

Electronic Thesis and Dissertation Repository

---

6-20-2014 12:00 AM

## Observational and Theoretical Investigation of Cylindrical Line Source Blast Theory Using Meteors

Elizabeth A. Silber  
*The University of Western Ontario*

Supervisor  
Dr. Peter Brown  
*The University of Western Ontario*

Graduate Program in Physics  
A thesis submitted in partial fulfillment of the requirements for the degree in Doctor of Philosophy  
© Elizabeth A. Silber 2014

Follow this and additional works at: <https://ir.lib.uwo.ca/etd>



Part of the [Physical Processes Commons](#)

---

### Recommended Citation

Silber, Elizabeth A., "Observational and Theoretical Investigation of Cylindrical Line Source Blast Theory Using Meteors" (2014). *Electronic Thesis and Dissertation Repository*. 2112.  
<https://ir.lib.uwo.ca/etd/2112>

This Dissertation/Thesis is brought to you for free and open access by Scholarship@Western. It has been accepted for inclusion in Electronic Thesis and Dissertation Repository by an authorized administrator of Scholarship@Western. For more information, please contact [wlsadmin@uwo.ca](mailto:wlsadmin@uwo.ca).

OBSERVATIONAL AND THEORETICAL INVESTIGATION OF  
CYLINDRICAL LINE SOURCE BLAST THEORY USING METEORS

(Thesis format: Integrated Article)

by

Elizabeth Allaryce Silber

Department of Physics and Astronomy  
Graduate Program in Physics and Planetary Science

A thesis submitted in partial fulfillment  
of the requirements for the degree of  
Doctor of Philosophy

The School of Graduate and Postdoctoral Studies  
The University of Western Ontario  
London, Ontario, Canada

© Elizabeth Allaryce Silber 2014



## Abstract

During their passage through the atmosphere meteoroids produce a hypersonic shock which may be recorded at the ground in the form of infrasound. The first objective of this project was to use global infrasound measurements to estimate the influx of large (meter/decameter) objects to Earth and investigate which parameters of their ablation and disruption can be determined using infrasound records. A second objective was to evaluate and extend existing cylindrical line source blast theory for meteoroids by combining new observations with earlier analytical models, and validate these against centimetre-sized optical meteor observations.

The annual terrestrial influx of large meteoroids (kinetic energies above a threshold  $E$ ) was found to be  $N=4.5E^{-0.6}$  where  $E$  is expressed in kilotons of TNT equivalent. This indicates that estimates of the influx derived from telescopic surveys of small asteroids near Earth are too low. Infrasound records from an event over Indonesia in 2009 were used to develop a technique to estimate the altitude of meteoroid terminal bursts and their energies. The burst altitude in this case was determined to be near 20 kilometers and the energy between 8 – 67 kilotons of TNT equivalent.

Using a network of optical cameras and an Infrasound Array in southern Ontario, Canada, 71 centimetre-sized meteoroids were optically detected and associated with infrasonic signals recorded at the ground. The shock source height and its uncertainty along the meteor trail from raytracing was determined including wind effects due to gravity waves perturbations, which were found to be significant for such short range (<300 km) infrasound propagation. Approximately 75% of signals were attributed to cylindrical line source geometry, while ray deviation angles greater than  $117^\circ$  were associated with spherical shocks. The ReVelle (1974) meteor infrasound model was found to be accurate when using infrasound period measurements, but systematically under-predicted blast radii when amplitude is used. The latter can be better modelled assuming the wave distortion distance is <6%, as opposed to the 10% adopted by ReVelle. Infrasonic masses found from ReVelle's theory deviate from photometric estimates largely due to meteoroid fragmentation.

## **Keywords**

meteor, meteoroid, bolide, infrasound, acoustics, shock waves

## Co-Authorship Statement

The core of this dissertation is based on 4 manuscripts:

1. **Chapter 3:** Silber, E.A., ReVelle, D.O., Brown, P.G. and W. N. Edwards (2009) An estimate of the terrestrial influx of large meteoroids from infrasonic measurements. *Journal of Geophysical Research - Planets* (1991–2012), 114(E8)
2. **Chapter 4:** Silber, E. A., Le Pichon, A. and P. G. Brown (2011), Infrasonic detection of a near-Earth object impact over Indonesia on 8 October 2009, *Geophysical Research Letters*, 38, L12201, doi:10.1029/2011GL047633
3. **Chapter 5:** Silber, E. A., and P. G. Brown (2014) Optical Observations of Meteors Generating Infrasonid – I: Acoustic Signal Identification and Phenomenology, *Journal of Atmospheric and Solar-Terrestrial Physics*, submission #ATP-S-13-00460-1, manuscript # ATP3766, in revision
4. **Chapter 6:** Silber, E. A., Brown, P. G. and Z. Krzeminski (2014) Optical Observations of Meteors Generating Infrasonid – II: Weak Shock Model Theory and Validation, submitted to *Journal of Geophysical Research – Planets*, manuscript # 2014JE004680

In each of the papers listed above, I performed research that included infrasonid data acquisition, data reductions, analysis, and algorithm development, writing and implementation. Over the course of my thesis project, I also wrote a number of *MATLAB*<sup>®</sup> programs. I was the lead author on all these manuscripts and also created all Tables and Figures (unless stated otherwise below). Peter Brown provided ongoing supervisory guidance and feedback, and assisted with manuscript revisions.

Chapter 3: I devised a way to digitize all scanned bolide records, wrote all the *MATLAB*<sup>®</sup> programs, performed all data reductions and measurements, derived the new flux rate and wrote the manuscript. The late Doug ReVelle provided the raw dataset in the form of

scanned bolide signal pressure records and also supplied Figure 3.4. Each author provided feedback on the manuscript prior to submission.

Chapter 4: I performed all infrasound data acquisition, reductions and analysis, developed new methodology to derive and estimate the likely altitude of the blast, wrote all the *MATLAB*<sup>®</sup> programs and finally wrote the manuscript. Alexis Le Pichon provided independent measurements in PMCC, calculated the bolide geolocation (Figure 4.2) and provided feedback on the manuscript.

The infrasound array and the camera network were already in place when I started working on my thesis project. Throughout my graduate studies, I was involved in regular infrasound equipment maintenance, as well as sensor and hose replacements. The camera system hardware, day-to-day operation of the system and automated detection software were prepared and handled by various members of the Meteor Research Group at Western.

In both Chapters 5 and 6, I performed data reductions, analysis and correlations, created *MATLAB*<sup>®</sup> programs, developed a new algorithm to derive the shock source heights, performed modelling, and wrote the manuscript.

Chapter 6: Zbyszek Krzeminski wrote all *IDL* programs which were used for video data reductions and photometry. Krzeminski also provided guidance in performing video data reductions, designed and helped carry out the laboratory experiments, and helped to model the light curve fits with the Fragmentation Model.

## **Dedication**

To my Family,  
without whose love I would not be who I am today

## Acknowledgments

First and foremost, I extend my sincere gratitude and big thanks my thesis supervisor, Dr. Peter Brown, for his guidance, encouragement and support throughout my graduate studies. Dr. Brown has been an inspirational supervisor and mentor who contributed immensely to the success of this project. I also thank Dr. Brown for giving me the opportunity to work on side research projects, which immensely contributed to my professional development.

I would like to honour and thank the late Dr. Doug ReVelle for his advice and for many useful discussions on meteor infrasound. Without his pioneering work on meteor generated infrasound this thesis would not have been possible. I also extend my thanks to Lou Sutherland for generously providing his program to calculate atmospheric absorption coefficients.

Dr. Wayne Hocking deserves credit and recognition for his willingness to help and discuss sometimes challenging issues regarding the numerical modeling of gravity waves. I thank Drs. Els Peeters and Carol Jones for serving on my advisory committee.

Furthermore, I would like to extend my sincere thanks and appreciation to Zbyszek Krzeminski for all his invaluable help, patience and many hours spent working with me on astrometry, photometry and the fragmentation model. Zbyszek also played an important role in designing and carrying out experimental work. Jason Gill must be credited for saving me many hours of computing by setting up and running my code on a parallel processing machine.

My project, which in part utilized the all-sky camera network data, would not have been possible without tremendous help of those who maintained the hardware, developed the software and oversaw day-to-day operations. For that, my sincere thanks goes to Rob Weryk, Zbyszek Krzeminski, Jason Gill and all others who have contributed in some way.

I thank all Meteor Physics Group members, past and present, whether they helped with my work in some way or not. I enjoyed working shoulder to shoulder with everyone.

I am grateful to Dr. Duncan Steel for taking his time to proofread part of my thesis and provide insightful and detailed feedback.

The administrative staff in the department of Physics and Astronomy have been absolutely amazing since my first day at Western. I sincerely thank Clara and Jodi, as well as Jackie and Anne who are now retired, for all their support over the years. I also thank Nelia, Loveleen and Donna for their kindness.

During my over a decade long stay at Western, I have had the pleasure to meet and interact with many great people, all of whom I would like to acknowledge. At this point, it is impossible to list everyone without inadvertently omitting someone, so I will just say thank you to all.

Last, but not the least, I would like to thank my family for their unlimited love, encouragement and support.

# Table of Contents

Abstract .....	ii
Co-Authorship Statement.....	iv
Dedication .....	vi
Acknowledgments.....	vii
List of Figures .....	xiii
List of Tables .....	xvii
List of Appendices .....	xviii
List of Symbols .....	xix
Chapter 1 .....	1
1. Introduction.....	1
1.1 Meteor Physics: History and Basic Background .....	1
1.1.1 A Brief History of Meteors .....	1
1.1.2 The Relevance of Meteor Studies .....	4
1.1.3 The Basics of Meteor Physics .....	5
1.2 Motivation.....	12
1.3 A Brief Primer on Infrasound .....	14
1.3.1 Physics of Sound and Infrasound.....	14
1.3.2 Infrasound Propagation and Attenuation .....	18
1.3.3 Historical Aspects of Infrasound .....	25
1.3.4 Infrasound Detection and Measurement Principles .....	28
1.3.5 Meteor Infrasound.....	29
1.4 Thesis Aim .....	31
References.....	34
Chapter 2.....	45
2. Shock Waves.....	45



2.1 A Brief Introduction to Shock Waves.....	45
2.2 Cylindrical Line Source Model of Meteoroid shocks: ReVelle’s Model .....	51
References.....	69
Chapter 3.....	72
3. An Estimate of the Terrestrial Influx of Bolides From Infrasonic Measurements .....	72
3.1 Introduction.....	72
3.2 Reduction Methods and Analysis .....	74
3.3 Estimating Source Energies for Fireballs .....	80
3.4 Results and Discussion .....	81
3.5 Conclusions.....	88
Acknowledgements.....	90
References.....	91
Chapter 4.....	93
4. Infrasonic Detection of a Near-Earth Object Impact over Indonesia .....	93
4.1 Introduction.....	93
4.2 Data Collection and Analysis.....	95
4.3 Estimating the Blast Radius and Source Energy.....	97
4.4 Results and Discussion .....	102
4.5 Conclusions.....	104
Acknowledgements.....	105
Chapter 5.....	110
5. Optical Observations of Meteors Generating Infrasound – I: Acoustic Signal Identification and Phenomenology .....	110
5.1 Introduction.....	110
5.2 Instrumentation .....	114
5.2.1 Infrasound Array .....	114
5.2.2 All Sky Camera System.....	117
5.3 Methodology.....	121
5.3.1 Astrometry .....	121
5.3.2 Meteor Infrasound Signal Identification .....	124

5.3.3 Signal Measurements .....	130
5.3.4 Raytracing and Atmospheric Variability Modelling.....	132
5.3.5 Analysis of Raytracing Results .....	137
5.4 Results and Discussion .....	143
5.4.1 Infrasound Signal Taxonomy and Phenomenology .....	146
5.4.2 Shock Source Heights and Entry Velocity Distributions.....	152
5.4.3 Definition of $S_h$ Parameter and Estimation of Shock Type .....	163
5.4.4 Multi Arrival Event Population.....	171
5.4.5 Correlation of Meteor Infrasound Signal Class and Ray Launch Deviation Angles .....	172
5.5 Conclusions.....	173
Acknowledgements.....	176
References.....	177
Chapter 6.....	185
6. Optical Observations of Meteors Generating Infrasound – II: Weak Shock Theory and Validation.....	185
6.1 Introduction.....	185
6.1.1 Meteor Generated Infrasound .....	185
6.1.2 A Brief Review of ReVelle (1974) Meteor Weak Shock Theory.....	188
6.2 Methodology and Results .....	195
6.2.1 Weak Shock: Model Updates and Sensitivities .....	195
6.2.2 Weak Shock: Bottom-up Modelling .....	198
6.2.3 Weak Shock: Top-Down Modelling.....	201
6.2.4 Infrasonic Mass .....	210
6.3 Discussion.....	212
6.4 Conclusions.....	222
Acknowledgements.....	224
References.....	225

Chapter 7.....	231
7. Conclusions and Future Work .....	231
7.1 Conclusions.....	231
7.1.1 Conclusions from Chapter 3 .....	231
7.1.2 Conclusions from Chapter 4 .....	231
7.1.3 Conclusions from Chapter 5 .....	232
7.1.4 Conclusions from Chapter 6 .....	234
7.2 Future Work .....	235
References.....	237
Appendix 1.....	238
Appendix 2.....	382
Appendix 3.....	473
Appendix 4.....	483
Appendix 5.....	519
Appendix 6.....	532
Copyright Permissions .....	564
Curriculum Vitae .....	578

## List of Figures

Figure 1.1: Basic terminology for meteors (from Ceplecha et al., 1998). .....	6
Figure 1.2: Lindsay’s wheel of acoustics.....	14
Figure 1.3: Thermal structure of the atmosphere.....	16
Figure 1.4: Model atmospheric profiles of effective speed of sound. ....	19
Figure 1.5: Representative infrasonic ray paths during summer .....	20
Figure 1.6: Theoretical acoustic wave absorption in dB/km as a function of height.....	21
Figure 1.7: Sources of infrasound. ....	23
Figure 1.8: Infrasound wave period (ordinate) and wavelength (abscissa). ....	23
Figure 1.9: An infrasound pressure wave recording from the Tunguska explosion. ....	26
Figure 1.10: The IMS infrasound network of the CTBTO as at the early 2014. ....	28
Figure 2.1: The shock wave phenomena.....	46
Figure 2.2: N wave pressure vs time.....	47
Figure 2.3: Evolution of slightly non-linear wave. ....	48
Figure 2.4: Shock wave pressure vs time.....	49
Figure 2.5: Typical explosion wave pressure-time signature at long range. ....	49
Figure 2.6: The flow field of a circular cylinder with a flat face.....	50
Figure 2.7: A simplified diagram depicting the meteoroid moving downward.....	53
Figure 2.8: The coordinate system as originally defined by ReVelle.....	54
Figure 2.9: A pictorial representation of the cylindrical line source. ....	55
Figure 2.10: A head on view of the meteoroid.. ....	61
Figure 2.11: Development of a shock front from nonlinear effects.....	62
Figure 3.1: Channel 1, 2 Nov 1960.....	76
Figure 3.2: A fully digitized waveform of the 2 November, 1960 event.....	77
Figure 3.3: The frequency response function adopted from Flores and Vega.....	79
Figure 3.4: AFTAC: Infrasonic probability of detection as a function of yield .....	83
Figure 3.5: Cumulative influx curve .....	85
Figure 4.1: An example of the bolide infrasound signal observed at I13CL.....	96
Figure 4.2: Map showing the intersection of infrasound bearings.....	97
Figure 4.3: The blast radius modeling results. ....	101
Figure 4.4: Numerical entry modeling results. ....	102

Figure 5.1: (a) ELFO vault diagram; (b) plane view of the array. ....	115
Figure 5.2: A power spectral density (PSD) plot. ....	117
Figure 5.3: The locations of the All-Sky Cameras. ....	118
Figure 5.4: An example of a stacked video image showing a meteor. ....	118
Figure 5.5: An automated trajectory solution for a meteor event. ....	120
Figure 5.6: A flowchart showing the process of generating astrometric solution. ....	124
Figure 5.7: An example of a meteor infrasound signal displayed in InfraTool. ....	126
Figure 5.8: Results from array processing using the PMCC algorithm. ....	127
Figure 5.9: Meteor trail raytrace modeling procedure. ....	134
Figure 5.10: An example of a gravity wave perturbed wind speed as a function of altitude. ....	136
Figure 5.11: An example composite plot showing the travel time (upper left), back azimuth (upper right) and arrival elevation angle (lower left) for an event. ....	139
Figure 5.12: The flow chart showing the logic used for calculating the meteor shock source heights and associated parameters. ....	140
Figure 5.13: A residuals composite plot. ....	142
Figure 5.14: Left: Distribution of begin and end heights for ASGARD meteors from 2006-mid 2013. Right: Detection rate of infrasonic meteor signals from simultaneously observed optical events for the entire network. ....	148
Figure 5.16: The relationship between the peak-to-peak amplitude of the meteor infrasound signal as a function of signal class. ....	151
Figure 5.17: The observed fall-off in the dominant signal frequency of bright regional fireballs as a function of range. ....	152
Figure 5.18: A map of Southwestern Ontario and surrounding lakes showing the array (middle) and the spatial orientation of ground projected meteor trajectories for all events (orange lines). ....	153
Figure 5.19: Pie charts showing the distribution of raytracing solution types. ....	157
Figure 5.20: Histograms showing the distribution of begin and end optical heights from camera data. ....	158
Figure 5.21: Meteor entry velocity populations. ....	159

Figure 5.22: Left: The dominant signal frequency as a function of meteoroid entry velocity for meteor infrasound events in this study. Right: Shock source altitude vs. dominant signal frequency.....	161
Figure 5.23: The scaled distributions of meteoroid entry angles (from the vertical) for all optically detected events (ASGARD data) and simultaneously detected events in this study.....	162
Figure 5.24: The distribution of $S_h$ parameter shown for all arrivals. ....	163
Figure 5.25: Left: Altitude vs. $S_h$ parameter Right: The mean value of $S_h$ parameter as a function of height.....	164
Figure 5.26: Examples of relative photometric light curves. Left: The shock source height was determined to have occurred at 104 km.....	166
Figure 5.27: The $S_h$ parameter vs $M_p$ for 50 arrivals. ....	168
Figure 5.28: Pie charts showing the distribution of spherical (S) shocks for events with ray deviations $\beta \leq 117^\circ$ , $\beta > 117^\circ$ , and cylindrical (C) shocks. ....	170
Figure 5.29: Ray launch deviation angles as a function of the signal Class type. ....	172
Figure 6.1: The change in signal (a) amplitude, (b) period and (c) overpressure ratio ( $dp/p_0$ ) as a function of height.....	191
Figure 6.2: An example of the predicted ground-level amplitude and period of a meteor shock using the ReVelle (1974) theoretical model. ....	197
Figure 6.3: The behaviour of $R_0$ in (a) linear and (b) weak shock regimes in the bottom-up modelling approach.....	200
Figure 6.4: The FM model fit to the light curve for a multi-station meteor recorded at 07:05:56 UT on 19 April 2006.....	206
Figure 6.5: The blast radius estimated from bottom-up modelling as compared to blast radii derived from application of the FM model.....	209
Figure 6.6: (a) Signal period and (b) amplitude obtained by running the top-down weak shock model with input $R_0$ as derived via FM model. ....	210
Figure 6.7: The comparison of the infrasonic and photometrically derived masses.. ....	211
Figure 6.8: Energy per unit path length comparison.....	212
Figure 6.9: The best fit $R_0$ from bottom-up modelling predictions .....	216
Figure 6.10: The comparison of the infrasonic and photometrically derived masses. ...	218

Figure 6.11: Blast radius produced by a single spherically shaped body.. ..... 218  
Figure 6.12: Blast radius from best fit bottom-up modelling versus observed signal .... 221

## List of Tables

Table 1. 1: Natural sources of infrasonic waves. ....	24
Table 2.1: Examples of expressions for $R_0$ as defined by various authors .....	56
Table 2.2: A summary of initial conditions, $Y_C$ and $Y_D$ . ....	67
Table 3.1: Summary of all ten bolide events from the historical data set.....	78
Table 3.2: Summary of all ten bolide events from the historical data set, sorted by date.	86
Table 4.1: Station details and signal measurements summary. ....	104
Table 5.1: A sample output from the automated optical meteor astrometric solutions..	119
Table 5.2: Infrasound signal measurements for meteors optically observed and which produced a single infrasonic arrival.....	131
Table 5.3: Infrasound signal measurements for optical meteors which produced more than one distinct infrasound arrival. ....	132
Table 5.4: All astrometric measurements.. ....	145
Table 5.5: Proposed meteor infrasound signal classification taxonomy.....	147
Table 5.6: Summary of infrasound signal characteristics by taxonomic class. ....	149
Table 5.7: The raytracing results and signal classification for single arrival events.. ....	155
Table 5.8: The raytracing results and signal classification for multi arrival events.. ....	156
Table 5.9: All events, categorized based on their solution quality. ....	157
Table 5.10: Optical meteor events producing single infrasonic arrivals divided into the slow (< 40 km/s) and the fast (> 40 km/s) meteor entry velocity population.....	160
Table 5.11: Average statistics for single arrival events and multi arrival events. ....	160
Table 6.1: A summary of orbital parameters for all events in our data set.....	199
Table 6.2: The range of PE parameter and the associated meteoroid group presumed type, type of the material and representative density.....	205
Table 6.3: A summary of the photometric mass measurements using observed light curves from meteor video records.....	208
Table 6.4: A summary of $R_0$ as derived from the FM model.....	217



## List of Appendices

Appendix 1.....	238
Appendix 2.....	382
Appendix 3.....	473
Appendix 4.....	483
Appendix 5.....	519
Appendix 6.....	532

## List of Symbols

$A$	Amplitude
$a$	Weighting constant; 0.8
$a$	Semi-major axis
$A_0$	-0.42
$A_l$	Predicted signal amplitude in the linear regime
$A_s$	Shape factor for a specific particle shape
$A_{ws}$	Predicted signal amplitude in the weak shock regime
$b$	Weighting constant; 0.02
$B_0$	1.49
$c$	Speed of sound
$c$	Weighting constant; 0.06
$C_0$	-1.29
$c_a$	Local ambient thermodynamic speed of sound
$C_D$	Coefficient of wave drag
$c_{eff}$	Effective speed of sound
$c_{obs}$	Sound speed as measured at observer
$C_p$	Specific heat per unit mass at constant pressure
$c_s$	Speed of sound
$C_v$	Specific heat per unit mass at constant volume
$\bar{c}_z$	Average speed of sound between source and observer
$d$	Weighting constant; 0.06
$d'$	Distortion distance
$d_a$	Remaining propagation distance of disturbance
$D_l$	Damping coefficient for a linear wave
$D_l$	Linear wave attenuation
$d_m$	Meteoroid diameter
$d_s$	Distance to the shocked state
$D_{ws}$	Damping coefficient for a weak shock wave

$e$	Eccentricity
$E$	Total energy of the event
$E_0$	Energy per unit trail length deposited by the meteoroid
$E_k$	Kinetic energy of the meteoroid
$f$	Wave frequency
$f(R)$	Dominant signal frequency as a function of detection range
$f(x)$	As defined by equations (2.14-15)
$f_0$	Fundamental frequency
$g$	Acceleration due to gravity on Earth
$g$	Weighting constant; 0.06
$H$	Scale height of the atmosphere
$h_b$	Meteor starting height
$I$	Luminous power
$k$	Wave number
$k$	Boltzmann's constant
$K$	Intrinsic shape density coefficient
$K$	Thermal conductivity
$\vec{k}$	Wave number in vector form
$K_n$	Knudsen number
$L$	Total path length of the entire visible meteor trajectory
$L_{\text{Bh-Mp}}$	Path length along the trajectory from beginning to point of peak luminosity
$L_{\text{Bh-S}}$	Path length along the trajectory from beginning to shock point
$m$	Mass
$M$	Mach number of meteoroid
$M_a$	Mach number of shock front
$M_{\text{HAD}}$	Absolute magnitude in the HAD bandpass
$m_{\text{infra}}$	Infrasonic mass
$M_{mw}$	Mean molecular weight

$M_p$	Maximum luminosity coefficient
$M_{ph}$	Photometric magnitude
$M_v$	Visual meteor luminosity
$\hat{n}$	Ray normal
$N$	Cumulative number of meteoroids impacting Earth per annum
$N^*$	Correction term for amplitude
$N_a$	Avogadro's number
$N_c$	Nonlinear propagation correction term
$p$	Atmospheric pressure
$P$	Period at maximum amplitude of the waveform
$P$	Pressure of a disturbance
$p'$	Acoustic pressure
$p_0$	Ambient pressure of atmosphere
$p_s$	Pressure amplitude of the disturbance
$Q_{model}$	Modelled quantity
$Q_{obs}$	Observed and experimentally measured quantity
$r$	Radius of meteoroid
$R$	Specific gas constant
$R'$	Universal gas constant
$R_0$	Relaxation or blast radius
$res$	Residual
$R_m$	Range of the bolide
$s$	Path length
$S$	Surface area
$S_A$	Raytracing solution viability type
$S_B$	Raytracing solution viability type
$S_C$	Raytracing solution viability type
$S_D$	Raytracing solution viability type
$S_F$	Raytracing solution viability type

$S_h$	Shock source height parameter ( $l_{bh-S} / L$ )
$S_m$	A condensation or overdensity ratio
$T$	Atmospheric temperature
$t$	Time
Tiss	Tisserand parameter
$\vec{u}$	Wind vector
$v$	Shock or object velocity
$V$	Volume
$v'$	Acoustic velocity
$v_0$	Ambient value for velocity
$V_a$	Ambient speed of sound
$v_g$	Geocentric velocity
$v_h$	Heliocentric velocity
$V_k$	Source-receiver wind speed
$x$	Distance between the point along the trail and the observer ( $R/R_0$ )
$x_1$	Signal celerity (speed) coefficient
$x_2$	Range coefficient
$x_3$	Arrival angle of the ray coefficient
$x_4$	Ray height from the receiver coefficient
$x_5$	Ray density at the source (1 / number of rays) coefficient
$X_{rms}$	Smallest root mean square
$Y_C$	Plooster's adjustable parameter
$Y_D$	Efficiency of shock wave generation
$z$	Altitude
$Z^*$	Correction term for variations in atmospheric density
$z_{obs}$	Altitude as measured at observer
$Z_R$	Zenith angle of the radiant
$z_t$	Transition height

$z_z$	Source altitude
$\alpha$	Right ascension of geocentric radiant
$\bar{\alpha}$	Total amplitude absorption coefficient
$\alpha_D$	Diffusion coefficient
$\alpha_K$	Thermal conductivity coefficient
$\alpha_{mol}$	Molecular relaxation absorption coefficient
$\alpha_{rad}$	Radiation coefficient
$\alpha_\mu$	Viscosity coefficient
$\beta$	Ray takeoff angle
$\Delta p$	$p - p_0$
$\Delta p_t$	Overpressure at transition height
$\Delta p_z$	Overpressure at the source height OR initial amplitude
$\Delta s$	Total path length from source
$\Delta \phi$	Infrasound ray deviation from the plane of entry
$\Gamma$	Drag coefficient
$\gamma$	ratio of the specific heat of air at constant pressure to that at constant volume
$\delta$	As defined by equation (2.28)
$\delta$	Declination of geocentric radiant
$\varepsilon$	Nadir angle of the infrasonic ray from the local vertical
$\zeta$	Shock strength
$\eta$	Mach angle
$\theta$	Entry elevation angle from the horizontal
$\Lambda$	Heat transfer coefficient
$\lambda$	Wavelength
$\mu$	Ordinary (shear) viscosity coefficient
$\xi$	Heat of ablation
$\rho$	Atmospheric density

$\rho'$	Acoustic density
$\rho_0$	Ambient density of atmosphere
$\rho_a$	Density of air
$\rho_E$	Density of air at the trajectory end height
$\rho_m$	Density of meteoroid
$\rho_{obs}$	Atmospheric density as measured at observer
$\rho_z$	Atmospheric density at the source
$\Sigma$	Ablation coefficient
$\tau_0$	Fundamental period of shock wave
$\tau_l$	Luminous efficiency factor
$\tau_1$	Period in the linear regime
$\tau_{ws}$	Period in the weak shock regime
$\varphi$	Azimuth angle of the meteoroid heading
$\varphi'$	Azimuth angle of a given infrasonic ray outside the entry plane
$\psi$	Bulk (volume) viscosity coefficient
$\omega$	Argument of perihelion
$\omega$	Angular frequency
$\Omega$	Intrinsic angular frequency
$\omega_B$	Brunt-Väisälä frequency
$\omega_g$	Brunt-Väisälä frequency in an isothermal atmosphere

# Chapter 1

## 1. Introduction

*If we knew what it is we were doing,  
it would not be called research, would it?*

- Albert Einstein

### 1.1 Meteor Physics: History and Basic Background

#### 1.1.1 A Brief History of Meteors

Following its rapid development after the end of World War II, meteor physics, as a sub-discipline of astronomy, experienced a renaissance (McKinley, 1961) and evolved into a mature science (Beech, 1988; Doel, 1996; Brown, 1999).

While the evolution of meteor studies as a credible scientific discipline can be traced to the mid-19<sup>th</sup> century, following the spectacular 1833 Leonid meteor shower (Burke, 1991; Brown, 1999), meteors had always been part of human history, either directly or indirectly, through religious and mythological interpretation and symbolism. Ancient Sumerian cuneiform writings and other subsequent records traced through history, including the ancient Greeks (e.g. Herodotus), Romans (e.g. AD 77 Pliny the Elder), ancient Chinese and Japanese, and continuing to the present age, show the importance attributed to meteoric phenomena (Burke, 1991; McSween, 1999; Ahn, 2003; D’Orazio, 2007). Correspondingly, the etymology of the word meteor shows that it originates from ancient Hellenic, and can be directly translated as “*things in the air*”.

The number of the small particles entering the Earth’s atmosphere on an annual basis likely exceeds the billions (Sugar, 1964), with an estimated yearly mass influx from sub-millimetre particles of up to 60,000 tonnes (Love and Brownlee, 1993), and total global meteoroidal influx of up to 200,000 t (Dyrud et al., 2008). However, long time-averaged and all size integrated mass influx may be significantly greater (Hughes, 1997).



The size distribution of those particles, which may have a cometary or asteroid belt origin (Brownlee, 1985; Ceplecha et al., 1998; Murad and Williams, 2002), range from dust sized grains (Campbell-Brown and Koschny, 2004; Briani et al., 2007) to large extra-terrestrial bodies 100s of meters in diameter (Ceplecha et al., 1998) that infrequently, as inferred from geological records, have the potential of ending human civilization and causing biological mass extinctions (O'Keefe and Ahrens, 1982). The most recent bolide over Chelyabinsk, Russia, the largest airburst on the Earth since the great Siberian bolide in 1908 (Brown et al., 2013; Popova, et al., 2013), attests to the practical importance of meteor studies and the need to quantify the potential impact hazard threat.

The average size of particles impacting the Earth's atmosphere on a daily basis is in the range of  $10^{-4}$  m (Kalashnikova, 2000; Havnes and Sigernes, 2005) with a mass input peak near  $1.5 \cdot 10^{-5}$  grams (Love and Brownlee, 1993).

The diurnally dependent velocity of these particles, upon entering the Earth's atmosphere, ranges from 11.2 km/s to 72.5 km/s (Baggaley, 2002) with a mass-averaged velocity of about 20 km/s (Taylor, 1995). The value of the mass averaged velocity has been a source of controversy primarily due to the results obtained from high power large aperture radars (Close et al., 2000; Erickson et al., 2001; Dyrud et al., 2004), although Nesvorny et al. (2011) suggest that these new data reflect changes in the dominant particle source populations as a function of size.

A particle, while traveling in space, outside of the boundary of the Earth's atmosphere, is classified as a meteoroid. Upon entering the atmosphere, the meteoroid sputters, ablates and may fragment as a result of frictional heating caused by hypervelocity collisions with the ambient atmosphere. Such a process produces ionization and luminous phenomena, which result from collisional de-excitation of the ablated meteoroid atoms (e.g. Murad and Williams, 2002). Such an event is collectively defined as a meteor.

The ablated material in the immediate wake of the meteor forms the meteor trail of some initial radius. The initial radius (Jones, 1995) is a term that defines the radius of the ionized column of ablated meteor vapour formed immediately after the passage of the meteoroid. The initial radius has a strong dependence on meteor velocity, size and mass, but is also a function of the air density (Bronshten, 1983). In the initial stages of

expansion, the meteor trail can be considered a quasi-neutral plasma that contains approximately an equal number of ablated positive ion species as electrons.

When the meteoroid's size, velocity, density and composition are such that the meteoroid does not ablate completely in the atmosphere (Wetherill and ReVelle, 1981), the residual mass arriving at the surface of Earth is defined as a meteorite.

Very bright meteors, exceeding the brightness of Venus, are generally referred to as fireballs or bolides (Ceplecha et al., 1998), whereas larger, more deeply penetrating meteoroids may be associated with shock waves which ultimately decay into low frequency acoustic waves (infrasound). Additionally, meteors may produce audible phenomena on the ground in the form of either instantaneously arriving electrophonic sounds, believed to be associated with electromagnetic emissions at audio frequencies (e.g. Wylie, 1932; Keay, 1980; Bronshten, 1983; Keay and Ceplecha, 1994), as well as delayed sound in the form of a sonic boom, similar to that of aircraft breaking the sound barrier (Ceplecha et al., 1998).

Based on their parent sources and occurrence frequency, it is possible to classify meteors into sporadics and meteor showers (Jenniskens, 2006; 2008), with the latter exhibiting annual periodicity. Most meteor showers are produced when the Earth travels through a stream of particles or debris left behind by a comet orbiting the Sun, resulting in a large number (10s to 100s per hour) of meteors coming from a fixed point in the sky, also called a radiant, as seen by an observer at the ground. Named after the constellation coinciding with the radiant, meteor showers occur at the same time each year and can often be associated with specific parent objects. For example, the Leonid meteor shower that occurs during the month of November has its radiant in the constellation Leo and is associated with the comet 55P/Tempel-Tuttle (Murad and Williams, 2002; Jenniskens, 2006).

The size distribution of sporadic meteoroids is such that there are roughly ten times as many particles with a mass of  $10^{-4}$  g than there are particles with mass of  $10^{-3}$  g. Thus, meteoroids are distributed according to  $N = C/m^{\alpha}$ , where  $\alpha$  is a constant (McIntosh, 1966; Belkovic, 1968), and often taken to approach unity for simplification purposes (McKinley, 1961) and because this value is near observational results (Ceplecha et al.,

1998). This explains why meteoroids associated with bolides are relatively rare compared with common shooting stars.

Usually meteors are studied using radar and optical means which include visual, photographic, video, and spectral methods (McKinley, 1961; Ceplecha et al., 1998). Less commonly, infrasonic and seismic observations of the shock waves produced by the meteor phenomena (e.g. ReVelle, 1997; Edwards and Hilderbrand, 2004; Arrowsmith et al., 2010; Silber et al., 2011) have been employed to define meteor properties not accessible by classical observational methods. The nature of infrasonic measurements in general makes it a valuable tool for independently determining the explosive yield of sources in the atmosphere, including fireballs. This technique may also yield flux and mass estimates for the meteoroids associated with fireballs (ReVelle, 1997; Edwards et al., 2008; Silber et al., 2009; Ens et al., 2012; Brown et al., 2013). This particular observational technique is the core of this thesis and therefore will be discussed in detail later in the text.

### **1.1.2 The Relevance of Meteor Studies**

Our knowledge about the rest of the universe, from distant stars to humanity's own backyard in the solar system, is gained from a variety of scientific disciplines. However, the most direct way of gaining further insight into the nature and origin of interplanetary and extra-terrestrial matter, as well as that of the planet-forming cloud of gas and dust that existed before our solar system, may be obtained from the study of meteoroids and meteorites (McSween, 1999). Closer to home, meteoroids are a real and ever-present danger to space platforms (Beech et al., 1995), thus the protection of human lives and spacecraft during space exploration depends strongly on understanding the nature of meteoric phenomena.

Furthermore, meteor trails in the atmosphere give us an insight about mesospheric parameters such as diffusion, temperature and turbulence (Hocking et al., 1997; Hocking, 1999), as well as the input of metallic ions into the atmosphere (Plane, 2012). The rain of such metallic atoms from above can be significant; it is estimated that the input of iron from meteoric deposition is the dominant form of bio-available iron in some parts of the

oceans (particularly off the coast of Antarctica) and thus controls growth of phytoplankton (Plane, 2012).

It has been suggested that comet and asteroid impacts in the past were conducive to the emergence of early life on Earth, creating favourable conditions necessary for life to evolve and perhaps even delivering the needed ingredients (Jenniskens, 2001; Abe et al., 2001; Jenniskens, 2004). Shocks from meteoroids can also affect and modify planetary surfaces, such as the surface of Venus (Zahnle, 1991). Studies of the meteoroid-atmosphere interaction provide insight into meteoroid energy deposition, shock production mechanisms, flux estimates and even assist in identifying threats from extraterrestrial impacts, allowing appropriate hazard mitigation.

### **1.1.3 The Basics of Meteor Physics**

The dynamics of meteoroid motion in the atmosphere and the resulting ionospheric chemical and plasma kinetics are fairly well understood (Dressler, 2001). Comprehensive treatments of meteor physics are given by McKinley (1961) and Bronshten (1983), and reviewed by Ceplecha et al. (1998).

For most meteoroids, the main meteoroid-atmosphere interaction occurs at ionospheric heights ( $>85$  km). However, larger meteoroids, capable of penetrating deeper into the atmosphere may cease ablation entirely while falling to the Earth in a dark flight ( $velocity_{meteor} < 3$  km/s) (Figure 1.1). Rarely does it occur that objects of sufficiently large size impact Earth; these may vary from city destroyers to ones capable of obliterating the human civilization; however, that category of objects is not part of this review.

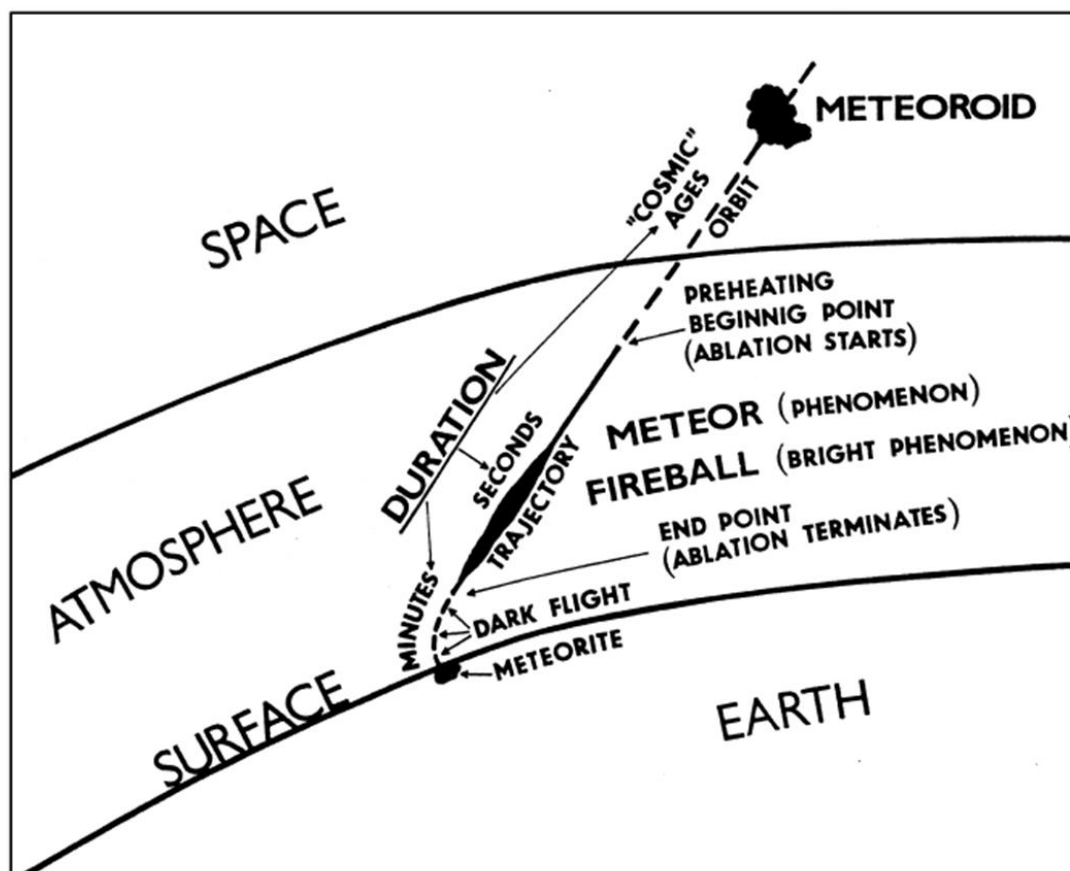


Figure 1.1: Basic terminology for meteors (from Ceplecha et al., 1998).

As a meteoroid enters the rarified atmosphere, it begins to heat up due to high energy collisions with atmospheric molecules. The heating of the meteoroid generally begins in the ionospheric F-region (~150 km) and is a function of the overall size and velocity of the impacting body. There are some exceptions to this, such as meteoroids associated with the very high speed Leonid meteor shower, which begin heating up and subsequently produce luminosity at altitudes as high as 200 km (Popova et al., 2001). When the mean free path of the atmosphere at a particular height is significantly larger than the diameter of the meteoroid, the particle is said to be moving in the free molecular flow regime (Campbell-Brown and Koschny, 2004). In this flow regime, the Knudsen number ( $K_n$ ) (the ratio of the molecular mean free path to the particle diameter) is larger than 10 (Popova, 2005). If the meteoroid diameter is larger than the mean free path of the

ambient atmosphere, and the Knudsen number is smaller than 0.01 (Ceplecha et al., 2000), then the flow regime is termed continuum (Popova et al., 2001; Campbell-Brown and Koschny, 2004). For intermediate Knudsen numbers, there is a transitional flow regime. Meteoroids capable of producing fireballs move in the continuum flow regime below 90 km (Popova, 2005).

In some cases, before the onset of ablation (i.e. very high altitude and high velocity meteoroids), the dominant mechanism of the mass loss is sputtering (Hill et al., 2005; Rogers et al., 2005). Sputtering is caused by the loss of individual atoms that get dislodged from the solid meteoroid lattice during high speed collisions (Öpik, 1958; Rogers et al., 2005). While sputtering is a relevant mass-loss mechanism for micrometeoroids ( $\sim 10^{-6}$  m,  $< 10^{-12}$  kg), and is a direct function of the physical characteristics of the target material, it is negligible in the case of slower meteoroids exceeding  $10^{-10}$  kg (Rogers et al., 2005). For a single non-fragmenting body meteoroid in a continuum flow, ablation represents the dominant mass-loss process. The presence of the metallic layer in the lower ionosphere is attributed to the metal deposition from meteoroids that ablate in this region of the atmosphere (ReVelle, 2005; Colestock et al., 2006; Feng et al., 2013). In continuum flow, a hydrodynamic layer forms in the front of the meteoroid and attenuates the rate of ablation (Öpik, 1958) by shielding the meteoroid surface from direct impacts with air molecules. The meteoroid type and composition play a significant role in ablation, as more volatile compounds ablate first at higher altitudes, while Ca, Al and Ti ablate last at lower heights (Vondrak et al., 2008), a process defined as differential ablation. The term ablation here refers to the evaporation of the material from the meteoroid surface, which occurs after some critical temperature, generally above 1800 K, has been reached (Marsh et al., 2013). It may also include the removal of material in the form of melted droplets. Meteoroid ablation reveals the physical and chemical properties of the ablating meteoroid through observation of its mass deposition, energy release and resulting emission spectrum (Borovička, 1993; Trigo-Rodriguez et al., 2003).

The kinetic energy of the incident particle colliding with the atmosphere is several orders of magnitude larger than the energy required to completely vaporize the meteoroid (Zinn

et al., 2004). Early studies suggested that the kinetic energy of the meteoroid is partitioned such that only 0.1% goes toward ionization, 1% toward light and the rest toward heating the surrounding atmosphere (Romig, 1965). More recently, however, the interpretation of other observations indicates that the percentage of energy distributed toward the production of light may be slightly larger (Ceplecha, 1996; Weryk and Brown, 2013).

Here, the review of the analytical treatment and fundamental equations of meteor ablation illustrating the dynamics of the meteoroid-atmosphere interactions is presented. However, it should be kept in mind that the primary focus in this work is centimetre-sized and larger meteoroids. These objects are large enough to always be in the continuum flow regime and produce a cylindrical shock wave which rapidly expands radially as a line source or in the case of gross fragmentation a spherical point source explosion (Ceplecha et al., 1998). Here, the discussion is limited to single body ablation and discrete, gross fragmentation (Ceplecha et al., 1993). A simplified treatment of the equations describing the ablation of a single particle impacting the atmosphere can be found in Zinn et al. (2004). It should be noted that while the dustball model (where micron sized grains are glued together by a volatile material to form a meteoroid) of meteor ablation proposed and developed by Hawkes and Jones (1975) explains certain anomalous behaviour observed in the ablation of faint meteoroids, it is not part of the present discussion in this review, as it does not pertain directly to the bolide and fireball dynamics examined in this work.

Consider a meteoroid with mass ( $m$ ), velocity ( $v$ ), of a spherical shape with projected cross-sectional surface area ( $S$ ) and having a drag coefficient ( $\Gamma$ ) (defined as the fraction of momentum transferred to the meteoroid from the oncoming air molecules). From the conceptual perspective, the single spherical body with the projected surface area ( $S$ ) enters the atmosphere (for the purpose of calculations assumed to be hydrostatic and isothermal) with hypersonic velocity and sweeps through a volume of air in a time increment ( $dt$ ), transferring kinetic energy from the meteoroid to the atmosphere. Hypersonic velocity refers to the aerodynamic flow where the Mach number, or the ratio

between the speed of an object (meteoroid) and the local atmospheric speed of sound, is greater than 5 (Anderson, 2006).

For a spherical meteoroid with radius  $r$ , the parameter  $S = \pi r^2$  can be related to the meteoroid mass  $m = 4/3 \pi \rho_m r^3$ , where  $\rho_m$  is the density of the meteoroid. Equating the radii in the aforementioned equations, one can solve for  $S$ . Generalizing the solution for any shape, it can be shown that:

$$S = A_s \left( \frac{m}{\rho_m} \right)^{2/3} \quad (1.1)$$

where  $A_s$  is the dimensionless shape factor for a specific particle shape. For the sphere,  $A_s$  is 1.209, and for a cube it can range from 1 to 1.7 depending on the orientation (McKinley, 1961). Because of rotation, irregularly shaped bodies will have their shape factor approaching the value for the spherical shape, a commonly used assumption.

The volume of the cylindrical parcel of swept air is then  $Svdt$ . The mass of the parcel can be considered in terms of the atmospheric density ( $\rho_a$ ) as  $dm_a = \rho_a Svdt$ . Substituting for  $S$  from equation (1.1), it is possible to write the expression for the rate of changing air mass ( $m_a$ ) encountered by the meteoroid (McKinley, 1961) as:

$$dm_a = \rho_a \left( \frac{m}{\rho_m} \right)^{2/3} A_s v dt \quad (1.2)$$

Now this parcel of air with a height specific mass density will transfer momentum as a result of impacts with the meteoroid, resulting in a rate of change of momentum of:

$$\frac{d(mv)}{dt} = v \frac{dm}{dt} + m \frac{dv}{dt} \quad (1.3)$$

In this volume, the air particles will gain momentum per unit time:

$$\Gamma \frac{dm_a}{dt} v = \Gamma A_s \left( \frac{m}{\rho_m} \right)^{2/3} \rho_a v^2 \quad (1.4)$$



The term  $v dm/dt$  in equation (1.3) is negligible for small meteoroids ( $m \gg dm$ ) and is therefore ignored. Equating the loss of momentum per second of the meteoroid ( $mdv/dt$ ) with the momentum gained by the air particles leads to the drag equation:

$$\frac{dv}{dt} = -\frac{\Gamma A_s \rho_a v^2}{m^{1/3} \rho_m^{2/3}} \quad (1.5)$$

where the presence of the negative sign indicates deceleration. The rate of mass loss, which is proportional to the kinetic energy, can be written in terms of the differential mass equation (McKinley, 1961), also known as the mass-loss equation (Ceplecha et al., 1998):

$$\frac{dm}{dt} = -\frac{\Lambda A_s \rho_a v^3 m^{2/3}}{2\xi \rho_m^{2/3}} \quad (1.6)$$

Above,  $\xi$  is the heat of ablation of the meteoroid material (or energy required to ablate a unit mass of the meteoroid, with dimensions:  $L^2, T^{-2}$ ) and  $\Lambda$  is the heat transfer coefficient, which is a measure of efficiency of the collision process in converting kinetic energy into heat (McKinley, 1961).

The ablated meteor vapour will decelerate from the initial meteoroid velocity as a result of collisions with the ambient atmosphere, and thermalization (Baggaley and Webb, 1977) will occur after approximately 10 collisions (Jones, 1995). In general, the stopping distance for the ablated meteoric ions and meteor vapour rapidly decreases with increasing air density, and while it depends on the initial meteoroid velocity, it is generally in the range of several hundred meters (Zinn et al., 2004).

The distribution of ions and electrons within the initially formed cylindrical meteor train is assumed to be approximately Gaussian. Following the formation of the initial trail, the subsequent post-adiabatic expansion and diffusion into the ambient atmosphere takes place under ambipolar diffusion (Jones and Jones, 1990). While an uncertainty about the size of the initial radius of the meteor train still persists (Baggaley and Fisher, 1980; Campbell-Brown and Jones, 2003; Jones and Campbell-Brown, 2005), it has been shown that it will strongly depend on the meteoroid velocity and that it is significantly larger

than the early estimate of 14 mean free paths of the ambient atmospheric region as proposed by Manning (1958).

The collisional and radiative transfer of translational energy from ablated ions will also heat up a volume of the ambient atmosphere surrounding the meteor train. Additionally, in the initial stages of the meteor trail formation, a strong shock wave will form, driven radially outward from the cylindrical meteor train by the rapidly expanding and extremely hot (~4000 K (Jenniskens, 2004)) ablated meteoric material (the initial translational energies in the ablated ions range in the hundreds of electron volts (Jones, 1975; Baggaley, 1980)).

It is possible to relate the visual meteor luminosity, expressed as the absolute visual magnitude  $M_v$ , to the luminous power  $I$  (in watts), which is a portion of the total radiation in the visual bandpass (400 nm – 700 nm) having a peak sensitivity at about 560 nm. The absolute visual magnitude of a meteor is defined as the magnitude it would have if the meteor was placed in the zenith at a height of 100 km (McKinley, 1961). The expression for  $M_v$  has been given by Opik (1958) as:

$$M_v = 6.8 - 2.5 \log_{10} I \quad (1.7)$$

This relation was derived from early theoretical considerations and suggests that a zero magnitude meteor radiates visible light at a rate of 525W (Opik, 1958). This luminous power depends on the spectral energy distribution of the meteor and recent observational measurements and related studies (e.g. Ceplecha and ReVelle, 2005; Weryk and Brown, 2013) give somewhat different values than equation (1.7). For meteoroids which have a sufficient size and velocity to produce luminous phenomena, it is assumed that the light production in a specific bandpass (e.g. panchromatic passband, appropriate to photographic film on which most early meteor measurements were made) is proportional to the rate of change of the particle's kinetic energy, and correspondingly proportional to the meteoroid mass loss rate.

The expression for luminous power is given as:

$$I = -\tau_l \frac{dE_k}{dt} = -\tau_l \left( \frac{v^2}{2} \frac{dm}{dt} + mv \frac{dv}{dt} \right) \quad (1.8)$$

where the term  $I$  can be more precisely defined as the power radiated in the specific instrument frequency passband. The symbol  $\tau_I$  represents the velocity dependent dimensionless luminous efficiency factor (Opik, 1958; Weryk and Brown, 2013) and  $E_k$  is the kinetic energy of the meteoroid. The term  $mv(dv/dt)$  is generally ignored for meteoroids with velocities exceeding 16 km/s as deceleration is negligible at higher speeds (Ceplecha et al., 1998). Considering that meteor light production is related to the mass loss, the initial mass of the meteoroid can be estimated from the observed luminosity by integrating equation (1.8) over the length of the entire light curve. Mass estimated in this way is termed photometric mass.

The lowermost size limit of the meteoroids capable of producing a sufficiently strong shock wave and subsequently an infrasonic signature at the ground is not well constrained, but is approximately in the cm-size range.

## 1.2 Motivation

Brilliant streaks in the sky, known as ‘shooting stars’, are produced by extraterrestrial solid particles as they enter the Earth’s atmosphere at high velocities. These particles, ranging from sub-millimetre to several meters (and very rarely 10s and 100s of meters) in size, can produce a range of phenomena, from intense light to destructive shock waves that can induce significant damage on the ground. Shock waves decay into very low frequency acoustic (infrasonic) waves at long distances from the source, and as such can propagate over many kilometers (100s – 1000s) away from the source. Those may eventually be detected on the ground by sensitive microphones. Meteor phenomena cannot be completely replicated or produced in a controlled environment, presenting a challenge in studying shock waves from meteors in the form of meteor infrasound.

The work in this thesis aims to address several still unanswered questions pertaining to what we can learn about meteoroids and their shock pattern using meteor infrasound, both experimentally and theoretically. Some of these questions are:

- Using infrasound only, can we determine meteoroid energy, meteor geolocation, meteor burst height and timing when other observational methods are not available?
- Can we establish and constrain the point along the meteor trail where the infrasound signal originates, thus allowing us to isolate the point of acoustic radiation from a meteor?
- Do meteor infrasound signals allow simple taxonomic classification based on their pressure-time signal alone?
- Can signal phenomenology tell us anything about the source?
- What is the effect of atmospheric variability on short range infrasound propagation?
- What are the mechanisms behind the shock production from high altitude sources (e.g. fragmentation or cylindrical line source) for meteoroids that produce infrasound detectable at ground and how common is each type of mechanism in producing signals?
- Can we independently, using infrasound only, determine meteoroid masses and meteoroid flux?
- Does the existing theoretical meteor cylindrical blast wave theory as developed by ReVelle (1974) reproduce observations?
- How does the ReVelle (1974) theory depend on underlying assumptions – which of these assumptions are robust and which may lead to errors in predicted model?

Before answering these questions, some basics about infrasound, shock wave dynamics and ReVelle's blast wave theory are presented.

## 1.3 A Brief Primer on Infrasound

### 1.3.1 Physics of Sound and Infrasound

The word acoustics stems from the Greek word ἀκουστικός (akoustikos), meaning ‘ready to hear’ and that from ἀκουστός (akoustos), meaning ‘heard, audible’ (Scott, 1901). The scientific study of sound, including its production, transmission and effects is called acoustics. The broad scope of acoustics, depicted by R. B. Lindsay in 1964 (Pierce, 1989 and references therein), is shown in Figure 1.2.

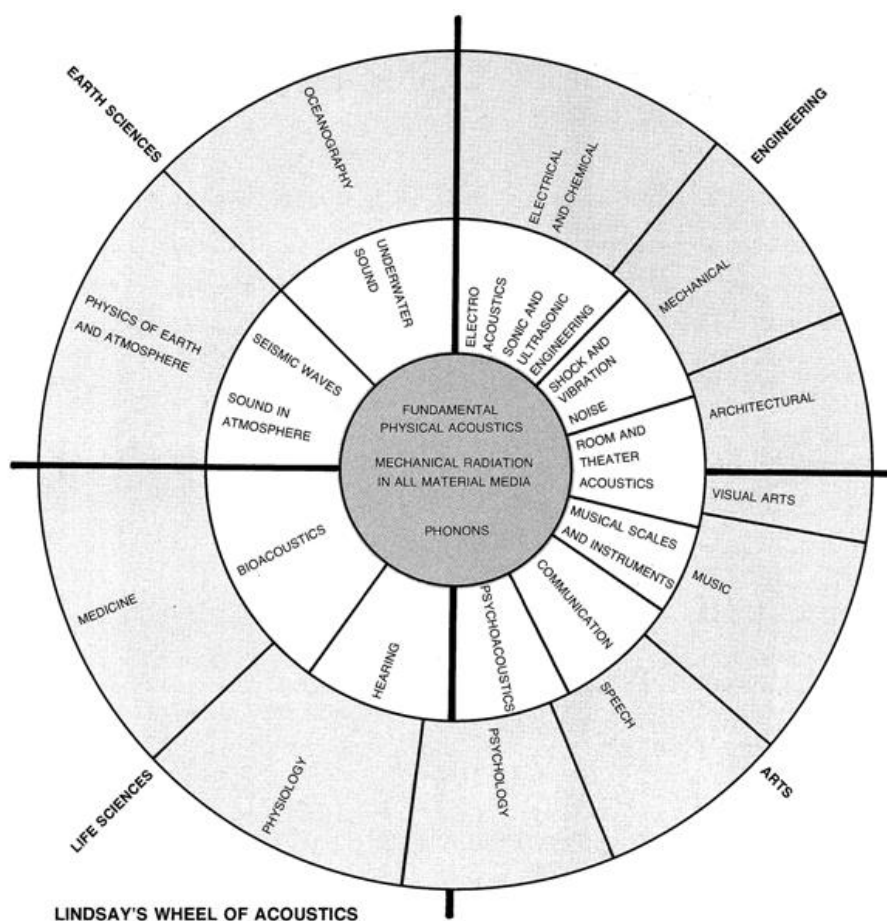


Figure 1.2: Lindsay’s wheel of acoustics describes the scope of acoustics. This diagram is not intended to rigorously represent all disciplines and subdisciplines (Pierce, 1989 and references therein).

Sound is a longitudinal (or pressure) wave whose particle motion is in the same direction as propagation, causing local regions of compression and rarefaction. In the absence of any external forces (e.g. gravitational) in a stationary fluid, the only type of wave that can exist is an acoustic wave (Beer, 1974). Sound audible to humans lies within the frequency range between 20 Hz and 20 kHz. Frequencies higher than 20 kHz are called ultrasound, while the frequencies lower than about 20 Hz are called infrasound. The lower frequency bound of infrasound is the natural buoyancy frequency of the atmosphere (Brunt-Väisälä frequency).

As gravity is a continual force acting on the atmosphere, it creates a density gradient and a restoring force, behaviours not present in a homogeneous fluid. Acoustic gravity waves (AGW) form when the force of gravity, coupled with the magnitude of the stabilizing restoring force, approaches the magnitude of compressibility forces. These waves are no longer purely longitudinal unless they undergo vertical propagation. Wave dispersion, the change in phase speed with frequency, occurs in two ways, either structural (caused by the properties of medium) or geometric (from interference effects induced by reflections at boundaries). It is usually written in terms of angular frequency  $\omega$  (Beer, 1974):

$$\begin{aligned}\omega &= \omega(k) \\ k &= 2\pi/\lambda\end{aligned}\tag{1.9}$$

where  $k$  is the wave number and  $\lambda$  is the wavelength. In a dispersive medium, the wave velocity is dependent on the wavelength, meaning that waves of different wavelengths travel at different phase velocities. Atmospheric waves undergo structural dispersion, especially in connection with the internal resonant frequencies, such as the Brunt-Väisälä frequency (Beer, 1974). A consequence of dispersion is that the energy flow may be in a direction other than the phase propagation direction of the wave (Beer, 1974).

The thermal structure of the atmosphere, driven by the absorption of the incoming and re-radiated solar energy, plays a major role in long range acoustic propagation (Figure 1.3). The temperature profile of the atmosphere is not ‘stationary’, but a complex function of solar radiation and how that radiation is absorbed by various molecular species in the atmosphere. In the troposphere, the temperature decreases with altitude until a local minimum is reached at the tropopause, the boundary layer located approximately 7-10 km in altitude depending on season and latitude (Beer, 1974). The temperature increases

up to the stratopause, where it starts to decrease again to a minimum at the mesopause (80-85 km). In the thermosphere, temperature increases up the altitude of 200 km and then remains constant since the thermal conductivity of the gas is sufficiently high to absorb energy and rapidly transport it downwards (Willmore, 1970; Beer, 1974).

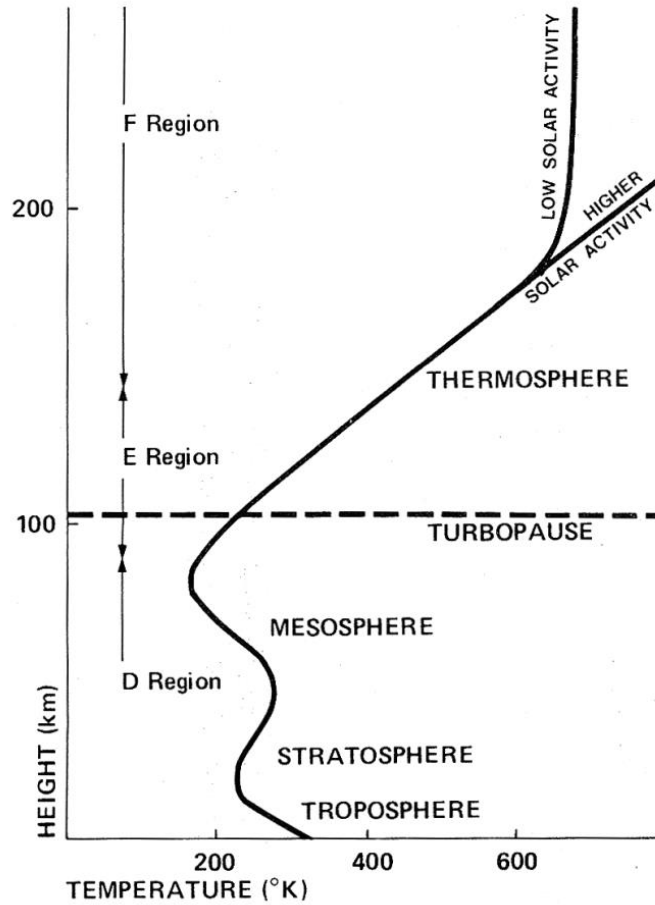


Figure 1.3: Thermal structure of the atmosphere (from Beer, 1974).

Taking the atmosphere as an ideal gas, the relationship between the pressure ( $p$ ) and density ( $\rho$ ) of the atmosphere as a function of temperature ( $T$ ) can be described as

$$p = \frac{\rho R' T}{M_{mw}} \quad (1.10)$$

where  $M_{mw}$  is the mean molecular weight,  $R'$  is the universal gas constant, defined in terms of Boltzmann's constant  $k$  ( $k = 1.38 \times 10^{-23}$  joule/K) and Avogadro's number  $N_a$  ( $N_a = 6.02 \times 10^{26}$  molecules/kmol/K). However, for simplicity, the specific gas constant  $R$  ( $R = R'/M$ ) can be used to eliminate  $M_{mw}$  and represent  $R'$  in terms of mean molecular weight. If the atmospheric process is adiabatic, then from the first law of thermodynamics:

$$p\rho^{-\gamma} = \text{constant} \quad (1.11)$$

$$\gamma = \frac{C_p}{C_v} \quad (1.12)$$

where  $C_p$  is the specific heat per unit mass at a constant pressure and  $C_v$  is the specific heat per unit mass at a constant volume. Values of  $\gamma$  range from a maximum of 5/3 for monoatomic gas, through 7/5 for diatomic gas and down to as low as 1 for polyatomic gasses at high temperature (Lighthill, 1978).

The speed of sound ( $c$ ) in the atmosphere is given by:

$$c^2 = \frac{\gamma p}{\rho} = \gamma RT \quad (1.13)$$

The speed of sound in air at 20°C and 1 atmosphere is 343 m/s. This was first correctly determined in the 1630s by the French mathematician and philosopher Marin Mersenne (Mersenne, 1636; Krehl, 2009). The fundamental equations of linear acoustic propagation are given by the linearized continuity equation, the linearized Euler's equation and the state equation (Pierce, 1989):

$$\frac{\partial \rho'}{\partial t} + \rho_0 \nabla \cdot v' = 0 \quad (1.14)$$

$$(1.15)$$

$$\rho_0 \frac{\partial v'}{\partial t} = -\nabla p' \quad (1.16)$$

$$p' = c^2 \rho'$$

where,  $\rho'$ ,  $p'$ ,  $v'$  are the acoustic density, pressure and velocity, respectively, and  $\rho_0$ ,  $p_0$  and  $v_0$  are the ambient values.



The equation of acoustic motion in a homogeneous stationary fluid is given by:

$$\nabla^2 p' - \frac{1}{c^2} \frac{\partial^2 p'}{\partial t^2} = 0 \quad (1.17)$$

where  $\nabla^2 = \frac{\partial^2}{\partial x^2} + \frac{\partial^2}{\partial y^2} + \frac{\partial^2}{\partial z^2}$  is the three dimensional Laplacian (Beer, 1974).

As previously mentioned, the limiting frequency for infrasound on the lower end of the spectrum is the Brunt-Väisälä frequency ( $\sim 0.003$  Hz in the lower atmosphere), or natural oscillation frequency of the atmosphere, given by:

$$\omega_B^2 = \omega_g^2 + \frac{g}{c^2} \frac{\partial c^2}{\partial z} \quad (1.18)$$

where  $\omega_B$  is the Brunt-Väisälä frequency,  $\omega_g$  is the Brunt-Väisälä frequency in an isothermal atmosphere and  $z$  is the height (Beer, 1974). As the frequency decreases, the wavelength becomes progressively longer, until it reaches the point where the gravitational restoring force becomes significant.

### 1.3.2 Infrasound Propagation and Attenuation

In considering acoustic propagation in the atmosphere, the speed of sound may be significantly affected by winds, especially if the channel propagation extends to the upper regions of the atmosphere, which is typical for infrasound. Therefore, the effective speed of sound ( $c_{eff}$ ) is given by sum of the adiabatic sound speed and the dot product between the ray normal ( $\hat{n}$ ) and the wind vector ( $\vec{u}$ ):

$$c_{eff} = c + \hat{n} \cdot \vec{u} \Rightarrow \sqrt{\gamma RT} + \hat{n} \cdot \vec{u} \quad (1.19)$$

Daily and seasonal variations in the atmospheric temperature and wind will modify the effective speed of sound as shown in Figure 1.4 (Donn and Rind, 1971; Rind and Donn, 1975).

With the emergence of satellites, it is possible to quantify atmospheric temperature variations, which in turn can be applied to determine the effective sound speed in the atmosphere and update atmospheric models (e.g. Hedin et al., 1996). Wind fields may vary significantly both temporally and spatially (e.g. Donn and Rind, 1971), consequently

affecting the effective speed of sound in the atmosphere, either by increasing it (downwind propagation) or reducing it (upwind propagation). Strong seasonal reversals of high altitude winds can significantly affect stratospheric propagation channels, and introduce anisotropy in wave propagation (e.g. Garcés et al., 1998). In midlatitudes, this propagation is predominantly west to east in winter, where the advective flow is up to 100 m/s at ~70 km altitude, and the opposite in the summer, where the advective flow is up to 60 m/s at ~ 50 km altitude (Gabrielson, 1997). Downwind propagation can increase the phase speed and dispersion of infrasound waves such as that these quantities are increased, as well as enhance signal amplitude and period (Mutschlecner and Whitaker, 2010). More recently, it has been recognized that the small scale structures in the atmosphere, such as gravity waves, may also significantly affect propagation (e.g. through partial reflection) of infrasound, especially over long distances (e.g. Chunchuzov, 2004; Ostashev et al., 2005; Kulichkov, 2010).

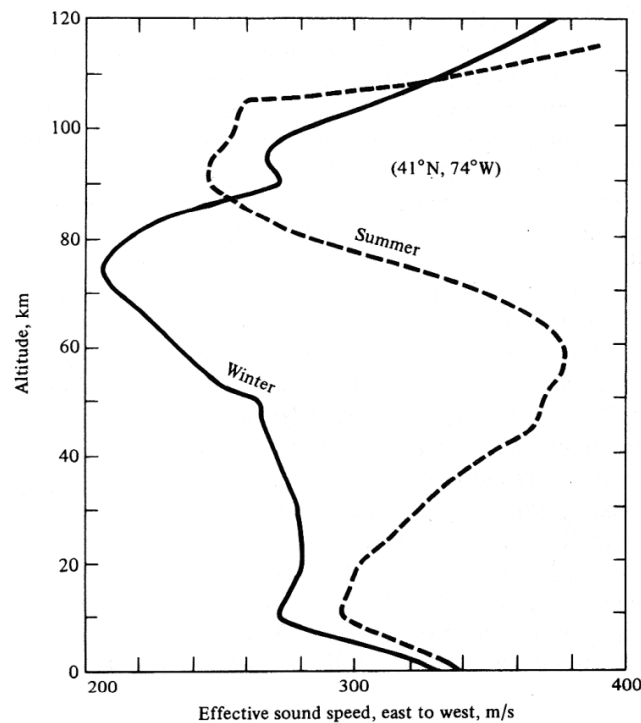


Figure 1.4: Model atmospheric profiles of effective speed of sound as a function of height and season for westward propagation in the USA (Rind and Donn, 1975).

Since the atmospheric temperature generally decreases as a function of height (see Fig 1.3), sound has a tendency to bend upward (Reynolds, 1876). Depending on the orientation of the wave as well as atmospheric conditions (e.g. changes in wind or temperature), wave turn over will occur at an altitude when  $c_{eff}$  becomes larger than its surface value. At this height the wave vector bends downward following Snell's law (Mutschlecner and Whitaker, 2010). This scenario is further complicated in regions of atmospheric temperature inversion zones.

Atmospheric waveguides (or ducts) are formed by temperature and wind variations in different atmospheric layers (Tolstoy, 1973; Georges and Beasley, 1977; Drob et al, 2003; Kulichkov, 2010). Consequently, infrasonic rays emanating from a source may become trapped in several atmospheric waveguides (ducts), which can lead to two or more infrasonic phases being recorded at the receiver. 'Zones of silence' or 'shadow zones' are the regions where geometrical ray theory predicts that no infrasound energy should reach the receiver (Figure 1.5). A number of studies, both historical (e.g. Evers and Haak, 2010) and recent, confirm that infrasound signals (sometimes called anomalous signals) can still be recorded in these zones as a result of scattering and diffraction effects not taken into account in geometrical ray theory (Golden et al., 2007; Herrin et al., 2007; Green et al., 2011; McKisic, 1997).

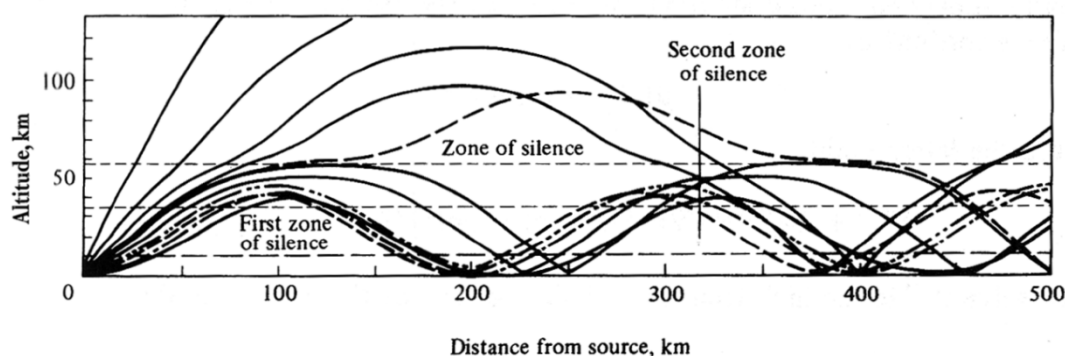


Figure 1.5: Representative infrasonic ray paths during summer in the northern hemisphere (from Gutenberg, 1951). Stratospheric and thermospheric waveguides are shown.

As infrasonic waves propagate outward from the source, they also undergo attenuation. Figure 1.6 shows the theoretical acoustic wave absorption as a function of height. Attenuation of sound in the atmosphere occurs due to spreading and absorption losses (Evans et al., 1972). Spreading losses can be uniform (spherical spreading, inverse square law) and nonuniform (reflection by finite boundaries, refraction, diffraction or scattering) (Evans et al., 1972). Atmospheric absorption occurs due to molecular relaxation (vibration and rotation) and classical (molecular diffusion, heat conduction and internal friction) effects (Evans et al., 1972; Sutherland and Bass, 2004). For the latter, internal friction and molecular diffusion are the largest contributors. These effects combined are a function of the square of the wave frequency, such that attenuation is proportional to  $1/f^2$  (Bass, 1972). Therefore, infrasonic waves are capable of propagating over very long distances with negligible attenuation, making them an excellent tool for studying distant explosive sources in the atmosphere.

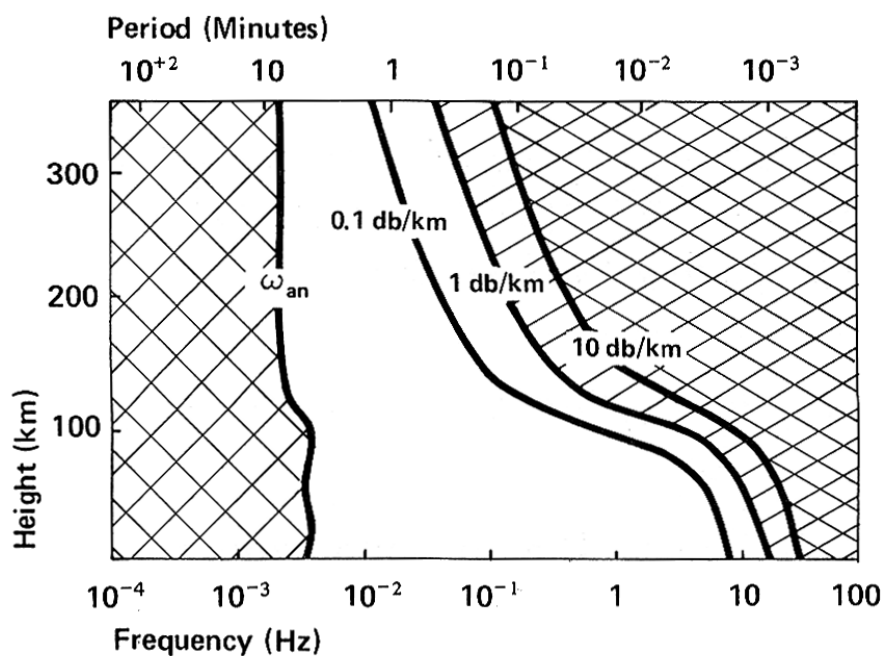


Figure 1.6: Theoretical acoustic wave absorption in dB/km as a function of height (after Georges, 1967 and from Beer, 1974). In the diagram,  $\omega_{an}$  is the acoustic frequency lower limit cutoff.

There are many sources of infrasound; both natural and anthropogenic (Figure 1.7). Natural sources of infrasound include ocean waves (microbaroms), avalanches (Bedard and Georges, 2000), lightning, aurorae, volcanoes (Evers and Haak, 2001; Garcés et al., 2008), earthquakes (Hedlin et al., 2002; Garcés and Le Pichon, 2009) and meteors (ReVelle, 1997; Silber et al., 2009; Brown et al., 2013). Even some animals (e.g. elephants, whales, giraffes) use infrasound for long range communication (e.g. Payne, 1995). Typical pressure levels associated with different natural sources are shown in Table 1.1. The natural source, which is a topic of this thesis, meteor generated infrasound, however, can fall within typical signal periods associated with other sources, such as microbaroms or severe weather (Figure 1.8), complicating the identification process. Interpreting infrasound source characteristics may be impeded by the complex dynamics of the atmosphere which modifies infrasound signals sometimes producing irreversible modifications to the signal as it travels between the source and the receiver. Often, as a consequence, it is not possible to determine the nature of the source without ground truth information or further observational data from other techniques. Dynamic changes of the atmosphere, which occur on a scale shorter than the infrasound wave propagation time, need to be adequately quantified in order to extract information about the source (e.g. de Groot-Hedlin, 2010; Norris et al., 2010).

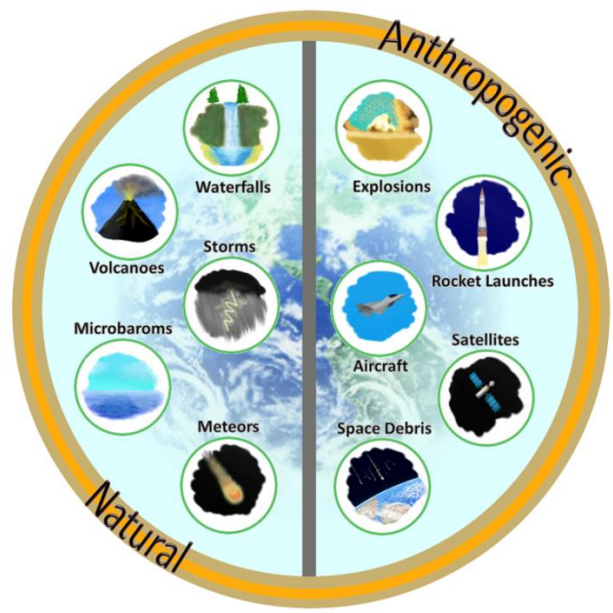


Figure 1.7: Sources of infrasound.

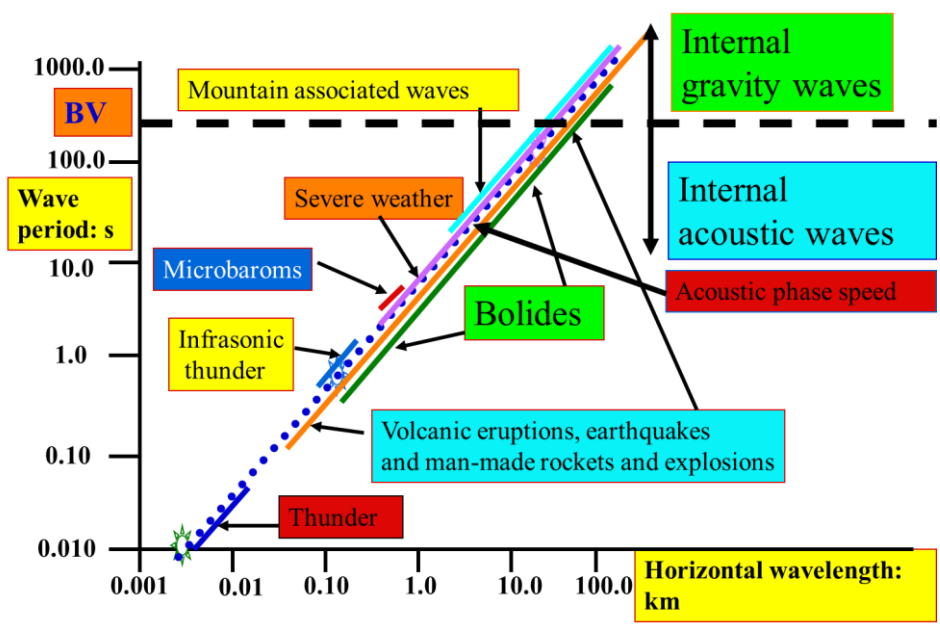


Figure 1.8: A diagram showing infrasound wave period (ordinate) and wavelength (abscissa) for some typical sources (adopted from ReVelle, 2003). Meteoroids (or bolides in the diagram) can produce infrasound within the period range of other sources, making the identification process more challenging. The dashed line (BV = Brunt-Väisälä frequency) denotes the boundary between the acoustic and internal gravity wave regions.

Table 1. 1: Natural sources of infrasonic waves (from Gabrielson, 1997).

Source	Period (s)	Typical Levels	Characteristics	Mechanism	Altitude
Microbaroms	2-8	0.01-1 Pa	Diurnal, semidiurnal, seasonal variations	Nonlinear interaction of ocean waves	Sea level
Aurora	10-100	0.1-0.5 Pa	Not observed from 1200-1600 local time	Supersonic motion of auroral arc, joule heating or electromagnetic force	100+ km
Meteors	0.2-18	0.05-1 Pa at 200-1200 km	Often observe both stratospheric and thermospheric arrivals	Explosive interaction with the atmosphere	25 km and above
Avalanches	0.5-2	0.02-0.05 Pa at 100 km	Dominant spectral peak	Monochromatic structure may result from periodic leading-edge roll of avalanche	Surface
Volcanic eruptions	>100	1.5 Pa at 10,000 km from Mt. St. Helens	Long duration (hours) at long distances, multiple arrivals	High-energy explosive compression of atmosphere	Surface to 10+ km
Strong earthquakes	8-30	0.1-2 Pa at thousands of kilometres for large events	In addition to airborne arrivals, locally generated seismic-acoustic arrivals	Ground motion at epicenter and from intermediate regions, ground motion from seismic waves at receiving station	Surface
Mountain-associated waves	10-50	0.1-3 Pa	No diurnal variation, long duration, -10.5 dB/octave power spectrum	Associated with wake turbulence from wind flow over mountain ridges	Surface to several kilometres
Severe storms	0.1-50	0.05-0.3 Pa at 30-800 km	Not correlated with lightning, -3 to -6 dB/octave power spectrum from 2-16 Hz	Mechanism uncertain: vigorous convection, tornadoes, fronts?	Surface to tropopause

### 1.3.3 Historical Aspects of Infrasound

The first documented instrumentally recorded infrasound dates back to 1883, when Krakatoa, a volcanic island in Indonesia, was almost completely eviscerated in a violent eruption. Starting on May 20, 1883 and reaching the peak with several explosions of unprecedented intensity between August 26-27, 1883, the aftermath of Krakatoa included pyroclastic flows, giant tsunamis, ash plumes, ash and pumice deposits, as well as the loudest noise ever recorded (Verbeek, 1884). The audible sound was heard as far as 4800 km away, in Alice Springs, Australia and 4653 km away on Rodriguez Island in the Indian Ocean, while the sub-audible acoustic waves enveloped the entire Earth. The atmospheric disturbances, caused by the shock waves emanating from the intense explosion of Krakatoa and recorded on barometers around the world, circled the globe seven times (Symons, 1888).

The first documented infrasound recording from an extraterrestrial body was not recorded until the early 20<sup>th</sup> century. In the morning hours of June 30, 1908, an extraterrestrial body entered the Earth's atmosphere and exploded approximately 5-10 km above the ground (Chyba et al., 1993) near the Podkamennaya Tunguska River (now Krasnoyarsk Krai) in Siberia, Russia, generating an intense blast wave which flattened much of the surrounding forest (Whipple, 1930; Krinov, 1966). It is estimated that this event released between 10 Mt (Hunt et al., 1960) and 20 Mt (Chyba et al., 1993) of energy (high explosive equivalent; 1 Mt =  $4.185 \times 10^{15}$  J). However, the origin, size and composition of the impactor and whether it was a comet or an asteroid (Chyba et al., 1993), remains unclear. The blast wave generated by this event was so intense that it generated low frequency acoustic waves recorded by microbarographs in England. Coincidentally, the microbarograph was invented only five years earlier, in 1903, by Shaw and Dines (1904). The recordings of the Tunguska event in Whipple (1930) represent perhaps the earliest published microbarograph records (Figure 1.9).



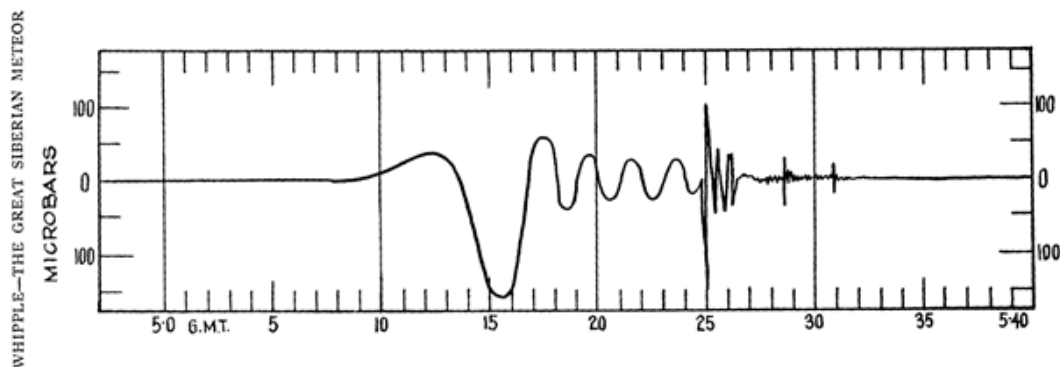


Figure 1.9: An infrasound pressure wave recording from the Tunguska explosion. This pressure form is a combined record from five microbarographs across the UK (Whipple, 1930). The x-axis is in minutes.

After the Tunguska explosion and until the onset of the Cold War, infrasound received very little attention. After the World War II, infrasound became a key technology for source identification and geolocation from explosive sources in the atmosphere, particularly nuclear explosions. The United States Air Force Technical Applications Centre (AFTAC) deployed a number of infrasound arrays worldwide, with sensor separations (6-12 km) optimized to detect large explosions (Cook and Bedard, 1972; ReVelle, 1997; Silber et al, 2009). Infrasonic signals emanating from nuclear explosions usually consist of Lamb waves (horizontally propagating waves), acoustic-gravity waves and various infrasonic phases. A number of approaches to estimate the explosive source yield from infrasound measurements were developed. These include the Lamb waves approach (Pierce and Posey, 1971; Pierce and Kinney, 1976), which utilizes the vertically evanescent surface waves; the period at maximum amplitude approach, which relates the period at maximum amplitude from stratospheric phases to the source energy (ReVelle, 1997) and other amplitude-based scaling relations (e.g. Posey and Pierce, 1971). The summary of attenuation relations, concurrently developed by Soviet and American scientists to estimate nuclear explosion yield is given by Stevens et al. (2002). Some of these empirical relations were applied to bolides in order to estimate their energy (ReVelle, 1997; Silber et al., 2009).

As previously mentioned, one by-product of global monitoring for nuclear explosions was detection of infrasound from other sources. Shoemaker and Lowery (1967) recognized that some of the signals recorded by the AFTAC network between 1960 and 1974, although belonging to seemingly energetic sources, were not associated with nuclear explosions, but with large bolides. If not for infrasound monitoring, these bolides would otherwise have gone undetected. This historical large bolide data set provides invaluable information on the influx of NEOs (ReVelle, 1997; Silber et al., 2009), especially since the global monitoring and recording of bolides only commenced during the 20<sup>th</sup> century. However, with advent of satellite monitoring in the 1960s and 1970s, infrasound fell out of favour as a monitoring technology and entered its own ‘dark age’ and becoming nearly forgotten.

The recent renaissance in infrasound studies is due to the Comprehensive Nuclear Test Ban Treaty (CTBT) which was opened for signature at the United Nations in on September 24, 1996. The CTBT Organization, stationed in Vienna, Austria, has implemented an International Monitoring Network (IMS), consisting of four monitoring technologies (radionuclide, seismic, hydroacoustic and infrasound), with stations distributed around the globe. A major advantage of infrasound monitoring is that it is a passive observational technique, fairly inexpensive and low maintenance. With the implementation of the IMS network, infrasound has experienced a revitalization. The infrasound component of the IMS consists of 60 certified arrays, 47 of which are fully operational (Figure 1.10), four are under construction and nine are planned as of the early 2014 (CTBTO, 2014). While the arrays developed during the Cold War were optimized for monitoring large explosions, the IMS network is set up to reliably detect and geolocate a 1 kiloton nuclear explosion anywhere on the globe (Christie and Campus, 2010).

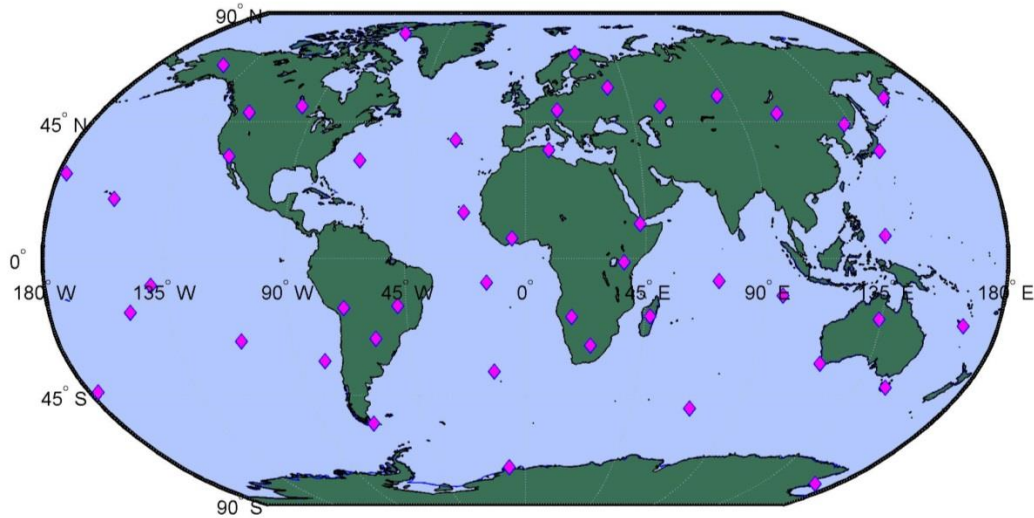


Figure 1.10: The IMS infrasound network of the CTBTO as of the early 2014. Each diamond represents an individual infrasound array consisting of four or more elements.

### 1.3.4 Infrasound Detection and Measurement Principles

Initially, the IMS infrasound arrays were to have a basic design of 4 elements. Each element consists of a very sensitive microphone, capable of detecting minute pressure disturbances above (or below) the ambient pressure of the atmosphere (e.g. Whittaker, 1995; Ponceau and Bosca, 2010). The amplitude (or overpressure) of an incoming wave is defined as:

$$A = \frac{p - p_0}{p_0} = \frac{\Delta p}{p_0} \quad (1.20)$$

where  $A$  is the amplitude, typically measured in units of pascals (Pa),  $p$  is the pressure of a disturbance and  $p_0$  is the ambient pressure. In a quiet environment, a sensor should be able to detect overpressure of about 0.1 Pa (Whittaker, 1995). Often, arrays are located in dense forests, where very little wind or noise interferes with the signal. Due to issues with aliasing, the arrays are commonly built with larger numbers of array elements and in a variety of configurations. A larger number of array sensors also increases the signal-to-noise ratio, which is especially important in naturally noisy sites. The sensors, along with their accompanied equipment are enclosed in a vault, typically with porous hoses

extending outward to reduce the local wind noise (Whittaker, 1995; CTBTO, 2014). The operating frequency of the network is up to 20 Hz, which translates to a Nyquist frequency of <10 Hz. As an infrasonic wave sweeps across the array, standard signal processing and analysis (e.g. Brachet et al., 2010) techniques make it possible to determine the signal arrival time, source bearings (back azimuth or direction of arrival), signal trace velocity, amplitude, correlation coefficients and spectra.

### **1.3.5 Meteor Infrasond**

Infrasonic waves detected at the ground offer valuable information and an insight into the shock wave phenomena generated by meteors. However, nonlinear influences, attenuation, dispersion, and other often irreversible propagation effects pose a great challenge when attempting to determine the source parameters such as the meteoroid's mass, energy deposition and source height. Without ground truth information (eyewitness reports, other instruments, etc.), infrasound records alone are often not sufficient in determining whether infrasound is generated ballistically (cylindrical line source) or from fragmentation.

Following early works on cylindrical line source related to exploding wires (Sakurai, 1964; Plooster, 1970), lightning phenomena (Jones et al., 1968; Few, 1969) and subsequently meteors, (Tsikulin, 1970), ReVelle (1974; 1976) developed an analytical blast wave model for meteors following the nonlinear disturbance initiated by an equivalent explosive line source. A major goal of this thesis is to experimentally test and validate ReVelle's (1974) meteor infrasound theory. This has never been done due to lack of observational data.

Constraining the source parameters, shock production mechanisms and establishing the source function are of great importance for calibrating meteoroid energy deposition and mass estimates as measured by infrasound, as well as in identification and measurement of signals produced by meteors. Thus, ground observatories with capabilities to detect and accurately measure meteors with multiple instruments are a necessary first step in identification and characterization of meteor infrasound (see Chapter 5). From ReVelle's theory, a prediction that up to ten infrasound producing meteoroids would be observed in

a six month period (ReVelle, 1974; Kraemer, 1977) at a single location, has yet to be documented for a single multi-instrument observatory (Silber and Brown, 2014). Earlier observational studies making use of camera systems as a cue for searching for meteor infrasound took place during the 1970s and the early 1980s. At that time, the Meteorite Observation and Recovery Program in Western Canada (Halliday et al., 1978), the U.S. Smithsonian Institution's Prairie Network (McCrosky and Boeschstein, 1965) and the Springhill Meteor Observatory (McKinley, 1961; Watson et al., 1976), in collaboration with the University of Michigan, started actively monitoring for meteor infrasound. Despite a five year span in active observations, only two detections were made, both by the Springhill Meteor Observatory in 1974 during the Geminid shower but without any directionality information (McIntosh et al., 1976). In 1975, the first confirmed infrasound signal from a meteoroid with a well-established trajectory was identified by the Prairie Network (McCrosky et al., 1979).

Following the inception of the CTBT IMS network, meteor infrasound observations experienced a renaissance. A number of ground meteor networks were established with the aim of recording meteor velocities and masses using optical and radar observations (e.g. Oberst et al., 1998; Trigo-Rodríguez, 2005; Weryk et al., 2008). Of these networks, the Southern Ontario Meteor Network (SOMN) was unique in purpose and design for simultaneous infrasound-optical meteor measurements, allowing a sufficiently large data base of well characterized near field (< 300 km) meteor events generated by centimetre-sized objects to be gathered (Silber and Brown, 2014).

Observations of large bolides capable of generating infrasound detectable over very long ranges (1000s of km) further attest the need for better constraining the shock production mechanisms. For example, one of the still pending problems is the issue of the dominant period, which may significantly deviate from station to station for a given infrasound producing bolide as observed by multiple stations on the ground, leading to the conclusion that the meteor shock production mechanisms (e.g. signals coming from different part of trajectory) may play a more significant role than previously thought (ReVelle, 1997; Silber et al., 2009; Silber et al., 2011). This complicates the already

obfuscating process of estimating infrasound bolide energy yield (which may vary by several orders of magnitude) and is further discussed in Chapters 3 and 4.

## 1.4 Thesis Aim

The first goal of this thesis was to determine the flux of large bolides impacting the Earth using recently declassified infrasonic records.

The second goal was to investigate the far-field (long range propagation) bolide infrasound with specific emphasis on:

- i. using infrasound only, determine meteoroid energy, meteoroid geolocation, burst height and timing;
- ii. investigate the issue of differences in observed dominant signal period at maximum amplitude as recorded by various stations and estimate the source height using infrasound signal properties alone;

In addition to these goals focused on larger bolides, regional meteor infrasound was examined to investigate the following:

- i. use astrometric optical measurements to positively identify infrasound from specific meteors;
- ii. establish and constrain the point (and its uncertainty) along the meteor trail where the observed infrasound signal emanates;
- iii. examine the influence of atmospheric variability on near-field infrasound propagation;
- iv. try to establish the type of shock production at the source (fragmentation, spherical vs. cylindrical);
- v. develop a phenomenological classification of meteor infrasound signals based on pressure-time waveforms
- vi. for meteors detected optically and with infrasound use the ReVelle (1974) weak shock theory to provide a bottom-up estimate of the blast radius;

- vii. test the influence of atmospheric variability, winds and Doppler shift on the weak shock solutions
- viii. determine an independent estimate of meteoroid mass from infrasonic signals alone and compare to photometric measurements;
- ix. critically evaluate and compare ReVelle's weak shock theory with observations;

The remainder of the thesis is structured as follows:

Chapter 2 presents a general review on shock waves and ReVelle's cylindrical blast wave theory.

Chapter 3 (published as Silber et al., 2009) outlines the infrasound measurements of large bolides recorded infrasonically by the Air Force Technical Applications Centre between 1960 and 1974 for derivation of the influx of meter to tens of meter-sized Near Earth Objects impacting the Earth.

Chapter 4 (published as Silber et al., 2011) presents a case study of instrumental recordings and analysis of infrasonic signals produced by a large Earth-impacting bolide, believed to be among the most energetic instrumentally recorded during the last century that occurred on 8 October, 2009 over Indonesia. This event was detected by 17 infrasonic stations of the global International Monitoring Network. No other observational data, other than eyewitness accounts, exists for this event. A new technique to estimate the source height using infrasonic data was developed and tested. Furthermore, this paper deals with the well-known fact that the bolide signal periods at maximum amplitude generally have different values as recorded by different stations, which is considered an anomaly.

Chapters 5 and 6 are an observational and theoretical pair of papers focusing on regional meteor infrasound. Chapter 5 (submitted as Silber and Brown, 2014) introduces the analysis procedures used to positively associate infrasonic signals with specific optically recorded meteors together with their infrasound phenomenology. The Elginfield infrasound array maintained by Western University, signal identification, processing and measurements are discussed in detail, followed by astrometric measurements. A new

taxonomic scheme for meteor generated infrasonic signals is proposed based on a large dataset of regionally recorded events. Raytracing with implementation of atmospheric variability was used to determine the source heights and uncertainty along the meteor trail for each event in the data set to investigate the type of shock production, as well as establish meteoroid population groups and signal phenomenology.

Chapter 6 (to be submitted as Silber et al., 2014) builds upon the paper in Chapter 5 and includes the theoretical comparison of ReVelle's weak shock theory to the observations, in addition to derivation of infrasonic masses and their comparison to photometric measurements.

Thesis appendices are organized as follows: Appendix 1 displays the infrasound signal identification methodology and phenomenology plots. Appendix 2 describes the raytracing results for all events analysed in Chapter 5. Appendix 3 describes photometric corrections and experiments. Appendix 4 displays the scaled, relative photometric lightcurve plots for all meteors for which infrasound was detected. Appendix 5 shows the measured light curves and the corresponding model fits. Appendix 6 displays the model fit to the observed light curve and dynamics plots for all events from Chapter 6.



## References

- Abe, S., Yano, H., Ebizuka, N., Kasuga, T., Sugimoto, M., Watanabe, J. I. (2002) Sowing the seeds of life: spectroscopic observations of possible prebiotic components in the Leonid meteor storm. *Astronomical Herald*, 95, 515-528.
- Ahn, S. H. (2003) Meteors and showers a millennium ago. *Monthly Notices of the Royal Astronomical Society*, 343(4), 1095-1100.
- Anderson, J. (2006) *Hypersonic and High-Temperature Gas Dynamics Second Edition*. AIAA Education Series
- Arrowsmith, S. J., Johnson, J. B., Drob, D. P., Hedlin, M. A. (2010) The seismoacoustic wavefield: a new paradigm in studying geophysical phenomena. *Reviews of Geophysics*, 48(4).
- Baggaley, W. J. (1980) Meteors and atmospheres. In *Solid Particles in the Solar System* (Vol. 90, pp. 85-100).
- Baggaley, W. J. (2002) Radar observations, in: Murad, E., and Williams, I. P. (Eds.) *Meteors in the Earth's Atmosphere: Meteoroids and Cosmic Dust and Their Interactions with the Earth's Upper Atmosphere*. Cambridge University Press. 123–148.
- Baggaley, W. J., Fisher, G. W. (1980) Measurements of the initial radii of the ionization columns of bright meteors. *Planetary and Space Science*, 28(6), 575-580.
- Baggaley, W. J., Webb, T. H. (1977) The thermalization of meteoric ionization. *Journal of Atmospheric and Terrestrial Physics*, 39(11), 1399-1403.
- Bass, H. E., Hetzer, C. H., Raspet, R. (2007) On the speed of sound in the atmosphere as a function of altitude and frequency. *Journal of Geophysical Research: Atmospheres* (1984–2012), 112(D15).
- Bass, H.E. (1972) Atmospheric absorption of sound: analytical expressions. *J Acoust Soc Am*, 52:821–825
- Bedard, A., Georges, T. (2000) Atmospheric infrasound. *Acoustics Australia*. 28(2), 47-52.
- Beech, M. (1988) Meteor astronomy: a mature science?. *Earth, Moon, and Planets*, 43(2), 187-194.
- Beech, M., Brown, P., Jones, J. (1995) The potential danger to space platforms from meteor storm activity. *Quarterly Journal of the Royal Astronomical Society*, 36, 127.
- Beer, T. (1974) *Atmospheric waves*. New York, Halsted Press; London, Adam Hilger, Ltd., 1974. 315 p.

- Belkovic, O. I., Pupysev, J. A. (1968) The variation of sporadic meteor radiant density and the mass law exponent over the Celestial Sphere. In *Physics and Dynamics of Meteors*, Vol. 33, p. 373.
- Borovička, J. (1993) A fireball spectrum analysis. *Astronomy and Astrophysics*, 279, 627-645.
- Brachet, N., Brown, D., Le Bras, R., Cansi, Y., Mialle, P., Coyne, J. (2009) Monitoring the earth's atmosphere with the global IMS infrasound network. In *Infrasound Monitoring for Atmospheric Studies* (pp. 77-118). Springer Netherlands.
- Briani, G., Pupillo, G., Aiello, S., Pace, E., Shore, S., Passaro, A. (2007) Study of the Interaction of Micrometeoroids with Earth's Atmosphere. *Memorie della Societa Astronomica Italiana Supplementi*, 11, 89.
- Bronshten, V. A. (1983) *Physics of meteoric phenomena*. Fizika meteornykh iavlenii, Moscow, Izdatel'stvo Nauka, 1981 Dordrecht, D. Reidel Publishing Co., 1983, 372 p. Translation., 1.
- Bronshten, V.A. (1983) *Physics of Meteoric Phenomena*. 372 pp. D. Reidel, Dordrecht, Netherlands
- Brown, P. (1999) The Leonid meteor shower: Historical visual observations. *Icarus*, 138(2), 287-308.
- Brown, P. G., Assink, J. D., Astiz, L., Blaauw, R., Boslough, M. B., Borovička, J., and 26 co-authors (2013) A 500-kiloton airburst over Chelyabinsk and an enhanced hazard from small impactors. *Nature*. 503, 238-241
- Brownlee, D. E. (1985) Cosmic dust-Collection and research. *Annual Review of Earth and Planetary Sciences*, 13, 147-173.
- Burke, J. G. (1991) *Cosmic debris: meteorites in history*. University of California Press.
- Campbell-Brown, M. D., Koschny, D. (2004) Model of the ablation of faint meteors. *Astronomy and Astrophysics-Berlin Then Les Ulis*, 418(2), 751-758.
- Campbell-Brown, M., Jones, J. (2003) Determining the initial radius of meteor trains: fragmentation. *Monthly Notices of the Royal Astronomical Society*, 343(3), 775-780.
- Cepplecha, Z. (1996) Luminous efficiency based on photographic observations of the Lost City fireball and implications for the influx of interplanetary bodies onto Earth. *Astronomy and Astrophysics*, 311, 329-332.
- Cepplecha, Z., Borovička, J., Elford, W. G., ReVelle, D. O., Hawkes, R. L., Porubčan, V., Šimek, M. (1998) Meteor phenomena and bodies. *Space Science Reviews*, 84(3-4), 327-471.

- Ceplecha, Z., Borovička, J., Spurný, P. (2000) Dynamical behavior of meteoroids in the atmosphere derived from very precise photographic records. *Astronomy and Astrophysics*, 357, 1115-1122.
- Ceplecha, Z., Revelle, D. O. (2005) Fragmentation model of meteoroid motion, mass loss, and radiation in the atmosphere. *Meteoritics & Planetary Science*, 40(1), 35-54.
- Ceplecha, Z., Spurny, P., Borovička, J., Keclikova, J. (1993) Atmospheric fragmentation of meteoroids. *Astronomy and Astrophysics*, 279, 615-626.
- Christie, D. R. Campus, P. (2010) The IMS Infrasound Network: Design and Establishment of Infrasound Stations, In: A. Le Pichon, E. Blanc and A. Hauchecorne, Eds., *Infrasound Monitoring for Atmospheric Studies*. Springer. New York, pp. 29-75
- Chunchuzov, I. P. (2004) Influence of internal gravity waves on sound propagation in the lower atmosphere. *Meteorology and Atmospheric Physics*. 85(1-3), 61-76
- Chyba, C. F., Thomas, P. J., Zahnle, K. J. (1993) The 1908 Tunguska explosion: atmospheric disruption of a stony asteroid. *Nature*, 361(6407), 40-44.
- Close, S., Hunt, S. M., Minardi, M. J., McKeen, F. M. (2000) Analysis of perseid meteor head echo data collected using the advanced research projects agency long-range tracking and instrumentation radar (altair). *Radio Science*, 35(5), 1233-1240.
- Colestock, P., Close, S., Zinn, J. (2006) Theoretical and Observational Studies of Meteor Interactions with the Ionosphere (No. LAUR-06-113). Los Alamos National Lab, NM.
- Cook, R.K. and A.J. Bedard Jr (1972) On the measurement of Infrasound Q. J. Roy. Astro. Soc. 67,pp 5-11
- CTBTO (2014) [www.ctbto.org](http://www.ctbto.org) (retrieved on 15 Feb, 2014)
- de Groot-Hedlin, C. D., Hedlin, M. A., Drob, D. P. (2010) Atmospheric variability and infrasound monitoring. In *Infrasound monitoring for atmospheric studies* (pp. 475-507). Springer Netherlands.
- Doel, R. E. (1996) *Solar System Astronomy in America, Communities, Patronage, and Interdisciplinary Science, 1920-1960*, Vol. 1
- Donn, W. L., Rind, D. (1971) Natural infrasound as an atmospheric probe. *Geophysical Journal of the Royal Astronomical Society*, 26(1-4), 111-133.
- D'Orazio, M. (2007) Meteorite records in the ancient Greek and Latin literature: between history and myth. *Geological Society, London, Special Publications*, 273(1), 215-225.

- Dressler, R. A., Murad, E. (2001) The gas-phase chemical dynamics associated with meteors. *Chemical Dynamics in Extreme Environments*, edited by RA Dressler, (Vol. 11). World Scientific. 268-348.
- Drob, D. P., Picone, J. M., Garcés, M. (2003) Global morphology of infrasound propagation. *Journal of Geophysical Research: Atmospheres* (1984–2012), 108(D21)
- Dyrud, L. P., Denney, K., Close, S., Oppenheim, M., Chau, J., Ray, L. (2004) Meteor velocity determination with plasma physics. *Atmospheric Chemistry and Physics*, 4(3), 817-824.
- Dyrud, L., Wilson, D., Boerve, S., Trulsen, J., Pecseli, H., et al. (2008) Plasma and electromagnetic simulations of meteor head echo radar reflections. *Earth, Moon, and Planets*, 102(1-4), 383-394.
- Edwards, W. N., Brown, P. G., Weryk, R. J., ReVelle, D. O. (2008) Infrasonic observations of meteoroids: Preliminary results from a coordinated optical-radar-infrasound observing campaign. *Earth, Moon, and Planets*. 102(1-4), 221-229.
- Edwards, W.N., Hildebrand, A. R. (2004) SUPRACENTER: Locating fireball terminal bursts in the atmosphere using seismic arrivals. *Meteoritics & Planetary Science*, 39(9), 1449-1460.
- Ens, T. A., Brown, P. G., Edwards, W. N., Silber, E. A. (2012) Infrasound production by bolides: A global statistical study. *Journal of Atmospheric and Solar-Terrestrial Physics*. 80, 208-229
- Erickson, P. J., Lind, F. D., Wendelken, S. M., Faubert, M. A. (2001) Meteor head echo observations using the Millstone Hill UHF incoherent scatter radar system. In *Meteoroids 2001 Conference*, Vol. 495, pp. 457-463.
- Evans, L. B., Bass, H. E., Sutherland, L. C. (1972) Atmospheric absorption of sound: theoretical predictions. *The Journal of the Acoustical Society of America*, 51, 1565.
- Evers, L. G., Haak, H. W. (2010) The characteristics of infrasound, its propagation and some early history. In *Infrasound Monitoring for Atmospheric Studies* (pp. 3-27). Springer Netherlands.
- Evers, L.G. H.W. Haak. (2001) Listening to sounds from an exploding meteor and oceanic waves. *Geophysical Research Letters*. 30: 41-44
- Feng, W., Marsh, D. R., Chipperfield, M. P., Janches, D., Höffner, J., Yi, F., Plane, J. (2013) A global atmospheric model of meteoric iron. *Journal of Geophysical Research: Atmospheres*, 118(16), 9456-9474.
- Few, A. A. (1969) Power spectrum of thunder, *J. Geophys. Res.*, 74, 6926-6934
- Gabrielson, T. B. (1997) Infrasound. *Encyclopedia of Acoustics*, Volume One, 367-372.

- Garcés, M. A., Hansen, R. A., Lindquist, K. G. (1998) Traveltimes for infrasonic waves propagating in a stratified atmosphere. *Geophysical Journal International*, 135(1), 255-263.
- Garces, M., Fee, D., Steffke, A., McCormack, D., Servranckx, R., Bass, H., Hetzer, C., Hedlin, M., Matoza, R., Yepes H., Ramon, P. (2008) Capturing the acoustic fingerprint of stratospheric ash injection, *EOS* 89(40), 377–378
- Garcés, M., Le Pichon, A. (2009) Infrasonics from Earthquakes, Tsunamis and Volcanoes, In: R. A. Meyers, Ed., *Encyclopedia of Complexity and Systems Science*. Springer, Berlin, pp. 663-679
- Georges, T. M. (1967) Ionospheric effects of atmospheric waves. Institute for Telecommunication Sciences and Aeronomy.
- Georges, T. M., Beasley, W. H. (1977) Refraction of infrasonics by upper-atmospheric winds. *The Journal of the Acoustical Society of America*, 61, 28.
- Golden P., E. T. Herrin and P. T. Negraru (2007) Infrasonics in the zone of silence, in *Proceedings of the European Geophysical Union*, Vienna, April 2007
- Green, D.N., Vergoz, J., Gibson, R., Le Pichon, A., Ceranna, L. (2011) Infrasonics radiated by the Gerdec and Chelapechene explosions: propagation along unexpected paths. *Geophysical Journal International*. 185(2), 890-910.
- Gutenberg, B. (1951) Sound propagation in the atmosphere, in *Compendium of Meteorology*, T. F. Malone (ed.), American Meteorological Society
- Halliday, I., Blackwell, A. T., Griffin, A. A. (1978) The Innisfree meteorite and the Canadian camera network, *Journal of the Royal Astronomical Society of Canada*, 72, 15-39
- Havnes, O., Sigernes, F. (2005) On the influence of background dust on radar scattering from meteor trails. *Journal of atmospheric and solar-terrestrial physics*, 67(6), 659-664
- Hawkes, R. L., Jones, J. (1975) A quantitative model for the ablation of dustball meteors. *Monthly Notices of the Royal Astronomical Society*, 173, 339-356.
- Hedin, A.E., Fleming, E.L., Manson, A.H., Schmidlin, F.J., Avery, S.K., Clark, R.R., Vincent, R.A. (1996) Empirical wind model for the upper, middle and lower atmosphere. *Journal of Atmospheric and Terrestrial Physics*. 58(13), 1421-1447
- Hedlin, M.A., Garcés, M., Bass, H., Hayward, C., Herrin, G., Olson, J., Wilson, C. (2002) Listening to the secret sounds of earth's atmosphere. *Eos* 83, 557, 564-565
- Herrin, E. T., Golden, P. W., Negraru, P. T., McKenna, M.H. (2007) Infrasonics in the zone of silence, *Proceedings of the 29th Monitoring Research Review: Ground-Based Nuclear Explosion Monitoring Technologies*, 25-27 Sep 2007, Denver, CO

- Hill, K. A., Rogers, L. A., Hawkes, R. L. (2005) Sputtering and high altitude meteors. *Earth, Moon, and Planets*, 95(1-4), 403-412.
- Hocking, W. K. (1999) Temperatures Using radar-meteor decay times. *Geophysical research letters*, 26(21), 3297-3300.
- Hocking, W. K., Thayaparan, T., Jones, J. (1997) Meteor decay times and their use in determining a diagnostic mesospheric Temperature-pressure parameter: Methodology and one year of data. *Geophysical research letters*, 24(23), 2977-2980.
- Hughes, D. W. (1997) Meteors and cosmic dust. *Endeavour*, 21(1), 31-35.
- Hunt, J. N., Palmer, R., Penney, W. (1960) Atmospheric waves caused by large explosions. *Philosophical Transactions of the Royal Society of London. Series A, Mathematical and Physical Sciences*, 252(1011), 275-315.
- Jenniskens, P. (2001) Meteors as a delivery vehicle for organic matter to the early Earth. In *Meteoroids 2001 Conference*, Vol. 495, pp. 247-254.
- Jenniskens, P. (2004) Meteor induced chemistry, ablation products, and dust in the middle and upper atmosphere from optical spectroscopy of meteors. *Advances in Space Research*, 33(9), 1444-1454.
- Jenniskens, P. (2008) Meteoroid streams that trace to candidate dormant comets. *Icarus*, 194(1), 13-22.
- Jenniskens, P. M. M. (2006) *Meteor showers and their parent comets*. Cambridge University Press.
- Jones, D. L., Goyer, G. G., Plooster, M. N. (1968) Shock wave from a lightning discharge. *J Geophys Res* 73:3121-3127
- Jones, J. (1975) On the decay of underdense radio meteor echoes. *Monthly Notices of the Royal Astronomical Society*, 173, 637-648.
- Jones, J., Campbell-Brown, M. (2005) The initial train radius of sporadic meteors. *Monthly Notices of the Royal Astronomical Society*, 359(3), 1131-1136.
- Jones, W. (1995) Theory of the initial radius of meteor trains. *Monthly Notices of the Royal Astronomical Society*, 275, 812-818.
- Jones, W., Jones, J. (1990) Ionic diffusion in meteor trains. *Journal of Atmospheric and Terrestrial Physics*, 52(3), 185-191.
- Kalashnikova, O., Horanyi, M., Thomas, G. E., Toon, O. B. (2000) Meteoric smoke production in the atmosphere. *Geophysical research letters*, 27(20), 3293-3296.
- Keay, C. S. (1980) Anomalous sounds from the entry of meteor fireballs. *Science*, 210(4465), 11-15.

- Keay, C. S. L., Ceplecha, Z. (1994) Rate of observation of electrophonic meteor fireballs. *Journal of Geophysical Research: Planets* (1991–2012), 99(E6), 13163-13165.
- Kraemer, D.R. (1977) *Infrasound from accurately measured meteor trails*, Ph.D. Thesis University of Michigan, Ann Arbor
- Krehl, P. O. (2009) *History of shock waves, explosions and impact: a chronological and biographical reference*. Springer.
- Krinov, E. L. (1966) *Giant meteorites*. Oxford, New York, Pergamon Press [1966][1st English ed.] Translated from the Russian by JS Romankiewicz. Translation edited by MM Beynon., 1.
- Kulichkov, S. (2010) On the prospects for acoustic sounding of the fine structure of the middle atmosphere. In *Infrasound monitoring for atmospheric studies* (pp. 511-540). Springer Netherlands.
- Lighthill, J. (1978) *Waves in Fluids*, 504 pp. Cambridge Univ.
- Love, S. G., Brownlee, D. E. (1993) A direct measurement of the terrestrial mass accretion rate of cosmic dust. *Science*, 262(5133), 550-553.
- Manning, L. A. (1958) The initial radius of meteoric ionization trails. *Journal of Geophysical Research*, 63(1), 181-196.
- Marsh, D. R., Janches, D., Feng, W., Plane, J. (2013) A global model of meteoric sodium. *Journal of Geophysical Research: Atmospheres*, 118(19), 11-442.
- McCrosky, R. E., Boeschenstein, H. (1965) *The Prairie Meteorite Network*, Smithsonian Astrophysical Observatory Special Report #173, 1-26
- McCrosky, R. E., Shao, C. Y., Posen, A. (1979) The Prairie Network bolide data. II – Trajectories and light curves, *Meteoritika*, 38, 106-156
- McIntosh, B. A. (1966) The determination of meteor mass distribution from radar echo counts. *Canadian Journal of Physics*, 44(11), 2729-2748.
- McIntosh, B. A., Watson, M. D., ReVelle, D. O. (1976) *Infrasound from a radar-observed meteor*. *Canadian Journal of Physics*, 54(6), 655-662.
- McKinley, D. W. R. (1961) *Meteor Science and Engineering*, McGraw-Hill Inc., New York, N.Y
- McKisic, J.M. (1997) *Infrasound and the Infrasonic Monitoring of Atmospheric Nuclear Explosions: A literature review*. Final report PL-TR-97-2123. Department of Energy and Phillips Laboratory, National Tech. Information Service, p. 310.
- McSween, H. Y. (1999) *Meteorites and their parent planets*. Cambridge University Press.

- Mersenne, M. (1636) *Harmonie Universelle*; transl. Chapman, R.: (1957). *The Books on Instruments*. Nijhoff, The Hague.
- Murad, E., Williams, I. P. (Eds.). (2002). *Meteors in the Earth's Atmosphere: Meteoroids and Cosmic Dust and Their Interactions with the Earth's Upper Atmosphere*. Cambridge University Press.
- Mutschlecner, J. P., Whitaker, R. W. (2010) Some atmospheric effects on infrasound signal amplitudes. In *Infrasound Monitoring for Atmospheric Studies*. (pp. 455-474). Springer Netherlands
- Nesvorný D. J., Janches D., Vokrouhlický D., Pokorný P., Bottke W. F., Jenniskens P. (2011) Dynamical Model for the Zodiacal Cloud and Sporadic Meteors. *The Astrophysical Journal* 743: 129.
- Norris, D., Gibson, R., Bongiovanni, K. (2010) Numerical methods to model infrasonic propagation through realistic specifications of the atmosphere. In *Infrasound monitoring for atmospheric studies* (pp. 541-573). Springer Netherlands.
- Oberst, J., Molau, S., Heinlein, D., Gritzner, C., Schindler, M., Spurny, P., Ceplecha, Z., Rendtel, J., Betlem, H. (1998) The 'European Fireball Network': Current status and future prospects, *Meteoritics and Planetary Science*, 33: 49-56
- O'Keefe, J. D., Ahrens, T. J. (1982) Impact mechanics of the Cretaceous-Tertiary extinction bolide. *Nature*, 298(5870), 123-127.
- Opik, E. J. (1958) *Physics of meteor flight in the atmosphere*. New York, Interscience Publishers, 1958, 1.
- Ostashev, V.E., Chunchuzov, I.P., Wilson, D.K. (2005) Sound propagation through and scattering by internal gravity waves in a stably stratified atmosphere. *The Journal of the Acoustical Society of America*. 118, 3420
- Payne, R. (1995) *Among Whales*. Scribner, New York, NY
- Pierce, A. D. (1989) *Acoustics: an introduction to its physical principles and applications*. Acoustical Soc of America.
- Pierce, A. D., Kinney, W. A. (1976) *Computational techniques for the study of infrasound propagation in the atmosphere*. Georgia Inst of Tech Atlanta School Of Mechanical Engineering
- Pierce, A. D., Posey, J. W. (1971) Theory of the excitation and propagation of Lamb's atmospheric edge mode from nuclear explosions. *Geophysical Journal of the Royal Astronomical Society*, 26(1-4), 341-368.
- Plane, J. M. (2012) Cosmic dust in the earth's atmosphere. *Chemical Society Reviews*, 41(19), 6507-6518.



- Plooster, M. N. (1970) Shock waves from line sources. Numerical solutions and experimental measurements. *Physics of fluids*, 13, 2665.
- Ponceau, D., Bosca, L. (2009) Low-noise broadband microbarometers. In *Infrasound Monitoring for Atmospheric Studies* (pp. 119-140). Springer Netherlands.
- Popova, O. (2005) Meteoroid ablation models. *Earth, Moon, and Planets*, 95(1-4), 303-319.
- Popova, O. P., Jenniskens, P., Emel'yanenko, V., Kartashova, A., Biryukov, E., Khaibrakhmanov, S., et al. (2013) Chelyabinsk Airburst, Damage Assessment, Meteorite Recovery, and Characterization. *Science*, 342(6162), 1069-1073.
- Popova, O. P., Sidneva, S. N., Strelkov, A. S., Shuvalov, V. V. (2001) Formation of disturbed area around fast meteor body. In *Meteoroids 2001 Conference*, Vol. 495, pp. 237-245.
- Posey, J. W., Pierce, A. D. (1971) Estimation of nuclear explosion energies from microbarograph records, *Nature*, 232, 253
- ReVelle, D. O. (1974) Acoustics of meteors-effects of the atmospheric temperature and wind structure on the sounds produced by meteors. Ph.D. Thesis, University of Michigan, Ann Arbor.
- ReVelle, D. O. (1976) On meteor-generated infrasound. *Journal of Geophysical Research*, 81(7), 1217-1230.
- ReVelle, D. O. (1997) Historical Detection of Atmospheric Impacts by Large Bolides Using Acoustic-Gravity Waves. *Annals of the New York Academy of Sciences*. 822(1), 284-302
- ReVelle, D. O. (2003) Bolide False Alarm Rate for the Global Infrasound Monitoring System, American Association for the Advancement of Science, Annual Meeting, Denver, Colorado, February 14, 2003
- ReVelle, D. O. (2005) The mesopause as a physical penetration boundary. *Journal of atmospheric and solar-terrestrial physics*, 67(13), 1159-1170.
- Reynolds, O. (1873) On the refraction of sound by the atmosphere. *Proceedings of the Royal Society of London*, 22(148-155), 531-548.
- Rind, D., Donn, W. L. (1975) Further use of natural infrasound as a continuous monitor of the upper atmosphere. *Journal of Atmospheric Sciences*, 32, 1694-1704.
- Rogers, L. A., Hill, K. A., Hawkes, R. L. (2005) Mass loss due to sputtering and thermal processes in meteoroid ablation. *Planetary and Space Science*, 53(13), 1341-1354.
- Romig, M. F. (1965) Physics of meteor entry. *AIAA Journal*, 3(3), 385-394.

- Sakurai, A. (1964) Blast Wave Theory, (No. MRC-TSR-497). Wisconsin Univ-Madison Mathematics Research Center.
- Scott, R. (1901) A greek-english lexicon. Clarendon Press.
- Shaw, W. N., Dines, W. H. (1905) The study of the minor fluctuations of atmospheric pressure. Quarterly Journal of the Royal Meteorological Society, 31(133), 39-52.
- Shoemaker, E. M., Lowery, C. J. (1967) Airwaves associated with large fireballs and the frequency distribution of energy of meteoroids, Meteoritics, 3, 123-124
- Silber, E. A., Brown, P. G. (2014) Optical Observations of Meteors Generating Infrasound – I: Acoustic Signal Identification and Phenomenology, JASTP, submitted (#ATP3766)
- Silber, E. A., Le Pichon, A., Brown, P. (2011) Infrasonic Detection of a Near-Earth Object Impact over Indonesia on 8 October, 2009, Geophysical Research Letters, Vol. 38, L12201
- Silber, E. A., ReVelle, D. O., Brown, P. G., Edwards, W. N. (2009) An estimate of the terrestrial influx of large meteoroids from infrasonic measurements. Journal of Geophysical Research: Planets (1991–2012), 114(E8).
- Stevens, J. L., Divnov, I. I., Adams, D. A., Murphy, J. R., Bouchik, V. N. (2002) Constraints on infrasound scaling and attenuation relations from Soviet explosion data. pure and applied geophysics, 159(5), 1045-1062.
- Sugar, G. R. (1964) Radio propagation by reflection from meteor trails. Proceedings of the IEEE, 52(2), 116-136.
- Sutherland, L. C., Bass, H. E. (2004) Atmospheric absorption in the atmosphere up to 160 km. The Journal of the Acoustical Society of America, 115, 1012.
- Symons, G. J., Judd, J. W., Strachey, S. R., Wharton, W. J. L., Evans, F. J., et al. (1888) The eruption of krakatoa: And subsequent phenomena. Trübner & Company
- Taylor, A. D. (1995) The Harvard radio meteor project meteor velocity distribution reappraised. Icarus, 116(1), 154-158.
- Tolstoy, I. (1973) Wave propagation. New York, NY (USA): McGraw-Hill, 466 p.
- Trigo-Rodríguez, J. M., Castro-Tirado, A. J., Llorca, J., Fabregat, J., Martínez, V. J., Reglero, V., Jelínek, M., Kubánek, P., Mateo, T., De Ugarte Postigo, A. (2005) The development of the Spanish Fireball Network using a new all-sky CCD system, In Modern Meteor Science An Interdisciplinary View (pp. 553-567). Springer Netherlands.
- Trigo-Rodríguez, J. M., Llorca, J., Borovička, J., Fabregat, J. (2003) Chemical abundances determined from meteor spectra: I. Ratios of the main chemical elements. Meteoritics & Planetary Science, 38(8), 1283-1294.

- Tsikulin, M. A. (1970). Shock waves during the movement of large meteorites in the atmosphere (No. NIC-Trans-3148). Naval Intelligence Command Alexandria VA Translation Div.
- Verbeek, R. D. M. (1884) The Krakatoa eruption. *Nature*, 30, 10-15.
- Vondrak, T., Plane, J. M. C., Broadley, S., Janches, D. (2008) A chemical model of meteoric ablation. *Atmospheric Chemistry and Physics*, 8(23), 7015-7031.
- Watson, M., McIntosh, B., ReVelle D. O. (1976) A meteor infrasound recording system, In: *Acoustics, Speech, and Signal Processing, IEEE International Conference on ICASSP'76*, 786-789
- Weryk, R. J., Brown, P. G. (2013). Simultaneous radar and video meteors-II: Photometry and ionisation. *Planetary and Space Science*.
- Weryk, R. J., Brown, P. G., Domokos, A., Edwards, W. N., Krzeminski, Z., Nudds, S. H., Welch, D. L. (2008) The Southern Ontario all-sky meteor camera network. *Earth, Moon, and Planets*, 102(1-4), 241-246.
- Wetherill, G. W., ReVelle, D. O. (1981) Which fireballs are meteorites? A study of the Prairie Network photographic meteor data. *Icarus*, 48(2), 308-328.
- Whipple, F. J. W. (1930) *The Great Siberian Meteor, and the Waves, Seismic and Aerial, which it Produces*.
- Whitaker, R. W. (1995) *Infrasonic monitoring*. Los Alamos National Lab, NM.
- Willmore, A. P. (1970) Electron and ion temperatures in the ionosphere. *Space Science Reviews*, 11(5), 607-670.
- Wylie, C. C. (1932) Sounds from meteors. *Popular Astronomy*, 40, 289.
- Zahnle, K. J. (1992) Airburst origin of dark shadows on Venus. *Journal of Geophysical Research: Planets* (1991–2012), 97(E6), 10243-10255.
- Zinn, J., O'Dean P. J., ReVelle, D. O. (2004) Leonid meteor ablation, energy exchange, and trail morphology." *Advances in Space Research* 33.9 (2004): 1466-1474.

## Chapter 2

### 2. Shock Waves

*No man is wise enough by himself.*

– Titus Maccius Plautus (254 BC - 184 BC)

Fundamentally, observations of meteor infrasound are possible due to hypersonic shock production during the ablation phase of the meteoroid. Here we review general characteristics of shocks in the atmosphere with emphasis on aspects relevant to meteor infrasound.

#### 2.1 A Brief Introduction to Shock Waves

Shock waves can be generated in all four states of matter. Gyözy Zemplén provided an operational definition of a shock in 1905: *“A shock wave is a surface of discontinuity propagating in a gas at which density and velocity experience abrupt changes. One can imagine two types of shock waves: (positive) compression shocks which propagate into the direction where the density of the gas is a minimum, and (negative) rarefaction waves which propagate into the direction of maximum density”* (Krehl, 2001).

Shock waves in the atmosphere are produced by a number of sources, both of anthropogenic and natural origin. Examples of the former are explosions (nuclear, chemical), supersonic craft, re-entry vehicles, and exploding wires, while examples of the latter are volcanic explosions, lightning and meteors. The intensity of a shock wave can be divided into two categories: the weak shock regime (waves of small, but finite pressure amplitude) and the strong-shock regime (waves of large pressure amplitude) (Krehl, 2009 and references therein). These are defined in terms of shock strength ( $\zeta = p/p_0$ ), or the pressure ratio across the shock front. In the strong shock regime  $\zeta \gg 1$  and shocks propagate supersonically displaying highly non-linear effects. In the weak shock regime,  $\zeta \sim 1$  (or barely exceeds 1), and shocks move at the speed of sound (Sakurai,

1964; Krehl, 2009; Needham, 2010). It is in the weak-shock regime that the signal can be treated as nearly linear (Sakurai, 1964). It is also convenient to define the strength of a shock wave with the Mach number, a dimensionless quantity which represents the ratio between the shock (or an object's) velocity ( $v$ ) and the velocity (ambient speed of sound or  $v_a$ ) with which a weak acoustic disturbance would travel in the undisturbed fluid (e. g. Hayes and Probstein, 1958; ReVelle, 1974; Emanuel, 2000):

$$M_a = \frac{v}{v_a} \quad (2.1)$$

The earliest imagery of meteor-like shocks was first made by Ernst Mach and Peter Salchner (Figure 2.1) (Hoffmann, 2009; Krehl, 2009 and references therein).

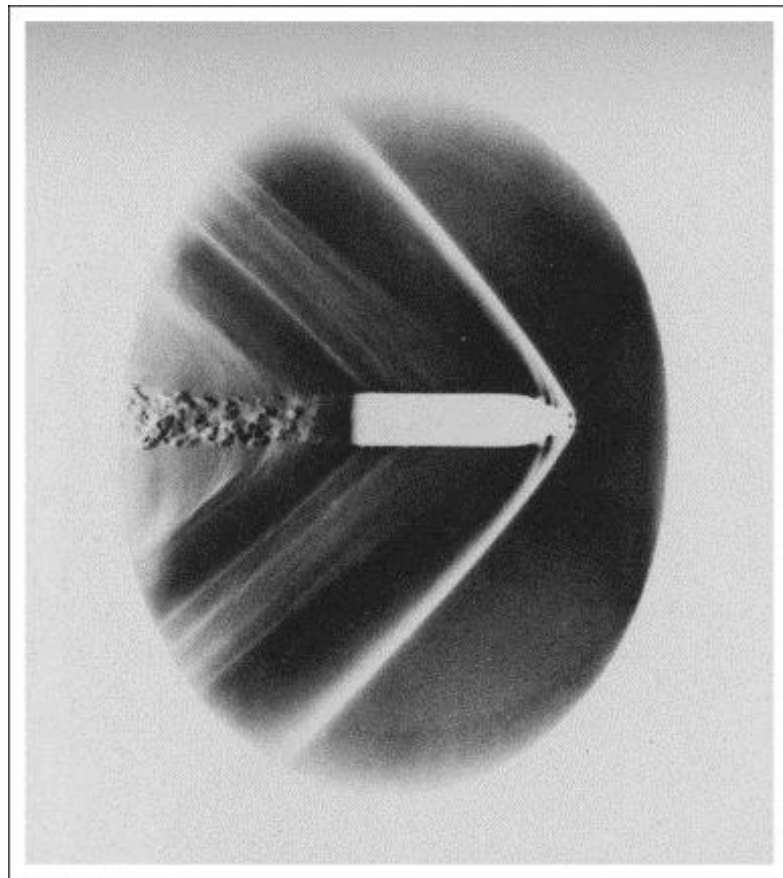


Figure 2.1: The shock wave phenomena captured by Ernst Mach and Peter Salchner in 1896 using schlieren photography (Hoffmann, 2009 and references therein).

The pressure-time behaviour of an initially small disturbance may grow in nonlinear acoustics into a significant distortion over many thousands of wavelengths due to a number of cumulative, long duration evolutionary processes (Krehl, 2009). In shock wave physics, the waveform is confined to a single pulse (Sakurai, 1964), which at some distance from the source take on the ubiquitous N-wave behaviour (DuMond et al, 1946) associated with sonic booms (Figure 2.2).

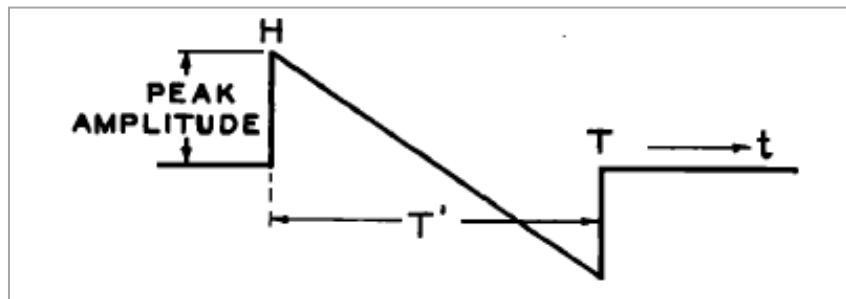


Figure 2.2: N wave pressure vs. time (from DuMond et al., 1946) waveform representing a typical sonic boom signature.

Landau (1945) showed that cylindrical and spherical N-waves should decay more rapidly than predicted by geometrical spreading and elongate as they travel away from the source. The second-order weak nonlinear effects are the cause of the wave elongation (or increase in the wave period) and enhanced decay (Wright, 1983; Maglieri and Plotkin, 1991), as shown in Figure 2.3. The same result was independently obtained by DuMond et al. (1946), albeit by a different method. DuMond et al. (1946) also attached the term N-wave to the resultant waveform as it resembles the capital letter “N” (Figure 2.2).

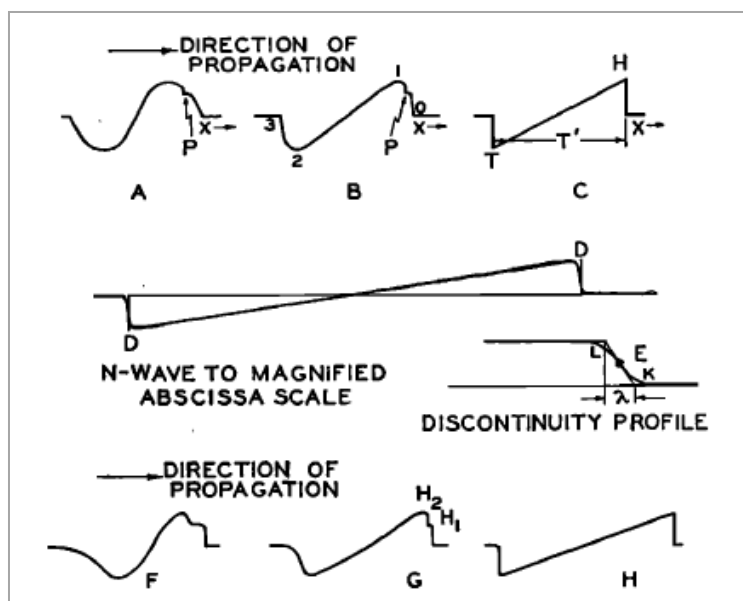


Figure 2.3: Evolution of slightly non-linear wave forms into N-waves (from DuMond et al., 1946).

A number of natural sources, such as thunder and meteors, generate shock waves in the form of a blast wave in the near field (Krehl, 2009). While the term shock wave is used in a more general context, a blast wave (Figure 2.4) is a shock wave in the air, such that it is accompanied by a strong wind (indicating a high dynamic pressure) as felt by an observer. Blast waves always propagate at supersonic velocity and at a sufficiently large distance from the source approach spherical geometry (Kinney and Graham, 1985; Krehl, 2009). Blast waves are characterized by a steep pressure rise time or shock intensity (or peak over pressure) and have a finite duration (usually defined as the length of the positive phase). The air blast produces an impulse per unit area resulting from its overpressure (Kinney and Graham, 1985), and if the blast wave is sufficiently strong, the air behind it may be accelerated to high velocities, creating a strong wind which in turn creates a dynamic pressure on objects in its path producing destructive effects collectively termed blast damage (Kinney and Graham, 1985; Krehl, 2009). Energetic bolide events are capable of producing significant blast damage on the ground, as demonstrated by the recent bolide over Chelyabinsk (Brown et al., 2013). At larger distances away from the source, however, the blast wave undergoes distortion and may propagate along multiple paths resulting in a more complicated waveform (Figure 2.5).

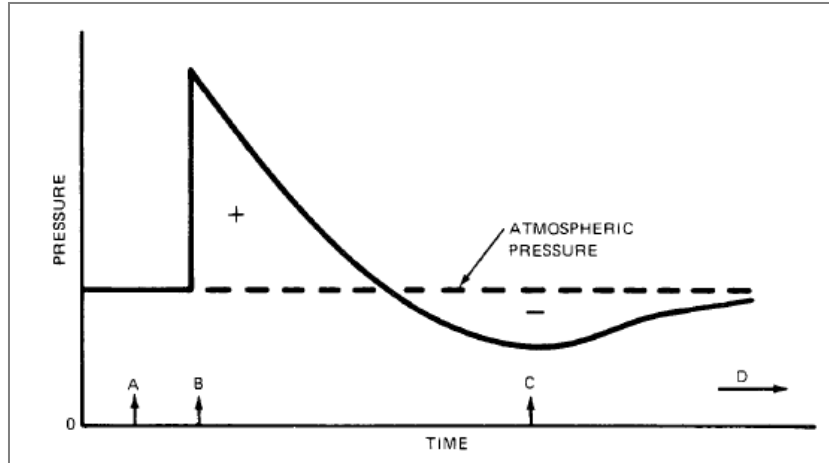


Figure 2.4: Shock wave pressure vs time (from Kinney and Graham, 1985) representing a typical blast wave signature.

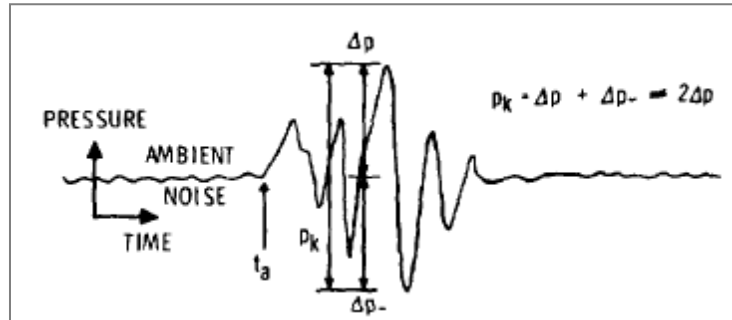


Figure 2.5: Typical explosion wave pressure-time signature at long range (from ANSI, 1983). Distortion effects as well as multi-pathing affect the appearance of the waveform some distance from the source.

The complex mathematical problem of wave propagation nonlinearity was resolved using the similarity principle (Sedov, 1946; Taylor, 1950), in which the number of independent variables are decreased, such that a set of fundamental partial differential equations is reduced to ordinary differential equations, while retaining the essential nature of the nonlinear behaviour (Sakurai, 1964; Sachdev, 2004). The problem of shock waves and the infrasound produced by meteors has been studied over the past several decades; however, compared to other problems of shock dynamics, not as extensively. Generally, an object moving at supersonic/hypersonic speeds will generate a conical bow shock as shown in Figure 2.6, where the Mach angle ( $\eta$ ) is defined as:

$$\eta = \sin^{-1} (1/M) \quad (2.2)$$



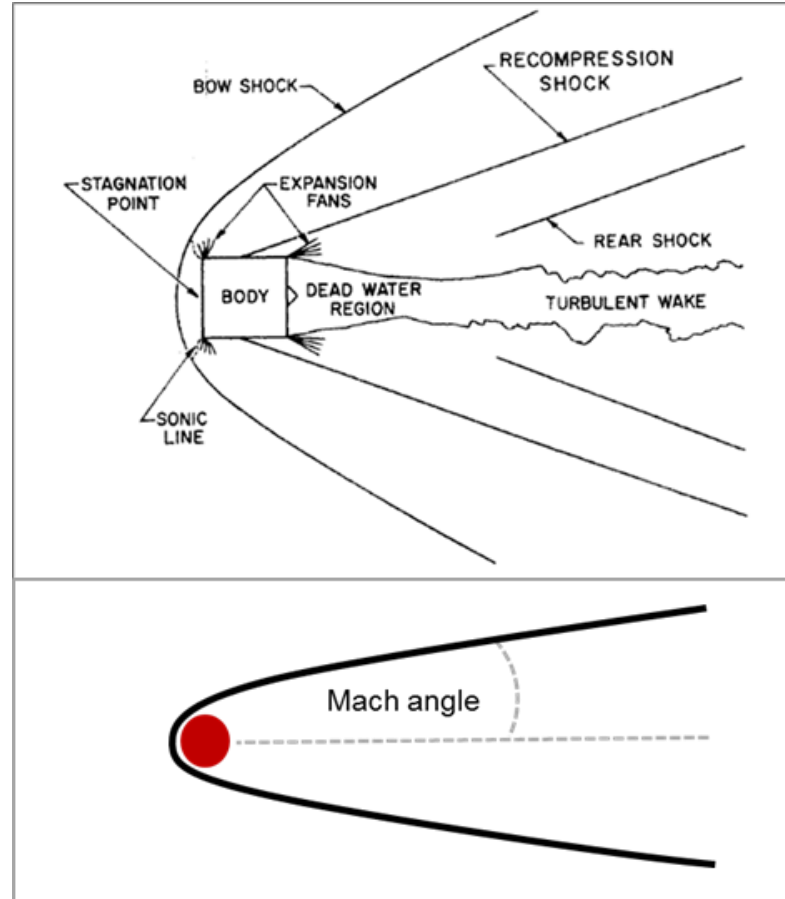


Figure 2.6: Top: Sketch of the flow field of a circular cylinder with a flat face forward in air at  $M = 3$  (from Hayes and Probstein, 1959). Bottom: Meteoroids produce a very narrow Mach cone and therefore a narrow Mach angle.

Meteoroids propagate through the Earth's atmosphere at high Mach numbers; from  $\sim 35$  up to 270 (e.g. Boyd, 1998) thereby producing a very narrow Mach cone ( $\eta < 1.7^\circ$ ), which can be approximated as a cylinder and has led to the concept of a meteor shock being equivalent to an instantaneous cylindrical line source charge (Tsikulin, 1970; ReVelle, 1976).

In the early 1950s, Whitham (1952) developed the F-function, a novel approach in treating the flow pattern of shock signatures generated by supersonic projectiles, now widely used in supersonics and classical sonic boom theory (e.g. Maglieri and Plotkin, 1991). It was realized early on that the F-function offers excellent correlation between

experiment and theory for low Mach numbers (up to  $M = \sim 3$ ), but was not as successful at hypersonic speeds (e.g. Carlson and Maglieri, 1972; Plotkin, 1989). The Whitham F-function theory has been recently applied to meteor shocks (Haynes and Millet, 2013), but detailed observational validation for meteor infrasound has not yet been obtained. We note, however, that this approach offers another theoretical pathway to predicting meteor infrasound, though we do not explore it further in this thesis.

## **2.2 Cylindrical Line Source Model of Meteoroid shocks: ReVelle's Model**

Early work on cylindrical shock waves during the 1940s and onward was done in connection with exploding wires (Sakurai, 1964; Plooster, 1968; 1970) and lightning (Jones et al., 1968; Few, 1969; Few, 1974). This theoretical and observational machinery was subsequently applied to meteoroids (e.g. Tsikulin, 1970; ReVelle, 1974; 1976). Following Lin (1954), Sakurai (1964), Few (1969), Jones et al. (1968), Plooster (1968; 1970) and Tsikulin (1970), ReVelle (1974; 1976) developed an analytic blast wave model of the nonlinear disturbance initiated by an explosive line source (meteor shock); this will be described in detail for the remainder of this chapter and where we draw extensively on the original treatment of ReVelle (1974).

Physically, as a meteoroid penetrates deeper into the denser regions of the atmosphere, stagnation pressure builds up (Figure 2.6) due to air molecules piling up in front of the body. If this stagnation pressure exceeds the internal strength of the meteoroid, gross fragmentation (or multiple fragmentation events) may occur, resulting in more complicated blast wave geometry, voiding the applicability of the cylindrical blast wave theory. For the cylindrical blast wave analogy to hypersonic flow to be valid (Pan and Sotomayer, 1972), certain conditions, in addition to  $M \gg 1$ , must be satisfied.

First, the energy release must be instantaneous, which is a good approximation for meteoroids which must encounter the Earth with  $v > 11$  km/s. Second, the cylindrical line source approximation is only valid if  $v \gg c_s$  (the Mach angle still has to be very small

many meteoroid diameters behind the body) and  $v = \text{constant}$  (Tsikulin, 1970). Therefore if there is significant deceleration ( $v < 0.95v_{\text{entry}}$ ) and strong ablation, the above criteria for the conditions necessary for the similarity principle in the cylindrical blast wave theory are not met (Bronshten, 1964; ReVelle, 1974; 1976). In this model, the line source is also considered to be in the free field, independent of any reflections due to finite boundaries, such as topographical features (ReVelle, 1974).

The cylindrical line shock decays to infrasonic waves which propagate to the ground as shown in Figure 2.7. Here the cylindrical line source is represented by a series of closely spaced discrete points. The shock wave expands radially outward in all directions away from the meteor trail (inset, Figure 2.7a).

The coordinate system to describe the motion and trajectory of the meteoroid, as originally developed by ReVelle (1974; 1976), is shown in Figure 2.8. The plane of meteoroid entry is referred to as the plane of entry. In this coordinate system, the variables are as follows:

$\varphi$  = azimuth angle of the meteoroid heading

$\varphi'$  = azimuth angle of a given infrasonic ray outside the entry plane

$\Delta\varphi = |\varphi - \varphi'|$  = infrasound ray deviation from the plane of entry ( $\Delta\varphi = 0$  in the plane of entry,  $\Delta\varphi = \pi/2$  out of the entry plane, i.e. purely horizontal)

$\theta$  = entry elevation angle from the horizontal ( $\theta = \pi/2$  is vertical entry)

$\varepsilon$  = nadir angle of the infrasonic ray with respect to the local vertical,  $\varepsilon \geq \theta$  ( $\varepsilon = 0$  is vertically downward,  $\varepsilon = \theta$  in the plane of entry), always viewed in a plane perpendicular to the plane of entry. ReVelle (1974) originally defined  $\varepsilon$  as zenith angle pointing downward.

$x$  = the distance between the point along the trail and the observer in units of blast radii (see definition later, equation (2.9)).

Azimuth angles, as viewed from the top looking downward, are measured clockwise from North. Other treatments (e.g. Edwards (2010)) have not always correctly and consistently defined these quantities relative to the original definitions given in ReVelle (1974).

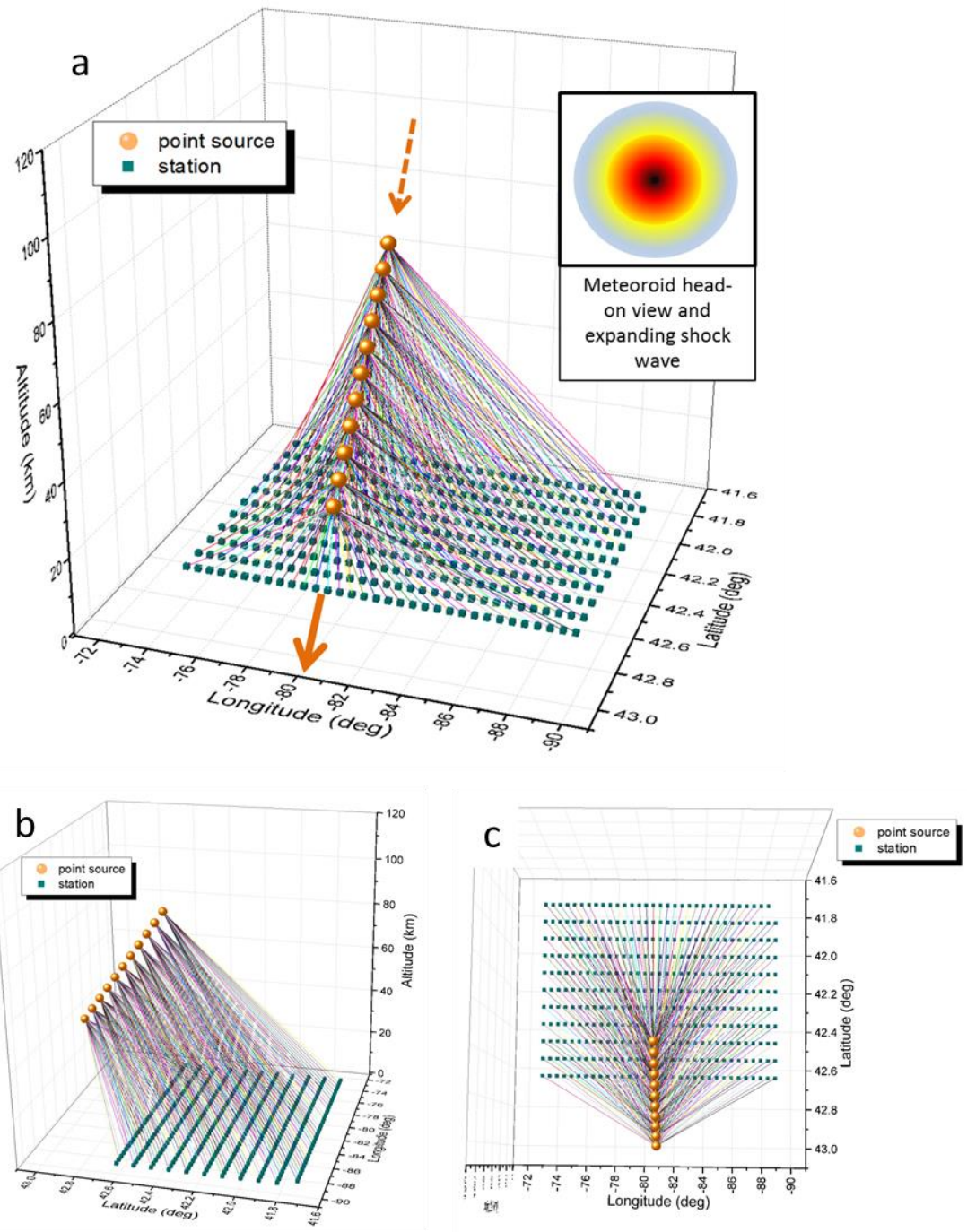


Figure 2.7: (a) Main figure: A simplified diagram depicting the meteoroid moving downward in the direction shown by the arrow. The lines are simulated infrasound rays reaching a grid of observers at the ‘ground’ (small squares). Only a limited number of distinct rays are shown for better visualization. Inset: The head-on view of the meteoroid (black dot in the centre) with the outward expanding shock front (the blue edge

boundary) with cylindrical symmetry. The color contours represent density. (b) Side view. (c) Top down view.

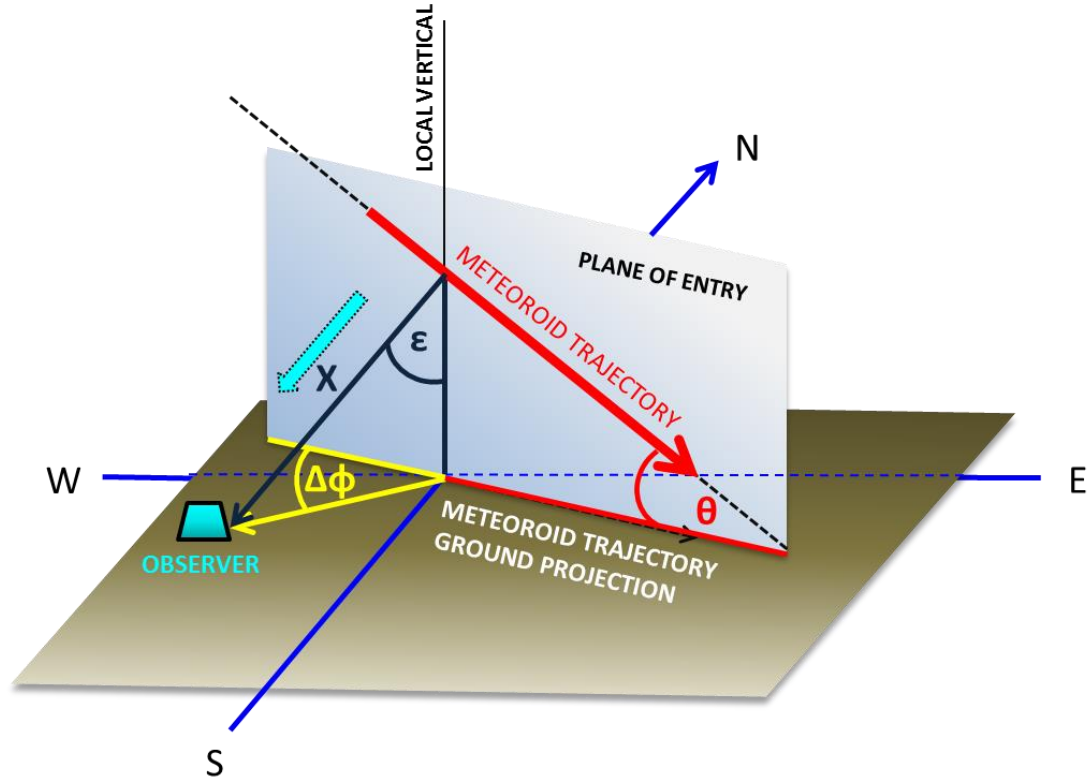


Figure 2.8: The coordinate system as originally defined by ReVelle (1974; 1976). The meteoroid trajectory is within the vertical entry plane. The variable  $x$  (eq. 2.9) refers to the distance between the point along the trail and the observer.

The relationship between the nadir angle ( $\epsilon$ ), entry elevation angle ( $\theta$ ) and ray deviation angle ( $\Delta\phi$ ) is as follows:

$$\epsilon = \tan^{-1} \left[ \left( 1 - \frac{2\Delta\phi}{\pi} \right) \cot \theta \right]^{-1} \quad (2.3)$$

$$\epsilon \neq 0; \theta \neq \frac{\pi}{2}; \epsilon \geq \theta$$

and

$$\Delta\phi = \frac{\pi}{2} (1 - \tan\theta \cot\epsilon) \quad (2.4)$$

In this model, only those rays which propagate downward (Figure 2.9, Figure 2.10) and are direct arrivals are considered. The requirement of direct arrival limits the source-observer distance to be less than 300 km. Only part of the shock generated along the trajectory will reach the observer; however, for certain propagation conditions no paths at all may be available between the source and the receiver. Hence meteors which produce infrasound may go undetected at any given receiver due to such effects

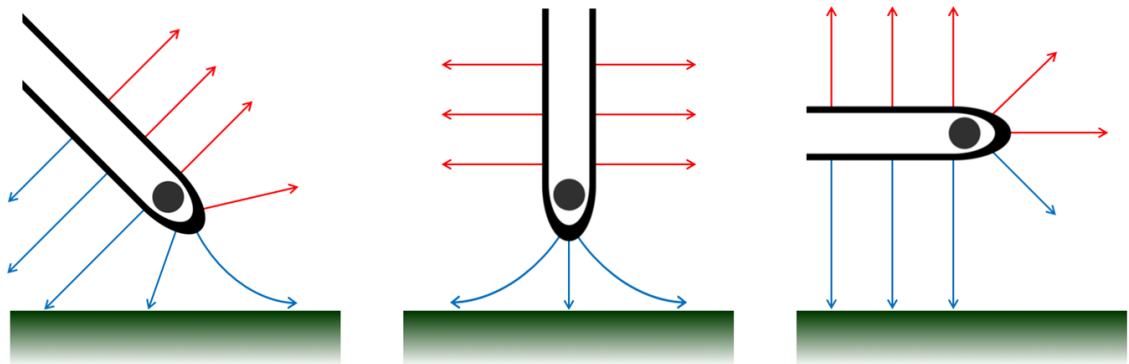


Figure 2.9: A pictorial representation of the cylindrical line source and possible meteoroid trajectory orientations. The middle and far right box show extreme orientations, such as a head on collision, and an Earth grazer, respectively. The red arrows represent those rays which are directed away from the ground – these will not form the primary hypersonic boom corridor, but may get reflected by the upper atmosphere and return in the form of the secondary sonic boom. The blue lines depict the direct path. Most of these rays are expected to reach the ground, given the existence refractive paths.

Once formed, the shock wave generated by a meteoroid is highly nonlinear, propagating outward at supersonic speed and absorbing the ambient air into the blast wave. The relaxation (or blast) radius  $R_0$  is the radius of the volume of the ‘channel’ that can be generated if all the explosion energy is used in performing work ( $pV$ ) on the surrounding atmosphere, at ambient pressure ( $p_0$ ) (e.g. Tsikulin, 1970):

$$R_0 = \left( \frac{E_0}{p_0} \right)^{1/2} \quad (2.5)$$

Here,  $E_0$  is the finite amount of energy deposited by the meteoroid per unit length, and  $p_0$  is the ambient hydrostatic atmospheric pressure (Sakurai, 1964; ReVelle, 1974). The blast radius, however, is expressed in a slightly different way by various authors, as shown in Table 2.1.

Table 2.1: Examples of expressions for  $R_0$  as defined by various authors. It should be remarked that all of these are fundamentally the same except the proportionality constant, leading to a maximum difference of a factor of 3.53 (ReVelle, 1974).

Blast Radius Definition		Author
$R_0 = \left(\frac{E_0}{\pi p_0}\right)^{1/2}$	(2.6a)	Few (1969)
$R_0 = \left(\frac{E_0}{\gamma b p_0}\right)^{1/2}$	(2.6b)	Jones et al. (1968) Plooster (1970) $b = 3.94$ and $\gamma = 1.4$
$R_0 = \left(\frac{E_0}{2\pi p_0}\right)^{1/2}$	(2.6c)	Sakurai (1964)
$R_0 = \left(\frac{E_0}{p_0}\right)^{1/2}$	(2.6d)	Tsikulin (1970) <i>standard definition</i>
$R_0 = \left(\frac{2E_0}{p_0}\right)^{1/2}$	(2.6e)	Tsikulin (1970) <i>modified definition</i>

For a non-fragmenting, single body meteoroid, the energy can also be written in terms of the drag force as (ReVelle, 1974):

$$E_0 = \frac{1}{2} \rho_0 v^2 C_D S \quad (2.7)$$

where  $C_D$  is the wave drag coefficient and  $S$  is meteoroid cross-sectional area.

Since the blast radius is directly related to the drag force, it can also be expressed as a function of Mach number and the meteoroid diameter:

$$R_0 \simeq M d_m \quad (2.8)$$

From the cylindrical blast wave similarity solution, the scaled distance ( $x$ ) from the trajectory is given by:

$$x = \frac{R}{R_0} \quad (2.9)$$

where  $R$  is the actual radius of the shock front at a given time. While the similarity solutions to the equations of hydrodynamics are applicable within the strong shock region, they are not valid for  $x < \sim 0.05$ , mainly due to severe nonlinear non-equilibrium processes, annulling the notion of local thermodynamic equilibrium, and subsequently voiding the existence of a classical equation of state. For  $x > 0.05$ , the size of the meteoroid no longer has a significant effect on blast wave propagation (Tsikulin, 1970; ReVelle, 1974). Once the wave reaches the state of weak nonlinearity (where the pressure at the shock front  $p_s \sim p_0$ ), using the Hugoniot relation between the overpressure ( $\Delta p/p_0$ ) and the shock front Mach number ( $M_a$ ) (Lin, 1954):

$$\frac{p}{p_0} = \left( \frac{2\gamma}{\gamma + 1} \right) M_a^2 \quad (2.10)$$

the shock front velocity approaches the local adiabatic velocity of sound ( $M_a \rightarrow 1$ ). When  $\Delta p/p_0 \lesssim 1$  (at  $x \gtrsim 1$ ), weak shock propagation takes place and geometric acoustics becomes valid (Jones et al., 1968; ReVelle, 1974). Moreover, beyond  $x = 1$ , steady state theory is applicable (Groves, 1963). The linear sound theory is derived under the assumption that:

$$\frac{\Delta p}{p_0} \rightarrow 0 \quad (2.11)$$

$$\frac{p_s}{p_0} \rightarrow 1 \quad (2.12)$$

In the strong shock regime, where  $p_s/p_0 > 10$ , the relationship between the shock front pressure and the ambient atmospheric pressure is given by (Jones et al., 1968):

$$\frac{p}{p_0} = \frac{\gamma}{2(\gamma + 1)} \frac{1}{x^2} \quad (2.13)$$

It should be noted that the main difference in the terms  $p_s/p_0$  and  $\Delta p/p_0$  is simply the convention of writing and describing the strong shock regime ( $p_s \gg p_0$ ) and the weak



shock regime ( $p_s \leq p_0$ ), respectively. As the shock propagates outward, it will reach the point where the strong shock similarity principle is no longer valid. Following Jones et al. (1968):

$$\lim_{x \rightarrow 0} f(x) = \frac{2(\gamma + 1) \Delta p}{\gamma p_0} \rightarrow x^{-2} \quad (2.14)$$

and

$$\lim_{x \rightarrow \infty} f(x) = \left(\frac{3}{8}\right)^{-3/5} \left\{ \left[ 1 + \left(\frac{8}{3}\right)^{8/5} x^2 \right]^{3/8} - 1 \right\}^{-1} \rightarrow x^{-3/4} \quad (2.15)$$

In the limit as  $x \rightarrow 0$  (eq.2.14), where  $\Delta p/p_0 > 10$ , attenuation is quite rapid ( $x^{-2}$ ), transitioning to  $x^{-3/4}$  as  $x \rightarrow \infty$ , where  $\Delta p/p_0 < 0.04$  (or  $M = 1.017$ ) (Jones et al., 1968). Both Landau (1945) and DuMond et al. (1946) obtained that the shock strength decay in the axisymmetric case clearly follows  $x^{-3/4}$ . Due to elevated temperature and forward velocity of the positive-pressure pulse, the wave steepens (Landau, 1945), becoming a shock resembling the well-known N-wave pressure signature in the far-field. The function  $f(x)$  can be slightly modified using constants  $Y_C$  and  $Y_D$  stemming from work of Plooster (1968).  $Y_C$  is Plooster's adjustable parameter (ReVelle, 1976) which defines the region where the nonlinear to weak shock transition occurs, while  $Y_D$  describes the efficiency with which cylindrical blast waves are generated as compared to the results of an asymptotic strong shock as numerically determined by Lin (1954). The variables  $Y_C$  and  $Y_D$  are the same as the variables  $C$  and  $\delta$ , respectively, in Plooster (1970) and ReVelle (1974; 1976); however they are renamed here to avoid confusion with other unrelated variables used in this work. The sensitivity to the final solutions in using different values of these parameters will be discussed later. For now we set,  $Y_C = Y_D = 1$ .

Taking advantage of both equations (2.14) and (2.15), and using results from experiments (Jones et al., 1968; Tsikulin, 1970), the overpressure (for  $x \geq 0.05$ ) can now be expressed as:

$$\frac{\Delta p}{p_0} = \frac{2(\gamma + 1)}{\gamma} \left(\frac{3}{8}\right)^{-\frac{3}{5}} \left\{ \left[ 1 + \left(\frac{8}{3}\right)^{\frac{8}{5}} x^2 \right]^{\frac{3}{8}} - 1 \right\}^{-1} \quad (2.16)$$

The limits within which this expression is applicable are  $0.04 \leq \Delta p/p_0 \leq 10$  (Jones et al., 1968). Note that this was incorrectly stated in Edwards (2010) as  $\Delta p/p_0 \geq 10$ . The above expression can also be written as:

$$\frac{\Delta p}{p_0} \cong \frac{2\gamma}{\gamma + 1} \left[ \frac{0.4503}{(1 + 4.803x^2)^{3/8} - 1} \right] \quad (2.17)$$

This implies that  $\Delta p \cong 0.0575p_0$  at  $x = 10$ . The assumption in the expressions above (equation 2.16 and equation 2.17) is that the ambient air density is uniform, which, in reality, is not completely true for the atmosphere proximal to the meteoroid in flight. The shock wave, as it travels from high altitudes down to the observer, encounters ambient pressures from low to high densities over many scale heights. Therefore, a correction term will need to be applied at a later point to account for variations in the atmospheric pressure between the source and the observer.

After the shock wave has travelled the distance of approximately  $10R_0$ , where the disturbance is still relatively strong, but remains in the weak shock regime, its fundamental period ( $\tau_0$ ) can be related to the blast radius via:

$$\tau_0 = \frac{2.81 R_0}{c_a} \quad (2.18)$$

where  $c_a$  is the local ambient thermodynamic speed of sound. The factor 2.81 at  $x = 10$  was determined experimentally (Few, 1969) and numerically (Plooster, 1968). The fundamental frequency ( $f_0$ ) is then simply  $1/\tau_0$ . The frequency of the wave at maximum amplitude of the pressure pulse as recorded by the receiver is referred to as the ‘dominant’ frequency (ReVelle, 1974). The choice of  $10R_0$  is somewhat arbitrary but it had arisen from the notion that nonlinear propagation effects may still be important at some distance from the origin (e.g. Yuldashev et al., 2010). It is also common usage to

begin model calculations at  $10R_0$  ( $x = 10$ ) under the assumption that the shock is clearly no longer in the strong shock regime.

From these relations, it should be clear that large meteoroids produce large blast radii, long fundamental periods and small fundamental frequencies. As a result given favourable infrasonic ray propagation paths they are more likely to produce infrasound detectable at the ground. As previously described, due to nonlinear effects, this fundamental period will lengthen as the shock propagates outward, eventually forming into an N-wave after it has travelled a certain distance from the source, as predicted by sonic boom theory (Landau, 1945; DuMond et al, 1946; Carlson and Maglieri, 1972; Maglier and Plotkin, 1991).

For sufficiently large  $R$  and assuming weakly nonlinear propagation, the line source wave period for ( $x \geq 10$ ) is predicted to increase with range as:

$$\tau(x) = 0.562 \tau_0 x^{1/4} \quad (2.19)$$

The above will be valid as long as the wave remains in the weak shock regime. Figure 2.10 shows the geometry of the meteoroid as viewed head-on, with the strong and weak shock regimes and propagation considerations.

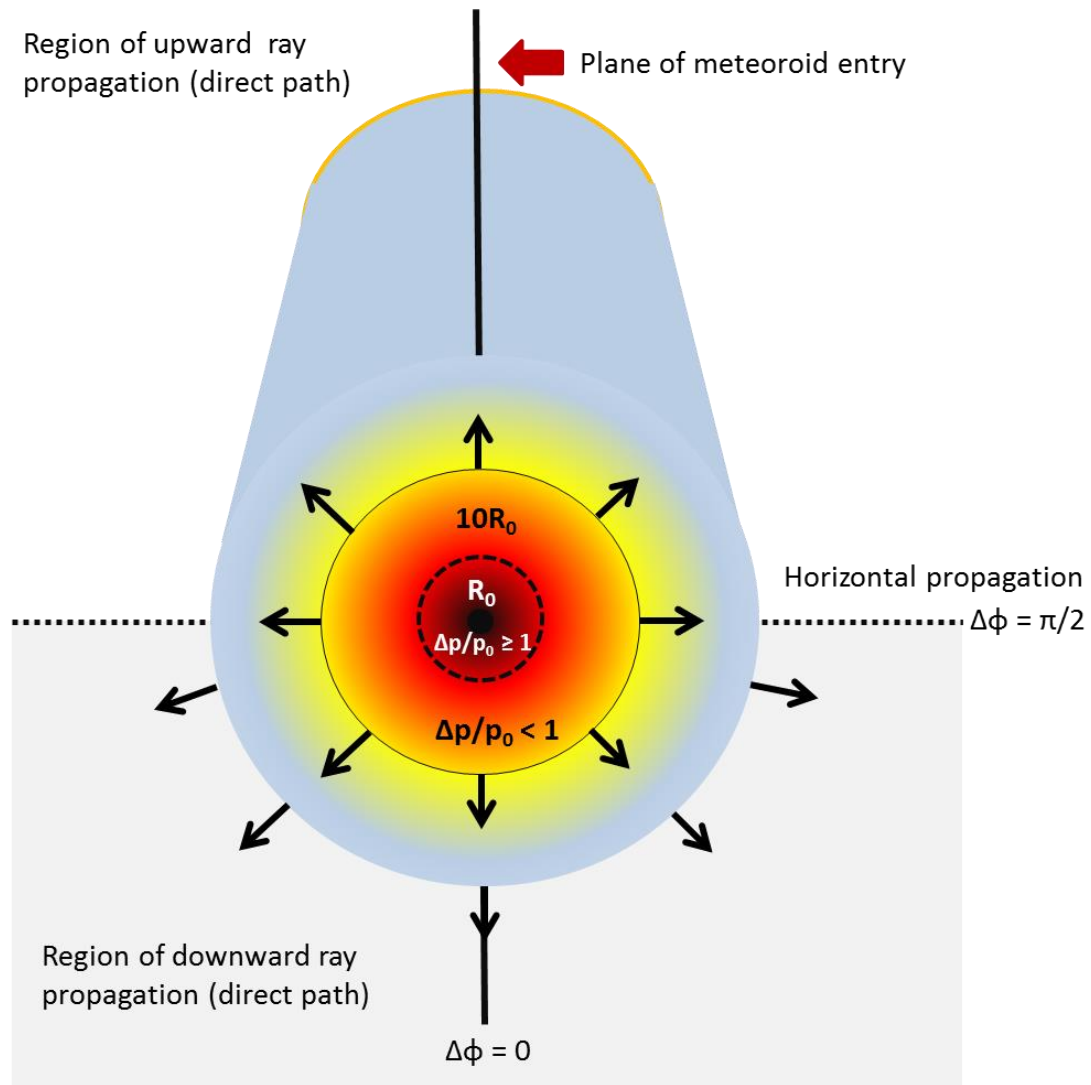


Figure 2.10: A head on view of the meteoroid. The grayed out area represents the region where the infrasonic rays will propagate downward and thus reach the observer via direct paths. Upward rays are not considered in this model. The plane of entry and infrasonic ray deviation angles are also shown.

Far from the source, the shape of the wave at any point will mainly depend on the two competing processes acting on the propagating wave – dispersion, which reduces the overpressure and ‘stretches’ the period; and steepening, which is the cumulative effect of small disturbances, increasing the overpressure (ReVelle, 1974) (Figure 2.11).

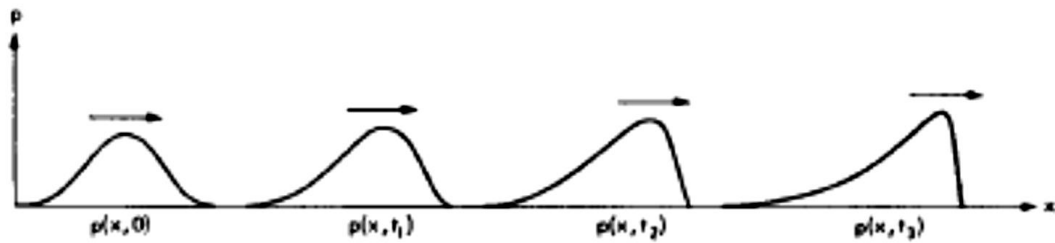


Figure 2.11: Development of a shock front from nonlinear effects (from Towne, 1967).

The precise transition, or the distortion distance, between the weak shock and linear regime is rather ambiguous. As per Sakurai (1964), the transition takes place when  $\Delta p/p_0 = 10^{-6}$ , while Morse and Ingard (1968) calculated the distortion distance ( $d_s$ ) to the ‘shocked’ state as:

$$d_s = \frac{c\tau}{5.38 \frac{\Delta p}{p_0}} \quad (2.20)$$

Towne (1967), however, defined the distortion distance ( $d'$ ) as the distance at which the acoustic period decays by 10%:

$$d' = \frac{\lambda}{20(\gamma + 1) \frac{\Delta \rho}{\rho_0}} = \frac{c\tau}{34.3 \frac{\Delta p}{p_0}} \quad (2.21)$$

Thus, from (2.20) and (2.21) it follows that:

$$d_s = 6.38 d' \quad (2.22)$$

$$d' > d_a \quad (2.23)$$

where  $d_a$  is the remaining propagation distance of the disturbance before it reaches the observer.

In the linear regime, equation (2.16) has to be modified to reflect the wave decay as  $x^{-1/2}$  (Officer, 1958) by applying the correction term  $x^{1/4}$  to the numerator. Since equation (2.23) assumes a straight source-observer path, an additional correction term, also needs

to be applied to account for a non-uniform (i.e. refracting) ray path (Pierce and Thomas, 1969), taking  $d_m \ll R_0 \ll H$  ( $M \gg 1$ ):

$$N^*(z) = \left( \frac{\rho(z)}{\rho_z} \right)^{1/2} \frac{c(z)}{\bar{c}_z} N_c \quad (2.24)$$

$$\bar{c}_z = \frac{\int_{z_{obs}}^{z_z} c(z) dz}{z_z - z_{obs}} \quad (2.25)$$

$$N_c < 1 + \frac{z_z}{12H} \quad (2.26)$$

where  $N_c$  is the nonlinear propagation correction term,  $c_{obs}$ ,  $\rho_{obs}$ ,  $z_{obs}$  are the sound speed, atmospheric density and altitude (0 if at the ground) at the observer, respectively, and  $\rho_z$  and  $z_z$  are the atmospheric density and altitude at the source,  $H$  is the scale height of the atmosphere, while  $\bar{c}_z$  is the average speed of sound between the source and the observer. Typical values for  $N_c$  as a function of height are:

$$N_c < \begin{cases} 2.1 (< \sim 100 \text{ km}) \\ 1.55 (< 50 \text{ km}) \end{cases} \approx 1$$

$N_c$  should be included only while weak shock effects are important. However, the correction term  $N_c$  is usually very small ( $\sim 1$  as shown above); the uncertainty in density is many more orders of magnitude greater than  $N_c$  over vertical paths (ReVelle, 1974). For simplicity, ReVelle (1974) set  $N_c = 1$  since his results coming from testing actual values of  $N_c$  and  $N_c = 1$  demonstrated that the correction factor indeed plays a negligible role in error estimates.

While the previous section focused on the shock period and waveform shape we now turn to the expected overpressure (amplitude) behaviour. For shock amplitudes, Morse and Ingard (1968) showed that the effects of nonlinear terms compared to viscous terms are not negligible until  $\Delta p$  is sufficiently small so that the mean free path becomes much greater than displacements of particles due to wave motion. Thus, the following equation

applies to ‘shocked’ acoustic waves (Morse and Ingard, 1968) at distances far from the source:

$$\frac{dp_s}{ds} = -\left(\frac{\gamma + 1}{\gamma^2 \lambda}\right) \left(\frac{\rho_0 c^2}{p_0^2}\right) p_s^2 - \left(\frac{3\delta}{2\rho_0 c \lambda^2}\right) p_s \quad (2.27)$$

where  $p_s$  is the pressure amplitude of the ‘shocked’ disturbance,  $\lambda$  is the wavelength of the ‘shocked’ disturbance, and  $\delta$  is defined as:

$$\delta = 4 \left[ \frac{4}{3} \mu + \psi + K \left( \frac{\gamma - 1}{C_p} \right) \right] \quad (2.28)$$

Here  $\mu$  is the ordinary (shear) viscosity coefficient,  $\psi$  is the bulk (volume) viscosity coefficient,  $K$  is thermal conductivity of the fluid, while  $C_p$  is the specific heat of the fluid at constant pressure. The term  $p_s^2$  in equation (2.27) is due to viscous and heat conduction losses across entropy jumps at the shock fronts, while  $p_s$  is due to the same mechanisms, but between the shock fronts (ReVelle, 1974). A more compact version of equation (2.27), represented in terms of coefficients A and B is given by:

$$dp_s = -(Ap_s^2 + Bp_s)ds \quad (2.29)$$

$$A(z) = \frac{\gamma + 1}{\gamma \lambda(z) p_0} \quad (2.30)$$

$$B(z) = \frac{3\delta}{2\rho_0(z)c(z)\lambda(z)^2} \quad (2.31)$$

$$\gamma H \gg \lambda(z); \quad \rho_0(z)c(z)^2 = \gamma p_0 \quad (2.32)$$

The above expression (eq. 2.32) is a valid approximation if the density ratio across the shock front does not significantly exceed a value of unity, which is applicable in the regime far from the source, where  $\rho/\rho_0 \leq 1.5$  (for  $x \geq 1$ , Plooster, 1968). It should be

remarked that the original weak shock treatment was developed for an isothermal atmosphere; however, a more realistic, non-isothermal case is shown here.

As mentioned earlier, distortion and dispersion are two competing mechanisms which affect the wave shape; however, an assumption implicit in this theory is that the wave shape is known during propagation (i.e. approximately sinusoidal). Now, integration over the path length ( $s$ ) leads to the solution to equation (2.27):

$$\frac{\Delta p}{\Delta p_z} \left( \frac{\Delta p + \frac{B}{A}}{\Delta p_z + \frac{B}{A}} \right) = \exp \left( - \int_{z_{obs}}^{z_z} \frac{B}{\cos \varepsilon} dz \right) \quad (2.33)$$

where it is assumed that  $z_z \geq z_0$ . The generalized form of the damping factor, or atmospheric attenuation, for a weak shock in a non-isothermal atmosphere (ReVelle, 1974) is given by:

$$D_{ws}(z) = \frac{\Delta p_t}{\Delta p_z} = \frac{\frac{B(z)}{A(z)} \exp \left( - \int_{z_z}^{z_t} \frac{B(z)}{\cos \varepsilon} dz \right)}{\Delta p_z \left[ 1 - \exp \left( - \int_{z_z}^{z_t} \frac{B(z)}{\cos \varepsilon} dz \right) \right] + \frac{B(z)}{A(z)}} \quad (2.34)$$

where  $\Delta p_z$  is the overpressure at the source height,  $\Delta p_t$  is the overpressure at transition height  $z_t$ . When the condition given in equation (2.23) is satisfied ( $d' > d_a$ ), the absorption decay law for a plane sinusoidal wave, given by Evans and Sutherland (1970) takes the following form:

$$\frac{\Delta p}{\Delta p_z} = \exp(-\bar{\alpha} \Delta s) \quad (2.35)$$

where  $\Delta s$  is the total path length from the source ( $\Delta s \geq 0$ ), and  $\bar{\alpha}$  is the total amplitude absorption coefficient. In general:

$$\bar{\alpha} = \alpha_\mu + \alpha_K + \alpha_D + \alpha_{rad} + \alpha_{mol} \quad (2.36)$$

where  $\alpha_\mu$ ,  $\alpha_K$ ,  $\alpha_D$ ,  $\alpha_{rad}$ ,  $\alpha_{mol}$  are viscosity, thermal conductivity, diffusion, radiation (collectively referred to as Stokes-Kirchhoff loss) and molecular relaxation absorption



coefficients, respectively. Since diffusion losses have a very small contribution, only about 0.3% of the total (Evans et al., 1972; Sutherland and Bass, 2004),  $\alpha_D$  can be ignored (ReVelle, 1974). In his treatment, however, ReVelle (1974) also excluded the effects of  $\alpha_{rad}$  and  $\alpha_{mol}$ . Furthermore, the possible effects of turbulent scattering on wave amplitude are also excluded, even though it may at times be even more important than  $\alpha_{rad}$  and  $\alpha_{mol}$  for frequencies  $< 10$  Hz. A more modern treatment for atmospheric absorption can be found in Sutherland and Bass (2004). It should be remarked that molecular vibration by nitrogen will be dominant at very high altitudes ( $> 130$  km), thus for meteors (which ablate typically below 120 km) it can be neglected.

The functional form of the total amplitude absorption coefficient (Morse and Ingard, 1968) as a function of height is given as:

$$\bar{\alpha}(z) = \frac{\omega^2}{2\rho(z)c(z)^3} \left[ \frac{4}{3}\mu + \psi + K \left( \frac{\gamma - 1}{C_p} \right) \right] = \frac{\pi^2}{\rho(z)c(z)\lambda(z)^2} \left( \frac{\delta}{2} \right) \quad (2.37)$$

where  $\omega$  is the angular frequency of the oscillation ( $\omega = 2\pi f$ ). Therefore, the generalized form of ReVelle's (1976) damping function for a linear wave is given by:

$$D_l(z) = \frac{\Delta p_{obs}}{\Delta p_t} = \exp \left( - \int_{z_t}^{z_{obs}} \frac{\bar{\alpha}(z)}{\cos \varepsilon} dz \right) \quad (2.38)$$

Note that the integration limits in equation (2.38) are from the transition height (weak-to-linear) down to the observer. The final correction term, accounting for variations in atmospheric density (Pierce and Thomas, 1969) is as follows:

$$Z^*(z) = \frac{\rho_z}{\rho(z)} \left( \frac{c_z}{c(z)} \right)^2 \quad (2.39)$$

Before concluding this section, an additional comment should be made about the choice for initial amplitude ( $\Delta p_z$ ) by revisiting the coefficients  $Y_C$  and  $Y_D$ , mentioned earlier. Using data from exploding wires to evaluate the cylindrical line source, Plooster (1968; 1970) used these coefficients to match the experimental results.

The functional form of  $f(x)$  (equation 2.15) including  $Y_C$  and  $Y_D$  can be expressed as:

$$f(x) = \left(\frac{3}{8}\right)^{-3/5} Y_C^{-8/5} \left\{ \left[ 1 + \left(\frac{8}{3}\right)^{8/5} Y_C^{-8/5} Y_D^{-1} x^2 \right]^{3/8} - 1 \right\}^{-1} \quad (2.40)$$

A high value of  $Y_D$  implies that the rate of internal energy dissipation is low, thereby leaving more energy available for driving the leading shock (Plooster, 1968). Table 2.2 includes all values for  $Y_C$  and  $Y_D$  found for a variety of initial conditions (Plooster, 1968).

Table 2.2: A summary of initial conditions,  $Y_C$  and  $Y_D$  as found by Plooster (1968). The values for low density gas were not established (Plooster, 1968). The last column represents the values of  $\Delta p_z$  extrapolated to  $x = 10$ . It should be remarked that the published value of  $0.563 p(z)$  in ReVelle (1976) refers to the  $\Delta p_z$  at  $x = 1$ . \*The value of  $\Delta p_z$  as determined by Jones et al. (1968) is included for the sake of completeness.

Initial conditions		$Y_C$	$Y_D$	Nonlinear to weak shock transition	$\Delta p_z$ at $x = 10$
Line source	Constant density Ideal gas	0.70	1.0	$< 7$	$0.0805 p(z)$
Isothermal cylinder	Constant density Real gas	0.70	0.66	$< 7$	$0.0680 p(z)$
Isothermal cylinder	High density gas Ideal gas	0.95	1.61	$> 2$	$0.0736 p(z)$
Isothermal cylinder	Best fit to experimental data	0.95	2.62	$\geq 3$	$0.0906 p(z)$
Isothermal cylinder	Low density gas Ideal gas	no determination made		--	--
Lightning*	--	1.00	1.0	10	$0.0575 p(z)$

At very large distances from the cylindrical line source, where  $R \gg L$  (where  $L$  is the line source path length), the source will appear spherical in nature. It is also at these longer ranges that the wave structure is more dependent on atmospheric variations rather than line source characteristics (ReVelle, 1974).

Having reviewed the basic foundation of ReVelle`s cylindrical line source blast theory of meteors we note that the theory predicts expected amplitudes and periods given knowledge at the source of the energy released per unit path length and source height. Chapters 5 and 6 will be devoted to validating this theory with emphasis on areas where the theory produces robust results in agreement with observations and vice versa.

## References

- ANSI (1983) Estimating Airblast Characteristics for Single Point Explosion in Air, with a Guide to Evaluation of Atmospheric Propagation and Effects, American National Standards Institute, Acoustical Society of America
- Boyd, I. D. (1998) Computation of atmospheric entry flow about a Leonid meteoroid. *Earth, Moon, and Planets*, 82, 93-108.
- Bronshten, V. A. (1964) Problems of the movements of large meteoric bodies in the atmosphere. National Aeronautics and Space Administration, TT-F-247.
- Brown, P. G., Assink, J. D., Astiz, L., Blaauw, R., Boslough, M. B., Borovička, J., and 26 co-authors (2013) A 500-kiloton airburst over Chelyabinsk and an enhanced hazard from small impactors. *Nature*. 503, 238-241
- Carlson, H. W., Maglieri, D. J. (1972) Review of Sonic-Boom Generation Theory and Prediction Methods. *The Journal of the Acoustical Society of America*, 51, 675
- DuMond, J. W., Cohen, E. R., Panofsky, W. K. H., Deeds, E. (1946) A determination of the wave forms and laws of propagation and dissipation of ballistic shock waves. *The Journal of the Acoustical Society of America*, 18, 97.
- Edwards, W. N. (2010) Meteor generated infrasound: theory and observation. In *Infrasound monitoring for atmospheric studies* (pp. 361-414). Springer Netherlands
- Emanuel, G. (2000) Theory of Shock Waves, in *Handbook of Shock Waves*, Ben-Dor, G., Igra, O., Elperin, T. (Eds.). Three Volume Set. Academic Press.
- Evans, L. B., Bass, H. E., Sutherland, L. C. (1972) Atmospheric absorption of sound: theoretical predictions. *The Journal of the Acoustical Society of America*, 51, 1565.
- Evans, L. B., Sutherland, L. C. (1970) Absorption of sound in air, Wylie Labs Inc., Huntsville, Alabama, AD 710291
- Few, A. A. (1969) Power spectrum of thunder, *J. Geophys. Res.*, 74, 6926-6934
- Groves, G. V. (1963) Initial expansion to ambient pressure of chemical explosive releases in the upper atmosphere. *Journal of Geophysical Research*, 68(10), 3033-3047.
- Hayes, W., Probstein, R. F. (1959) *Hypersonic flow theory* (Vol. 5). Elsevier.
- Haynes, C. P., Millet, C. (2013) A sensitivity analysis of meteoric infrasound. *Journal of Geophysical Research: Planets*, 118(10), 2073-2082.
- Hoffmann, C. (2009) Representing difference: Ernst Mach and Peter Salcher's ballistic-photographic experiments. *Endeavour*, 33(1), 18-23.

- Jones, D. L., Goyer, G. G., Plooster, M. N. (1968) Shock wave from a lightning discharge. *J Geophys Res* 73:3121–3127
- Kinney, G. F., Graham, K. J. (1985) Explosive shocks in air. Berlin and New York, Springer-Verlag, 1985, 282 p., 1.
- Krehl, P. (2001) History of shock waves. In: (G. Ben-Dor et al.) Handbook of shock waves. Academic Press, New York; vol. 1, pp. 1-142.
- Krehl, P. O. (2009) History of shock waves, explosions and impact: a chronological and biographical reference. Springer.
- Landau, L. D. (1945) On shock waves at a large distance from the place of their origin, *Sov. J. Phys.*, 9, 496
- Lin, S. C. (1954) Cylindrical shock waves produced by instantaneous energy release. *J Appl Phys* 25:54–57
- Maglieri, D. J., Plotkin, K. J. (1991) Sonic boom. In *Aeroacoustics of Flight Vehicles: Theory and Practice. Volume 1: Noise Sources*, Vol. 1, pp. 519-561
- Morse P. M., Ingard K. U. (1968) *Theoretical Acoustics*, McGraw-Hill, New York.
- Needham, C. E. (2010) *Blast Waves, Shock Wave and High Pressure Phenomena*, Springer, pp. 339.
- Officer, C. B. (1958) *Introduction to the theory of sound transmission: With application to the ocean* (p. 284). New York: McGraw-Hill.
- Pan, Y. S., Sotomayer, W. A. (1972) Sonic boom of hypersonic vehicles, *AIAA J.*, /0, 550-551
- Pierce, A. D., Thomas, C. (1969) Atmospheric correction factor for sonic-boom pressure amplitudes, *Journal of the Acoustical Society of America*, 46, 1366-1380
- Plooster, M. N. (1968) *Shock Waves from Line Sources*, National Center for Atmospheric Research, Report TN, 1-93
- Plooster, M. N. (1970) Shock waves from line sources. Numerical solutions and experimental measurements. *Physics of fluids*, 13, 2665.
- Plotkin, K. (1989) Review of sonic boom theory, *AAIA 12th Aeronautics Conference*, April 10-12, 1989, San Antonio, TX, USA
- ReVelle, D.O. (1974) *Acoustics of meteors-effects of the atmospheric temperature and wind structure on the sounds produced by meteors*. Ph.D. Thesis University of Michigan, Ann Arbor.
- ReVelle, D.O. (1976) On meteor-generated infrasound. *Journal of Geophysical Research*, 81(7), 1217-1230.

- Sachdev, P. L. (2004) *Shock Waves & Explosions*. CRC Press.
- Sakurai, A. (1953) On the propagation and structure of the blast wave, I. *Journal of the Physical Society of Japan*, 8, 662.
- Sakurai, A. (1964) *Blast Wave Theory*, (No. MRC-TSR-497). Wisconsin Univ-Madison Mathematics Research Center.
- Sedov, L. I. (1946) Propagation of intense blast waves. *Prikl Mat Mekh*, 10, 241-250.
- Sutherland, L. C., Bass, H. E. (2004) Atmospheric absorption in the atmosphere up to 160 km. *The Journal of the Acoustical Society of America*, 115, 1012
- Taylor, G. (1950) The formation of a blast wave by a very intense explosion. I. Theoretical discussion. *Proceedings of the Royal Society of London. Series A, Mathematical and Physical Sciences*, 201(1065), 159-174.
- Towne, D.H. (1967) *Wave Phenomena*, Addison-Wesley Publications, Reading, Massachusetts
- Tsikulin, M. A. (1970) Shock waves during the movement of large meteorites in the atmosphere (No. NIC-Trans-3148). Naval Intelligence Command Alexandria VA Translation Div.
- Whitham, G. B. (1952) The flow pattern of a supersonic projectile. *Communications on pure and applied mathematics*. 5(3), 301-348
- Wright, W. M. (1983) Propagation in air of N waves produced by sparks. *The Journal of the Acoustical Society of America*, 73, 1948.
- Yuldashev, P., Ollivier, S., Averiyarov, M., Sapozhnikov, O., Khokhlova, V., Blanc-Benon, P. (2010) Nonlinear propagation of spark-generated N-waves in air: Modeling and measurements using acoustical and optical methods. *The Journal of the Acoustical Society of America*, 128, 3321.

## Chapter 3

### 3. An Estimate of the Terrestrial Influx of Bolides From Infrasonic Measurements

*A version of this chapter has been published as:*

Silber, E.A., ReVelle, D.O., Brown, P.G., Edwards, W.N. 2009. An estimate of the terrestrial influx of large meteoroids from infrasonic measurements. *Journal of Geophysical Research: Planets* (1991–2012), 114(E8)

#### 3.1 Introduction

The flux of meter to tens of meter-sized meteoroids in near Earth space is poorly known. It is near this size threshold (below 100m) where impactors may penetrate the atmosphere and crater the Earth's surface (Bland and Artemieva, 2003) and where impact effects may result in localized climate perturbations (cf. Toon et al., 1997). More generally, the flux of meter-class meteoroids is critical to dating young planetary surfaces and understanding the delivery mechanisms of meteoroids from the main asteroid belt, as, for example, it is in the size range of meter to tens of meters where the Yarkovsky drift effect is most significant (Farinella et al., 1998). The most comprehensive measurement of the meteoroid flux in this size range to date by Brown et al. (2002) examined satellite data of light flashes produced by the disintegration of meter-sized objects in the Earth's atmosphere. This analysis, however, was dependent on assumptions about both the spectral distribution and efficiency of light production which are uncertain. More recently, Harris (2008) has produced estimates of the flux of 10m and larger near Earth objects from telescopic survey data. The new Harris (2008) analysis suggests a dip of as much as one order of magnitude in the population relative to a constant power-law extrapolation (as presumed by Brown et al. (2002)) in the few tens – 100m size range. Both of these studies have (generally different) built-in assumptions which would make another, independent estimate of the flux in this size regime desirable.

Here we make use of the acoustic waves produced by large meteoroid impacts over a 13 year study period to estimate the influx rate for meter-sized and larger meteoroids. Meteoroid impacts produce infrasound, low frequency acoustic waves below the frequency threshold of human hearing ( $\sim 20$  Hz) and above the Brunt-Väisälä frequency of the atmosphere  $\sim 10^{-3}$  Hz. These waves are of special interest as attenuation in the atmosphere at these frequencies is low and hence the waves can be detected over large distances, approaching global scales at the lowest frequencies corresponding to large explosive sources. It is also possible to estimate the source energies for fireballs using acoustic records alone (Ceplecha et al., 1998). Our data set consists of historical detections of airwaves from 10 large fireballs made by a global network of microbarometers operated by the U.S. Air Force Technical Applications Center (AFTAC) covering the period from the early 1960s until the mid-1970s. This data set has been previously analyzed in part by Shoemaker and Lowery (1967), and in complete form by ReVelle (1997, 2001) for the purpose of measurement of meteoroid influx rates. The current study differs from these earlier works in that we have digitized all the original hardcopy records, corrected the cylindrical pen recordings to linear scales, applied instrument responses to the airwave signals and re-measured all signal quantities. We note that the major remaining unknown correction is for wind-pipe filtering; details of the wind-pipe design are now lost. Here we re-examine the signal processed records estimating yields using the original period-approach of ReVelle (1997) and independently apply a recent energy-amplitude relation derived from simultaneous satellite-infrasound measurements (Edwards et al., 2006).

Each infrasonic array consisted of a minimum of four microbarometer pressure sensors (channels), placed approximately 6-12 km apart, with two distinct passbands: (i) Infrasonic wave band, high frequency (HF), 3 dB down at 0.04 to 8.2 Hz, and (ii) Internal gravity wave band, low frequency (LF), 3 dB down at periods of 440 - 44 s (ReVelle et al., 2008). The global network of these stations was designed to detect large nuclear explosions anywhere on the planet; hence this design is well suited to global fireball monitoring. The AFTAC operated network differs from the currently established International Monitoring System (IMS), (which is under the umbrella of the Comprehensive Nuclear-Test-Ban Treaty (CTBT) commission) in several respects, such



as the setup, sampling rates, noise processing, array element separations and signal processing. For example, the AFTAC operated network utilized infrasonic arrays with a large separation of sensor elements (6-12 km) compared to the IMS network (1-3 km), and a comparably lower signal-to-noise ratio compared to the IMS network. The complete AFTAC setup was geared towards monitoring and detections of large nuclear explosions, predominantly occurring in the atmosphere and yielding low frequency infrasound, while the IMS network is designed to detect lower yield explosions underground as well as in the atmosphere with a correspondingly higher infrasonic frequency range. In short, the historical infrasonic records that come from the AFTAC operated network are profoundly unique and fundamentally different from those coming from the presently operated IMS network. More details of the AFTAC network, areal coverage and instruments can be found in ReVelle (1997). Our current analyzed data set consists of HF detections only, although the LF data exists and were fully digitized as well.

We note that this data set is unique in that it covers a long time period (13.67 years) and has several large energy events, the detection of which set useful limits to the influx for larger (10m) meteoroids. One event is of particular interest, it occurred off the coast of South Africa on 3 August, 1963, originally estimated by ReVelle (1997) at ~1100 kt TNT (1 kt TNT =  $4.185 \times 10^{12}$  J). Our flux values will necessarily be lower limits as not all fireball events detected by the AFTAC network have been made available for analysis and only relatively deeply penetrating fireballs produce significant infrasound.

### **3.2 Reduction Methods and Analysis**

All original waveforms were recorded to strip-chart paper as well as on magnetic tape at the time of observation, with events being identified in real-time by station operators who noted increased cross-correlation among a given station's microbarometers. A total of ten events were identified as being fireballs, nine of them with a certain confirmation by other techniques, such as seismic and VLF (ReVelle, 1997). The only event that did not have confirmation by any other technique is the South African event of 3 August 1963.

These original chart paper records were scanned in .tiff format. Even though the scans were saved in high resolution, they were not in a suitable state for data digitization, as the

original records were contaminated with various markings, such as stamps, smudges, handwritten measurements and dates, all entered by the equipment operators. In almost all cases these markings were directly on top of a waveform, impairing the clarity of the signal; hence, a careful image cleaning was necessary to proceed to the next step. It is important to note that these scanned waveforms are very large in size (up to 84,000 pixels), limiting the choice of image manipulation software which would be capable of efficiently handling the clean-up procedure. For this purpose we used the open LINUX software program Gimp, as it can facilitate large file handling and seamless computer resource management (all raw waveforms can be found in the auxiliary material<sup>1</sup>).

Once cleaned, the images were saved in their native form (.tiff) for archiving and further processing. Several *MATLAB*<sup>®</sup> programs were written for post-processing. For example, it was necessary to correct for the cylindrical pen and ‘straighten’ the signal for all records except for events recorded in 1971 and 1972, as those were already recorded digitally. Figure 3.1 shows a representative example of the raw waveform as scanned from the paper record, and the corresponding example of this ‘straightening’, for channel 1 of the 2 Nov 1960 event.

---

<sup>1</sup> Auxiliary material is available at:  
[http://aquarid.physics.uwo.ca/infra\\_pub/2009je003334/Supplemental\\_material/](http://aquarid.physics.uwo.ca/infra_pub/2009je003334/Supplemental_material/)

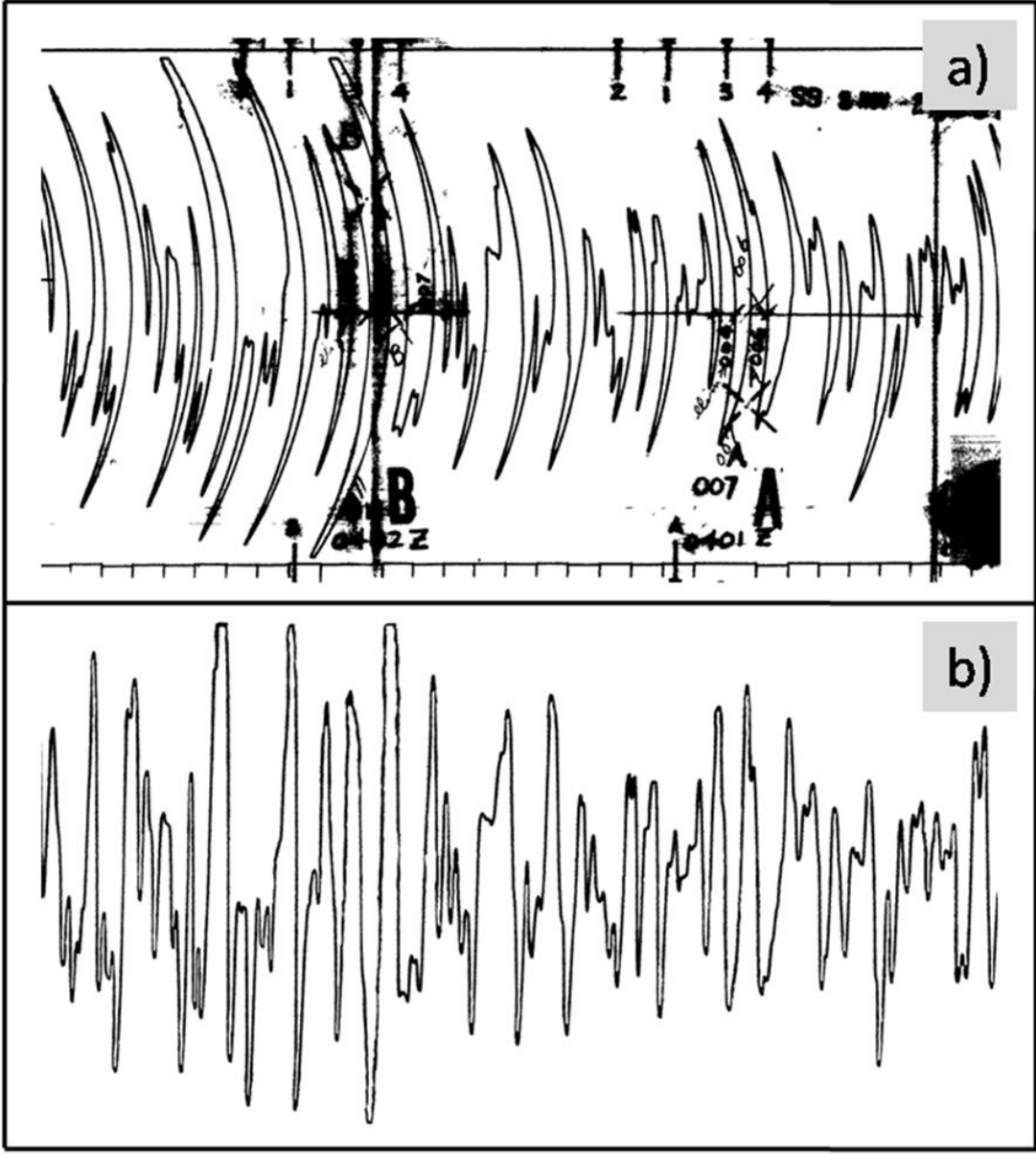


Figure 3.1: Channel 1, 2 Nov 1960: (a) A representative example of the segment of the raw waveform as scanned from the original paper record, and (b) cleaned and straightened (corrected for the cylindrical pen) corresponding segment of the waveform. At this point, the cleaned and straightened waveform is subjected to further processing in order to produce a final, digitized waveform which is as close as possibly attainable to the original one.

The final stages of the process generated fully digitized waveforms which are identical to that of the scanned original. Once this was achieved, the calibration based on the original paper records was applied to each waveform. This calibration consisted of three main components: (i) the gain setting correction, (ii) the amplitude scaling, and (iii) the sampling rates. An example of the finalized fully digitized and calibrated waveform for channel 1 of the 2 November, 1960 event is shown in Figure 3.2.

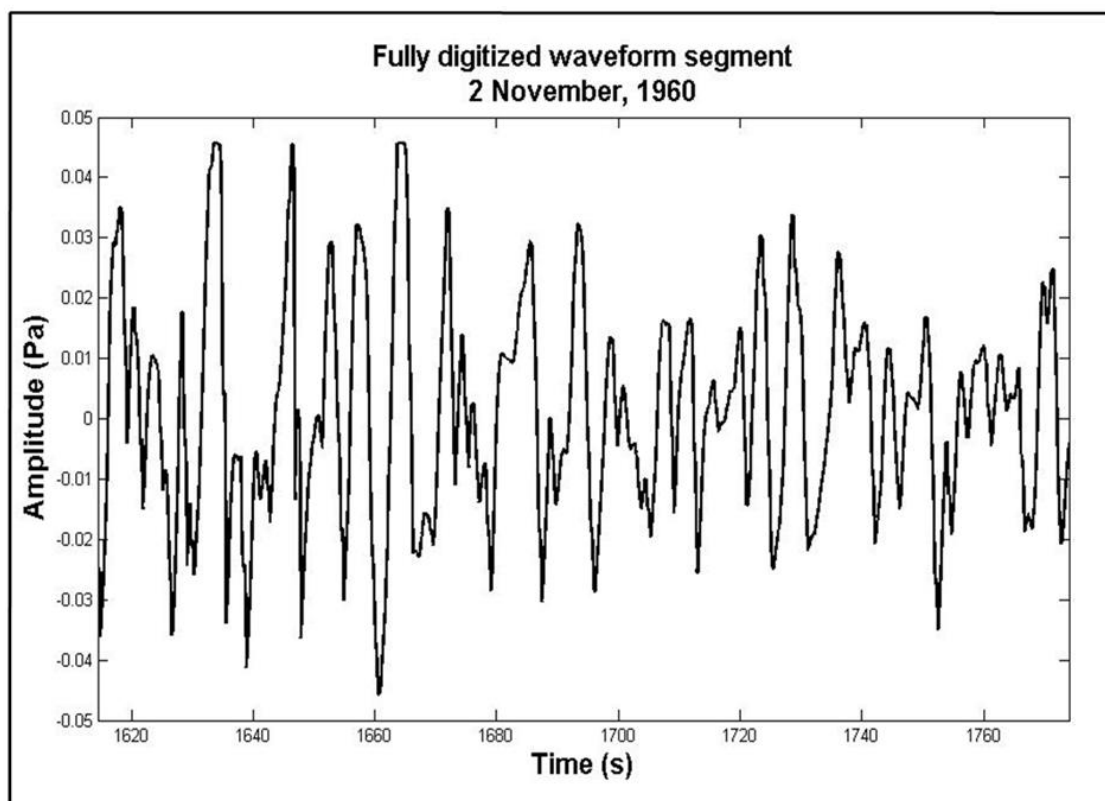


Figure 3.2: A fully digitized waveform of the 2 November, 1960 event, channel 1: this is the same segment as in Figure 3.1, now fully digitized and calibrated.

From these digitized records, we verified that the original measurements made by ReVelle (1997) were reproducible to within pen width uncertainty which (with the exception of some transcription errors) was generally found to be the case (Table 3.1 contains all measurements of the original digitized and calibrated waveforms). The digital

waveforms then had the instrument response of the microphones applied (Flores and Vega, 1975) and a final best estimate for the original waveform was produced.

Table 3.1: Summary of all ten bolide events from the historical data set, sorted by date. The data includes the measurements of the digitized and calibrated original waveforms: maximum peak-to-peak amplitude, the period at maximum amplitude and the standard deviation of the period.

Event date	Channel	Digitized Peak to peak amplitude (Pa)	Digitized Period at maximum amplitude (s)	Digitized Period Standard Deviation (s)	Event date	Channel	Digitized Peak to peak amplitude (Pa)	Digitized Period at maximum amplitude (s)	Digitized Period Standard Deviation (s)
3-Aug-1963	JB-1	0.23	35.29	1.83	14-Apr-1972	GE-4	0.14	6.65	0.72
<b>3-Aug-1963</b>	JB-2	0.15	25.49	1.05	14-Apr-1972	FH-1	0.07	7.33	2.39
3-Aug-1963	JB-3	0.16	25.49	1.05	14-Apr-1972	FH-2	0.02	6.87	0.99
<b>3-Aug-1963</b>	JB-4	0.14	25.49	1.05	14-Apr-1972	FH-3	0.10	9.03	2.31
<b>3-Aug-1963</b>	PB-1	0.21	40.51	2.10	14-Apr-1972	FH-4	0.13	7.46	2.64
3-Aug-1963	PB-2	0.23	37.55	1.01	14-Apr-1972	GK-1	0.49	13.18	3.43
<b>3-Aug-1963</b>	PB-3	0.19	37.24	5.70	14-Apr-1972	GK-2	0.49	11.50	0.50
3-Aug-1963	PB-4	0.29	46.71	4.89	14-Apr-1972	GK-3	0.69	14.29	0.22
<b>31-Mar-1965</b>	MF-1	0.20	15.44	1.67	14-Apr-1972	GK-4	0.59	12.83	2.23
<b>31-Mar-1965</b>	MF-2	0.21	15.72	2.45	14-Apr-1972	GS-1	0.19	21.06	3.80
<b>31-Mar-1965</b>	MF-3	0.21	11.27	1.97	14-Apr-1972	BO-1	1.27	15.36	1.70
<b>31-Mar-1965</b>	MF-4	0.20	15.24	1.05	14-Apr-1972	BO-2	1.21	10.20	1.32
<b>31-Mar-1965</b>	PD-1	1.23	13.86	1.32	14-Apr-1972	BO-3	0.60	11.82	0.44
<b>31-Mar-1965</b>	PD-2	0.65	13.12	1.68	14-Apr-1972	BO-4	0.28	9.84	4.27
<b>31-Mar-1965</b>	PD-3	1.76	14.40	1.63	2-Nov-1960	TD-1	0.24	8.23	0.91
<b>31-Mar-1965</b>	PD-4	1.75	13.28	1.52	2-Nov-1960	TD-2	0.23	9.98	3.65
12-Jun-1966	FH-1	0.12	8.59	1.13	2-Nov-1960	TD-3	0.16	7.98	1.64
12-Jun-1966	FH-2	0.12	6.79	0.34	2-Nov-1960	TD-4	0.22	9.84	3.83
12-Jun-1966	FH-3	0.10	7.37	0.27	<b>26-Sep-1962</b>	SS-1	0.09	12.84	1.20
12-Jun-1966	FH-4	0.12	7.99	1.04	26-Sep-1962	SS-2	0.06	17.76	2.21
12-Jun-1966	GE-1	0.11	11.70	0.80	<b>26-Sep-1962</b>	SS-3	0.11	27.47	3.15
12-Jun-1966	GE-2	0.11	8.47	0.84	26-Sep-1962	SS-4	0.06	8.73	1.70
12-Jun-1966	GE-3	0.11	9.48	0.97	<b>27-Sep-1962</b>	DC-1	0.59	8.89	0.99
12-Jun-1966	GE-4	0.06	10.59	1.07	27-Sep-1962	DC-2	0.66	16.49	3.20
12-Jun-1966	MF-1	0.06	7.98	2.17	<b>27-Sep-1962</b>	DC-3	0.48	9.21	0.73
12-Jun-1966	MF-2	0.07	6.45	0.64	27-Sep-1962	DC-4	0.50	13.36	5.73
12-Jun-1966	MF-3	0.06	7.96	0.95	<b>30-Nov-1964</b>	PB-1	0.54	6.89	1.18
12-Jun-1966	MF-4	0.06	7.36	0.43	30-Nov-1964	PB-2	0.42	8.55	0.40
12-Jun-1966	RW-1	0.24	6.63	0.55	<b>30-Nov-1964</b>	PB-3	0.23	8.26	0.92
12-Jun-1966	RW-2	0.27	7.06	0.45	30-Nov-1964	PB-4	0.33	7.80	1.26
12-Jun-1966	RW-3	0.25	6.78	0.07	<b>3-Jan-1965</b>	KP-1	0.12	5.38	1.24
12-Jun-1966	RW-4	0.28	6.60	0.51	3-Jan-1965	KP-2	0.15	6.02	0.91
<b>14-Apr-1972</b>	GE-1	0.53	8.48	1.27	<b>3-Jan-1965</b>	KP-3	0.12	4.76	0.18
<b>14-Apr-1972</b>	GE-2	0.10	8.77	0.20	3-Jan-1965	KP-4	0.12	4.71	1.22
<b>14-Apr-1972</b>	GE-3	0.20	8.63	0.42	<b>8-Jan-1971</b>	TT-4	0.06	9.46	0.29

Figure 3.3 shows an example of this process and the instrument response function. The period at the maximum amplitude of the signal and peak-to-peak amplitude were measured on both the instrument response corrected and original waveforms for all station channels.

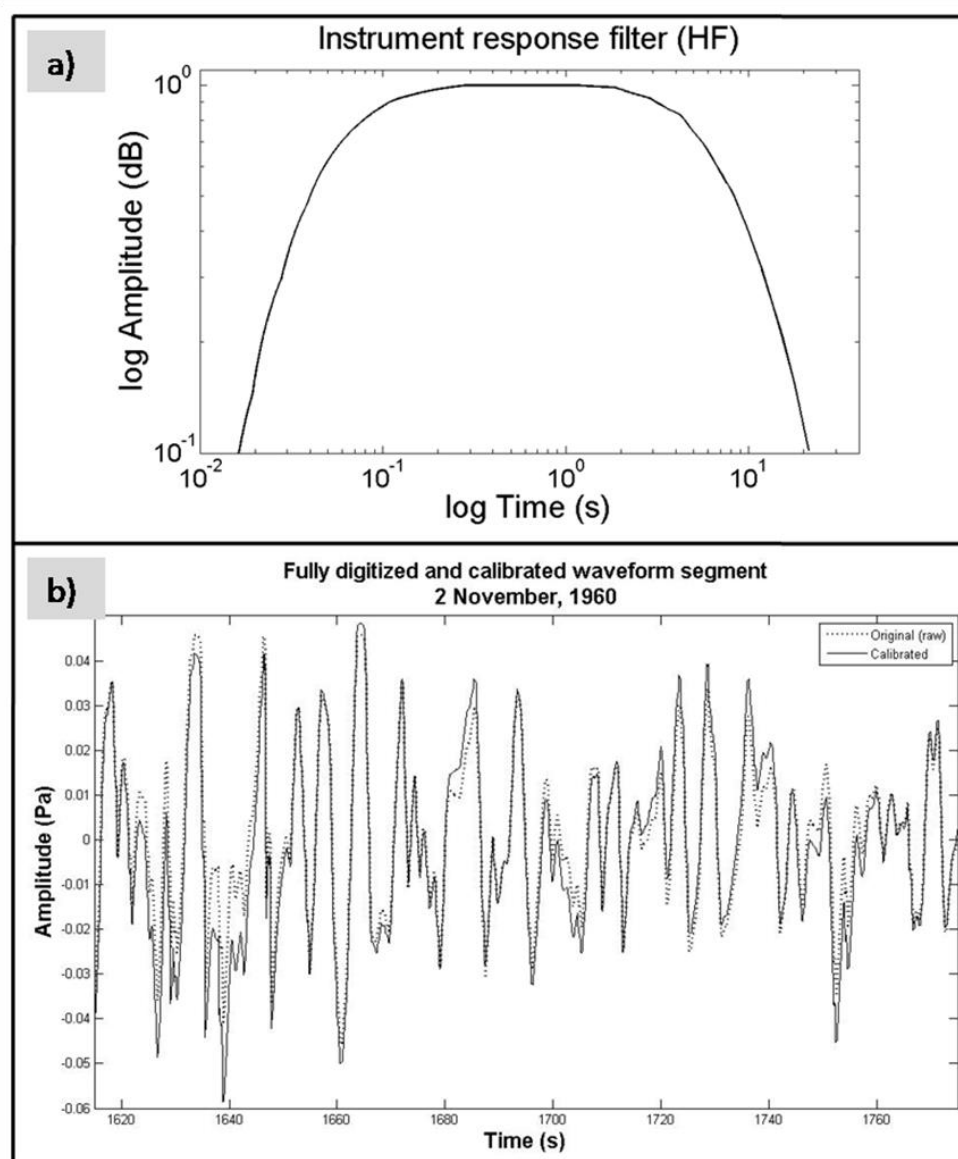


Figure 3.3: (a) The frequency response function adopted from Flores and Vega [1975], with 3 dB down between 0.04 – 8.2 Hz; (b) the original digitized (dotted line) and corrected waveforms (solid line) superimposed.

To apply the empirical yield relation from Edwards et al. (2006) it is desirable to know the wind conditions between the source and receiver at the time of the event. Since these events all occurred at a time before upper wind measurements were globally available (except for the NASA rocket grenade network) we could only perform statistical averages of the wind from more recent years data over the same great circle paths from the United Kingdom Meteorological Office (UKMO) model atmosphere (Swinbank and O'Neill, 1994) to estimate the original stratospheric wind field. However, we find that the average wind values are often smaller than their standard deviations, making wind corrections almost meaningless. We choose instead to use these amplitude relations without wind corrections with the understanding that this will necessarily produce greater uncertainty in the final energy estimates. We note, however, that for very large events, the previous work by Edwards et al. (2006) shows the wind corrections to be relatively minor for the largest energy events and since most of our fireballs fall into the large energy category as defined by Edwards et al. (2006) we expect the impact of this simplification to be minor in most cases.

### 3.3 Estimating Source Energies for Fireballs

Estimating the source energy for a large impulsive atmospheric infrasonic source generally relies on empirical relations derived from sources with known provenance. Among these, the most often cited for fireballs is the relation first introduced by ReVelle (1997) derived from infrasonic measurements of ground level nuclear explosions recorded by AFTAC. These relations make use of the period at maximum amplitude, which is generally more insensitive to propagation effects than amplitude only.

These relations are:

$$\log(E/2) = 3.34\log(P) - 2.58 \quad E/2 \leq 100kt \quad (3.1)$$

$$\log(E/2) = 4.14\log(P) - 3.61 \quad E/2 \geq 40kt \quad (3.2)$$

Here,  $E$  is the total energy of the event (in kilotons of TNT),  $P$  is the period (in seconds) at maximum amplitude of the waveform, and the factor  $\frac{1}{2}$  is present because these

relations were originally derived for nuclear explosions, where 50% of the source energy was presumed lost into radiation.

Most recently, Edwards et al. (2006) examined a large number of fireballs detected simultaneously with infrasound and by satellite measurements and found:

$$E = 10^{3(2.58 - 0.0018v_h) / -1.35} R^3 A^{3/1.35} \quad E > 7kt \quad (3.3)$$

$$E = 10^{3(3.36 - 0.0177v_h) / -1.74} R^3 A^{3/1.74} \quad E < 7kt \quad (3.4)$$

where E is the energy yield of a bolide (in tons of TNT) (presumed to be larger than 7 kt TNT in equation (3.3) and less than 7 kt TNT in equation (3.4)), R is the range to the bolide (in km), A is the maximum peak-to-peak amplitude (in Pa) and  $v_k$  is the source – receiver wind speed (in m/s). Since it is unclear which of these relations is most applicable to fireballs, we use all approaches in the next section to derive energy and recurrence intervals.

### 3.4 Results and Discussion

We performed several energy calculations on digitized original and response function corrected waveforms, including applying the original AFTAC relations (3.1), (3.2), and the empirical relation equations (3.3) and (3.4) (Edwards et al., 2006). As previously mentioned, all events, except for the 3 August 1963 event, were reliably detected by methods and instruments (ReVelle, 1997) other than just infrasound. For the 3 January 1965 event, because the signal is concentrated at such a high acoustic frequency where the relationship between period and yield is less sensitive to meteorological conditions and the range is very low, the yield is believed to be known most reliably of all the events in our data set. This event was subsequently used as a check on the AFTAC energies to scale all other events by adding a correction factor to the AFTAC period relation (3.1). This method reduced kinetic energy estimates of the corrected waveforms by approximately one half, but did not produce a significant change to the slope of the cumulative number vs. energy meteoroid flux profile.



There are 14 distinct AFTAC stations included in the data we have used. Generally few explosions are recorded by many stations, particularly at lower energies. This is because the propagation and detection of infrasound depends on signal attenuation, upper atmosphere wind conditions, time of the day and local noise, all of which vary dramatically from site to site. For comparison, the current IMS network is designed generally to have a minimum two-station detection of a one kt explosion anywhere on Earth (Christie, 2007), but this is with 60 stations and modern digital instruments and signal processing. A detailed analysis of the AFTAC network sensitivity as a function of yield and wind conditions was performed by AFTAC during the operational years of the network. That system sensitivity bias is shown in Figure 3.4 and forms the basis for our flux corrections. Note that the probability is shown for a two-station detection where the range to the fireball would be unambiguously resolved with the infrasound measurements alone. We emphasize that the current fireball data set is only a portion of the total AFTAC fireball data set; some events are not included and we expect others may not have met the detection thresholds discussed earlier. As such, our flux values should be considered lower limits.

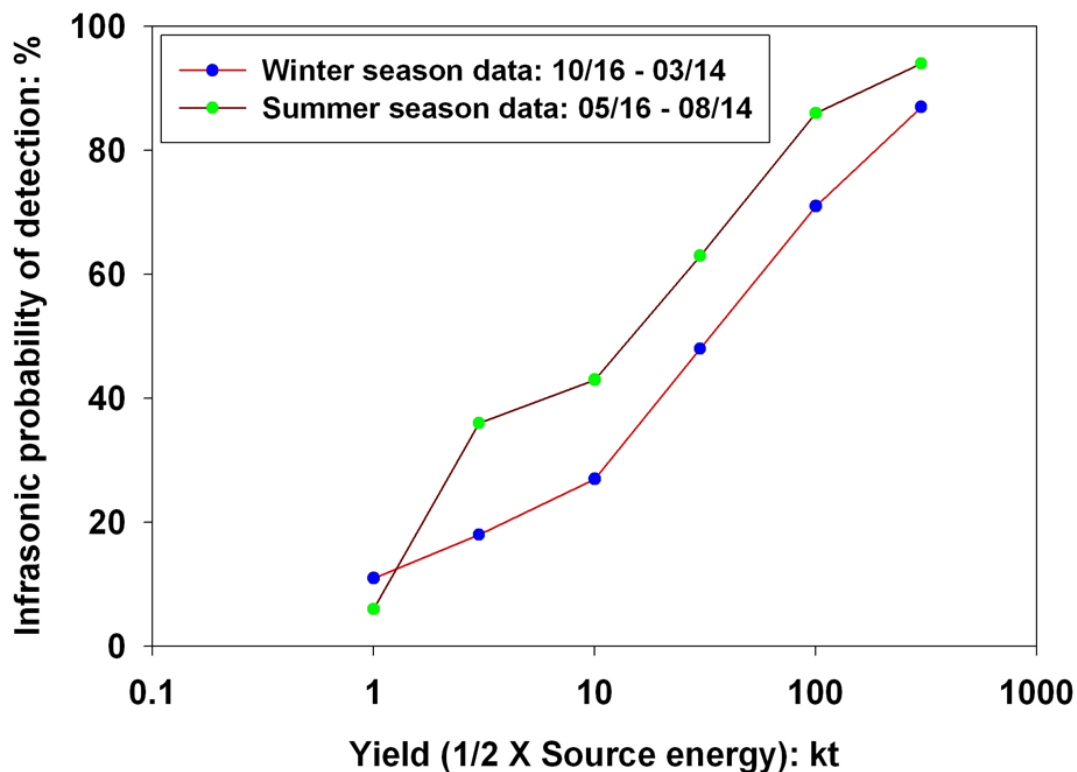


Figure 3.4: AFTAC: Infrasonic probability of detection as a function of yield and the time of year, derived for low altitude nuclear explosions and with detection declared using two or more infrasonic arrays (ReVelle, 1997). Winter and summer seasons are defined as Oct 16 – March 14 and May 16 – Aug 14 each year, respectively. Events falling between these dates, during times of the stratospheric wind jet transition used interpolated versions of the probability.

The total collection duration of the AFTAC network was 13.67 years and using the percent coverage of Earth (Figure 3.4) as a function of yield, season and hemisphere (ReVelle, 1997), we computed an equivalent time-area collection product which together with our infrasound derived source energies produces an equivalent meteoroid flux at the Earth. Our final results are shown in Figure 3.5. Note that the range to each event is determined by the great circle intersections from two or more stations – range errors are typically of the order of a few hundred kilometers at most and form a negligible contribution to the overall error in flux estimation. Here we exhibit the difference between our computed influx rate using the AFTAC – period relation and the empirical source energy estimate from Edwards et al. (2006) appropriate to each event depending

on whether it had  $E > 7$  kt or  $E < 7$  kt. Note that we include for comparison various other flux estimates from telescopic surveys of near-earth objects, satellite measurements of fireball light flashes in the Earth's atmosphere and scaling from lunar crater statistics. The errors for our measurements are shown for each point and reflect counting statistics (error in ordinate) as well as the standard deviation in measured energy due to station and individual channel differences (error in abscissa).

Events recorded by two or more stations generally show noticeable variations in estimated energy – this may be due to the source shock wave originating from different locations along a bolide's trajectory, variations in meteorological conditions along differing source-receiver paths, and factors such as local noise and seasonal variations. Consequently, these events are averaged across all stations and channels to give a single kinetic energy estimate (Table 3.2) per event. We have also computed the mean infrasonic signal speeds between the bolides and each receiving station for which we have location information and find the signal speeds to range from 258.9 – 341.2 m/s, consistent with stratospheric ducting in almost all cases (cf. Ceplecha et al., 1998). As stratospheric signal arrivals are presumed for both energy relations, this implies that the energy estimates are internally self-consistent.

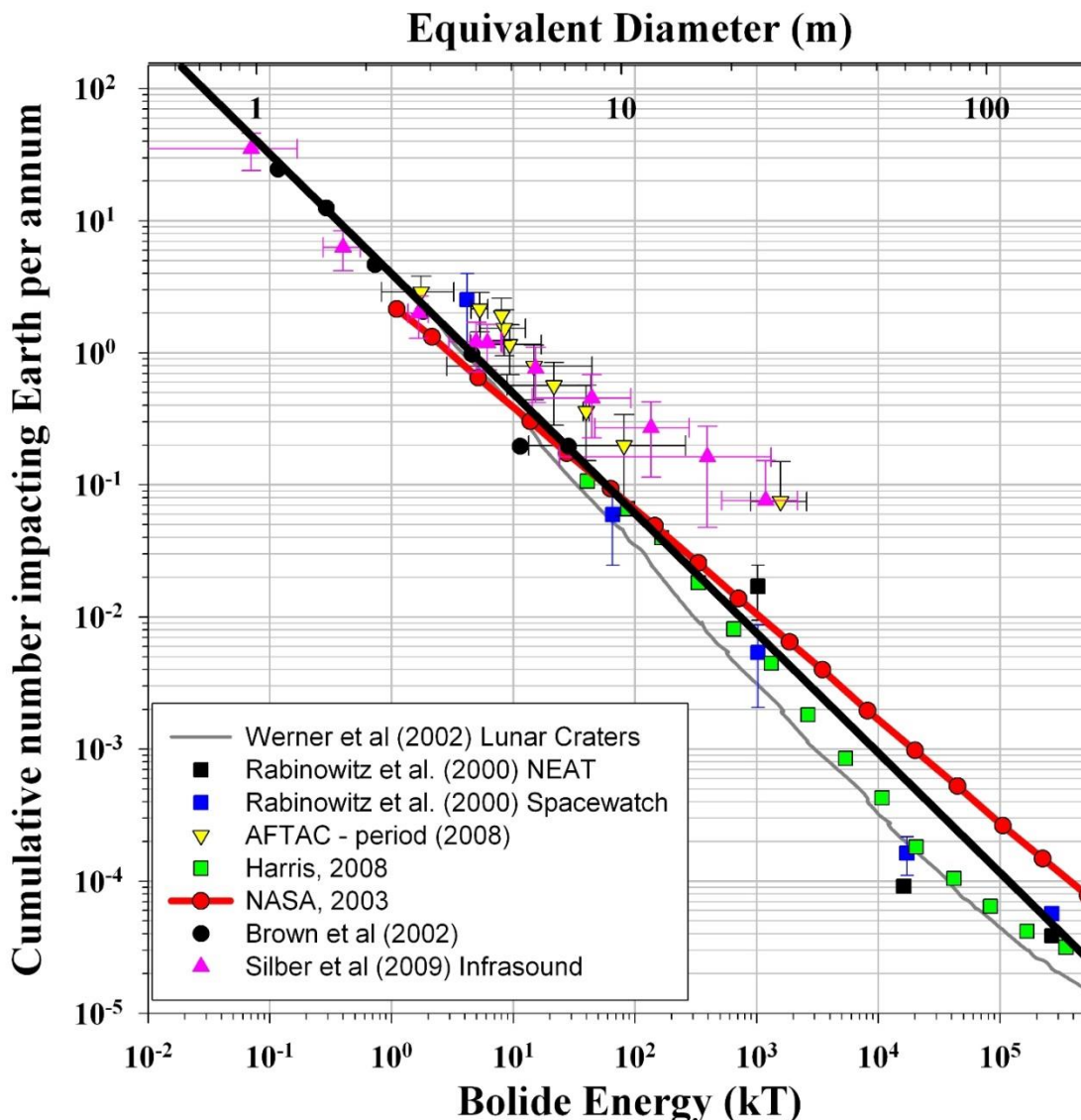


Figure 3.5: Cumulative influx curve showing data from a global debiasing of all telescopic surveys (Harris, 2008), and from individual detailed debiased flux values from the Spacewatch and NEAT programs (Rabinowitz et al., 2000). Also shown are the equivalent impact flux inferred from lunar cratering data (Werner et al., 2002) and from satellite observed bolide impacts in the atmosphere (Brown et al., 2002) as well as the power law fit and extrapolation for these data (solid black line with  $N=3.7E^{-0.90}$ ). The NASA 2003 NEO Science Definition Team report estimated flux is shown and is well represented by a relationship of  $N=2.4E^{-0.79}$  (Stokes et al., 2003). Note that this power law is an extrapolation from larger (km-sized) NEOs. Our two new sets of data points from the digitized historic bolide data set using: i) the AFTAC energy-period relation (ReVelle, 1997) using periods derived in this work (labeled AFTAC – period 2008), and ii) the empirical relation using signal amplitudes (Edwards et al., 2006) are shown for comparison.

Table 3.2: Summary of all ten bolide events from the historical data set, sorted by date. The back azimuth entered as n/a indicates this information is not published for a particular station. We include results for two methods of source kinetic energy estimation: i) AFTAC period-energy relation (ReVelle, 1997), where equation (3.1) was applied to all bolide events except for the 3 August 1963 event, and equation (3.2) to the latter; and ii) empirical relation for  $E > 7$  kt and  $E < 7$  kt, where appropriate, from (Edwards et al., 2006). These results are based on digitized and instrument response-corrected waveforms. For multi-station events, kinetic energy is averaged across all stations and channels. Error estimates in the final energies are based on the spread in measurement errors. Signal velocities for the 12 Jun 1966 fireball are below that expected of stratospheric returns at two stations. It is possible either thermospheric returns or strong counter-wind returns are responsible.

Event date	Station	Back Azimuth (deg)	Great Circle Range (km)	Signal velocity (m/s)		Empirical Relation (kt)	AFTAC Period-Energy Relation (kt)
2-Nov-60	TD	n/a	4004.0	306.1		<b>4.9549</b>	<b>8.4135</b>
					STDev (-)	1.9753	3.0770
					STDev (+)	2.5382	4.1454
26-Sep-62	SS	173	1112.0	294.2		<b>0.0677</b>	<b>81.2511</b>
					STDev (-)	0.0590	67.9152
					STDev (+)	0.1004	179.5343
27-Sep-62	DC	118.7	872.7	303.0		<b>0.4039</b>	<b>14.7872</b>
					STDev (-)	0.1306	11.9476
					STDev (+)	0.1514	29.6139
3-Aug-63	JB PB	170 n/a	11282.1 13824.0	298.0 293.5		<b>1182.8468</b>	<b>930.2768</b>
					STDev (-)	665.9478	337.3165
					STDev (+)	983.2660	453.0749
30-Nov-64	PB	n/a	5219.1	312.9		<b>44.0152</b>	<b>9.3240</b>
					STDev (-)	29.7263	4.8407
					STDev (+)	48.5490	7.6692
3-Jan-65	KP	84.1	3123.6	272.6		<b>1.6695</b>	<b>1.7538</b>
					STDev (-)	0.3062	0.9263
					STDev (+)	0.3318	1.4832
31-Mar-65	MF PD	145.8 196.8	2497.7 3497.1	333.0 303.6		<b>135.3897</b>	<b>39.7627</b>
					STDev (-)	88.9490	2.2432
					STDev (+)	142.9545	2.3356
12-Jun-66	FH GE MF RW	60.6 77.4 222.5 n/a	4828.0 6678.8 4425.7 2896.8	258.9 335.3		<b>6.0986</b>	<b>5.2929</b>
					STDev (-)	1.7123	0.7829
					STDev (+)	2.0424	0.8735
8-Jan-71	TT	n/a	13892.0		<b>15.2560</b>	<b>8.0222</b>	
				STDev (-)	n/a	n/a	
				STDev (+)	n/a	n/a	
14-Apr-72	GE FH GK BO	220.6 236.4 n/a n/a	3701.5 5471.8 7805.3 4345.2	293.8 294.2 316.5 341.2		<b>393.7589</b>	<b>21.5462</b>
					STDev (-)	369.8045	12.6370
					STDev (+)	917.7597	21.7458

In general, the two different approaches produce flux values which are in agreement within error. It is notable that the flux estimates agree best with all other techniques in the lower energy ranges (a few kilotons and smaller) where number statistics are the best. However, the significant feature of this influx curve is the relatively high predicted impact flux at the Earth for ~10-20 m diameter objects, independent of the choice of yield relation.

Caution must be exercised in interpretation at this high energy end – only a few events contribute to each of these points and errors in energy estimates in some cases span an order of magnitude. Among these is the Revelstoke fireball of 31 March 1965. Our energy estimates of 40 – 140 kt are order of magnitude consistent with those of Shoemaker (1983) who suggested 20 kt and by ReVelle (2007) whose entry modeling predicts energy of 13 kt. Most critical to the flux at the high end is the energy estimate for the 3 August 1963 bolide, the most energetic event in this data set. Depending on the method used, source energies range from 540 – 1990 kt, which broadly agrees with the recent estimate of 1100 kt (ReVelle, 1997). Shoemaker (1983) estimated this event to have an energy of 500 kt, while Edwards et al. (2006) found an energy of  $270 \pm 90$  kt; both of these earlier estimates used the instrumentally uncorrected waveforms, having smaller amplitudes and lower periods than the corrected versions we employed, and hence are extreme lower limits. Even accounting for possible uncertainties due to upper air winds and variations in the observed period of the waveforms, the extreme lower bound for this event is  $> 300$  kT. The nature of this one bolide remains a mystery; no other reports exist of the effects of this large impact (as may be expected of an event occurring far from land in this time period) and unlike most other events in the AFTAC database this one did not have independent confirmation from other techniques. It remains possible that this event was not a bolide but rather another source.

The discrepancy in the infrasonically estimated flux at the 5 – 20 m size range may reflect a systematic overestimation in source energies by our two different techniques; neither has been calibrated with bolides at these high energies so we are extrapolating from lower bolide energy estimates for the amplitude estimates and from nuclear tests for the AFTAC case. Furthermore, seasonal variations play a significant role in efficiency of

signal propagation and detection with the summer season preferentially producing lower energy estimates. Alternatively, the infrasonic measurements may be detecting an impacting population of objects not easily seen telescopically, perhaps with low albedos. The order of magnitude difference in apparent flux rates in this case could reflect a large population of darker objects. The differences in the slopes of the distributions are harder to explain unless asteroid albedos change substantially over a very small size range, a situation we view as improbable. Satellite data, however, are also most consistent with the telescopic flux numbers in slope and magnitude and would not be obviously biased in the same way as telescopic measurements by albedo properties alone. Using these two energy scales, if we presume the influx follows a power law (which is only very crudely correct), over our observed size range we find:

$$N = 4.05_{-0.49}^{+0.56} E^{-0.578 \pm 0.034} \quad (3.5)$$

$$N = 4.49_{-0.79}^{+0.95} E^{-0.603 \pm 0.055} \quad (3.6)$$

for the empirical yield and AFTAC-period approaches respectively. Here, N is the cumulative number of objects hitting the Earth per annum and E is the energy in kilotons TNT equivalent. These relations predict approximately one 11-12 kiloton (or larger) impact globally per annum, roughly a factor of 2-3 higher in energy than other techniques. Our relations predict a megaton event once every ~15 years, approximately 5-10 times more frequently than telescopic surveys suggest.

### 3.5 Conclusions

We have presented new estimates for the flux of meter – tens of meter sized objects impacting the Earth based on acoustic recordings made by the AFTAC infrasound network during the period from the early 1960s until the mid 1970s. We have digitized and applied corrections to the original paper analog infrasonic records of ten large fireballs and then applied several different yield relations, to estimate the kinetic energy of each event. From these energy estimations and coverage estimates of the original AFTAC network, we have estimated the global meteoroid influx of meter- tens of meter

sizes. Our findings suggest a shallower slope of cumulative number vs. energy than is found from either satellite observed fireball flashes in the terrestrial atmosphere or fluxes inferred from telescopic surveys.

Much of this difference is due to the very high inferred flux rate at the largest sizes produced due to inclusion of a single event, namely the 3 August 1963 fireball which occurred off the coast of South Africa. From examination of many different yield relations, application of plausible wind corrections and accounting for uncertainties in period and amplitude measurement we conclude that this large event is plausibly in the megaton yield range, with extreme lower energy bounds of  $\sim 300$  kt. If this event is removed from our data set, our inferred cumulative influx values based on the AFTAC-period relationship becomes  $N=6.5E^{-0.76}$ , much closer to the slope of the NASA Science definition team study and largely in agreement within error to flux measurements made by satellite and telescopic surveys. Removal of the 3 August 1963 fireball from the curve using the Edwards et al. (2006) empirical relation does not change its slope significantly. While the difference in slope and intercept produced using our full data set may reflect a true difference in flux between the various recording techniques, it is also possible that this event is a statistical anomaly, a non-meteoritic event or perhaps was of much lower energy but somehow produced a much larger acoustic signature than is typical for fireballs. From our measurements and presuming that the flux curve should follow a power law (equations (3.5) and (3.6)), we find that the largest annual impact event expected, would be in that 11-12 kiloton range, a factor of several higher than found with other techniques. However, at the upper end, a large event of a megaton would occur on the order of every 15 years, approximately 5-10 times more than that estimated using telescopic data. The underlying cause for the disparity between these data sets, particularly at the high end, remains unclear.



## **Acknowledgements**

PGB thanks the Natural Sciences and Engineering Research Council of Canada and the Canada Research Chairs program for funding. EAS wishes to thank the UK Met Office for supplying the initial stratospheric assimilated data via the British Atmospheric Data Center. The authors thank Alan W. Harris (USA) for helpful comments on an earlier version of this manuscript.

## References

- Bland, P. A. and Artemieva, N. A. (2003), Efficient disruption of small asteroids by Earth's atmosphere, *Nature*, 424(6946), 288-291, doi: 10.1038/nature01757
- Brown, P. G., Spalding, R. E., ReVelle, D. O., Tagliaferri, E. and Worden, S. P. (2002), The flux of small near-Earth objects colliding with the Earth, *Nature*, 420, 294-296, doi: 10.1038/nature01238
- Cepplecha, Z., Borovička, J., Elford, W. G., ReVelle, D. O., Hawkes, R. L., Porubčan, V. and Šimek, M. (1998), Meteor Phenomena and Bodies, *Space Science Reviews*, 84 (3/4), 327-471, doi: 10.1023/A:1005069928850
- Christie, D. R. (2007), Recent Developments in infrasound monitoring technology: application to CTBT verification, *CTBTO Spectrum*, 10
- Edwards, W. N., Brown, P. G. and ReVelle, D. O. (2006), Estimates of meteoroid kinetic energies from observations of infrasonic airwaves, *Journal of Atmospheric and Solar-Terrestrial Physics*, 68 (10), 1136-1160, doi: 10.1016/j.jastp.2006.02.010
- Farinella, P., Vokrouhlicky, D. and Hartmann, W. K. (1998), Meteorite Delivery via Yarkovsky Orbital Drift, *Icarus*, 132 (2), 378-387, doi: 10.1006/icar.1997.5872
- Flores, J. S. and Vega, A. J. (1975), Some relations between energy yield of atmospheric nuclear tests and generated infrasonic waves, *The Journal of the Acoustical Society of America*, 57 (5), 1040-1043, doi: 10.1121/1.380571
- Harris, A. (2008), What Spaceguard did, *Nature*, 453, 1178-1179, doi: 10.1038/4531178a
- Rabinowitz, D. L., Helin, E. F., Lawrence, K. J., Pravdo, S. H. (2000), A reduced estimate of the number of kilometer-sized Near-Earth Asteroids, *Nature*, 403, 165-166, doi: 10.1038/35003128
- ReVelle, D. O. (1976), On Meteor-generated infrasound, *J. Geophys. Res.*, 81 (7), 1217-1230, doi: 10.1029/JA081i007p01217
- ReVelle, D. O. (1997), Historical Detection of Atmospheric Impacts by Large Bolides Using Acoustic-Gravity Waves, *Ann N Y Acad Sci*, 822 (1 near-earth ob), 284, doi: 10.1111/j.1749-6632.1997.tb48347.x
- ReVelle, D. O. (2001), Global infrasonic monitoring of large bolides, In: *Proceedings of the Meteoroids 2001 Conference*, 6 - 10 August 2001, Kiruna, Sweden, ESA SP-495, Noordwijk: ESA Publications Division, ISBN 92-9092-805-0, 483 - 489
- ReVelle, D.O., Sukara (Silber), E. A., Edwards, W. N., Brown, P. G. (2008), Reanalysis of the Historic AFTAC Bolide Infrasound Database, *Earth, Moon, and Planets*, 102 (1-4), 337-344, doi: 10.1007/s11038-007-9173-3

- Shoemaker, E. M. (1983), Asteroid and comet bombardment of the Earth, Annual review of Earth and Planetary Sciences, 11 (A83-33477 14-42). Palo Alto, CA, Annual Reviews, Inc., 461-494, doi: 10.1146/annurev.ea.11.050183.002333
- Shoemaker, E. M. and Lowery, C. J. (1967), Airwaves associated with large fireballs and the frequency distribution of energy of meteoroids, Meteoritics, 3, 123-124
- Stokes, G. H., Yeomans, D. K., Bottke, W. F., Chesley, S. R., Evans, J. B., Gold, R. E., Harris, A. W., Jewitt, D., Kelso, T. S., McMillan, R. S., Spahr, T. B., Worden, S. P. (2003), Study to Determine the Feasibility of Extending the Search for Near-Earth Objects to Smaller Limiting Diameters. Report of the Near-Earth Object Science Definition Team, NASA Office of Space Science, Solar system Exploration Division, 154 pp
- Swinbank, R. and O'Neill, A. A. (1994), Stratosphere-Troposphere Data Assimilation System, Monthly Weather Review, 122 (4), 686-702, doi: 10.1175/1520-0493(1994)122
- Toon, O. B., Zahnle, K., Morrison, D., Turco, R. P. and Covey, C. (1997), Environmental Perturbations Caused by the Impacts of Asteroids and Comets, Ann N Y Acad Sci, 822 (1 near-earth ob), 401, doi: 10.1111/j.1749-6632.1997.tb48357.x
- Werner, S. C., Harris, A. W., Neukum, G. and Ivanov, B. A. (2002), The near-Earth asteroid size-frequency distribution: a snapshot of the lunar impactor size-frequency distribution, Icarus, 156, 287-290, doi: 10.1006/icar.2001.6789

## Chapter 4

### 4. Infrasonic Detection of a Near-Earth Object Impact over Indonesia

*A version of this chapter has been published as:*

Silber, E. A., A. Le Pichon, and P. G. Brown (2011), Infrasonic detection of a near-Earth object impact over Indonesia on 8 October 2009, *Geophys. Res. Lett.*, 38, L12201, doi:10.1029/2011GL047633

#### 4.1 Introduction

Impacts of medium-sized (meter to 10s of meters in diameter) Near Earth Objects (NEOs) at the Earth may cause physical damage at ground level (e.g. Chapman and Morrison, 1994) and could perturb climate on regional scales (Toon et al., 1997). However, the impactor size at which these effects begin to occur is poorly understood from models (Artemieva and Bland, 2003) with little constraining observational data (cf. Chapman, 2008). Records of significant NEO impacts are rare. McCord et al. (1995) reported a ~40 kT impactor detected by satellite over the Pacific on Feb 1, 1994 while Klekociuk et al. (2005) and Arrowsmith et al. (2008) report multi-instrumental observations of two different impactors with energies of 20-30 kilotons of TNT ( $1 \text{ kT} = 4.185 \times 10^{12} \text{ J}$ ) occurring in the fall of 2004. In all cases these events occurred over open ocean and much of the energetics information was compiled from records of satellite data or the associated airwaves detected by infrasonic stations.

Infrasound is low frequency sound (<20 Hz down to the atmospheric Brunt-Väisälä frequency) which experiences little attenuation during propagation over large distances making it an excellent tool for studying distant explosive sources (Hedlin et al., 2002). Among the phenomena which have been detected and extensively studied with

infrasound are fireballs (bright meteors) (ReVelle, 1976, 1997; Brown et al., 2002a). Fireballs are produced by large meteoroids which may penetrate deep into the atmosphere and may generate a cylindrical ballistic shock wave and a quasi-spherical ablational shock during their hypersonic passage, which decays to low frequency infrasonic waves that propagate over great distances (Bronsthen, 1983; ReVelle, 1976; Edwards, 2010; Le Pichon et al., 2002a, Brown et al., 2002; Brown et al., 2003). Infrasonically detected impacts can provide a valuable tool in estimation and validation of the influx rate of meter sized and larger meteoroids (Brown et al., 2002; Silber et al., 2009), as well as trajectory and energetics information for interesting events which otherwise lack such data (e.g. the Carancas crater forming impact in Peru in 2007 (Brown et al., 2008; Le Pichon et al., 2008)). Here we present evidence that a significant NEO impact occurred on 8 October, 2009 over Indonesia based primarily on infrasound recordings of the infrasonic wave detected across the globe; our analysis suggests that this may have been one of the most energetic impactors to collide with the Earth in recent history.

On October 8, 2009 at 2:57 UT (10:57 a.m. local time), thunder like sounds and ground shaking were reported near the city of Bone, South Sulawesi, Indonesia (Surya News<sup>[1]</sup>). Local eyewitnesses also reported the aftermath of an atmospheric explosion, describing a thick gray-white dusty smoke trail in the sky (Surya News<sup>[2]</sup>), which was also captured on amateur video (You Tube<sup>[3]</sup>). The video shows a smoke trail consistent with other fireball dust trails, such as the Tagish Lake fireball (Hildebrand et al., 2006), probable confirmation of the meteoric nature of the event. According to the Jakarta Globe<sup>[4]</sup> news report there was one casualty; a nine year old with an underlying heart condition who was terrified by the explosion and went into shock. Several houses were also damaged in Bone's Panyula village, while the police department in Bone received numerous calls and reports of unusual audible sounds as far as 11 km away from Latteko, Bone district, South Sulawesi (The Jakarta Globe<sup>[5]</sup>). Thomas Djamaluddin, head of the Lapan Center for Climate and Atmosphere Science, confirmed that the blast was caused by an extraterrestrial object (The Jakarta Post<sup>[6]</sup>). Motivated by these initial reports, we undertook a detailed examination of infrasonic records of all International Monitoring System (IMS) infrasound stations to search for possible signals from the airburst.

## 4.2 Data Collection and Analysis

We were able to examine waveform data from 31 infrasound stations in the IMS network, which is operated by the Comprehensive Nuclear-Test-Ban Treaty Organization (CTBTO) and consists in part of 43 globally distributed infrasonic stations to detect nuclear explosions (CTBTO web: <http://www.ctbto.org>). Infrasonic data were analyzed for probable signals associated with the fireball using the Progressive Multi-Channel Correlation Method (PMCC) (Cansi, 1995) (Figure 4.1). PMCC is sensitive to coherent signals with very low signal-to-noise ratio (SNR) and has been successfully employed in searching for infrasound from other large bolides (e.g. Arrowsmith et al., 2008). It searches for coherent signals in frequency and time windows and selects detections of similar parameters to identify ‘families’ (e.g. Brachet et al., 2010). In total 17 positive detections were identified, using the approximate location (4.5°S, 120°E) and timing from media reports and expected typical stratospheric propagation speeds as a guide to isolate the signal arrival on each array. The signal was remarkable in that: (i) it was detected by many infrasonic stations, some at extreme ranges (>17 000 km); and (ii) it had substantial signal energy at very low frequencies, consistent with a source of very high energy. Table 4.1 summarizes findings signal properties from all detecting stations.

To ensure robustness of our period estimates, the dominant period was obtained via two independent techniques using the same bandpass. The dominant period at maximum frequency was acquired from the residual power spectral density (PSD) of the signal alone, and the maximum peak-to-peak amplitude was determined by measuring the zero crossings of the stacked waveform at each station (cf. ReVelle, 1997). This methodology is robust in itself, as the periods obtained using these two techniques agree to better than 10% in all cases.

Using the nine closest stations it was possible to perform a source geolocation (Figure 4.2). The location of the signal was computed using an inverse location algorithm based on Geiger’s approach (1910) modified in order to also take station azimuth into account (see Coleman and Yi, 1996 for details of this method).

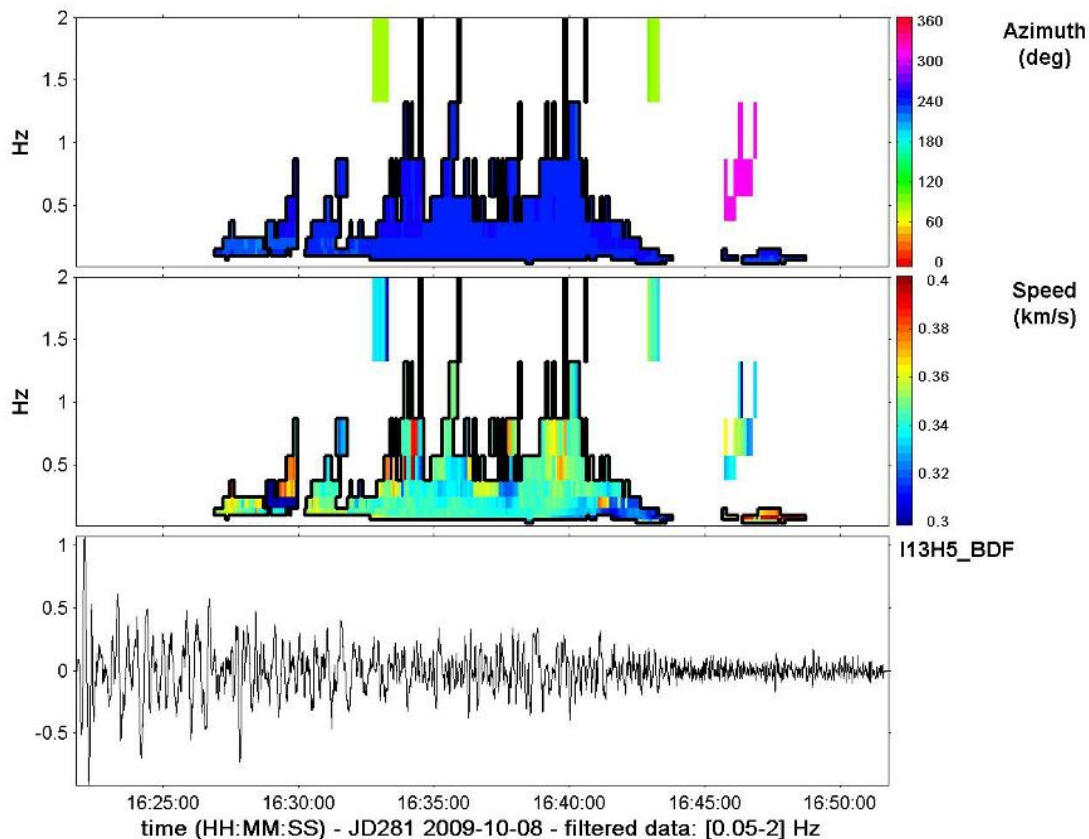


Figure 4.1: An example of the bolide infrasound signal observed at I13CL (27.13°S, 109.36°W, Easter Island), 13 636 km from the source. The top window is the best estimate for the signal back-azimuth in the direction of maximum F-statistic (a measure of the relative coherency of the signal across all array elements in any particular window; essentially an SNR measure for coherent signals), the second window represents the apparent trace velocity of the acoustic signal across the array in the direction of the peak F-stat, while the third window is the raw pressure signal for one array element bandpassed according to the chosen frequency combination, shown in the boxes of the lower plot.

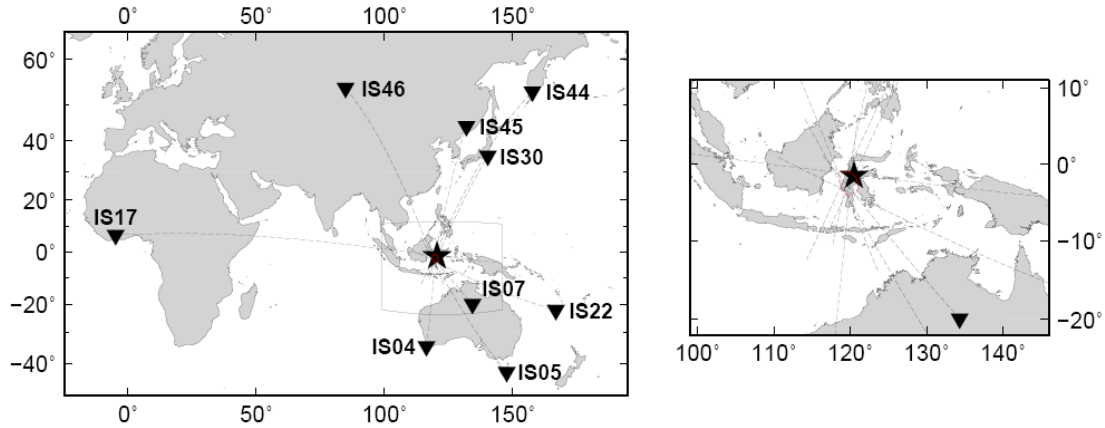


Figure 4.2: Map showing the intersection of infrasound bearings. Left: map showing nine closest stations; Right: area of uncertainty, geolocation ellipse. The uncertainties account for both propagation effects and measurement uncertainties. The best fit solution is obtained using the nine stations closest to the main burst. In order to determine the location errors, the 95% confidence ellipses are estimated by repeatedly running the linearized least-squares inversion with arbitrary sub-sets of the input data within  $\pm 10^\circ$  and  $\pm 30$  m/s ranges of uncertainties for the azimuths (azimuths are not wind corrected) and celerity, respectively.

### 4.3 Estimating the Blast Radius and Source Energy

There are several empirical relations, relying on either the period at maximum amplitude or range and signal amplitude, which can be utilized in estimating source energy for bolides from infrasound measurements (Edwards et al., 2006). Typically, infrasonic period is less modified during propagation than amplitude (cf. Mutschlecner et al., 1999; ReVelle 1997; ReVelle 1974) and thus the period relationship is expected to be more robust. The Air Force Technical Application Centre (AFTAC) period-yield relations which are commonly used for large atmospheric explosions, are given by ReVelle (1997), as:

$$\log(E/2) = 3.34 \log(P) - 2.58 \quad E/2 \leq 100kt \quad (4.1)$$

$$\log(E/2) = 4.14 \log(P) - 3.61 \quad E/2 \geq 40kt \quad (4.2)$$



Here,  $E$  is the total energy of the event (in kilotons of TNT),  $P$  is the period (in seconds) at maximum amplitude of the waveform. Infrasound for a given bolide event in general shows a large variation in observed periods from different stations (Silber et al., 2009; ReVelle et al., 2008; Edwards et al., 2006). The exact origin of this variation is not well known; large (Mton) nuclear explosions, for example, do not show period variances as large as we find for bolides (cf. Flores and Vega, 1975). One possibility is that signals are arriving from different portions of the fireball trajectory. In this interpretation, the period measurement at each station is a 'sample' of the size of the cylindrical blast cavity at that particular segment of the trail (ReVelle 1974) having an acoustically accessible path to the receiver. With this working hypothesis, we have developed a novel technique to correlate the observed period to a most probable source height and compute the equivalent size of the bolide blast cavity at that height and therefore synthesize the blast radius as a function of height from observations across multiple stations.

As an initial step, we performed ray tracing to obtain the most likely source height as observed by the five closest stations, situated within 5 000 km from the event. The InfraMap ray tracing package (Norris and Gibson, 2001) was used to find all eigenrays reaching the given station for source heights extending from 15 – 55 km in 5 km increments at the bolide source location. The eigenray model results were then analyzed by comparing the model predictions to observed parameters, such as the celerity, range, arrival angle, ray height from the receiver, as well as the number density of the model eigenray population to establish the most likely source height observed by each of the five stations with  $R < 5000$  km. Using the bolide weak shock theory developed by ReVelle (1974), we then modeled the period decay to find the size of the blast cavity and the fundamental period at each height (Figure 4.3). The most probable heights for the five closest stations (up to 5,000 km range) were obtained using the InfraMap ray tracing package (Norris and Gibson, 2001) by shooting eigenrays from the source to the receiver between 15 km and 55 km in 5 km steps and comparing the results to observations. The discrimination parameters used to compare observations to the model are: signal celerity ( $x_1$ ), range ( $x_2$ ), arrival angle of the ray ( $x_3$ ), ray height from the receiver ( $x_4$ ) and the number density of rays at the source ( $x_5=1/\text{number of rays}$ ). We define the most likely model source height as having the smallest root mean square ( $X_{\text{rms}}$ ) of the form:

$$X_{\text{rms}} = \text{sqrt} [(ax_1^2 + bx_2^2 + cx_3^2 + dx_4^2 + gx_5^2)/5] \quad (4.3)$$

where a, b, c, d and g are the weighting constants (a=0.8, b=0.02, c=0.06, d=0.06, g=0.06). Since eigenrays coming from any particular source height to the receiver may take different propagation paths, and therefore exhibit large variation in values (from 220 m/s up to 340 m/s, depending whether the ray is thermospherically or stratospherically ducted, respectively), the most weight was assigned to signal celerities. The least weight was given to the range (the great circle distance) as there was the least amount variation in this quantity. The remaining weights were equally distributed among the remaining three quantities. Once a most probable height is established for each station with this methodology, we utilized the bolide weak shock treatment (ReVelle, 1974) to determine the fundamental period ( $\tau$ ) as well as the blast radius ( $R_0$ ) at the source for each height using only the observed period at each station and the known range to the source. The blast radius is the region of highly non-linear /strong shock proximal to the propagating meteoroid (given by  $R_0 = E_0/p = Md$ , where  $E_0$  is the drag force per unit trail length exerted on the meteoroid by the fluid,  $p$  is the ambient hydrostatic pressure,  $M$  is the Mach number, and  $d$  is the meteoroid diameter). The blast radius is related to the fundamental signal wave period via  $\text{Tau} = C_s/(2.81 R_0)$ , where  $c_s$  is the adiabatic speed of sound. The non-linear shock ultimately transitions into a weak shock (at one blast radii) and then decays into a linear wave. In this treatment, once the wave transitions to linear propagation, its period does not change; this is what is recorded by the receiver. Once a series of model estimated blast radii as a function of height were determined, we employed a numerical bolide entry model (ReVelle, 2001) to determine limits to the most likely source energy.

With this blast radius as a function of height as our main constraint, we then applied the numerical entry model of ReVelle (2001) to model the blast radius and establish limits to the most probable source energy using plausible values for entry velocity, entry angle and compositional type. The numerical entry modeling (more details can be found in ReVelle, 2001) includes full meteoroid ablation and fragmentation in a realistic atmosphere and calculates the meteoroid blast radius as a function of altitude. The model input entry parameters are as follows: initial bolide diameter and velocity, zenith angle, shape, and

porosity. As many of these parameters are unknown for the Indonesia bolide, we have chosen values typical for bolides in an effort to identify combinations that produce our derived trend in the blast radii as a function of height established using the weak shock treatment. The total range of input parameters that we explored using the model covered the following parameter ranges:

- Initial bolide radius = 4 – 12 m
- Entry velocity = 12 – 25 km/s
- Zenith angle = 10 – 60 degrees
- Meteoroid porosity = 5 – 50 % (ordinary to carbonaceous chondrites)

Here we have explored initial bolide radii of 4 – 10 m, entry velocities from just above Earth escape (12 km/s) to approximately the mean entry velocity for NEAs colliding with the Earth (Brown et al., 2002), zenith angles from 10 – 60 degrees, while the meteoroid porosity range examined extended from those expected for chondritic bodies to highly porous carbonaceous chondrites (Britt and Consolmagno, 2003). 7000 runs were made using various combinations of these parameters and the resulting model predicted blast radius profile with height compared to Figure 4.3. From this range of input parameters we found the best fit to the modelled blast radius as a function of height was reproduced using:

- Initial bolide radius = 6.5 – 10 m
- Entry velocity = 12 – 20 km/s
- Zenith angle = 20 – 40 degrees
- Meteoroid porosity = 5 – 42 % (ordinary to carbonaceous chondrites)

Using a bulk mass density of  $3300 \text{ kg/m}^3$  (Wilkinson and Robinson, 2000), we obtain an energy range between 8 kT to 67 kT. The results shown in Figure 4.4 are based on the following input values (these were used for the lowest energy estimate of 8 kT of TNT, shown in Figure 4.3):

- Diameter = 6.5 m

- Entry velocity = 12.5 km/s
- Porosity = 42 %
- Zenith angle = 20 degrees

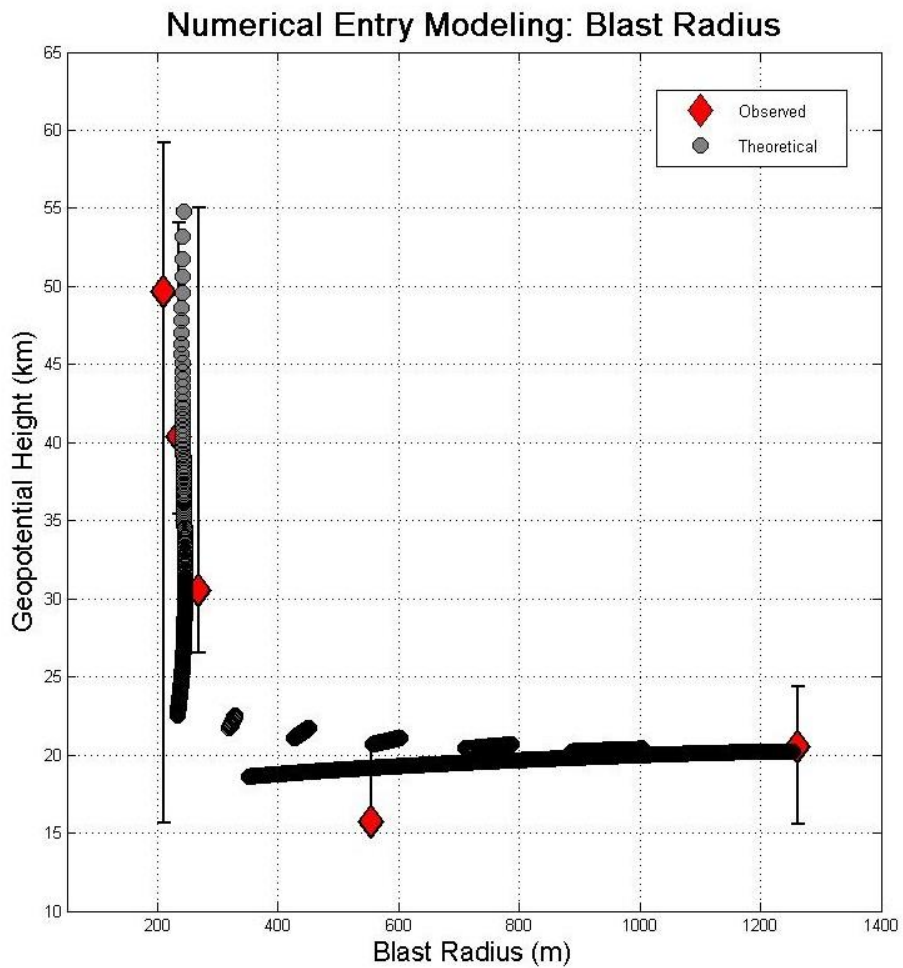


Figure 4.3: The blast radius modeling results (where marker size is proportional to the model-inferred blast radius at the source).

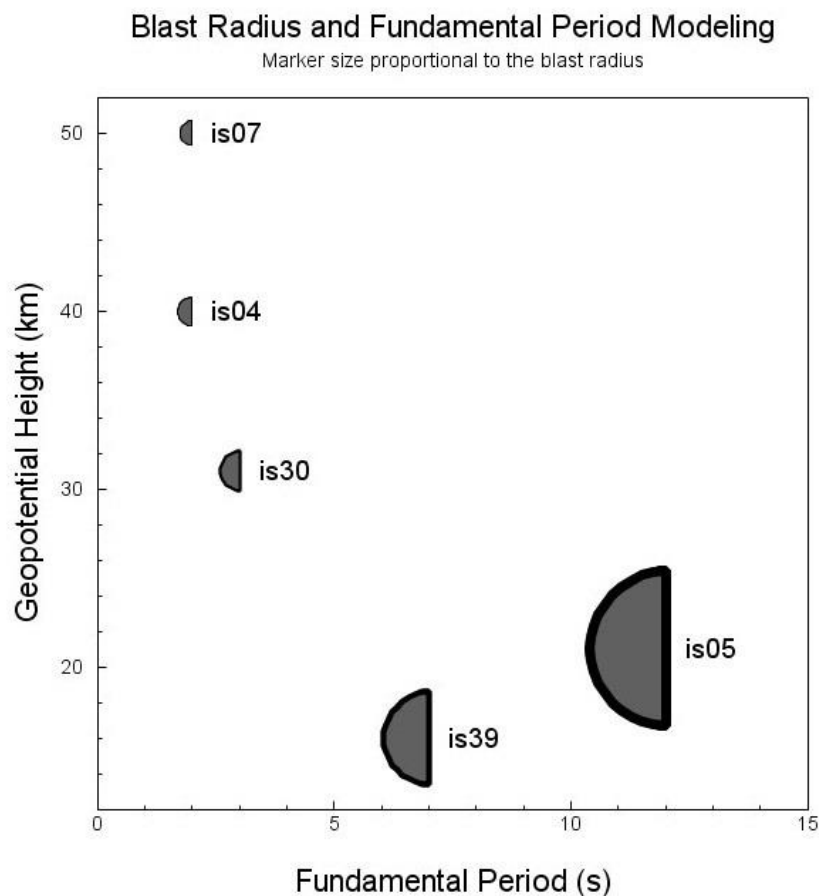


Figure 4.4: Numerical entry modeling results.

#### 4.4 Results and Discussion

The first bolide - related signal arrived at 04:39:51 UT to I39PW (Palau), the closest detecting station, while the latest signal arrived to I08BO nearly 15 hours later. Average signal celerities (defined by the ratio between the horizontal propagation range and the travel time) are between 0.27 and 0.32 km/s, which is consistent with stratospheric duct signal returns (Ceplecha et al., 1998). The geolocation ellipse, computed using azimuths and arrival times points to 4.9°S and 122.0°E with mean residuals of 2.9°. The source time estimated from this location is 02:52:22 UT with a residual of 1320 s (Figure 4.1).

While recognizing the inherent limitation of combining periods across all stations as discussed earlier, for comparison with earlier bolide energy analyses we found the

combined average periods of all phase-aligned stacked waveforms at each station - this produced a global average of 14.8 seconds using zero crossings and 15.3 seconds using PSD analysis. This corresponds to a mean source energy of 43 kt of TNT and 48 kt of TNT, respectively, using the AFTAC period-yield relation (Equation 4.1). However, as emphasized earlier, since the periods observed by individual stations show a factor of five variation (Table 4.1), our new modeling technique has placed more solid constraints on upper and lower bounds beyond this traditional approach to energy estimation. We include results for two methods of dominant period measurements. First, the dominant period at maximum frequency was acquired from the residual power spectral density (PSD), where the latter was obtained by first computing the PSD of the entire signal, then using a series of identically sized windows before and after the signal to establish the background noise PSD and finally subtracting the noise from the total signal PSD. Second, the maximum peak-to-peak amplitude was determined by bandpassing the stacked, raw waveform using a second-order Butterworth filter and then applying the Hilbert Transform (Dziewonski and Hales, 1972) to obtain the peak of the envelope. We then computed the period at maximum amplitude by measuring the zero crossings of the stacked waveform at each station (e.g. ReVelle, 1997). Due to sensitivity thresholds and low SNR, it was not possible to reliably calculate the period for I26DE and I46RU. Ray tracing and numerical modeling for the five closest stations reveal a distinctive pattern of the increasing fundamental period, and consequently the blast radius, with decreasing altitude (Figure 4.3). This implies that the short period signal originates in the upper portions of the fireball trail (50 km), while the long period signal emanates from an altitude as low as 15 km. This is consistent with the expected large blast cavity resulting from a terminal detonation/airburst and fragmentation, which typically accompany large bolide events. This gives us confidence that the technique is physically reasonable. We note that inclusion of stations more distant than 5 000 km does not change this basic picture, a finding we did not expect a priori given the large uncertainties in atmospheric propagation over paths in excess of ~5 000 km. This is consistent with the fact that bolides in general exhibit much more variation in the observed period (as much as factor of six), than spherical explosions do (factor of ~2). By matching our derived pattern of blast radii with height to entry modeling (Figure 4.4) we estimate the true total source

energy to be between 8 – 67 kt of TNT, corresponding to a chondritic object 6 – 10 m in diameter.

Table 4.1: Station details and signal measurements summary.

Distance (km)	Station ID	Latitude (deg)	Longitude (deg)	True Back Azimuth (deg)	Observed Back Azimuth (deg)	Arrival time	Signal Duration (s)	Minimum Celerity (m/s)	Maximum Celerity (m/s)	Peak-to-peak Amplitude via PMCC (Pa)	Peak-to-peak Amplitude via MatSeis (Pa)	Period at max Amplitude via PSD (s)
2099	I39PW	7.5	134.5	230	264	04 :39 :51	1235	283	340	...	1.57	18.22
2291	I07AU	-19.9	134.3	316	318	04 :55 :46	850	287	320	2.823	3.091	6.77
3350	I04AU	-34.6	116.4	7	9	05 :59 :18	1370	271	305	0.471	0.526	7.23
4920	I30JP	35.3	140.3	210	211	07 :33 :43	1280	280	302	0.642	0.6077	7.06
5009	I05AU	-42.5	147.7	319	319	07 :37 :01	690	280	292	0.542	0.874	23.95
5386	I22FR	-22.2	166.8	284	285	07 :45 :08	1340	290	312	0.165	0.127	6.92
5543	I45RU	44.2	132.0	196	197	08 :04 :54	1450	278	300	1.192	1.1873	14.02
7296	I46RU	53.9	84.8	222	224	09 :46 :19	1490	281	298	0.803	...	...
7323	I44RU	53.1	157.7	141	141	09 :49 :46	2450	268	294	0.363	0.7896	15.24
8577	I55US	-77.7	167.6	311	305	10 :55 :07	1060	289	299	0.168	0.145	14.06
10573	I53US	64.9	-147.9	270	270	12 :49 :47	830	291	297	0.488	0.418	11.81
11594	I26DE	48.8	13.7	80	80	14 :28 :51	185	278	279	0.04	...	...
11900	I18DK	6.7	-4.9	350	340	14 :15 :26	1100	284	292	0.693	0.645	23.62
12767	I56US	48.3	-117.1	293	322	14 :54 :45	1520	286	292	0.765	0.764	13.03
13636	I13CL	15.3	-23.2	244	240	16 :26 :53	1310	273	281	0.618	0.606	16.43
13926	I17CI	-33.7	-78.8	91	87	17 :05 :34	615	270	274	0.128	0.1347	12.04
17509	I08BO	-16.2	-68.5	203	218	18 :54 :45	30	...	305	...	0.933	16.71

## 4.5 Conclusions

The Indonesian bolide of 8 October, 2009, detected infrasonically on a global scale, was perhaps the most energetic event since the bolide of 1 February, 1994 (McCord et al., 1995) and may have exceeded it in total energy. We have no other instrumental records of this event other than casual video records of the dust trail emphasizing again the value of infrasound monitoring of atmospheric explosive sources. Infrasonic waves from this bolide observed at 17 IMS stations are all characterized by very low frequency content, consistent with a large energy source and a large blast cavity (ReVelle, 1976).

Our best estimate of the object's energy (8 – 67 kt of TNT) is derived from an inferred blast radius pattern matched to entry modeling and suggests an object 6 – 10 m in diameter. Based on the flux rate from Brown et al. (2002), such objects are expected to

impact the Earth on average every 2 – 10 years, while the infrasonic flux rate from Silber et al. (2009) suggests an impact every 5 years. Global events of such magnitude can be utilized to calibrate infrasonic location and propagation tools at global scale, evaluate energy yield formula, and event timing. Our large uncertainty in energy for this event can only be refined if additional instrumental records of this unique event become available.

### **Acknowledgements**

EAS and PGB thank the Natural Sciences and Engineering Research Council of Canada and Natural Resources Canada. PGB thanks the Canada research chairs program for funding support.



## References

- Arrowsmith, S.J., Revelle, D.O., Edwards, W. and P. Brown (2008) Global Detection of Infrasonic Signals from Three Large Bolides, *Earth, Moon, and Planets*, 102 (1-4), 357-363, doi: 10.1007/s11038-007-9205-z
- Artemieva, N.A. and P.A. Bland (2003) The Largest Meteorites on Earth, *Meteoritics & Planetary Science*, 38, Supplement, abstract no.5153
- Brachet, N., Brown D., Le Bras R., Mialle P. and J. Coyne (2010) Monitoring the earth's atmosphere with the global IMS infrasound network, *Infrasound Monitoring for Atmospheric Studies*, Springer Netherlands, pp. 77-118, doi: 10.1007/987-1-4020-9508-5\_16, ISBN: 978-1-4020-9507-8
- Britt, D. T. and G. J. Consolmagno (2003) Stony meteorite porosities and densities: A review of the data through 2001, *Meteoritics & Planetary Science*, 38(8), 1161-1180, doi: 10.1111/j.1945-5100.2003.tb00305.x
- Bronshten, V. A. (1983), *Physics of Meteoric Phenomena*, D.Reidel, Dordrecht, Netherlands, p. 372, ISBN: 9027716544
- Brown P., ReVelle D. O., Silber E. A., Edwards W. N., Arrowsmith S., Jackson L. E., Tancredi G. and D. Eaton (2008) Analysis of a crater forming meteorite impact in Peru, *Journal of Geophysical Research* 113 (E09007), doi:10.1029/2008JE003105
- Brown, D., Katz, C.N., Le Bras, R., Flanagan, M.P., Wang, J. and A.K. Gault (2002) Infrasonic signal detection and source location at the Prototype International Data Center, *Pure and Appl. Geophys.* 159(5), 1081-1125, doi: 10.1007/s00024-002-8674-2
- Brown, P. G., Spalding, R. E., ReVelle, D. O., Tagliaferri, E. and S. P. Worden (2002) The flux of small near-Earth objects colliding with the Earth, *Nature*, 420, 294-296, doi: 10.1038/nature01238
- Brown, P.G, Kalenda, P., ReVelle, D.O. and J. Borovička (2003) The Moravka meteorite fall:2. Interpretation of infrasonic and seismic data, *Meteoritics and Planetary Science*, 38, 989-1003, doi: 10.1111/j.1945-5100.2003.tb00296.x
- Brown, P.G., Whitaker, R.W., ReVelle, D.O. and E. Tagliaferri, (2002) Multi-Station Infrasonic Observations of Two Large Bolides: Signal Interpretation and Implications for Monitoring of Atmospheric Explosions, *Geophysical Research Letters*, 29 (13), 1-6, doi: 10.1029/2001GL013778
- Cansi, Y. (1995) An automatic seismic event processing for detection and location: The PMCC method, *Geophysical Research Letters*, 22, 1021-1024, doi: 10.1029/95GL00468

- Ceplecha, Z., Borovička, J., Elford, W. G., ReVelle, D. O., Hawkes, R. L., Porubčan, V. and M. Šimek (1998), Meteor Phenomena and Bodies, *Space Science Reviews*, 84 (3/4), 327-471, doi: 10.1023/A:1005069928850
- Chapman, C.R. (2008) Meteoroids, Meteors, and the Near-Earth Object Impact Hazard, *Earth Moon Planet*, 102, 417–424, doi:10.1007/s11038-007-9219-6
- Chapman, C.R. and D. Morrison (1994) Impacts on the Earth by asteroids and comets: assessing the hazard, *Nature*, 367, 33-40, doi: 10.1038/367033a0
- Coleman, T.F. and Y. Li (1996) An Interior, Trust Region Approach for Nonlinear Minimization Subject to Bounds, *SIAM Journal on Optimization*, 6, 418-445
- Dziewonski, A. and A. Hales (1972) *Methods in Computational Physics*, Academic Press, New York, 11, 39–84
- Edwards, W. (2010) Meteor Generated Infrasound: Theory and Observation, *Infrasound Monitoring for Atmospheric Studies*, Springer Netherlands, pp. 361-414, doi: 10.1007/987-1-4020-9508-5\_12, ISBN: 978-1-4020-9507-8
- Edwards, W. N., Brown, P. G. and D. O. ReVelle (2006) Estimates of meteoroid kinetic energies from observations of infrasonic airwaves, *Journal of Atmospheric and Solar-Terrestrial Physics*, 68 (10), 1136-1160, doi: 10.1016/j.jastp.2006.02.010
- Flores, J. S. and A. J. Vega (1975), Some relations between energy yield of atmospheric nuclear tests and generated infrasonic waves, *The Journal of the Acoustical Society of America*, 57 (5), 1040-1043, doi: 10.1121/1.380571
- Geiger, L. (1910), Herdbestimmung bei Erdbeben aus den Ankunftszeiten, *K. Ges. Wiss. Gött.*, 4, 331-349
- Hedlin, M., Garces, M., Bass, H., Hayward, C., Herrin, E., Olson, J. and C. Wilson (2002) Listening to the secret sounds of earth's atmosphere, *EOS*, 83, 564–565, doi: 10.1029/2002EO000383
- Hildebrand, A.R., McCausland, P.J.A., Brown, P.G., Longstaffe, F.J., Russell, S.D.J., Tagliaferri, E., Wacker, J.F. and M.J. Mazur (2006) The fall and recovery of the Tagish Lake meteorite, *Meteoritics & Planetary Science*, 41 (3), 407-431, doi: 10.1111/j.1945-5100.2006.tb00471.x
- Kenney, J. F. and E.S. Keeping (1962) Root Mean Square, Section 4.15 in *Mathematics of Statistics*, Pt. 1, 3rd ed. Princeton, NJ: Van Nostrand, pp. 59-60
- Klekociuk, A.R., Brown, P.G., Pack, D.W., ReVelle, D.O., Edwards, W.N., Spalding, R.E., Tagliaferri, E., Yoo, B.B. and J. Zagari (2005) Meteoritic dust from the atmospheric disintegration of a large meteoroid, *Nature*, 436, 1132-1135, doi: 10.1038/nature03881
- Le Pichon A., Guérin J. M., Blanc E. and D. Raymond (2002a) Trail in the atmosphere of the December 29, 2000, meteorite as recorded in Tahiti: Characteristics and

trajectory reconstitution, *Journal of Geophysical Research*, 107, doi:10.29/2001JD001283

- Le Pichon, A., Antier, K., Cansi, Y., Hernandez, B., Minaya, E., Burgoa, B., Drob, D., Evers, L. G. and J. Vaubaillon (2008) Evidence for a meteoritic origin of the September 15, 2007, Carancas crater, *Meteoritics and Planetary Science*, 43 (11), 1797-1809, doi: 10.1111/j.1945-5100.2008.tb00644.x
- McCord, T.B., Morris, J., Persing, D., Tagliaferri, E., Jacobs, C., Spalding, R., Grady, L. and R. Schmidt (1995) detection of a meteoroid entry into the Earth's atmosphere on February 1, 1994, *Journal of Geophysical Research*, 100(E2), 3245-3249, doi: 0148-0227/95/94JE-0280250
- Mutschlecner, J.P., Whitaker, R.W. and L.H. Auer (1999) An empirical study of infrasonic propagation, Los Alamos National Laboratory Technical Report, LA-13620-MS. Los Alamos, NM
- Norris, D. and R. Gibson (2001) Infrasonic propagation modeling enhancements and the study of recent bolide events, 23rd Seismic Research Review Conference: Worldwide Monitoring of Nuclear Explosions, Jackson Hole, Wyoming, USA, October 2-5, 2001, Contract No. DTRA01-00-C-0063
- ReVelle, D. O. (1976) On Meteor-generated infrasound, *J. Geophys. Res.*, 81 (7), 1217-1230, doi: 10.1029/JA081i007p01217
- ReVelle, D.O. (1974) *Acoustics of Meteors*, PhD Dissertation, University of Michigan
- ReVelle, D.O. (1997) Historical Detection of Atmospheric Impacts by Large Bolides using Acoustic-Gravity Waves, *Annals of the New York Academy of Sciences, Near-Earth Objects - The United Nations International Conference*, editor J.L. Remo, New York Academy of Sciences, 822, 284-302, doi: 10.1111/j.1749-6632.1997.tb48347.x
- ReVelle, D.O. (2001) Theoretical Leonid Modeling, *Proceedings of the Meteoroids 2001 Conference*, 6 - 10 August 2001, Kiruna, Sweden. Ed.: Barbara Warmbein. ESA SP-495, Noordwijk: ESA Publications Division, ISBN 92-9092-805-0, 2001, p. 149 - 154
- Revelle, D.O., Sukara, E. A., Edwards, W. N. and P. G. Brown (2008) Reanalysis of the Historic AFTAC Bolide Infrasound Database, *Earth, Moon, and Planets*, 102 (1-4), 337-344, doi: 10.1007/s11038-007-9173-3
- Silber, E.A., ReVelle, D.O., Brown, P.G. and W.N. Edwards (2009) An estimate of the terrestrial influx of large meteoroids from infrasonic measurements, *Journal of Geophysical Research*, 114 (E8), CiteID E08006, doi: 10.1029/2009JE003334
- Toon, O.B., Zahnle, K., Morrison, D., Turco, R.P. and C. Covey (1997) Environmental perturbations caused by the impacts of asteroids and comets, *Reviews of Geophysics*, 35(1), 41-78, doi: 10.1029/96RG03038

Wilkinson, S.L., and M.S. Robinson (2000) Bulk density of ordinary chondrite meteorites and implications for asteroidal internal structure, *Meteoritics & Planetary Science*, 35(6), 1203-1213, doi: 10.1111/j.1945-5100.2000.tb01509.x

[1] Surya news report, available at:

<http://www.surya.co.id/2009/10/09/ledakan-misterius-guncang-sulsel.html>

[2] Surya news report, available at:

<http://www.surya.co.id/2009/10/09/ledakan-misterius-guncang-sulsel.html>

[3] You Tube, available at:

<http://www.youtube.com/watch?v=yeQBzTkJNhs&videos=jkRJgbXY-90>

[4] The Jakarta Globe, available at:

<http://www.thejakartaglobe.com/home/astronomer-sulawesi-blast-bigger-t7an-atom-bomb-and-caused-by-meteorite/338073>

[5] The Jakarta Globe, available at:

<http://www.thejakartaglobe.com/home/astronomer-sulawesi-blast-bigger-than-atom-bomb-and-caused-by-meteorite/338073>

<http://thejakartaglobe.com/home/mysterious-explosion-panics-locals-in-south-sulawesi-police-still-investigating/334246>

[6] The Jakarta Post, available at:

<http://www.thejakartapost.com/news/2009/10/08/blast-may-be-result-falling-space-waste-or-meteorite-lapan.html>

## Chapter 5

### 5. Optical Observations of Meteors Generating Infrasound – I: Acoustic Signal Identification and Phenomenology

*A version of this chapter has been submitted for a publication as:*

Silber, E. A., and P. G. Brown (2014) Optical Observations of Meteors Generating Infrasound – I: Acoustic Signal Identification and Phenomenology, Journal of Atmospheric and Solar-Terrestrial Physics, manuscript # ATP3766, in revision

#### 5.1 Introduction

Low frequency sound extending from below the human hearing range of 20 Hz and down to the natural oscillation frequency of the atmosphere (Brunt-Väisälä frequency) is known as infrasound (Beer, 1974; Jones, 1982). There are many sources of infrasound, both natural and anthropogenic. Some examples of natural sources are ocean waves (microbaroms), storms, lightning, aurorae, volcanoes (Evers and Haak, 2001; Garcés et al., 2003a; Garcés, et al., 2003b; Rieppe et al, 1996), avalanches (Bedard and Georges, 2000) and earthquakes (Hedlin et al., 2002; Garcés and LePichon, 2009), while some animal species (Payne, 1995; von Muggenthaler, et al., 2003; Günther et al., 2004) use infrasound for long range communication (elephants, giraffes, whales). Examples of anthropogenic sources are heavy machinery, mining activities, nuclear and chemical explosions, missile launches, helicopters, and supersonic jets (Hedlin et al., 2002).

Infrasonic waves undergo little attenuation at ground level compared to audible sound because the attenuation is proportional to the square of frequency (Bass et al., 1972; Sutherland and Bass, 2004). This means that infrasound can be used for global monitoring of explosions. Since the mid-1990s the International Monitoring System (IMS) of the Comprehensive Test-Ban Treaty Organization (CTBTO) in Vienna, Austria, utilizes infrasound as one of its monitoring technologies. At present, the IMS has 45

certified and fully operational global infrasound stations (Christie and Campus, 2010; [www.ctbto.org](http://www.ctbto.org)).

Meteors are one of the most elusive sources of infrasound. When small cosmic particles, also known as meteoroids, collide with the Earth's atmosphere at hypersonic velocities (11.2 – 72.8 km/s), they produce a wide range of phenomena, including heat, light, and ionization (collectively known as a meteor) as well as an atmospheric shock (Ceplecha et al., 1998). If a meteoroid survives its flight through the atmosphere and makes it all the way to the ground, it becomes a meteorite. These objects contain invaluable information about the dynamics and composition of the solar nebula, hence aiding in understanding of the early Solar System. A typical visual meteor is produced by a particle larger than 1 mm; however, the size limit is a strong function of the entry velocity (Ceplecha et al., 1998).

The most famous historical example of meteor infrasound occurred on June 30, 1908, when a large meteoroid exploded over the Podkamennaya Tunguska River, generating an intense shock wave (Chyba et al., 1993). It was later discovered that infrasound generated during this massive explosion travelled twice around the globe and was recorded by microbarometers in Europe, primarily in England (Whipple, 1930). After the event, meteor infrasound observations became rare, only to be reinvigorated during the Cold War when infrasound was used to monitor nuclear explosions. It was realized however, that some explosive sources were not nuclear explosions, but in fact large meteoroid (1 – 10 m in size) airbursts (ReVelle, 1997; Silber et al., 2009). A theoretical treatment predicting the nature of infrasound generated by meteoroids was first developed in 1974 (ReVelle, 1974, 1976). However, the difficulty in unambiguously identifying infrasound produced by a particular meteor has left much of this theory unverified (e.g. Kraemer, 1977). Recently, Haynes and Millet (2013) have adapted the Whitham sonic boom theory (Whitham, 1974) to produce a theoretical model to predict the overpressure and period from meteor shocks.

In general, infrasound source characteristics (such as energy) are often estimated by purely empirical means (e.g. Mutschlecner and Whitaker, 2010); however, this process is of limited use for meteor infrasound where the source altitudes are very high and few

empirical measurements exist. Consequently, a strong need exists for a large dataset of meteor events with independently known speed, trajectories and energies as a first step in validating theoretical frameworks.

During the late 1970s and early 1980s, there were attempts by several groups (McIntosh et al, 1976; Kraemer, 1977) to observe bright meteors simultaneously with optical, radar and infrasound instruments. In five years of observations only two events were positively detected (Kraemer, 1977). It was not until the inception of the IMS network that some well documented cases of infrasound from meteors were observed (ReVelle and Whitaker, 1999; Evers and Haak, 2003). More recently, several regional optical meteor networks emerged using modern technologies to monitor bright meteors (e.g. Oberst et al, 1998), resulting in an additional handful of meteor infrasound observations (Edwards et al, 2008).

In most cases, meteor infrasound signals have been associated with meteors whose flight characteristics were poorly known, limiting the ability to validate ReVelle's (1974, 1976) analytic meteor infrasound theory. In addition to validating existing models, the frequency of occurrence of meteor infrasound from any given location remains poorly known as does the diversity of the meteor infrasound source functions - either cylindrical (associated with the main ballistic wave) or spherical (associated with fragmentation event) and their relative importance. The relationship between the meteor energy deposition as a function of height and shock production as well as the effects of the varying atmospheric conditions on meteor infrasound propagation remain only partially explored.

To address these questions, we have measured a large dataset of meteors with the purpose of model testing and statistical studies. This has been accomplished by associating infrasound from meteors (also referred to as events) using optical measurements as a cue to search for meteor infrasound. We employed the Southern Ontario Meteor Network (SOMN) (Weryk et al., 2007; Brown et al., 2010) which uses integrated optical, and infrasound technologies to monitor, detect and measure the trajectory of bright regional meteor events. Between 2006 and 2011, a total of 6989 meteor events were recorded optically and of these 80 were also infrasonically detected. The advantage of studying

short range ( $< 300$  km) infrasonic events is that these direct signals are detected before they undergo substantial (and sometimes poorly defined) modifications during propagation due to atmospheric variability.

The specific goals of this coordinated optical-infrasound meteor study are to: (i) use astrometric optical measurements to positively identify infrasound from meteors; (ii) establish and constrain the point (and its uncertainty) along the meteor trail where the infrasound signal emanates; (iii) estimate the potential importance of atmospheric variability due to winds on meteor infrasound propagation; (iv) determine the type of shock production mechanism for meteor generated infrasound; and (v) classify meteor infrasound and correlate meteor infrasound classes using pressure-time waveforms. A major goal is to develop an observational foundation for future work to understand the underlying physical mechanisms which modify meteor infrasound signals and relate to sonic boom theory.

The second paper in this study will use the results from this work as the basis to critically evaluate the meteor weak shock theory of ReVelle (1974; 1976) as applied to meteors and use photometric measurements of infrasonically detected meteors to compare masses derived infrasonically from photometric/dynamic measurements.

Our paper builds upon an earlier study (Edwards et al., 2008) and extends it by using a large data base of optically detected meteor generated infrasound events (in the current study 71 vs. 12 simultaneously detected events in the earlier study). Our work also has an implementation of a new methodology for infrasonic signal association, verification and measurement and it uses an improved optical meteor astrometric measurement technique, hence providing better ground truth and constraints. With a larger ensemble of events we have also been able to develop a taxonomy of infrasound signal classification and define a new algorithm for determining the meteor shock source heights. Finally, this study takes into consideration atmospheric variations in meteor infrasound propagation and interpretation to constrain the uncertainty in source height.

Our global goals in this and the forthcoming paper are to: (i) critically examine the weak shock theory developed for meteors (ReVelle, 1976) experimentally, (ii) use weak shock theory to provide a bottom up estimate (using the infrasound signal alone) of the meteor



blast radius and compare this with the equivalent blast radius from entry modelling as determined photometrically, and (iii) develop a homogenous dataset of meteor infrasound detections with known source characteristics (trajectory, energy, speed) for statistical examination of shock characteristics. Point (iii) will also allow others to test and compare infrasound shock models, both analytic and numerical. In the following sections, we first present a detailed instrumentation description of the infrasound array and cameras used in this study followed by our infrasound and optical measurement methodology. Our criteria for meteor infrasound detection and association is then developed together with a proposed meteor infrasound classification system. Next we discuss the identification of the source height for our meteor infrasound signals using a ray trace model with a Monte Carlo implementation of gravity waves to simulate wind variability. The final section presents our overall results, together with a discussion and conclusions.

## **5.2 Instrumentation**

The first step in our study is to identify infrasound from meteors by correlating bright meteors detected optically with local infrasound observations. We begin by describing the infrasound array used in this study.

### **5.2.1 Infrasound Array**

The Elginfield Infrasound Array (ELFO), situated near the town of Elginfield (43°.1907N, 81°.3152W, 322 m), some 20 km north of London, Ontario, Canada, is a four sensor tripartite (microbarograph) array, positioned in a traditional triangular formation with an off-centre central element (Figure 5.1).

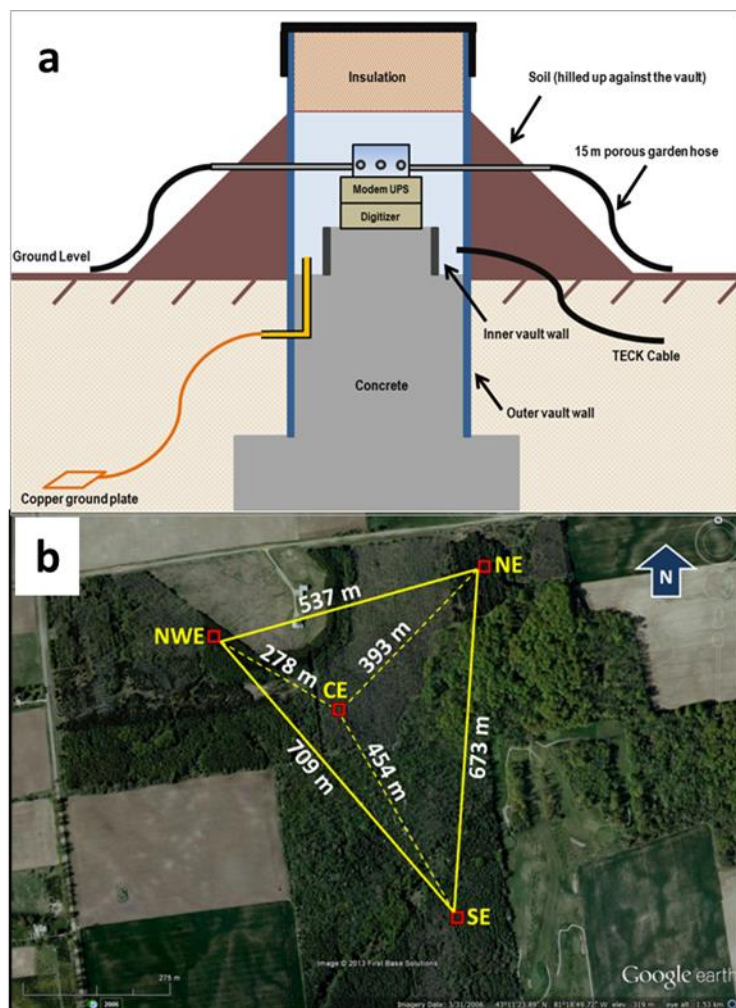


Figure 5.1: (a) ELFO vault diagram; (b) plane view of the array configuration of ELFO.

Since it is expected from theory (ReVelle, 1976) that infrasound from regional ( $< 300$  km range) meteors will have a peak infrasound frequency in the range of  $\sim 1$  Hz, the array element spacing was optimized for this frequency (Christie et al, 2011). Each microbarograph is placed in a vault designed to protect it from the elements and minimize temperature variations and all vaults are located in forest to reduce noise. The sensors are 12-port Chapparals, model 2.5 made by Chapparral Physics, with a flat response (3 dB points) from 0.1 to 200 Hz. Three elements use 15m long porous garden hoses laid out in a star pattern to minimize the local wind noise (Christie and Campus, 2010), while the fourth element (Northwest Element) features a wind shelter, built in August 2007. A snow fence is installed around all elements to further reduce local wind noise. Data from

each element is digitized at 100 Hz and transmitted via a buried and steel armoured TECK cable to a centralized data system, where it is stored locally and streamed to Natural Resources Canada in Ottawa. A GPS antenna at each element enables timing to be embedded in the data stream.

Since beginning operation on January 25, 2006, the array has been continuously collecting infrasound data, capturing signals produced by a number of phenomena, such as machinery, lightning, storms, mining activities, local explosions, etc. During the time period of this study, the array has experienced occasional temporary equipment issues. For example, the sensor at the Centre Element experienced systematic gain problems, where the amplitude was either higher or lower by some factor ( $\sim 0.5 - 2x$ ). In the summer of 2009, a delay in the sensor replacement resulted in only three functional array channels for a period of several months. Regular preventative maintenance visits are conducted in order to inspect all equipment, perform repairs (e.g. re-install snow fence) and replacements if necessary (e.g. garden hoses can break down due to elements or animal interference).

The most prominent source of seasonally dependent persistent background noise is the Niagara Falls, located about 150 km NE from London. From late April to early October, it produces a constant coherent signal with the mean frequency of 2 Hz, which falls within the same frequency range as most meteors, and hence reduces detection efficiency during those months. Figure 5.2 shows the infrasound noise level and variation as a function of local time of day at ELFO during the summer of 2006. In contrast with earlier studies (e.g. Kraemer, 1977) which detected  $\sim 1$  meteor/year, during our study we find on average about one optically measured meteor is infrasonically detected per month at ELFO. This meteor infrasound data base is particularly unique as meteor infrasound is correlated with meteor optical data obtained with a multi-station all-sky camera network. This has allowed detection of small, short-range meteor infrasound events and ensures robust confirmation of each meteor infrasound event based on timing and directionality determined from optical data as described later.

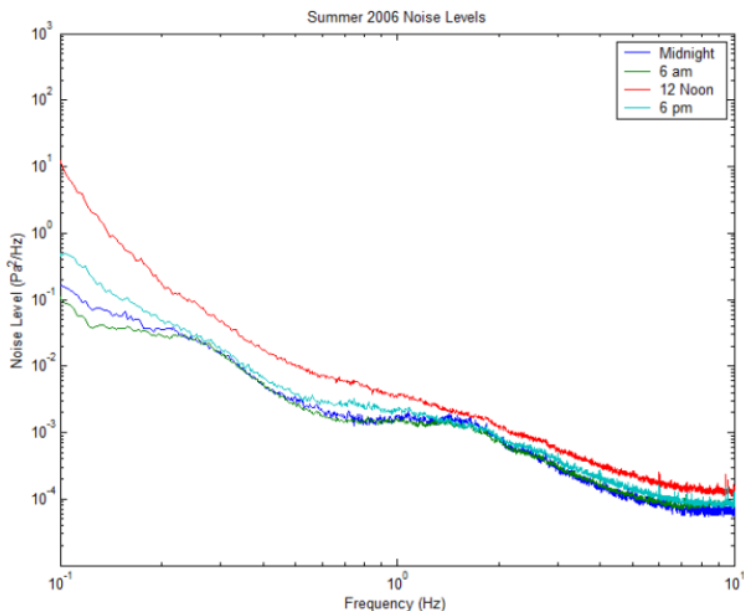


Figure 5.2: A power spectral density (PSD) plot for the entire array for the summer 2006 showing the noise levels as a function of day/night hour. The average noise levels at ELFO at 10 Hz, 1 Hz and 0.1 Hz are  $\sim 10^{-4}$  Pa<sup>2</sup>/Hz,  $\sim 10^{-3}$  Pa<sup>2</sup>/Hz and  $\sim 10^{-1}$  Pa<sup>2</sup>/Hz, respectively.

We note that not every meteor will produce infrasound detectable at the ground, and not every meteor that does produce infrasound is detected by all-sky cameras, the latter being limited to night-time operations under clear skies. Here we consider only those events which are simultaneously recorded by at least two stations of the all-sky camera network (thus permitting trajectory solutions) as well as having an associated infrasound signal. We provide average detection frequency estimates and lower energy bounds in the results section based on these considerations, updating the earlier work by Edwards et al (2008).

### 5.2.2 All Sky Camera System

The All-Sky and Guided Automatic and Realtime Detection (ASGARD) camera network is comprised of 8 stations throughout Southwestern Ontario (Figure 5.3).

These use 8-bit HiCam HB-710E cameras with Sony Hole Accumulation Diode (HAD) CCDs and Rainbow L163VDC4 1.6-3.4 mm f/1.4 lenses producing all-sky views from each station (see Figure 5.4 for an of example all-sky view from a typical camera).

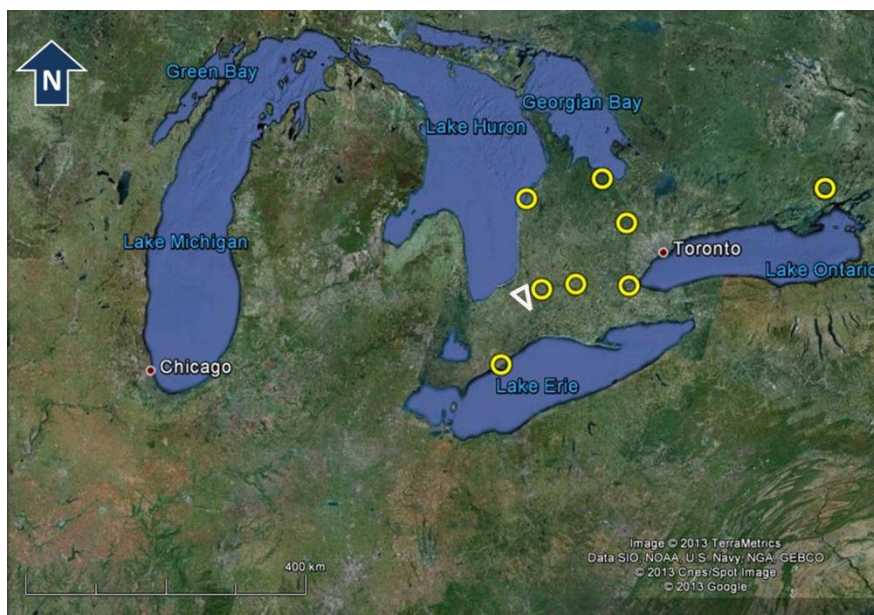


Figure 5.3: The locations of the All-Sky Cameras (yellow circles) of the Southwestern Ontario Meteor Network (SOMN). The white triangle shows the location of ELFO.



Figure 5.4: An example of a stacked (100 frames) video image showing a meteor captured by one of the all sky cameras. North is shown by the arrow. This particular event has a long trail. Most of the events have much shorter trails and are often low in the horizon, where the atmospheric collecting area is largest.

The cameras operate with a gamma setting of 0.45. Each camera is enclosed in a waterproof 30cm in diameter acrylic dome, and set up to observe the entire sky (Weryk et al., 2007) during the night. Each site records video at 29.97 frames per second with 640 x 480 pixel resolution, corresponding to a pixel scale of 0.2 degrees resulting in typical trajectory solutions on order of  $\sim 250$  m precision. The system hardware and software are described in Weryk et al. (2007) and Brown et al (2010).

The all-sky camera system uses an automated detection algorithm in real time (Weryk et al., 2007), triggered by bright visual meteors (brighter than -2 magnitude). Meteors of this brightness correspond roughly to masses ranging from 100g (at 15 km/s) to 0.1g at 70 km/s (Jacchia et al., 1967). When a meteor is detected by two or more cameras, an automated astrometric solution (Table 5.1 and Figure 5.5) is also produced and saved together with raw video comprising 30 frames prior to and 30 frames post event. All stations have Network Time Protocol (NTP) calibrated time using GPS signals. For this study, automated astrometric solutions were used only for initial optical meteor association to locate infrasound detections; all final astrometric solutions were obtained using manual processing in IDL.

Table 5.1: A sample output from the automated optical meteor astrometric solutions. N is the number of cameras detecting the event and used in the trajectory solution, Q\* is the maximum angle between camera's local observation planes of the meteor, shw indicates if the event is associated with a known meteor shower using the three letter codes from the International Astronomical Union (<http://www.ta3.sk/IAUC22DB/MDC2007/>), vel and err are the entry speed and error (in km/s), respectively, H\_beg and H\_end are the begin and end heights in km, respectively.

date	time	N	Q*	shw	vel	err	H_beg	H_end
20131125	10:44:03	2	75.8	...	57.4	3.9	105.5	94.1
20131125	10:33:26	3	48.2	...	60.6	2.4	106	96.5
20131125	08:44:44	4	89.5	...	68.6	0.7	113	89.8
20131125	08:36:05	2	48.6	...	67.7	3.2	107.1	98.4
20131125	08:14:50	2	79.5	LEO	67.8	1.4	112.4	102.5
20131125	07:41:19	2	41.7	...	30.4	0	87.7	72.6
20131125	07:28:17	2	24.5	NOO	44.8	1.1	95.2	81.9
20131125	06:35:39	2	57.9	NOO	40.1	1.3	89.2	76.4
20131125	03:54:53	3	74.5	...	57.8	5	95.9	90.7
20131125	03:53:16	3	76.2	...	60.6	0.4	108.2	86.6
20131125	03:42:27	2	13.1	...	29	1.6	88.2	80
20131124	23:54:28	4	88.6	...	28.4	1	99.1	65
20131124	11:24:58	2	40.6	...	53.4	3.2	94.2	84.3
20131124	10:44:56	2	55.5	LEO	67.4	6.5	106.7	90.4



The meteor astrometric measurements for this study are used to establish the begin and end points of the luminous meteor trail (latitude, longitude and height), radiant (apparent direction in the sky from which a meteor emanates) as well as the meteor speed at any point of the trajectory. These quantities are used to associate potential infrasound signals with meteors and identify source heights of the infrasound signal as described later. In this initial study we focus on astrometry, trajectory solutions and establishing the infrasound source height for each event. The second paper in this series presents photometry and entry modelling of our dataset to compare predictions of infrasound weak shock theory to observations.

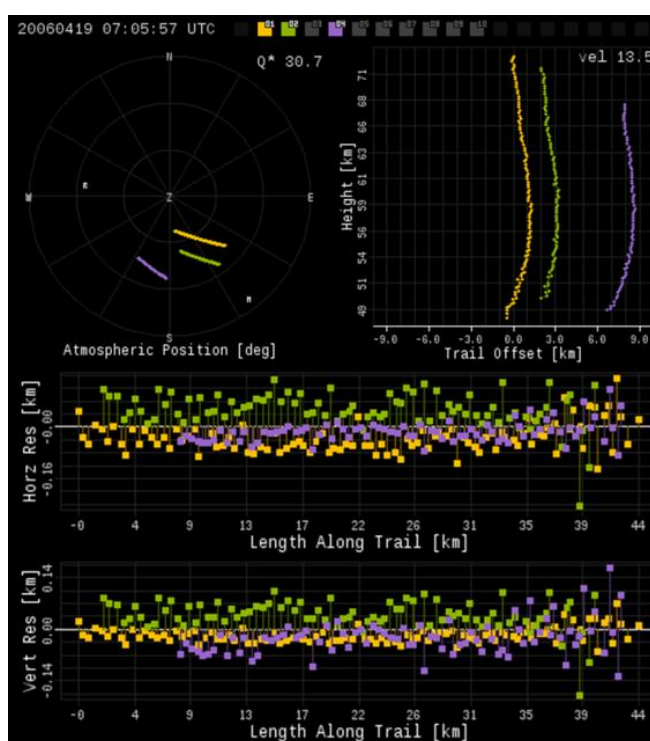


Figure 5.5: An automated trajectory solution for a meteor event recorded by three cameras of the ASGARD system. The top left panel shows the apparent path of the meteor as seen from the three different camera sites where the event was detected. The upper right panel shows the apparent height vs. model height of the meteor where the latter uses an average constant speed of 13.5 km/s - the curved lines demonstrate that the meteor noticeably decelerated. The bottom plots show the individual meteor picks on each frame projected to the meteor trail - deviations are shown from the horizontal and vertical relative to the best fit straight line solution in the atmosphere.

## 5.3 Methodology

### 5.3.1 Astrometry

#### 5.3.1.1 Astrometric Plates

To make precise measurements of the position in the sky and movement of a meteor detected by a camera, calibrations of the plates use known stars to establish plates which map x,y pixel coordinates to local coordinates (elevation and azimuth). Since cameras can move slightly and lose calibration over time, for the highest degree of accuracy in astrometry it is helpful to ensure that the camera plates are made from stellar observations as close to the time of the meteor event as possible. Each camera produces a number of calibration images throughout the night (typically every 20 – 30 minutes) which can later be used for making astrometric plates. For the automated system, new plates are normally generated every 30 – 45 days using Meteor Analysis (METAL), in-house software (Weryk et al, 2007; Weryk and Brown, 2012), which uses the RedSky routine to define the plate (Borovička et al, 1995). The sensitivity of the cameras allows use of stars to magnitude +3.5 for calibration in 30 second image stacks, where the magnitude refers to a stellar magnitude in the R band found in the SKY2000v4 catalogue (Myers et al, 2002).

In order to do astrometric measurements for each optical/infrasonic meteor in this study, first it was necessary to make new plates for each camera and for each night having an event. To make useable plates for any given camera, the all-sky calibration images have to satisfy the condition that there have to be at least nine identifiable stars throughout the entire image, but less than ~50, after which plate residuals slowly increase due to random errors. However, this is not always possible to achieve due to weather. To overcome this shortcoming, the plates are made using multiple images spanning several hours. For those nights which remain cloudy throughout, the plates are made on the closest clear night (ideally a day or two before or after the actual event date). Even though there are instances of two or more meteor events analysed in this study occurring within a time frame of order a week, the new plates were still produced for each night to ensure astrometric solution accuracy. Since astrometric stellar fits undergo significant degradation at low elevations (high zenith angle), it is most desirable to choose



calibration stars at elevations  $20^\circ$  or more above the horizon, where a plate fit solution has smaller stellar residuals ( $< 0.2$  degrees). However, since many optically detected meteors which produce infrasound tend to be low to the horizon, it is desirable to select a good balance of stars throughout the entire image and at all elevations. In this process we use plates where the mean residuals (difference between the fit position and the actual position for stars used in the fit) do not exceed 0.2 degrees. As the functional form of the fit has nine degrees of freedom at least 9 stars are needed to make a plate fit. This initial fit is later refined by adding more stars. METAL displays the star residuals on the screen, thus allowing for outliers to be removed interactively. The plate can be fit and re-fit at any point until a desired average or maximum stellar residual is achieved. The interested reader is referred to Weryk et al. (2007), Brown et al. (2010), and Weryk and Brown (2012) for further details about METAL.

#### ***5.3.1.2 Astrometric Data Reduction and Event Time***

Although it was possible to generate astrometric trajectory solutions using automated picks, these solutions generally had high residuals ( $>0.2$  km) and often were affected by unusual effects, such as hot pixels, weather conditions (i.e. overcast), blemishes or reflections on the dome, meteor fragmentation, very bright flares and occasional insects that adversely affect the quality of the automated picks (positions of the meteor as a function of time in the plane of the sky). Therefore, manual reductions were performed for the final set of complete trajectory solutions for those meteor events having a probable infrasound signal association based on the initial automated solution.

Once the plates were made, in-house programs/functions written in IDL were used to generate astrometric solutions for each event. The procedure includes: (i) select images containing the meteor; (ii) use either automated meteor position picks or a rough version of the manual picks as an approximate guideline in selecting new meteor picks manually, (iii) apply the plate; (iv) generate a trajectory solution using the software MILIG (Borovička, 1990); (v) verify if the solution is acceptable (i.e. residuals from each camera are less than 0.2 km from the trajectory straight line solution and good ( $<10\%$ ) average speed agreement among all cameras); (vi) repeat as necessary until the solution meets the residual and interstation speed consistency (Figure 5.6). Each frame had the meteor

position measured using a manual centroid, since an automatic centroid may suffer from undesirable shifting under certain conditions, such as pixels being close to a star, in very dim and/or overly bright regions (e.g. blooming and oversaturation).

The other criteria we use to define a good astrometric solution also include: the intersecting planes of any two cameras have to be at an angle ( $Q$ ) of more than  $20^\circ$  (in most instances the trajectory solution is unstable and unreliable otherwise), the entire meteor trail should be clearly visible, the meteor should be at elevation of  $>20^\circ$  above the horizon from cameras used in the solution and the event lasts at least 10 frames. Complications in reduction occur due to poor sky conditions, flares on the meteor trail and spurious reflections on the camera dome. These complications are dealt with manually on an event by event basis. For example, many optically detected meteors which produce infrasound tend to be low to the horizon, making the astrometric reductions less accurate as the pixel scale is larger at low elevations. In these cases, the trajectory solution is made using local plate fits, obtained by concentrating on the sky region around the meteor and choosing nearby stars rather than stars throughout the image. Due to poor sky conditions and/or poor camera angle view geometry, astrometric solutions were judged to be of low quality for four optical events having simultaneous infrasound signals and rejected from the final simultaneous infrasound - optical meteor data set.

We computed the event time, accounting for both any interstation camera time discrepancies and time of the first detected frame for each camera. Establishing absolute timing is important in raytracing analysis, when the ray travel time (time between the airwave arrival time and the event start time measured by the camera) has to be known accurately. We estimate the absolute time from any one camera based upon the first frame used for astrometry by subtracting from the trigger time any additional frames from a particular camera where manual examination shows the meteor to be visible. All event start times from all cameras included in the astrometric solution were averaged to give one global event start time. The standard deviations of the averaged camera times were generally less than one second, except in two cases, which were manually corrected when raytracing was performed (further discussed in Section 3.5). This is the estimated

maximum uncertainty in our travel time due to uncertainty in the absolute camera event time. The time error was included in our overall travel time uncertainty for each event start time using the standard deviation between cameras calculated in the previous step and applied to the total uncertainty/error in the observed signal travel time.

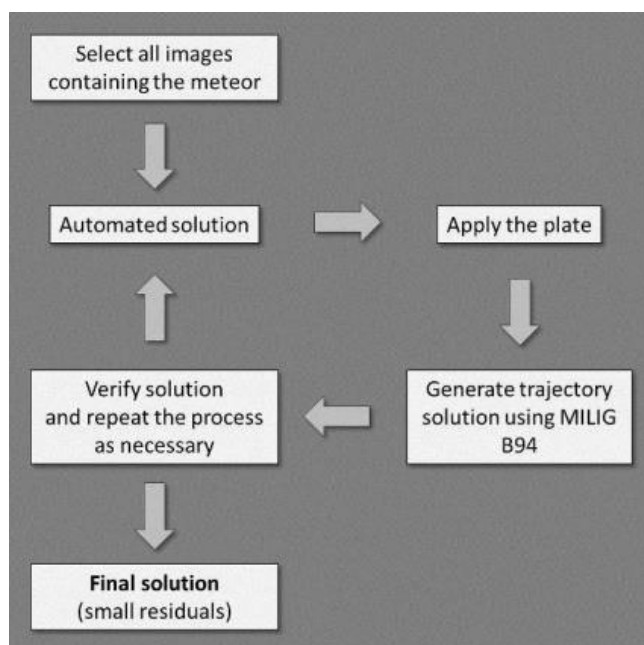


Figure 5.6: A flowchart showing the process of generating astrometric solution from an automated solution.

### 5.3.2 Meteor Infrasonic Signal Identification

Two software packages are used to identify possible infrasonic signals, MatSeis1.7 (Harris and Young, 1997; Young et al., 2002) and the Progressive Multi-Channel Correlation (PMCC) algorithm (Cansi, 1995; Cansi and Klinger, 1997; Garcès et al., 2003a). MatSeis (Figure 5.7) implements the standard form of cross-correlation of the output between each element of the array and performs beamforming of the signals across the array (Evers and Haak, 2001). PMCC (Figure 5.8) is sensitive to signals with very low signal-to-noise ratio (SNR) and uses element pair-wise correlation techniques to declare detections on the basis of signal coherency and back azimuth identifying return

‘families’ in time and frequency space (Cansi and Klinger, 1997; Cansi and LePichon, 2009).

Even though the near field events, especially if they are discrete point source explosions (expected to be produced from fragmenting meteoroids), tend to produce diverging spherical waves, the plane wave geometry approximation in both MatSeis and PMCC is still fairly good when calculating the back azimuth from sources many times further away than the array size; however, it should be noted that the wave distortion effects and atmospheric variability, winds in particular, may produce additional uncertainty. For example, the observed back azimuth deviations for far field infrasonic events due to the variability of atmospheric winds can be as large as  $\pm 15^\circ$  (Garcés, 2013).

Even when a positive detection is found (here defined as an SNR of at least 3 dB) in the correlation indicating a coherent infrasonic wave crossing the array, the infrasonic signal cannot be confidently associated with a source without additional information. An infrasonic signal at short range from a typical local meteor is usually short in duration (1–10s is typical), and in the majority of cases appears as a single N-wave with duration on order of seconds. Thus, it is imperative to have some sort of discriminative methodology which allows for convincing association of meteor events with an infrasound signal.

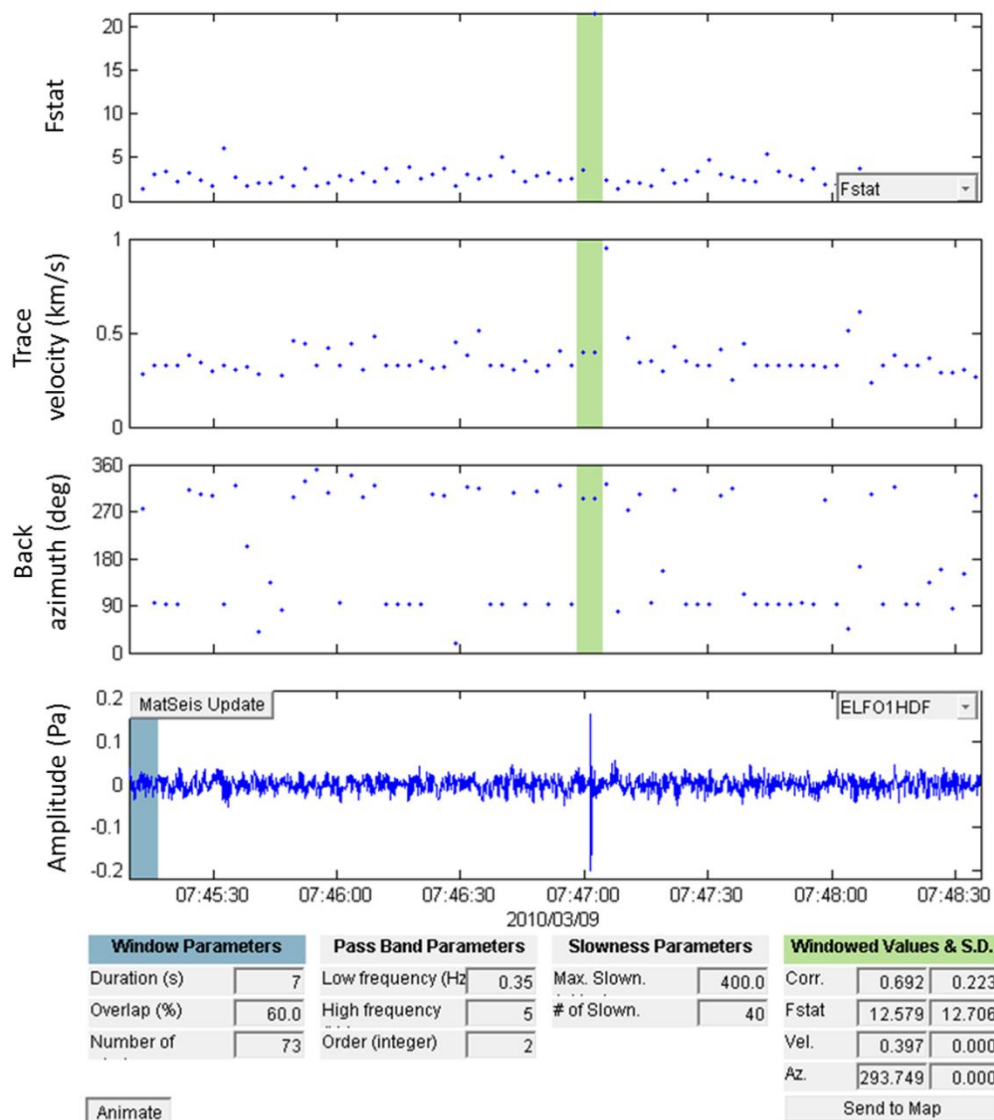


Figure 5.7: An example of a meteor infrasound signal displayed in InfraTool (MatSeis 1.7). The top window is the F-statistic, a measure of the relative coherency of the signal across the array elements, the second window is the apparent trace velocity of the infrasound signal across the array in the direction of the peak F-stat, and the third window shows the best estimate for the signal back-azimuth. The fourth window shows the bandpassed raw pressure signal for the Centre Element of ELFO.

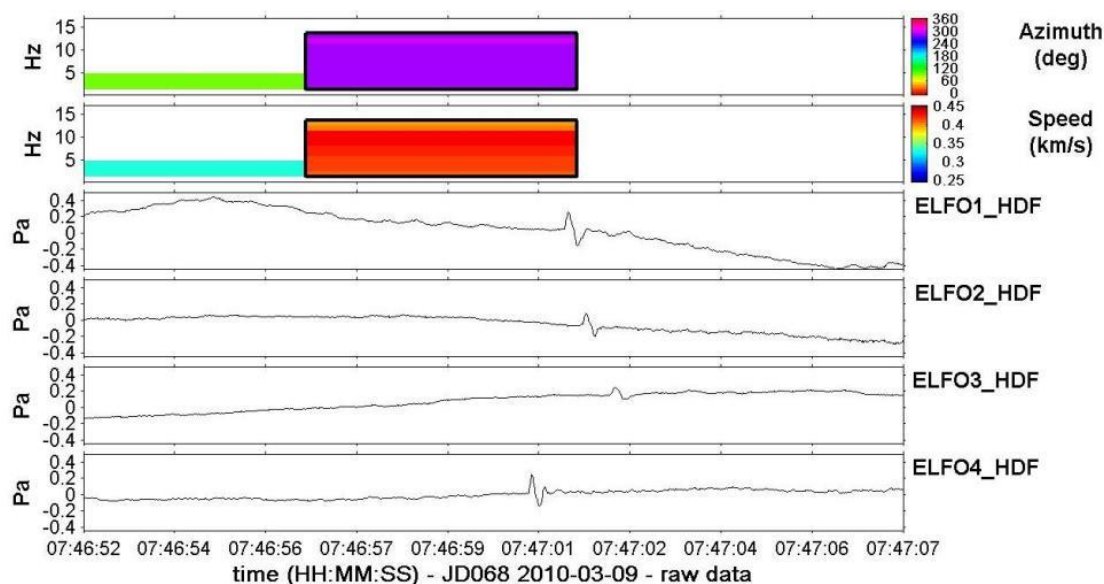


Figure 5.8: Results from array processing using the PMCC algorithm. The top window gives the observed azimuth, the middle window represents the trace velocity of the signal, while the bottom window shows the bandpassed raw pressure signal for all four array elements.

Here we use the automated optical trajectory solutions from each detected meteor for each night, with the date, time, begin and end coordinates and altitudes as inputs, to calculate the following values for both the meteor begin and end points as seen from ELFO: the expected back azimuth, range (great circle path between the source and receiver) and expected travel and arrival time for tropospheric (0.340 km/s average speed or celerity), stratospheric (0.285 km/s) and thermospheric (0.220 km/s) signals. Using these values as guides, we then perform a targeted search for possible infrasonic signals at ELFO associated with the meteor. Although it is not likely to observe thermospheric arrivals for near field events, we still perform a full signal search (from fastest possible to slowest possible celerity). A typical ground-projected distance for most of the camera detected meteors is on average 120 km (and up to 250 km) from ELFO; thus if the meteor trail has a significant horizontal length (on order of tens of kilometers) and depending on the overall spatial geometry of the meteor relative to ELFO, the expected back azimuth, range and travel time windows may vary significantly between the begin point and the end point. This is especially important during meteor showers, when many bright meteors are detected in a single night. Note that we check all meteors optically detected

independent of brightness, where the optical network limiting meteor magnitude is near -2 (corresponding to gram-sized meteoroids at speeds of 40 km/s). The travel time search 'window' thresholds are bounded by the expected signal travel times given the fastest and the slowest infrasonic celerity at the begin point and end point, as well as the closest point to the array with an added five seconds of buffer. Due to the close range of most events to the array, when calculating expected arrival times, we include the true distance (3D) from the source to the receiver, rather than ground projected horizontal distance. The search 'window' thresholds for back azimuth are given by the azimuthal fan sweep from the begin point up to the end point (with a 5° buffer at each end to account for other possible deviations due to the measurement uncertainty, atmospheric effects and array response).

For each optical meteor, a search for possible infrasonic detections is performed using both MatSeis and PMCC guided by the expected arrival time and back azimuth windows. These two quantities are expected to be much more constrained than trace velocity (or signal elevation angle) (McIntosh and ReVelle, 1984). Both signal search approaches (MatSeis and PMCC) are expected to have a high degree of confidence when declaring a positive detection (i.e. within the expected travel time and back azimuth window), which is then flagged for further analysis.

To search for possible signals from typical, small regional meteor events using MatSeis, we used the following detection parameter ranges: window size 7 – 10s, window overlap 50 – 70%, Butterworth bandpass 2<sup>nd</sup> order filter cutoffs between 0.2-1 Hz on the lower end and 2 Hz up to 45 Hz on the upper end. A series of separate independent runs employing different filter and window settings within these ranges for each possible event are used for every meteor to isolate a possible associated infrasound signal recorded by ELFO. Additionally, the correlation and Fisher F-statistics (Melton and Bailey, 1957) have to be above the background values (F-statistics >3) for a positive detection to be declared. Even if the arrival time and back azimuth fall within the previously determined search window, before any coherent event is declared a possible correlated detection, it has to satisfy the additional conditions that the back azimuth and trace velocity have small standard deviations (<2° and < 0.010 km/s, respectively),

without any abrupt variations or spread within the correlation window. Other nearby moving signal sources (e.g. storms, helicopters) generally give infrasonic signals with a spread over several or even tens of degrees in the back azimuth, last for many tens of seconds and in some cases show significant variations in trace velocity; characteristics not typically expected for most meteors. Therefore, such coherent signals would not qualify as possible correlated meteor detections. Based on our experience examining meteor infrasound signals in the past, we also rejected signals which had the following characteristics: signals containing only high frequency ( $>15$  Hz) content, repetitive signals (more than 4 impulsive instances in 15 or less seconds), signals with trace velocity  $< 0.30$  km/s, and long duration signal clusters ( $>30$ s).

Typical detection parameter settings for PMCC were as follows: 5 – 8s window length with 5s time step with default ‘family’ settings (e.g. Brachet et al., 2010; Cansi and LePichon, 2009). The Chebyshev filter parameters were: 2<sup>nd</sup> order, 15 bands with ripple size of 0.005. As with MatSeis, a series of independent runs are performed to search for ‘families’. Once a ‘family’ is detected, additional runs are performed to narrow down the frequency range, arrival time, duration and other signal characteristics.

The results from both MatSeis and PMCC are then compared to look for inconsistencies with the detected signal and determine whether a given positive detection is associated within the window range of our criteria for each meteor. All signal properties found by PMCC were recorded and then used as a secondary means of event and signal measurement verification by comparing to MatSeis results.

The uncertainty in the signal onset (arrival time) was set to 1s, in order to account for potential windowing and intrinsic biases, including the probable discrepancies between MatSeis and PMCC, though we expect in most cases we have localized the start time with better precision. We found empirically that the signal arrival times as calculated in both MatSeis and PMCC generally agree within  $\sim 1$ s for the majority of our meteor infrasound events.

Once positive detections are declared correlated with an optical meteor and selected for further processing, manual optical astrometric solutions are used to re-run the *MATLAB*<sup>®</sup> program in order to refine the timing, distance and back azimuth predictions. These new



values are then used to further check the observations against predicted quantities according to our criteria. If necessary, the entire process of signal detection is repeated. This happens in cases of a significant difference between the automated and manual optical astrometric trajectory solutions, which in turn affects the expected back azimuth and propagation time. In only five cases did this secondary check produce a rejection after initial acceptance on the basis of the automated solutions (of  $\sim 80$  initial events), suggesting a  $<10\%$  loss rate due to poor initial automated optical solutions.

### 5.3.3 Signal Measurements

Following positive infrasound signal correlations with an optical meteor, the meteor infrasonic signal parameters were measured, using the measurement technique described in Ens et al. (2012).

The dominant signal period was calculated using two separate approaches; first, by measuring the zero crossings of the waveform at the maximum Hilbert envelope (max peak-to-peak amplitude) and second, by finding the inverse of the frequency at the maximum signal PSD after subtracting the noise. In contrast to the Ens et al. (2012) procedure, where the signal is stacked using a best beam across the array and where long duration, often high SNR infrasonic bolide signals on large arrays were examined, here signal measurements on each separate channel were performed. This included calculating the maximum amplitude, peak-to-peak amplitude and the period at maximum amplitude to check for any intra-array discrepancies. As there were periods when one of the elements (Centre Element) experienced digitizing issues and thus the amplitude was either systematically higher or lower by some factor ( $\sim 2\times$  or  $0.5$ ) than the rest of the elements, this approach ensured our amplitudes, in particular, did not suffer biases due to equipment problems. In cases where one element was rejected from amplitude measurements, while all four channels were used in cross-correlating, beamforming the period and isolating the signal, the remaining three channels were used for the maximum and peak-to-peak amplitude measurements. The final signals quantities measured for our meteor infrasound database are given in Table 5.2 and Table 5.3.

Table 5.2: Infrasound signal measurements for meteors optically observed and which produced a single infrasonic arrival. Event time denotes the onset of luminous trail as seen by the All-Sky cameras. The remaining columns represent the signal parameters observed at the infrasound array.

Date	Event Time			Observed	Observed	$\pm$	Trace	Dominant	Dominant	$\pm$	Max Amp	$\pm$	P2P Amp	$\pm$	Amp SNR	Integrated
	hh	mm	ss	Travel Time	Back Azimuth											
				s	$^{\circ}$	$^{\circ}$	km/s	Hz	s	s	Pa	Pa	Pa	Pa		
20060419	4	21	28	345	319.9	2.8	0.488	2.2	0.53	0.02	0.05	0.01	0.09	0.03	29.5	3.5
20060419	7	5	56	280	144.5	0	0.42	9.6	0.12	0.07	0.10	0.04	0.13	0.07	29.7	4.3
20060813	9	42	26	554	147.0	0.3	0.358	1.0	0.98	0.06	0.03	0.01	0.05	0.02	18.3	8.1
20061101	6	46	12	527	275.3	1.4	0.421	0.6	1.55	0.44	0.05	0.01	0.08	0.02	13.4	4.9
20061104	3	29	29	354	293.1	0.1	0.439	6.4	0.16	0.00	0.06	0.02	0.09	0.03	29.7	5.2
20061121	10	45	46	526	133.5	1.8	0.395	0.8	1.18	0.11	0.03	0.01	0.06	0.01	16.7	4.3
20070125	10	2	5	398	289.4	4.1	0.601	0.9	1.35	0.03	0.06	0.01	0.08	0.02	7.6	5.6
20070421	9	21	1	636	36.7	0.6	0.379	1.7	0.64	0.04	0.02	0.00	0.03	0.01	18.8	6.8
20070511	7	41	14	439	326.1	1.1	0.442	1.4	0.80	0.04	0.01	0.00	0.02	0.01	14.9	6.9
20070725	4	42	44	392	25.6	2.4	0.425	2.7	0.38	0.06	0.03	0.02	0.05	0.04	31.7	6.0
20070727	4	51	58	467	29.9	0.4	0.41	1.1	0.94	0.08	0.06	0.01	0.09	0.03	20.0	5.4
20070917	7	55	43	572	259.3	0.3	0.368	0.9	1.07	0.12	0.06	0.01	0.09	0.01	28.7	11.8
20071004	4	55	9	557	19.5	0.2	0.352	1.9	0.52	0.03	0.13	0.01	0.15	0.02	41.8	12.0
20071004	5	19	27	307	98.6	0.7	0.345	7.5	0.15	0.04	0.05	0.05	0.08	0.10	43.5	6.3
20071021	10	26	25	700	38.9	3.1	0.347	0.5	2.21	0.03	0.11	0.00	0.20	0.01	51.0	72.4
20071130	10	28	49	645	64.0	0.4	0.332	1.3	0.81	0.18	0.10	0.01	0.12	0.02	12.5	6.2
20071215	11	18	13	318	66.3	4.4	0.397	2.1	0.42	0.06	0.11	0.05	0.17	0.10	39.0	10.6
20080325	0	42	3	341	305.0	4	0.379	7.0	0.14	0.01	0.10	0.06	0.14	0.12	47.2	9.3
20080520	3	29	47	288	80.9	0.5	0.439	10.0	0.11	0.00	0.05	0.05	0.09	0.10	47.2	7.9
20080602	5	44	44	505	221.6	1.6	0.378	0.4	2.56	0.36	0.07	0.01	0.11	0.01	24.2	15.2
20080801	4	22	20	348	329.9	6.4	0.494	2.8	0.33	0.01	0.07	0.02	0.10	0.03	33.7	13.2
20080801	8	19	30	375	350.0	2.4	0.628	0.8	1.40	0.09	0.09	0.01	0.14	0.03	19.4	12.3
20080804	4	17	14	393	148.4	0.3	0.439	2.5	0.44	0.02	0.01	0.01	0.03	0.01	10.7	3.8
20080812	6	0	34	424	197.4	0.5	0.451	2.0	0.53	0.05	0.02	0.00	0.03	0.01	18.5	10.1
20080908	4	3	12	592	292.0	1.5	0.352	0.6	1.63	0.10	0.04	0.01	0.07	0.01	30.5	16.2
20081005	1	50	12	406	337.8	0.3	0.372	6.3	0.19	0.01	0.06	0.03	0.10	0.06	42.1	7.2
20081018	6	53	39	292	83.7	0.2	0.367	12.9	0.07	0.00	0.07	0.13	0.12	0.26	50.4	16.4
20081028	3	17	35	240	306.5	0.7	0.379	11.1	0.10	0.01	0.06	0.06	0.10	0.12	33.1	7.1
20081102	6	13	26	576	292.2	9.5	0.372	2.3	0.44	0.03	0.08	0.04	0.12	0.08	32.6	8.1
20081107	7	34	16	378	330.4	0.6	0.494	1.5	0.59	0.05	0.06	0.01	0.09	0.01	23.9	8.5
20090126	7	16	24	320	231.4	0	0.831	2.2	0.34	0.09	0.13	0.04	0.21	0.08	32.2	16.7
20090523	7	7	25	428	62.2	0.1	0.41	3.0	0.35	0.02	0.20	0.04	0.32	0.07	64.3	18.1
20090530	6	35	20	312	254.3	0.6	0.451	5.3	0.19	0.09	0.07	0.04	0.11	0.07	24.4	3.3
20090709	5	24	23	460	357.1	3.3	0.349	1.7	0.58	0.08	0.10	0.01	0.15	0.02	15.0	4.5
20090813	6	47	53	540	356.9	0.2	0.366	2.9	0.31	0.03	0.02	0.00	0.03	0.00	15.0	1.8
20090906	1	27	55	460	269.0	1.8	0.409	1.9	0.51	0.10	0.02	0.01	0.03	0.01	6.8	2.0
20090917	1	20	38	429	358.0	2.1	0.401	3.0	0.37	0.12	0.08	0.02	0.13	0.04	22.4	13.5
20091025	11	5	58	579	15.0	1.3	0.349	1.3	0.91	0.11	0.03	0.01	0.05	0.02	14.1	8.0
20100111	5	41	5	450	313.8	0.4	0.383	2.6	0.38	0.13	0.15	0.08	0.21	0.16	4.5	0.5
20100307	6	3	26	480	300.1	1.2	0.417	0.7	1.54	0.46	0.08	0.01	0.11	0.01	8.2	2.6
20100309	7	40	44	376	295.0	0.9	0.416	2.0	0.54	0.04	0.15	0.07	0.25	0.13	37.1	3.5
20100316	5	7	44	492	297.3	0.1	0.362	2.4	0.42	0.04	0.10	0.02	0.13	0.04	13.8	1.8
20100421	4	49	43	709	5.7	0.5	0.36	1.0	1.21	0.27	0.05	0.01	0.07	0.01	20.9	8.9
20100423	8	32	35	567	100.5	0.6	0.345	1.9	0.51	0.04	0.03	0.00	0.05	0.01	11.1	3.1
20100429	5	21	35	617	320.4	0.5	0.363	0.9	0.99	0.35	0.07	0.01	0.11	0.02	24.7	8.0
20100814	3	0	42	686	298.2	1.2	0.332	1.2	0.76	0.09	0.04	0.02	0.07	0.05	5.4	1.1
20100914	5	42	26	667	107.2	0.3	0.357	1.3	0.73	0.17	0.04	0.01	0.05	0.02	16.5	4.5
20101129	9	12	44	425	22.4	1.5	0.349	2.6	0.38	0.03	0.09	0.02	0.10	0.05	13.6	5.9
20110208	8	59	33	437	340.3	0.7	0.381	1.8	0.53	0.04	0.13	0.03	0.24	0.05	24.1	4.7
20110402	8	46	52	529	0.0	0.1	0.374	2.3	0.39	0.04	0.05	0.00	0.08	0.01	24.2	4.1
20110520	6	2	9	565	62.5	0.3	0.385	1.9	0.65	0.02	0.03	0.01	0.06	0.01	17.3	5.3
20110630	3	39	38	535	186.2	0.3	0.348	3.0	0.40	0.00	0.03	0.01	0.04	0.02	8.6	3.4
20110808	5	22	6	565	170.2	0.4	0.368	1.5	0.50	0.03	0.03	0.01	0.04	0.02	12.0	4.4
20111005	5	8	53	407	306.6	0.8	0.379	4.6	0.18	0.01	0.13	0.06	0.20	0.12	68.9	15.5
20111202	0	31	4	449	339.1	0.8	0.381	2.8	0.38	0.11	0.15	0.06	0.21	0.12	24.3	7.0

Table 5.3: Infrasound signal measurements for optical meteors which produced more than one distinct infrasound arrival.

Date	Event Time			Observed	Observed	±	Trace	Dominant	Dominant	±	Max Amp	±	P2P Amp	±	Amp	Integrated
				Travel	Back											
	hh	mm	ss	Time	Azimuth	°	Velocity	Freq	Period	s	Pa	Pa	Pa	Pa	SNR	SNR
20060305	5	15	36	349	342.6	0.9	0.381	3.5	0.33	0.02	0.11	0.04	0.18	0.08	50.8	3.6
20060305	5	15	36	358	343.7	1.2	0.357	2.1	0.44	0.09	0.05	0.01	0.07	0.01	17.0	3.8
20060305	5	15	36	359	342.8	1.2	0.357	3.0	0.29	0.04	0.04	0.01	0.06	0.02	16.4	4.3
20060405	3	3	27	394	86.4	0.4	0.335	3.9	0.34	0.07	0.10	0.07	0.15	0.14	33.0	7.1
20060405	3	3	27	397	86.6	0.3	0.339	2.9	0.31	0.05	0.08	0.03	0.10	0.05	25.2	1.1
20060805	8	38	50	427	255.5	1.3	0.372	0.9	1.19	0.10	0.49	0.10	0.68	0.20	162.9	30.8
20060805	8	38	50	450	257	0.2	0.41	0.6	2.01	0.17	0.10	0.02	0.18	0.05	44.5	0.4
20061223	6	27	26	479	341.4	1.6	0.381	2.0	0.53	0.07	0.05	0.03	0.09	0.05	28.9	9.3
20061223	6	27	26	489	346.3	1	0.351	1.0	0.96	0.05	0.09	0.04	0.15	0.07	21.2	8.7
20061223	6	27	26	516	346.4	0.9	0.386	1.2	0.74	0.06	0.18	0.07	0.31	0.14	53.3	48.8
20070102	10	42	3	579	33.1	0.3	0.358	0.8	1.30	0.17	0.04	0.01	0.07	0.02	11.1	2.9
20070102	10	42	3	581	32.8	0.3	0.372	2.0	0.51	0.07	0.04	0.02	0.05	0.05	9.8	3.4
20080511	4	22	17	371	24.8	0.4	0.516	1.3	0.77	0.03	0.03	0.01	0.04	0.01	13.8	2.8
20080511	4	22	17	381	24.8	0.4	0.425	2.9	0.36	0.00	0.01	0.00	0.02	0.01	13.2	2.7
20080612	5	58	29	388	71.2	0.2	0.408	3.5	0.25	0.00	0.04	0.01	0.06	0.02	13.8	0.3
20080612	5	58	29	391	64.7	0.2	0.425	1.4	0.72	0.09	0.10	0.04	0.16	0.07	42.4	20.3
20080812	3	27	25	400	170.3	0.3	0.446	1.5	0.62	0.13	0.20	0.06	0.35	0.12	110.1	20.2
20080812	3	27	25	406	176.2	0.6	0.431	1.6	0.66	0.17	0.11	0.01	0.15	0.02	3.9	0.3
20080812	8	19	29	554	249.4	0.1	0.349	1.6	0.59	0.05	0.02	0.00	0.03	0.01	16.5	6.5
20080812	8	19	29	557	249.8	0.5	0.349	1.8	0.58	0.01	0.02	0.00	0.03	0.01	14.0	2.8
20090428	4	43	37	456	53.6	1.7	0.345	4.1	0.21	0.03	0.16	0.03	0.22	0.06	45.1	4.6
20090428	4	43	37	460	55.3	1.5	0.345	2.7	0.32	0.01	0.06	0.02	0.11	0.04	26.3	6.4
20090812	7	55	58	522	204.5	1.2	0.372	1.6	0.59	0.05	0.09	0.02	0.16	0.03	26.6	1.0
20090812	7	55	58	525	204.3	1.1	0.372	1.8	0.58	0.01	0.07	0.01	0.09	0.02	10.9	1.0
20090825	1	14	35	811	46.2	0.1	0.349	1.2	0.76	0.10	0.07	0.03	0.12	0.05	18.0	1.6
20090825	1	14	35	835	47.2	0	0.348	1.5	0.54	0.01	0.03	0.01	0.05	0.02	5.6	1.4
20090825	1	14	35	842	47.4	0.4	0.348	1.8	0.58	0.03	0.03	0.01	0.05	0.02	6.0	1.3
20090926	1	2	58	424	82.8	0.8	0.347	2.0	0.59	0.01	0.28	0.02	0.49	0.04	112.2	50.0
20090926	1	2	58	439	79.7	0.1	0.363	2.2	0.49	0.03	0.05	0.01	0.08	0.02	3.2	0.4
20100530	7	0	31	530	324.4	0.4	0.358	1.5	0.64	0.01	0.03	0.01	0.06	0.02	16.1	1.7
20100530	7	0	31	535	325.2	0.1	0.358	1.9	0.84	0.21	0.03	0.01	0.05	0.01	10.9	1.7
20100802	7	18	25	406	74.5	0.3	0.417	4.0	0.22	0.00	0.03	0.01	0.06	0.02	16.1	1.7
20100802	7	18	25	410	73.7	0.1	0.417	1.6	0.30	0.01	0.03	0.01	0.05	0.01	10.9	1.7
20110815	5	50	16	550	328.3	0.4	0.347	2.0	0.66	0.02	0.04	0.02	0.06	0.04	14.5	2.1
20110815	5	50	16	556	328.9	0.4	0.372	1.2	0.87	0.09	0.03	0.01	0.05	0.02	9.0	1.1

### 5.3.4 Raytracing and Atmospheric Variability Modelling

Having linked infrasonic signals with optical meteor events and performed signal measurements, the next step in event characterization is establishing where along the optical meteor trail the infrasonic signal originates. This was done by raytracing using the range independent *SUPRACENTER* program (Edwards and Hildebrand, 2004) and a real atmospheric profile for the day of each event. The raytracing results provide expected model timing and model arrival direction of the infrasound signal at ELFO which are then compared with the observed signal. The total uncertainty in signal arrival time consists of the event start time uncertainty (generally <1s except in two cases; see Section

3.1) and uncertainty produced by signal processing (1s). A non-isothermal and vertically inhomogeneous realistic atmospheric profile for each event was generated using wind data from the daily United Kingdom Meteorological Office (UKMO) assimilated dataset (Swinbank and O'Neill, 1994). The UKMO data extends to only 50-70 km in altitude; thus to reconstruct the atmospheric profile (atmospheric pressure, temperature and horizontal winds) from that point to 200 km altitude, HMW95 (Horizontal Wind Model; Hedin et al., 1996) and the NRL-MSIS00 (Naval Research Laboratories – Mass Spectrometer and Incoherent Scatter Radar; Picone et al., 2002) models were combined by a smooth spline interpolation following the same procedure as adopted by Edwards et al. (2008).

Typically, optical meteor events last for 30 video frames or less; each frame corresponds to a different portion along the meteor's path. For raytracing, we used 100 discrete heights along the meteor trajectory (latitude, longitude and altitude) as source 'points' for raytracing. A version of the *SUPRACENTER* (Edwards and Hildebrand, 2004) was used to follow rays from each model point along the meteor trajectory (Figure 5.9) toward the infrasound station and find probable arrivals, which we define as any rays which arrive within 1 km from the central element, horizontally or vertically.

Note that we only follow direct arrivals— ducted arrivals are not computed. The modelled infrasound travel times are adjusted for the finite meteor flight time. The modelled quantities recorded for each discrete point along the trajectory are travel time, back azimuth and elevation angle at the receiver (station) and ray takeoff angle  $\beta$ , which is the angle between the meteor velocity and the ray wave vector as well as vertical and infrasound ray elevation angle at the source.

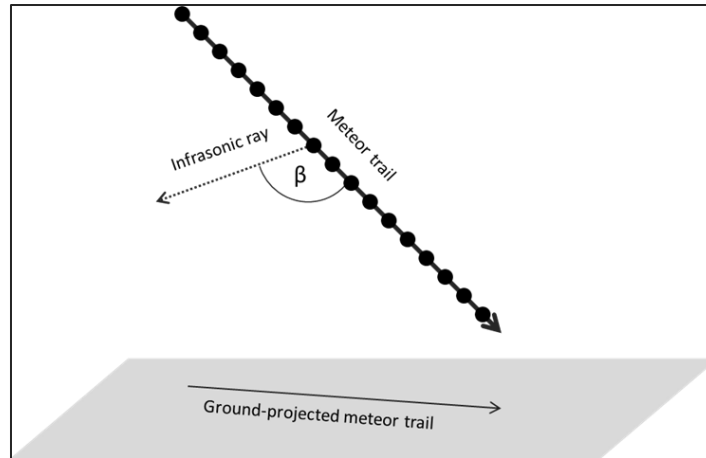


Figure 5.9: Meteor trail raytrace modeling procedure. Black circles depict distinct source points along the trail which are used for raytracing. Infrasonic rays are generated at each point source and propagated towards the array; however, for simplification, only one ray is shown here. The ray deviation angle is the angle of the infrasonic ray wave vector and the meteor velocity vector (in 3D), referred to as angle  $\beta$ .

Using our average atmosphere we found that many events showed no model propagation path or only a model propagation path from the part of the trajectory when winds were applied, though a signal was clearly recorded at the infrasound array. This emphasizes how the atmospheric variability and scattering can play a significant role in infrasound signal propagation (Balachandran et al., 1971; Brown and Hall, 1978; Green et al, 2011). Hourly, daily and seasonal variations in atmospheric infrasound propagation have been observed and well documented (e.g. Le Pichon et al., 2005; 2009). Many factors affect the propagation and detection of infrasound including attenuation (e.g. molecular absorption of sound in the air), non-linear effects, atmospheric turbulence, the effect of the ground surface on acoustic reflection, temperature and wind stratification, barriers, scattering, and atmospheric tidal effects (Brown and Hall, 1978; Ostashev, 2002; Sutherland and Bass, 2004; Kulichkov, 2010; Hedlin et al., 2012). Among these, gravity waves in particular (e.g. Hines and Reddy, 1967; Fritts and Alexander, 2003; Nappo, 2012) have been previously identified as having a significant impact on infrasound signal propagation as they perturb the local wind field on short timescales (Churchuzov, 2004; Ostashev et al., 2005; Green et al, 2011). Furthermore, gravity waves are especially important in perturbing the average windfield in the stratosphere and lower thermosphere,

since this is where the gravity wave amplitudes and scale heights are the largest (e.g. Walterscheid and Hocking, 1991; Gardner et al., 1993; Fritts and Alexander, 2003; Bhattacharyya et al., 2003; Mutschlecner and Whitaker, 2006).

In more general terms, the scattering of infrasonic energy in the middle and upper atmosphere has also been recognized (Chunchuzov, 2004; Kulichkov, 2004; Ostashev et al., 2005; Millett et al., 2007), albeit still not fully understood. Case studies involving well documented large explosive events, such as the Buncefield oil depot explosion in the UK (Ceranna et al., 2009) and the Misty Picture experiment at White Sands Missile Range in New Mexico, USA (Gainville et al., 2010) have explicitly demonstrated noticeable effects on propagation produced by gravity wave perturbations.

However, the implications of gravity-wave induced wind perturbations on regional (near-field, <300 km) infrasound propagation from high altitude explosive sources have not been comprehensively investigated due to a lack of sufficient data. Because we expect wind perturbations to affect the propagation of meteor infrasound *a priori*, we have implemented a Monte Carlo - type approach to estimate the sensitivity of our raytrace solution to uncertainties in the wind field produced by gravity waves. We note that this is only one of several sources of uncertainty in infrasound propagation at regional distances; scattering, diffraction and local reflections may also play a role, but we do not explore these further in this work. Many physical models of gravity waves exist (e.g. Mengel et al., 1995; Fritts and Alexander, 2003); however for the purpose of this study we used the gravity wave wind perturbation scheme implemented in the *InfraMap* raytracing software (Norris and Gibson, 2001; Gibson and Norris, 2000; 2003). Note that the perturbation to the temperature field (and hence indirectly to the sound speed) due to gravity waves is ignored, as this is much smaller than the direct perturbations to the effective sound speed through gravity wave-induced wind variability at our heights of interest.

In this approach the vertical mean wind profile is perturbed, using the Gardner et al (1993) gravity wave model to simulate the spectral character of gravity waves with height and a random-phase technique (Peitgen and Saupe, 1998). This model has been shown to explain propagation in shadow zones and counter-wind returns for other infrasound sources (Green et al, 2011). In our case the gravity-wave wind perturbation model

provides an estimate of the variation in modelled travel-time and backazimuth due to variability in the atmosphere, resulting in a source height uncertainty.

To estimate the maximum expected deviation in model travel time and back azimuth due to gravity waves, perturbations along the great circle propagation path (tailwind or headwind) and transverse to the great circle propagation path (crosswind) were applied to each atmospheric profile (Gibson and Norris, 2000). In total, 1400 perturbation realizations in vertical wind profile per event were generated and then applied to each UKMO-HWM95 profile, forming a sample of 1400 individual atmospheric profiles, upon which raytracing was performed once again for each event. With the exception of a very small number of events (~10), nearly all meteors showed accessible propagation paths along the entire meteor trail. An example of some gravity wave perturbation realizations are shown in Figure 5.10.

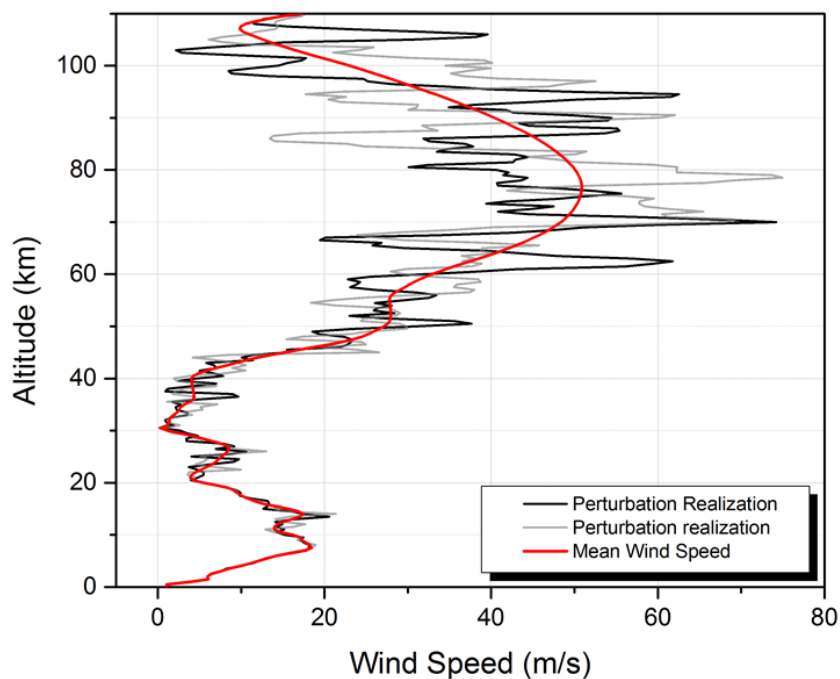


Figure 5.10: An example of a gravity wave perturbed wind speed as a function of altitude. The black and gray lines represent a sample of two separate realizations applied to the to the UKMO-HWM07 mean wind model (red line). For ray-trace modelling, 1400 realizations were applied to the mean atmospheric profile for each event and the resulting spread in travel times and backazimuths recorded.

### 5.3.5 Analysis of Raytracing Results

From the raytracing for each point on the meteor trajectory, we have the expected travel time, back azimuth, arrival elevation angle, the horizontal range (along the great circle path), total range, signal celerity and ray deviation from the trajectory (angle between the meteor velocity vector and the infrasound ray launch direction, Figure 5.11) at ELFO. When combined with the infrasound meteor measurements this produces residuals in the time, the back azimuth and the elevation angle between the model rays and the observations at the ELFO array. Our final dataset consists of 71 meteor infrasound events having a common optical record. To determine where along the meteor trail the infrasound signal originates, the raytracing model results were compared with the observed travel time, back azimuth and elevation angle measured at ELFO.

The ray deviation from the trajectory is important in understanding the nature of the shock production. On theoretical grounds, we expect that there are two types of shock production mechanisms – ablational, due to fragmentation; and ballistic, due to the production of cylindrical line source shock along the entire trail (ReVelle, 1976; Bronshten, 1983). A 90 degree ray deviation angle ( $\pm 25^\circ$ ) is indicative of the ballistic shock (ReVelle, 1976; Brown et al., 2007) and a cylindrical line source geometry, while the ablational shock is expected to be more omnidirectional. However, it remains unknown which of these shock modes is dominant at small meteoroid sizes and what the range of allowable deviation from  $90^\circ$  for true ballistic shocks is. Quantifying these unknowns is one of the goals of this study.

Uncertainties in the signal arrival elevation at ELFO were computed assuming a possible variation of up to  $7^\circ\text{C}$  in the local temperature, which was measured either by a weather station located at ELFO or by UKMO model estimates of the surface temperature.

Our raytracing model using Monte Carlo perturbation realizations produces a ‘cloud’ of possible airwave arrivals from each point along the trajectory. To decide from this ensemble the most likely shock source heights, we developed an algorithm to find the best estimate for the source shock height and its associated uncertainty.



The algorithm works as follows: from our model runs, four modelled arrival quantities were extracted to compare with the observations – travel time, back azimuth, elevation angle and ray deviation from the trajectory. The travel time was used as the primary source height discriminant while the back azimuth was used as a secondary discriminant. We note that the ray arrival elevation angle can vary significantly and is the least reliable measure of all observed quantities (McIntosh and ReVelle, 1984), as atmospheric turbulence, for example, may cause local temperature changes of 5°C in a few seconds (Embleton, 1996). As a result, it was not used to determine the final source heights, only as a tertiary check with the first two quantities. The best estimate of source height then produces an estimate for the ray launch angle, and its deviation from 90 degrees gives an indication of the shock type (ballistic =  $90 \pm 25$  degrees, ablational = any angle). While the majority of the solutions appeared to have a height solution (i.e. fall within the range of the observed quantity and its uncertainty) (S), some solutions were degenerate (could have two possible height solutions) (D), or showed no solution (i.e. did not fall within the observed quantity and our range of adopted uncertainty) (NS).

Even for events showing unique source height solutions, the two quantities used to define source height independently (travel time and back azimuth) would frequently have height solutions which differed from each other, in some instances by up to as much as 20 km much, larger than the uncertainty from the various realizations). To reconcile these differences we developed a set of heuristic rules to try and best objectively quantify the height uncertainty based on our experience with past solutions. For events showing multiple signal arrivals, each arrival was treated as a distinct infrasonic 'signal'. The algorithmic logic for deciding on a best estimate for source height and error is summarized in Figure 5.12.

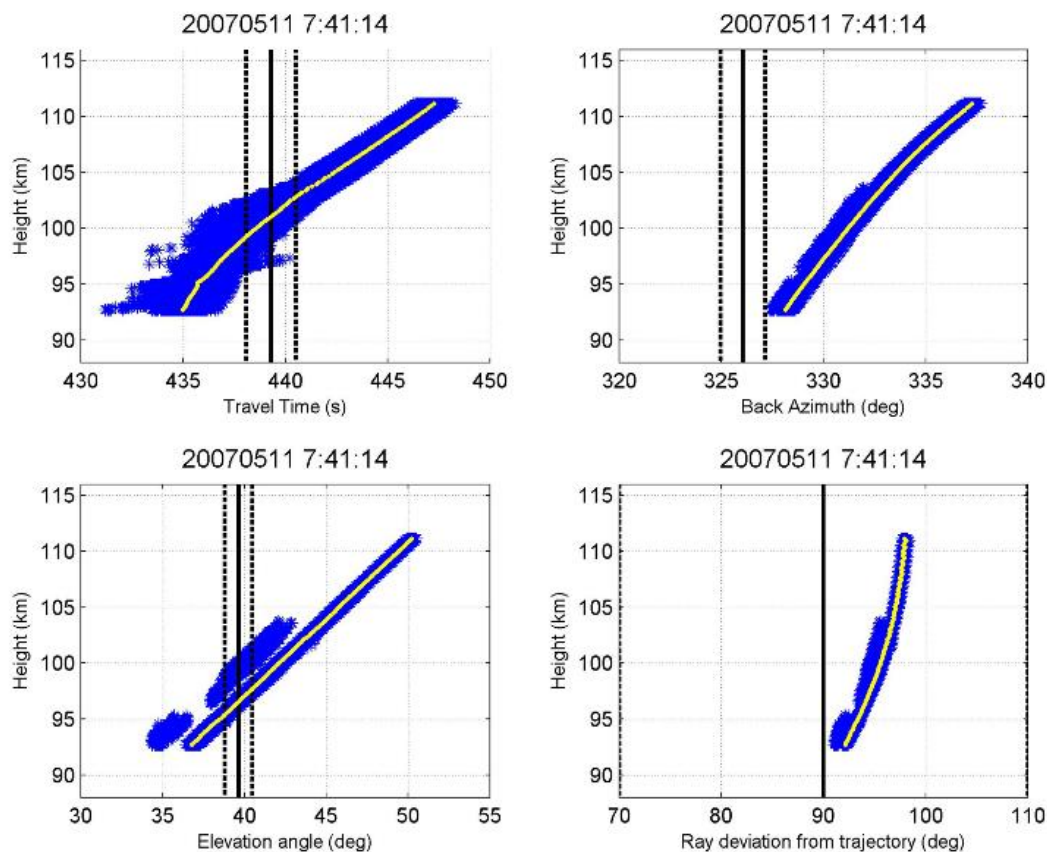


Figure 5.11: An example composite plot showing the travel time (upper left), back azimuth (upper right) and arrival elevation angle (lower left) for an event on May 11, 2007 occurring at 07:41 UT. The lower right plot is the ray launch deviation angle as a function of height along the meteor trail. The blue points represent modelled arrivals for 1400 gravity wave realizations for this event. The yellow model points in all plots are the simulation means along the meteor trail for each height (averaging along the x-axis). The vertical solid black line corresponds to the observed quantity with its uncertainty (dotted line), except in the case of ray deviation angle, which is simply a reference to the expected ballistic angle ( $90^\circ$ ). This particular event is an example which shows a unique solution as defined by our height selection algorithm. The composite plot also shows that the back azimuth determined model source height differs from the model source height determined by the travel time residuals.

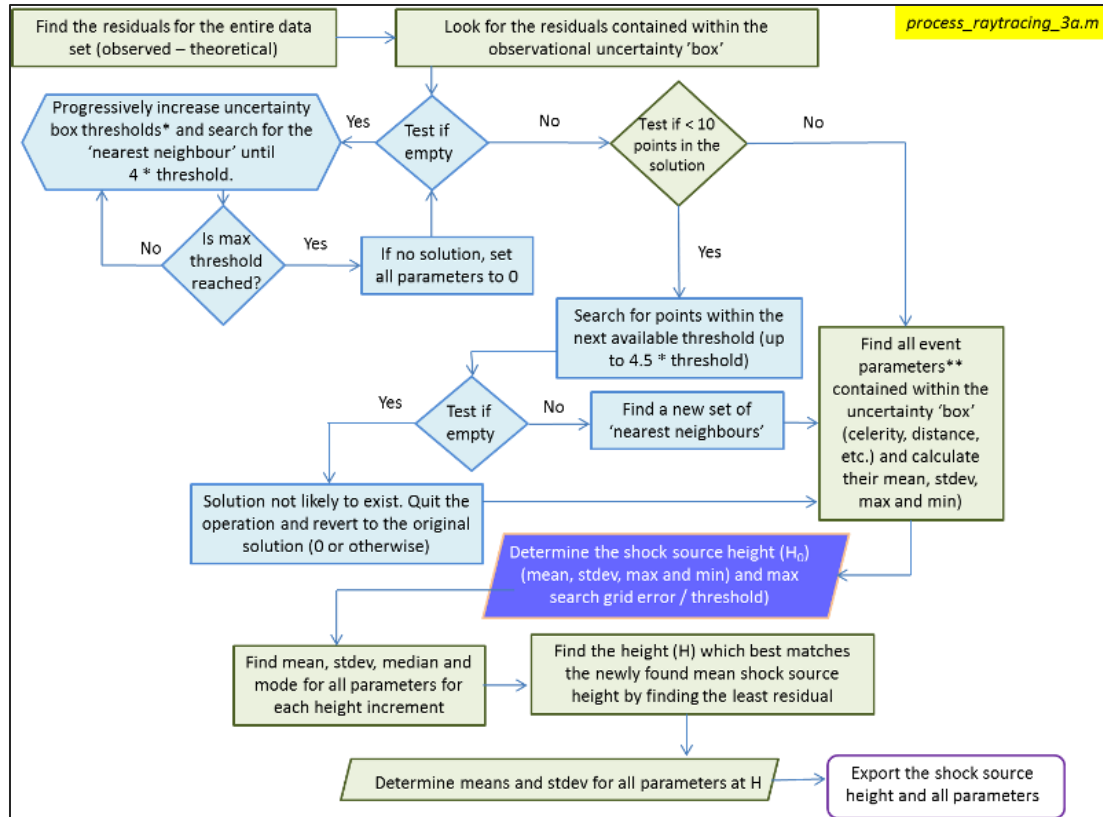


Figure 5.12: The flow chart showing the logic used for calculating the meteor shock source heights and associated parameters.

For each modelled quantity, the absolute value of the difference between each model run and observation is first computed, as shown in equation (5.1) - we refer to these as the model residuals. Here,  $res$  is the residual,  $Q_{obs}$  is the observed and experimentally measured quantity, while  $Q_{model}$  is the modelled quantity:

$$res = |Q_{obs} - Q_{model}| \quad (5.1)$$

All residuals lying within a window containing the observed value and its uncertainty were found. A model residual of zero indicates quantitative agreement between the model value and the measurement (Figure 5.13). This produces a 2-dimensional grid with all the possible heights along one dimension, and the model residuals along the other dimension where all residuals are weighted equally. Even though the arrival ray elevation angle and launch ray deviation angle from the trajectory were not used to establish the source height, the residuals were still calculated in order to get an overall sense of the goodness

of the solution in qualitative terms. To make a best estimate for source height, we use equally weighted measurement residuals of source height from the travel time and backazimuths produced by the model runs (equation (5.1)), first using only those residuals within the measurement error (red points in Figure 5.13).

If no residuals are found within the measurement uncertainty window the range of allowable residuals was increased beyond the one sigma in measurement uncertainty. Here we used expected uncertainties in the atmospheric models and back azimuth uncertainties to gauge the size of the initial allowable increases starting at 1% for travel time (which translates to 1% variation in signal celerity),  $1.5^\circ$  for back azimuth,  $5^\circ$  for elevation angle and  $10^\circ$  for the ray deviation angle. These values are chosen based on the expectation that the signal celerity may vary by a few percent and back azimuth is often not exactly a plane wave in the near field (Pearce and Posey, 1973; Picone et al., 1997; Brown et al, 2003). The choices for the elevation angle and ray deviation were arbitrarily set to the above mentioned values, as these quantities were not used to determine the shock source height but only as a secondary check.

The final shock source height selection was made primarily based on the arrival times, with the back azimuth as a secondary measurement, except for degenerate solutions. In the cases where the two source height solutions were possible for modelled travel times a subjective determination of the best fit was made, using the best fit height from the back azimuth to isolate the most likely ‘true’ source height. We note that the high fidelity astrometric solutions ( $\pm 0.2$  km for begin and end points in horizontal and vertical directions) in this study allow for accurate trajectory measurements and event timing, thus final source heights matched to the model travel times will have atmospheric variability as the main source of uncertainty.

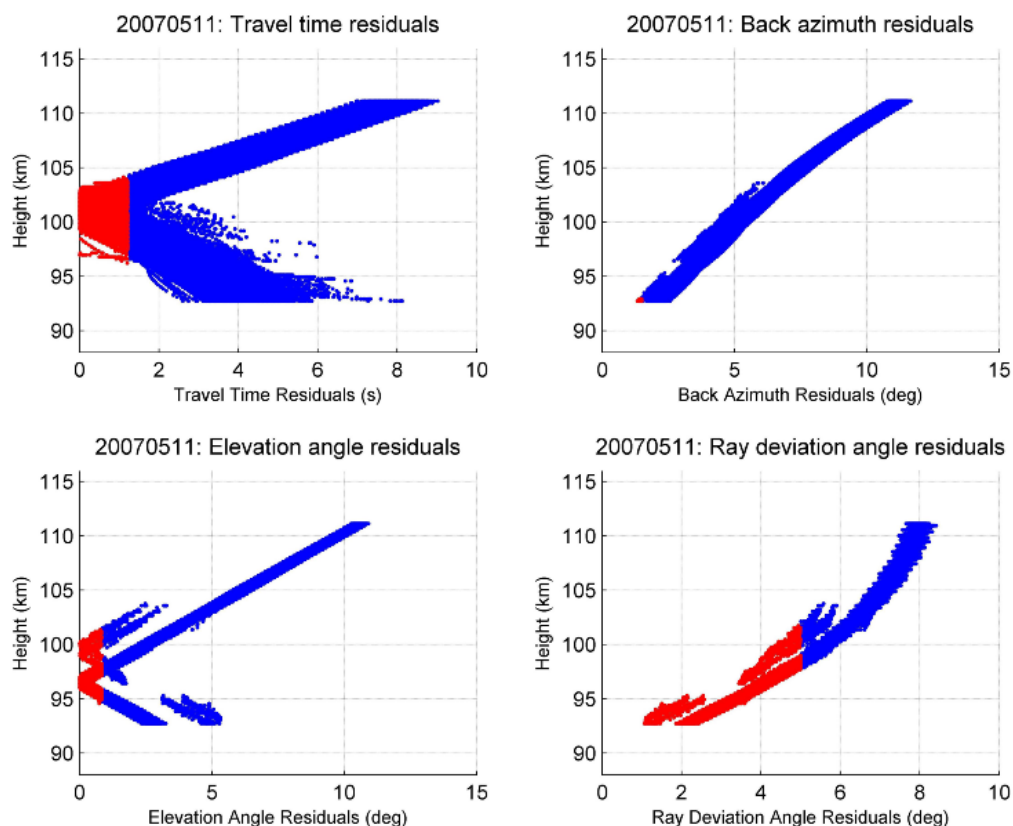


Figure 5.13: A residuals composite plot showing the difference between the model values for each realization and the observed value. Red points show the residuals contained within the height-residual grid where model points agree with observations within the observational uncertainty. Here the ray deviation angle residuals are relative to a ballistic arrival (i.e. residual of zero = 90 degree ray deviation angle).

The implementation of the atmospheric variability in both the direction along and transverse to the propagation path from source to receiver delineates our maximum expected deviations in travel time and back azimuth. Direct arrival, short range (<300 km as in this study) infrasound signals do not undergo significant ducting (channeling) and thus do not suffer from additional modification as seen in far-field (long distance) propagation. To determine the quality of the final source height solution, the travel time and back azimuth residuals were evaluated. The quality of the solutions were classified by the amount the estimated source height primary parameter deviates (percent in travel time and degrees in back azimuth) from the observed quantity. If both travel time and back azimuth were within 1% and  $1^\circ$ , respectively, then the solution was deemed well constrained and of high quality (solution quality Type  $S_A$ ). For the remainder of the

solution quality categories ( $S_B = 2\%$  or  $2^\circ$ ,  $S_C = 3\%$  or  $3^\circ$ ,  $S_D = 4-5\%$  or  $4-5^\circ$ ,  $S_F = >5\%$  or  $>5^\circ$ ), the event was assigned based on the highest deviation of either travel time or back azimuth. For example, if the travel time was within 2%, but back azimuth deviation was greater than  $5^\circ$ , the event was assigned to the  $S_F$  quality category.

## 5.4 Results and Discussion

The initial 80 simultaneously detected infrasound events were reduced to 71 as some events did not have useable optical astrometric solutions while for others there was no raytracing solution, or there were no direct arrivals. The lowermost limit on the detection rate of the array during the 6 year period covered in this study is approximately 1% - out of the total sample of 6989 optically detected meteors, ~80 were also detected by infrasound. This translates into an average of one meteor optical detection on our network producing noticeable infrasound at ELFO per month. However, not all these automated solutions represent physically reasonable solutions as evidenced by unreasonable begin height, end height and entry velocity. Furthermore, the true total infrasonic detection rate is 3-4 times higher accounting for daylight, weather conditions and moonlight which restrict the optical detections to a 20%-30% duty cycle throughout the entire year. This implies that for a site with the noise characteristics of ELFO approximately one meteor per week is expected to be detected infrasonically as a direct arrival. Though rarer, bolides producing ducted infrasonic arrivals (energies above 1 kiloton TNT) on a nearly global scale are expected a few times per year (Brown et al., 2013). On this basis we expect direct arrival meteor infrasound from regional sources to be the dominant type of meteor infrasound detectable at any one station by close to an order of magnitude. We emphasize that identification of an infrasound signal with a meteor or bolide requires separate cuing (in our case optical detection) as the meteor infrasound signal is indistinguishable from most other infrasound sources. In this sense, most meteor infrasound signals can be expected to go unrecognized in the absence of other information. The distribution of begin and end heights for all optically detected meteors, irrespective of infrasound production, as well as the infrasound detected fraction as a function of end height for our study, are shown in Figure 5.14. It is clear that deep penetrating fireballs are much more likely, compared to those ending at higher altitudes,

to produce infrasound detectable at the ground; however, only a very small number of all optical meteors detected by the SOMN network penetrate below 50 km. For example, only about 13% of all SOMN detected meteors have their end height below 70 km, 4% reach below 60 km, while <1% of our optically detected gram-sized and larger meteors have their end heights between 20-40 km. We note, however, that the sole event with an end height below 30 km is the meteorite-dropping Grimsby fireball (Brown et al., 2011); the rest of our data have end heights above 30 km. Our final dataset of events and their astrometric measurements are shown in Table 5.4. Out of 71 events, 55 had associated single infrasound arrivals and 16 produced multiple infrasound arrivals. The 16 multi arrival events produced 35 separate infrasound signal arrivals (three events were triple arrivals, while the remaining 13 were double arrivals).

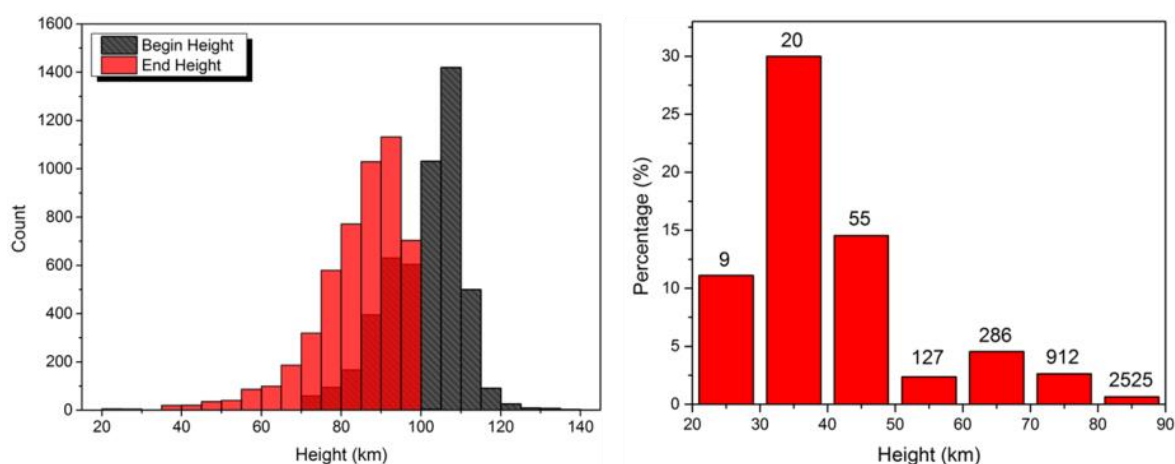


Figure 5.14: Left: Distribution of begin and end heights for ASGARD meteors from 2006-mid 2013. Outliers and events beyond the upper and lower cutoff limits are excluded. Outliers arise as a result of non-converging automated solutions or incorrect picks. Right: Detection rate of infrasonic meteor signals from simultaneously observed optical events for the entire network as a function of end height during the period between 2006 and 2011 in 10 km bins. The percentage represents the ratio between the number with end height of our final data set of all infrasound producing meteors (71 events) and all optically detected meteors in the given height bin during the 6 year period as a function of height. The count number (given at the top of the vertical bar in each bin) represents the total number of optically detected meteors in that height bin (3934 out of 6989 events were in the end height range between 20 – 90 km).

Table 5.4: All astrometric measurements. N is the number of cameras which recorded the event, meteor azimuth and zenith angles refer to the location of the meteor radiant (direction in the sky), and meteor trajectory length is the ground projected length.

Date	Event Time			N	Entry Velocity km/s	$\pm$ km/s	Meteor Azimuth °	Meteor Zenith °	Begin Height °	End Height °	Meteor Trajectory Length km	Meteor Flight Time s	Camera Error Time s
	hh	mm	ss										
20060419	4	21	28	2	18.8	0.6	13.1	64.1	81.3	68.1	26.7	1.57	0.22
20060419	7	5	56	3	14.2	0.1	98.9	56.1	72.0	47.7	35.6	3.30	0.53
20060813	9	42	26	3	62.7	0.3	216.1	19.2	105.4	75.8	10.1	0.50	0.04
20061101	6	46	12	4	57.1	0.9	245.2	14.7	106.0	83.4	5.8	0.40	0.05
20061104	3	29	29	2	30.3	0.4	293.8	35.7	89.9	65.8	17.1	1.03	0.01
20061121	10	45	46	5	71.1	1.3	325.2	25.8	124.3	83.0	19.5	0.63	0.32
20070125	10	2	5	2	71.2	0.4	340.0	75.0	119.2	88.5	109.5	1.64	0.30
20070421	9	21	1	3	33.3	1.0	144.5	14.6	104.4	70.2	8.7	1.00	0.13
20070511	7	41	14	3	64.5	0.6	297.4	52.9	111.1	92.7	23.8	0.47	0.21
20070725	4	42	44	3	26.3	0.2	344.6	34.2	91.5	72.8	12.5	0.87	0.09
20070727	4	51	58	3	26.3	0.0	350.8	51.2	96.2	70.6	31.3	1.57	0.79
20070917	7	55	43	2	59.5	0.3	224.4	40.5	103.7	87.1	13.9	0.33	0.09
20071004	4	55	9	3	28.9	0.5	156.5	47.0	97.3	69.6	29.1	1.37	0.13
20071004	5	19	27	3	16.1	0.2	36.2	53.1	75.9	45.1	40.5	3.50	0.35
20071021	10	26	25	6	75.6	2.7	24.5	22.4	130.8	81.7	19.8	0.70	0.06
20071130	10	28	49	3	71.7	0.5	357.3	25.0	112.9	73.5	18.1	0.60	0.02
20071215	11	18	13	5	35.7	0.5	96.3	44.6	93.6	60.7	31.8	1.30	0.41
20080325	0	42	3	6	13.5	0.3	15.3	45.3	76.2	32.8	43.3	5.21	0.47
20080520	3	29	47	4	14.1	0.1	104.2	29.5	75.2	40.4	19.4	3.24	16.26
20080602	5	44	44	6	63.5	0.7	269.1	61.2	118.1	90.0	49.6	0.90	2.92
20080801	4	22	20	4	23.6	0.4	344.0	50.6	93.3	78.9	17.3	0.93	0.24
20080801	8	19	30	7	65.2	1.2	314.9	68.3	115.5	92.4	56.5	0.97	0.98
20080804	4	17	14	5	58.3	0.3	218.2	59.8	110.7	80.3	50.8	1.00	0.49
20080812	6	0	34	5	60.7	3.5	222.6	48.5	105.9	89.6	18.2	0.43	0.47
20080908	4	3	12	5	62.3	1.2	265.5	56.1	117.6	81.7	52.0	1.04	0.10
20081005	1	50	12	3	22.8	1.5	278.0	24.0	88.4	43.4	18.4	2.10	0.37
20081018	6	53	39	3	21.3	0.3	74.1	38.9	84.1	49.8	27.2	2.24	0.57
20081028	3	17	35	3	15.8	0.1	0.4	57.1	81.2	41.1	60.9	5.21	0.19
20081102	6	13	26	6	31.1	0.7	356.7	28.2	96.5	62.6	17.9	1.33	0.08
20081107	7	34	16	6	70.2	0.9	297.2	62.0	113.5	81.5	58.5	0.97	0.34
20090126	7	16	24	5	67.7	0.9	272.4	75.0	115.6	81.7	119.6	1.87	0.49
20090523	7	7	25	4	29.5	1.0	40.2	42.4	95.9	72.4	21.1	1.14	0.12
20090530	6	35	20	4	17.3	1.2	213.4	59.6	81.7	60.3	35.9	2.47	0.80
20090709	5	24	23	5	18.6	0.7	53.6	39.9	90.2	75.2	12.4	1.03	0.15
20090813	6	47	53	6	60.9	0.4	228.4	42.1	116.2	74.2	37.0	0.94	0.01
20090906	1	27	55	4	60.6	0.4	213.8	69.9	110.9	77.4	88.4	2.50	0.61
20090917	1	20	38	6	23.0	0.4	296.9	65.4	85.7	72.4	28.5	1.60	0.90
20091025	11	5	58	4	28.7	0.3	284.1	88.4	72.6	69.2	92.2	3.40	0.46
20100111	5	41	5	3	54.6	0.4	239.0	73.0	93.9	63.4	95.5	1.47	0.88
20100307	6	3	26	4	49.0	1.3	257.0	53.3	105.8	93.0	16.9	0.43	0.16
20100309	7	40	44	6	48.3	0.9	259.2	44.1	106.9	67.2	37.6	1.17	0.10
20100316	5	7	44	6	22.0	0.3	8.3	60.5	78.0	48.6	51.2	2.08	0.30
20100421	4	49	43	6	46.2	2.0	281.5	48.1	108.5	74.6	37.0	1.07	0.09
20100423	8	32	35	6	48.8	1.1	308.6	13.5	103.4	71.6	7.5	0.63	0.13
20100429	5	21	35	4	46.3	0.8	268.4	49.3	105.7	89.9	18.0	0.50	0.05
20100814	3	0	42	4	57.7	1.1	207.4	65.6	112.9	80.3	69.8	1.34	0.09
20100914	5	42	26	4	43.9	0.1	175.7	40.5	104.4	79.4	20.9	0.73	0.09
20101129	9	12	44	3	29.2	0.4	82.7	42.7	100.1	56.5	39.4	2.10	0.03
20110208	8	59	33	3	59.2	2.6	290.2	28.2	112.8	71.9	21.5	0.80	0.04
20110402	8	46	52	4	28.4	0.4	53.9	53.4	94.8	73.3	28.4	1.30	0.42
20110520	6	2	9	3	23.5	0.8	21.6	51.5	95.7	84.1	14.3	0.80	0.22
20110630	3	39	38	6	33.7	0.3	209.2	23.6	100.5	71.7	12.4	0.87	0.16
20110808	5	22	6	5	24.8	0.4	156.1	49.3	86.6	39.9	53.3	2.84	0.10
20111005	5	8	53	3	29.2	0.2	342.2	43.4	96.2	64.5	29.5	1.50	0.12
20111202	0	31	4	4	26.9	0.1	265.1	67.8	97.0	53.8	101.8	4.40	0.42
20060305	5	15	36	3	18.6	0.1	8.8	30.9	81.2	35.5	27.0	3.17	0.30
20060405	3	3	27	2	11.5	1.7	89.7	26.9	67.8	36.4	15.7	3.54	0.76
20060805	8	38	50	4	67.5	2.7	268.5	29.3	126.4	74.5	28.5	0.80	0.19
20061223	6	27	26	4	22.9	0.8	29.7	32.1	91.5	31.1	37.2	3.00	0.93
20070102	10	42	3	2	43.6	2.6	242.8	30.0	94.0	66.2	15.8	0.77	0.04
20080511	4	22	17	4	21.7	0.3	20.6	67.1	95.2	77.3	41.5	1.97	0.72
20080612	5	58	29	3	15.5	0.4	130.6	52.2	88.3	69.7	23.7	1.97	0.14
20080812	3	27	25	2	59.4	0.8	211.0	64.0	115.8	77.0	77.2	1.47	0.75
20080812	8	19	29	3	56.2	1.4	224.9	28.1	105.7	82.0	12.4	0.47	0.34
20090428	4	43	37	4	18.2	0.0	351.0	32.8	83.5	38.0	29.0	2.97	0.29
20090812	7	55	58	3	58.7	0.2	225.7	32.6	108.5	80.4	17.7	0.57	0.80
20090825	1	14	35	4	23.4	1.6	297.0	48.5	85.4	45.7	44.1	2.50	0.40
20090926	1	2	58	7	20.5	1.2	129.4	36.3	100.5	19.6	56.3	6.07	0.03
20100530	7	0	31	4	28.4	0.5	16.3	61.9	96.0	78.3	32.5	1.33	0.06
20100802	7	18	25	3	41.2	3.2	358.3	57.8	93.6	64.8	44.9	1.27	0.18
20110815	5	50	16	2	57.1	2.2	292.1	30.5	104.3	77.7	15.4	0.57	0.21



### 5.4.1 Infrasound Signal Taxonomy and Phenomenology

The summary of infrasonic signal characteristics as measured for meteors producing single infrasound arrivals is shown in Table 5.2 and for meteors which produced multi infrasound arrival events in Table 5.3. All analysed signal celerities are consistent with the refractive, direct path propagation from the source to the receiver.

Using our dataset of 71 meteor infrasound events, a new taxonomic classification was developed based on the pressure-time coda of the signal. While the majority of the signals in our dataset showed N-wave (DuMond et al., 1946) type arrivals typical of sonic boom signatures (Whitham, 1952; Seebass, 1967; Crow, 1969; Gottlieb and Ritzel, 1988), some signals have double or even triple N-waves, while others exhibit more complex features, such as variability in amplitude, wave appearance, ripples, and humps. Additionally, there were some signals which appeared ‘diffuse’, meaning that they have four or more pressure cycle maxima, all with comparable amplitudes meaning it is difficult to discern specific N-wave features. The amplitude and duration of the N-wave signature are linked to the body’s shape and speed following Whitham’s F-function theory and the sonic boom area rule (Whitham, 1952; Seebass, 1967). However, we do not specifically investigate these here, as the main focus of our study is the signal phenomenology, our intent being to lay the observational foundations for future theoretical studies.

Note we only use the apparent shape of pressure vs. time for classification. The theoretical interpretation and treatment are left for future studies. Our infrasound taxonomic signal classification is described in Table 5.5 and shown in Figure 5.15. Class I signals clearly dominate the data set. In total, 57% of all arrivals were Class I signals, while 22% were Class II, 7% Class III and 14% Class IV signals. Table 5.6 summarizes all signal and source height properties associated with each meteor infrasound taxonomic class.

Table 5.5: Proposed meteor infrasound signal classification taxonomy.

<b>Class I</b>	<b>Single N-wave</b> <ul style="list-style-type: none"> <li>- Clean, no noticeable features, a single most prominent and complete cycle with the P2P amplitude significantly above any other cycles within the signal portion of the waveform (any other peak which is less than one 1/2 of the P2P amplitude would not be counted)</li> </ul>
<b>Class II</b>	<b>Double N-wave</b> <ul style="list-style-type: none"> <li>- Clean, no noticeable features, two prominent and complete cycles similar in size, with the main (dominant) cycle significantly above any others within the signal segment and with the second peak at least 1/2 the P2P amplitude (any other peak which is less than one 1/2 of the P2P amplitude would not be counted)</li> </ul>
<b>Class III</b>	<b>Triple N-wave</b> <ul style="list-style-type: none"> <li>- Clean, no noticeable features, similar in size, classification same as above</li> </ul>
<b>Class IV</b>	<b>Diffuse</b> <ul style="list-style-type: none"> <li>- 4+ complete cycles all within 1/2 the P2P amplitude of the dominant cycle</li> <li>- If the signal is barely above the noise (low SNR), then it is classified as the class IV</li> </ul>
<b>Subclasses</b>	<p><b>a</b> - with a slowly decaying wavetrain and/or trailing reverberations (noticeable for additional 1+ cycles)</p> <p><b>b</b> – subtle to noticeable additional features within the main wave/cycle (humps, ripples, spikes, dips, widening (but not a typical U-wave), etc) confined to the main cycle</p> <p><b>c</b> – complex. Presence of ‘sub-cycles’ and other complex features in the main cycle and beyond. ‘c’ can also be considered a combination of ‘a’ + ‘b’. Presence of leading reverberations.</p> <p><b>d</b> – mixed U- and N- waves (instead of a typical sharp turn as seen in N-waves, a U-wave displays significant widening, after which it gets its destination)</p>
<b>Signal phase</b> (first motion above RMS)	(+) Positive phase (-) Negative phase
	Positive phase (+) Negative phase (-) Indistinguishable (indeterminate) phase (*)

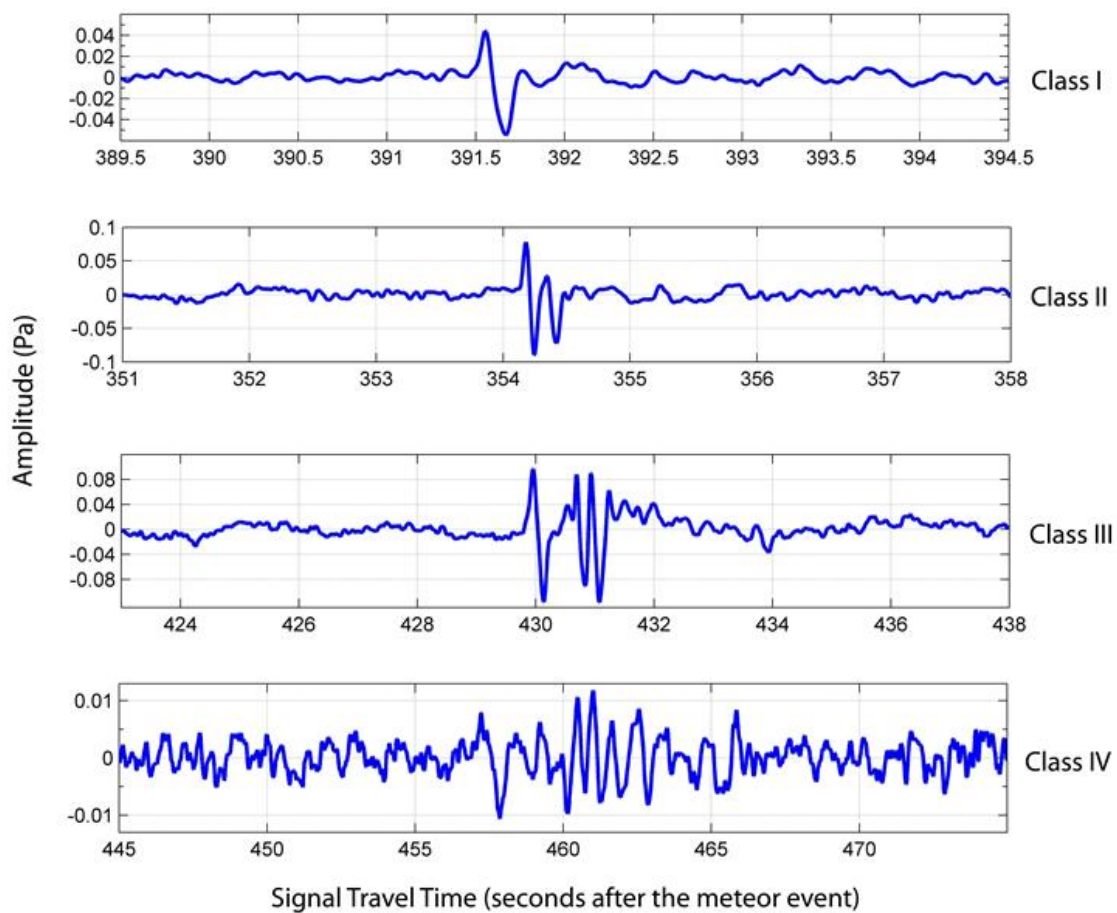


Figure 5.15: Examples of each taxonomic class.

Table 5.6: Summary of infrasound signal characteristics by taxonomic class.

	Source Altitude (km)	Signal celerity (km/s)	Total range (km)	Horiz range (km)	Ray deviation (°)	Sh parameter	Meteor Entry Velocity (km/s)	Begin Altitude (km)	End Altitude (km)	Flight Time (s)	Trace Velocity (km/s)	Dominant Freq (Hz)	Dominant Period (s)	Max Amplitude (Pa)	P2P Amplitude (Pa)	Bolide Integrated Energy SNR
<b>Class I (51 arrivals)</b>																
Avg	77.5	0.306	140.6	115.3	102.0	0.6	38.5	97.6	65.6	1.7	0.394	2.64	0.70	0.09	0.14	8.50
Std. dev.	15.6	0.015	32.8	36.3	16.7	0.3	20.1	15.5	17.2	1.2	0.080	2.56	0.50	0.07	0.10	11.16
Min	38.1	0.274	73.3	47.4	75.2	0.1	11.5	67.8	31.1	0.4	0.332	0.39	0.10	0.02	0.03	0.28
Max	111.4	0.334	216.6	198.6	146.7	1.0	75.6	130.8	93.0	5.2	0.831	12.89	2.60	0.49	0.68	72.40
<b>Class II (20 arrivals)</b>																
Avg	78.2	0.313	151.8	127.8	99.4	0.6	37.3	97.6	63.2	2.2	0.393	2.29	0.60	0.07	0.12	9.15
Std. dev.	17.0	0.015	28.0	33.4	13.7	0.3	17.7	12.0	22.0	1.8	0.057	1.70	0.30	0.06	0.11	14.13
Min	20.2	0.288	113.1	72.5	70.3	0.0	13.5	72.6	19.6	0.3	0.332	0.88	0.10	0.01	0.02	0.31
Max	102.7	0.336	206.9	189.7	122.6	1.0	71.2	119.2	88.5	6.1	0.601	7.03	1.30	0.28	0.49	50.03
<b>Class III (6 arrivals)</b>																
Avg	77.0	0.298	118.1	87.9	92.2	0.8	35.8	95.2	71.7	1.5	0.429	3.63	0.40	0.05	0.08	9.59
Std. dev.	19.7	0.008	16.0	15.1	3.2	0.1	21.3	13.3	20.1	1.1	0.049	3.16	0.20	0.03	0.04	3.24
Min	46.9	0.287	92.6	68.2	87.0	0.5	14.1	75.2	40.4	0.4	0.349	1.37	0.10	0.01	0.02	5.92
Max	101.0	0.307	132.6	108.2	95.9	0.9	64.5	111.1	92.7	3.2	0.494	9.96	0.80	0.09	0.13	13.55
<b>Class IV (13 arrivals)</b>																
Avg	78.6	0.309	174.8	150.6	111.7	0.6	40.8	99.6	65.3	1.6	0.386	2.01	0.70	0.04	0.06	3.94
Std. dev.	17.9	0.019	57.9	69.9	17.8	0.3	19.0	12.2	19.5	1.0	0.050	1.43	0.40	0.02	0.03	2.46
Min	46.4	0.282	111.7	59.3	83.9	0.0	21.7	85.4	31.1	0.4	0.348	0.59	0.20	0.01	0.03	1.34
Max	103.8	0.338	277.1	267.9	151.5	1.0	71.1	124.3	83.4	3.0	0.52	6.25	1.60	0.07	0.12	9.26

Meteor generated infrasound signals with slowly decaying wavetrains (in this study referred to as subclass ‘a’), as well as double and triple brief cycle pulses with nearly identical amplitudes were also observed and reported by Edwards (2010). These peculiar types of multiple N-wave signals are defined in our classification table as Class II and Class III. Edwards (2010) suggested that these repeating N-wave like pulses could be due to the relaxation of the atmosphere as it restores itself to the ambient levels. Alternatively, local turbulence in the lowest layers of the atmosphere could cause some of these distortions as has been found for sonic booms (e.g. Pierce, 1968; Hayes et al., 1971).

These waveform signatures, however, are not unique to meteor generated infrasound. Gainville et al. (2010) modelled the infrasonic waveforms from the Misty Picture experiment (a spherical blast induced by the explosion of ammonium nitrate and fuel oil (ANFO)) and showed the measured waveforms as recorded at the Alpine, White River and Roosevelt sites, all of which were within a few hundred kilometers from the source (248 km, 324 km and 431 km, respectively). The waveform from Alpine bears a close resemblance to the Class II signals typically observed in our study (irrespective of the frequency content and signal amplitude). The signals in our study originated at high altitudes and had a direct propagation path to the detection location, while the signal from Alpine was a thermospherically refracted arrival. We note that the typical signal

amplitudes in our study are at least two orders of magnitude smaller than those of the Misty Picture experiment. Gainville et al. (2010) showed that both scattering and nonlinear effects influence the shock front evolution and propagation and local effects near the receiver array may affect our meteor infrasound signals in a similar manner.

Brown et al. (2007) suggested that a very high temperature region near the edge of the blast cavity induced by rapid deposition of energy as the meteoroid propagates through the atmosphere may enable, due to non-linear refractive effects, outward shocks to have ray deviations up to  $25^\circ$  from the ballistic regime. Successive shocks, potentially originating at different points along the hypersonic path (cylindrical line source) may then undergo interference (e.g. converging shocks) and produce a complex flow pattern, similar to that around an axisymmetric slender body (e.g. Whitham, 1952). For example, a ballistic shock (which reaches an observer at the ground) from a certain height may get ‘mixed’ with a refracted ray emanating from an adjacent portion of the trail, thus forming complex shock features at the source. Meteoroids which fragment and have two or more distinct fragments with independent shocks might also produce multiple N-wave signatures provided the transverse spread is of order 100m or more, values consistent with transverse spread for some larger meteorite producing fireballs (Borovička and Kalenda, 2003). Moreover, events with ballistic arrivals having fragmentation episodes within a few kilometers of the specular point would have the cylindrical and spherical N-waves arrive close in time. Further studies and numerical modelling are needed to investigate the connection between the non-linear and refractive effects, and shock pattern at the source and their subsequent manifestations in the waveform as received by the observer.

Infrasound observations from the large sample of events in this study suggest that Subclass ‘a’ can be generated anywhere in the meteor region (middle and upper atmosphere) and it does not show any particular association to source altitudes. Signal class also shows no correlation with source heights, suggesting that there is no association between these two parameters.

The correlation between the signal peak-to-peak amplitude and the signal class is shown in Figure 5.16. There is a general pattern in the peak-to-peak signal amplitude, which

shows an apparent decrease as the taxonomic class increases. This may hint at a change in the acoustic radiation efficiency with an angle from the ballistic direction or that longer duration shocks showing more N wave cycles have a larger wavetrain to "spread" similar energy and hence the peak amplitudes appear to be smaller. Indeed, classical Whitham's theory indicates that the quantity *pressure x duration* is conserved and hence the longer durations of the higher classes would expect to be correlated with attenuated amplitudes. However, the underlying cause of this correlation for meteor infrasound remains unclear. 'Outliers', which appear to be far beyond the peak-to-peak amplitude limits of any of the other meteors, are associated with higher energy bright fireballs which exhibit evident gross fragmentation events; one of these 'outliers' is the Grimsby meteorite-producing fireball (Brown et al., 2011). These large events more strongly reinforce the correlation between the signal class and peak-to-peak amplitude.

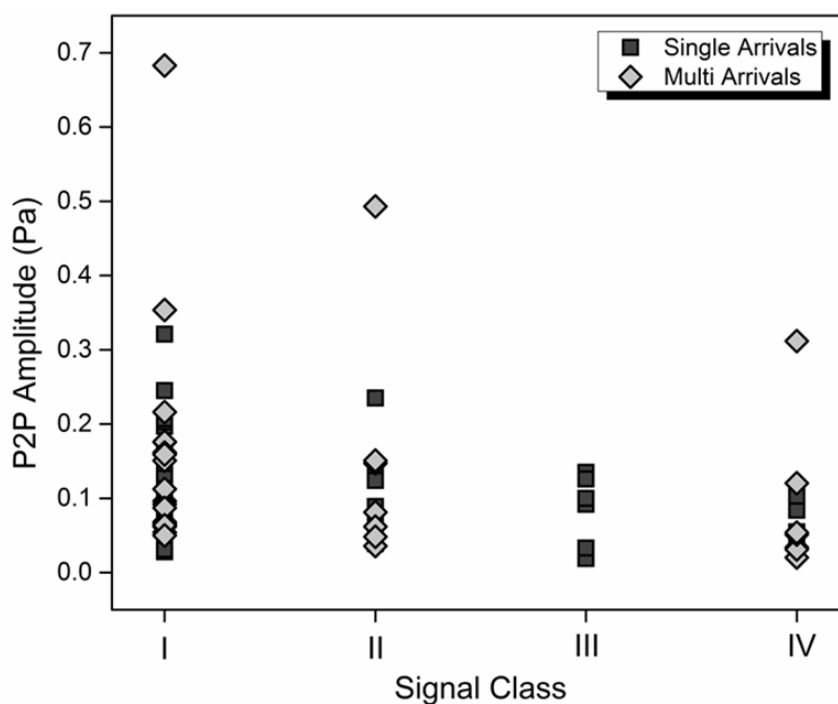


Figure 5.16: The relationship between the peak-to-peak amplitude of the meteor infrasound signal as a function of signal class. There is an evident fall-off in amplitude as the signal class increases.

The dominant signal frequency shows a clear relationship with range, as expected (Figure 5.17). As a zeroth order empirical discriminant for direct arrival meteor infrasound we can use the upper envelope shown in Figure 5.17 to estimate the maximum likely detection range for typical regional meteor events using dominant frequency:

$$Frequency(R) = 2.05 + 290 \exp(-R/31) \quad (5.2)$$

where the dominant signal frequency in Hz and  $R$  is the range in km.

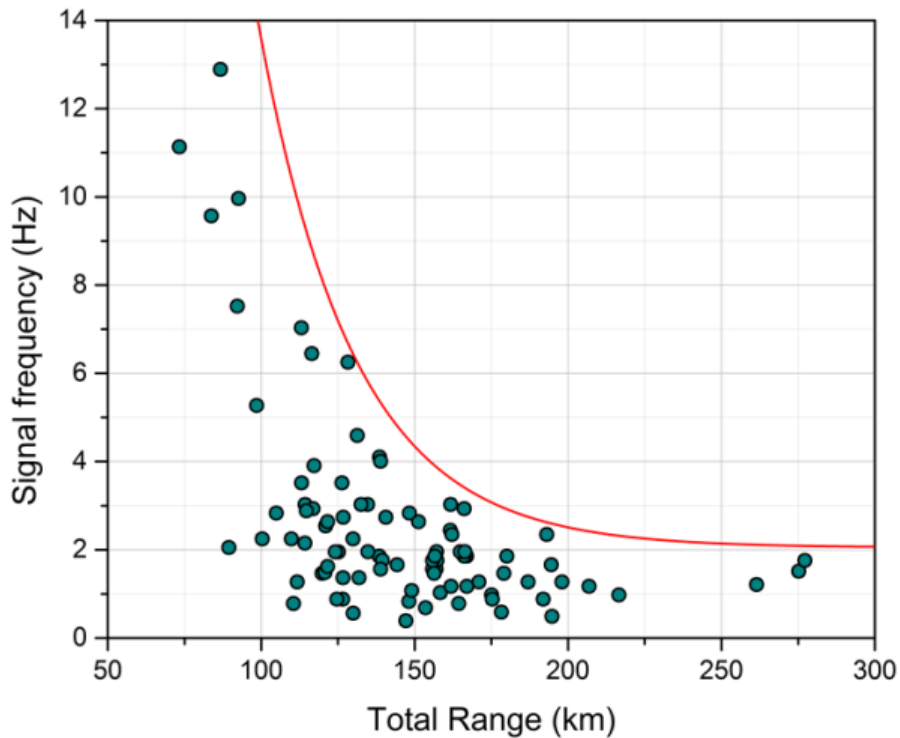


Figure 5.17: The observed fall-off in the dominant signal frequency of bright regional fireballs as a function of range. The exponential decay curve is given by equation (5.2).

#### 5.4.2 Shock Source Heights and Entry Velocity Distributions

Using our new algorithm to determine the shock source heights from raytracing using a sequence of 1400 *InfraMap* gravity wave perturbation realizations, we found best estimates for the height (and its uncertainty) along the meteor path where the infrasound was produced and subsequently detected at ELFO for single arrivals and multi arrival

events. These results are summarized in Table 5.7 and Table 5.8, respectively. For the purpose of quantifying the shock source parameters, each infrasound arrival was treated as a separate event. An overview map with the ground trajectories showing the point along the meteor trail where the infrasound is produced as detected at ELFO is shown in Figure 5.18.

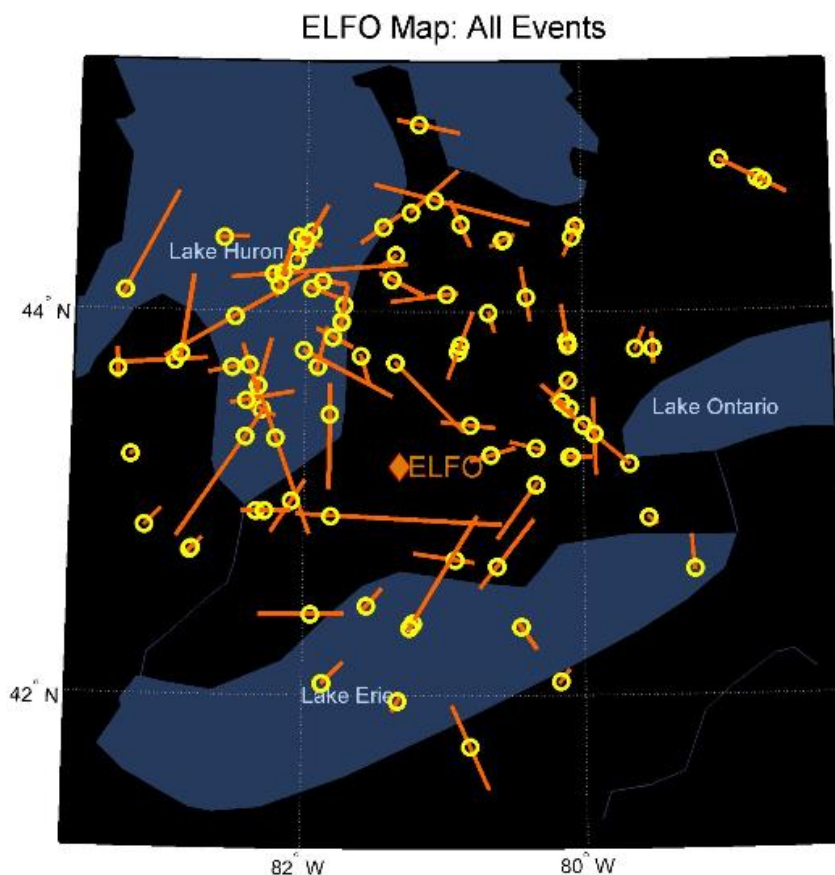


Figure 5.18: A map of Southwestern Ontario and surrounding lakes showing the array (middle) and the spatial orientation of ground projected meteor trajectories for all events (orange lines), including the point along the trail where infrasound was produced and subsequently detected at ELFO (yellow circles).

Overall, we find that the travel time is the most robust estimator for the true shock source heights; secondary estimates from other parameters usually agreed with the height found from travel time residuals. Taking into account gravity-wave induced variability through



our model we were able to match all observed arrivals, demonstrating in a model sense that wind perturbations can be a major factor in permitting infrasound propagation paths which do not otherwise exist using an average atmosphere only. Typically, the model predicted spread in the travel time due to atmospheric variability was between 2 s and 7 s, and the spread in the back azimuth was  $1^\circ - 4^\circ$ . Most events had source height agreement between both travel time and back azimuths, while others showed poorer agreement (Table 5.9).

We compared our results with a previous study which explored 12 common optical-infrasound events recorded during the period between 2006 and the early 2007 (Edwards et al., 2008). These were also analysed as part of our study. In terms of raytracing, the main difference between the two studies is that in the current study there is a much smaller overall spread in the source height uncertainties per event. The shock source heights derived in this study differ from those found previously by 7 km on average. We attribute this difference to three major factors: (i) better astrometric solutions (e.g. improvements in the processing software have been made since 2007); (ii) the incorporation of atmospheric variability in raytracing solutions; and (iii) the method of finding the source heights using our new algorithm which differs from that used in the Edwards et al. (2008) study.

Table 5.7: The raytracing results and signal classification for single arrival events. All raytracing parameters represent the modelled quantities at shock source height, which are then compared to the observed quantities to determine which source heights best match the observations. Here Solution type code is: NS - no source height solution; D - degenerate source height solution and S - unique source height solution.

Date	Event Time			Source $H_{mean}$ km	$\pm$ km	Total Range km	Hor. Range km	Ray Dev °	Back Azimuth °	Travel Time s	Sol Type	Sh Param	Signal Class
	hh	mm	ss										
20060419	4	21	28	79.8	0.2	109.8	75.4	88.2	327.4	349	NS	0.11	I
20060419	7	5	56	54.4	1.1	83.7	63.5	80.7	143.9	279	D	0.72	I
20060813	9	42	26	80.3	0.4	175.1	155.6	122.6	146.8	554	S	0.85	II
20061101	6	46	12	85.7	0.5	178.3	156.4	121.8	273.6	527	S	0.90	IV
20061104	3	29	29	77.0	1.1	116.4	87.2	104.3	294.1	354	S	0.53	II
20061121	10	45	46	91.4	0.4	148.1	116.7	151.5	136.0	526	S	0.80	IV
20070125	10	2	5	102.7	0.5	126.6	73.7	89.3	287.5	399	S	0.53	II
20070421	9	21	1	89.6	0.4	194.6	172.7	130.8	36.5	636	S	0.43	I
20070511	7	41	14	101.0	1.2	131.9	84.8	95.9	331.7	439	S	0.55	III
20070725	4	42	44	73.3	0.5	126.7	103.3	105.5	28.6	403	NS	0.97	I
20070727	4	51	58	85.0	1.5	149.0	122.5	94.6	30.2	469	S	0.44	I
20070917	7	55	43	87.9	0.8	175.3	151.7	95.6	257.8	589	NS	0.96	II
20071004	4	55	9	83.0	0.2	166.9	144.9	146.7	18.1	557	S	0.52	I
20071004	5	19	27	46.4	0.8	92.2	79.7	82.1	96.6	311	NS	0.96	I
20071021	10	26	25	101.2	1.4	194.8	166.3	105.2	39.8	700	S	0.60	I
20071130	10	28	49	93.2	0.6	187.0	162.1	114.2	68.2	645	S	0.50	I
20071215	11	18	13	75.9	0.9	89.5	47.4	94.0	65.3	328	NS	0.54	I
20080325	0	42	3	61.6	0.6	113.1	94.9	107.4	304.9	343	S	0.34	II
20080520	3	29	47	46.9	1.0	92.6	79.8	87.0	82.2	305	NS	0.81	III
20080602	5	44	44	111.4	3.9	147.2	96.2	89.0	212.9	508	S	0.24	I
20080801	4	22	20	79.8	0.5	104.9	68.2	93.2	332.5	348	NS	0.93	III
20080801	8	19	30	92.6	0.3	110.5	60.3	86.3	346.4	373	S	0.99	I
20080804	4	17	14	90.0	0.4	121.0	80.8	108.6	140.7	392	S	0.68	IV
20080812	6	0	34	93.8	2.7	125.2	82.8	94.4	200.8	430	NS	0.74	III
20080908	4	3	12	104.3	1.0	178.3	144.6	75.2	294.2	614	NS	0.37	I
20081005	1	50	12	54.3	1.8	128.3	116.3	102.4	341.1	405	S	0.76	IV
20081018	6	53	39	67.9	1.0	86.7	53.3	101.4	84.6	303	NS	0.47	I
20081028	3	17	35	52.7	3.6	73.3	50.9	92.2	307.2	239	S	0.71	I
20081102	6	13	26	85.0	0.5	193.1	173.4	117.3	292.4	576	S	0.34	II
20081107	7	34	16	81.9	0.6	119.9	87.6	85.3	332.0	377	D	0.99	I
20090126	7	16	24	87.3	0.8	100.3	49.1	88.4	219.9	329	NS	0.83	I
20090523	7	7	25	78.1	2.3	134.7	109.8	96.0	60.8	429	S	0.76	I
20090530	6	35	20	74.0	2.5	98.5	65.7	88.1	256.1	325	NS	0.39	I
20090709	5	24	23	75.9	0.5	144.3	122.7	107.3	352.3	468	NS	0.95	I
20090813	6	47	53	75.4	0.2	166.1	148.0	144.4	359.1	541	S	0.97	I
20090906	1	27	55	103.8	1.0	138.5	91.5	92.1	282.6	469	NS	0.21	IV
20090917	1	20	38	76.6	2.1	132.6	108.2	90.3	358.4	437	NS	0.68	III
20091025	11	5	58	70.5	0.2	171.0	155.8	91.4	14.6	595	NS	0.62	II
20100111	5	41	5	78.6	1.7	151.3	129.2	100.3	326.1	458	S	0.50	I
20100307	6	3	26	103.6	0.8	153.5	113.4	99.9	304.3	480	S	0.18	I
20100309	7	40	44	77.8	0.9	124.2	96.6	102.4	297.3	375	S	0.73	I
20100316	5	7	44	75.2	0.9	161.6	143.1	94.3	301.3	493	S	0.10	I
20100421	4	49	43	86.3	0.8	216.6	198.6	109.4	5.7	709	S	0.65	I
20100423	8	32	35	76.5	0.4	166.2	147.5	136.5	100.8	566	S	0.85	I
20100429	5	21	35	93.0	1.9	191.9	167.9	94.6	322.3	622	NS	0.81	I
20100814	3	0	42	82.5	0.6	206.9	189.7	109.2	300.7	711	NS	0.93	II
20100914	5	42	26	80.6	0.6	198.1	180.9	105.8	108.1	667	S	0.96	I
20101129	9	12	44	63.7	1.0	121.6	103.5	92.2	25.3	426	S	0.83	III
20110208	8	59	33	78.0	0.5	139.5	115.6	109.8	340.6	437	S	0.85	II
20110402	8	46	52	82.7	2.8	162.1	139.4	89.5	359.6	529	S	0.56	II
20110520	6	2	9	94.5	0.7	180.0	153.2	88.0	62.0	570	NS	0.09	II
20110630	3	39	38	87.7	0.5	161.7	135.8	113.6	186.0	535	S	0.45	IV
20110808	5	22	6	63.6	0.3	179.1	167.4	70.3	169.5	565	S	0.49	II
20111005	5	8	53	77.8	4.2	131.3	105.7	97.1	307.2	407	S	0.58	I
20111202	0	31	4	64.0	0.6	148.3	133.7	91.3	339.4	448	D	0.76	I

Table 5.8: The raytracing results and signal classification for multi arrival events. All raytracing parameters represent the modelled quantities at shock source height, which are then compared to the observed quantities to determine the solution viability. Here Solution type code is: NS - no source height solution; D - degenerate source height solution and S - unique source height solution.

Date	Event Time			Source		Total Range km	Hor. Range km	Ray Dev °	Back Azimuth °	Travel Time s	Sol Type	Sh Param	Signal Class
	hh	mm	ss	H <sub>mean</sub> km	± km								
20060305	5	15	36	54.8	2.3	113.1	99.0	91.3	346.6	349	S	0.58	I
20060305	5	15	36	38.9	1.7	114.2	107.4	93.7	346.0	358	D	0.93	I
20060305	5	15	36	38.1	1.4	114.3	107.7	93.3	346.1	358	S	0.94	I
20060405	3	3	27	63.5	3.1	117.2	98.6	90.7	86.2	400	D	0.14	I
20060405	3	3	27	60.6	2.7	116.9	100.3	87.9	86.0	398	D	0.24	I
20060805	8	38	50	87.8	0.6	124.7	88.3	110.5	254.8	427	S	0.74	I
20060805	8	38	50	101.4	0.4	130.0	81.2	112.8	254.1	450	S	0.48	I
20061223	6	27	26	54.3	2.4	157.2	147.6	98.1	341.9	480	S	0.62	IV
20061223	6	27	26	74.7	1.7	158.4	139.7	103.9	341.4	489	S	0.28	I
20061223	6	27	26	90.6	0.7	161.9	133.9	112.9	338.3	508	NS	0.01	II
20070102	10	42	3	79.7	0.2	164.4	143.7	143.2	31.8	579	S	0.52	I
20070102	10	42	3	80.3	0.3	164.9	144.0	144.6	32.6	581	S	0.49	I
20080511	4	22	17	94.6	0.4	111.7	59.3	83.9	25.5	372	S	0.03	IV
20080511	4	22	17	88.9	0.5	114.7	72.5	78.6	25.1	382	S	0.35	II
20080612	5	58	29	71.8	0.5	126.3	104.0	101.2	70.2	388	S	0.89	I
20080612	5	58	29	76.0	0.3	126.7	101.3	104.6	67.3	391	S	0.66	I
20080812	3	27	25	79.4	0.7	120.7	91.0	100.5	181.4	400	D	0.94	I
20080812	3	27	25	77.7	0.2	121.6	93.6	101.9	182.3	405	S	0.98	II
20080812	8	19	29	86.2	0.8	157.0	131.3	103.8	249.6	555	S	0.83	IV
20080812	8	19	29	87.9	0.8	157.3	130.4	104.0	250.1	558	S	0.75	IV
20090428	4	43	37	60.7	6.2	138.6	124.8	95.6	52.4	454	S	0.50	I
20090428	4	43	37	70.9	1.1	140.6	121.5	105.1	55.2	459	S	0.28	I
20090812	7	55	58	80.6	0.3	155.9	133.4	101.1	205.5	526	NS	0.99	I
20090812	7	55	58	80.5	0.3	155.9	133.4	101.1	205.5	526	S	1.00	I
20090825	1	14	35	46.4	0.3	261.4	257.2	116.0	46.0	811	S	0.98	IV
20090825	1	14	35	68.3	1.8	275.2	266.5	127.4	47.9	846	NS	0.43	IV
20090825	1	14	35	70.9	2.0	277.1	267.9	129.0	48.4	852	S	0.36	IV
20090926	1	2	58	20.2	0.9	134.8	133.2	88.3	89.0	423	S	0.99	II
20090926	1	2	58	70.8	1.0	129.9	109.1	103.9	77.0	440	D	0.37	II
20100530	7	0	31	92.7	2.4	156.4	125.9	87.2	322.7	535	NS	0.18	I
20100530	7	0	31	92.1	2.8	156.6	126.7	86.9	323.2	536	S	0.21	II
20100802	7	18	25	78.9	0.3	138.9	114.3	110.8	81.3	422	NS	0.51	II
20100802	7	18	25	78.9	0.3	138.9	114.3	110.8	81.3	422	NS	0.51	II
20110815	5	50	16	79.1	0.6	166.4	146.4	102.6	332.5	550	S	0.95	I
20110815	5	50	16	84.1	0.7	167.0	144.3	105.2	333.4	556	S	0.76	I

Table 5.9: All events, categorized based on their solution quality.

Solution Viability	Travel time (%)	Back azimuth (°)	Single arrivals	Multi arrivals	All
S <sub>A</sub>	< 1	< 1	19	11	30
S <sub>B</sub>	1 ≤ n < 2	1 ≤ n < 2	7	8	15
S <sub>C</sub>	2 ≤ n < 3	2 ≤ n < 3	9	5	14
S <sub>D</sub>	3 ≤ n < 5	3 ≤ n < 5	12	5	17
S <sub>F</sub>	≥ 5	≥ 5	8	6	14

The raytracing solution types (unique solution (S), degenerate solution (D) and no solution (NS)) for all events, broken down by single and multi arrival categories, are shown in Figure 5.19. For events falling into the no solution category, to find an estimate using the travel time and thus determine the best estimated shock source altitude, the residuals threshold grid had to be increased. Degenerate solutions are found only in those events which occur at ranges of less than 150 km. We note that almost half (45%) of single arrival events lie within 150 km, while nearly all (94%) multi arrival events are found within that range. The begin/end height for optical events with detectable infrasound together with the inferred source shock height distributions for single arrival events are shown in Figure 5.20.

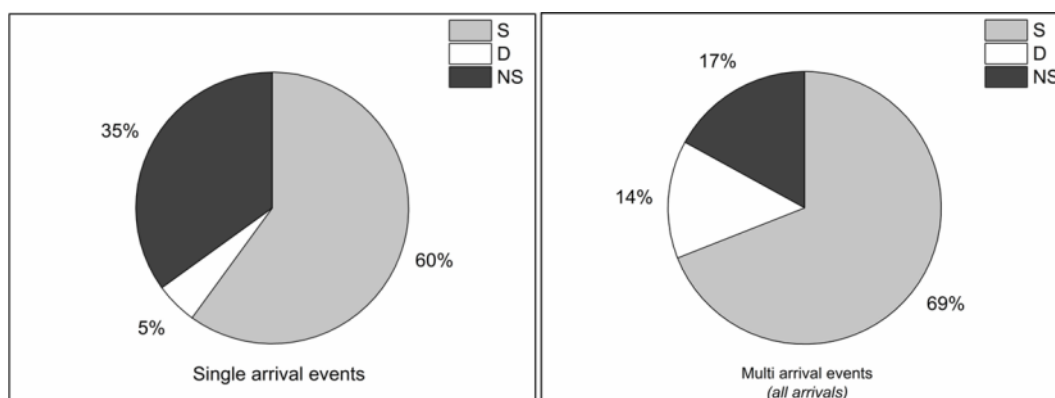


Figure 5.19: Pie charts showing the distribution of raytracing solution types (S – solution, D – degenerate and NS – no solution). Left: Single arrival events; Right: Multi arrival events (all arrivals).

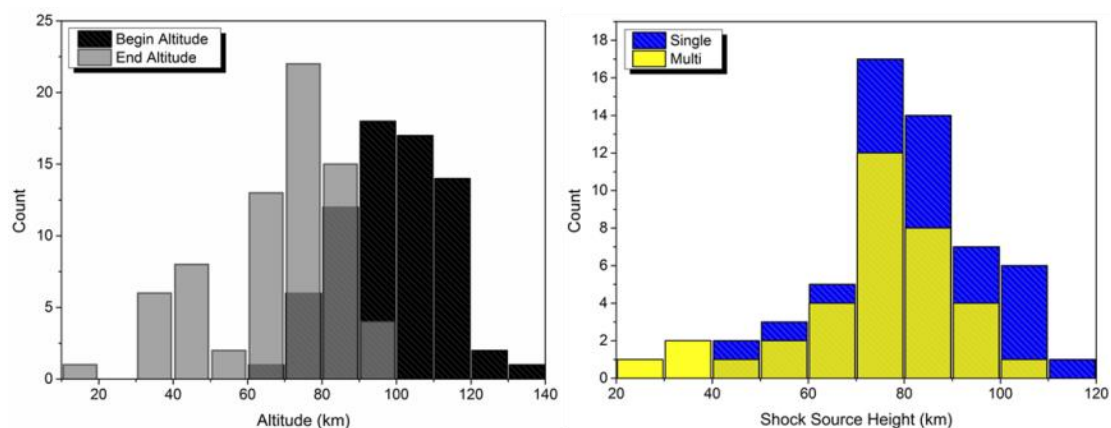


Figure 5.20: Histograms showing the distribution of begin and end optical heights from camera data, as well as the infrasound source height from ray trace modelling. Left: begin and end height distribution for all events. Right: the shock source height distribution for single (blue) and multi (transparent yellow) arrivals.

The luminous trails for all meteoroids in this study start at altitudes between 75 – 140 km, and end as low as 35 km for single arrivals and 20 km for multi-arrivals. It is evident from Figure 5.21 that there are two distinct meteoroid populations in terms of entry velocity, one population has entry velocities  $< 40$  km/s (31 single arrival events or 56%), while the other population has entry velocities  $> 40$  km/s (24 single arrival events or 44%). The same trend can be seen in the multi arrival events; nine out of 16 events are in the slow entry velocity population, while the remaining seven events are in the fast entry velocity population. These local peaks in the apparent speed of meteoroids at the Earth have been recorded by other systems, both optical and radar (e.g. McKinley, 1961). They represent asteroidal/Jupiter family comet material (low speed peaks) and the near-isotropic comet or the Halley-type comet material (high speed peak) following the classification convention of Levison (1996). In this study, the slow meteoroid populations ( $< 40$  km/s) often produce fireballs with long lasting luminous trails ( $> 2$  s), which penetrate substantially deeper into the atmosphere, consistent with their stronger structure (Ceplecha and McCrosky, 1976). In contrast, the fast meteoroid population ( $> 40$  km/s) usually produce shorter lasting luminous trails ( $\sim 1$  s), and have end heights above 63 km, due to their cometary origins (Borovička, 2006). Furthermore, high velocity meteors,

which are mostly cometary in origin, are more likely to produce flares, which are associated with fragmentation processes (Ceplecha et al., 1998).

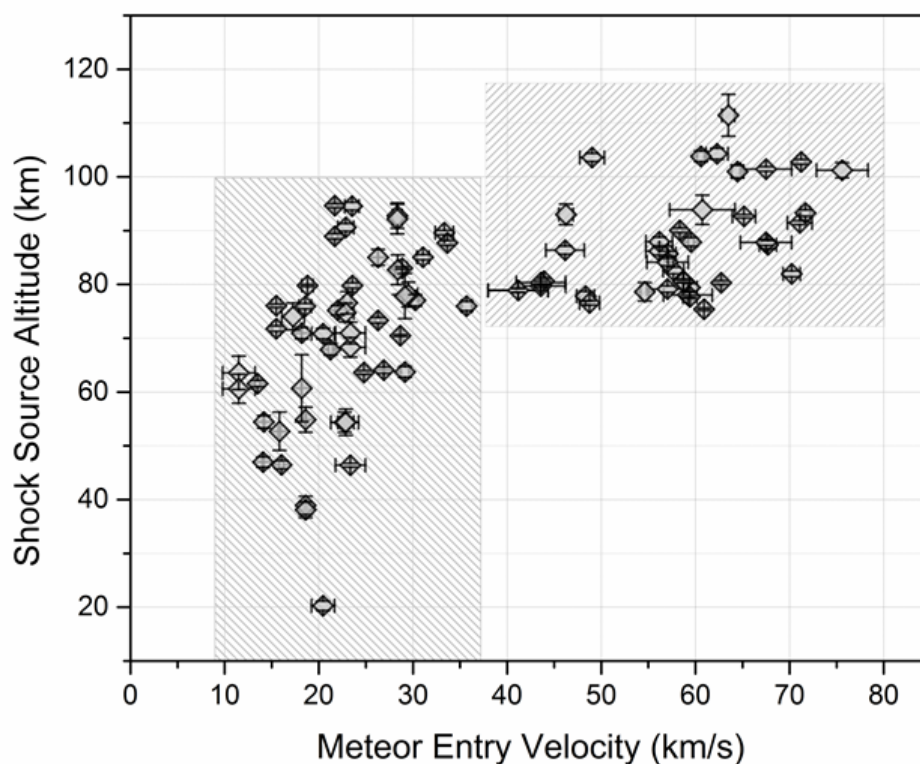


Figure 5.21: Meteor entry velocity populations. There appears to be a ‘dip’ between 36 – 43 km/s, a feature seen in most raw meteor speed distributions (e.g. Brown et al., 2004). The slow meteor population has their velocities  $< 40$  km/s, while the fast population is defined as having the entry velocity  $> 40$  km/s.

There is a strong correlation between meteoroid entry velocity, ablation heights (luminous trail) and the duration of luminous flight in the atmosphere (Ceplecha et al., 1998) (Figure 5.21), demonstrating the correlation between entry speed, total luminous path length and meteoroid population types (Ceplecha and McCrosky, 1976). A summary of average properties and standard deviations as well as extreme values for the two velocity populations in the single arrival category are given in Table 5.10. These same properties for the entire data set are summarized in Table 5.11. The infrasound signal characteristics reflect the velocity-duration-altitude interdependence - namely higher

speed meteoroids ablate higher and have shorter durations because they are also lower in mass for a similar brightness threshold.

Table 5.10: Optical meteor events producing single infrasonic arrivals divided into the slow (< 40 km/s) and the fast (> 40 km/s) meteor entry velocity population. Multi arrival events are excluded from this tabulation.

	Slow Population (30 events)			Fast Population (25 events)		
	Mean $\pm$ error	Min	Max	Mean $\pm$ error	Min	Max
Entry Velocity (km/s)	24.4 $\pm$ 6.3	13.5	35.7	59.9 $\pm$ 8.8	43.9	75.6
Begin Point Altitude (km)	88.7 $\pm$ 9.2	72.0	104.4	111.2 $\pm$ 7.6	93.9	130.8
End Point Altitude (km)	60.7 $\pm$ 13.7	32.8	84.1	81.0 $\pm$ 8.0	63.4	93
Meteor Flight Time (s)	2.1 $\pm$ 1.3	0.8	5.2	0.9 $\pm$ 0.5	0.3	2.5
Meteor Radiant Zenith Angle (deg)	47.0 $\pm$ 15.5	14.6	88.4	47.4 $\pm$ 19.3	13.5	75
Shock Source Altitude (km)	72.3 $\pm$ 12.7	46.4	94.5	90.0 $\pm$ 10.3	75.4	111.4
Total Range (km)	132.7 $\pm$ 34.9	73.3	194.6	156.6 $\pm$ 32.0	100.3	216.6
Ray Deviation (deg)	97.8 $\pm$ 15.2	70.3	146.7	104.9 $\pm$ 18.4	75.2	151.5
Signal Trace Velocity (km/s)	0.392 $\pm$ 0.040	0.345	0.494	0.422 $\pm$ 0.111	0.332	0.831
Signal Celerity (km/s)	0.310 $\pm$ 0.015	0.274	0.336	0.305 $\pm$ 0.016	0.278	0.338
Dominant Signal Frequency (Hz)	4.24 $\pm$ 3.25	1.07	12.89	1.35 $\pm$ 0.71	0.39	2.93
Dominant Signal Period (s)	0.38 $\pm$ 0.23	0.07	0.94	0.98 $\pm$ 0.58	0.31	2.56
Signal Duration (s)	6.3 $\pm$ 1.5	3.0	10.0	7.9 $\pm$ 2.8	5.0	19.7

Table 5.11: Average statistics for single arrival events and multi arrival events. The 16 multi arrival events include statistics for all 35 arrivals, except for meteor entry velocity, meteor flight time and meteor zenith angle, which are global across all arrivals in each event.

	Single Arrival	Min	Max	Multi Arrival	Min	Max	All Events
	Events			Events			
Shock Source Height (km)	80.7 $\pm$ 14.6	46.4	111.4	73.2 $\pm$ 17.8	20.2	101.4	77.8 $\pm$ 16.2
Begin Altitude (km)	99.3 $\pm$ 14.1	72.0	130.8	95.24 $\pm$ 13.7	67.8	126.4	97.7 $\pm$ 14.0
End Altitude (km)	70.3 $\pm$ 15.2	32.8	93.0	57.7 $\pm$ 21.1	19.6	82.0	65.4 $\pm$ 18.6
Signal Celerity (km/s)	0.307 $\pm$ 0.015	0.274	0.338	0.307 $\pm$ 0.016	0.282	0.329	0.307 $\pm$ 0.016
Total Range (km)	144.0 $\pm$ 35.4	73.3	216.6	150.5 $\pm$ 41.8	111.7	277.1	146.5 $\pm$ 37.9
Horizontal Range (km)	117.7 $\pm$ 41.3	47.4	198.6	128.4 $\pm$ 47.5	59.3	267.9	121.3 $\pm$ 43.3
Horizontal Trajectory Length (km)	37.0 $\pm$ 27.4	5.8	119.6	32.7 $\pm$ 16.6	12.4	77.3	35.3 $\pm$ 23.8
Ray Deviation (deg)	101.2 $\pm$ 17.0	70.3	151.5	103.8 $\pm$ 15.0	78.6	144.6	102.2 $\pm$ 16.2
Meteor Entry Velocity (km/s)	41.2 $\pm$ 19.4	13.5	75.6	34.1 $\pm$ 18.3	11.5	67.5	38.4 $\pm$ 19.2
Meteor Flight Time (s)	1.55 $\pm$ 1.15	0.33	5.21	2.10 $\pm$ 1.42	0.47	6.07	1.8 $\pm$ 1.3
Meteor Radiant Zenith Angle (deg)	47.2 $\pm$ 17.2	13.5	88.3	42.2 $\pm$ 14.6	26.9	67.1	46.1 $\pm$ 16.7
Signal Dominant Period (s)	0.7 $\pm$ 0.5	0.1	2.6	0.6 $\pm$ 0.4	0.2	2.0	0.6 $\pm$ 0.5
Signal Dominant Frequency (Hz)	2.9 $\pm$ 2.8	0.4	12.9	2.0 $\pm$ 0.9	0.6	4.1	2.5 $\pm$ 2.3
Maximum Amplitude (Pa)	0.07 $\pm$ 0.04	0.01	0.20	0.09 $\pm$ 0.08	0.01	0.49	0.07 $\pm$ 0.06
Peak-to-peak Amplitude (Pa)	0.10 $\pm$ 0.06	0.02	0.32	0.13 $\pm$ 0.10	0.02	0.68	0.12 $\pm$ 0.10
Observed Travel Time (s)	466 $\pm$ 119	240	709	489 $\pm$ 127	349	842	475 $\pm$ 122

The shock wave, as it propagates away from the meteor source height, undergoes attenuation proportional to the altitude, with the high frequency content preferentially removed due to absorptive losses, turbulence, heat conduction and molecular relaxation (ReVelle, 1976). As higher velocity meteoroids deposit more energy at high altitudes and have correspondingly lower frequency signals reaching the ground, there is a direct relationship between meteor entry velocity and dominant period and dominant frequency of the infrasonic signal received at the array for these small regional events. In general, we find that the dominant signal period is significantly smaller and confined to below 1 s in the slow entry velocity meteor population. Only low velocity meteors ( $< 40$  km/s) produced infrasonic signals with dominant frequencies  $> 4$  Hz (Figure 5.22). This characteristic might be exploitable for stand-alone meteor infrasound measurement as a means to roughly constrain entry speed. Additionally, there is a strong inverse relationship between the shock source height and the dominant signal frequency (Figure 5.22).

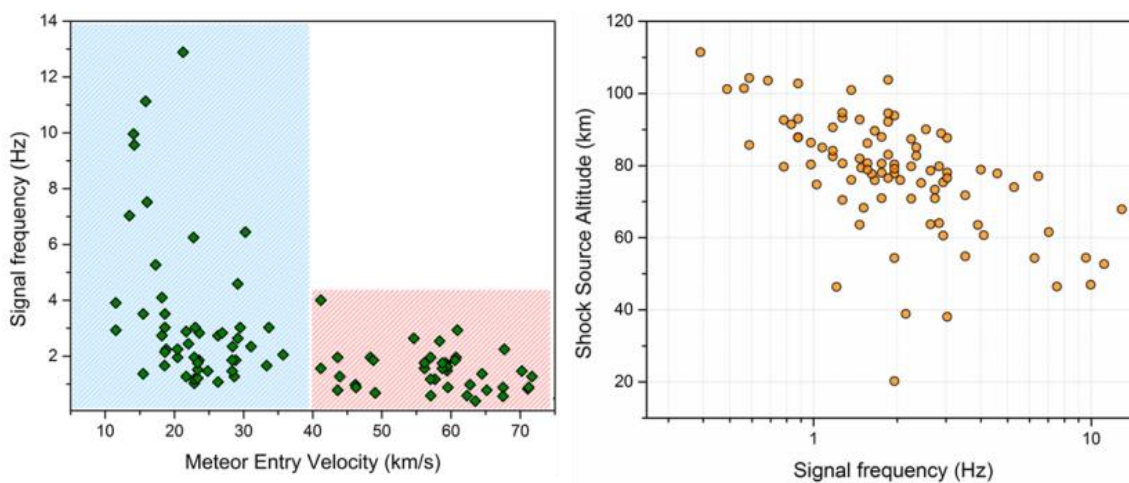


Figure 5.22: Left: The dominant signal frequency as a function of meteoroid entry velocity for meteor infrasound events in this study. The blue region denotes the slow velocity population ( $< 40$  km/s), while the red region is the high velocity meteoroid population ( $> 40$  km) which correspond roughly to asteroidal and cometary meteoroids, respectively. Right: Shock source altitude vs. dominant signal frequency.



Compared to the slow velocity, deep penetrating meteoroids, the high velocity, very high altitude (>100 km) meteoroid population is less likely to produce infrasound that propagates to the ground, though other studies have reported rare instances of infrasound from high altitude meteors, especially those associated with meteor showers (McIntosh et al., 1976; ReVelle and Whitaker, 1999; Brown et al., 2007). Out of the total population of 71 single arrival events, 7 high altitude (>100 km) events generated infrasound detectable at the ground, suggesting that high-altitude ablation from meteoroids, even though not in the continuum flow, may still be capable of producing infrasound detectable at the surface, an effect also noted in studies of high altitude rocket-produced infrasound (Cotten and Donn, 1971).

Finally, we note that meteoroids with shallow entry angles (from the horizontal) are more likely to produce detectable infrasound due to the line source geometry having better propagation paths to the ground. The entry angle distributions for all events in this data set, as well as the ASGARD data, are shown in Figure 5.23.

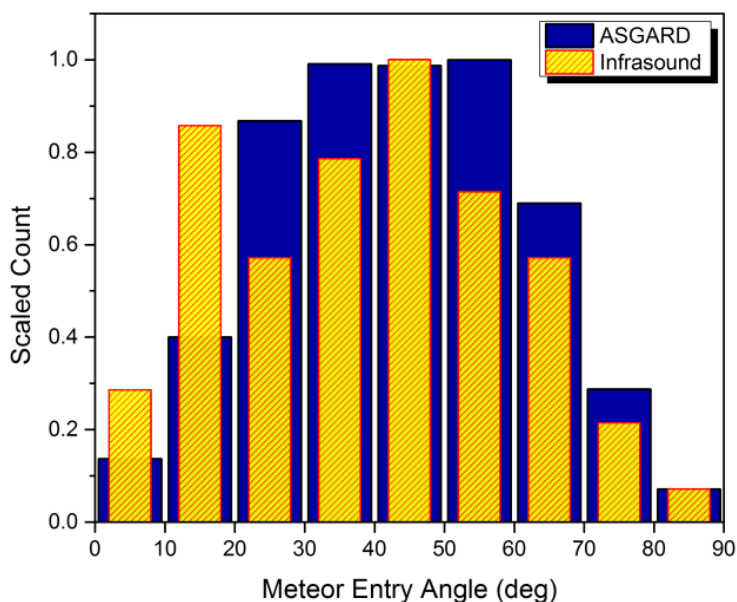


Figure 5.23: The scaled distributions of meteoroid entry angles (from the vertical) for all optically detected events (ASGARD data) and simultaneously detected events in this study. In ASGARD data, the maximum is between  $30^\circ - 60^\circ$ , while the simultaneously detected meteors in this study show a peak at  $45^\circ$  and another one at  $15^\circ$ . The meteoroids with small entry angles (as measured from the vertical) are more likely to produce infrasound via spherical shock than cylindrical line source. In our dataset, the limiting

meteoroid radiant zenith angle for spherical shocks is  $64^\circ$  (average  $38^\circ$ ) and for cylindrical line source it is  $88^\circ$  (average  $49^\circ$ ).

### 5.4.3 Definition of $S_h$ Parameter and Estimation of Shock Type

To examine the possible shock source types (spherical vs. cylindrical) we first define a source height parameter ( $S_h$ ) as:

$$S_h = L_{Bh-S} / L \quad (5.3)$$

where  $L_{Bh-S}$  is the path length along the trajectory from the begin point of the meteor to the shock source point, and  $L$  is the total path length of the entire visible meteor trajectory. Thus if  $S_h \approx 1$ , the shock originates at the meteor's luminous end point and as  $S_h \rightarrow 0$ , the shock originates closer to the luminous begin point of the meteor trail. The distribution of  $S_h$  for all arrivals (Figure 5.24) exhibits two peaks, one around the middle of the trail, and another one closer to the end point.

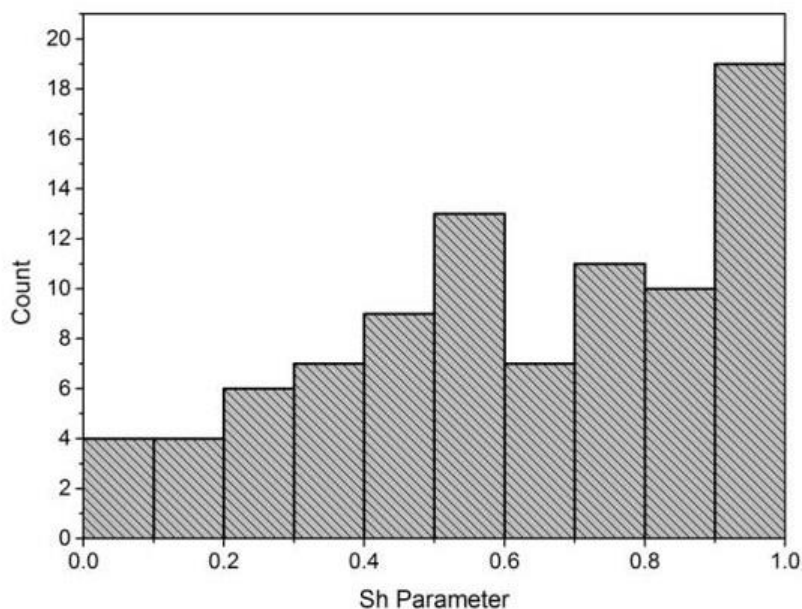


Figure 5.24: The distribution of  $S_h$  parameter shown for all arrivals.

As expected, there is a weak inverse relationship between the shock source height and the  $S_h$  parameter with the shock source heights for the  $S_h$  parameter  $< 0.5$  constrained to the altitude region above 60 km (Figure 5.25).

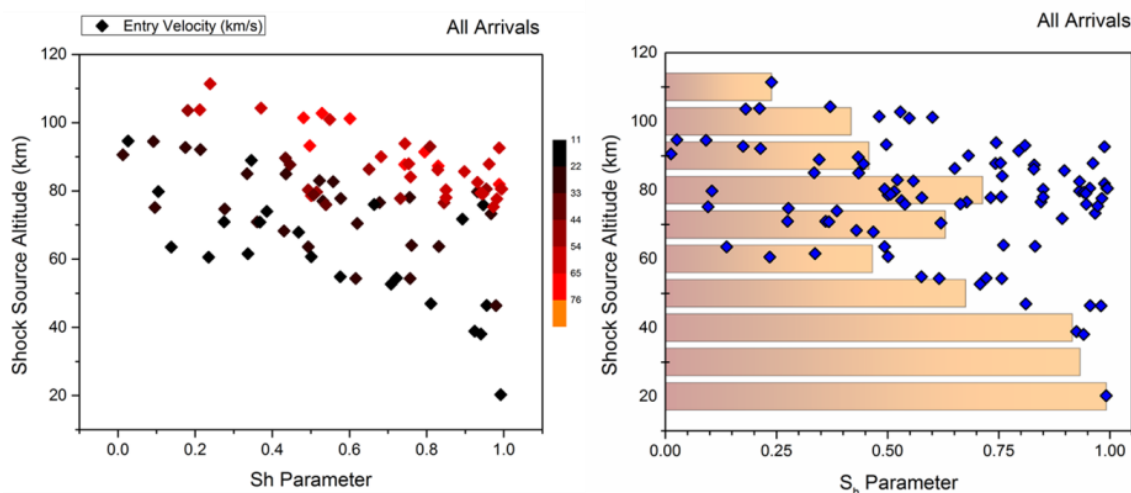


Figure 5.25: Left: Altitude vs.  $S_h$  parameter, where the colour coded diamonds represent meteor entry velocity (high intensity red denotes highest velocity events, gradually shifting towards dark shades and to black, denoting slowest velocities). Right: The mean value of  $S_h$  parameter as a function of height (orange bars) in 10 km increments (bins) overlaid with  $S_h$  parameter as a function of height (blue diamonds).

We expect the statistical behaviour of the  $S_h$  parameter to be diagnostic of the shock production mechanism, and thus examine this supposition further. For ballistic (cylindrical line) sources any portion of the trail is geometrically likely, though we expect a bias toward the end of the trail due to lower attenuation from lower source heights. The point of fragmentation, associated with spherical source geometry, depends on many factors, such as the meteoroid velocity, composition, tensile strength, etc. (Cepilecha, 1998, Cepilecha and ReVelle, 2004), but such fragmentation points tend to occur lower in the trail, particularly for asteroidal-type meteoroids. Several well documented meteor events have provided valuable information shedding more light on the fragmentation and breakup characteristics of larger meteoroids (e.g. Borovička and Kalenda, 2003) during meteoroid flight through the atmosphere (e.g. Brown et al., 2003; ReVelle et al., 2004),

which may be similar to several deep penetrating events in our multi arrival population (e.g. Brown et al., 2011), but not representative of the entire population.

In our study, five multi arrival events and eight single arrival events have ray deviation angles ( $\beta$ ) greater than  $115^\circ$ , which may indicate spherical shock production based on earlier interpretations (e.g. Edwards et al., 2008). If a fragmentation episode (which we expect to act as a quasi omni-directional acoustic emission source) can be linked directly to the shock production point along the trail, then the ray deviation angle is not expected to be confined to the ballistic regime ( $90^\circ \pm 25^\circ$ ) (see Brown et al. (2007) for a discussion of the theoretical variance in the ballistic angle from considerations of the expected gradient introduced in the local sound speed by the cylindrical shock).

Edwards et al. (2008) suggested the presence of a quasi-ballistic regime, defined as the region with ray deviation,  $\beta$ , of  $110^\circ - 125^\circ$ , where the waveform exhibits ballistic shock features (interpreted as a typical N-wave appearance), but does not fall within the true ballistic regime (in Edwards et al. (2008) referred to as  $90^\circ \pm 20^\circ$ ). Following Edwards et al. (2008) and Edwards (2010), any signals beyond  $125^\circ$  would therefore suggest spherical shock production at the source.

In this study we find an absence of a clear boundary in the waveform features that would phenomenologically distinguish ballistic shock from non-ballistic shock (identification based solely on the basis of N-wave appearance), or place it in the transition region. Spherical shocks, depending on the overall geometry and propagation effects, are also expected to produce N-wave signals and have ray deviations within the ballistic region (ray deviation angle  $90^\circ \pm 25^\circ$  as defined by Brown et al. (2007)), as the decay of any shock at large distances tends to exhibit N-wave behaviour due to the cumulative effects of non-linearity in the waveform, independent of the source characteristics (e.g. Whitham, 1972). This implies that the infrasound pressure-time signal alone may not be sufficient to clearly identify of the shock source type (point vs. line source) and that some information about the geometry of the source has to be known. In our dataset, a number of events with ray deviations larger than  $125^\circ$  (beyond the quasi-ballistic as defined by Edwards et al. (2008)) still show Class I signals (i.e. N-wave signature), interpreted earlier as being typical of the ballistic regime. Conversely, it is not unusual to find a Class

IV signal within the ballistic region (though this might still be due to a fragmentation event).

To investigate this question, along with the behaviour of the  $S_h$  parameter as a function of shock type, we tried to determine if flares (produced by fragmentation) in a meteor lightcurve were a source of infrasound at the ground, as such fragmentation episodes are expected to produce quasi-spherical shock sources. The photometric lightcurve for each event was produced following standard photometric procedures (e.g. Brown et al., 2010). Since the visual magnitude was not calibrated to an absolute visual magnitude at this stage, it was normalized to -1 for each event and the differential lightcurve used to identify flares. An example of a brightness vs. meteoroid height lightcurve for two representative events is shown in Figure 5.26. The full photometric methodology and reduction procedure will be discussed in detail in Chapter 6.

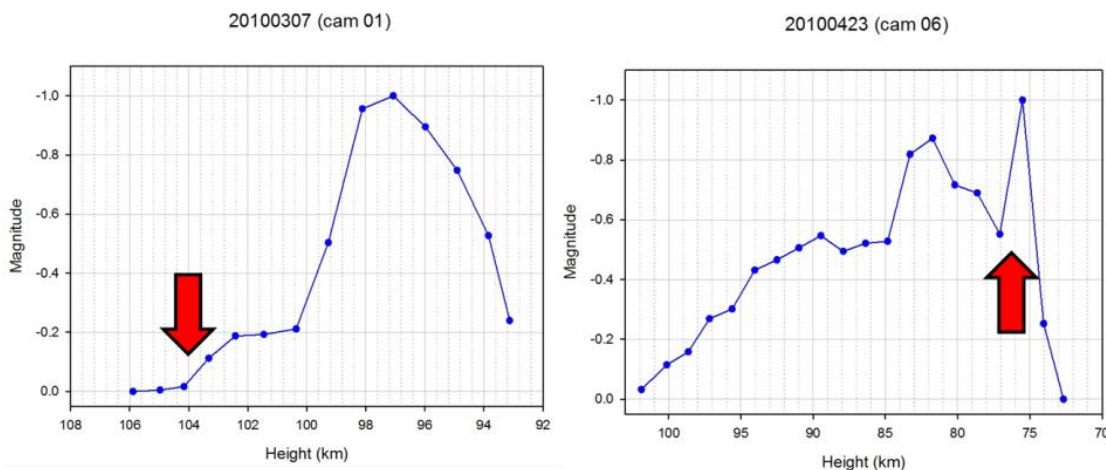


Figure 5.26: Examples of relative photometric light curves. Left: The shock source height was determined to have occurred at 104 km. Thus, this event most likely produced infrasound via hypersonic shock (cylindrical line source) as the shock source height does not correlate with any local brightening (flare) suggestive of a fragmentation episode. Right: The onset of the flare (fragmentation) coincides with the best estimate of the source height, suggesting that the signal was most likely produced by a spherical shock. On both panels the red arrow shows the most probable shock source height. For the first event, the ray deviation angle is  $100^\circ$  and for the event on the right, it is  $136^\circ$  degrees.

If the height of the optical flare falls within the uncertainty bounds of the infrasonically estimated shock source height derived from raytracing, then this suggests that the shock

type is spherical in nature. We assume that infrasound shock source heights showing no association with flares are more likely to be cylindrical line sources. In all but one case (event 20071004) it was possible to determine the most probable nature of shock production based on correlation with the lightcurve. This one ambiguous event, which was excluded from the lightcurve shock-source type analysis, shows continuous fragmentation in the video records which is indicative of a spherical shock generated by a rapidly moving point source; however, there is an absence of a clearly defined flare in the light curve. The distributions of shock type in the single arrival and multi arrival event categories, as well as the distribution of the  $S_h$  parameter as a function of shock type, are shown in Figure 5.28.

The photometric light curves were also used to establish the height of peak brightness; this is the region associated with the maximum energy deposition and ablation/mass loss along the trail (Zinn et al., 2004). The location of the peak brightness along the trail was used to define an  $M_p$  parameter, which is defined (in analogy with the  $S_h$  parameter) as:

$$M_p = L_{Bh-Mp} / L \quad (5.4)$$

where  $L_{Bh-Mp}$  is the path length along the trajectory from the begin point of the meteor to the point of peak luminosity, and  $L$  is the total path length of the entire visible meteor trajectory.

This information was then used to examine the correlation between the  $S_h$  parameter and the  $M_p$  (Figure 5.27). We note that if the shock source height occurs at the point of peak luminosity  $S_h=M_p$ .

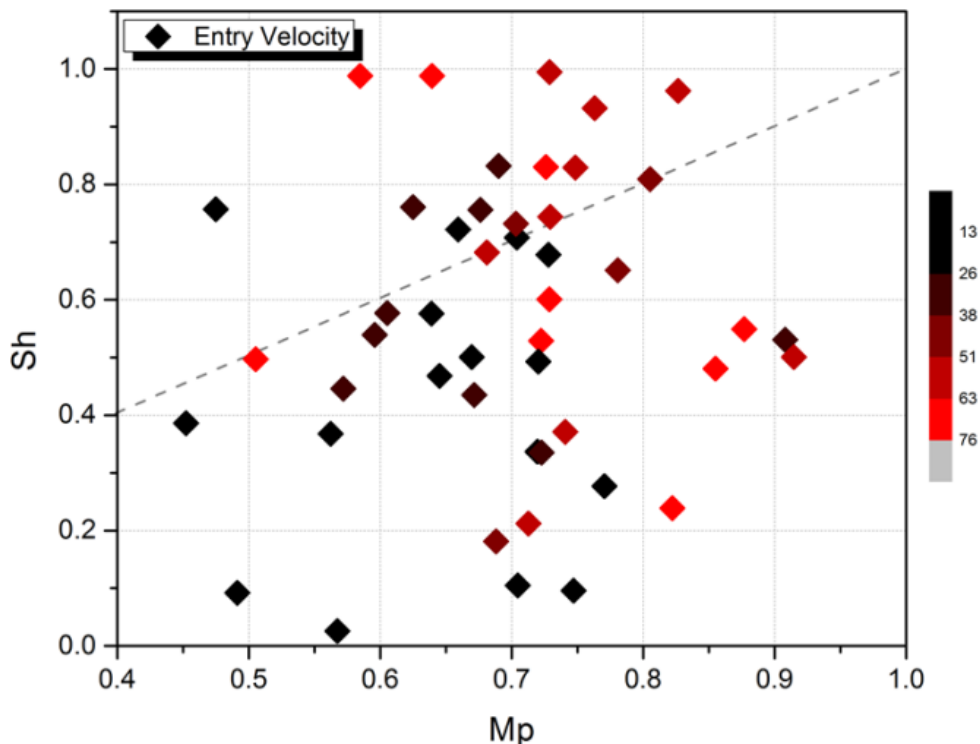


Figure 5.27: The  $S_h$  parameter vs  $M_p$  for 50 arrivals (single and multi arrival populations combined) generated by a cylindrical line source (i.e. not showing a shock source height which can be obviously correlated with a local maximum in the lightcurve). Due to complex light curve features (e.g. flares), it was not possible to determine the height of the peak brightness with certainty for the remaining 10 arrivals. Therefore, those arrivals are excluded from the plot. The dotted line is the 1:1 line.

Our examination of the correlation between optical meteor flares and infrasound production suggests:

- (i) There are events with ray deviation angles  $\beta$ , in the ballistic regime ( $90^\circ \pm 25^\circ$ ) which are most likely generated by a spherical shock (rapidly moving point source or terminal burst) based on their association with a visible flare or fragmentation - the fraction of these events differs between the single and multiple meteor infrasound arrival populations as shown in Figure 5.28;
- (ii) From (i) it follows that infrasound produced in the single arrival population is predominantly generated by a meteor's hypersonic passage through the atmosphere (cylindrical line source), while a significant portion of multi

arrivals tend to be produced by fragmentation. This implies that most meteor infrasound direct signals showing multiple arrivals are not due to atmospheric multi-pathing, but fragmentation based on our observed optical correlation to flares;

- (iii) All events with large ray launch deviation angles ( $\beta > 117^\circ$ ) were found to be associated with optical fragmentation points (flares) and hence likely originate from a spherical type of shock. It should be remarked that it may not be possible to determine this based on the infrasound signal alone;
- (iv) A small number of events (12% of cases, or 7 arrivals out of 60) which were not associated with flares and hence we interpret to be generated as a cylindrical line source have their shock source height closely associated with the height of maximum brightness along the luminous trail (Figure 5.27). Taking into account the uncertainty in the  $M_p$  parameter, this percentage may actually be closer to ~25%.
- (v) The  $S_h$  parameter for events showing flares is skewed towards larger values (i.e. closer to  $S_h=1$ ), while events showing no flares (which are most likely ballistic shocks) are predominantly generated in the region around the middle of the trail (i.e.  $S_h \sim 0.5$ ) (Figure 5.28).

The  $S_h$  parameter for events showing flares is skewed towards larger values (ie. closer to  $S_h=1$ ), while events showing no flares (which are most likely ballistic shocks) are predominantly generated in the region around the middle of the trail (i.e.  $S_h \sim 0.5$ ).



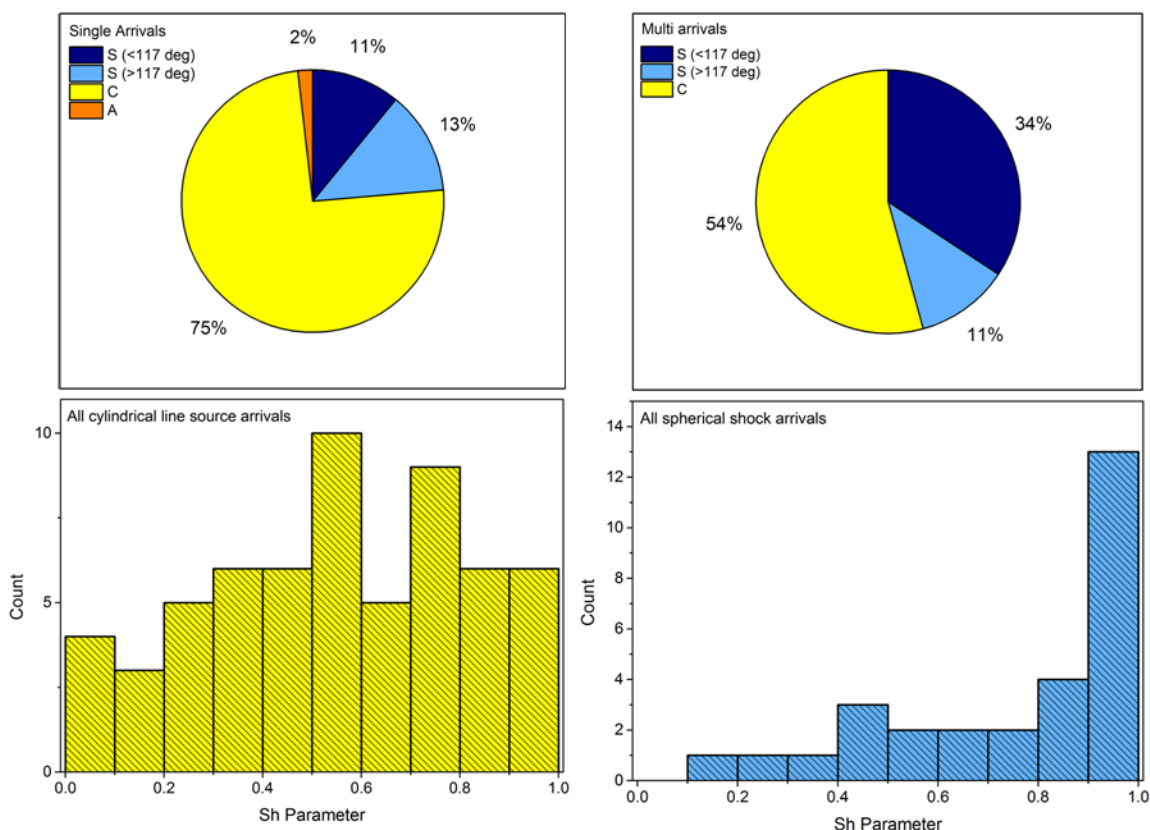


Figure 5.28: Pie charts showing the distribution of spherical (S) shocks for events with ray deviations  $\beta \leq 117^\circ$ ,  $\beta > 117^\circ$ , and cylindrical (C) shocks, where identification of a probable spherical shock source is defined as association with an optical flare and vice versa. Only one arrival in our entire data set is of ambiguous nature (A). Nearly half of the multi arrivals are found to be associated with probable spherical shocks, while a much greater proportion of the single arrivals are generated by a cylindrical shock. The histograms represent the distribution of the  $S_h$  parameter, separated by the shock source type.

As shown by Zinn et al. (2004), the region of maximum luminosity is also where energy deposition peaks and hence is the point where the blast radius is the largest. This would also be the location where the refractive effects (i.e. gradient in local sound speed produced by the shock) are the largest. Nevertheless, point source shocks are still present in the ballistic region, based on the occurrence of flares in the trail along the ballistic launch zone, indicating that it is not only necessary to investigate the type of signal, but also understand the geometry of each event to uniquely associate it with a meteor infrasound signal and a particular source shock type.

#### 5.4.4 Multi Arrival Event Population

Meteor infrasound signals showing multiple arrivals display source height and shock type characteristics different than those events with single meteor infrasound arrivals as shown in Table 5.11. In the majority of cases, the main arrival (i.e. arrival with the maximum pressure amplitude) is associated with the lowermost part of the meteor trajectory (higher value of  $S_h$ ). There are two distinct categories of multi arrival events. One category (9 out of 16 events) shows shock source heights which are nearly identical within uncertainty for at least 2 arrivals (Group M1), while the other group (7 out of 16 events) is associated with clearly different shock source heights for each infrasound arrival (Group M2). Three events in the M1 group were most likely generated by a cylindrical line source, while the remaining 6 we associate with spherical shocks based on a common association with optical flares.

The M2 group may be interpreted as either a ballistic shock and/or a spherical shock occurring at different locations along the meteor trail at different heights, while the M1 group may be associated with different ray paths from a single source, similar to the cause of secondary sonic booms (Rickleby and Pierce, 1980). The former was observed in several well documented meteorite producing fireballs (e.g. Brown et al., 2011; Brown et al., 2003). Fragmentation processes may lead to complex shock configurations (Artemieva and Shuvalov, 2001; Borovička and Kalenda, 2003). Multiple fragments, if sufficiently large, may each generate individual shocks (Artemieva and Shuvalov, 2001) that could therefore produce distinct infrasonic arrivals possibly appearing to originate from the same altitude, though only the Grimsby event in our dataset is large enough for this mechanism to be plausible. Among our multi arrival events, only one was found to have a shock source height at an altitude greater than 90 km (20100530); all others occur at lower altitudes with a mean height of  $72 \pm 15$  km. This suggests that meteoroids capable of producing multiple infrasonic signals detectable at the ground are both typically slower (and hence more likely to be of asteroidal origin) and/or may be intrinsically more energetic than a typical single arrival producing fireball. This is further supported by the observation that the maximum dominant frequency for the multi arrival population does not exceed  $\sim 4$  Hz.

### 5.4.5 Correlation of Meteor Infrasound Signal Class and Ray Launch Deviation Angles

In general, while meteor infrasound taxonomic classes I, II and IV are evenly spread over nearly all ray launch deviation angles, all class III events occur only when ray deviations are strictly around the ballistic regime of  $90^\circ$  (Figure 5.29). The significance of this correlation is hard to gauge as there are a very small number of Class III signals compared to other classes and the triple N-wave pressure signal is not obviously linked to any purely ballistic process. Although the multi infrasound arrival sample is smaller (16 individual events showing a total of 35 arrivals) than the single infrasound arrival group, it is notable that there are no multi infrasound arrivals in Class III. Again, this may simply be due to small number statistics. Another interesting aspect of Class III signals is that they are all emanate from the meteors with the  $S_h$  parameter  $> 0.5$ , which means that the shock was generated in the lower  $\frac{1}{2}$  of the trajectory.

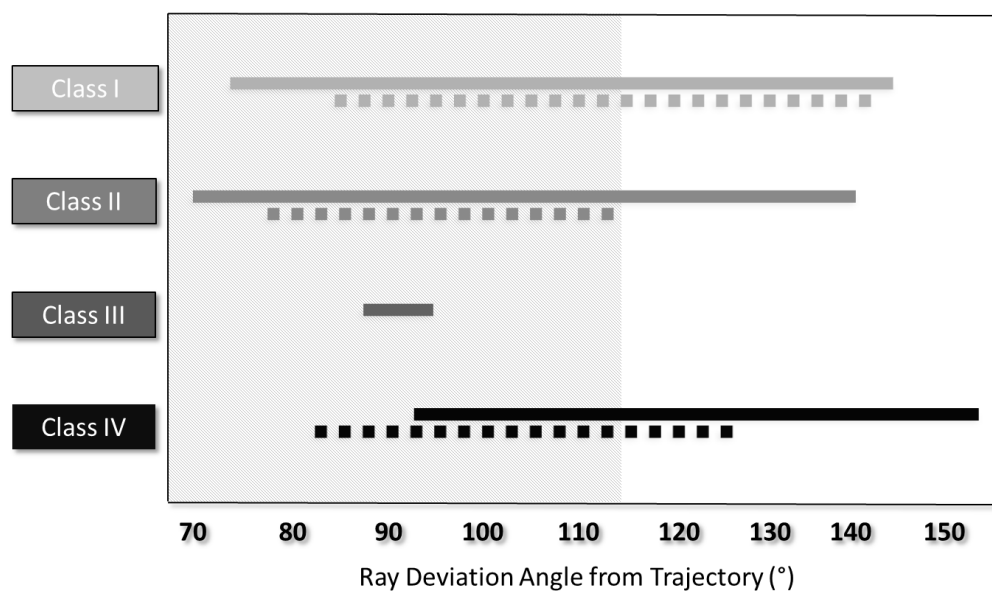


Figure 5.29: Ray launch deviation angles as a function of the signal Class type. Solid line: single arrival event category; Dotted line: multi arrival event category (all arrivals). The shaded region represents the ballistic region ( $90^\circ \pm 25^\circ$ ) as originally defined on theoretical ground by Brown et al (2007).

## 5.5 Conclusions

In this first paper in a two part series, we present the experimental investigation, phenomenology and analysis of a data set of meteors simultaneously detected optically and infrasonically. The specific goals of this coordinated optical-infrasound meteor study were to: (i) use astrometric optical measurements to positively identify infrasound from meteors; (ii) establish and constrain the point (and its uncertainty) along the meteor trail where the infrasound signal emanates; (iii) examine the role of atmospheric variability due to winds on the infrasound solution; (iv) determine the type of shock production mechanism for meteor generated infrasound; and (v) classify meteor infrasound and correlate meteor infrasound classes with structures seen in meteor infrasound signals to establish the foundation for future work to understand the underlying physical mechanisms and possibly relate to sonic boom theory. Our main conclusions related to these initial goals are:

- (i) Seventy one optically recorded meteor events were positively identified with infrasound signals using the observed travel time and arrival azimuths in comparison to the expected values from the measured trajectories. Among these data, some 16 events also produced more than one distinct infrasound arrival. We have found that there are two entry velocity meteor populations which produced infrasound detectable at the ground, slow ( $< 40$  km/s) and fast ( $> 40$  km/s), which we associate with predominantly asteroidal and cometary populations, respectively. These exhibit different astrometric, source height, and signal characteristics. The findings in this study also suggest that infrasound from high altitude meteors may be more common than previously thought. The slow and fast velocity meteoroid populations also exhibit an apparent upper limit on the dominant infrasound signal period and frequency. The slow velocity population appears to be capped at a dominant signal frequency of  $\sim 14$  Hz, while the fast velocity population is limited to the upper dominant signal frequency bound of  $< 4$  Hz. There is a strong inverse relationship between the shock source height and the dominant signal frequency.

- (ii) By comparing travel time and arrival azimuths with raytracing model values and incorporating the perturbations in the wind field we determined the altitude and uncertainty of the infrasound source height production and its location along the meteor trail. We find that meteors preferentially produce infrasound toward the end of their trails with a smaller number showing a preference for mid-trail production.
- (iii) We show that the atmospheric variability may play a nontrivial role even for short range ( $< 300$  km) infrasound propagation from meteors, with our model variations due to gravity wave induced winds producing spreads in the travel time between 2 s and 7 s, and spreads in the back azimuth from  $1^\circ - 4^\circ$  for our meteor dataset which averaged  $\sim 150$  km in range and 70-80 km in source altitude. Some of the differences observed between our raytracing predictions and observations may also be due to scattering, diffraction and range dependent changes in the atmosphere which we do not explicitly examine.
- (iv) We linked the type of shock production (cylindrical and spherical) at the source based on whether or not the infrasound source height corresponds with an optical flare. We find that large deviation angles ( $\beta > 117^\circ$ ) are generally associated with spherical sources (point source or a moving point source). Approximately one quarter of single arrival meteor infrasound events are associated with fragmentation episodes (spherical shocks); while almost half of all multi arrival events are correlated with fragmentation events. Notably, the multi arrival population shows a strong source height skewness to the end of trails; this reflects the larger masses involved as well as the predominance of asteroidal meteoroids in the multi-arrival category. We find that the ray deviation angle cannot be used as a sole discriminant of the type of shock at the source, as both spherical and hypersonic line sources, depending on the geometry and orientation with respect to the observer, may produce signals which apparently have ray deviation angles confined to the ballistic regime.
- (v) We have developed a new signal taxonomic scheme based on the appearance and qualitative characteristics of the waveforms. This taxonomic scheme may

be extended to infrasound signals from other explosive sources located at a relatively short distance from the source (within ~300 km, to remain consistent with our dataset). For example, N-waves are common features of all shocks at some distance from their sources (not only in meteors). Further studies, theoretical and experimental, are required to better explain certain shock features, such as double and triple N-waves (Table 1), and link them to the source and propagation effects. We also found an association between the signal peak-to-peak amplitude and the signal class, which may relate to the sonic boom equal area rule. The signal amplitude tends to decrease as a function of signal class; this is clearly observable when all our data is plotted. All four classes of signals can be found in any source (spherical or line source) category.

We find that about 1% of all our optically detected meteors have associated infrasound. For a typical infrasound station such as ELFO we estimate that regional meteor infrasound events should occur on the order of once per week and dominate in numbers over infrasound associated with more energetic (but rarer) bolides detectable at large (>500 km) propagation distances. While a significant fraction of our meteors generating infrasound (~1/4 of single arrivals) are produced by fragmentation events, we find no instances where acoustic radiation is detectable more than  $60^\circ$  beyond the ballistic regime at our meteoroid sizes (grams - tens of kilograms). Indeed, the average deviation angles among our population are within  $10^\circ$ - $15^\circ$  of purely ballistic. This emphasizes the strong anisotropy in acoustic radiation for meteors which are dominated by cylindrical line source geometry, even in the presence of fragmentation.

## **Acknowledgements**

Funding in support for part of this project was provided by the CTBTO Young Scientist Award funded through the European Union Council Decision 2010/461/CFSP IV. EAS thanks Dr. W. K. Hocking for discussions about gravity waves, Zbyszek Krzeminski for his help with astrometric reductions and Jason Gill for his help with setting up a parallel processing machine to run raytracing. Funding in support of this work from NASA Co-operative agreement NNX11AB76A, from the Natural Sciences and Engineering Research Council and the Canada Research Chairs is gratefully acknowledged.

## References

- Artemieva, N. A., and Shuvalov, V. V. 2001. Motion of a fragmented meteoroid through the planetary atmosphere. *Journal of geophysical research*, 106(E2), 3297-3309.
- Balachandran, N. K., Donn, W. L., Kaschak, G. 1971. On the propagation of infrasound from rockets: Effects of winds. *The Journal of the Acoustical Society of America*. 50, 397.
- Bass, H. E., Bauer, H. J., Evans, L. B. 1972. Atmospheric absorption of sound: Analytical expressions. *The Journal of the Acoustical Society of America*. 52, 821
- Bedard, A., Georges, T. 2000. Atmospheric infrasound. *Acoustics Australia*. 28(2), 47-52.
- Beer, T. 1974. *Atmospheric waves*. New York. Halsted Press. London, Adam Hilger, Ltd. 315p.
- Bhattacharyya, J., Bass, H., Drob, D., Whitaker, R., ReVelle, D., Sandoval, T. 2003. Description and Analysis of Infrasound and Seismic Signals Recorded from the Watusi Explosive Experiment, in *Proceedings of the 25th Seismic Research Review—Nuclear Explosion Monitoring: Building the Knowledge Base*. LA-UR-03-6029, Vol. 2, pp. 587–596
- Borovička J., Spurný P., Keclikova J. 1995. A new positional astrometric method for all-sky cameras. *Astronomy and Astrophysics-Supplement Series*. 112: 173–178
- Borovička, J. 1990. The comparison of two methods of determining meteor trajectories from photographs. *Bulletin of the Astronomical Institutes of Czechoslovakia*. 41, 391-396.
- Borovička, J. 1992. *Astrometry with all-sky cameras*. Publications of the Astronomical Institute of the Czechoslovak Academy of Sciences. 79.
- Borovička, J., Kalenda, P. 2003. The Morávka meteorite fall: 4. Meteoroid dynamics and fragmentation in the atmosphere. *Meteoritics & Planetary Science*. 38(7). 1023-1043.
- Brachet, N., Brown, D., Le Bras, R., Cansi, Y., Mialle, P., Coyne, J. 2009. Monitoring the earth's atmosphere with the global IMS infrasound network. In *Infrasound Monitoring for Atmospheric Studies*, pp. 77-118. Springer Netherlands.
- Bronsthen, V.A. 1983. *Physics of Meteoric Phenomena*. 372 pp. D. Reidel, Dordrecht, Netherlands.



- Brown, E.H., Hall, F.F. 1978. Advances in atmospheric acoustics. *Reviews of Geophysics*. 16(1), 47-110.
- Brown, P. G., Assink, J. D., Astiz, L., Blaauw, R., Boslough, M. B., Borovička, J., and 26 co-authors (2013). A 500-kiloton airburst over Chelyabinsk and an enhanced hazard from small impactors. *Nature*.
- Brown, P., McCausland, P.J.A., Fries, M., Silber, E., Edwards, W.N., Wong, D.K., Krzeminski, Z. 2011. The fall of the Grimsby meteorite—I: Fireball dynamics and orbit from radar, video, and infrasound records. *Meteoritics & Planetary Science*. 46(3), 339-363.
- Brown, P., Weryk, R. J., Kohut, S., Edwards, W. N., Krzeminski, Z. 2010. Development of an All-Sky Video Meteor Network in Southern Ontario, Canada The ASgard System. *WGN, Journal of the International Meteor Organization*, 38, 25-30.
- Brown, P.G., Edwards, W.N., ReVelle, D.O., Spurny, P. 2007. Acoustic analysis of shock production by very high-altitude meteors – I: infrasonic observations, dynamics and luminosity, *Journal of Atmospheric and Solar-Terrestrial Physics*. 69: 600–620.
- Brown, P.G., Kalenda, P., Revelle, D.O., Borovička, J. 2003. The Morávka meteorite fall: 2. Interpretation of infrasonic and seismic data. *Meteoritics & Planetary Science*. 38(7), 989-1003.
- Cansi, Y., 1995. An automatic seismic event processing for detection and location: the P.M.C.C. method. *Geophysical Research Letters* 22 (9), 1021-1024
- Cansi, Y., Klinger, Y. 1997. An automated data processing method for mini-arrays. *Newsletter of the European Mediterranean Seismo-logical Centre*. 11, 2-4
- Cansi, Y., Le Pichon, A. 2008. Infrasound Event Detection using the Progressive Multi-Channel Correlation Algorithm,” In: D. Havelock, S. Kuwano and M. Vorlander, Eds., *Handbook of Signal Processing in Acoustics*. Springer, New York, pp. 1424-1435. doi:10.1007/978-0-387-30441-0\_77
- Cansi, Y., Le Pichon, A. 2009. Infrasound event detection using the progressive multi-channel correlation algorithm. In *Handbook of signal processing in acoustics* (pp. 1425-1435). Springer New York.
- Cepelcha, Z., Borovička, J., Elford, W. G., ReVelle, D. O., Hawkes, R. L., Porubčan, V., Šimek, M. 1998). Meteor phenomena and bodies. *Space Science Reviews*. 84(3-4), 327-471.
- Cepelcha, Z., McCrosky, R. E. 1976. Fireball end heights: a diagnostic for the structure of meteoric material. *Journal of Geophysical Research*. 81(35), 6257-6275.

- Ceranna, L., Le Pichon, A., Green, D. N., Mialle, P. 2009. The Buncefield explosion: a benchmark for infrasound analysis across Central Europe. *Geophysical Journal International*. 177(2), 491-508.
- Christie, D. R. Campus, P. The IMS Infrasound Network: Design and Establishment of Infrasound Stations, In: A. Le Pichon, E. Blanc and A. Hauchecorne, Eds., *Infrasound Monitoring for Atmospheric Studies*. Springer. New York, 2010, pp. 29-75. doi:10.1007/978-1-4020-9508-5\_2
- Chunchuzov, I. P. 2004. Influence of internal gravity waves on sound propagation in the lower atmosphere. *Meteorology and Atmospheric Physics*. 85(1-3), 61-76.
- Chyba, C.F., Thomas, P.J., Zahnle, K.J. 1993. The 1908 Tunguska explosion: atmospheric disruption of a stony asteroid. *Nature*. 361: 40-44
- Cotten, D., Donn, W. L. 1971. Sound from Apollo rockets in space. *Science*. 171(3971), 565-567.
- Crow, S.C. 1969. Distortion of sonic bangs by atmospheric turbulence. *Journal of Fluid Mechanics* 37(03): 529-563.
- DuMond, J. W., Cohen, E. R., Panofsky, W. K. H., Deeds, E. 1946. A determination of the wave forms and laws of propagation and dissipation of ballistic shock waves. *The Journal of the Acoustical Society of America*. 18, 97.
- Edwards, W. N. 2010. Meteor generated infrasound: theory and observation. In *Infrasound monitoring for atmospheric studies* (pp. 361-414). Springer Netherlands.
- Edwards, W. N., Brown, P. G., Weryk, R. J., ReVelle, D. O. 2008. Infrasonic observations of meteoroids: Preliminary results from a coordinated optical-radar-infrasound observing campaign. *Earth, Moon, and Planets*. 102(1-4), 221-229.
- Edwards, W.N., Hildebrand, A.R. 2004. SUPRACENTER: Locating fireball terminal bursts in the atmosphere using seismic arrivals. *Meteoritics & Planetary Science*, 39(9), 1449-1460.
- Embleton, T. F. 1996. Tutorial on sound propagation outdoors. *The Journal of the Acoustical Society of America*. 100, 31.
- Ens, T. A., Brown, P. G., Edwards, W. N., Silber, E. A. 2012. Infrasound production by bolides: A global statistical study. *Journal of Atmospheric and Solar-Terrestrial Physics*. 80, 208-229.
- Evers, L.G. H.W. Haak. 2001. Listening to sounds from an exploding meteor and oceanic waves. *Geophysical Research Letters*. 30: 41-44.

- Evers, L.G. Haak, H.W. 2003. Tracing a meteoric trajectory with infrasound. *Geophysical Research Letters*. 30(24): 1-4.
- Fritts, D. C., Alexander, M. J. 2003. Gravity wave dynamics and effects in the middle atmosphere. *Reviews of geophysics*. 41(1), 1003.
- Gainville, O., Blanc-Benon, P., Blanc, E., Roche, R., Millet, C., Le Piver, F., Depress, B., Piserchia, P. F. 2010. Misty picture: a unique experiment for the interpretation of the infrasound propagation from large explosive sources. In *Infrasound Monitoring for Atmospheric Studies* (pp. 575-598). Springer Netherlands.
- Garcés, M. 2013. On Infrasound Standards, Part 1: Time, Frequency, and Energy Scaling, *InfraMatics*. 2013, 2, 13-35, doi:10.4236/inframatics.2013.22002
- Garcés, M., Harris, A. Hetzer, C. Johnson, J., Rowland. S. 2003a. Infrasonic tremor observed at Kilauea Volcano, Hawai'i. *Geophysical Research Letters*. 30: 2023-2026.
- Garcés, M., Hetzer, C. Merrifield, M. Willis, M., Aucan. J. 2003b Observations of surf infrasound in Hawai'i. *Geophysical Research Letters*. 30: 2264-226
- Garcés, M., Le Pichon, A. 2009. Infrasound from Earthquakes, Tsunamis and Volcanoes, In: R. A. Meyers, Ed., *Encyclopedia of Complexity and Systems Science*. Springer, Berlin, pp. 663-679.
- Gardner, C.S., Hostetler, C.A., Franke, S.J. 1993. Gravity wave models for the horizontal wave number spectra of atmospheric velocity and density fluctuations. *Journal of geophysical research*. 98(D1), 1035-1049.
- Gibson, R., Norris, D. (2000). The infrasound analysis tool kit InfraMap: Capabilities, enhancements and applications. BBN Technologies Arlington VA.
- Gibson, R.G., Norris, D.E. 2003. Integration of InfraMap with Near-Real-Time Atmospheric Characterizations and Applications to Infrasound Modeling, *Proceedings of the 25th Seismic Research Review – Nuclear Explosion Monitoring ‘Building the Knowledge Base’, 23-25 September, 2003, Tuscon, AZ, Vol II*, pp 638-645
- Gottlieb, J.J., Ritzel, D.V. 1988. Analytical study of sonic boom from supersonic projectiles *Progress in Aerospace Sciences*. 25(2): 131-188
- Green, D.N., Vergoz, J., Gibson, R., Le Pichon, A., Ceranna, L. 2011. Infrasound radiated by the Gerdec and Chelophechene explosions: propagation along unexpected paths. *Geophysical Journal International*. 185(2), 890-910.
- Günther, R.H., O'Connell-Rodwell, C.E., Klemperer, S.L. 2004. Seismic waves from elephant vocalizations: a possible communication mode?. *Geophysical Research Letters*. 31: L11602

- Harris, M., and Young, C. 1997. MatSeis: a seismic GUI and tool-box for MATLAB. *Seism. Res. Lett.*, 68(2), 267-269.
- Haynes, C. P., Millet, C. 2013. A sensitivity analysis of meteoric infrasound. *Journal of Geophysical Research: Planets.* 118, 2073-2082
- Hedin, A.E., Fleming, E.L., Manson, A.H., Schmidlin, F.J., Avery, S.K., Clark, R.R., Vincent, R.A. 1996. Empirical wind model for the upper, middle and lower atmosphere. *Journal of Atmospheric and Terrestrial Physics.* 58(13), 1421-1447.
- Hedlin, M. A. H., Walker, K., Drob, D. P., de Groot-Hedlin, C. D. 2012. Infrasound: Connecting the Solid Earth, Oceans, and Atmosphere. *Annual Review of Earth and Planetary Sciences.* 40, 327-354.
- Hedlin, M.A., Garcés, M., Bass, H., Hayward, C., Herrin, G., Olson, J., Wilson, C. 2002. Listening to the secret sounds of earth's atmosphere. *Eos* 83 (2002). 557, 564-565.
- Hines, C.O., Reddy, C.A. 1967. On the propagation of atmospheric gravity waves through regions of wind shear. *Journal of Geophysical Research.* 72(3), 1015-1034.
- Jacchia, L., Verniani, F., Briggs, R. E. 1967. An analysis of the atmospheric trajectories of 413 precisely reduced photographic meteors. *Smithsonian Contributions to Astrophysics.* 10, 1-139.
- Jones, T.B. 1982. Generation and propagation of acoustic gravity waves. *Nature.* 299: 488-290.
- Kraemer, D.R. 1977. Infrasound from accurately measured meteor trails. Ph.D. Thesis University of Michigan, Ann Arbor
- Kulichkov, S. 2010. On the prospects for acoustic sounding of the fine structure of the middle atmosphere. In *Infrasound monitoring for atmospheric studies* (pp. 511-540). Springer Netherlands.
- Kulichkov, S. N. 2004. Long-range propagation and scattering of low-frequency sound pulses in the middle atmosphere. *Meteorology and Atmospheric Physics.* 85(1-3), 47-60.
- Le Pichon, A., Blanc, E., Drob, D. 2005. Probing high-altitude winds using infrasound. *Journal of geophysical research.* 110(D20), D20104.
- Le Pichon, A., Vergoz, E. Blanc, J. Guilbert, L. Ceranna, L. G. Evers, N. Brachet. 2009. Assessing the performance of the International Monitoring System infrasound network: Geographical coverage and temporal variabilities. *J. Geophys. Res.* 114. D08112

- Levison, H. F. 1996. Comet taxonomy. In *Completing the Inventory of the Solar System*. Vol. 107, pp. 173-191.
- McIntosh, B. A., Watson, M. D., ReVelle, D. O. 1976. Infrasound from a radar-observed meteor. *Canadian Journal of Physics*. 54(6), 655-662.
- McIntosh, B.A., ReVelle, D.O. 1984. Traveling atmospheric pressure waves measured during a solar eclipse. *Journal of Geophysical Research: Atmospheres* (1984–2012), 89(D3), 4953-4962.
- McIntosh, B.A., Watson, M.D., ReVelle, D.O. 1976. Infrasound from a radar-observed meteor. *Canadian Journal of Physics*. 54(6), 655-662.
- McKinley, D. W. R. 1961. *Meteor science and engineering*. New York, McGraw-Hill, 1961., 1.
- Melton, B.S., Bailey, L.F. 1957. Multiple signal correlators, *Geophysics*, 22, 565
- Mengel, J.G., Mayr, H.G., Chan, K.L., Hines, C.O., Reddy, C.A., Arnold, N.F., Porter, H.S. 1995. Equatorial oscillations in the middle atmosphere generated by small scale gravity waves. *Geophysical research letters*. 22(22), 3027-3030.
- Millet, C., Robinet, J. C., and Roblin, C. 2007. On using computational aeroacoustics for long-range propagation of infrasounds in realistic atmospheres. *Geophysical Research Letters*. 34(14), L14814.
- Mutschlecner, J. P., Whitaker, R. W. 2010. Some atmospheric effects on infrasound signal amplitudes. In *Infrasound Monitoring for Atmospheric Studies*. (pp. 455-474). Springer Netherlands.
- Mutschlecner, J., Whitaker, R. 2006. *Infrasound Signals from the Henderson, Nevada, Chemical Explosion*, LA-UR-06-6458
- Myers, J. R., Sande, C. B., Miller, A. C., Warren Jr, W. H., and Tracewell, D. A. 2002. *SKY2000 Master Catalog*. Version 4. Goddard Space Flight Center. Flight Dynamics Division, 109.
- Nappo, C. J. 2012. *An introduction to atmospheric gravity waves*. International Geophysics. Vol. 102. Academic Press. 1st Edition.
- Norris, D., Gibson, R. 2001. *InfraMAP Propagation Modeling Enhancements and the Study of Recent Bolide Events*. 23rd Seismic Research Review: Worldwide Monitoring of Nuclear Explosions. Jackson Hole, Wyoming
- Oberst, J., Molau, S., Heinlein, D., Gritzner, C., Schindler, M., Spurny, P., Ceplecha, Z., Rendtel, J. Betlem, H. 1998. The “European Fireball Network”: current status and future prospects. *Meteoritics & Planetary Science*. 33(1), 49-56.

- Ostashev, V. 2002. Acoustics in moving inhomogeneous media. Taylor & Francis.
- Ostashev, V.E., Chunchuzov, I.P., Wilson, D.K. 2005. Sound propagation through and scattering by internal gravity waves in a stably stratified atmosphere. *The Journal of the Acoustical Society of America*. 118, 3420.
- Payne, R. 1995. *Among Whales*. Scribner, New York, NY
- Peitgen, H., Saupe, D. eds., 1998. *The Science of Fractal Images*, Springer-Verlag
- Picone J. M., Hedin A. E., Coffey S. L., Lean J., Drob D. P., Neal, H., Melendez-Alvira D. J., Meier R. R., Mariska J. T. 1997. The Naval Research Laboratory Program on empirical models of the neutral upper atmosphere. In *Advances in the astronomical sciences*, edited by Hoots F. R., Kaufman B., Cefola P. J., and Spencer D. B. San Diego: American Astronautical Society. 2184 p.
- Picone, J.M., Hedin, A.E., Drob, D.P., Aikin, A.C. 2002. NRLMSISE-00 empirical model of the atmosphere: Statistical comparisons and scientific issues. *Journal of Geophysical Research: Space Physics*. (1978–2012), 107(A12), SIA-15.
- Pierce, A.D., Posey, J.W. 1970. *Theoretical Prediction of Acoustic-Gravity Pressure Waveforms Generated by Large Explosions in the Atmosphere*, Technical Report AFCRL-70-0134, Air Force Cambridge Research Laboratories, Bedford, Mass.
- ReVelle, D. O. 2004. Recent advances in bolide entry modeling: A bolide potpourri. *Earth, Moon, and Planets*, 95(1-4), 441-476.
- Revelle, D. O., Brown, P. G., Spurný, P. 2004. Entry dynamics and acoustics/infrasonic/seismic analysis for the Neuschwanstein meteorite fall. *Meteoritics & Planetary Science*. 39(10). 1605-1626.
- ReVelle, D.O. 1974. *Acoustics of meteors-effects of the atmospheric temperature and wind structure on the sounds produced by meteors*. Ph.D. Thesis University of Michigan, Ann Arbor.
- ReVelle, D.O. 1976. On meteor-generated infrasound. *Journal of Geophysical Research*. 81(7), 1217-1230.
- ReVelle, D.O. 1997. Historical Detection of Atmospheric Impacts by Large Bolides Using Acoustic-Gravity Waves. *Annals of the New York Academy of Sciences*. 822(1), 284-302.
- Revelle, D.O., Whitaker, R.W. 1999. Infrasonic detection of a Leonid bolide: 1998 November 17. *Meteoritics & Planetary Science*. 34(6), 995-1005.
- Rickle, E. J., Pierce, A. D. 1981. Detection and assessment of secondary sonic booms in New England. *The Journal of the Acoustical Society of America*. 69(S1). S100-S100.

- Ripepe, M., Poggi, P., Braun, T., Gordeev, E. 1996. Infrasonic waves and volcanic tremor at Stromboli. *Geophysical research letters*. 23(2), 181-184.
- Seebass, A.R. 1967. Sonic boom research, Proceedings of a conference held at the National Aeronautics and Space Administration. Washington, D. C., April 12, 1967
- Silber, E.A., ReVelle, D.O., Brown, P.G., Edwards, W.N. 2009. An estimate of the terrestrial influx of large meteoroids from infrasonic measurements. *Journal of Geophysical Research: Planets* (1991–2012), 114(E8).
- Sutherland, L.C., Bass, H.E. 2004. Atmospheric absorption in the atmosphere up to 160 km. *The Journal of the Acoustical Society of America*, 115, 1012.
- Swinbank, R., O'Neill, A. 1994. A stratosphere-troposphere data assimilation system. *Monthly Weather Review*. 122(4), 686-702.
- von Muggenthaler, E., Reinhart, P., Lympany, B., Craft, R.B. 2003. Songlike vocalizations from the Sumatran Rhinoceros (*Dicerorhinus sumatrensis*). *Acoustics Research Letters Online*. 4: 83-8.
- Walterscheid, R.L., Hocking, W.K. 1991. Stokes diffusion by atmospheric internal gravity waves. *Journal of Atmospheric Sciences*. 48, 2213-2230.
- Weryk, R. J., and Brown, P. G. 2012. Simultaneous radar and video meteors—I: Metric comparisons. *Planetary and Space Science*. 62(1), 132-152.
- Weryk, R.J., Brown, P.G., Domokos, A., Edwards, W.N., Krzeminski, Z., Nudds, S.H., Welch D.L. 2007. The Southern Ontario All-sky Meteor Camera Network. *Earth Moon and Planets*. doi: 10.1007/s11038-007-9183-1.
- Whipple, F. 1930. The great Siberian meteor and the waves, seismic and aerial, which it produced. *Quarterly Journal of the Royal Meteorological Society*. 56: 287-304
- Whitham, G. B. 1952. The flow pattern of a supersonic projectile. *Communications on pure and applied mathematics*. 5(3), 301-348.
- Whitham, G. B. 1974. *Linear and Nonlinear Waves*. Wiley-Interscience, New York.
- Young, C. J., Chael, E. P., Merchant, B. J. 2002. Version 1.7 of MatSeis and the GNEM R&E regional seismic analysis tools. In *Proc. of the 24th Annual Seismic Research Symposium*.
- Zinn, J., Judd, O. D. P., ReVelle, D. O. 2004. Leonid meteor ablation, energy exchange, and trail morphology. *Advances in Space Research*. 33(9). 1466-1474

## Chapter 6

# 6. Optical Observations of Meteors Generating Infrasound – II: Weak Shock Theory and Validation

*A version of this chapter was submitted for a publication as:*

Silber, E. A., Brown, P. G. and Z. Krzeminski (2014) Optical Observations of Meteors Generating Infrasound – II: Weak Shock Model Theory and Validation, JGR-Planets, submission # 2014JE004680

### 6.1 Introduction

#### 6.1.1 Meteor Generated Infrasound

Well documented and constrained observations of meteor generated infrasound (Edwards et al., 2008; Silber and Brown, 2014) are an indispensable prerequisite for testing, validating and improving theoretical hypersonic shock propagation and prediction models pertaining to meteors (e.g. ReVelle, 1974). However, due to the lack of a sufficiently large and statistically meaningful observational dataset, linking the theory to observations had been a challenging task, leaving this major area in planetary science underexplored.

Infrasound is low frequency sound extending from below the range of human hearing of 20 Hz down to the natural oscillation frequency of the atmosphere (the Brunt-Väisälä frequency). Due to its negligible attenuation when compared to audible sound, infrasound can propagate over extremely long distances (Sutherland and Bass, 2004), making it an excellent tool for the detection and characterization of distant explosive sources in the atmosphere. Infrasound studies have gained momentum with the implementation of the global IMS network after the Comprehensive Nuclear Test Ban Treaty (CTBT) opened for signature in 1996. The IMS network includes 60 infrasound stations, 45 of which are



presently certified and operational, designed with the goal of detecting a 1 kt (TNT equivalent;  $1 \text{ kt} = 4.185 \times 10^{18} \text{ J}$ ) explosion anywhere on the globe (Christie and Campus, 2010).

Included among the large retinue of natural (e.g. volcanoes, earthquakes, aurora, lightning) (e.g. Bedard and Georges, 2000; Garces and Le Pichon, 2009) and anthropogenic (e.g. explosions, re-entry vehicles, supersonic aircraft) (Hedlin et al., 2002) sources of infrasound are meteors (ReVelle, 1976; Evers and Haak, 2001). A number of meteoritic events have been detected and studied (e.g. Brown et al., 2008; Le Pichon et al., 2008; Arrowsmith et al., 2008) since the deployment of the IMS network. Often, no other instrumental records for these bolides are available; hence infrasound serves as the sole means of determining the bolide location and energy. A notable example of such an observation is the daylight bolide/airburst over Indonesia, which occurred on 8 October, 2009 and produced estimated tens of kilotons in energy (Silber et al., 2011).

Most recently, on 15 February, 2013, an exceptionally energetic bolide exploded over Chelyabinsk, Russia, causing significant damage on the ground as well as a number of injuries (Brown et al., 2013; Popova et al., 2013). Such events attest to the need to better understand the nature of the shock wave produced by meteors.

The shocks produced by meteoroids may be detected as infrasound signals at the ground. As meteoroids enter the Earth's atmosphere at hypersonic velocities (11.2 – 72.8 km/s) (Ceplecha et al., 1998), corresponding to Mach numbers from ~35 to 270 (Boyd, 1998), they produce luminous phenomena known as a meteor through sputtering, ablation and in some cases fragmentation (Ceplecha et al., 1998). Meteoroids can produce two distinct types of shock waves which differ principally in their acoustic radiation directionality. Their hypersonic passage through the atmosphere may produce a ballistic shock, which radiates as a cylindrical line source. Episodes of gross fragmentation, where a sudden release of energy occurs at a nearly fixed point (ReVelle, 1974; Bronshten, 1983) may result in a quasi-spherical shock (e.g. Brown et al, 2007; ReVelle, 2010).

Meteoroids can produce two distinct types of shock waves which differ principally in their acoustic radiation directionality. Their hypersonic passage through the atmosphere may produce a ballistic shock, which radiates as a cylindrical line source. Episodes of gross fragmentation, where a sudden release of energy occurs at a fixed point (ReVelle, 1974; Bronshten, 1983) may result in a quasi-spherical shock (e.g. Brown et al, 2007; ReVelle, 2010).

Although infrasound does not suffer from significant attenuation over long distances, it is susceptible to dynamic changes that occur in the atmosphere. Nonlinear influences, atmospheric turbulence, gravity waves and winds, all have the potential to affect the infrasonic signal as it propagates between the source and the receiver (Ostashev, 2002; Kulichkov, 2004; Mutschlecner and Whittaker, 2010). Consequently, distant explosive sources, such as bolides, are generally difficult to fully model or uniquely separate from other impulsive sources based on infrasound records alone.

The first complete quantitative model of meteor infrasound was developed by ReVelle (1974). In this model predictions are made, starting with a set of source parameters, for the maximum infrasound signal amplitude and dominant period at the receiver. Due to a lack of observational data, ReVelle's (1974) cylindrical blast wave theory for meteors has never been experimentally and observationally validated. In particular, regional (<300 km) meteor infrasound signals have been studied infrequently in favor of larger bolide events, despite the fact that regional meteor infrasound is likely to reveal more characteristics of the source shock, having been substantially less modified during the comparatively short propagation distances involved (Silber and Brown, 2014).

A central goal of meteor infrasound measurements is to estimate the size of the relaxation or blast radius ( $R_0$ ), as this is equivalent to an instantaneous estimate of energy deposition, which is the key to defining the energetics in meteoroid ablation. Indeed, all meteor measurements ultimately try to relate observational information back to energetics either through light, ionization or shock (infrasound) production. In order to better define meteoroid shock production, evaluate energy deposition mechanisms and estimate meteoroid mass and energy, it is helpful to first investigate near field meteor infrasound (ranges < 300 km) for well documented and characterized meteors, because this offers the

most plausible route in validating the cylindrical blast wave model of meteor infrasound. Near field infrasonic signals are generally direct arrivals and suffer less from propagation effects.

In this work, we attempt to validate the existing ReVelle (1974) meteor infrasound theory, using a survey of centimeter-sized and larger meteoroids recorded by a multi-instrument meteor network (Silber and Brown, 2014). This network, designed to optically detect meteors which are then used as a cue to search for associated infrasonic signals, utilizes multiple stations containing all sky video cameras for meteor detection and an infrasound array located near the geographical centre of the optical network.

### **6.1.2 A Brief Review of ReVelle (1974) Meteor Weak Shock Theory**

In the early 1950s, Whitham (1952) developed the F-function approach to sonic boom theory, a novel method of treating the flow pattern of shock signatures generated by supersonic projectiles, now widely used in supersonics and classical sonic boom theory (e.g. Maglieri and Plotkin, 1991). It was soon realized that although the F-function offers an excellent correlation between experiment and theory for low Mach numbers ( $< \sim 3$ ), it is not an optimal tool in the hypersonic regime (e.g. Carlson and Maglieri, 1972; Plotkin, 1989). Recently, the Whitham F-function theory has been applied to meteor infrasound (Haynes and Millet, 2013), but it has not yet received a detailed observational validation. We note, however, that this approach offers another theoretical pathway to predicting and interpreting meteor infrasound, though we do not explore it further in this study.

Drawing on the early works of Lin (1954), Sakurai (1964), Few (1969), Jones et al. (1968), Plooster (1968; 1970) and Tsikulin (1970), ReVelle (1974; 1976) developed an analytic blast wave model of the nonlinear disturbance initiated by an explosive line source as an analog for a meteor shock.

In cylindrical line shock theory, the magnitude of the characteristic blast wave relaxation radius ( $R_0$ ) is defined as the region of a strongly nonlinear shock.

$$R_0 = (E_0/p_0)^{1/2} \quad (6.1)$$

Here,  $E_0$  is the energy deposited by the meteoroid per unit trail length and  $p_0$  is the ambient hydrostatic atmospheric pressure. Physically this is the distance from the line source at which the overpressure approaches the ambient atmospheric pressure. For a single body ablating in the atmosphere, ignoring fragmentation, the blast radius can be directly related to the drag force and ultimately expressed as a function of Mach number ( $M$ ) and meteoroid diameter ( $d_m$ ) (ReVelle, 1974):

$$R_0 \sim M d_m \quad (6.2)$$

While the original ReVelle (1974) model assumes propagation through an isothermal atmosphere, here we use an updated version incorporating a non-isothermal atmosphere. As shown in an earlier study (Edwards et al., 2008), the isothermal approximation leads to unrealistic values of signal overpressure. The following summary of ReVelle's (1974) meteor infrasound theory is similar to that presented in Edwards (2010), though with some corrections and emphasis on the approximations used by ReVelle (1974) and aspects of the treatment most applicable to our study. The ReVelle (1974) approach begins with a set of input parameters characterizing the entry conditions of the meteoroid, and from these initial conditions predicts the infrasonic signal overpressure (amplitude) and period at the ground. As part of this analysis, the blast radius and the height (distortion distance) at which the shock transitions from the weakly nonlinear regime to the linear regime is also determined. The model inputs are:

- (i) station (observer) location (latitude, longitude and elevation);
- (ii) meteoroid parameters (mass, density, velocity, and entry angle as measured from the horizontal);
- (iii) infrasonic ray parameters at the source which reach the station based on ray-tracing results (angular deviation from the meteoroid plane of entry and shock source location along the trajectory in terms of latitude, longitude and altitude).

In the ReVelle (1974) meteor cylindrical blast wave theory the following assumptions are made:

- i. The energy release must be instantaneous.
- ii. The cylindrical line source is valid only if  $v \gg c_s$  (the Mach angle has to be very small many meteoroid diameters behind the body) and  $v = \text{constant}$  (Tsikulin, 1970). Therefore, it follows that if there is significant deceleration ( $v < 0.95v_{\text{entry}}$ ) and strong ablation, the above criteria are not met and the theory is invalid.
- iii. The line source is considered to be in the free field, independent of any reflections due to finite boundaries, such as topographical features (ReVelle, 1974).
- iv. Ballistic entry (no lifting forces present - only drag terms)
- v. The meteoroid is a spherically shaped single body and there is no fragmentation
- vi. The trajectory is a straight line (i.e. gravitational effects are negligible). The nonlinear blast wave theory does not include the gravity term.

The coordinate system to describe the motion and trajectory of the meteoroid, as originally developed by ReVelle (1974; 1976), is described in Chapter 2. In this model, only those rays which propagate downward and are direct arrivals are considered (i.e. direct source-observer path). The predicted signal period, amplitude and overpressure ratio as a function of altitude are shown in Figure 6.1.

Note that due to severe nonlinear processes, the solutions to the shock equations are not valid for  $x \leq 0.05$ , where  $x$  is the distance in units of blast radii (e.g.  $R/R_0$ ). Once the wave reaches a state of weak nonlinearity (i.e. the shock front pressure ( $p_s$ )  $\sim$  ambient pressure ( $p_0$ )), the shock velocity approaches the local adiabatic speed of sound ( $c$ ). When  $\Delta p/p_0 \leq 1$  (at  $x \geq 1$ ), weak shock propagation takes place and geometric acoustics becomes valid (Jones et al., 1968; ReVelle, 1974). It is also assumed that at beginning, near the source ( $x < 1$ ), the wave energy is conserved except for spreading losses (Sakurai, 1964).

Vertically Inhomogeneous Atmosphere Predictions  
(Meteor Event 20110630\_033938)

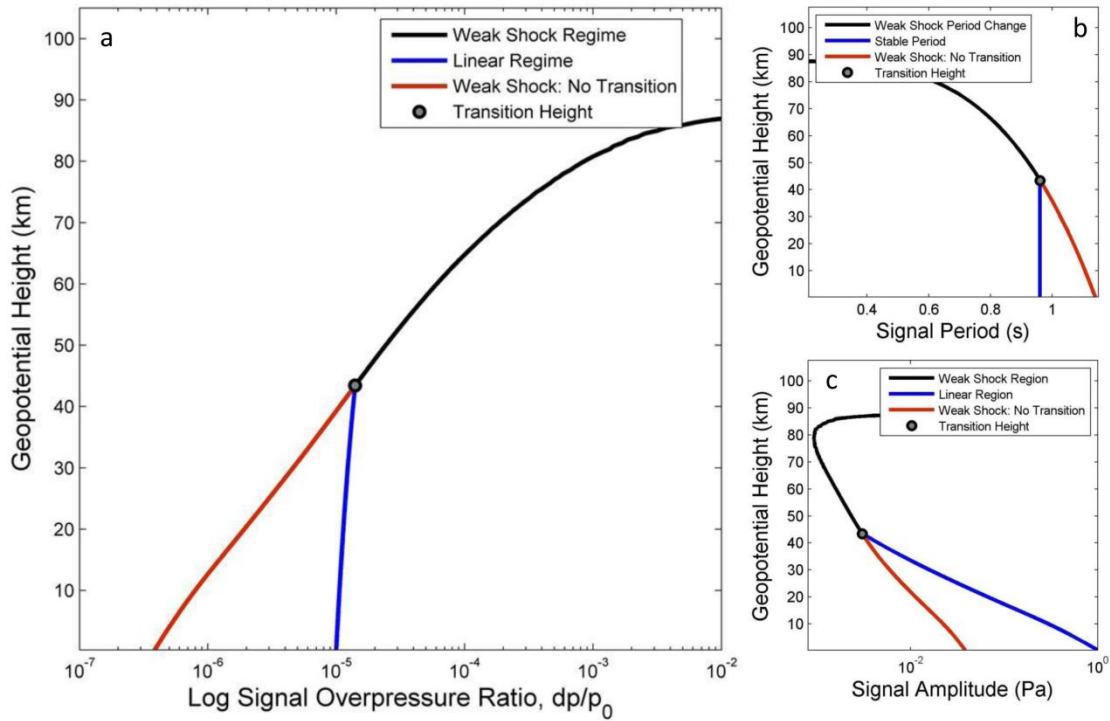


Figure 6.1: The change in signal (a) amplitude, (b) period and (c) overpressure ratio ( $dp/p_0$ ) as a function of height from source to receiver in a fully realistic atmosphere (with winds and true temperature variations with height) according to the ReVelle (1974) theory. In this case the meteor blast radius ( $R_0$ ) = 5 m, entry angle =  $43^\circ$ , speed = 29 km/s and source height = 88.7 km.

Drawing upon theoretical and observational work on shock waves from lightning discharges (Jones et al., 1968) the functional form of the overpressure has limiting values of:

$$\lim_{x \rightarrow 0} f(x) = \frac{2(\gamma + 1) \Delta p}{\gamma p_0} \rightarrow x^{-2} \quad (6.3a)$$

and

$$\lim_{x \rightarrow \infty} f(x) = \left(\frac{3}{8}\right)^{-3/5} \left\{ \left[ 1 + \left(\frac{8}{3}\right)^{8/5} x^2 \right]^{3/8} - 1 \right\}^{-1} \rightarrow x^{-3/4} \quad (6.3b)$$

Here,  $\gamma$  is the specific heat ratio ( $\gamma=C_p/C_v=1.4$ ) and  $\Delta p/p_0$  is the overpressure. In the limit as  $x \rightarrow 0$ , where  $\Delta p/p_0 > 10$ , attenuation is quite rapid ( $x^{-2}$ ), transitioning to  $x^{-3/4}$  as  $x \rightarrow \infty$ , where  $\Delta p/p_0 < 0.04$  (or  $M = 1.017$ ) (Jones et al., 1968). Taking advantage of equations (3a) and (3b), and using results obtained from experiments (Jones et al., 1968; Tsikulin, 1970), the overpressure (for  $x \geq 0.05$ ) can be expressed as:

$$\frac{\Delta p}{p_0} = \frac{2(\gamma + 1)}{\gamma} \left(\frac{3}{8}\right)^{-\frac{3}{5}} \left\{ \left[ 1 + \left(\frac{8}{3}\right)^{\frac{8}{5}} x^2 \right]^{\frac{3}{8}} - 1 \right\}^{-1} \quad (6.4a)$$

The limit within which this expression is applicable is  $0.04 \leq \Delta p/p_0 \leq 10$  (Jones et al., 1968). The above expression can also be written as:

$$\frac{\Delta p}{p_0} \cong \frac{2\gamma}{\gamma + 1} \left[ \frac{0.4503}{(1 + 4.803x^2)^{\frac{3}{8}} - 1} \right] \quad (6.4b)$$

After the shock wave has travelled a distance of approximately  $10R_0$ , where it is assumed that strong nonlinear effects are no longer important, its fundamental period ( $\tau_0$ ) can be related to the initial blast radius via:  $\tau_0 = 2.81R_0/c$ , where  $c$  is the local ambient thermodynamic speed of sound. The factor 2.81 at  $x = 10$  was determined experimentally (Few, 1969) and found to compare favorably to numerical solutions (Plooster, 1968). The frequency of the wave at maximum is referred to as the ‘dominant’ frequency (ReVelle, 1974). For a sufficiently large  $R$ , and assuming weakly nonlinear propagation, the line source wave period ( $\tau$ ) for  $x \geq 10$  is predicted to increase with range as:

$$\tau(x) = 0.562 \tau_0 x^{1/4} \quad (6.5)$$

Far from the source, the shape of the wave at any point will mainly depend on the two competing processes acting on the propagating wave: dispersion, which reduces the overpressure and ‘stretches’ the period; and steepening, which is the cumulative effect of small disturbances, tending to increase the overpressure amplitude (ReVelle, 1974). In ReVelle’s (1974) model, however, it is assumed that the approximate wave shape is known at any point. After a short distance beyond  $x = 10$ , the waveform is assumed to remain an N-wave (DuMond et al., 1946) type-shape (ReVelle, 1974).

For the analytic implementation of ReVelle's theory, it is necessary to choose some transition distance from the source where we consider the shock as having moved from weakly nonlinear propagation to fully linear. The precise distance at which the transition between the weak shock and linear regime occurs is poorly defined. Physically, it occurs smoothly, as no finite amplitude wave propagating in the atmosphere is truly linear; this is always an approximation with different amplitudes along the shock travelling with slightly different speeds. This distance was originally introduced by Cotten et al. (1971) in the context of examining acoustic signals from Apollo rockets at orbital altitudes. Termed by Cotten et al. (1971) the "distortion distance", it is based upon Towne's (1967) definition of the distance ( $d'$ ) required for a sinusoidal waveform to distort by 10%. ReVelle (1974) adopted this distance, together with the definition of Morse and Ingard (1968), to define the distance ( $d_s$ ) an initially sinusoidal wave must travel before becoming "shocked". Thus, it follows that  $d_s = 6.38 d'$ , where  $d' > d_a$  and  $d_a$  is the remaining propagation distance of the disturbance before it reaches the observer. Further details summarizing the ReVelle (1974) model are given in Chapter 2.

In summary, according to the ReVelle (1974) weak shock model, there are two key sets of expressions to estimate the predicted infrasonic signal period and the amplitude at the ground. The first is the expression for the predicted dominant signal period in the weak shock regime ( $d' \leq d_a$ ). Once the shock is assumed to propagate linearly, by definition the period remains fixed.

The second expression relates to the overpressure amplitude. In the weak shock regime the predicted maximum signal amplitude is given by:

$$\Delta p_{z \rightarrow obs} = (f(x) D_{ws}(z) N^*(z) Z^*(z)) p_0 \quad (6.6a)$$

where  $f(x)$  is the expression given in equation (4b),  $N^*$  and  $Z^*$  are the correction factors as described in Chapter 2 and  $D_{ws}$  is the weak shock damping coefficient.

Once the wave transitions into a linear wave, the maximum signal amplitude is given by:

$$\Delta p_{z \rightarrow obs} = \left[ \Delta p_{z \rightarrow t} D_l(z) \frac{N^*(z)_{z \rightarrow obs} Z^*(z)_{z \rightarrow obs}}{N^*(z)_{z \rightarrow t} Z^*(z)_{z \rightarrow t}} \left( \frac{x_{z \rightarrow t}}{x_{z \rightarrow obs}} \right)^{1/2} \right] p_0 \quad (6.6b)$$



where  $\Delta p_{z \rightarrow t}$  is identical to the expression given in equation (6a) and  $D_l$  is the linear damping coefficient. The subscripts  $z$ ,  $t$  and  $obs$  in equations (6a) and (6b) denote the source altitude, transition altitude and the receiver's altitude, respectively, following the notation in ReVelle (1974).

The ReVelle (1974) model as just described has been coded in *MATLAB*<sup>®</sup> to allow comparison between the predicted amplitudes and periods of meteor infrasound at the ground with the observations, the focus of this paper. In our first paper in the series (Silber and Brown, 2014 in review), we used optical measurements to positively identify infrasound from specific meteors and constrain the point (and its uncertainty) along the meteor trail where the observed infrasound signal emanated. That work also examined the influence of atmospheric variability on near-field meteor infrasound propagation and established the type of meteor shock production at the source (spherical vs. cylindrical). We also developed a meteor infrasound taxonomy using the pressure-time waveforms of all the identified meteor events as a starting point to gain insight into the dominant processes which modify the meteor infrasound signal as observed at the ground.

Here, we use the dataset constructed in the first part of our study and select the best constrained (ie. those for which we have accurate infrasound source heights) meteor events to address the following:

- i. for meteors detected optically and with infrasound, use the ReVelle (1974) weak shock theory to provide a bottom-up estimate of the blast radius (i.e. from observed amplitude and period at the ground can we self-consistently estimate the blast radius at the source);
- ii. test the influence of atmospheric variability, winds, Doppler shift and initial shock amplitude on the weak shock solutions within the context of ReVelle (1974) meteor infrasound theory;
- iii. determine an independent estimate of meteoroid mass/energy from infrasonic signals alone and compare to photometric mass/energy measurements;

- iv. critically evaluate and compare ReVelle's (1974) weak shock theory with observations, establishing which parameters/approximations in the theory are valid and which may require modification.

## 6.2 Methodology and Results

### 6.2.1 Weak Shock: Model Updates and Sensitivities

The ReVelle (1974) weak shock model algorithm was implemented in *MATLAB*<sup>®</sup> and updated to include full wind dependency, as well as Doppler shift for period (Morse and Ingard, 1968) as a function of altitude. The influence of the winds is reflected in the effective speed of sound ( $c_{eff}$ ), which is given by the sum of the adiabatic sound speed ( $c$ ) and the dot product between the ray normal ( $\hat{n}$ ) and the wind vector ( $\vec{u}$ ):

$$c_{eff} = c + \hat{n} \cdot \vec{u} \quad (6.7)$$

The signal amplitude is affected by winds such that the amplitude will intensify for downwind propagation and diminish in upwind propagation (Mutschlecner and Whittaker, 2010). In the linear regime, the signal period (equation 6.5), does not suffer any decay with distance, but the winds do induce a Doppler shift. Following Morse and Ingard (1968), the Doppler shift due to the wind is given by:

$$\Omega = \omega - \vec{k} \cdot \vec{u} \quad (6.8)$$

where  $\Omega$  is the intrinsic angular frequency (frequency in the reference frame of the moving wind with respect to the ground),  $\omega$  is the angular frequency in the fixed earth frame of reference and  $\vec{k}$  is the wave number. Since the contribution of winds in the vertical direction is generally 2-4 orders of magnitude smaller than the horizontal wind contribution (Wallace and Hobbs, 2006; Andrews, 2010), it is neglected.

Another addition to the weak shock model was the inclusion of updated absorption coefficients (Sutherland and Bass, 2004), applicable in the linear propagation regime.

In the first part of our study (Silber and Brown, 2014) we described the influence on the raytracing results of small scale perturbations in the wind profile due to gravity waves on raytracing results. While the effects were small, they were significant enough to produce

propagation paths which were non-existent using the average atmosphere from the source to the receiver. Here we have used the same ‘perturbed’ atmospheric profiles to test the influence of gravity-wave-induced perturbations on the predicted signal amplitude and period as calculated using the weak shock model. We selected five events which span the global range of our final data (i.e. meteors with different entry velocity, blast radius, and shock heights), and ran the weak shock code using 500 ‘perturbed’ atmospheric profiles. For each event and each realization we computed the magnitude of the modelled infrasonic signal period and amplitude while simultaneously testing the effect of different absorption coefficients in the linear regime using the set given by ReVelle (1974) and that of Sutherland and Bass (2004).

The overall effect of both winds and Doppler shift on the weak shock model was found to be relatively small, resulting in  $R_0$  differences of no more than 13% for the period (average 4%) and as high as 9% for the amplitude (average 3%). The perturbations to the atmospheric winds expected from gravity-waves were found to have even smaller effects on estimates of  $R_0$ , typically of 10% or less.

In addition, the predicted ground-level period and amplitude outputs of the weak shock model were tested using a synthetically generated meteor (Figure 6.2).

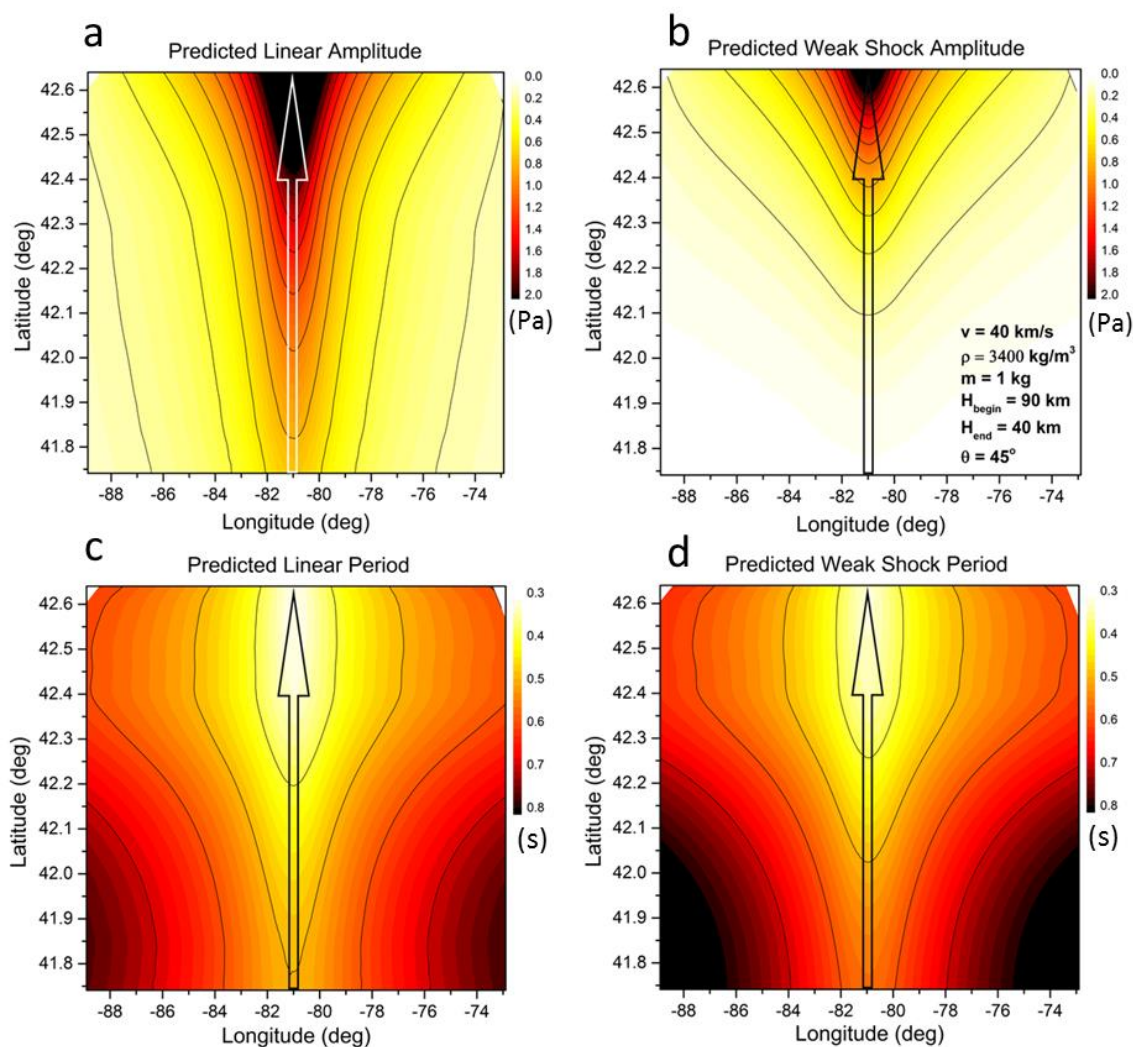


Figure 6.2: An example of the predicted ground-level amplitude and period of a meteor shock using the ReVelle (1974) theoretical model. In these figures, the meteor moves northward, as shown with the arrow in each plot, starting ablation at an altitude of 90 km and ending at 40 km. A representative realistic atmosphere was applied, accounting for the wind. The top two panels show the predicted (a) linear and (b) weak shock amplitude. The bottom two panels show the predicted (c) linear and (d) weak shock period. The amplitude in the linear regime has a larger magnitude than that in the weak shock regime, while the opposite is true for the signal period. The synthetic meteor parameters are shown in the lower right of plot (b).

### 6.2.2 Weak Shock: Bottom-up Modelling

The first approach we adopt to testing the ReVelle (1974) theory is a bottom-up methodology. This provides an indirect method of estimating the blast radius at the meteor using infrasound and optical astrometric measurements of the meteor only (i.e. without prior independent knowledge of the meteoroid mass and density). Given the input parameters, all of which are known except the blast radius, the goal is to answer the following question: what is the magnitude of the blast radius required to produce the observed signal amplitude and period at the station if we assume (i) the signal remained a weak shock all the way to the ground and (ii) if it transitioned to the linear regime? Additionally, we want to define the blast radius uncertainty given the errors in signal measurements.

Drawing upon the results obtained in Silber and Brown (2014), the 24 well constrained optical meteors which were also consistent with cylindrical line sources (as determined through optical measurements and raytracing) were used to observationally test the weak shock model. The orbital parameters and meteor shower associations for our data set are listed in Table 6.1. Out of these 24 events, 18 produced a single infrasonic arrival, while six events produced two distinct infrasonic arrivals at the station. The meteor shock source altitude in our data set ranges from 53 km to 103 km, the observed signal amplitude ( $A_{obs}$ ) is from 0.01 Pa to 0.50 Pa, while the observed dominant signal period ( $\tau_{obs}$ ) is between 0.1 s and 2.2 s. Typical values of overpressure from meteors in this study are 1-2 orders of magnitude smaller than those associated with the signals from Apollo rockets as reported by Cotten et al. (1971), the last comparable study to this one.

For the model to be self-consistent a single blast radius should result from the period and amplitude measurements. In practice, we find estimates of blast radii for period and amplitude independently in both linear and weak shock regimes such that the measured signal amplitude or period is matched within its measurement uncertainty. Therefore, for each amplitude/period measurement there are two pairs of theoretical quantities produced from ReVelle's (1974) theory: the predicted signal amplitude ( $A_{ws}$ ) and period ( $\tau_{ws}$ ) in the weak shock regime, and the signal amplitude ( $A_l$ ) and period ( $\tau_l$ ) in the linear regime. The iterations began with a seed-value of the initial  $R_0$ , and then based on the computed

results the process is repeated with a new (higher or lower) value of  $R_0$  and the results again compared to measurements until convergence is reached. The result of this bottom-up procedure is a global estimate of the blast radius matching the observed amplitude or period assuming either weak-shock or linear propagation ( $A_{ws}$ ,  $\tau_{ws}$ ,  $A_l$ ,  $\tau_l$ ). In the second phase of this bottom-up approach, this global modelled initial blast radius was used as an input to iteratively determine the minimum and maximum value of the model  $R_0$  required to match the observed signal (period or amplitude) within the full range of measurement uncertainty.

Table 6.1: A summary of orbital parameters for all events in our data set. The columns are as follows: (1) event date, (2) Tisserand parameter, a measure of the orbital motion of a body with respect to Jupiter (Levison, 1996), (3) semi-major axis (AU), (4) eccentricity, (5) inclination ( $^\circ$ ), (6) argument of perihelion ( $\omega$ ) ( $^\circ$ ), (7) longitude of ascending node ( $^\circ$ ), (8) geocentric velocity (km/s), (9) heliocentric velocity (km/s), (10)  $\alpha$  – right ascension of geocentric radiant ( $^\circ$ ), (11)  $\delta$  – declination of geocentric radiant ( $^\circ$ ), (12) perihelion (AU), (13) aphelion (AU), (14) meteor shower associations. The meteor shower codes are:  $\alpha$ -Capricornids (CAP), Orionids (ORI), Perseids (PER), and Southern Taurids (STA). Note all angular quantities are J2000.0.

1	2	3	4	5	6	7	8	9	10	11	12	13	14
Date	Tiss	a	e	inc	$\omega$	asc node	$v_g$	$v_h$	$\alpha$ geo	$\delta$ geo	q per	q aph	Showers
20060419	2.8	3.2	0.69	2.2	195.5	29.021	10.0	38.6	153.0	20.2	0.989	5.4	--
20060805	hyp	-8.4	1.12	144.9	164.9	132.716	69.0	43.1	38.7	37.1	0.996	-17.7	--
20061104	3.1	2.2	0.83	4.3	292.1	221.472	28.0	37.3	49.0	22.0	0.371	4.1	--
20070125	hyp	-1.7	1.57	156.4	342.6	124.950	76.6	48.3	214.3	-28.9	0.957	-4.3	--
20070727	2.7	2.8	0.80	8.3	269.9	123.717	23.8	37.8	303.7	-9.3	0.566	5.1	CAP
20071021	1.2	2.5	0.80	172.9	94.6	27.535	63.4	37.9	95.6	20.1	0.519	4.6	ORI
20080325	3.7	1.9	0.48	7.3	358.8	184.634	7.7	36.3	95.8	-13.2	0.997	2.9	--
20080511	hyp	-26.1	1.03	9.3	42.6	230.738	19.6	42.3	191.2	-25.4	0.874	-53.1	--
20080812	1.0	3.7	0.74	110.8	157.7	139.878	56.4	38.9	41.3	57.8	0.981	6.4	PER
20081028	2.7	3.2	0.71	6.9	31.6	34.961	12.1	38.8	2.4	-23.0	0.932	5.4	--
20081102	3.5	1.8	0.82	5.2	118.2	40.086	27.9	36.1	52.7	14.6	0.335	3.3	STA
20081107	hyp	-8.8	1.11	152.8	10.0	45.144	71.5	43.5	130.2	1.7	0.983	-18.7	--
20090428	3.1	2.4	0.68	10.6	244.7	37.916	18.0	37.3	211.2	8.9	0.773	4.1	--
20090523	hyp	-41.8	1.02	21.3	250.7	62.169	27.9	42.1	240.2	6.4	0.671	-84.3	--
20090812	0.5	5.4	0.82	111.9	154.0	139.617	57.5	39.8	44.0	57.8	0.967	9.8	PER
20090917	2.5	3.2	0.81	0.3	263.0	174.168	22.4	38.6	350.9	-3.4	0.610	5.8	--
20100421	0.4	93.7	0.99	71.7	257.8	30.847	45.3	41.9	252.1	21.2	0.610	186.9	--
20100429	1.0	5.8	0.85	82.8	229.2	38.658	47.2	40.1	274.4	27.9	0.846	10.8	--
20100530	2.5	3.0	0.86	4.6	284.4	68.652	28.2	38.1	254.4	-18.4	0.429	5.6	--
20110520	2.6	3.2	0.78	6.0	252.8	58.759	20.9	38.5	229.8	-8.5	0.699	5.8	--
20110630	1.5	7.9	0.87	45.0	187.8	97.886	28.6	40.4	274.9	61.5	1.012	14.7	--
20110808	2.3	3.8	0.74	37.1	156.9	135.191	24.2	38.9	223.8	70.6	0.980	6.6	--
20111005	2.6	2.8	0.85	7.9	103.2	11.464	27.2	38.2	19.9	0.1	0.437	5.2	--
20111202	2.9	2.4	0.81	5.5	100.8	69.314	26.0	37.9	74.8	16.8	0.461	4.4	--

The summary of the bottom-up blast radius modelling results are presented in Figure 6.3. There is a significant discrepancy between the period-based blast radii and amplitude-based blast radii in both the linear and weak shock regimes. The average blast radius from amplitude determinations in the linear regime is approximately 30 times smaller than that in the weak shock regime, indicating that the transition to linearity approach employed in the ReVelle (1974) weak shock model perhaps significantly underestimates the blast radius. In the weak shock regime, where we assume the signal can be treated as a weak shock all the way to the ground, we find that the amplitude-estimated  $R_0$  in most cases is larger than that estimated from the period, but the difference is much smaller than the linear case, being no more than a factor of 15 between the amplitude and period. Almost half of the events show agreement within uncertainty.

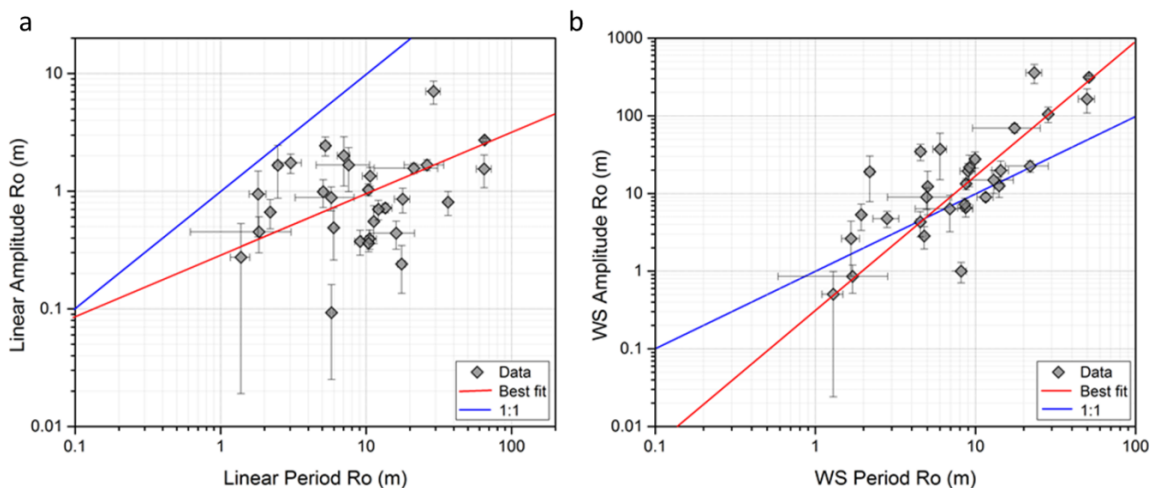


Figure 6.3: The behaviour of  $R_0$  in (a) linear and (b) weak shock regimes in the bottom-up modelling approach. In the linear regime, the amplitude blast radius appears underestimated relative to the  $R_0$  estimated from the period, while in the weak shock regime, the behaviour is reversed. In all plots, the blue line represents the 1:1 correspondence, while the red line is the best fit.

### 6.2.3 Weak Shock: Top-Down Modelling

#### 6.2.3.1 Photometric Measurements

The fundamental equations of motion (Bronshten, 1983; Ceplecha et al., 1998) for a meteoroid of mass  $m$  and density  $\rho_m$  entering the Earth's atmosphere at velocity  $v$  are given by the drag and mass-loss equations:

$$\frac{dv}{dt} = -\frac{\Gamma A \rho_a v^2}{m^{\frac{1}{3}} \rho_m^{\frac{2}{3}}} \quad (6.9)$$

$$\frac{dm}{dt} = -\frac{\Lambda A \rho_a v^3 m^{\frac{2}{3}}}{2\xi \rho_m^{\frac{2}{3}}} \quad (6.10)$$

Here,  $\Gamma$  is a drag coefficient,  $\xi$  is the heat of ablation of the meteoroid material (or energy required to ablate a unit mass of the meteoroid),  $\Lambda$  is the heat transfer coefficient, which is a measure of efficiency of the collision process in converting kinetic energy into heat (McKinley, 1961),  $\rho_a$  is density of the air, and  $A$  is the dimensionless shape factor ( $A_{sphere} = 1.209$ ).

The all-sky meteor camera system used for this survey and details of the astrometric reductions and measurements methodology are presented in Silber and Brown (2014). Here we briefly describe the photometric analysis.

A series of laboratory experiments were performed to determine the camera response in an effort to model the effects of camera saturation (which affect many of our events). In the field, measurements were performed to model the lens roll-off (the apparent drop in sensitivity of the camera as the edges of the all-sky field are reached). The lens roll-off correction becomes significant for meteors as a  $>0.8$  astronomical magnitude attenuation results for elevations below  $\sim 15$  degrees. Other standard photometric corrections were applied including extinction correction (e.g. Vargas et al., 2001; Burke et al., 2010) and apparent instrumental magnitude converted to an absolute magnitude by referencing all meteors to a standard range of 100 km (McKinley, 1961).



Bright meteors (magnitude  $> -4$ ) are typically saturated on the 8-bit cameras. In our laboratory setup, an artificial star of variable brightness was created using a fixed light source and a turning wheel with a neutral density filter of varying density following the procedure used by Swift et al. (2004). Standard photometric procedures (Hawkes, 2002) were used to determine the apparent instrumental magnitude of the artificial star and a power law fit between the observed and known brightness of the artificial star was then computed to find a correction for the saturation which we applied to meteors to deduce their true apparent magnitude.

The instrumental magnitude of any given star (or meteor) varies as a function of distance from the optical center (or zenith distance if the camera is vertically directed) of the camera lens. For our cameras a star appears about 2.5 stellar magnitudes dimmer near the horizon than at the zenith due to the natural vignetting in the optical system. The in-field experiment was performed on a clear night by setting up the camera on a turntable attached to a fixed frame and taking a series of video frames starting from the horizon and sweeping through an angle of  $180^\circ$  through the zenith. Several bright stars then had their instrumental magnitudes computed as a function of distance from the optical axis to compute the lens roll-off which was found to functionally behave as  $\cos^4\theta$ . Applying all these corrections we then followed standard photometric routines (Hawkes, 2002), to compute the light curves for each meteor in our instrumental passband. Our cameras use hole accumulation diode CCD chips (Weryk and Brown, 2013). The CCDs have both a wide passband and high QE making them extremely sensitive in low-light conditions. Our limiting meteor sensitivity is approximately  $M_{\text{HAD}} = -2$  corresponding to meteoroids of  $\sim 5$  g or roughly 1cm in diameter at 30 km/s.

There are two approaches which can be used to determine the mass of a meteoroid given optical data. First, we may appeal to empirical estimates of the magnitude-mass-speed determined from earlier photographic surveys (e.g. Jacchia et al. (1967)) which yields:

$$M_{\text{HAD}} = 55.34 - 8.75 \log v - 2.25 \log m - 1.5 \log \cos Z_R \quad (6.11)$$

where  $M_{\text{HAD}}$  is the absolute magnitude in the HAD bandpass,  $m$  is the mass of the meteoroid in grams,  $Z_R$  is the zenith angle of the radiant and where the meteoroid velocity ( $v$ ) is expressed in cgs units. The original relation was computed in the photographic

bandpass. We estimated the color correction term between our instrumental system and the photographic system, ( $M_{\text{HAD}} = M_{\text{Ph}} + 1.2$ ) by assuming each meteor radiates as a 4500K blackbody and computing the energy falling into our HAD bandpass as compared to the photographic bandpass following the synthetic photometry procedure described in Weryk and Brown (2013).

A second approach to estimate photometric mass is to directly integrate the light emission ( $I$ ) of the meteoroid throughout the time of its visibility:

$$m = \frac{2 \int I dt}{\tau_l v^2} \quad (6.12)$$

where  $\tau_l$  is the luminous efficiency defined as the fraction of the meteoroid's kinetic energy produced converted into radiation (Ceplecha et al., 1998). More about this approach can be found in Ceplecha et al. (1998) and Weryk and Brown (2013).

The magnitude of the blast radius at any point along the meteor trail can be thought of as a 'snapshot' of the energy per unit path length deposited into the atmosphere by a meteoroid. This may also be equated to the meteoroid mass times the Mach number at that point assuming single body ablation (ReVelle, 1976).

While the single body approach is much more simple if the source region along the trail where the shock observed at the microphone location on the Earth's surface is produced close to the end of the meteor trail the total initial photometric mass poorly represents the actual energy/mass at the source location. If the initial mass is used to test the weak shock model, it produces erroneous results as the actual mass (and energy deposited per unit path length) would be much smaller as the initial meteoroid mass is much larger than the remnant mass near the end of the trail.

### **6.2.3.2 The Fragmentation (FM) Model**

A third approach to estimating mass using optical data is to apply an entry model code to fit the observed brightness and length vs. time measured for the meteor. Here we use the fragmentation (FM) model of meteoroid motion, mass loss and radiation in the atmosphere (Ceplecha and ReVelle, 2005) to fit the observed brightness and length vs. time measured for the infrasound-producing meteor. As fragmentation is explicitly

accounted for, the FM model should provide a more realistic estimate of energy deposition along the trail, and thus  $R_0$ .

The first step in constructing an entry model solution was to begin with the approximate (starting) values for intrinsic shape density coefficient ( $K$ ) and intrinsic ablation coefficient ( $\sigma$ ), which are defined by the following expressions (Ceplecha and ReVelle, 2005):

$$\sigma = \frac{\Lambda}{2\xi\Gamma} \quad (6.13)$$

$$K = \frac{\Gamma A_s}{\rho^{2/3}} \quad (6.14)$$

The intrinsic shape density coefficient ( $K$ ) and intrinsic ablation coefficient ( $\sigma$ ) are then modified together with the initial mass in a forward modeling process. We do this statistically by first classifying each of our meteors according to the fireball types defined by Ceplecha and McCrosky (1976) (hereafter CM). This is done by calculating the PE parameter (Ceplecha and McCrosky, 1976), defined as:

$$PE = \log \rho_E + A_0 \log m + B_0 \log v + C_0 \log \cos Z_R \quad (6.15)$$

where  $\rho_E$  is the density of air (in cgs units) at the trajectory end height,  $m$  is the estimated initial mass in grams, and the meteoroid entry velocity ( $v$ ) is expressed in km/s. From fits to a large suite of photographically observed fireballs, CM found  $A_0 = -0.42$ ,  $B_0 = 1.49$  and  $C_0 = -1.29$ . As an estimate for the initial mass we use the mass computed from equation (6.31) and assume a +1.2 color term between the HAD and photographic bandpasses. In this way we derive estimates for the PE for each of our events. The range of values of PE and presumed corresponding meteoroid types as proposed by CM are given in Table 6.2. The observed light curve from photometric measurements, in conjunction with the astrometric solution (event time, path length as a function of height and entry angle) for each event, was used to match the theoretical light curve and model length vs. time to observations through forward modelling (Figure 6.4).

As our average meteoroid mass is intermediate between fireball and small camera data, we *a priori* expect our distribution of fireball types (I-III) to be intermediate between

these two classes, if our mass scale is reasonable. As shown in Table 6.2, within the limitations of our small number statistics, our distribution is broadly consistent with being intermediate between the percentage distribution of these two categories given by Ceplecha et al. (1998) indicating our choice of color term is physically reasonable.

Table 6.2: The range of PE parameter and the associated meteoroid group presumed type, type of the material and representative density as given by Ceplecha et al. (1998). The percentage of observed meteoroids in each group according to mass category typical of fireball networks (mass range 0.1 - 2000 kg) and small cameras (mass range  $10^{-4}$  kg to 0.5 kg) as published in (Ceplecha et al., 1998) and the percentages found in this study (masses  $10^{-4}$  kg to 1.0 kg). The range of values for  $\sigma$  and K found in our study within the framework of the FM model are given in the last two columns.

PE range	Group type	Type of the meteoroid material	$\rho_m$ (kg/m <sup>3</sup> )	% observed (fireball networks)	% observed (small cameras)	% observed (this study)	$\sigma$	K
PE > -4.6	I	ordinary chondrites, asteroids	3700	29	5	13	0.006-0.021	0.46-1.29
-4.6 $\geq$ PE > -5.25	II	carbonaceous chondrites, comets, asteroids	2000	33	39	37	0.002-0.19	0.1-3.09
-5.25 $\geq$ PE > -5.7	IIIa	regular cometary material	750	26	41	13	0.002-0.009	1.93-3.29
PE $\leq$ -5.7	IIIb	soft cometary material	270	9	19	37	0.001-0.06	1.2-4.89

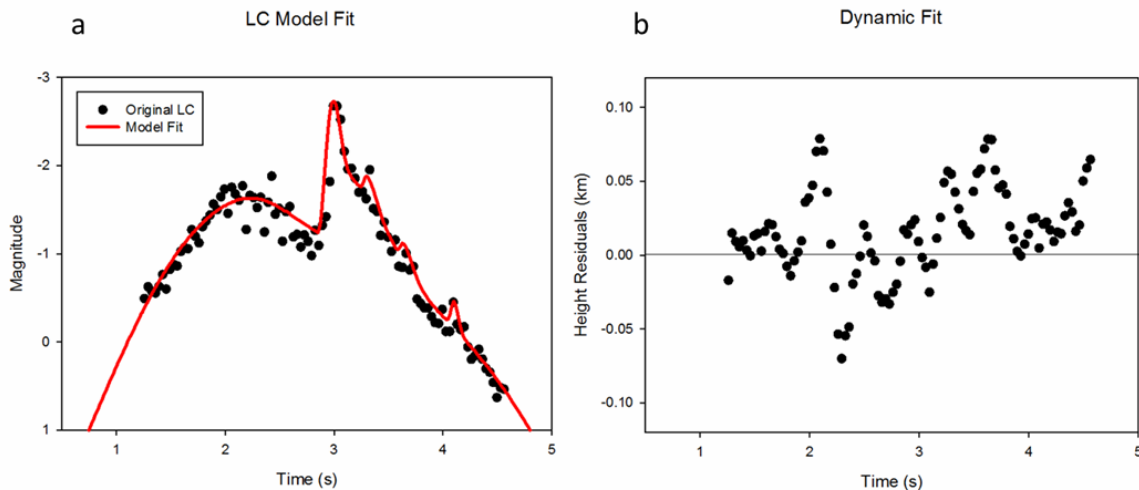


Figure 6.4: The FM model fit to the light curve for a multi-station meteor recorded at 07:05:56 UT on 19 April 2006. The model is matched in both (a) magnitude vs. time and (b) height residuals vs. time (dynamic fit). In this case the FM model provides a best fit of 14.18 km/s initial speed and 20 g mass. Full details can be found in Table 6.3.

Depending on the shape of the light curve (e.g. obvious flares or a smooth light curve), the model is used to implement either a single body approach or discrete fragmentation points. Using the results for 15 bolides obtained by Ceplecha and ReVelle (2005) as a starting reference point, the following parameters were forward modeled until a best fit to the observed light curve as well as magnitude as a function of height and path length were found:  $K$ ,  $\sigma$ , integration altitude, the initial mass, the mass loss at each fragmentation point (if applicable), duration of the flare, interval from the start of the flare until the flare maximum and part of mass fragmented as large fragments. From the model we have the following to match to the meteor: time, path length, altitude, velocity,  $dv/dt$ , mass,  $dm/dt$ , meteor luminosity, meteor magnitude,  $\sigma$ ,  $K$ , luminous efficiency and zenith distance of the radiant. The summary of photometric and dynamic masses, as well as meteoroid types, is given in Table 6.3. While the FM model performs very well in matching the observed light curves, it should be noted that the final solution is representative, but not necessarily unique. For example, if the shape coefficient is increased, then similar output results are found by reducing the initial mass. These differences in initial parameters and their variation at fragmentation points may result in an uncertainty of up to factor of several in the initial mass and therefore affect the mass

loss in a similar fashion as a function of altitude. The ranges of the  $\sigma$  and  $K$  values used for modelling are given in Table 6.3.

In the general case, the energy lost by the meteoroid per unit path length is:

$$\frac{dE}{dL} = \left( \frac{v^2}{2} \frac{dm}{dL} + mv \frac{dv}{dL} \right) \quad (6.16)$$

To determine the blast radius using the dynamics from the FM model, we applied equation (6.16), also accounting for mass loss during fragmentation episodes, or single-body mass at the height corresponding to the shock height.

Table 6.3: A summary of the photometric mass measurements using observed light curves from meteor video records. The columns are as follows (column numbers are in the first row): (1) meteor event date, (2) meteor velocity (km/s) at the onset of ablation, (3) begin height (km), (4) end height (km), (5) instrument corrected peak magnitude ( $M_{\text{HAD}}$ ) from the observed light curve, (6-7) minimum and maximum values of shape coefficient ( $K$ ) (in c.g.s. units), and (8-9) minimum and maximum values of ablation coefficient ( $\sigma$ ) ( $\text{s}^2/\text{km}^2$ ) used in the FM model fitting, (10) estimated meteor mass (g) from equation (6.30), (11) estimated meteor mass (g) using integrated light curve, (12) initial (entry) meteor mass (g) from the FM model, (13) PE coefficient and (14) meteoroid group type.

1	2	3	4	5	6	7	8	9	10	11	12	13	14
	Entry	H	H								FM		
	Velocity	begin	end	Peak					Mass	Mass	Model		
Date	(km/s)	(km)	(km)	Mag	K min	K max	$\sigma$ min	$\sigma$ max	(JVB) (g)	(int) (g)	Mass (g)	PE	Type
20060419	14.2	72.0	47.7	-2.7	0.14	0.53	0.009	0.009	107.4	23.5	20.0	-4.69	II
20060805	28.4	126.4	74.5	-12.8	1.4	2.3	0.002	0.004	5927.6	432.9	74.0	-6.20	IIIB
20061104	67.5	89.9	65.8	-7.2	1.8	4.18	0.002	0.005	459.9	12.5	12.0	-6.39	IIIB
20070125	30.3	119.2	88.5	-5.9	1.99	3.69	0.001	0.004	9.5	2.7	0.9	-5.12	II
20070727	71.2	96.2	70.6	-8.2	0.46	2.68	0.002	0.004	2583.9	91.5	63.0	-6.22	IIIB
20071021	26.3	130.8	81.7	-8.8	2.5	2.5	0.004	0.004	57.5	10.6	4.3	-5.82	IIIB
20080325	75.6	76.2	32.8	-5.9	0.69	0.79	0.015	0.015	2912.0	792.9	917.0	-4.51	I
20080511	23.5	95.2	77.3	-3.8	2.54	2.54	0.06	0.06	85.8	5.2	8.0	-5.90	IIIB
20080812	33.7	105.7	82.0	-1.8	3.29	--	0.009	--	0.2	0.1	0.1	-4.93	II
20081028	13.5	81.2	41.1	-4.1	0.66	0.66	0.014	0.014	309.8	79.6	110.0	-4.40	I
20081102	21.7	96.5	62.6	-7.7	1.73	2.05	0.002	0.002	663.9	53.3	18.0	-5.58	IIIA
20081107	56.2	113.5	81.5	-3.1	1.99	2.59	0.003	0.006	0.4	0.2	0.1	-4.56	I
20090428	24.8	83.5	38.0	-7.2	0.14	1.09	0.003	0.005	3086.5	784.1	330.0	-4.77	II
20090523	15.8	95.9	72.4	-2.0	0.2	0.86	0.042	0.044	2.7	0.7	2.2	-5.10	II
20090812	29.2	108.5	80.4	-6.7	1.29	3.29	0.008	0.01	20.6	3.4	1.8	-5.65	IIIA
20090917	31.1	85.7	72.4	-2.7	3.05	3.05	0.004	0.004	20.7	6.6	8.5	-5.31	IIIA
20100421	70.2	108.5	74.6	-9.3	1.5	1.5	0.005	0.0055	861.5	45.7	17.0	-5.95	IIIB
20100429	18.2	105.7	89.9	-2.6	4.89	4.89	0.014	0.014	0.9	0.2	0.3	-5.79	IIIB
20100530	26.9	96.0	78.3	-0.8	2.19	2.99	0.01	0.012	1.2	0.3	0.3	-5.12	II
20110520	29.5	95.7	84.1	-3.1	2.79	2.99	0.039	0.039	21.3	2.3	2.5	-6.35	IIIB
20110630	58.7	100.5	71.7	-7.8	2.49	2.49	0.003	0.003	527.5	18.0	10.0	-6.05	IIIB
20110808	23.0	86.6	39.9	-9.3	0.99	1.49	0.002	0.002	9990.9	2586.4	1003.0	-4.77	II
20111005	46.2	96.2	64.5	-2.9	1.09	1.59	0.004	0.004	6.8	2.6	20.0	-4.78	II
20111202	46.3	97.0	53.8	-3.1	0.29	0.69	0.008	0.009	18.0	8.8	9.0	-4.06	I

### 6.2.3.3 Top-Down Weak Shock Modelling

To perform the top-down weak shock modelling, we start at the "top" by using the FM model estimates for  $R_0$  in conjunction with the other optically measured parameters for each meteor and calculate the predicted signal period and amplitude at the ground, assuming both weak shock and linear propagation. This provides an independent

comparison between the bottom-up modeling and forms a potential cross-calibration between infrasonically derived energy/mass and the same photometrically estimated quantities.

Figure 6.5 shows the comparison of the blast radius as obtained via FM model versus the blast radius from bottom-up modelling including all four outputs (the period and amplitude in linear and weak shock regimes). In the linear regime, the amplitude-based  $R_0$  from the bottom-up modelling is clearly underestimated compared to the  $R_0$  derived from the FM model. The comparison between the predicted signal period and amplitude using  $R_0$  from the top-down modelling and that observed is shown in Figure 6.6. The predicted signal amplitude is somewhat underestimated in the weak shock regime and markedly overestimated in the linear regime. The predicted signal period, however, shows a near 1:1 agreement with the observed period.

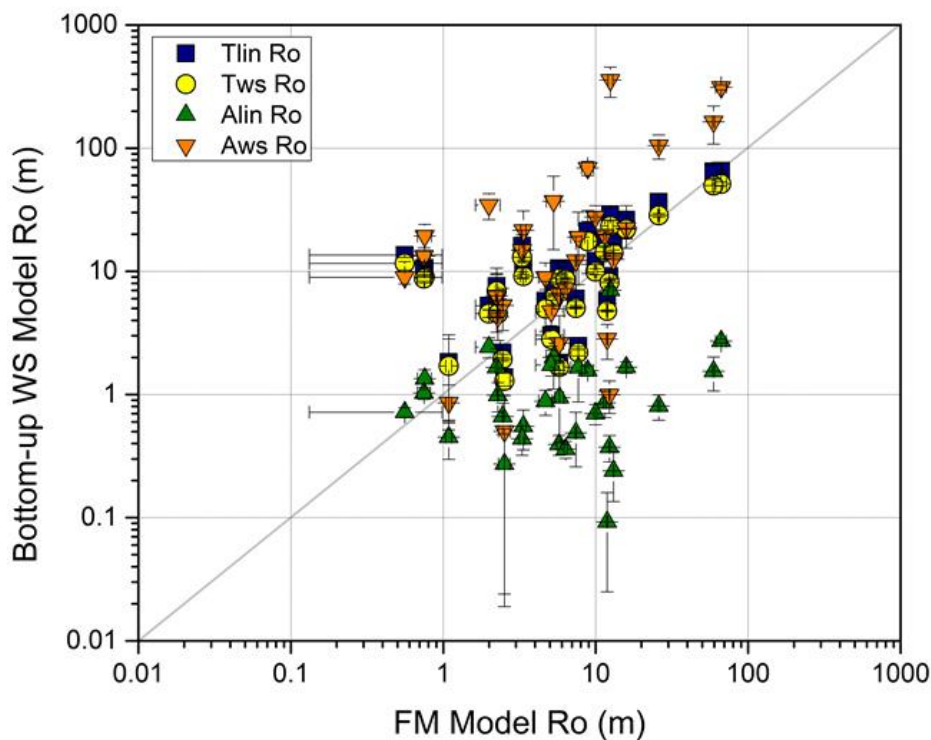


Figure 6.5: The blast radius estimated from bottom-up modelling as compared to blast radii derived from application of the FM model. Tlin and Tws are the period in linear and weak shock regime, respectively. Alin and Aws are the amplitude in linear and weak shock regime, respectively.



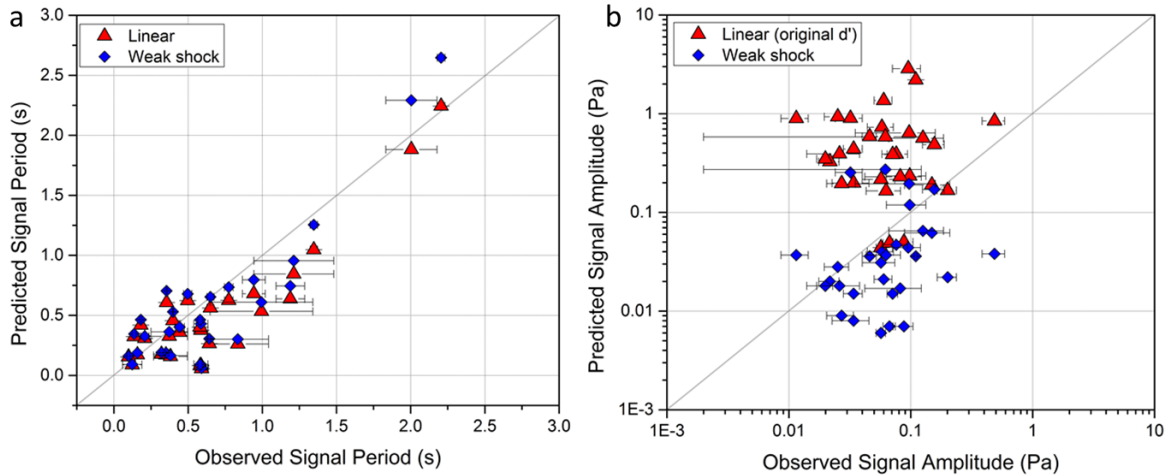


Figure 6.6: (a) Signal period and (b) amplitude obtained by running the top-down weak shock model with input  $R_0$  as derived via FM model.

#### 6.2.4 Infrasonic Mass

From the optical measurements of the meteor and appealing to the fireball classification work of Ceplecha and McCrosky (1976) it is possible to correlate the fireball type with its likely physical properties (i.e. density) (Ceplecha et al., 1998) (Table 6.2) and thus compute an infrasonic mass (Edwards et al., 2008) through  $m = \pi \rho d_m^3 / 6$ , assuming a spherical shape and single body ablation (i.e. no fragmentation) from the bottom-up modelling. Using equation (6.2) and the relationship between the meteoroid density and diameter, infrasonic mass ( $m_{infrac}$ ) is then given by:

$$m_{infrac} = \frac{\pi \rho}{6} \left( \frac{R_0}{M} \right)^3 \quad (6.17)$$

Considering that the bottom-up modelling yields four values of blast radii as described in section 6.2.2, there are four resultant infrasonic masses. These are compared to photometric masses derived through the FM model (Figure 6.7). The infrasonic masses derived from the period-based  $R_0$  are in better agreement with the photometric masses than are the infrasonic masses derived from the amplitude-based  $R_0$  in either regime.

Drawing upon equation (6.1), meteoroid energy can be derived from  $R_0$  (bottom-up and top-down) without needing to make any assumption about single body (Figure 6.8).

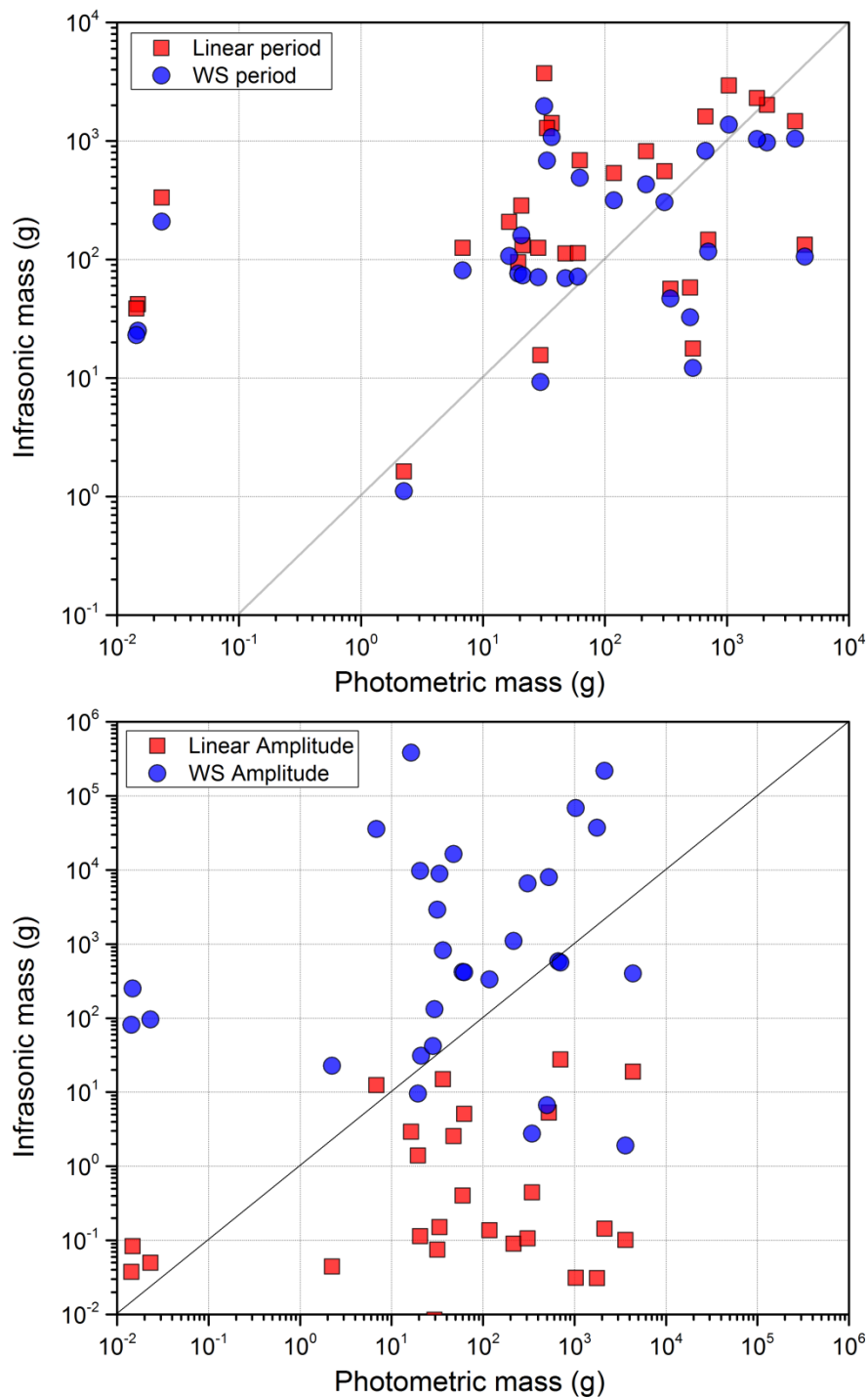


Figure 6.7: The comparison of the infrasonic and photometrically derived masses. The abscissa in both panels represents the equivalent photometric mass derived from the FM model blast radius and equation (6.17). The infrasonic masses derived from the amplitude-based (top panel) and period-based (bottom panel) blast radius in the linear and weak shock regimes are shown. The grey line is the 1:1 line in all plots.

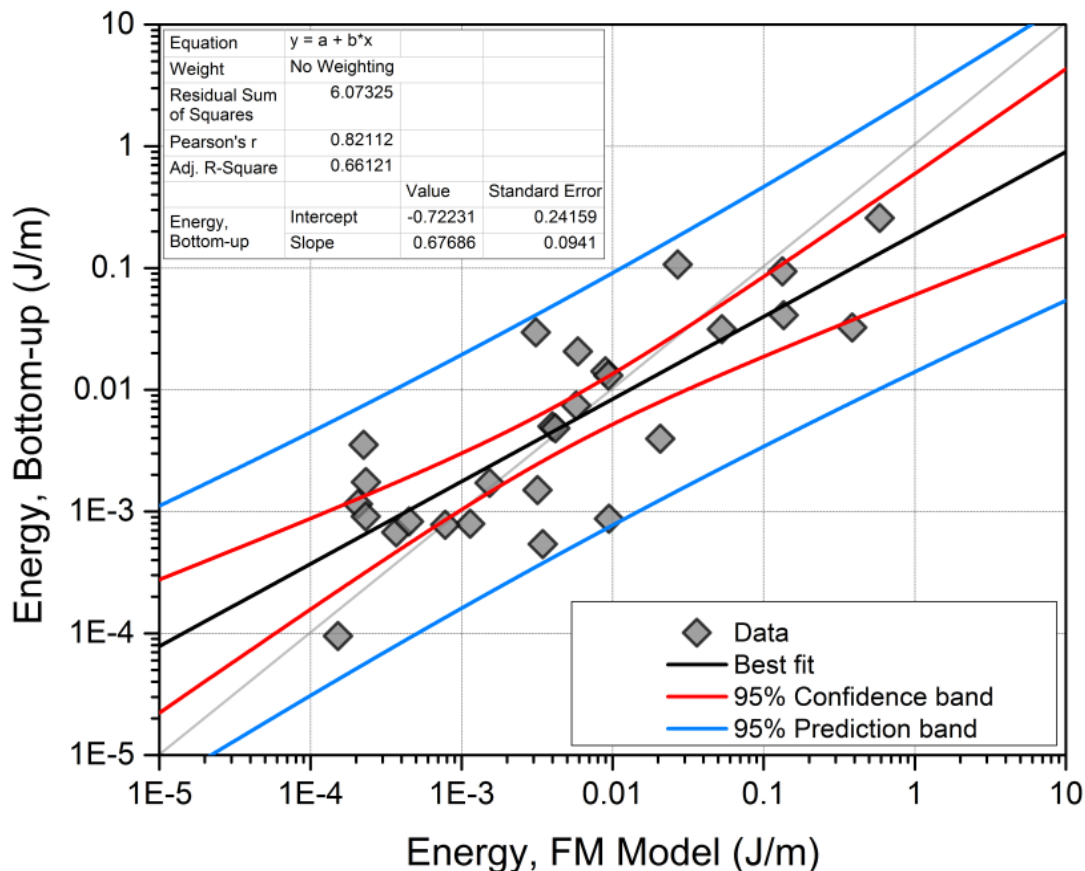


Figure 6.8: Energy per unit path length comparison between the bottom-up modelling, where  $R_0$  is determined entirely from the infrasound signal properties at the ground, and the FM model. The grey line is the 1:1 line.

### 6.3 Discussion

The linear amplitude-derived  $R_0$  was on average 12% larger when the Sutherland and Bass (2004) coefficients were applied. To put this in perspective, the range of  $R_0$  from matching the amplitude in the linear regime was from 0.15 m to 7.4 m with the Sutherland and Bass (2004) coefficients and from 0.09 m to 7 m using the classical coefficients (ReVelle, 1974). The most significant difference was found for signals with a dominant frequency  $> 12$  Hz (at the weak shock to linear regime transition altitude point). However, even in this case, the difference is still within the uncertainty bounds in  $R_0$  fits.

ReVelle (1974) suggested that the lower threshold for the blast radius of meteors generating infrasound, which should be detectable at the ground, should be in the range

of  $\sim 5$  m. Having well constrained observational data, we derive the blast radii between 1.1 m and 51 m from our best fit bottom-up weak shock modelling and 0.4 – 41 m from the top-down FM model. A smaller blast radius is typically associated with lower source altitudes ( $< 80$  km). This suggests that the original ReVelle (1974) estimate may well be too high by a factor of almost ten.

The dominant signal period is more robust than signal amplitude when estimating meteoroid energy deposition, as it is less susceptible to adverse propagation effects in the atmosphere (ReVelle, 1974; Edwards et al., 2008; Ens et al., 2012). The dominant signal period is proportional to the blast radius, and therefore energy deposition by a meteoroid (mass and velocity) and the shock altitude. We remark that the signal period undergoes very small overall changes during propagation as it changes slowly in the weak shock regime (e.g. equation (6.5), Figure 6.1) and remains constant once it transitions to the linear regime. Therefore, the weak shock period is closer to the fundamental period at the source and expected to be a more robust indicator of the initial blast radius and hence energy of the event.

In contrast, the signal amplitude is generally more susceptible to a myriad of changes during propagation. The effects of non-linearity and wave steepening, as well as the assumed transition point from weak shock to a linear regime of propagation, are poorly constrained for meteors. Indeed, accurately predicting signal amplitudes for high altitude infrasonic sources (e.g. meteors), especially in the linear regime has been recognized as a long standing problem (e.g. ReVelle, 1974; 1976; Edwards et al., 2008). Edwards et al. (2008) noted the significant differences in predicted amplitude for simultaneously observed optical-infrasound meteors, especially that in the linear regime, and determined that meteor infrasound reaches the ground predominately as a weak shock. While a similar empirical deduction can be made from Figure 6.3 in our study, this does not physically explain the discrepancy.

As shown earlier through top-down modeling, we expect the period-estimated blast radius in either regime to be relatively close to true values, as the observed period is much less modified during propagation compared to the amplitude. With this in mind, it becomes evident that the transition altitude is a major controlling factor in the linear

amplitude predictions. We observe that the consistently smaller amplitude-based blast radius in the linear regime originates from the fact that depending on the transition altitude, the amplitude grows in the linear regime as a result of the change in ambient pressure. This leads to two questions: (i) is it possible to find the distortion distance and therefore a transition height which would predict both the period and amplitude such that the observed quantities are matched? (ii) given enough adjustment in the distortion distance, would any wave eventually transition to the linear regime?

We investigated the effect of the transition altitude by varying the distortion distance. The distortion distance was originally defined as the distance a wave would have to travel before distorting by 10% (Towne, 1967). The original definition of the distortion distance (Towne, 1967) is:

$$d' = \frac{\lambda}{20(\gamma + 1)S_m} = \frac{c\tau}{34.3 \left(\frac{\Delta p}{p}\right)} \quad (6.18)$$

where  $\lambda$  is the wavelength,  $S_m$  is the overdensity ratio ( $\Delta\rho/\rho_0$ ),  $c$  is the adiabatic speed of sound and  $\Delta p/p$  is the overpressure. The distortion distance is a constant number of wavelengths for waves of different frequency (Towne, 1967). There are two major assumptions in equation (6.18): (i) the wave is initially sinusoidal, (ii)  $S_m$  is small but not negligible. An intense sound wave ( $S_m = 10^{-4}$ ) would therefore distort by 10% within 200 wavelengths (Towne, 1967; Cotten et al., 1971).

By varying the constant in the denominator in the right hand side of equation (6.18) to reflect an ‘adjustable’ distortion distance factor and by using the weak shock period-determined  $R_0$  value as an input, a series of bottom-up modelling runs were performed. These were aimed at finding simultaneously both the predicted linear regime amplitude and the period which would match the observed quantities within their measurement uncertainty (Figure 6.9). Physically, this corresponds to adopting a series of different distortion distance definitions (rather than using the original distance with 10% distortion remaining assumption) with the goal of matching the signal properties and deriving the new set of bottom-up  $R_0$ . Henceforth, these new blast radii are referred to as the best fit  $R_0$ . The outcome of this investigation was:

- It was possible to find the converging amplitude-period solution in the linear regime for the majority of arrivals (22/24). Three fits are as much as 20% beyond the measurement uncertainty bounds for amplitude, while all others are within the measurement uncertainty bounds for both period and amplitude.
- When varying the constant in equation (6.18), the resultant distortion distance percentage is well below 6%. The distribution is shown in Figure 6.9(d). Moreover, it is not possible to define a set percentage that would be applicable to all events. Some of these values may in fact not be realistic or feasible - we are assuming that the entire cause of the difference in the linear amplitude vs. period is due to the definition of the distortion distance, an assumption probably not fully correct.
- Smaller distortion distance leads to lower transition altitudes (Table 6.4). Half of the arrivals (12/24) had their transition height below 5 km. The maximum transition altitude was 25 km, with the mean altitude of 9 km; this means that no weak shock wave can be approximated as transitioning to a linear acoustic wave prior to reaching this height within the context of the original ReVelle (1974) model and still produce physically reasonable amplitude estimates. With the original definition for  $d'$ , the transition altitudes for our data were as high as 56 km, with a mean of 33 km. Cotten et al. (1971) examined propagation of shock waves generated by Apollo rockets and noted that a wave would not be expected to be acoustic above the altitude of 35-40 km at the large blast radii characteristic of those vehicles.
- Regardless of the extent of adjustment to the distortion distance, within the context of the ReVelle (1974) model, self-consistent amplitudes and periods are not possible unless some weak shock waves are assumed to never transition to linear waves. – i.e. even using a 0% distortion in our data set, two arrivals had no transition at all. However, these two arrivals also had a poor fit overall for any distortion distance.
- The lower transition altitude also implies that the difference between the classical and Sutherland and Bass (2004) absorption coefficients is negligible in the frequency range of our events.

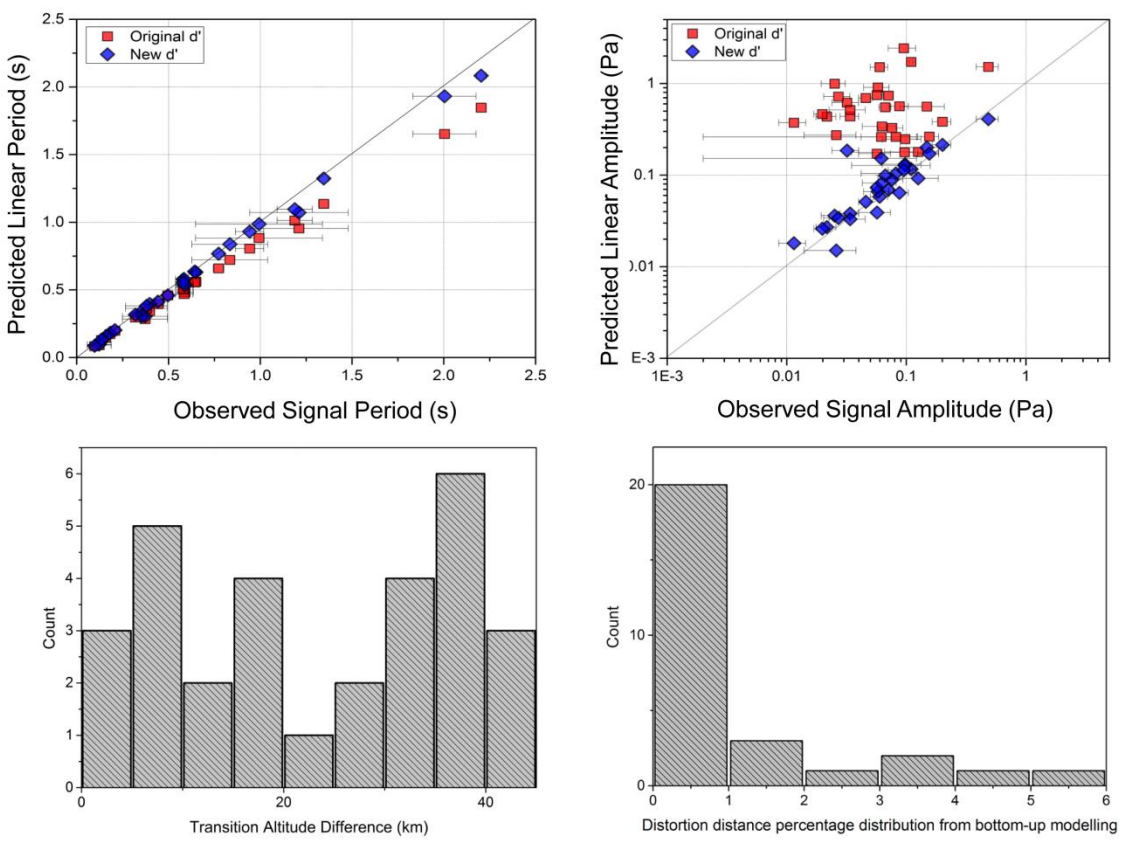


Figure 6.9: The best fit  $R_0$  from bottom-up modelling predictions for amplitude and period vs observed using (a) linear period and (b) linear amplitude. The square data points represent model output for the original definition for the distortion distance (Towne, 1967), while the diamonds represent the new values. The solid gray line is the 1:1 fit. (c) Distribution of transition altitudes for the original and new distortion distance. (d) Distribution of the transition altitude difference ( $\Delta H_{\text{transition}}$ ) between the original and new distortion distance percentage values that were used to find the optimal  $R_0$  fit; note original definition was 10%.

Table 6.4: A summary of  $R_0$  as derived from the FM model. The associated outputs from top-down modelling are also shown. The two entries in the Taltitude, which is the transition height, in the “New d’” section denote events that never transition to the linear regime. Therefore, the original definition for d’ was used by default.

Date	Ro		Original d' [Towne, 1967]					New d'				
			Tlin	Tws	Alin	Aws	Taltitude	Tlin	Tws	Alin	Aws	Taltitude
20060419	1.09	0.05	0.09	0.09	0.234	0.119	10.0	0.09	0.09	0.125	0.119	1.1
20061104	2.45	0.01	0.17	0.19	0.216	0.031	25.4	0.18	0.19	0.048	0.031	7.1
20070125	25.95	0.36	1.05	1.26	1.363	0.021	55.0	1.22	1.26	0.053	0.021	12.8
20070727	11.48	0.21	0.68	0.80	0.731	0.04	38.4	0.79	0.80	0.054	0.04	5.0
20071021	66.66	5.36	2.24	2.65	2.202	0.036	54.5	2.53	2.65	0.148	0.036	19.3
20080325	5.79	0.39	0.32	0.35	0.639	0.195	16.1	0.33	0.35	0.452	0.195	12.0
20081028	2.52	0.22	0.15	0.16	0.582	0.272	10.9	0.16	0.16	0.317	0.272	2.6
20081102	5.30	0.55	0.36	0.40	0.23	0.017	33.2	0.38	0.40	0.091	0.017	22.2
20081107	0.56	0.43	0.06	0.06	0.044	0.006	25.8	0.06	0.06	0.007	0.006	1.3
20090523	1.99	0.36	0.17	0.19	0.167	0.022	26.5	0.18	0.19	0.094	0.022	19.5
20090917	4.68	0.47	0.33	0.36	0.39	0.047	27.8	0.35	0.36	0.105	0.047	11.9
20100421	15.88	0.07	0.85	0.96	0.587	0.036	36.2	0.95	0.96	0.044	0.036	3.5
20100429	8.87	0.79	0.53	0.61	0.387	0.015	42.5	0.59	0.61	0.037	0.015	12.7
20110520	9.97	0.20	0.56	0.65	0.439	0.015	42.0	0.63	0.65	0.038	0.015	11.9
20110630	7.42	0.05	0.46	0.53	0.392	0.018	40.6	0.53	0.53	0.021	0.018	2.4
20110808	12.32	0.06	0.62	0.68	0.9	0.254	17.2	0.62	0.68	0.9	0.254	17.2*
20111005	7.69	0.82	0.42	0.46	0.565	0.065	28.3	0.44	0.46	0.285	0.065	20.0
20111202	2.24	0.04	0.16	0.17	0.19	0.062	15.4	0.16	0.17	0.075	0.062	3.4
20060805	12.50	0.44	0.64	0.75	0.844	0.038	41.2	0.69	0.75	0.228	0.038	23.9
20060805	59.42	0.76	1.88	2.29	2.861	0.044	56.5	2.20	2.29	0.132	0.044	15.4
20080511	13.10	0.03	0.63	0.74	0.932	0.028	46.9	0.73	0.74	0.034	0.028	3.7
20080511	11.90	0.10	0.61	0.70	0.895	0.037	42.0	0.61	0.70	0.895	0.037	42.0*
20080812	5.75	0.19	0.38	0.43	0.326	0.02	37.0	0.43	0.43	0.021	0.02	1.4
20080812	6.34	0.15	0.40	0.46	0.348	0.018	39.1	0.46	0.46	0.02	0.018	2.2
20090428	5.11	1.08	0.31	0.33	0.486	0.171	14.6	0.32	0.33	0.306	0.171	8.7
20090428	2.28	0.01	0.18	0.19	0.165	0.037	20.2	0.19	0.19	0.043	0.037	2.8
20090812	0.76	0.08	0.08	0.09	0.05	0.007	26.7	0.09	0.09	0.008	0.007	2.6
20090812	0.75	0.07	0.08	0.09	0.049	0.007	26.6	0.09	0.09	0.011	0.007	7.6
20100530	3.35	0.13	0.26	0.31	0.198	0.008	41.8	0.30	0.31	0.014	0.008	7.7
20100530	3.29	0.14	0.26	0.30	0.196	0.009	41.1	0.30	0.30	0.011	0.009	3.6

We compared the infrasonic masses from the best fit  $R_0$  to the photometric masses (Figure 6.10(a)) and found a much better agreement (on average to within order of magnitude) than that resulting from the comparison between photometric and the infrasonic masses from  $R_0$  using the original definition of distortion distance.

The mass from the FM model  $R_0$  should not exceed the mass used as the model input; however, the contrary can be observed (Figure 6.10(b)). For a single spherical body and no fragmentation and/or significant ablation, the blast radius can be estimated via equation (6.2). However, if there is fragmentation and/or significant ablation, then the



contributions from the particles/fragments falling off the main body may alter the blast radius (Figure 6.11) such that there is an over-prediction of the meteoroid mass.

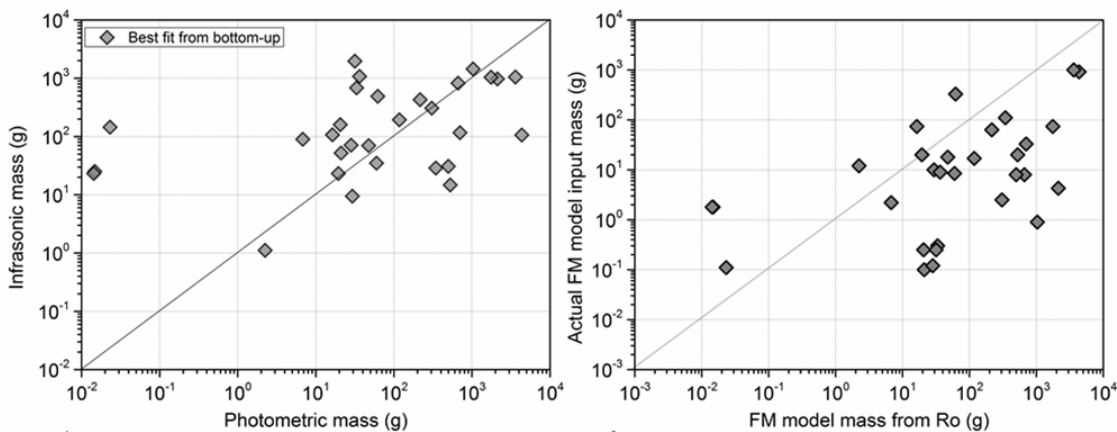


Figure 6.10: The comparison of the infrasonic and photometrically derived masses. (a) Infrasonic mass from the best fit  $R_0$ . The three points on the far left are from the two events, which were poorly constrained in terms of the transition height and distortion distance. The abscissa represents the equivalent photometric mass derived from the FM model blast radius and equation (6.17); (b) The comparison between the FM model input mass and the mass derived from the blast radius as per equation (6.17). The grey line is the 1:1 line in all plots.

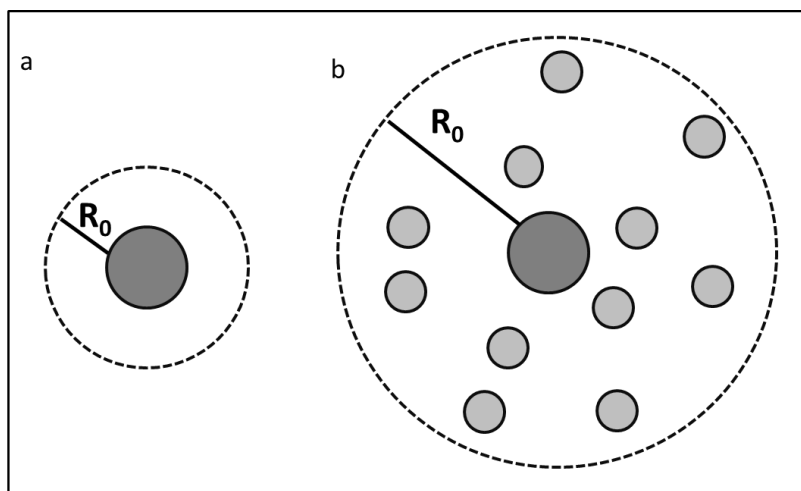


Figure 6.11: Blast radius produced by a single spherically shaped body. (b) Blast radius produced during fragmentation or significant ablation.

Therefore, in such instances, the blast radius, while a good measure of energy deposition by the meteoroid ( $R_0 \sim (dE/dL)^{1/2}$ ), is not a reliable means of obtaining the meteoroid mass. Recall from section 6.1.2 that there are several crucial assumptions in the weak shock model: (i) the meteoroid is a spherically shaped single body, (ii) there is no fragmentation, and (iii) there is no significant deceleration and strong ablation. ReVelle (2010) suggested that  $R_0$  from a fragmenting bolide may be as much as 5-20 times larger (depending on height) than a non-fragmenting blast radius. Our study shows that strong ablation is indeed an important effect, even for centimeter sized meteoroids. In fact, this contribution is up to a factor of 10 and on average a factor of 3. Therefore, use of the  $R_0 = Md_m$  is not valid in most cases. The blast radius estimated from purely energy-based (optical) considerations appears to be more robust.

Having done bottom-up and top down analysis, and blast radius and mass comparisons, it is evident that without having some information about the source function (i.e. measurements from video observations) the signal amplitude exhibits too much scatter to be utilized in empirical blast radius estimates. Although the dominant signal period may undergo variations due to competing processes of distortion and dispersion (ReVelle, 1974), this study demonstrates that the dominant signal period is much closer to ‘true’ values of  $R_0$  (e.g. Figures 6.5 and 6.6(a)).

In Figure 6.12 we show best fit  $R_0$  derived through the bottom-up modelling. For the centimeter-sized meteoroids we may estimate an empirical period- $R_0$  relation for the blast radius from these bottom-up values. We have divided the final fits into two distinct blast radius prediction populations: the short period ( $\tau_{obs} \leq 0.7s$ ) and the long period ( $\tau_{obs} > 0.7s$ ) based on the source altitudes. The short period population, predicting  $R_0 \leq 10$  m, is confined to the shock source altitudes between 53 km and 95 km. The long period population, predicting  $R_0 > 10$  m, is associated with the shock source altitudes extending above 85 km. For short period population, the bottom-up based blast radius can be estimated within 1.5 meters, and for long periods within ~5 m, although the number statistics for the latter is small. We suspect much of the uncertainty at larger periods reflects the greater role fragmentation may play for larger meteoroids. The overlap altitude (85 – 95 km) between these two populations occurs at the mesopause and near

the transitional slip-flow regime for meteoroids  $\sim 1$  centimetre in diameter (Campbell-Brown and Koschny, 2004), suggesting that the weak shock model may not be correctly predicting  $R_0$  in the free molecular flow regime.

For completeness, we also fitted the  $R_0$  calculated from the FM model. Recall that the FM based  $R_0$  is derived from the energy deposition determined by fitting optical measurements to the entry model. The FM based  $R_0$  has much more scatter, thus resulting in the blast radius estimate uncertainty of up to 17 m.

The empirical relations for the blast radius derived from the bottom-up approach are:

$$R_0 = 15.4231 \tau - 0.5294 \quad (\tau_{obs} \leq 0.7s) \quad (6.19a)$$

$$R_0 = 29.14597 \tau - 11.5811 \quad (\tau_{obs} > 0.7s) \quad (6.19b)$$

Even though there are a number of simplifications and assumptions in the weak shock model, in its new modified form it offers a reasonable initial estimate for the blast radius as a function of observed signal period, and therefore energy deposition for small regional meteoroids, without making any assumptions about the fragmentation process. Consequently, this methodology could be extended to high altitude explosive sources in the atmosphere. The applicability of the weak shock model can also be further investigated and extended to spherical shocks, especially if observational data can be used in a similar fashion as in this study.

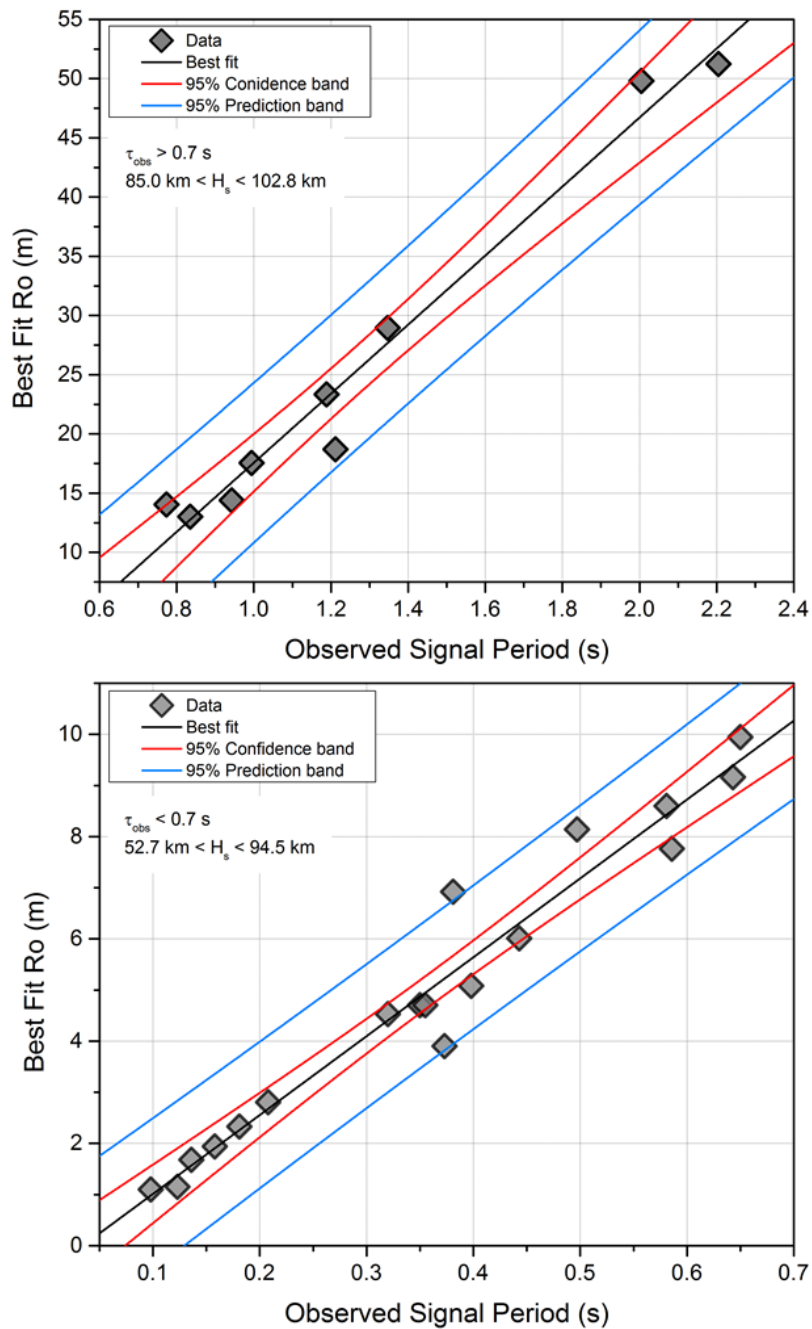


Figure 6.12: Blast radius from best fit bottom-up modelling versus observed signal for (a) the short signal period ( $\tau_{\text{obs}} \leq 0.7 \text{ s}$ ) and (b) the long signal period ( $\tau_{\text{obs}} > 0.7 \text{ s}$ ) populations.  $H_s$  is the shock source height as derived from raytracing (Silber and Brown, 2014).

## 6.4 Conclusions

In this paper we extend the study of Silber and Brown (2014, in review) to critically investigate the analytic blast wave model of the nonlinear disturbance initiated by an explosive line source as an analog for a meteor shock as developed by ReVelle (1974). We applied the updated ReVelle (1974) model to 24 of the best constrained simultaneously optical and infrasound detected regional meteors to critically examine the weak shock model. Here we summarize our main conclusions:

- i. We analyzed the weak shock model behavior using a synthetic meteor, and performed the sensitivity analysis on a set of meteor events from our data set to examine the effect of the winds, perturbed wind fields due to gravity waves, and Doppler shift. The overall effect of these factors on the initial value of the blast radius is relatively small (<10%) for regional meteor events.
- ii. We performed bottom-up modelling using the ReVelle (1974; 1976) approach to determine the blast radius required to predict both the signal amplitude and period at the ground such that it matches that observed by the receiver within uncertainty. While the period-based  $R_0$  appears to have realistic values, the amplitude-based  $R_0$  exhibits large systematic deviations in the linear and weak shock regimes, as well as large deviations when compared to the period-based blast radius. The amplitude-based  $R_0$  estimate severely under-predicts the observed amplitude in the linear regime, and overestimates it in the weak shock regime.
- iii. Drawing upon the results from (ii), we varied the distortion distance to examine its effect on the weak shock to linear transition altitude. We empirically established that to match the observed amplitude of the meteor infrasound at the ground within the context of the ReVelle (1974) model, the distortion distance for our dataset must always be less than six percent, contrary to the proposed fixed 10 percent (Towne, 1967). The choice of definition of the distortion distance has a strong effect on the predicted linear amplitude. We established the ‘best fit’ linear regime  $R_0$  which matched both amplitude and period within their respective measurement uncertainties. No one definition of modified distortion distance

worked for all events, but we found acceptable fits when the distortion distance was assumed to be of an order half or less than the original ReVelle (1974) adopted value.

- iv. We applied the FM entry model (Ceplecha and ReVelle, 2005) to photometric data as measured from video observations of meteor events to independently calculate the blast radius using the fundamental definition for  $R_0$  in terms of energy deposition per path length derived from the FM model. This blast radius was used as an input for top-down modelling to determine the predicted signal amplitude and period in both weak shock and linear regimes. Both the predicted period and amplitude as obtained from the best fit  $R_0$  are nearly 1:1. This validates the basic definition of blast radius and its fundamental linkage to energy deposition during the hypervelocity meteor entry.
- v. The infrasonic mass estimate is systematically larger than the mass estimated from FM modeling and is not a reliable predictor of the true meteoroid mass using any set of assumptions which we interpret as being mainly due to the ubiquitous presence of fragmentation during ablation of centimeter-sized meteoroids. The fragmentation tends to artificially increase the equivalent single-body mass, making infrasonically determined mass less reliable for larger events.
- vi. We derived new empirical relations which link the observed dominant signal period to the meteoroid blast radius:  $R_0 = 15.4231 \tau - 0.5294$  ( $\tau_{obs} \leq 0.7s$ ) and  $R_0 = 29.14597 \tau - 11.5811$  ( $\tau_{obs} > 0.7s$ ). The blast radius can be estimated to within 15 percent.

Even though the premise of the ReVelle (1974) weak shock model is to require some knowledge about the source *a priori* to be able to predict the signal amplitude and the period at receiver located at the ground, we have obtained an empirical relation which can be used to estimate the source blast radius for centimeter-sized bright fireballs, regardless of the meteoroid's velocity, entry angle and other parameters which are generally difficult to determine without video observations. In conclusion, the weak shock model of meteor infrasound production (ReVelle, 1974) in its analytical form offers a good first order estimate in determining the blast radius and therefore energy

deposition by small meteoroids, particularly if period alone is used or if no fragmentation is present.

## **Acknowledgements**

The authors would like to thank: J. Borovička, P Spurny and Z. Ceplecha for kindly providing trajectory solution software and the FM model code. EAS thanks: CTBTO Young Scientist Award (through European Union Council Decision 2010/461/CFSP IV) for funding part of this project; L. Sutherland for generously providing worked out atmospheric absorption coefficients; R. Weryk for assistance with the synthetic photometry and all-sky camera development; J. Gill for setting up the parallel processing machine; the British Atmospheric Data Centre for providing UKMO Assimilated atmospheric data set. PGB thanks the Natural Sciences and Engineering Research Council of Canada, the Canada Research Program and NASA cooperative agreement NNX11AB76A for funding this work.

## References

- Andrews, D. G. (2010) An introduction to atmospheric physics. Cambridge University Press, ISBN: 0521693187.
- Arrowsmith, S. J., ReVelle, D., Edwards, W., & Brown, P. (2008) Global detection of infrasonic signals from three large bolides. *Earth, Moon, and Planets*, 102(1-4), 357-363, doi: 10.1007/978-0-387-78419-9\_50.
- Baggaley, W. J. (2002) Radar observations, in: Murad, E., and Williams, I. P. (Eds.) *Meteors in the Earth's Atmosphere: Meteoroids and Cosmic Dust and Their Interactions with the Earth's Upper Atmosphere*, Cambridge University Press, 123–148, doi: 10.1029/1999JA900383.
- Bedard, A., Georges, T. (2000) Atmospheric infrasound, *Acoustics Australia*, 28(2), 47-52, doi: 10.1063/1.883019.
- Boyd, I. D. (1998) Computation of atmospheric entry flow about a Leonid meteoroid. *Earth, Moon, and Planets*, 82, 93-108, doi: 10.1023/A:1017042404484.
- Bronsthen, V.A. (1983) *Physics of Meteoric Phenomena*, 372 pp., D. Reidel, Dordrecht, Netherlands, ISBN: 978-94-009-7222-3.
- Brown, P. G., Assink, J. D., Astiz, L., Blaauw, R., Boslough, M. B., Borovička, J., and 26 co-authors (2013) A 500-kiloton airburst over Chelyabinsk and an enhanced hazard from small impactors, *Nature*, 503, 238-241, doi: 10.1038/nature12741.
- Brown, P., ReVelle, D. O., Silber, E. A., Edwards, W. N., Arrowsmith, S., Jackson, L. E., Tancredi, G., Eaton, D. (2008) Analysis of a crater-forming meteorite impact in Peru. *Journal of Geophysical Research: Planets* (1991–2012), 113(E9), doi: 10.1029/2008JE003105.
- Brown, P.G., Edwards, W.N., ReVelle, D.O., Spurny, P. (2007) Acoustic analysis of shock production by very high-altitude meteors – I: infrasonic observations, dynamics and luminosity, *Journal of Atmospheric and Solar-Terrestrial Physics*, 69: 600–620, doi: 10.1016/j.jastp.2006.10.011.
- Burke, D. L., Axelrod, T., Blondin, S., Claver, C., Ivezić, Ž., Jones, L., Jones, L., Saha, A., Smith, A., Smith, R. C., Stubbs, C. W. (2010) Precision determination of atmospheric extinction at optical and near-infrared wavelengths. *The Astrophysical Journal*, 720(1), 811, doi:10.1088/0004-637X/720/1/811.
- Campbell-Brown, M. D., Koschny, D. (2004) Model of the ablation of faint meteors. *Astronomy and Astrophysics-Berlin Then Les Ulis*, 418(2), 751-758, doi: 10.1051/0004-6361:20041001-1.



- Carlson, H. W., Maglieri, D. J. (1972) Review of Sonic-Boom Generation Theory and Prediction Methods, *The Journal of the Acoustical Society of America*, 51, 675, doi: 10.1121/1.1912901.
- Cepplecha, Z., and R. E. McCrosky. (1976) Fireball end heights: A diagnostic for the structure of meteoric material. *Journal of Geophysical Research*, 81(35), 6257-6275, doi: 10.1029/JB081i035p06257.
- Cepplecha, Z., and Revelle, D. O. (2005) Fragmentation model of meteoroid motion, mass loss, and radiation in the atmosphere, *Meteoritics & Planetary Science*, 40(1), 35-54, doi: 10.1111/j.1945-5100.2005.tb00363.x.
- Cepplecha, Z., Borovička, J., Elford, W. G., ReVelle, D. O., Hawkes, R. L., Porubčan, V., and Šimek, M. (1998) Meteor phenomena and bodies, *Space Science Reviews*, 84(3-4), 327-471, doi: 10.1023/A:1005069928850.
- Christie, D. R. Campus, P. (2010) The IMS Infrasound Network: Design and Establishment of Infrasound Stations, In: A. Le Pichon, E. Blanc and A. Hauchecorne, Eds., *Infrasound Monitoring for Atmospheric Studies*, Springer, New York, pp. 29-75, doi: 10.1007/978-1-4020-9508-5\_2.
- Chyba, C. F., Thomas, P. J., Zahnle, K. J. (1993) The 1908 Tunguska explosion: atmospheric disruption of a stony asteroid. *Nature*, 361(6407), 40-44, doi: 10.1038/361040a0.
- Cook, R.K. and A.J. Bedard Jr (1972) On the measurement of Infrasound, *Q. J. Roy. Astro. Soc.* 67, pp 5-11, doi: 10.1038/361040a0.
- Cotten, D. E., Donn, W. L., and Oppenheim, A. (1971) On the generation and propagation of shock waves from Apollo rockets at orbital altitudes, *Geophysical Journal of the Royal Astronomical Society*, 26(1-4), 149-159, doi: 10.1111/j.1365-246X.1971.tb03388.x.
- DuMond, J. W., Cohen, E. R., Panofsky, W. K. H., Deeds, E. (1946). A determination of the wave forms and laws of propagation and dissipation of ballistic shock waves. *The Journal of the Acoustical Society of America*. 18, 97, doi: 10.1121/1.1916347.
- Edwards, W. N. (2010) Meteor generated infrasound: theory and observation. In *Infrasound monitoring for atmospheric studies* (pp. 361-414). Springer Netherlands, doi: 10.1007/978-1-4020-9508-5\_12
- Edwards, W. N., Brown, P. G., Weryk, R. J., ReVelle, D. O. (2008) Infrasonic observations of meteoroids: Preliminary results from a coordinated optical-radar-infrasound observing campaign, *Earth, Moon, and Planets*. 102(1-4), 221-229, doi: 10.1007/s11038-007-9154-6.

- Ens, T. A., Brown, P. G., Edwards, W. N., Silber, E. A. (2012) Infrasound production by bolides: A global statistical study, *Journal of Atmospheric and Solar-Terrestrial Physics*, 80, 208-229, doi: 10.1016/j.jastp.2012.01.018.
- Evans, L. B., Sutherland, L. C. (1971) Absorption of Sound in Air. *The Journal of the Acoustical Society of America*, 49(1A), 110-110, doi: 10.1121/1.1975615.
- Evers, L.G. H.W. Haak. (2001) Listening to sounds from an exploding meteor and oceanic waves, *Geophysical Research Letters*, 30: 41-44, doi: 10.1029/2000GL011859.
- Few, A. A. (1969) Power spectrum of thunder, *J. Geophys. Res.*, 74, 6926-6934, doi: 10.1029/JC074i028p06926.
- Garcés, M., Le Pichon, A. (2009) Infrasound from Earthquakes, Tsunamis and Volcanoes, In: R. A. Meyers, Ed., *Encyclopedia of Complexity and Systems Science*, Springer, Berlin, pp. 663-679, doi: 10.1007/978-0-387-30440-3\_286.
- Hawkes R. L. (2002) Detection and analysis procedures for visual, photographic and image intensified CCD meteor observations. In *Meteors in the Earth's Atmosphere*, edited by Murad E., and Williams I. Cambridge Univ Press, pp. 97–122, ISBN: 0521804310.
- Haynes, C. P., Millet, C. (2013) A sensitivity analysis of meteoric infrasound, *Journal of Geophysical Research: Planets*, 118(10), 2073-2082, doi: 10.1002/jgre.20116.
- Hedlin, M.A., Garcés, M., Bass, H., Hayward, C., Herrin, G., Olson, J., Wilson, C. (2002) Listening to the secret sounds of earth's atmosphere, *Eos* 83, 557, 564-565, doi: 10.1029/2002EO000383.
- Hunt, J. N., Palmer, R., and Penney, W. (1960) Atmospheric waves caused by large explosions. *Philosophical Transactions of the Royal Society of London, Series A, Mathematical and Physical Sciences*, 252(1011), 275-315, doi: 10.1098/rsta.1960.0007.
- Jacchia, L., Verniani, F., and Briggs, R. E. (1967) An analysis of the atmospheric trajectories of 413 precisely reduced photographic meteors, *Smithsonian Contributions to Astrophysics*, 10, 1-139.
- Jones, D. L., Goyer, G. G., Plooster, M. N. (1968) Shock wave from a lightning discharge. *J Geophys Res*, 73, 3121–3127, doi: 10.1029/JB073i010p03121.
- Kraemer, D.R. (1977) *Infrasound from accurately measured meteor trails*, Ph.D. Thesis Michigan Univ., Ann Arbor, MI, USA.
- Kulichkov, S. N. (2004) Long-range propagation and scattering of low-frequency sound pulses in the middle atmosphere, *Meteorology and Atmospheric Physics*, 85(1-3), 47-60, doi: 10.1007/s00703-003-0033-z.

- Levison, H. F. (1996) Comet taxonomy, in *Completing the Inventory of the Solar System*, Astronomical Society of the Pacific Conference Proceedings, T.W. Rettig and J.M. Hahn, Eds., Vol. 107, pp. 173-191.
- Lin, S. C. (1954) Cylindrical shock waves produced by instantaneous energy release, *J Appl Phys*, 25, 54–57, doi: 10.1063/1.1721520.
- Maglieri, D. J., Plotkin, K. J. (1991) Sonic boom, In *Aeroacoustics of Flight Vehicles: Theory and Practice, Volume 1: Noise Sources*, Vol. 1, pp. 519-561
- McKinley, D. W. R. (1961) *Meteor Science and Engineering*, McGraw-Hill Inc., New York, NY, USA
- Morse P. M., Ingard K. U. (1968) *Theoretical Acoustics*, McGraw-Hill, New York, ISBN: 0691024014.
- Mutschlecner, J. P., Whitaker, R. W. (2010) Some atmospheric effects on infrasound signal amplitudes. In *Infrasound Monitoring for Atmospheric Studies*, pp. 455-474, Springer Netherlands, doi: 10.1007/978-1-4020-9508-5\_14.
- Officer, C. B. (1958) *Introduction to the theory of sound transmission: With application to the ocean*, pp. 284, New York: McGraw-Hill, USA.
- Ostashev, V. (2002) *Acoustics in moving inhomogeneous media*, CRC Press, USA, ISBN: 0419224300.
- Pichon, A. L., Antier, K., Cansi, Y., Hernandez, B., Minaya, E., Burgoa, B., ... & Vaubaillon, J. (2008) Evidence for a meteoritic origin of the September 15, 2007, Carancas crater. *Meteoritics & Planetary Science*, 43(11), 1797-1809, doi: 10.1111/j.1945-5100.2008.tb00644.x.
- Pierce, A. D., Thomas, C. (1969) Atmospheric correction factor for sonic-boom pressure amplitudes, *Journal of the Acoustical Society of America*, 46, 1366-1380, doi: 10.1121/1.1911861.
- Plooster, M. N. (1970) Shock waves from line sources, Numerical solutions and experimental measurements, *Physics of fluids*, 13, 2665, doi: 10.1063/1.1692848.
- Plotkin, K. (1989) Review of sonic boom theory, AAIA 12th Aeronautics Conference, April 10-12, 1989, San Antonio, TX, USA
- Popova, O. P., Jenniskens, P., Emel'yanenko, V., Kartashova, A., Biryukov, E., Khaibrakhmanov, S., et al. (2013) Chelyabinsk Airburst, Damage Assessment, Meteorite Recovery, and Characterization. *Science*, 342(6162), 1069-1073, doi: 10.1126/science.1242642.
- ReVelle, D. O. (1974) *Acoustics of meteors-effects of the atmospheric temperature and wind structure on the sounds produced by meteors*. Ph.D. Thesis Michigan Univ., Ann Arbor MI, USA.

- ReVelle, D. O. (1976) On meteor-generated infrasound, *Journal of Geophysical Research*, 81(7), 1217-1230, doi: 10.1029/JA081i007p01217.
- ReVelle, D. O. (1997) Historical Detection of Atmospheric Impacts by Large Bolides Using Acoustic-Gravity Waves, *Ann N Y Acad Sci*, 822 (1 near-earth ob), 284, doi: 10.1111/j.1749-6632.1997.tb48347.x.
- ReVelle, D. O. (2010) Acoustic-gravity waves from impulsive sources in the atmosphere, In *Infrasound Monitoring for Atmospheric Studies*, pp. 305-359, Springer Netherlands, doi: 10.1007/978-1-4020-9508-5\_11.
- Sakurai, A. (1964) Blast Wave Theory, Report No. MRC-TSR-497, Wisconsin Univ-Madison Mathematics Research Center, USA.
- Silber, E. A., Brown, P. G. (2014) Optical Observations of Meteors Generating Infrasound – I: Acoustic Signal Identification and Phenomenology, *JASTP*, submitted (#ATP3766)
- Silber, E. A., Le Pichon, A. Brown, P. (2011) Infrasonic Detection of a Near-Earth Object Impact over Indonesia on 8 October, 2009, *Geophysical Research Letters*, Vol. 38, L12201, doi: 10.1029/2011GL047633.
- Silber, E. A., ReVelle, D. O., Brown, P. G., Edwards, W. N. (2009) An estimate of the terrestrial influx of large meteoroids from infrasonic measurements, *Journal of Geophysical Research: Planets* (1991–2012), 114(E8), doi: 10.1029/2009JE003334.
- Sutherland, L. C., Bass, H. E. (2004) Atmospheric absorption in the atmosphere up to 160 km. *The Journal of the Acoustical Society of America*, 115, 1012, doi: 10.1121/1.1631937.
- Swift, W. R., Suggs, R. M., and Cooke, W. J. (2004) Meteor44 video meteor photometry, *Earth, Moon, and Planets*, 95(1-4), 533-540, doi: 10.1007/1-4020-5075-5\_49.
- Towne, D.H. (1967) *Wave Phenomena*, Addison-Wesley Publications, Reading, Massachusetts, USA
- Tsikulin, M. A. (1970) Shock waves during the movement of large meteorites in the atmosphere, Report No. NIC-Trans-3148, Naval Intelligence Command Alexandria, VA Translation Div., USA
- Vargas, M. J., Benítez, P. M., Bajo, F. S., Vivas, A. A. (2002) Measurements of atmospheric extinction at a ground level observatory, *Astrophysics and space science*, 279(3), 261-269, doi: 10.1023/A:1015184127925
- Wallace, J. M. and Hobbs, P.V. (2006) *Atmospheric Science: An Introductory Survey*, Academic Press, 2nd edition, ISBN: 012732951X.

Weryk, R. J., and Brown, P. G. (2013) Simultaneous radar and video meteors—II: Photometry and ionisation. *Planetary and Space Science*, 81, 32-47, doi: 10.1016/j.pss.2011.12.023.

Whitham, G. B. (1952) The flow pattern of a supersonic projectile. *Communications on pure and applied mathematics*. 5(3), 301-348, doi: 10.1002/cpa.3160050305.

## Chapter 7

### 7. Conclusions and Future Work

*There is no real ending. It's just the place where you stop the story.*

– Frank Herbert

#### 7.1 Conclusions

The main goals of this dissertation were to investigate observationally and theoretically meteor infrasound, and to address several previously unanswered questions as outlined in Section 1.2.

##### 7.1.1 Conclusions from Chapter 3

The influx rate of meteoroids hitting the Earth is most uncertain at sizes of ~10 meters. In Chapter 3, a declassified historical data base of 13 large bolides recorded infrasonically over a period of 13 years by the United States Air Force Technical Applications Center (AFTAC) was digitized and re-examined using modern techniques in order to refine our knowledge of the terrestrial influx rate at these sizes. From this infrasound study, the best estimate for the cumulative annual flux of impactors with energy equal to or greater than  $E$  (in kilotons of TNT equivalent) is  $N=4.5 E^{-0.6}$ . This influx value is found to be several times higher than predicted from telescopic surveys and indicates that a megaton-class impact should occur somewhere on Earth every few decades.

##### 7.1.2 Conclusions from Chapter 4

In Chapter 4, instrumental recordings of infrasonic signals produced by a large Earth-impacting fireball, believed to be one of the most energetic instrumentally recorded during the last century that occurred on 8 October, 2009 over Indonesia, were analysed. This event, detected by 17 infrasonic stations of the global International Monitoring Network, generated stratospherically ducted infrasound returns at distances up to 17,500

km, the greatest range at which infrasound from a fireball had been detected since the 1908 Tunguska explosion, being surpassed only by the Chelyabinsk bolide of 15 February 2013. A new methodology to determine the most likely source height for infrasound signals reaching the closest stations (within <5,000 km) was developed and tested.

The measured differences in the dominant signal periods were attributed to signals coming from different parts of the meteoroid trail. The signal with the longest period most likely originated at an altitude near 20 km, suggesting that the terminal burst occurred near this altitude. Newly released US Government Sensor data (<http://neo.jpl.nasa.gov/fireballs/>) independently indicates the height of the terminal burst to have occurred at 19 km, in agreement with the height determined purely from infrasound records using the new methodology presented in the paper. Using the AFTAC infrasonic period-yield relation, it was found that the most probable source energy for this bolide as 8 – 67 kt of TNT equivalent explosive yield. This is in an acceptable agreement with the estimated energy of 33 kt from optical radiation reported at (<http://neo.jpl.nasa.gov/fireballs/>), given that optical efficiency estimates are known to be subject to considerable uncertainty due to assumptions required in performing their derivations. The satellite derived influx rate (Brown et al., 2002) indicates that impact events of such energy are expected only once per decade, while infrasonic influx rate derived in Chapter 3 indicates that such events would occur once every 5 years. The study of impact effects and modes of disintegration of large bolides in the atmosphere can provide insight into the threshold levels at which ground damage and climate perturbations may be caused by airbursts as exemplified by the recent Chelyabinsk airburst (Brown et al., 2013).

### **7.1.3 Conclusions from Chapter 5**

In Chapter 5, infrasound signals from 71 simultaneously detected bright optical meteors were examined to investigate the phenomenology and characteristics of meteor near-field infrasound (< 300 km) and shock production. It was found that approximately 1% of all optically detected meteors recorded by the Southern Ontario Meteor Network (SOMN) have associated infrasound. It was found that there are two entry velocity meteor

populations which produced infrasound detectable at the ground, slow ( $< 40$  km/s) and fast ( $> 40$  km/s). These exhibit different astrometric, source height, and signal characteristics, consistent with the differing physical origins of the populations as asteroidal (slow) and cometary (fast). For our regional infrasound measurements, the slow velocity population produces maximum dominant frequency of up to  $\sim 14$  Hz, while the fast velocity population is bounded by an upper dominant signal frequency of  $< 4$  Hz. There is a strong inverse relationship between the shock source height and the dominant signal frequency.

A new algorithm was developed to determine the most probable point along the meteor trail where the infrasound signal is generated. Small scale atmospheric perturbations in the winds due to gravity waves were introduced to the model so to investigate their role on short range infrasound propagation ( $< 300$  km) and the effect on shock source heights. It was shown that these wind perturbations play a significant role, and also result in infrasound propagation paths which are not present when only averaged atmospheric profiles are used in the model. The findings in this study also indicate that infrasound generated by high altitude meteors may be more common than previously thought.

Based on the location along the meteor trail where the infrasound signal originates, it was found that for centimetre-sized meteoroids most signals are associated with cylindrical shocks, with some  $\sim 25\%$  of events displaying spherical shocks associated with fragmentation events/optical flares. The video data suggests that all events with large ray launch angles ( $\beta > 117^\circ$ ) from the trajectory heading are most likely generated by a spherical shock as evidenced by a correlation with point-like flares in the meteor light curves, while infrasound produced by the meteors with ray launch angles  $\leq 117^\circ$  can be attributed to both a cylindrical line source and a spherical shock. It was found that centimetre-sized meteoroids predominantly produce infrasound toward the end of their trails, with a smaller number generating infrasound in the mid-trail regions. While a significant fraction of the observed meteors producing infrasound ( $\sim 1/4$  of single arrivals) also exhibit fragmentation events, we find no instances where acoustic emission is detectable more than  $\sim 60^\circ$  beyond the ballistic regime at the meteoroid masses observed here (ranging from grams to tens of kilograms). This emphasizes the strong anisotropy in



acoustic emission by meteors, which is dominated by a cylindrical line source geometry, even in the presence of fragmentation.

A new taxonomic signal classification scheme for meteor generated infrasound was established. Meteors producing multiple infrasound arrivals show a strong preference for infrasound source heights concentrated at the end of trails and are much more likely to be associated with optical flares. The new taxonomic scheme could be extended to infrasound signals from other explosive sources located at relatively short distance from the source (within ~300 km, to remain consistent with our dataset).

#### **7.1.4 Conclusions from Chapter 6**

In Chapter 6, 24 optically and infrasonically detected meteors were used to test, validate and update the meteor infrasound weak shock model (ReVelle, 1974).

The weak shock model behaviour was examined in a sensitivity analysis to estimate the effects of (a) winds; (b) perturbed wind fields due to gravity waves; (c) Doppler shift; and (d) Sutherland and Bass (2004) absorption coefficients. The overall effect of these factors on the initial value of the blast radius is relatively small (~10%) for regional meteor events.

A bottom-up modelling approach which uses the observed infrasound signal period and amplitude together with the weak shock model to predict the blast radius ( $R_0$ ) at altitude was employed. It was found that the period-based  $R_0$  appears to have realistic values. However, the amplitude-based  $R_0$  exhibits a large systematic deviation in the linear and weak shock regimes, as well as large deviations when compared to the period-based blast radius. The amplitude-based  $R_0$  is severely underestimated in the linear regime, and overestimated in the weak shock regime.

We isolated one possible cause of the amplitude-based  $R_0$  estimate mismatch as being due to the Towne's (1967) definition for the distortion distance, which was subsequently adopted by ReVelle (1974). Assuming this arbitrary definition is not correct, it was empirically determined that a modified distortion distance for the data set of <6% explained the linear amplitude observations, contrary to the proposed value of 10% (Towne, 1967). A 'best fit' linear regime  $R_0$  which simultaneously matched both

amplitude and period within their measurement uncertainties was established using this modified distortion distance. The Fragmentation Model of meteoroid ablation was applied (Ceplecha and ReVelle, 2005) to photometric data as measured from optical observations of meteor events to calculate independently the blast radius using the fundamental definition for  $R_0$  in terms of energy deposition per unit path length. This blast radius was used as an input for top-down modelling to determine the predicted signal amplitude and period in both the weak shock and linear regimes. We found good agreement with the observed period, while the linear amplitude using the nominal distortion distance of 10% was again underestimated. The predicted values of the period and amplitude agree when the modified distortion distance as obtained from the best fit  $R_0$  was used.

New empirical relations which link the observed dominant signal period ( $\tau$ ) to the meteoroid blast radius were derived:

$$R_0 = 15.4231 \tau - 0.5294 \text{ (for observed signals } \tau \leq 0.7\text{s) and}$$

$$R_0 = 29.14597 \tau - 11.5811 \text{ (for observed signals } \tau > 0.7\text{s).}$$

## 7.2 Future Work

Meteor generated infrasound provides valuable insights into high altitude explosive events in the atmosphere. There is still much to be learned from well documented simultaneously observed meteors; given the infrequency of such events such records provide invaluable data sources. To further understand meteor generated infrasound, propagation effects and the source function, the following possible avenues might be explored in the future:

- i. Validate the method for determining the likely burst altitude for long range propagation using other well documented events;
- ii. Expand the experimental data set of simultaneously observed regional (< 300 km) meteors to improve statistics;

- iii. Automate detection techniques and algorithms to improve regional detection rates;
- iv. Investigate local effects on signal characteristics (e.g. ground cover, reflection);
- v. Investigate effects of turbulence in the atmosphere;
- vi. Apply an improved propagation model which includes full gravity wave implementation and atmospheric variability for raytracing and signal prediction;
- vii. Expand this study to investigate regional infrasound generated by spherical explosions (i.e. fragmenting meteoroids);
- viii. Further investigate the effects responsible for shock wave deviation angles at the source – (and this could be broken into two distinctive parts: first, numerically examine interactions of successive shocks at the source to understand how these may affect ray deviation angles and features seen in the shock; second, examine the effect of temperature near the source on ray deviations);
- ix. Revisit the taxonomic scheme from a theoretical standpoint;
- x. Rigorously (numerically and experimentally) investigate the distortion distance and transition altitude of a weak shock wave to the linear regime on a larger set of well documented events;
- xi. Modify the updated version of ReVelle's model to validate it against infrasound generated by spherical shocks;
- xii. Expand the data base with meteoroids which generate infrasound at very high altitudes (above 85 km) to improve statistics and build upon the results found in this project;
- xiii. Apply the newly derived period-blast radius relation to a larger data set to determine its general applicability;
- xiv. Apply what was learned through the study in Chapters 5 and 6 of this thesis and expand to medium range bolides (distances of 300 km to 1000 kilometers from the observation point).

- xv. Apply numerical modelling (e.g. hydrocode) and investigate Witham's F-function (Whitham, 1952).

## References

- Brown, P. G., Assink, J. D., Astiz, L., Blaauw, R., Boslough, M. B., Borovička, J., and 26 co-authors (2013) A 500-kiloton airburst over Chelyabinsk and an enhanced hazard from small impactors. *Nature*. 503, 238-241
- Brown, P. G., Spalding, R. E., ReVelle, D. O., Tagliaferri, E. and Worden, S. P. (2002) The flux of small near-Earth objects colliding with the Earth, *Nature*, 420, 294-296, doi: 10.1038/nature01238
- Ceplecha, Z., and Revelle, D. O. (2005) Fragmentation model of meteoroid motion, mass loss, and radiation in the atmosphere. *Meteoritics & Planetary Science*, 40(1), 35-54
- ReVelle, D. O. (1974) Acoustics of meteors-effects of the atmospheric temperature and wind structure on the sounds produced by meteors. Ph.D. Thesis University of Michigan, Ann Arbor
- Sutherland, L. C., Bass, H. E. (2004) Atmospheric absorption in the atmosphere up to 160 km. *The Journal of the Acoustical Society of America*, 115, 1012
- Towne, D.H. (1967) *Wave Phenomena*, Addison-Wesley Publications, Reading, Massachusetts
- Whitham, G. B. (1952) The flow pattern of a supersonic projectile. *Communications on pure and applied mathematics*. 5(3), 301-348

## Appendix 1

### Signal Identification and Phenomenology Plots: Single and Multi Arrival Events

This section displays in detail the meteor infrasound signal identification methodology and phenomenology plots analysed in Chapters 5 and 6. There are three figures shown for each event: (i) an example of infrasound signal displayed in InfraTool (MatSeis 1.7), (ii) filtered waveform for all functional channels (sensors), and (iii) best beam signal with Hilbert envelope. The signal classification scheme is shown in Table 5.5 (Chapter 5). The latter two figures show the appearance and features of infrasonic signals produced by regional meteors in the data set developed in Chapter 5.

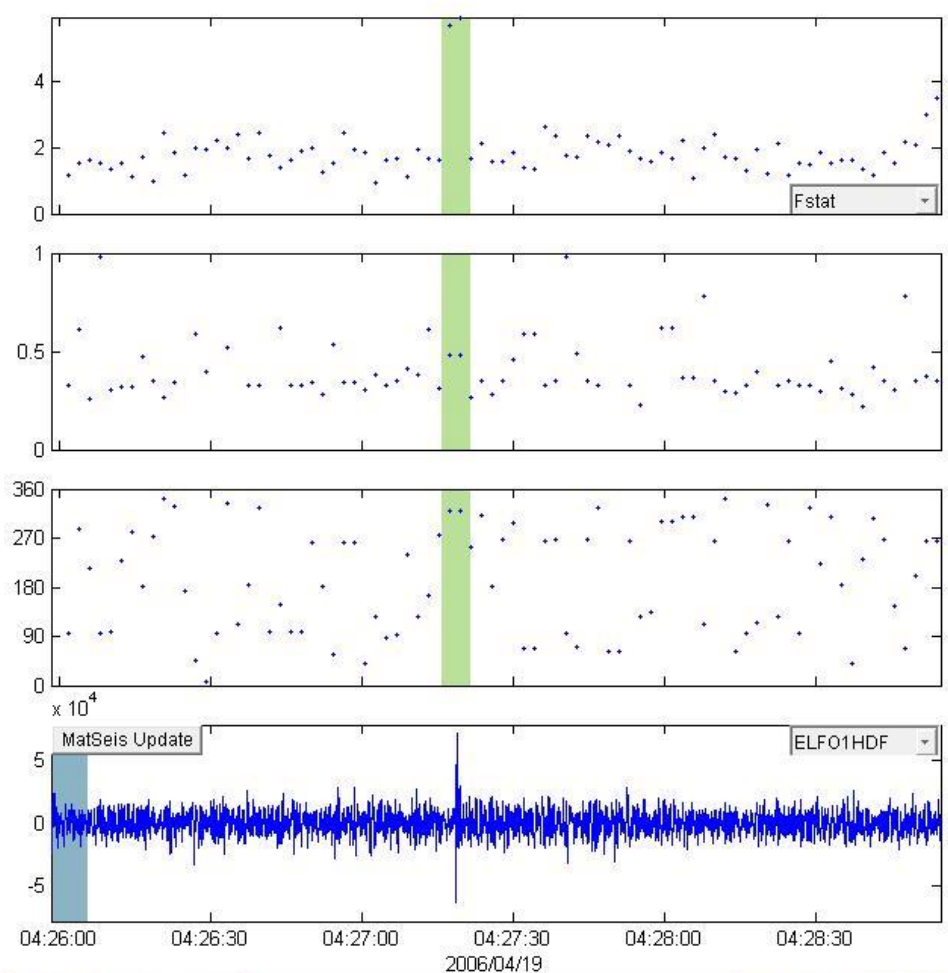
**InfraTool plot:** As described in detail in Chapter 5, one of the steps in signal identification is to search for possible signals using InfraMap within the parameters determined a priori (e.g. time window, back azimuth). The plots shown here represent a typical MatSeis output when a signal is initially identified; however, they do not represent the final signal measurements. The top window is either the signal correlation or the F-statistic, a measure of the relative coherency of the signal across the array elements, the second window is the apparent trace velocity of the infrasound signal across the array in the direction of the peak F-stat, and the third window shows the best estimate for the signal back-azimuth. The fourth window shows the bandpassed raw pressure signal for the Centre Element of ELFO.

**Filtered waveform:** Filtered (2<sup>nd</sup> order Butterworth) waveform as recorded at each array sensor. The filter bandpass for each event is shown in the associated figure title.

**Best beam plot:** Phase aligned and stacked filtered signal (black) from all elements. The filter band is shown in figure titles. The peak of the envelope (red) represents the maximum amplitude, which is calculated using the Hilbert Transform (Dziewonski and Hales, 1972).

# SINGLE EVENTS

20060419\_042128



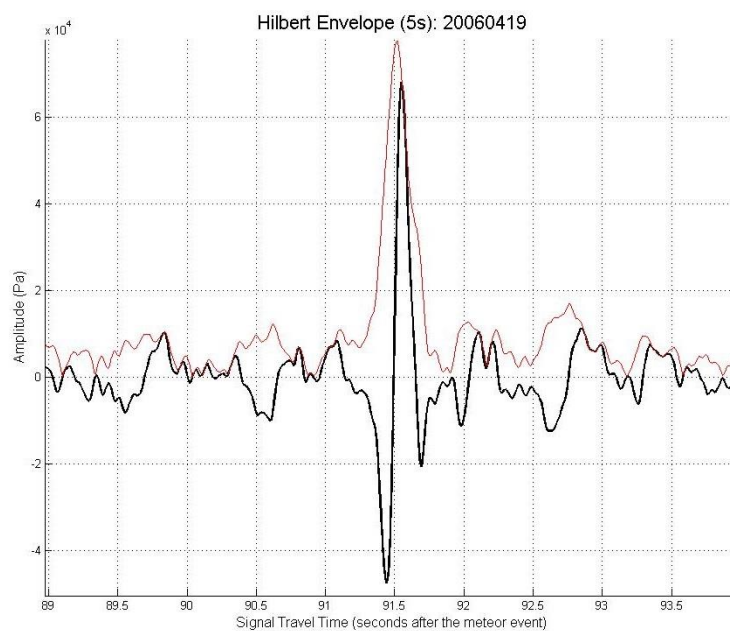
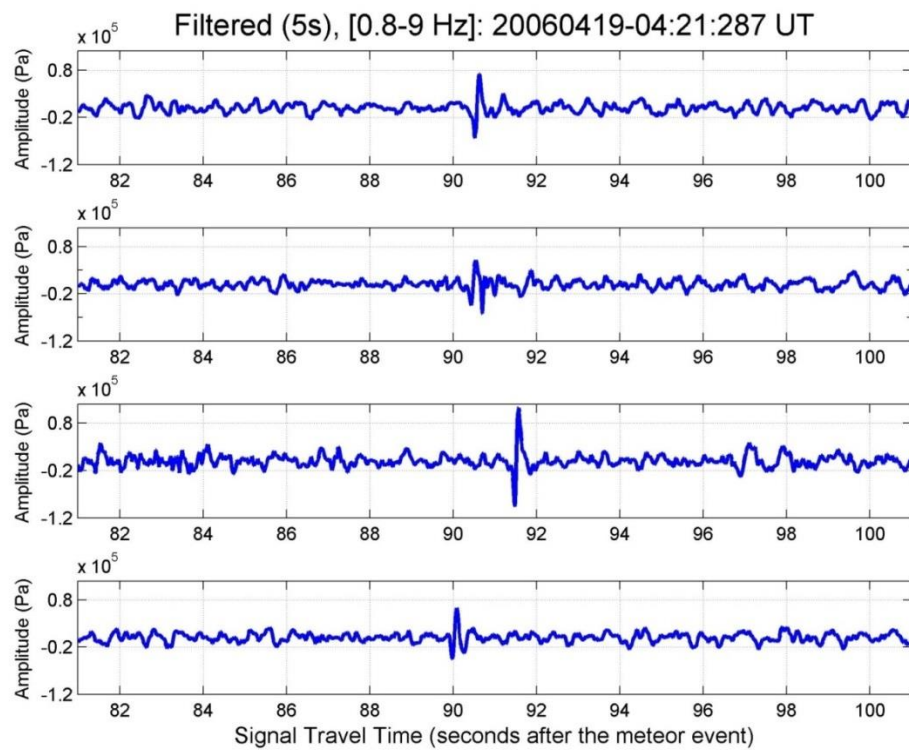
Window Parameters		Pass Band Parameters		Slowness Parameters		Windowed Values & S.D.	
Duration (s)	7.0	Low frequency (Hz)	0.8	Max. Slown.	400.0	Corr.	0.631 0.006
Overlap (%)	70.0	High frequency	9	# of Slown.	40	Fstat	5.832 0.163
Number of	83	Order (integer)	2			Vel.	0.478 0.000
						Az.	318.576 0.000

MatSeis Update

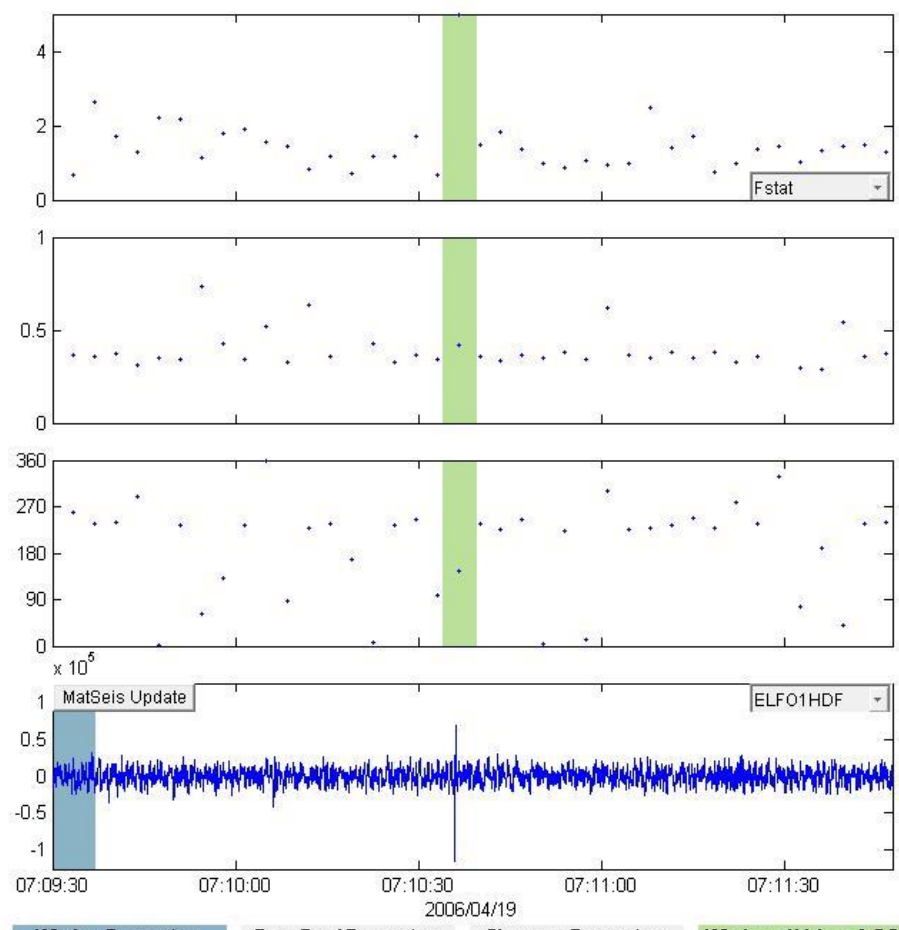
ELFO1HDF

2006/04/19

Calculate 0 Write File D:\Research\Research - Elizabeth\l Cancel



### 20060419\_070557

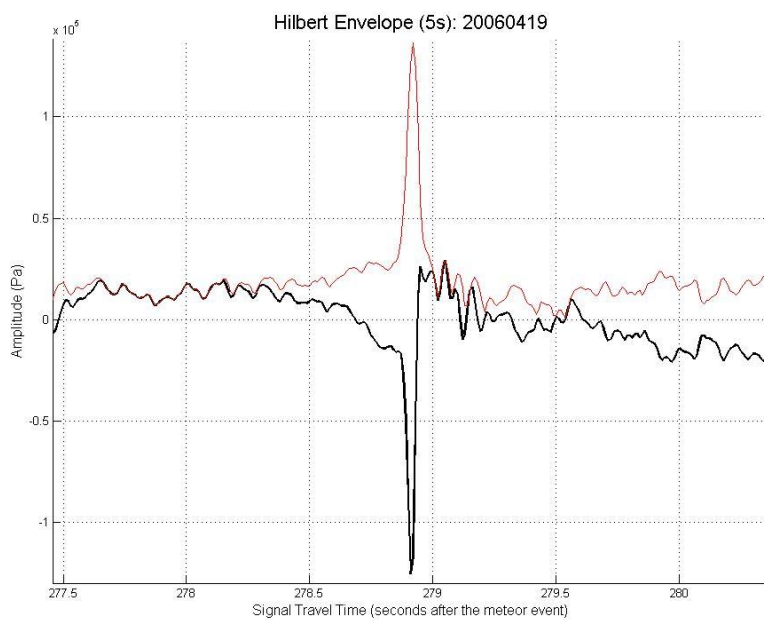
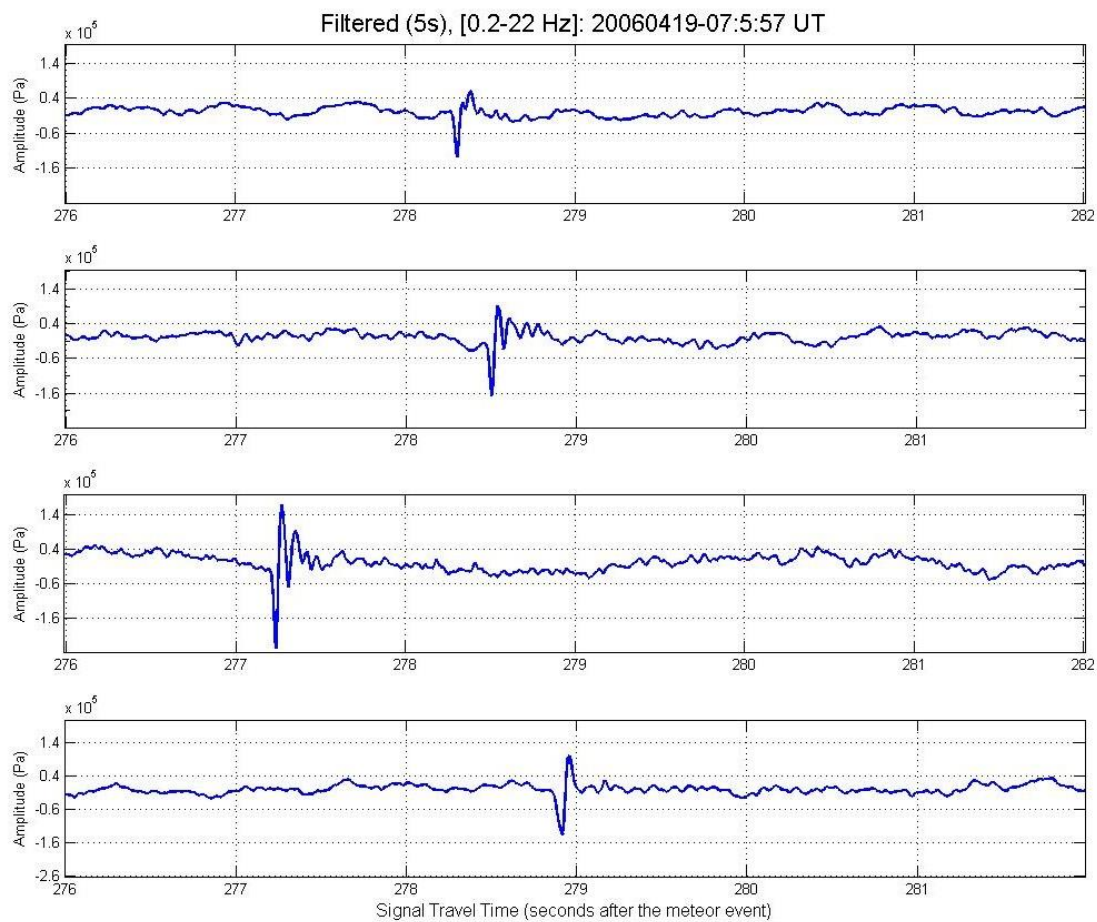


Window Parameters		Pass Band Parameters		Slowness Parameters		Windowed Values & S.D.	
Duration (s)	7.0	Low frequency (Hz)	0.6	Max. Slown.	400.0	Corr.	0.600 0.000
Overlap (%)	50.0	High frequency	20	# of Slown.	40	Fstat	5.001 0.000
Number of	39	Order (integer)	2			Vel.	0.420 0.000
						Az.	144.462 0.000

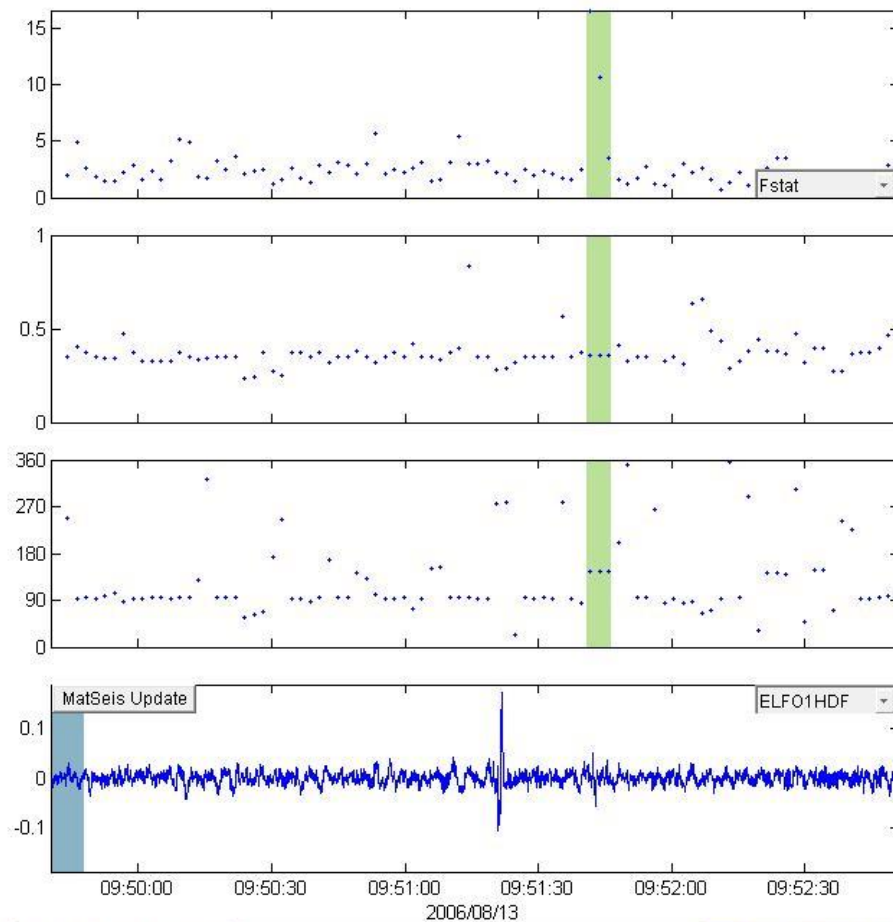
  

Animate			
Calculate	0	Write File	D:\Research\Research - Elizabeth\l
			Cancel

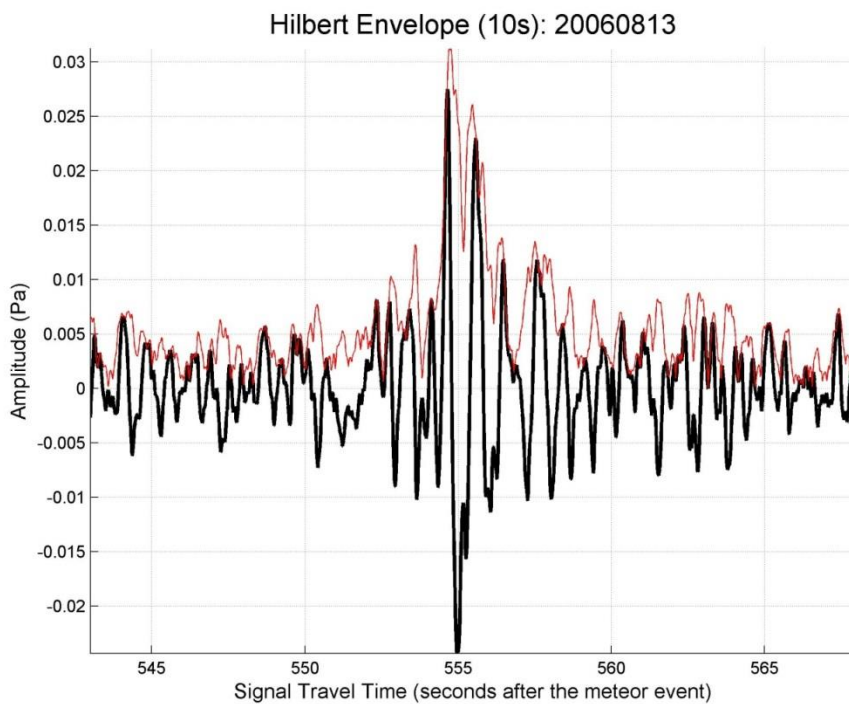
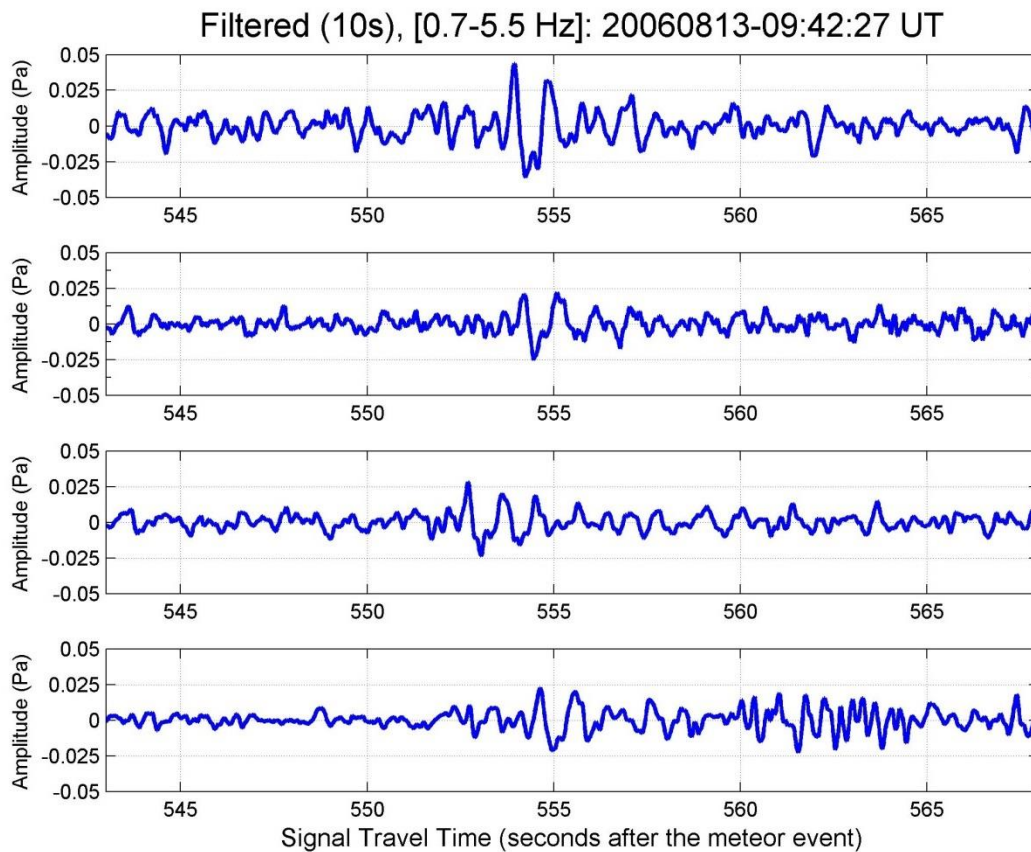




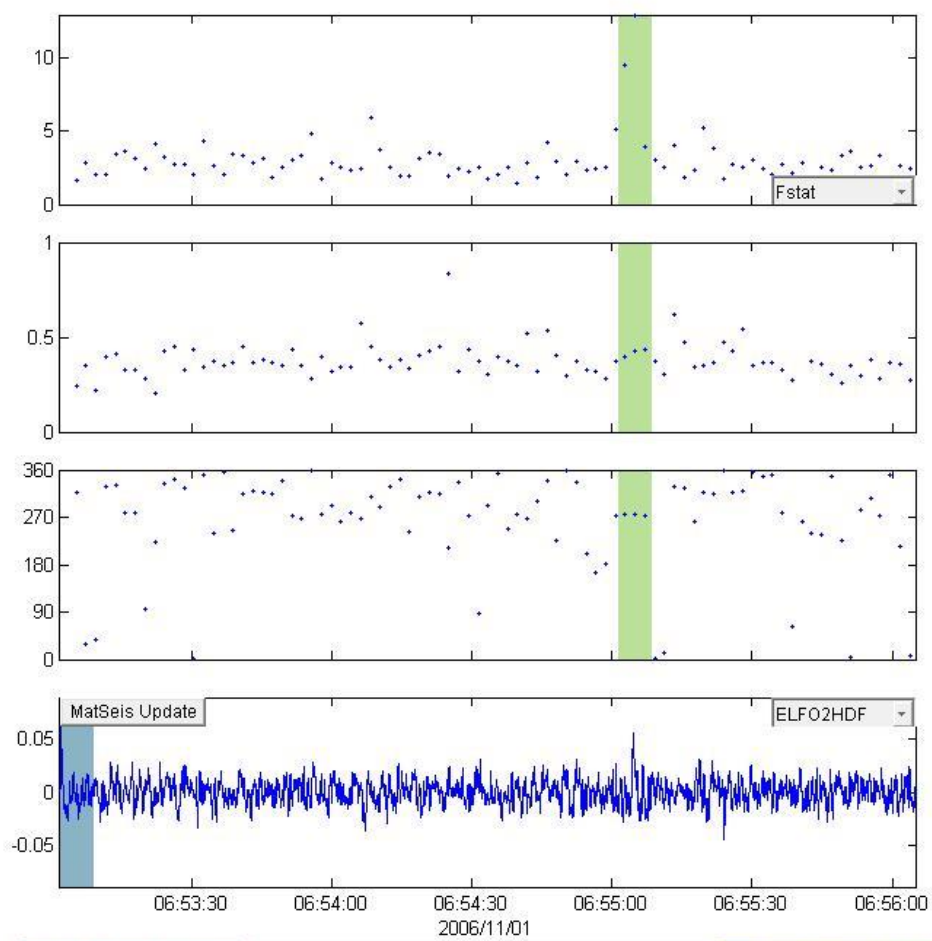
20060813\_094227



Window Parameters		Pass Band Parameters		Slowness Parameters		Windowed Values & S.D.	
Duration (s)	7.0	Low frequency (Hz)	0.4	Max. Slown.	400.0	Corr.	0.696 0.149
Overlap (%)	70.0	High frequency	12	# of Slown.	40	Fstat	10.242 6.546
Number of	89	Order (Integer)	2			Vel.	0.358 0.000
						Az.	145.784 0.000
						Send to Map	
Animate		Write File				D:\Research\Research - Elizabeth\lr	
Calculate	0					Cancel	

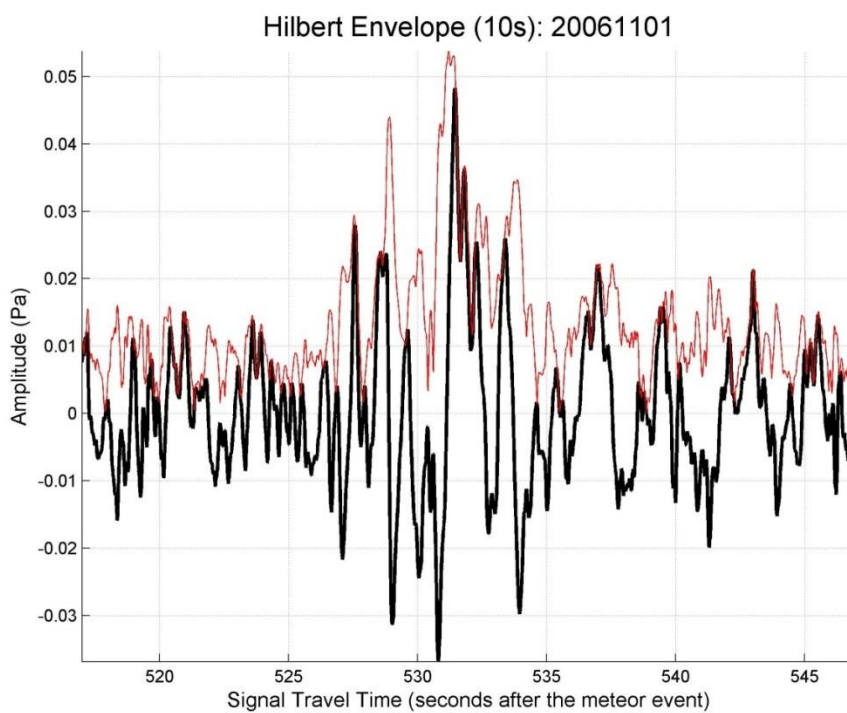
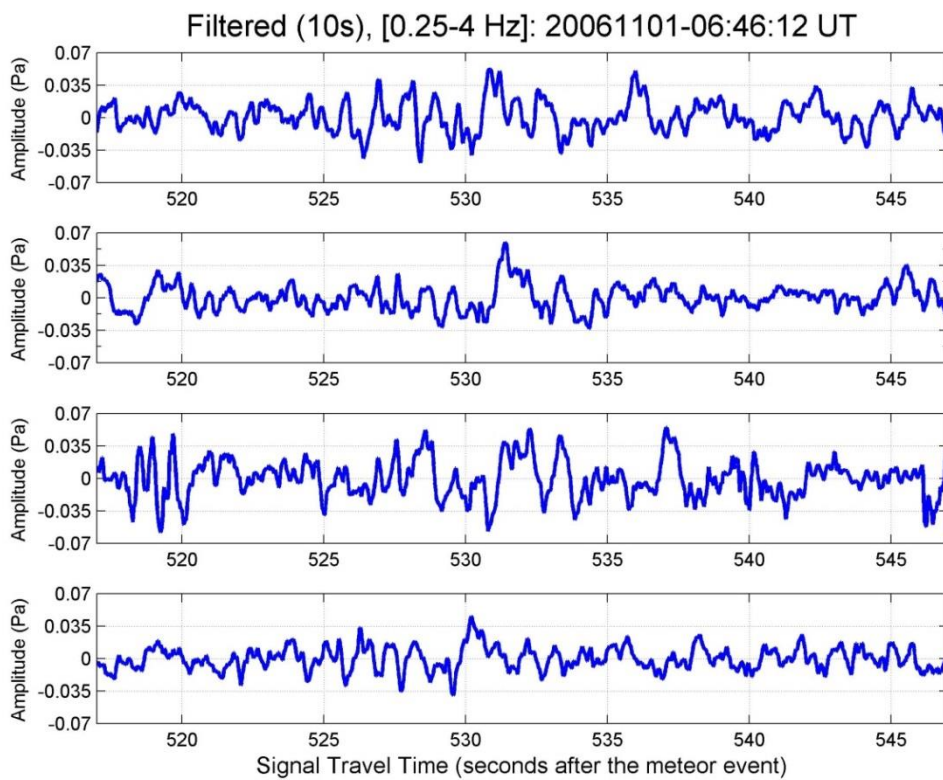


### 20061101\_064612



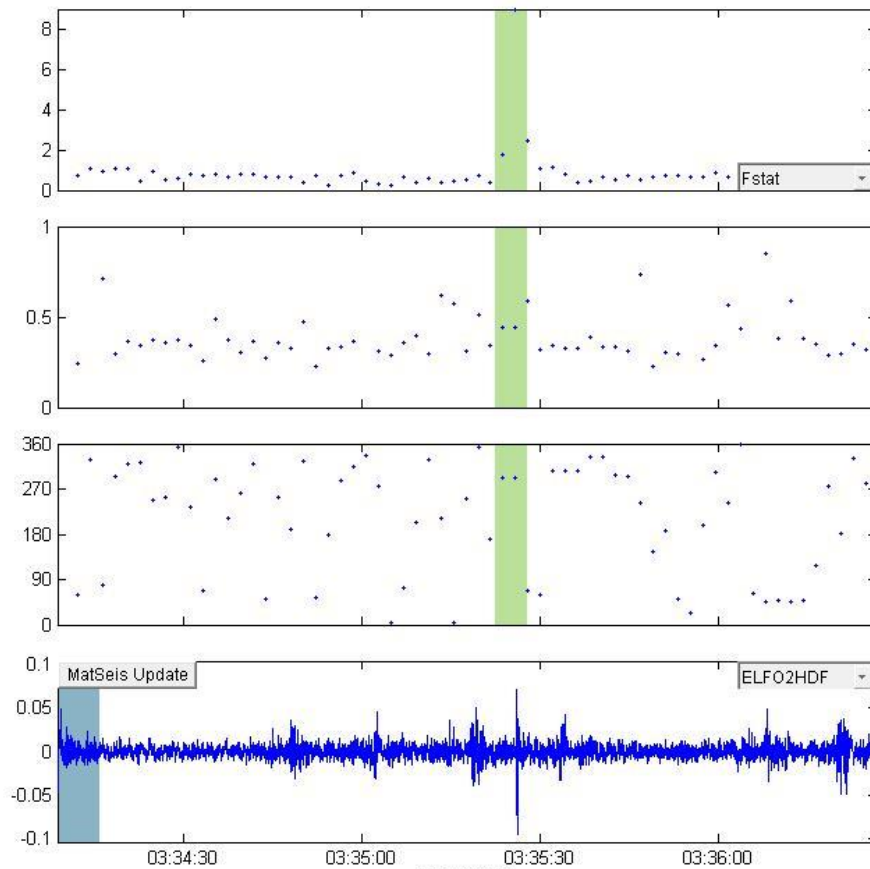
Window Parameters		Pass Band Parameters		Slowness Parameters		Windowed Values & S.D.	
Duration (s)	7.0	Low frequency (Hz)	0.3	Max. Slown.	400.0	Corr.	0.684 0.119
Overlap (%)	70.0	High frequency	4	# of Slown.	40	Fstat	8.804 4.586
Number of	86	Order (integer)	2			Vel.	0.421 0.019
						Az.	275.158 2.496

Buttons: Animate, Calculate 0, Write File D:\Research\Research - Elizabeth\l, Send to Map, Cancel





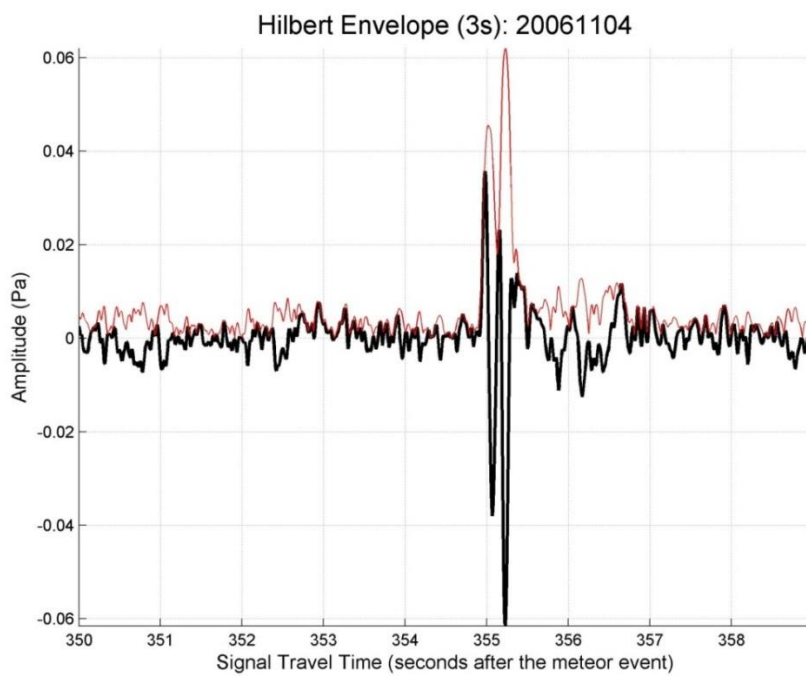
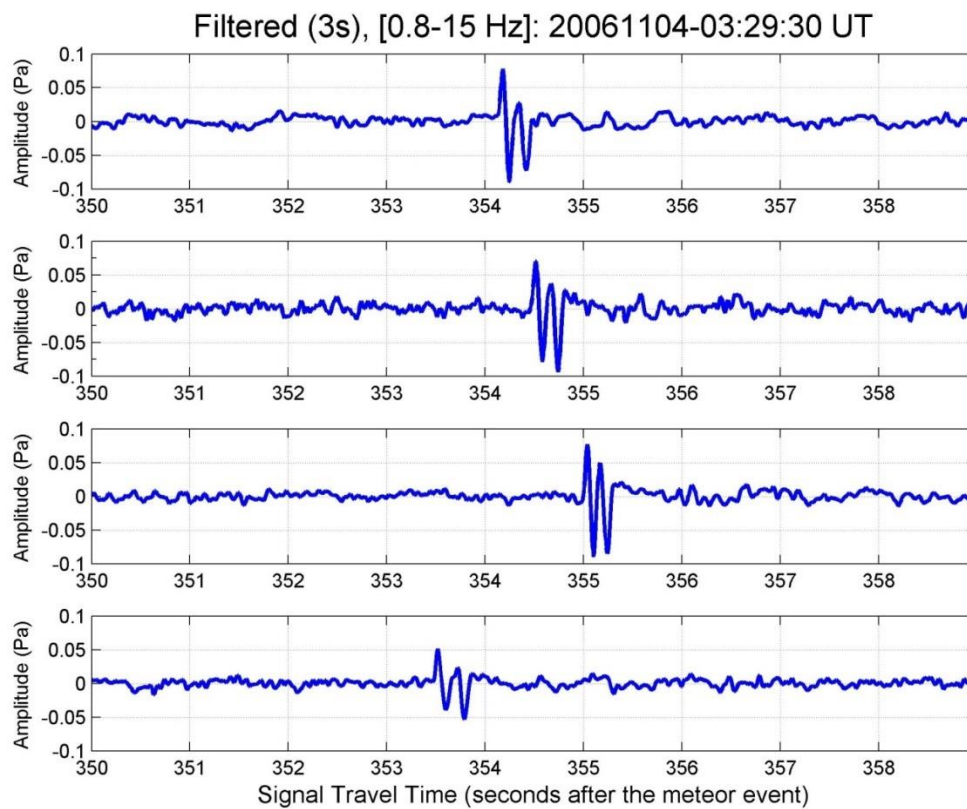
### 20061104\_032930



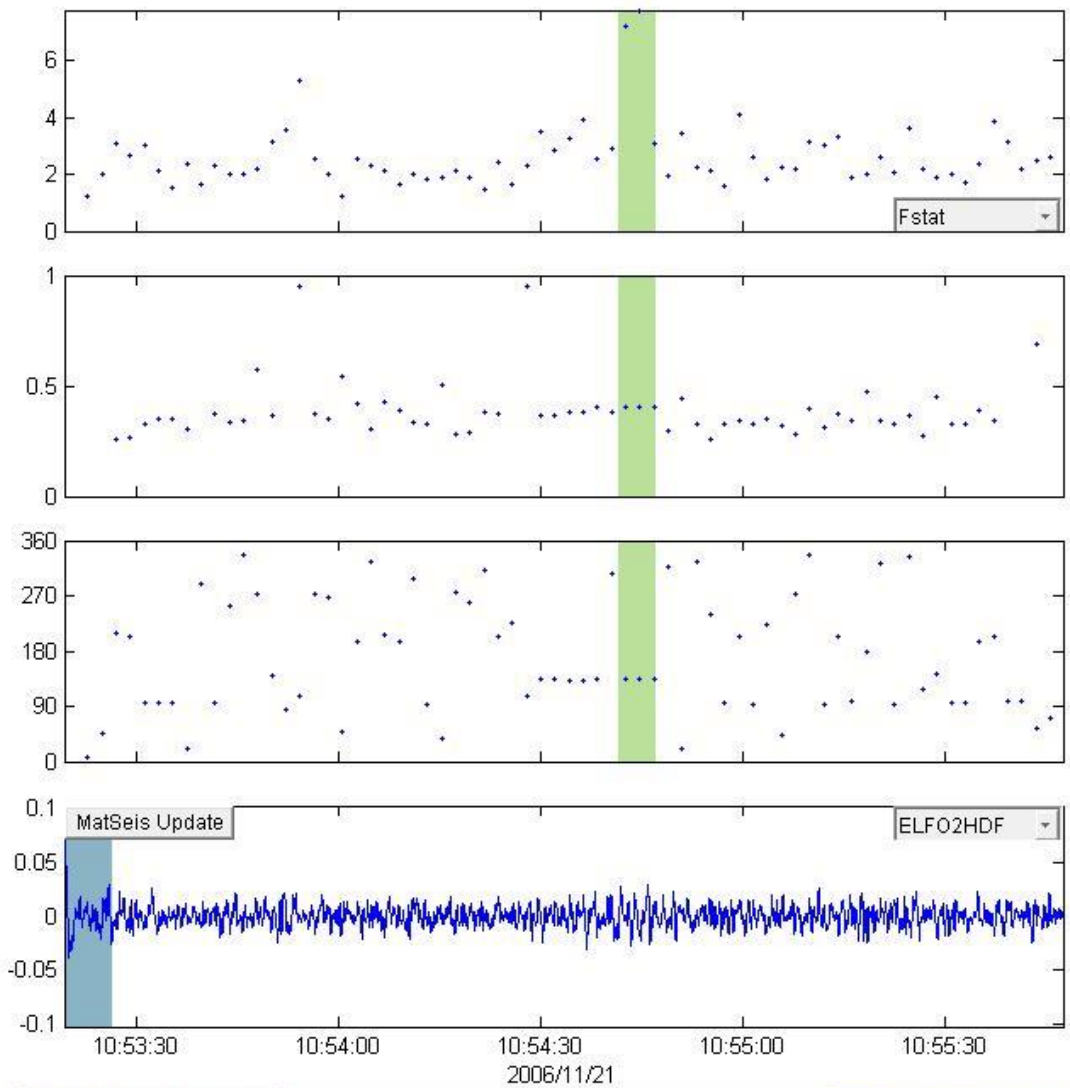
2006/11/04

Window Parameters		Pass Band Parameters		Slowness Parameters		Windowed Values & S.D.	
Duration (s)	7.0	Low frequency (Hz)	0.8	Max. Slown.	400.0	Corr.	0.562 0.215
Overlap (%)	70.0	High frequency	15	# of Slown.	40	Fstat	5.381 5.087
Number of	64	Order (integer)	2			Vel.	0.439 0.000
						Az.	291.371 0.000

0
  D:\Research\Research - Elizabeth\lr



### 20061101\_064612



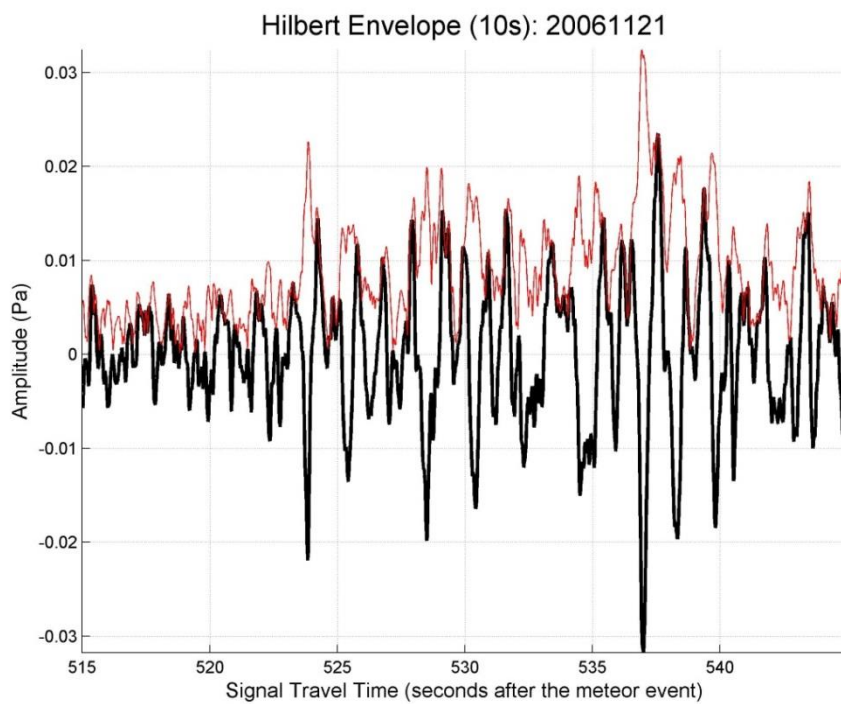
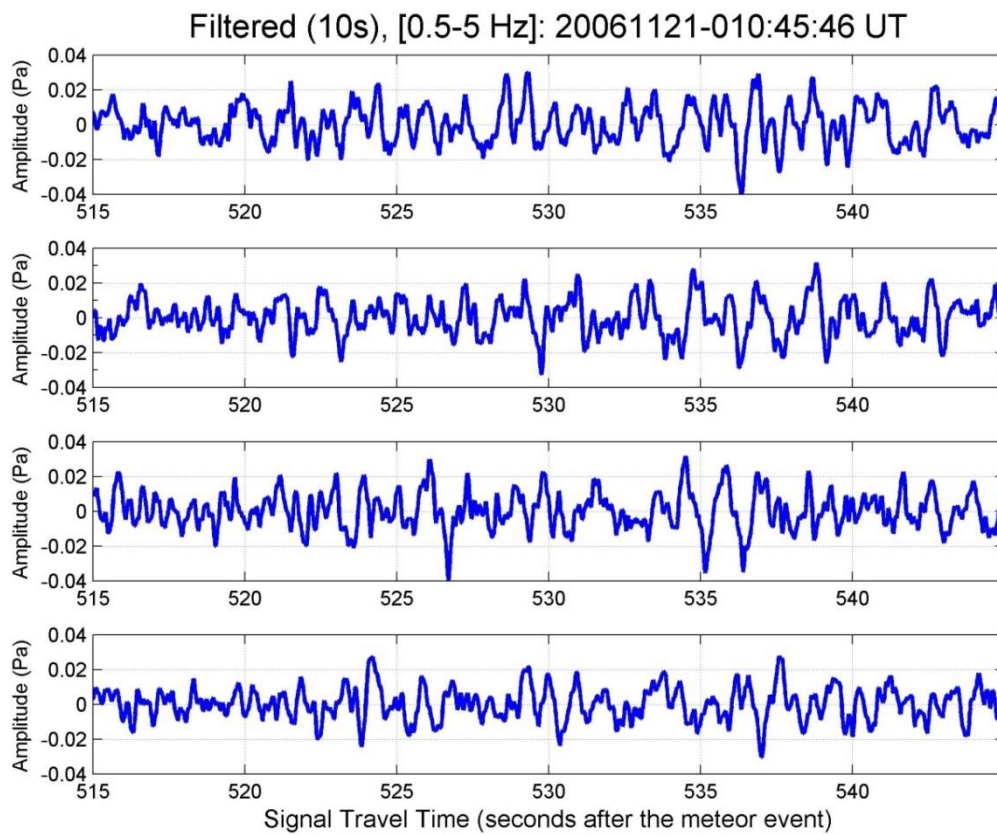
Window Parameters		Pass Band Parameters		Slowness Parameters		Windowed Values & S.D.	
Duration (s)	7.0	Low frequency (Hz)	0.5	Max. Slown.	400.0	Corr.	0.622   0.101
Overlap (%)	70.0	High frequency	3.5	# of Slown.	40	Fstat	6.032   2.561
Number of	69	Order (integer)	2			Vel.	0.403   0.000
						Az.	135.000   0.000

MatSeis Update ELFO2HDF

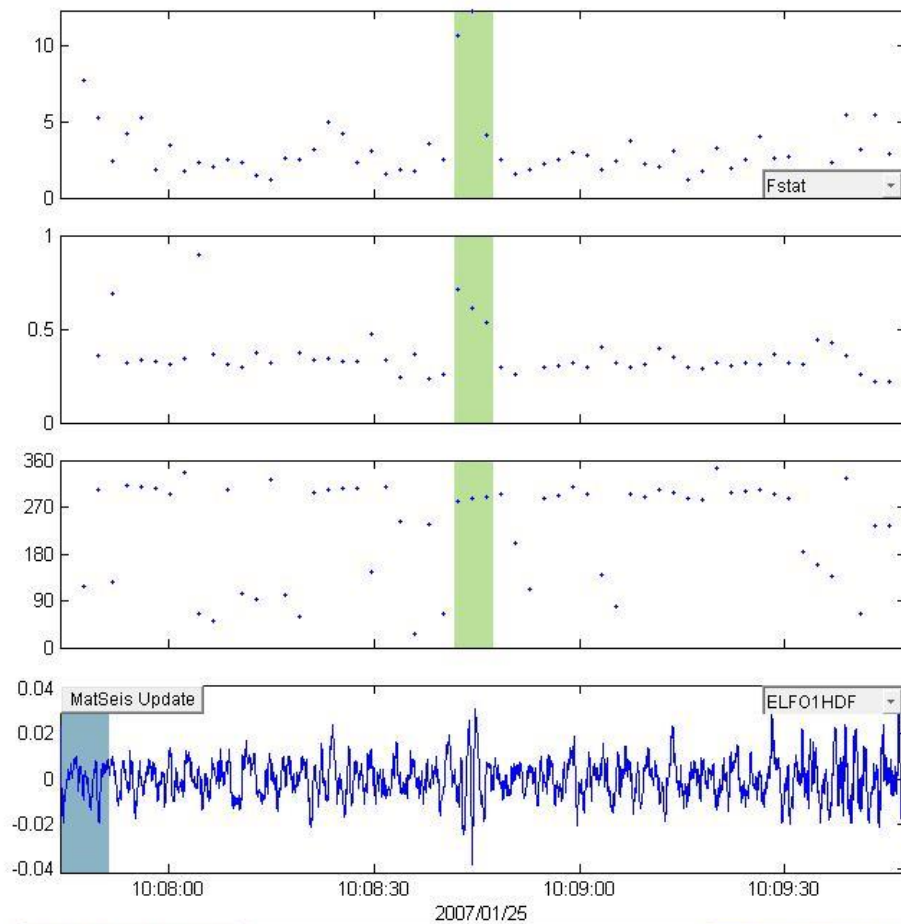
10:53:30 10:54:00 10:54:30 10:55:00 10:55:30  
2006/11/21

Animate  Calculate 0  D:\Research\Research - Elizabeth\



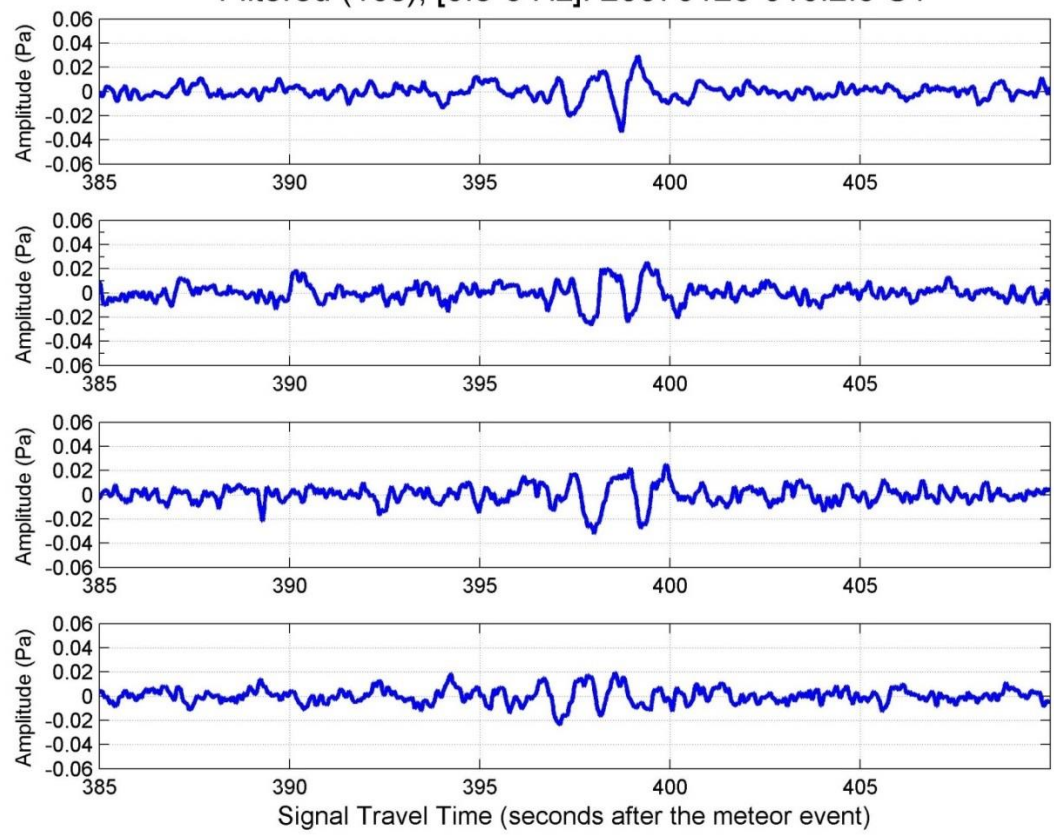


## 20070125\_100205

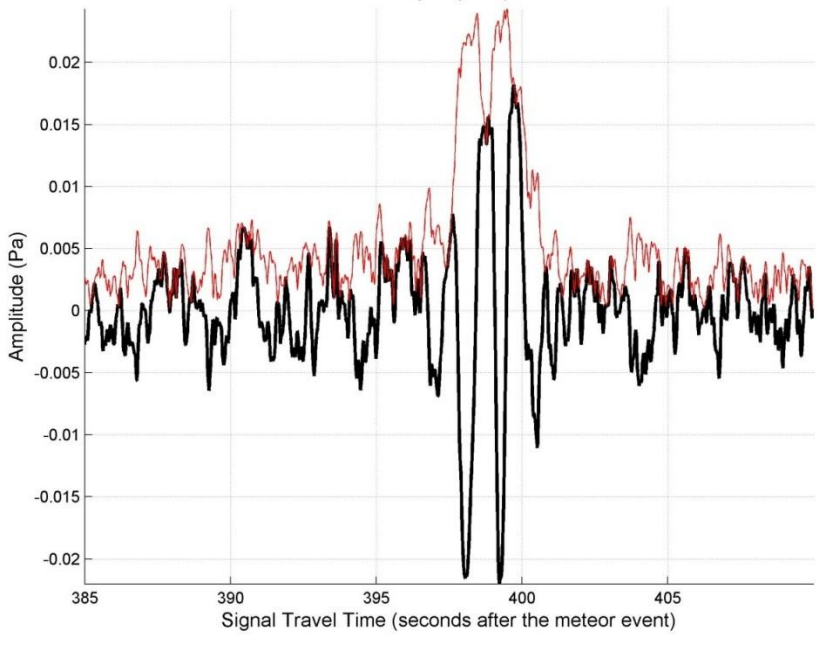


Window Parameters		Pass Band Parameters		Slowness Parameters		Windowed Values & S.D.	
Duration (s)	7.0	Low frequency (Hz)	0.6	Max. Slown.	400.0	Corr.	0.692 0.114
Overlap (%)	70.0	High frequency	6	# of Slown.	40	Fstat	9.055 4.371
Number of	57	Order (integer)	2			Vel.	0.618 0.087
						Az.	285.975 4.472
Animate						Send to Map	
Calculate	0	Write File	D:\Research\Research - Elizabeth\lr			Cancel	

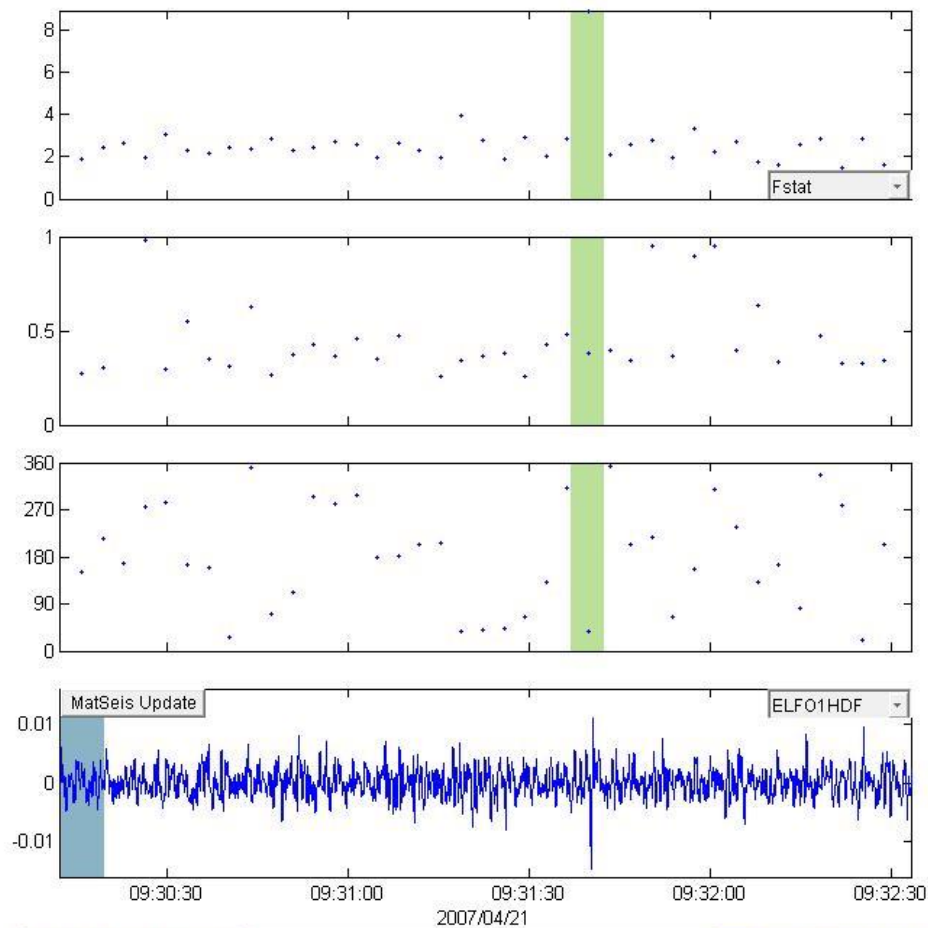
Filtered (10s), [0.8-6 Hz]: 20070125-010:2:5 UT



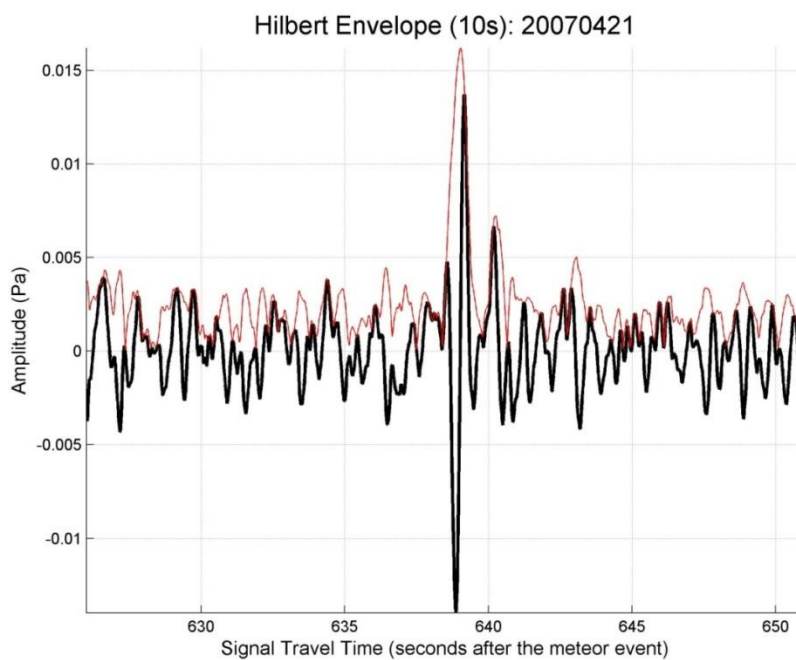
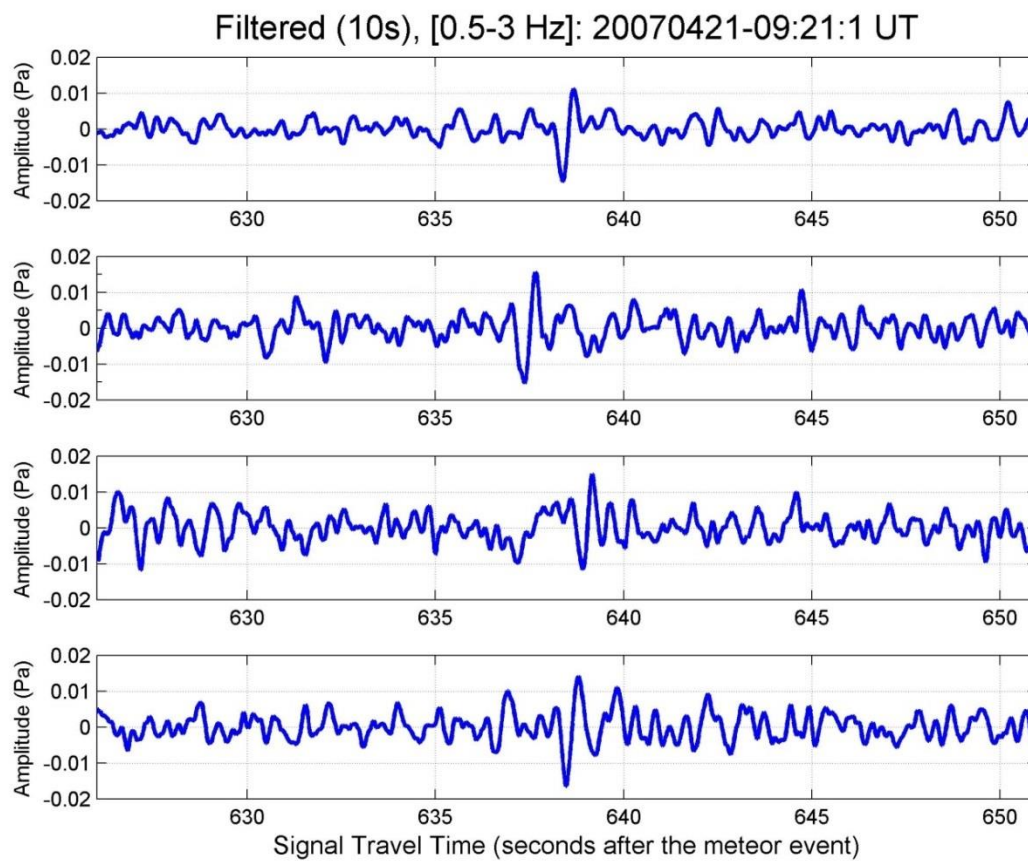
Hilbert Envelope (10s): 20070125



## 20070421\_092101

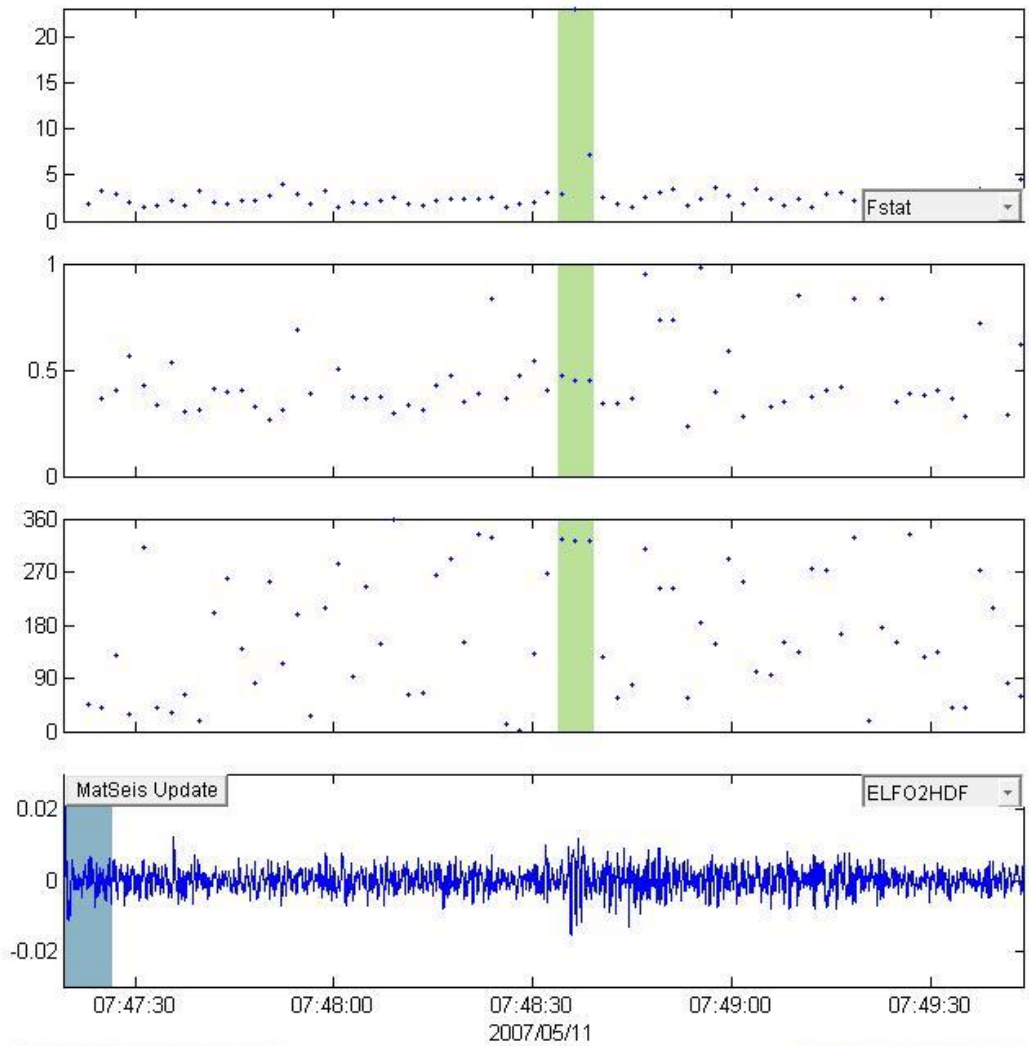


Window Parameters		Pass Band Parameters		Slowness Parameters		Windowed Values & S.D.	
Duration (s)	7.0	Low frequency (Hz)	0.5	Max. Slown.	400.0	Corr.	0.712 0.000
Overlap (%)	50.0	High frequency	3	# of Slown.	40	Fstat	8.890 0.000
Number of	39	Order (integer)	2			Vel.	0.379 0.000
						Az.	36.469 0.000
Animate						Send to Map	
Calculate	0	Write File	D:\Research\Research - Elizabeth\lr			Cancel	





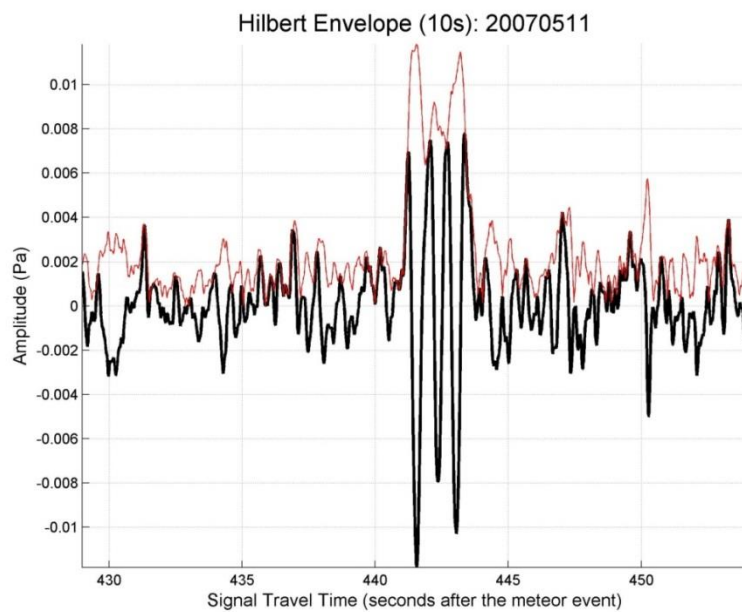
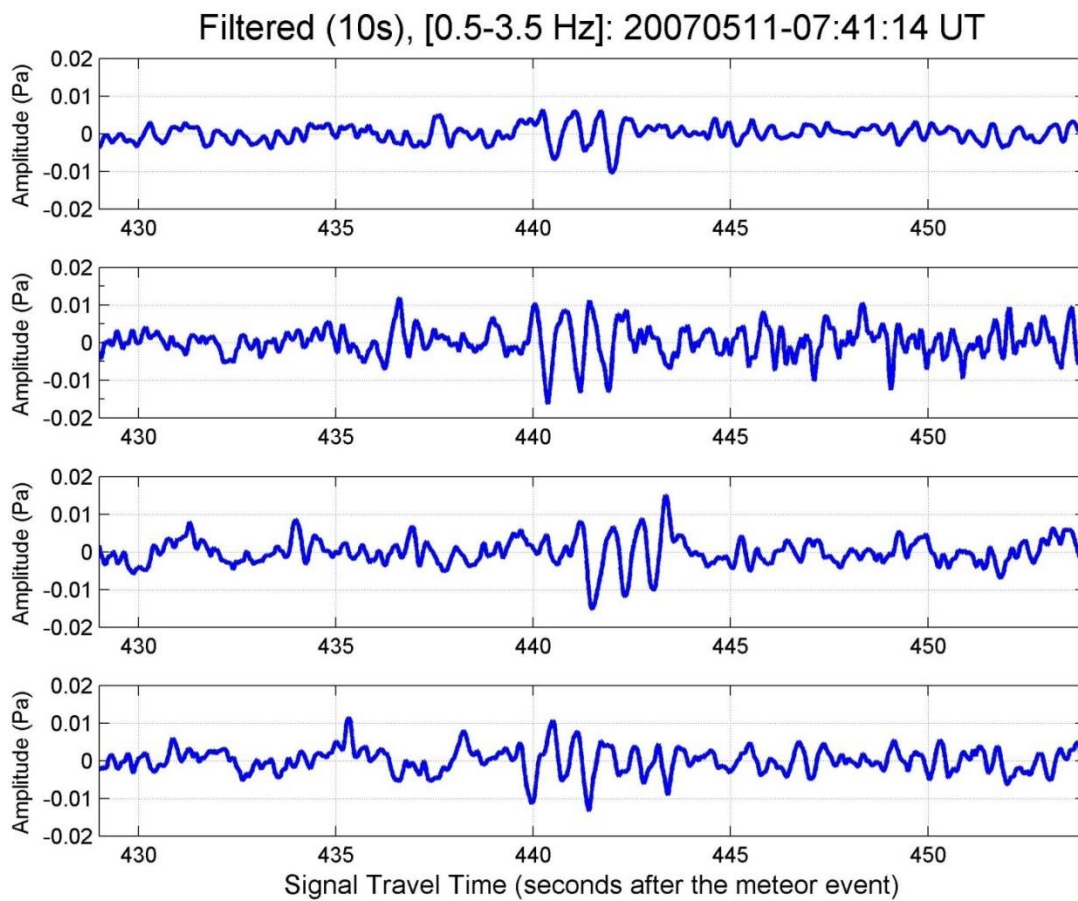
### 20070511\_074114



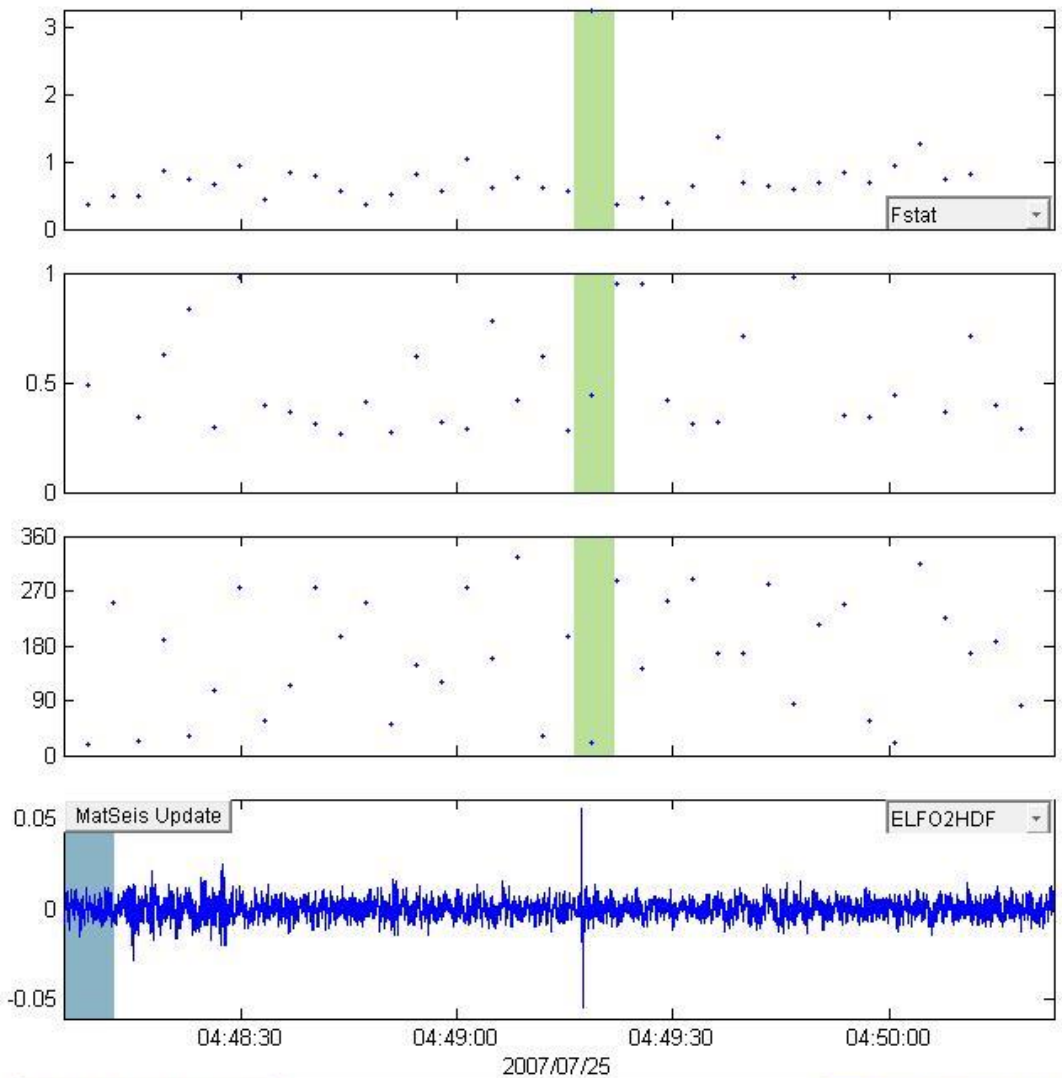
Window Parameters		Pass Band Parameters		Slowness Parameters		Windowed Values & S.D.	
Duration (s)	7.0	Low frequency (Hz)	0.7	Max. Slown.	400.0	Corr.	0.674   0.183
Overlap (%)	70.0	High frequency	4	# of Slown.	40	Fstat	11.074   10.705
Number of	68	Order (integer)	2			Vel.	0.455   0.013
						Az.	323.013   2.257

Animate				
Calculate	0	Write File	D:\Research\Research - Elizabeth\lr	Cancel



### 20070725\_044245



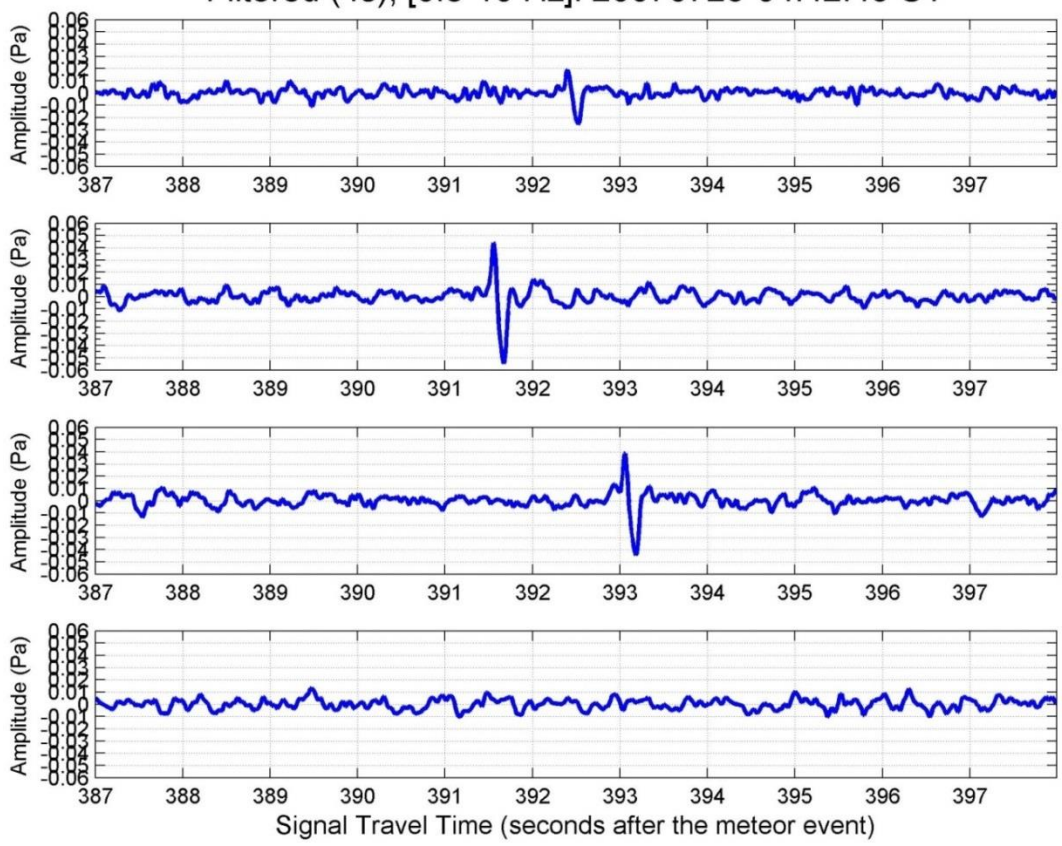
Window Parameters		Pass Band Parameters		Slowness Parameters		Windowed Values & S.D.		
Duration (s)	7.0	Low frequency (Hz)	0.6	Max. Slown.	400.0	Corr.	0.516	0.000
Overlap (%)	50.0	High frequency	15	# of Slown.	40	Fstat	3.272	0.000
Number of	38	Order (integer)	2			Vel.	0.439	0.000
						Az.	21.371	0.000

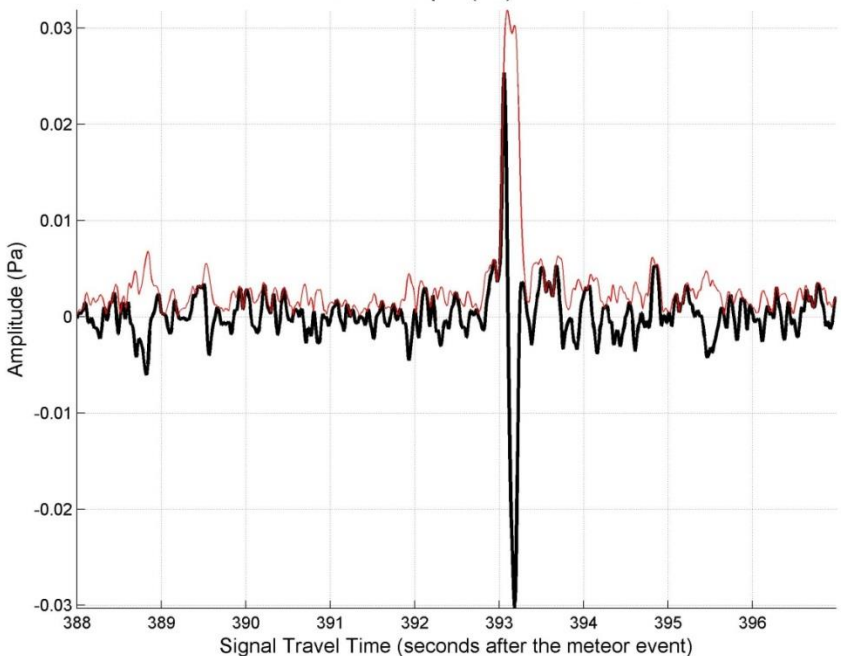
Animate				
Calculate	0	Write File	D:\Research\Research - Elizabeth\lr	Cancel



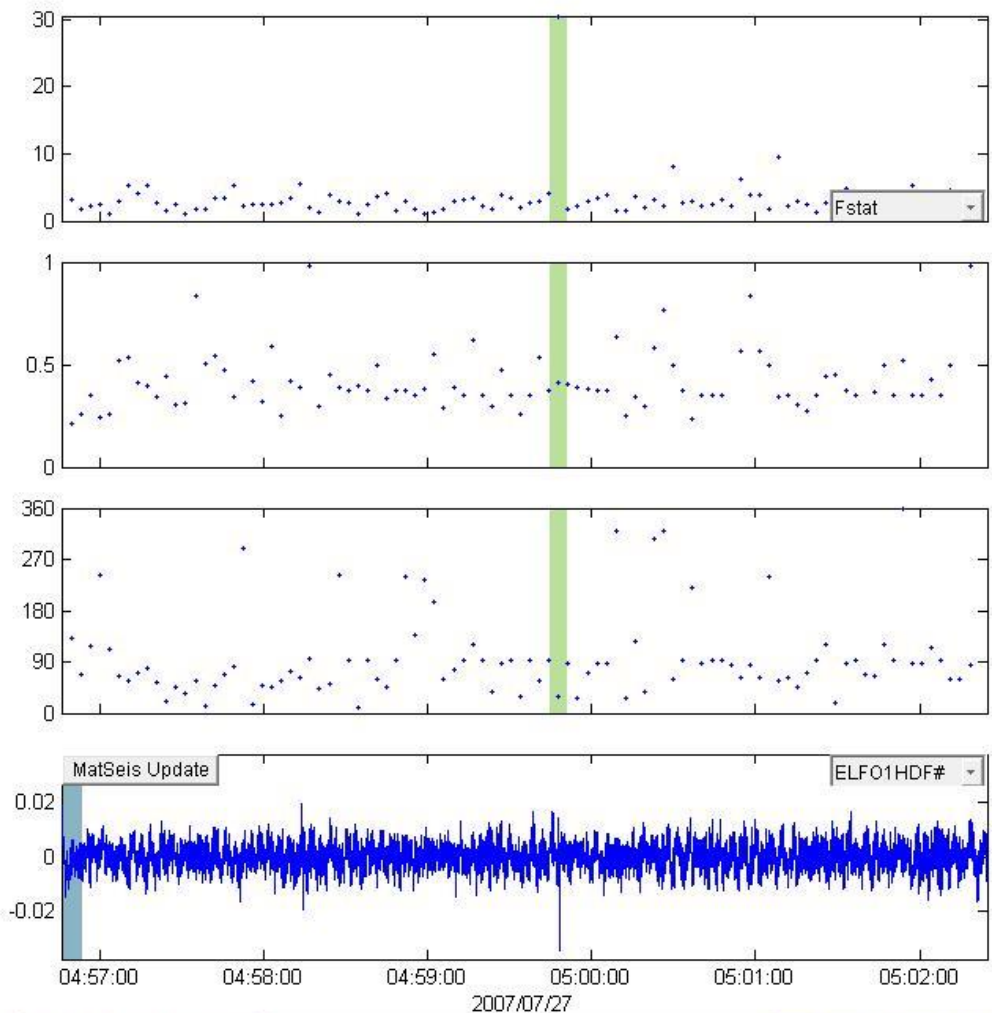
Filtered (4s), [0.8-10 Hz]: 20070725-04:42:45 UT



Hilbert Envelope (3s): 20070725



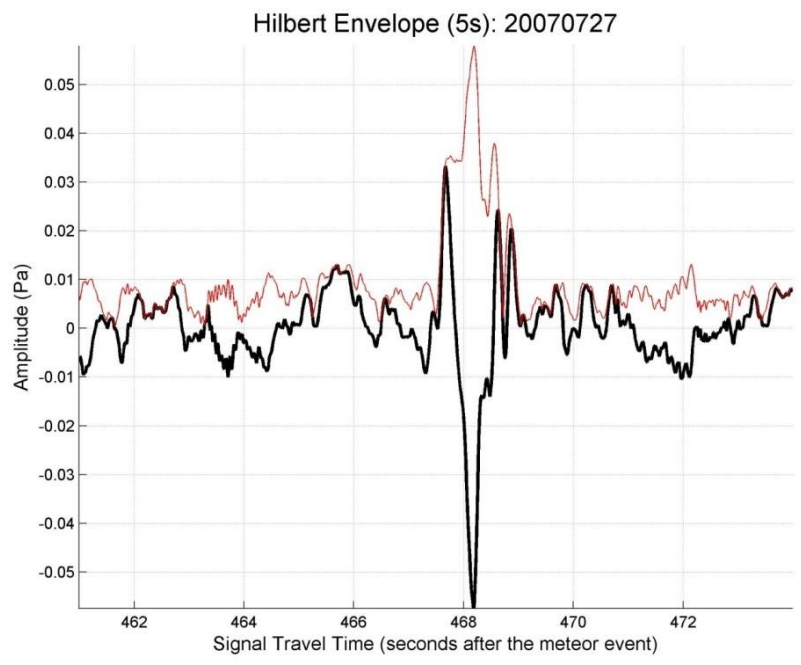
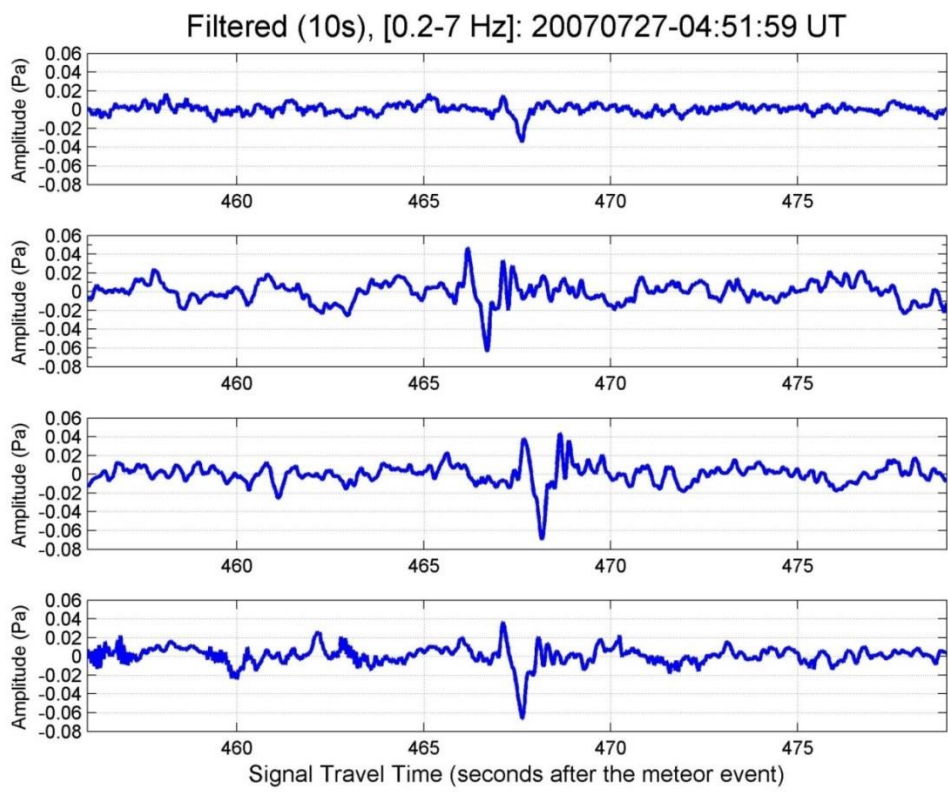
### 20070727\_045159



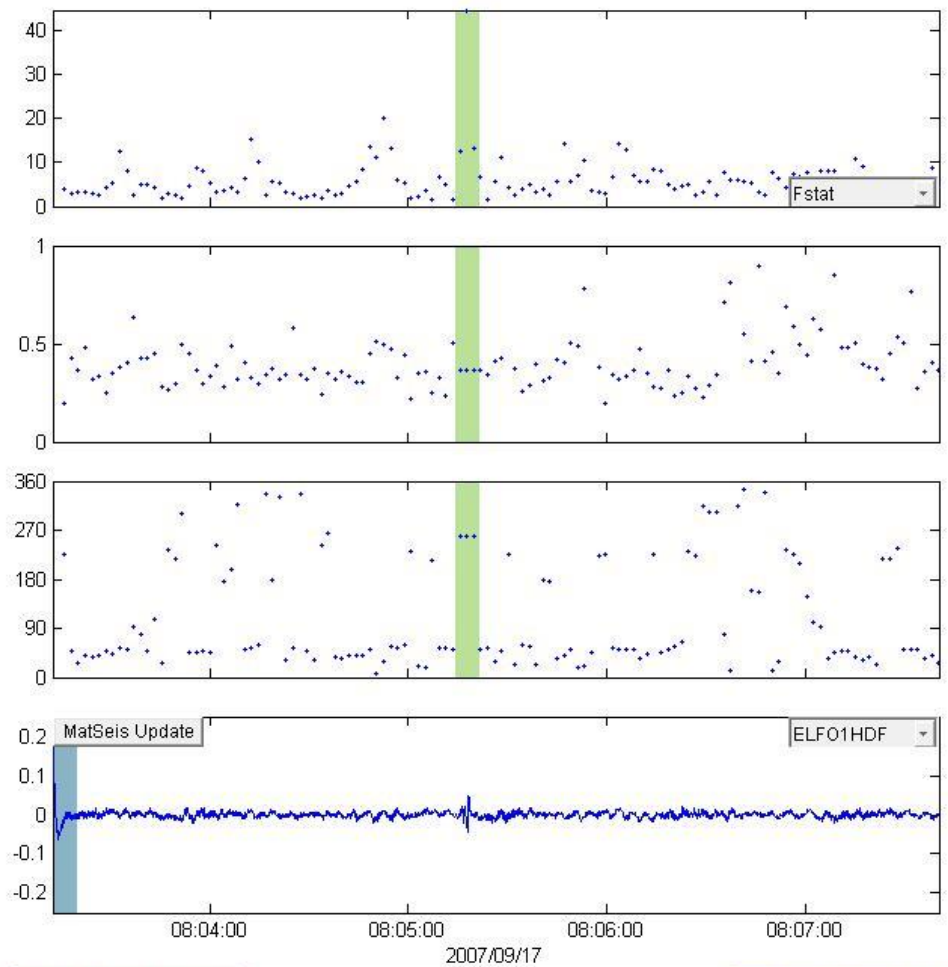
Window Parameters		Pass Band Parameters		Slowness Parameters		Windowed Values & S.D.	
Duration (s)	7.0	Low frequency (Hz)	0.2	Max. Slown.	400.0	Corr.	0.887 0.000
Overlap (%)	50.0	High frequency	7	# of Slown.	40	Fstat	30.507 0.000
Number of	95	Order (integer)	2			Vel.	0.410 0.000
						Az.	29.476 0.000

Animate			
Calculate	0	Write File	D:\Research\Research - Elizabeth\lr
			Cancel

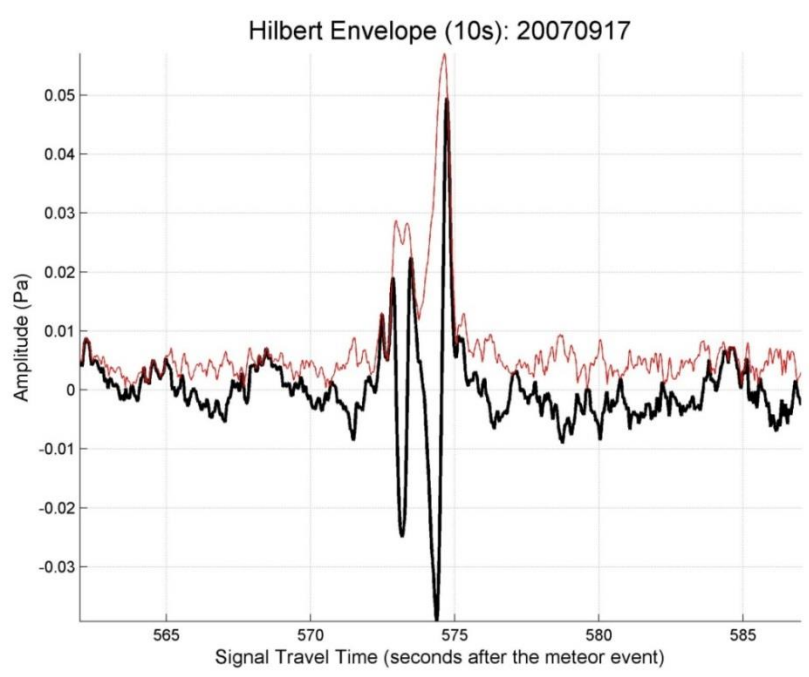
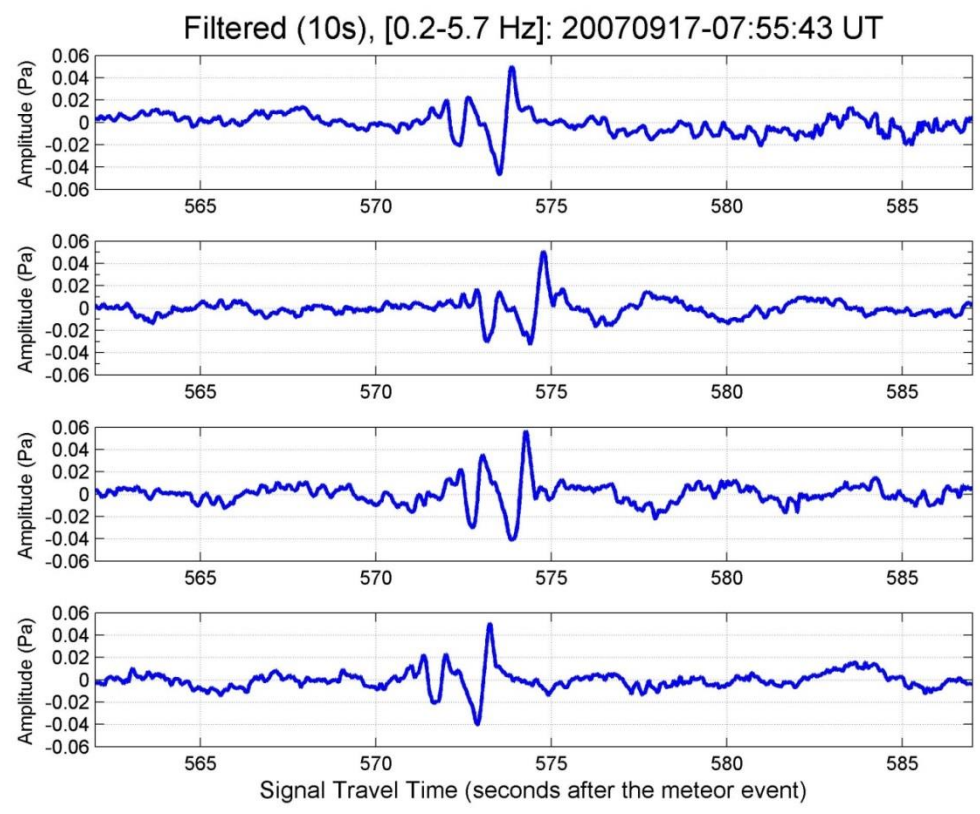


### 20070917\_075543



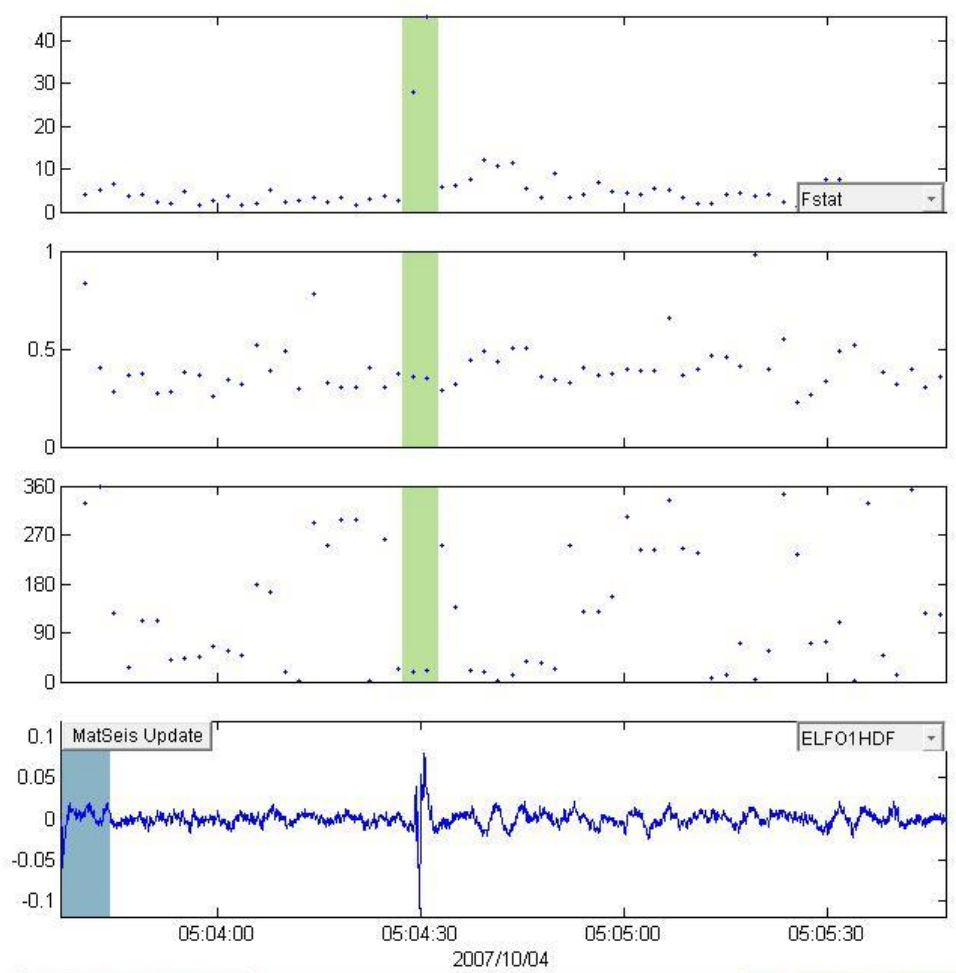
Window Parameters		Pass Band Parameters		Slowness Parameters		Windowed Values & S.D.	
Duration (s)	7.0	Low frequency (Hz)	0.2	Max. Slown.	400.0	Corr.	0.824 0.083
Overlap (%)	70.0	High frequency	6	# of Slown.	40	Fstat	23.454 18.355
Number of	127	Order (integer)	2			Vel.	0.368 0.000
						Az.	260.218 0.000

0
  D:\Research\Research - Elizabeth\lr





### 20071004\_045509



Window Parameters		Pass Band Parameters		Slowness Parameters		Windowed Values & S.D.	
Duration (s)	7.0	Low frequency (Hz)	0.2	Max. Slown.	400.0	Corr.	0.900   0.030
Overlap (%)	70.0	High frequency	8.2	# of Slown.	40	Fstat	36.850   12.469
Number of	61	Order (integer)	2			Vel.	0.353   0.005
						Az.	19.007   2.497

MatSeis Update ELFO1HDF

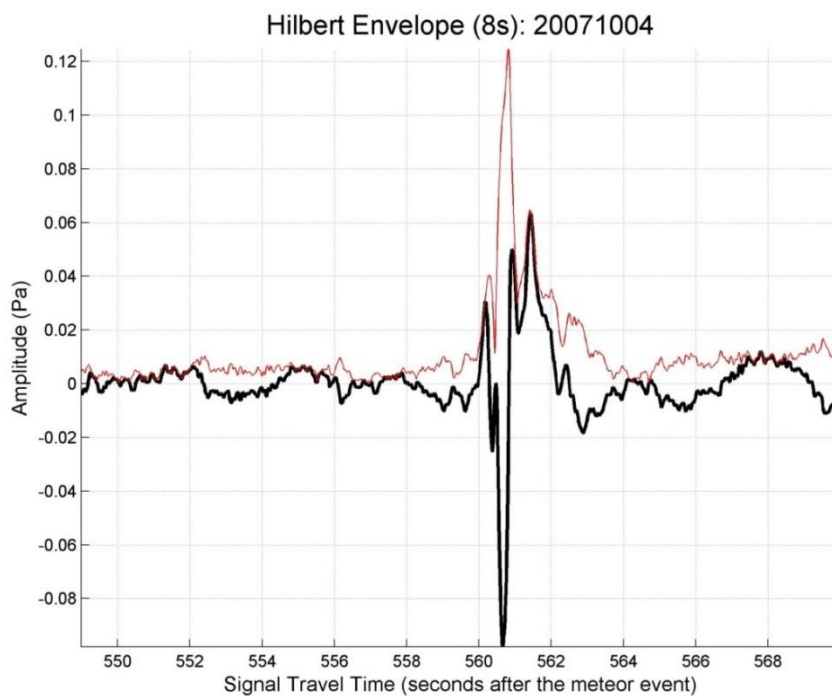
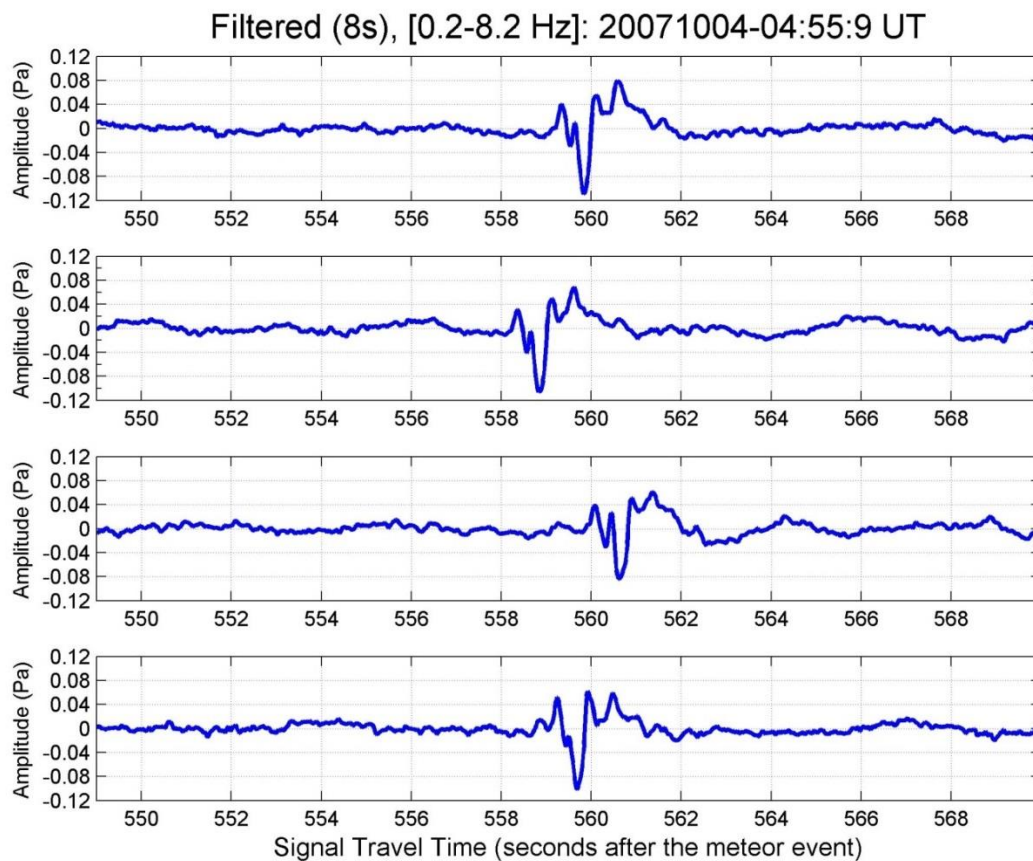
2007/10/04

05:04:00 05:04:30 05:05:00 05:05:30

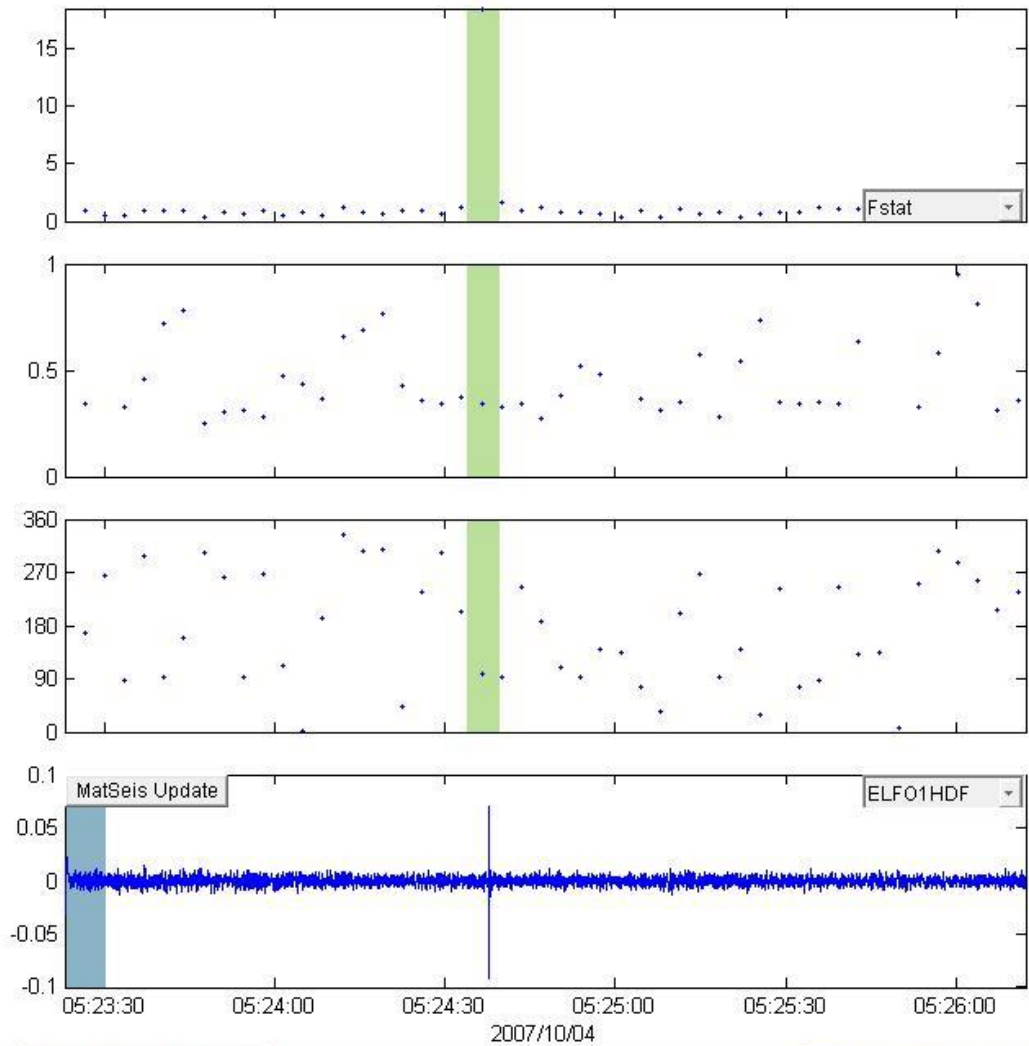
Animate

Calculate 0 Write File D:\Research\Research - Elizabeth\lr Cancel

Send to Map



### 20071004\_051927



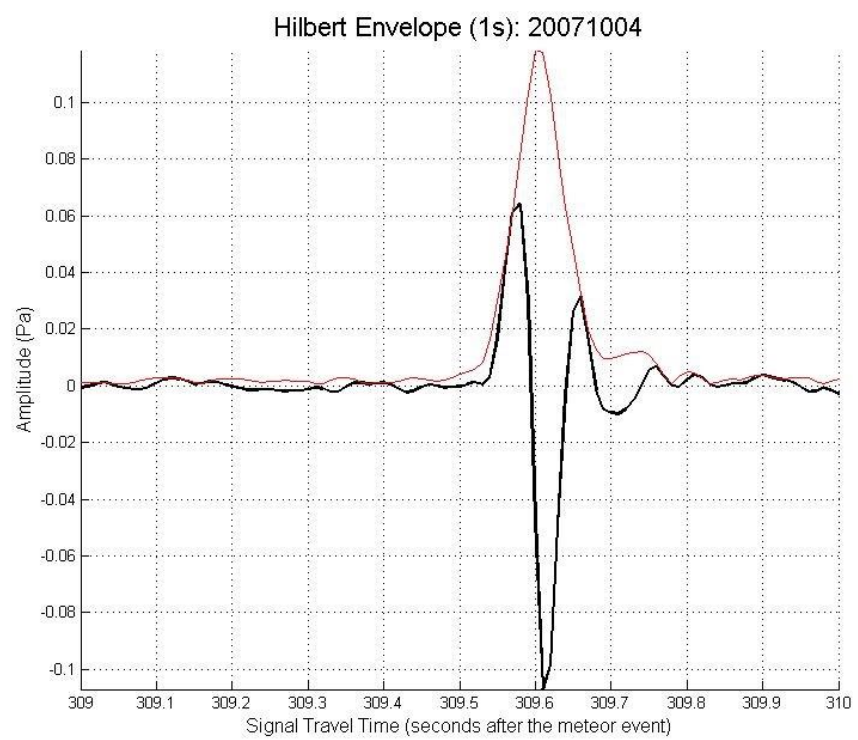
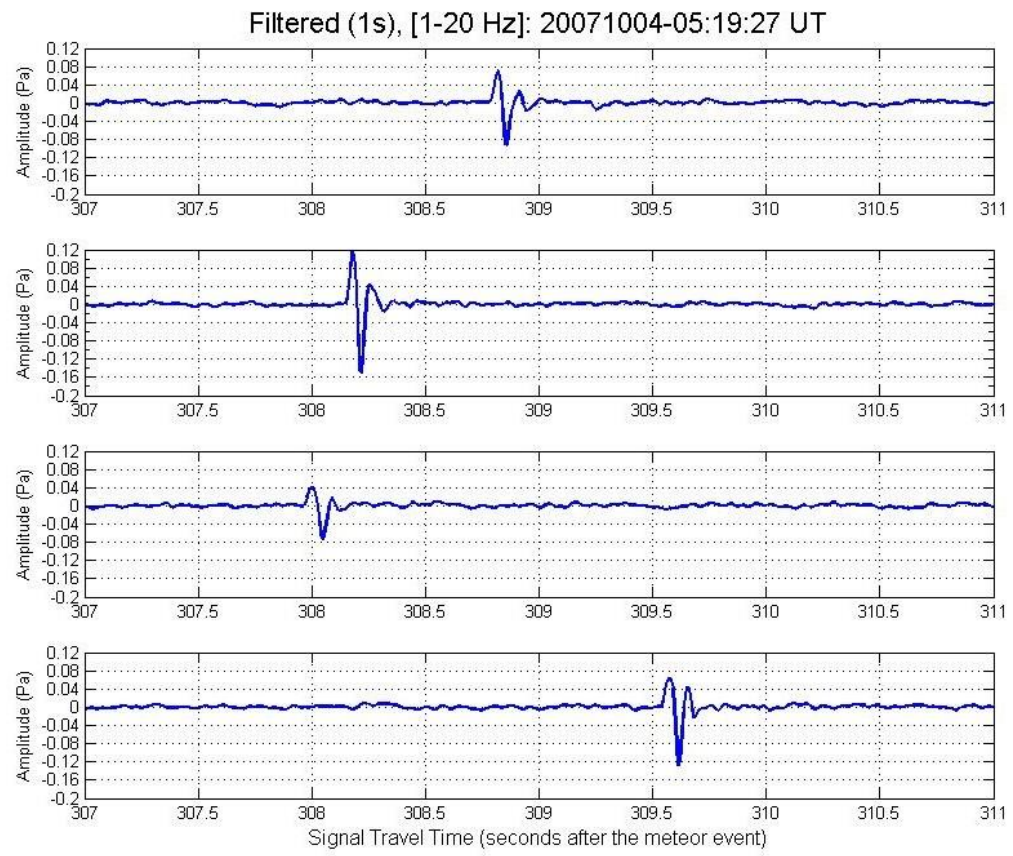
Window Parameters		Pass Band Parameters		Slowness Parameters		Windowed Values & S.D.	
Duration (s)	7.0	Low frequency (Hz)	1	Max. Slown.	400.0	Corr.	0.829   0.000
Overlap (%)	50.0	High frequency	20	# of Slown.	40	Fstat	18.446   0.000
Number of	48	Order (integer)	2			Vel.	0.345   0.000
						Az.	99.162   0.000

MatSeis Update ELFO1HDF

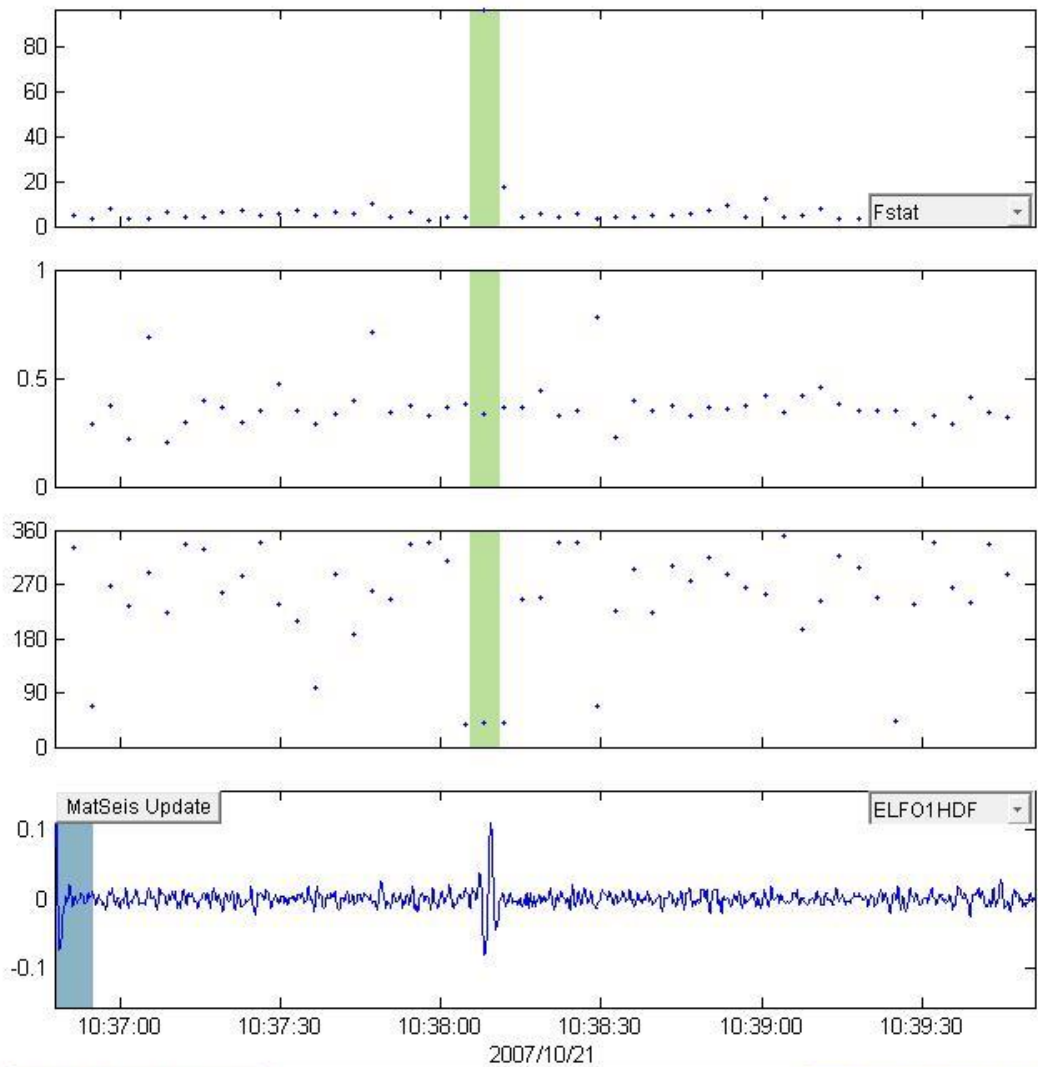
2007/10/04

Animate  Calculate  0  D:\Research\Research - Elizabeth\lr





### 20071021\_102625

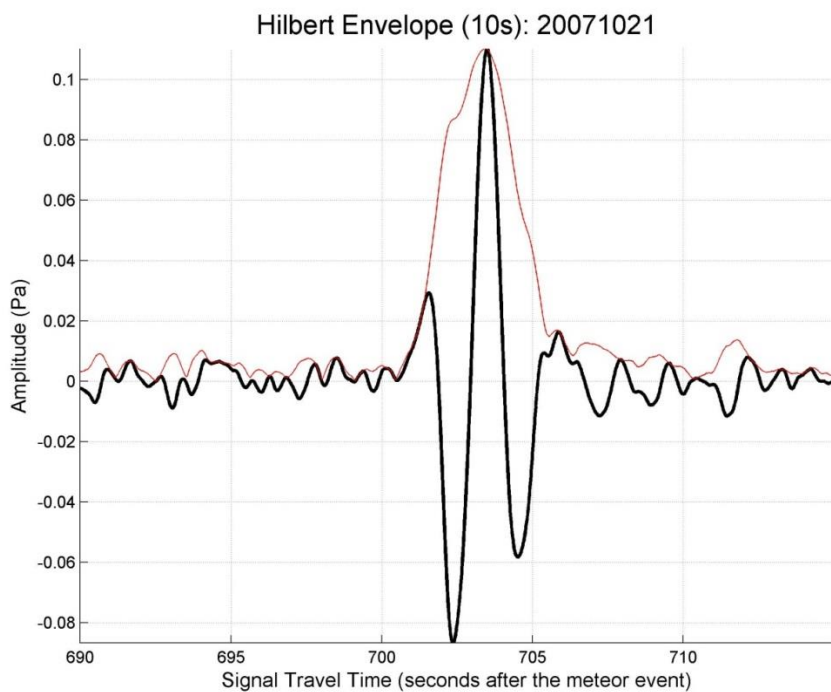
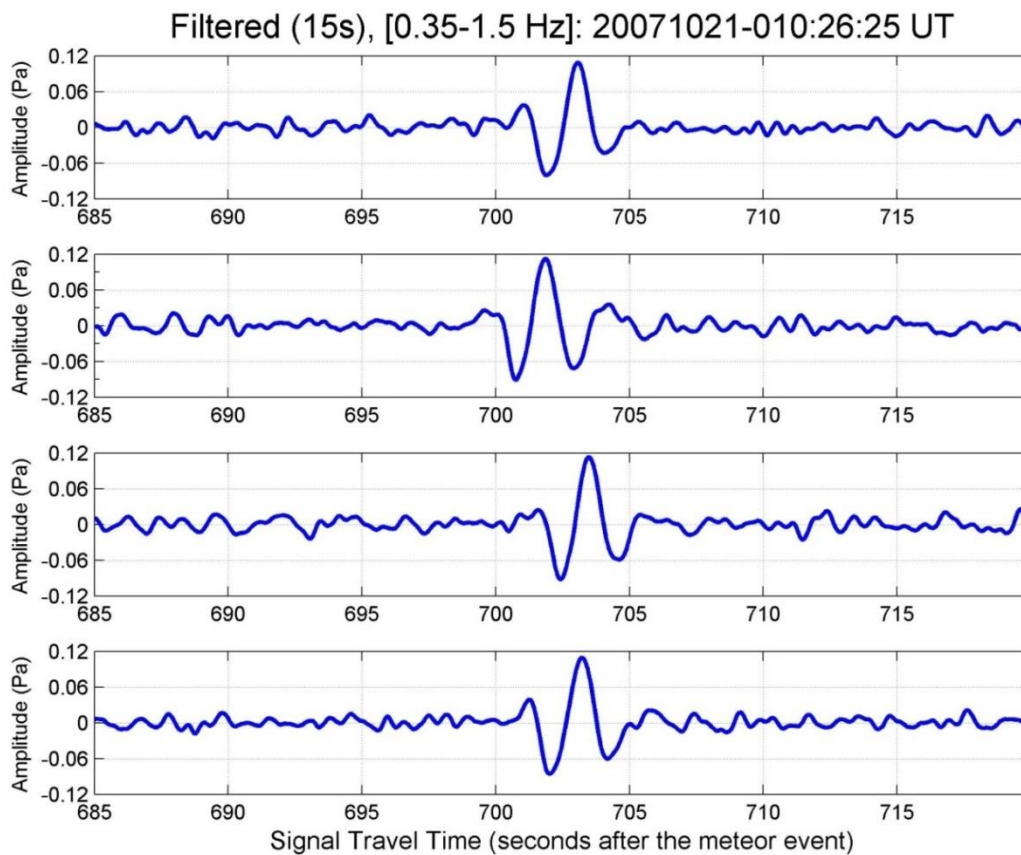


Window Parameters		Pass Band Parameters		Slowness Parameters		Windowed Values & S.D.	
Duration (s)	7.0	Low frequency (Hz)	0.35	Max. Slown.	400.0	Corr.	0.961   0.000
Overlap (%)	50.0	High frequency	1.5	# of Slown.	40	Fstat	97.113   0.000
Number of	51	Order (integer)	2			Vel.	0.332   0.000
						Az.	40.030   0.000

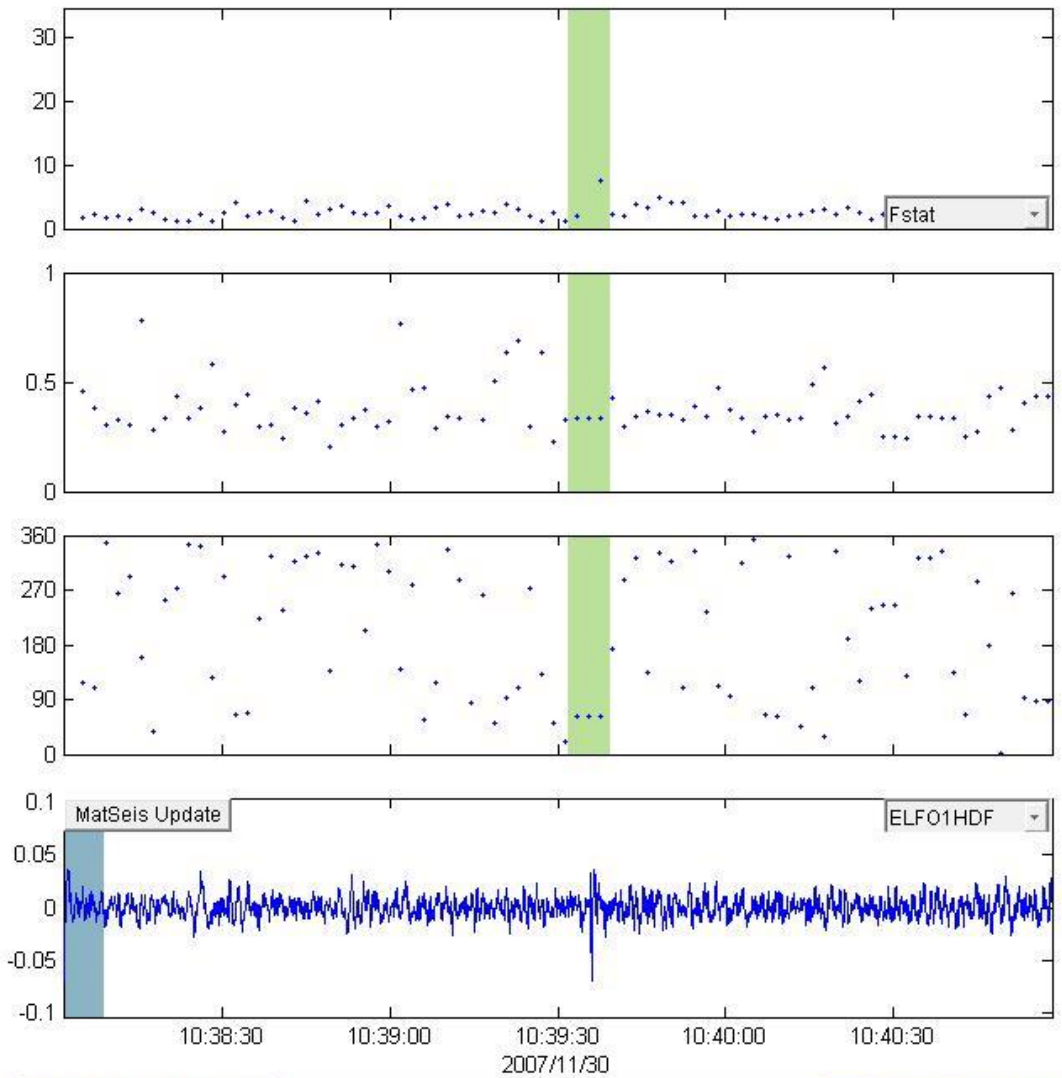
MatSeis Update ELFO1HDF

2007/10/21

Animate  Calculate  Write File  Send to Map



### 20071130\_102849



Window Parameters		Pass Band Parameters		Slowness Parameters		Windowed Values & S.D.	
Duration (s)	7.0	Low frequency (Hz)	0.5	Max. Slown.	400.0	Corr.	0.672 0.233
Overlap (%)	70.0	High frequency	6	# of Slown.	40	Fstat	14.716 17.321
Number of	83	Order (integer)	2			Vel.	0.332 0.000
						Az.	62.650 0.000

MatSeis Update

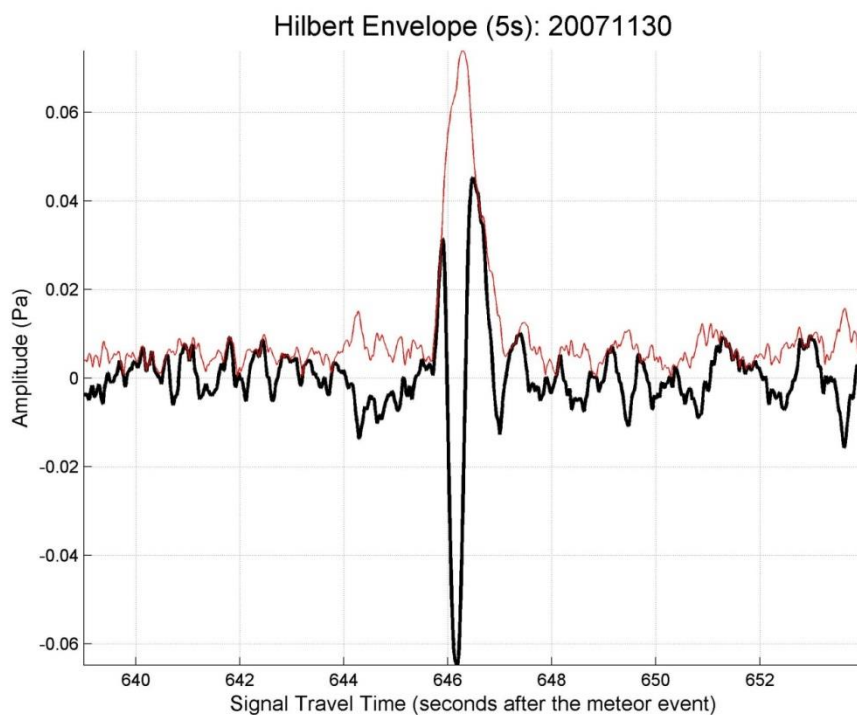
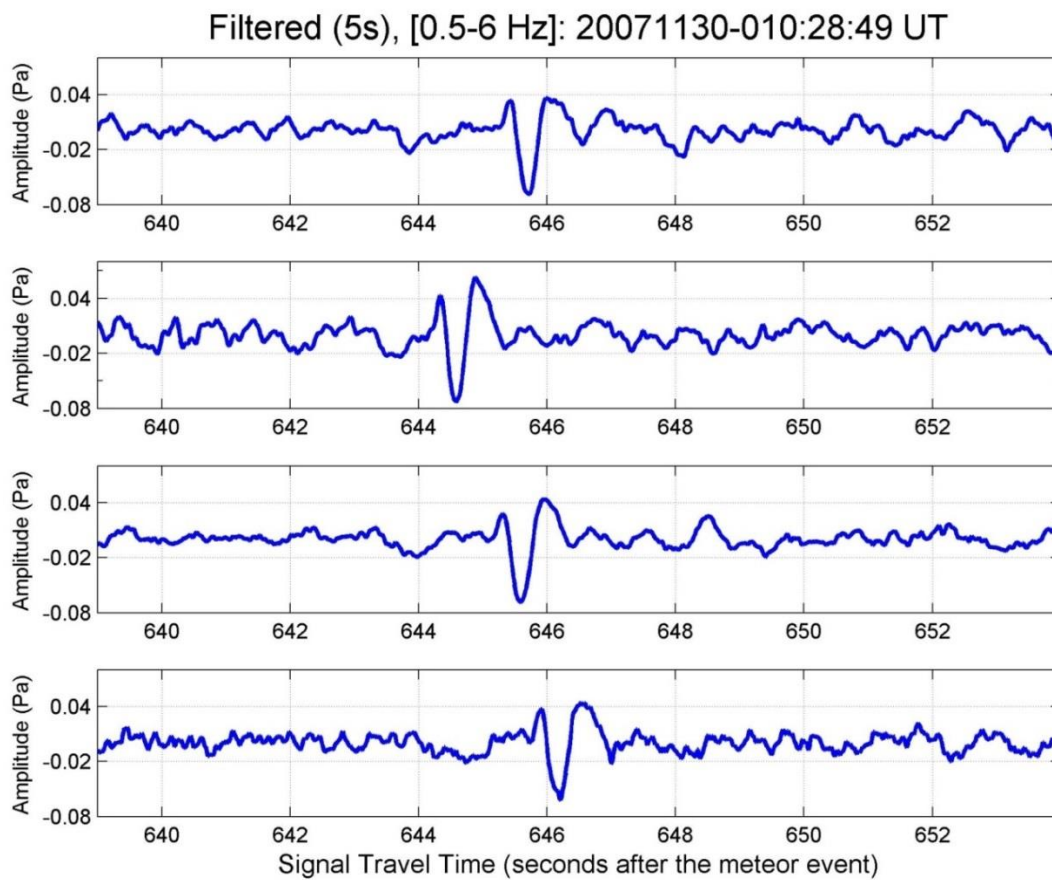
Animate

Calculate

Write File

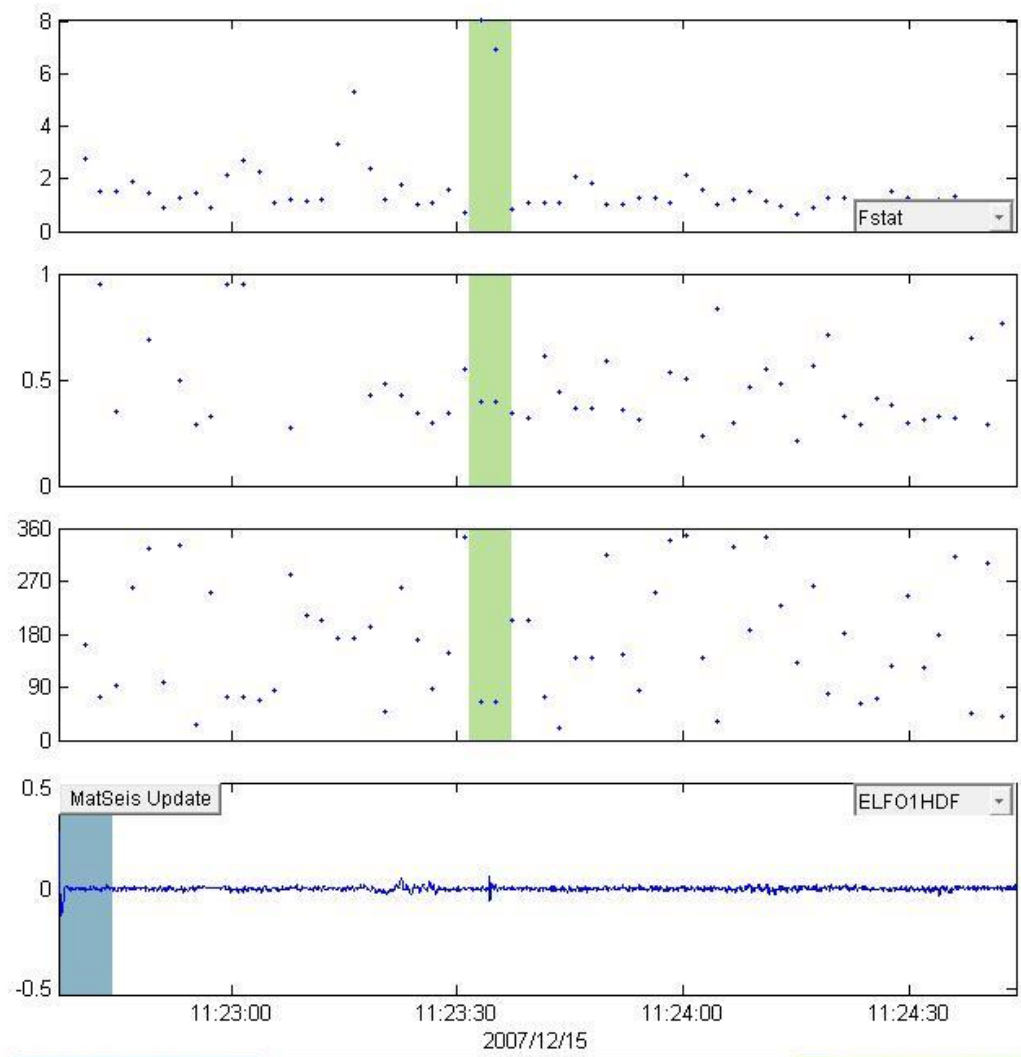
Send to Map

Cancel





### 20071215\_111813

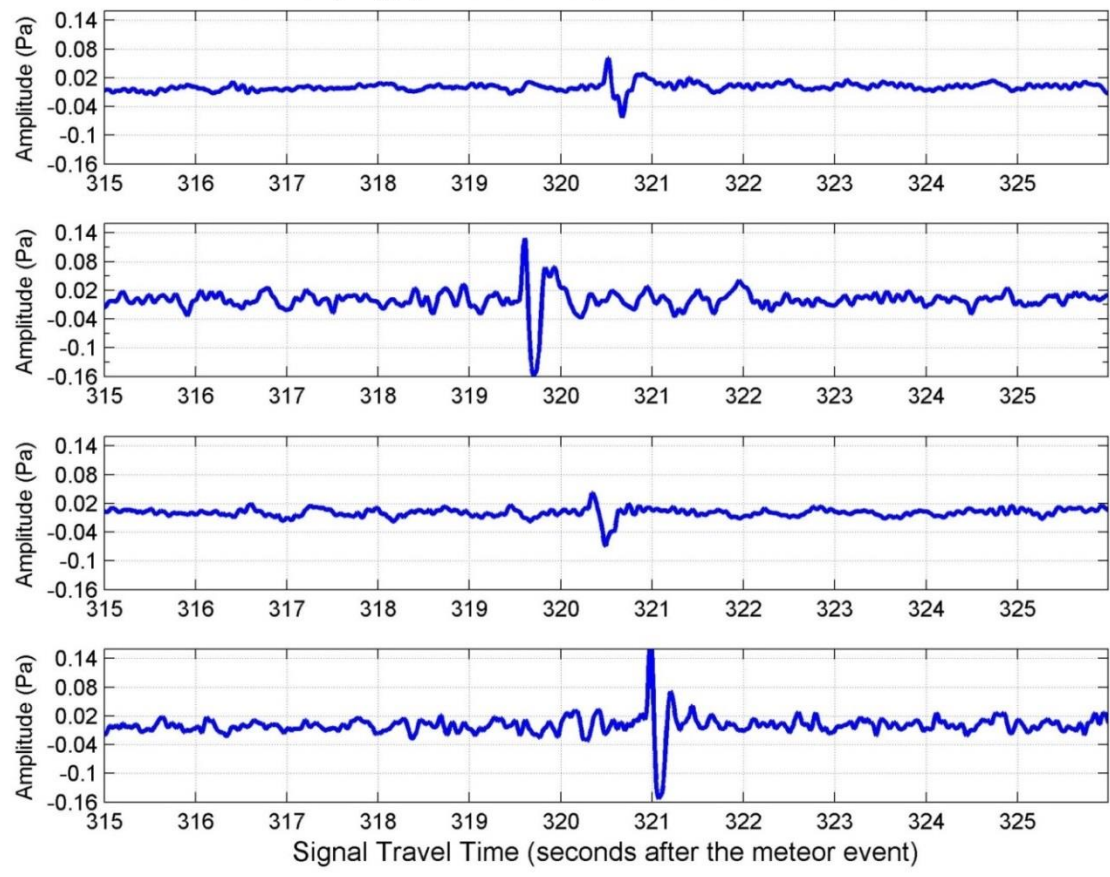


Window Parameters		Pass Band Parameters		Slowness Parameters		Windowed Values & S.D.	
Duration (s)	7.0	Low frequency (Hz)	0.9	Max. Slown.	400.0	Corr.	0.680 0.021
Overlap (%)	70.0	High frequency	11	# of Slown.	40	Fstat	7.511 0.802
Number of	59	Order (integer)	2			Vel.	0.397 0.000
						Az.	66.251 0.000

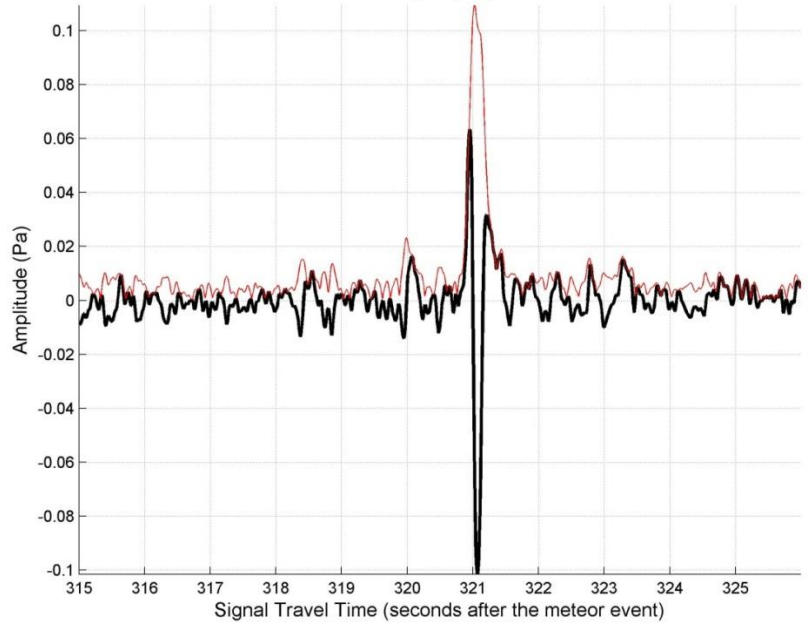
  

Animate			
Calculate	0	Write File	D:\Research\Research - Elizabeth\lr
			Send to Map
			Cancel

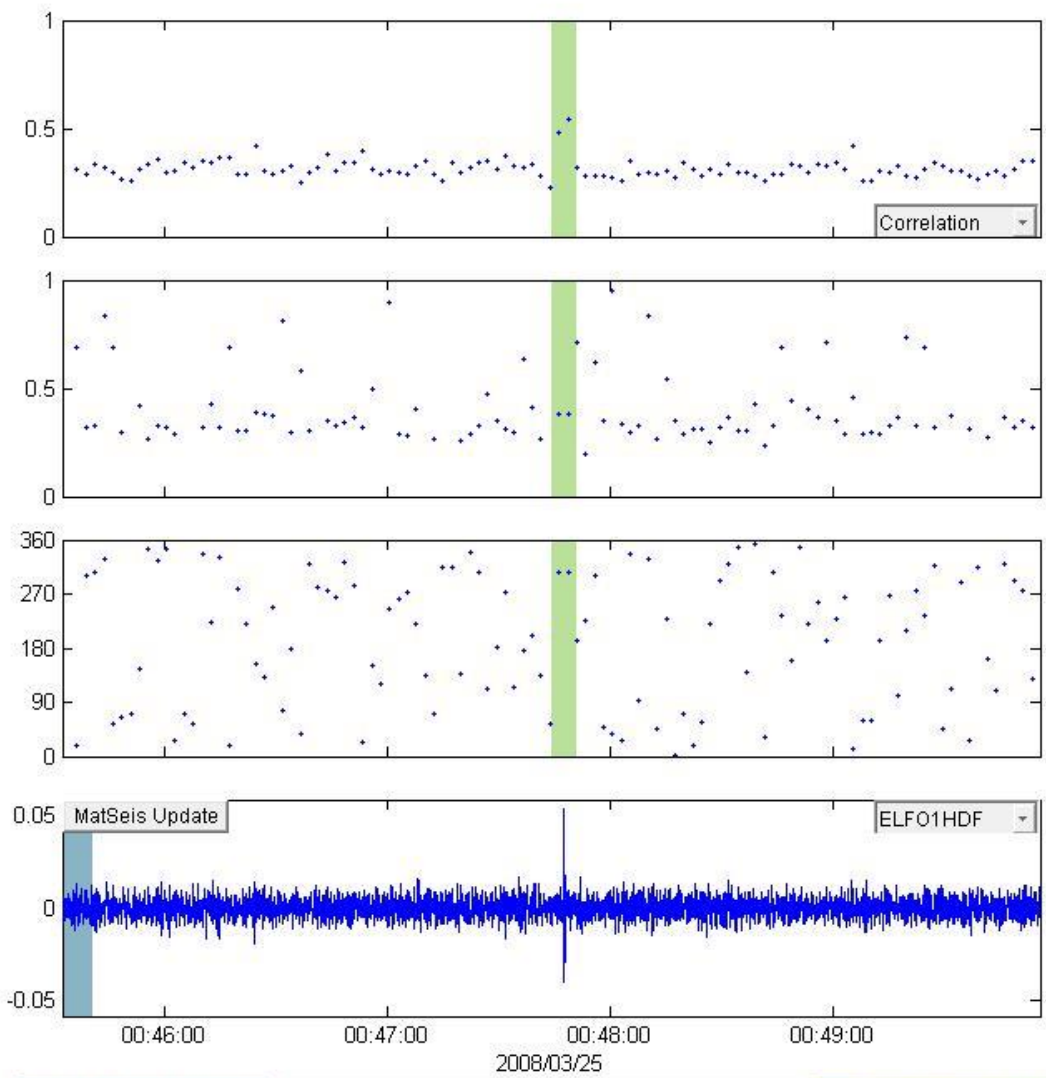
Filtered (3s), [0.85-11 Hz]: 20071215-011:18:13 UT



Hilbert Envelope (3s): 20071215



### 20080325\_004203

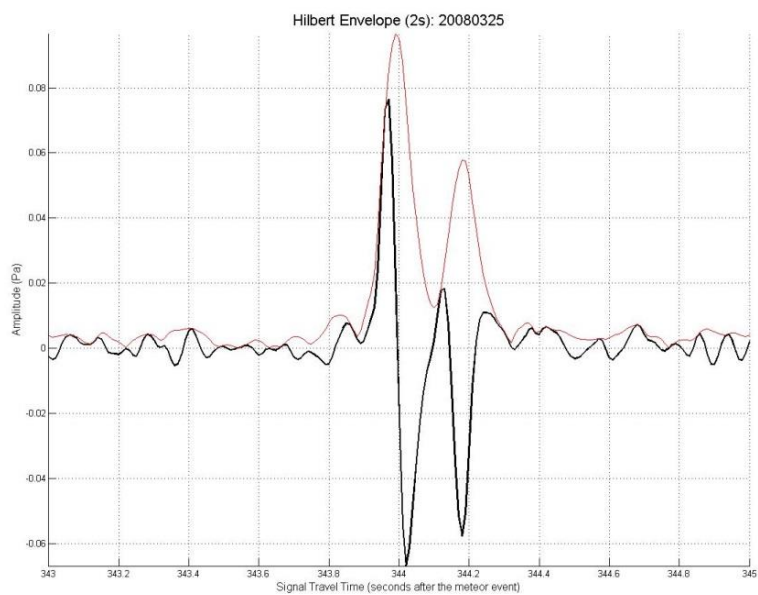
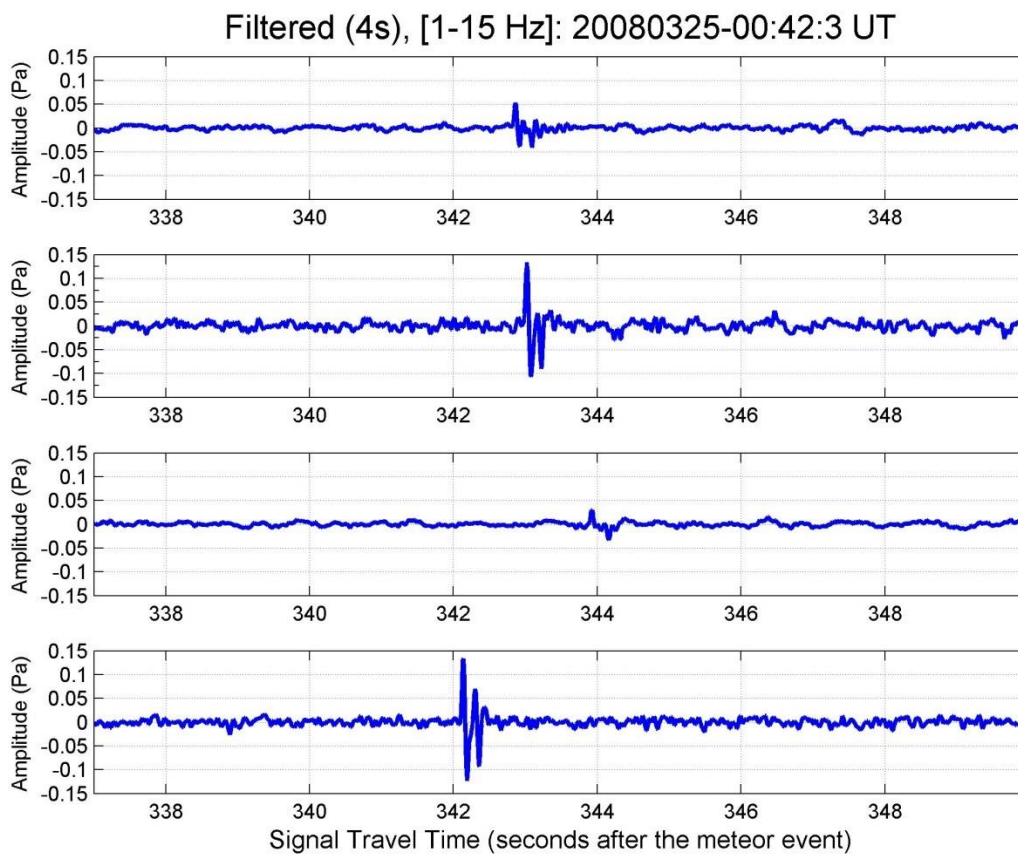


Window Parameters		Pass Band Parameters		Slowness Parameters		Windowed Values & S.D.	
Duration (s)	8.0	Low frequency (Hz)	1	Max. Slown.	400.0	Corr.	0.511   0.040
Overlap (%)	70.0	High frequency	15	# of Slown.	40	Fstat	3.214   0.666
Number of	108	Order (integer)	2			Vel.	0.379   0.000
						Az.	306.469   0.000

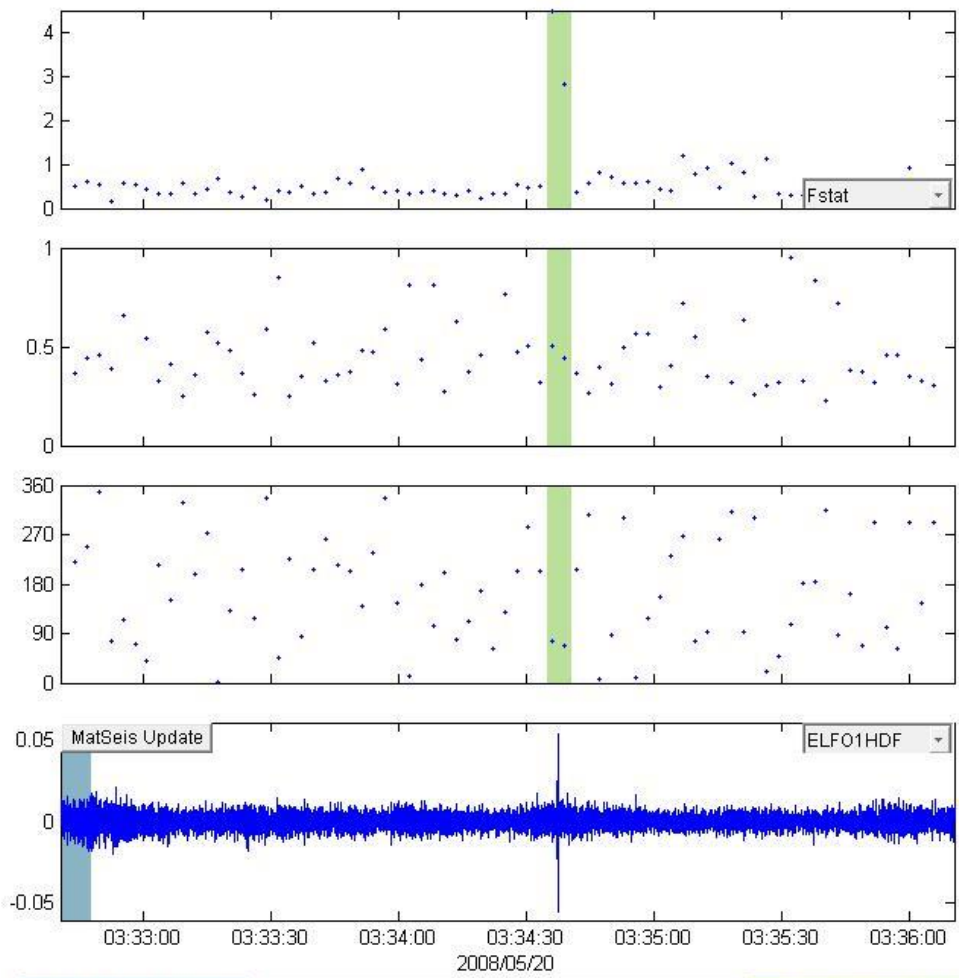
MatSeis Update      ELFO1HDF

Animate      Calculate      0      Write File      D:\Research\Research - Elizabeth\lr      Send to Map      Cancel



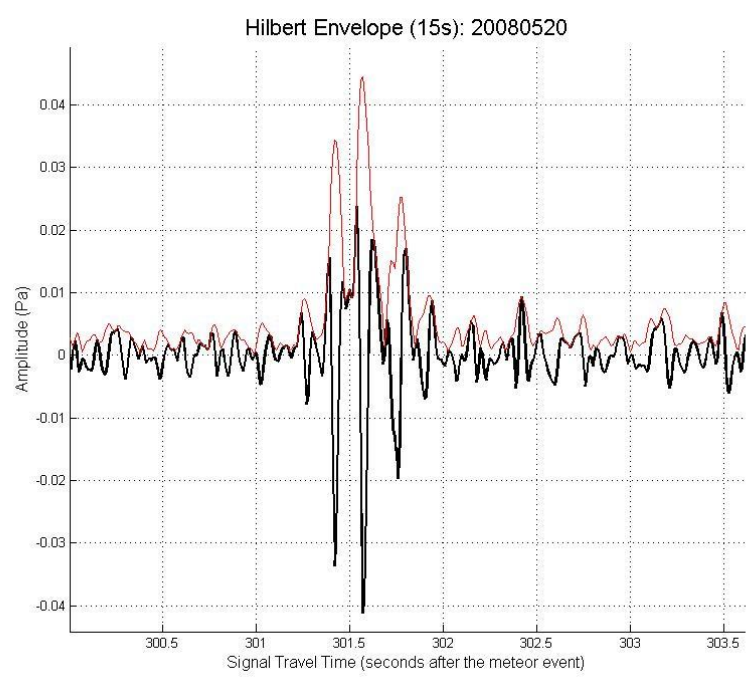
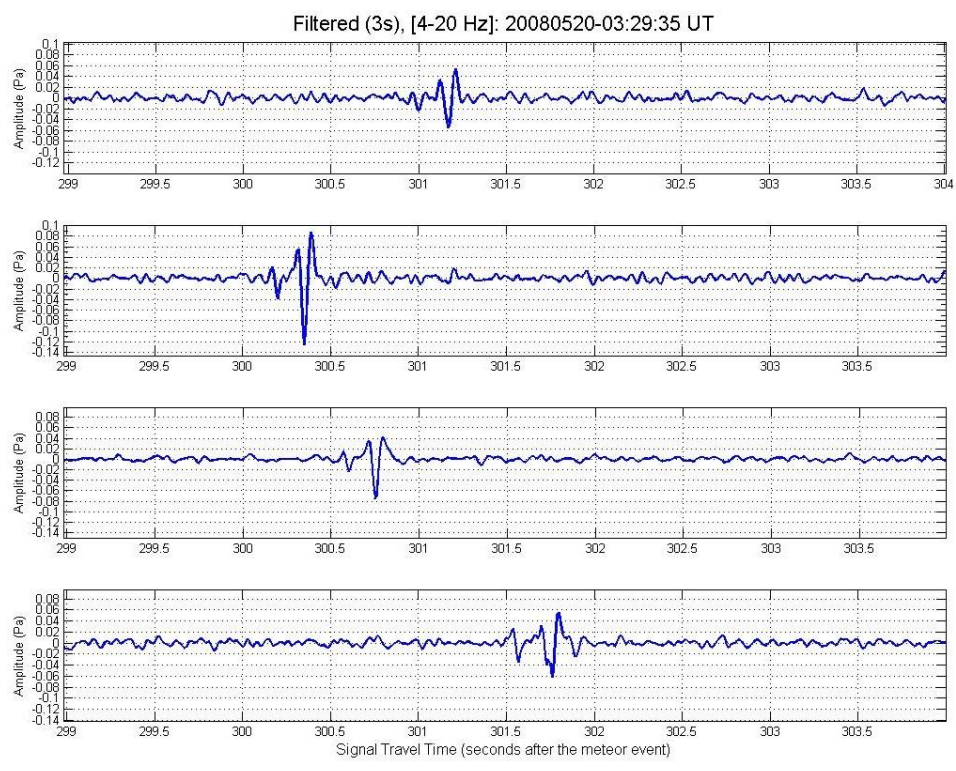


### 20080520\_032935

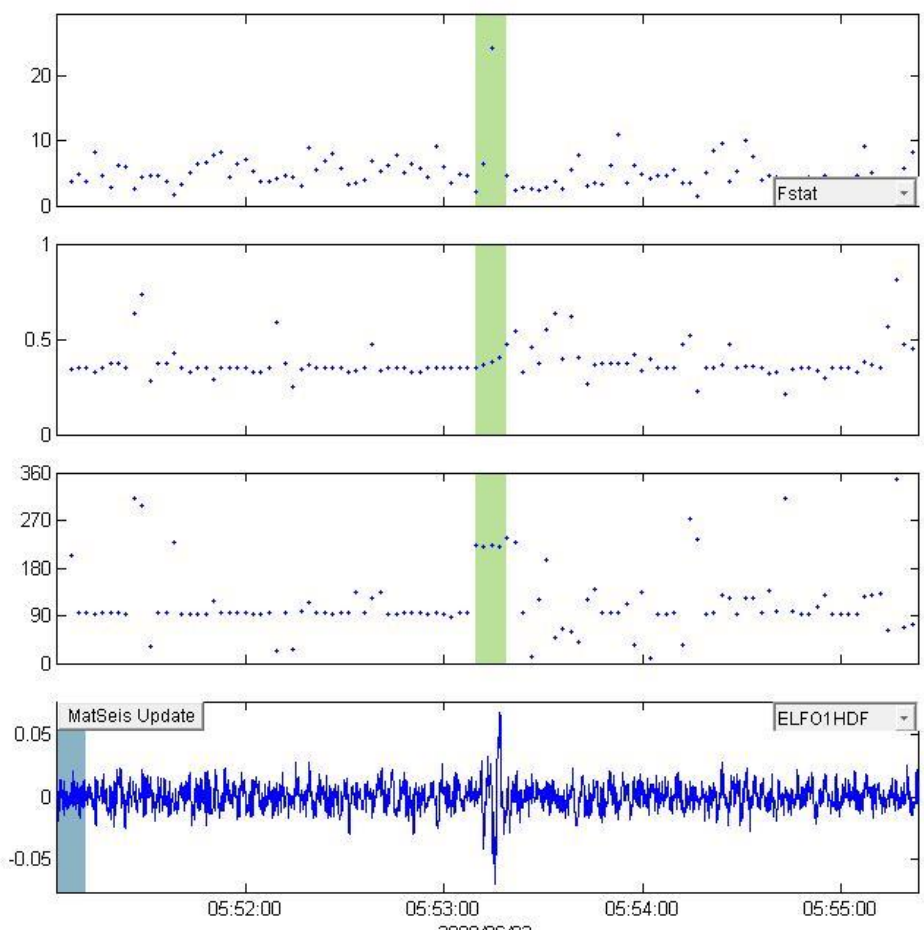


Window Parameters		Pass Band Parameters		Slowness Parameters		Windowed Values & S.D.		
Duration (s)	7	Low frequency (Hz)	4	Max. Slown.	400.0	Corr.	0.533	0.064
Overlap (%)	60.0	High frequency	20	# of Slown.	40	Fstat	3.652	1.188
Number of	73	Order (integer)	2			Vel.	0.470	0.045
						Az.	72.618	5.641

Animate  Calculate 0 Write File D:\Research\Research - Elizabeth\lr Send to Map Cancel



### 20080602\_054441



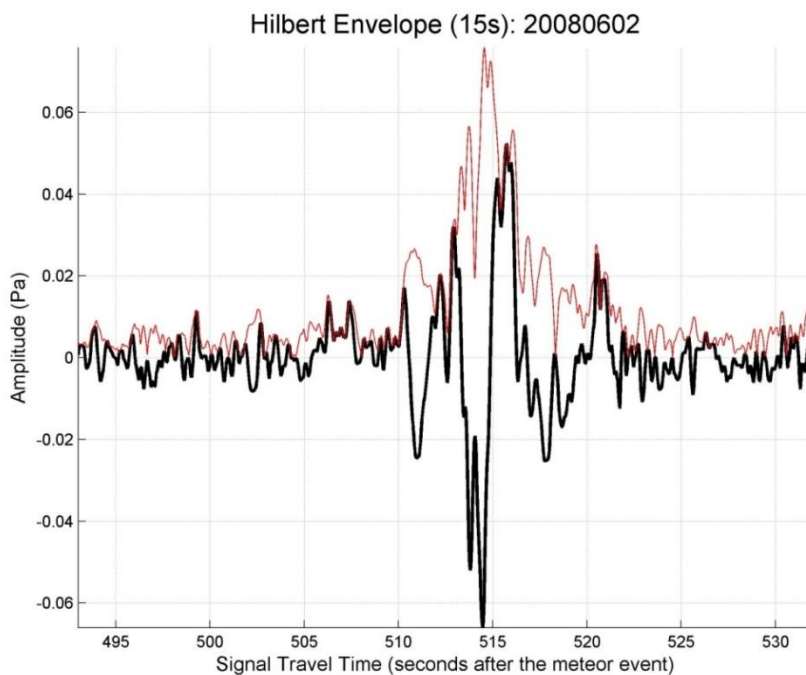
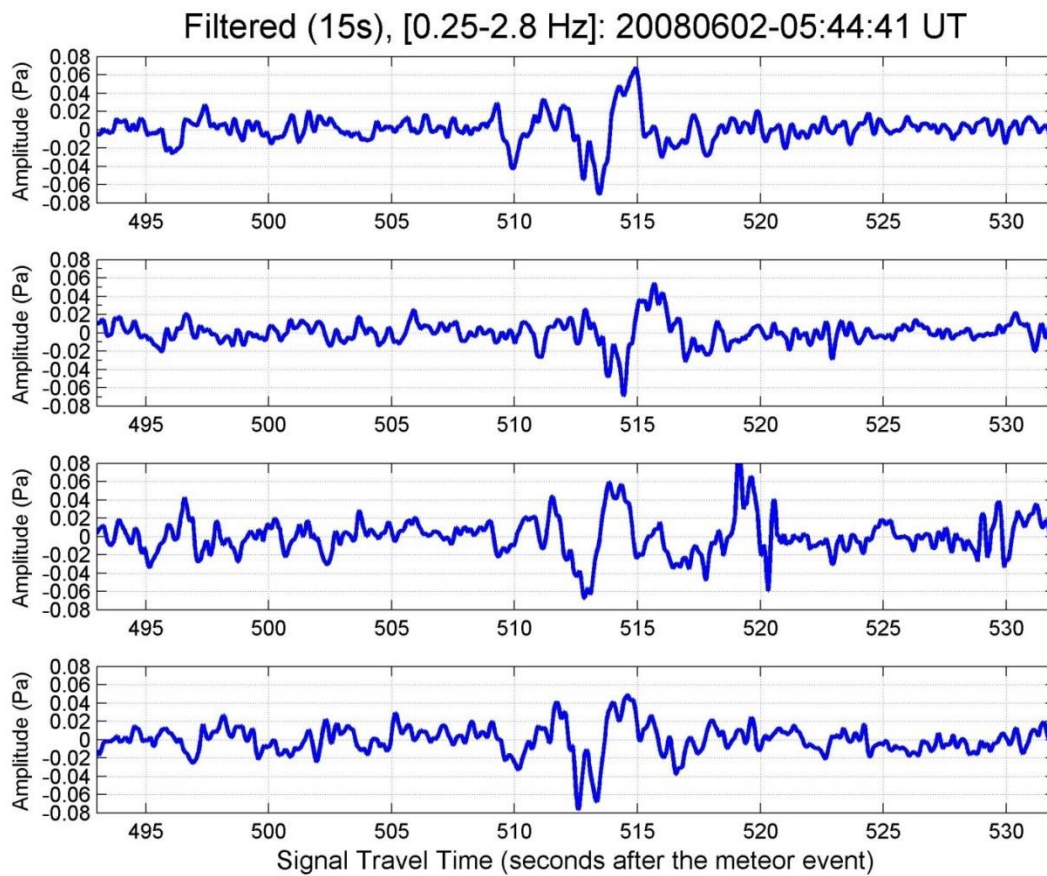
Window Parameters		Pass Band Parameters		Slowness Parameters		Windowed Values & S.D.	
Duration (s)	8	Low frequency (Hz)	0.25	Max. Slown.	400.0	Corr.	0.798 0.130
Overlap (%)	70.0	High frequency	2.8	# of Slown.	40	Fstat	19.884 11.987
Number of	107	Order (integer)	2			Vel.	0.382 0.019
						Az.	220.229 1.677

MatSeis Update ELF01HDF

2008/06/02

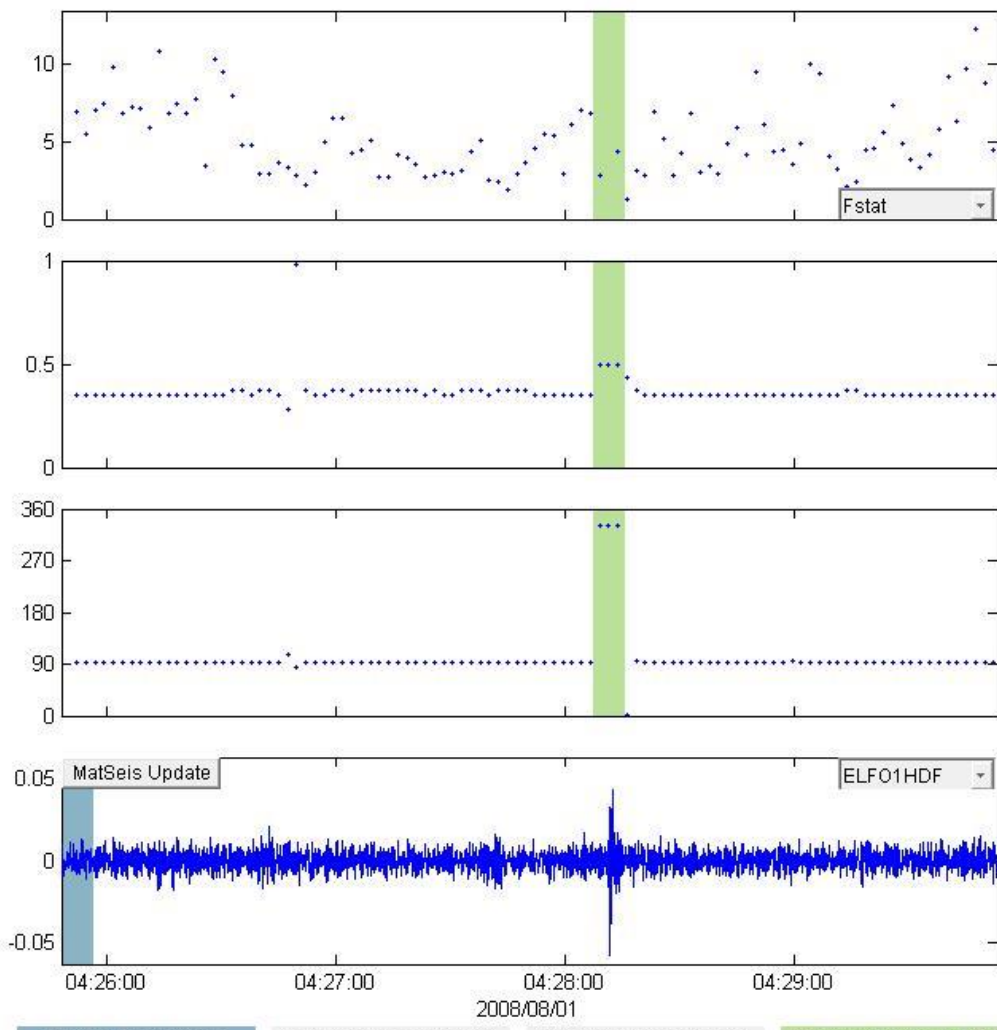
05:52:00 05:53:00 05:54:00 05:55:00

Calculate  0  \20080325\_004203\infrasound-da





### 20080801\_042220



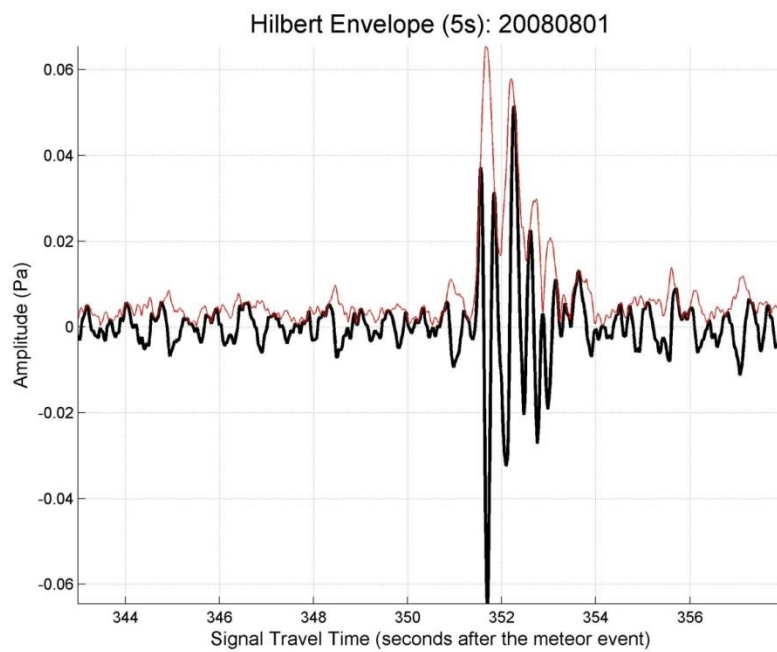
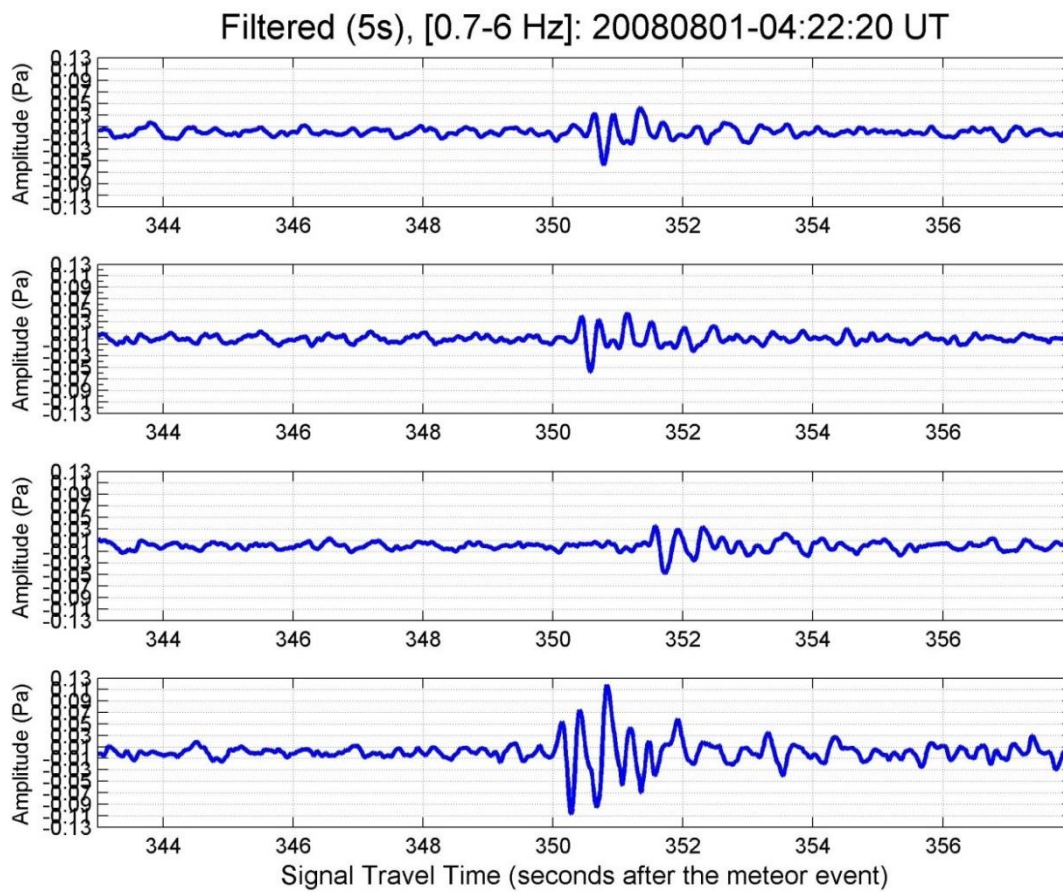
Window Parameters		Pass Band Parameters		Slowness Parameters		Windowed Values & S.D.	
Duration (s)	8	Low frequency (Hz)	0.7	Max. Slown.	400.0	Corr.	0.612 0.153
Overlap (%)	70.0	High frequency	6	# of Slown.	40	Fstat	6.800 5.698
Number of	101	Order (integer)	2			Vel.	0.494 0.000
						Az.	329.931 0.000

MatSeis Update ELFO1HDF

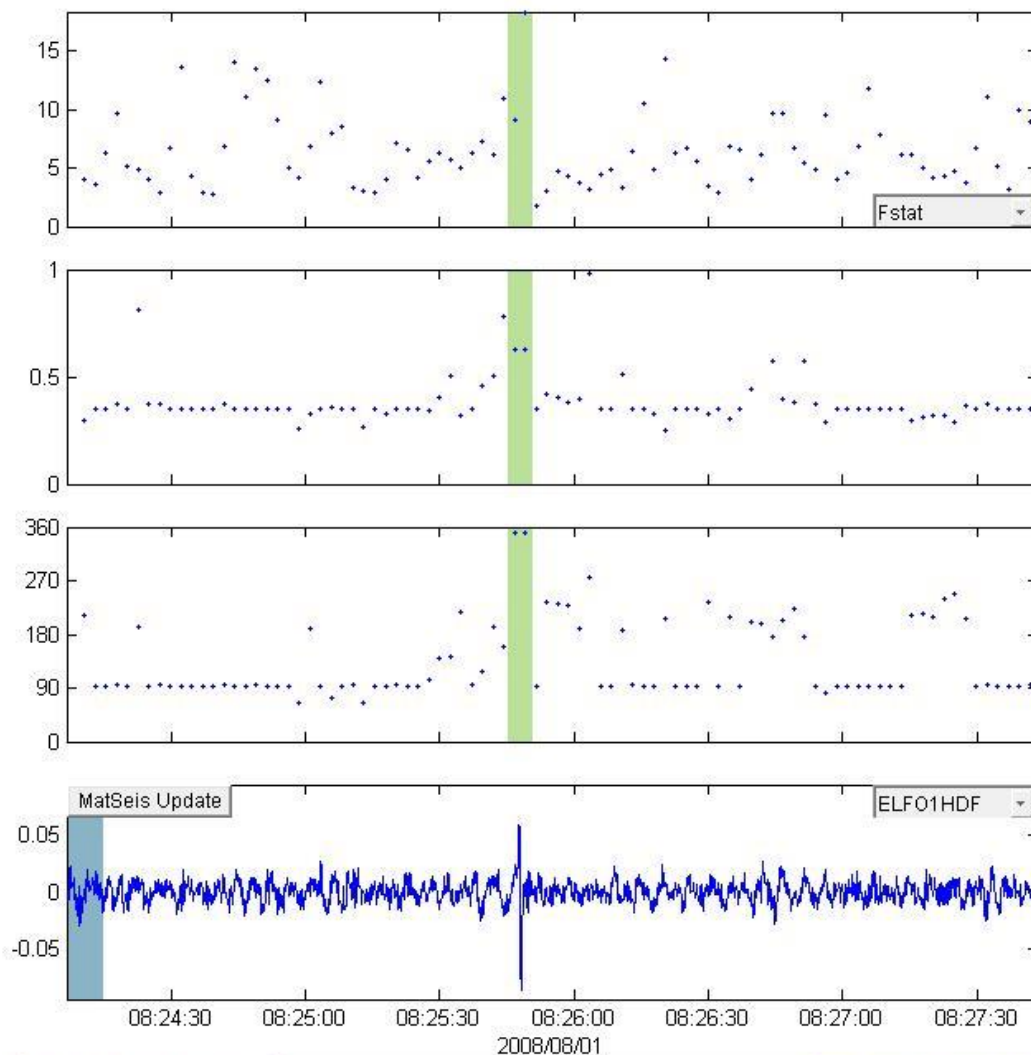
2008/08/01

Animate  Calculate 0

Write File 8\20080325\_004203\infrasound-da Send to Map Cancel

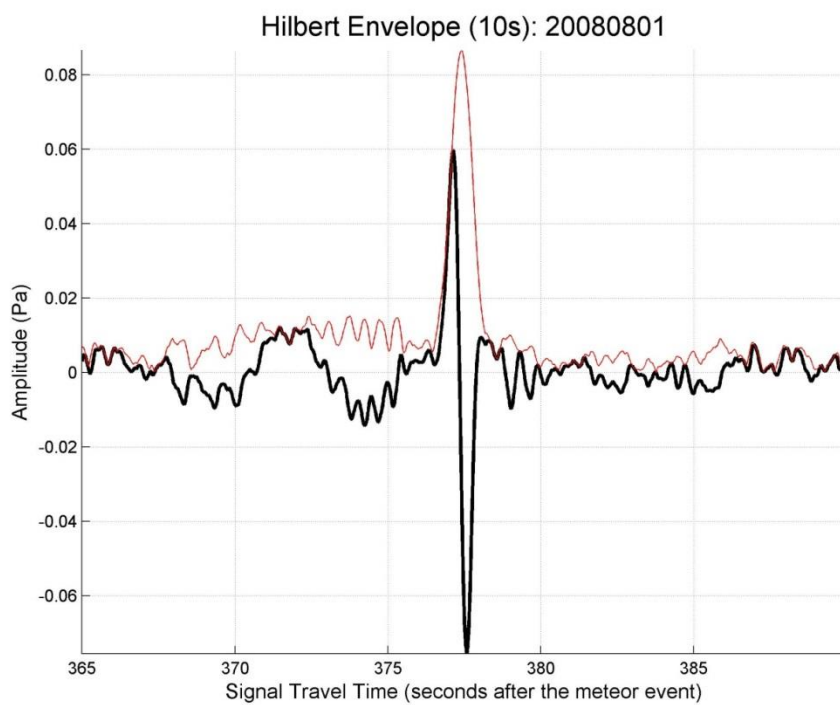
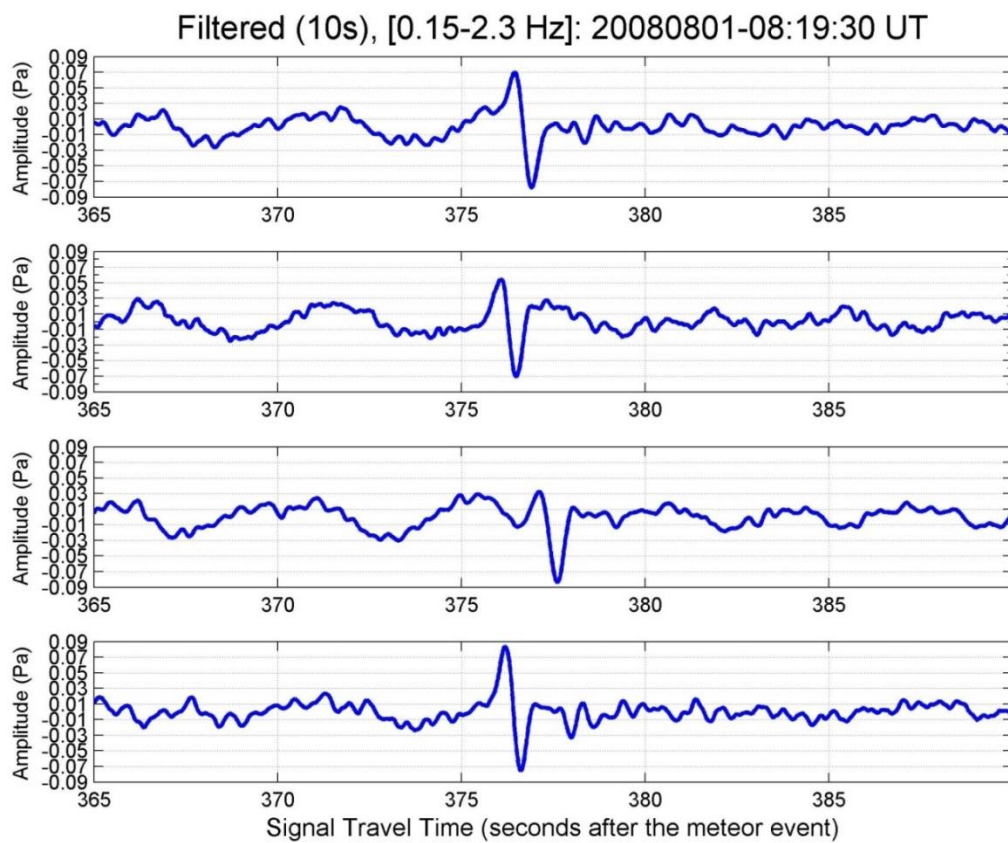


### 20080801\_081930

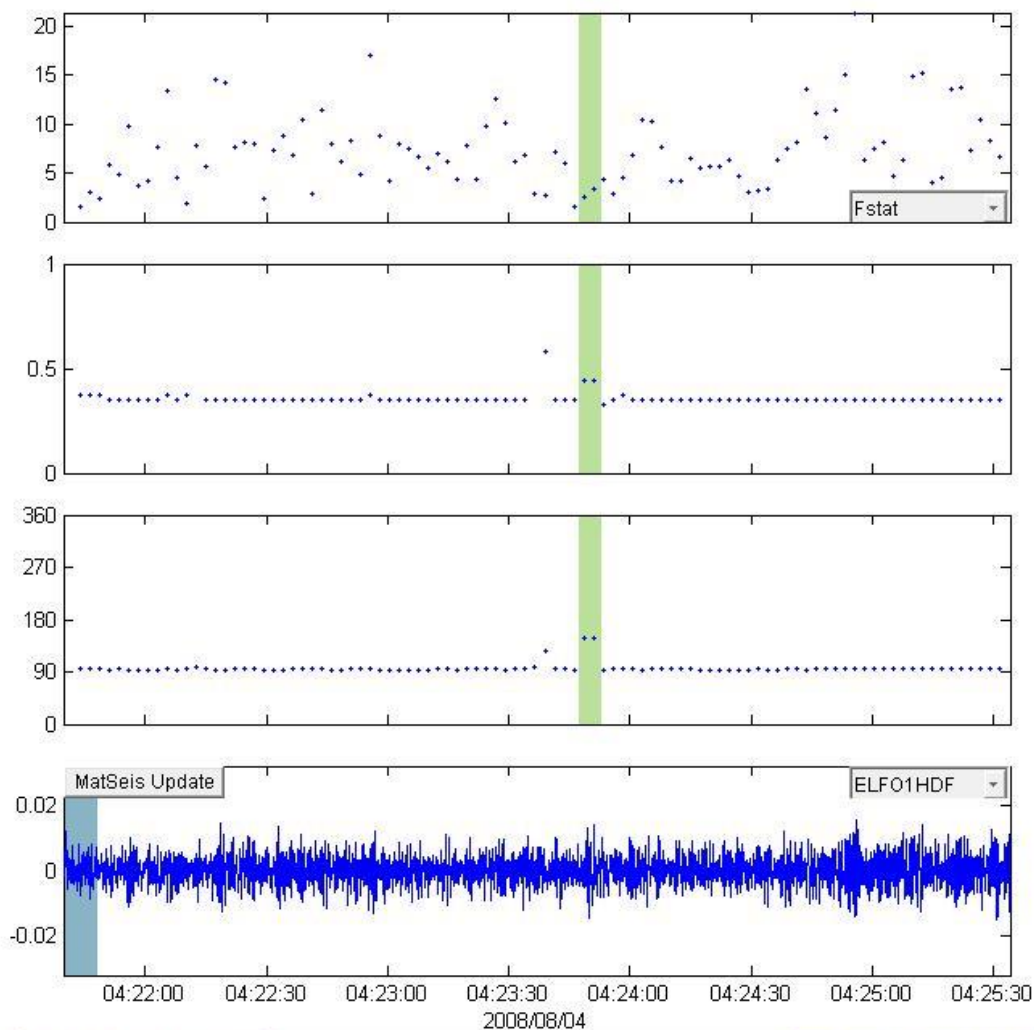


Window Parameters		Pass Band Parameters		Slowness Parameters		Windowed Values & S.D.	
Duration (s)	8	Low frequency (Hz)	0.2	Max. Slown.	400.0	Corr.	0.772 0.079
Overlap (%)	70.0	High frequency	3	# of Slown.	40	Fstat	13.712 6.504
Number of	89	Order (integer)	2			Vel.	0.628 0.000
						Az.	349.992 0.000
						Send to Map	
Animate		Write File	8\20080325_004203\infrasound-da			Cancel	
Calculate	0						

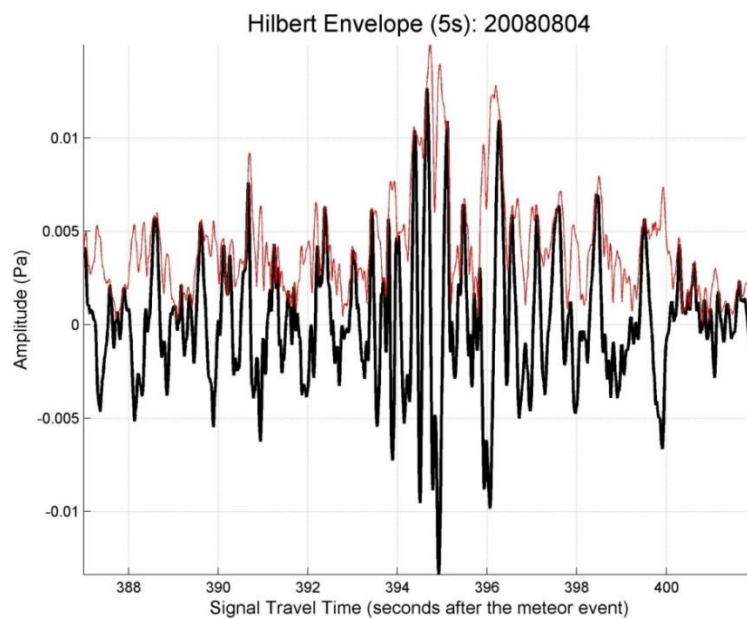
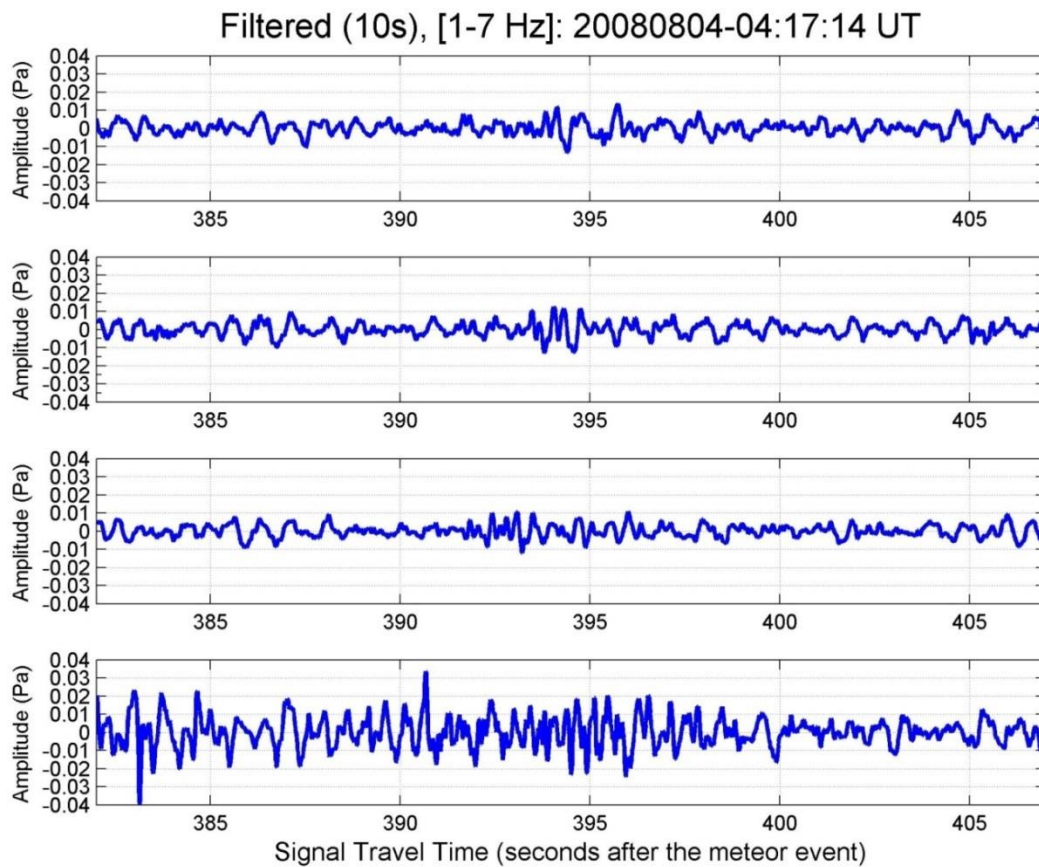




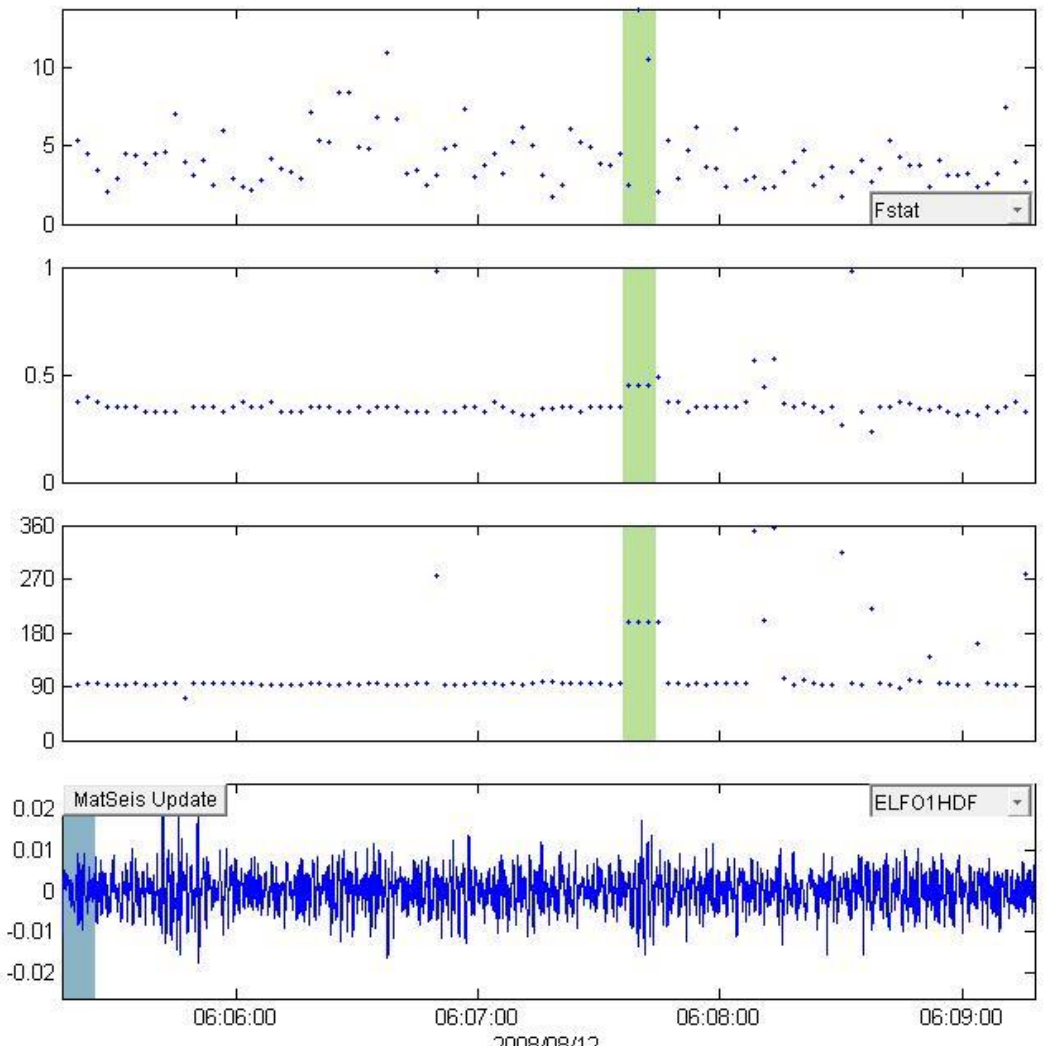
## 20080804\_041714



Window Parameters		Pass Band Parameters		Slowness Parameters		Windowed Values & S.D.	
Duration (s)	8	Low frequency (Hz)	0.9	Max. Slown.	400.0	Corr.	0.496 0.038
Overlap (%)	70.0	High frequency	7	# of Slown.	40	Fstat	2.963 0.594
Number of	96	Order (integer)	2			Vel.	0.439 0.000
						Az.	148.241 0.000
Animate						Send to Map	
Calculate	0	Write File	8120080325_004203\infrasound-da			Cancel	



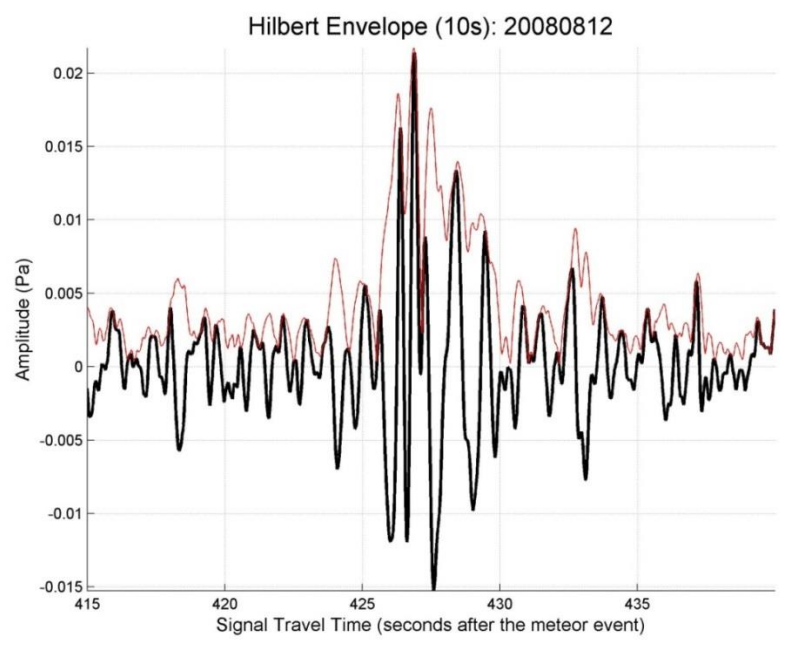
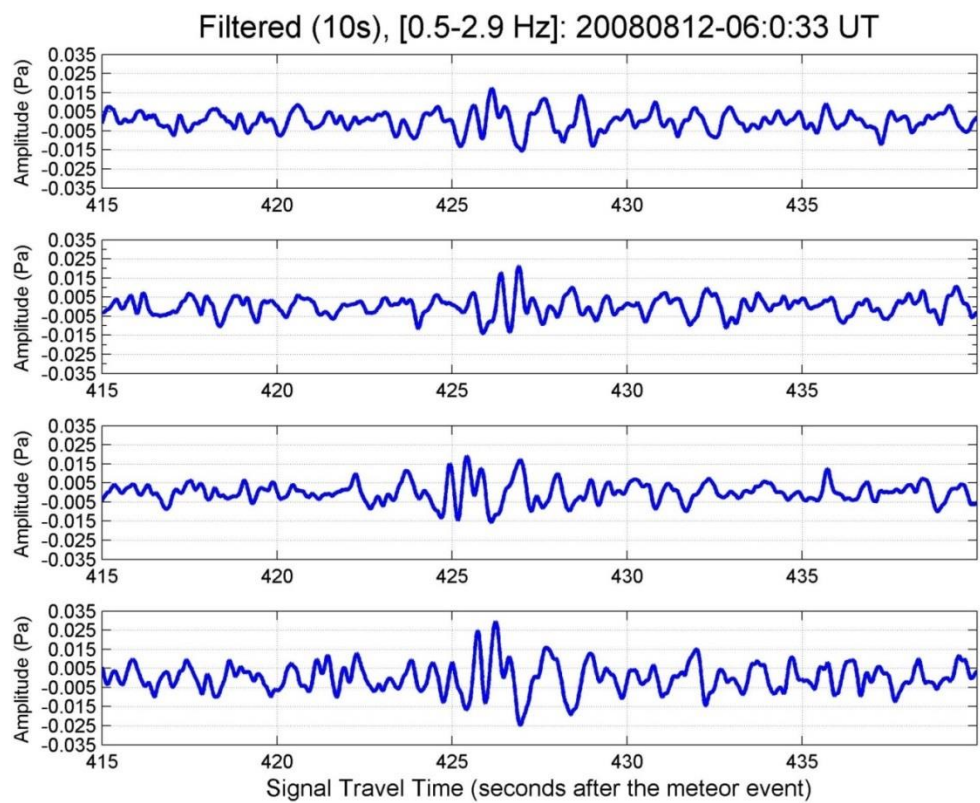
### 20080812\_060033



Window Parameters		Pass Band Parameters		Slowness Parameters		Windowed Values & S.D.	
Duration (s)	8	Low frequency (Hz)	0.5	Max. Slown.	400.0	Corr.	0.665 0.175
Overlap (%)	70.0	High frequency	2.9	# of Slown.	40	Fstat	8.919 5.816
Number of	99	Order (Integer)	2			Vel.	0.451 0.000
						Az.	196.928 0.000

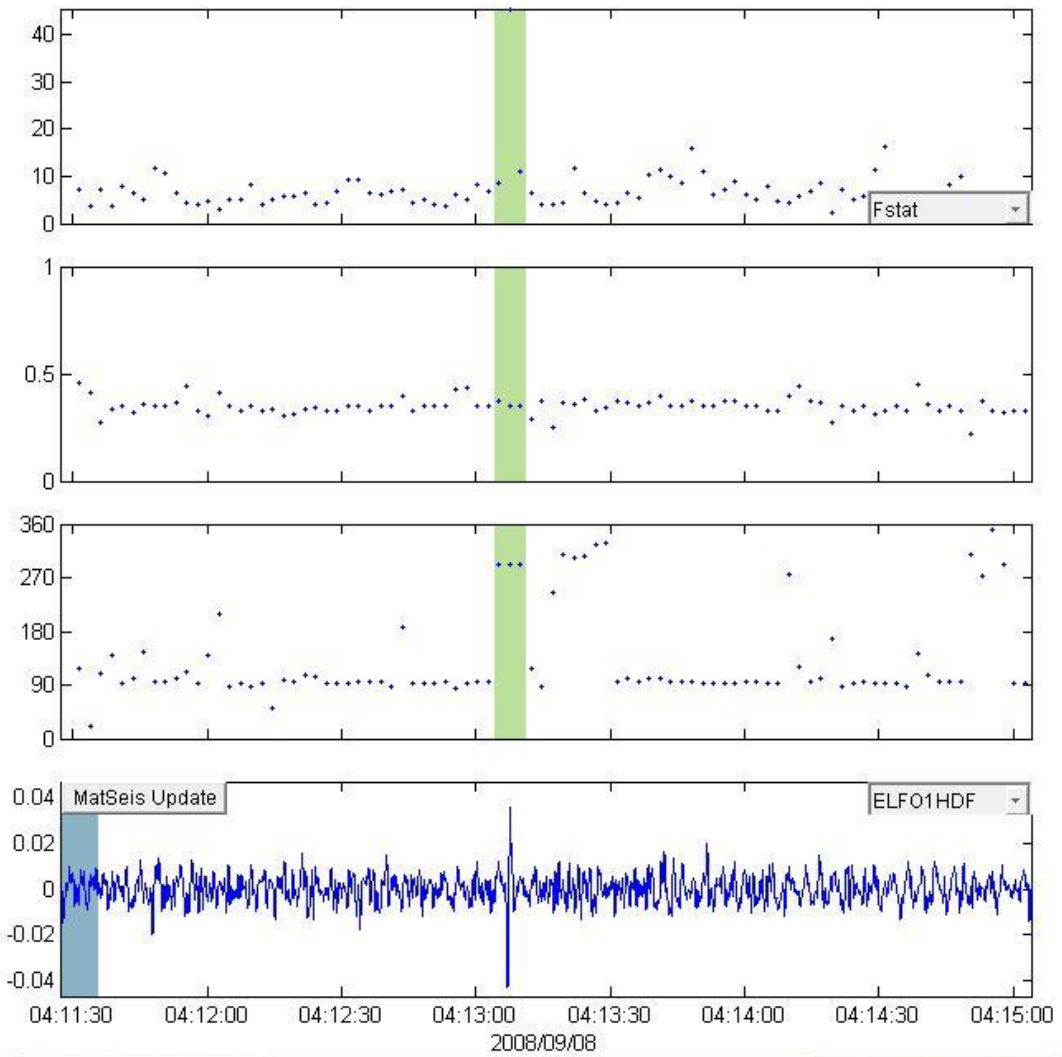
  

Animate			
Calculate	0	Write File	D:\Research\Research - Elizabeth\lr
			Cancel





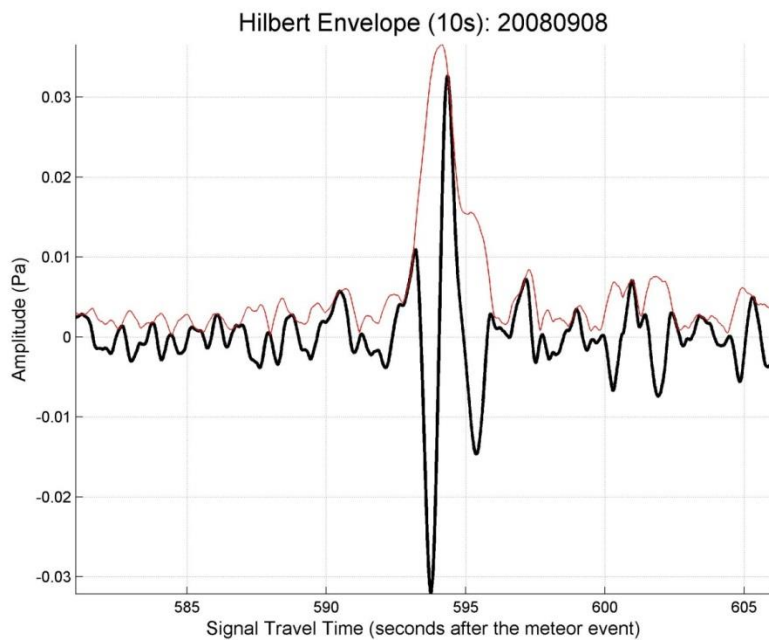
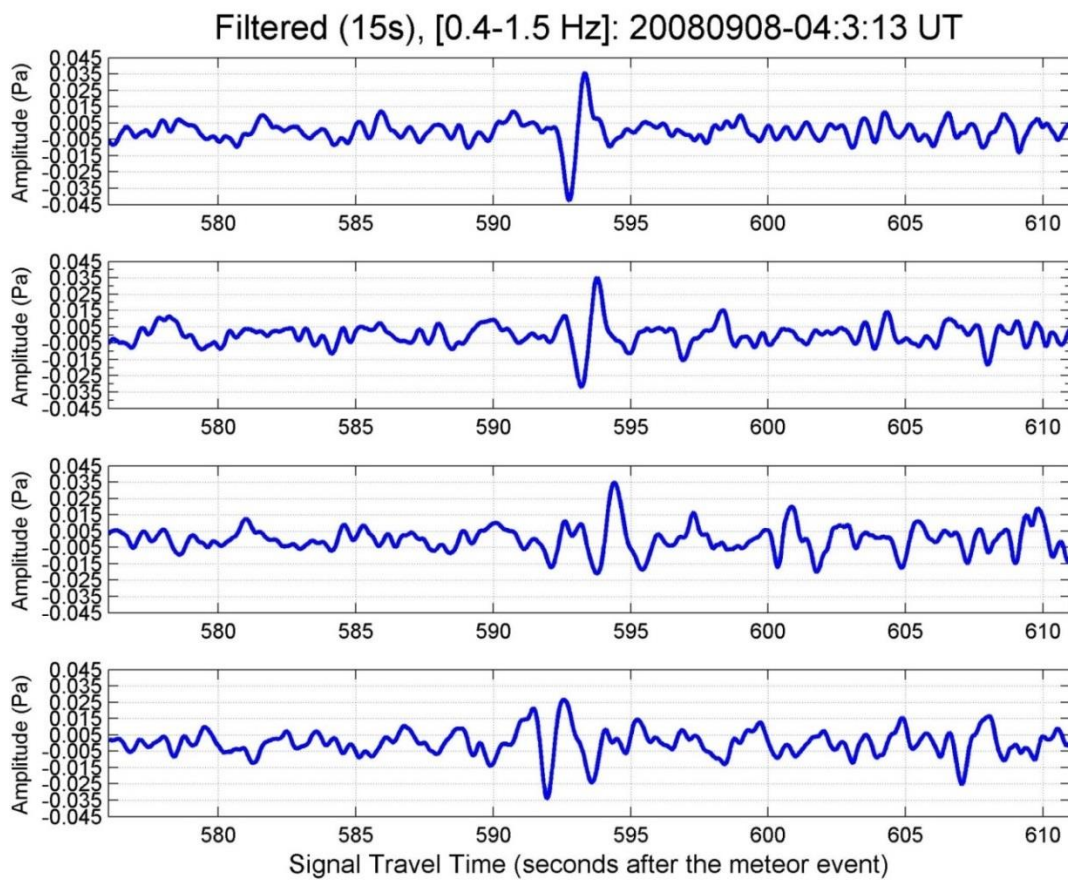
### 20080908\_040313



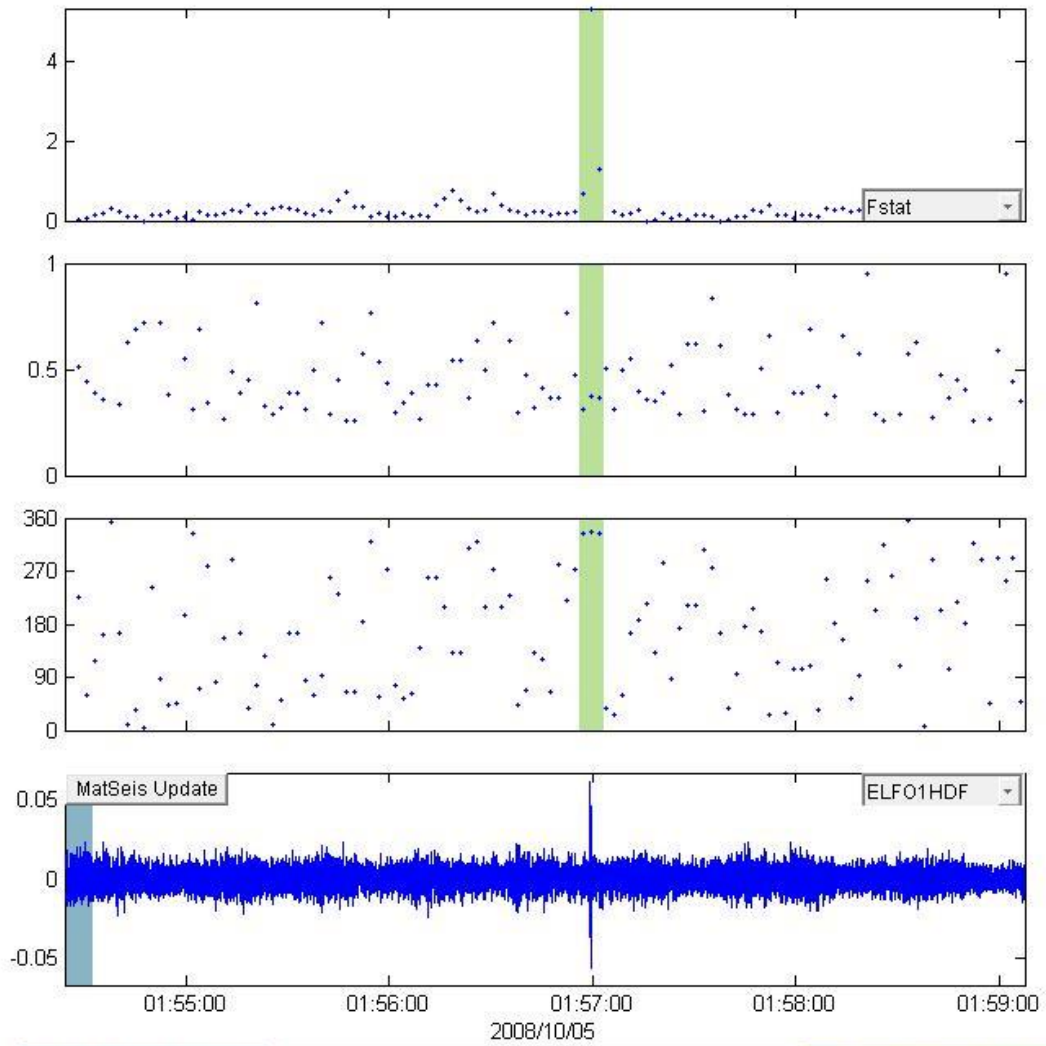
Window Parameters		Pass Band Parameters		Slowness Parameters		Windowed Values & S.D.	
Duration (s)	8	Low frequency (Hz)	0.4	Max. Slown.	400.0	Corr.	0.793 0.113
Overlap (%)	70.0	High frequency	1.5	# of Slown.	40	Fstat	21.754 20.638
Number of	89	Order (integer)	2			Vel.	0.357 0.013
						Az.	291.237 0.805

Animate			
Calculate	0	Write File	8\20080325_004203\infrasound-da
			Cancel



### 20081005\_015012

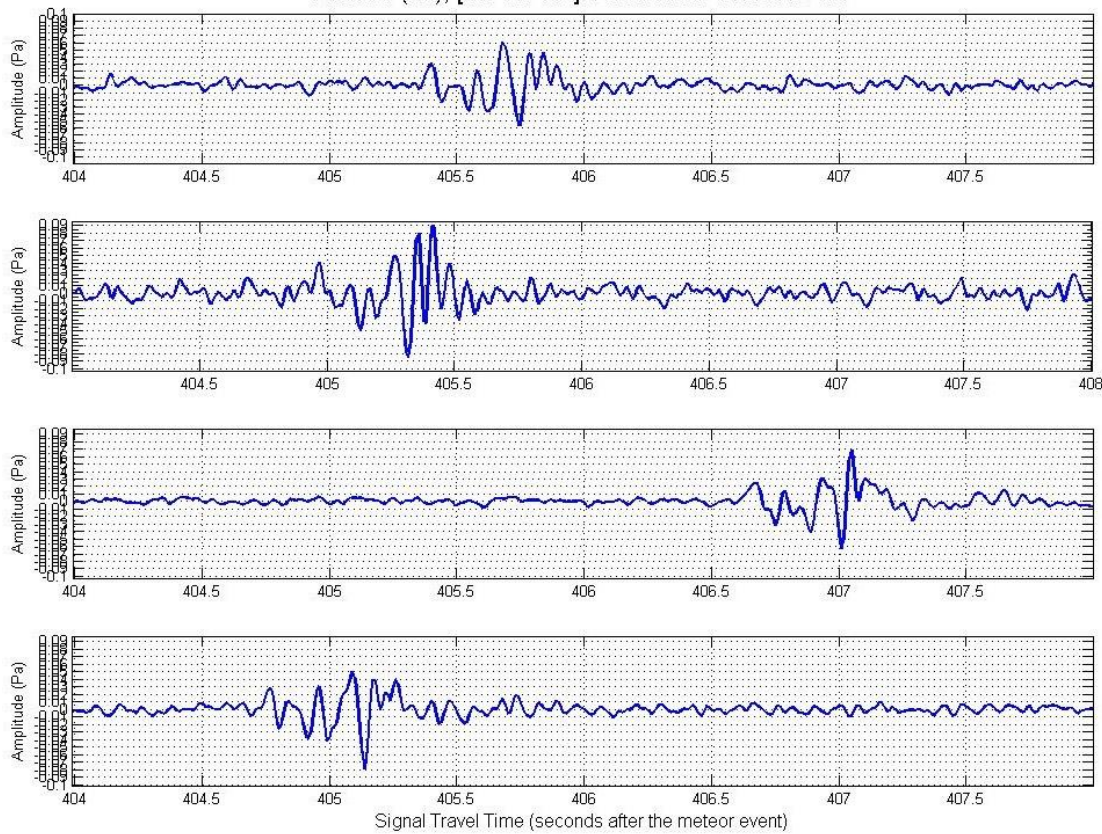


Window Parameters		Pass Band Parameters		Slowness Parameters		Windowed Values & S.D.		
Duration (s)	8	Low frequency (Hz)	1.5	Max. Slown.	400.0	Corr.	0.425	0.166
Overlap (%)	70.0	High frequency	20	# of Slown.	40	Fstat	2.437	2.520
Number of	117	Order (integer)	2			Vel.	0.349	0.030
						Az.	335.434	2.079

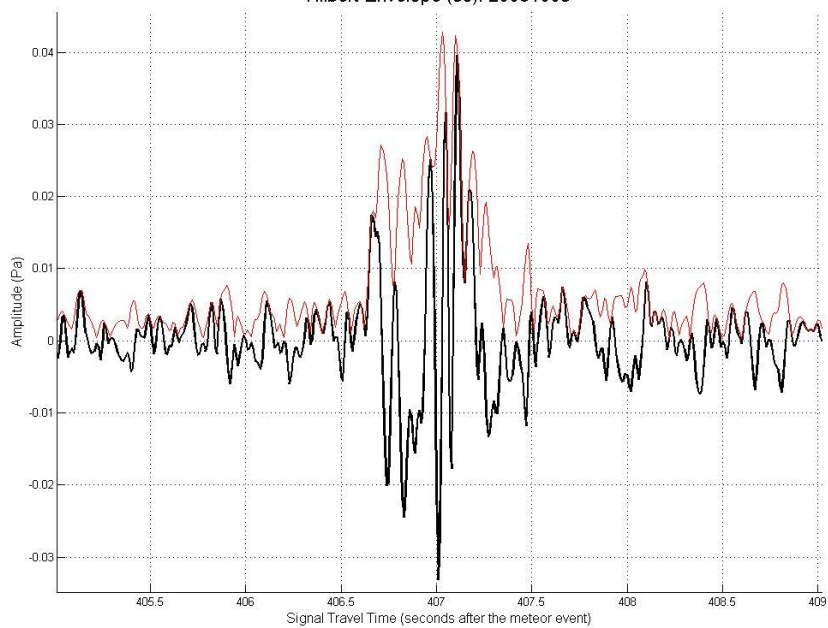
Animate  Calculate 0 Write File | 8\20080325\_004203\infrasound-da



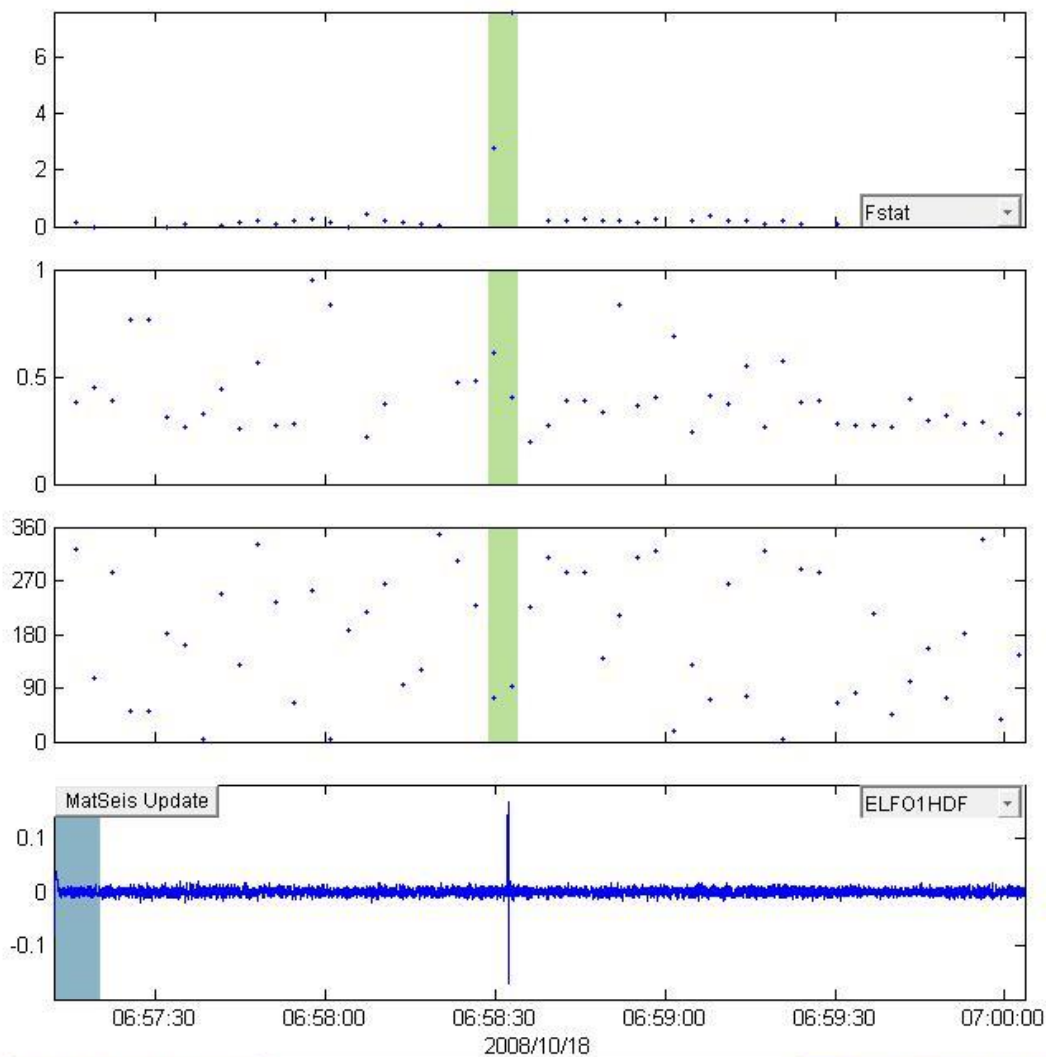
Filtered (3s), [1.5-20 Hz]: 20081005-01:50:12 UT



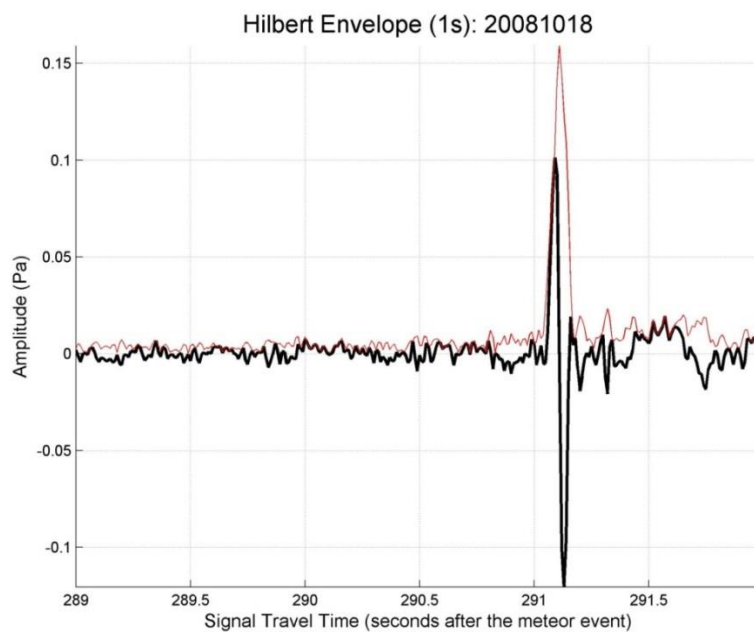
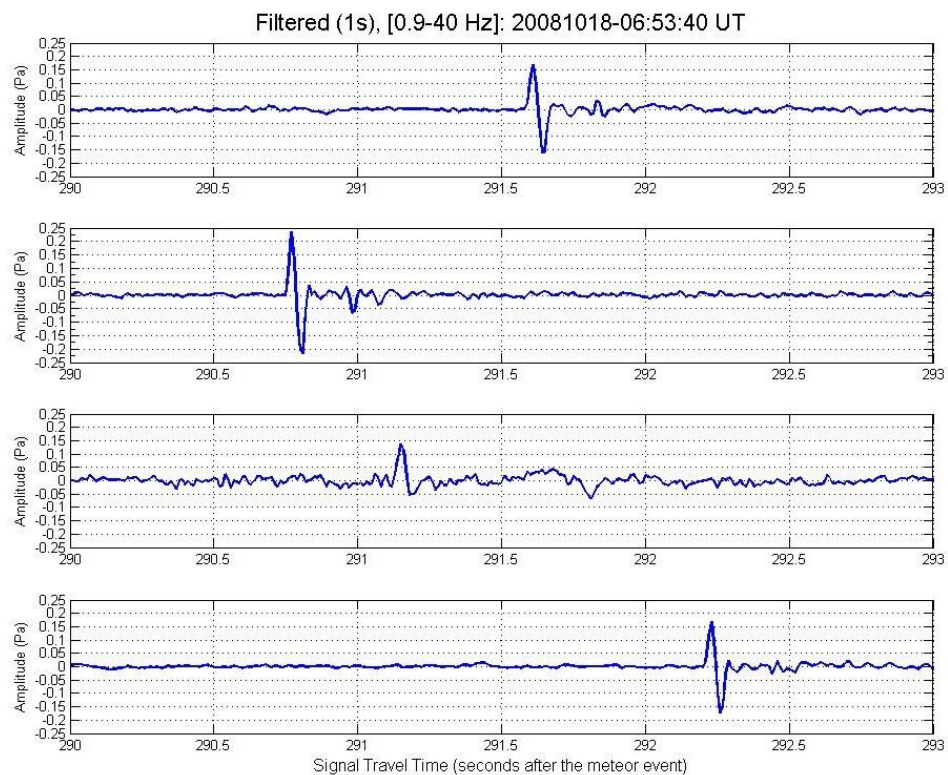
Hilbert Envelope (3s): 20081005



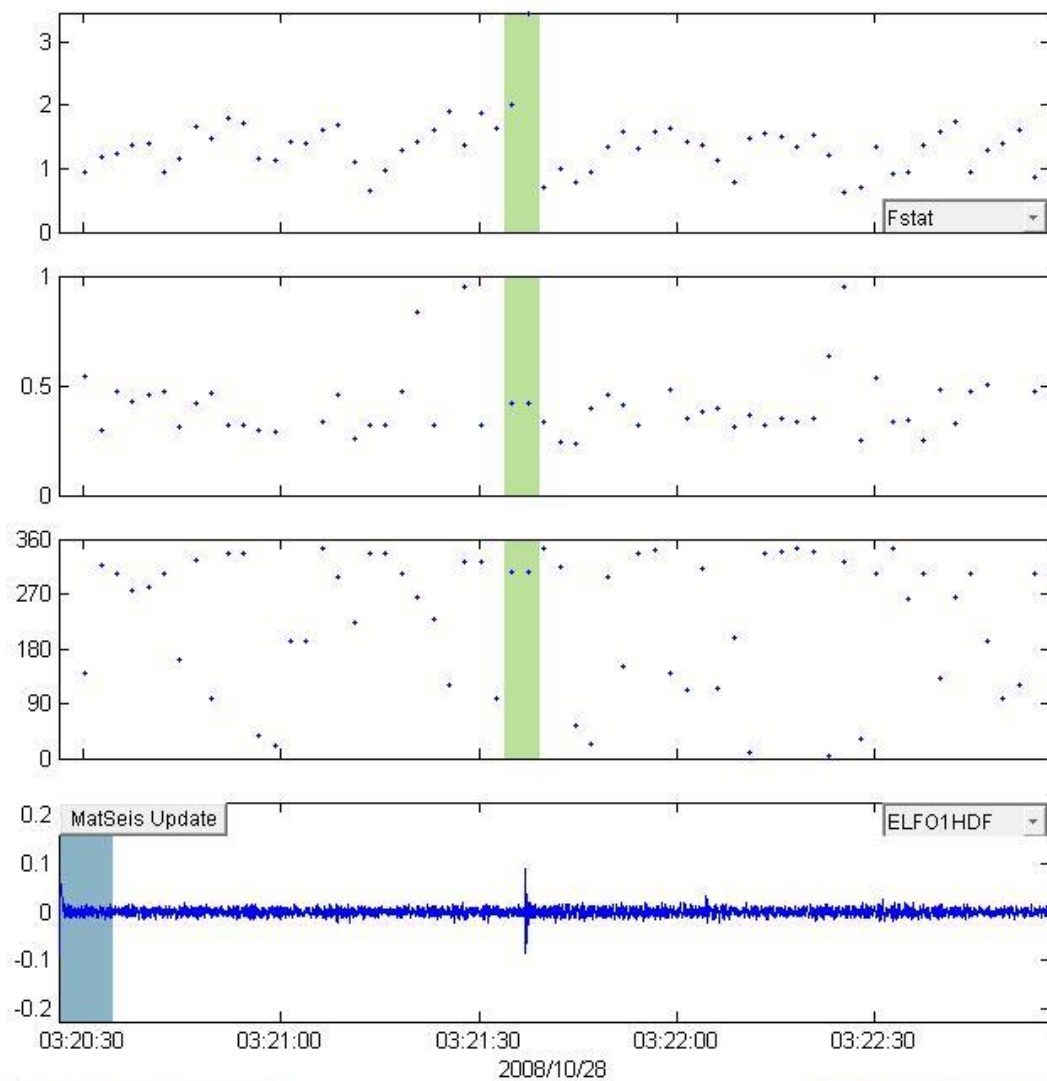
### 20081018\_065340



Window Parameters		Pass Band Parameters		Slowness Parameters		Windowed Values & S.D.	
Duration (s)	8	Low frequency (Hz)	0.9	Max. Slown.	400.0	Corr.	0.583 0.140
Overlap (%)	60.0	High frequency	45	# of Slown.	40	Fstat	5.175 3.424
Number of	53	Order (integer)	2			Vel.	0.506 0.149
						Az.	82.866 13.089
						Send to Map	
Animate		Write File   8\20080325_004203\infrasound-da				Cancel	
Calculate	0						

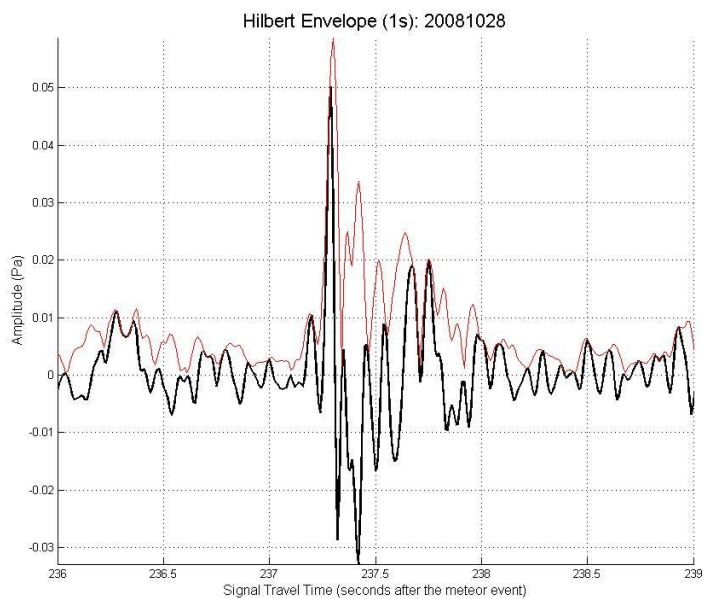
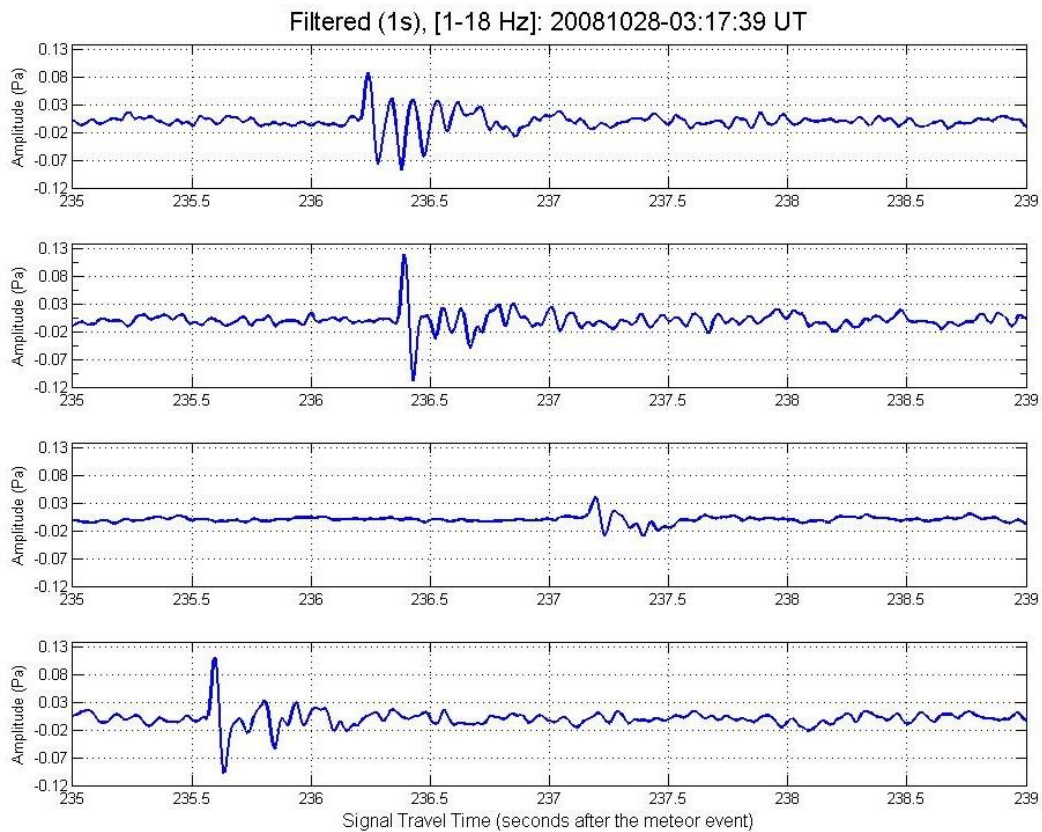


20081028\_031739

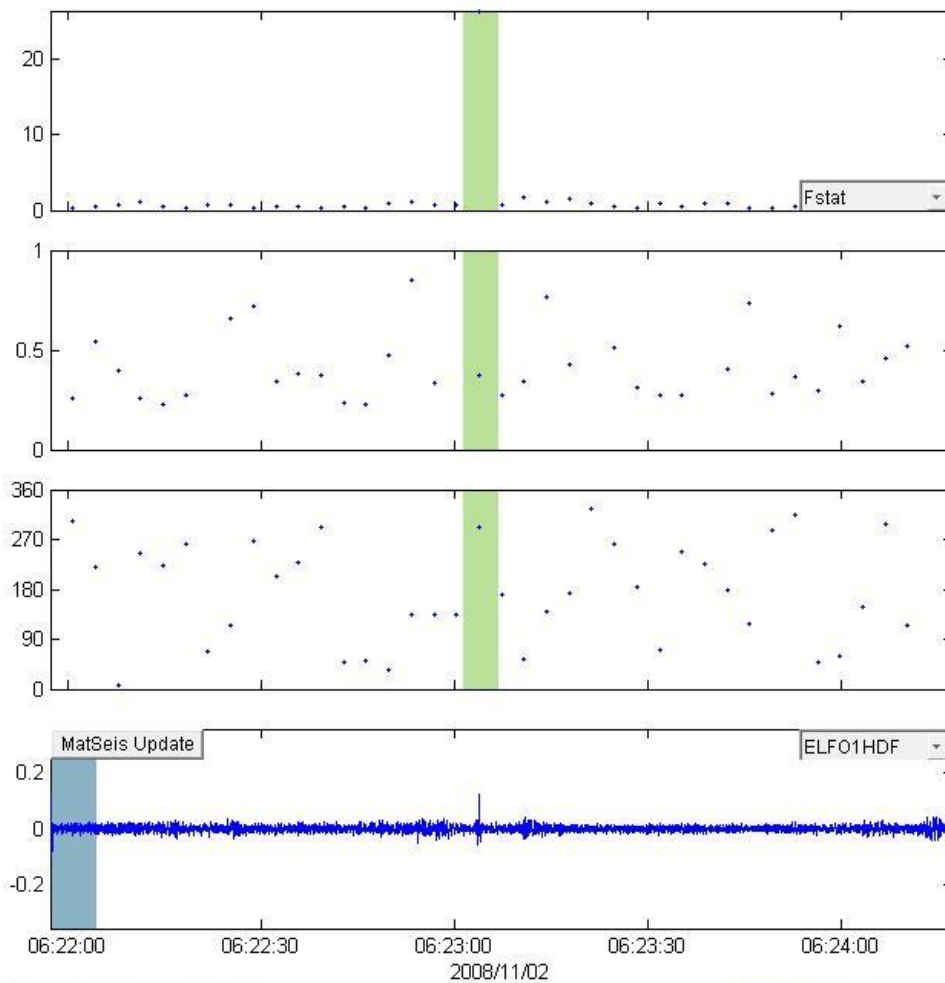


Window Parameters		Pass Band Parameters		Slowness Parameters		Windowed Values & S.D.	
Duration (s)	8	Low frequency (Hz)	1	Max. Slown.	400.0	Corr.	0.479 0.069
Overlap (%)	70.0	High frequency	18	# of Slown.	40	Fstat	2.739 1.029
Number of	62	Order (integer)	2			Vel.	0.420 0.000
						Az.	305.538 0.000
Animate						Send to Map	
Calculate	0	Write File	8\20080325_004203\infrasound-da			Cancel	





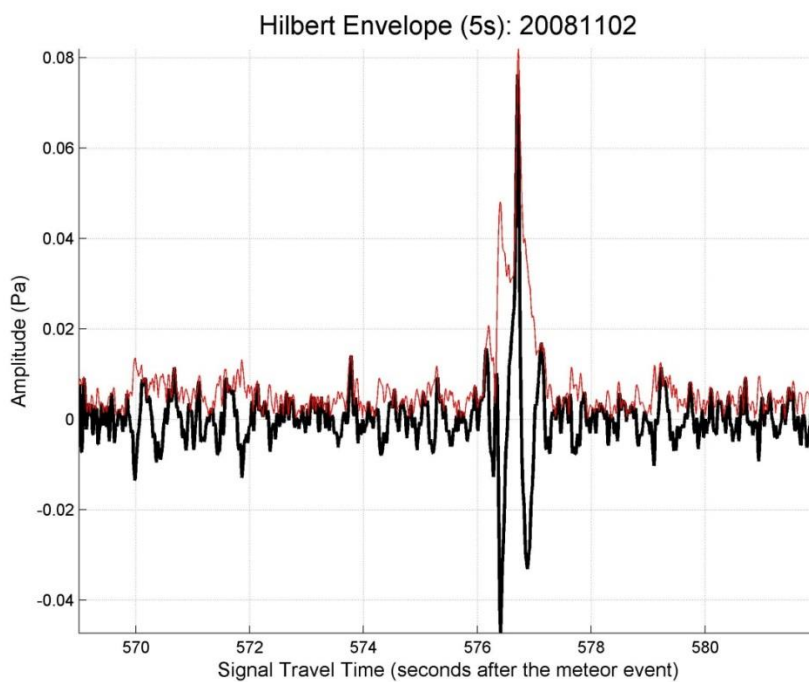
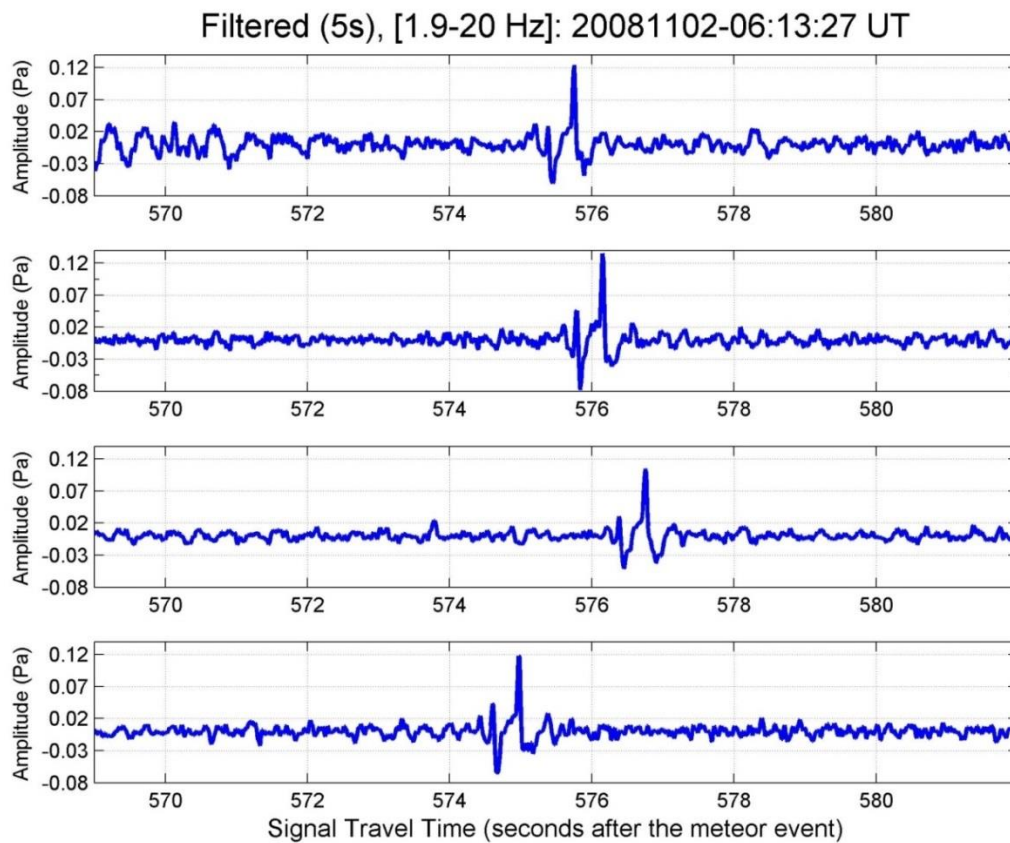
### 20081102\_061327



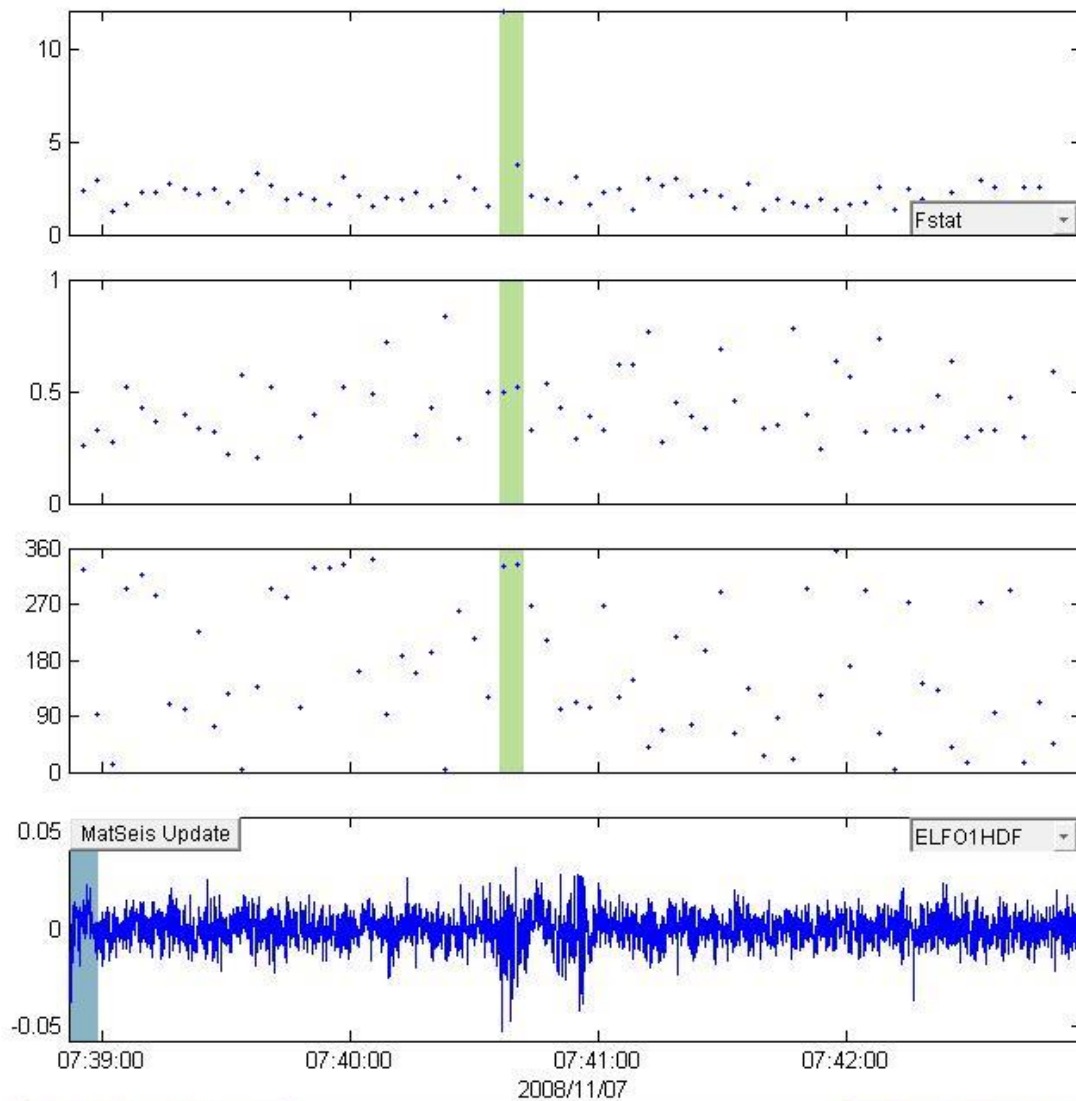
Window Parameters		Pass Band Parameters		Slowness Parameters		Windowed Values & S.D.	
Duration (s)	7	Low frequency (Hz)	1.9	Max. Slown.	400.0	Corr.	0.872 0.000
Overlap (%)	50.0	High frequency	20	# of Slown.	40	Fstat	26.348 0.000
Number of	38	Order (integer)	2			Vel.	0.372 0.000
						Az.	292.166 0.000

Animate		Write File	8\20080325_004203\infrasound-da	Send to Map	
Calculate	0				Cancel

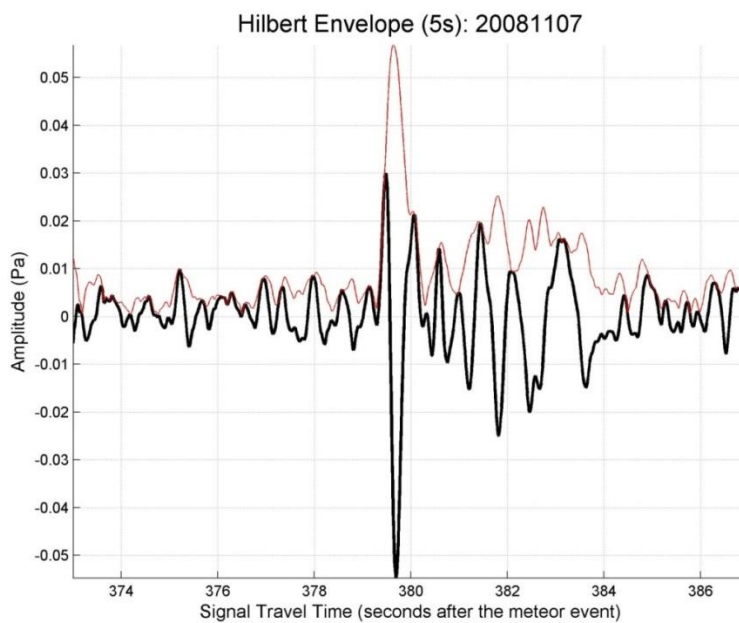
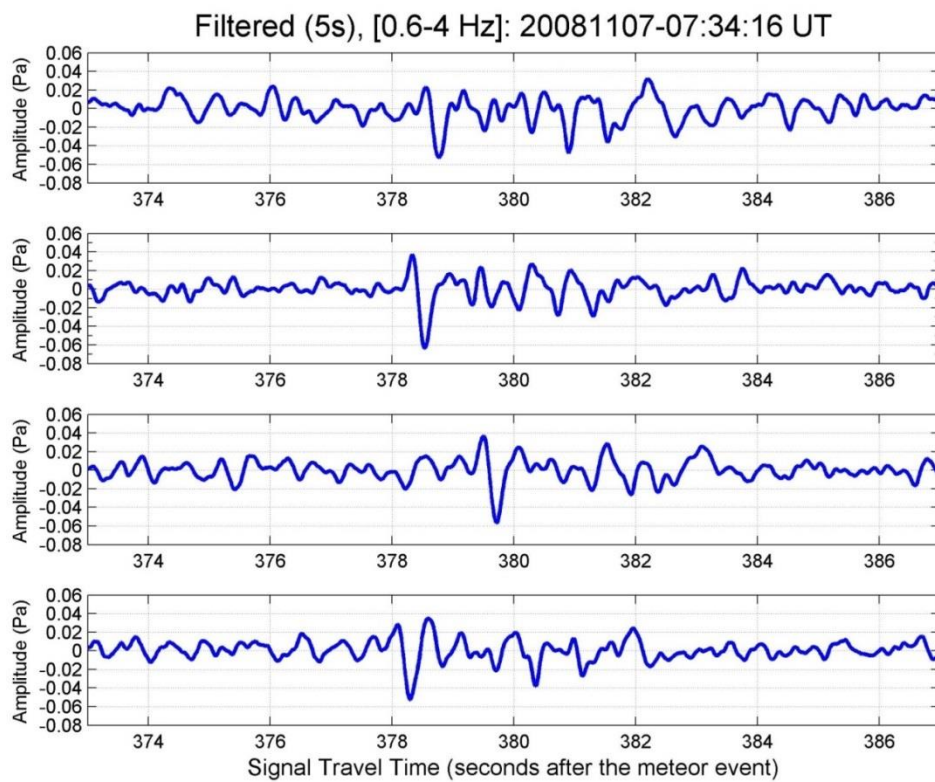


## 20081107\_073416

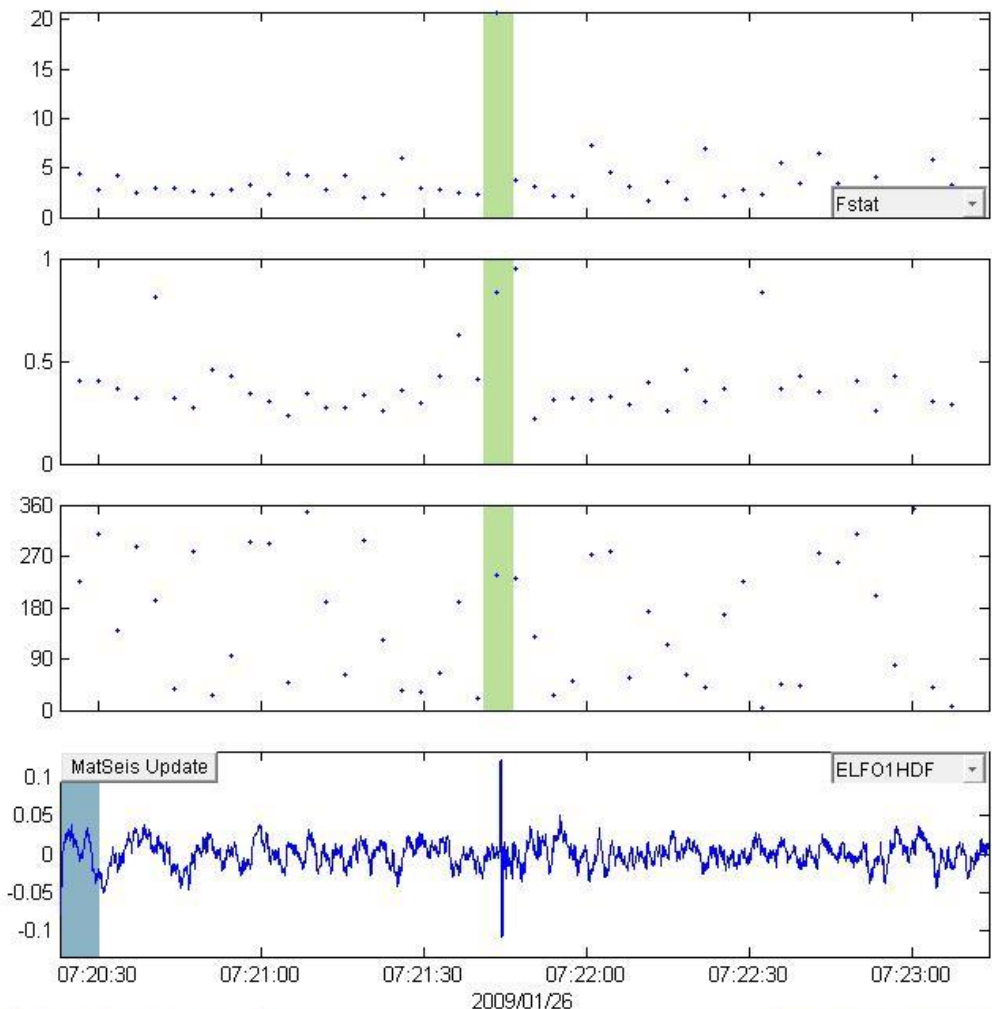


Window Parameters		Pass Band Parameters		Slowness Parameters		Windowed Values & S.D.	
Duration (s)	7	Low frequency (Hz)	0.6	Max. Slown.	400.0	Corr.	0.656 0.156
Overlap (%)	50.0	High frequency	4	# of Slown.	40	Fstat	7.941 5.858
Number of	68	Order (integer)	2			Vel.	0.505 0.015
						Az.	332.293 3.339
Animate						Send to Map	
Calculate	0	Write File	8\20080325_004203\infrasound-da			Cancel	





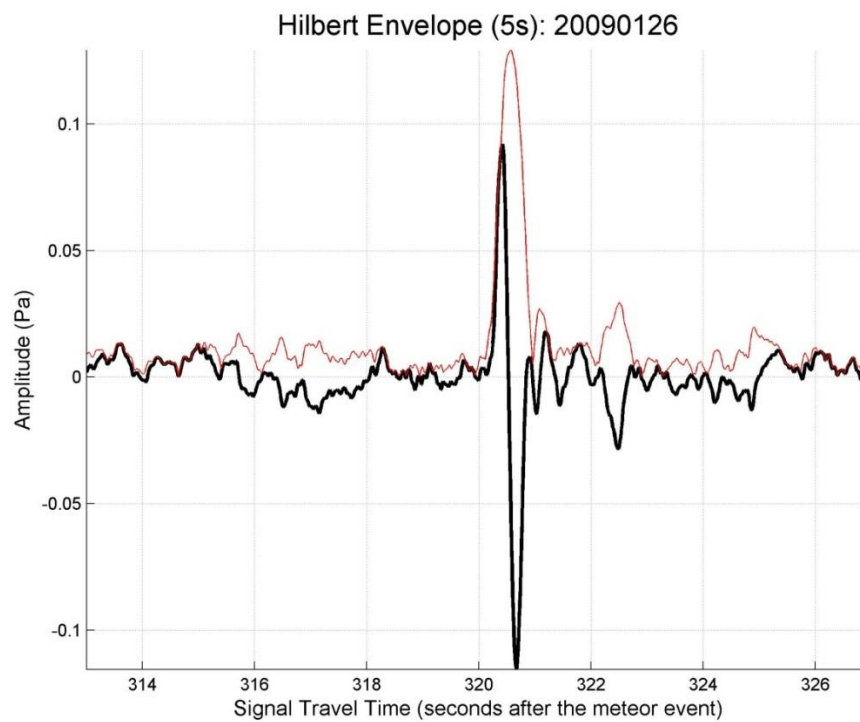
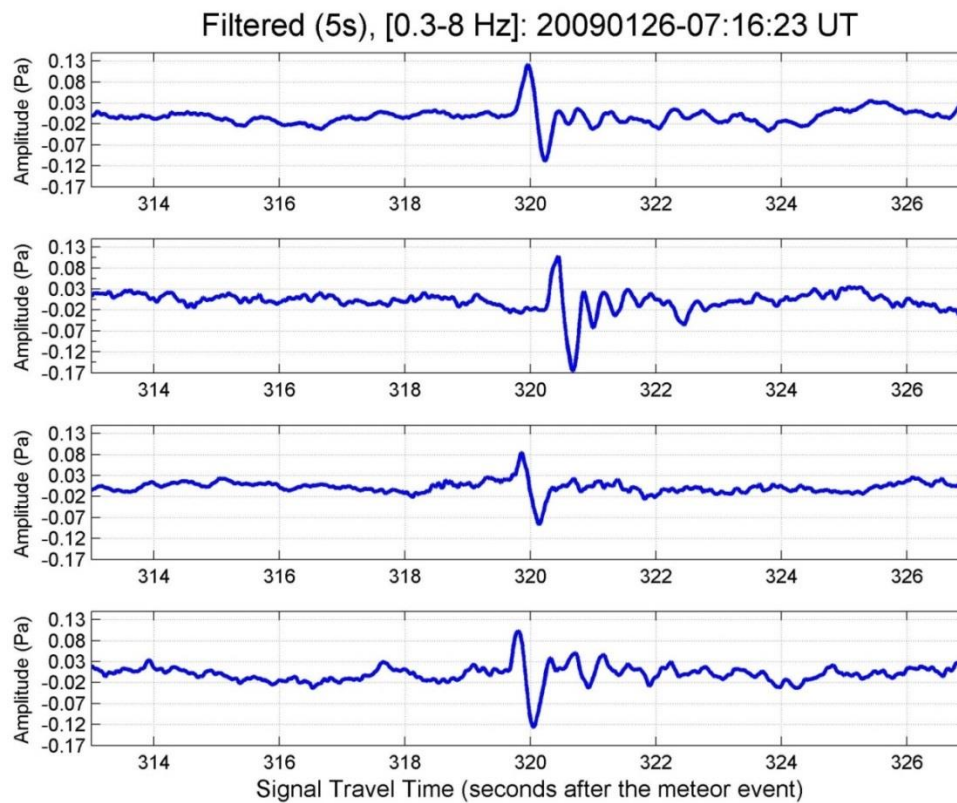
### 20090126\_071623



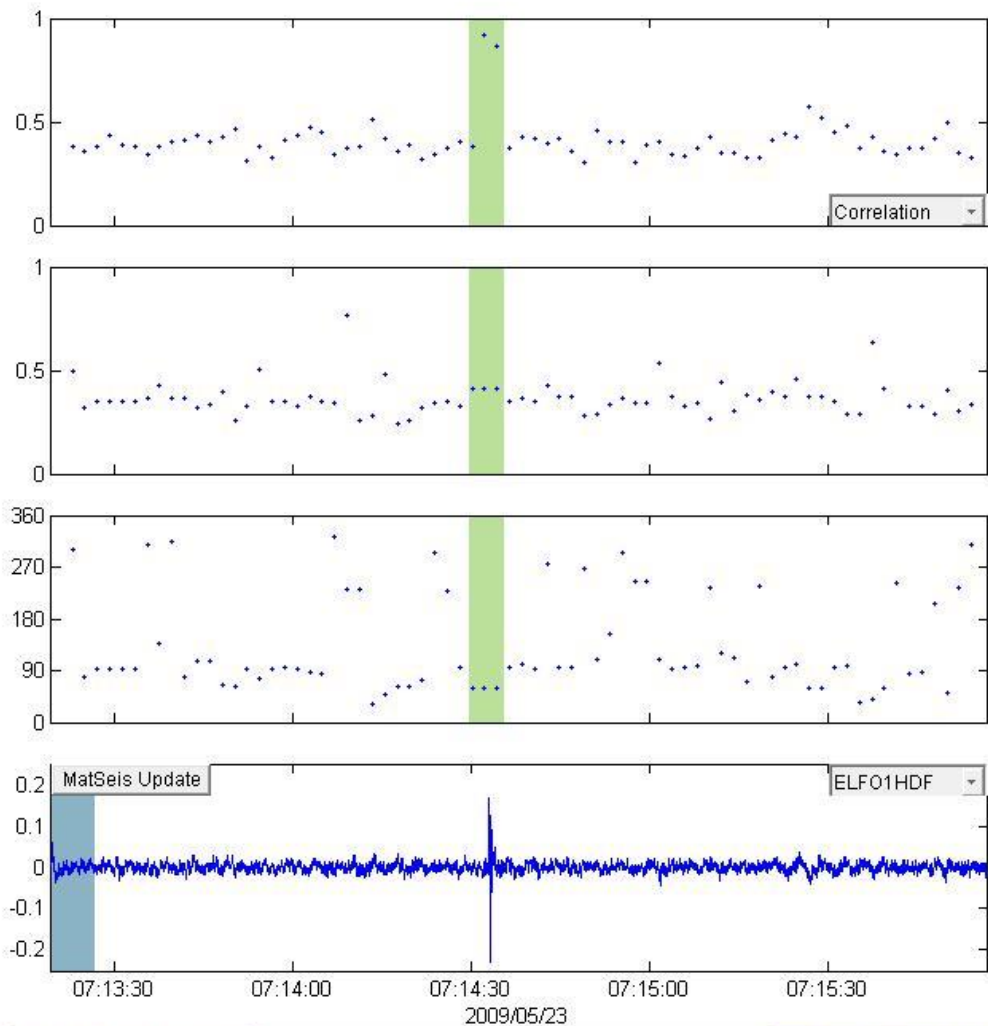
Window Parameters		Pass Band Parameters		Slowness Parameters		Windowed Values & S.D.	
Duration (s)	7	Low frequency (Hz)	0.3	Max. Slown.	400.0	Corr.	0.845   0.000
Overlap (%)	50.0	High frequency	8	# of Slown.	40	Fstat	20.755   0.000
Number of	47	Order (integer)	2			Vel.	0.831   0.000
						Az.	237.529   0.000

Animate			
Calculate	0	Write File	8\20080325_004203\infrasound-da
			Cancel



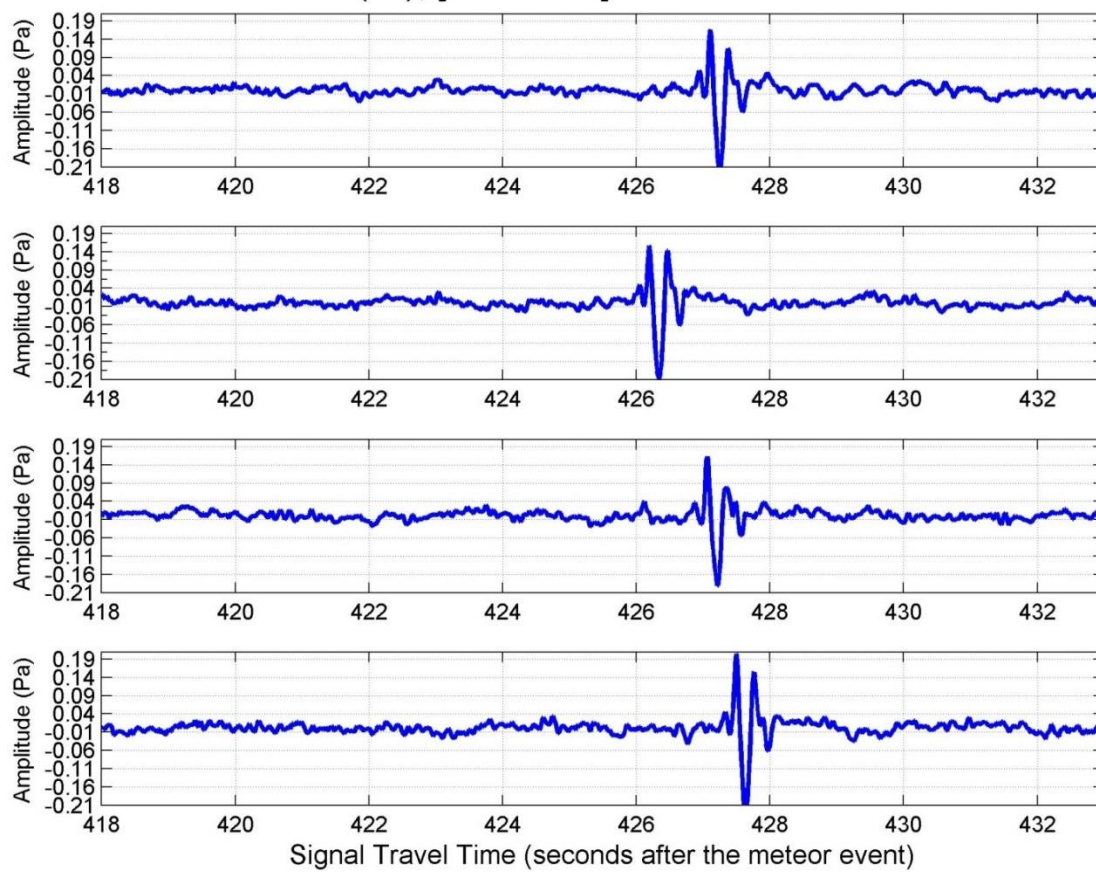
### 20090523\_070725



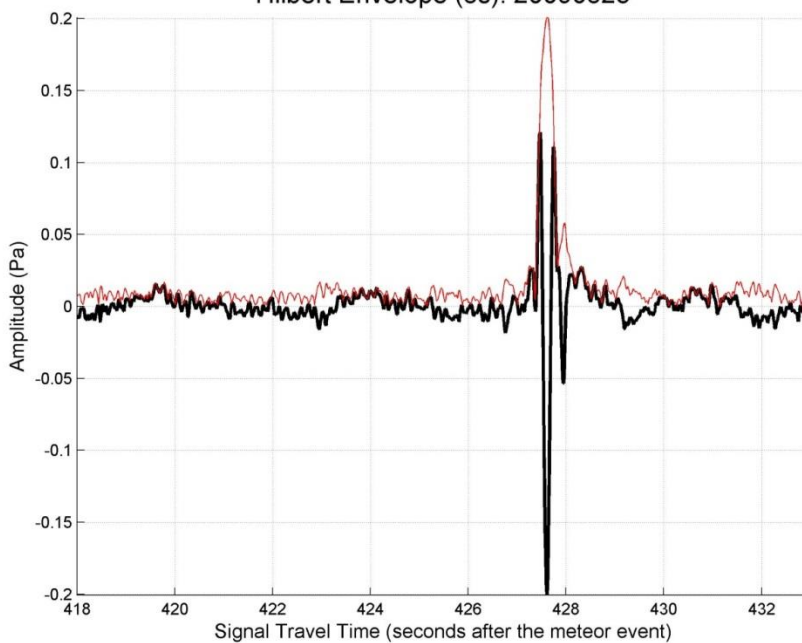
Window Parameters		Pass Band Parameters		Slowness Parameters		Windowed Values & S.D.	
Duration (s)	7	Low frequency (Hz)	0.3	Max. Slown.	400.0	Corr.	0.722 0.298
Overlap (%)	70.0	High frequency	12	# of Slown.	40	Fstat	23.561 21.286
Number of	73	Order (integer)	2			Vel.	0.410 0.000
						Az.	60.524 0.000

0
  8\20080325\_004203\infrasound-da

Filtered (5s), [0.3-12 Hz]: 20090523-07:7:25 UT

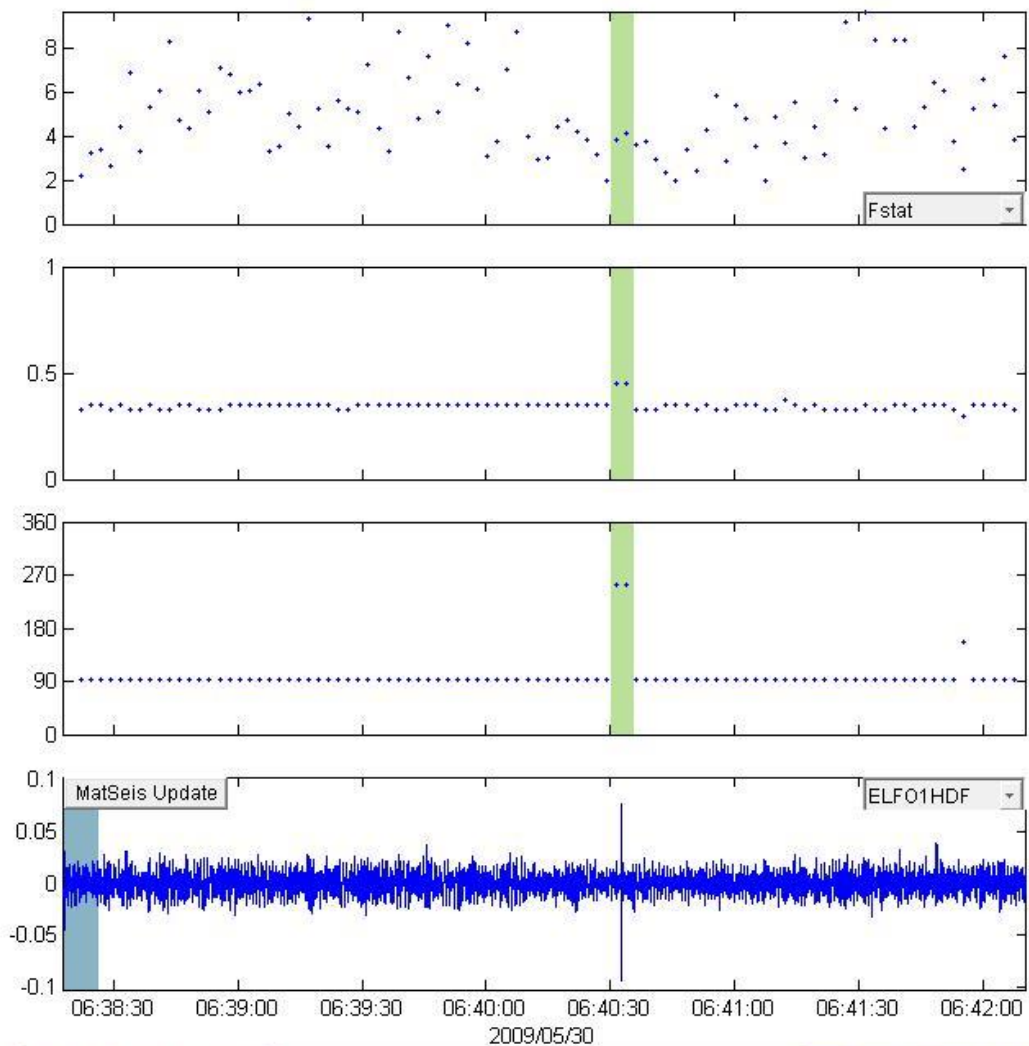


Hilbert Envelope (5s): 20090523





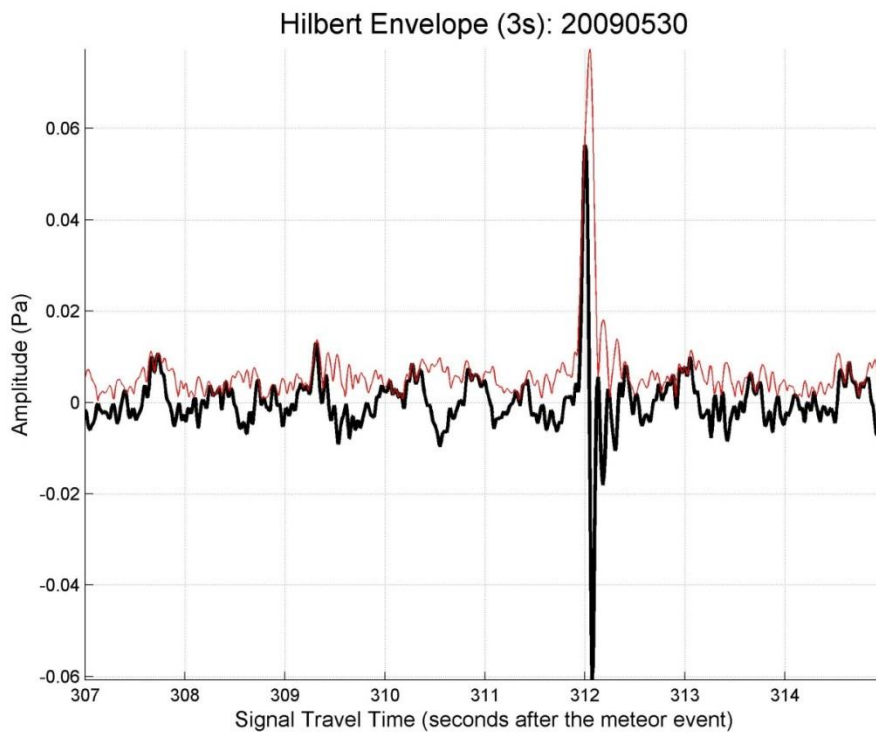
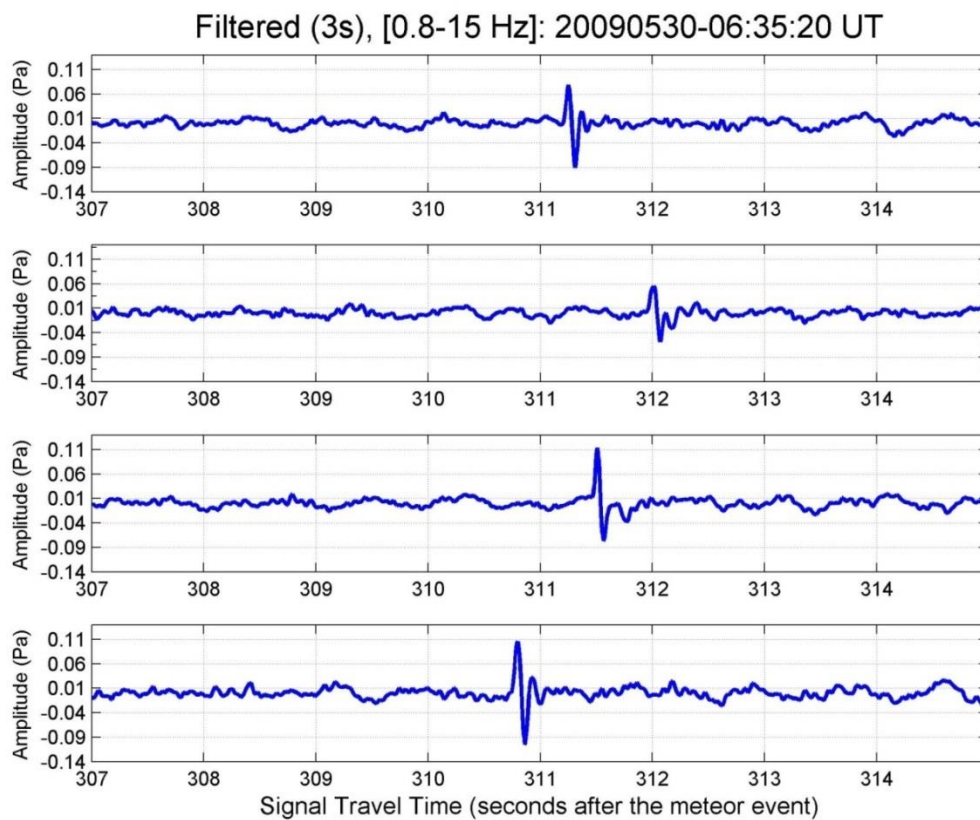
### 20090530\_063520



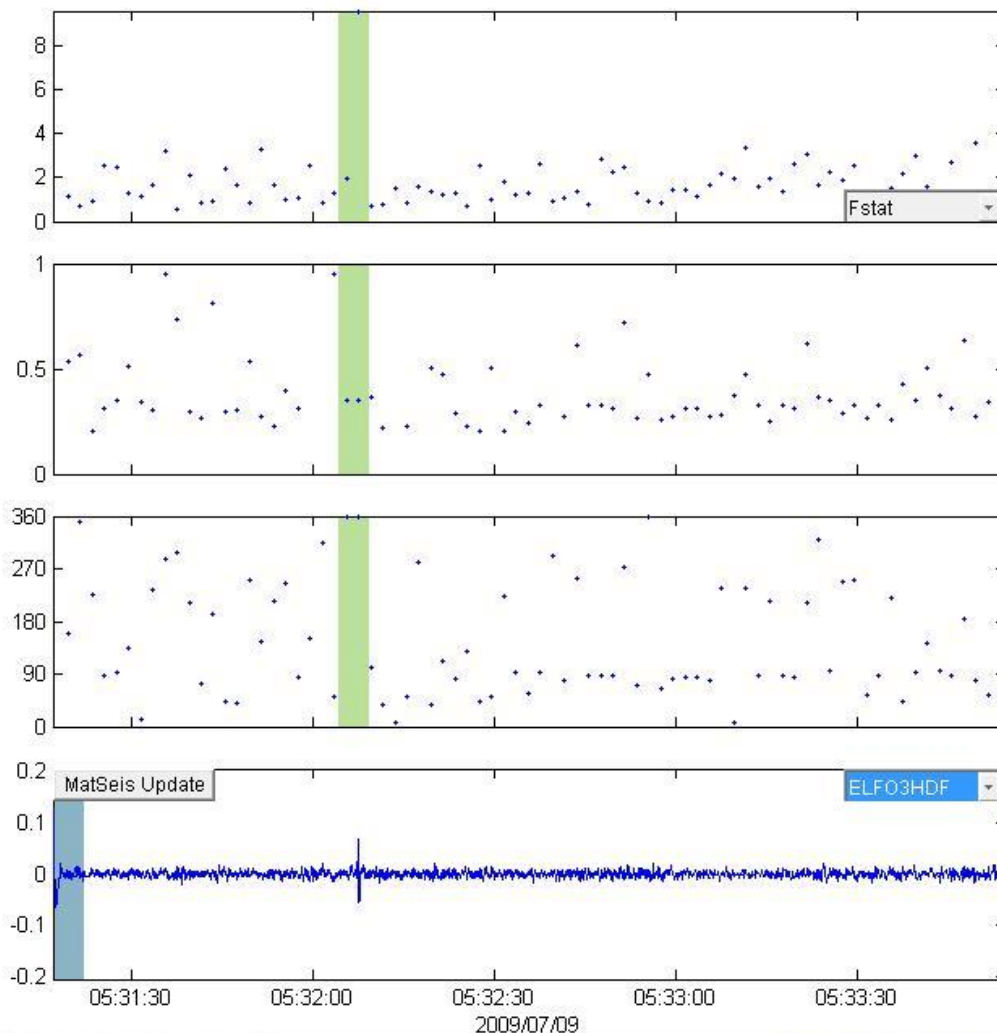
Window Parameters		Pass Band Parameters		Slowness Parameters		Windowed Values & S.D.	
Duration (s)	8.0	Low frequency (Hz)	0.9	Max. Slown.	400.0	Corr.	0.554   0.009
Overlap (%)	70.0	High frequency	15	# of Slown.	40	Fstat	3.978   0.180
Number of	95	Order (integer)	2			Vel.	0.451   0.000
						Az.	253.072   0.000

Animate			
Calculate	0	Write File	D:\Research\Research - Elizabeth\lr
			Send to Map
			Cancel



### 20090709\_052424

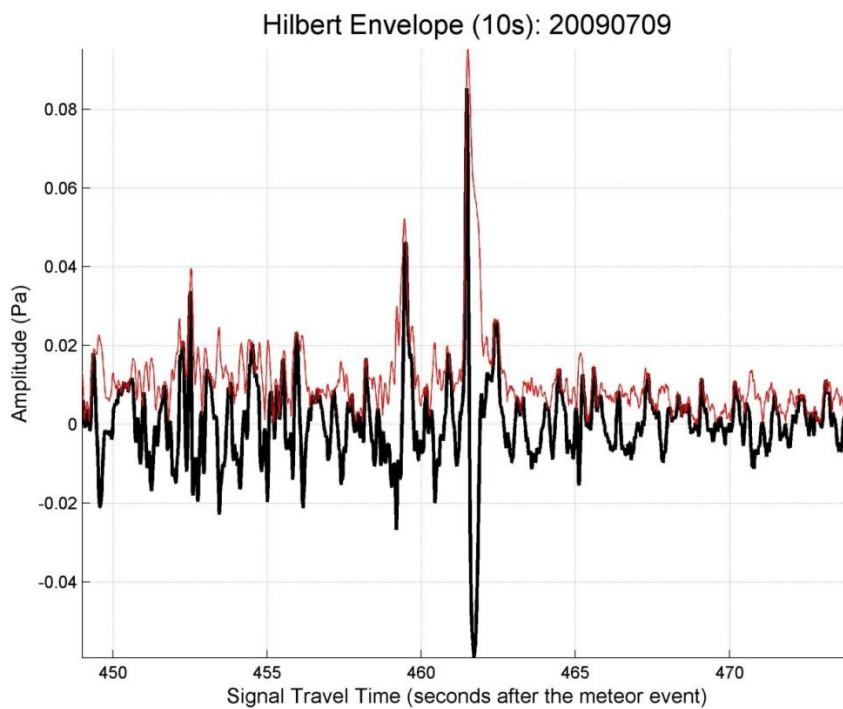
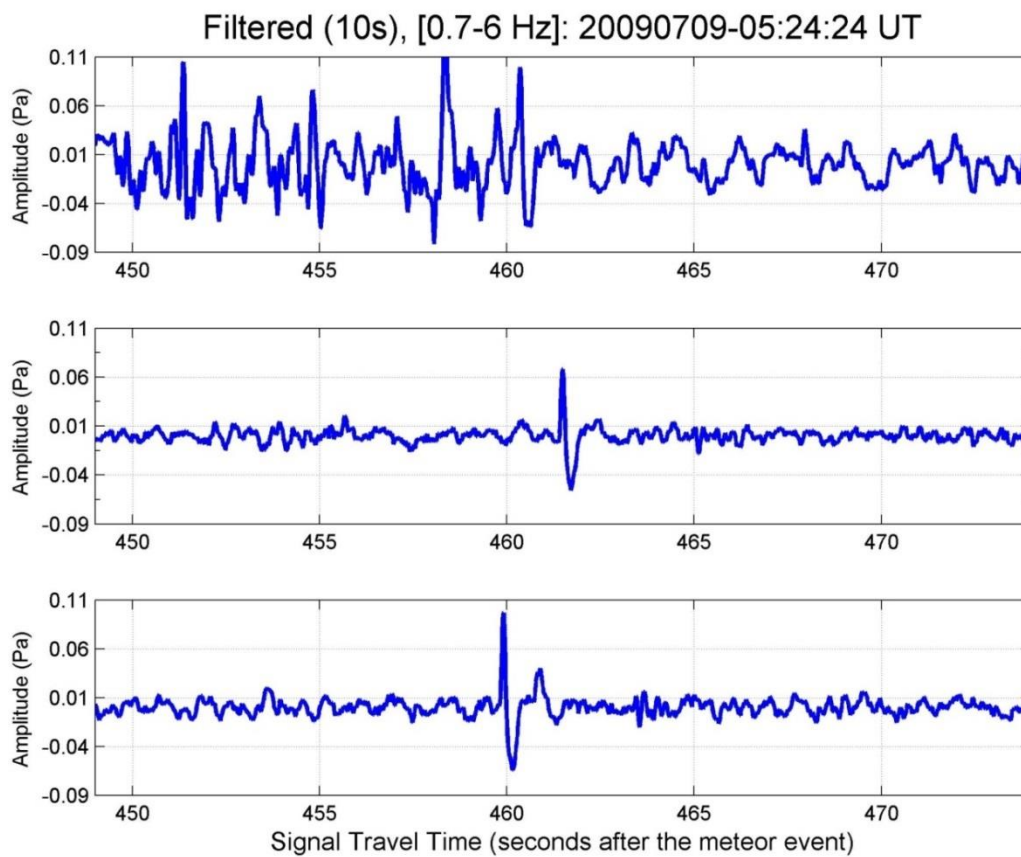


2009/07/09

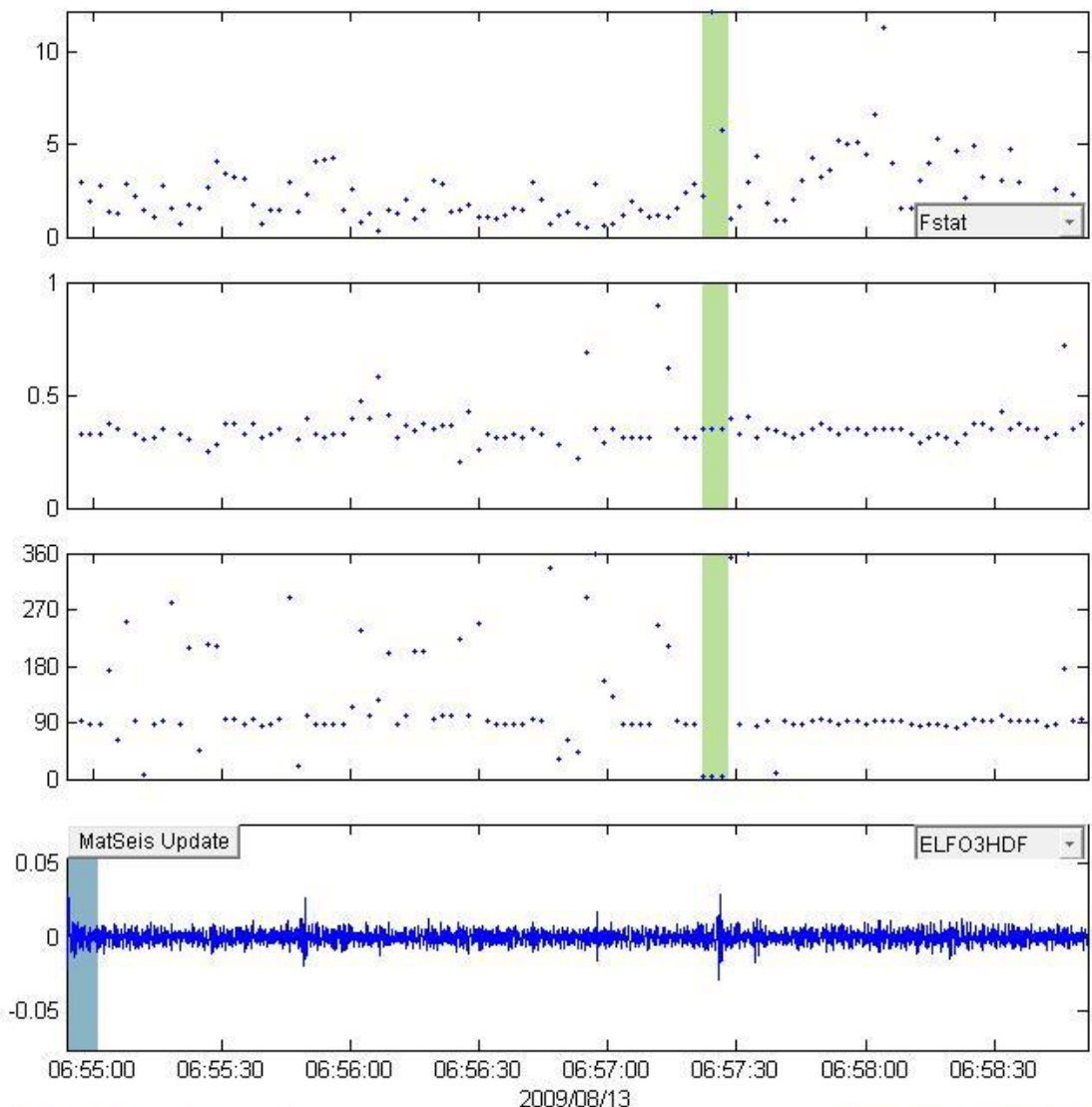
Window Parameters		Pass Band Parameters		Slowness Parameters		Windowed Values & S.D.	
Duration (s)	5	Low frequency (Hz)	0.7	Max. Slown.	400.0	Corr.	0.636 0.202
Overlap (%)	60.0	High frequency	6	# of Slown.	40	Fstat	5.736 5.398
Number of	77	Order (integer)	2			Vel.	0.349 0.000
						Az.	358.152 0.000

0  8|20080325\_004203|infrasound-da



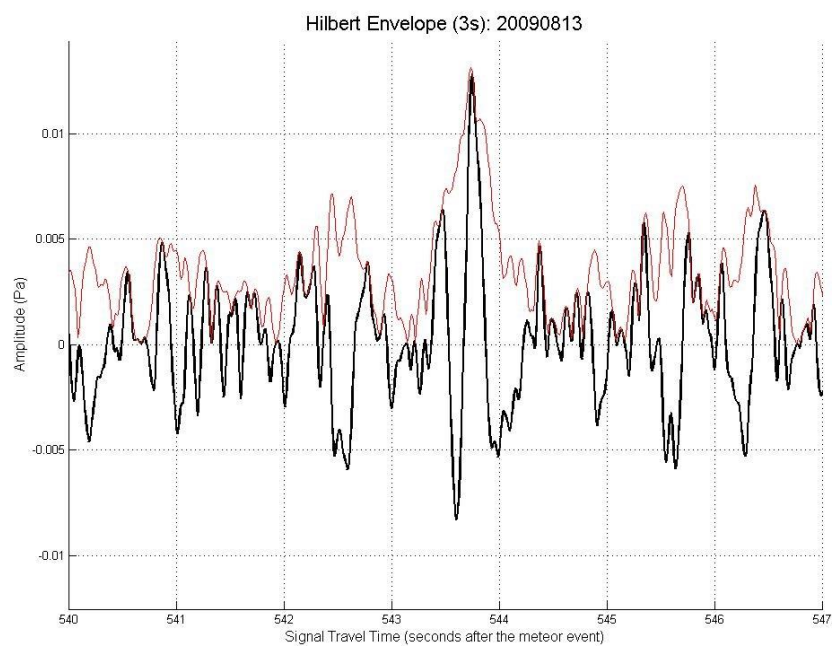
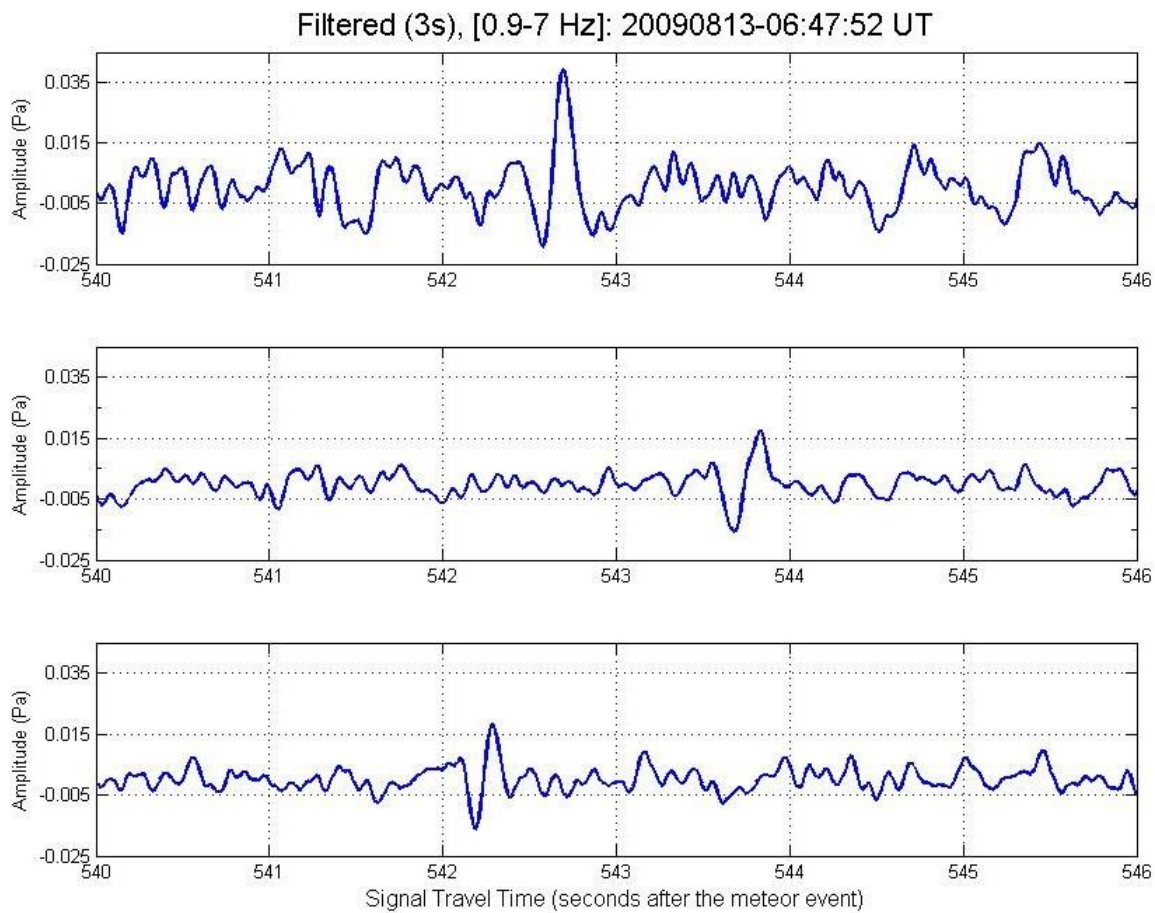


### 20090813\_064752

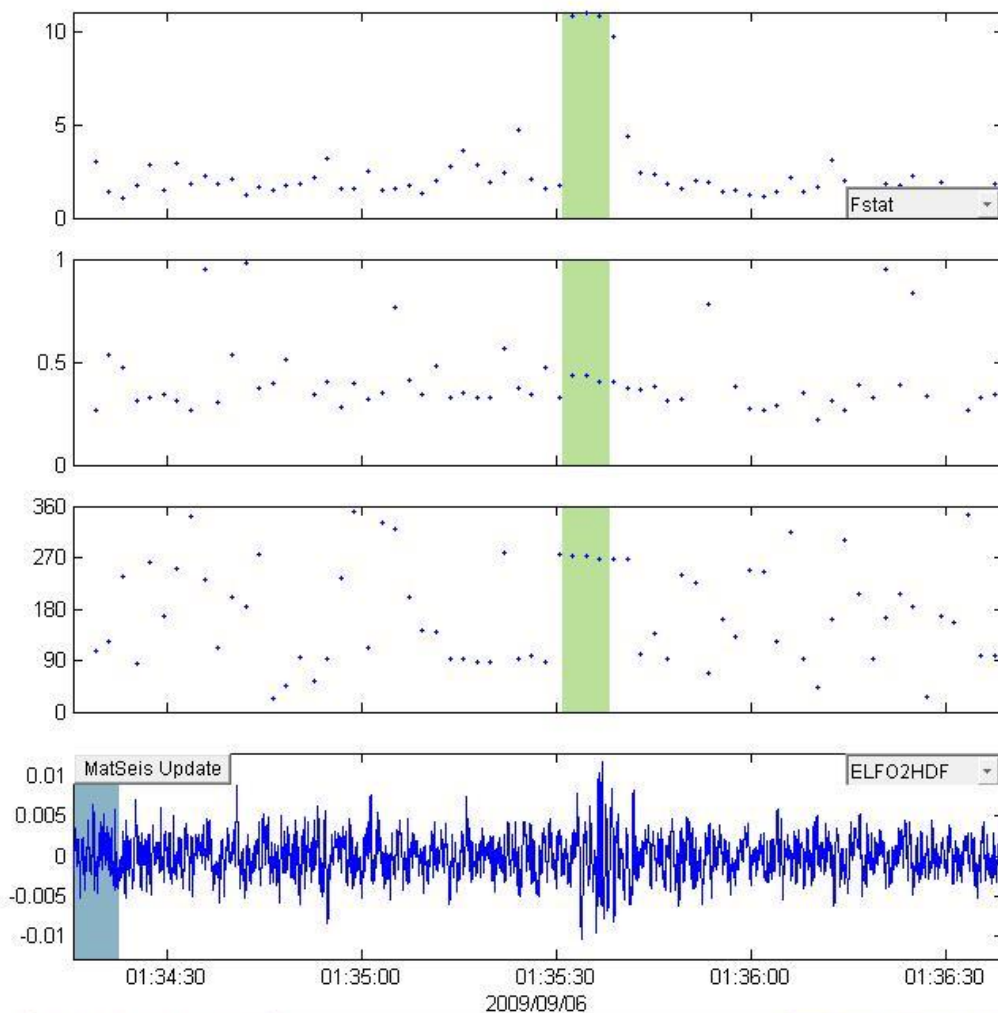


Window Parameters		Pass Band Parameters		Slowness Parameters		Windowed Values & S.D.		
Duration (s)	7	Low frequency (Hz)	0.9	Max. Slown.	400.0	Corr.	0.676	0.148
Overlap (%)	70.0	High frequency	7	# of Slown.	40	Fstat	6.758	5.045
Number of	112	Order (integer)	2			Vel.	0.348	0.000
						Az.	5.528	0.000

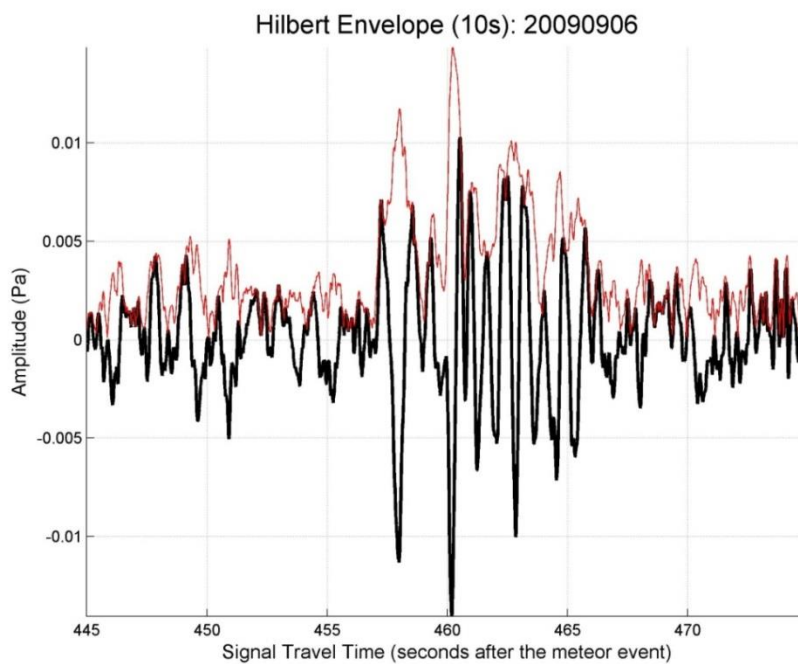
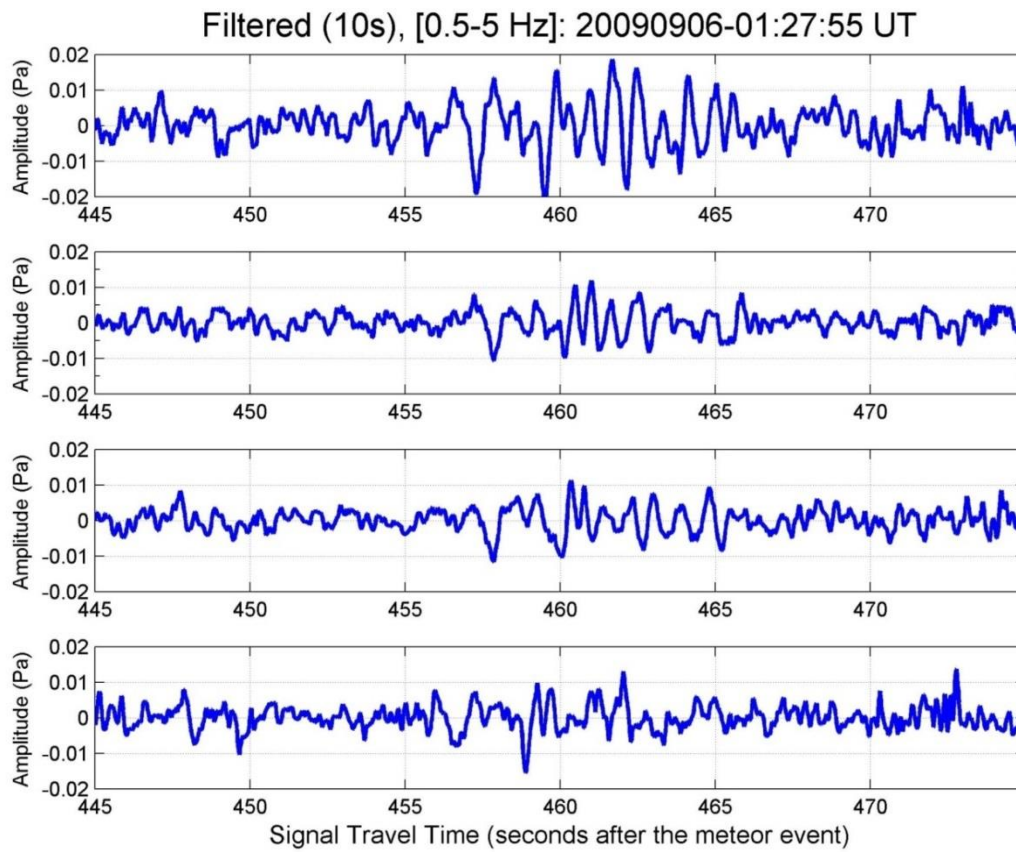
0



## 20090906\_012755

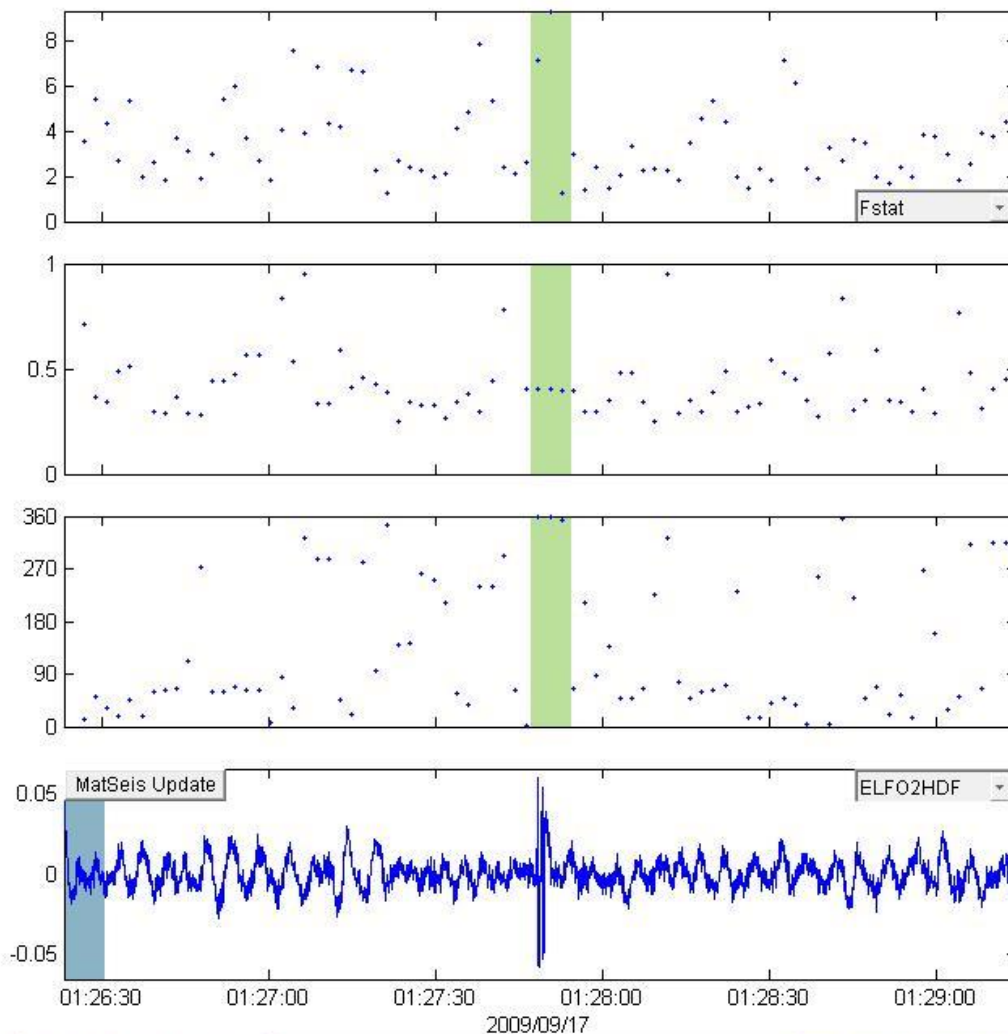


Window Parameters		Pass Band Parameters		Slowness Parameters		Windowed Values & S.D.	
Duration (s)	7	Low frequency (Hz)	0.5	Max. Slown.	400.0	Corr.	0.748 0.002
Overlap (%)	70.0	High frequency	5	# of Slown.	40	Fstat	10.887 0.113
Number of	67	Order (integer)	2			Vel.	0.422 0.018
						Az.	270.820 2.547
						Send to Map	
Animate		Write File				8\20080325_004203\infrasound-da	
Calculate	0					Cancel	





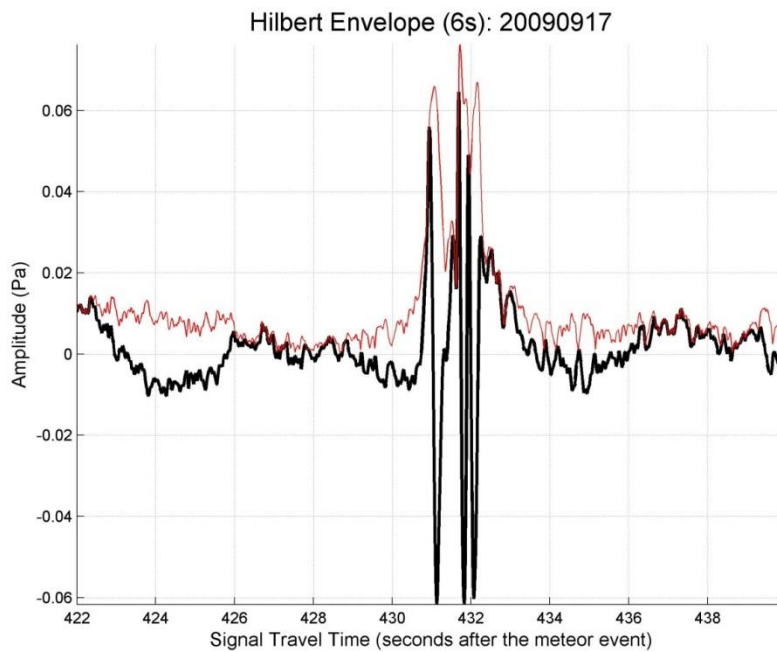
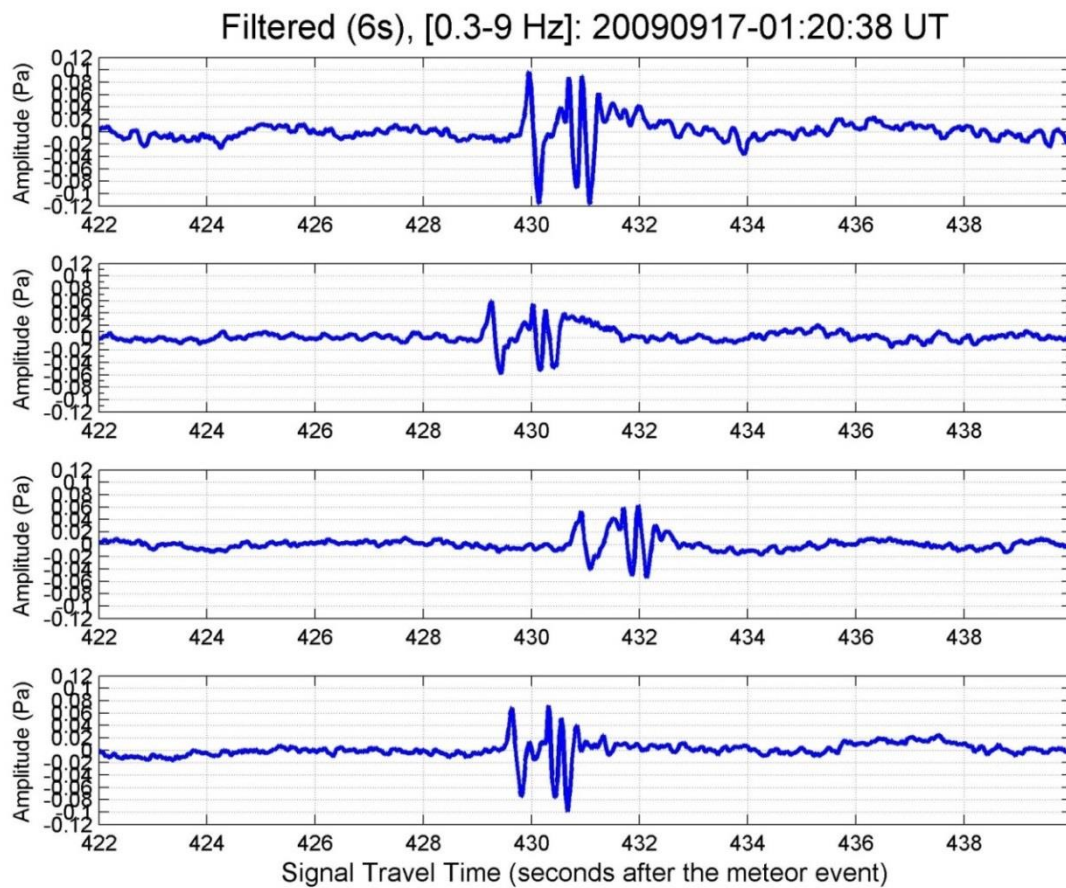
### 20090917\_012038



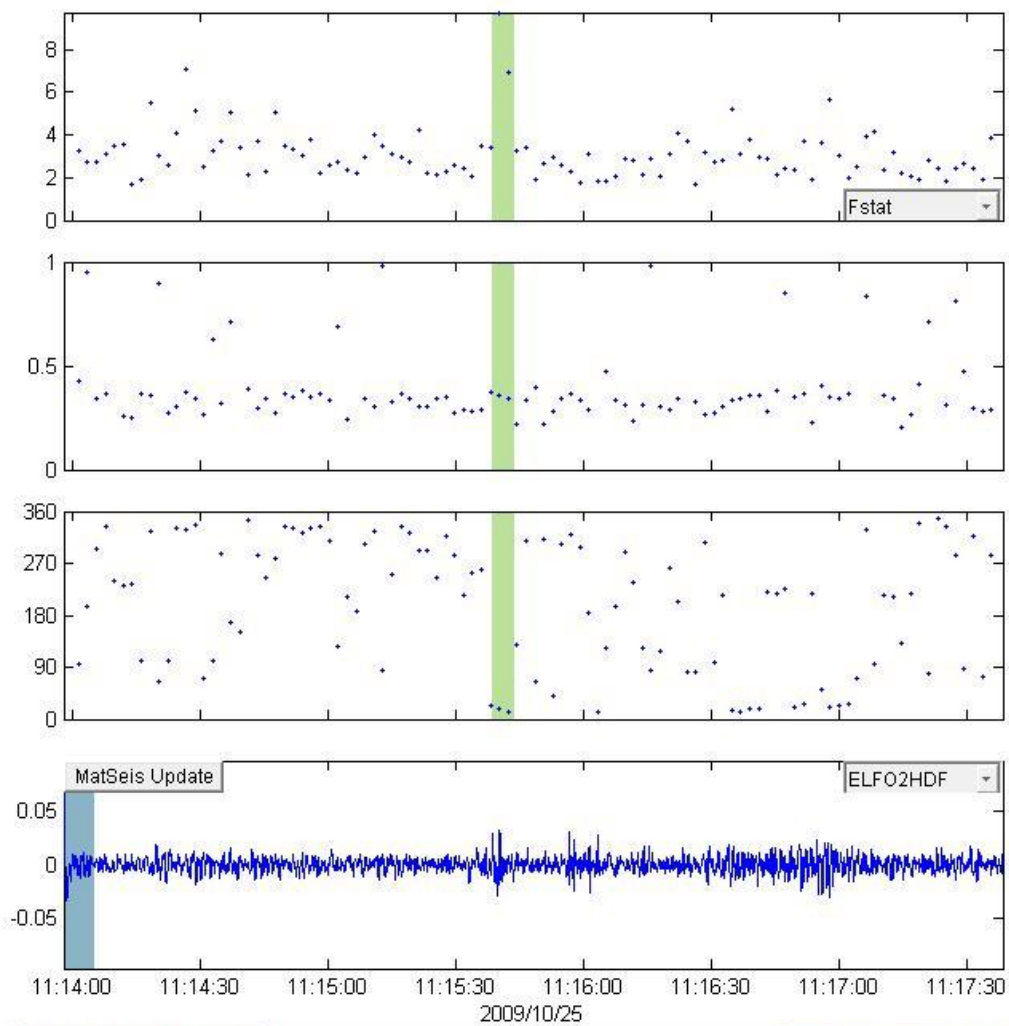
2009/09/17

Window Parameters		Pass Band Parameters		Slowness Parameters		Windowed Values & S.D.	
Duration (s)	7	Low frequency (Hz)	0.3	Max. Slown.	400.0	Corr.	0.584 0.196
Overlap (%)	70.0	High frequency	9	# of Slown.	40	Fstat	5.923 4.201
Number of	80	Order (integer)	2			Vel.	0.400 0.001
						Az.	356.473 2.436

0
  8|20080325\_004203|infrasound-da

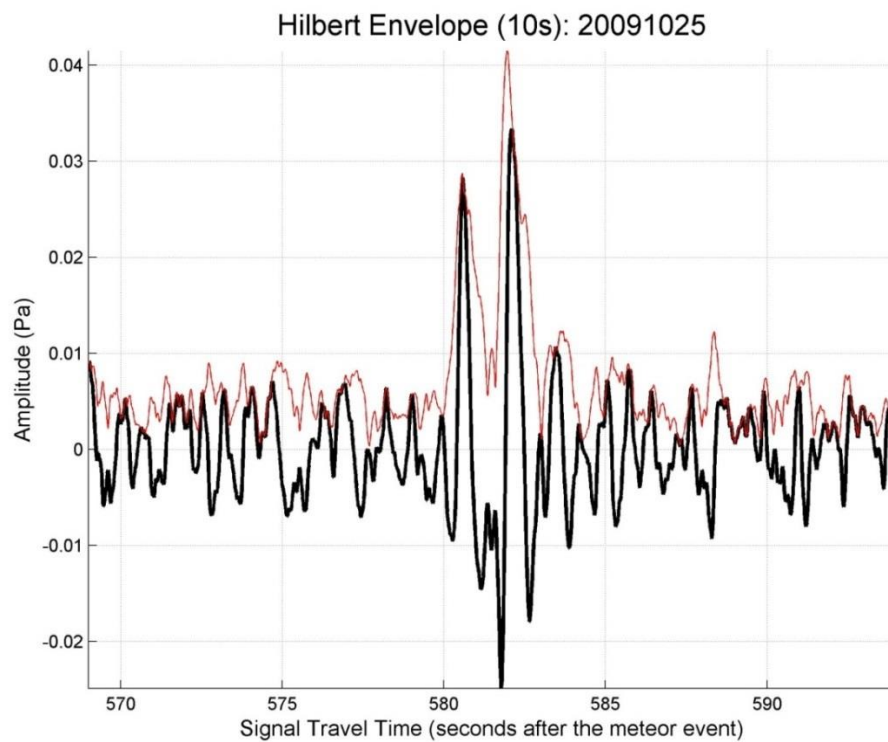
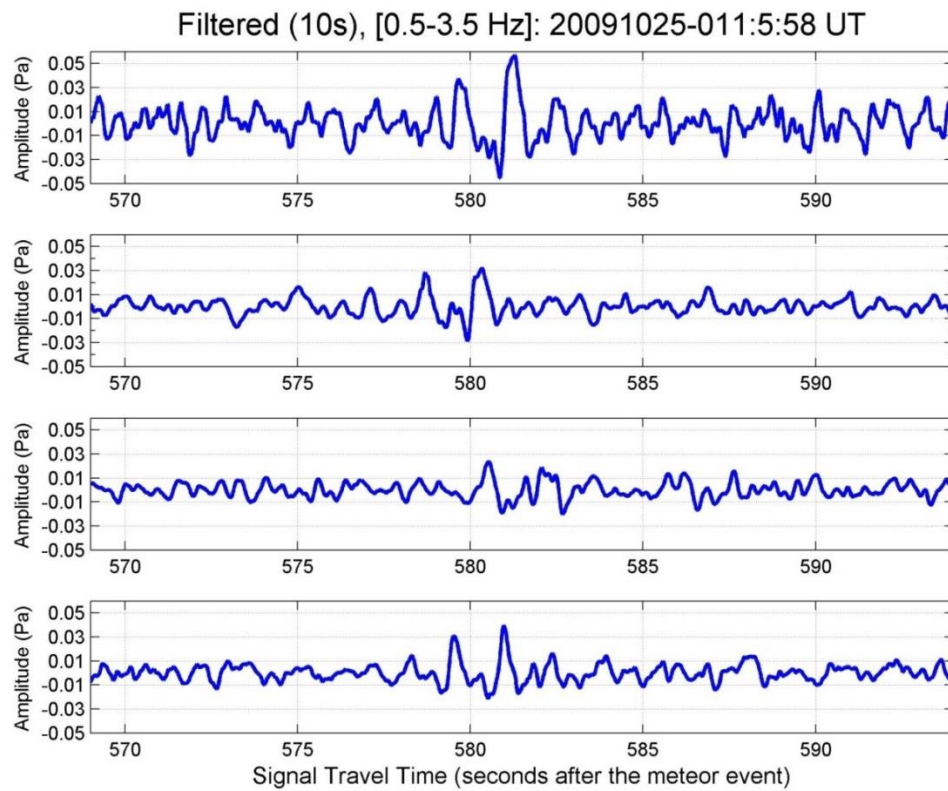


20091025\_110558

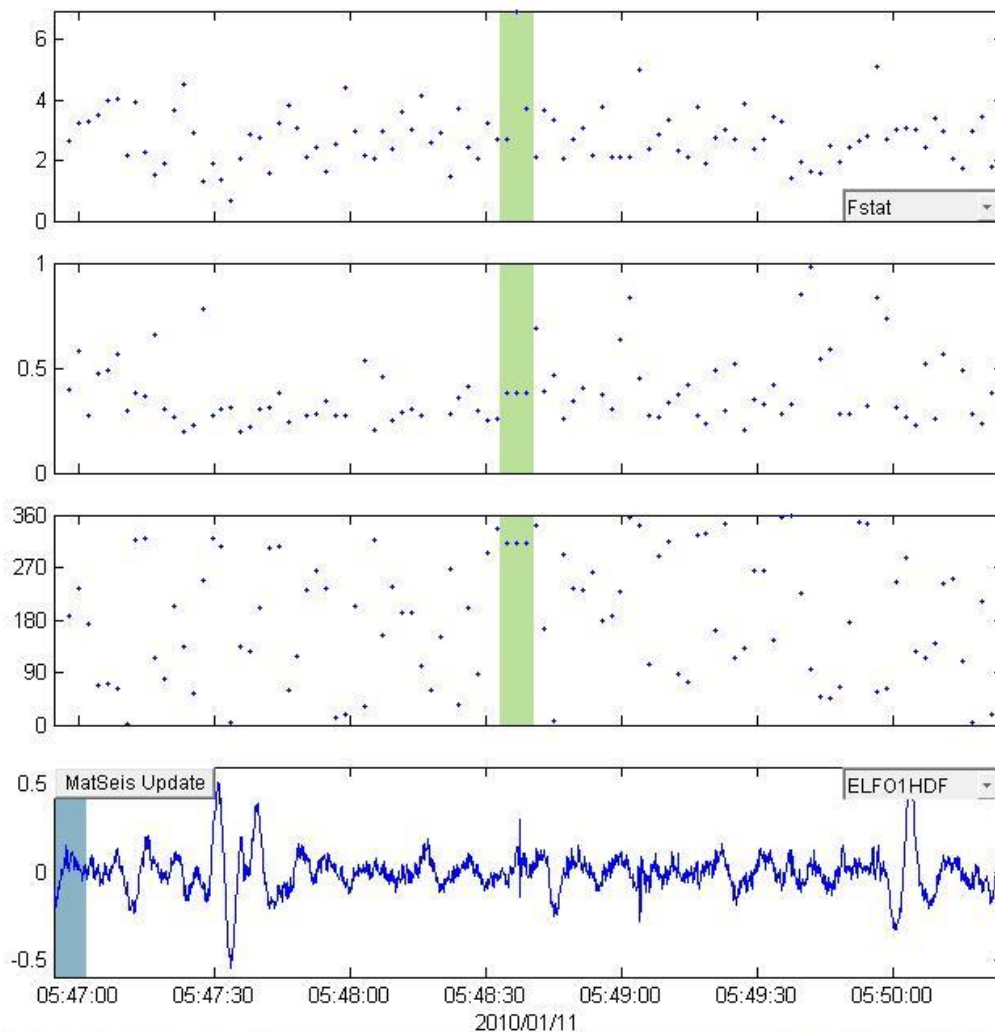


Window Parameters		Pass Band Parameters		Slowness Parameters		Windowed Values & S.D.	
Duration (s)	7	Low frequency (Hz)	0.5	Max. Slown.	400.0	Corr.	0.697 0.044
Overlap (%)	70.0	High frequency	3.5	# of Slown.	40	Fstat	8.356 1.961
Number of	103	Order (integer)	2			Vel.	0.349 0.011
						Az.	14.983 3.194
<input type="button" value="Animate"/>		<input type="button" value="Write File"/>		<input type="button" value="Send to Map"/>		<input type="button" value="Cancel"/>	
<input type="button" value="Calculate"/> 0		<input type="text" value="8\20080325_004203\infrasound-da"/>					

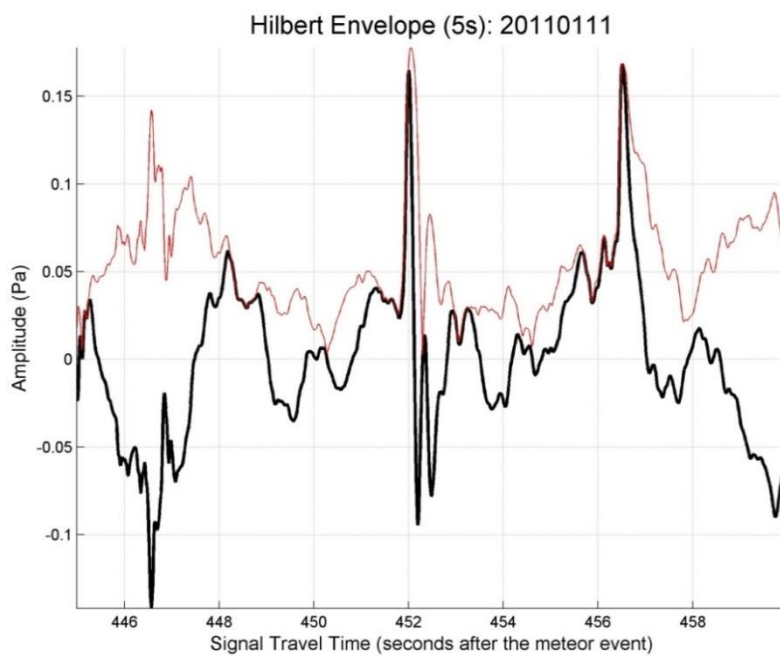
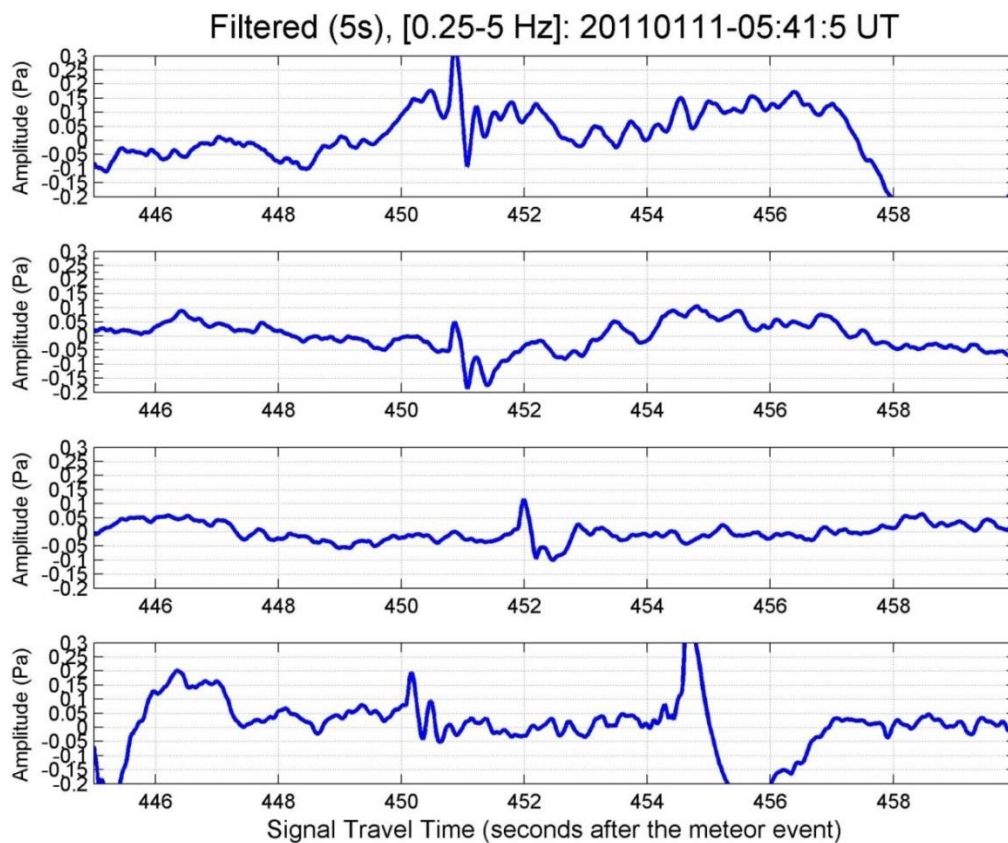




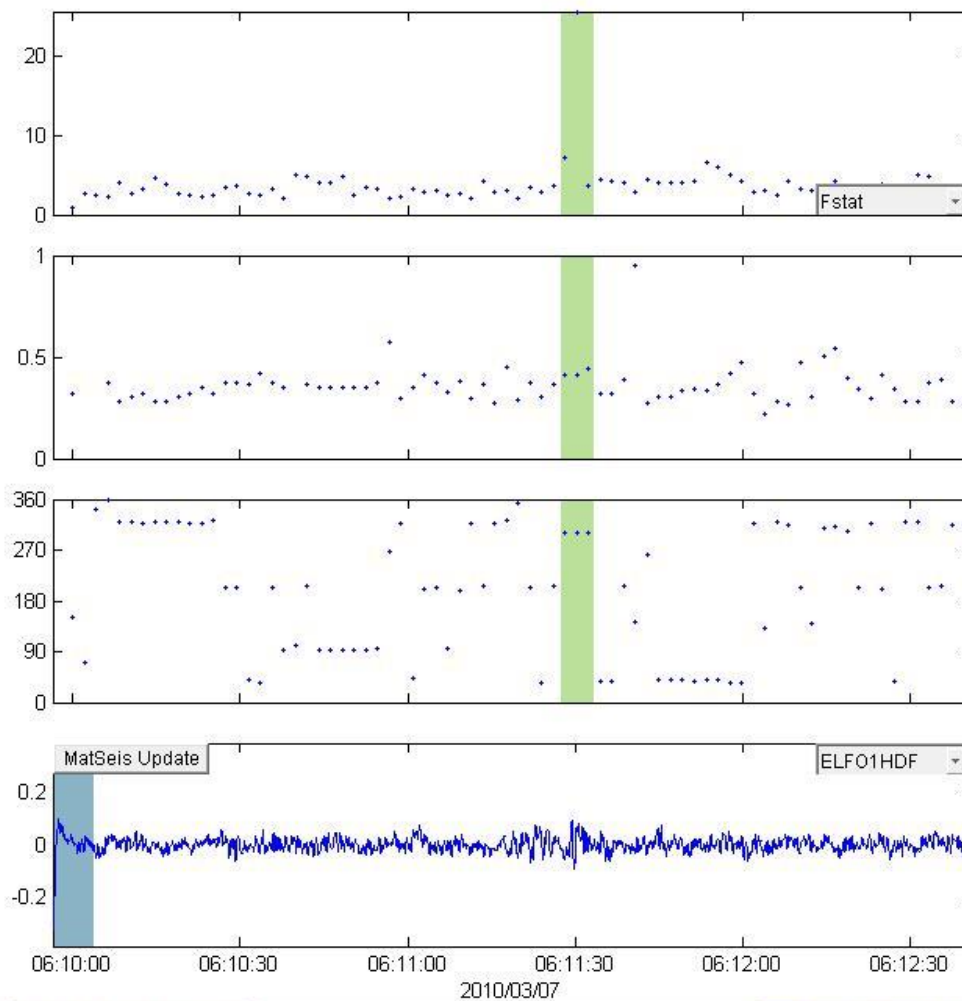
## 20100111\_054105



Window Parameters		Pass Band Parameters		Slowness Parameters		Windowed Values & S.D.	
Duration (s)	7	Low frequency (Hz)	0.3	Max. Slown.	400.0	Corr.	0.563 0.094
Overlap (%)	70.0	High frequency	5	# of Slown.	40	Fstat	4.468 2.218
Number of	98	Order (integer)	2			Vel.	0.383 0.000
						Az.	312.138 0.000
Animate						Send to Map	
Calculate	0	Write File	8\20080325_004203\infrasound-da			Cancel	

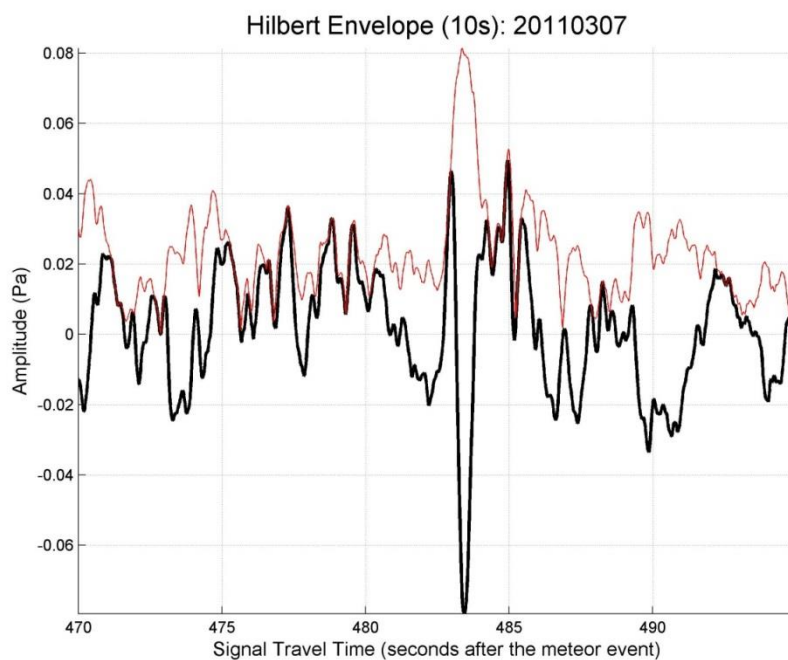
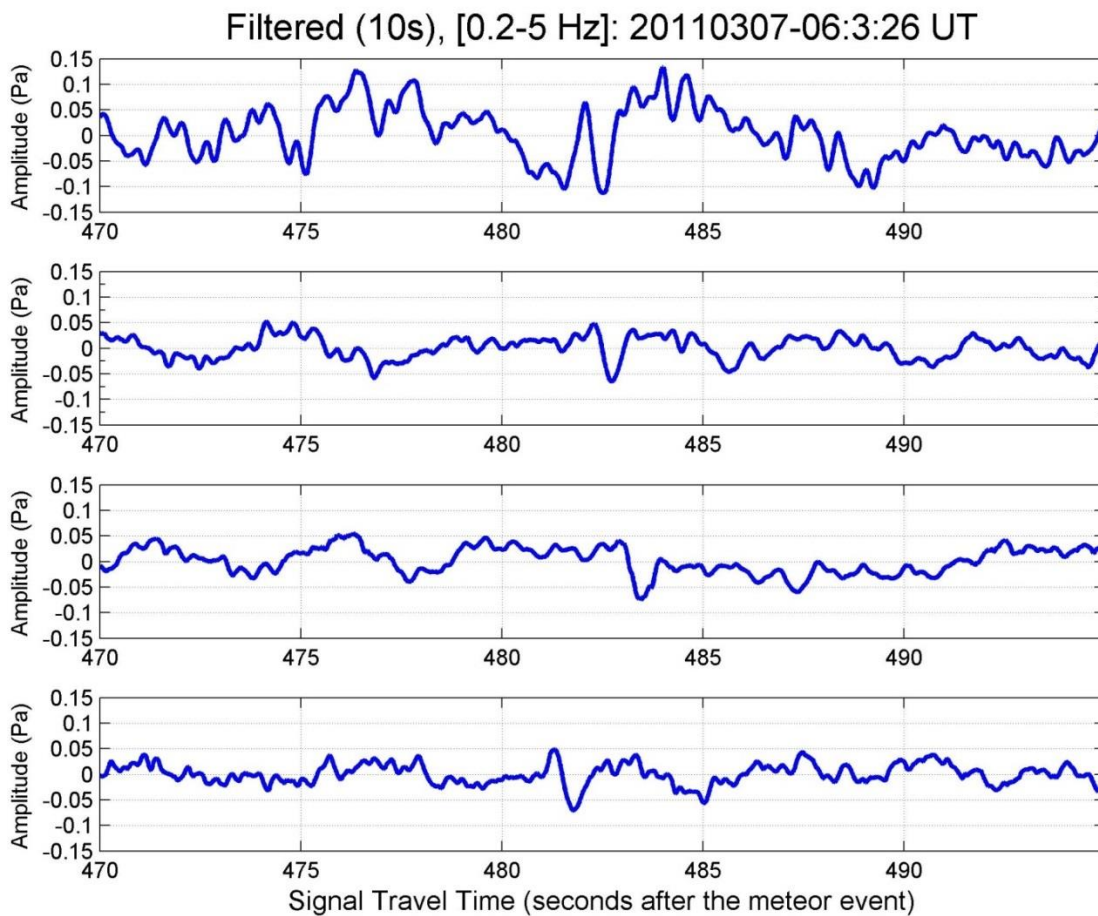


20100307\_060326



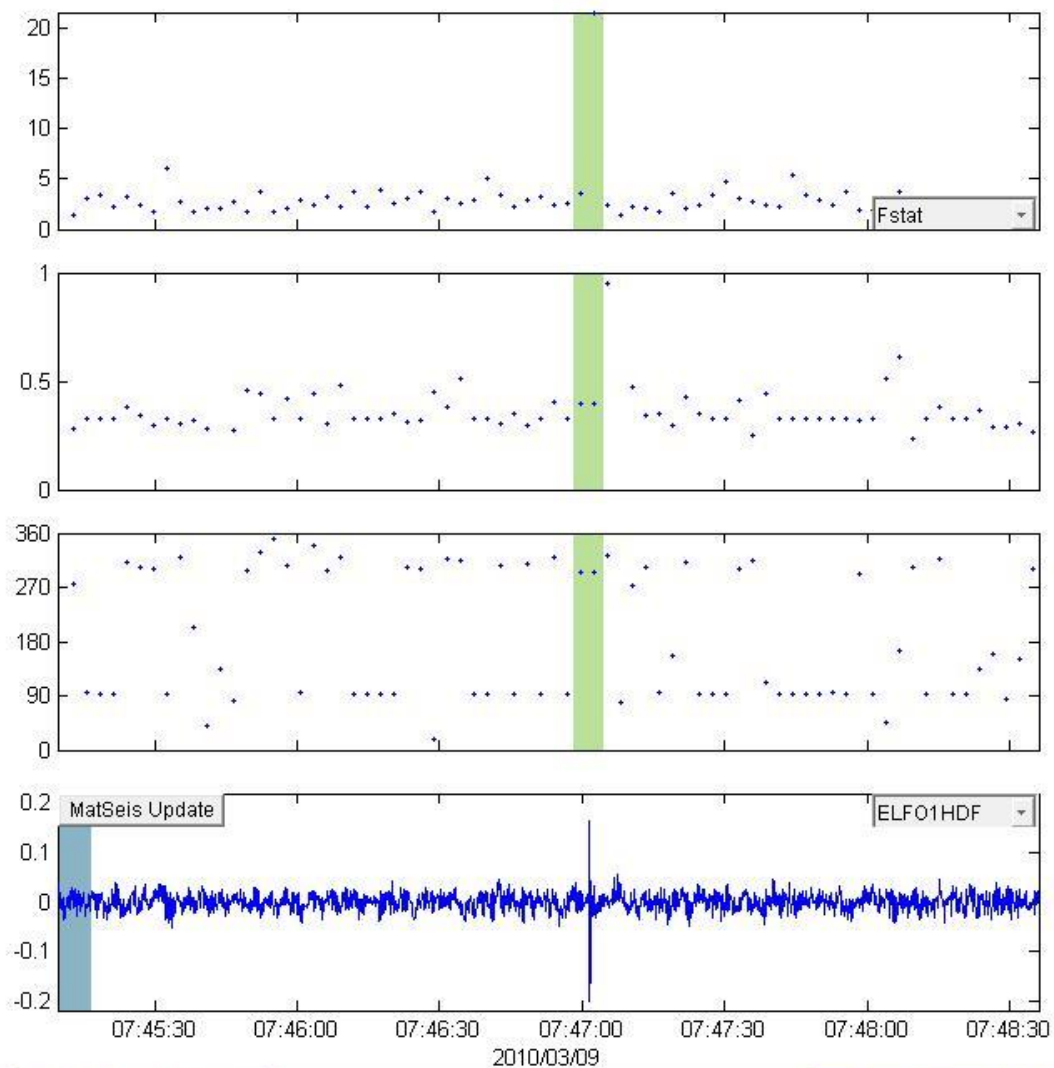
Window Parameters		Pass Band Parameters		Slowness Parameters		Windowed Values & S.D.	
Duration (s)	7	Low frequency (Hz)	0.35	Max. Slown.	400.0	Corr.	0.692 0.168
Overlap (%)	70.0	High frequency	5	# of Slown.	40	Fstat	12.128 11.842
Number of	77	Order (integer)	2			Vel.	0.420 0.017
						Az.	300.237 1.318
<input type="button" value="Animate"/> <input type="button" value="Calculate"/> 0						<input type="button" value="Send to Map"/>	
<input type="button" value="Write File"/>						<input type="button" value="Cancel"/>	

8\20080325\_004203\infrasound-da





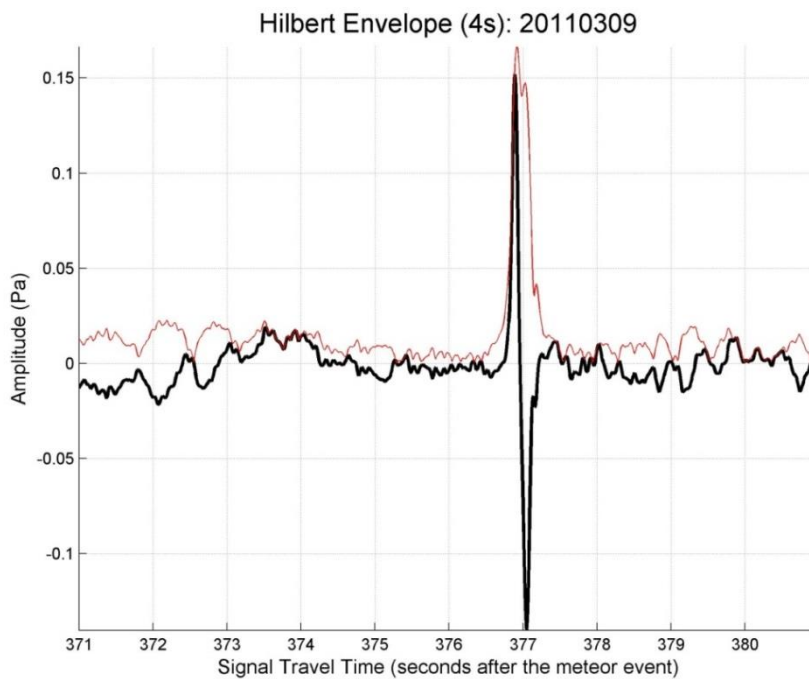
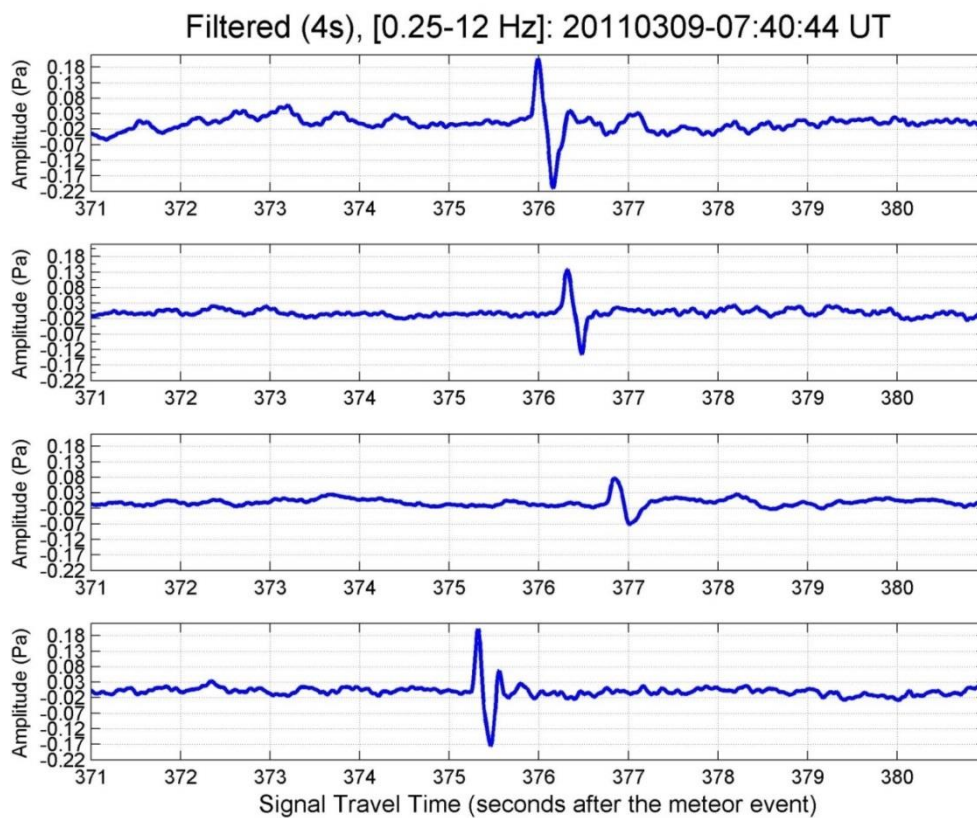
### 20100309\_074044



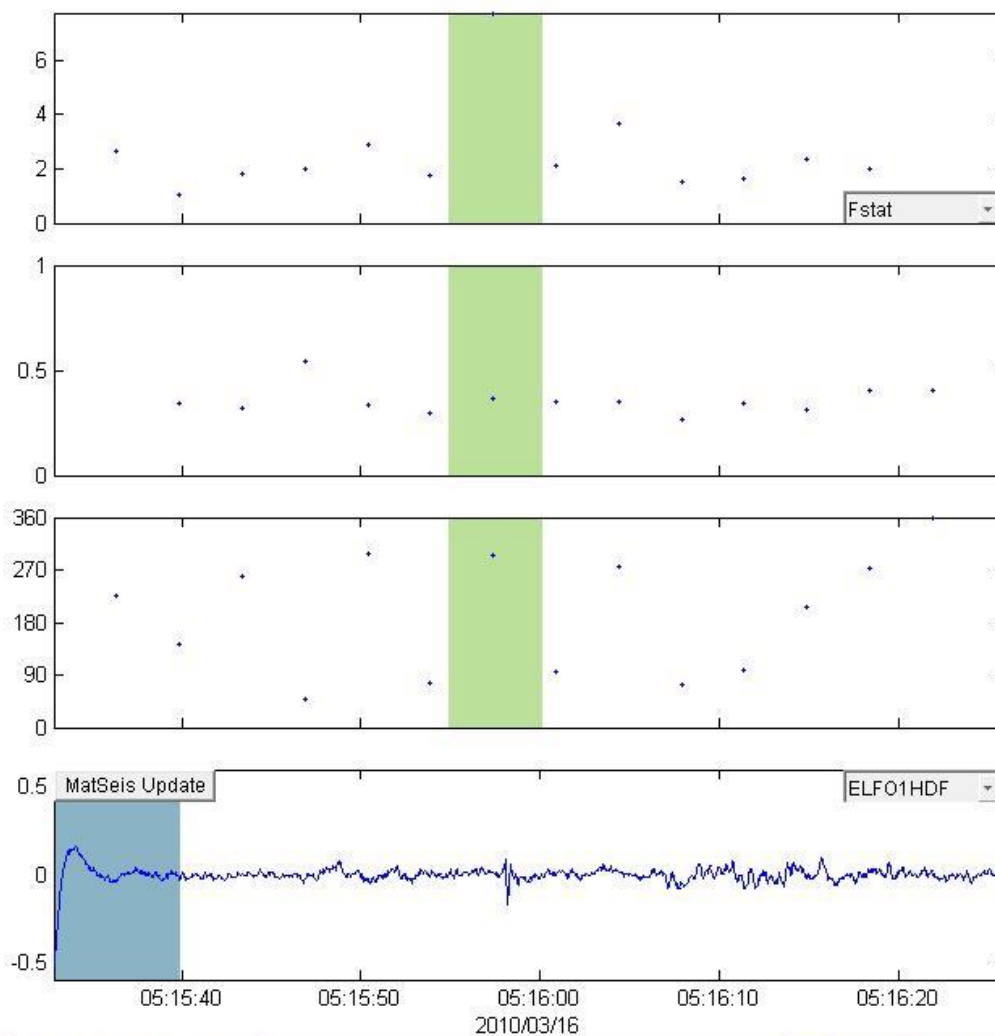
Window Parameters		Pass Band Parameters		Slowness Parameters		Windowed Values & S.D.	
Duration (s)	7	Low frequency (Hz)	0.35	Max. Slown.	400.0	Corr.	0.692   0.223
Overlap (%)	60.0	High frequency	5	# of Slown.	40	Fstat	12.579   12.706
Number of	73	Order (integer)	2			Vel.	0.397   0.000
						Az.	293.749   0.000

Animate			
Calculate	0	Write File	8\20080325_004203\infrasound-da
			Cancel

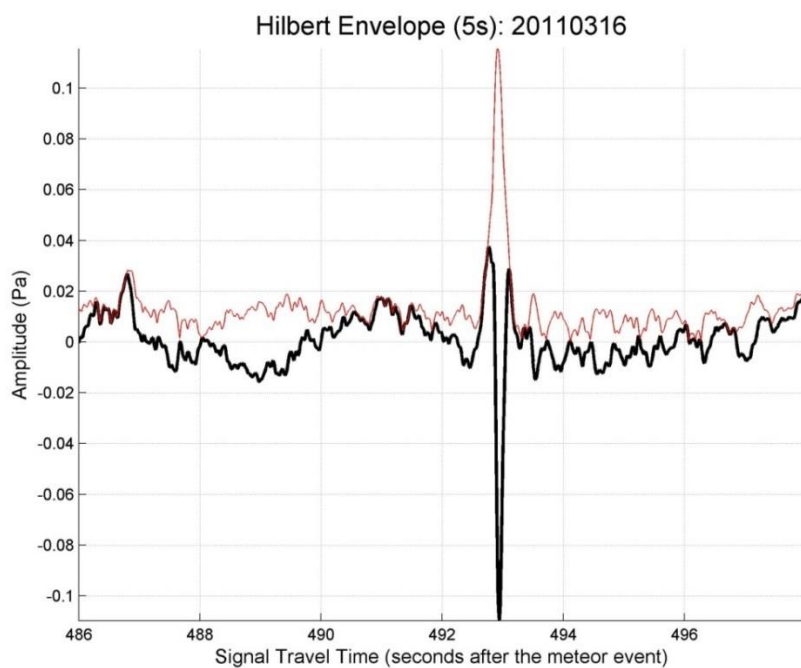
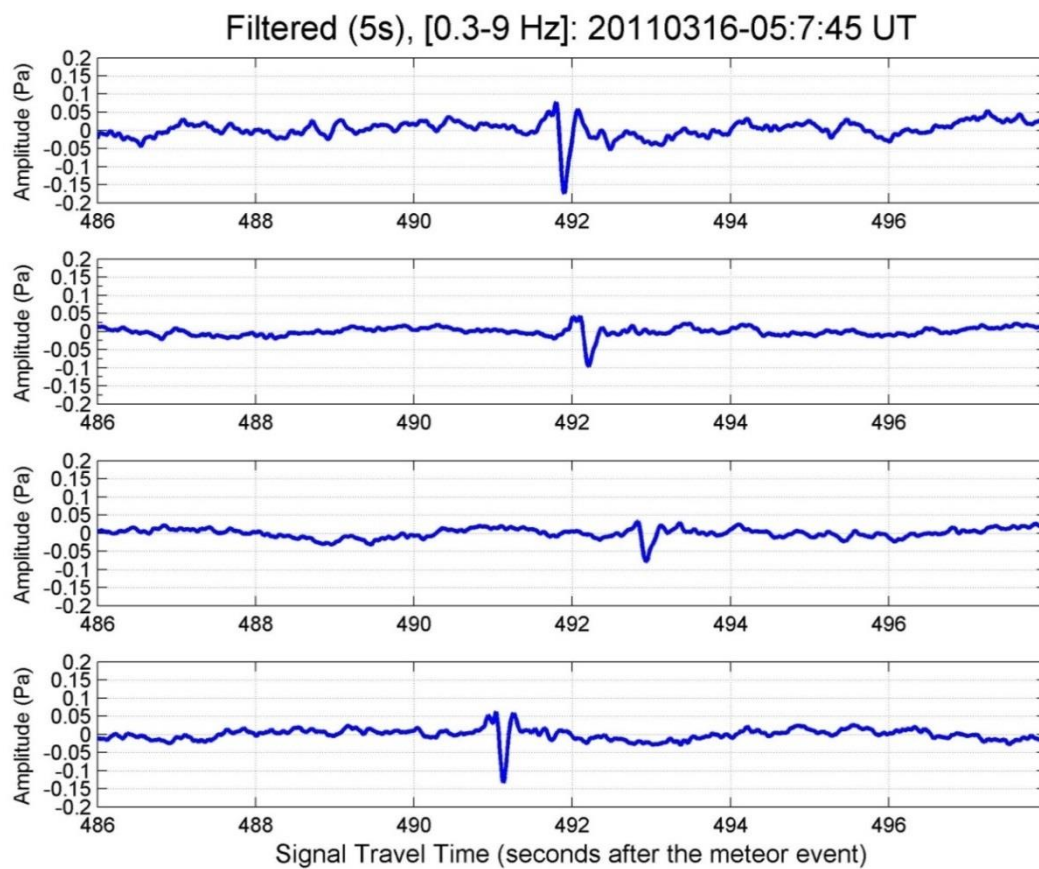


## 20100316\_050745

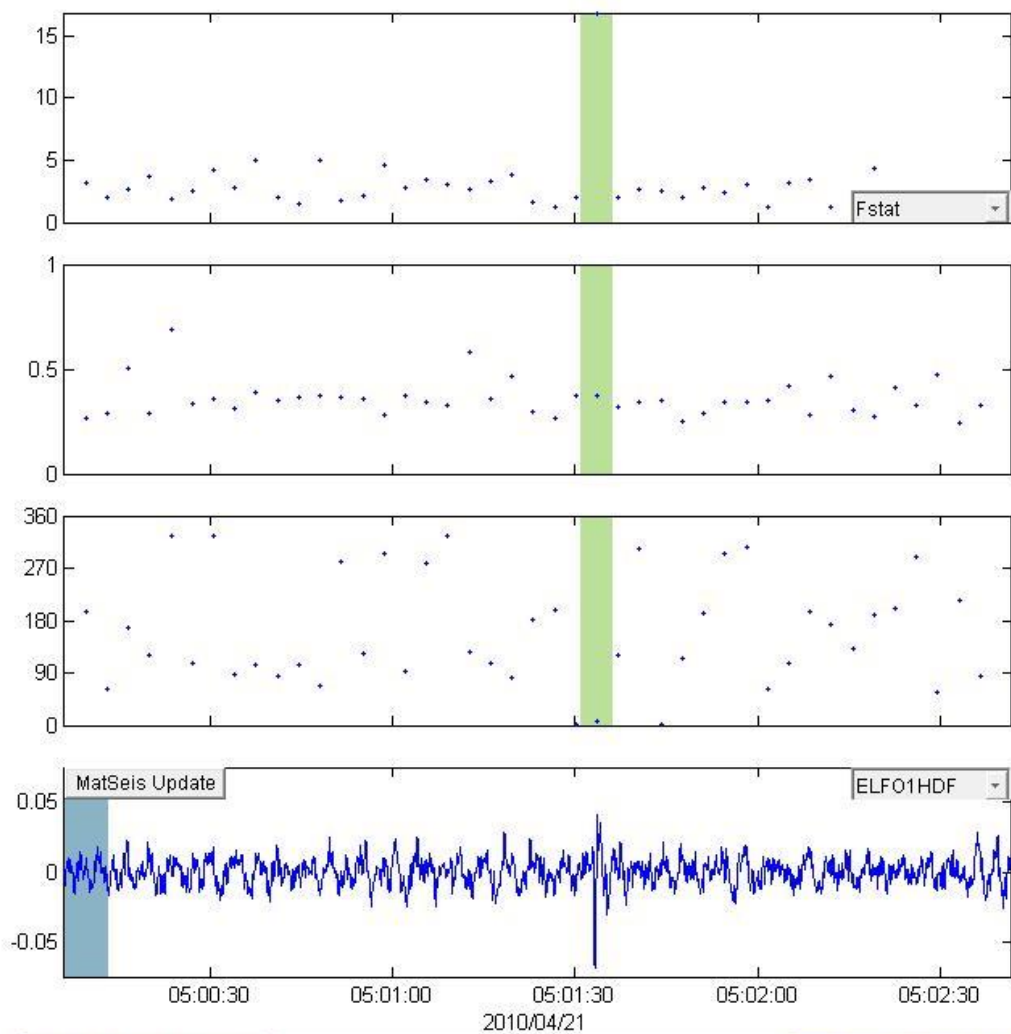


Window Parameters		Pass Band Parameters		Slowness Parameters		Windowed Values & S.D.	
Duration (s)	7	Low frequency (Hz)	0.3	Max. Slown.	400.0	Corr.	0.686 0.000
Overlap (%)	50.0	High frequency	15	# of Slown.	40	Fstat	7.749 0.000
Number of	14	Order (integer)	2			Vel.	0.362 0.000
						Az.	295.710 0.000
						Send to Map	
Animate		Write File	8\20080325_004203\infrasound-da		Cancel		
Calculate	0						

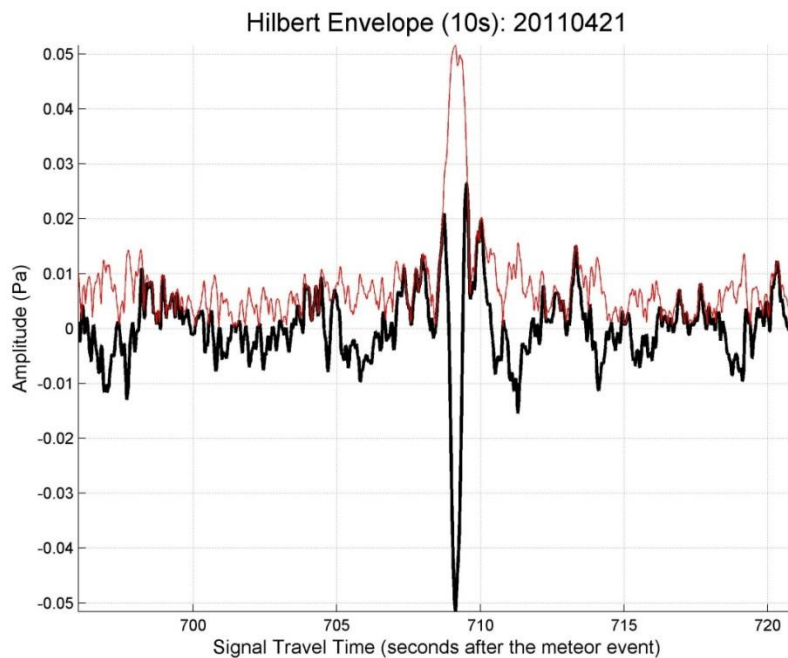
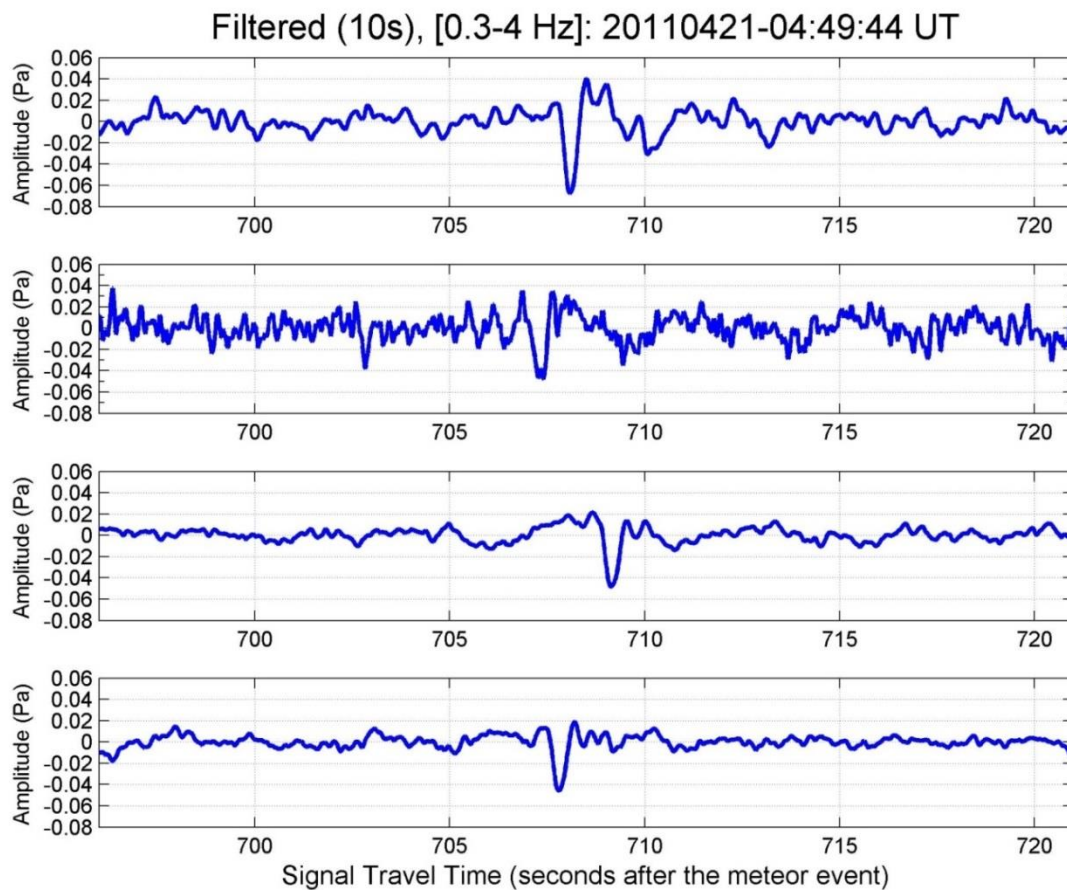




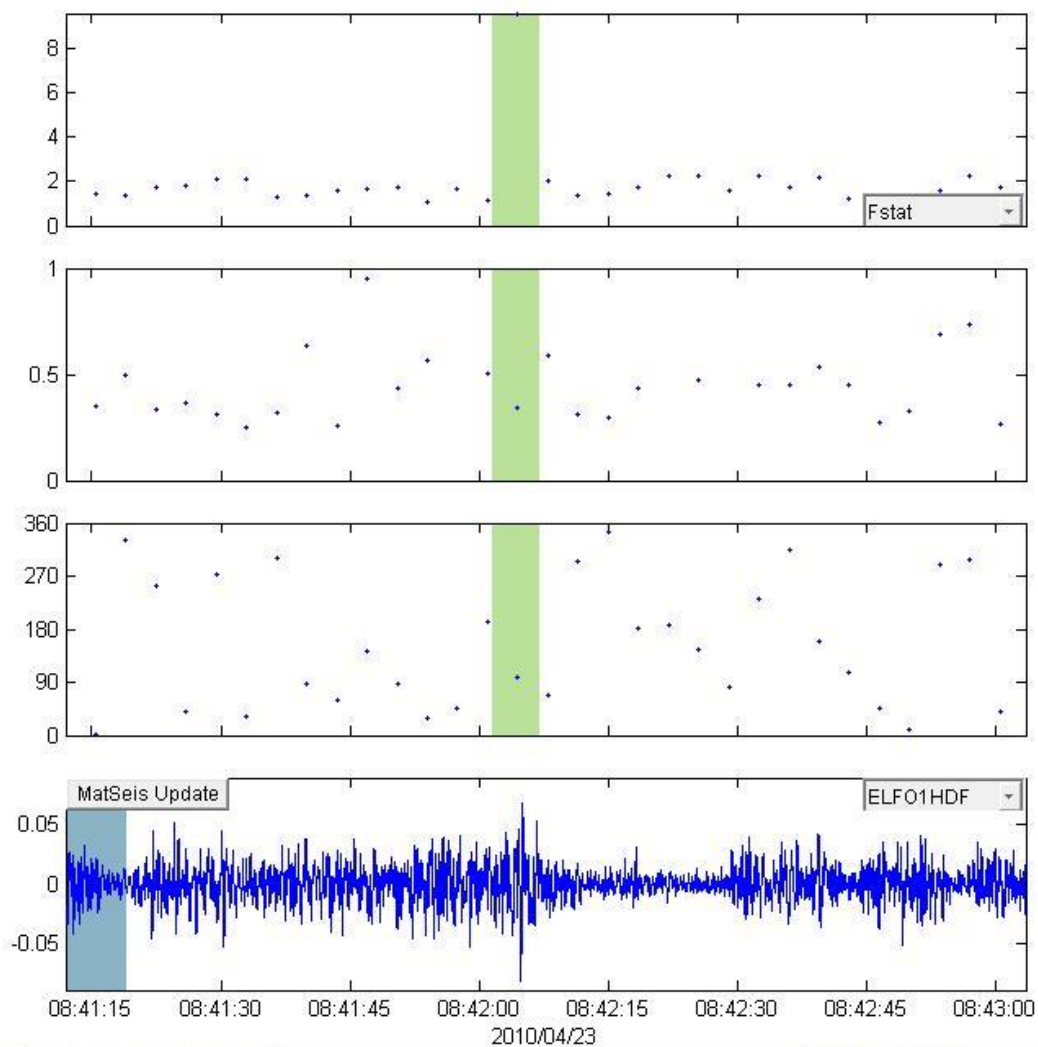
20100421\_044944



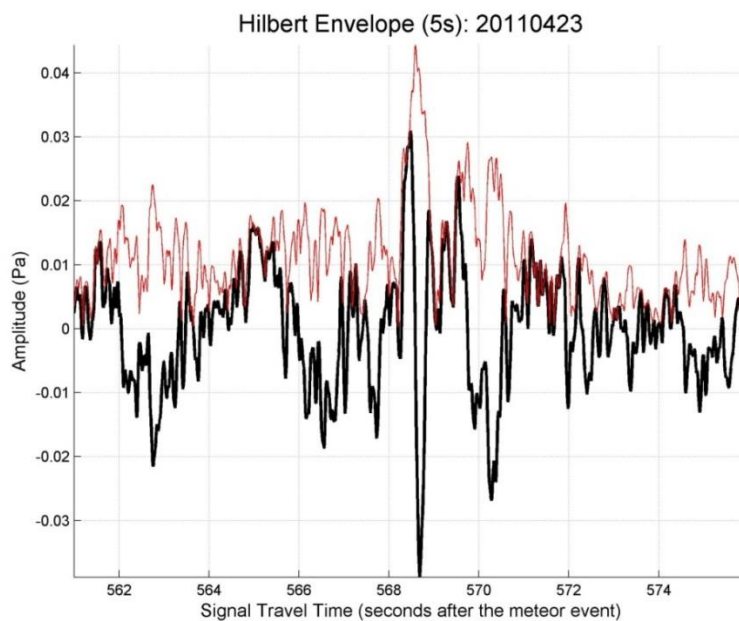
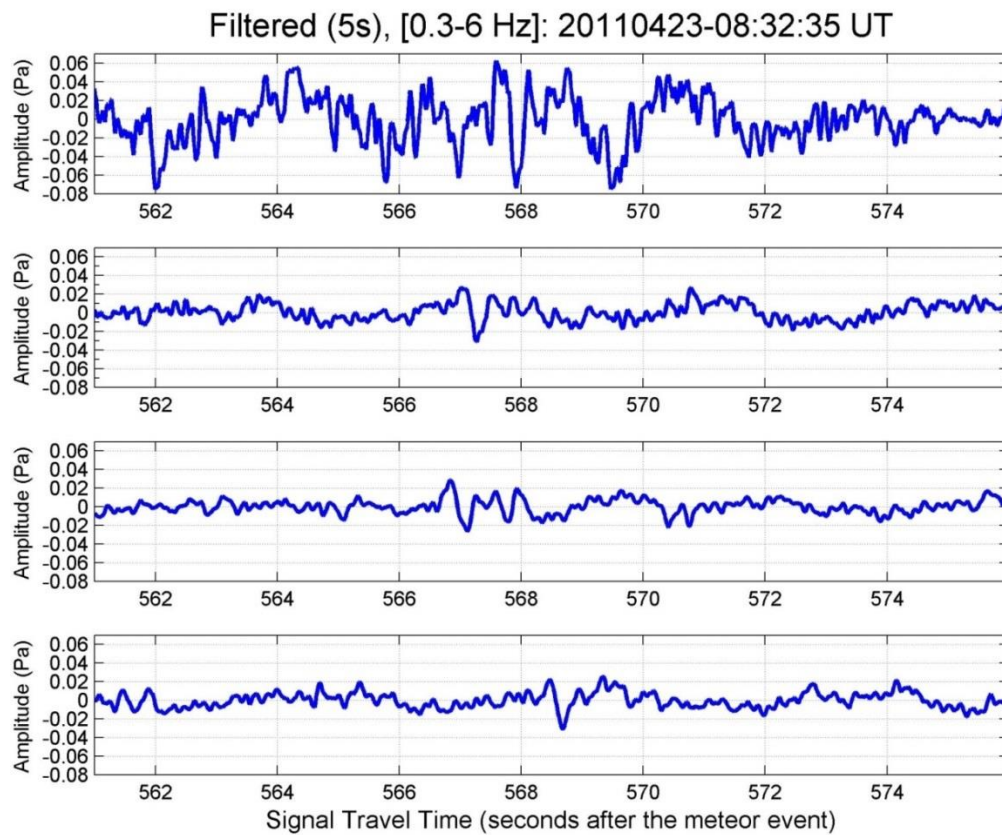
Window Parameters		Pass Band Parameters		Slowness Parameters		Windowed Values & S.D.	
Duration (s)	7	Low frequency (Hz)	0.3	Max. Slown.	400.0	Corr.	0.817 0.000
Overlap (%)	50.0	High frequency	4	# of Slown.	40	Fstat	16.833 0.000
Number of	43	Order (integer)	2			Vel.	0.372 0.000
						Az.	5.906 0.000
Animate						Send to Map	
Calculate	0	Write File	8\20080325_004203\infrasound-da			Cancel	



20100423\_083235

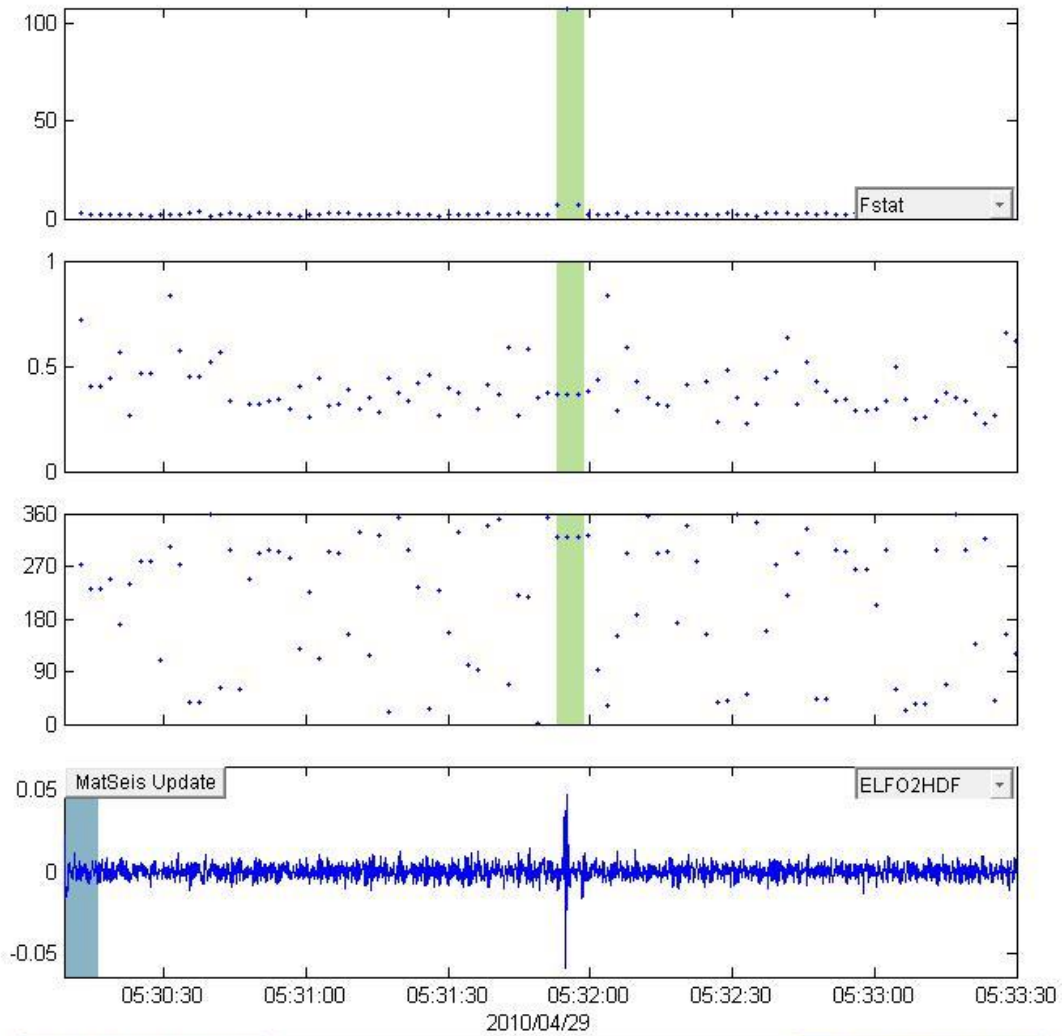


Window Parameters		Pass Band Parameters		Slowness Parameters		Windowed Values & S.D.	
Duration (s)	7.0	Low frequency (Hz)	0.8	Max. Slown.	400.0	Corr.	0.727   0.000
Overlap (%)	50.0	High frequency	5	# of Slown.	40	Fstat	9.626   0.000
Number of	31	Order (integer)	2			Vel.	0.345   0.000
						Az.	99.162   0.000
						Send to Map	
Animate		Write File				D:\Research\Research - Elizabeth\lr	
Calculate	0					Cancel	



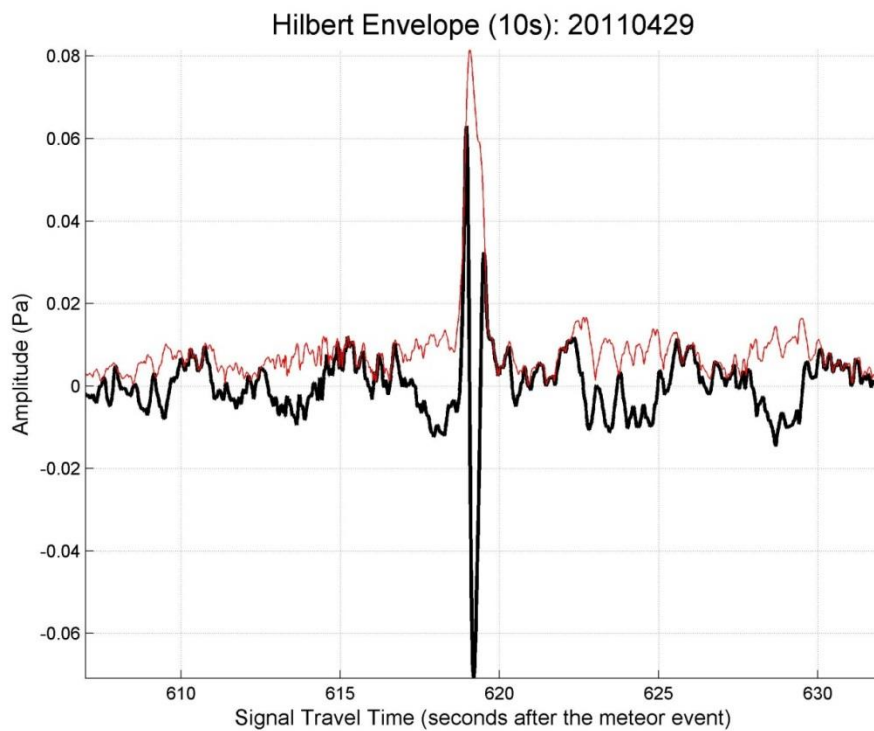
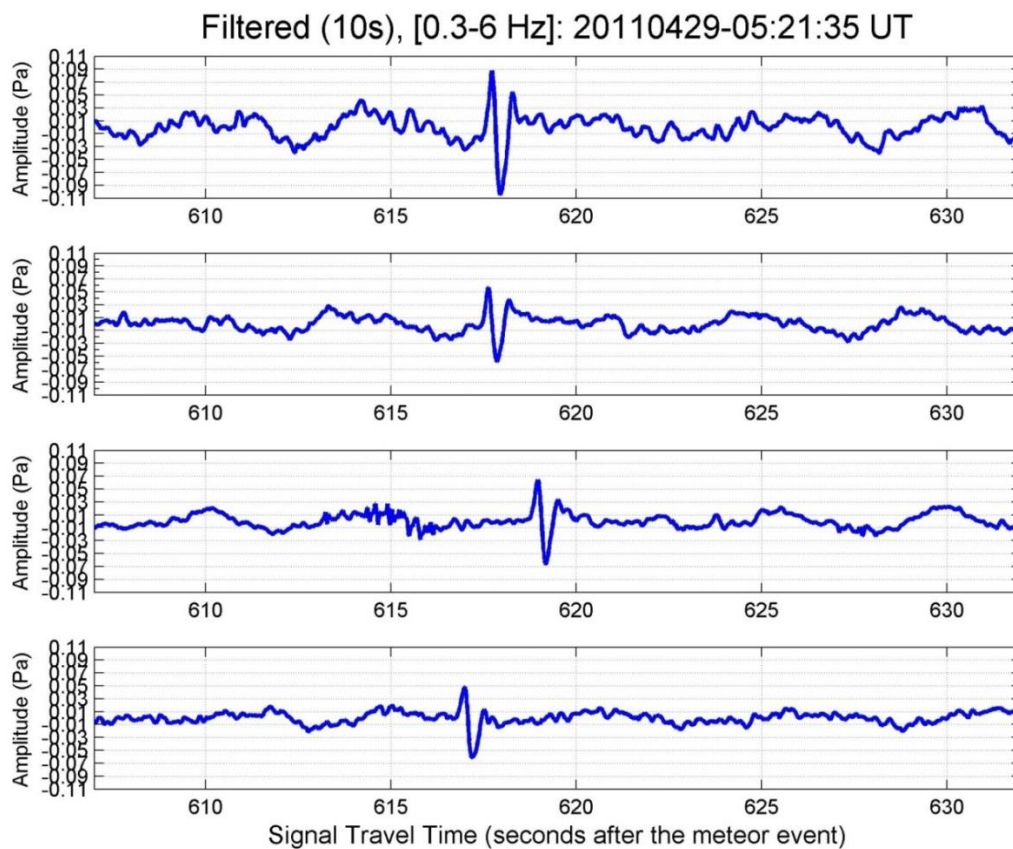


### 20100429\_052135

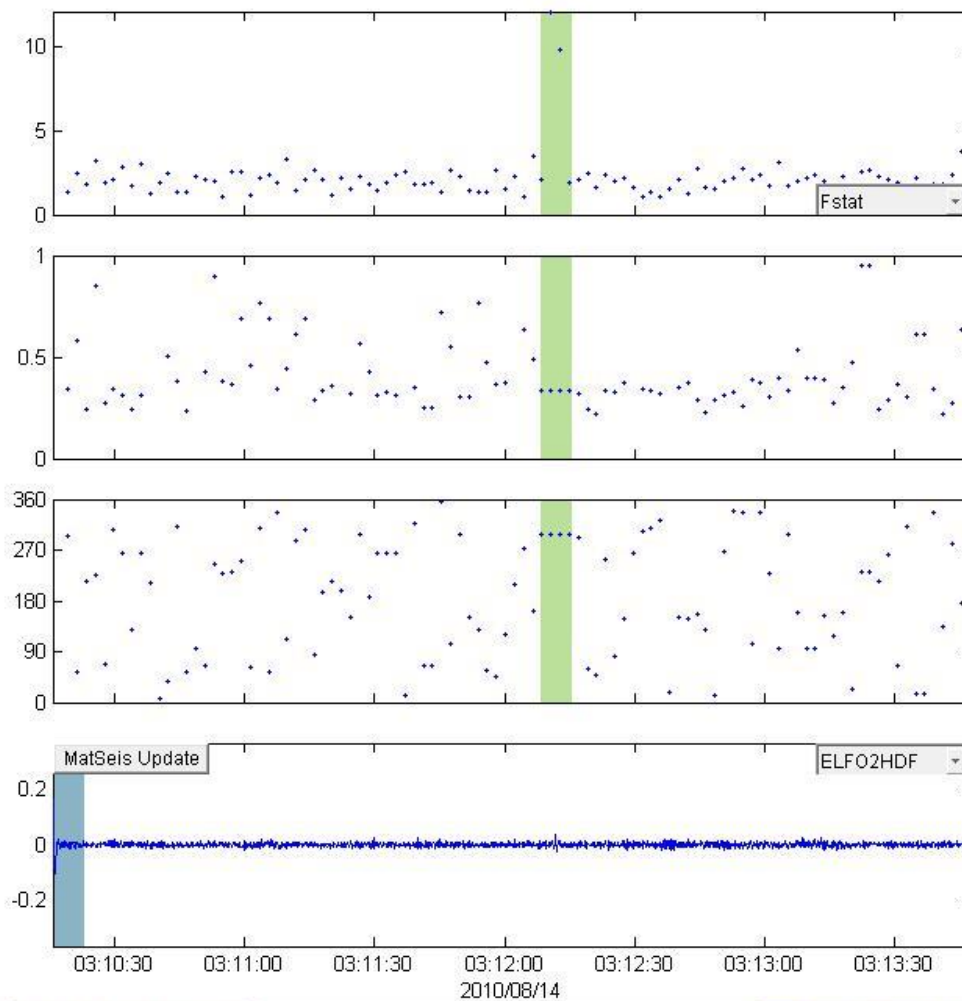


Window Parameters		Pass Band Parameters		Slowness Parameters		Windowed Values & S.D.	
Duration (s)	7.0	Low frequency (Hz)	0.8	Max. Slown.	400.0	Corr.	0.765   0.173
Overlap (%)	70.0	High frequency	5	# of Slown.	40	Fstat	40.713   58.437
Number of	95	Order (integer)	2			Vel.	0.363   0.000
						Az.	320.440   0.000

0  D:\Research\Research - Elizabeth\l...



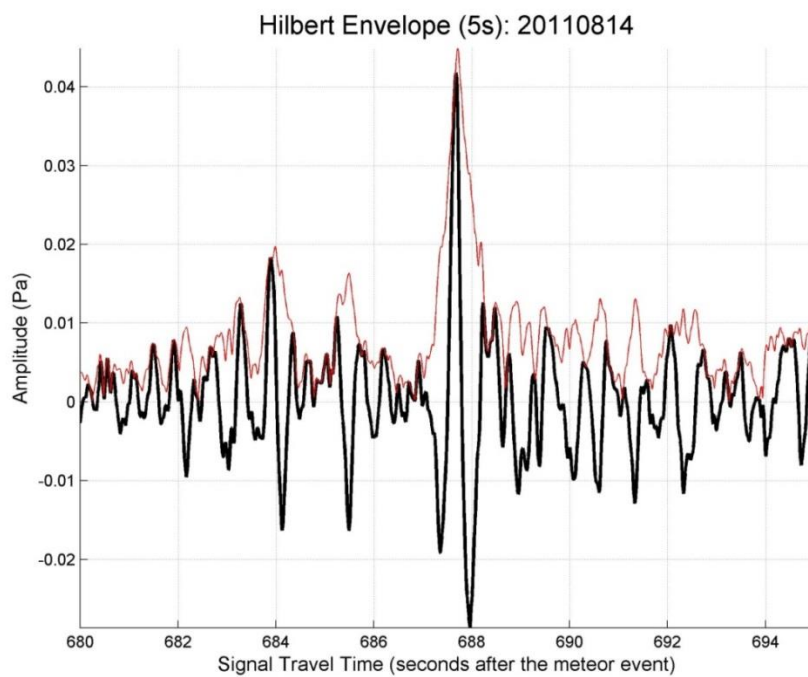
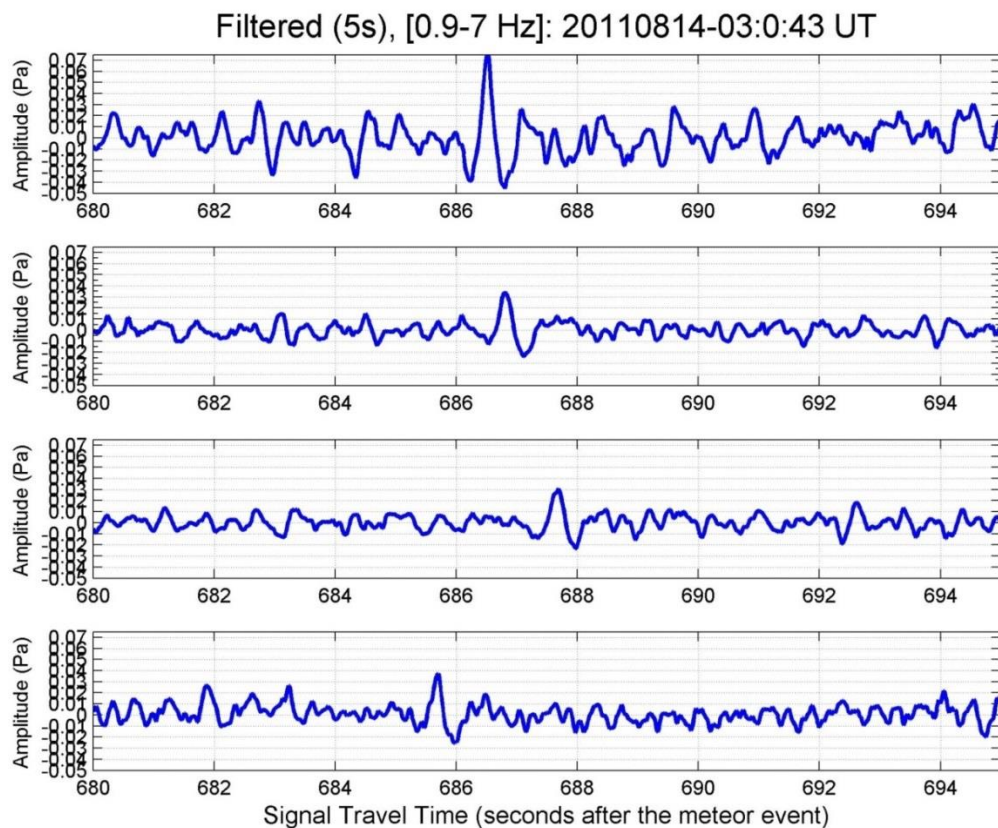
## 20100814\_030043



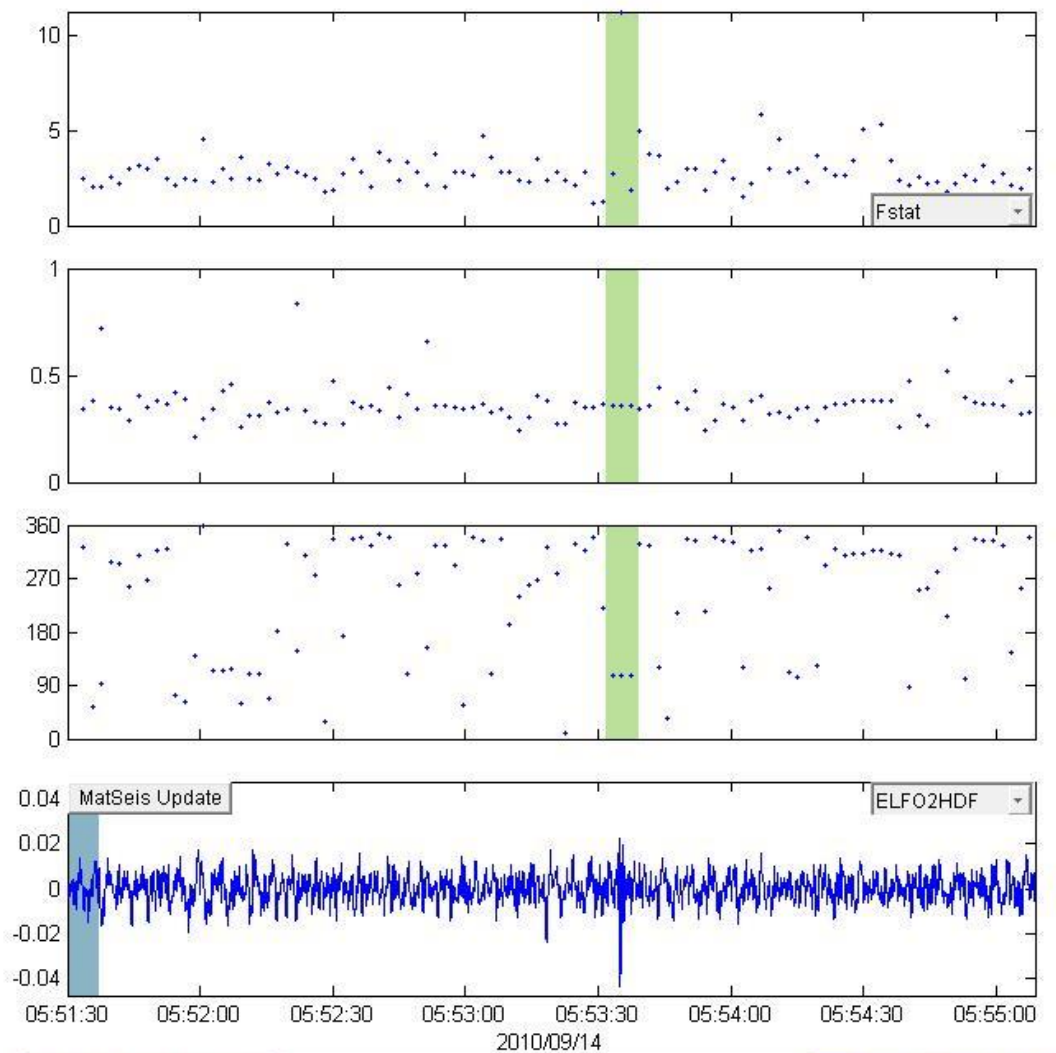
Window Parameters		Pass Band Parameters		Slowness Parameters		Windowed Values & S.D.	
Duration (s)	7.0	Low frequency (Hz)	0.8	Max. Slown.	400.0	Corr.	0.587 0.186
Overlap (%)	70.0	High frequency	7	# of Slown.	40	Fstat	6.461 5.260
Number of	99	Order (integer)	2			Vel.	0.332 0.000
						Az.	297.350 0.000

0
  D:\Research\Research - Elizabeth\ur

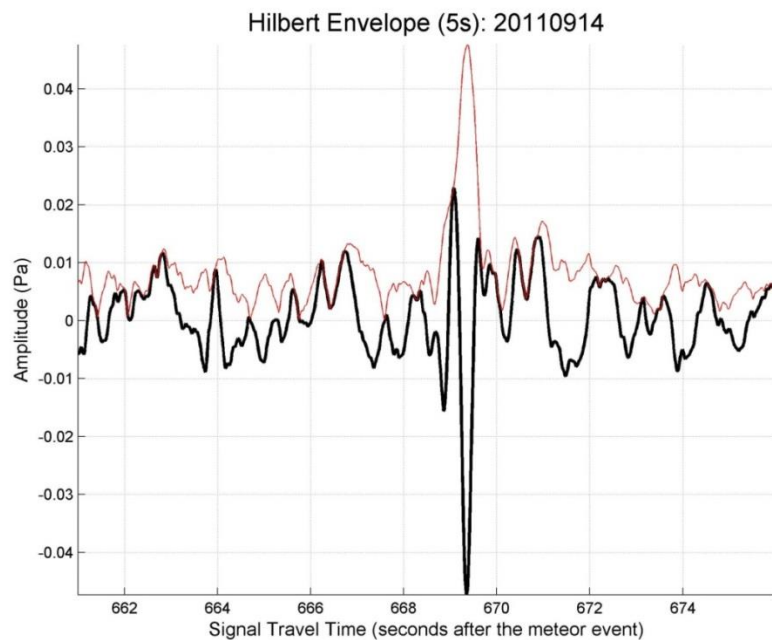
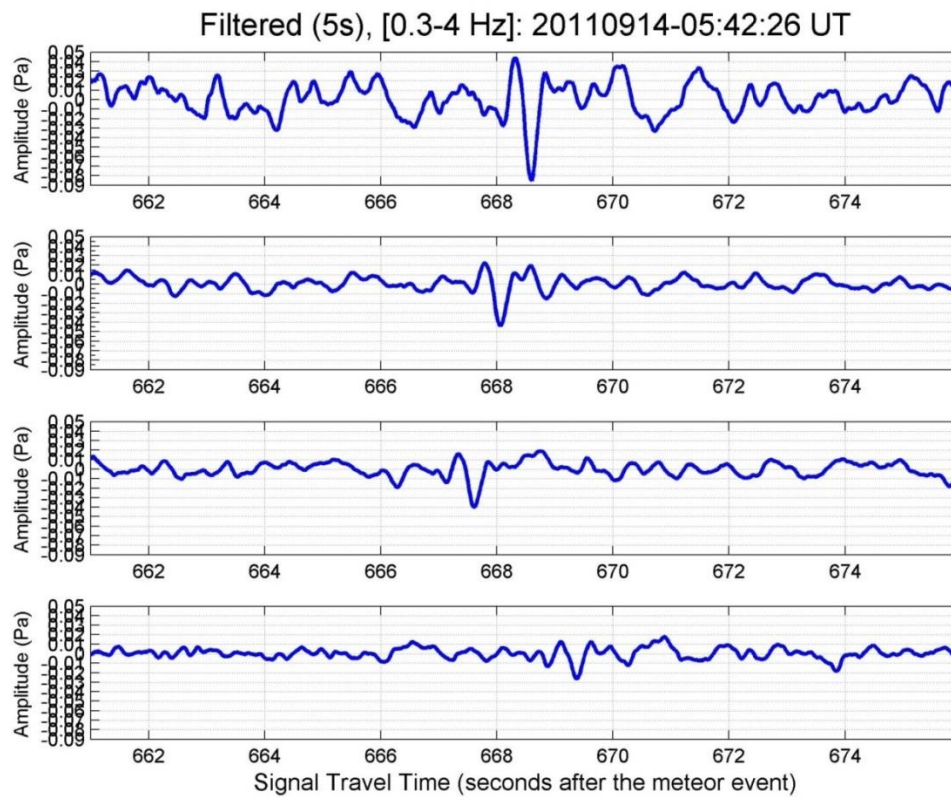




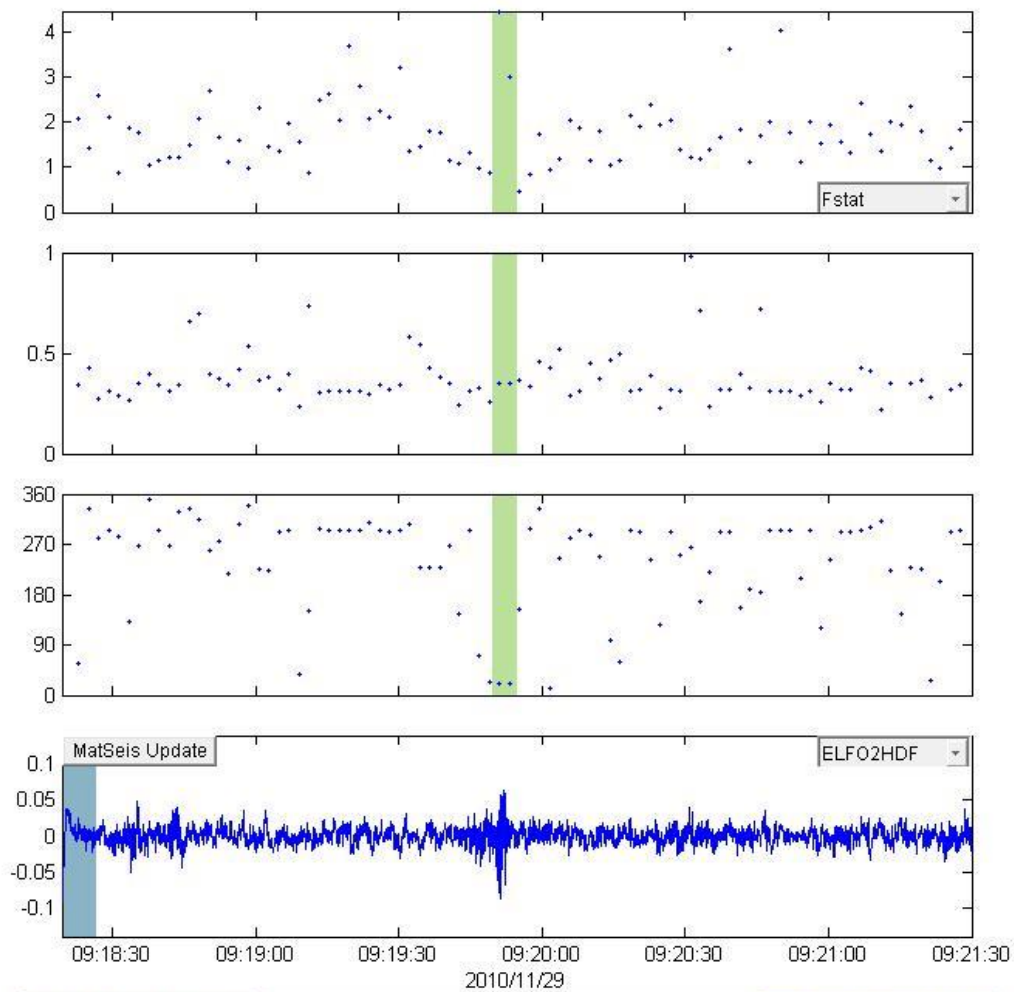
20100914\_054226



Window Parameters		Pass Band Parameters		Slowness Parameters		Windowed Values & S.D.	
Duration (s)	7.0	Low frequency (Hz)	0.3	Max. Slown.	400.0	Corr.	0.551 0.178
Overlap (%)	70.0	High frequency	4	# of Slown.	40	Fstat	5.280 5.182
Number of	103	Order (integer)	2			Vel.	0.357 0.000
						Az.	107.241 0.000
						Send to Map	
Animate		Write File				D:\Research\Research - Elizabeth\lr	
Calculate	0					Cancel	



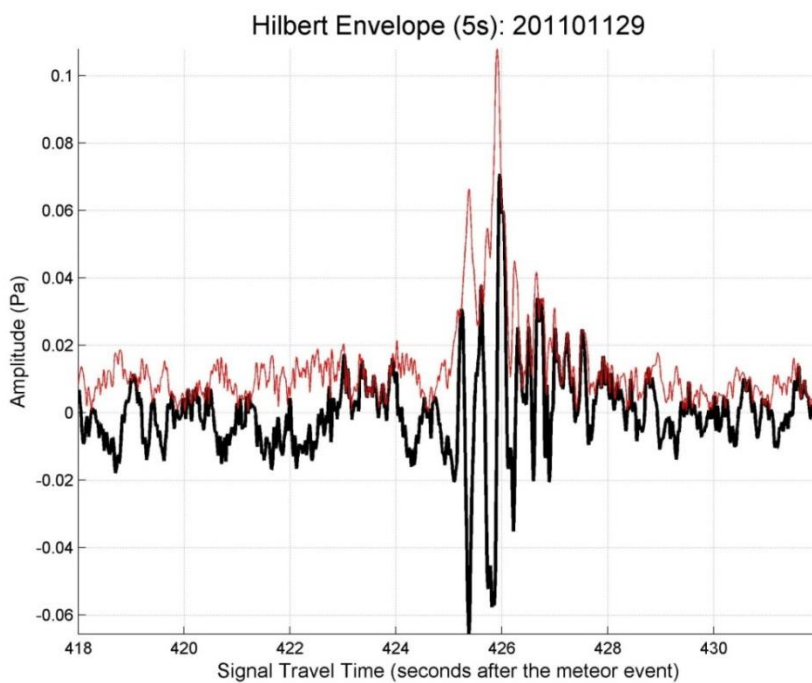
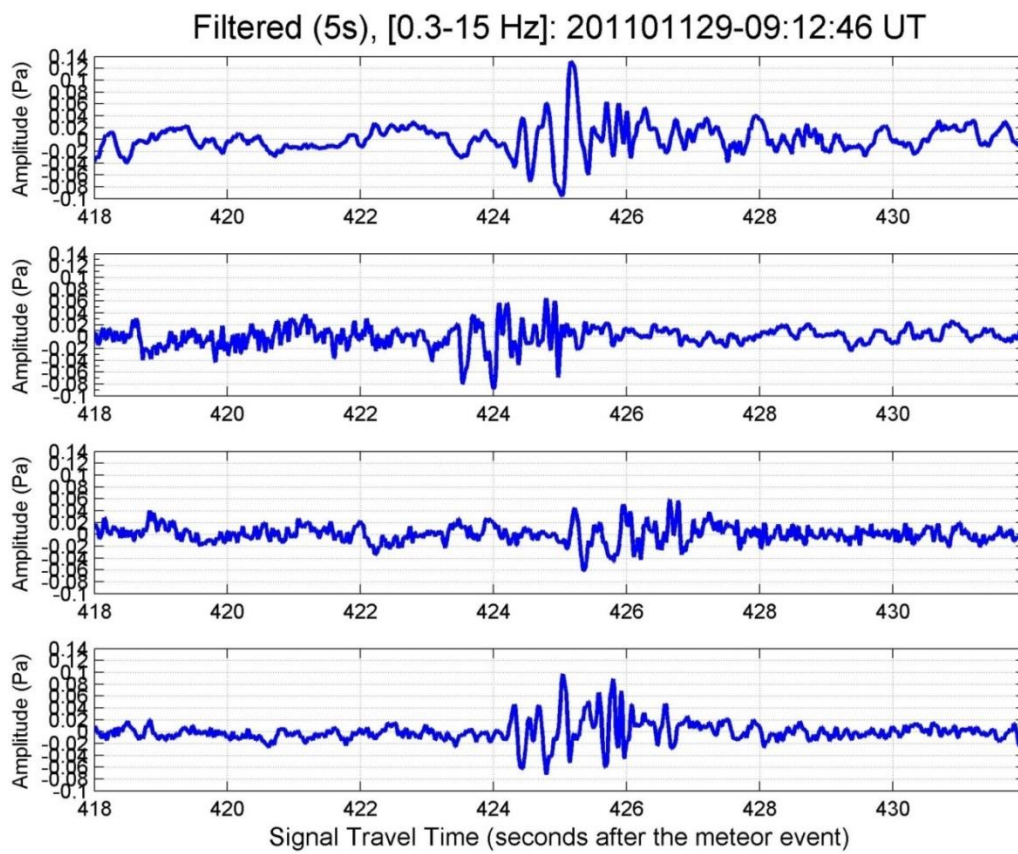
## 20101129\_091246



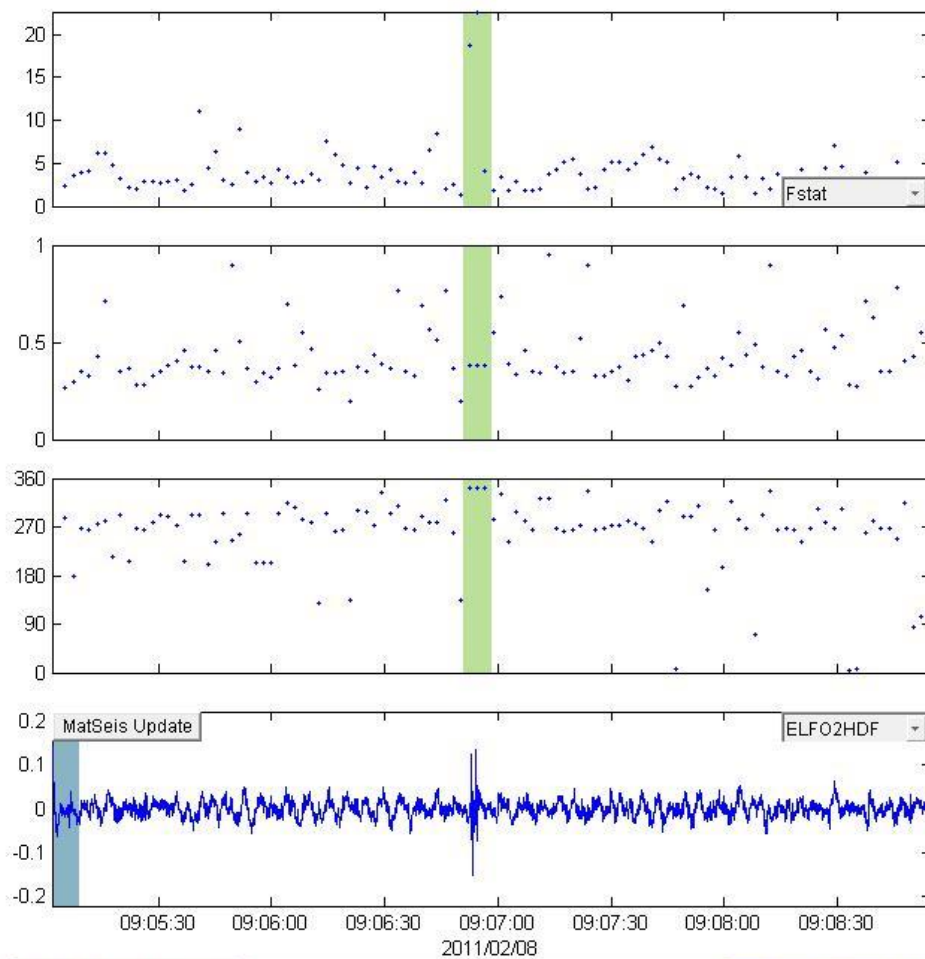
Window Parameters		Pass Band Parameters		Slowness Parameters		Windowed Values & S.D.	
Duration (s)	7.0	Low frequency (Hz)	0.3	Max. Slown.	400.0	Corr.	0.540 0.054
Overlap (%)	70.0	High frequency	15	# of Slown.	40	Fstat	3.748 1.033
Number of	89	Order (integer)	2			Vel.	0.349 0.000
						Az.	20.772 0.000

0
  D:\Research\Research - Elizabeth\lr





20110208\_085933



Window Parameters		Pass Band Parameters		Slowness Parameters		Windowed Values & S.D.	
Duration (s)	7.0	Low frequency (Hz)	0.3	Max. Slown.	400.0	Corr.	0.749 0.164
Overlap (%)	70.0	High frequency	10	# of Slown.	40	Fstat	15.178 9.803
Number of	109	Order (integer)	2			Vel.	0.381 0.000
						Az.	341.565 0.000

Animate

Calculate

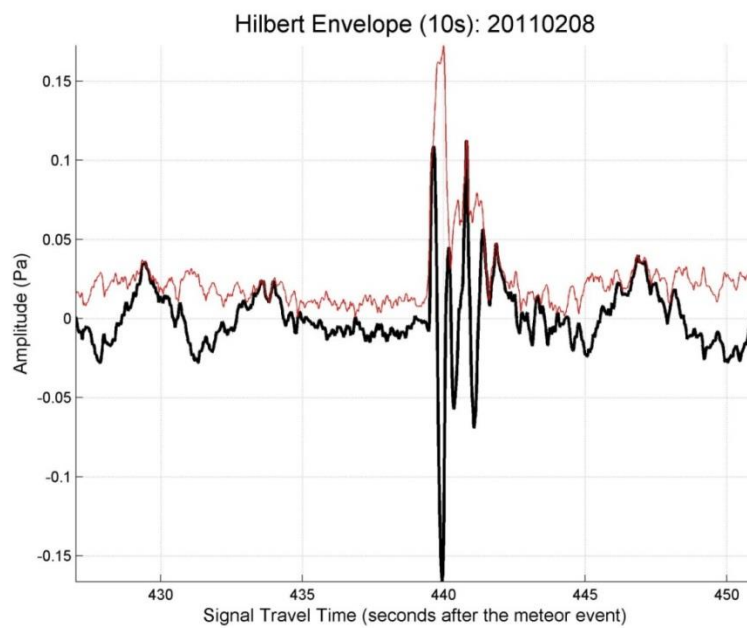
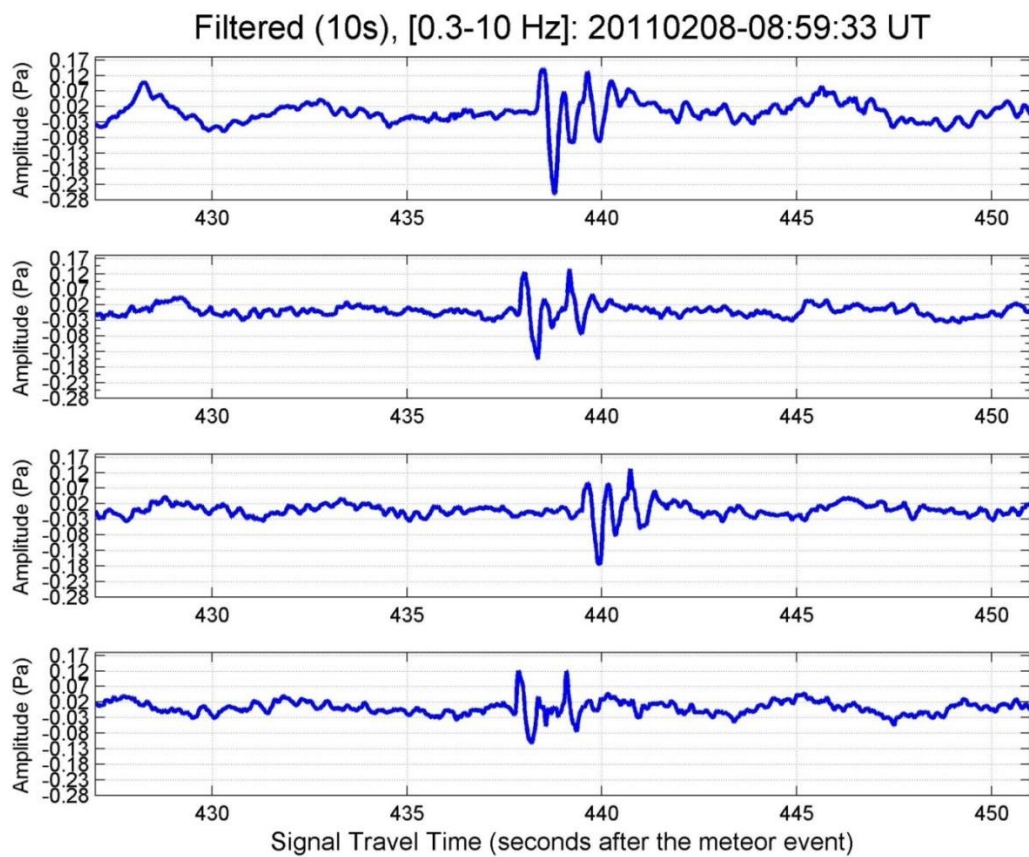
0

Write File

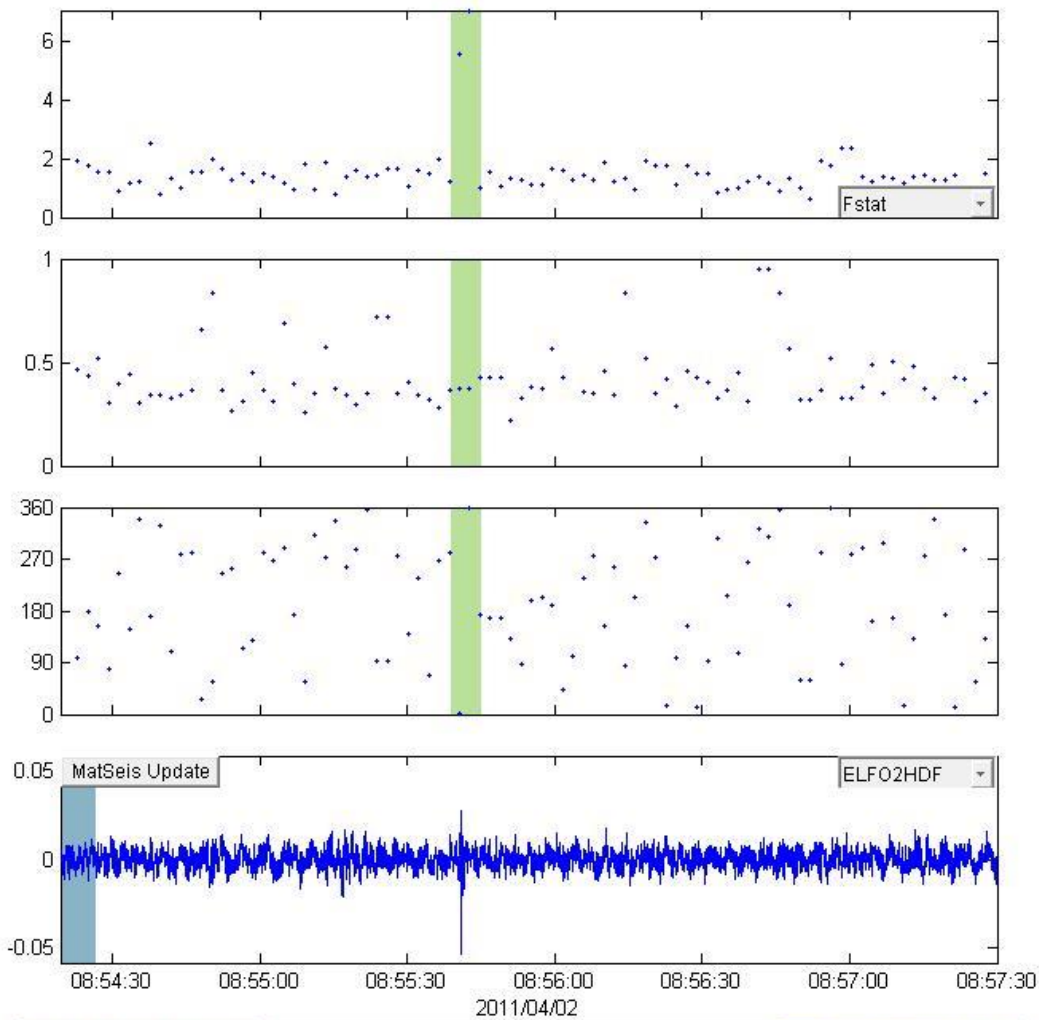
D:\Research\Research - Elizabeth\lr

Send to Map

Cancel



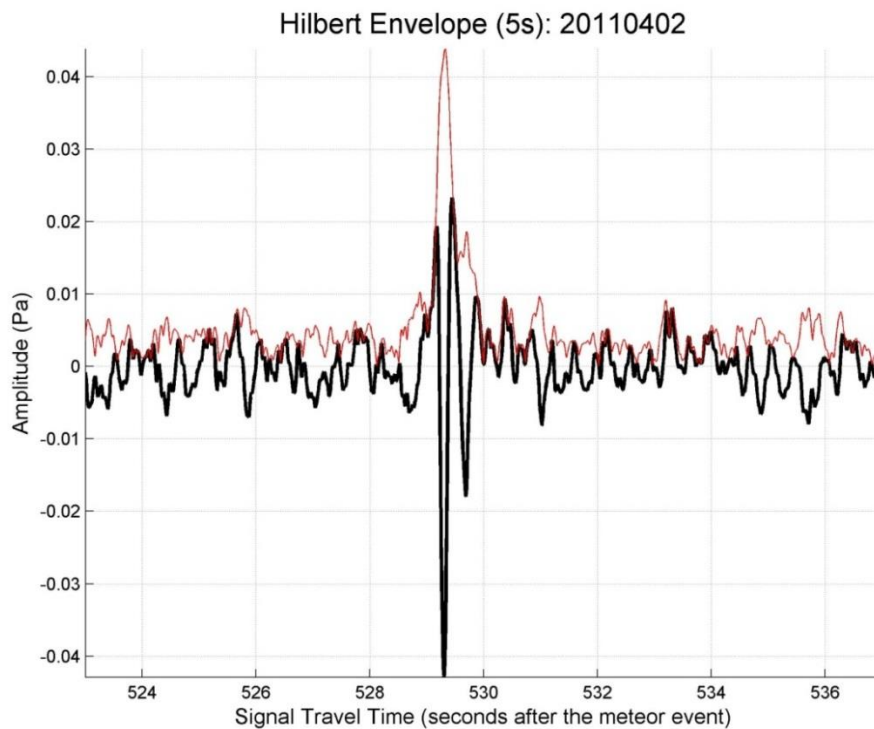
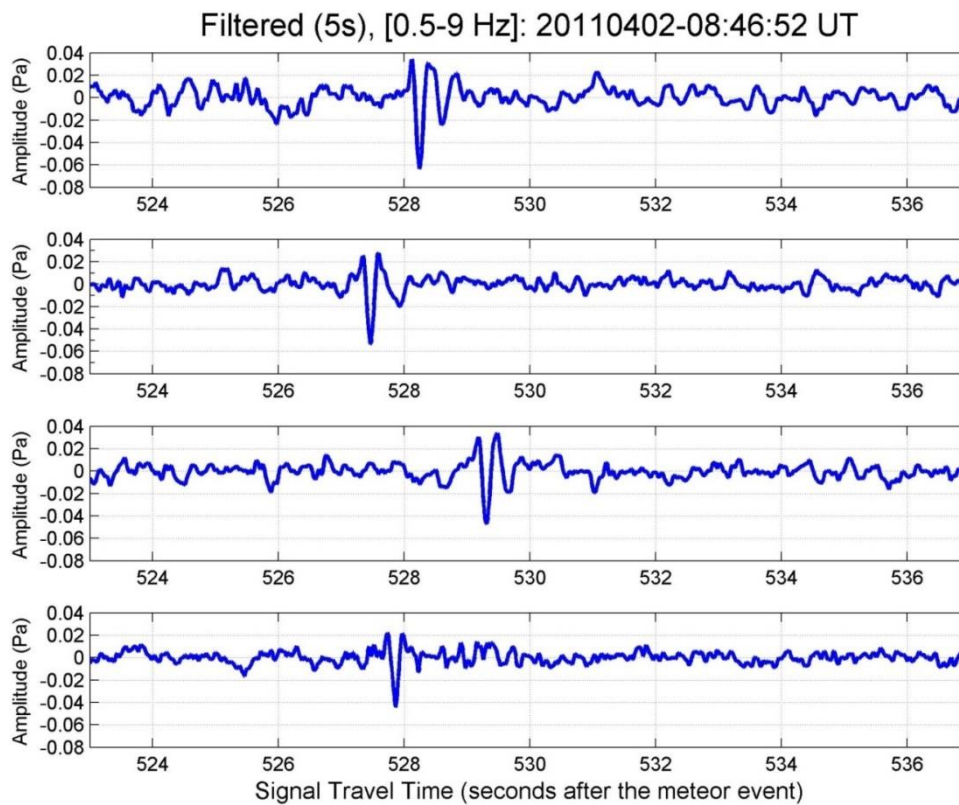
### 20110402\_084652



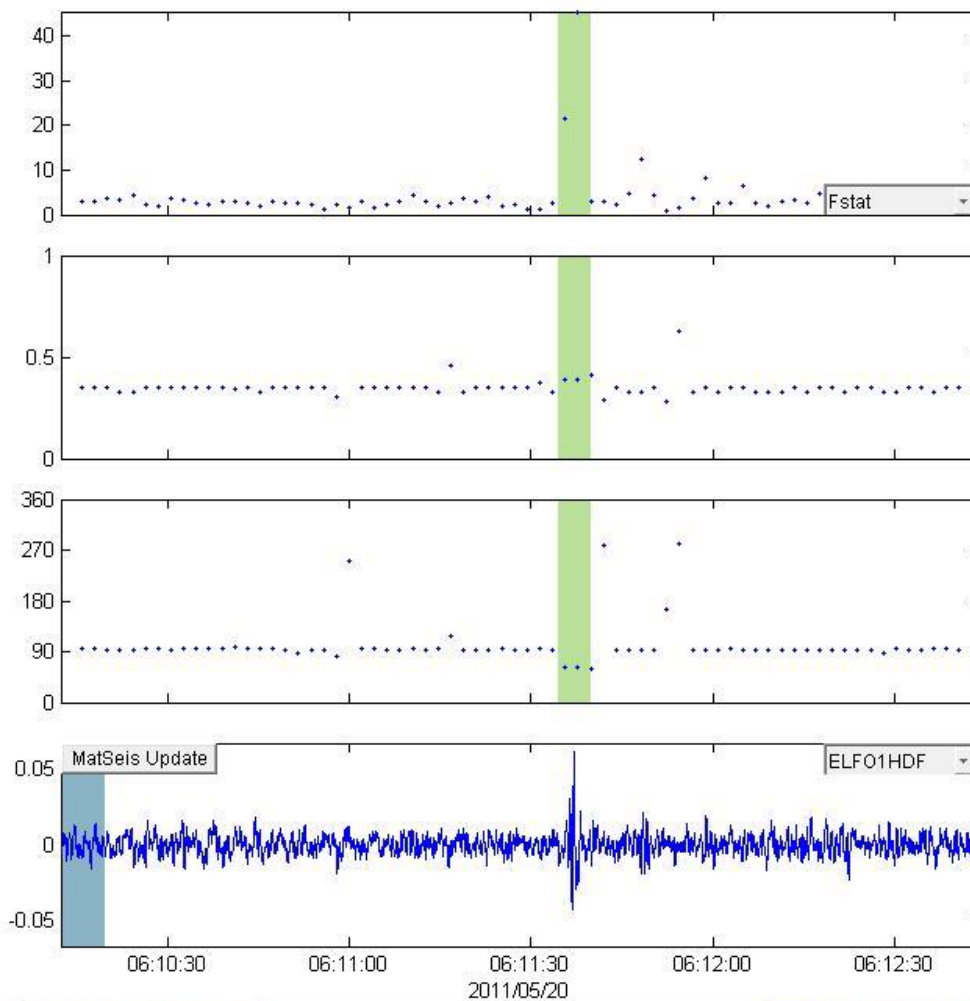
Window Parameters		Pass Band Parameters		Slowness Parameters		Windowed Values & S.D.	
Duration (s)	7.0	Low frequency (Hz)	0.5	Max. Slown.	400.0	Corr.	0.541 0.181
Overlap (%)	70.0	High frequency	9	# of Slown.	40	Fstat	4.531 3.153
Number of	89	Order (integer)	2			Vel.	0.392 0.033
						Az.	177.719 178.069

0
  D:\Research\Research - Elizabeth\lr

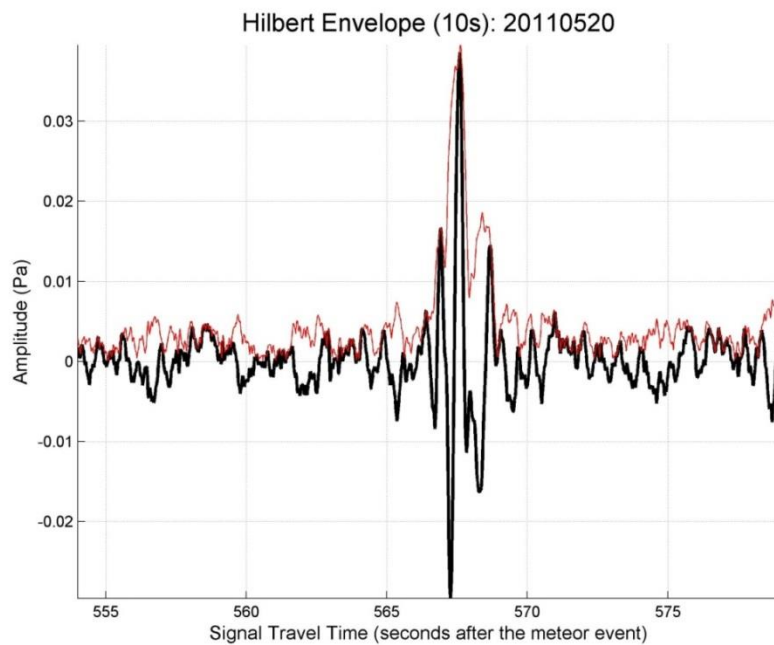
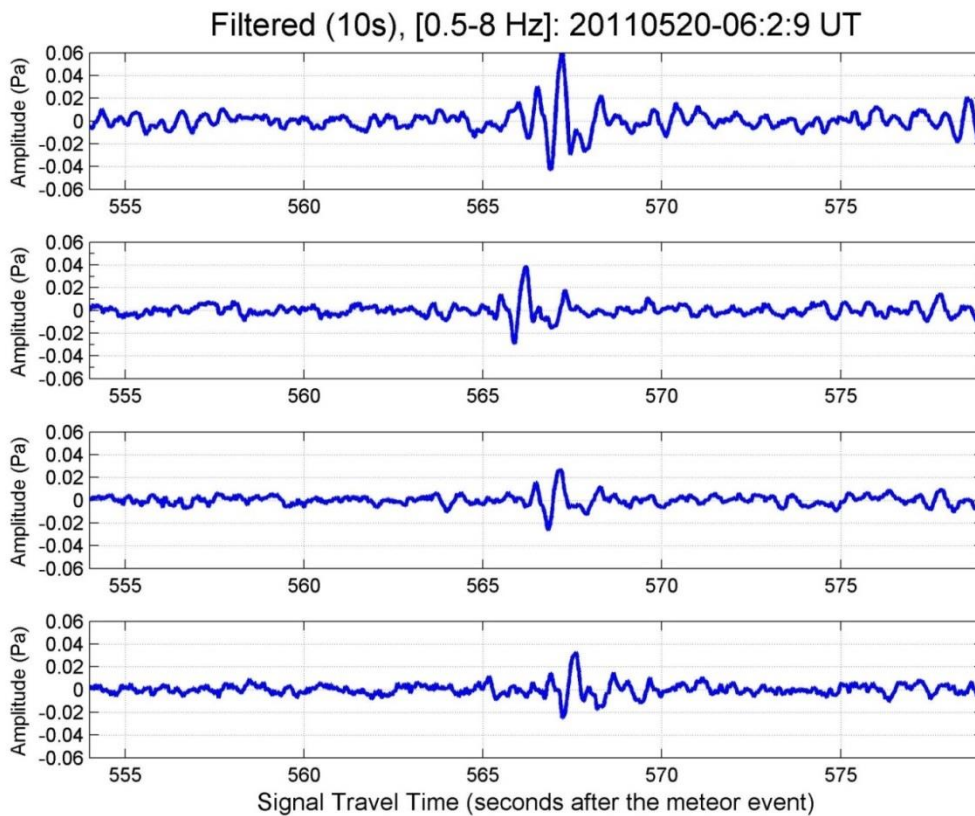




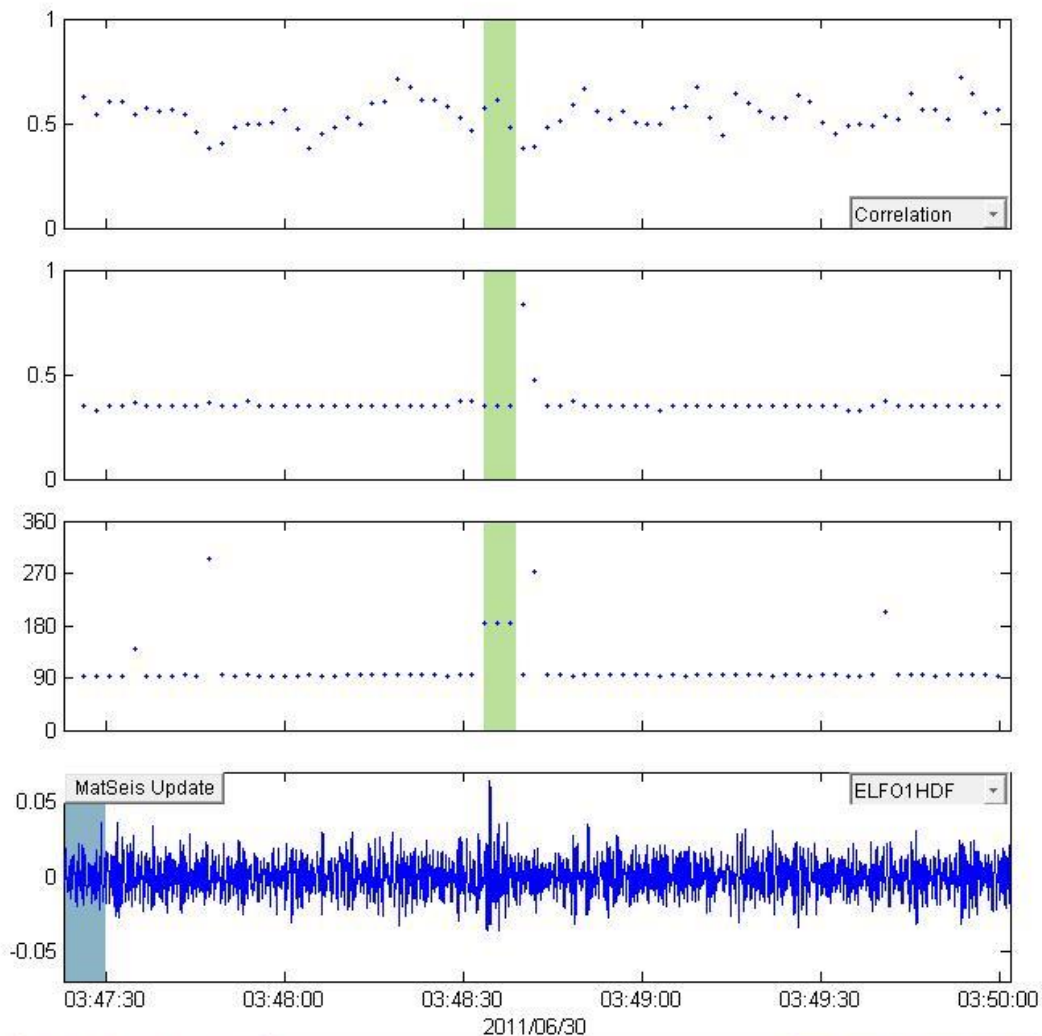
## 20110520\_060209



Window Parameters		Pass Band Parameters		Slowness Parameters		Windowed Values & S.D.	
Duration (s)	7.0	Low frequency (Hz)	0.5	Max. Slown.	400.0	Corr.	0.885 0.051
Overlap (%)	70.0	High frequency	8	# of Slown.	40	Fstat	33.526 17.023
Number of	71	Order (integer)	2			Vel.	0.385 0.000
						Az.	62.526 0.000
Animate						Send to Map	
Calculate	0	Write File	D:\Research\Research - Elizabeth\hr			Cancel	

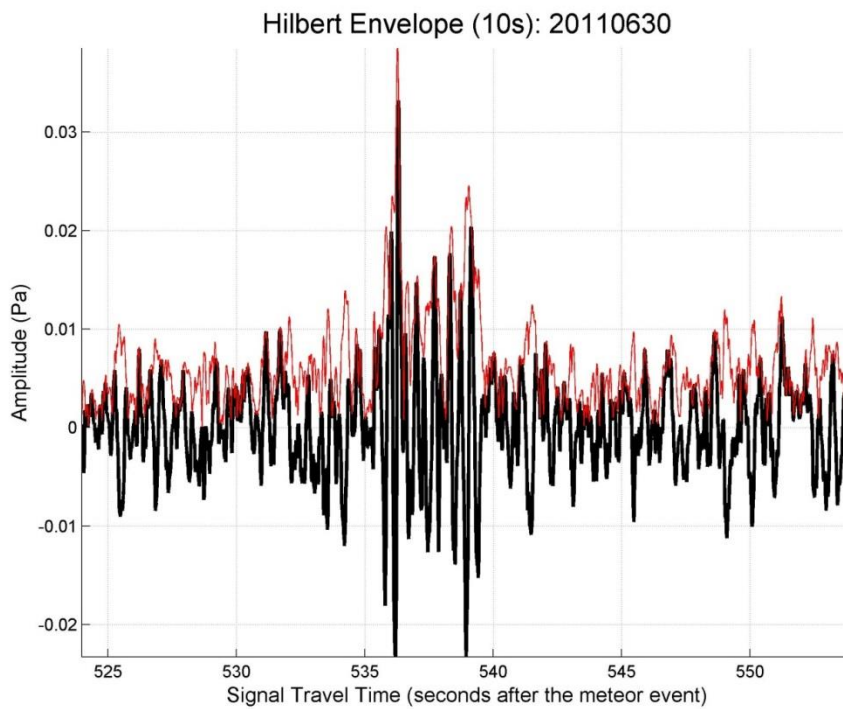
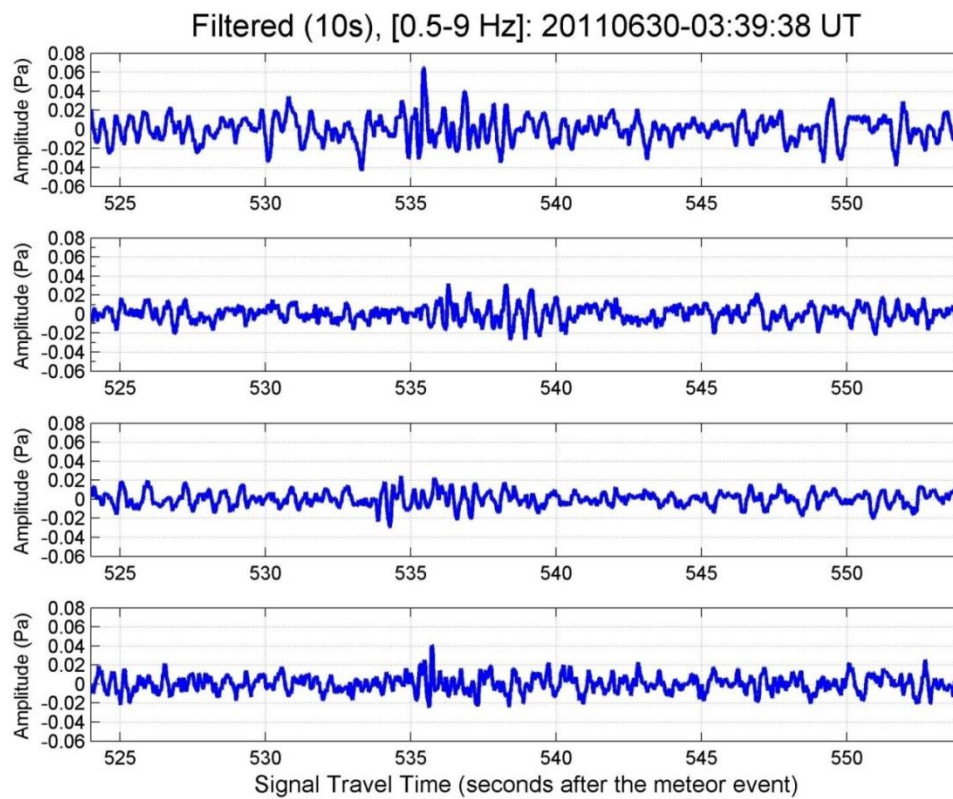


### 20110630\_033938



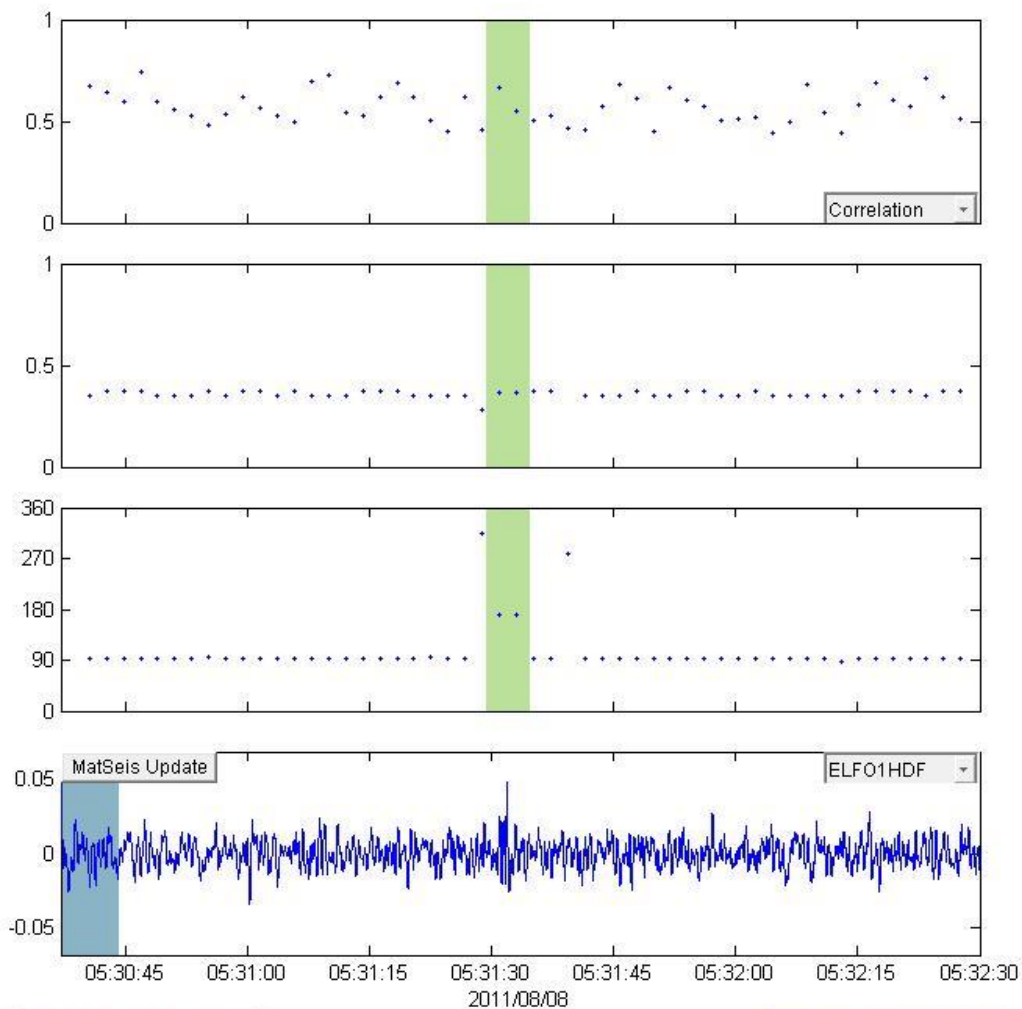
Window Parameters		Pass Band Parameters		Slowness Parameters		Windowed Values & S.D.	
Duration (s)	7.0	Low frequency (Hz)	1	Max. Slown.	400.0	Corr.	0.556 0.067
Overlap (%)	70.0	High frequency	10	# of Slown.	40	Fstat	4.139 1.325
Number of	74	Order (integer)	2			Vel.	0.348 0.000
						Az.	185.528 0.000

0  D:\Research\Research - Elizabeth\l...

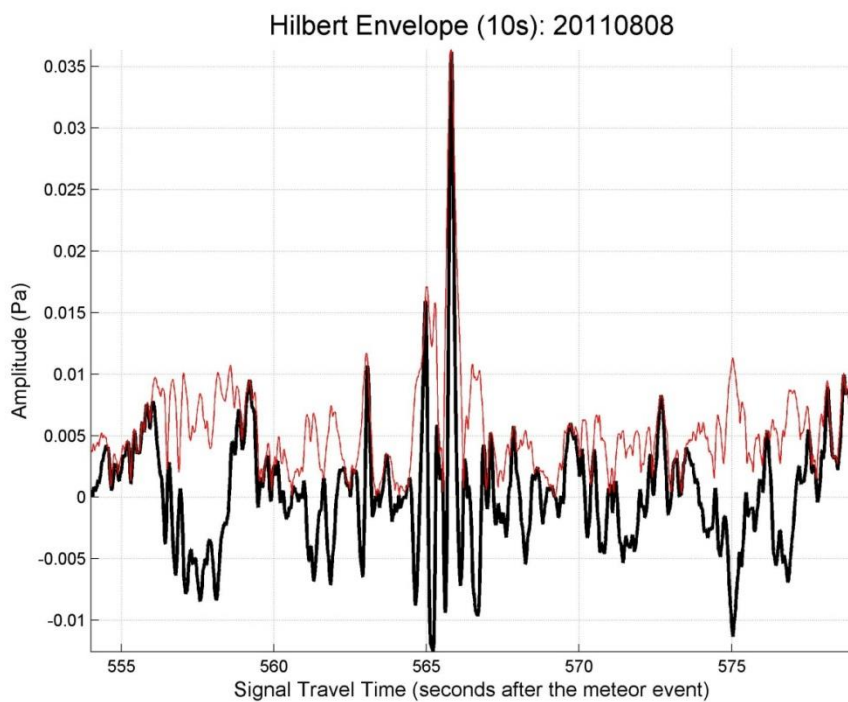
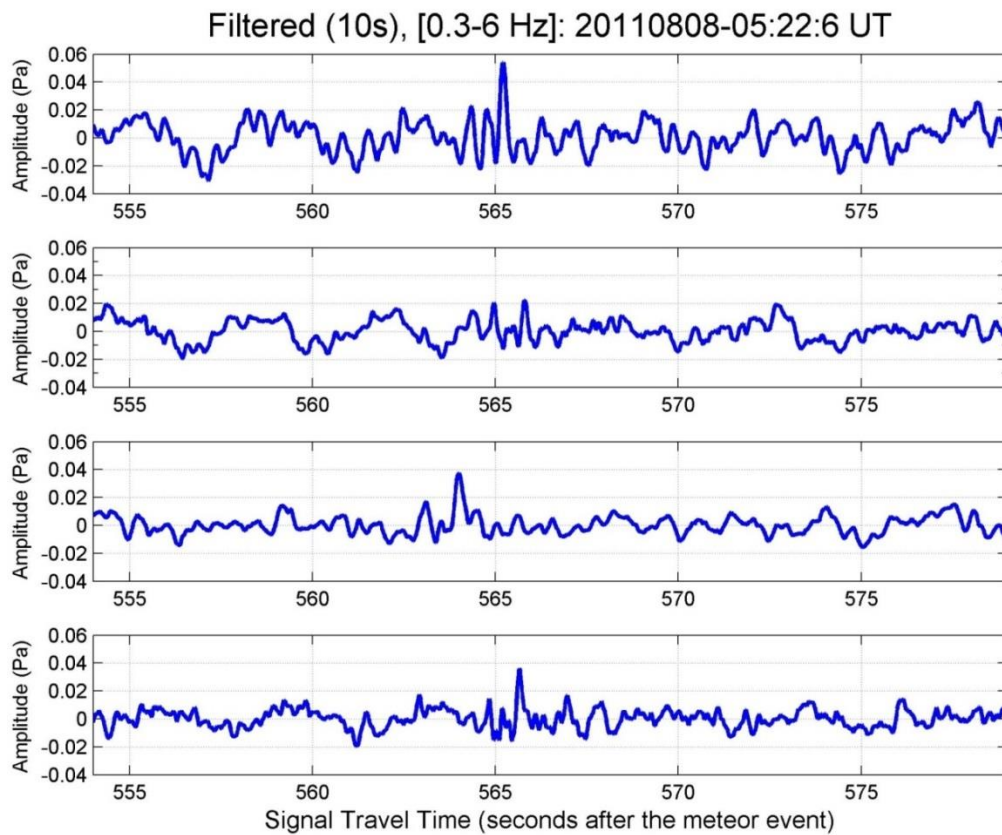




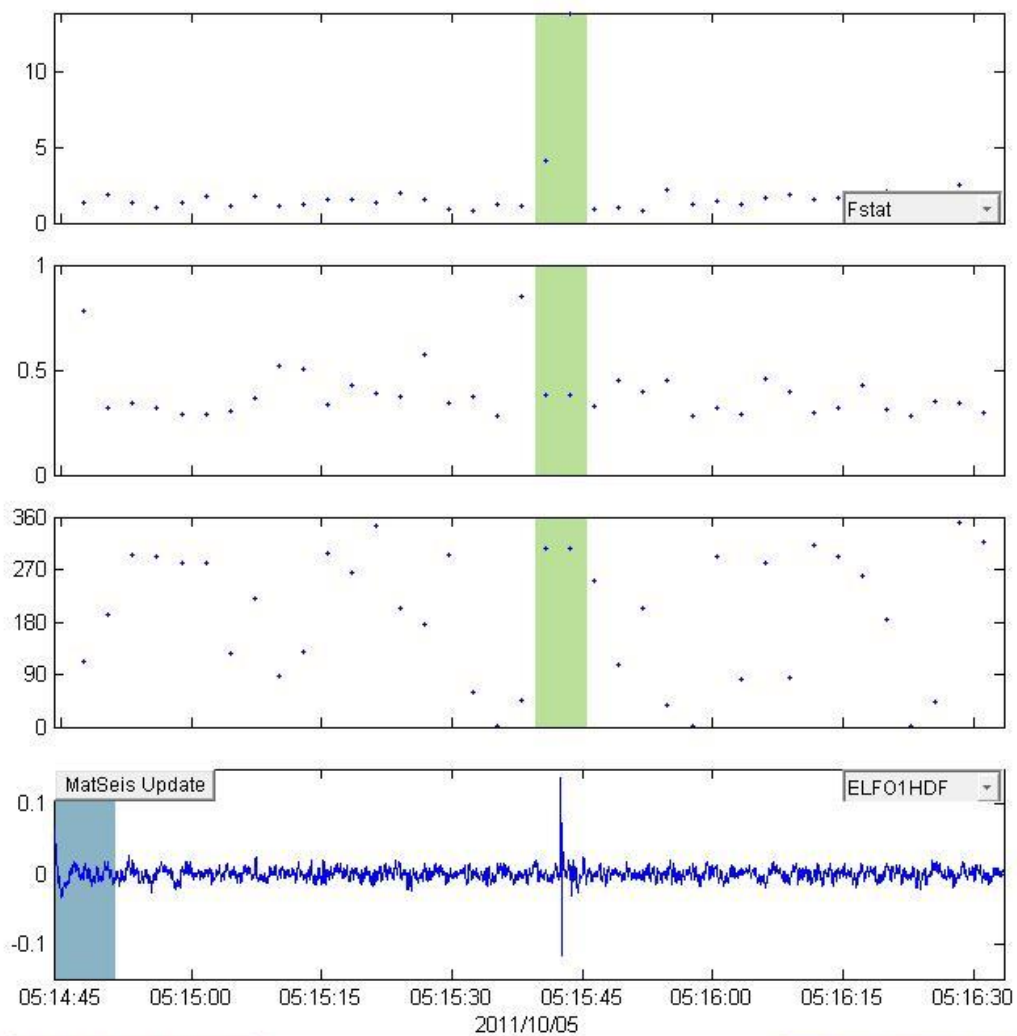
## 20110808\_052206



Window Parameters		Pass Band Parameters		Slowness Parameters		Windowed Values & S.D.	
Duration (s)	7.0	Low frequency (Hz)	0.5	Max. Slown.	400.0	Corr.	0.610 0.082
Overlap (%)	70.0	High frequency	8	# of Slown.	40	Fstat	5.499 2.219
Number of	52	Order (integer)	2			Vel.	0.368 0.000
						Az.	170.218 0.000
Animate						Send to Map	
Calculate	0	Write File	D:\Research\Research - Elizabeth\ur			Cancel	

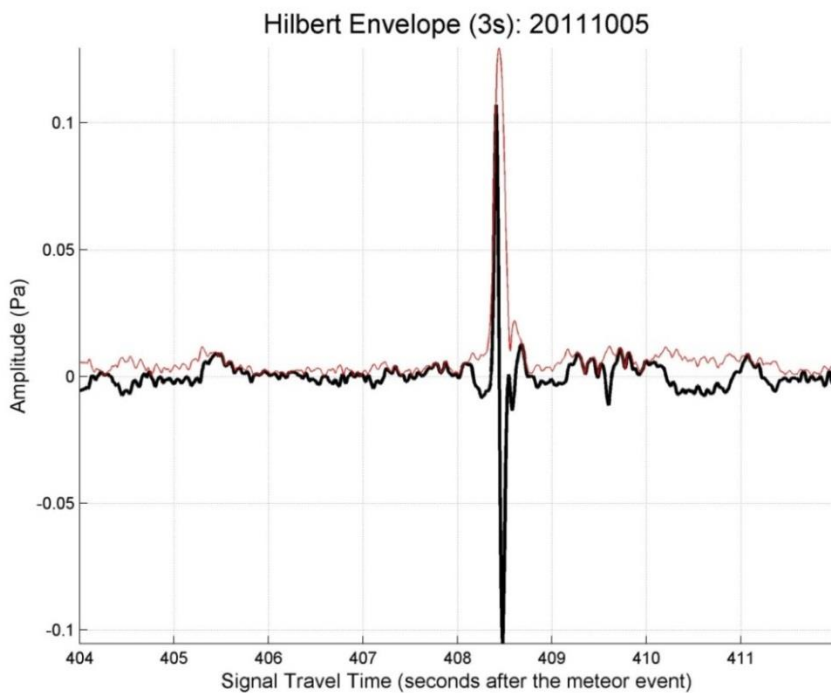
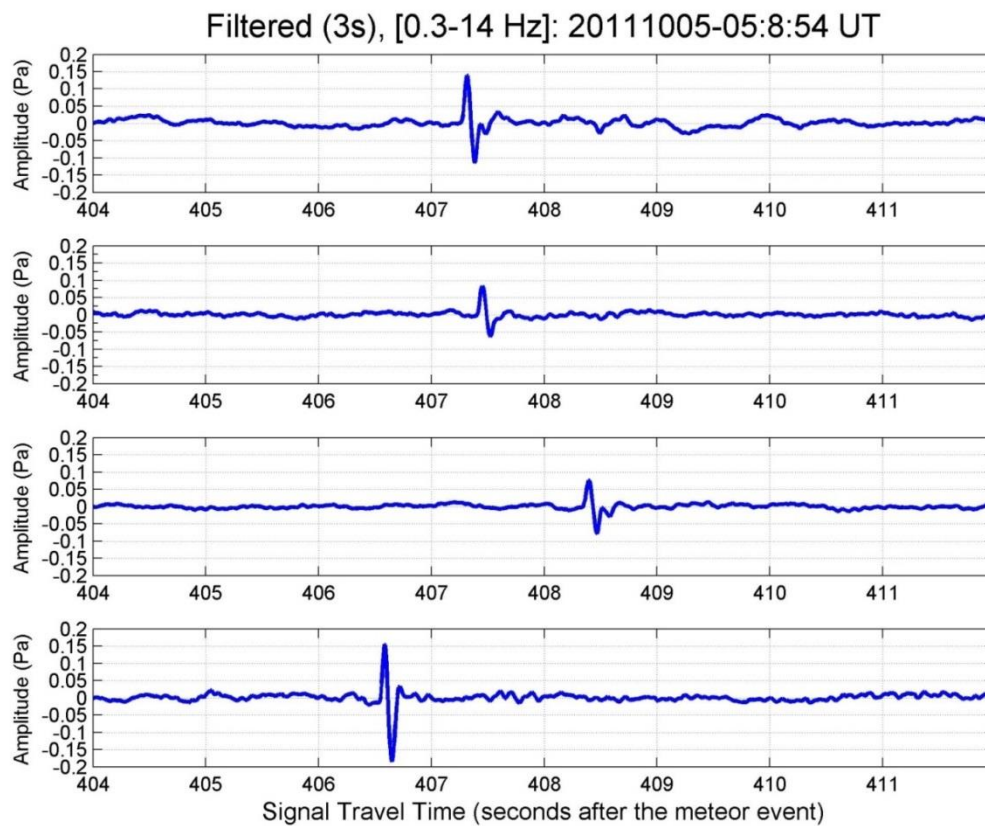


## 20111005\_050854

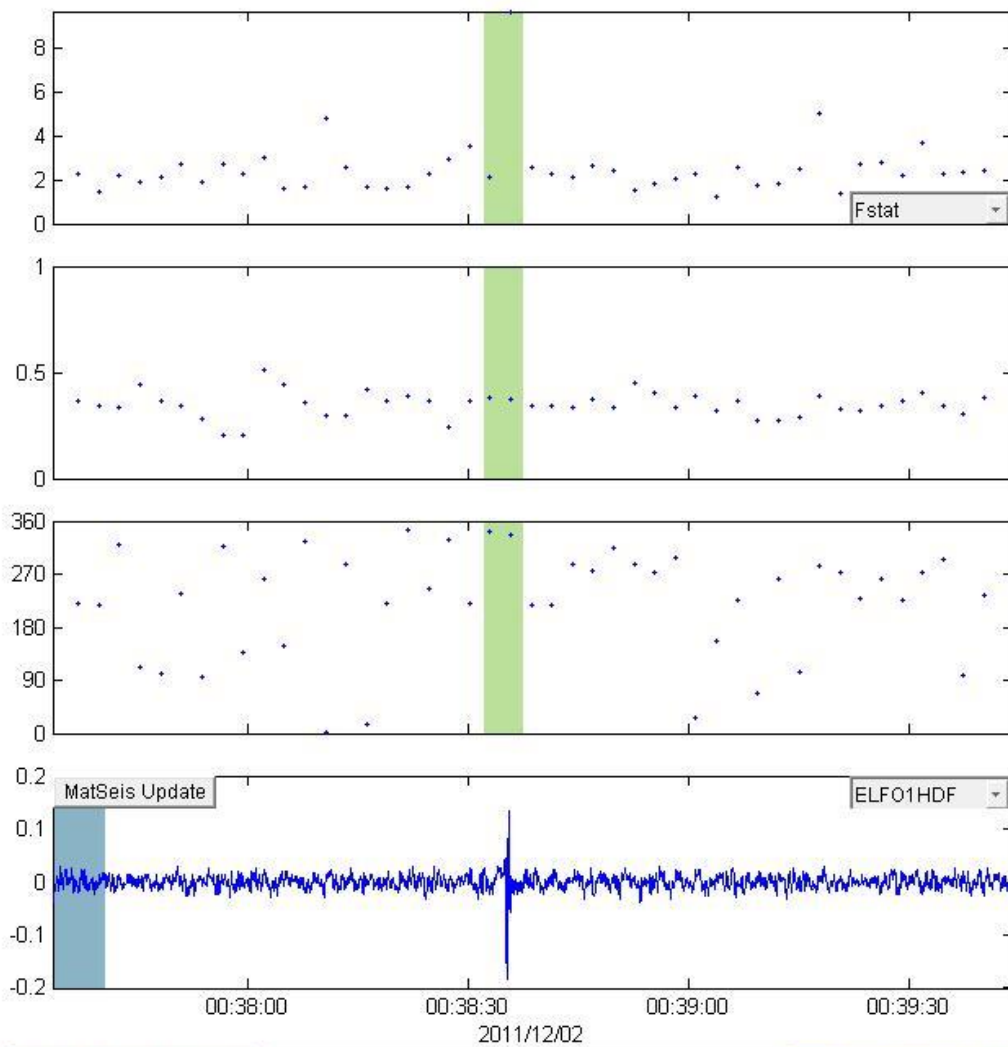


Window Parameters		Pass Band Parameters		Slowness Parameters		Windowed Values & S.D.	
Duration (s)	7.0	Low frequency (Hz)	0.4	Max. Slown.	400.0	Corr.	0.675 0.161
Overlap (%)	60.0	High frequency	14	# of Slown.	40	Fstat	9.005 6.913
Number of	38	Order (integer)	2			Vel.	0.379 0.000
						Az.	306.469 0.000
Animate						Send to Map	
Calculate	0	Write File	D:\Research\Research - Elizabeth\lr			Cancel	

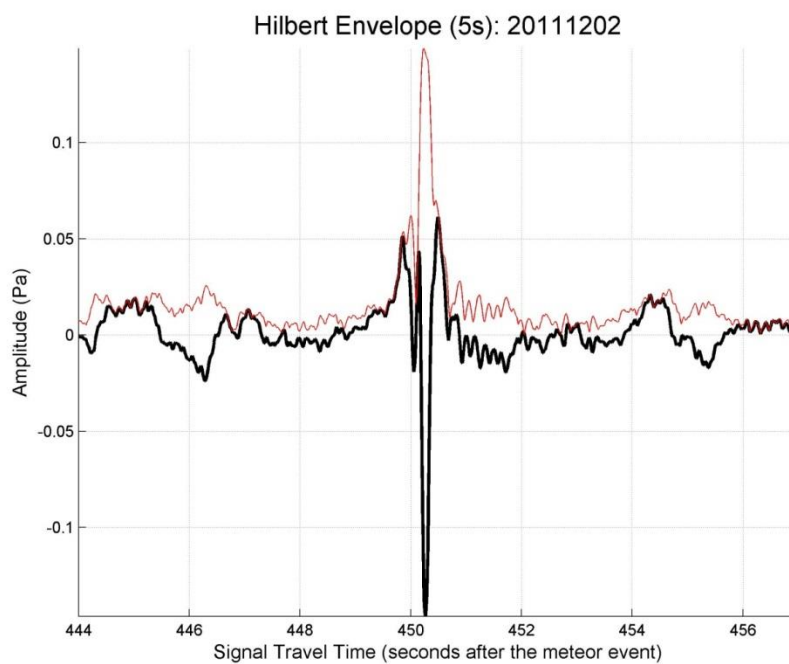
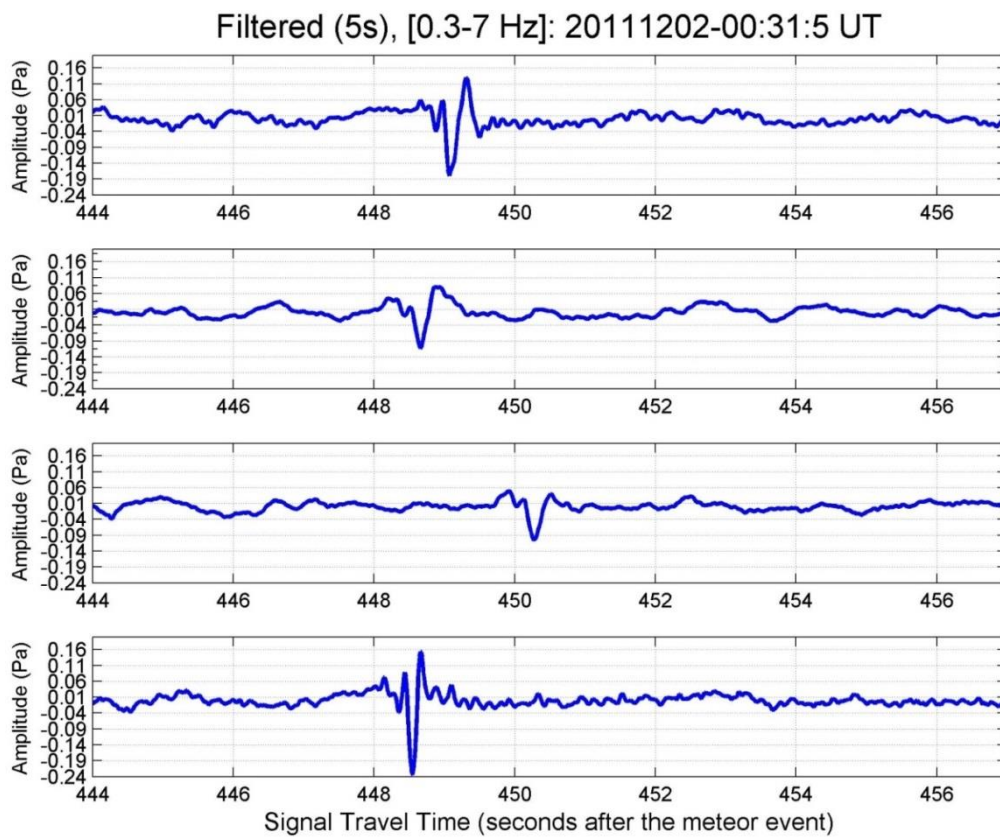




20111202\_003105

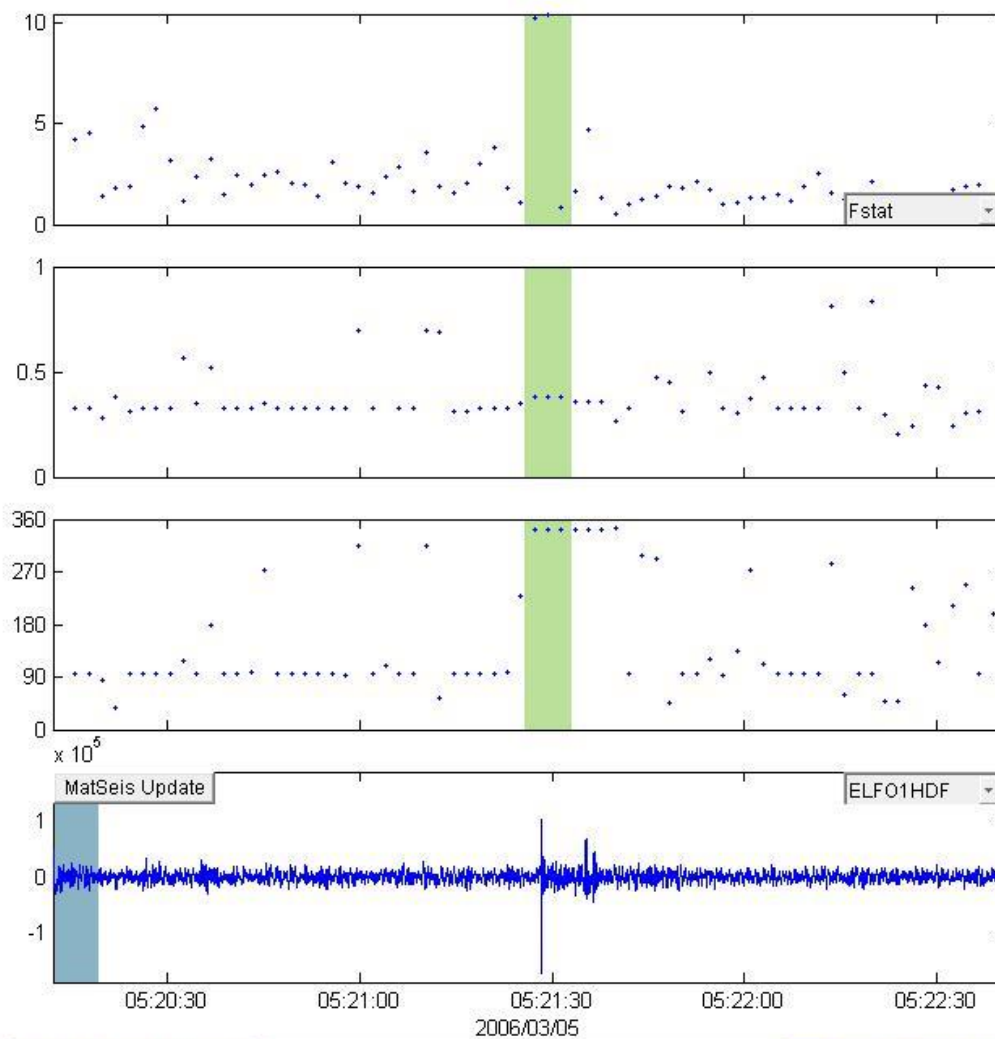


Window Parameters		Pass Band Parameters		Slowness Parameters		Windowed Values & S.D.	
Duration (s)	7.0	Low frequency (Hz)	0.4	Max. Slown.	400.0	Corr.	0.583   0.204
Overlap (%)	60.0	High frequency	7	# of Slown.	40	Fstat	5.878   5.309
Number of	45	Order (integer)	2			Vel.	0.376   0.006
						Az.	339.699   2.638
						Send to Map	
Animate		Write File   D:\Research\Research - Elizabeth\lr				Cancel	
Calculate	0						



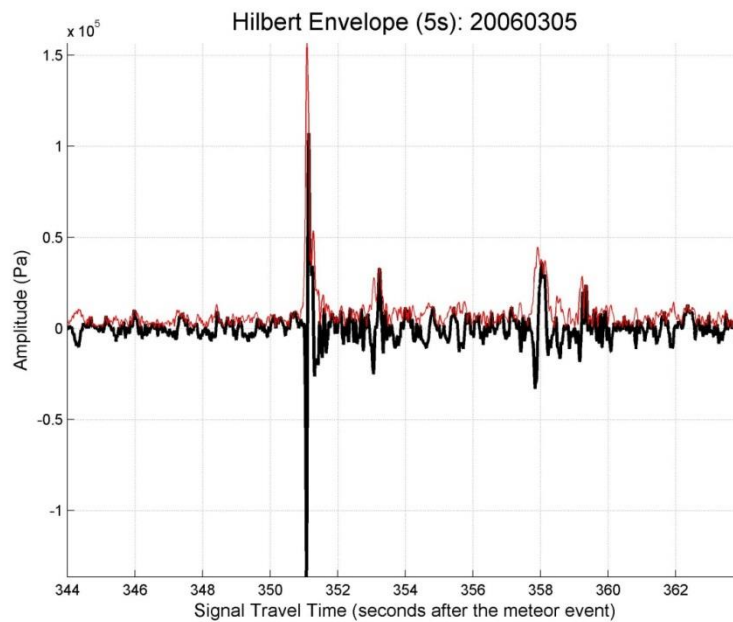
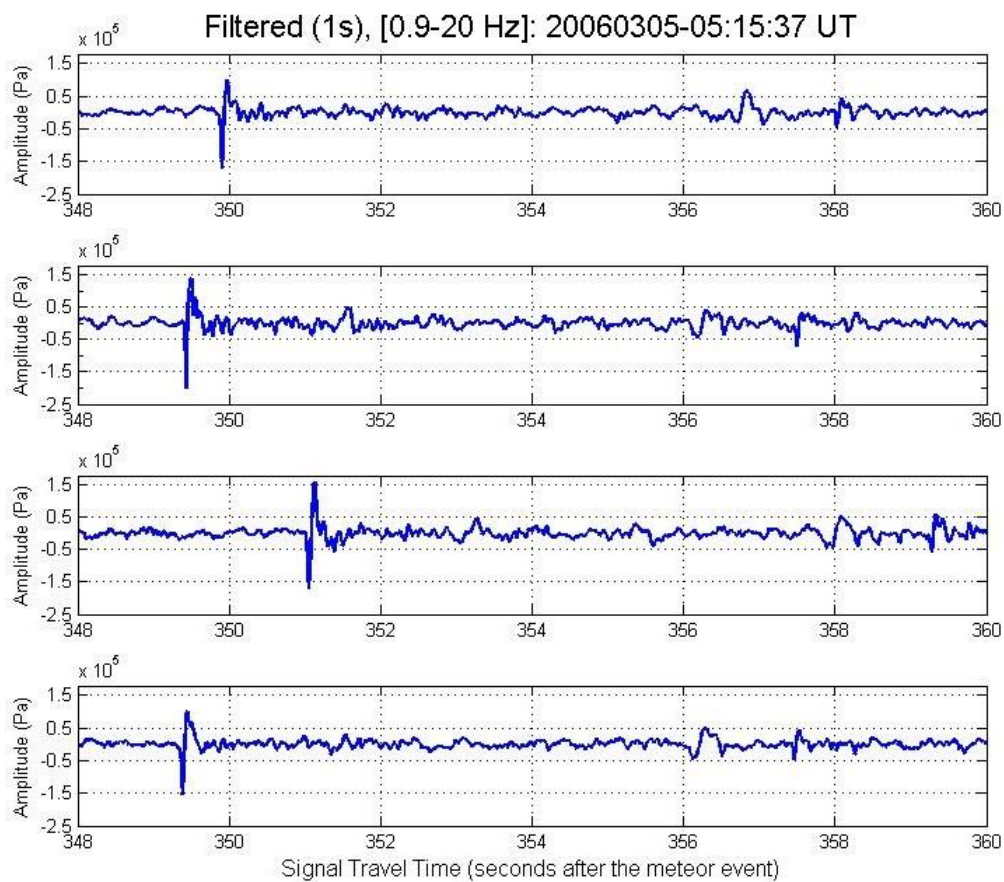
# MULTIPLE ARRIVALS

## 20060305\_051537

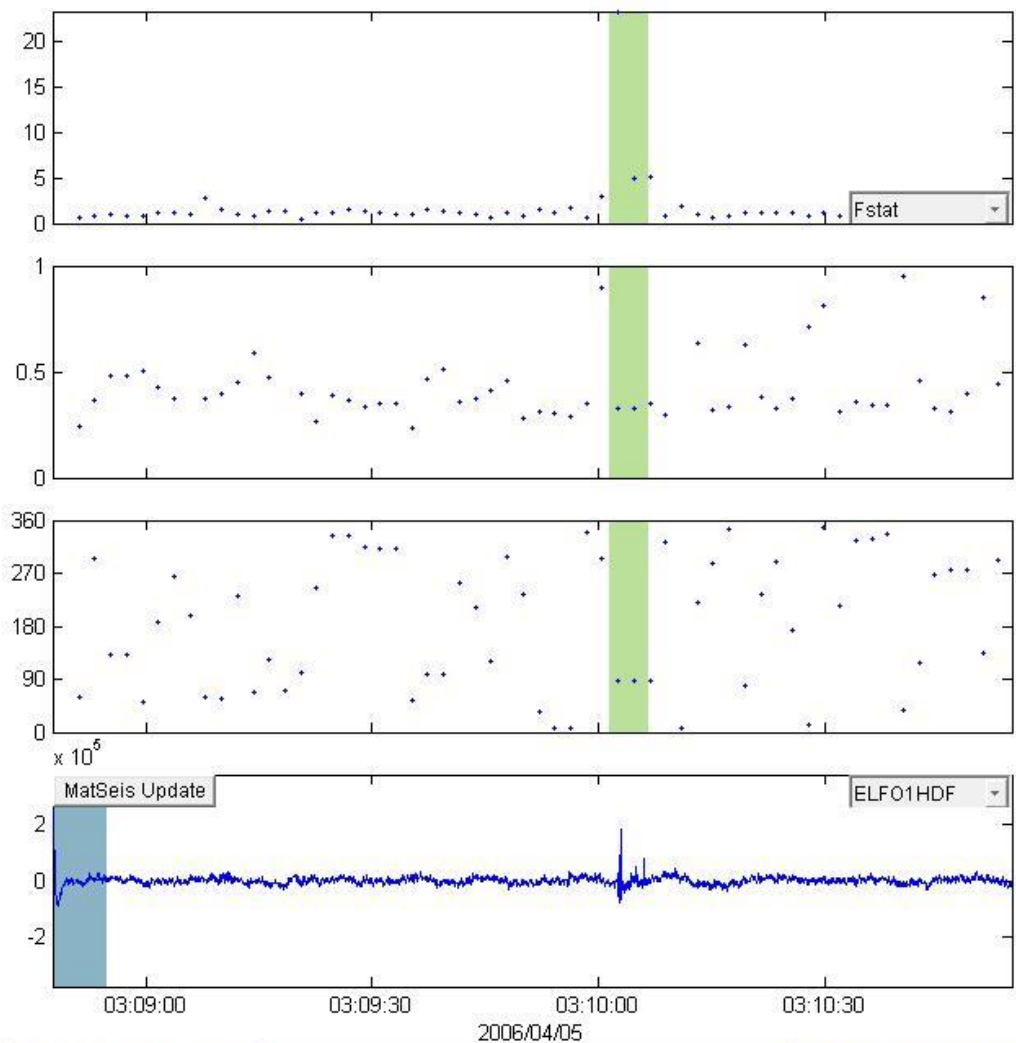


Window Parameters		Pass Band Parameters		Slowness Parameters		Windowed Values & S.D.	
Duration (s)	7.0	Low frequency (Hz)	0.9	Max. Slown.	400.0	Corr.	0.597 0.247
Overlap (%)	70.0	High frequency	20	# of Slown.	40	Fstat	7.184 5.520
Number of	69	Order (integer)	2			Vel.	0.381 0.000
						Az.	341.565 0.000

0
  D:\Research\Research - Elizabeth\lr



20060405\_030327

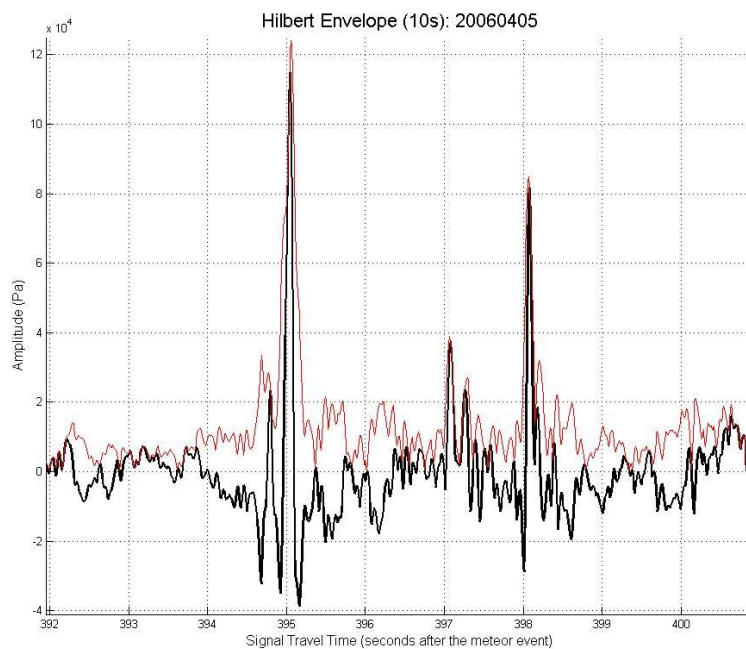
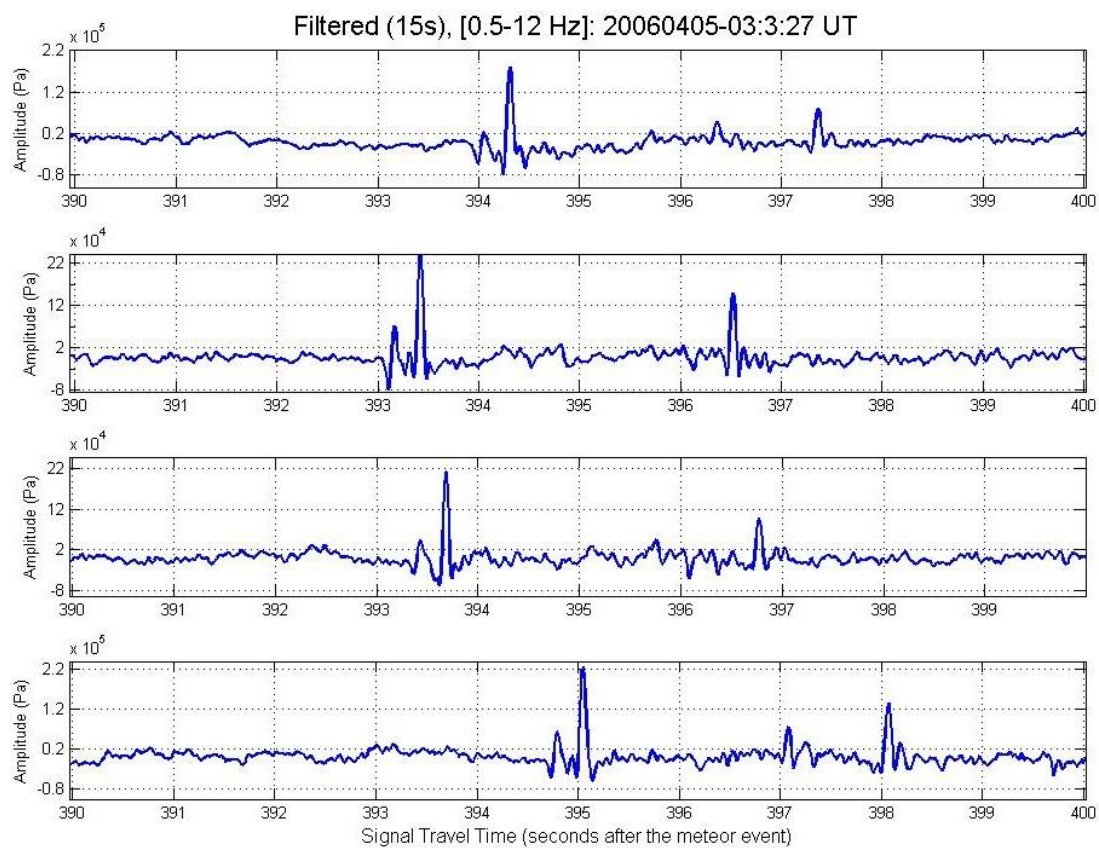


Window Parameters		Pass Band Parameters		Slowness Parameters		Windowed Values & S.D.	
Duration (s)	7.0	Low frequency (Hz)	0.5	Max. Slown.	400.0	Corr.	0.727   0.187
Overlap (%)	70.0	High frequency	12	# of Slown.	40	Fstat	14.103   13.056
Number of	59	Order (integer)	2			Vel.	0.328   0.000
						Az.	88.264   0.000

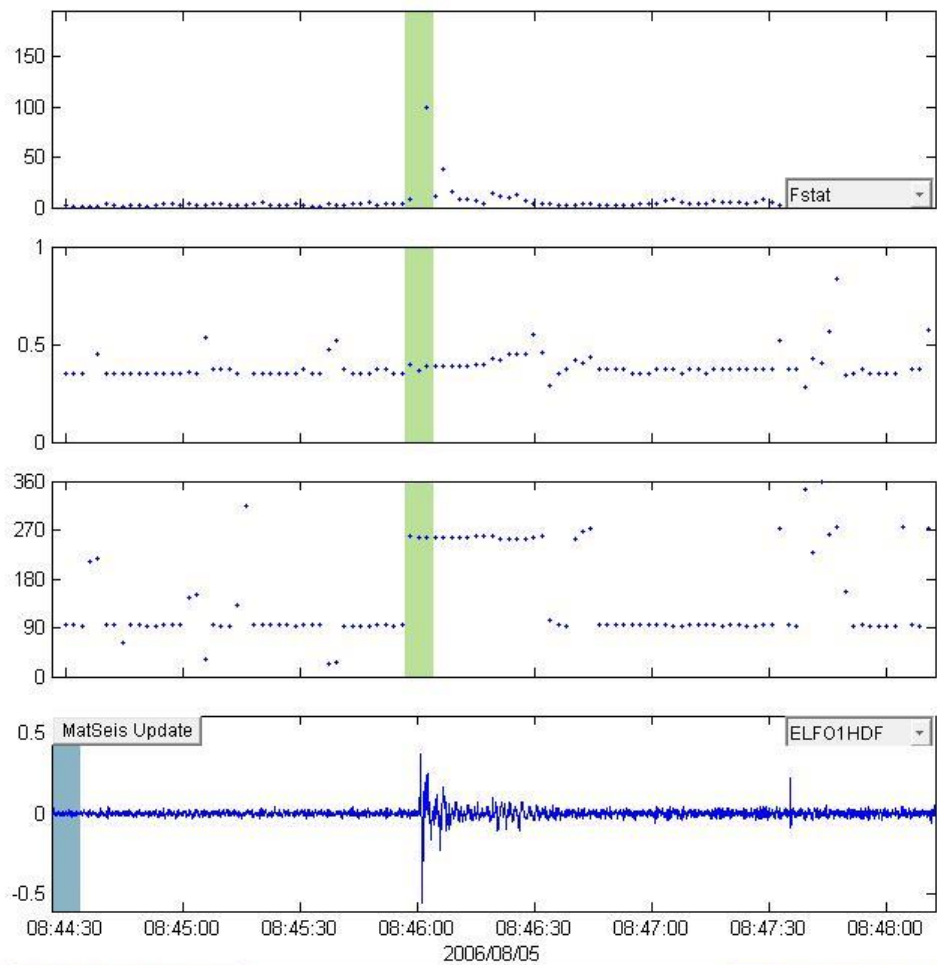
  

Animate			
Calculate	0	Write File	D:\Research\Research - Elizabeth\lr
			Send to Map
			Cancel



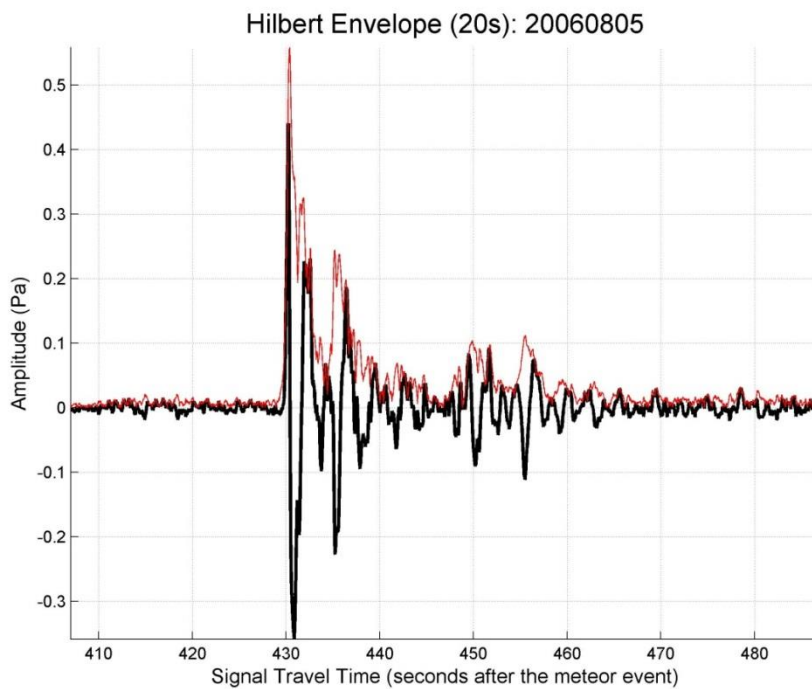
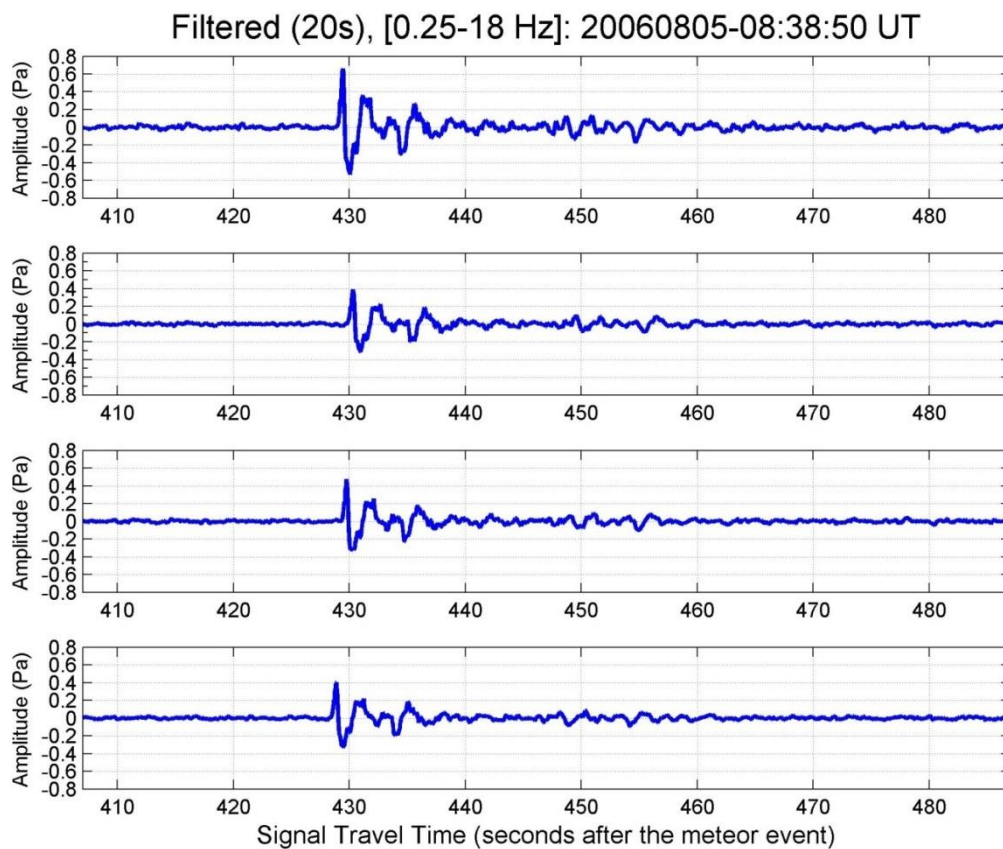


20060805\_083850

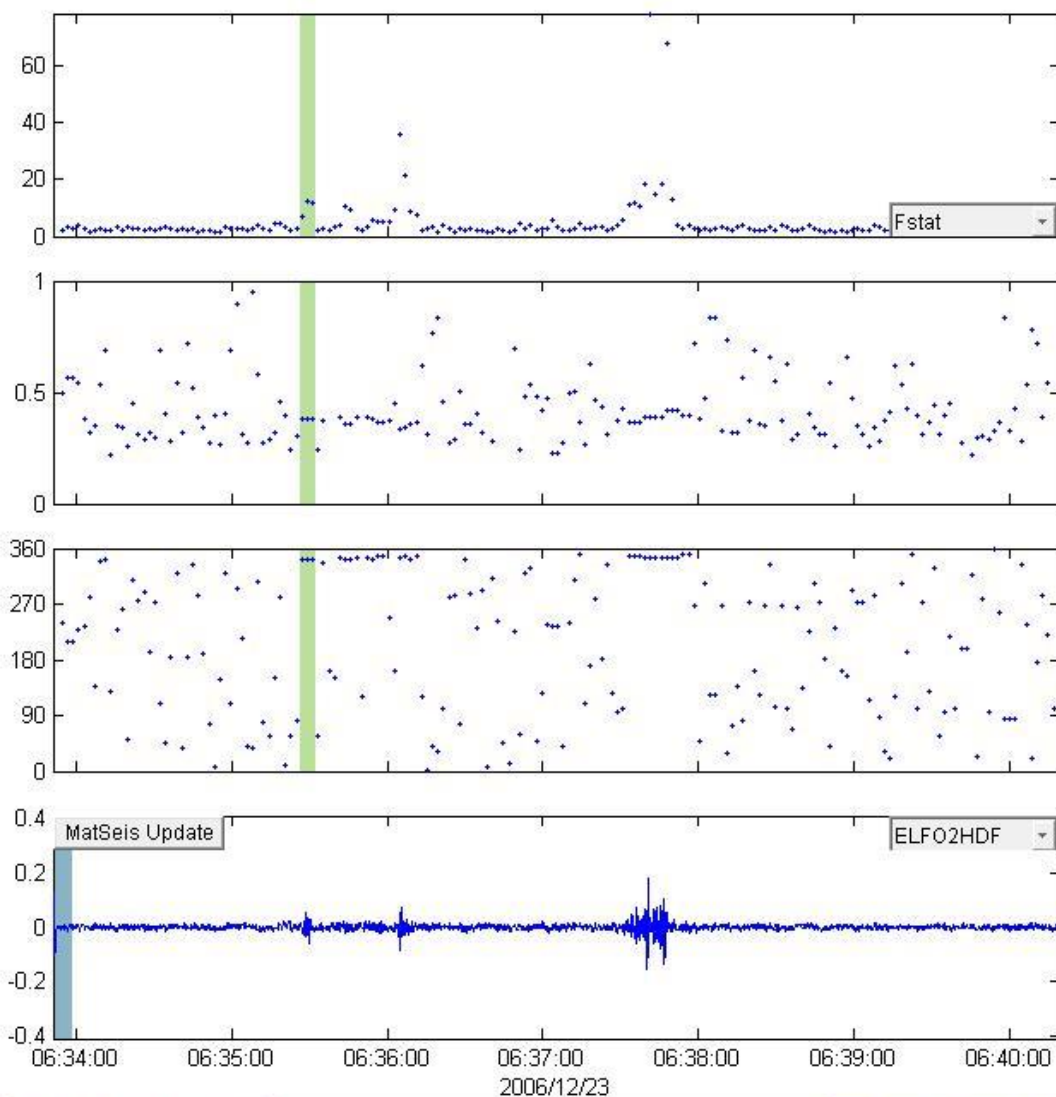


Window Parameters		Pass Band Parameters		Slowness Parameters		Windowed Values & S.D.	
Duration (s)	7.0	Low frequency (Hz)	0.6	Max. Slown.	400.0	Corr.	0.876   0.165
Overlap (%)	70.0	High frequency	20	# of Slown.	40	Fstat	100.942   93.568
Number of	106	Order (Integer)	2			Vel.	0.382   0.017
						Az.	257.135   2.112
						Send to Map	
Animate		Write File   D:\Research\Research - Elizabeth\lr				Cancel	
Calculate	0						



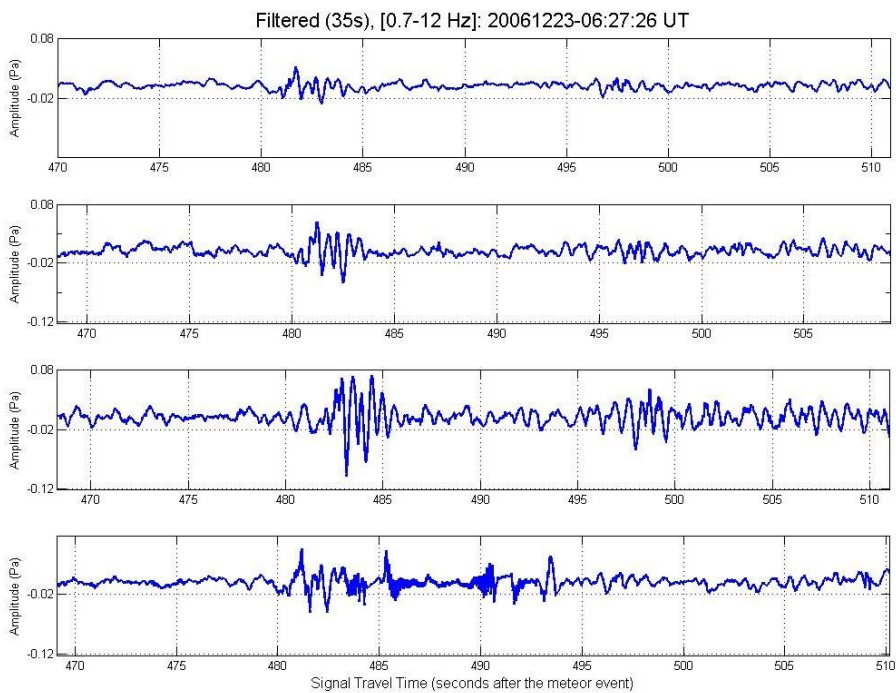


20061223\_062726

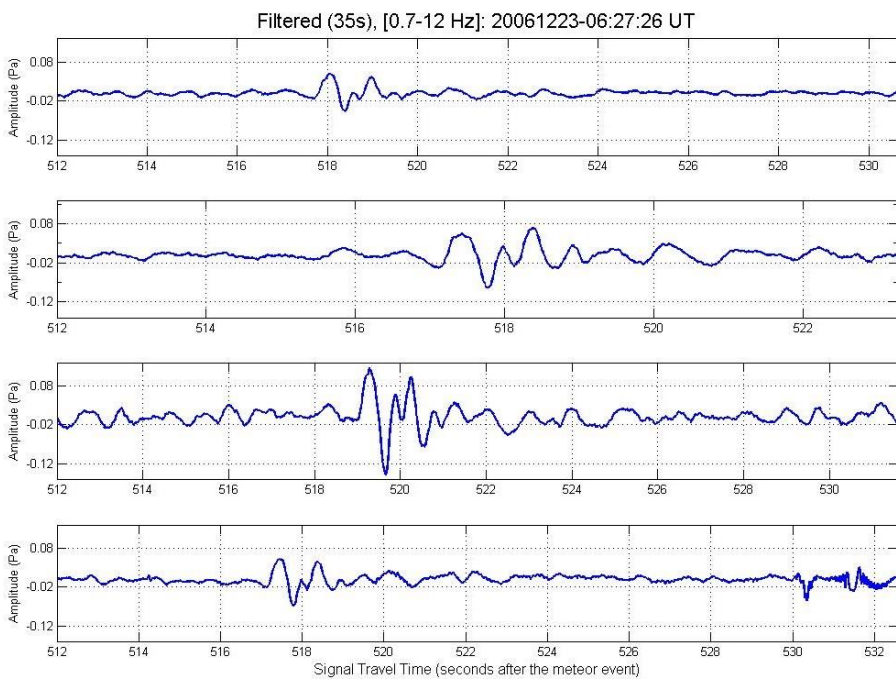


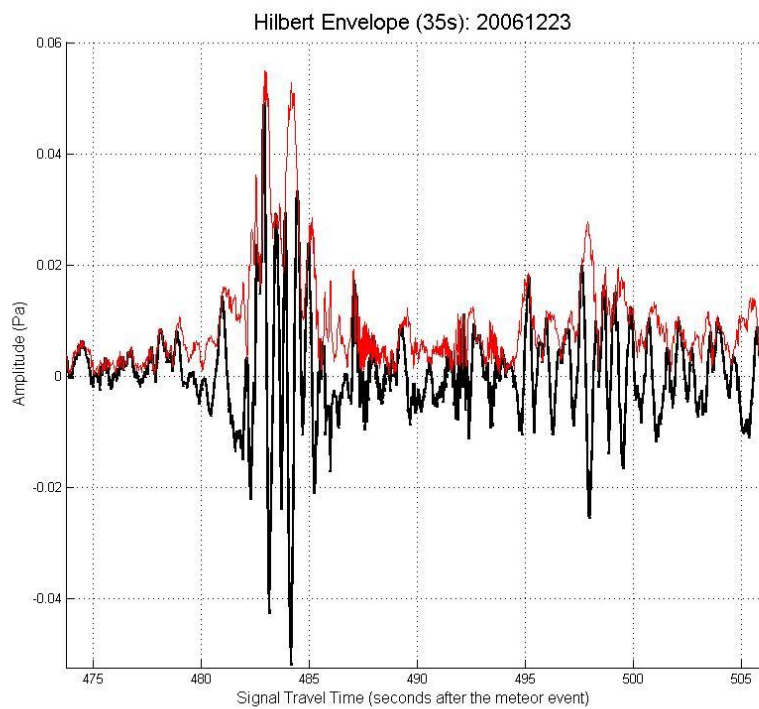
Window Parameters		Pass Band Parameters		Slowness Parameters		Windowed Values & S.D.	
Duration (s)	7.0	Low frequency (Hz)	0.6	Max. Slown.	400.0	Corr.	0.732   0.058
Overlap (%)	70.0	High frequency	8	# of Slown.	40	Fstat	10.372   2.974
Number of	183	Order (integer)	2			Vel.	0.381   0.000
						Az.	341.565   0.000
Animate						Send to Map	
Calculate	0	Write File	D:\Research\Research - Elizabeth\lr			Cancel	

## First and second arrival

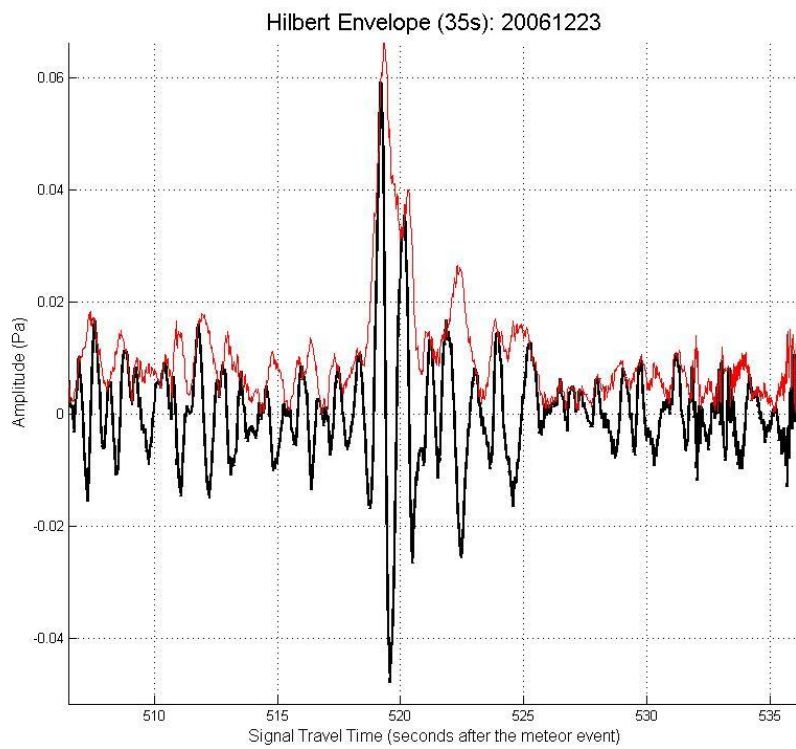


## Third arrival

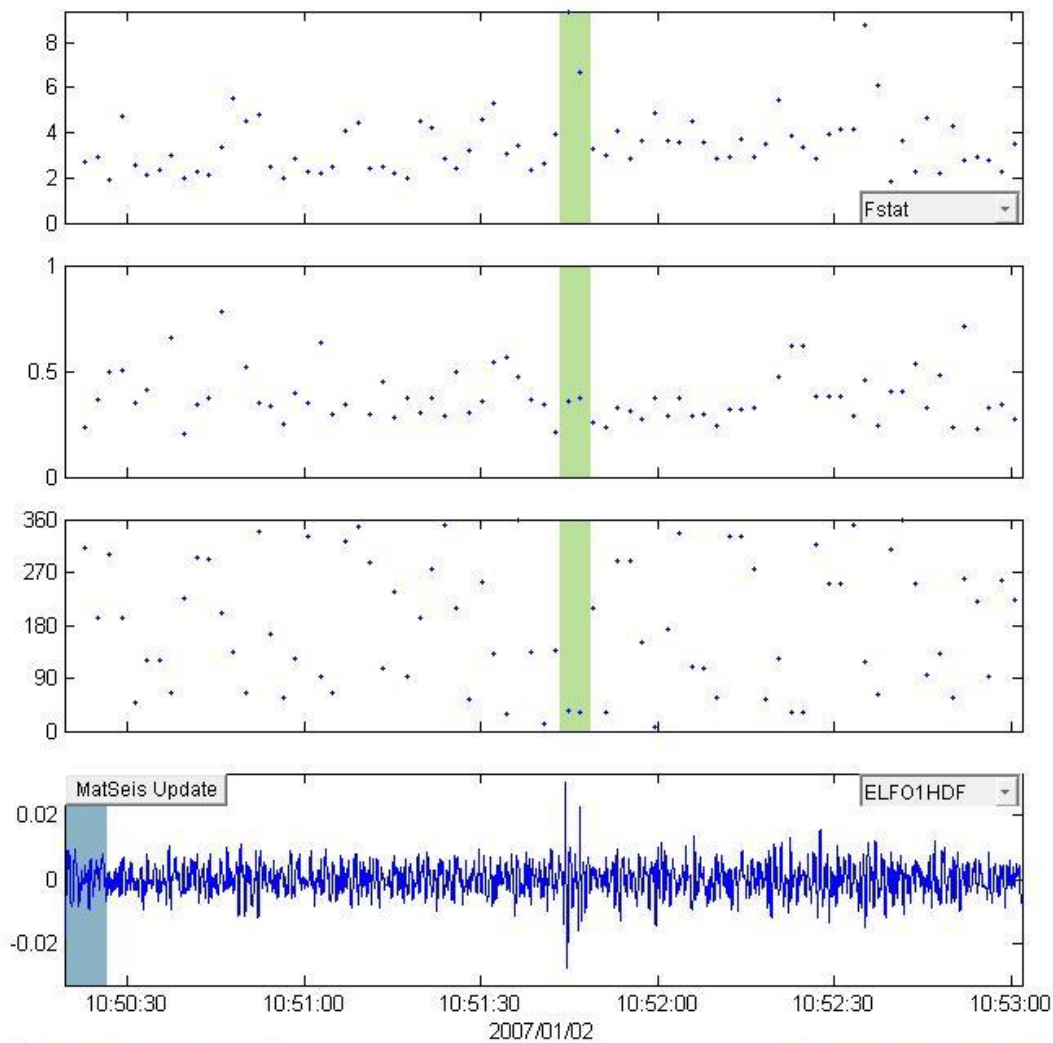




**Upper plot (1<sup>st</sup> and 2<sup>nd</sup> arrivals), Lower plot (3<sup>rd</sup> arrival)**



### 20070102\_104203

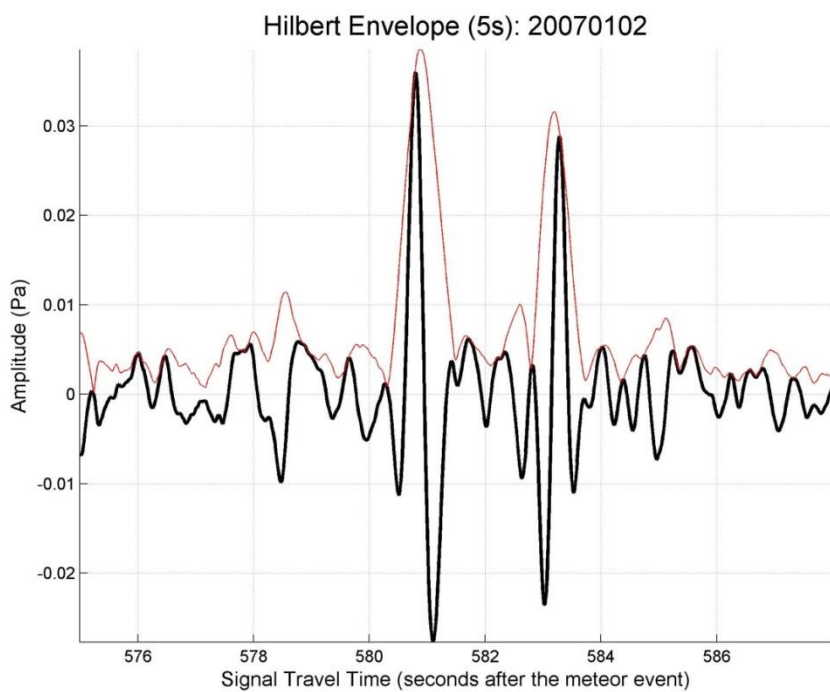
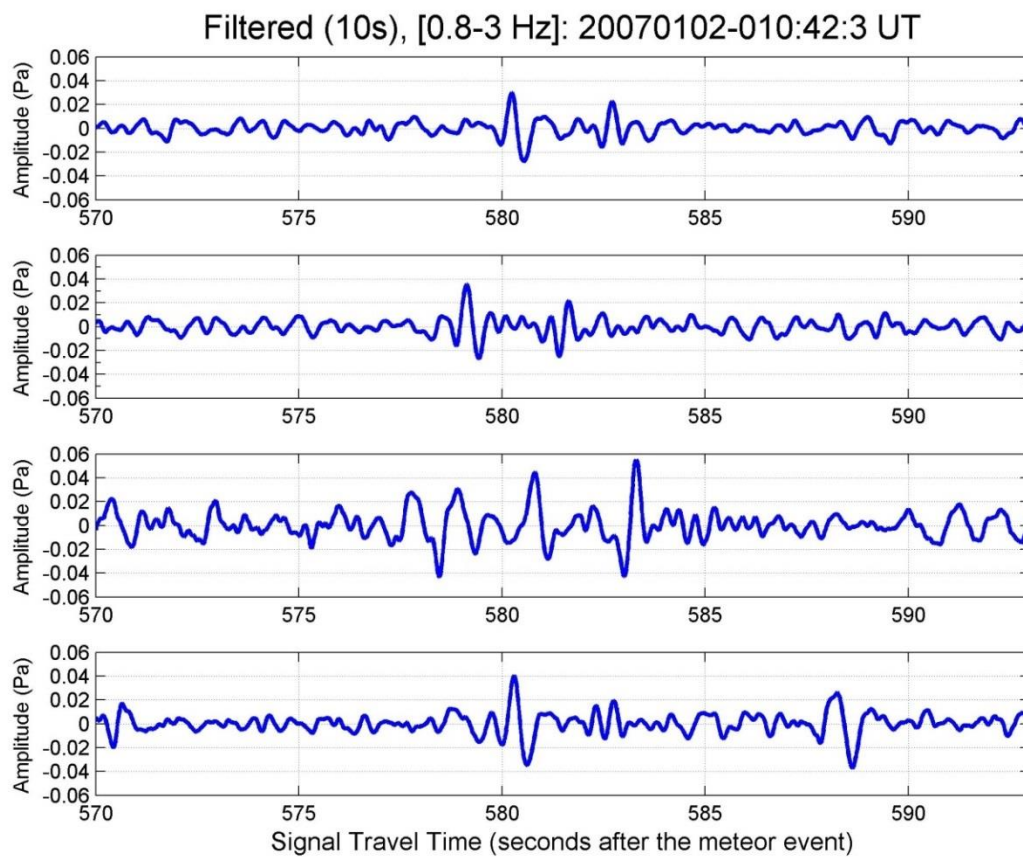


Window Parameters		Pass Band Parameters		Slowness Parameters		Windowed Values & S.D.	
Duration (s)	7.0	Low frequency (Hz)	0.8	Max. Slown.	400.0	Corr.	0.690 0.045
Overlap (%)	70.0	High frequency	3	# of Slown.	40	Fstat	8.035 1.908
Number of	77	Order (integer)	2			Vel.	0.365 0.009
						Az.	32.590 2.299

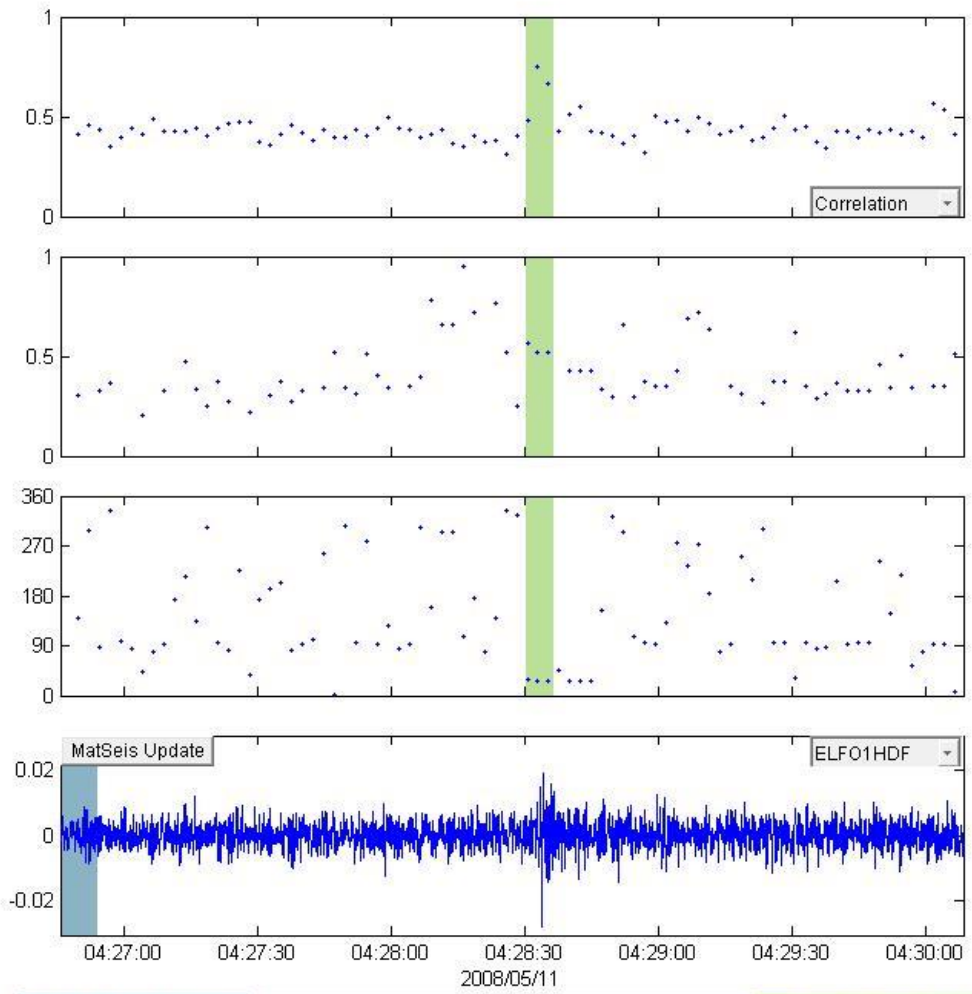
  

Animate			
Calculate	0	Write File	D:\Research\Research - Elizabeth\lr
			Send to Map
			Cancel



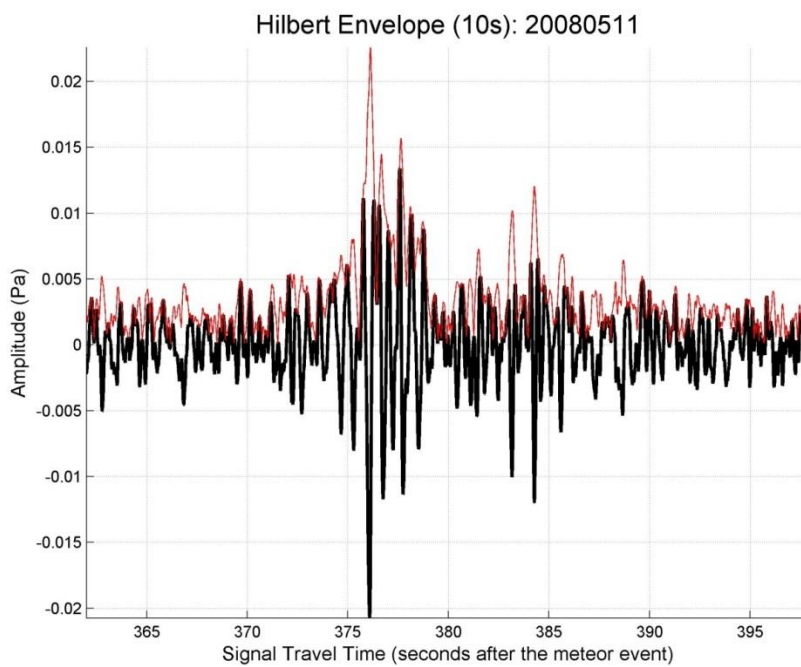
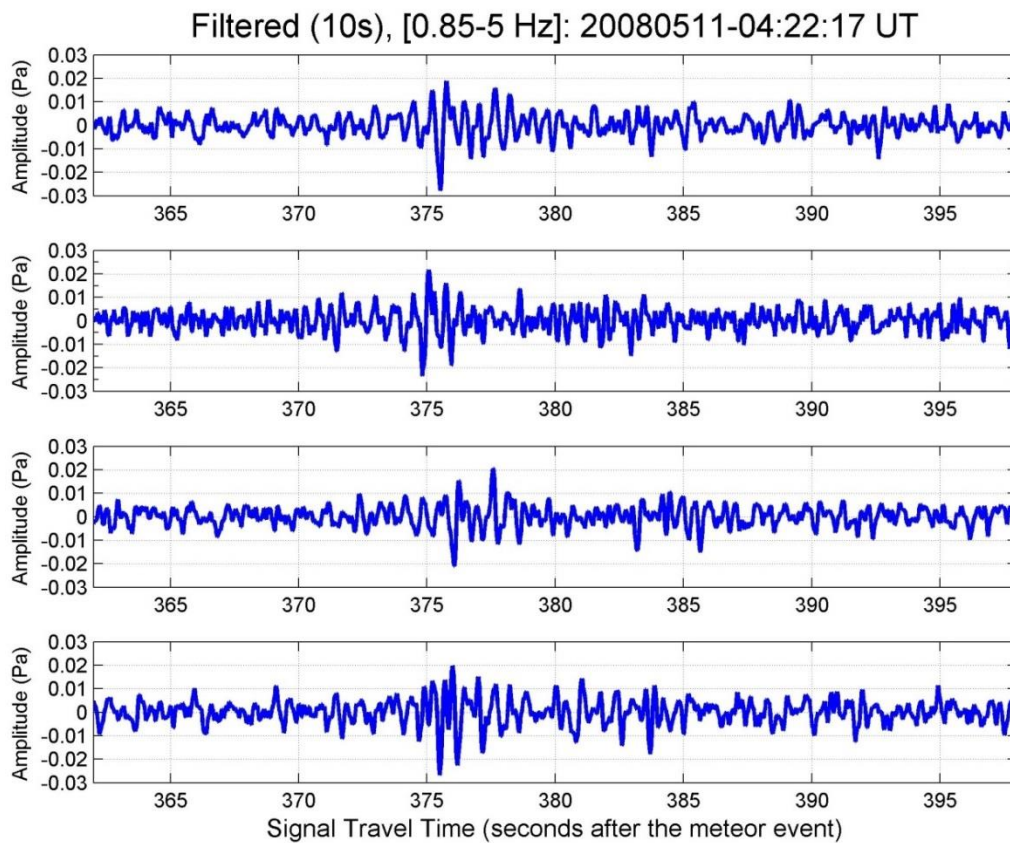


### 20080511\_042217



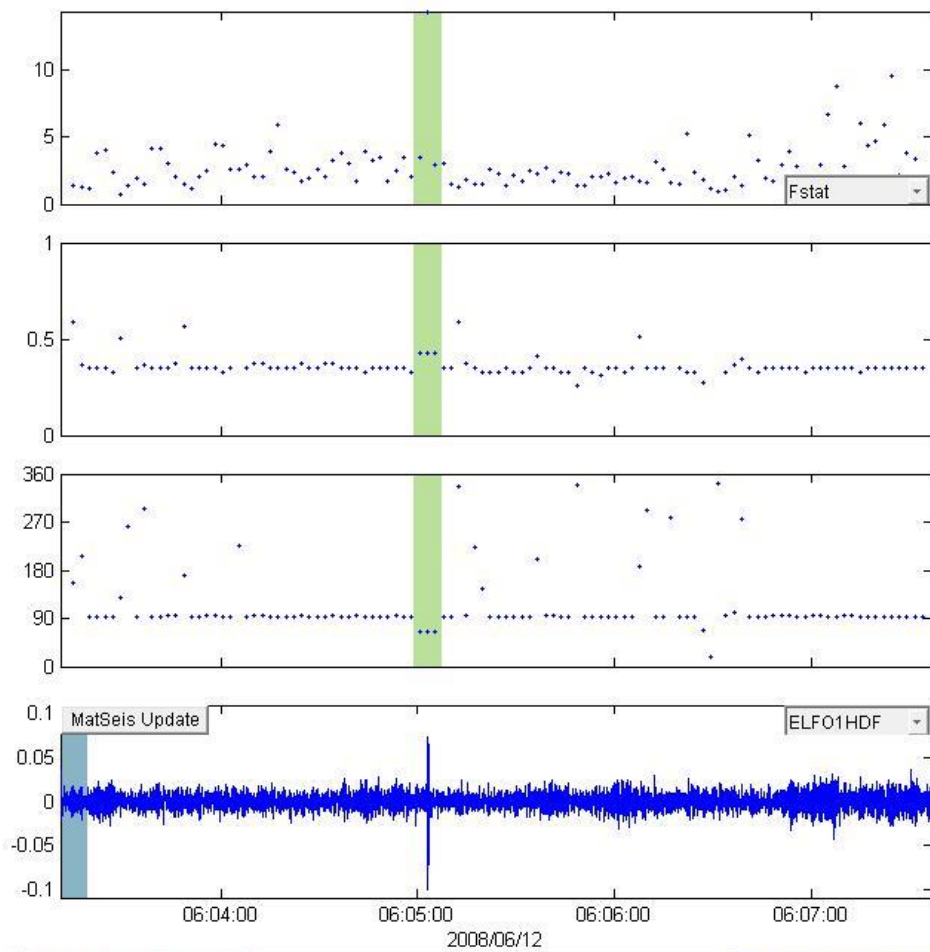
Window Parameters		Pass Band Parameters		Slowness Parameters		Windowed Values & S.D.	
Duration (s)	8.0	Low frequency (Hz)	0.85	Max. Slown.	400.0	Corr.	0.631 0.134
Overlap (%)	70.0	High frequency	5	# of Slown.	40	Fstat	6.789 4.019
Number of	83	Order (integer)	2			Vel.	0.531 0.028
						Az.	26.197 1.473

Buttons: Animate, Calculate 0, Write File, D:\Research\Research - Elizabeth\lr, Send to Map, Cancel

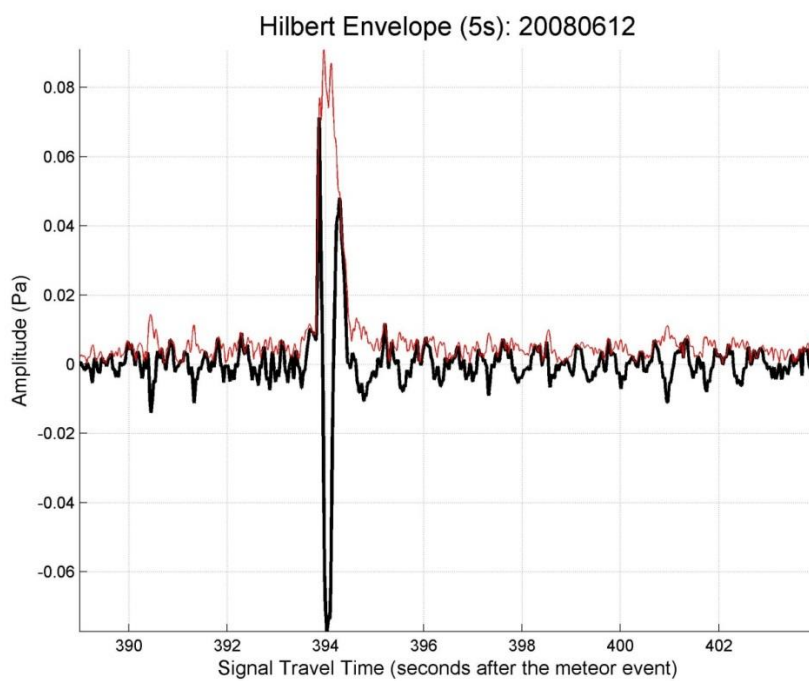
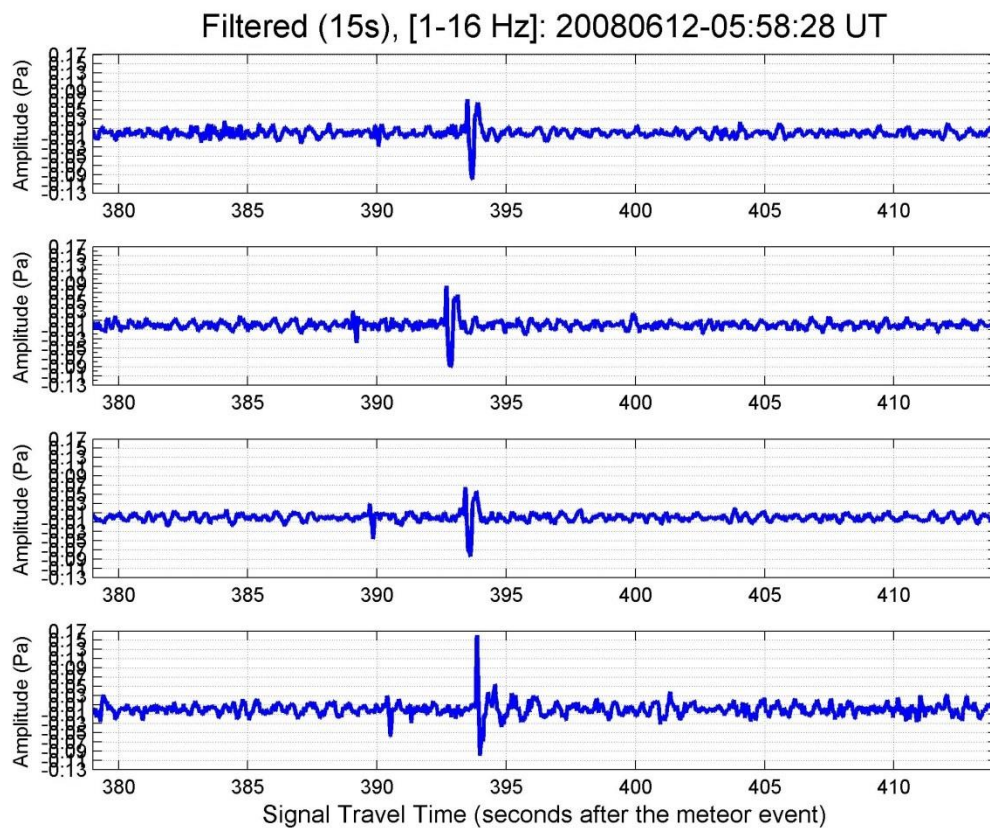




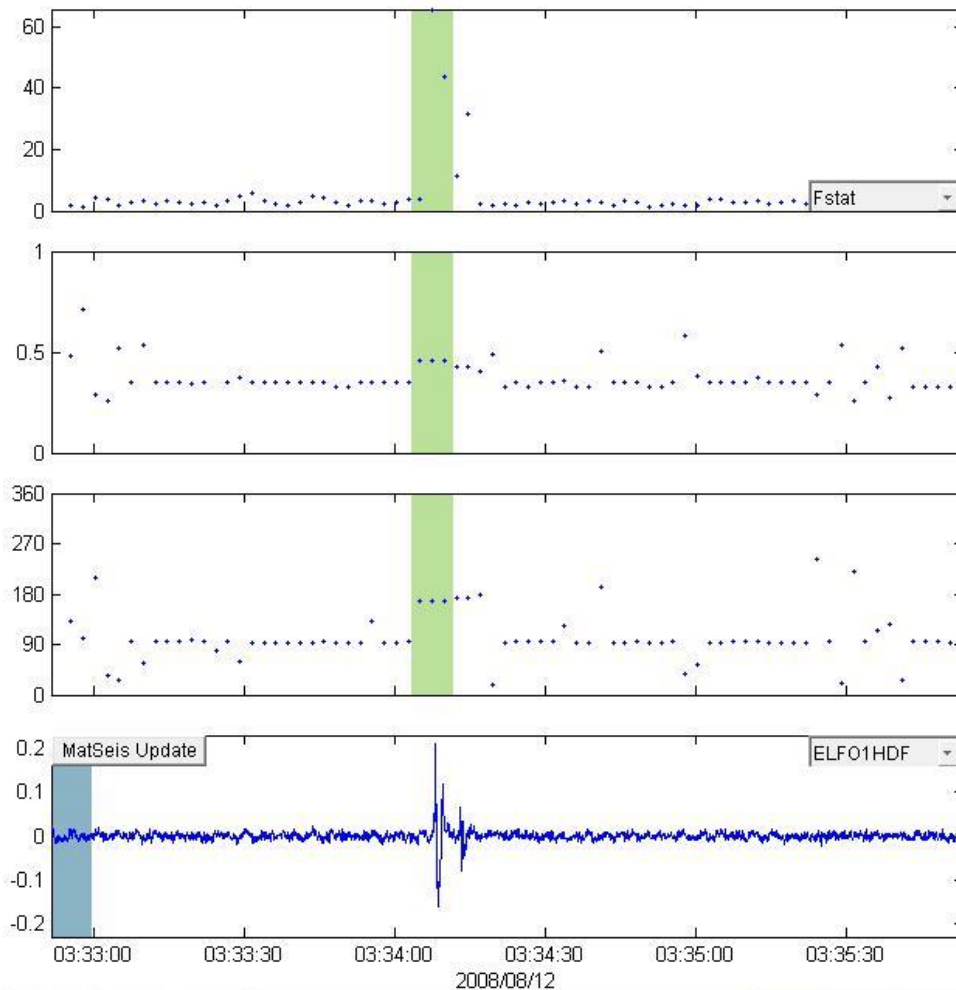
20080612\_055828



Window Parameters		Pass Band Parameters		Slowness Parameters		Windowed Values & S.D.	
Duration (s)	8	Low frequency (Hz)	1	Max. Slown.	400.0	Corr.	0.604 0.165
Overlap (%)	70.0	High frequency	16	# of Slown.	40	Fstat	6.892 6.453
Number of	109	Order (integer)	2			Vel.	0.425 0.000
						Az.	64.440 0.000
						Send to Map	
Animate		Write File				Cancel	
Calculate	0	8\20080325_004203\infrasound-da					



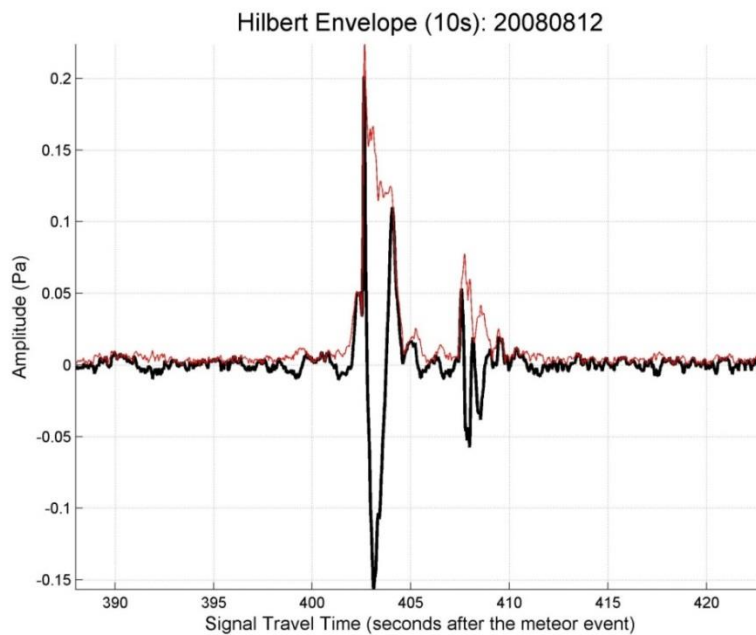
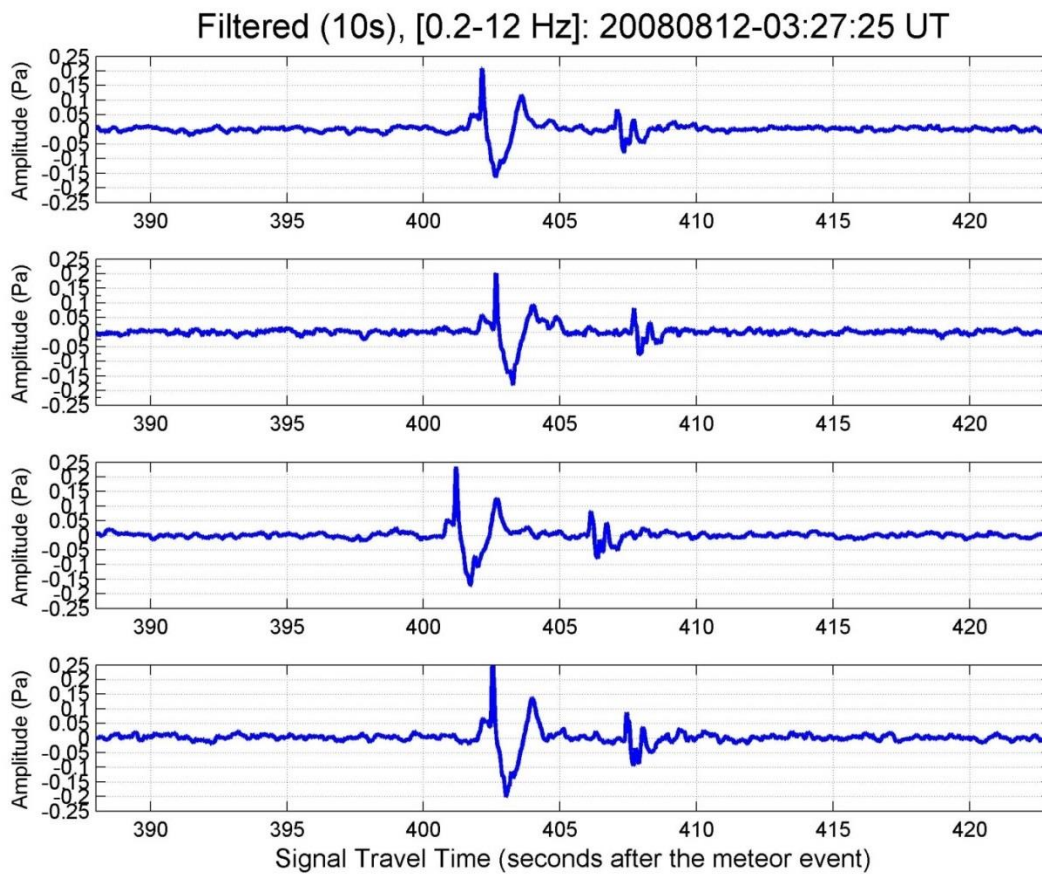
### 20080812\_032725



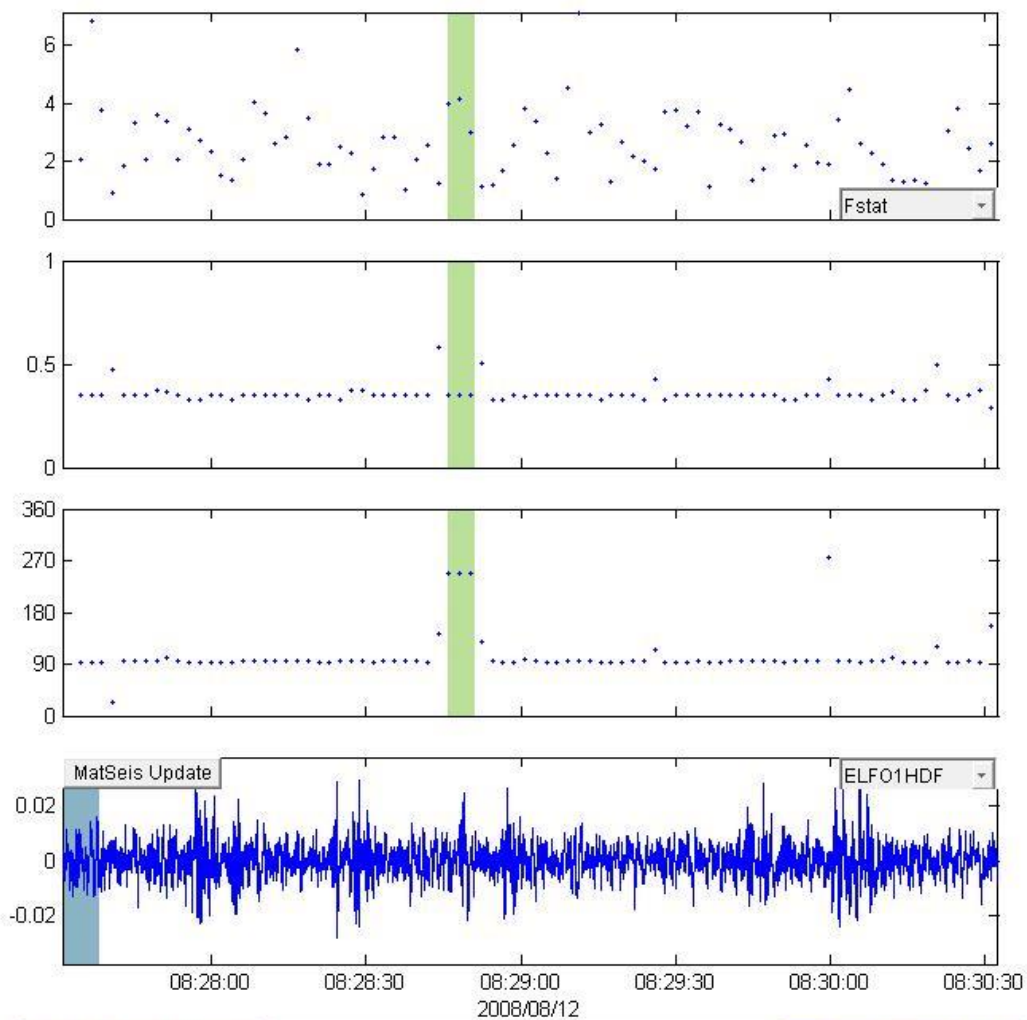
Window Parameters		Pass Band Parameters		Slowness Parameters		Windowed Values & S.D.	
Duration (s)	8	Low frequency (Hz)	0.2	Max. Slown.	400.0	Corr.	0.804 0.220
Overlap (%)	70.0	High frequency	12	# of Slown.	40	Fstat	37.672 31.261
Number of	74	Order (integer)	2			Vel.	0.460 0.000
						Az.	167.735 0.000

Animate		Write File	8\20080325_004203\infrasound-da	Send to Map
Calculate	0			Cancel

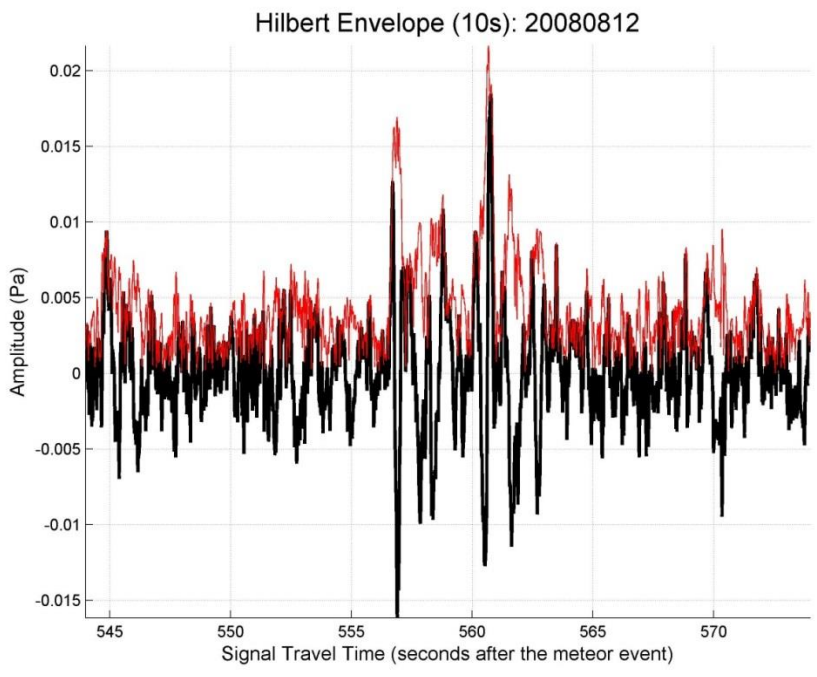
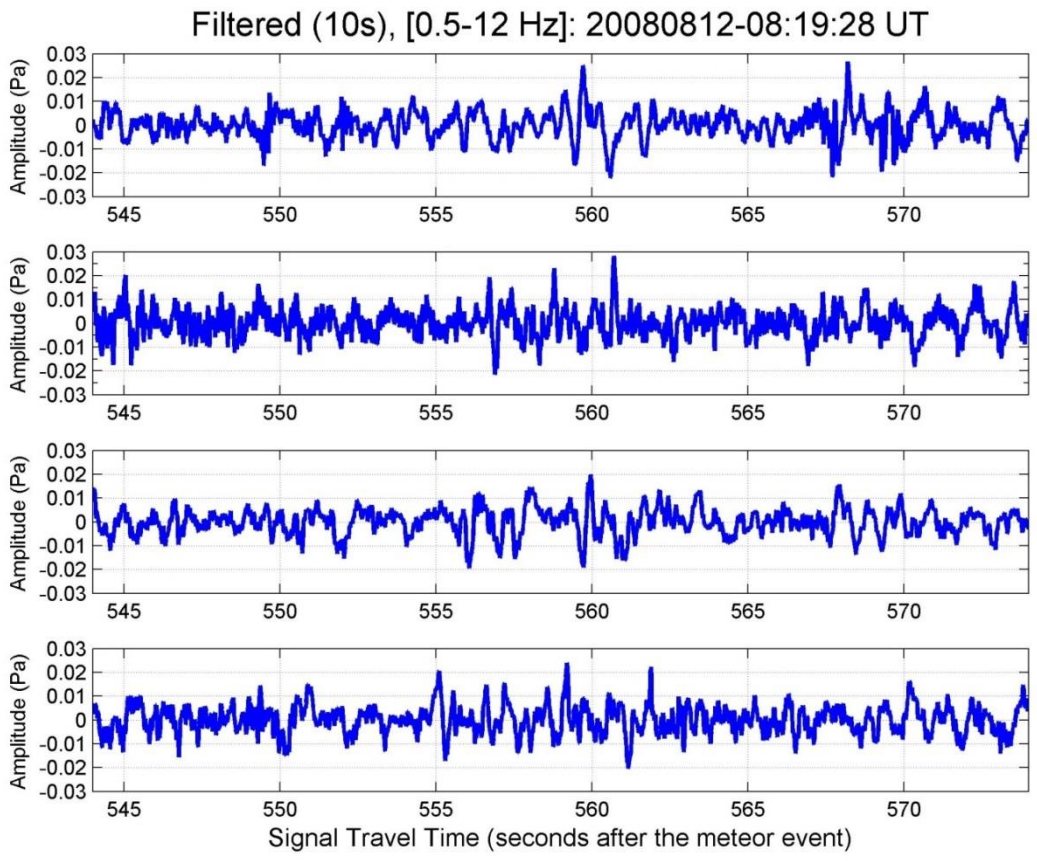


20080812\_081928

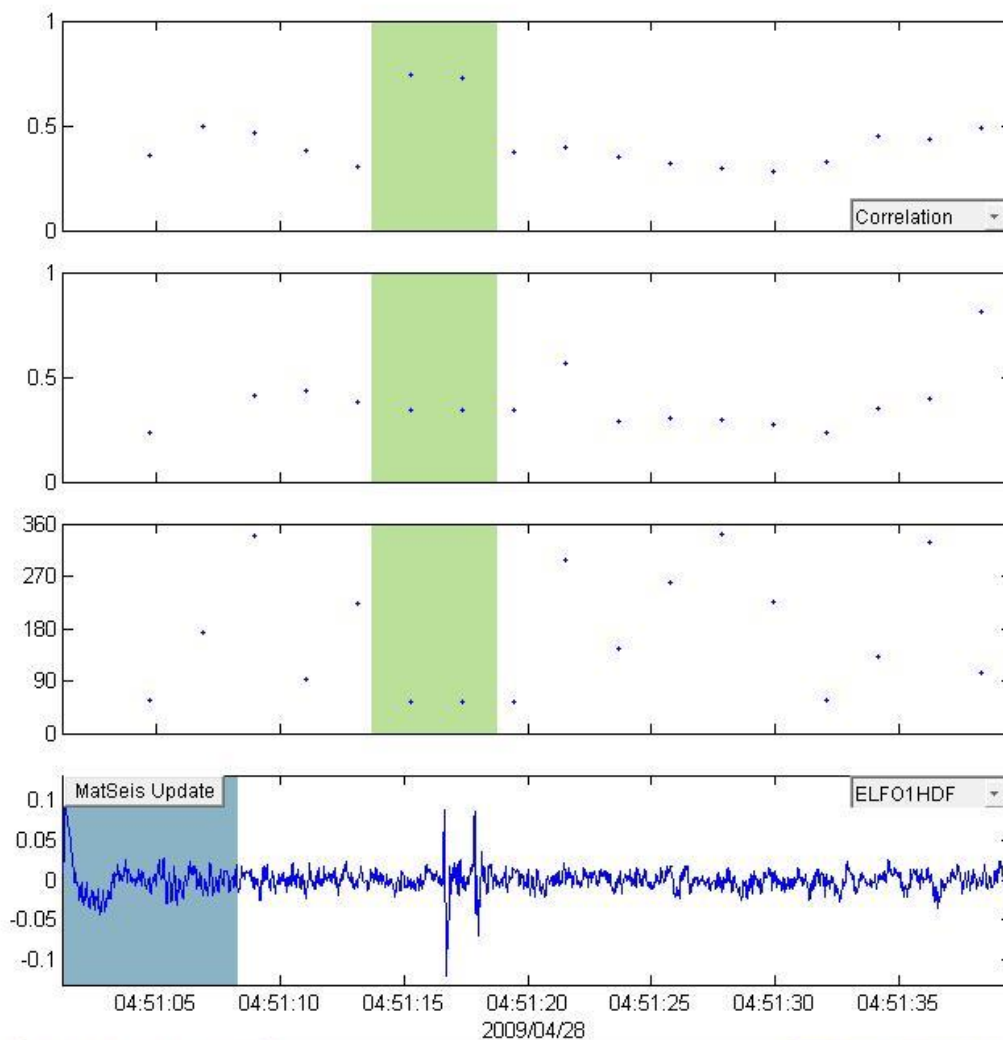


Window Parameters		Pass Band Parameters		Slowness Parameters		Windowed Values & S.D.	
Duration (s)	7.0	Low frequency (Hz)	0.5	Max. Slown.	400.0	Corr.	0.539 0.036
Overlap (%)	70.0	High frequency	12	# of Slown.	40	Fstat	3.713 0.644
Number of	86	Order (integer)	2			Vel.	0.349 0.000
						Az.	249.228 0.000
Animate						Send to Map	
Calculate	0	Write File	D:\Research\Research - Elizabeth\lr			Cancel	

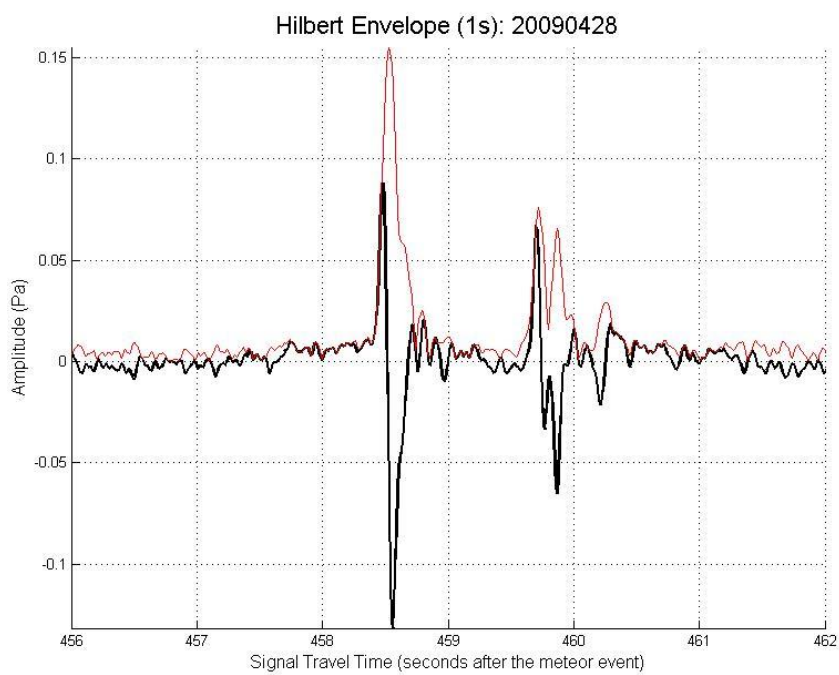
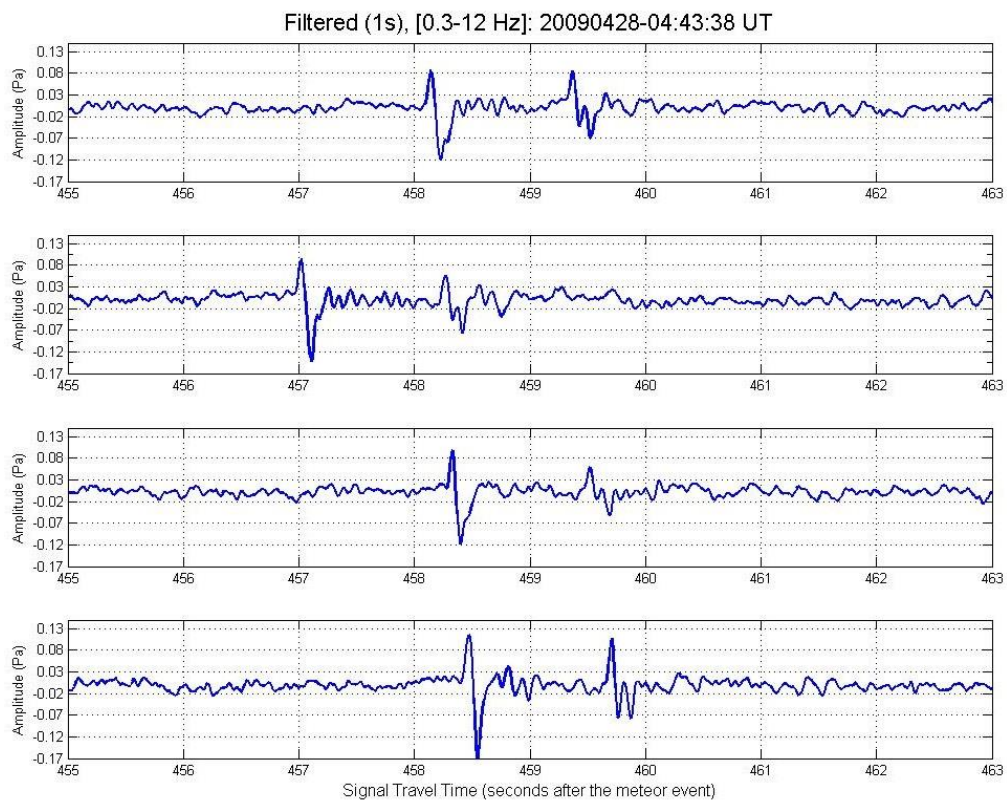




## 20090428\_044338

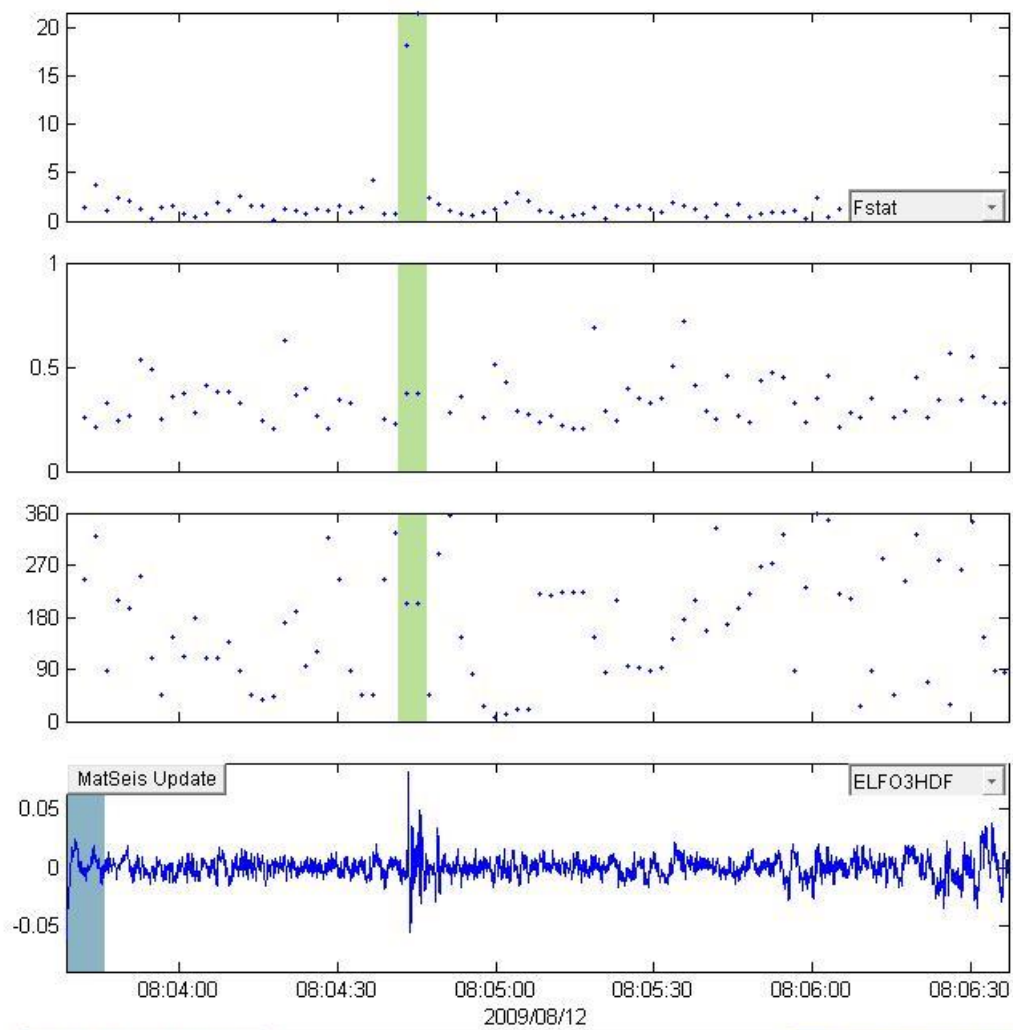


Window Parameters		Pass Band Parameters		Slowness Parameters		Windowed Values & S.D.	
Duration (s)	7	Low frequency (Hz)	0.3	Max. Slown.	400.0	Corr.	0.736 0.014
Overlap (%)	70.0	High frequency	12	# of Slown.	40	Fstat	10.161 0.803
Number of	17	Order (integer)	2			Vel.	0.345 0.000
						Az.	52.765 0.000
Animate						Send to Map	
Calculate	0	Write File	8\20080325_004203\infrasound-da			Cancel	

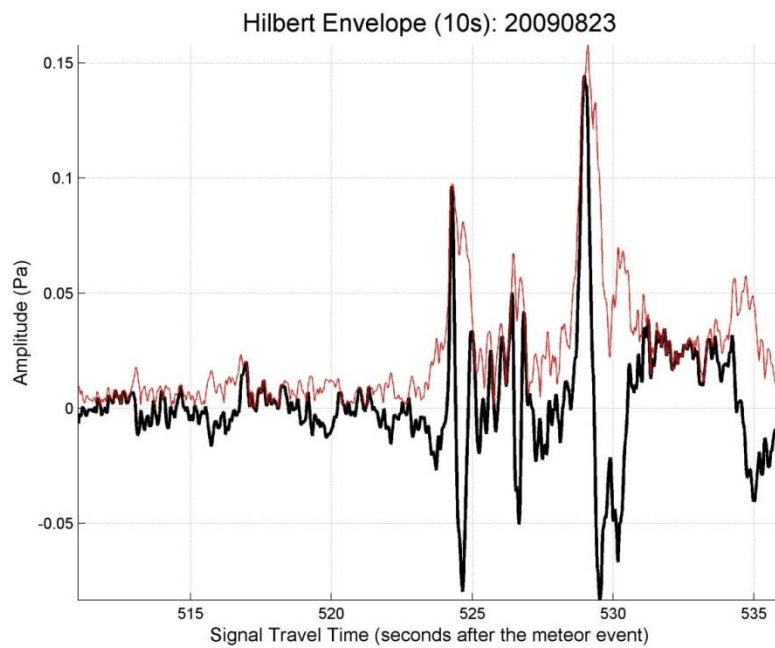
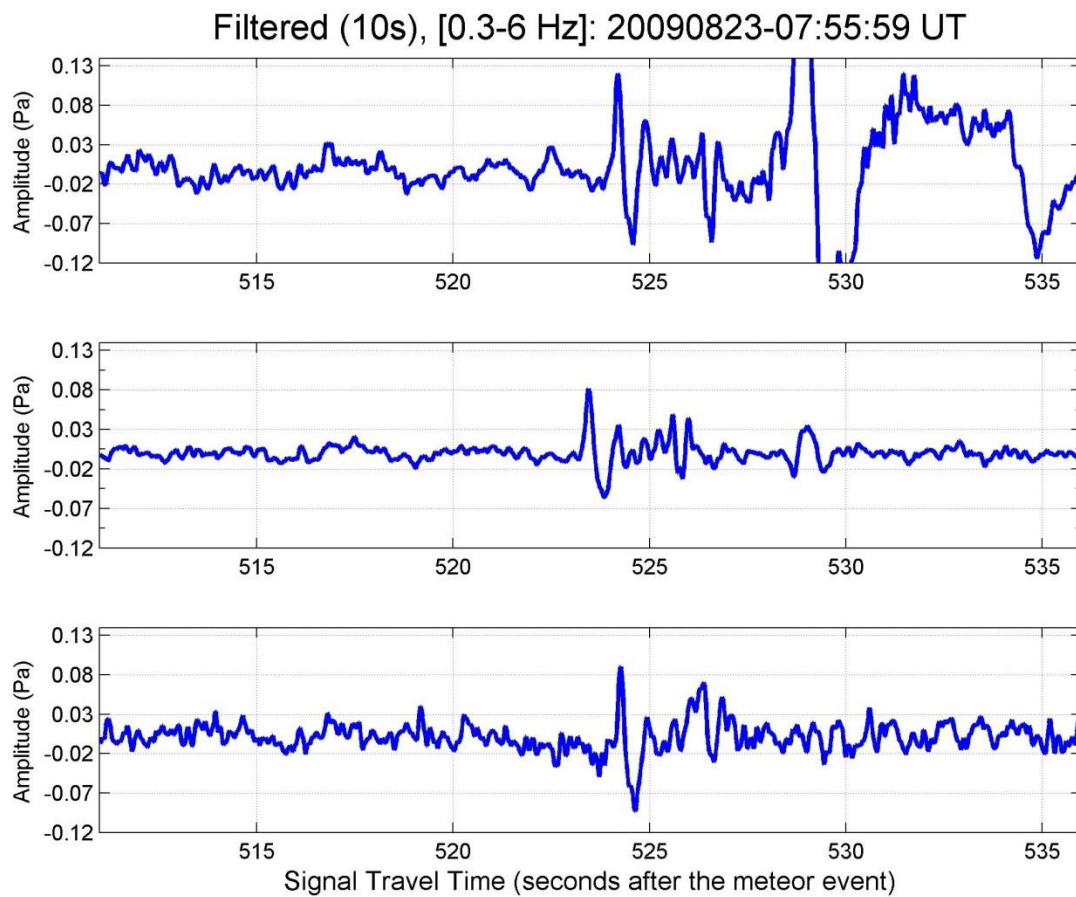




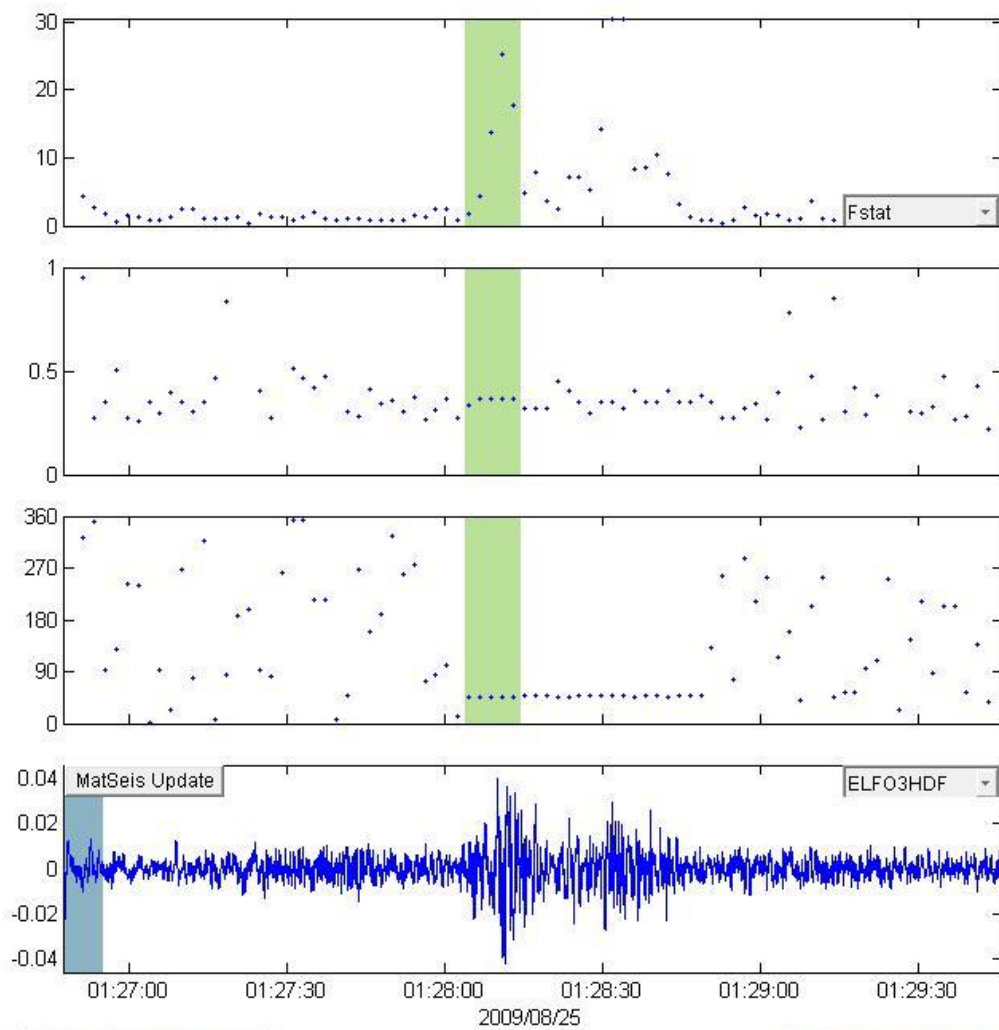
20090812\_075559



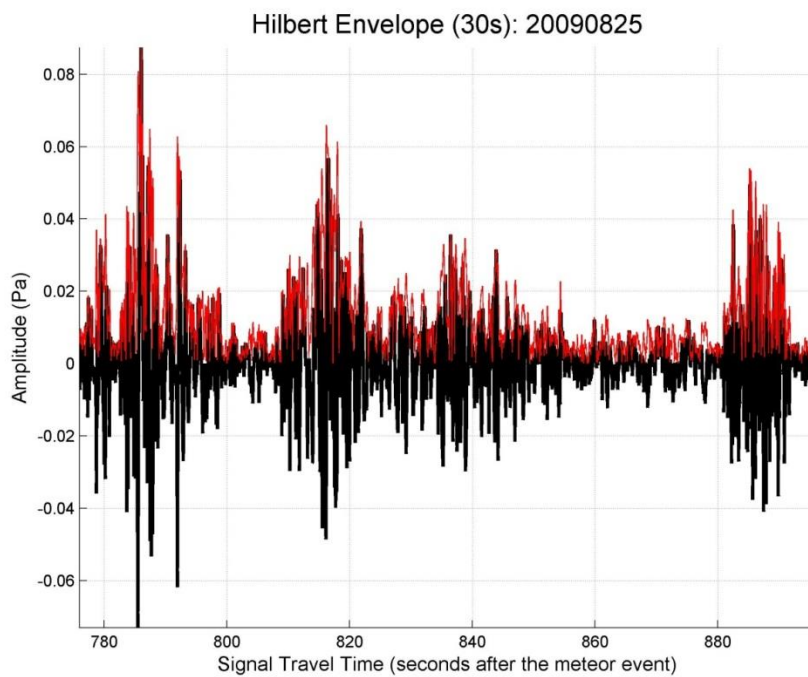
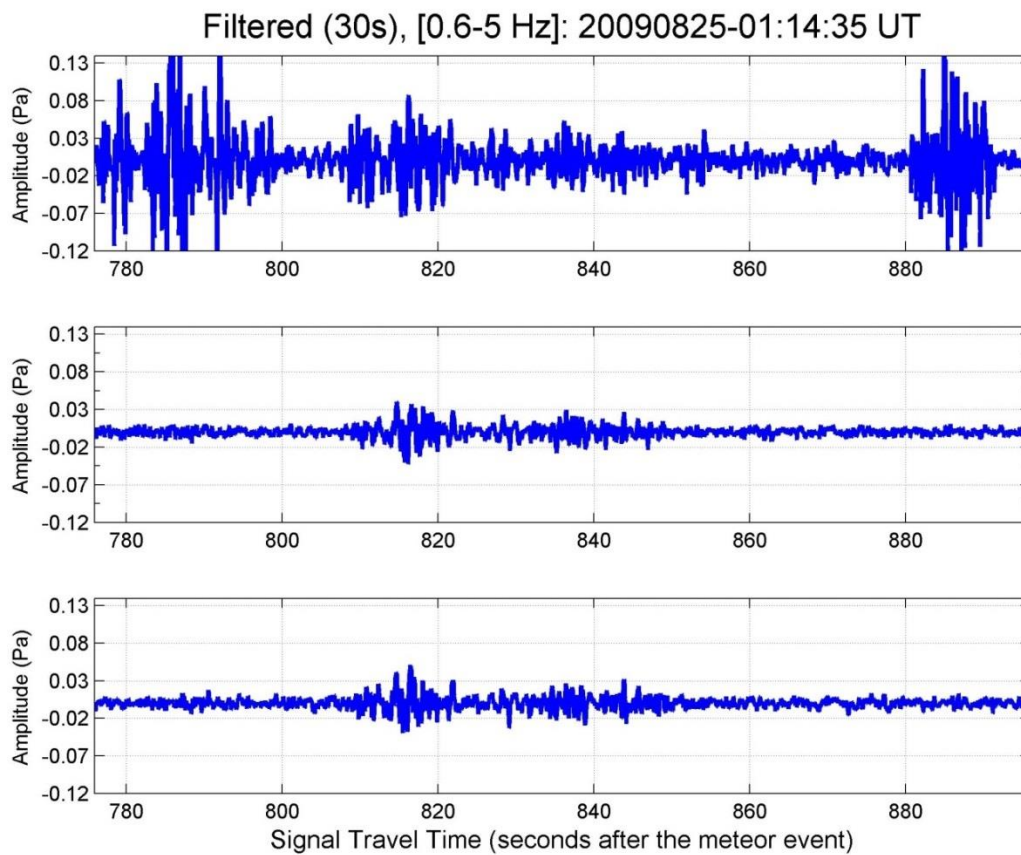
Window Parameters		Pass Band Parameters		Slowness Parameters		Windowed Values & S.D.	
Duration (s)	7	Low frequency (Hz)	0.3	Max. Slown.	400.0	Corr.	0.874 0.013
Overlap (%)	70.0	High frequency	6	# of Slown.	40	Fstat	19.926 2.437
Number of	84	Order (integer)	2			Vel.	0.372 0.000
						Az.	202.166 0.000
<input type="button" value="Animate"/> <input type="button" value="Calculate"/> 0						<input type="button" value="Send to Map"/>	
<input type="button" value="Write File"/> 8120080325_004203infrasound-da						<input type="button" value="Cancel"/>	



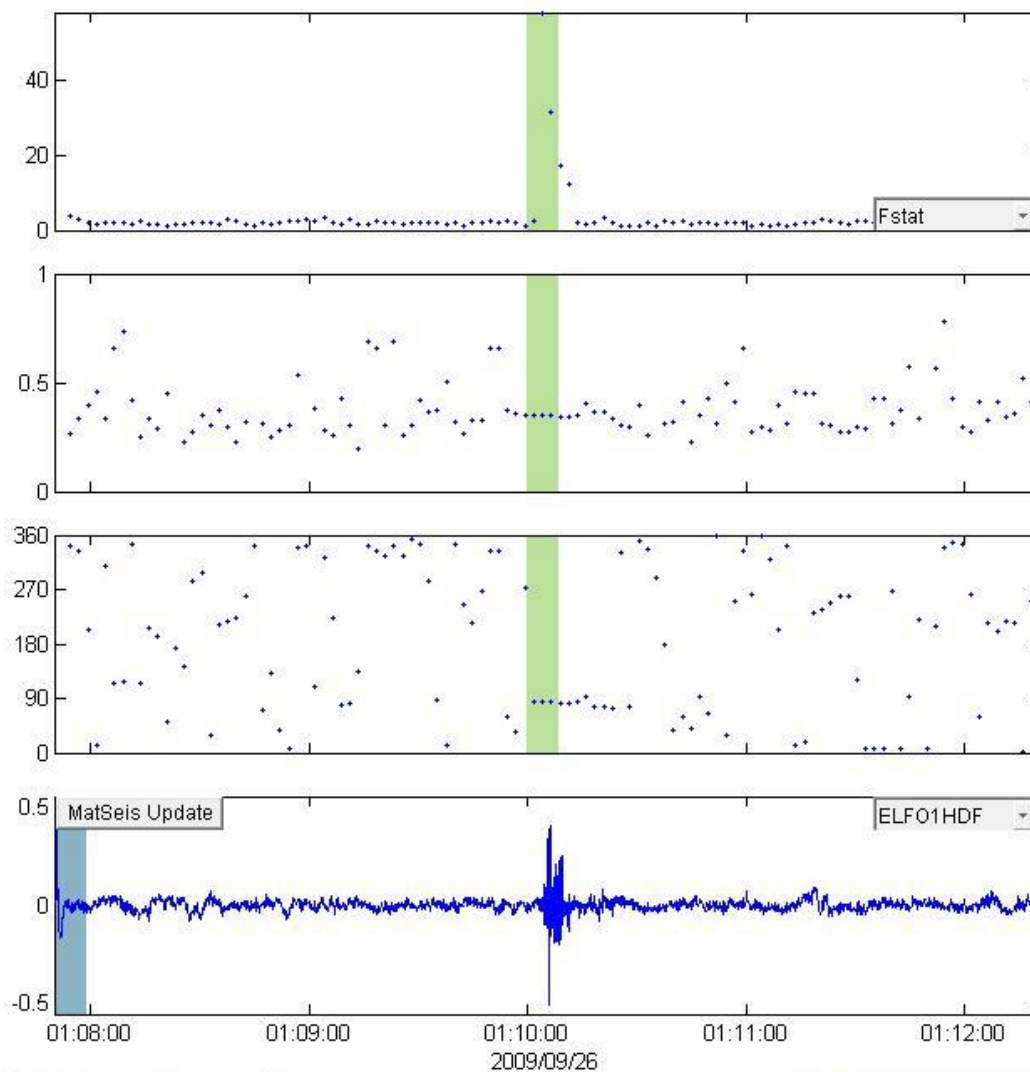
20090825\_011435



Window Parameters		Pass Band Parameters		Slowness Parameters		Windowed Values & S.D.	
Duration (s)	7	Low frequency (Hz)	0.6	Max. Slown.	400.0	Corr.	0.743 0.175
Overlap (%)	70.0	High frequency	5	# of Slown.	40	Fstat	12.538 9.613
Number of	83	Order (integer)	2			Vel.	0.359 0.014
						Az.	45.000 0.000
Animate						Send to Map	
Calculate	0	Write File	8\20080325_004203\infrasound-da			Cancel	



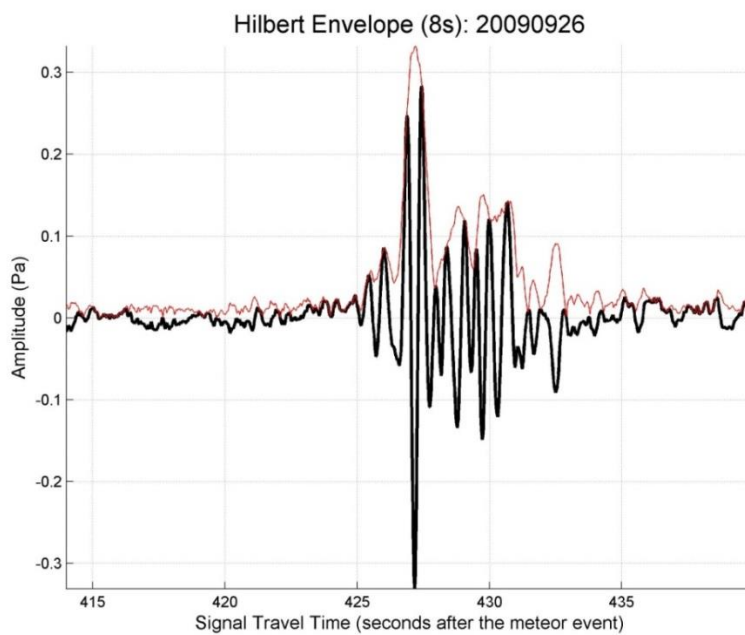
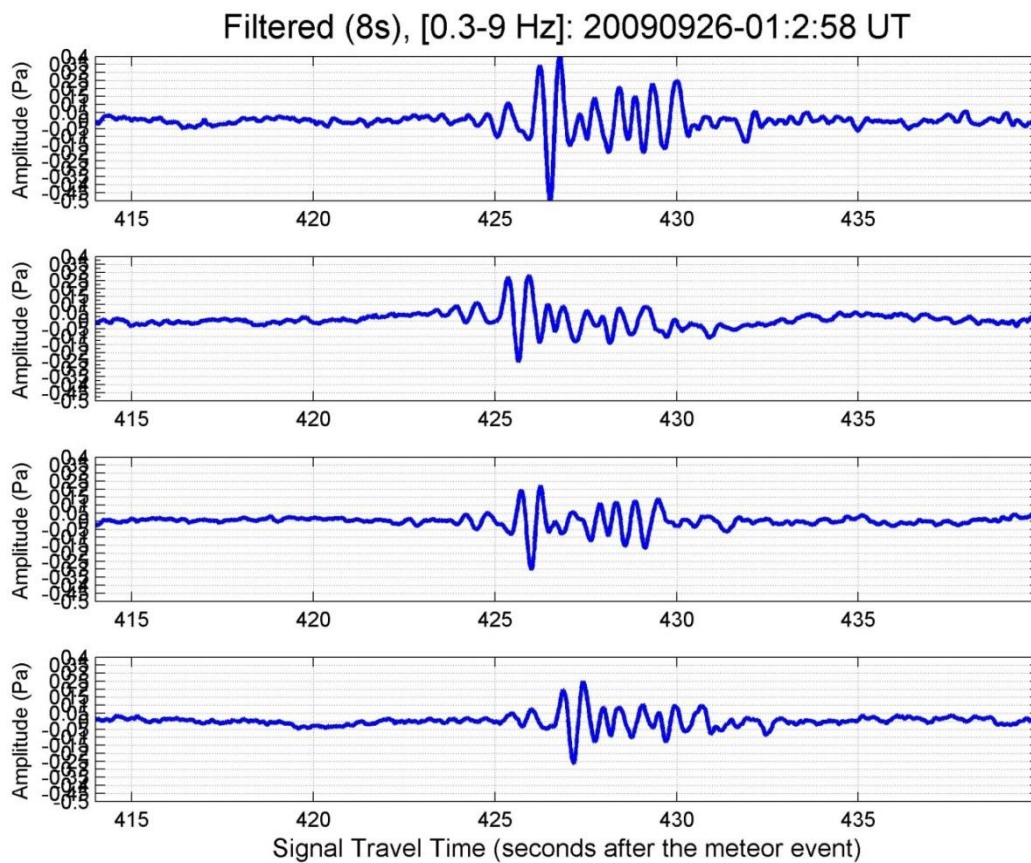
### 20090926\_010258



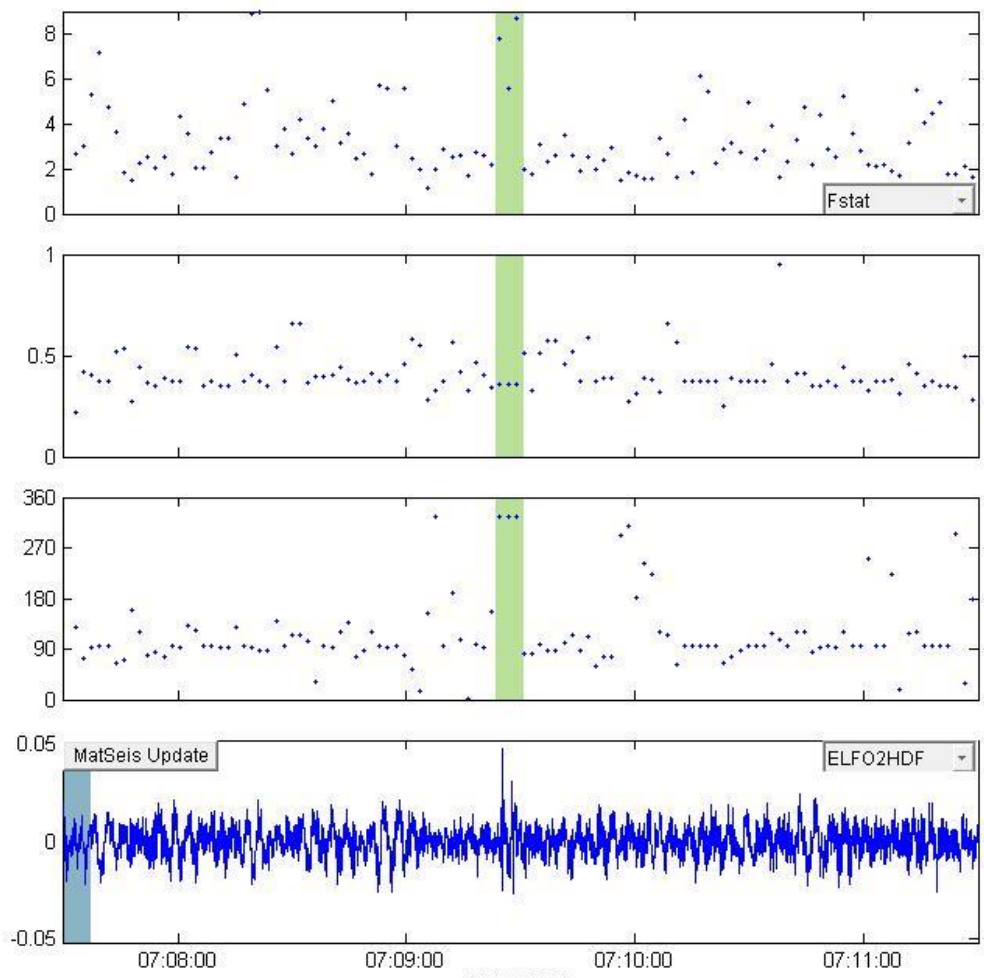
Window Parameters		Pass Band Parameters		Slowness Parameters		Windowed Values & S.D.	
Duration (s)	8.0	Low frequency (Hz)	0.3	Max. Slown.	400.0	Corr.	0.763 0.262
Overlap (%)	70.0	High frequency	5	# of Slown.	40	Fstat	30.712 27.801
Number of	111	Order (integer)	2			Vel.	0.348 0.000
						Az.	84.472 0.000

0
  D:\Research\Research - Elizabeth\lr





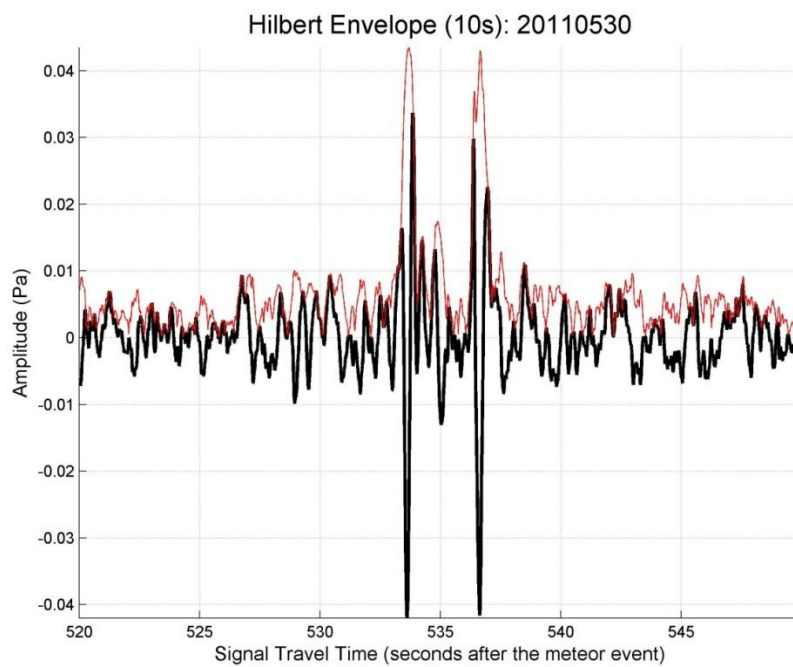
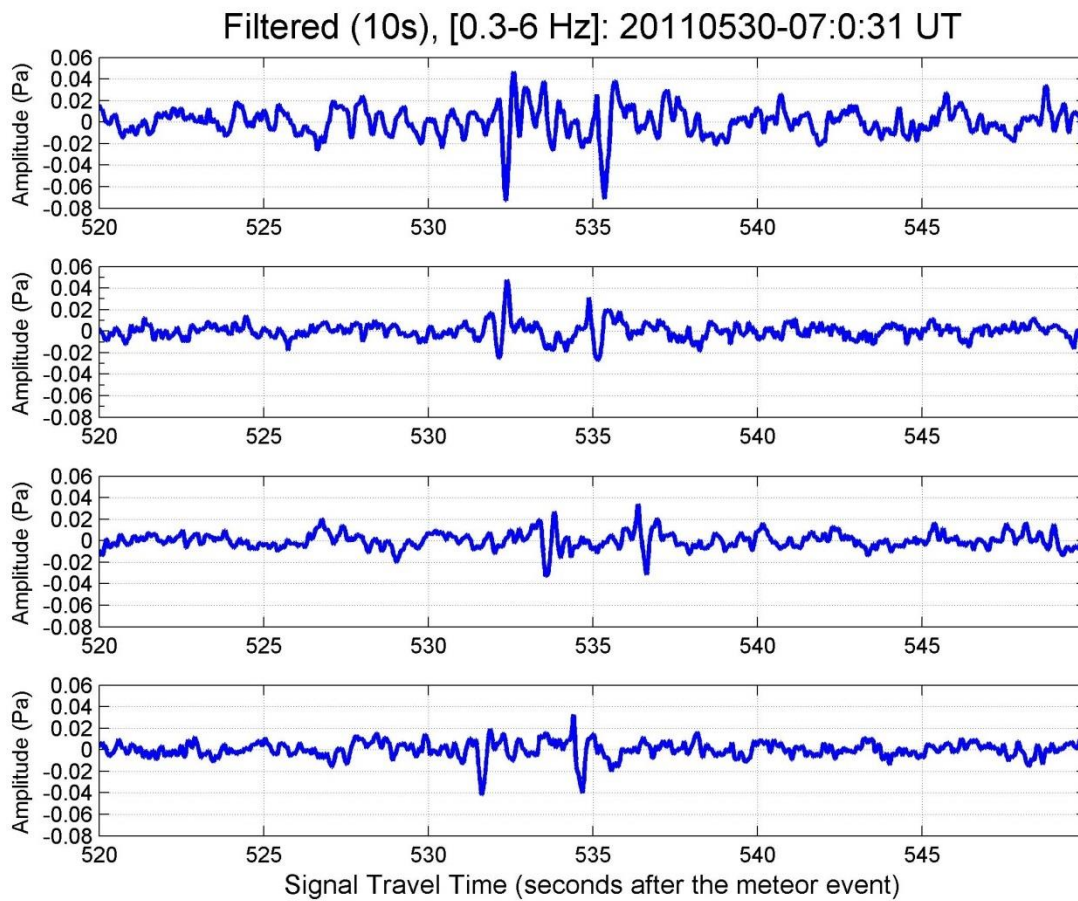
### 20100530\_070031



Window Parameters		Pass Band Parameters		Slowness Parameters		Windowed Values & S.D.	
Duration (s)	7.0	Low frequency (Hz)	0.3	Max. Slown.	400.0	Corr.	0.673 0.045
Overlap (%)	70.0	High frequency	6	# of Slown.	40	Fstat	7.363 1.592
Number of	113	Order (integer)	2			Vel.	0.358 0.000
						Az.	325.784 0.000

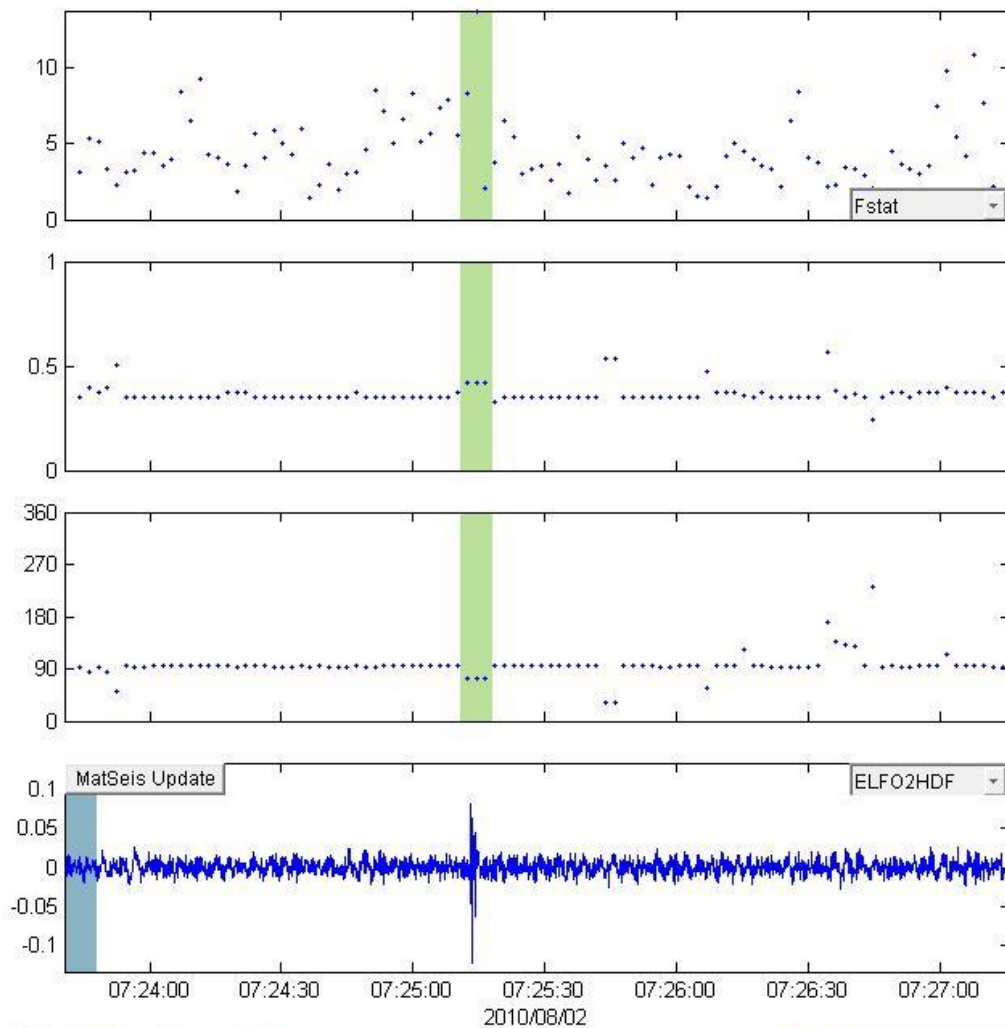
  

Animate		Write File	D:\Research\Research - Elizabeth\lr	Send to Map	
Calculate	0			Cancel	



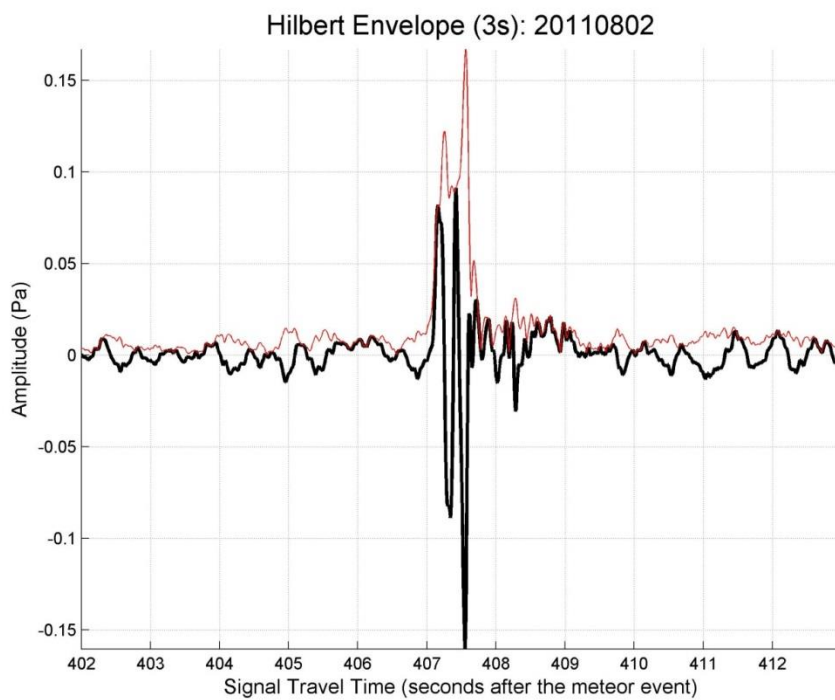
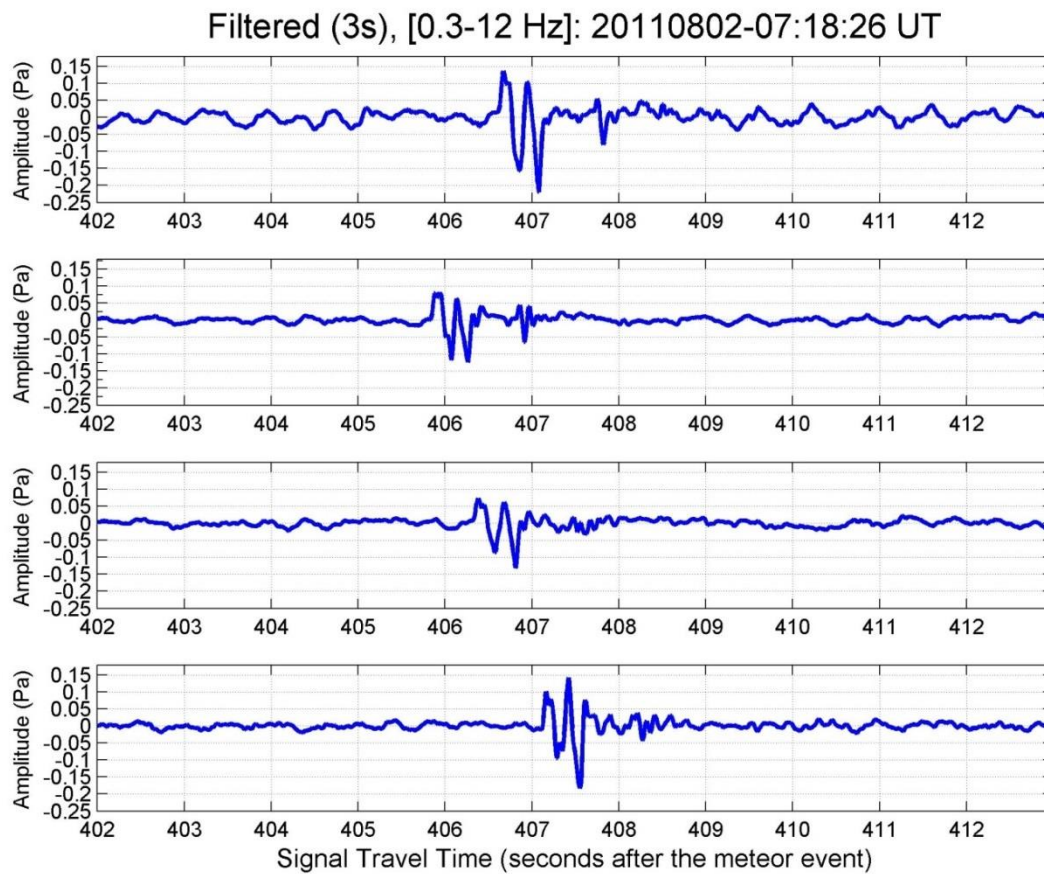


### 20100802\_071826

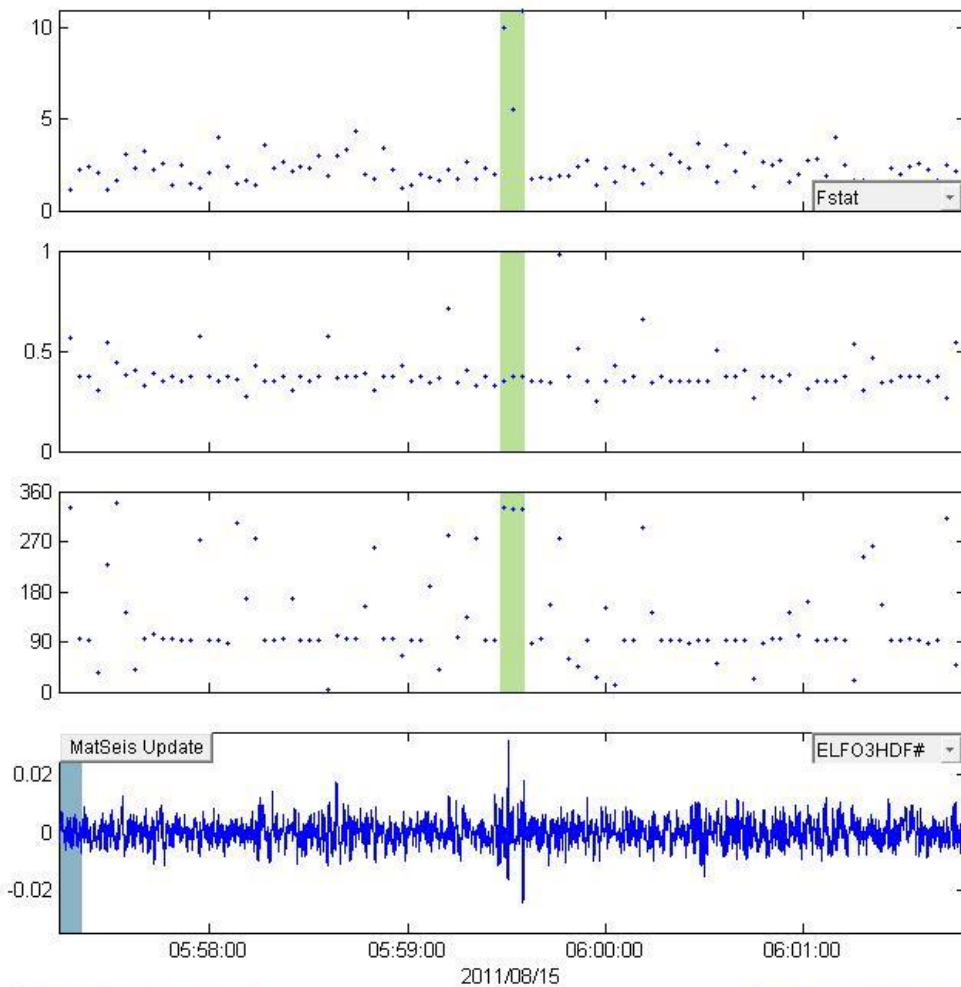


Window Parameters		Pass Band Parameters		Slowness Parameters		Windowed Values & S.D.	
Duration (s)	7.0	Low frequency (Hz)	0.3	Max. Slown.	400.0	Corr.	0.640 0.185
Overlap (%)	70.0	High frequency	12	# of Slown.	40	Fstat	8.058 5.888
Number of	101	Order (integer)	2			Vel.	0.417 0.000
						Az.	74.358 0.000

0
  D:\Research\Research - Elizabeth\lr

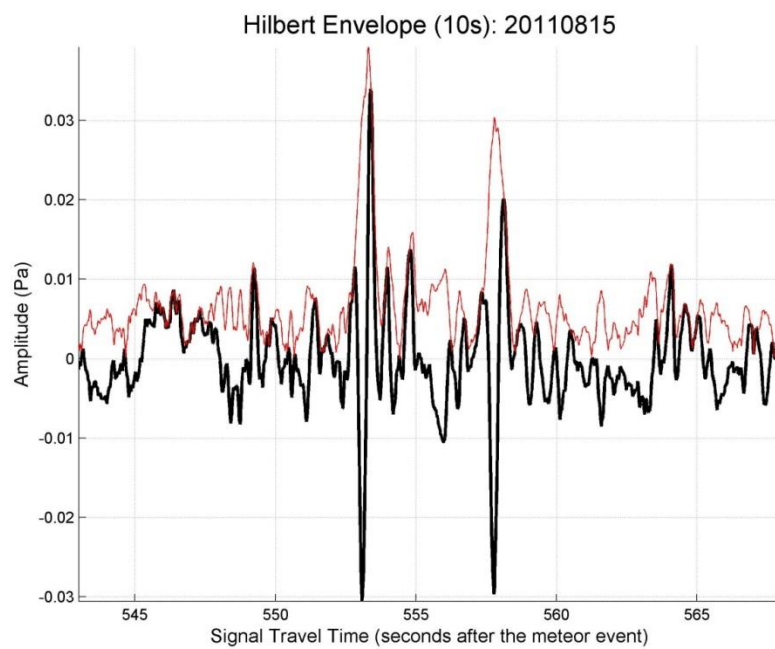
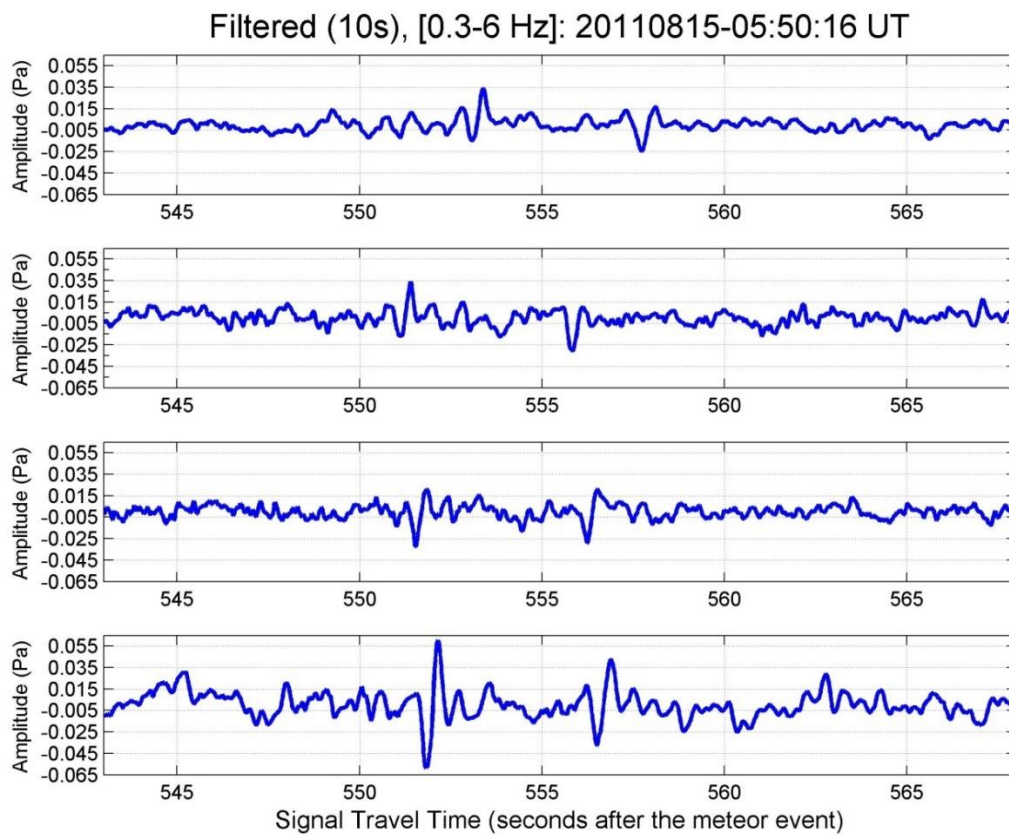


### 20110815\_055016



Window Parameters		Pass Band Parameters		Slowness Parameters		Windowed Values & S.D.	
Duration (s)	7.0	Low frequency (Hz)	0.4	Max. Slown.	400.0	Corr.	0.701 0.070
Overlap (%)	60.0	High frequency	6	# of Slown.	40	Fstat	8.848 2.894
Number of	97	Order (integer)	2			Vel.	0.365 0.012
						Az.	329.673 1.102

0
  D:\Research\Research - Elizabeth\lr



## Appendix 2

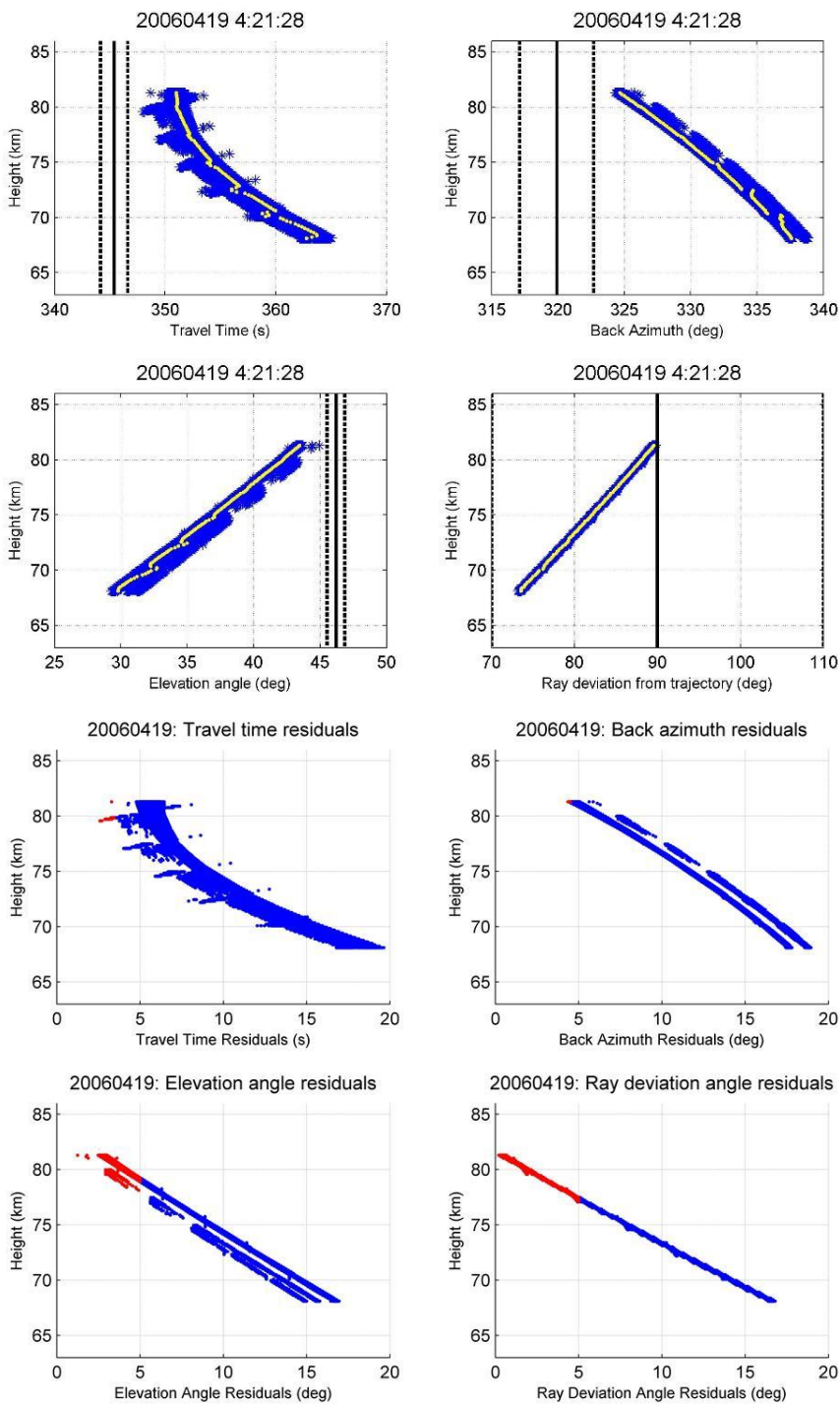
### Raytracing Results: Single Arrival Events and Multi Arrival Events

This section describes in detail the raytracing results for all events analysed in Chapter 5. There are two 4-panel plots for each event (or for each arrival for multi arrival events): (i) raytracing results as shown in Figure 5.11, and (ii) raytracing residuals as shown in Figure 5.13. Rather than repeating the two identical captions, they are described in the paragraph below and apply to each plot. Event dates and times are shown in figure titles. Each page corresponds to a single meteor event or arrival.

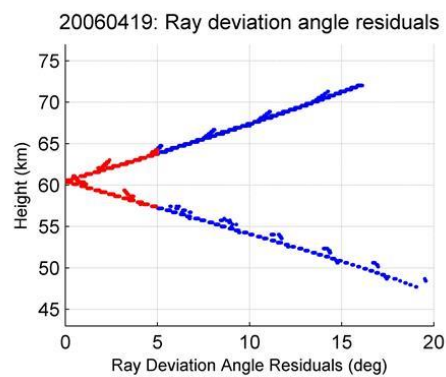
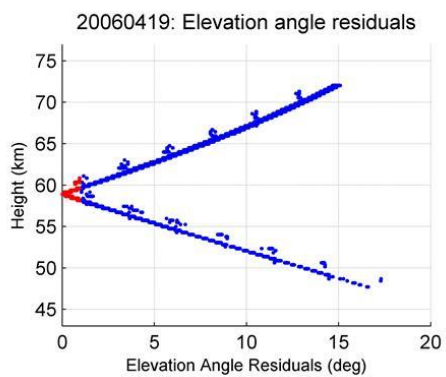
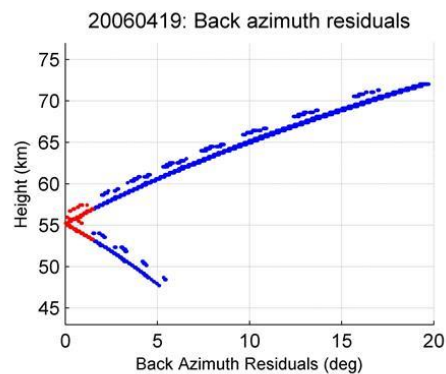
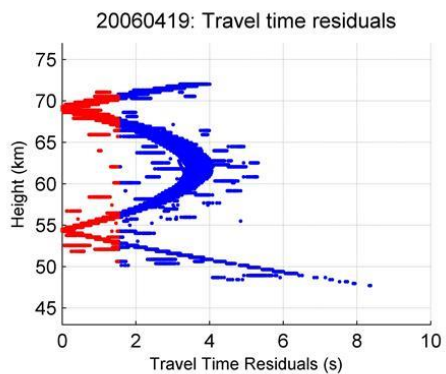
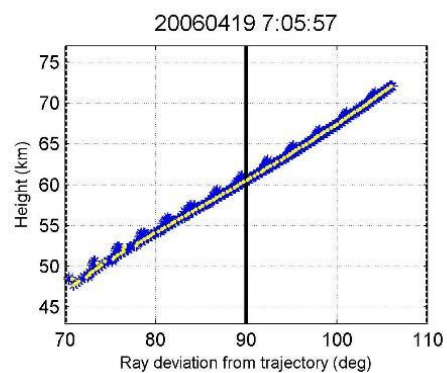
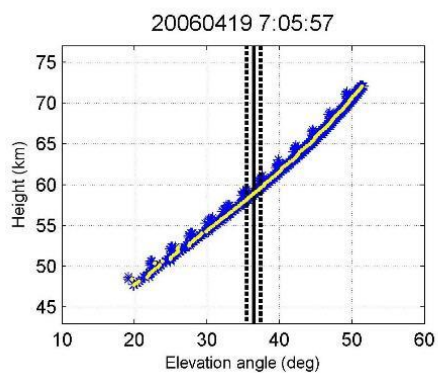
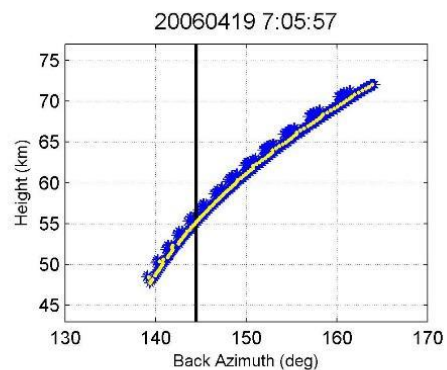
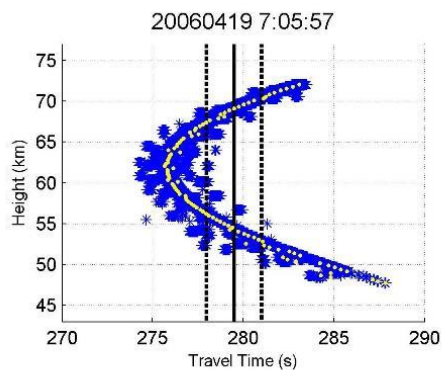
**Raytracing results:** A composite plot showing the travel time (upper left), back azimuth (upper right) and arrival elevation angle (lower left) for a given event. The lower right plot is the ray launch deviation angle as a function of height along the meteor trail. The blue points represent modelled arrivals for 1400 gravity wave realizations for this event. The yellow model points in all plots are the simulation means along the meteor trail for each height (averaging along the x-axis). The vertical solid black line corresponds to the observed quantity with its uncertainty (dotted line), except in the case of ray deviation angle, which is simply a reference to the expected ballistic angle ( $90^\circ$ ). The composite plot also shows how the back azimuth determined model source height differs from the model source height determined by the travel time residuals.

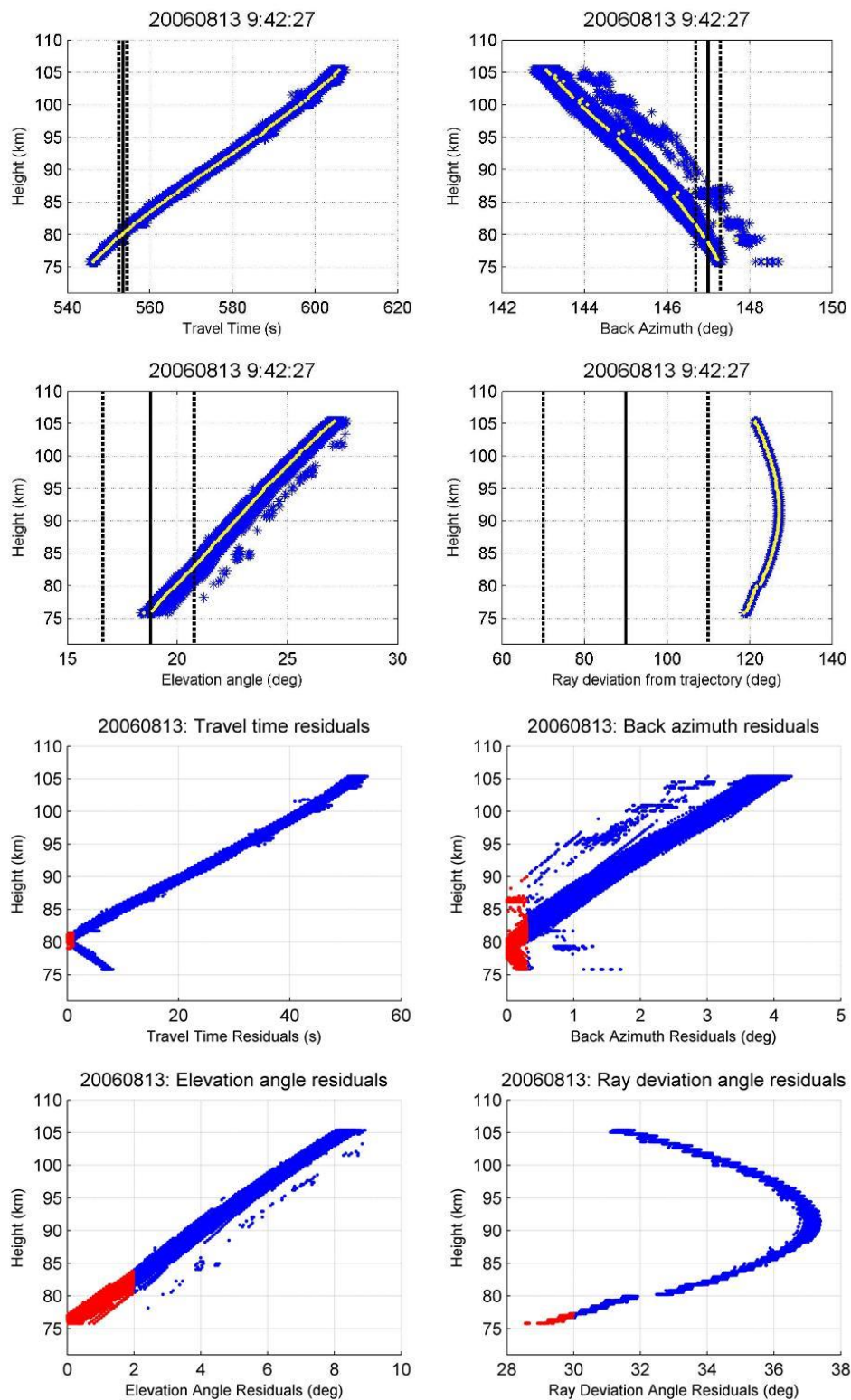
**Raytracing residuals:** A residuals composite plot showing the difference between the model values for each realization and the observed value. Red points show the residuals contained within the height-residual grid where model points agree with observations within the observational uncertainty. The ray deviation angle residuals are relative to a ballistic arrival (i.e. residual of zero = 90 degree ray deviation angle).

## Single Arrival Events

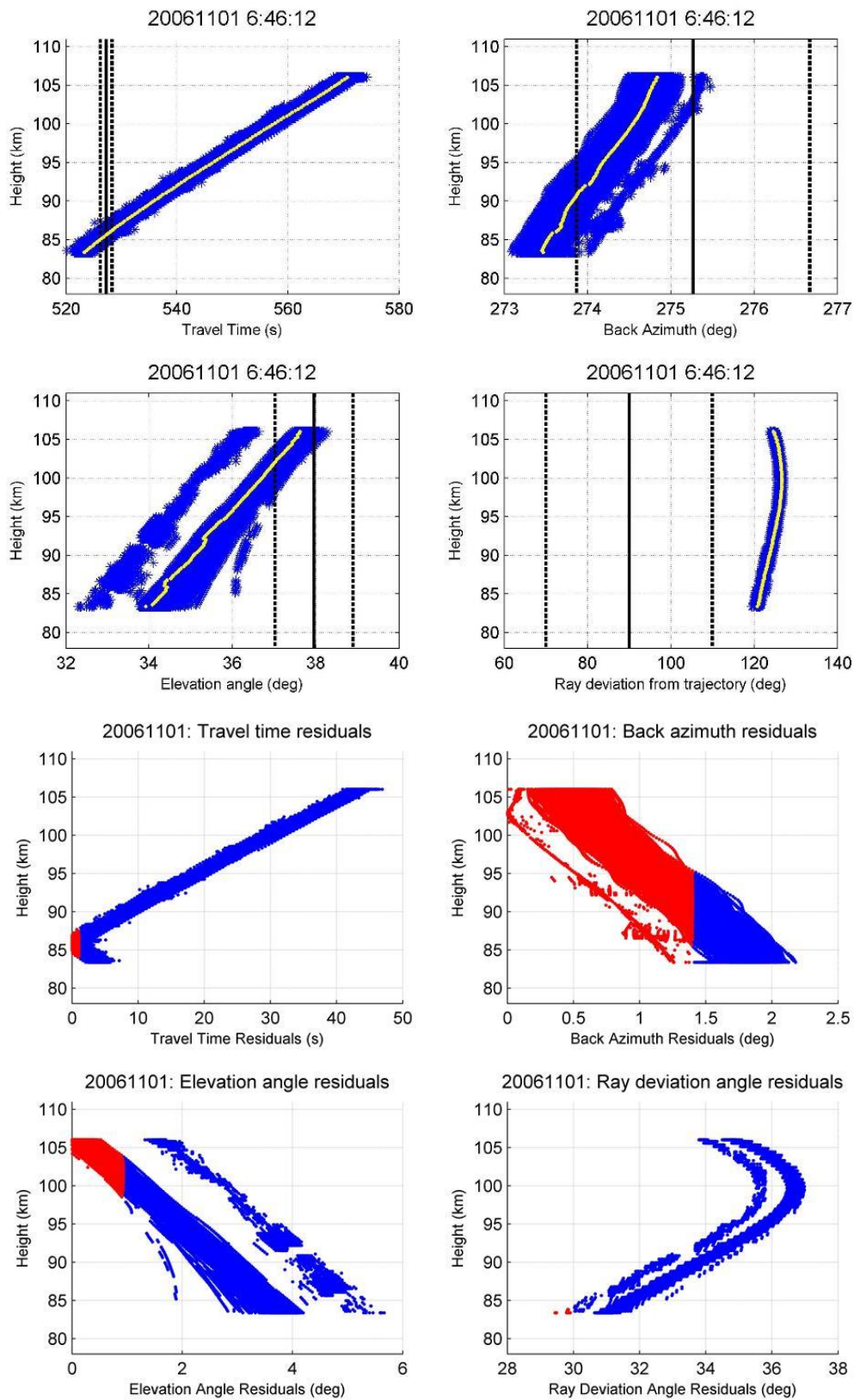


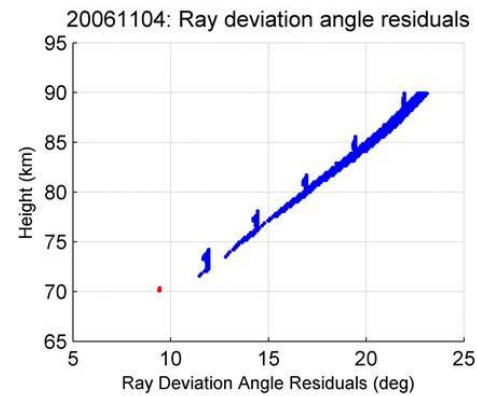
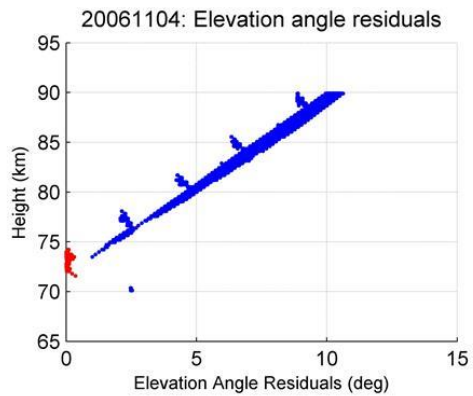
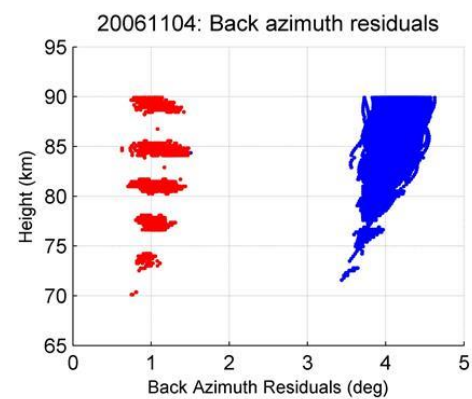
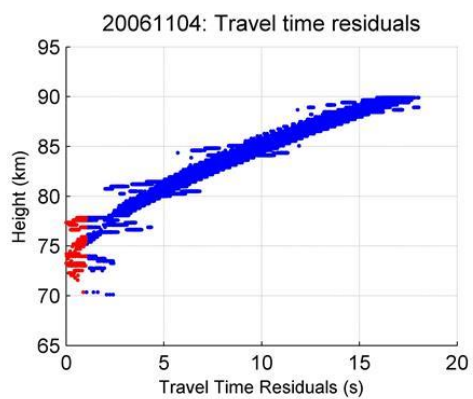
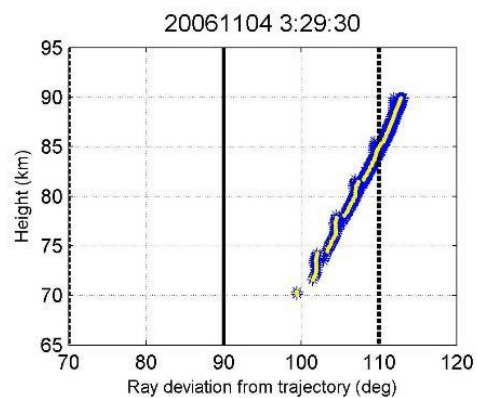
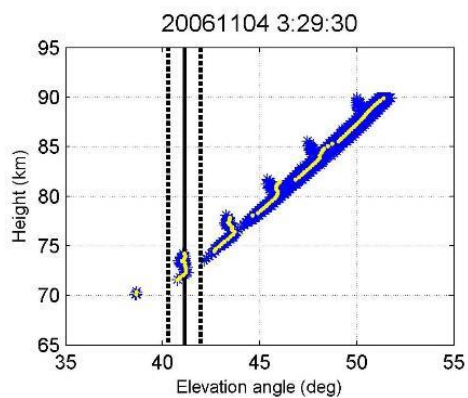
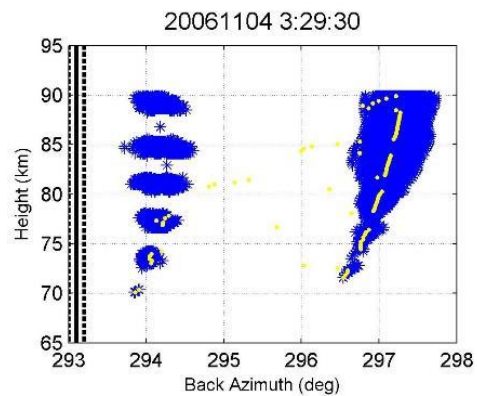
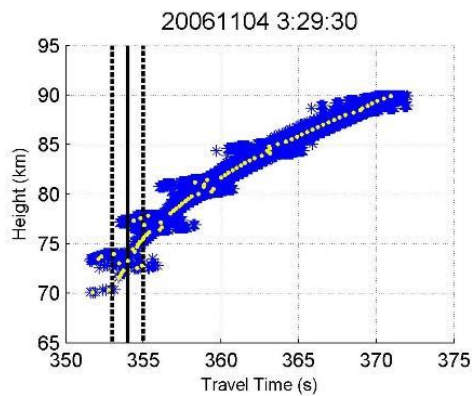


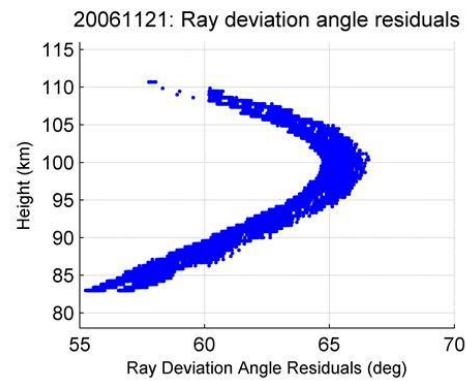
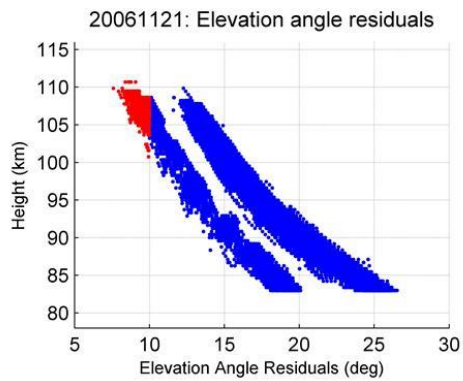
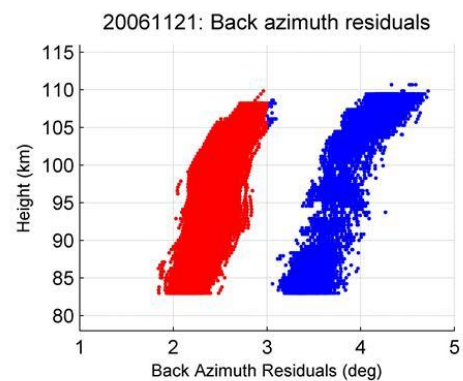
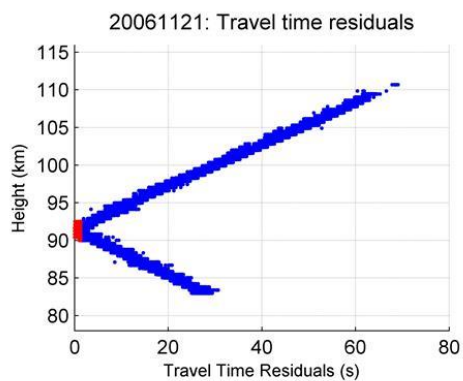
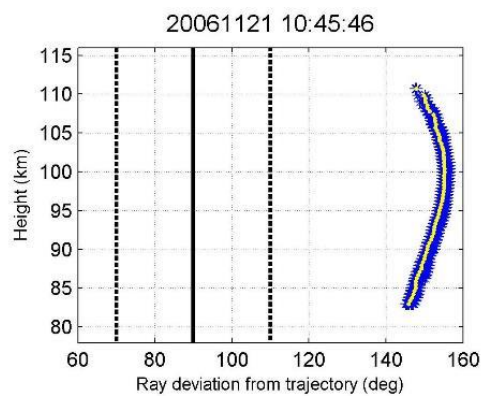
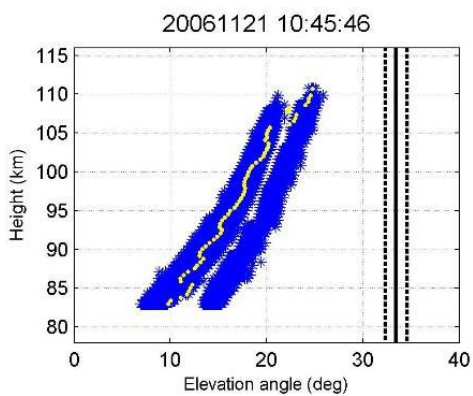
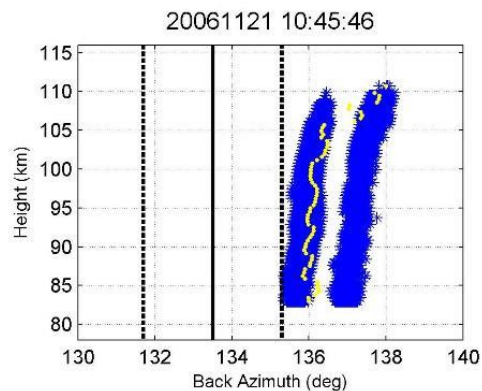
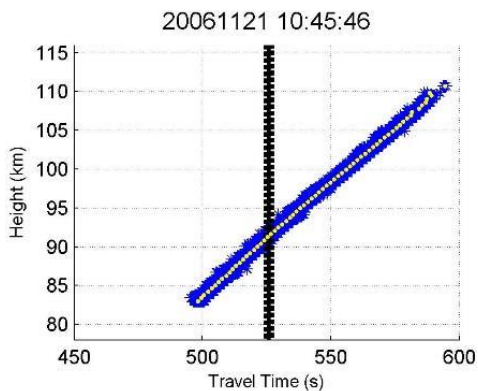


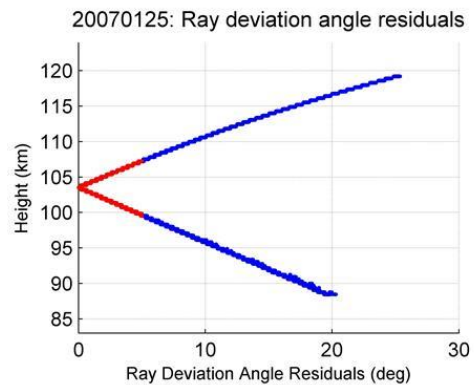
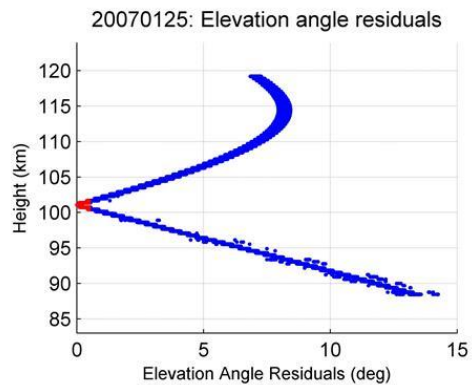
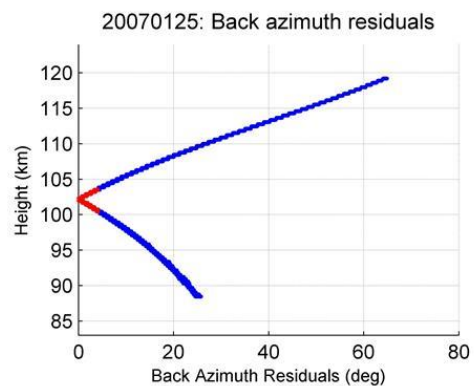
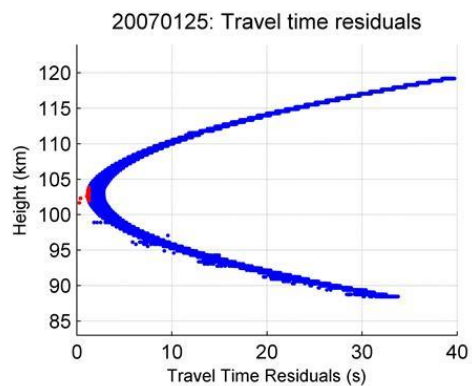
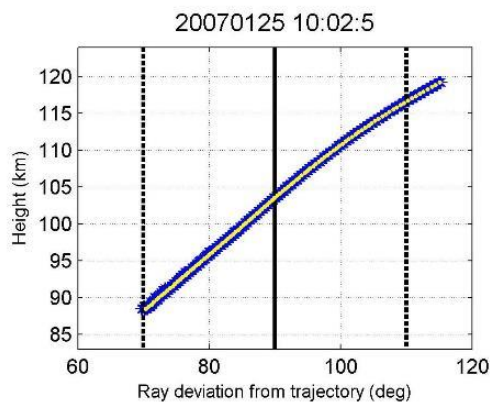
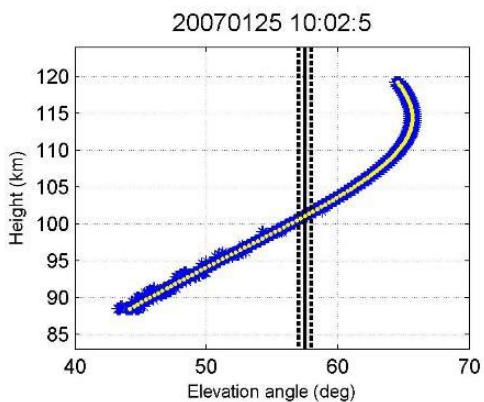
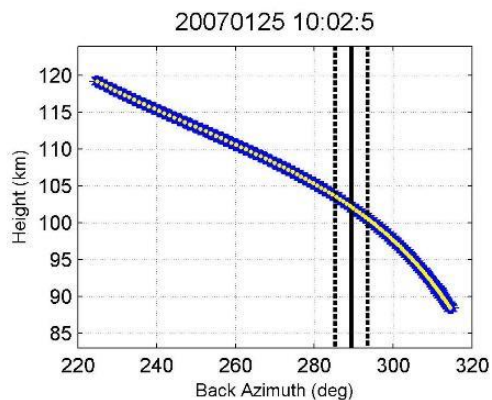
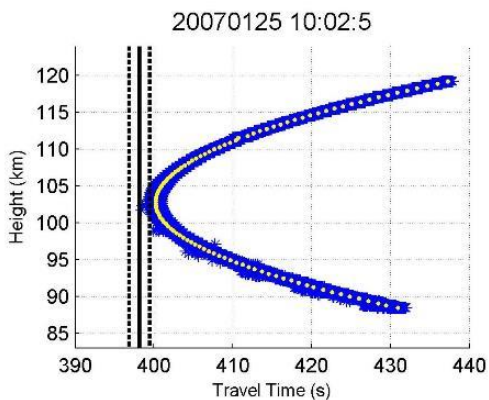




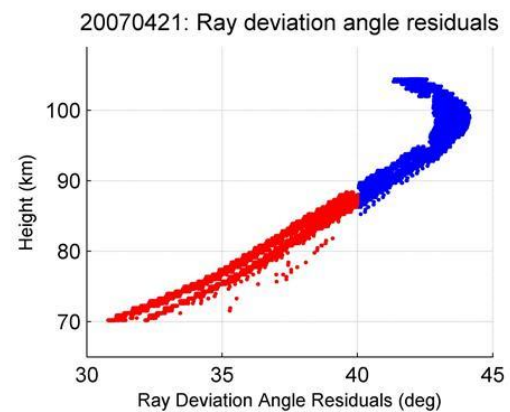
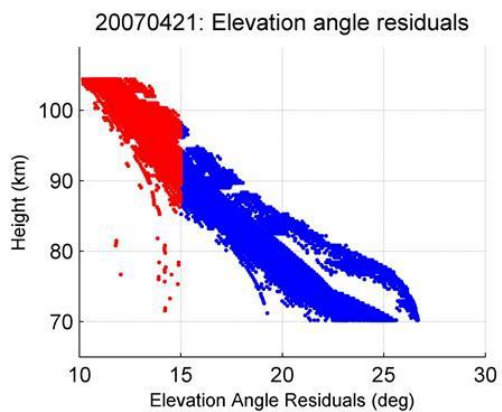
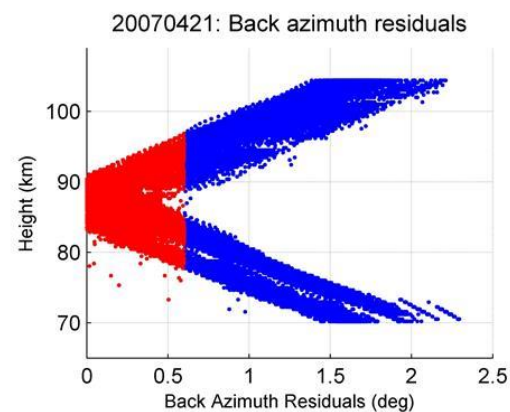
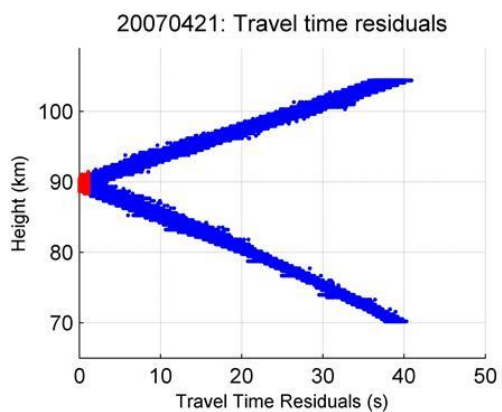
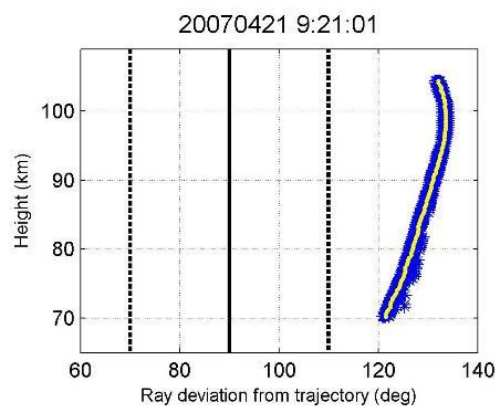
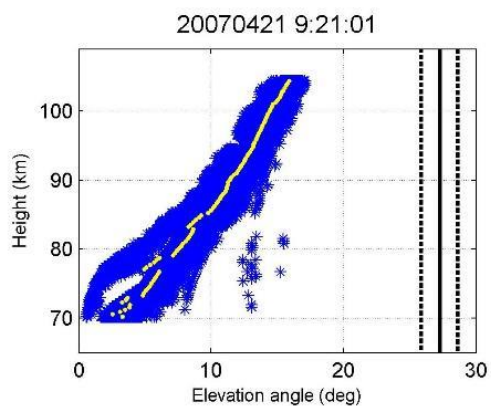
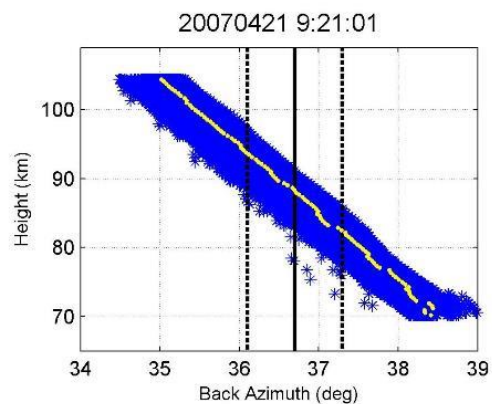
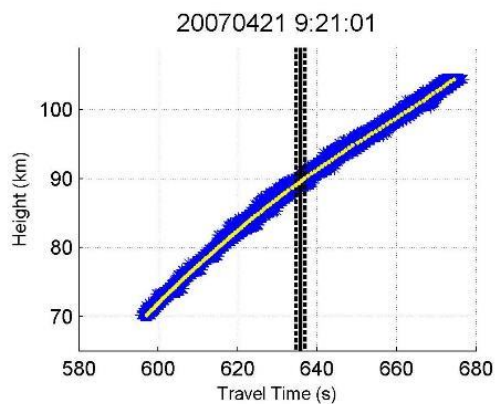


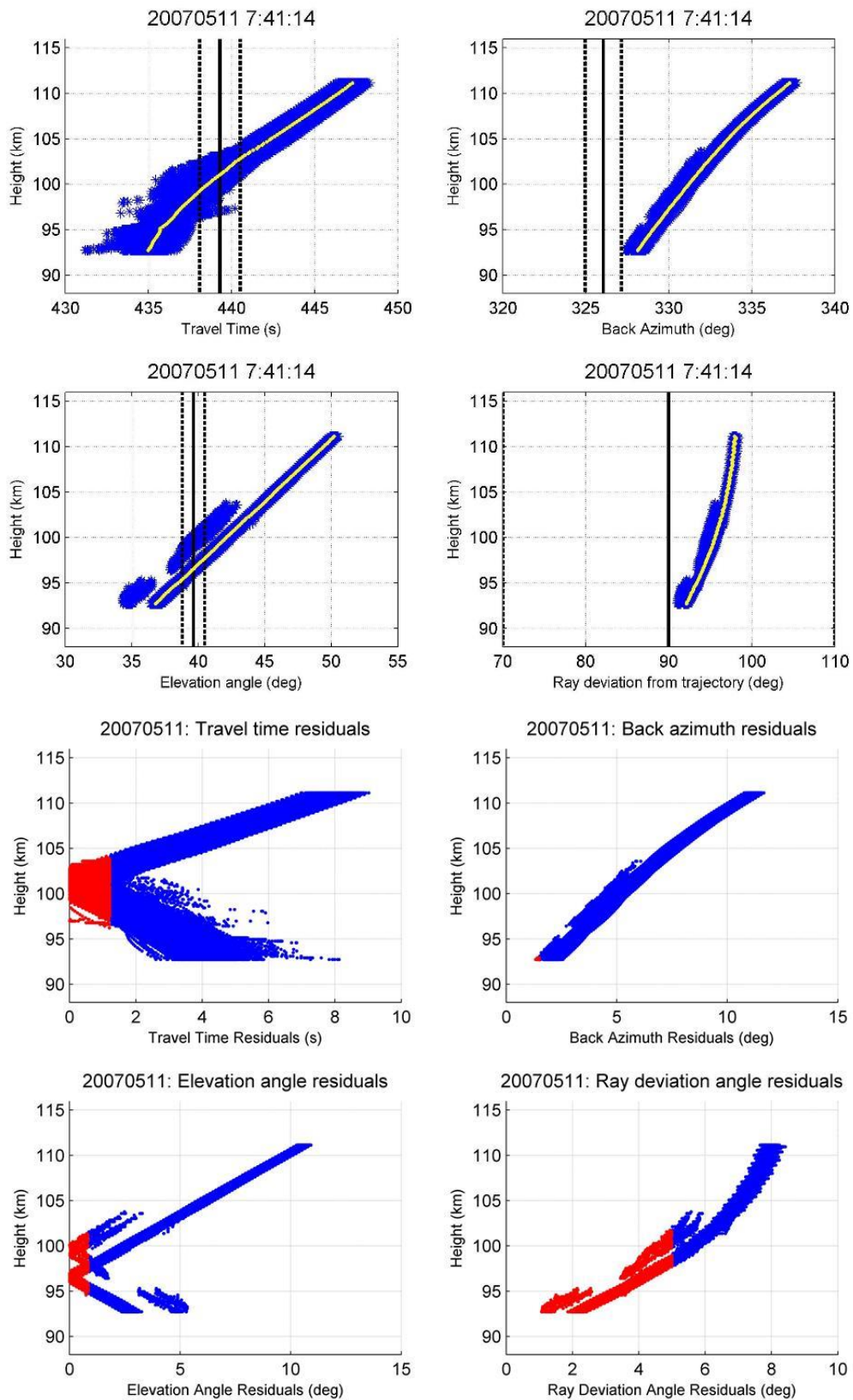


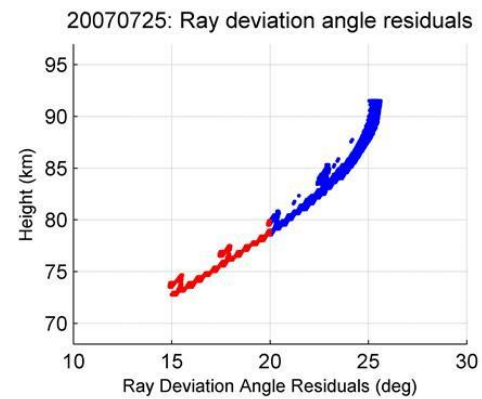
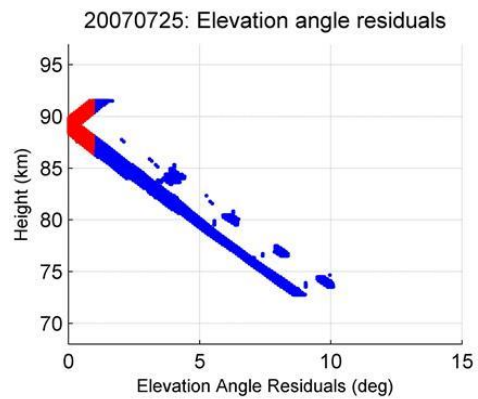
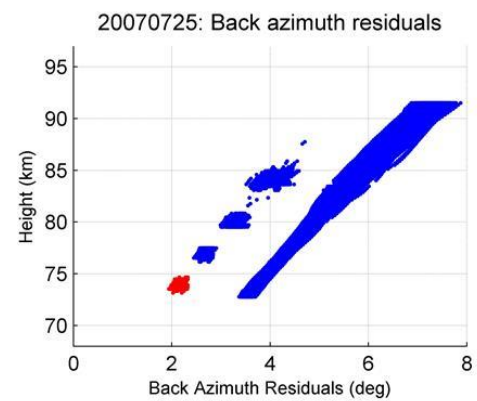
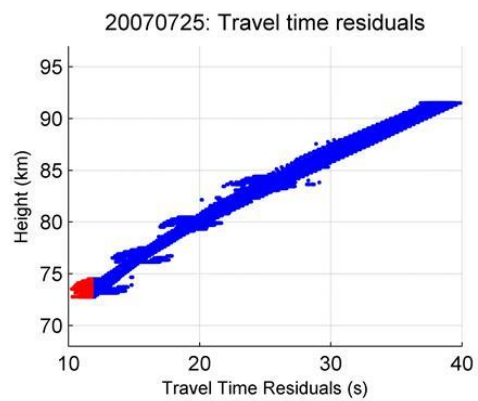
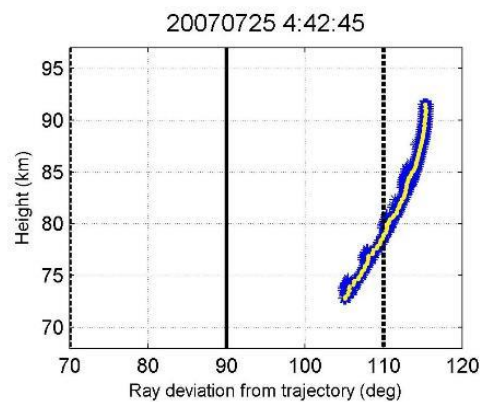
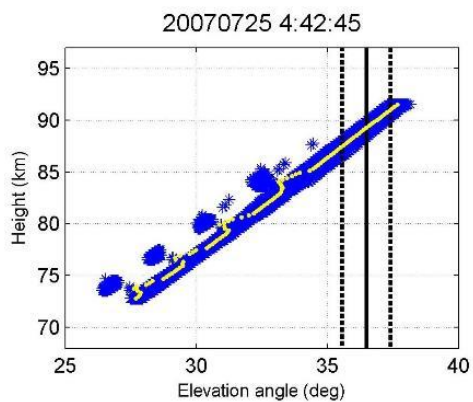
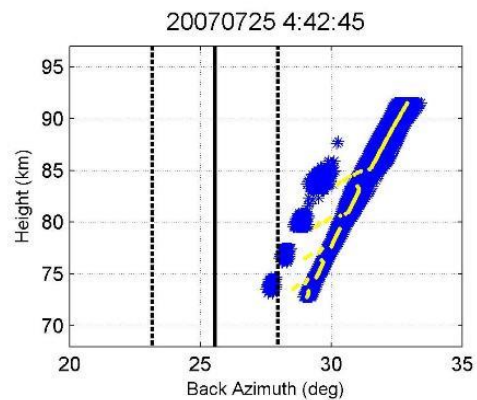
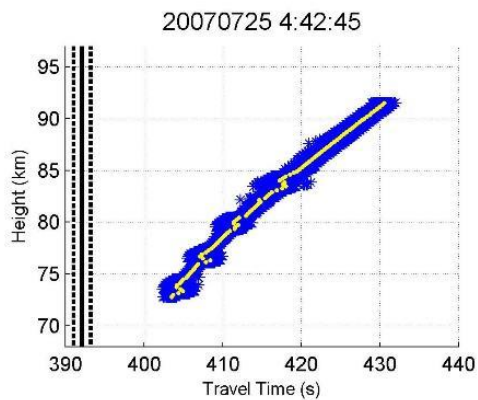


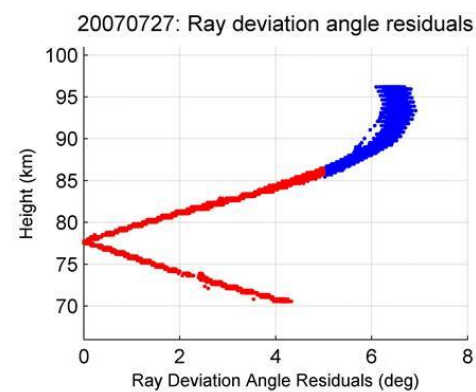
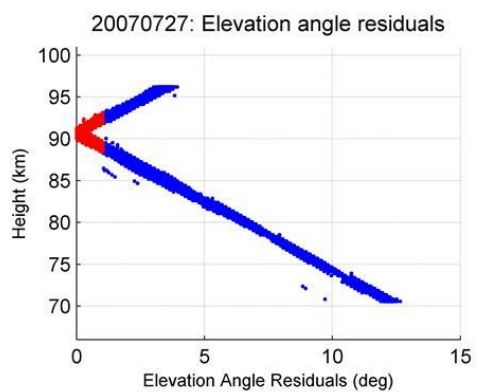
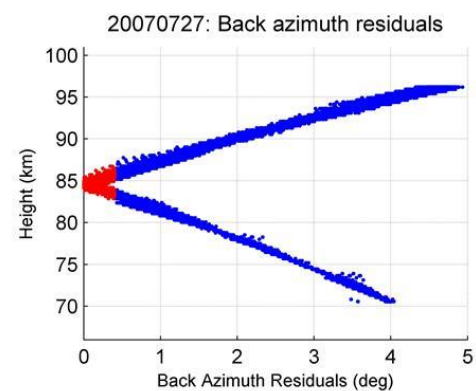
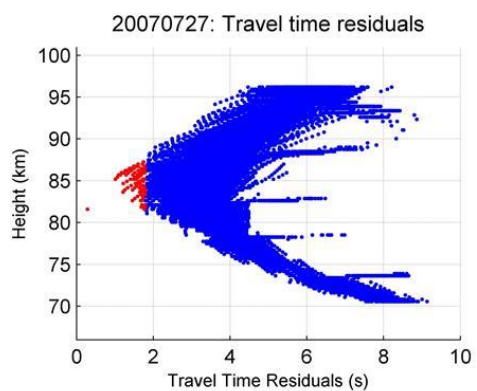
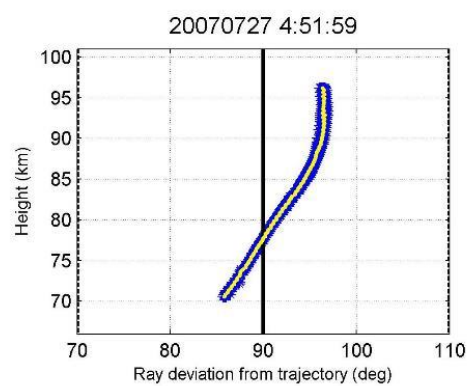
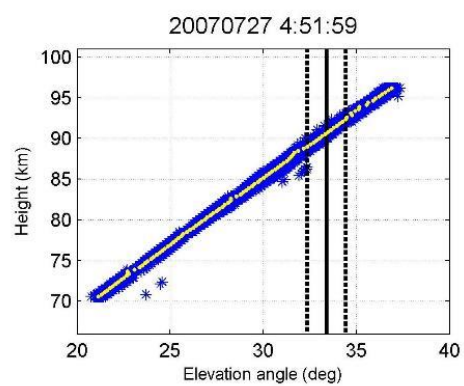
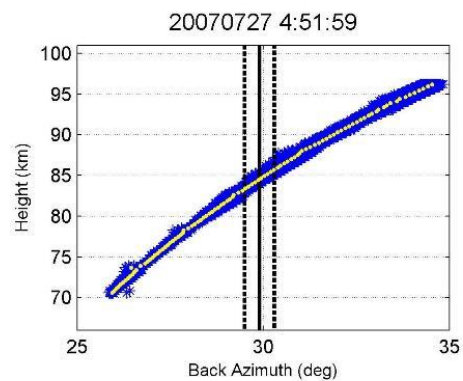
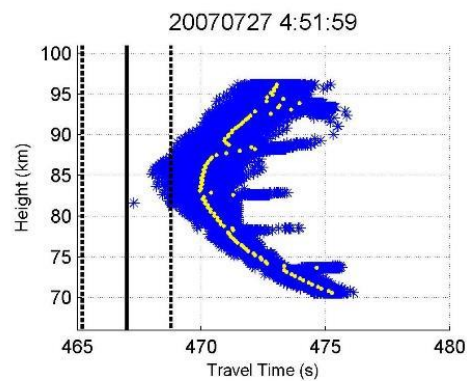




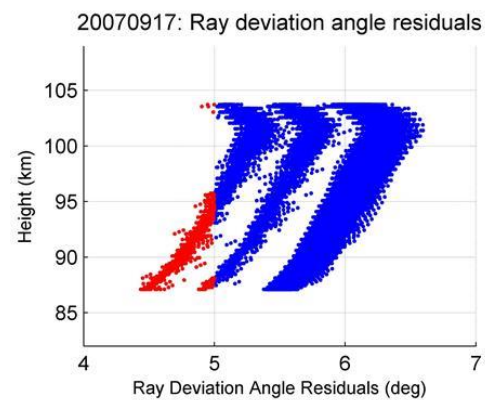
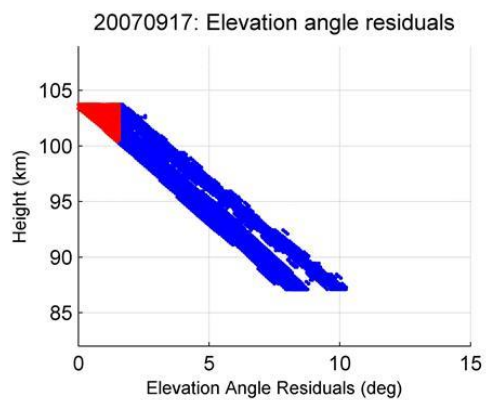
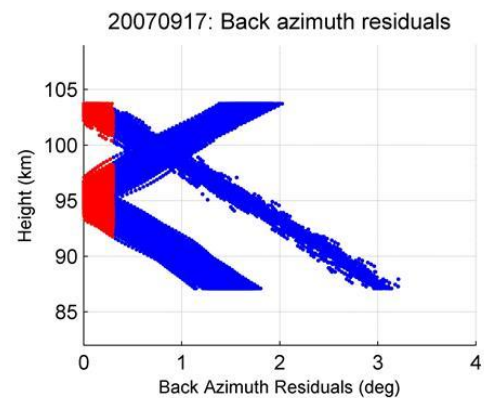
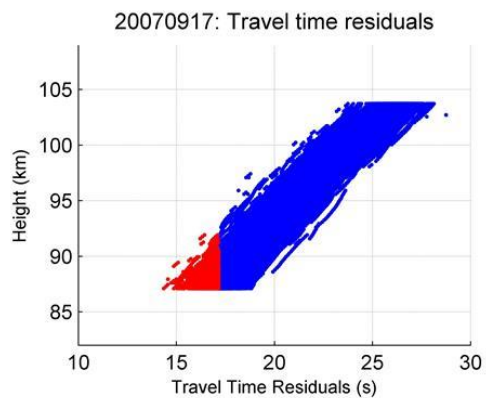
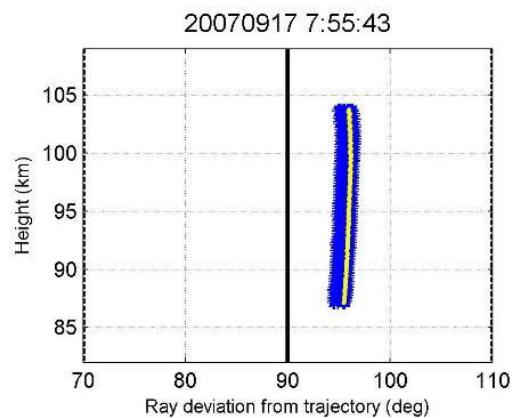
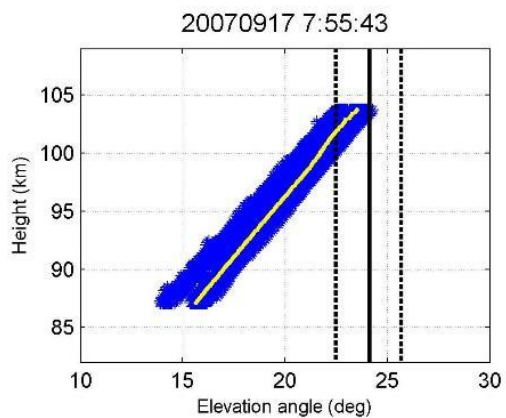
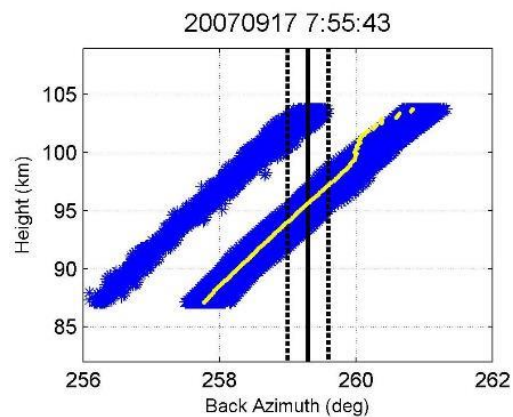
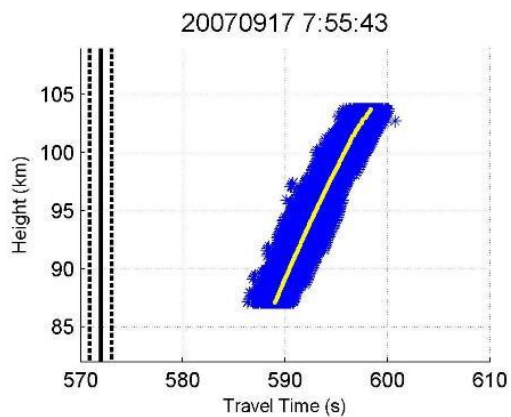


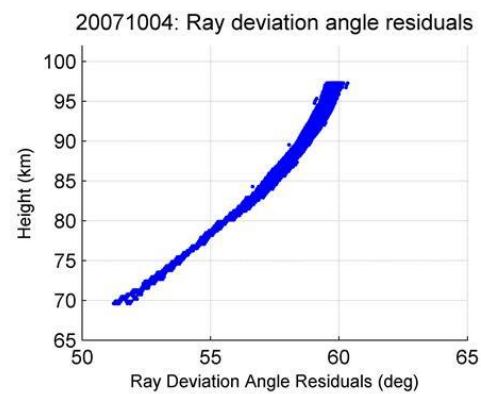
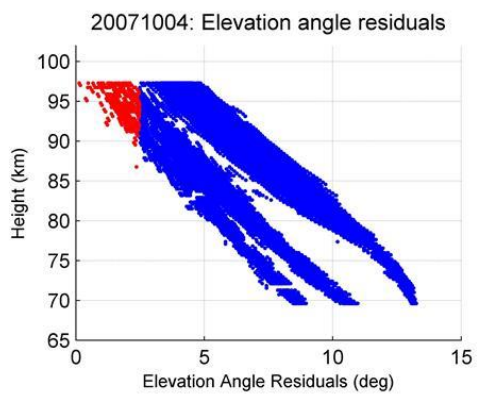
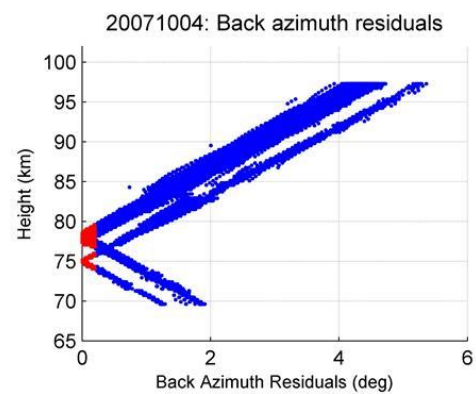
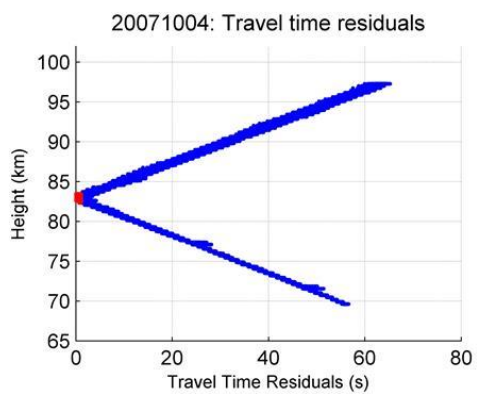
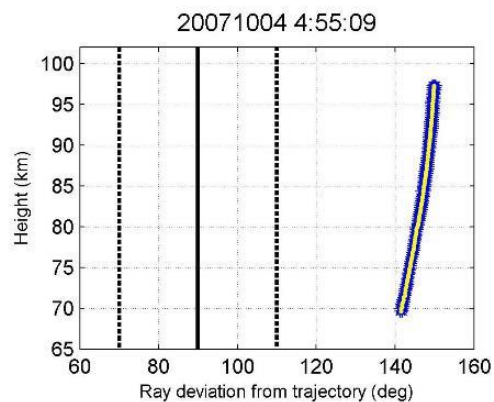
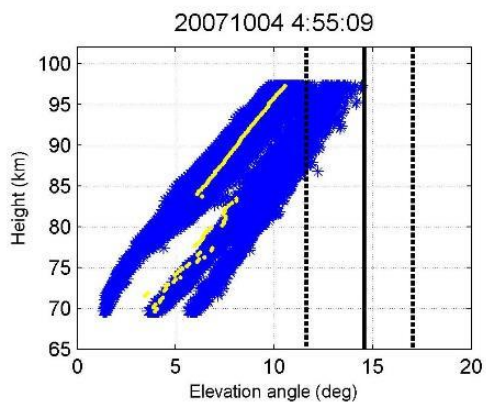
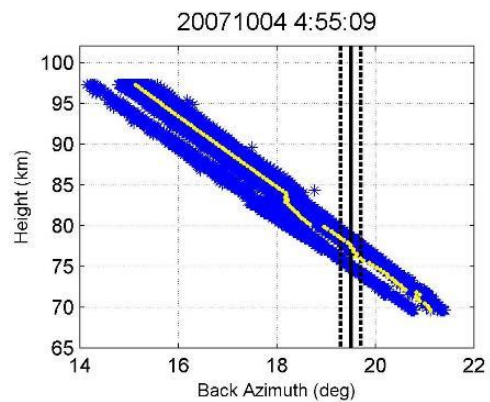
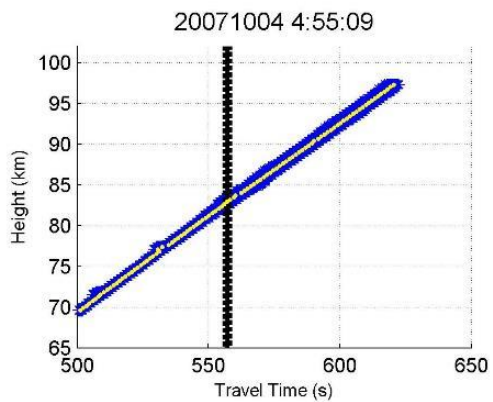


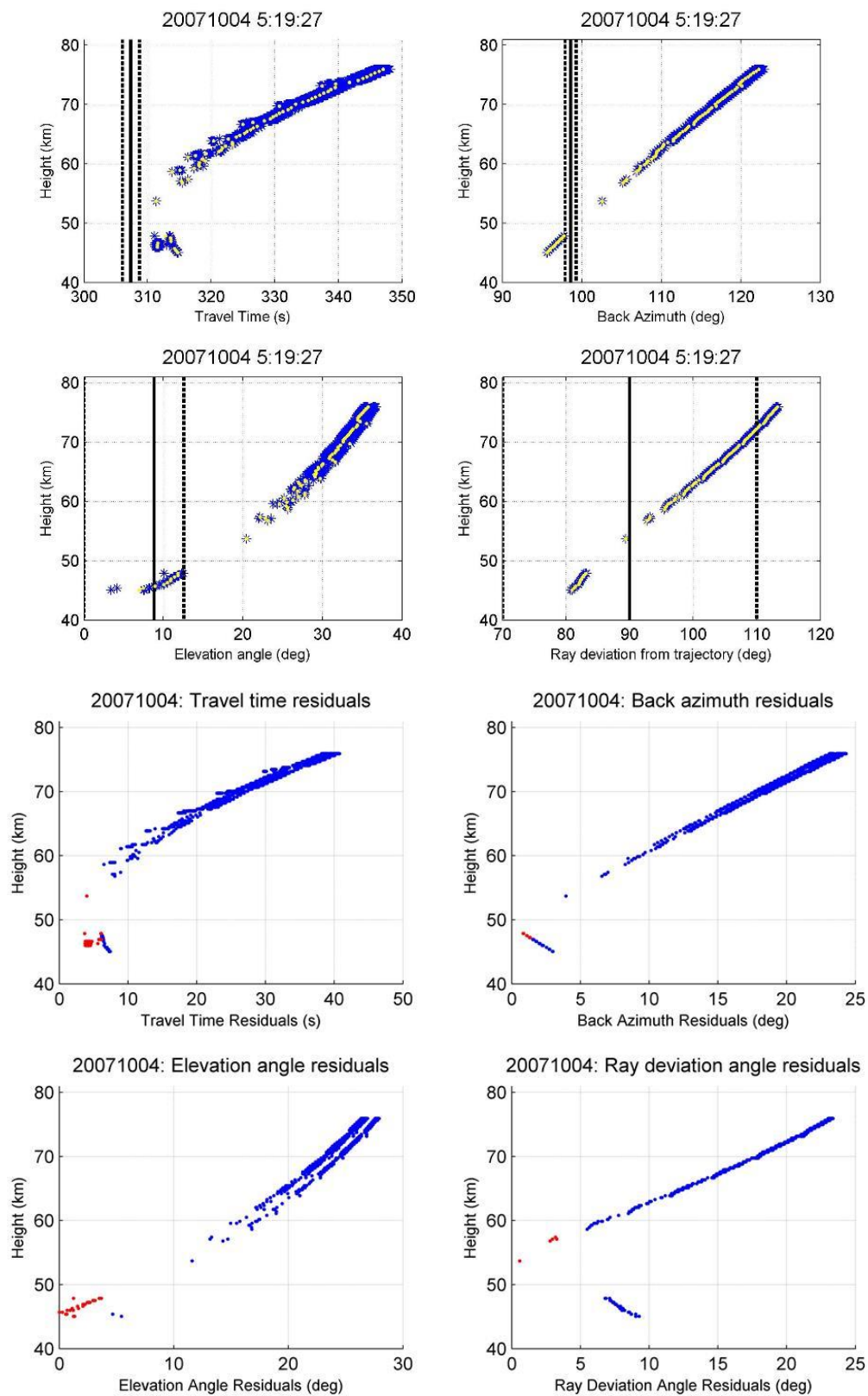


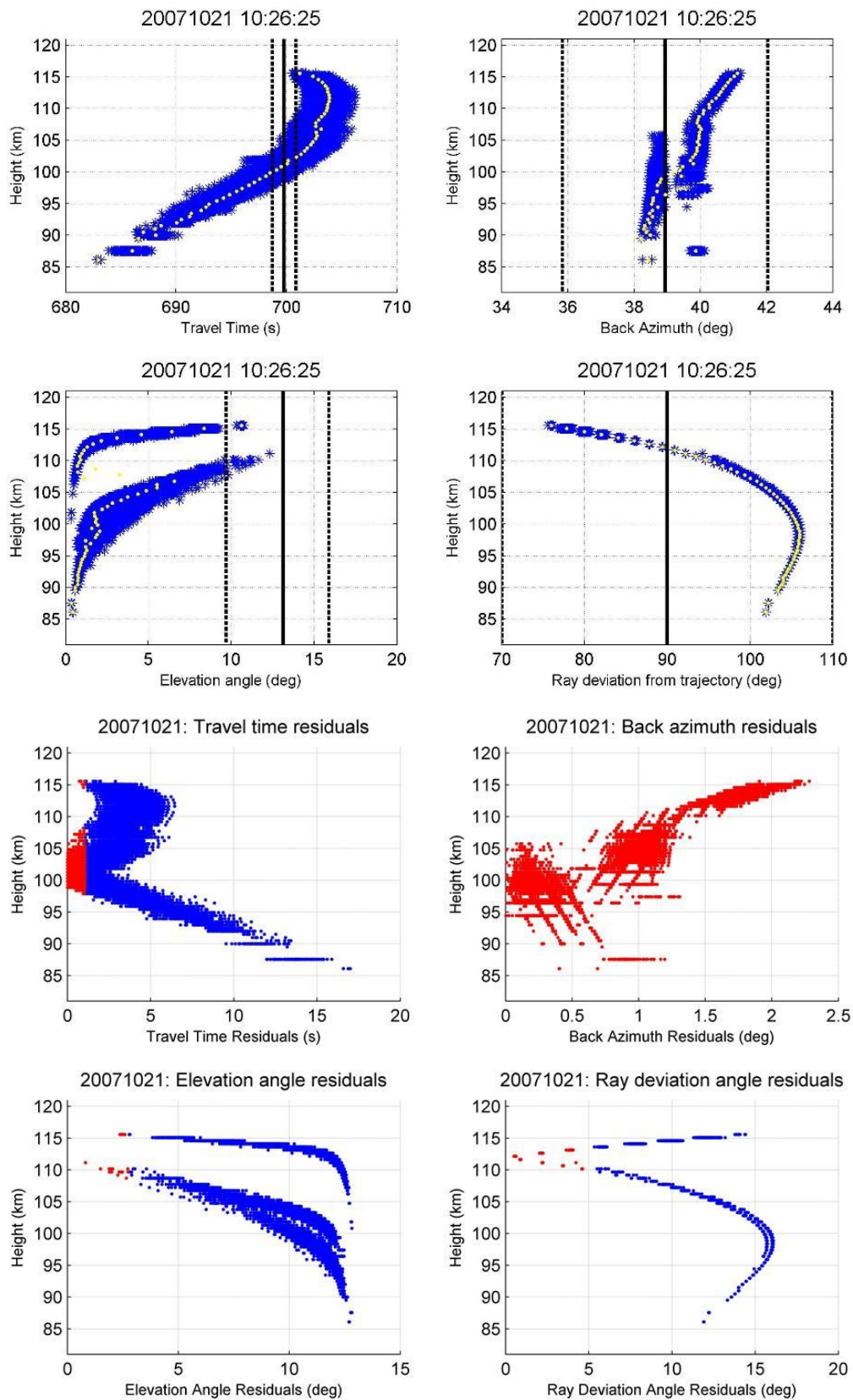




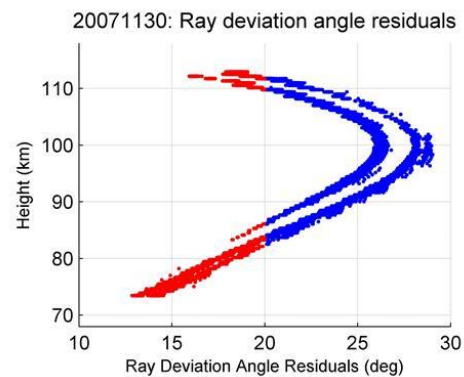
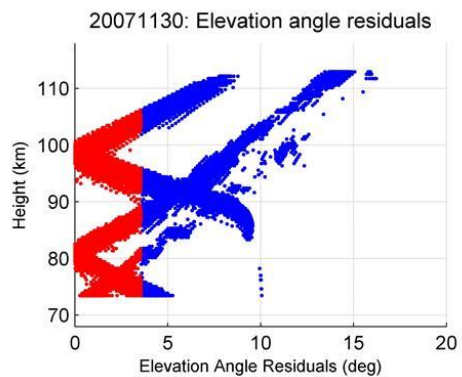
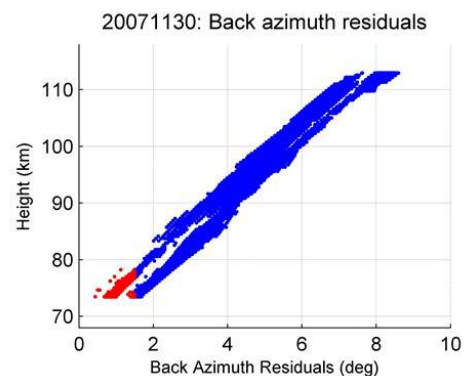
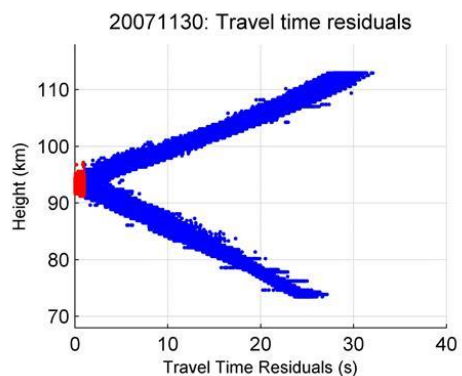
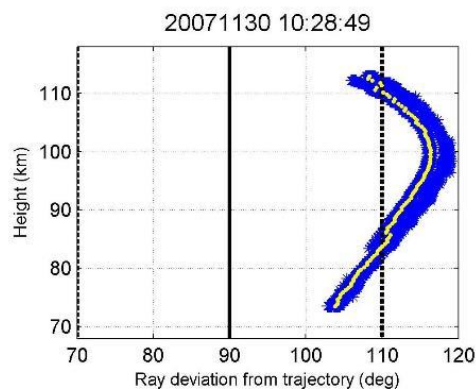
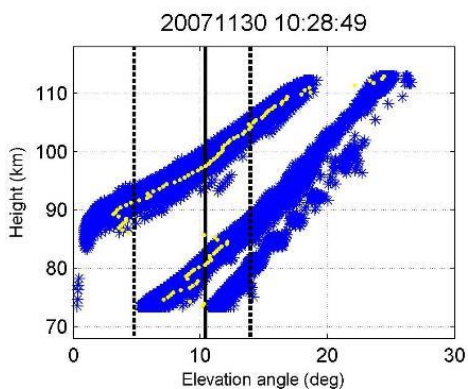
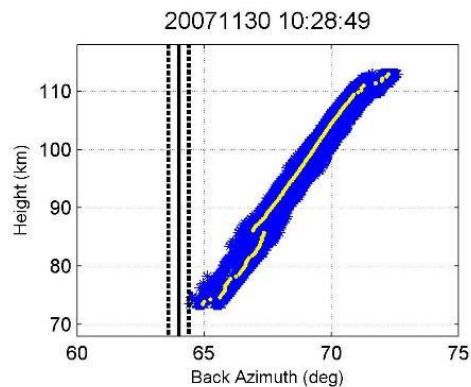
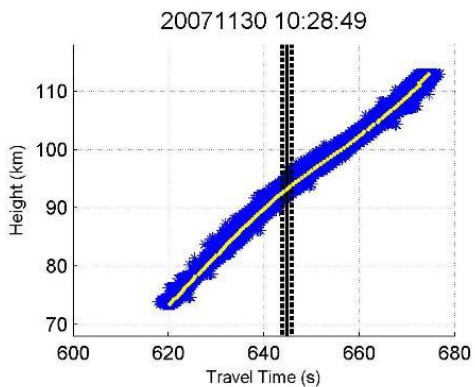


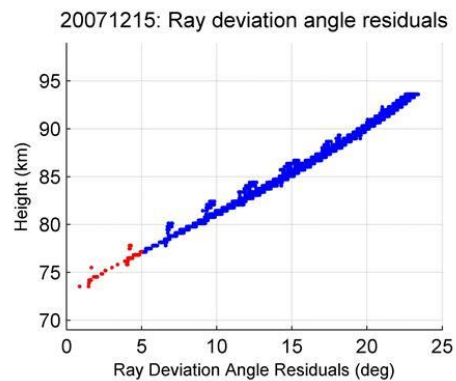
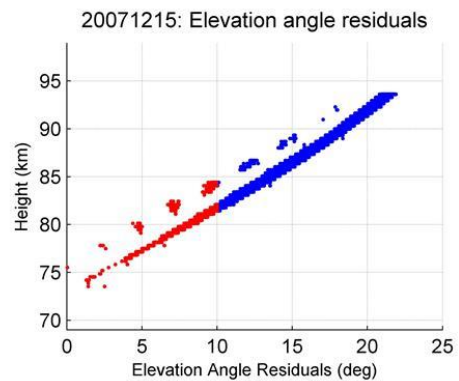
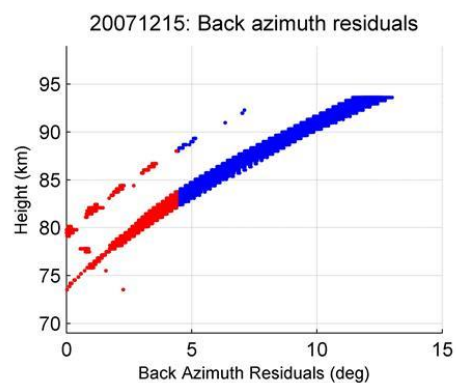
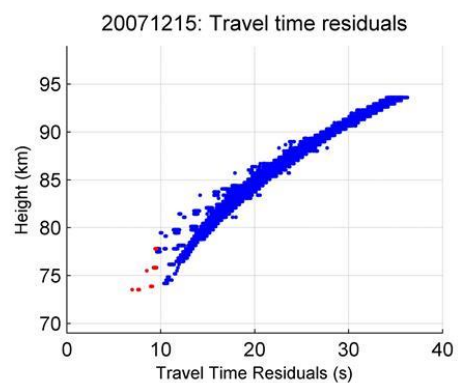
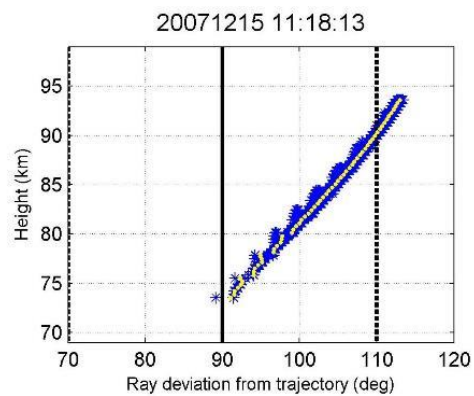
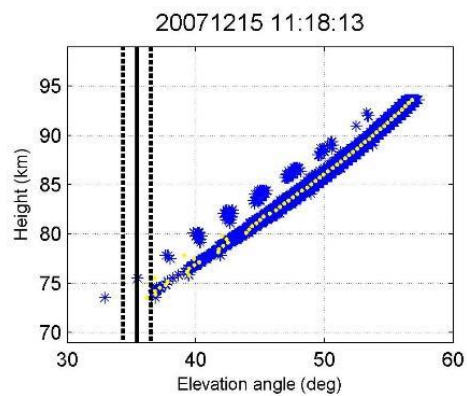
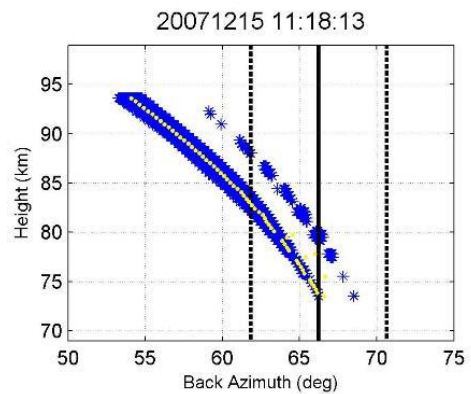
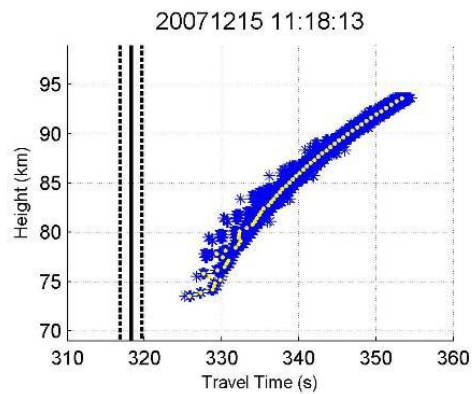


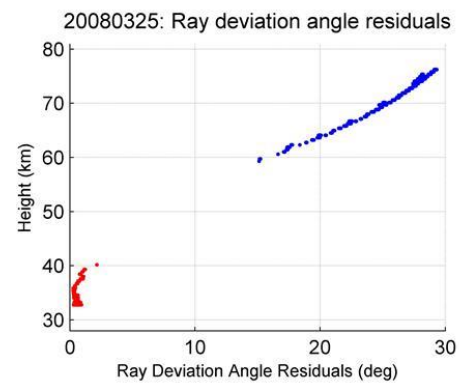
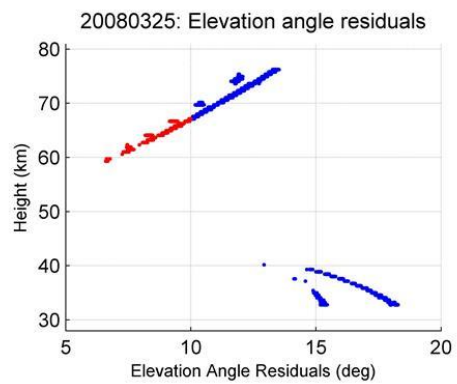
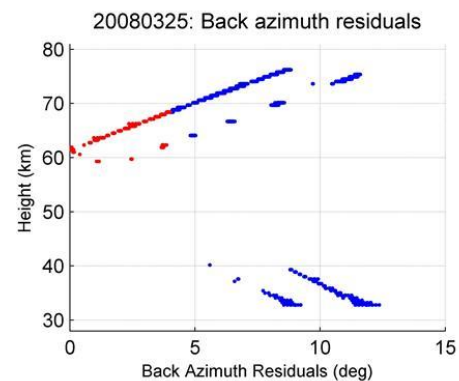
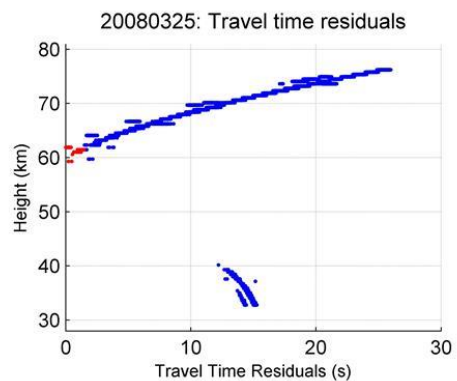
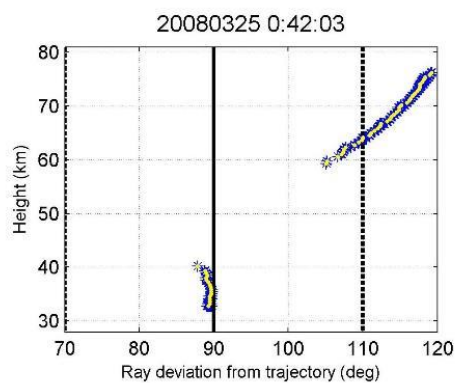
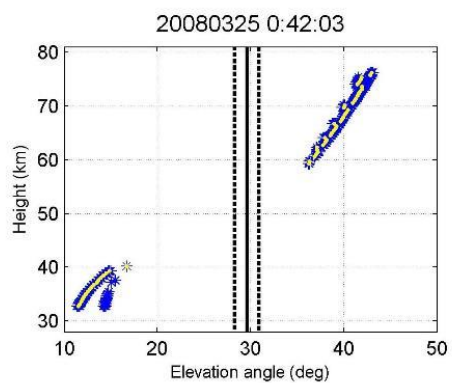
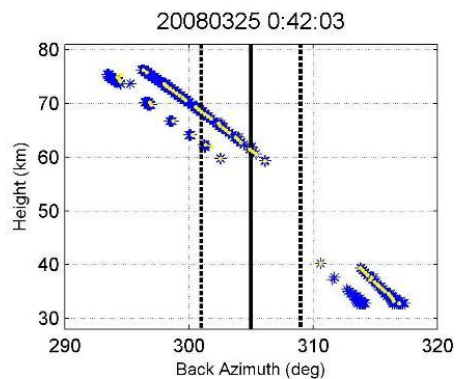
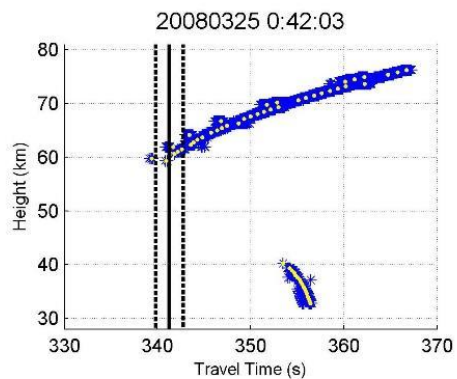


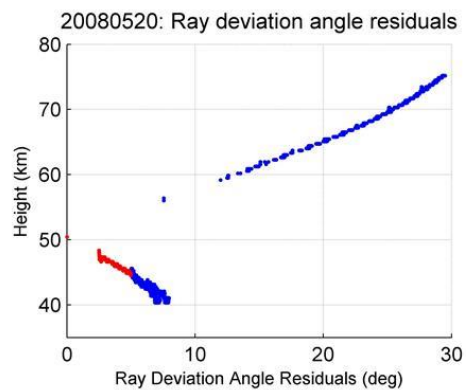
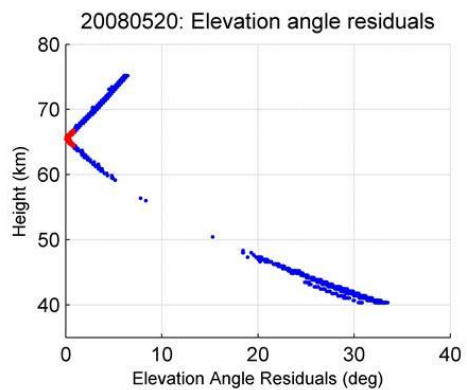
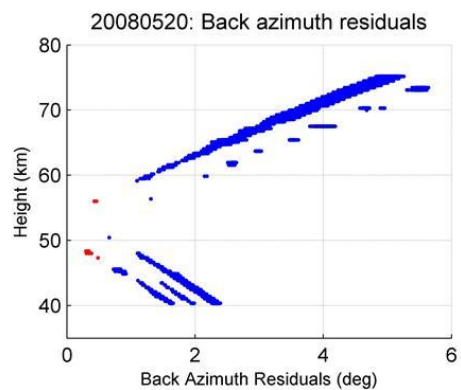
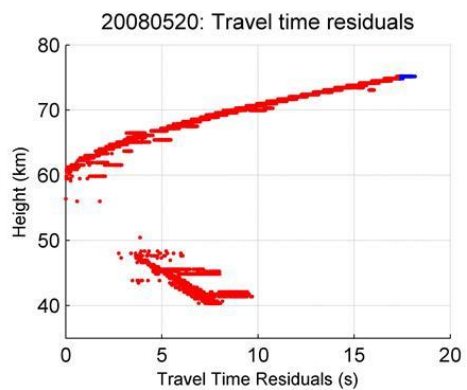
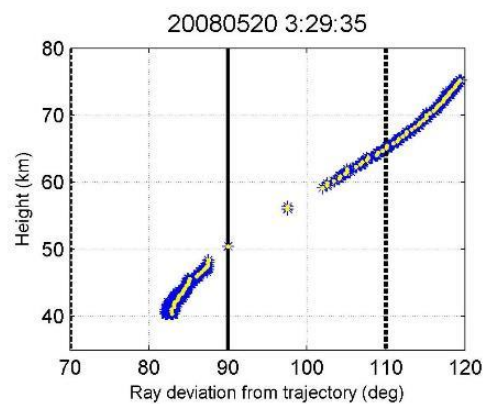
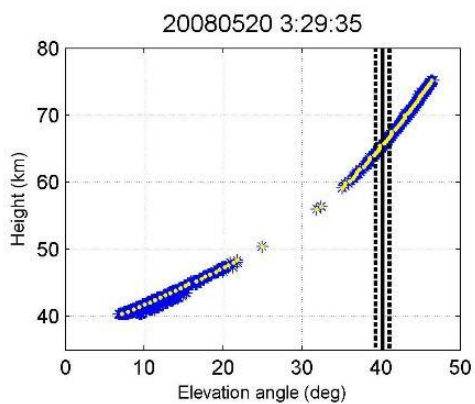
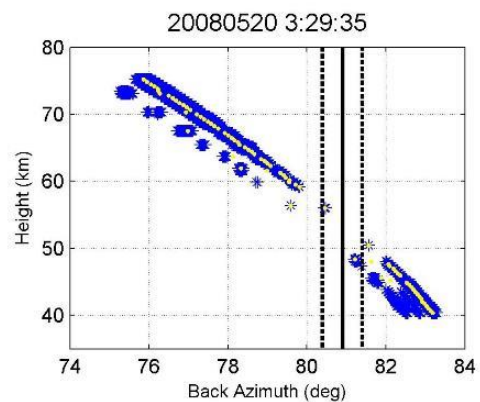
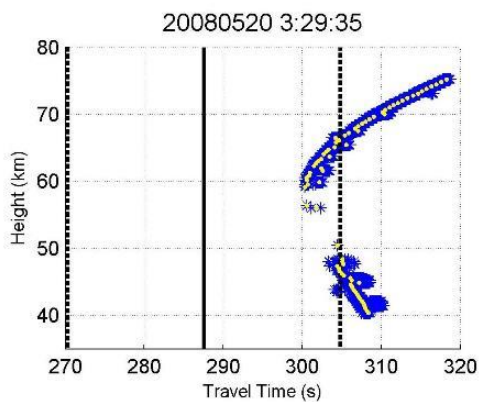




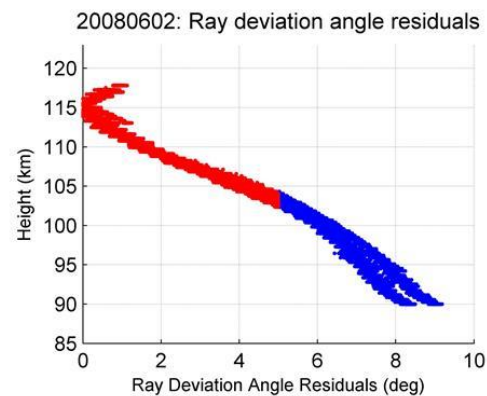
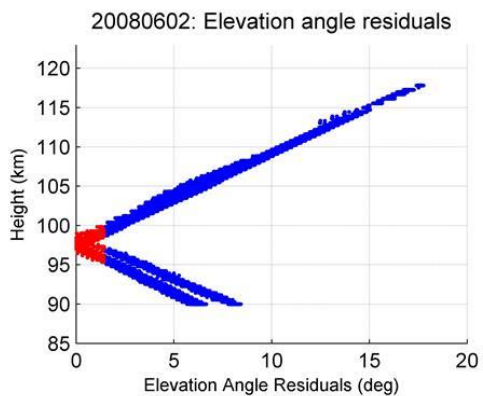
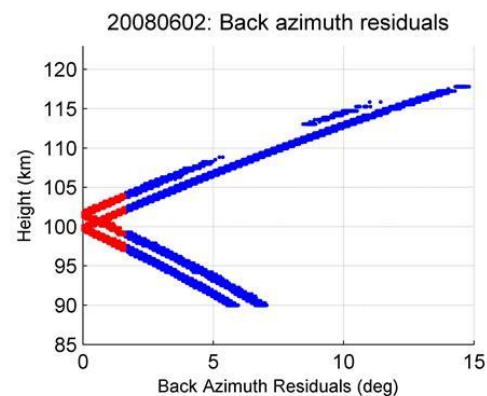
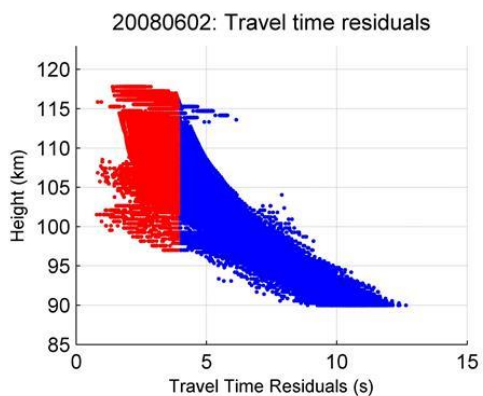
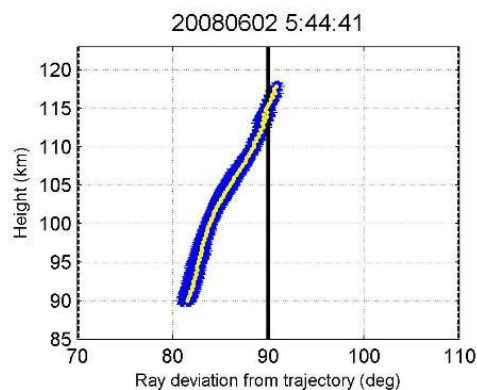
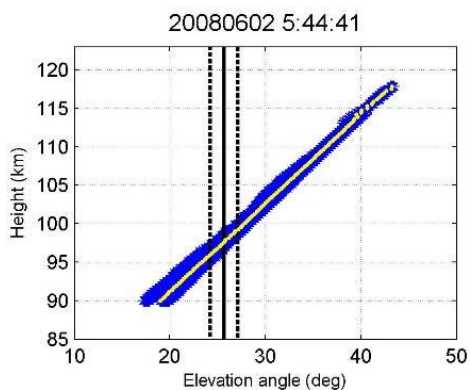
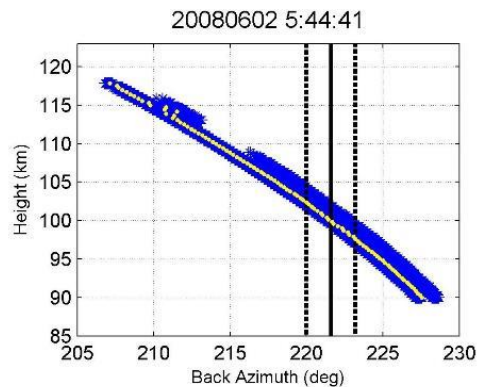
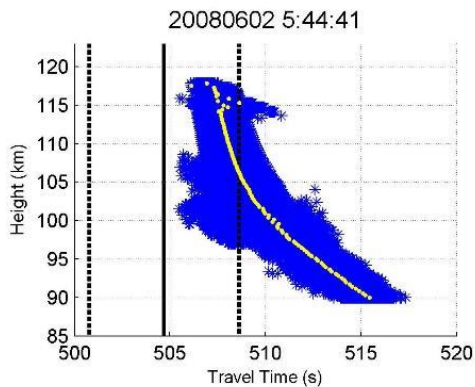


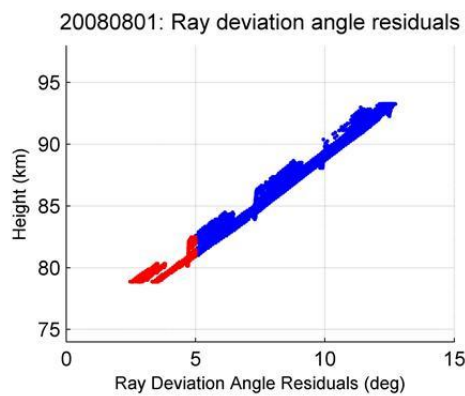
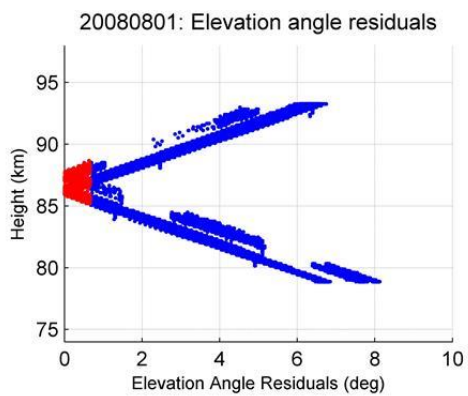
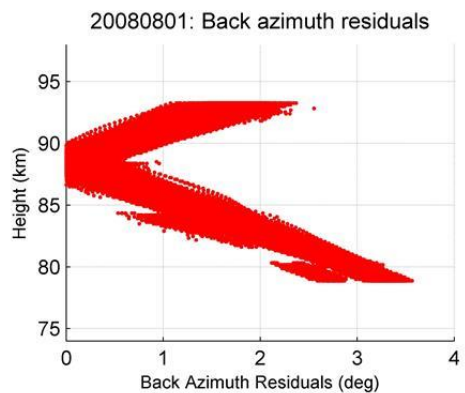
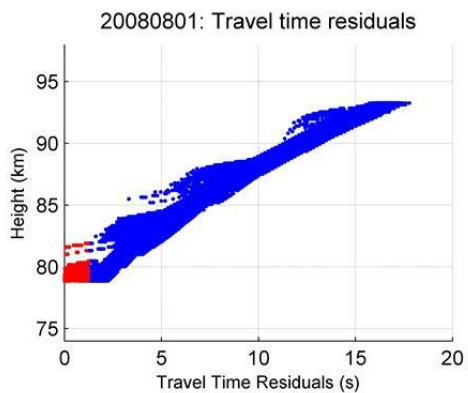
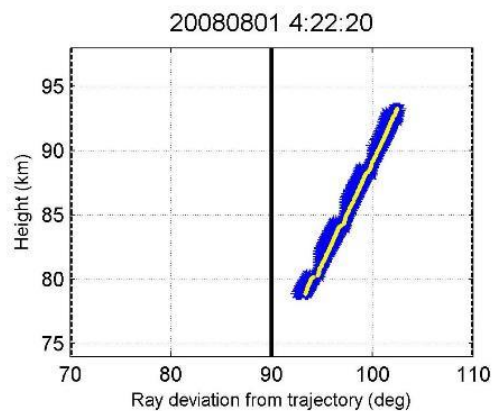
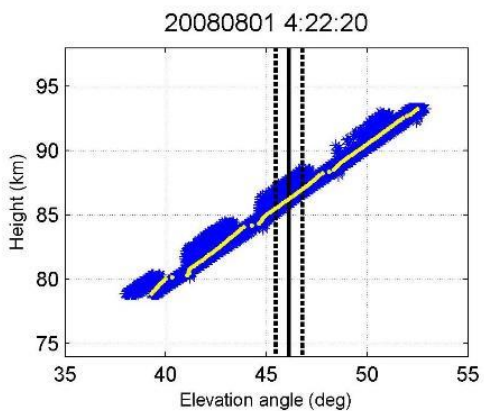
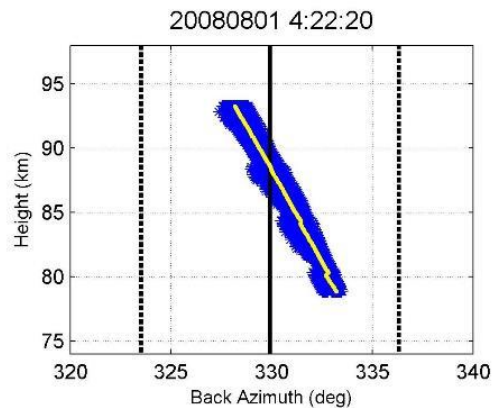
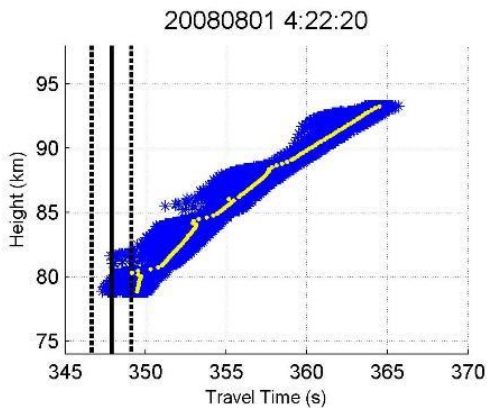


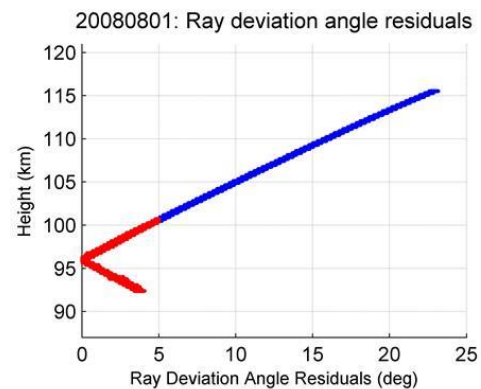
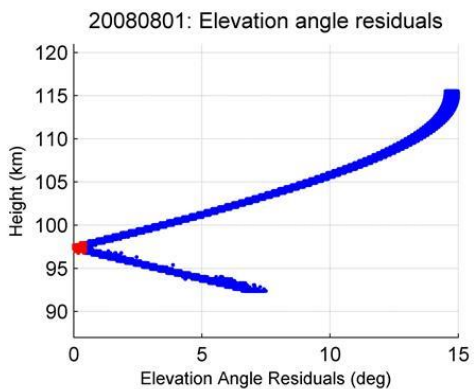
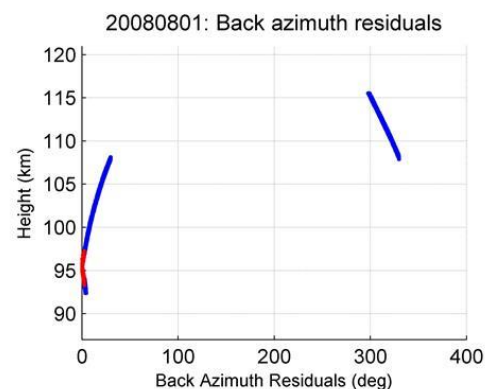
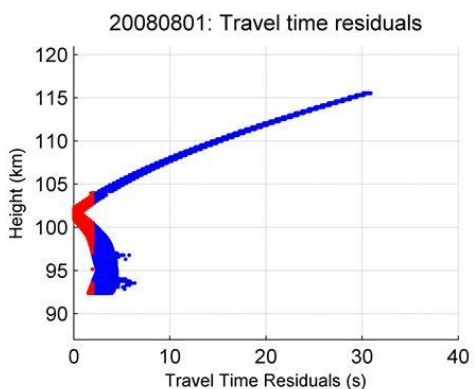
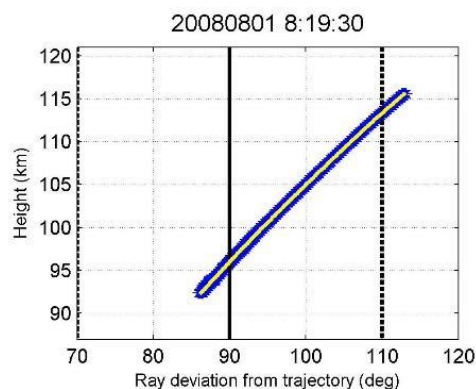
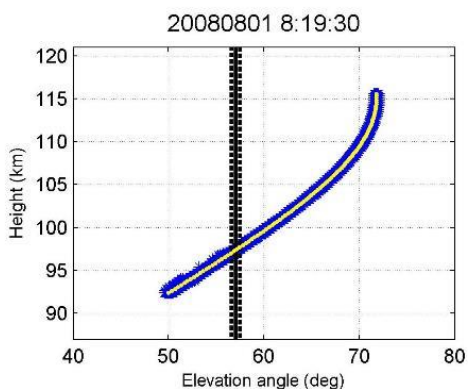
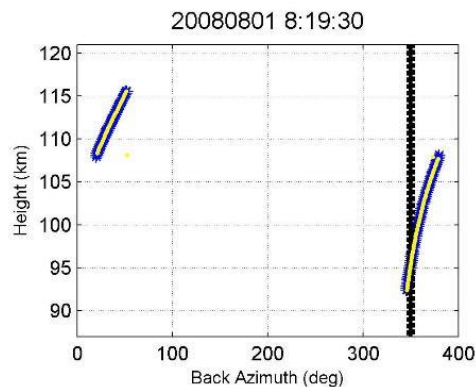
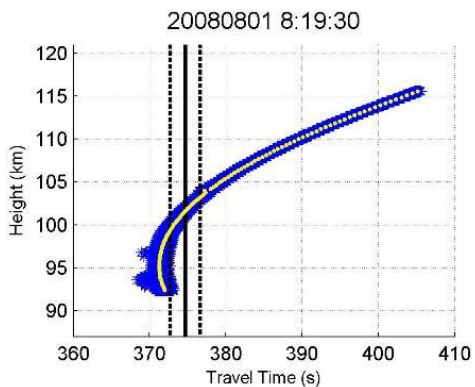


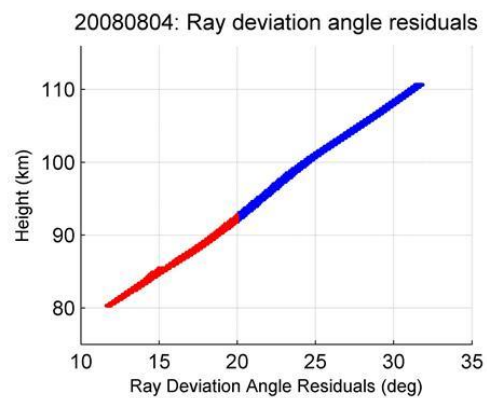
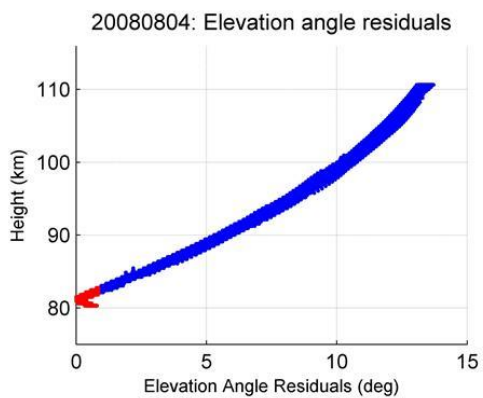
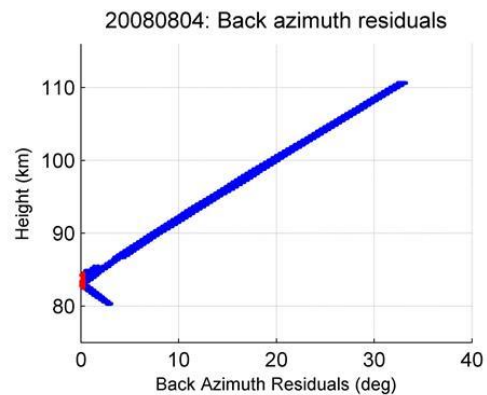
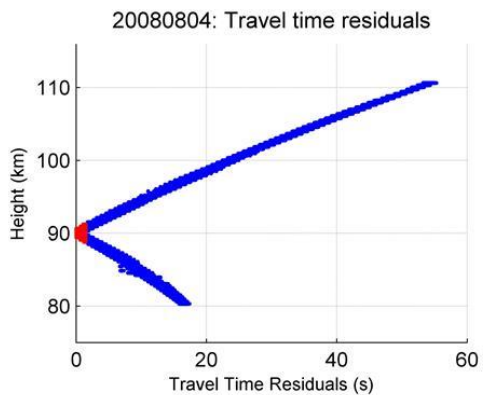
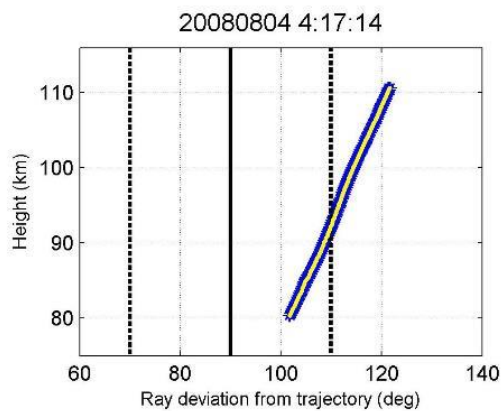
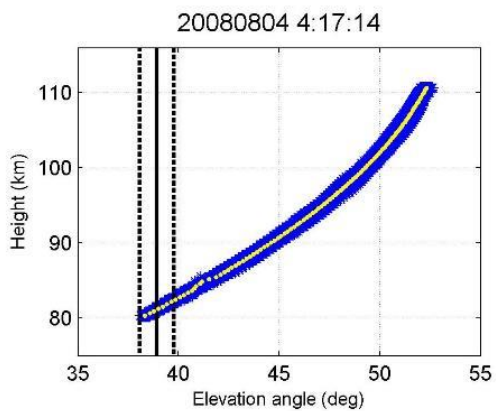
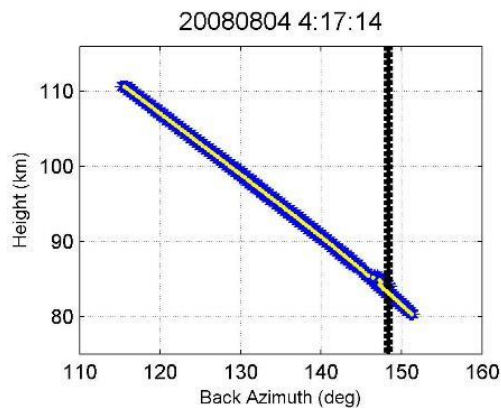
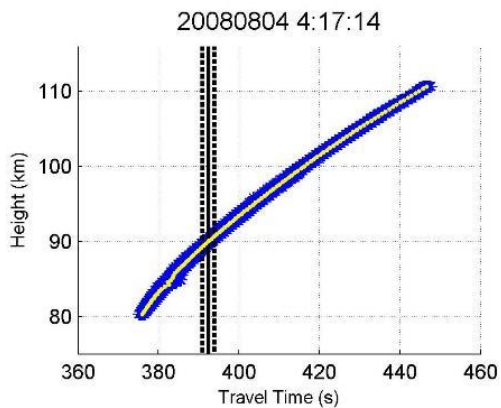




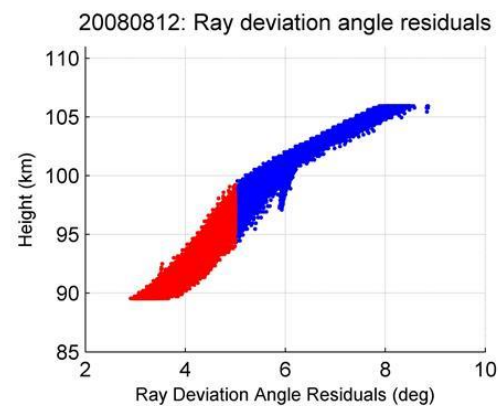
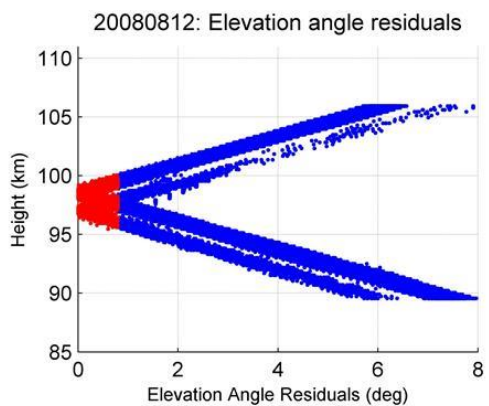
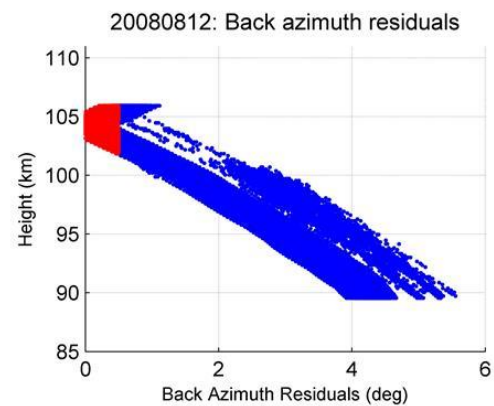
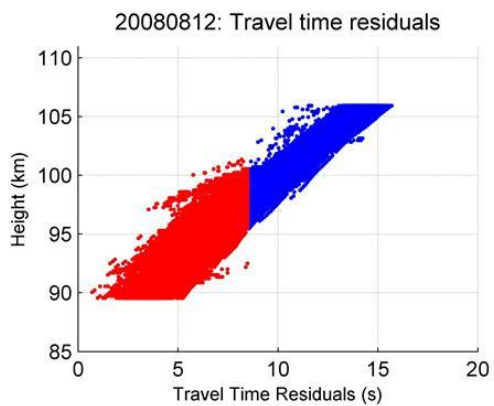
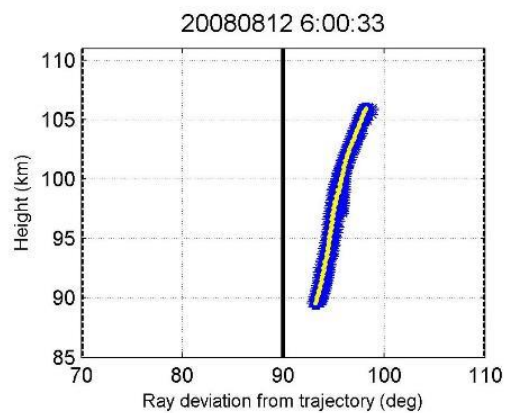
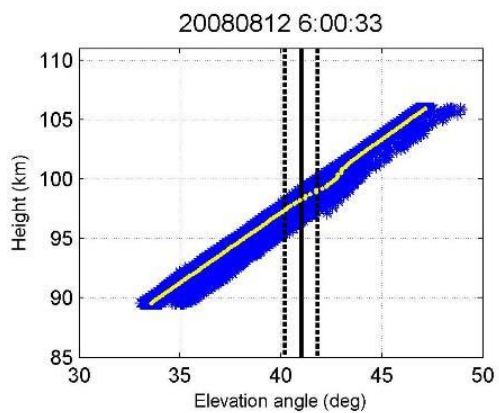
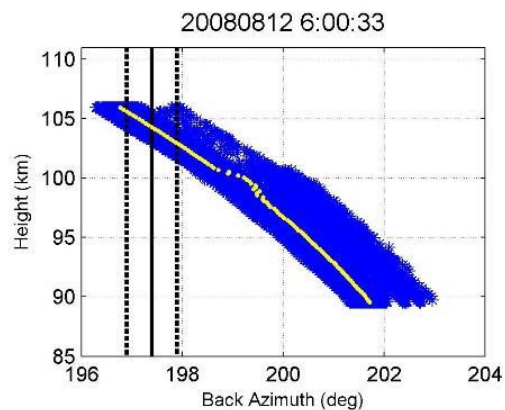
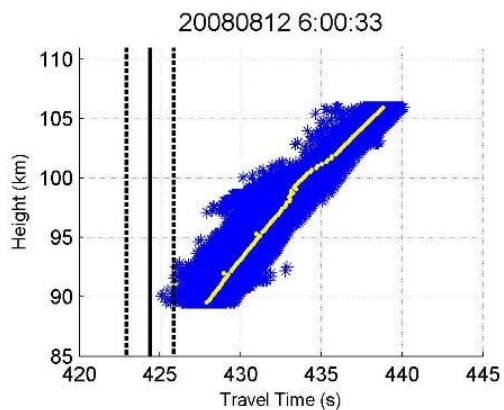


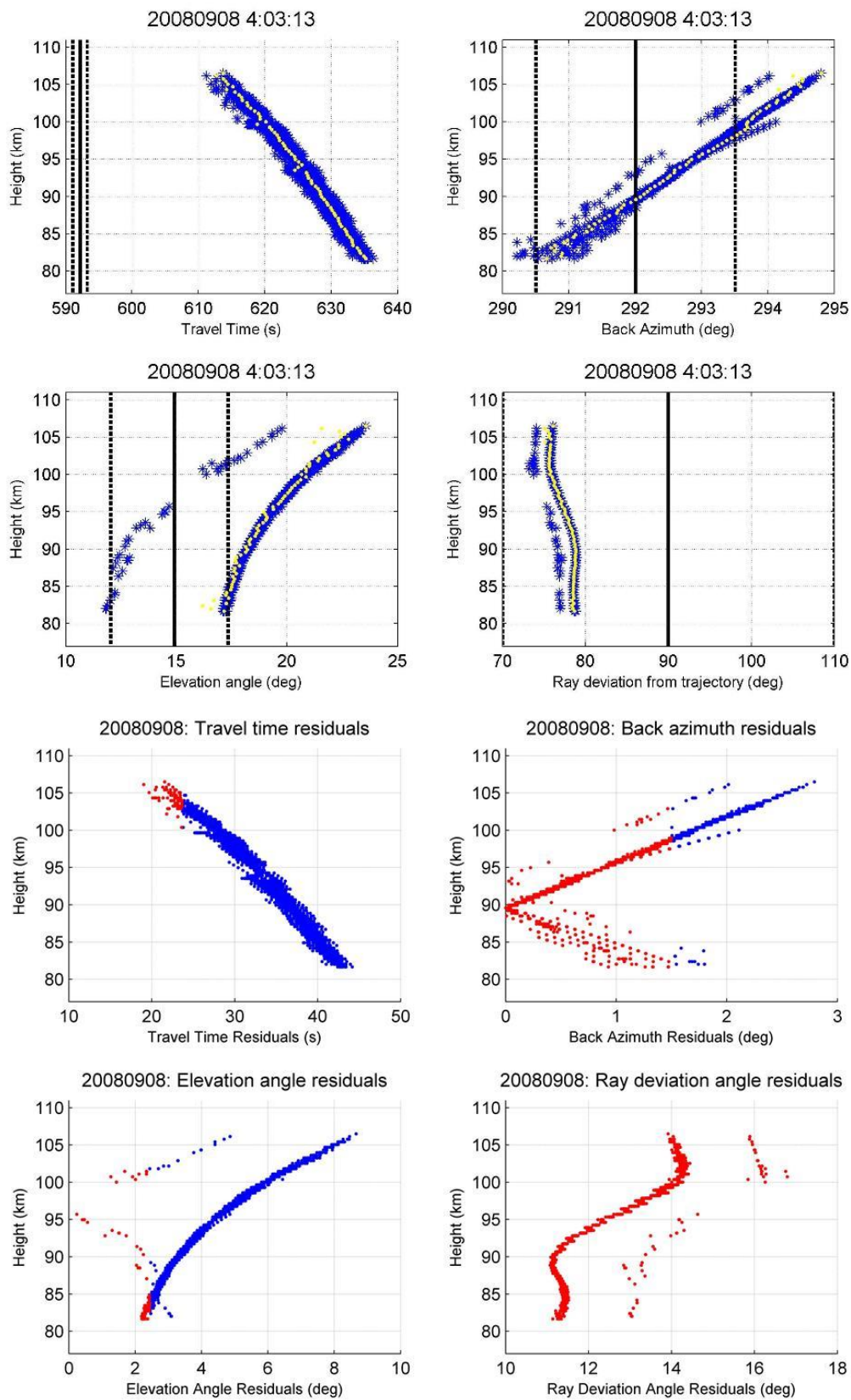


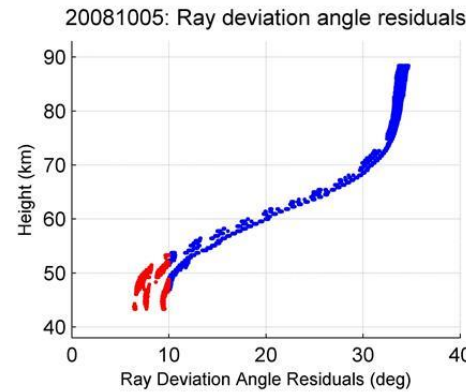
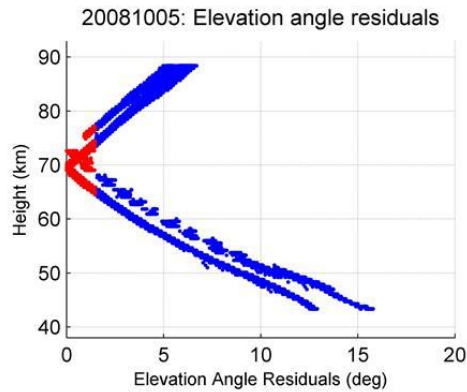
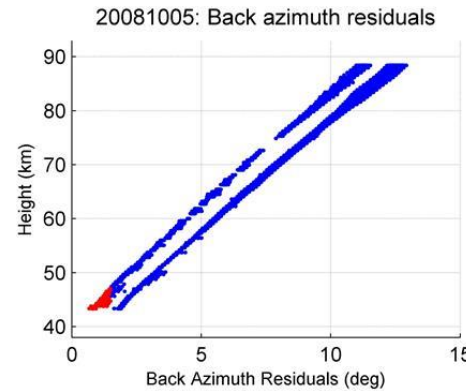
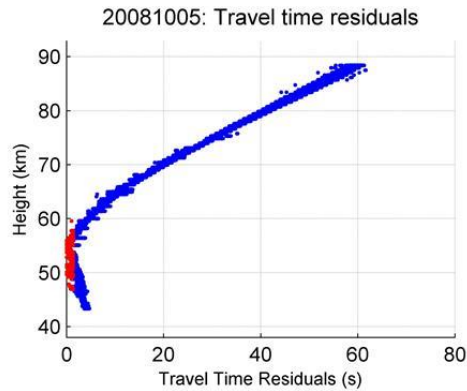
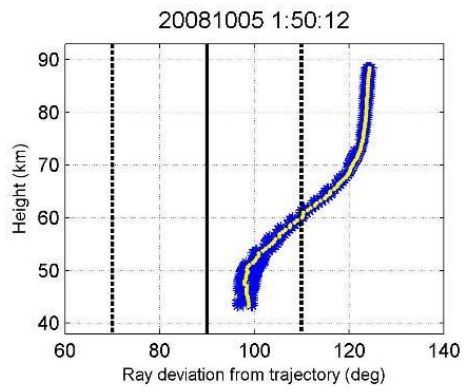
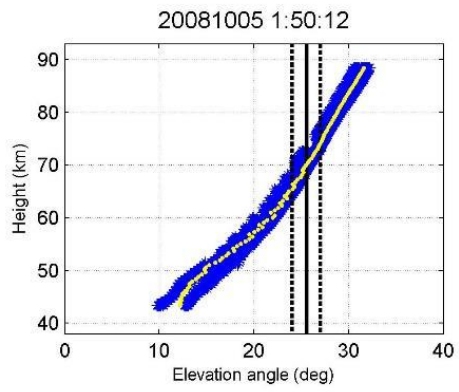
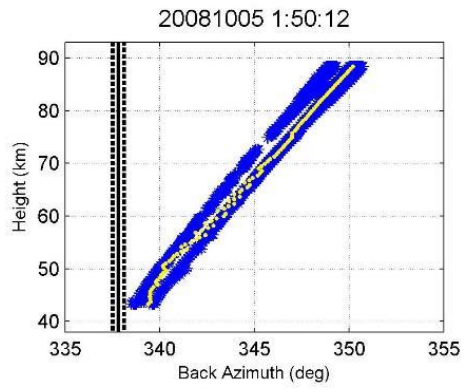
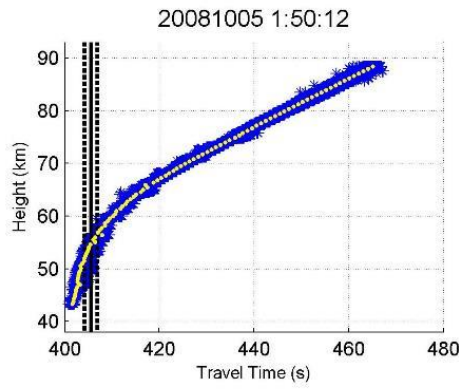


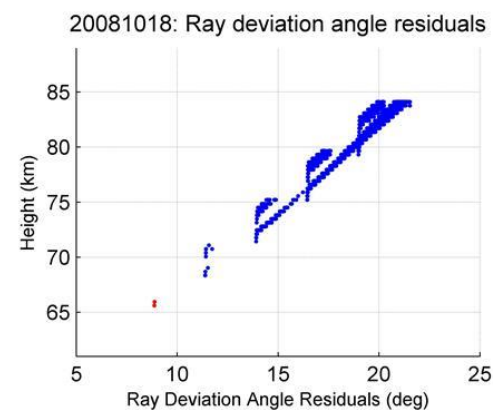
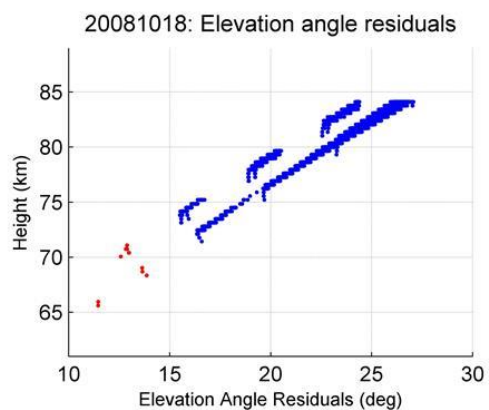
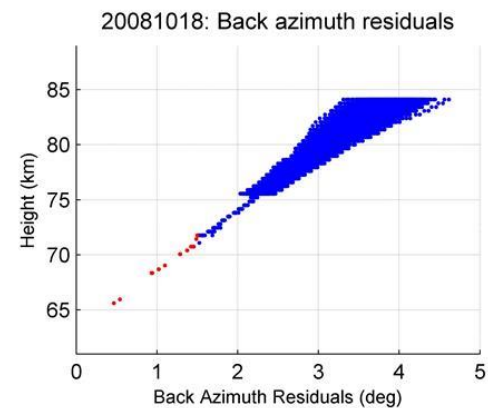
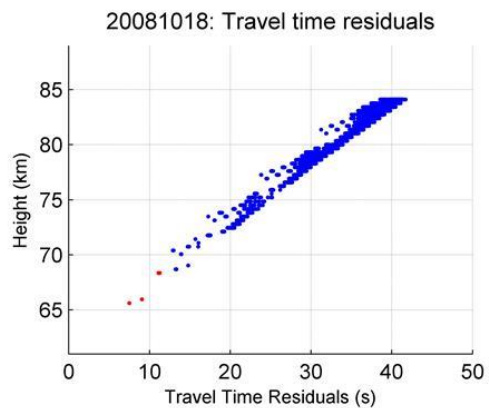
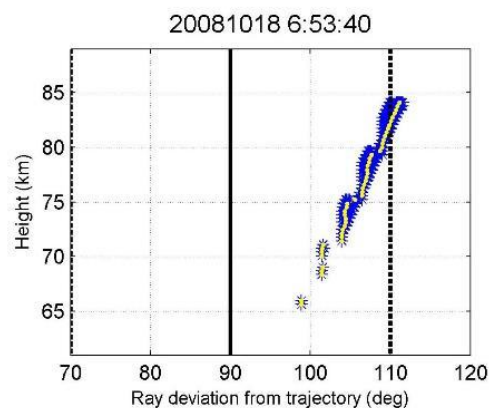
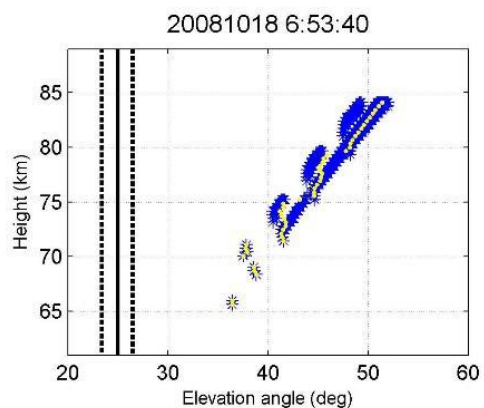
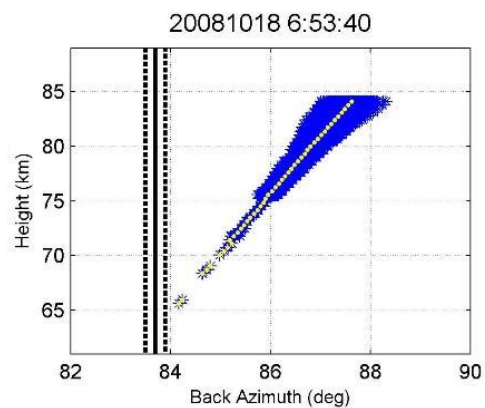
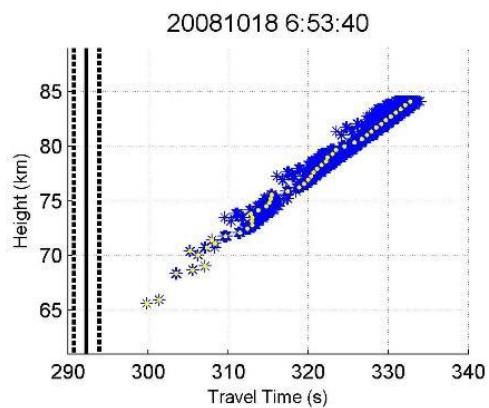




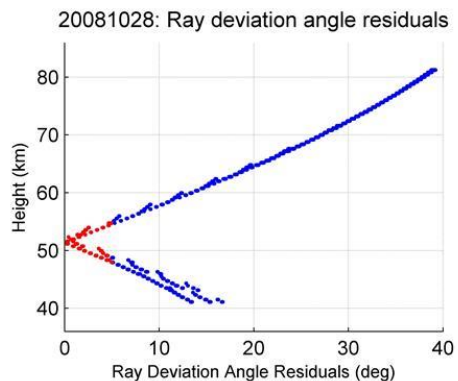
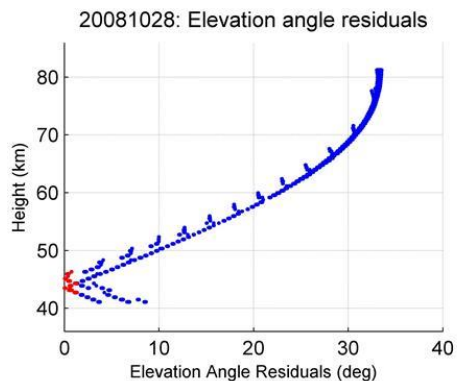
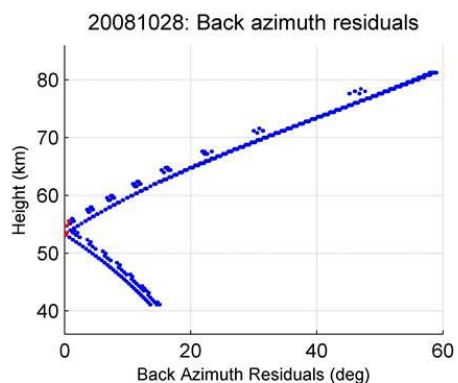
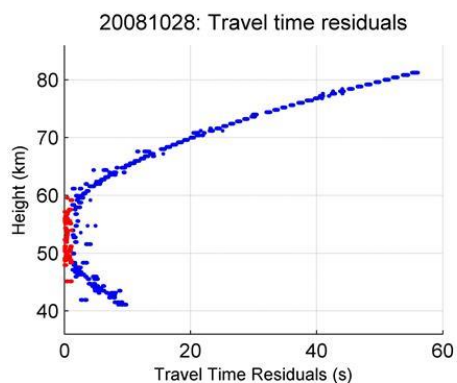
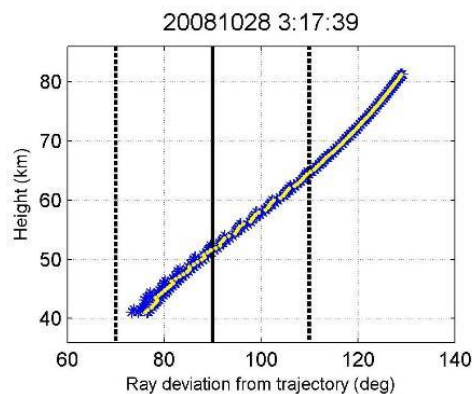
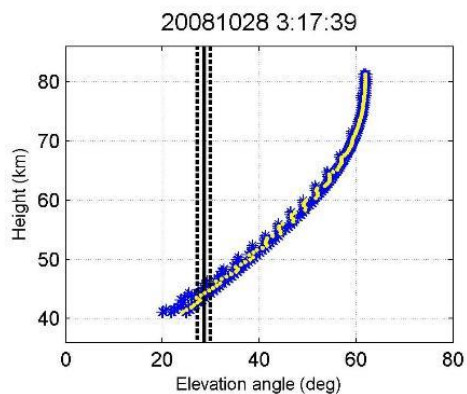
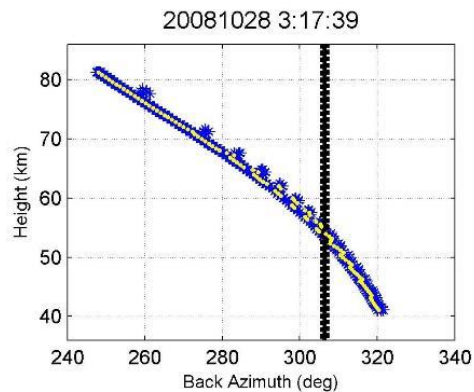
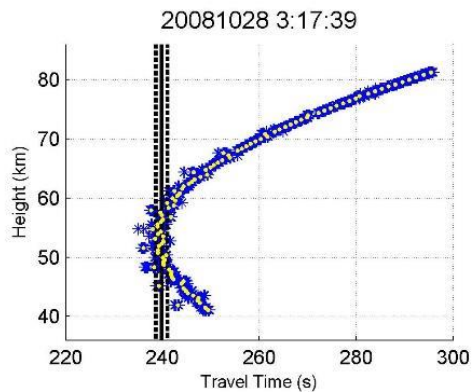


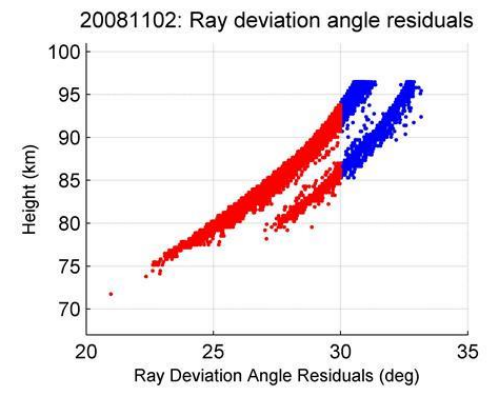
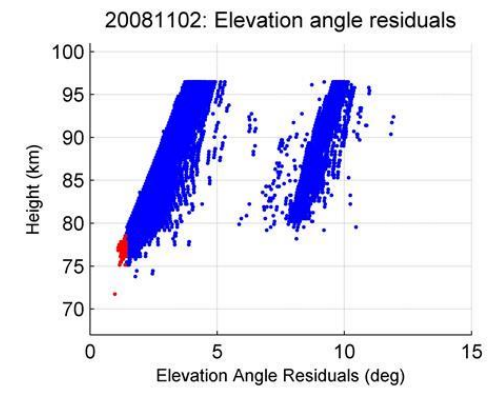
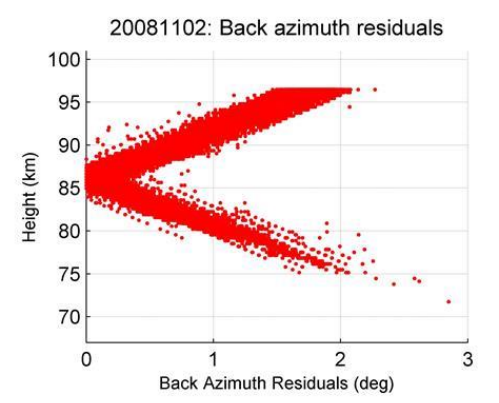
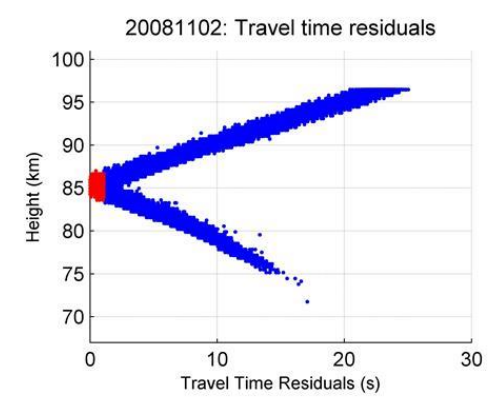
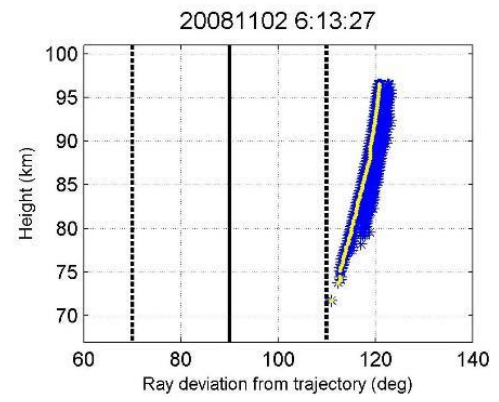
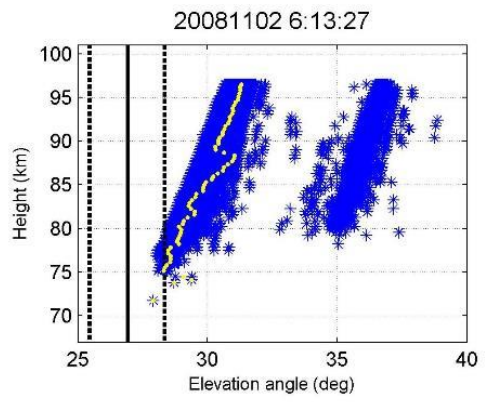
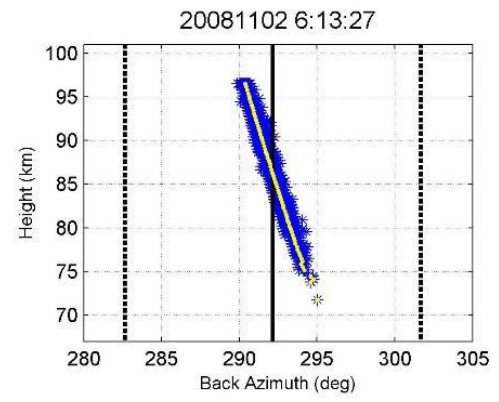
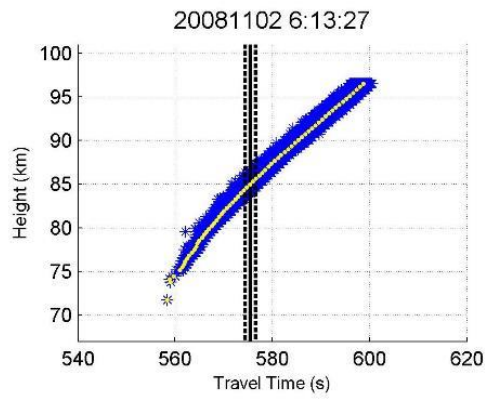


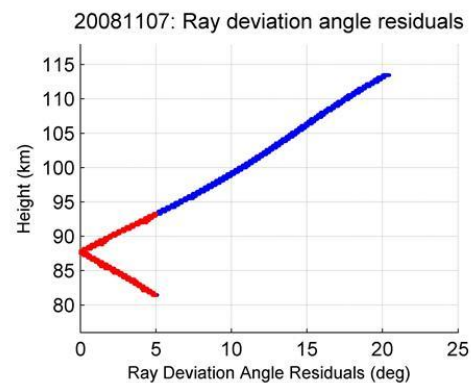
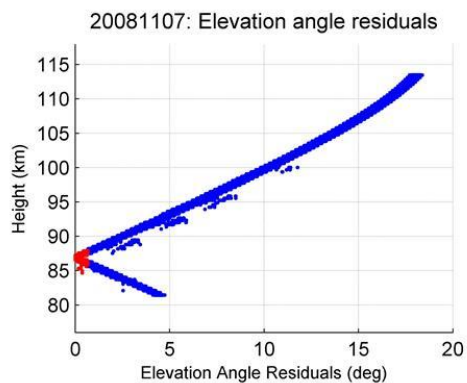
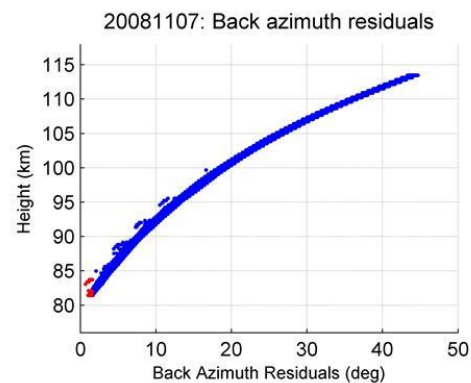
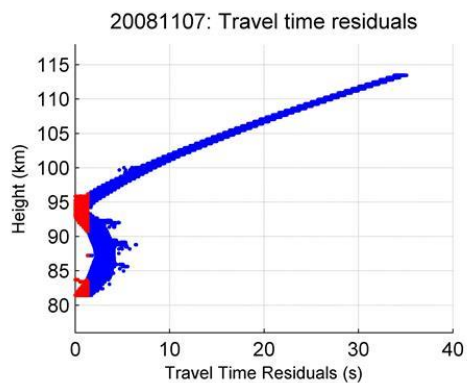
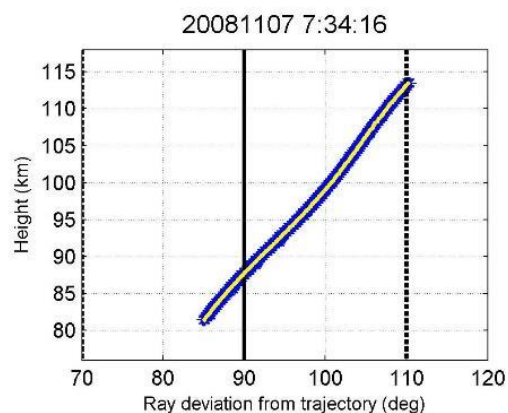
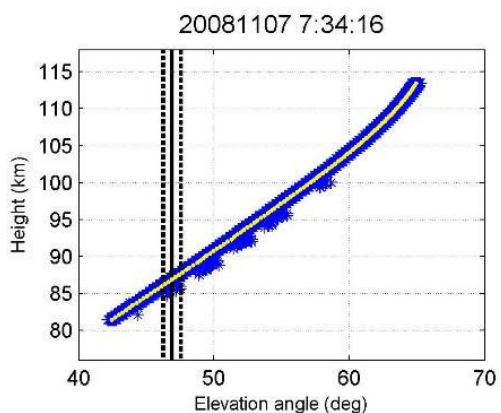
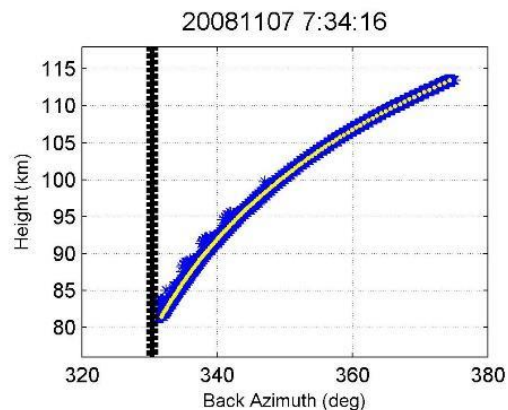
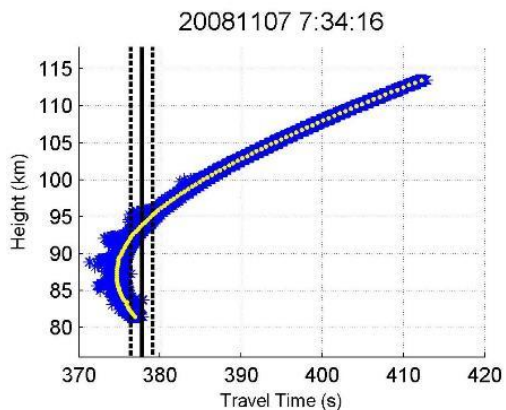


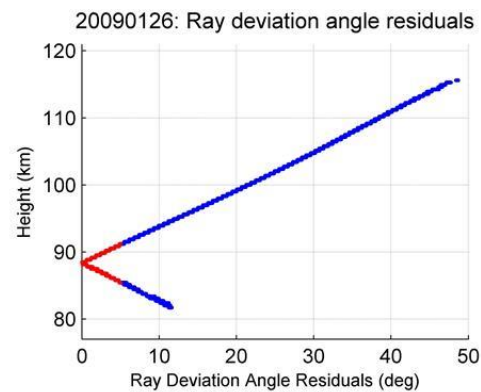
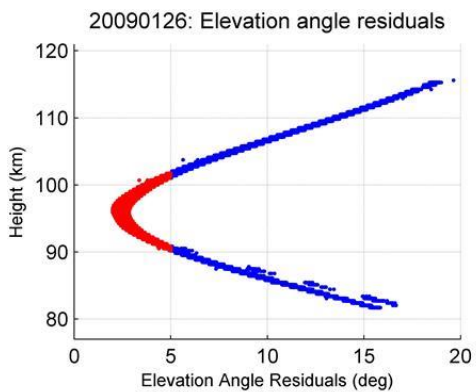
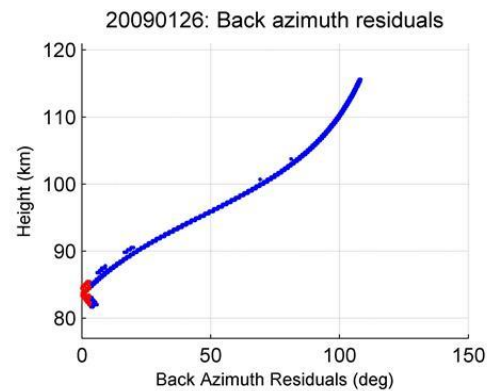
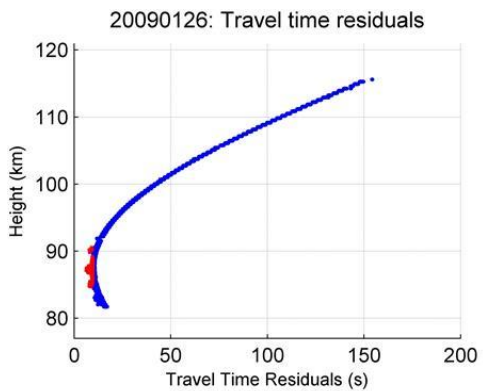
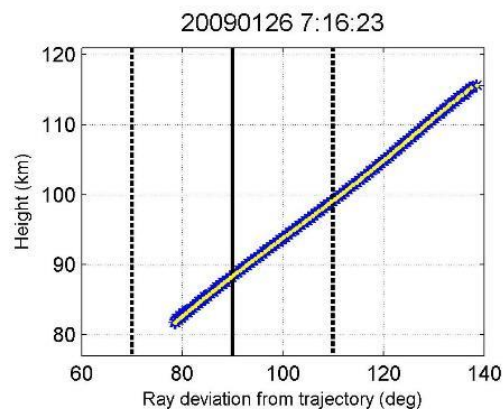
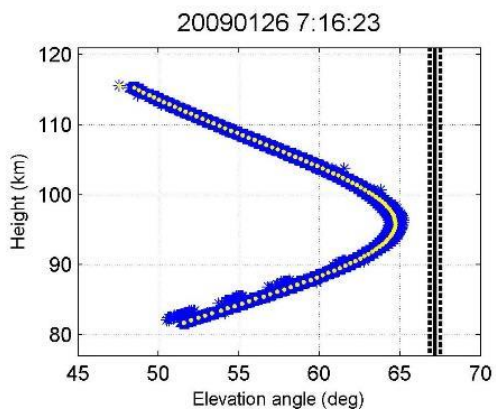
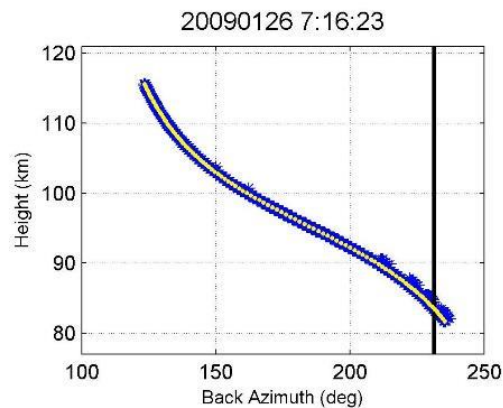
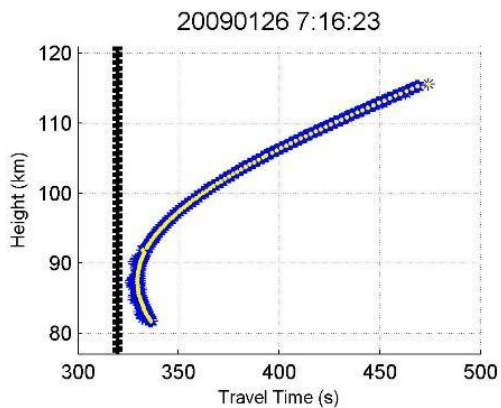




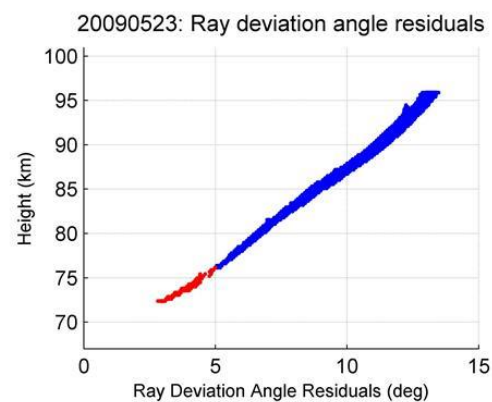
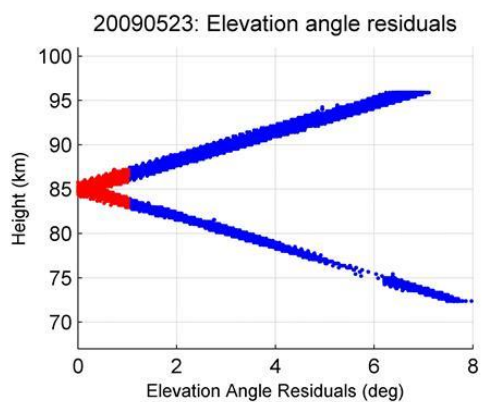
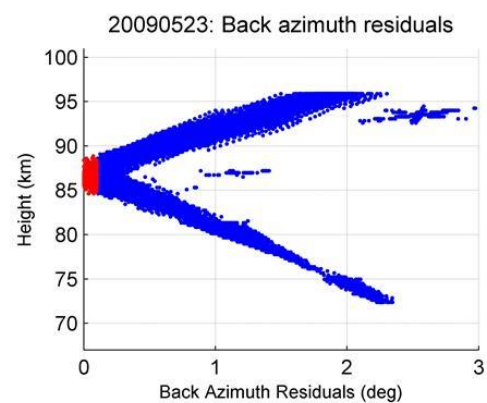
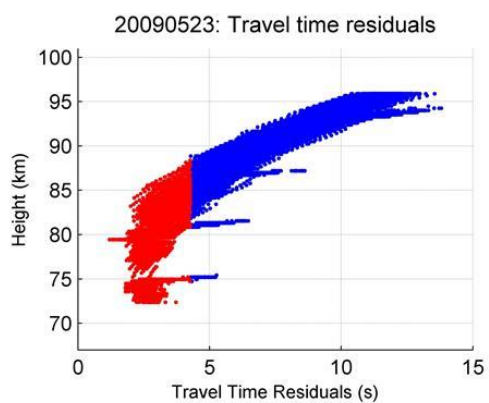
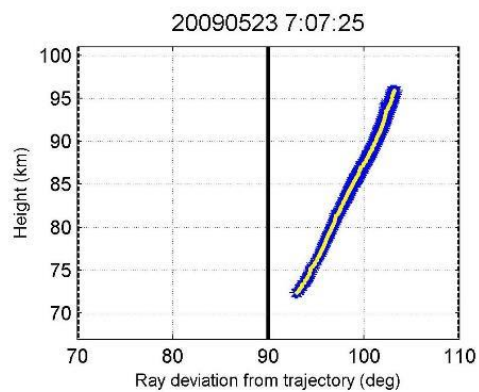
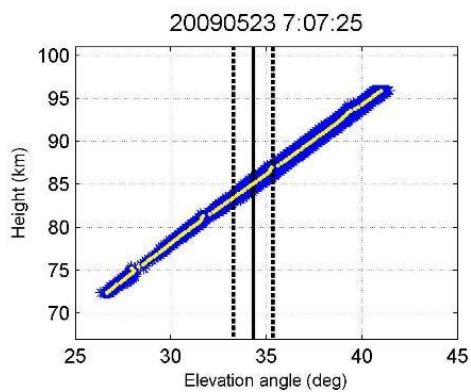
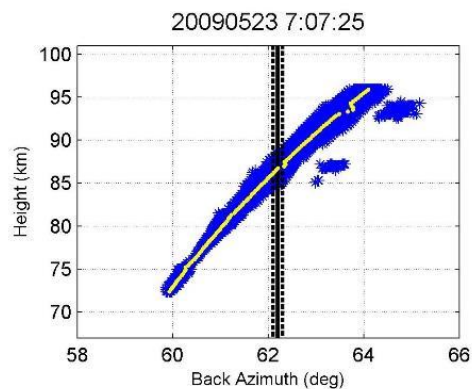
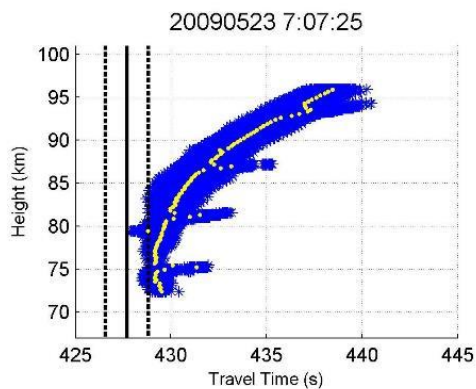


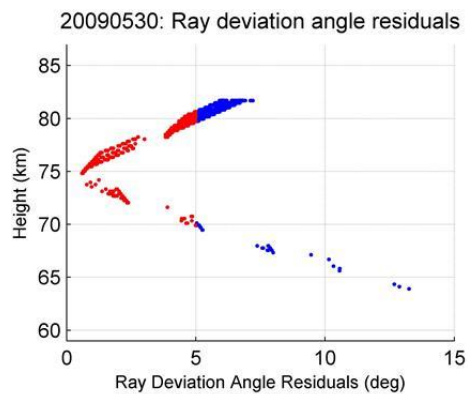
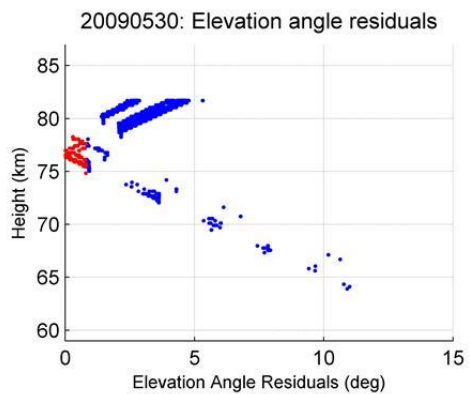
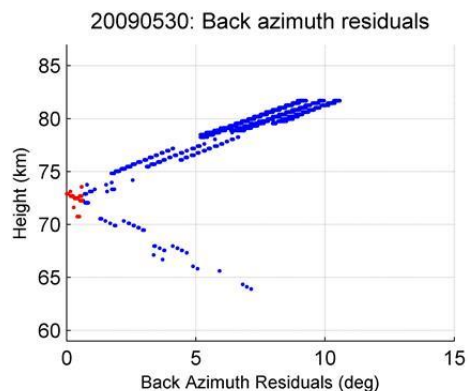
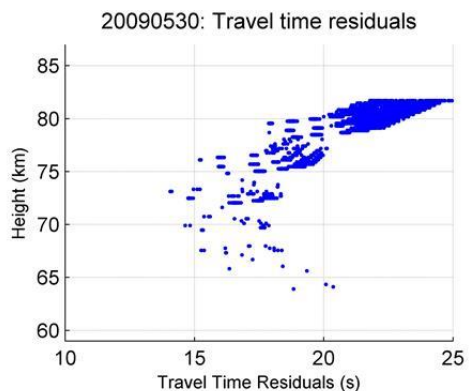
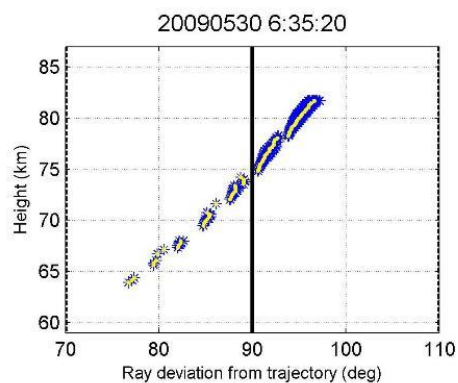
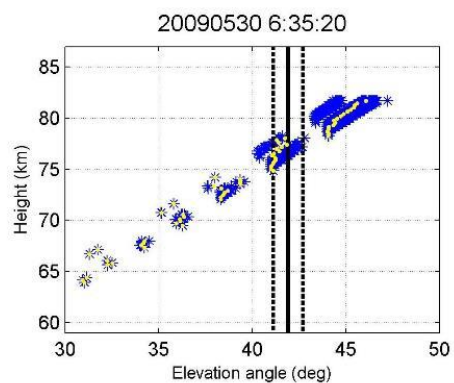
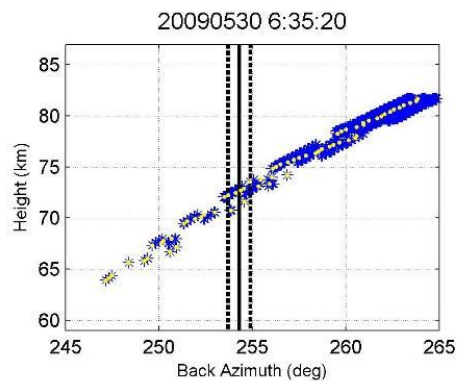
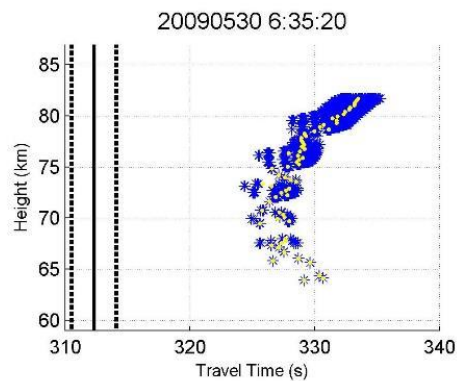


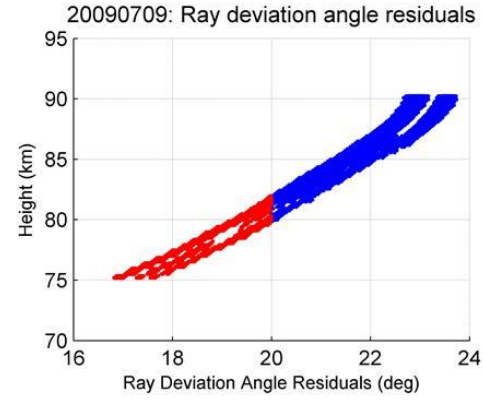
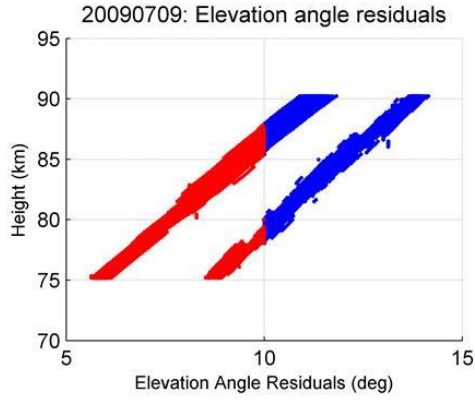
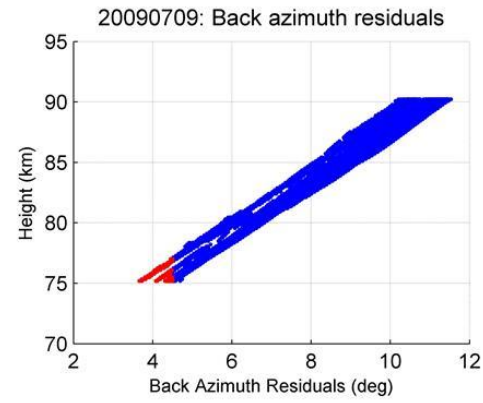
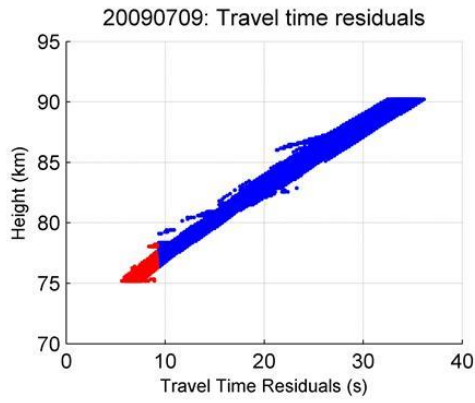
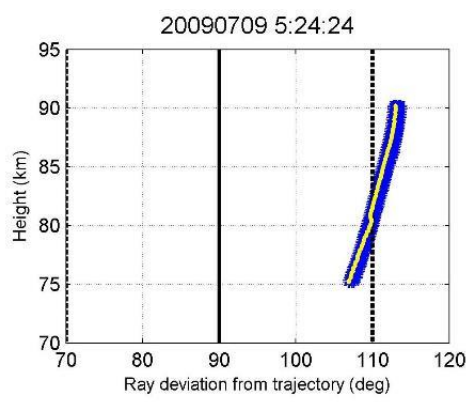
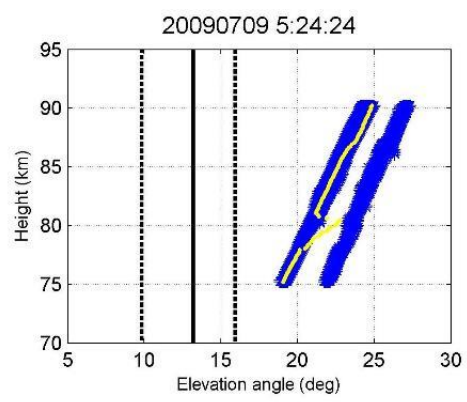
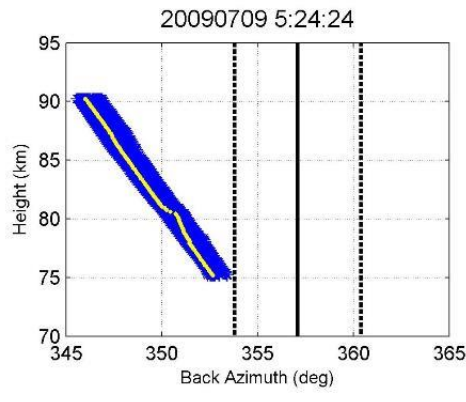
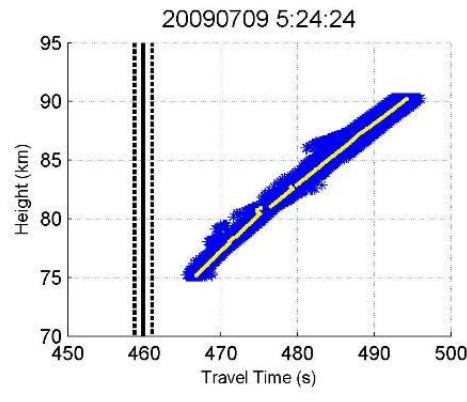


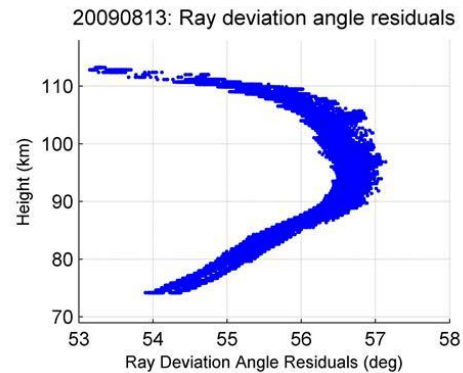
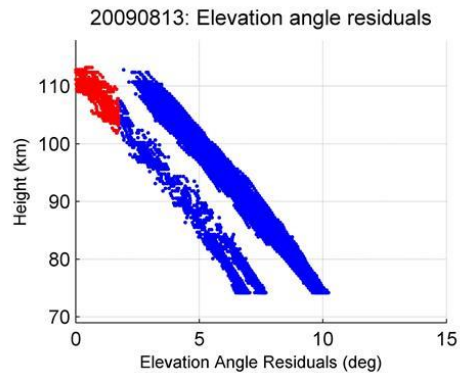
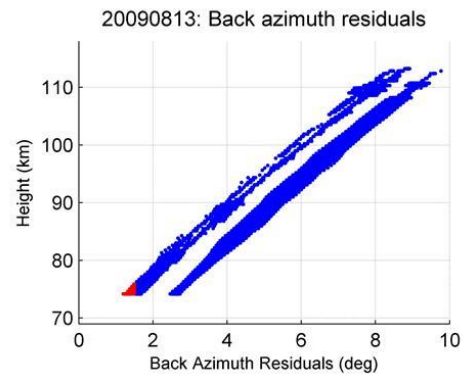
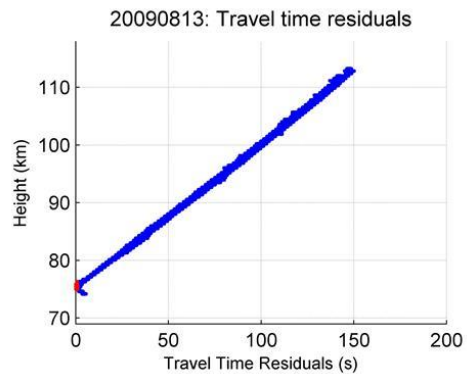
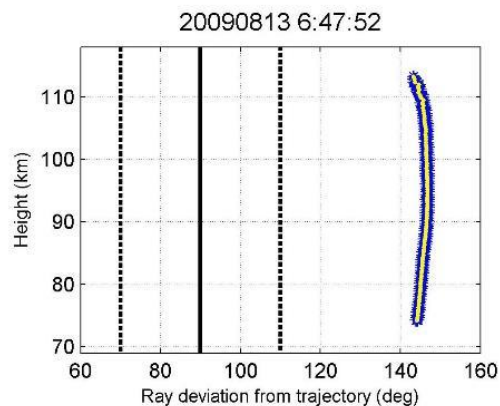
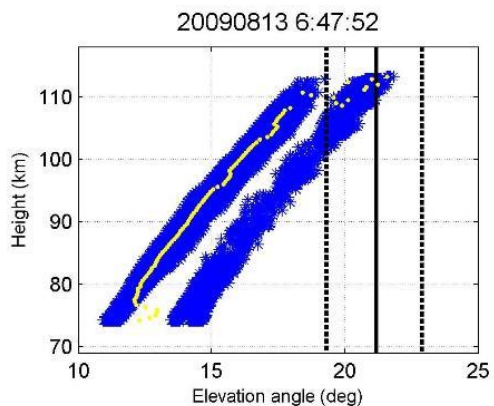
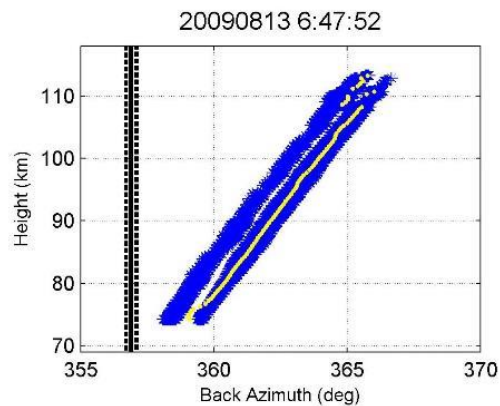
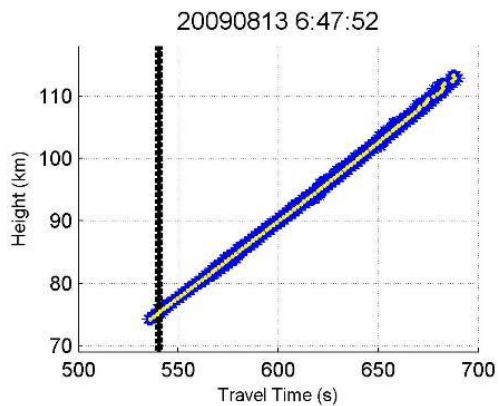




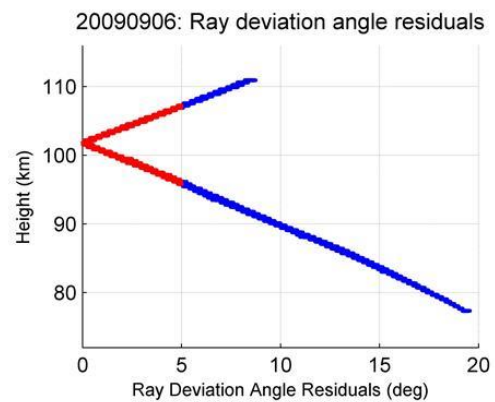
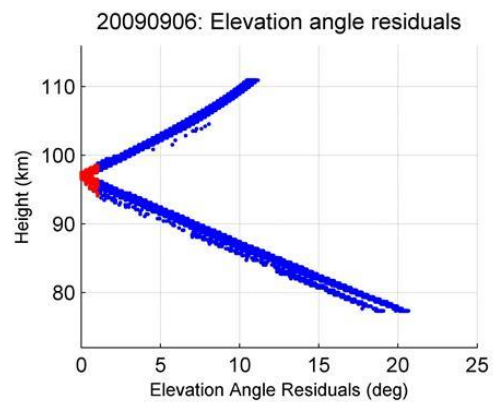
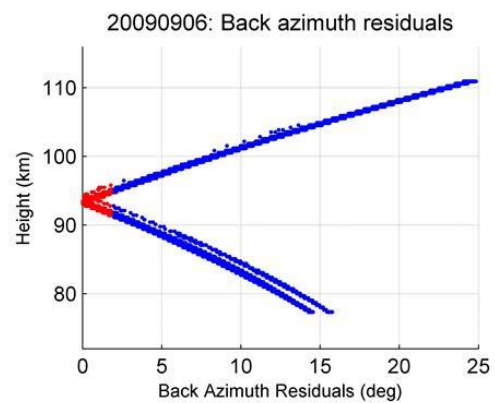
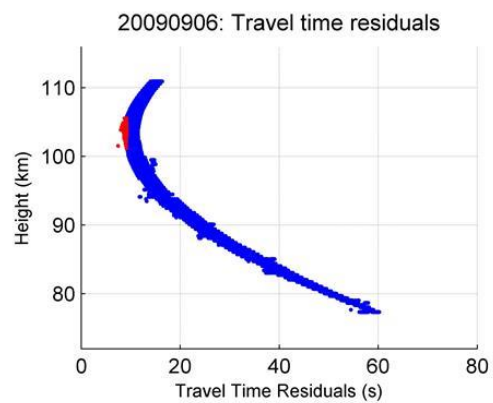
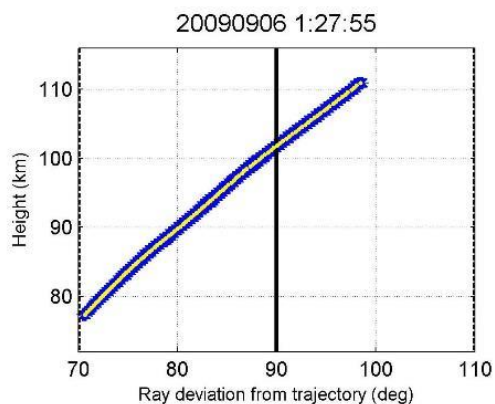
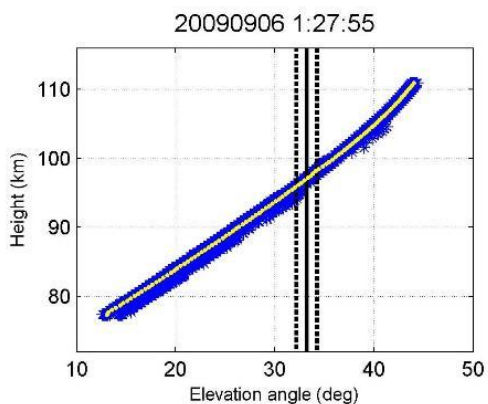
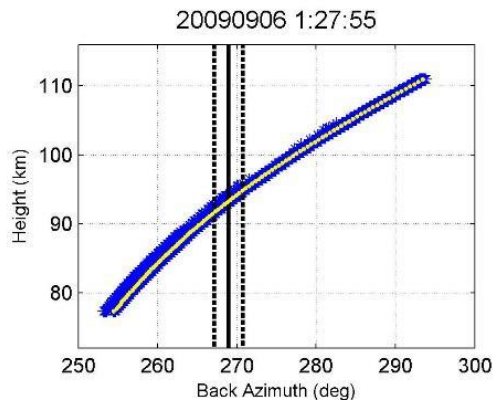
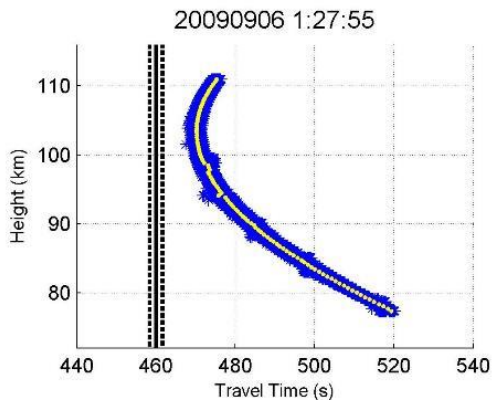


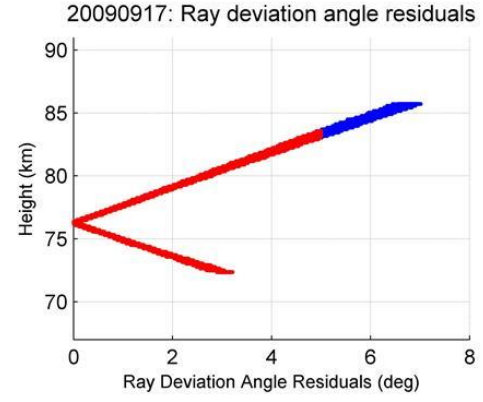
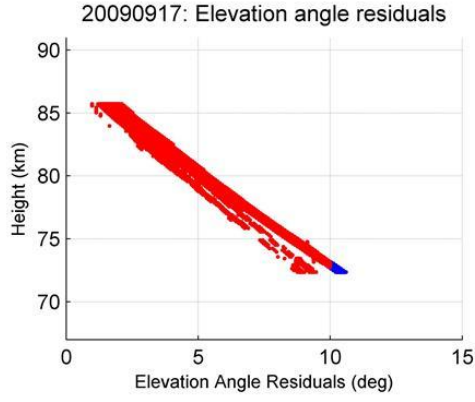
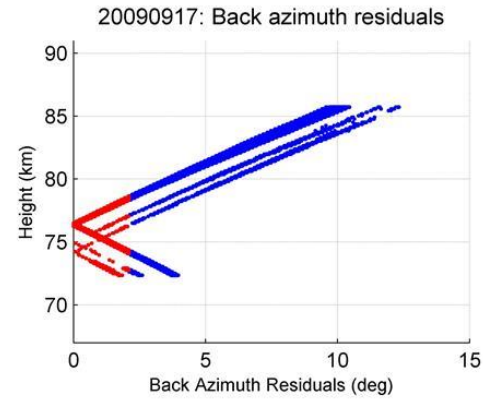
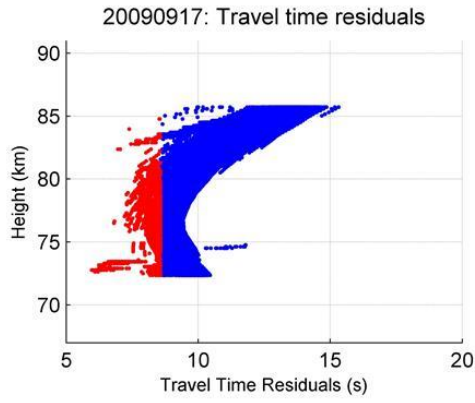
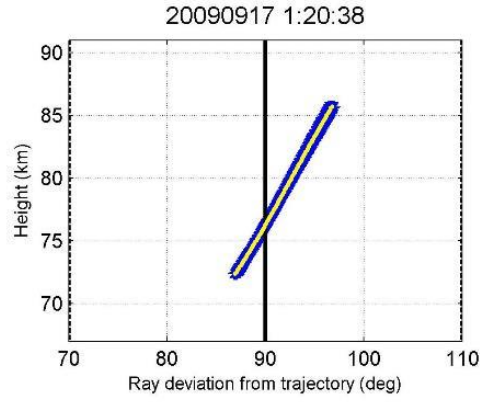
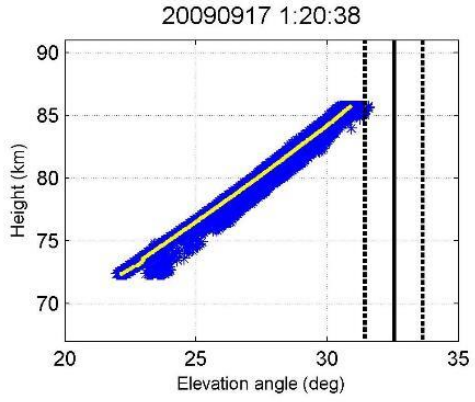
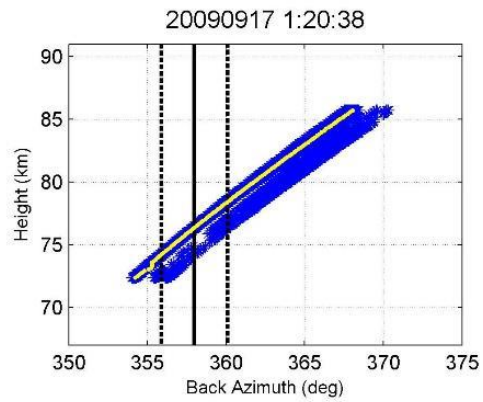
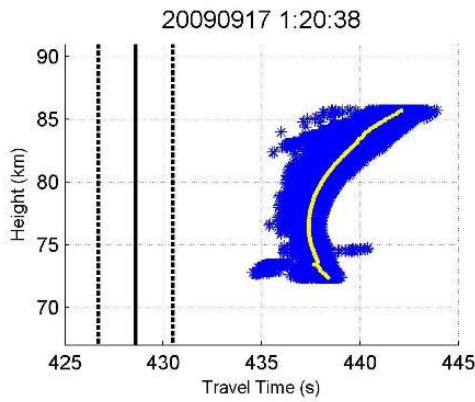


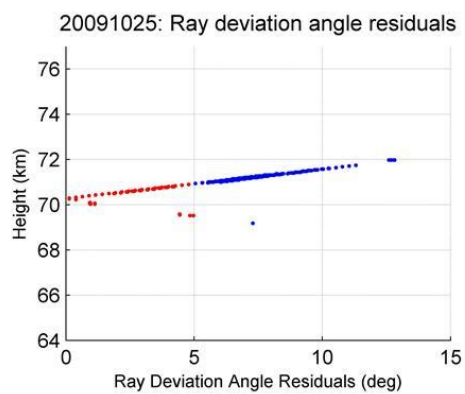
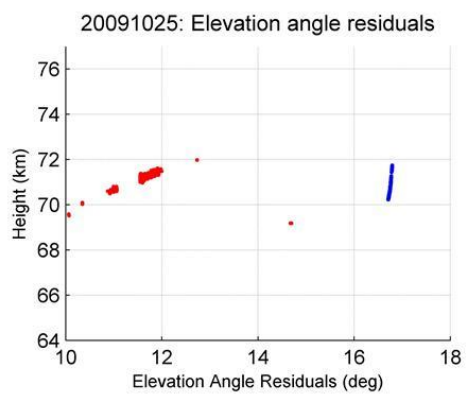
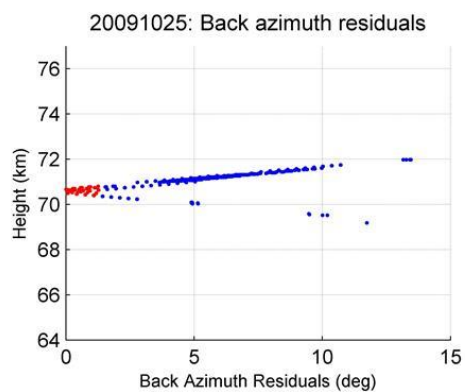
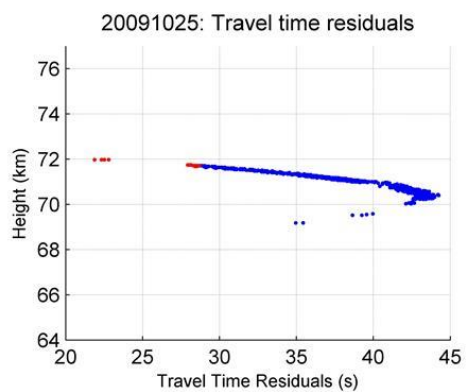
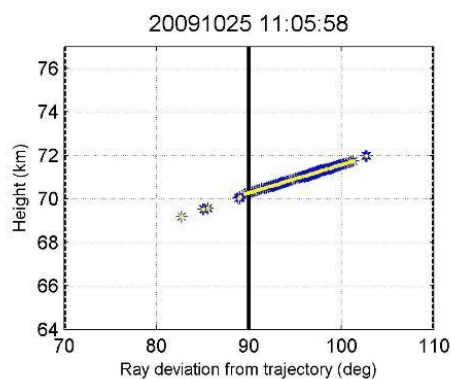
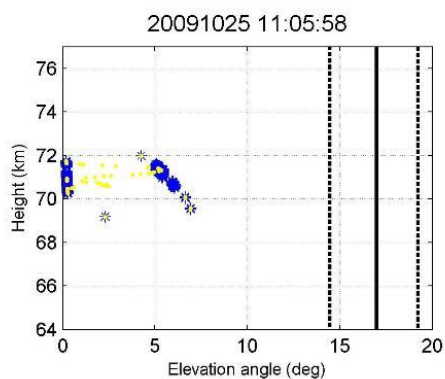
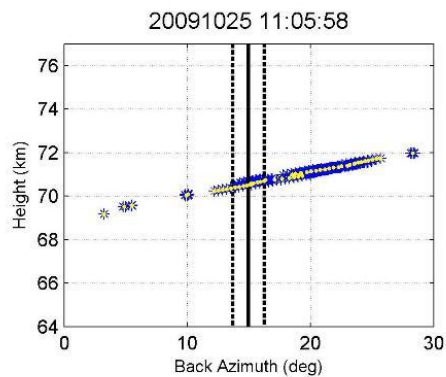
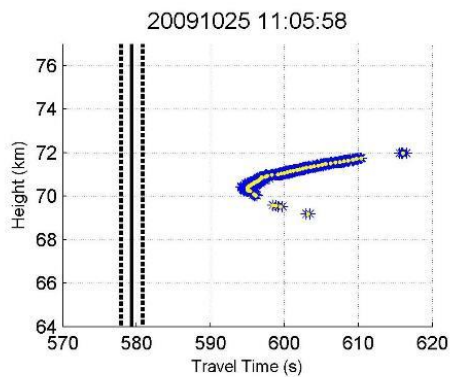


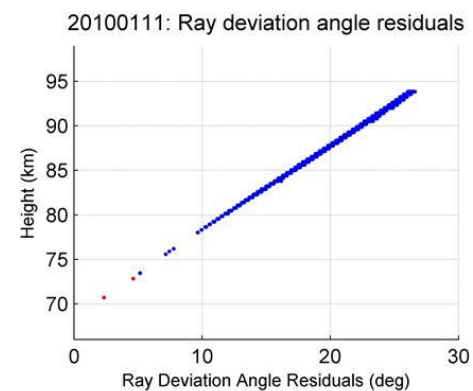
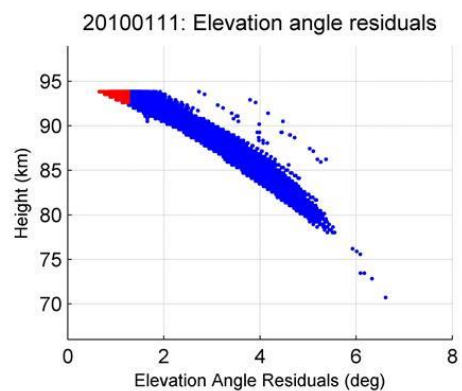
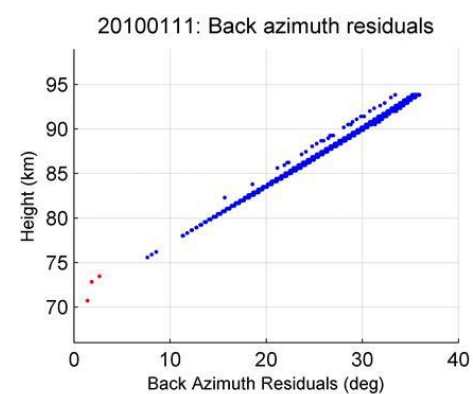
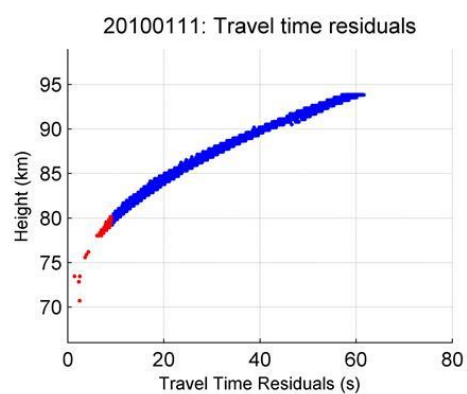
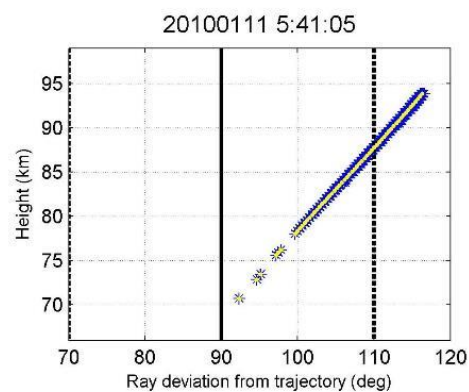
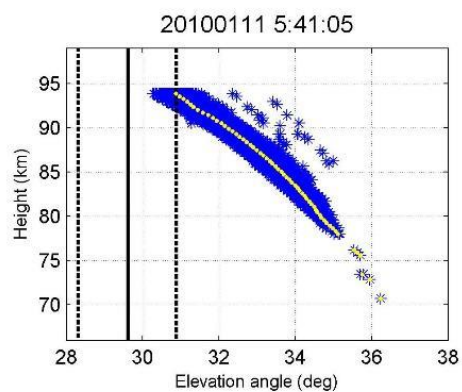
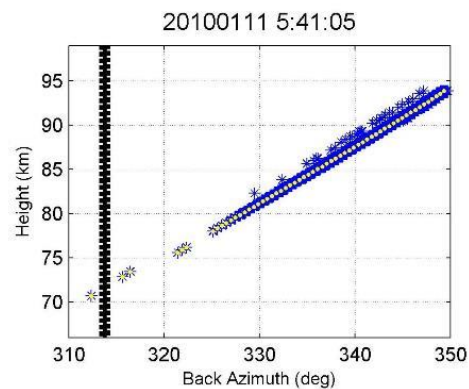
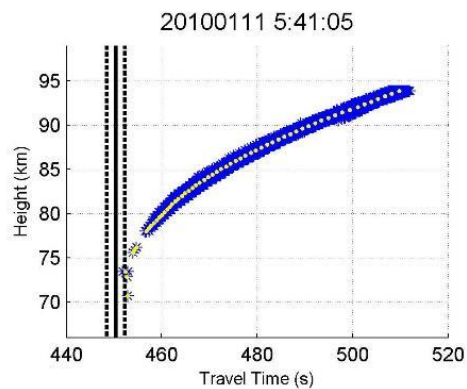


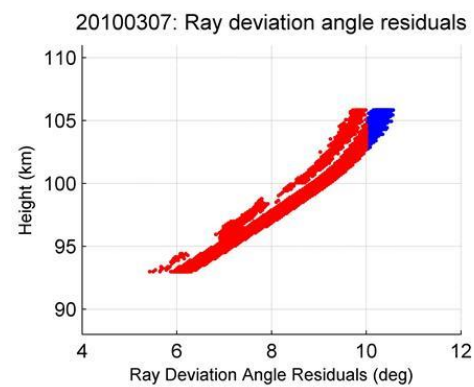
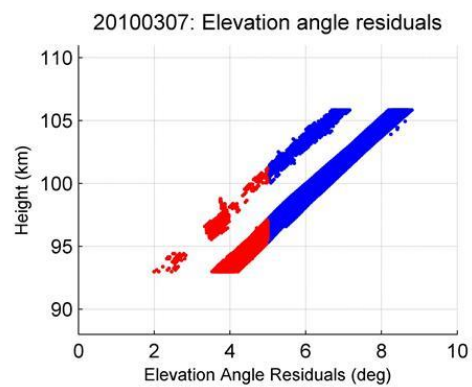
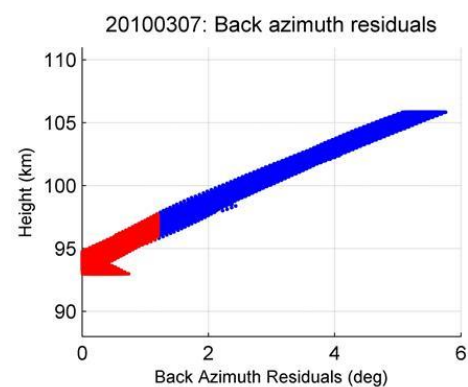
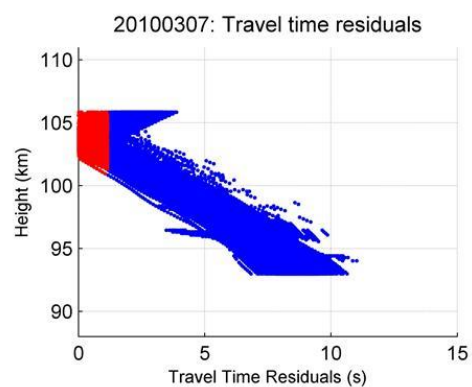
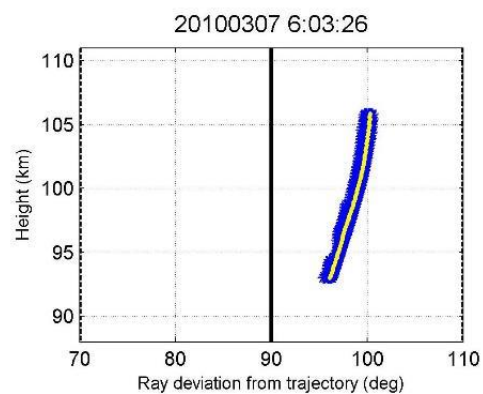
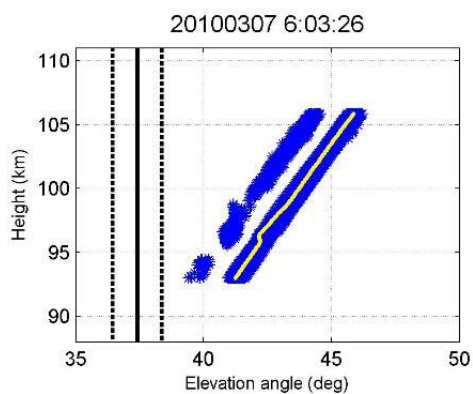
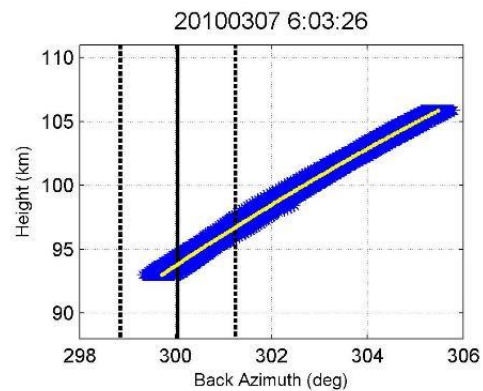
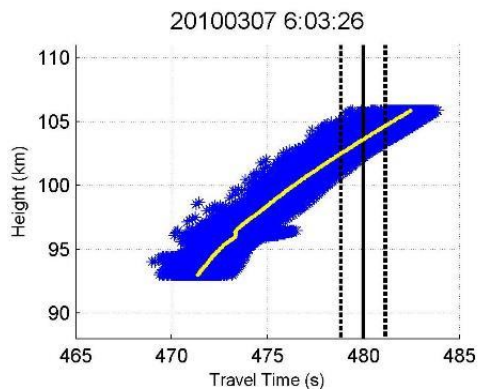




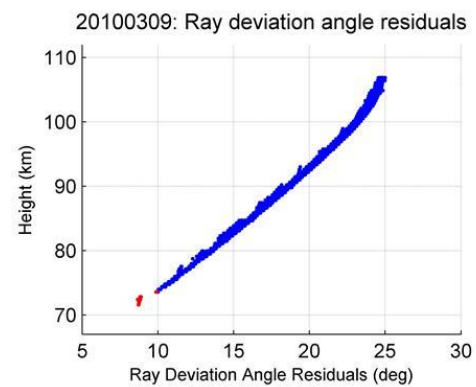
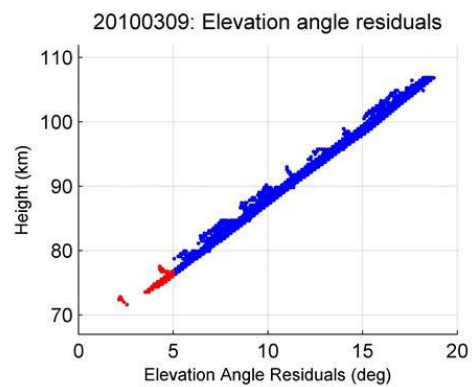
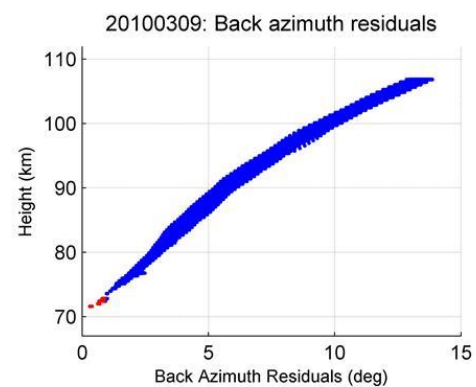
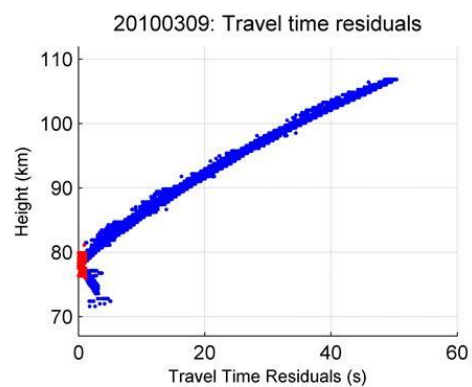
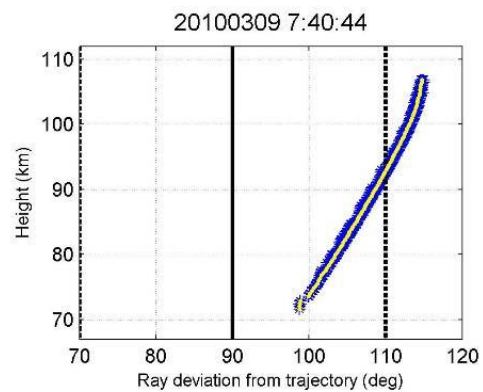
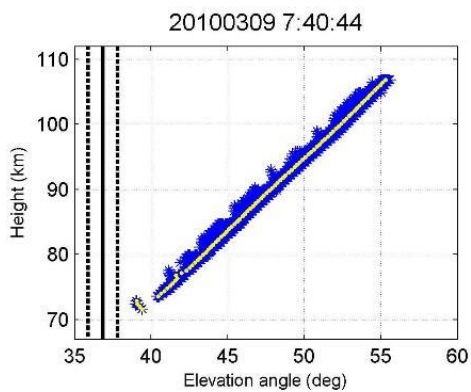
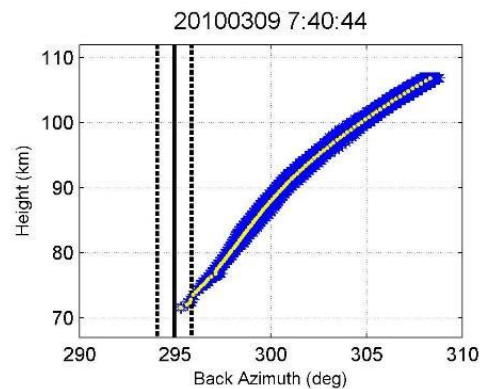
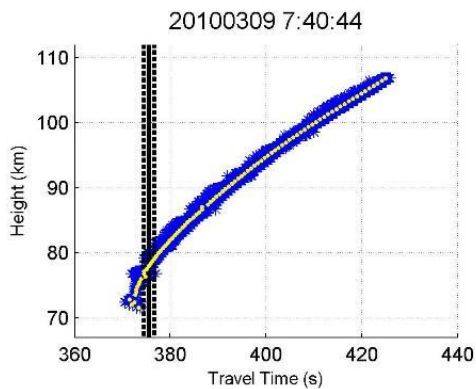


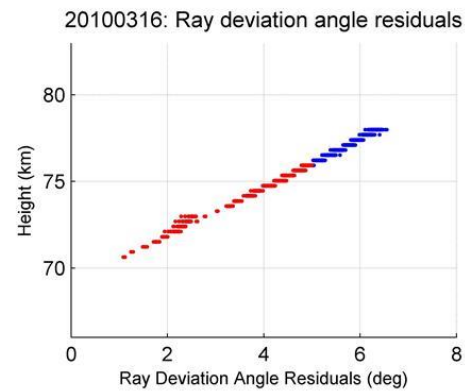
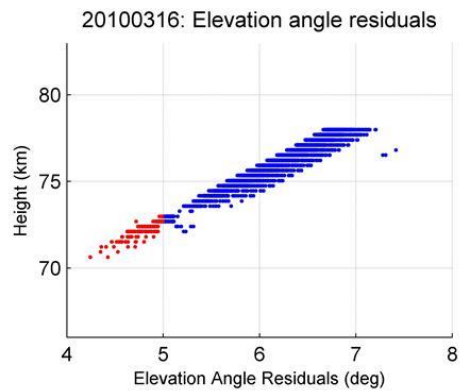
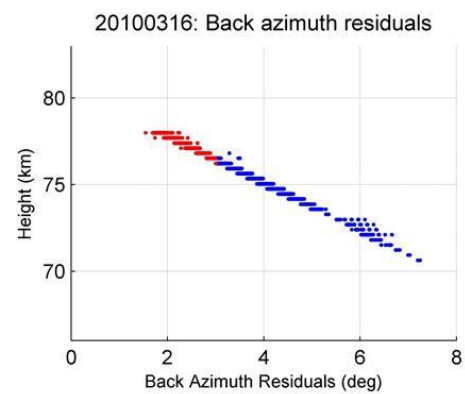
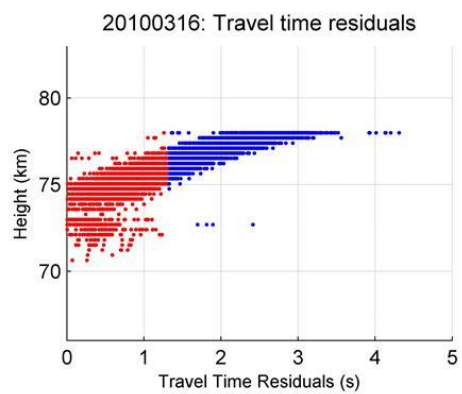
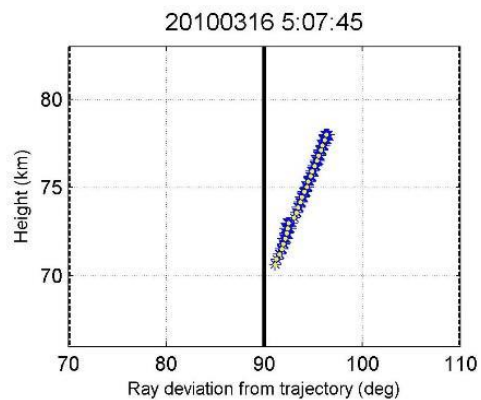
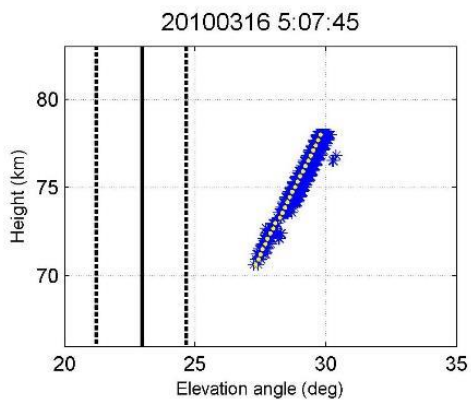
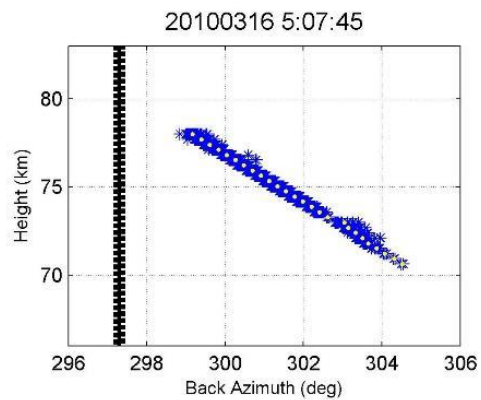
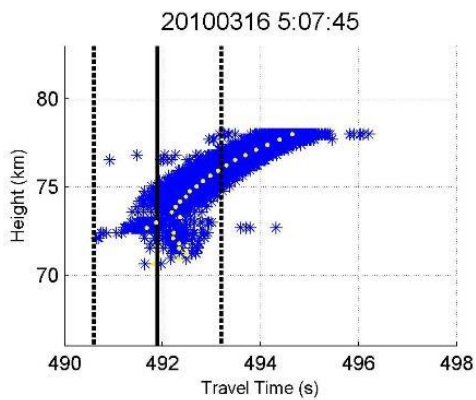


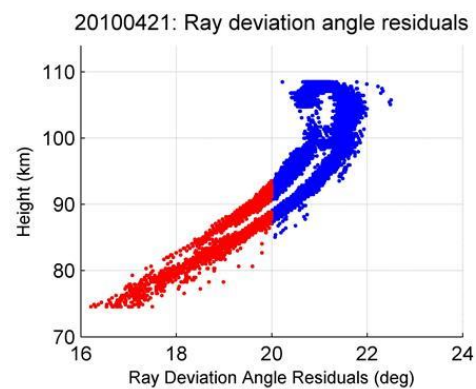
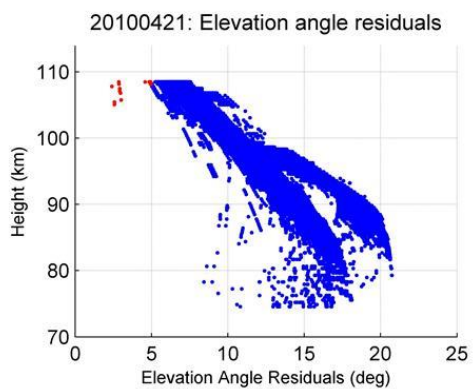
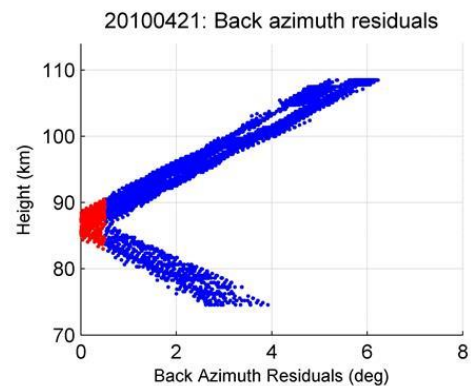
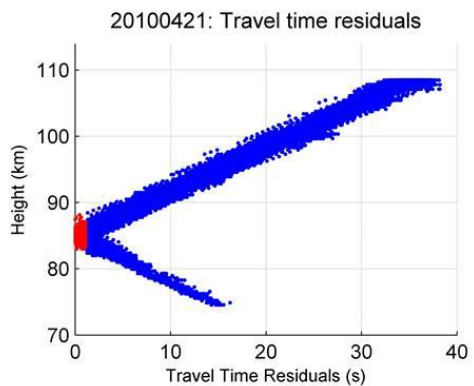
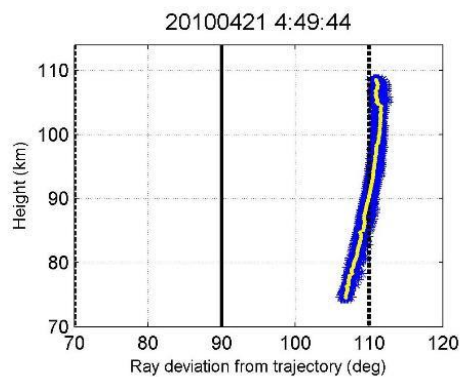
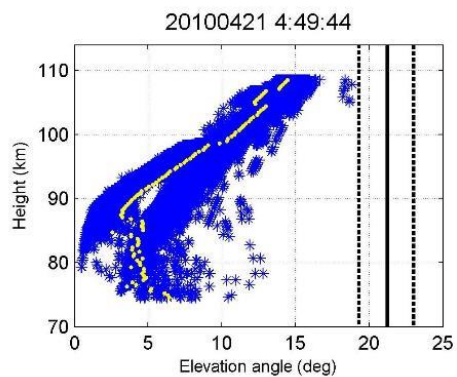
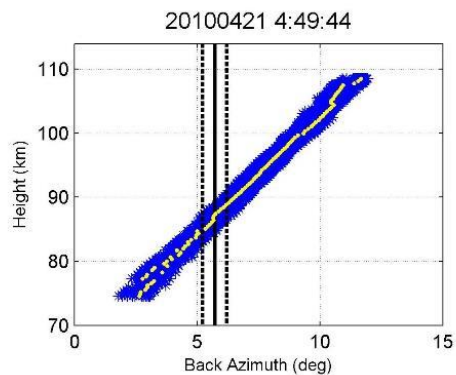
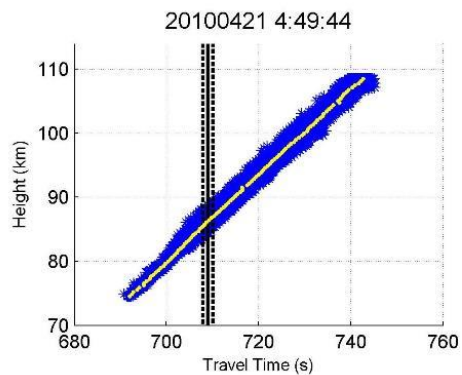




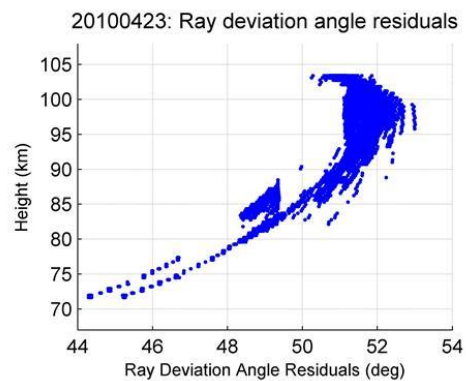
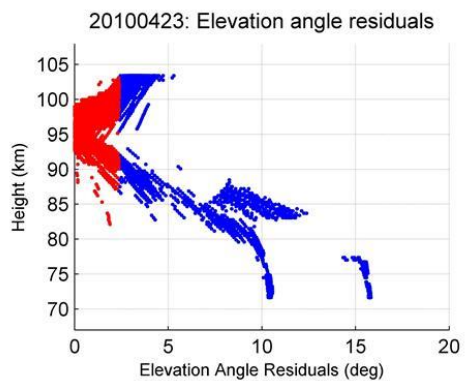
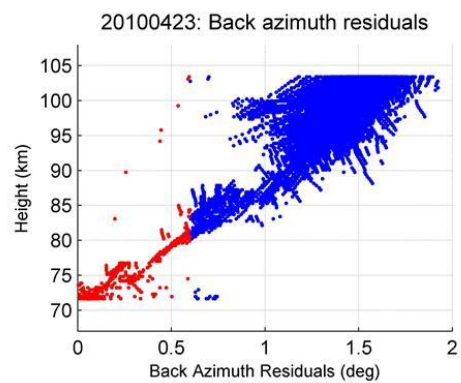
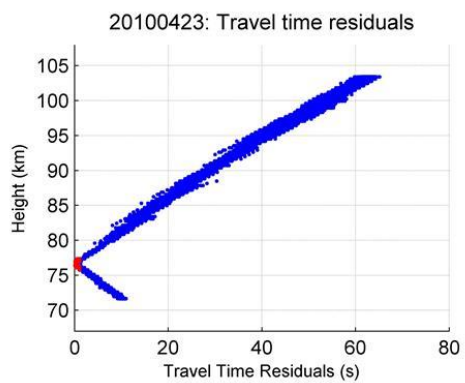
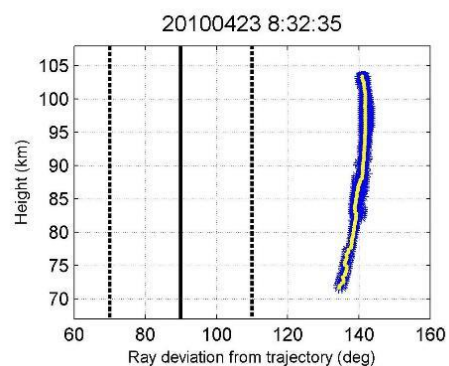
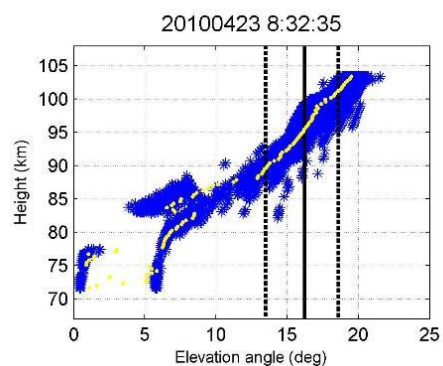
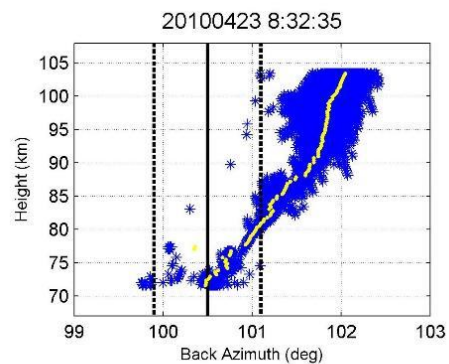
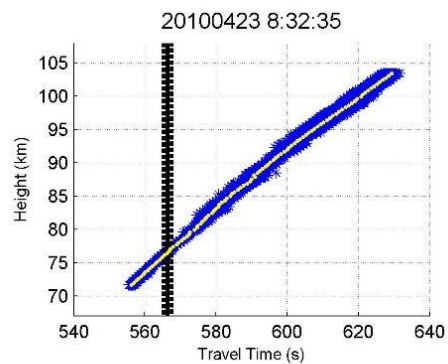


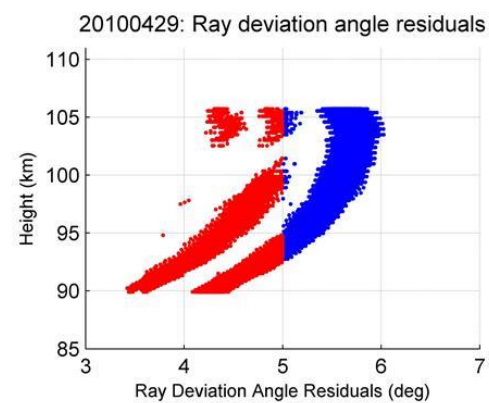
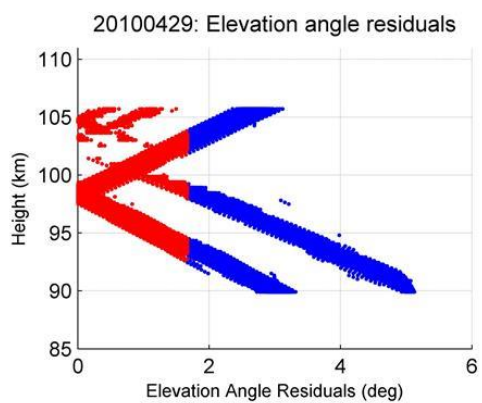
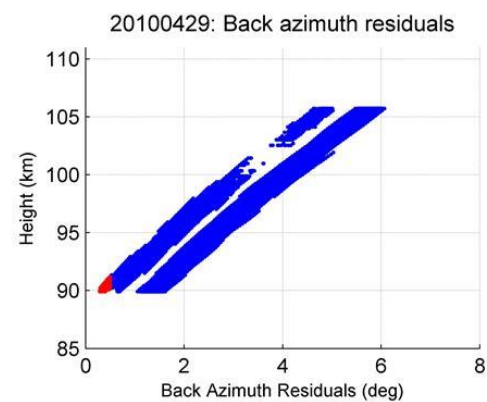
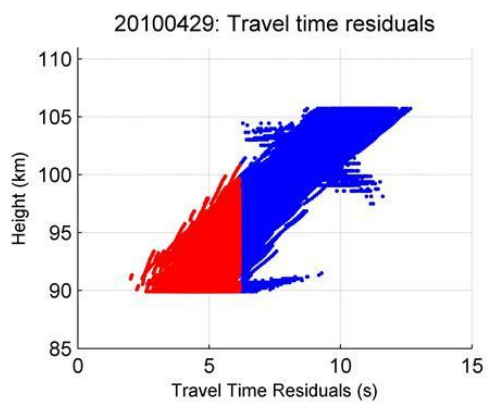
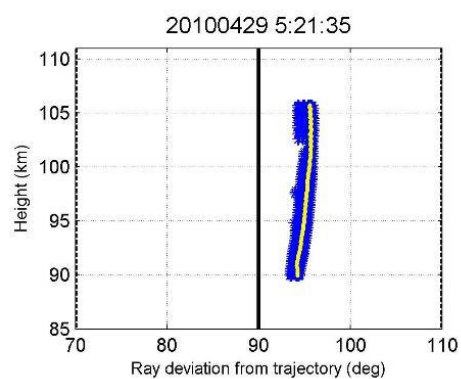
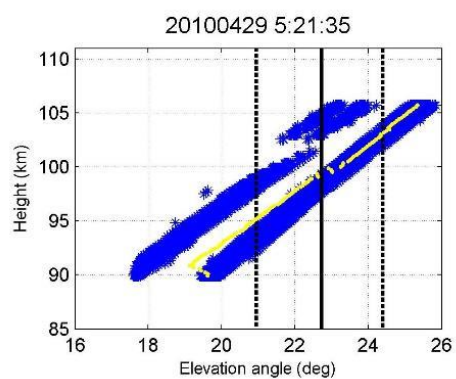
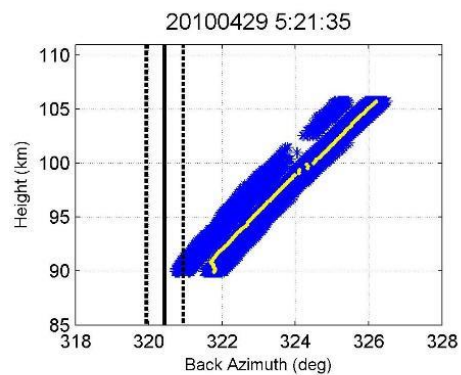
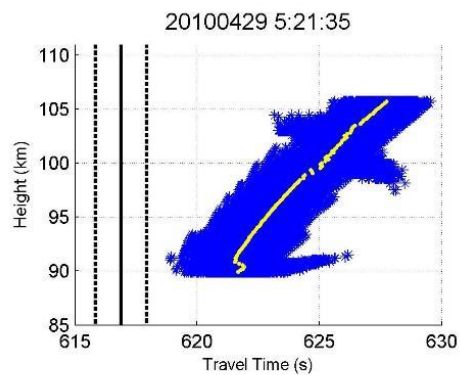


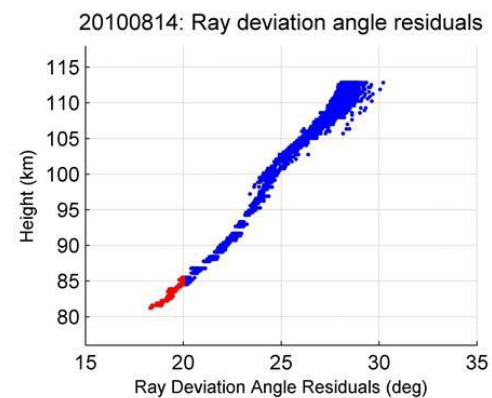
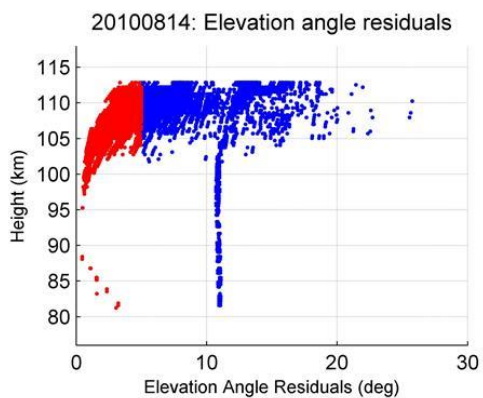
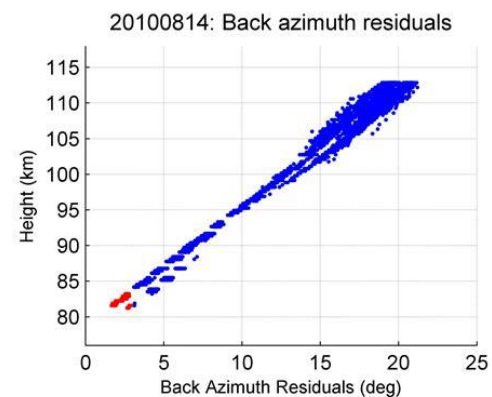
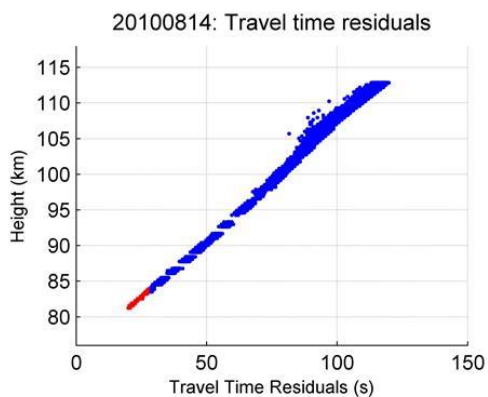
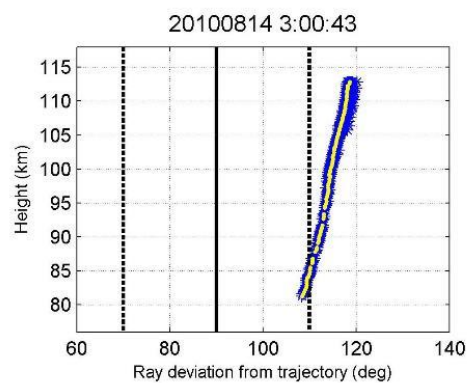
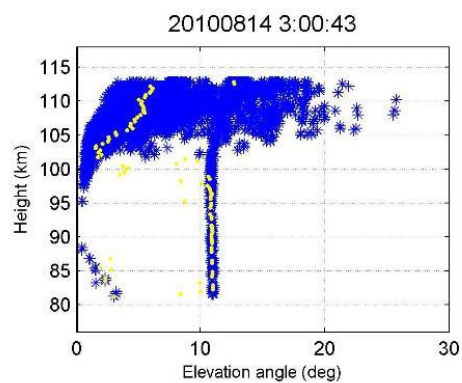
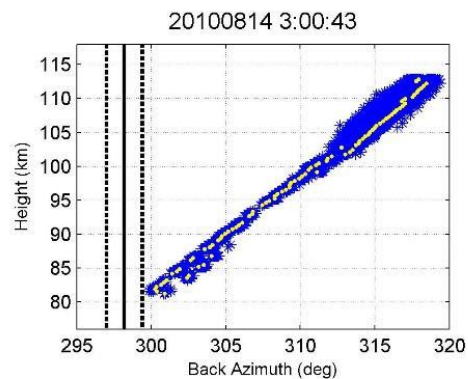
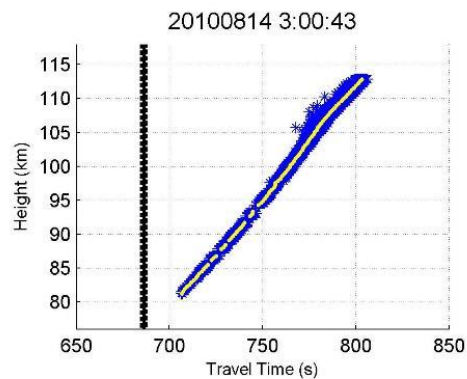


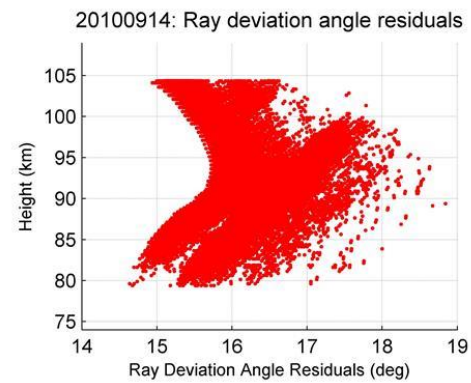
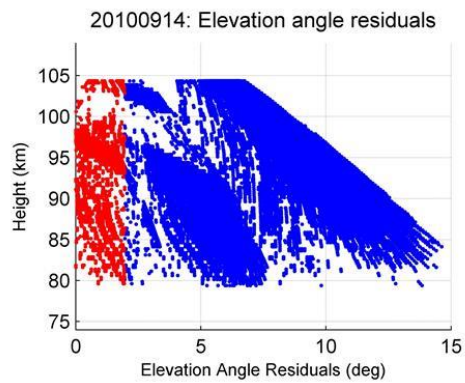
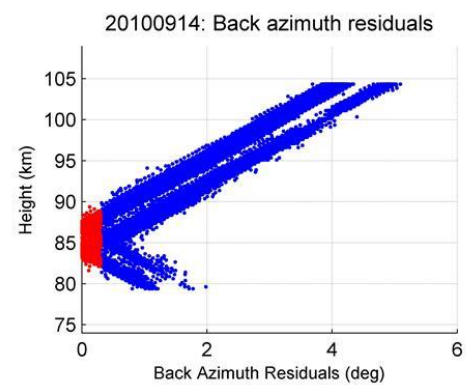
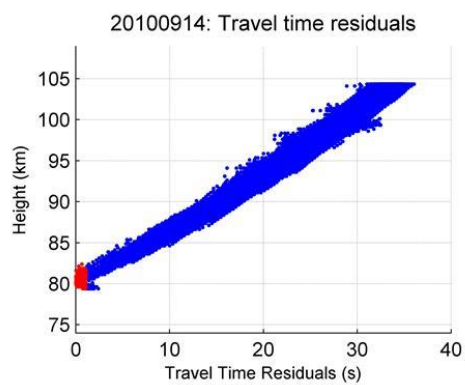
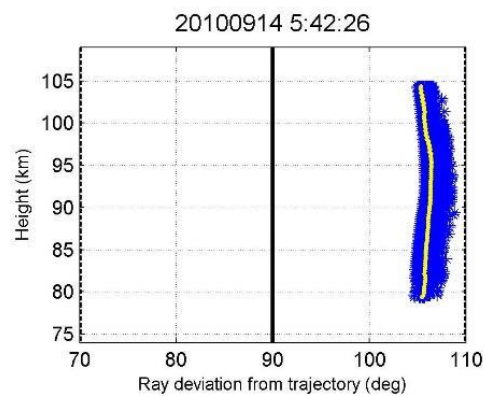
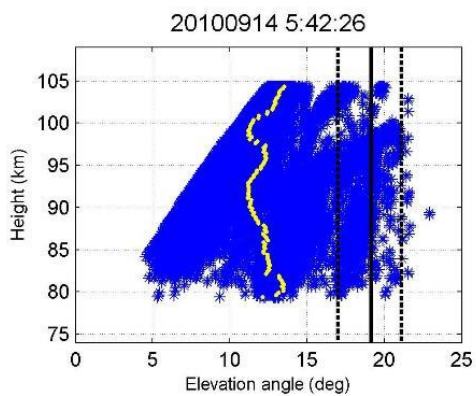
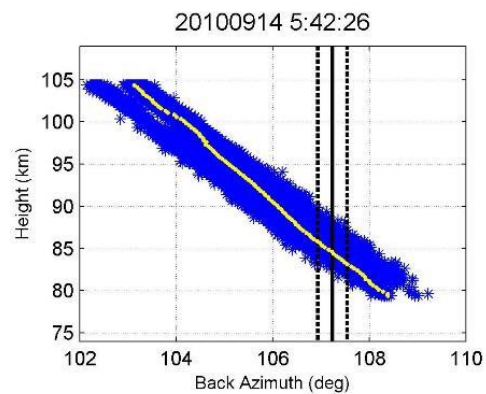
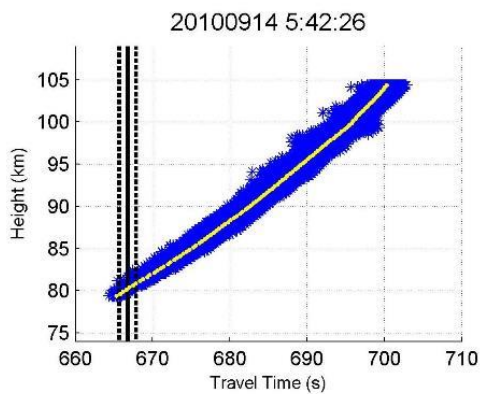




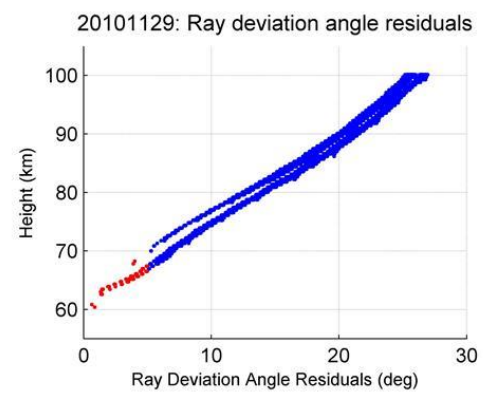
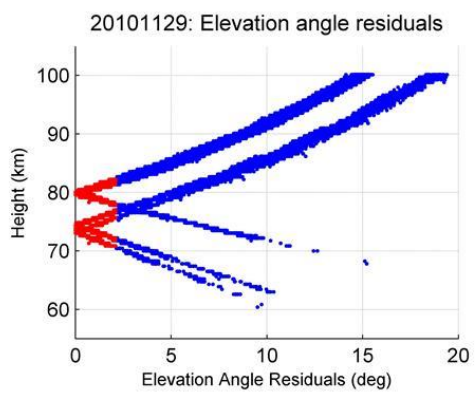
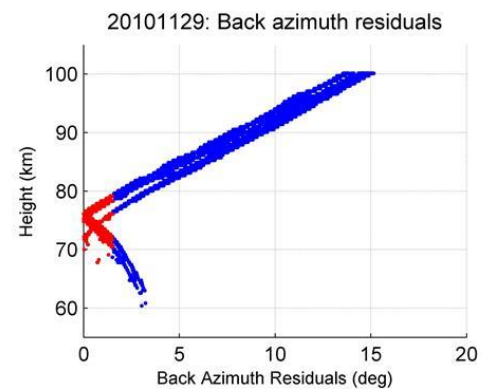
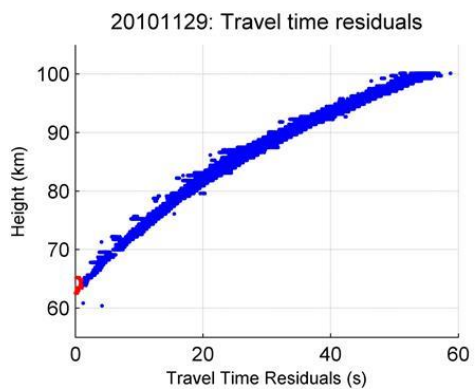
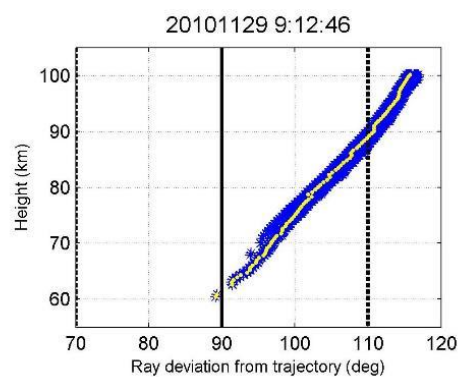
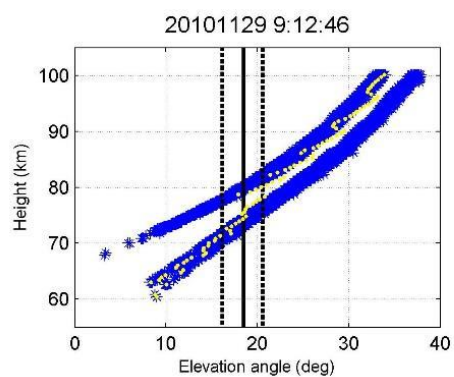
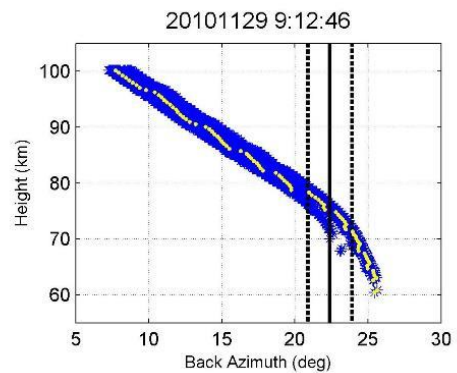
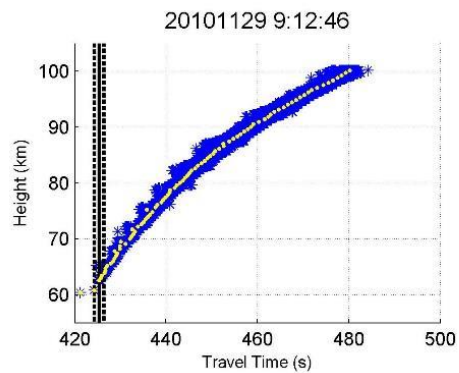


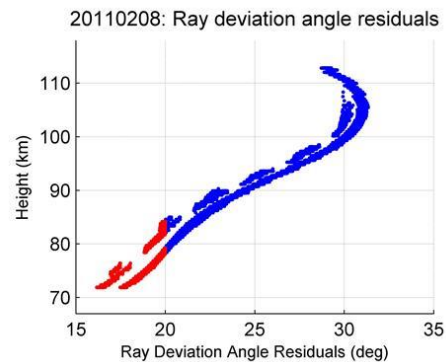
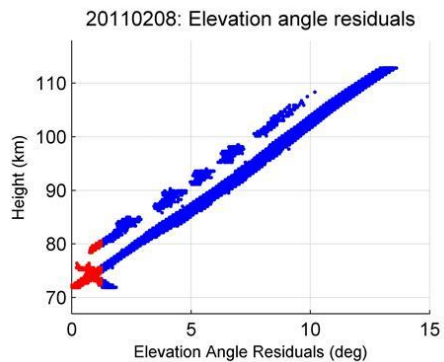
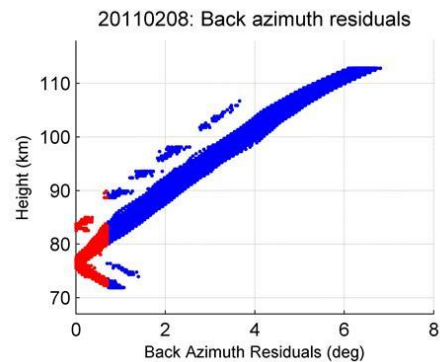
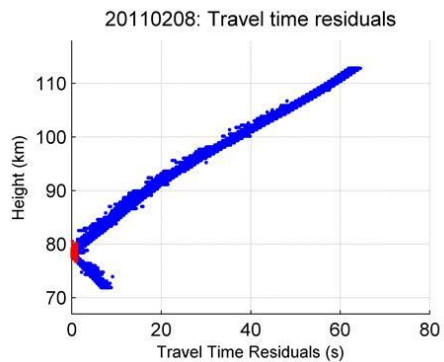
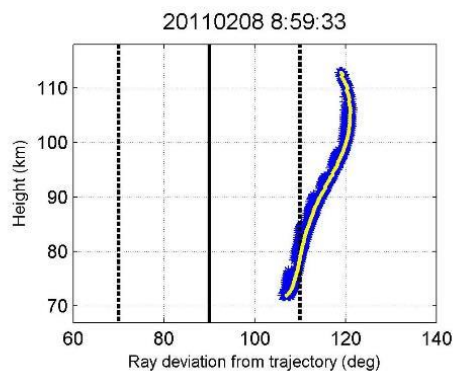
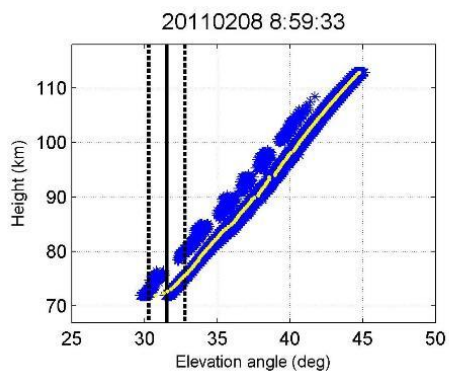
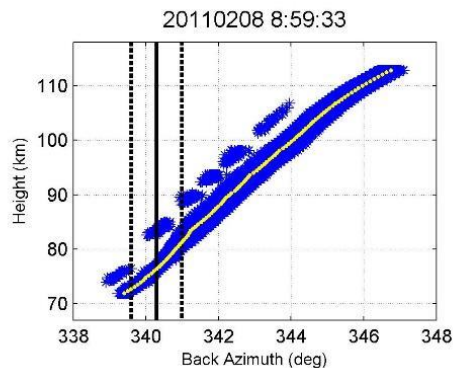
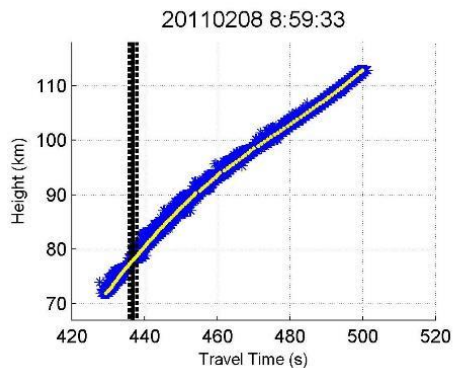


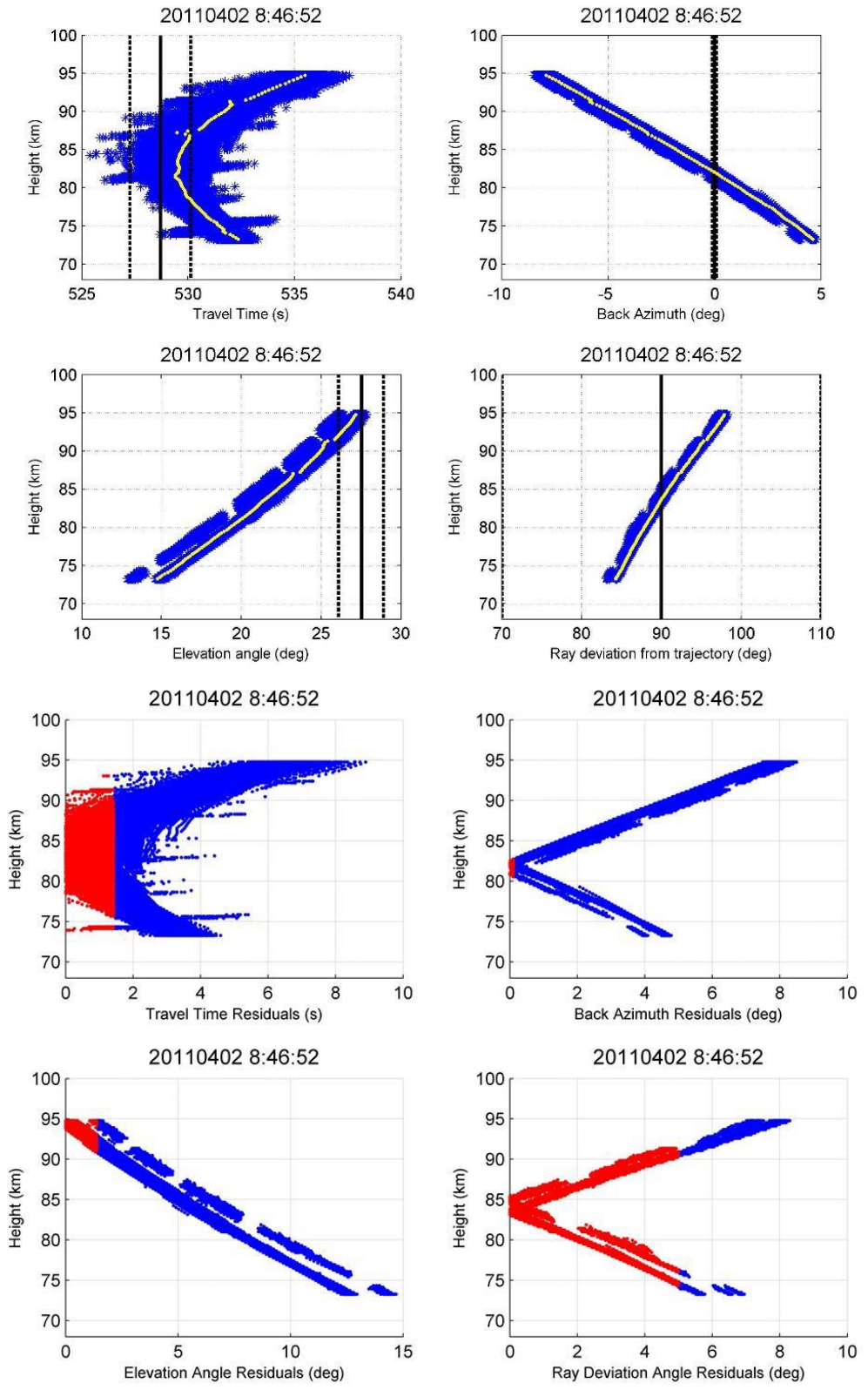


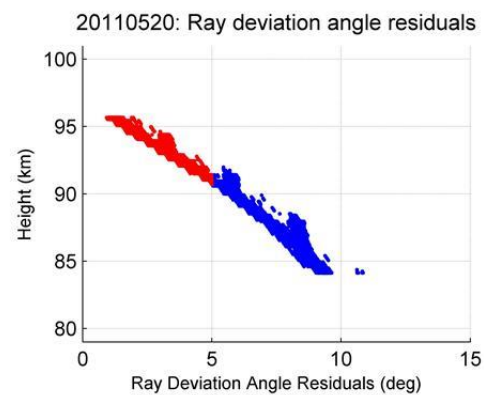
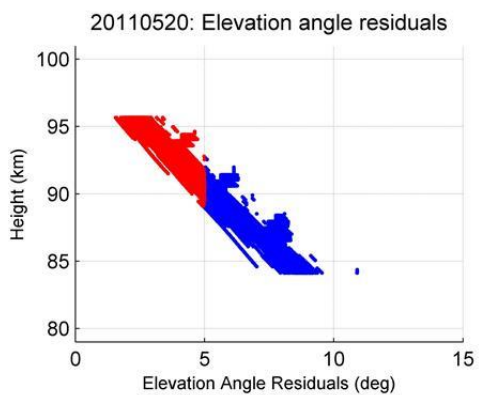
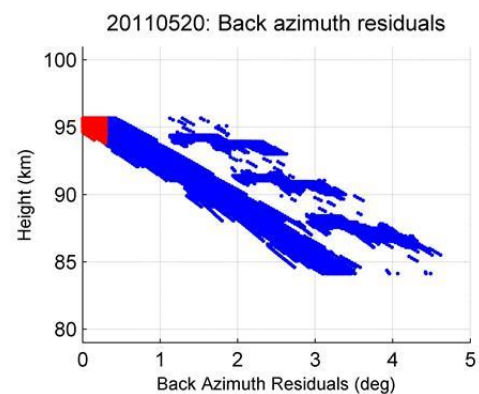
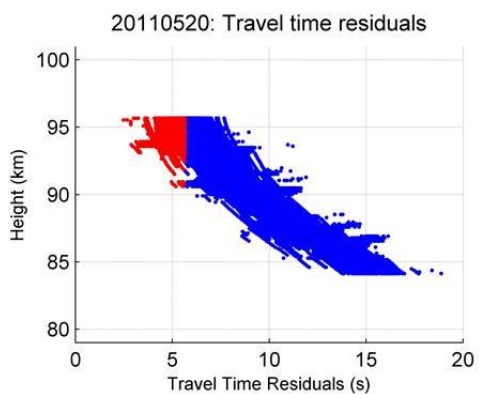
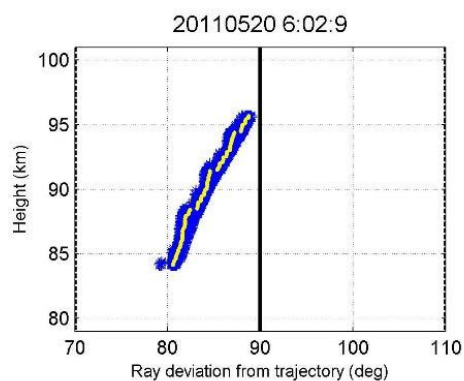
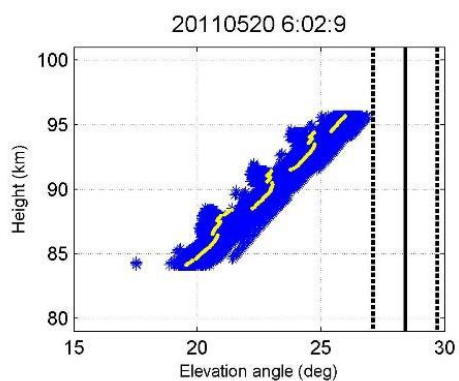
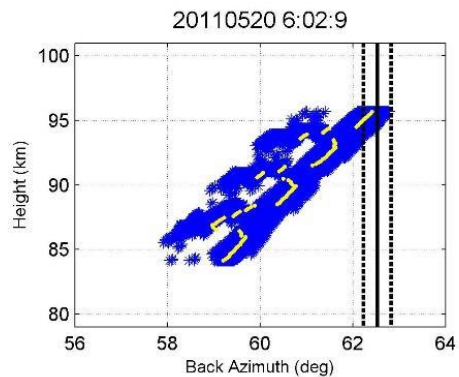
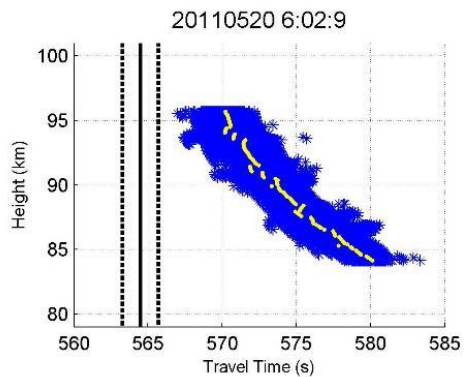




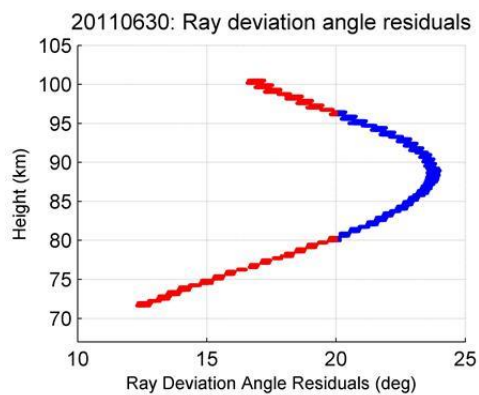
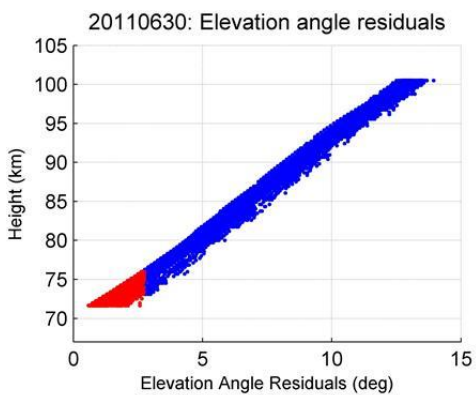
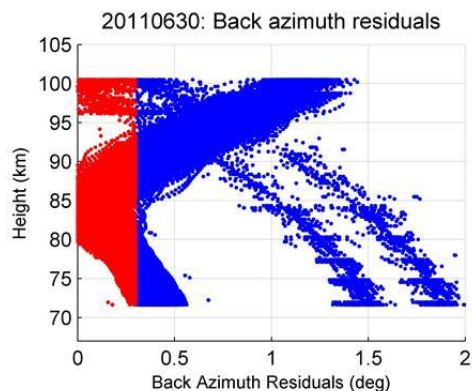
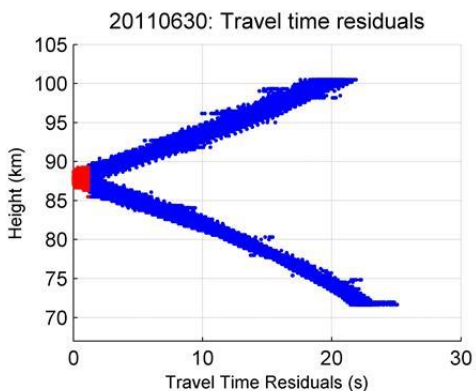
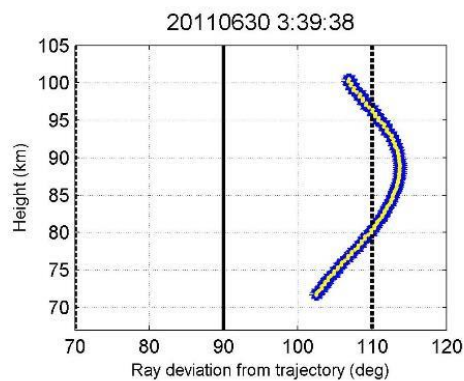
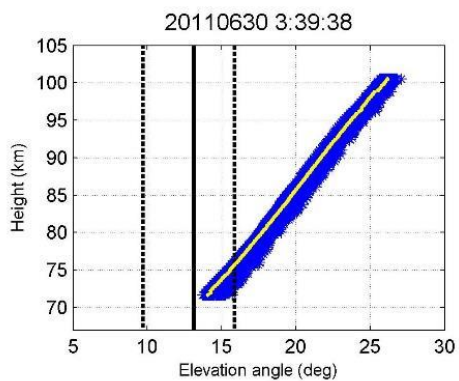
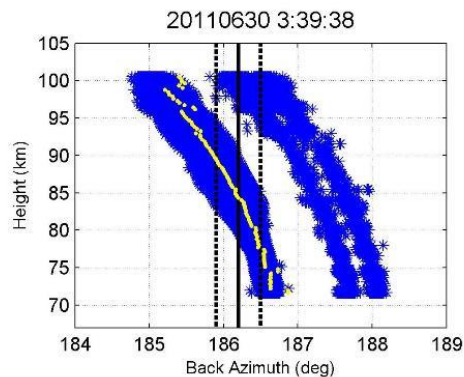
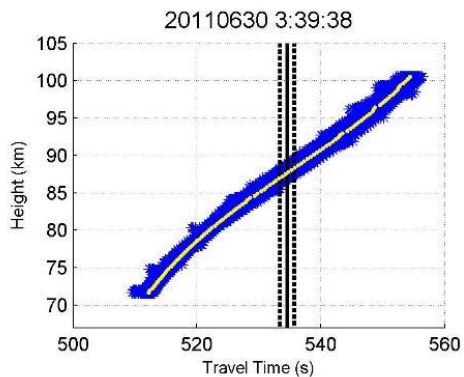


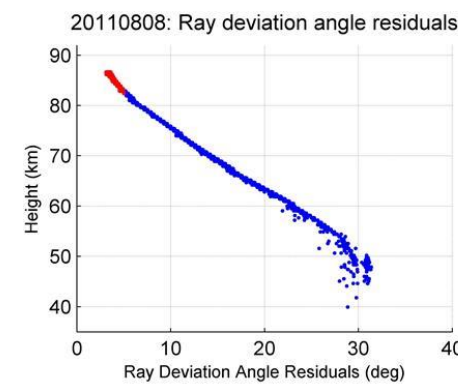
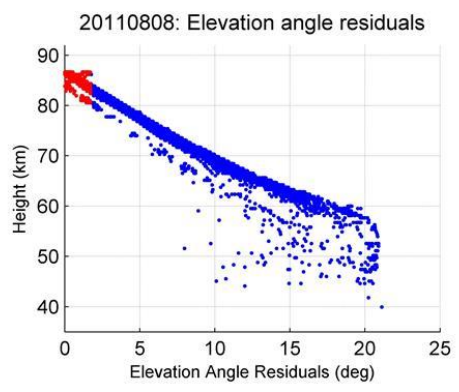
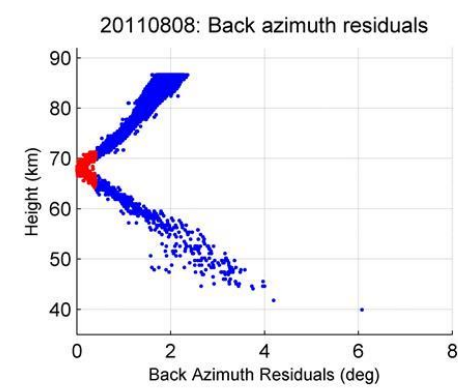
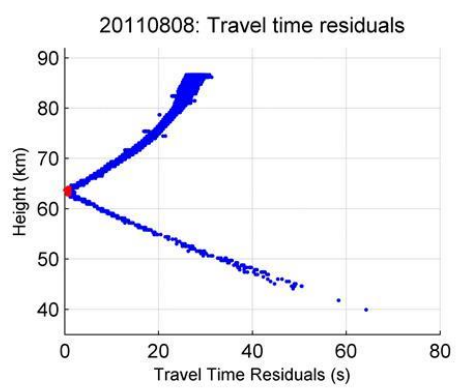
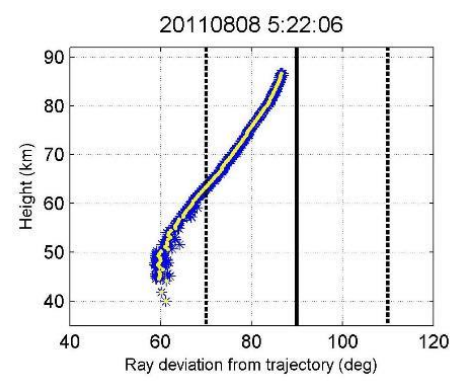
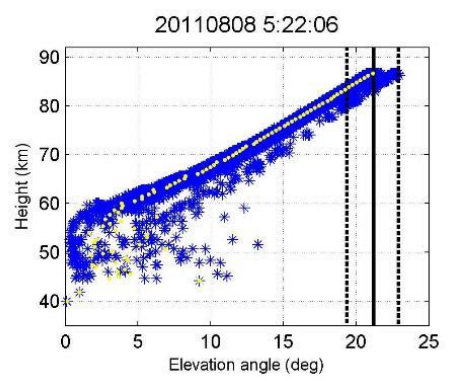
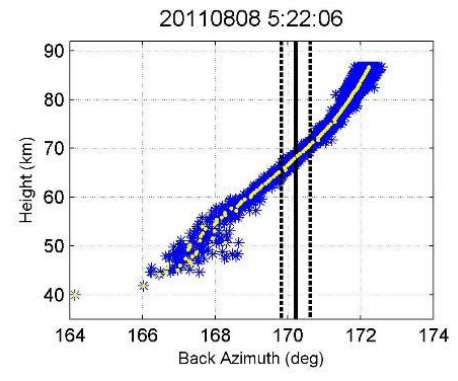
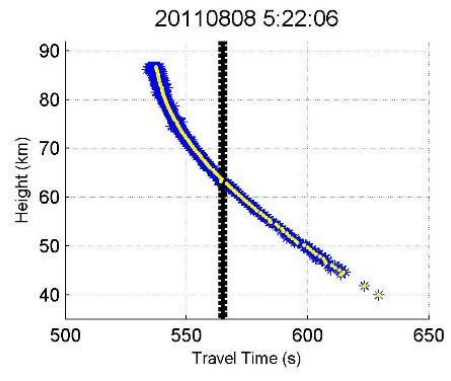


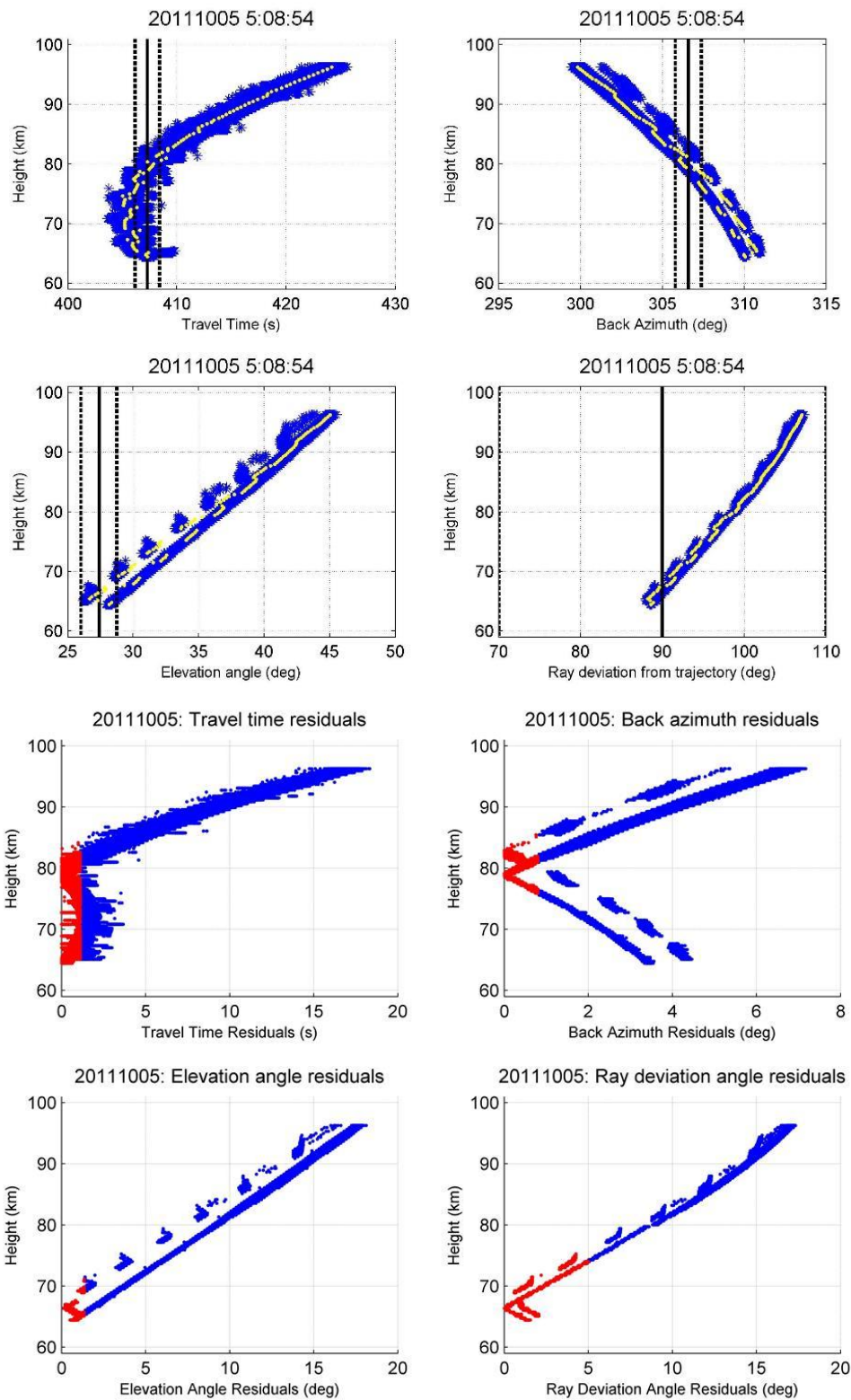


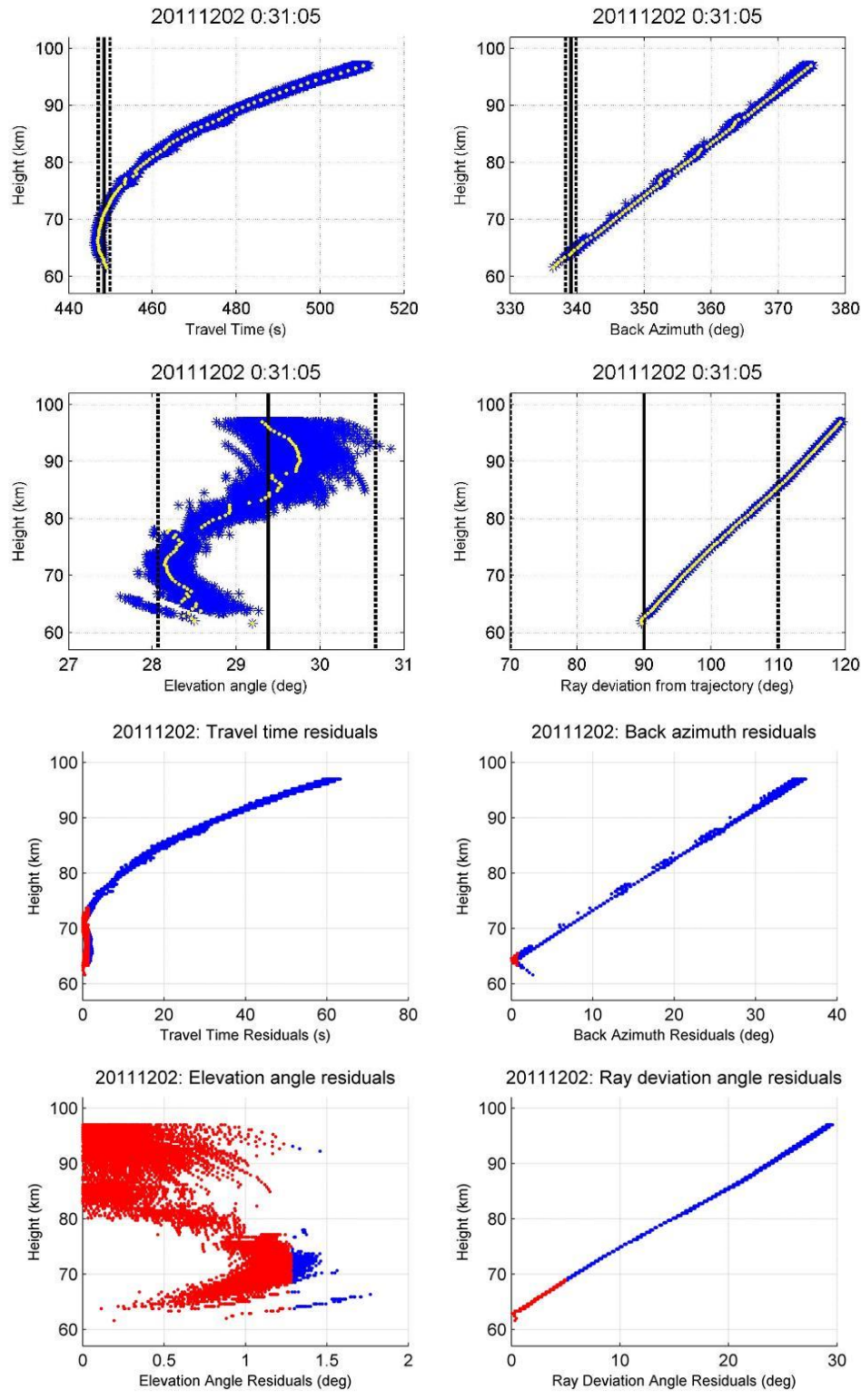






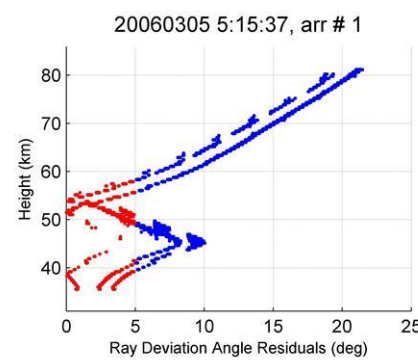
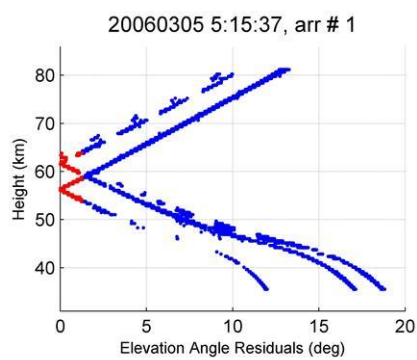
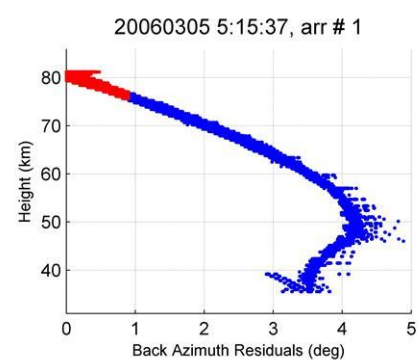
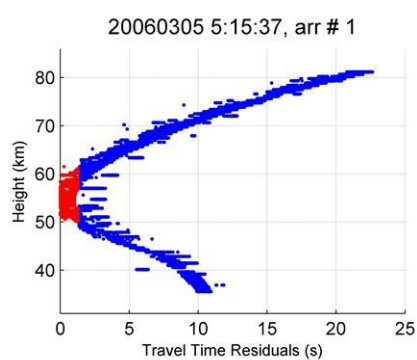
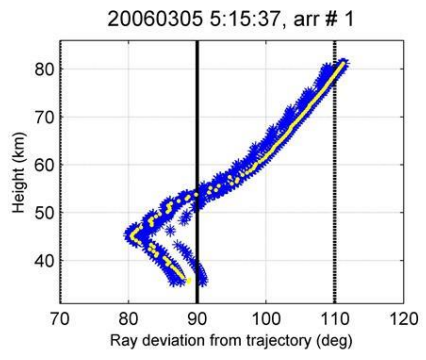
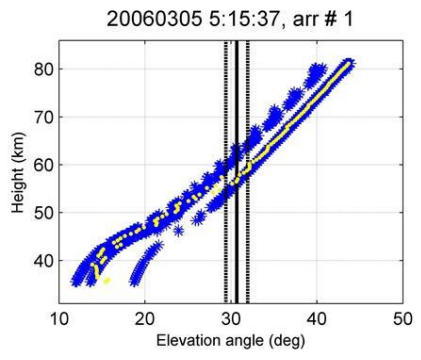
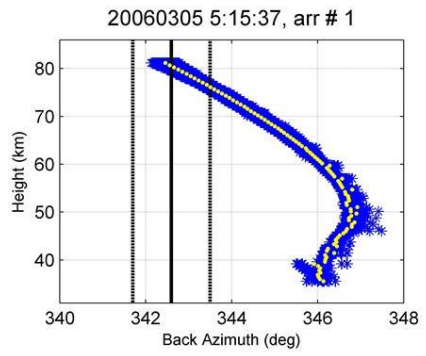
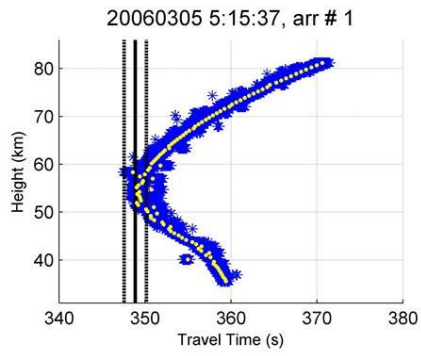


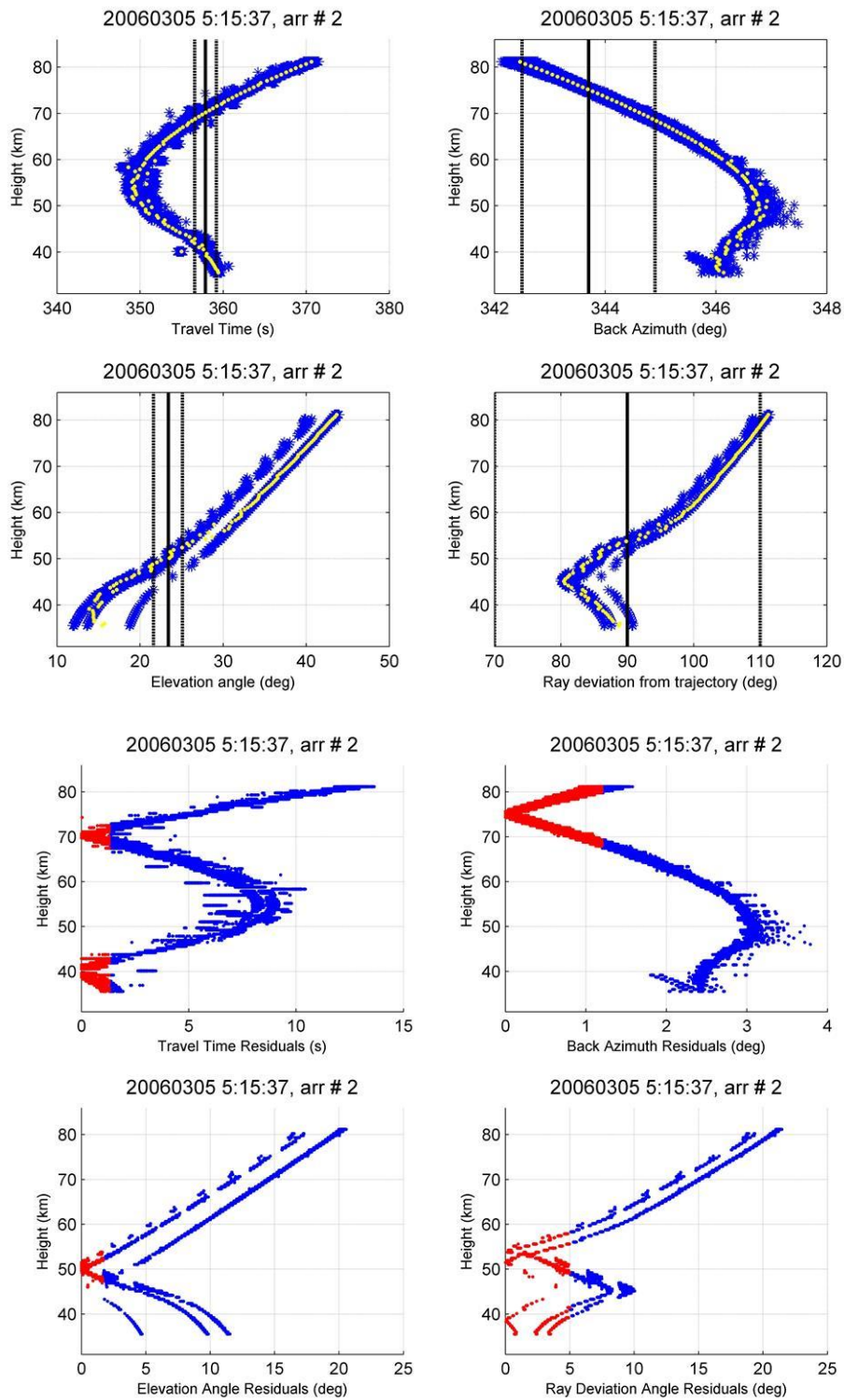


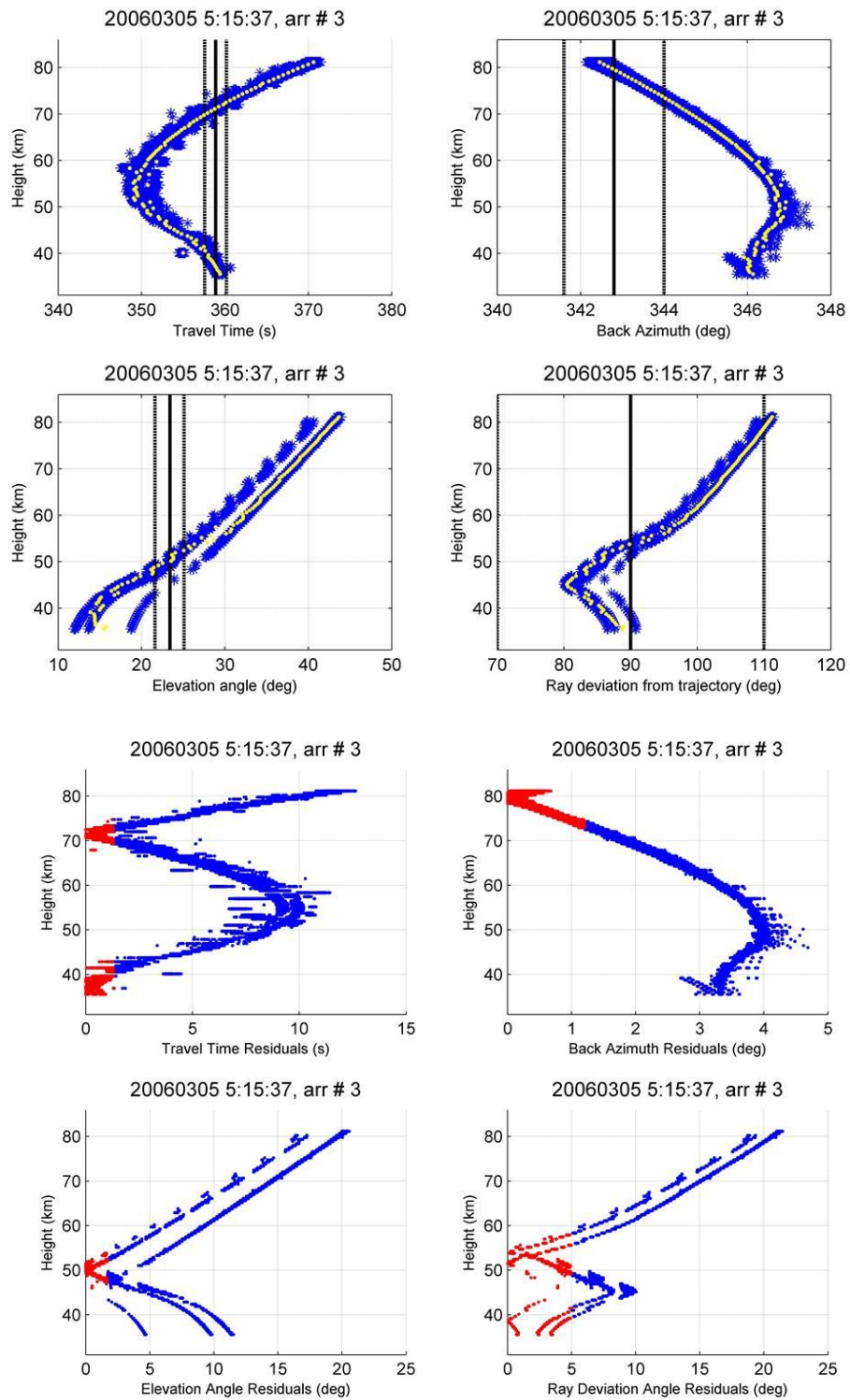


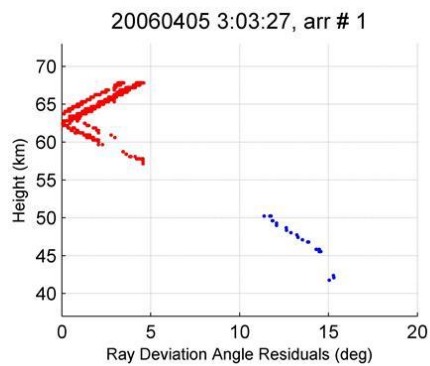
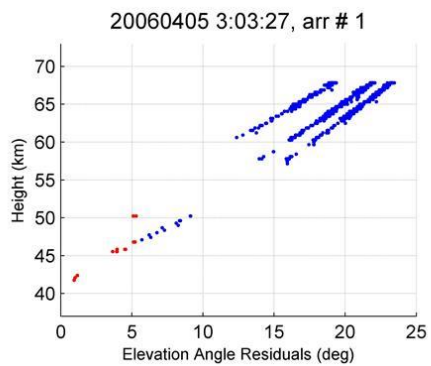
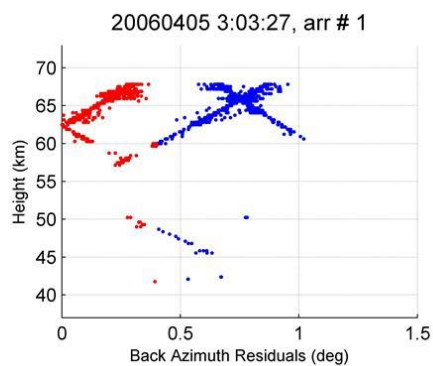
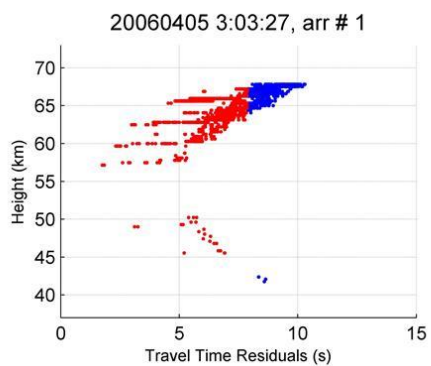
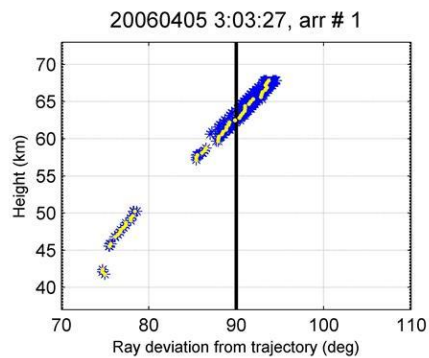
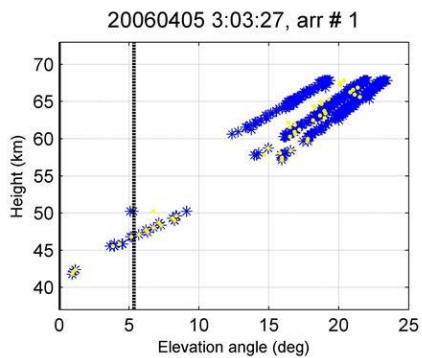
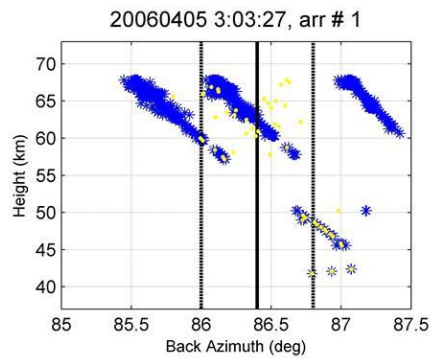
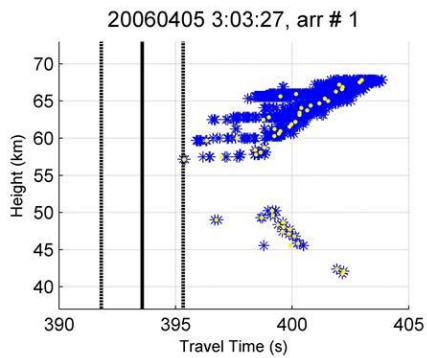
### Multi Arrival Events



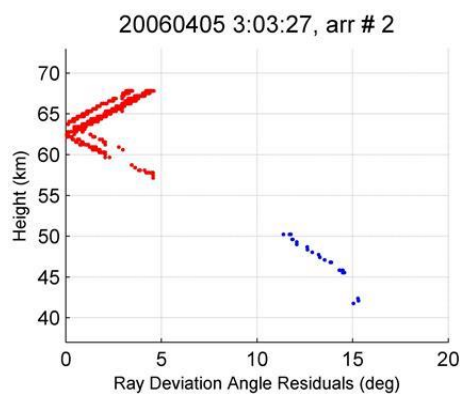
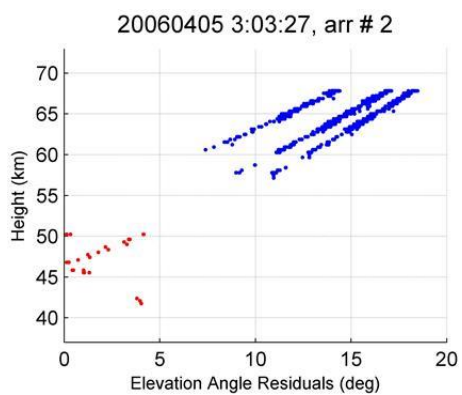
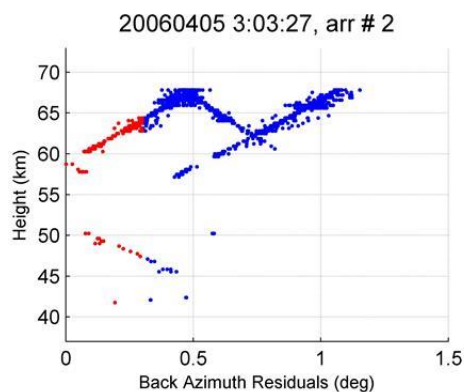
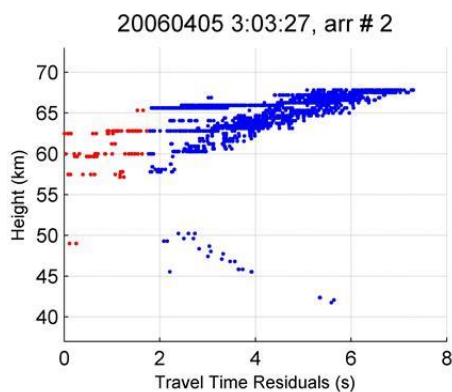
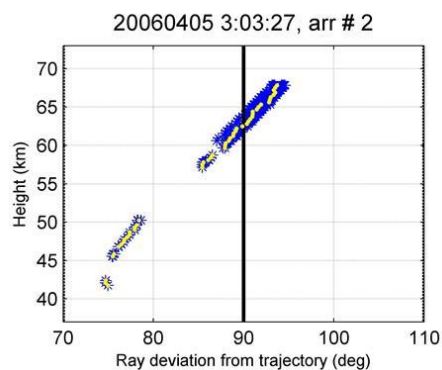
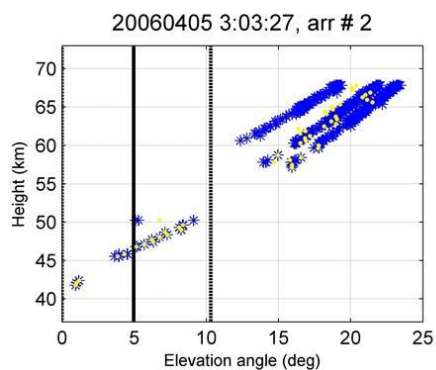
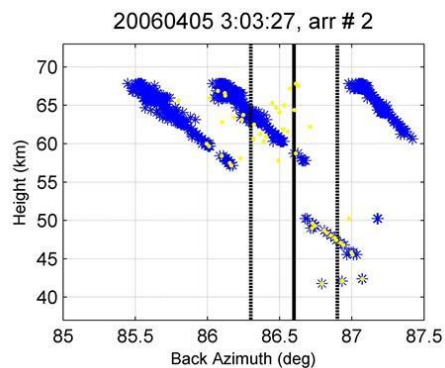
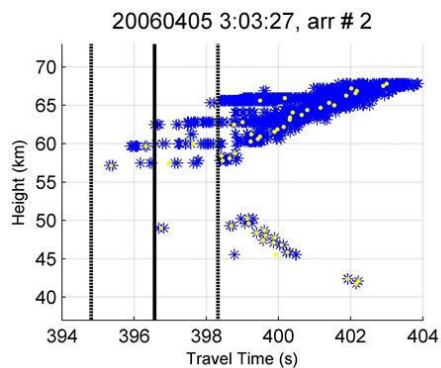


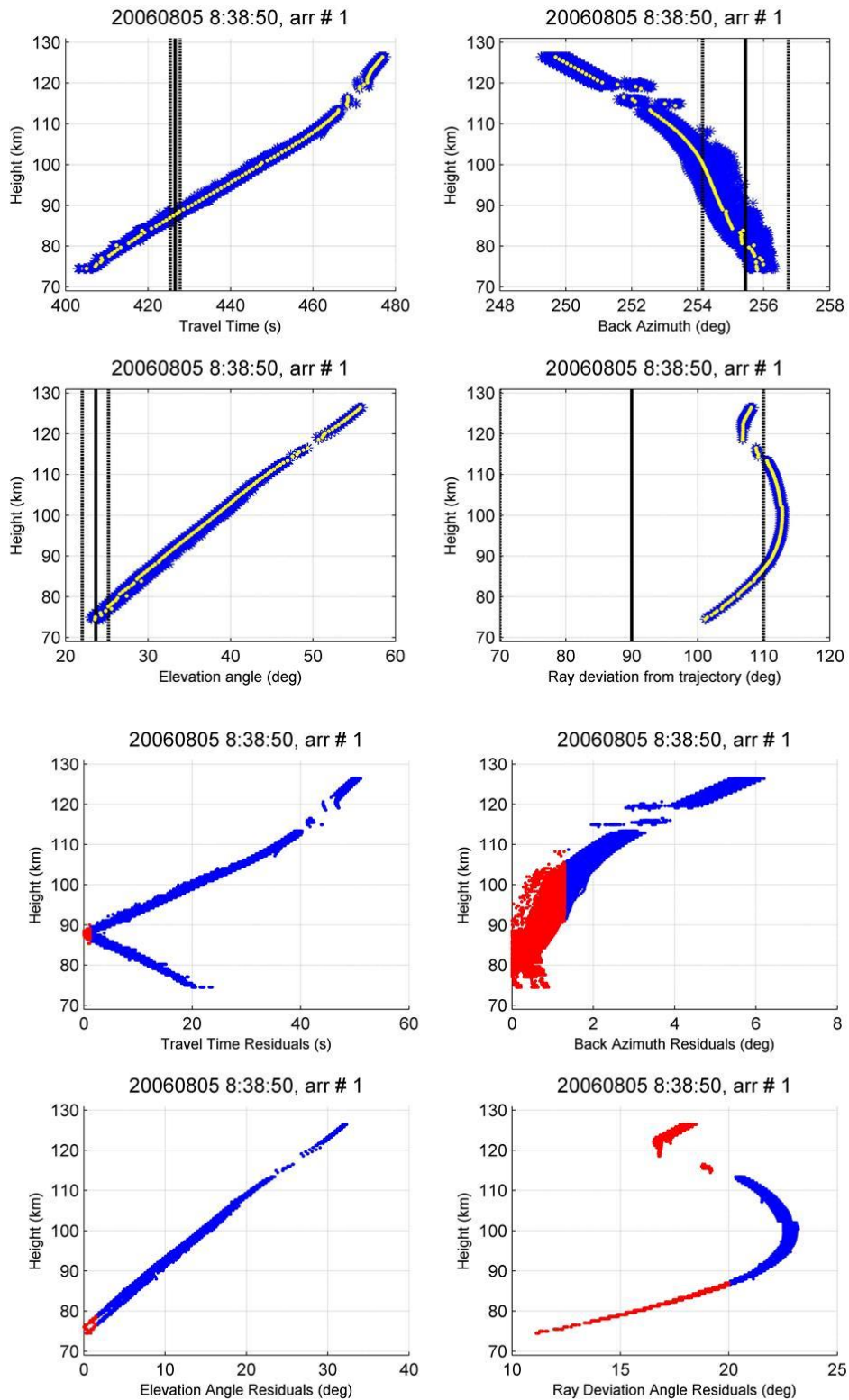


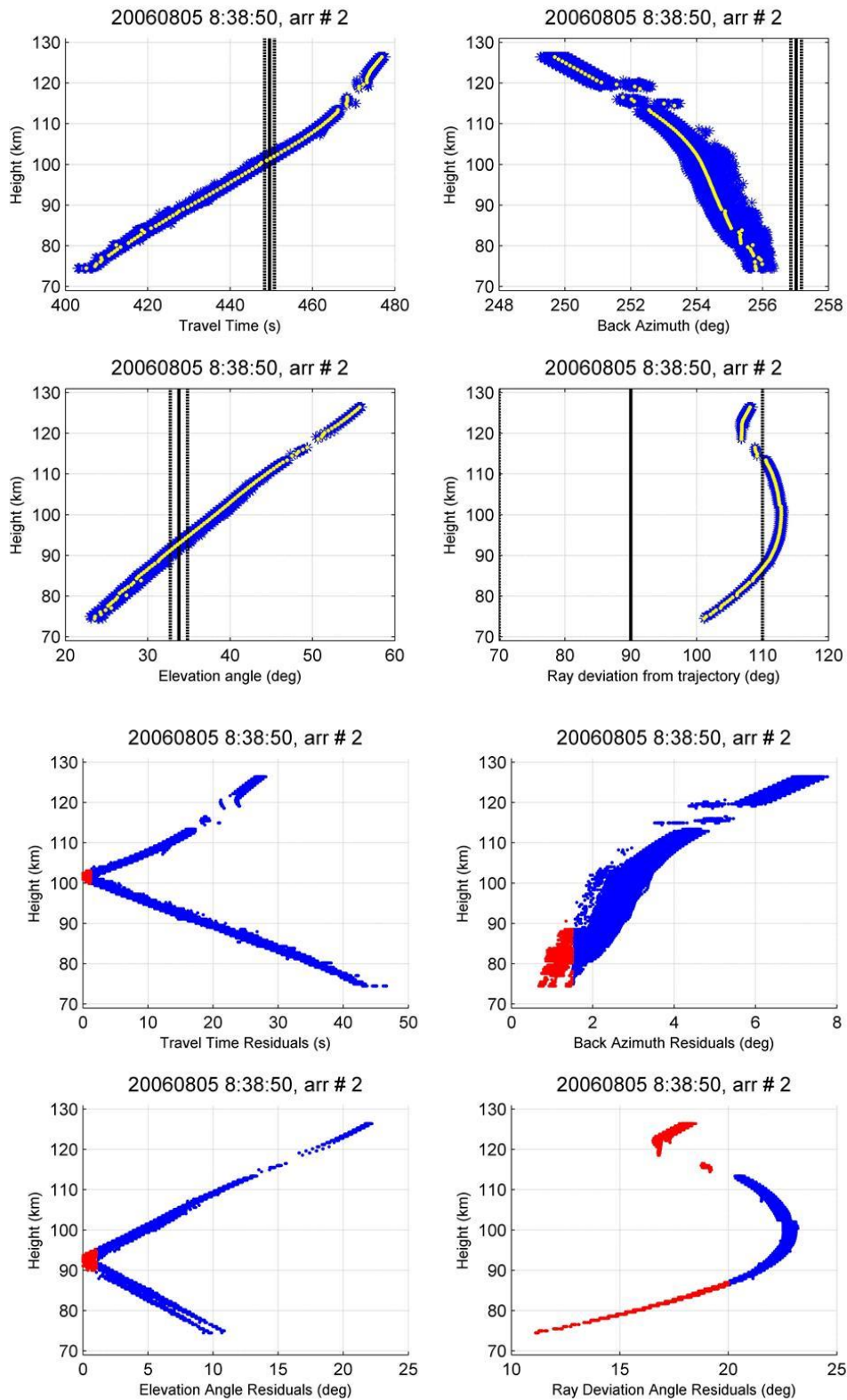


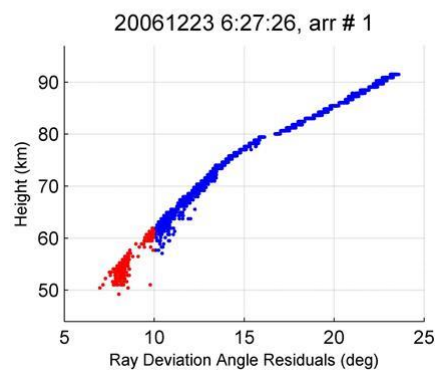
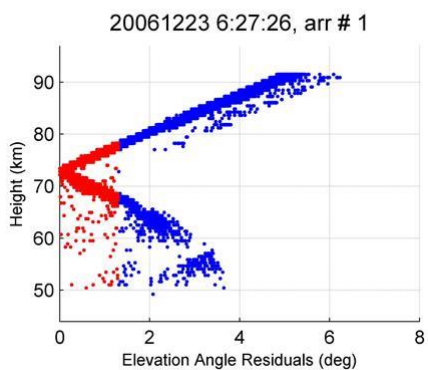
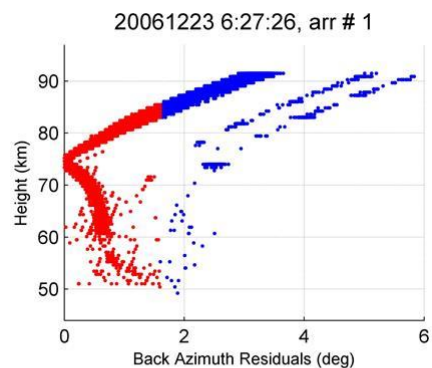
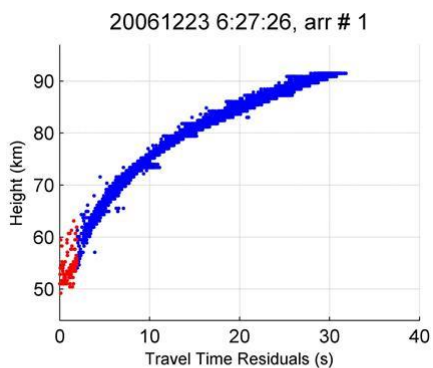
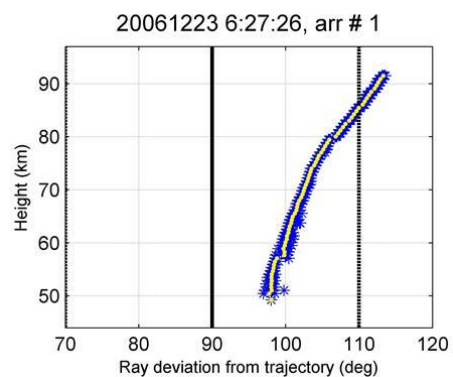
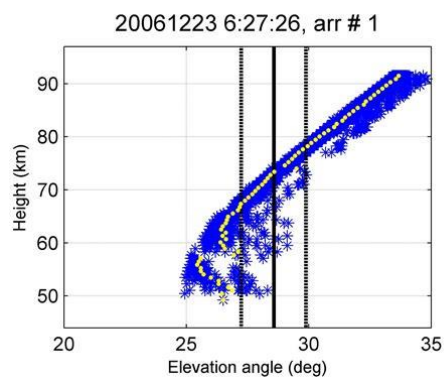
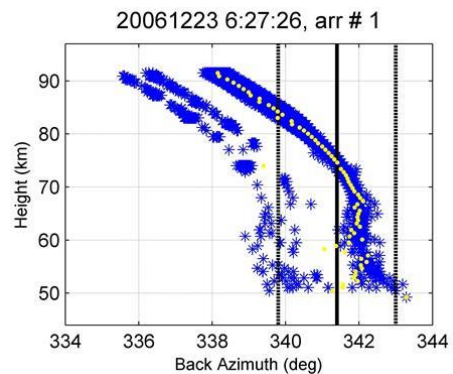
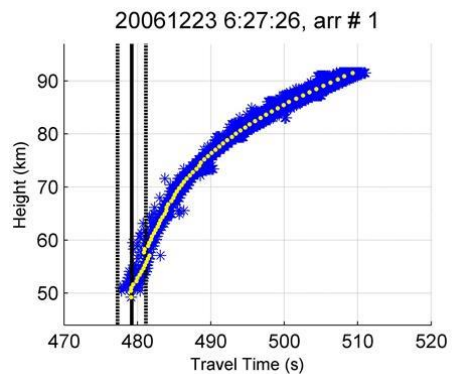


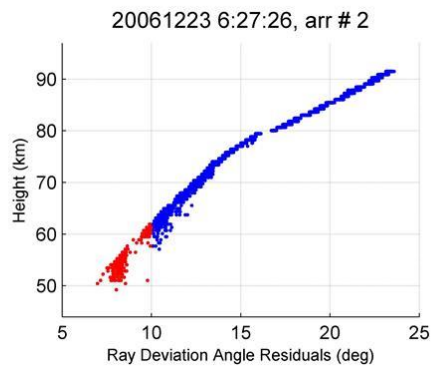
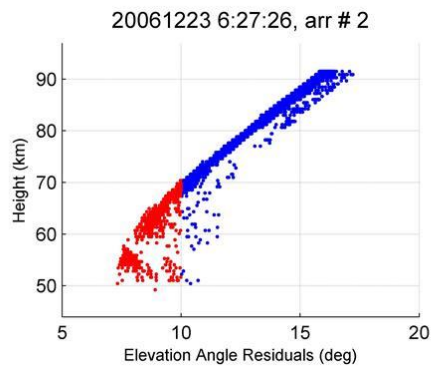
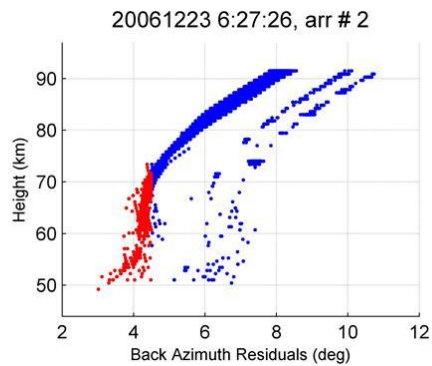
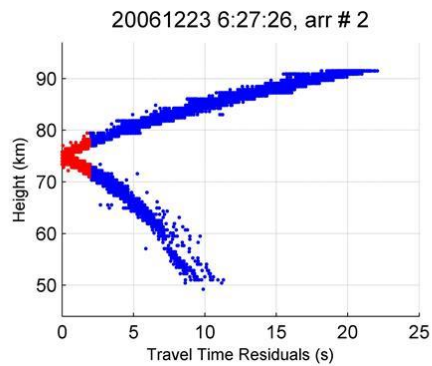
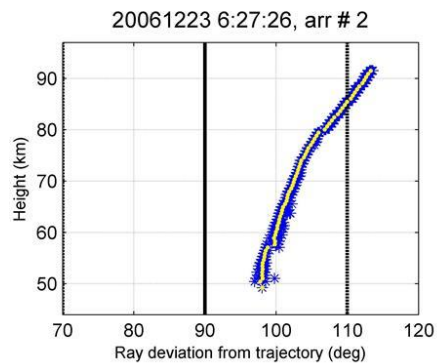
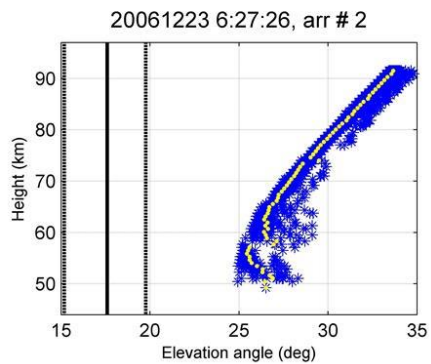
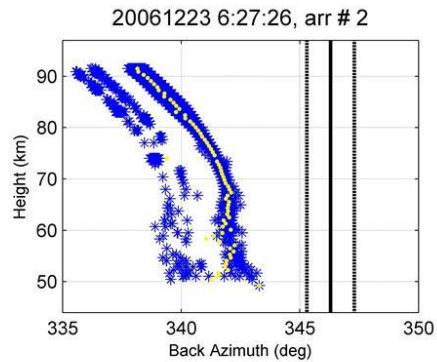
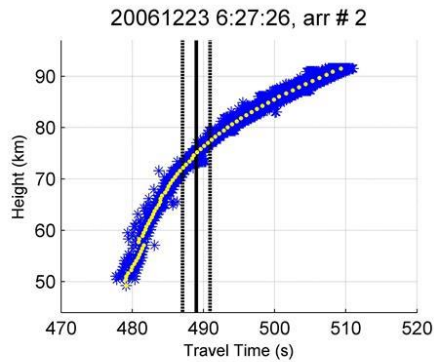




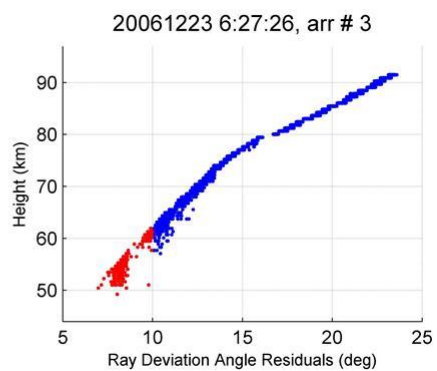
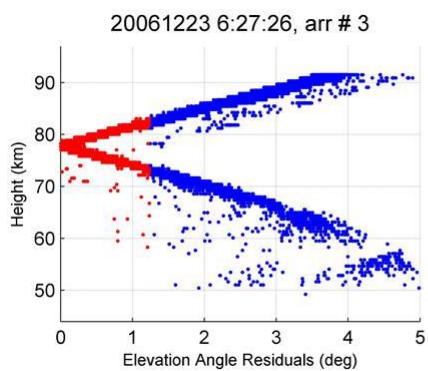
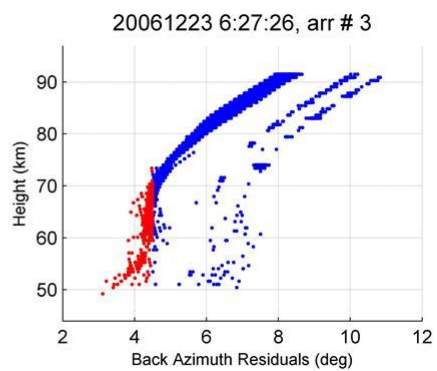
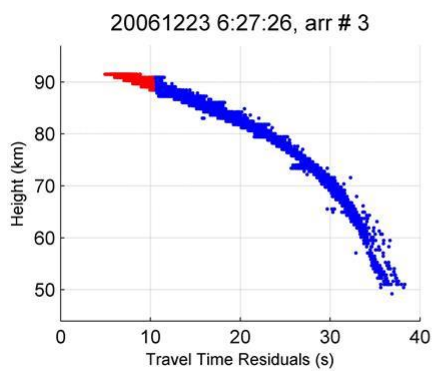
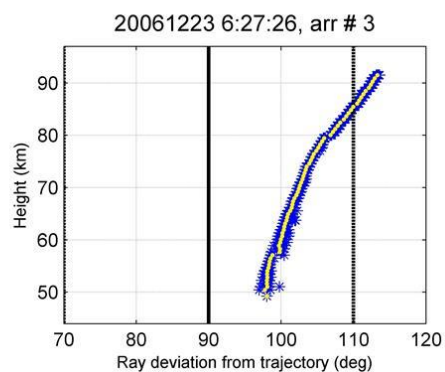
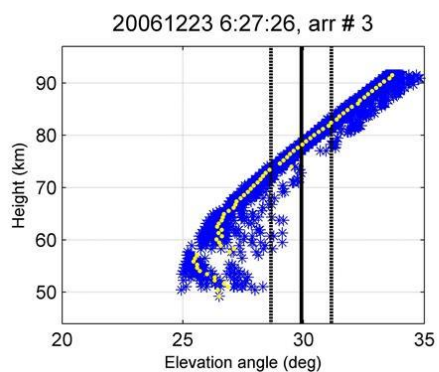
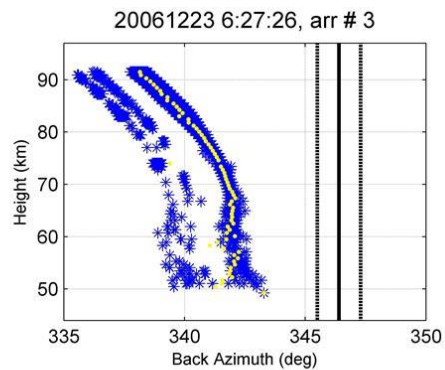
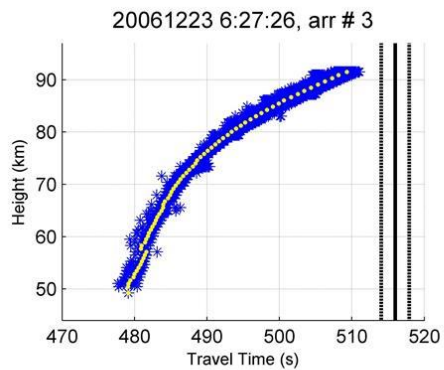


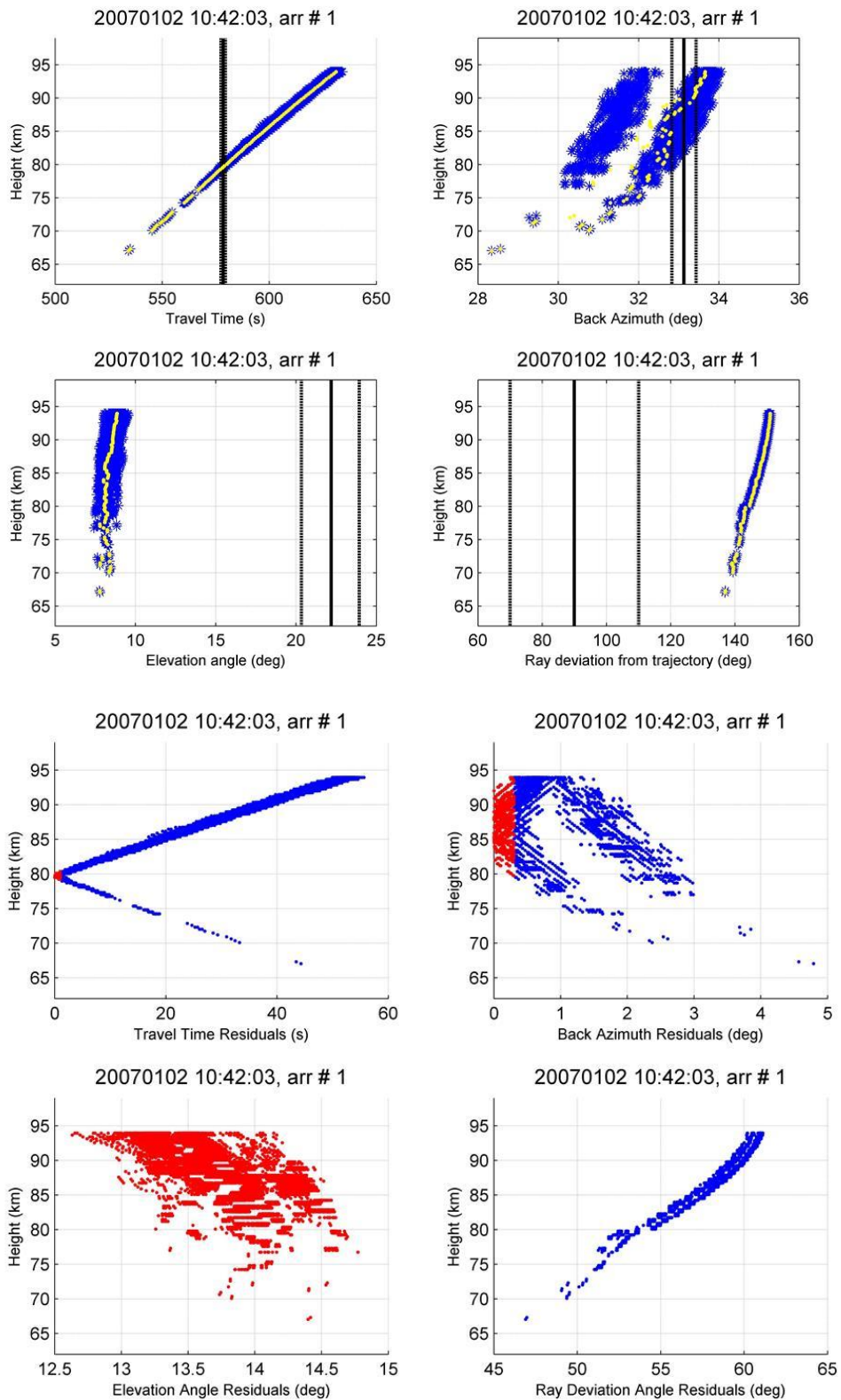






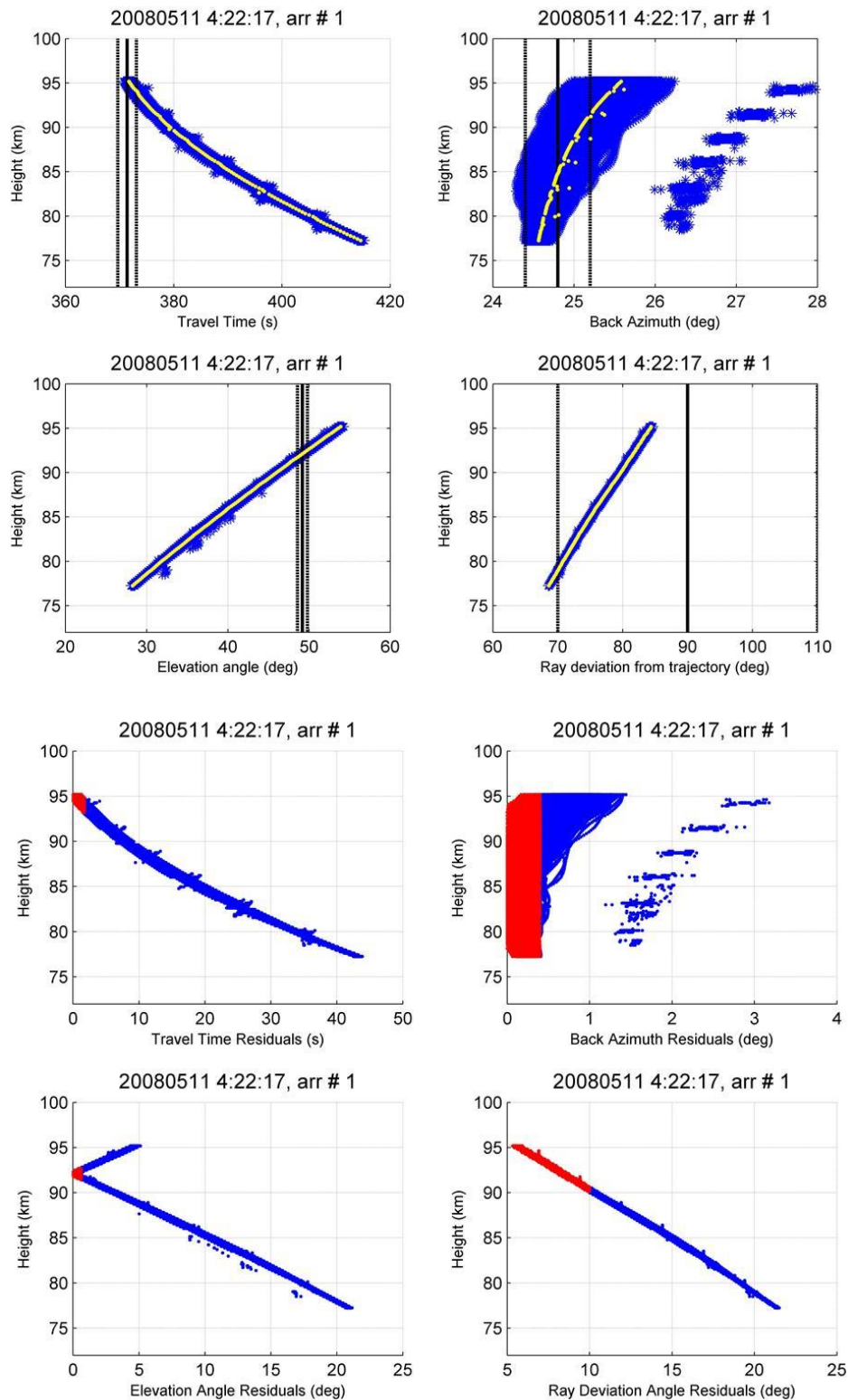


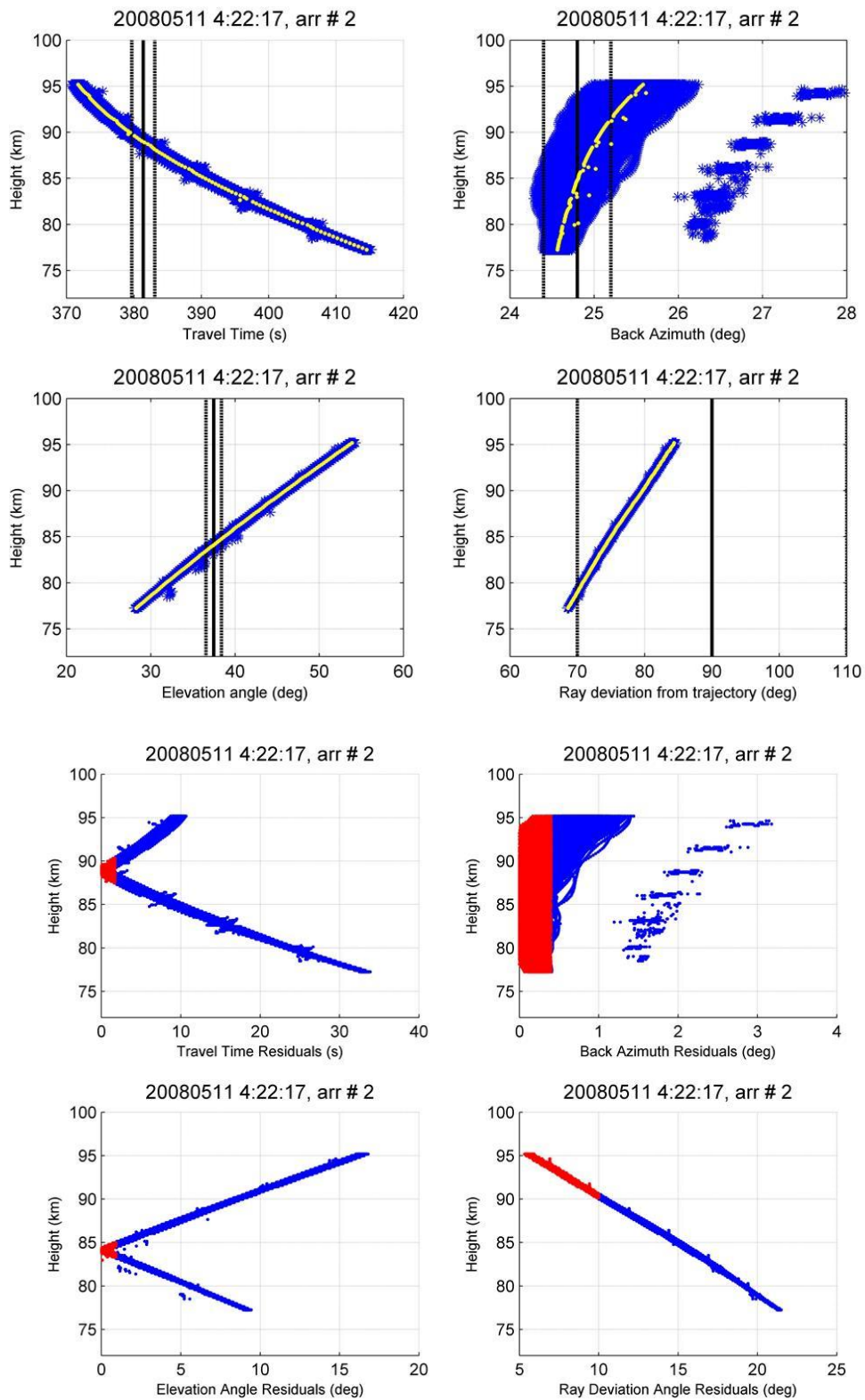


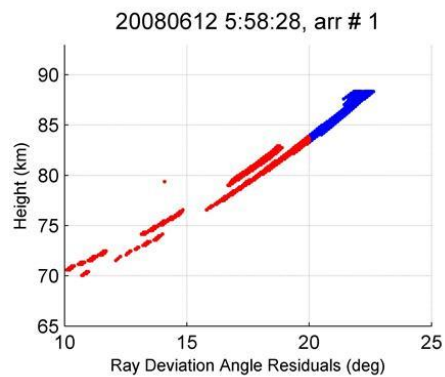
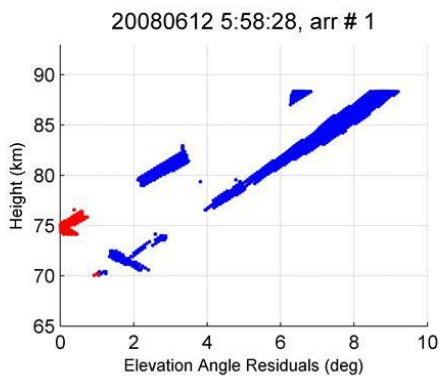
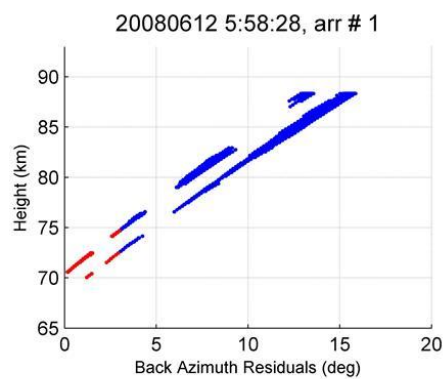
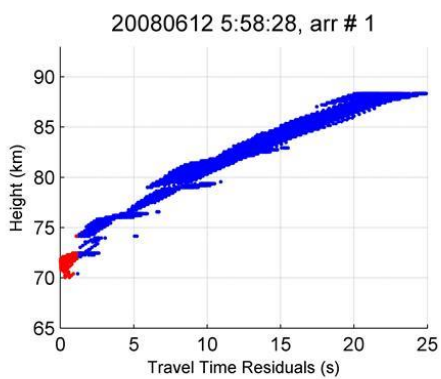
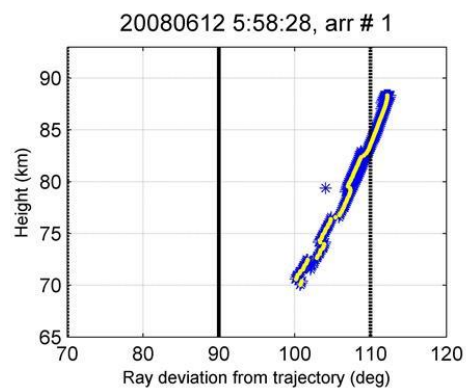
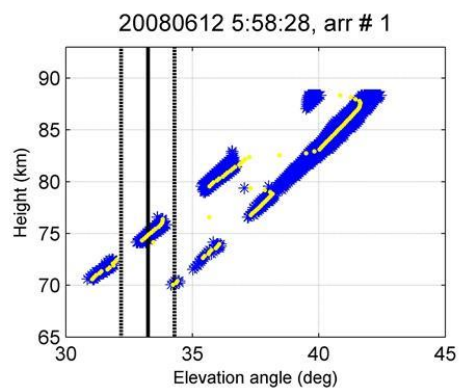
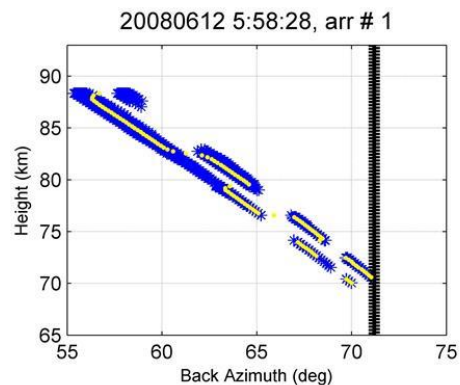
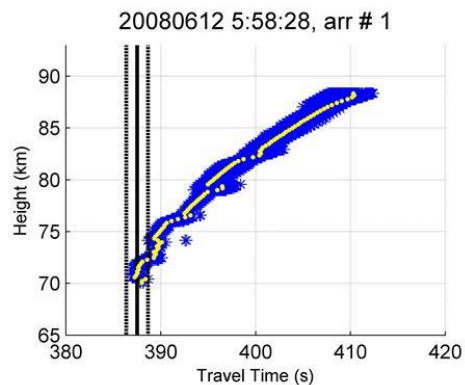


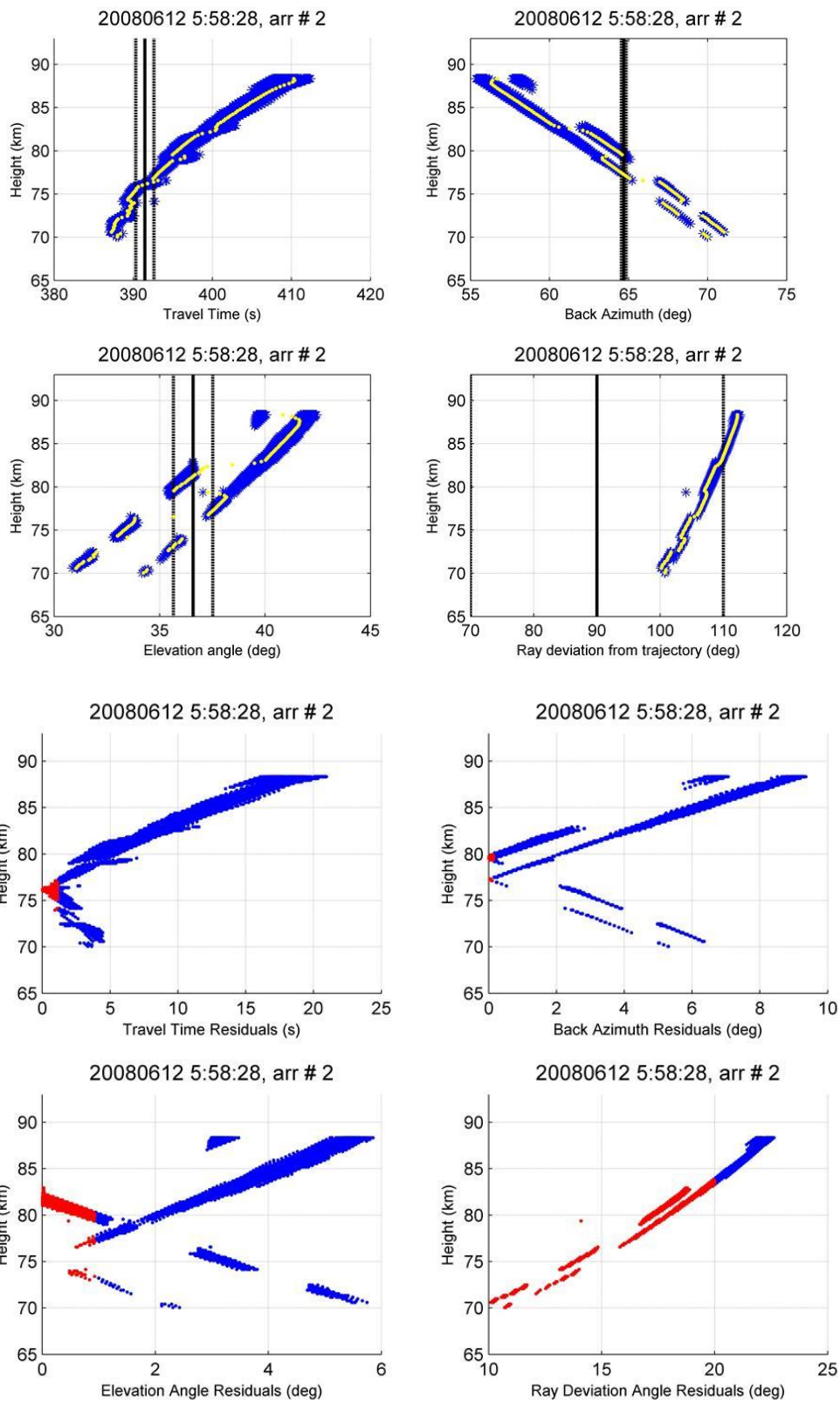


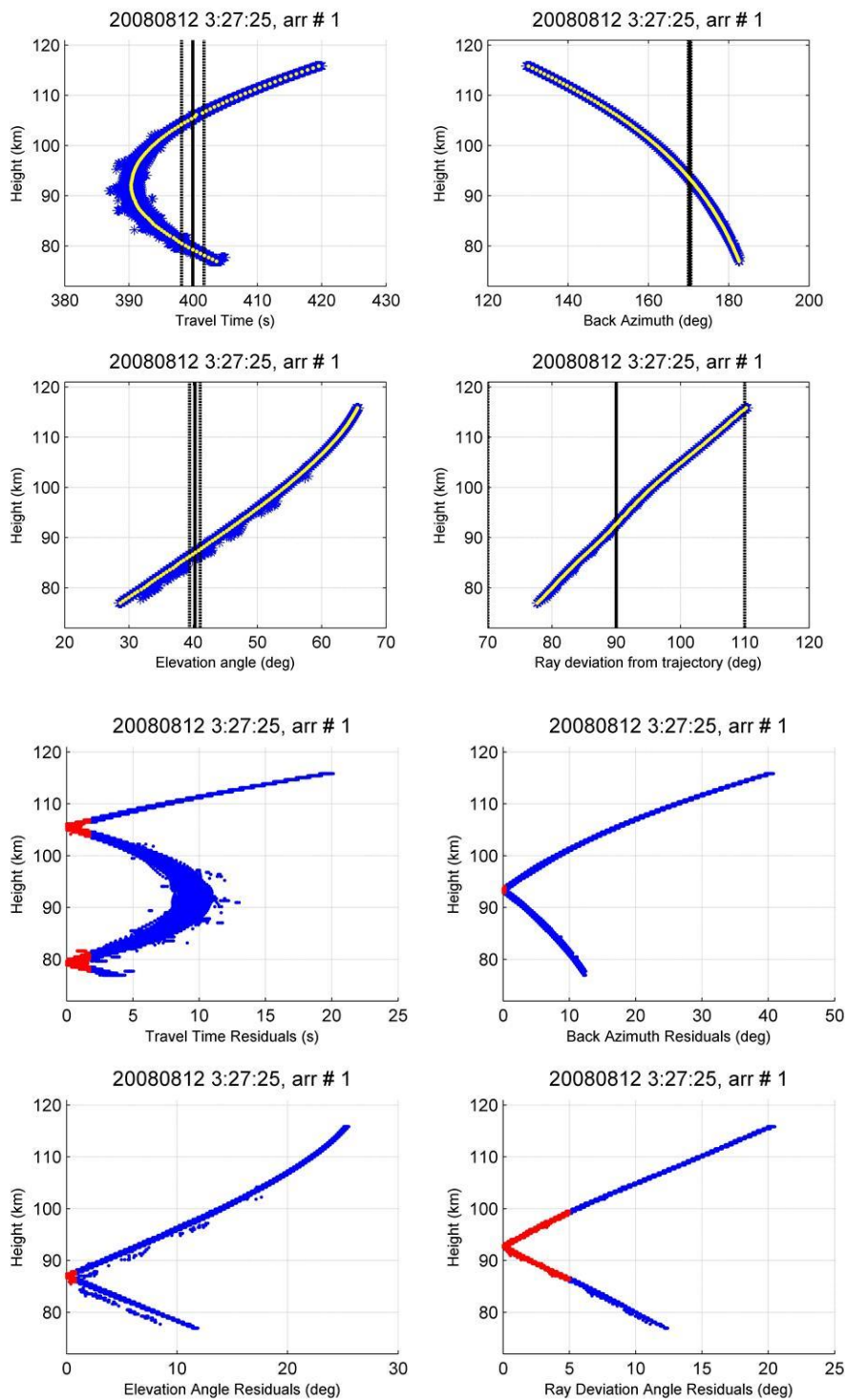




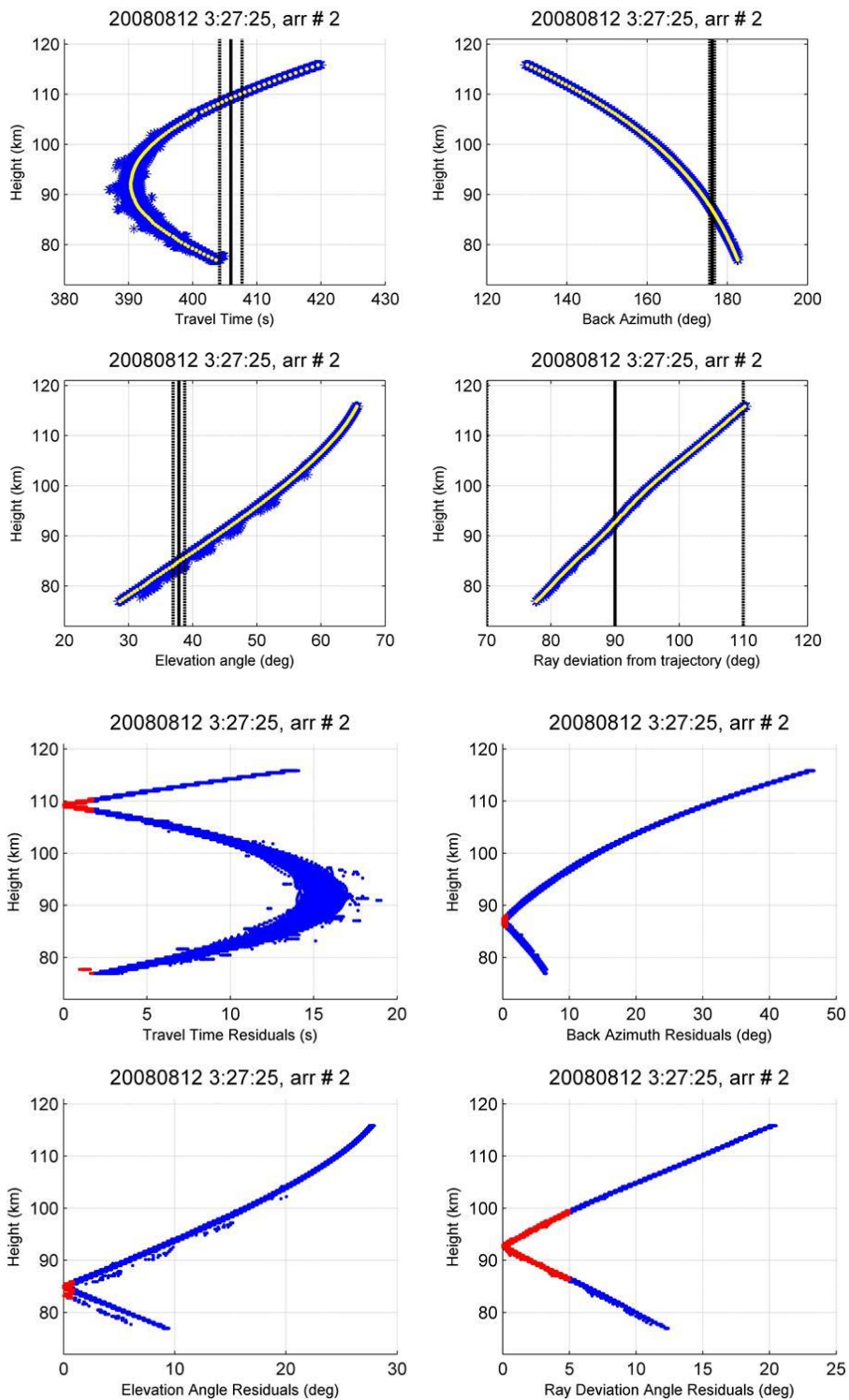


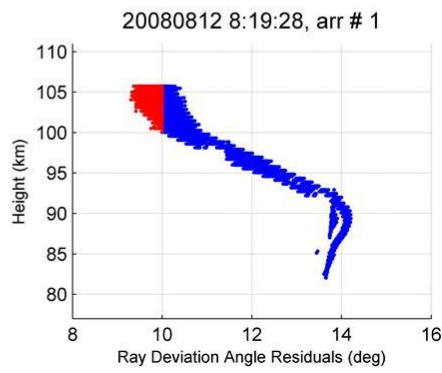
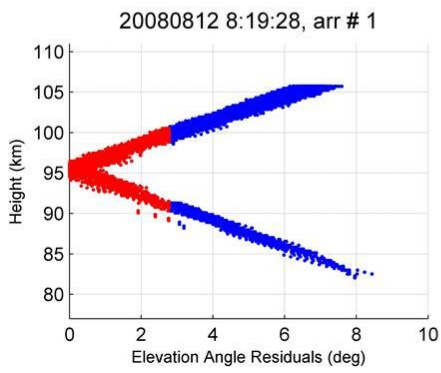
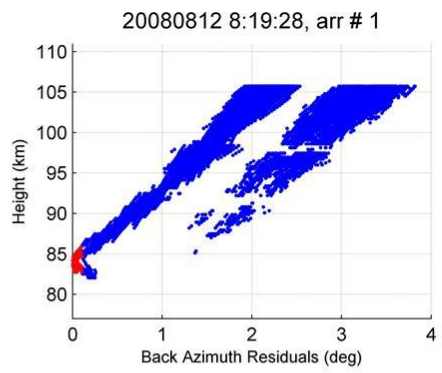
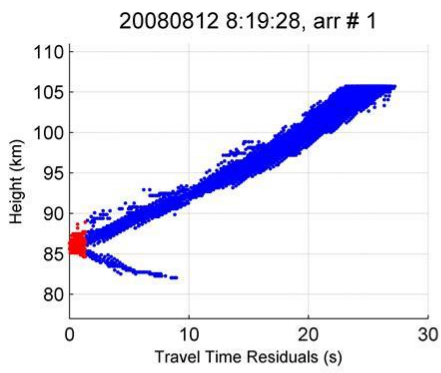
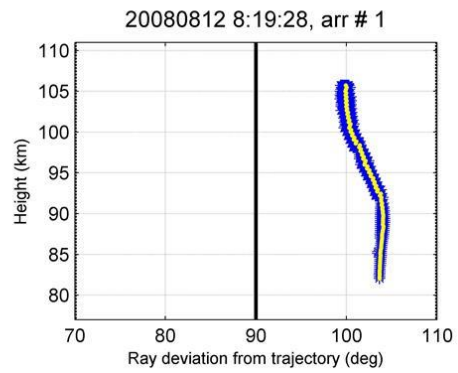
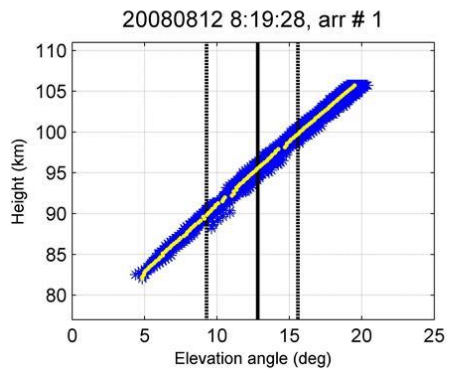
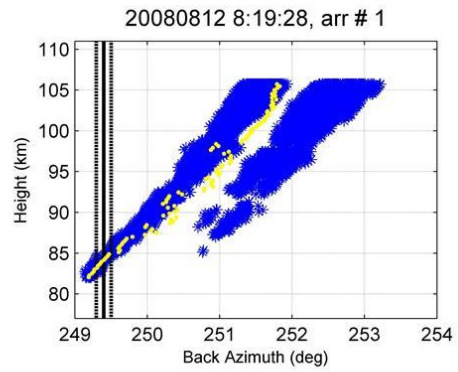
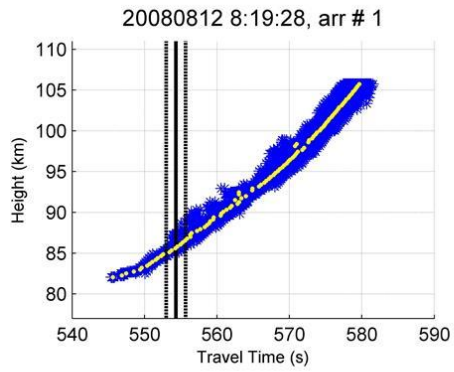


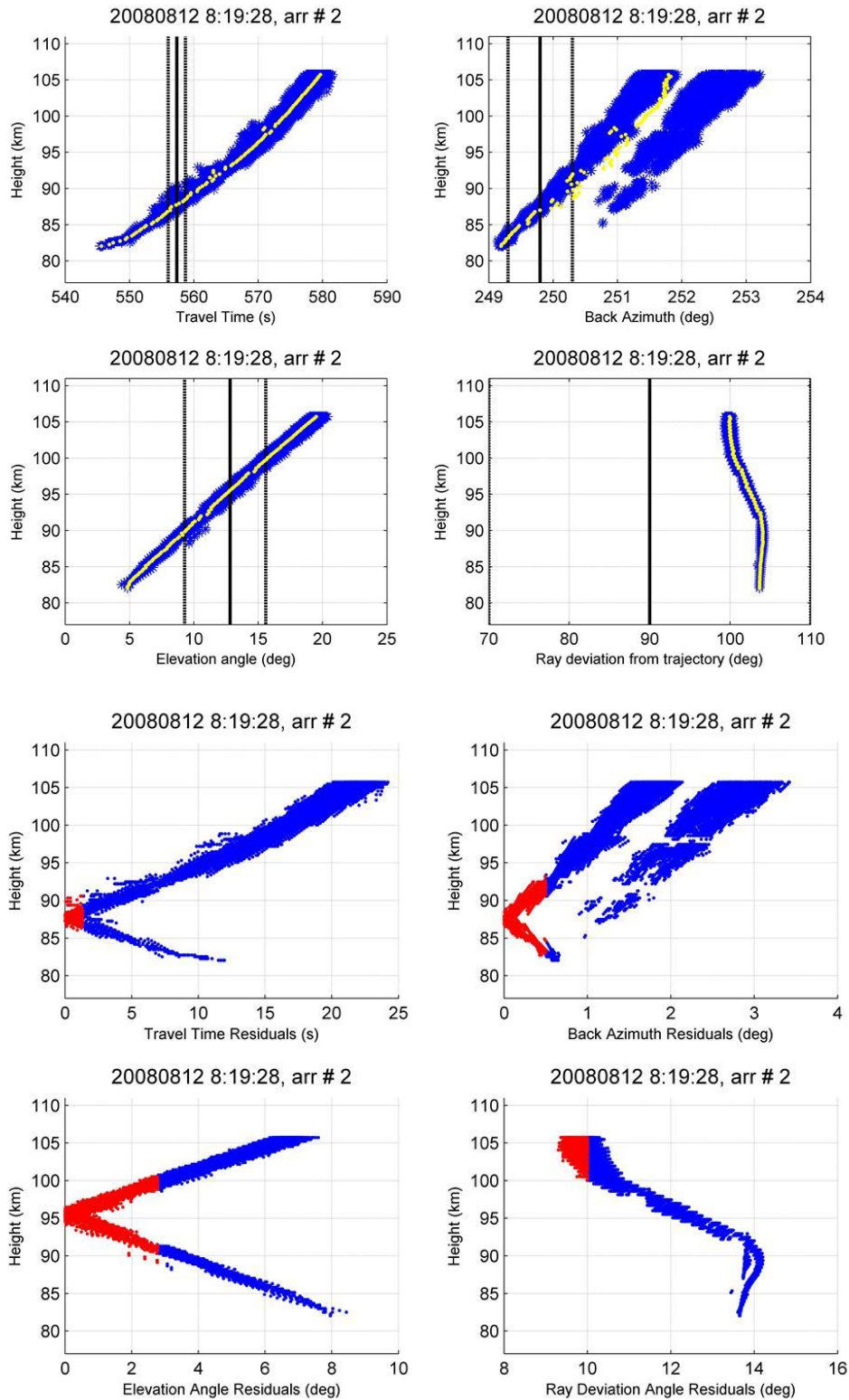




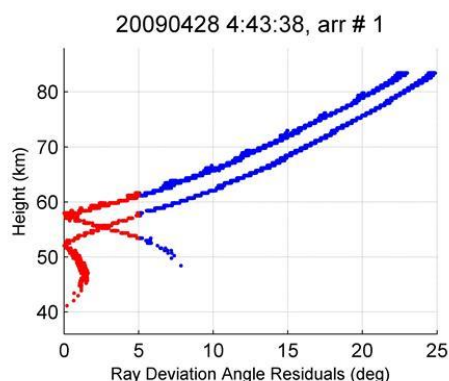
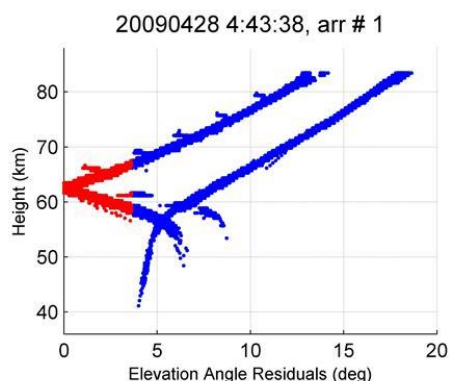
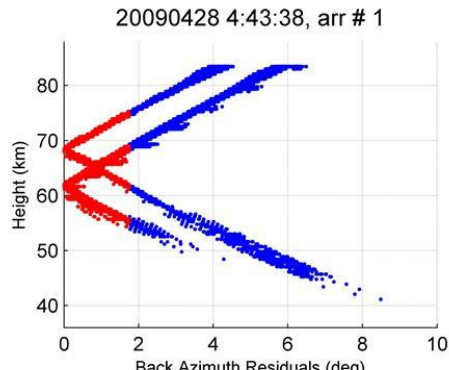
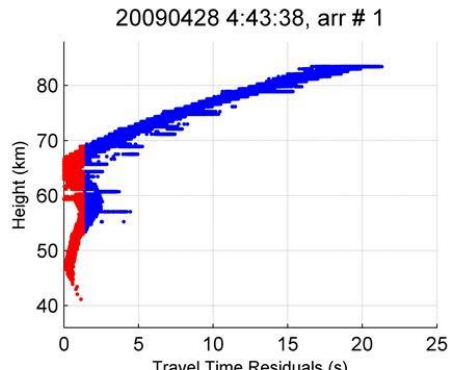
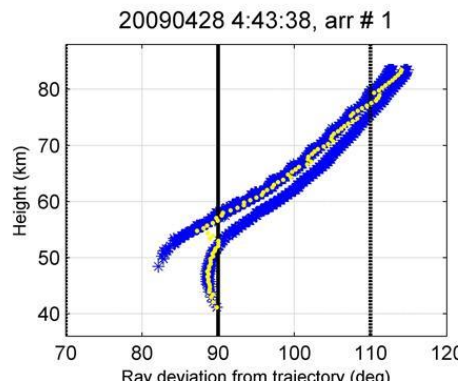
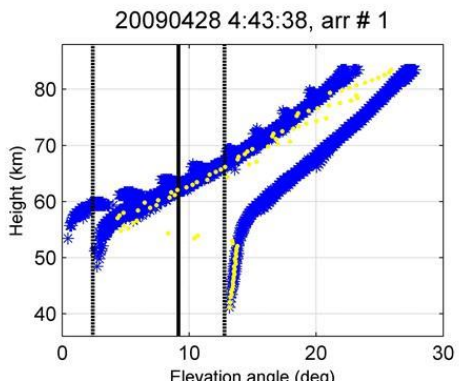
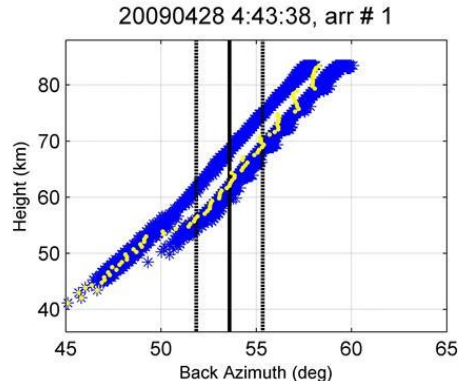
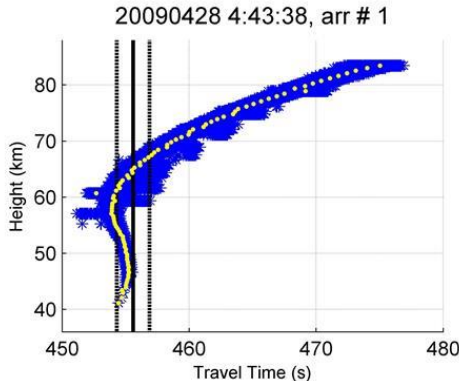


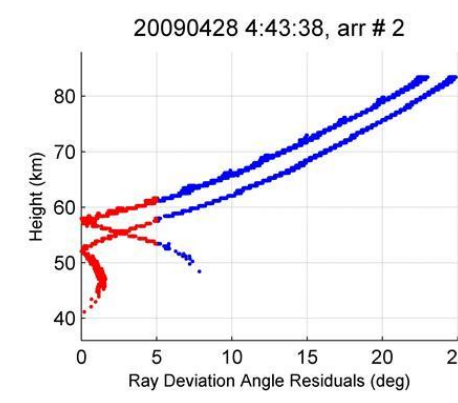
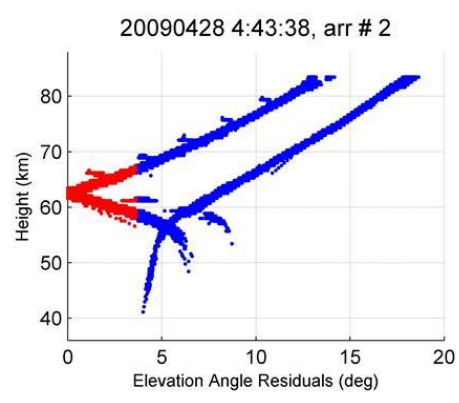
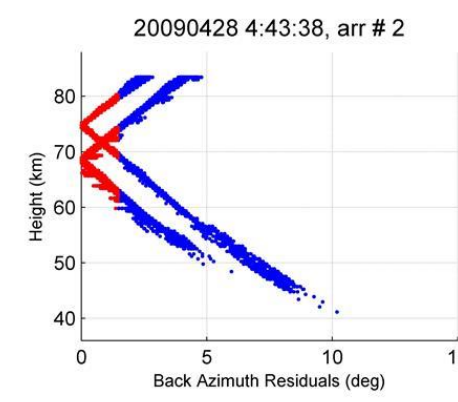
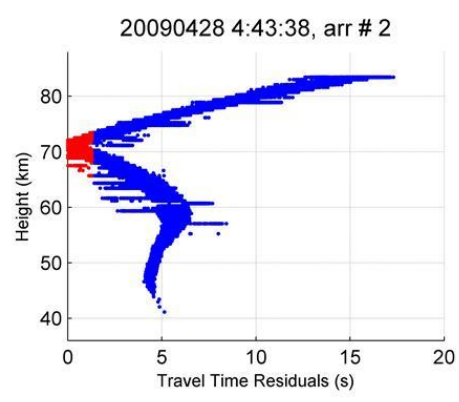
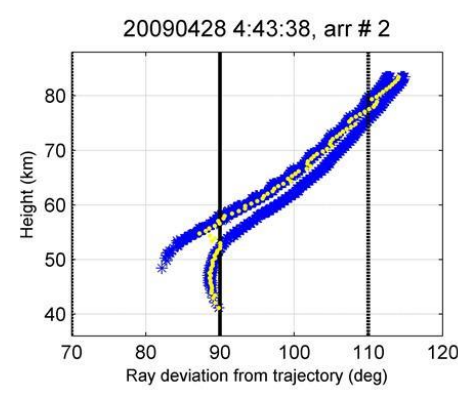
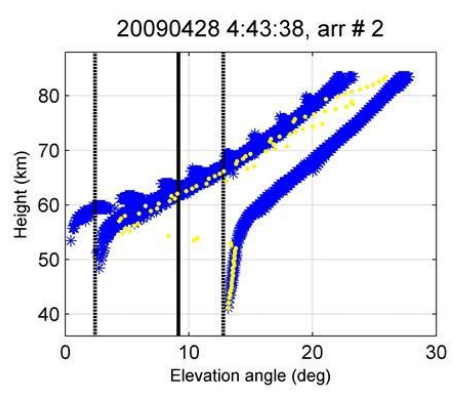
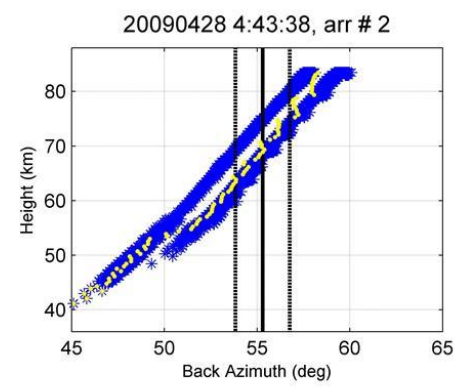
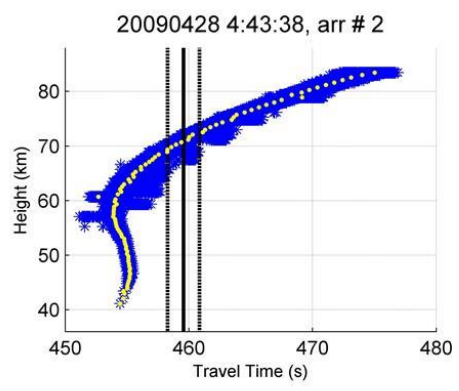




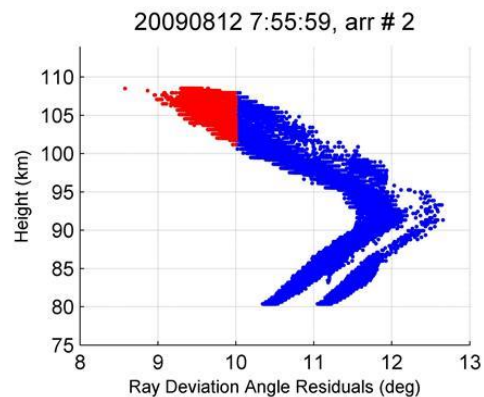
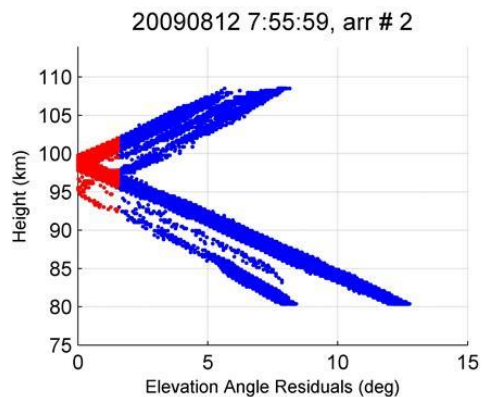
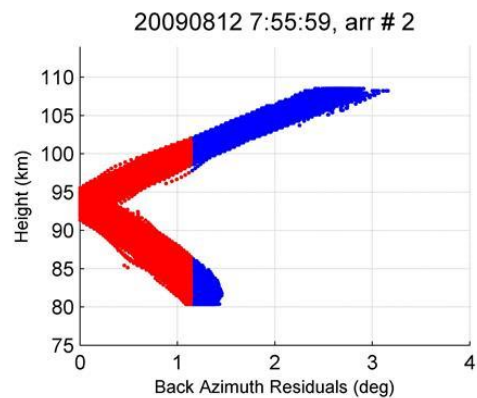
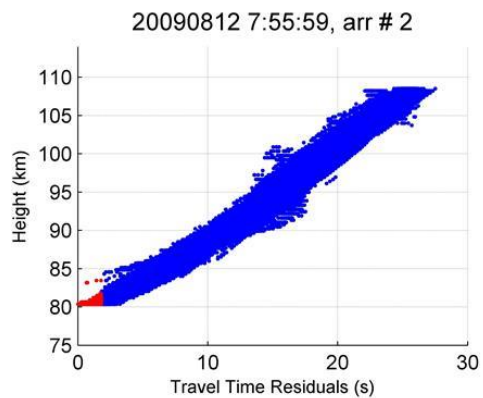
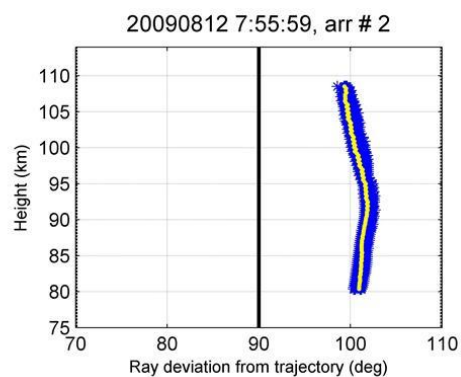
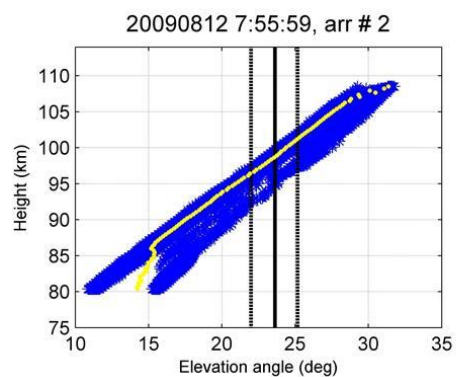
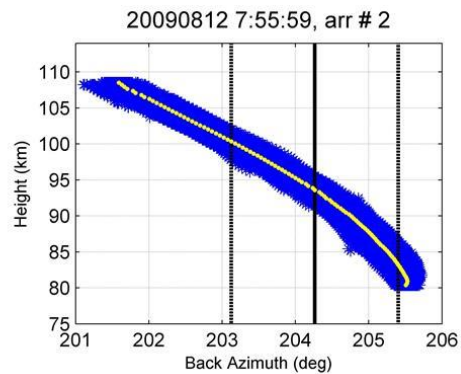
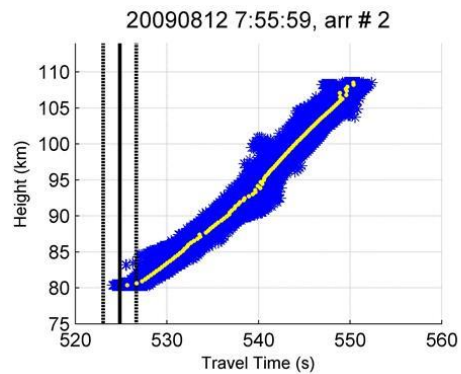


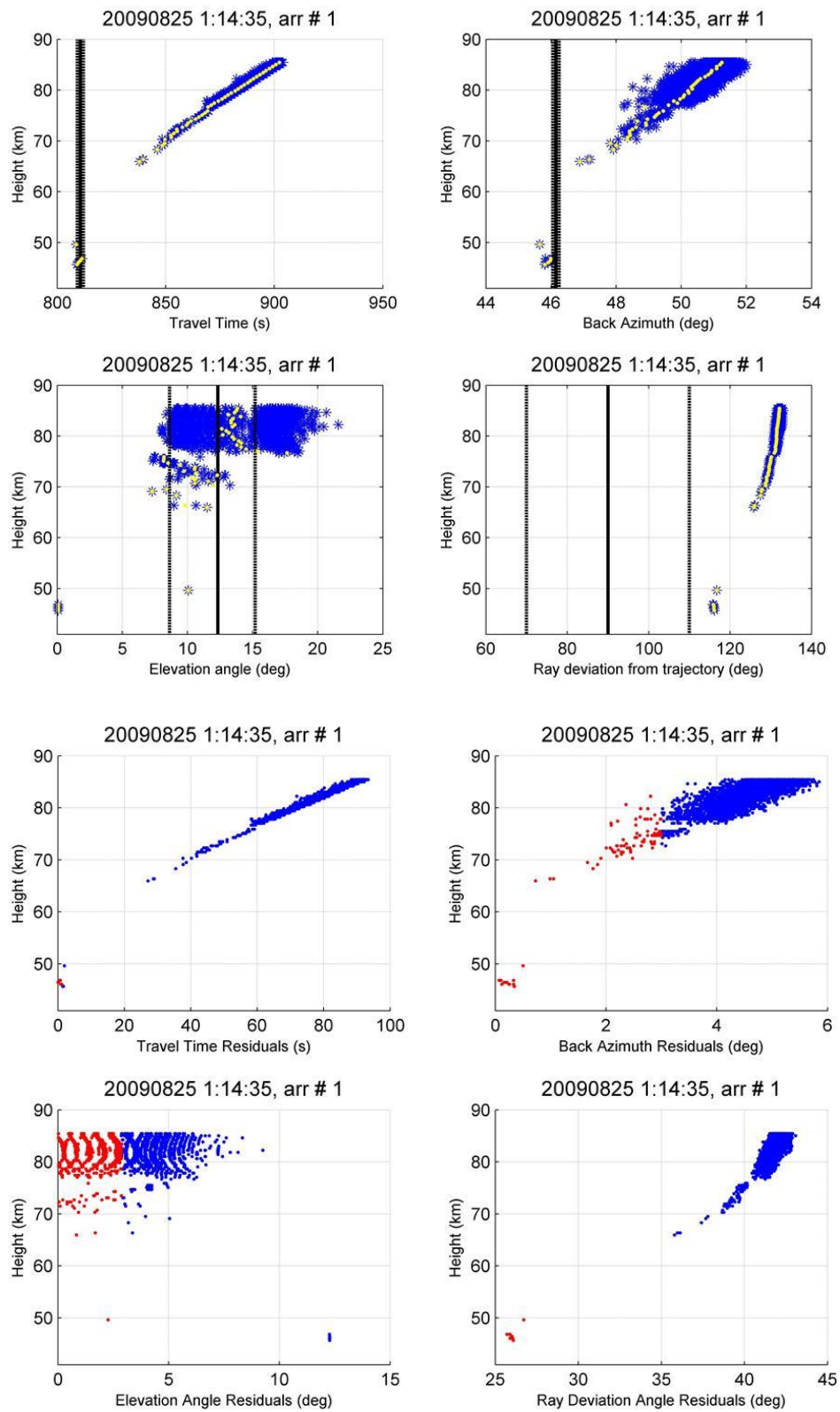




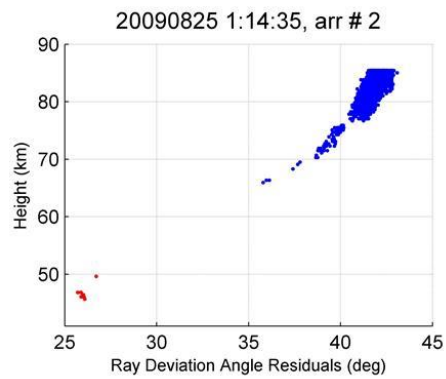
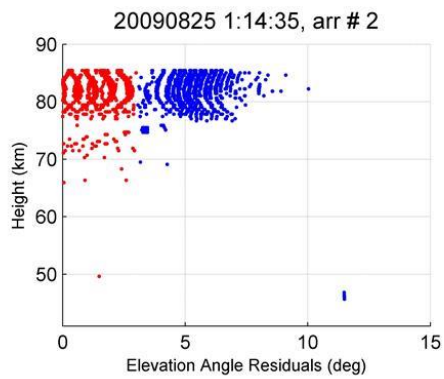
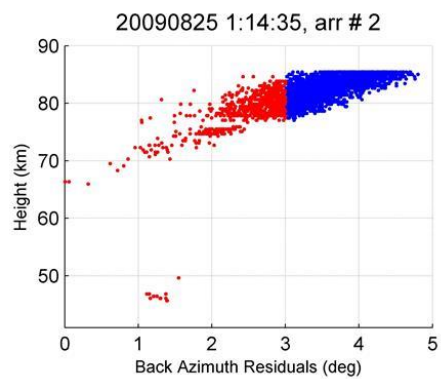
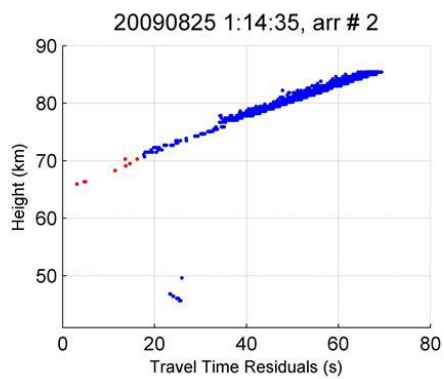
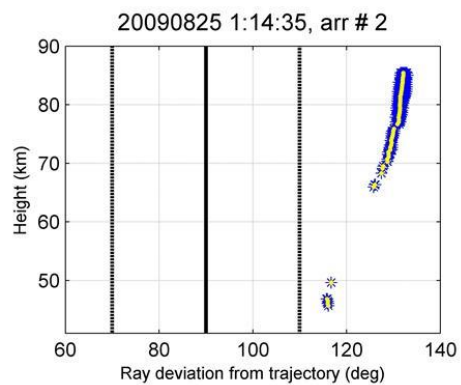
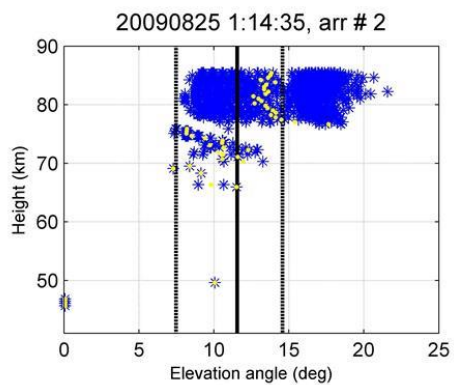
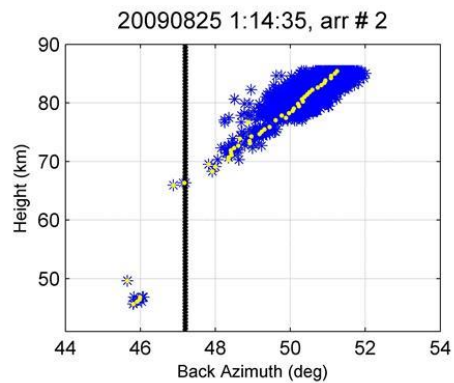
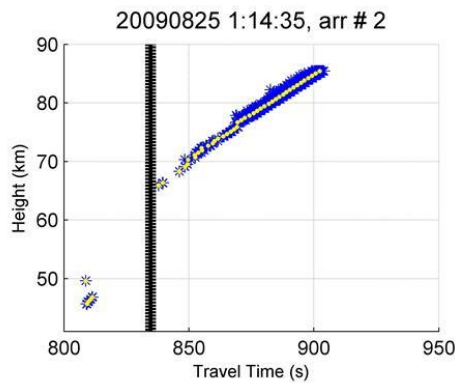


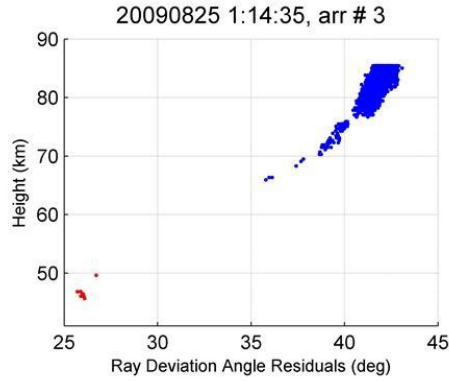
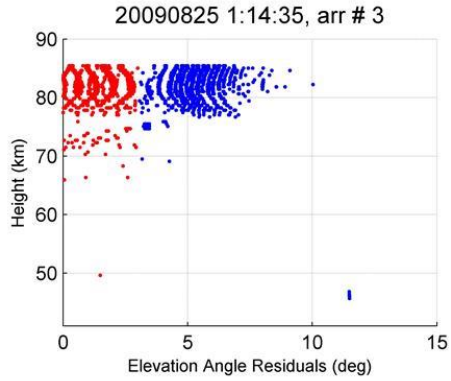
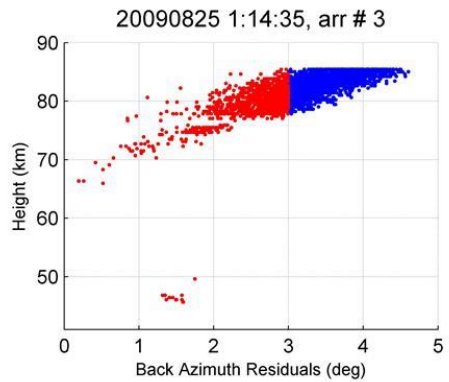
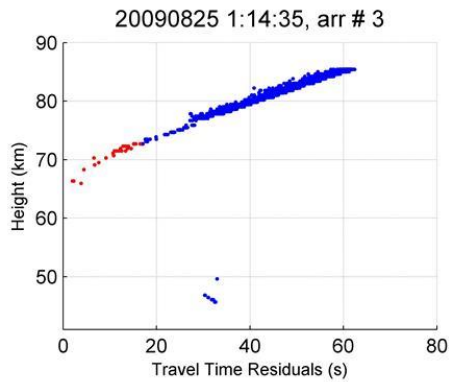
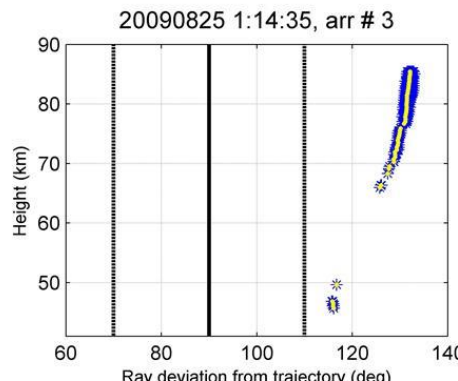
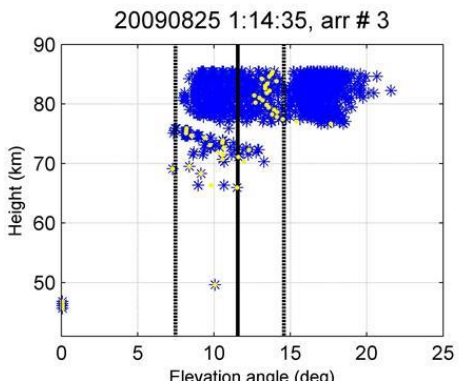
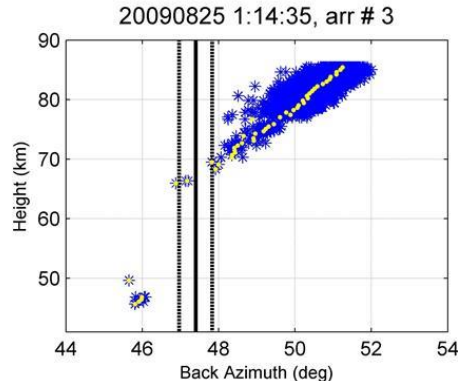
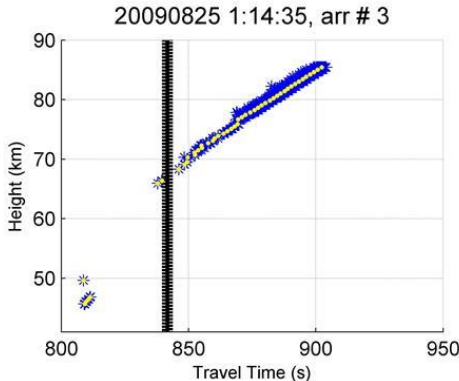


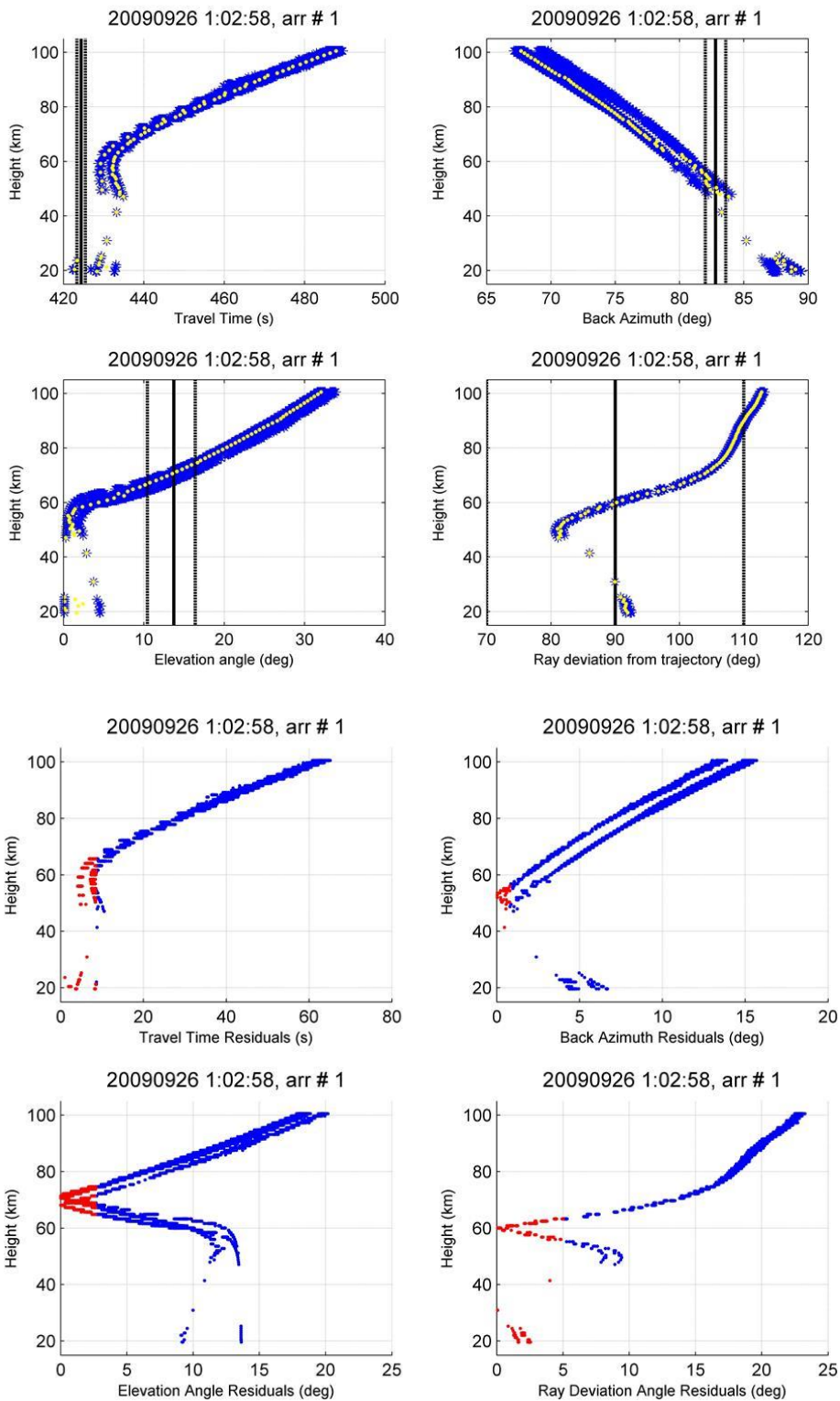




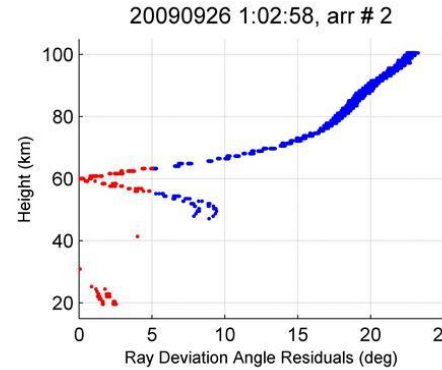
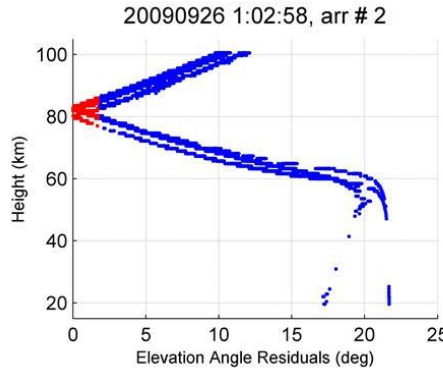
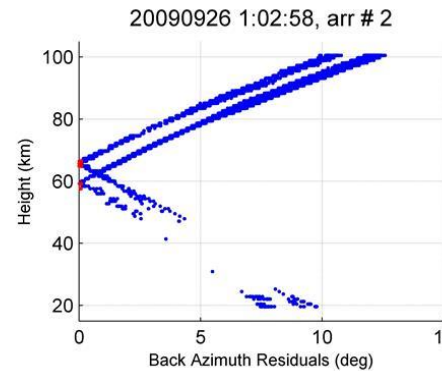
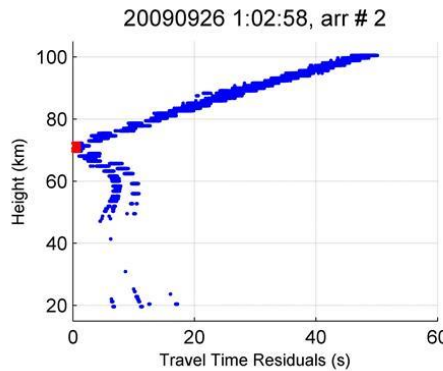
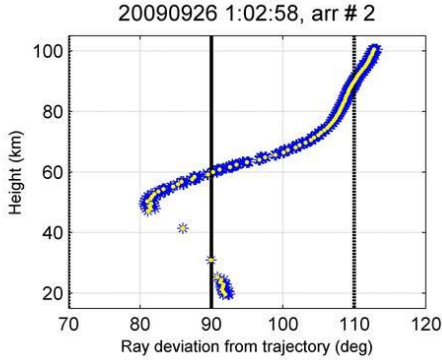
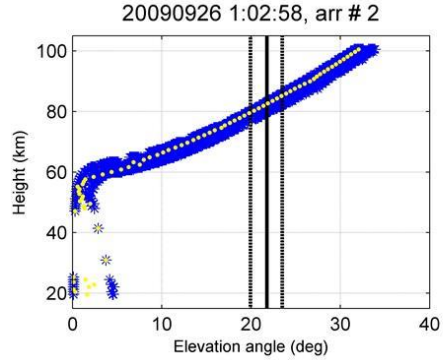
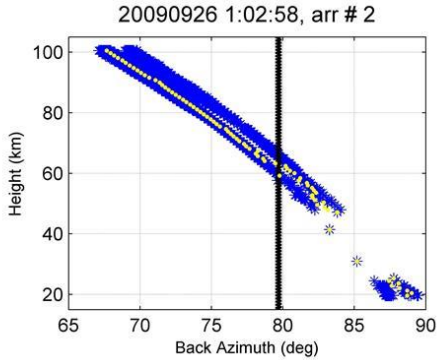
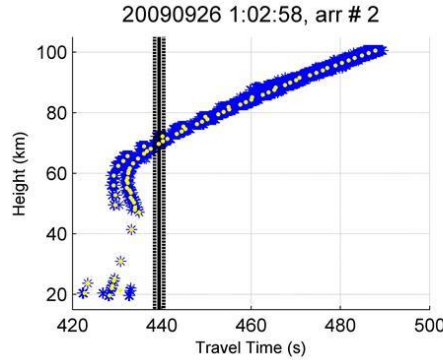


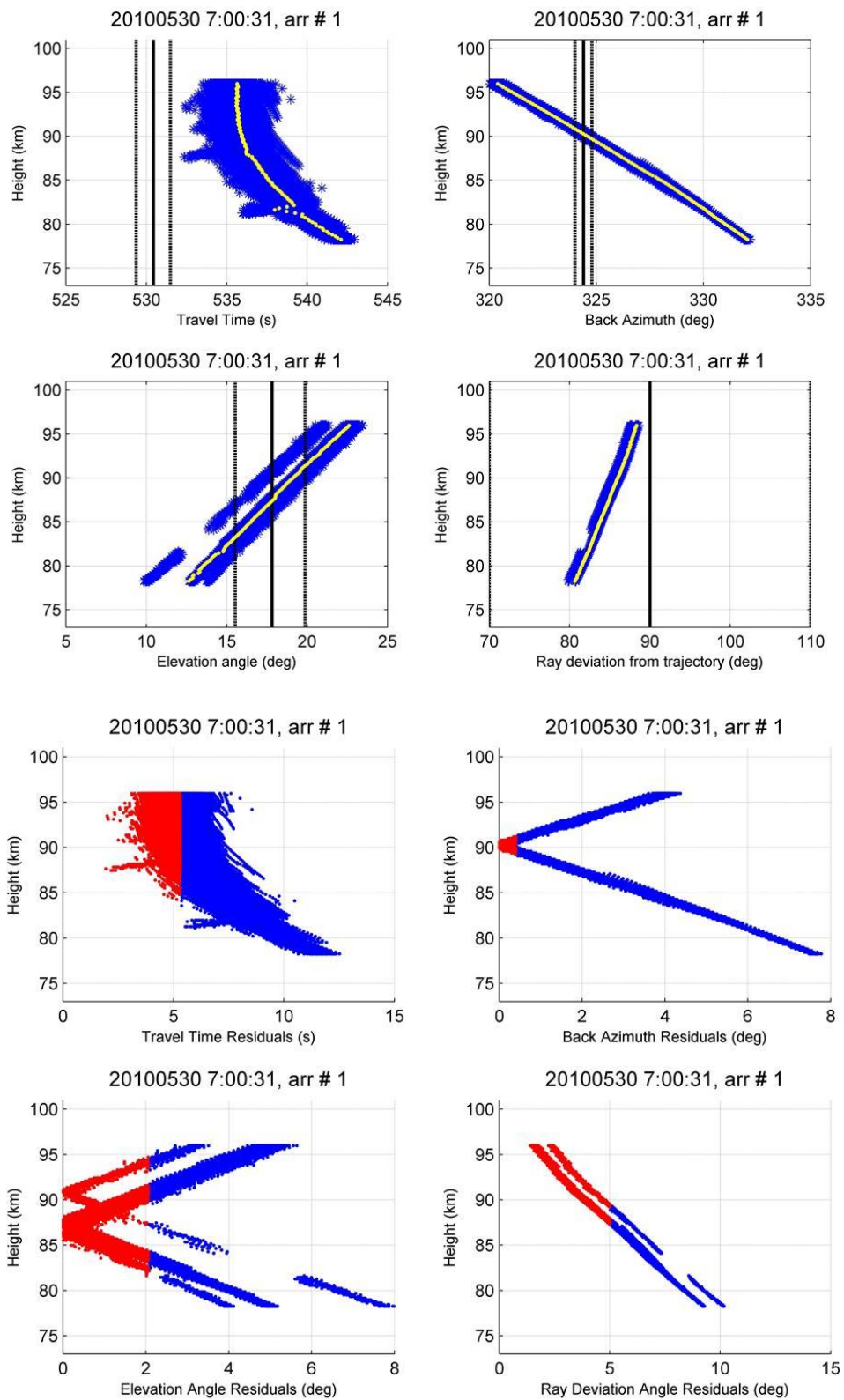


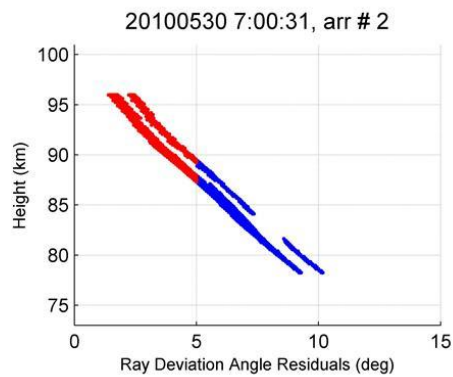
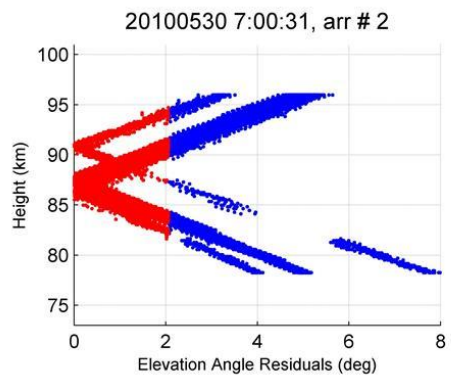
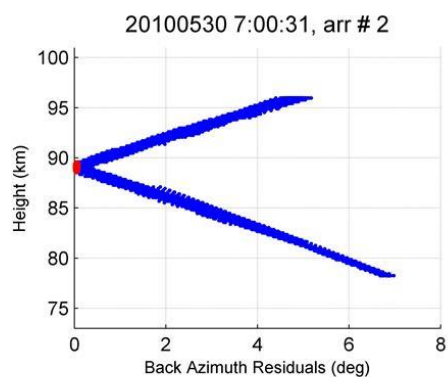
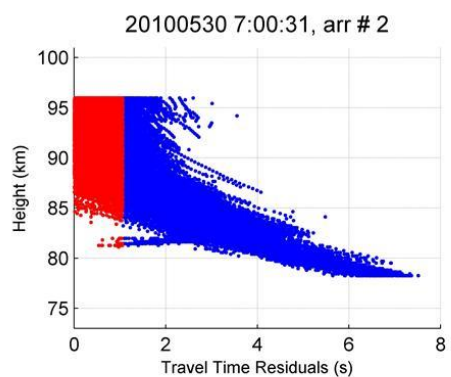
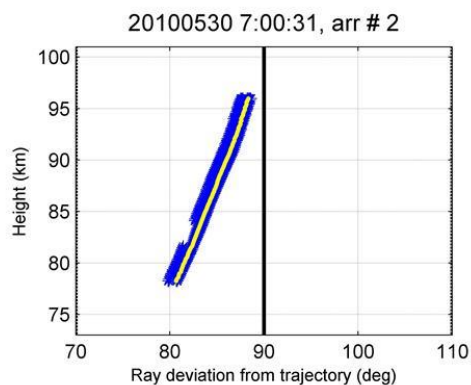
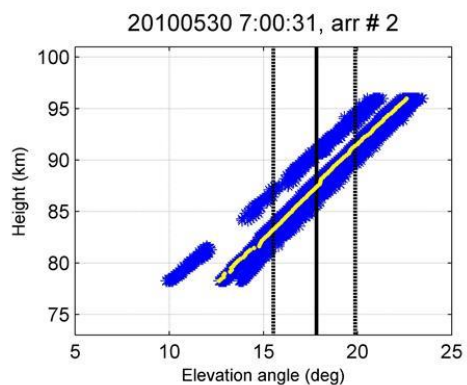
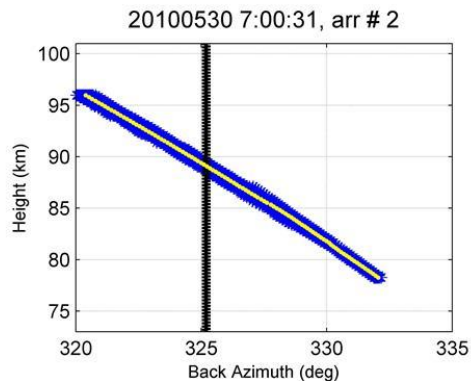
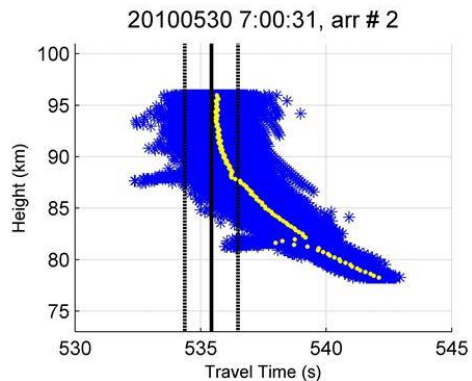


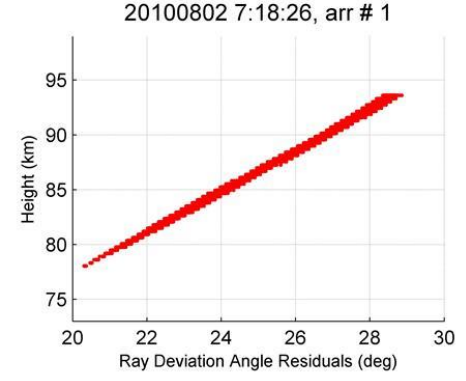
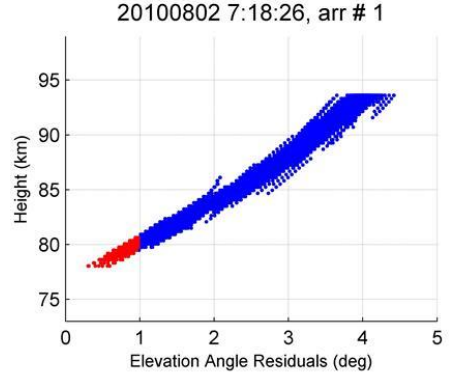
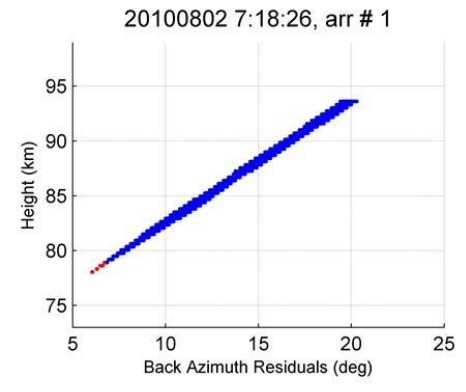
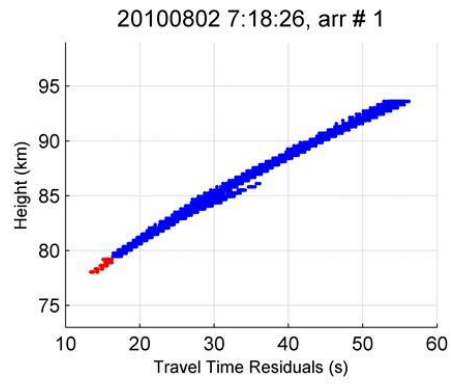
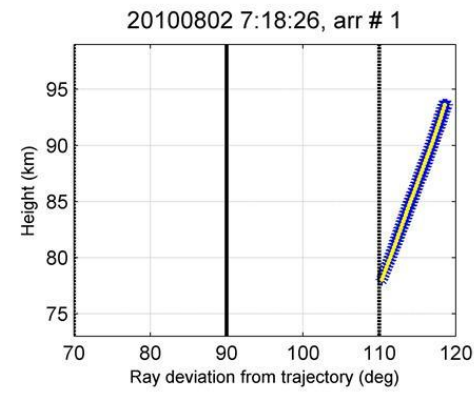
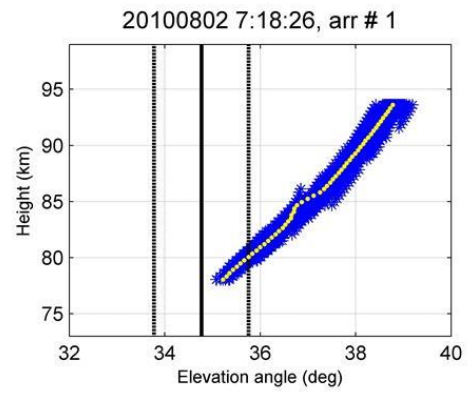
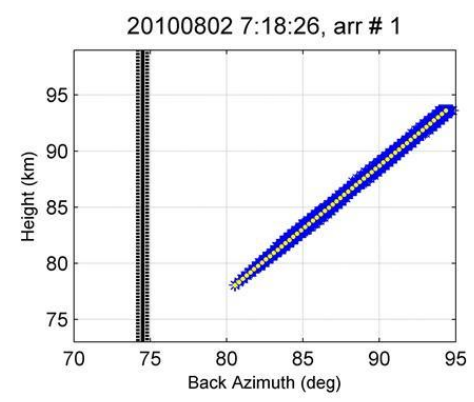
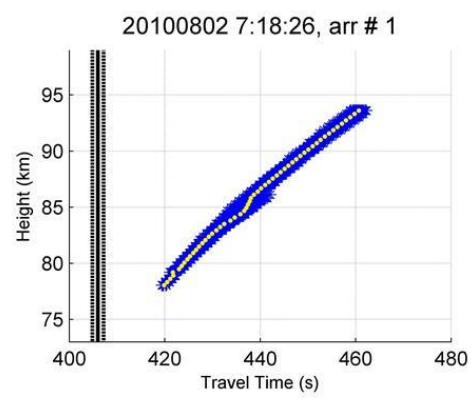


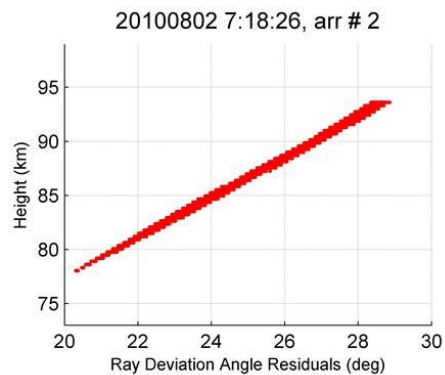
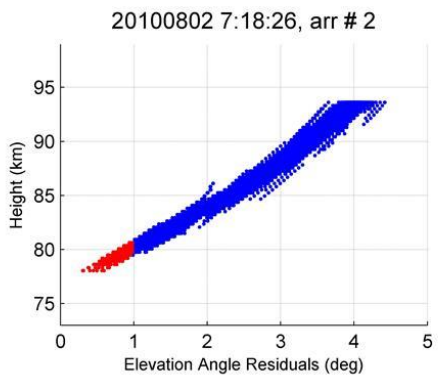
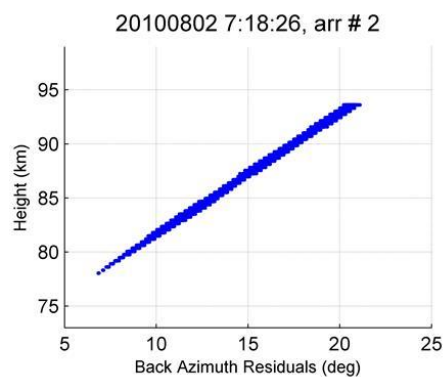
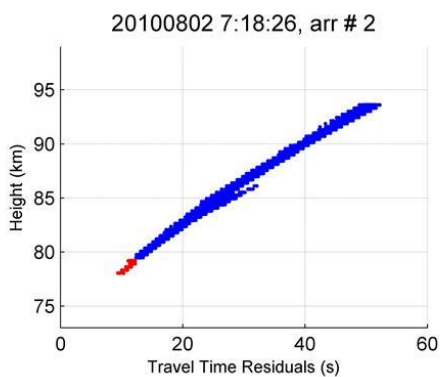
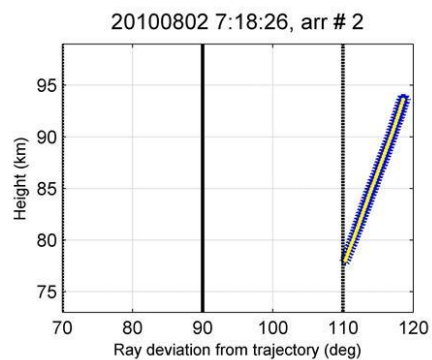
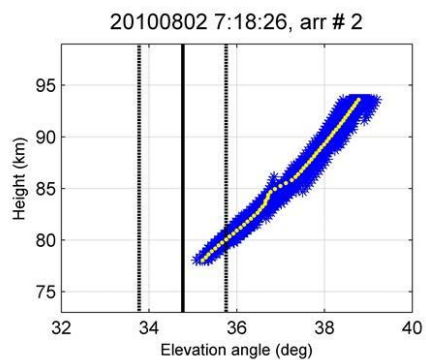
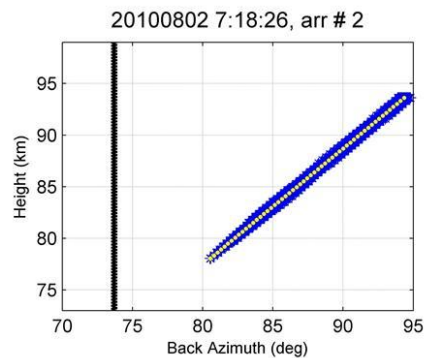
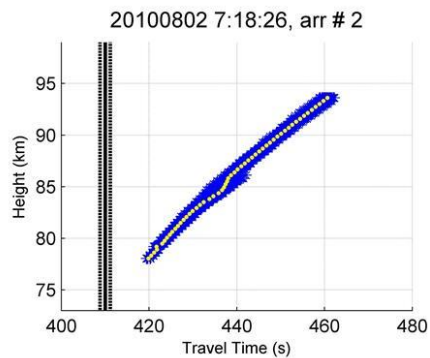




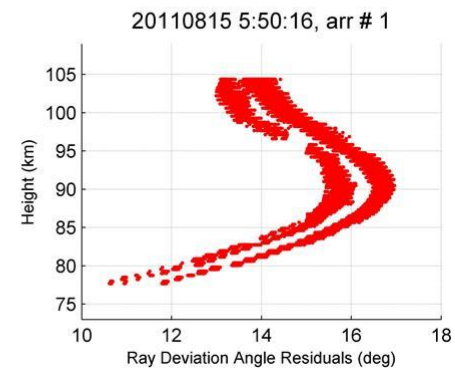
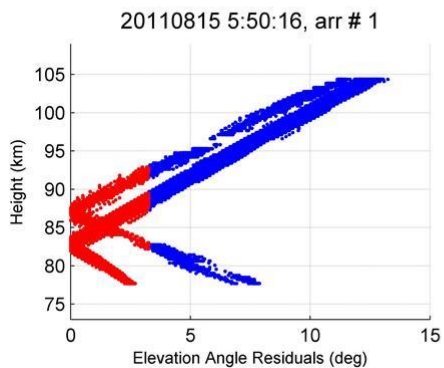
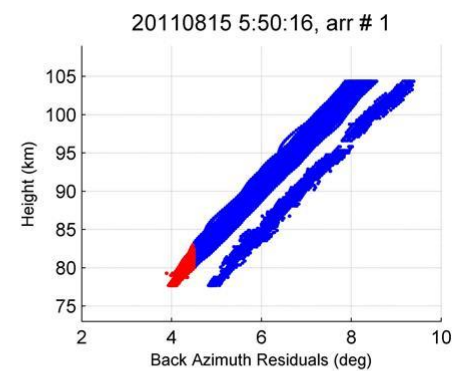
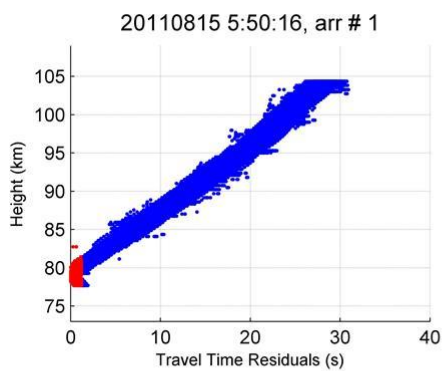
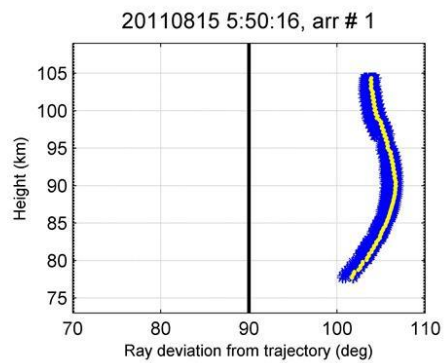
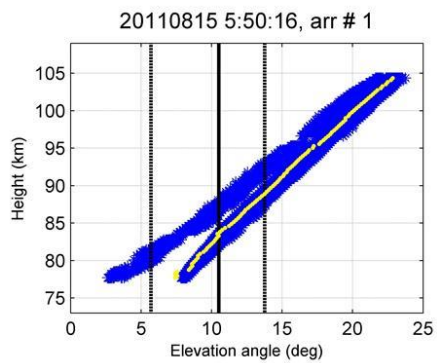
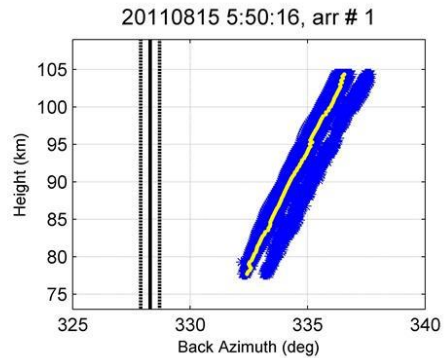
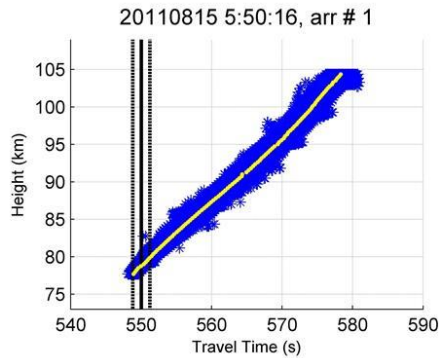


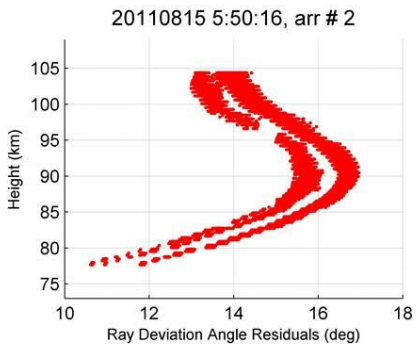
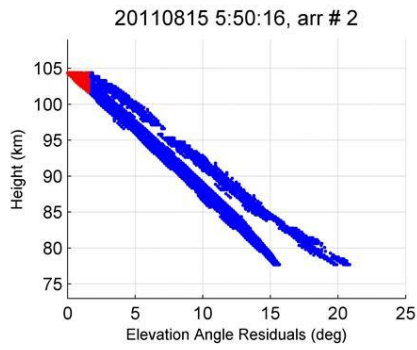
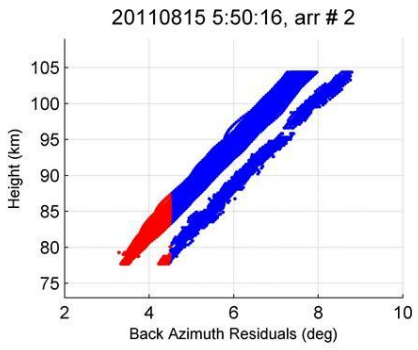
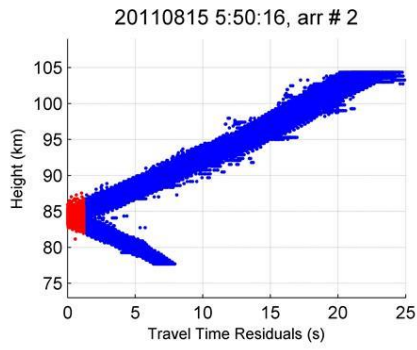
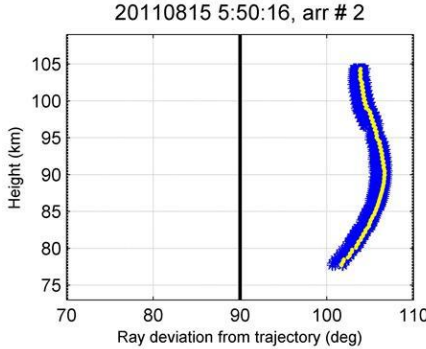
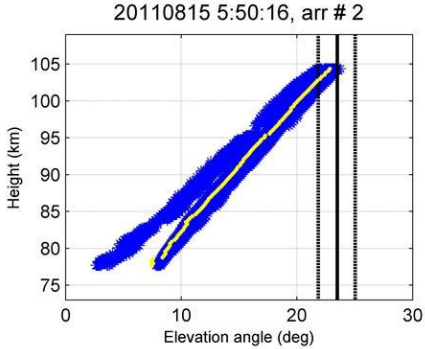
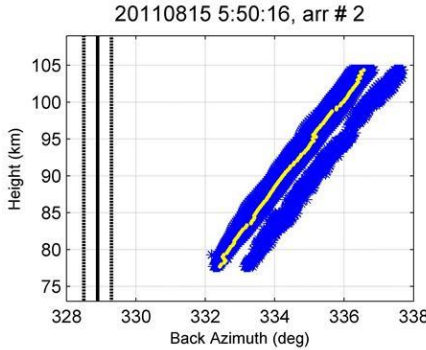
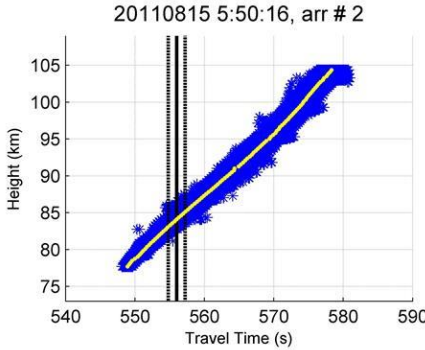












## Appendix 3

### Photometric Corrections: A Brief Overview

The camera system used by the Southern Ontario Meteor Network to gather optical data for simultaneous optical-infrasound meteor events includes the following hardware:

- The camera: a Sony HiCam HB-710E (8 bit) as shown in Figure A3.1. The camera specifications are listed in Table A3.1.
- The CCD (Charge Coupled Device): a 1.27 cm (0.5 inch) interlined chip with 410K pixels, with 768 (Horizontal) X 494 (Vertical) effective pixels. It has a super-low illumination environment of 0.0005 Lux (F1.2 /20 IRE at AGC Max).
- The lens: Rainbow L163VDC4P fisheye lens with a 180 degree field.
- Power: +12VDC (energy consumption 150 mA at maximum load).



Figure A3.1: Sony HiCam HB-710E (<http://www.hicam.co.kr/main/710.htm>).



Table A3.1: All sky camera specifications (<http://www.hicam.co.kr/main/710.htm>). The abbreviations are as follows: CCD – charged coupled device, EIA - Electronics Industries Association, CCIR – digital video encoding standard (International Telecommunication Union)

<b>MODEL</b>	<b>HB-710E</b>
<b>Image Device</b>	1/2" Interline Transfer B/W Ex-view HAD CCD
<b>Total Pixels</b>	811(H) x 508(V)
<b>Effective Pixels</b>	768(H) x 494(V)
<b>Unit Cell Size [<math>\mu\text{m}</math>]</b>	8.40(H) x 9.80(V)
<b>Scanning System</b>	2 : 1 Interlace
<b>Sync. System</b>	Internal
<b>TV Mode</b>	EIA
<b>Resolution (H) [TV Lines]</b>	580
<b>Video Output</b>	Composite Video Output (1 Vp-p, 75 Ohm, Unbalanced)
<b>AGC Max.</b>	32 dB
<b>S/N Ratio (AGC Off)</b>	50dB Over
<b>Gamma</b>	0.45 / 0.65 (selectable)
<b>Minimum Illumination</b>	0.0003 Lux (F-1.2 scene)
<b>Auto Iris</b>	Video / DC Iris
<b>Electronic Shutter</b>	EIA : 1/60 ~ 1/100,000 sec CCIR : 1/50 ~ 1/100,000 sec
<b>Flickerless</b>	EIA : 1/100 sec CCIR : 1/120 sec (optional)
<b>Manual Shutter</b>	EIA : 1/60 ~ 1/100,000 sec CCIR : 1/50 ~ 1/100,000 sec (optional)
<b>Lens Mount</b>	C / CS Mounted
<b>Supply Voltage</b>	DC +12V( $\pm 10\%$ )
<b>Power Consumption</b>	150 mA(Max)
<b>Operating Temperature</b>	- 10 ~ 60 $^{\circ}\text{C}$
<b>Storage Temperature</b>	- 30 ~ 80 $^{\circ}\text{C}$
<b>Dimensions [mm]</b>	61.5 (H) x 50.0 (V) x 53.0 (D) - Not Included Lens
<b>Weight [g]</b>	(Approx) 220.0 - Not Included Lens

### A.3.1 Procedure for Saturation Correction

To correct for light saturation in the camera CCD and therefore estimate the total amount of light reading the camera, the following laboratory experiment was constructed as shown in Figures A3.2 and A3.3. Here a light source is placed at the focal point of a Newtonian reflecting telescope with a fixed neutral density filter to reduce intensity to just above saturation for the camera and then rotating filter having smooth gradations in neutral density as a function of angle placed between the light source and the main mirror. This permits the light source to be smoothly attenuated from above saturation, through normal unsaturated detection down to the noise level of the camera (no signal from the source is then detectable). The camera is placed along the main optical axis where the point source light is defocussed to a plane wave. The procedure for gathering data for estimating the saturation effect is:

- The step motor was used to rotate the wheel in equal increments (71.47 steps over  $310^\circ$ ) and take 60 second image stacks in both clockwise and counter clockwise directions.
- The raw images were processed using IDL and plotted in Sigma Plot. Here the log sum of the pixel intensity of the source is taken as a direct estimate for the source intensity (hereafter this is termed instrumental magnitude) following Hawkes et al (2002).
- Only the best experimental data (i.e. no reflections) extending through the wheel and ND filters was used to determine the saturation correction. This is accomplished by comparing the known intensity (from the stepper motor position and angular position of the filter wheel) with the instrumental magnitude measured through the camera. Note that this produces relative changes in brightness but not absolute.
- The final saturation correction fit for data and the corresponding residuals are shown in Figure A3.5 and Figure A3.6, respectively.
- A sample meteor light curve, corrected for saturation and uncorrected, is shown in Figure A3.7.

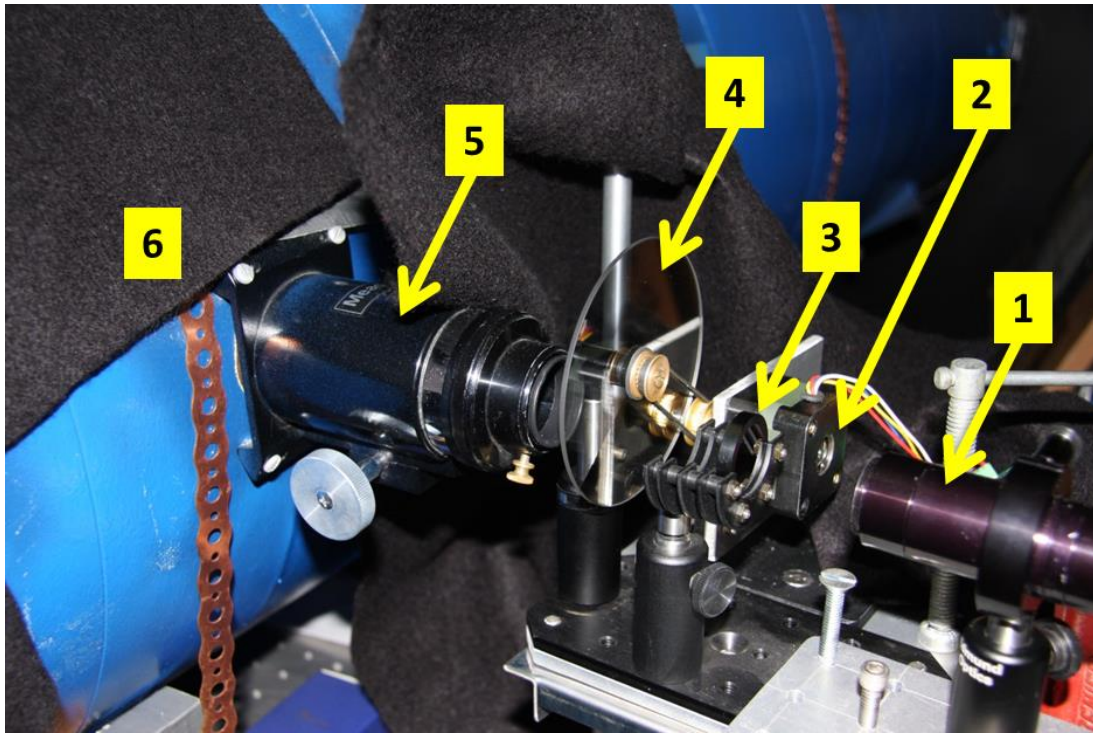


Figure A3.2: The beam of light from the constant intensity lightsource (#1) is passed through the pinhole (front of lightsource) and then through a neutral density (ND) filter (#3) and the neutral density wheel (#4) before entering the eyepiece holder (#5) of the telescope (#6). The ND wheel is composed of the clear region through  $50^\circ$  and neutral density gradient filter (0.04 – 4) through the remaining  $310^\circ$  with the wheel powered by the stepper motor (#2).

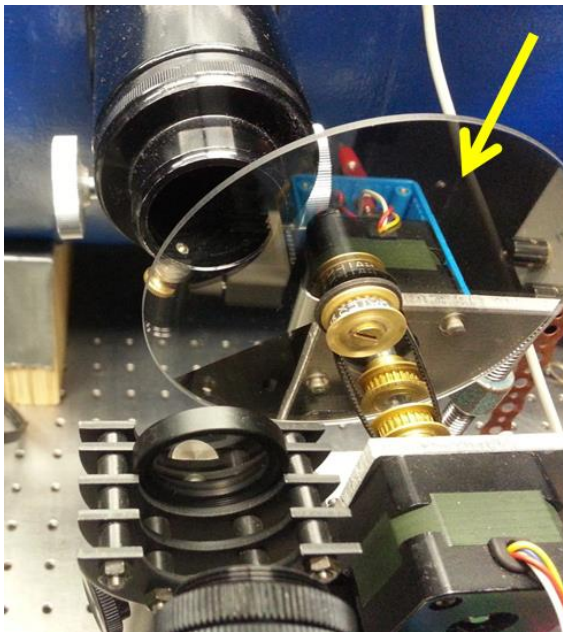


Figure A3.3: The transition between the clear portion and the densest filter of the ND wheel is shown with the yellow arrow in the image. The experiment can be set up to run with the ND wheel alone, or with both the wheel and the ND filter, depending on the light intensity dynamic range required. The ND filter, which sits in front of the wheel, can range in ND value from 1 ND – 3 ND. Note that every 1 unit in ND corresponds to a linear factor of ten in brightness change.

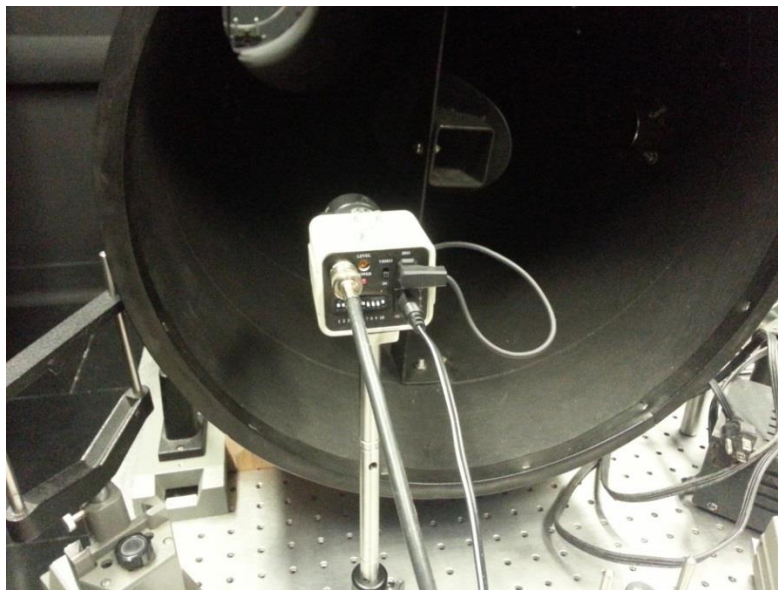


Figure A3.4: The camera is anchored in front of the telescope where it measures a plane wave which mimics characteristics of star with connections to power and the computer where the analog signal is digitized using a frame grabber (based on the Brooktree line of video capture cards).

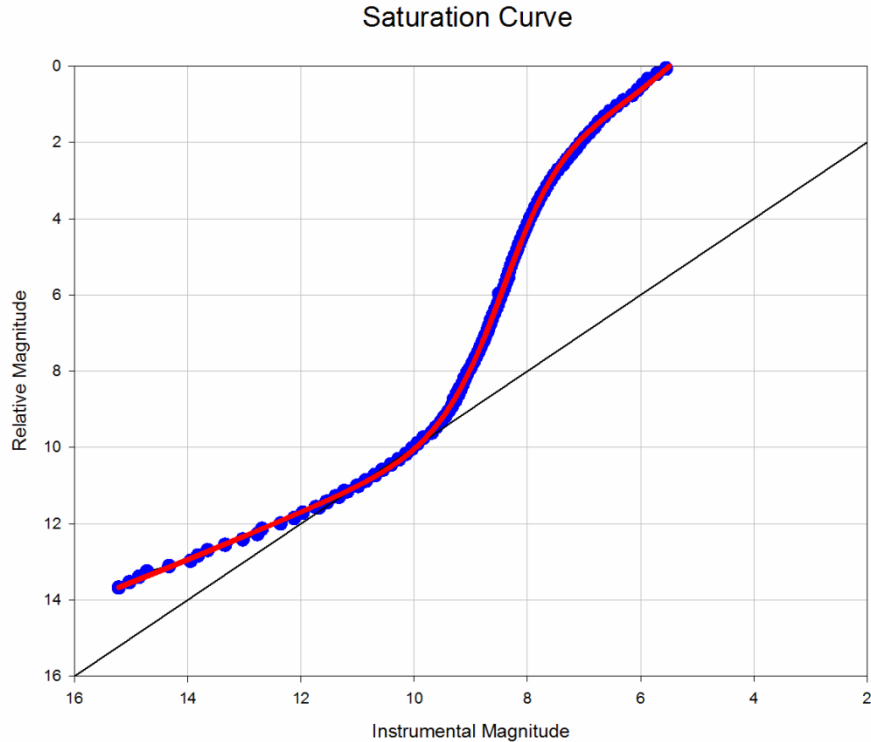


Figure A3.5: The blue points correspond to the raw data, while the red line is an empirical best fit. The graph shows the actual (known) brightness of the source (relative magnitude) and the measured brightness (Instrumental Magnitude). If saturation were not present this would be a straight line - saturation is evident by the small change in the x-variable relative to a large change in the y variable, reflecting the loss of photons once saturation is reached.

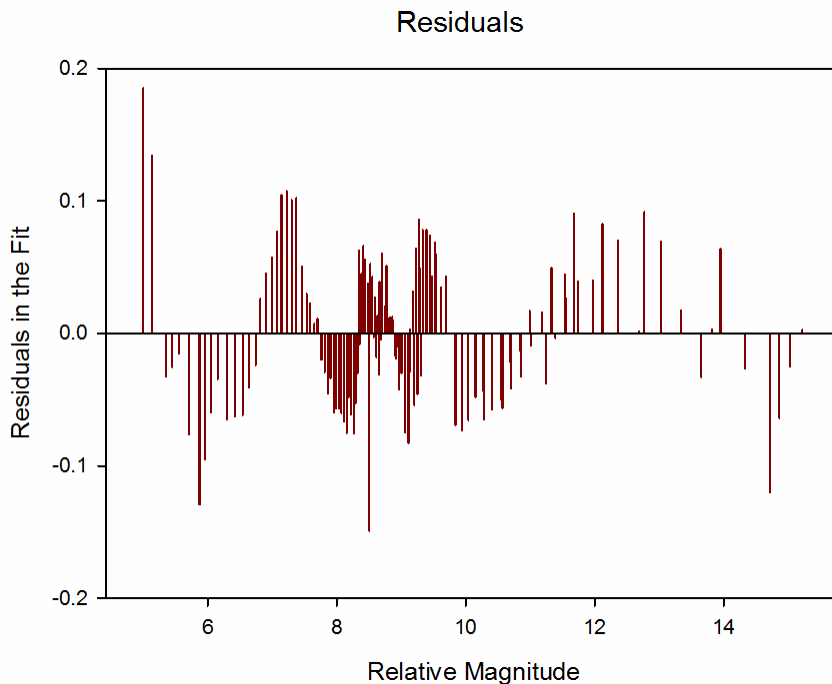


Figure A3.6: The residuals for the saturation correction fit between the instrumentally measured magnitude with saturation correction applied and the true (relative) magnitude.

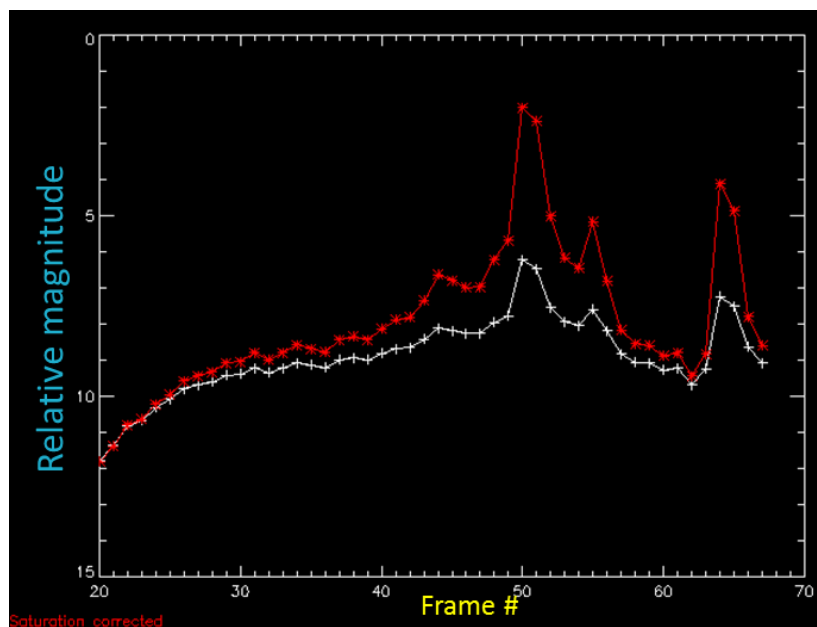


Figure A3.7: The white data points represent the camera measured light curve uncorrected for saturation (the roll-off correction, described in the next section, is included). The red data points represent the fully corrected apparent light curve – i.e. our best estimate of the relative magnitude of the meteor as seen from the camera..

### A.3.2 Lens Roll-off Correction

Near the edges of any lens, the amount of light reaching the sensor naturally is truncated (termed vignetting). To estimate the attenuation of the light from vignetting, which is very pronounced in wide field optics, an experiment in the field was constructed. The roll-off correction experiment was performed in-field during a clear, dark night. The experiment was set up as shown in Figure A3.8 and Figure A3.9.

- Starting with the lens centre oriented slightly below the horizontal, the camera was rotated in  $5^\circ$  increments to sweep an angle just over  $180^\circ$  across the sky.
- A one second video (30 frames) was captured at each step.
- Additional calibration images were taken and subsequently used to generate the astrometric plate.
- Multiple stars had their instrumental magnitude measured in a relative sense across the field of view while at a fixed elevation in the sky to estimate the lens roll-off correction.
- The final lens roll-off was empirically fit as:  $y = a + bx^{2.5} + cx^3 + de^x$ , where  $a = 2.619384896465613$ ,  $b = -1.86730696627234e-5$ ,  $c = 3.689985963834343e-6$  and  $d = 3.768268975434104e-40$ . Here  $x$  is  $\theta$  in degrees, where  $\theta$  is the zenith angle (0 degrees overhead, 90 degrees at the zenith).

The lens roll-off correction plot and the residuals are shown in Figure A3.10 and Figure A3.11, respectively.



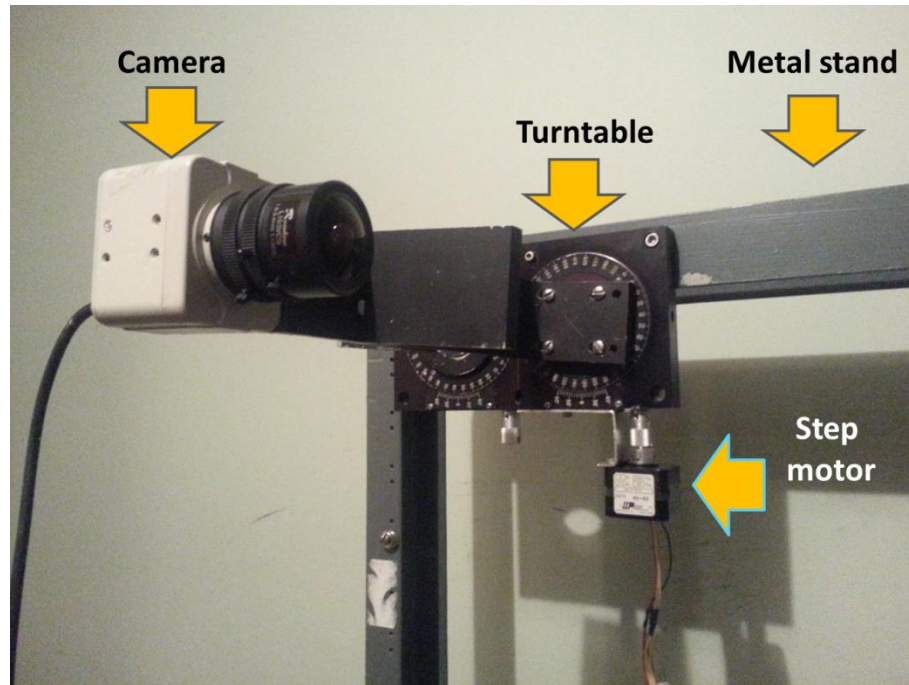


Figure A3.8: The camera, identical to those used for meteor measurements, attached to the turntable. This structure was in turn attached to a metal frame to keep the apparatus firmly in place once in the field. The step motor was used to turn the wheel in equal  $5^\circ$  increments.

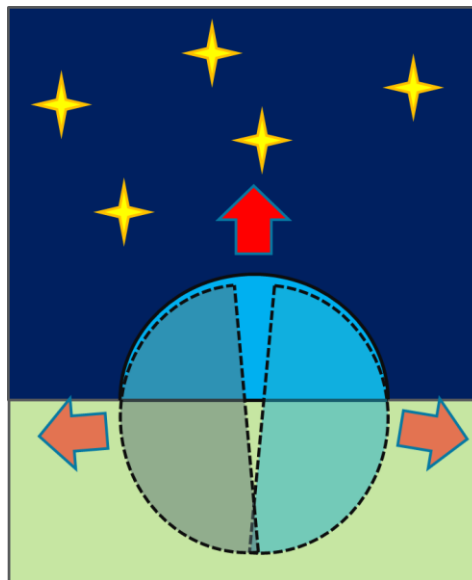


Figure A3.9: A diagram showing the orientation of the lens with respect to the sky. The red arrows correspond to the centre of the lens.

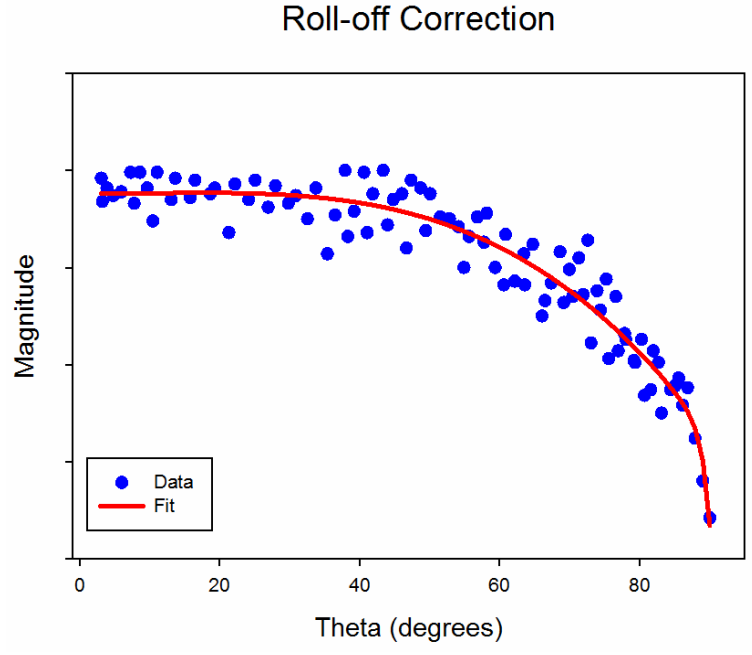


Figure A3.10: The lens roll-off correction. The blue points represent the relative instrumental magnitude for raw data collected during the night of the experiment, while the red curve is the best fit. The magnitude decreases a function of  $\theta$  due to vignetting.

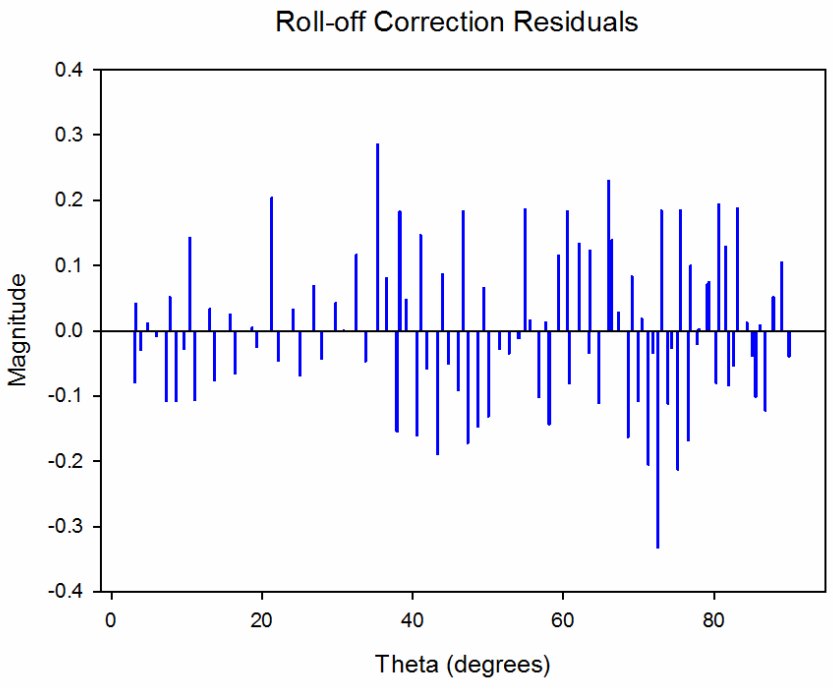


Figure A3.11: The roll-off correction fit residuals.

## Appendix 4

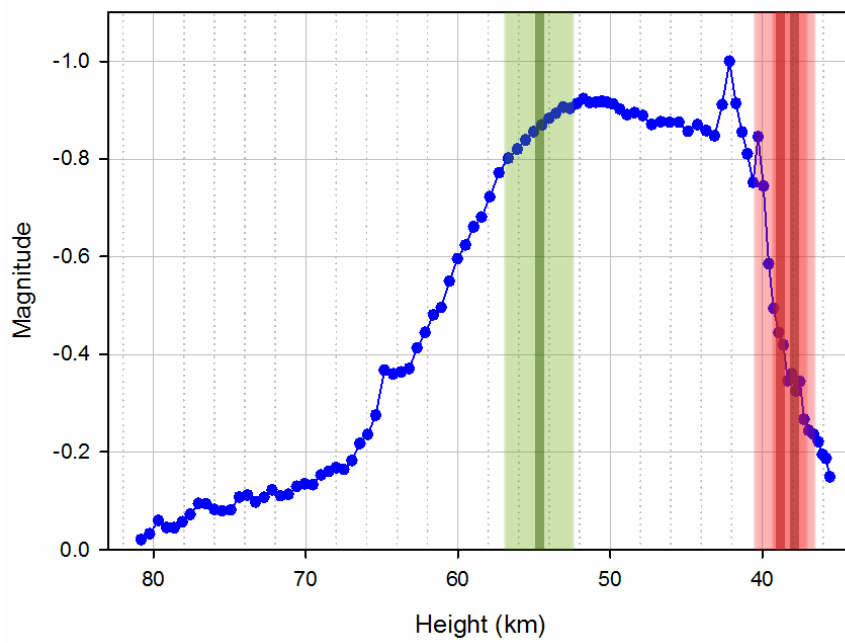
### Relative Magnitude Light Curves: Associations to Shock Production

The plots shown in this appendix are scaled, relative photometric lightcurves for each meteor event for which infrasound signals were detected. These plots depict the relationship between the point of shock production and light curve as derived from the video data, as described in Chapter 5 (e.g. Figure 5.26).

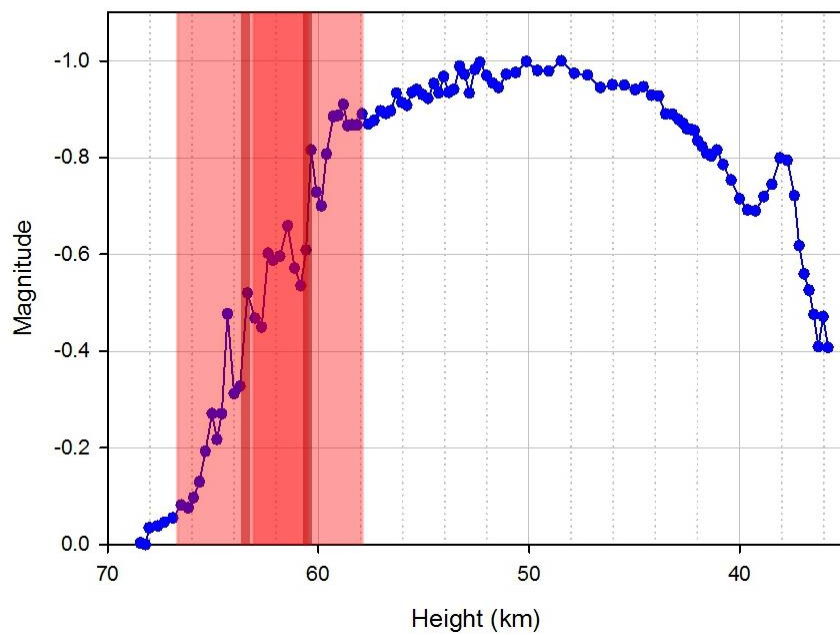
The scaled relative magnitude shown for all events has been normalized on a scale from 0 to -1, simply to allow the point of maximum brightness (-1) to be easily portrayed. These light curves were also used to determine the  $M_p$  parameter as described in Chapter 5. The photometric corrections for saturation, lens roll-off and extinction were applied to all events. The choice of the camera site for any light curve in this set was based on the highest fidelity video data – the best site with best sky conditions for each given event was used to produce the relative light curve.

The solid lines with shaded (transparent regions) correspond to the inferred shock source heights and their uncertainties as determined in Chapter 5. The green colour is associated with shock heights determined to be most likely line source-type shocks, while the red colour corresponds to likely spherical shocks. The identification methodology used for shock type is described in detail in Chapter 5. In general, flares are likely to be associated with spherical shock production, while the absence of flares is indicative of cylindrical line source. There is only one event (yellow line) for which it was not possible to determine with any certainty whether the type of shock is cylindrical or spherical. In some cases, however, the positioning of relatively small flares on the light curve alone was not sufficient to determine the type of shock. Sometimes, the location of the signal would correspond to the region between flares. Therefore, in addition to light curve examination, a careful inspection of frame-by-frame video records was performed to look for signs of visible fragmentation or continuous fragmentation to make the best possible estimate of shock production.

20060305 (cam 04)

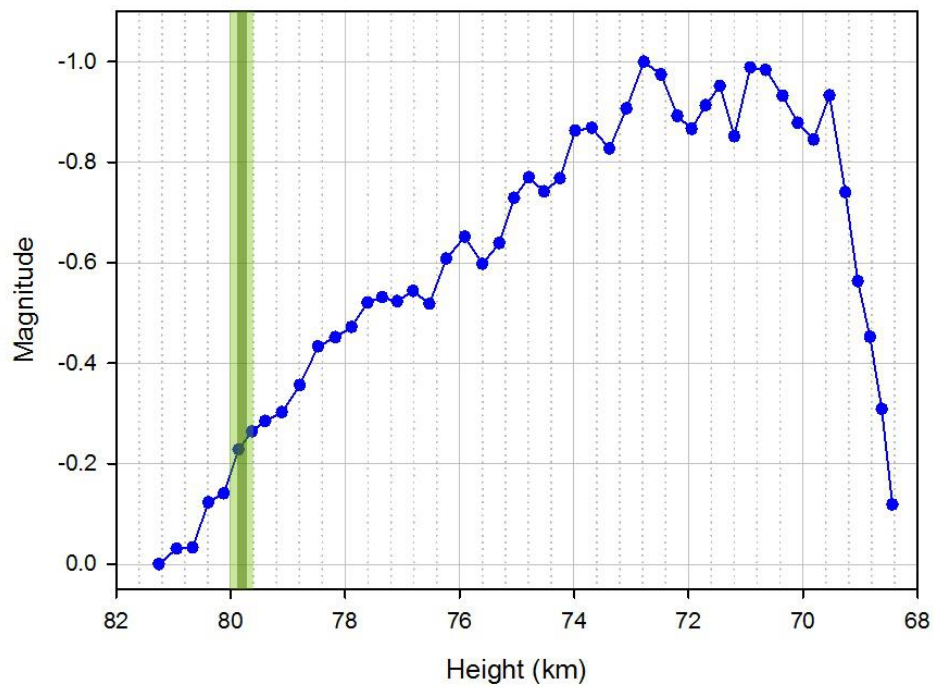


20060405 (cam 03)



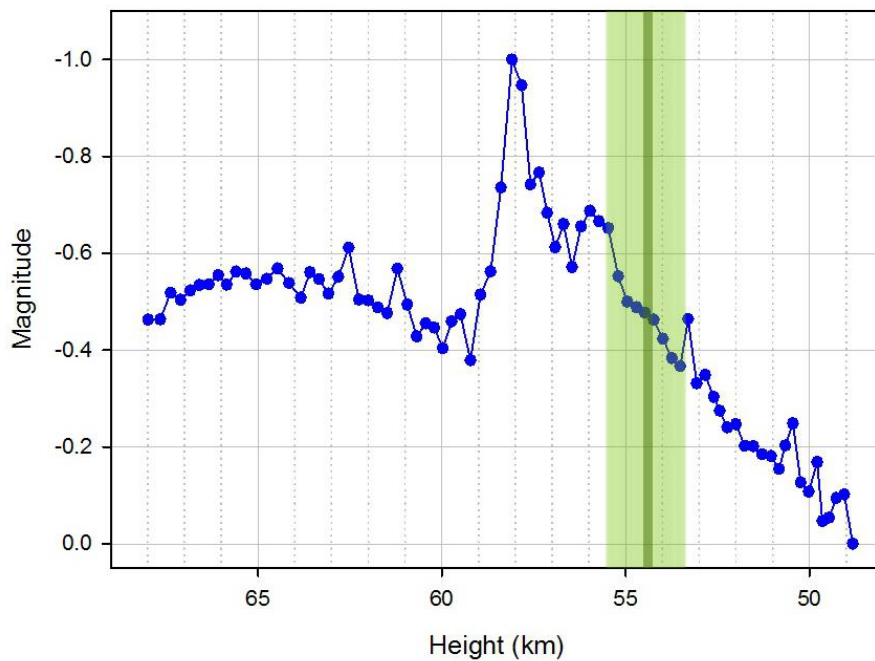
20060419 (cam 04)

04:21:28

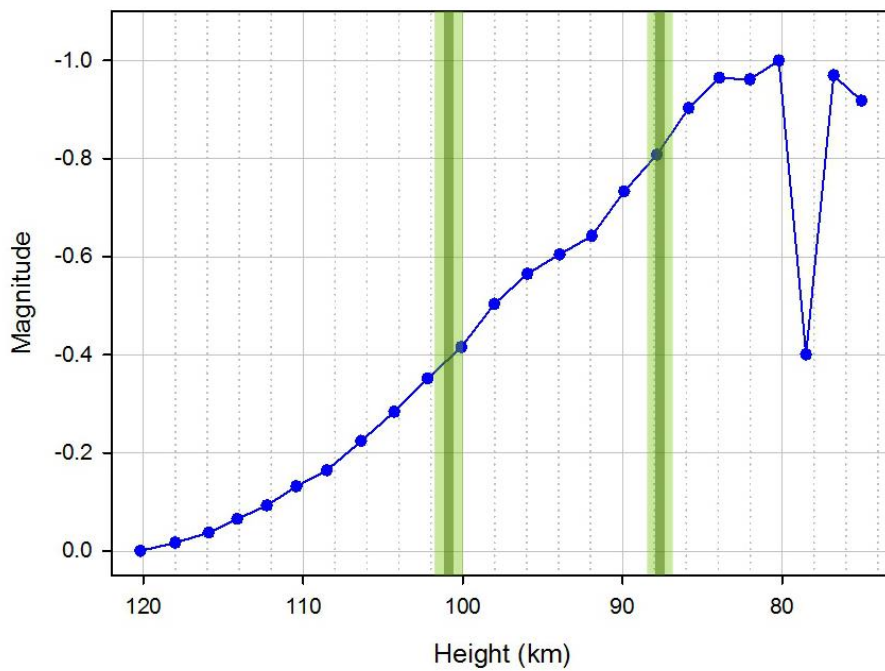


20060419 (cam 04)

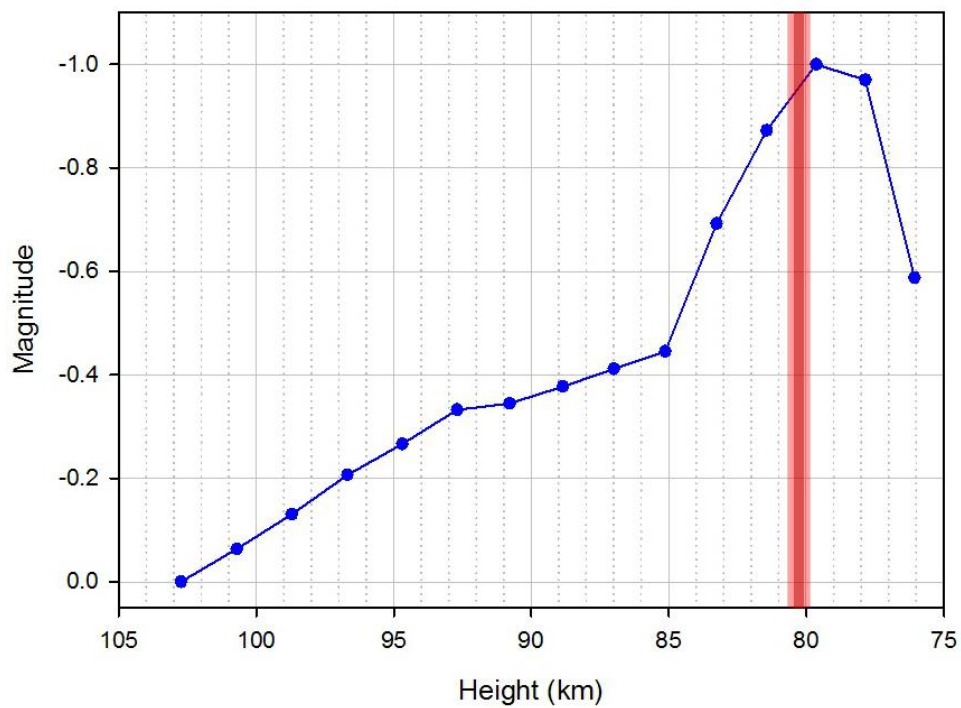
07:05:57



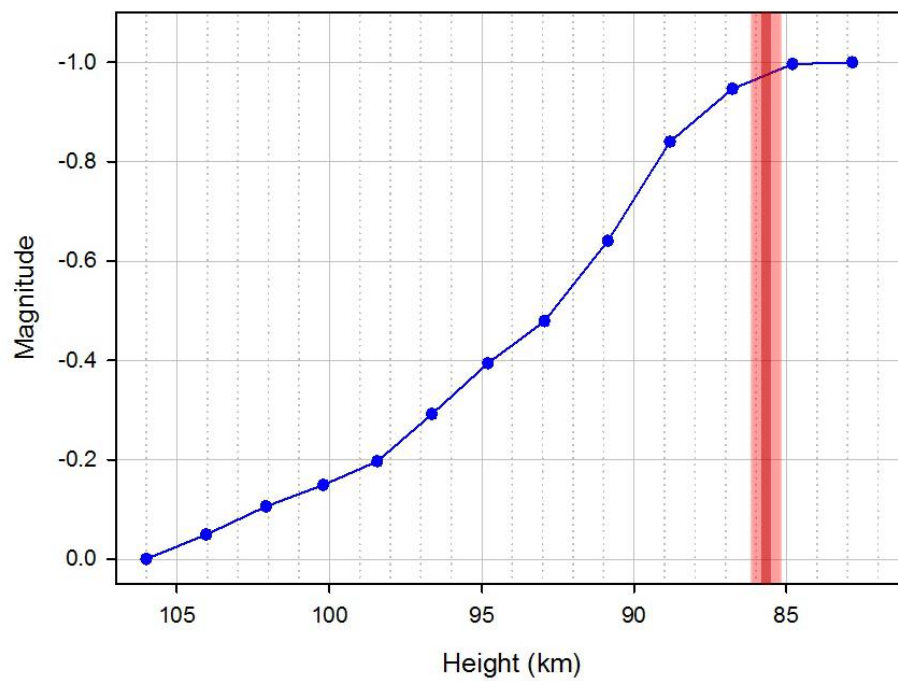
20060805 (cam 03)



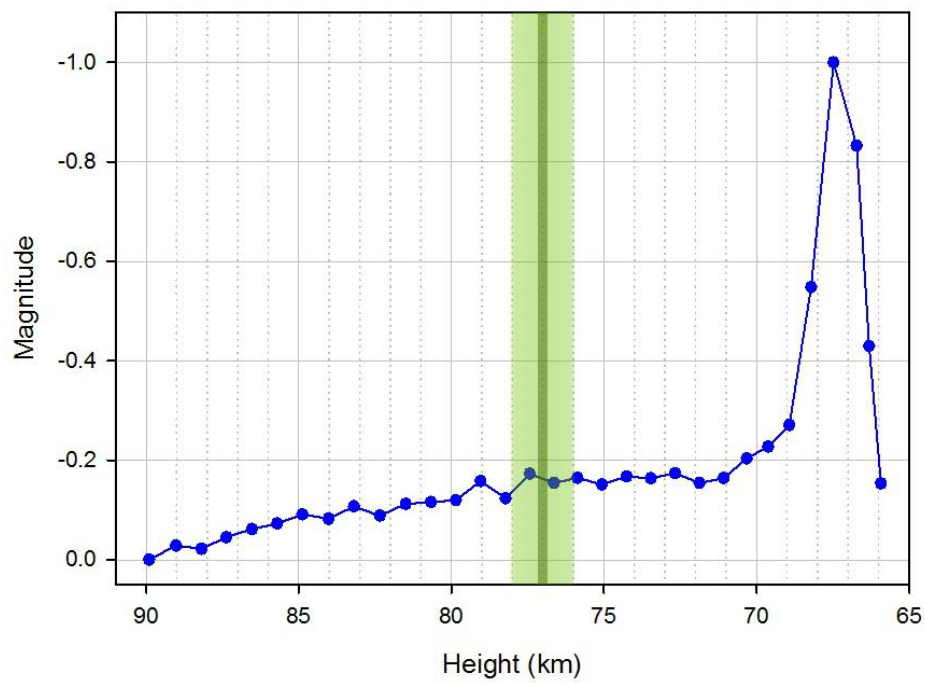
20060813 (cam 02)



20061101 (cam 02)

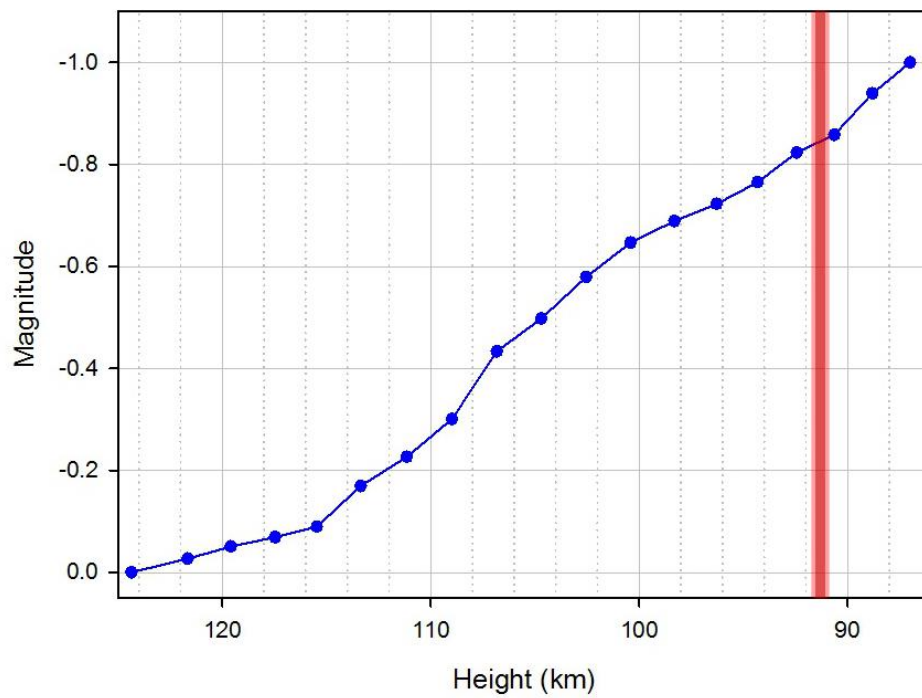


20061104 (cam 04)

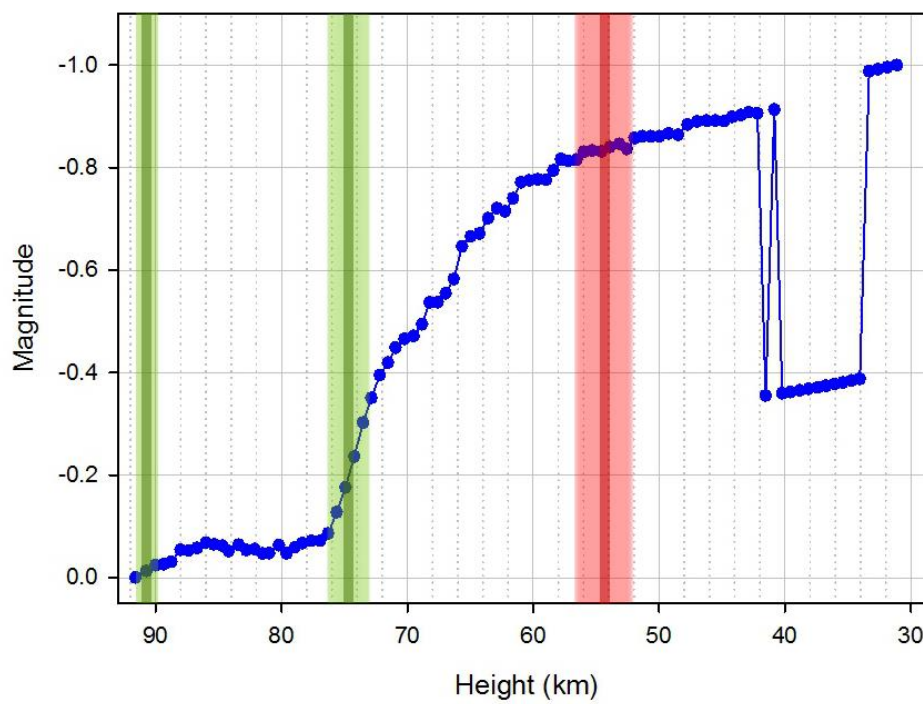




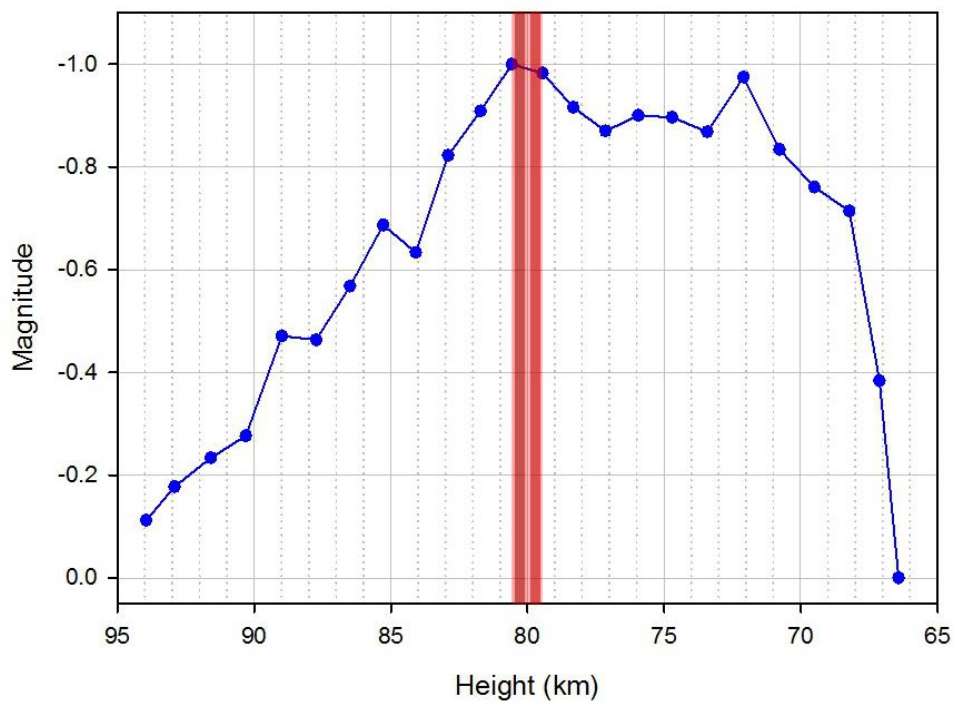
20061121 (cam 03)



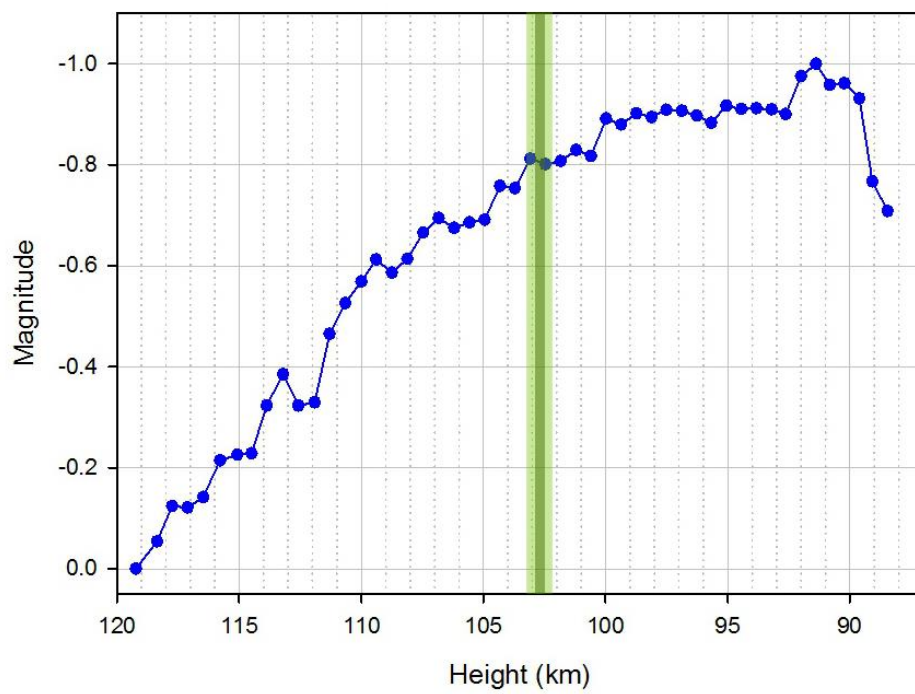
20061223 (cam 03)



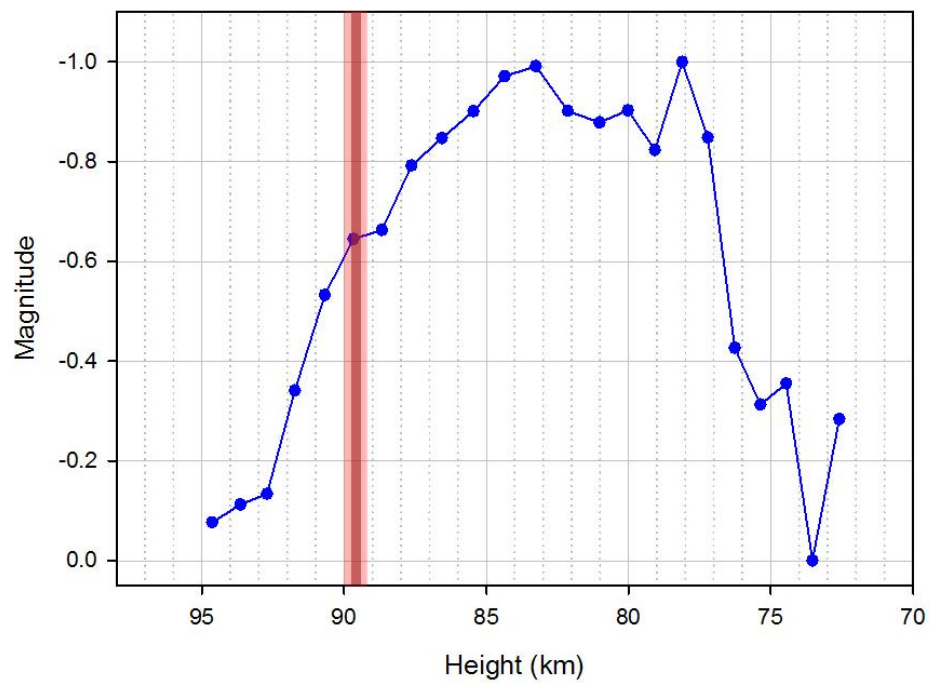
20070102 (cam 05)



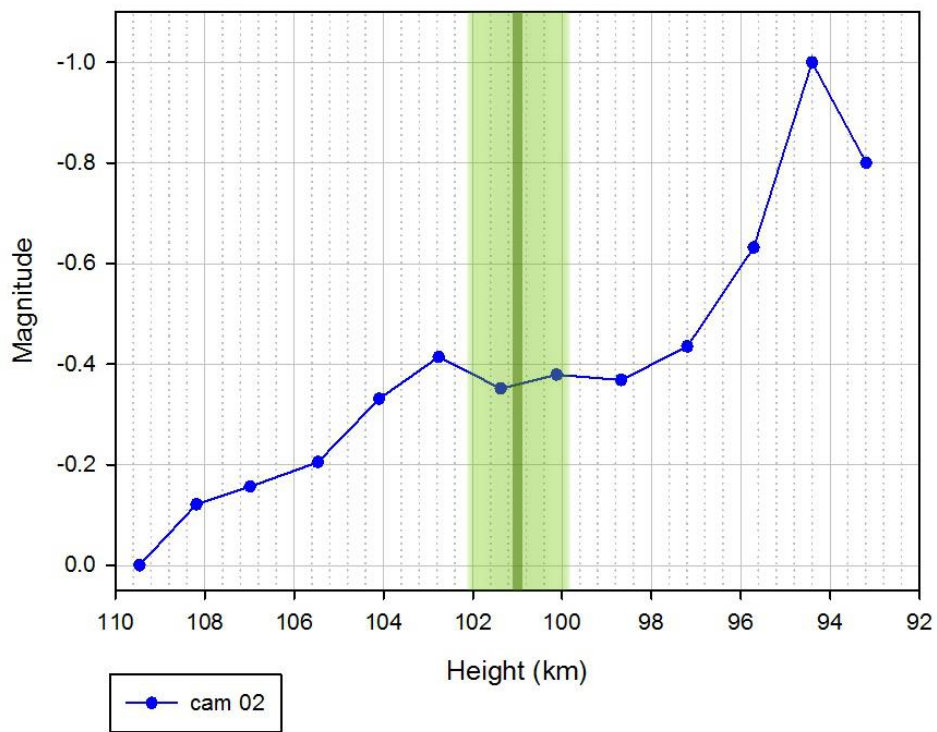
20070125 (cam 02)



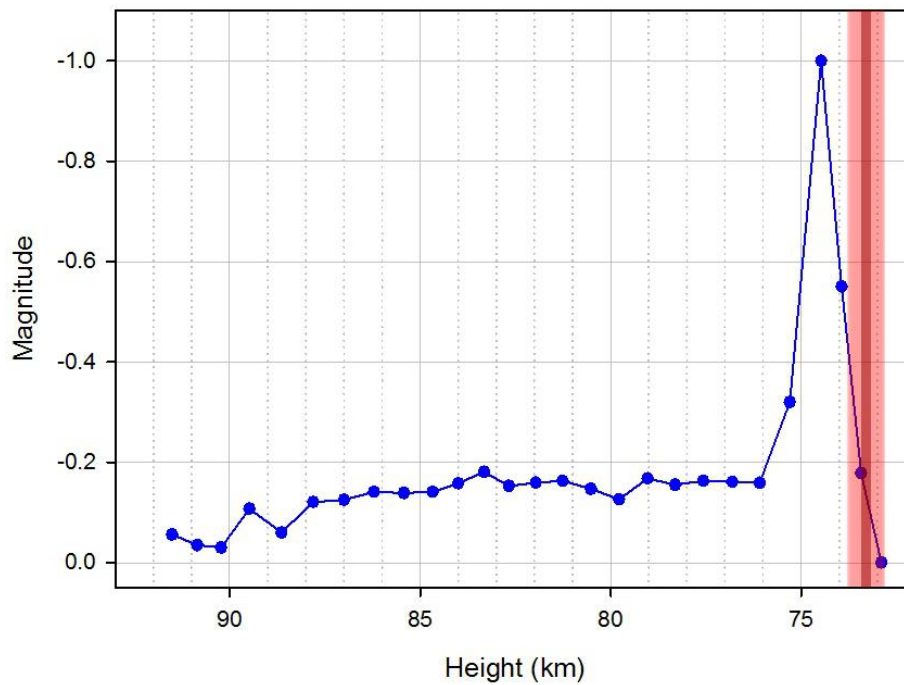
20070421 (cam 02)



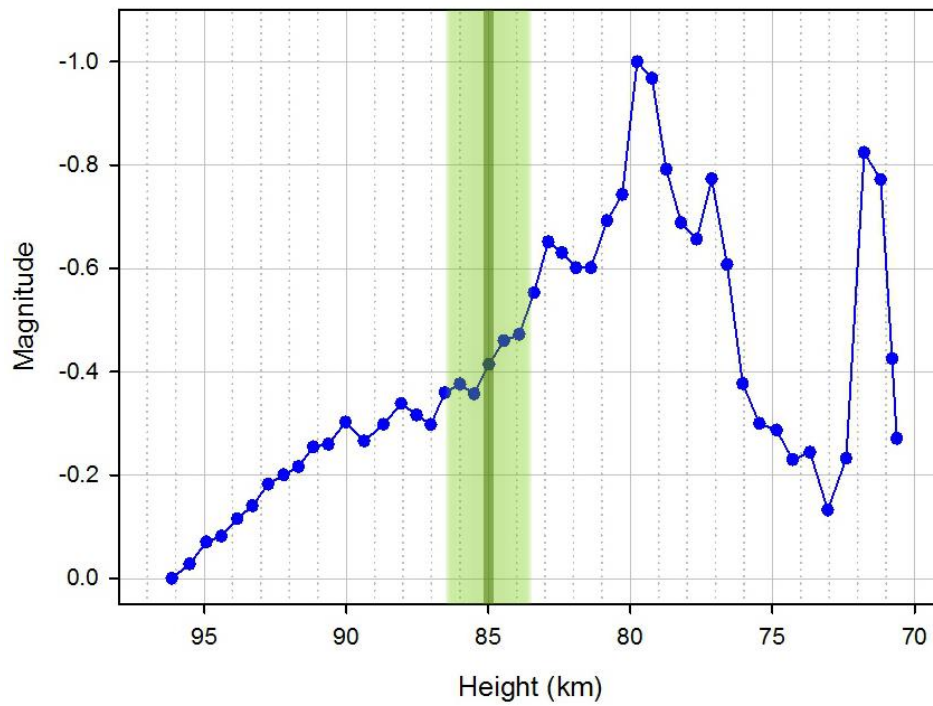
20070511 (cam 04)



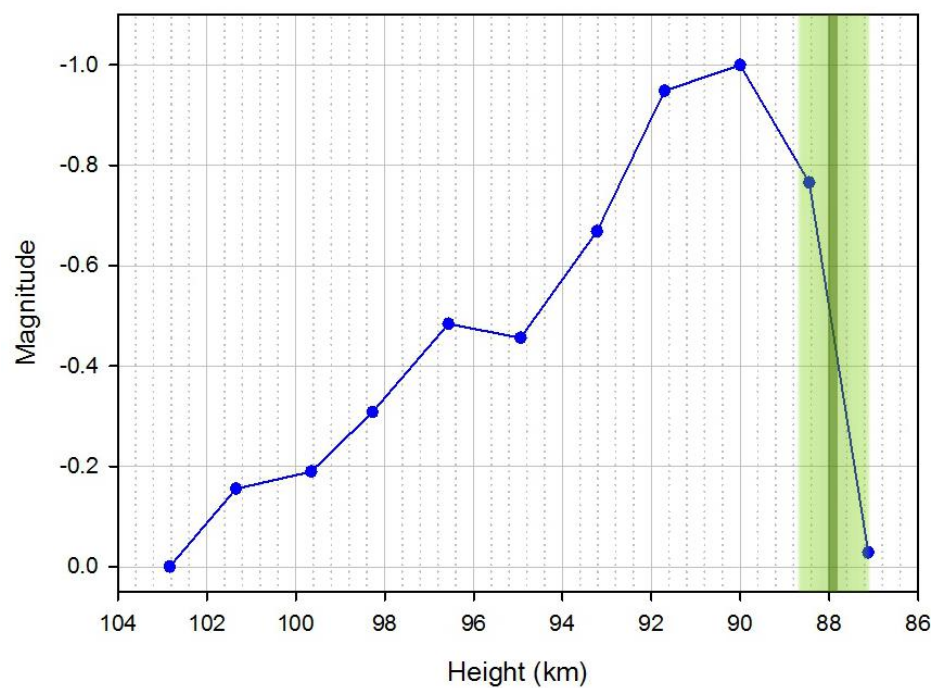
20070725 (cam 04)



20070727 (cam 04)

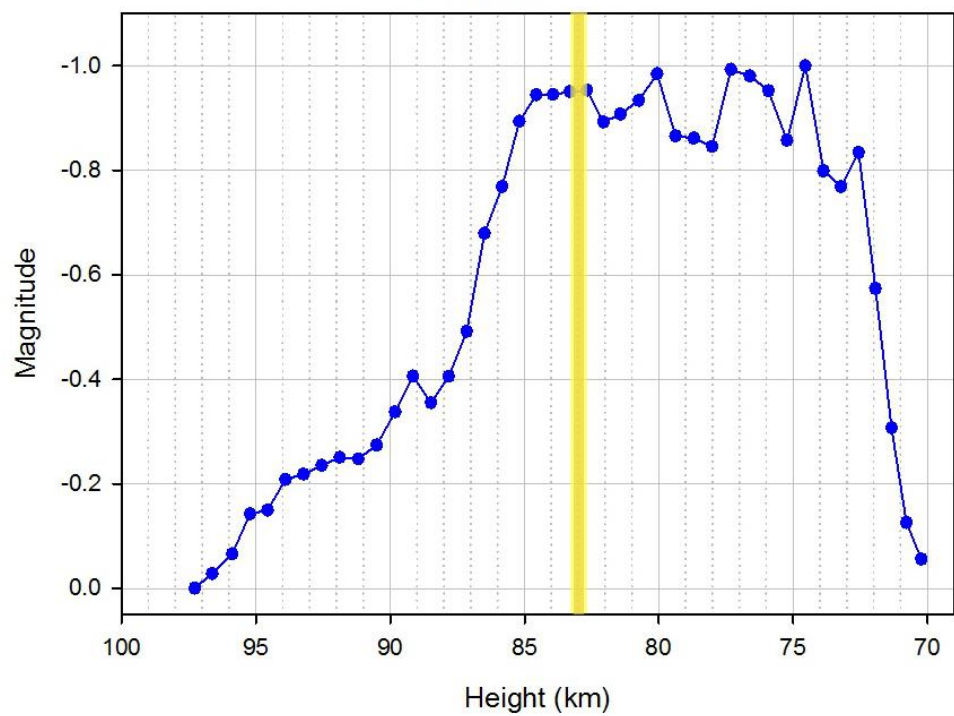


20070917 (cam 02)



20071004 (cam 05)

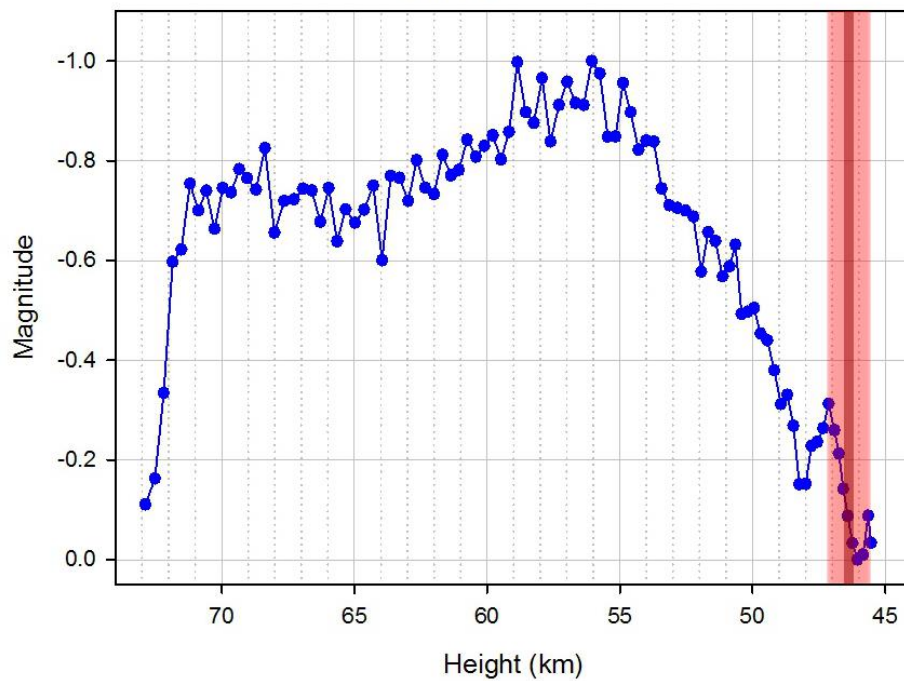
04:55:09



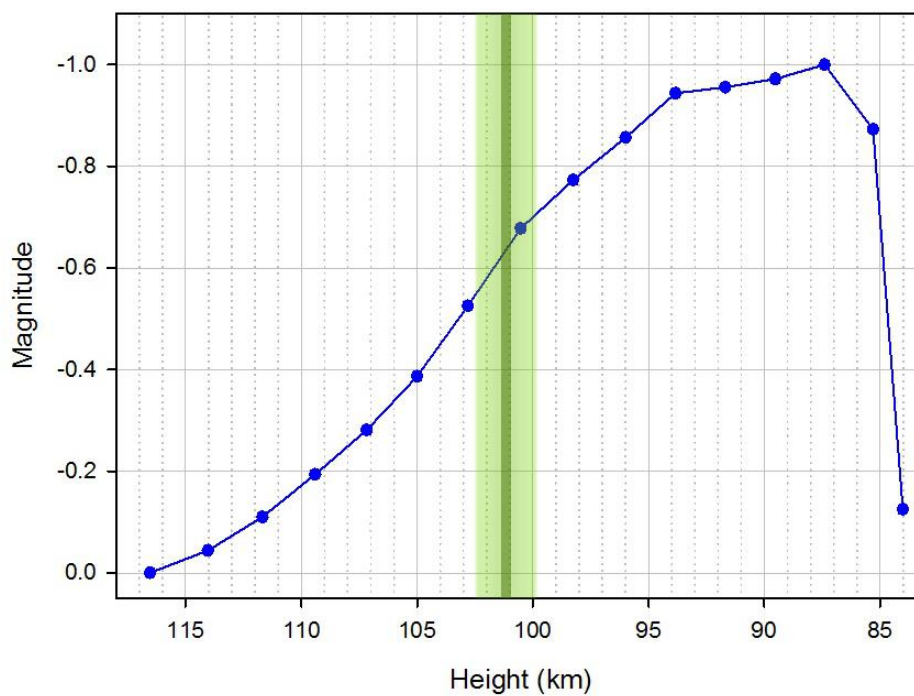


20071004 (cam 04)

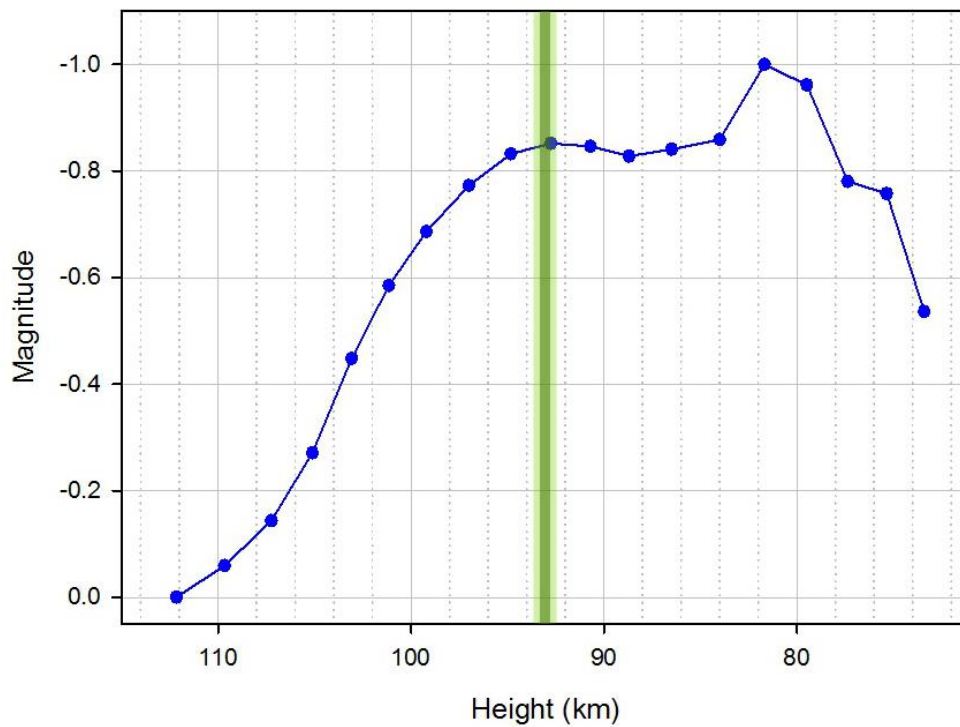
05:19:27



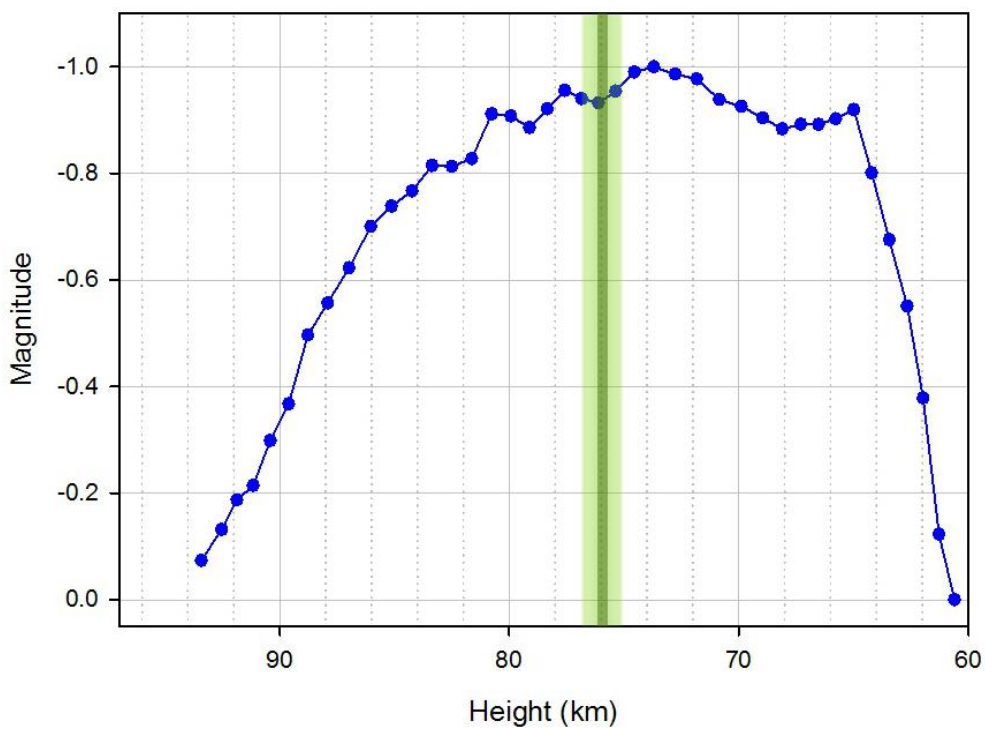
20071021 (cam 04)



20071130 (cam 06)

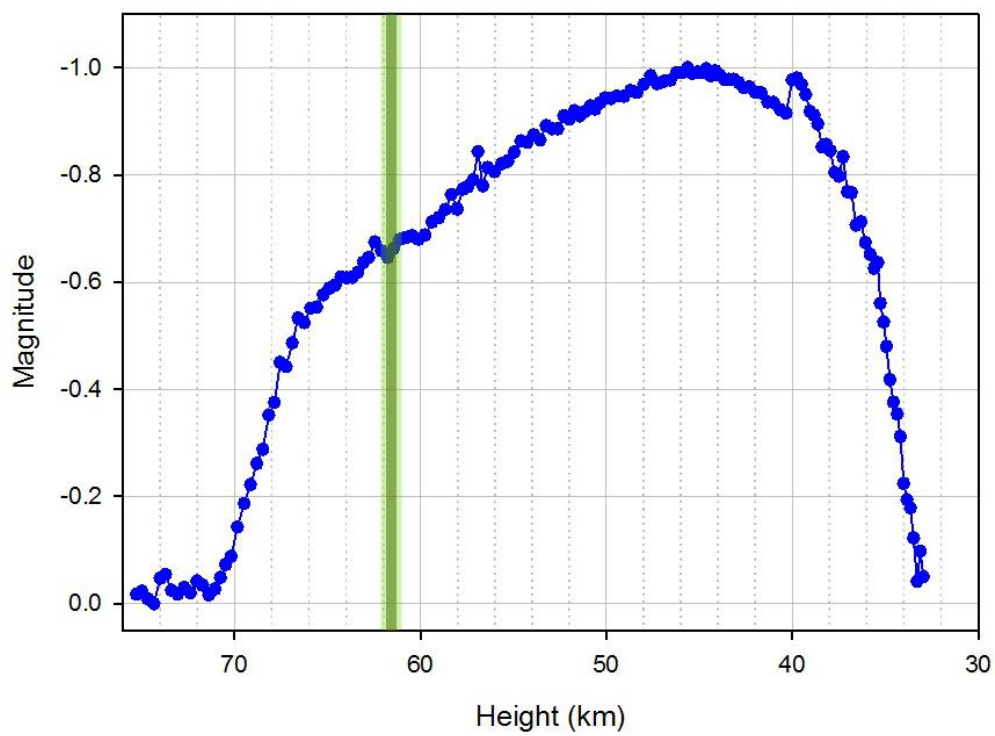


20071215 (cam 06)

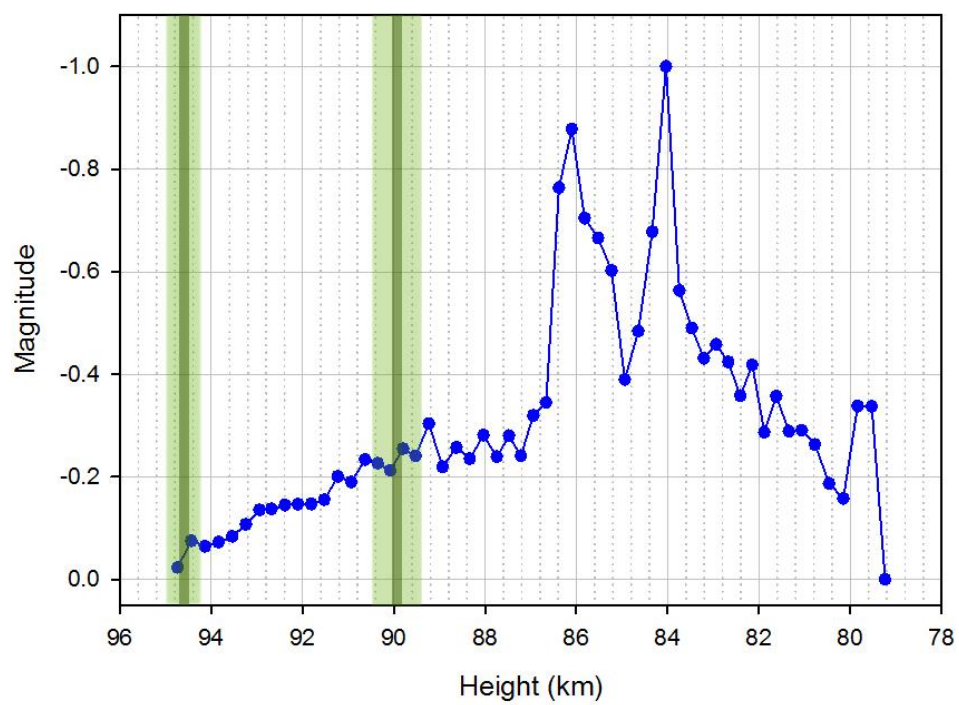




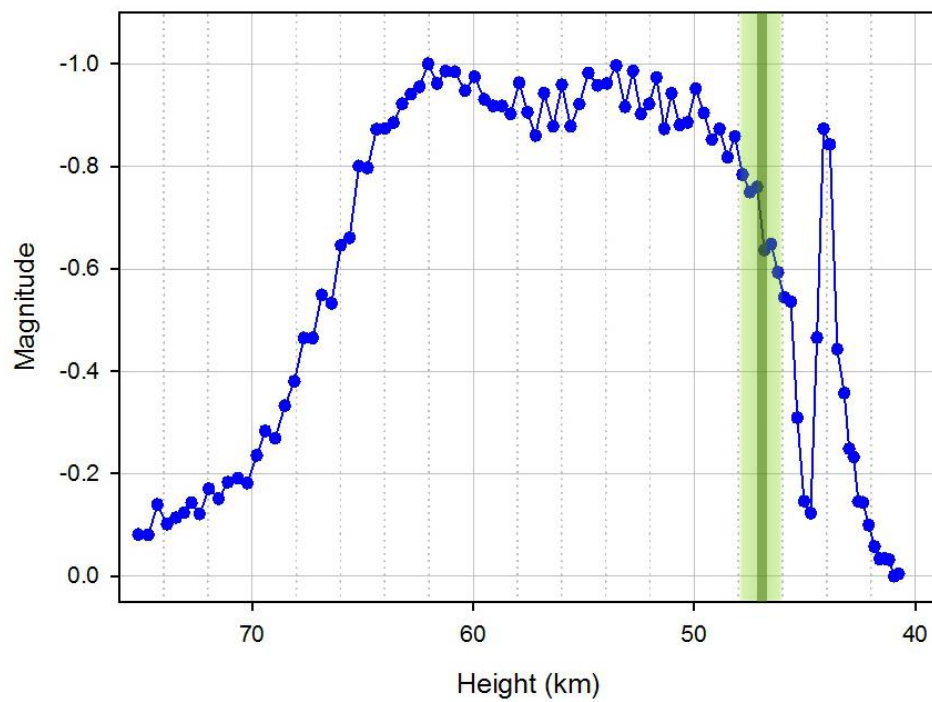
20080325 (cam 02)



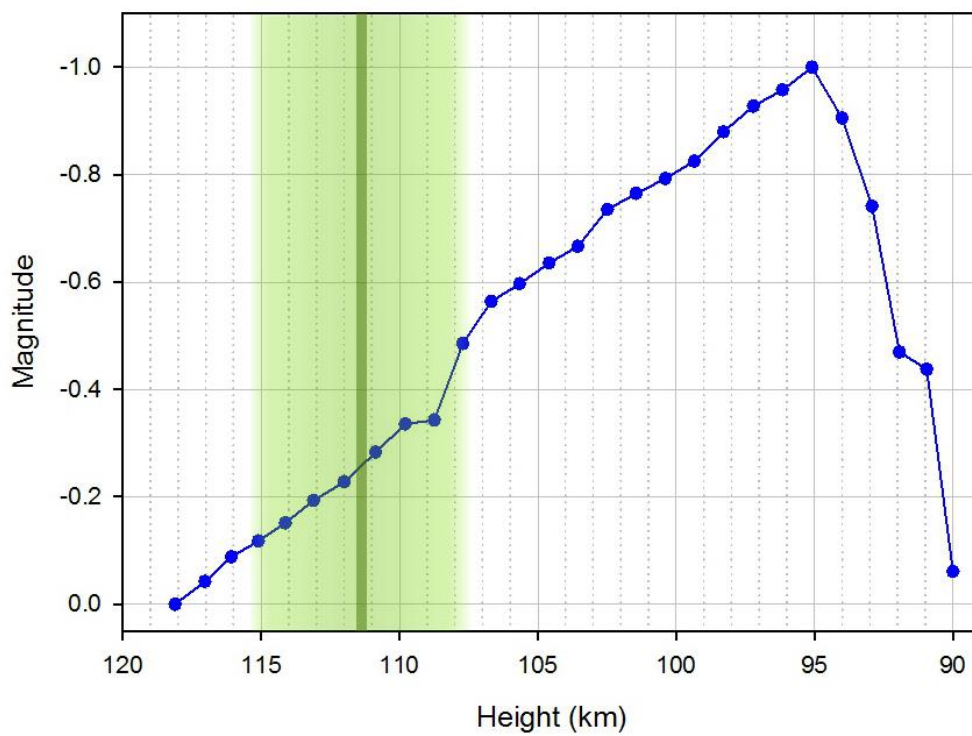
20080511 (cam 06)



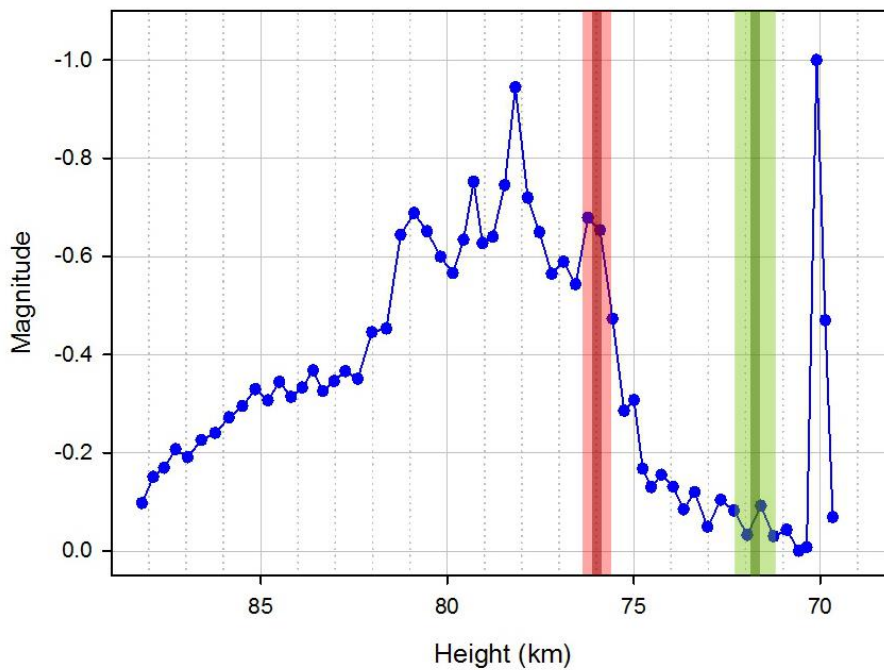
20080520 (cam 04)



20080602 (cam 02)

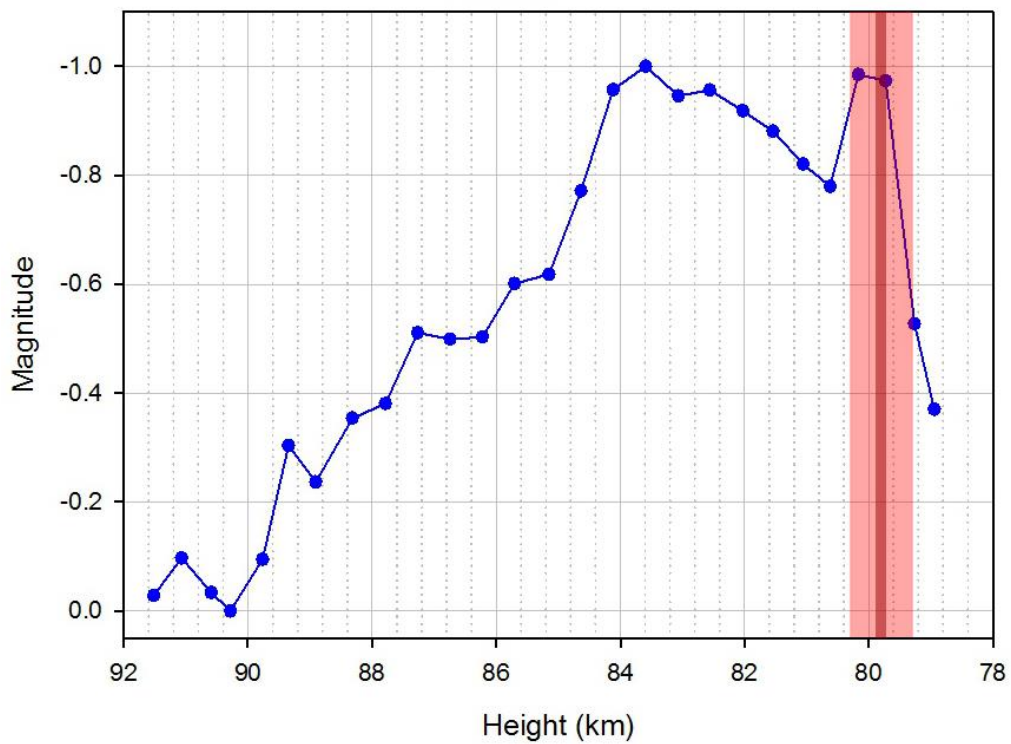


20080612 (cam 05)



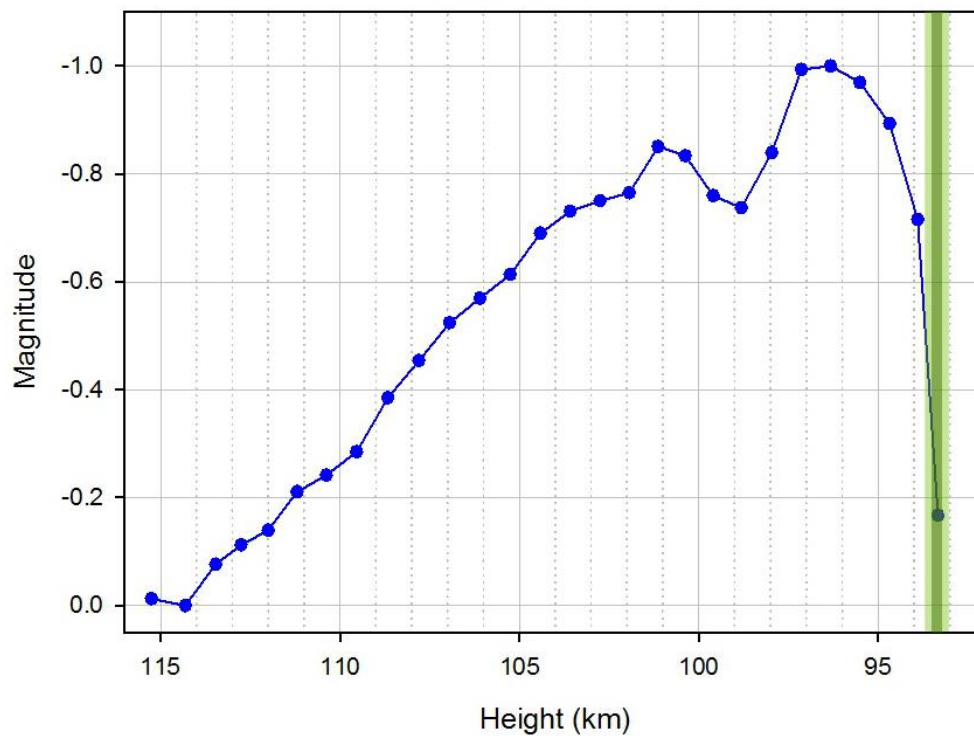
20080801 (cam 05)

04:22:20

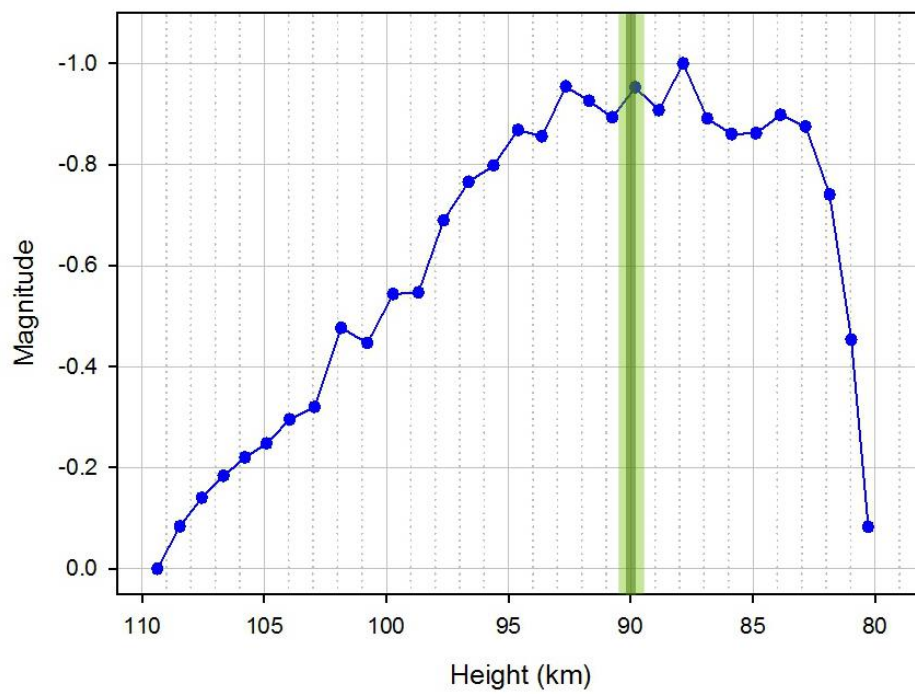


20080801 (cam 04)

08:19:30

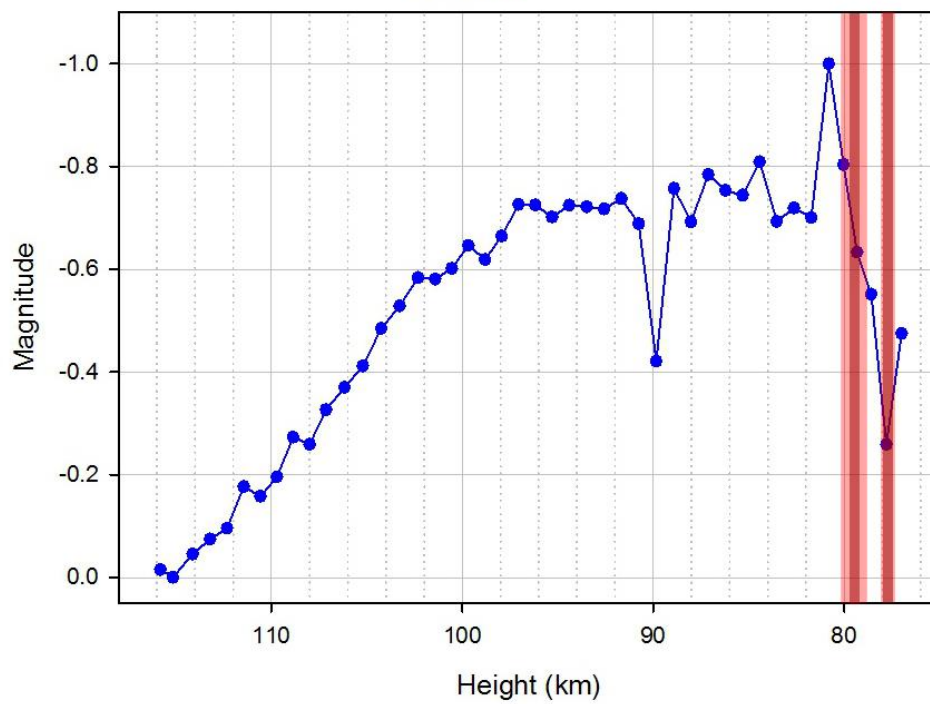


20080804 (cam 04)



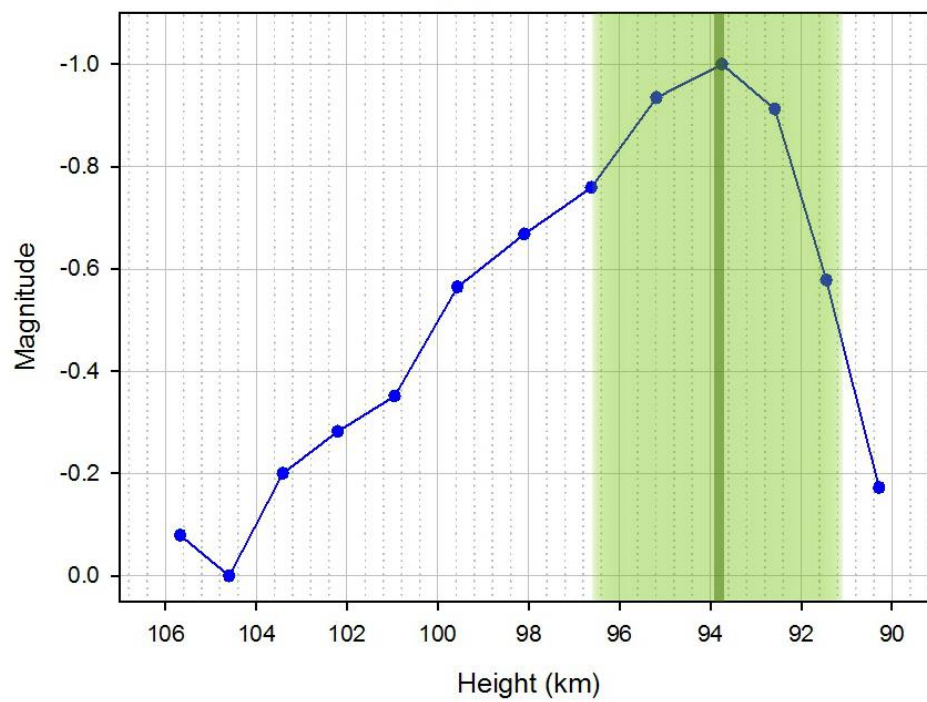
20080812 (cam 02)

03:27:25



20080812 (cam 07)

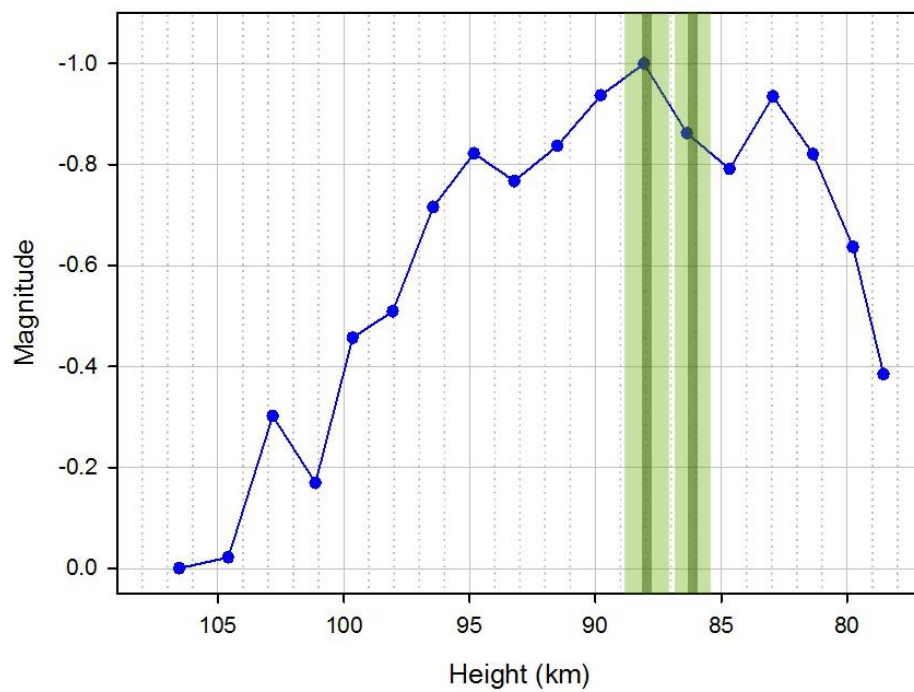
06:00:33



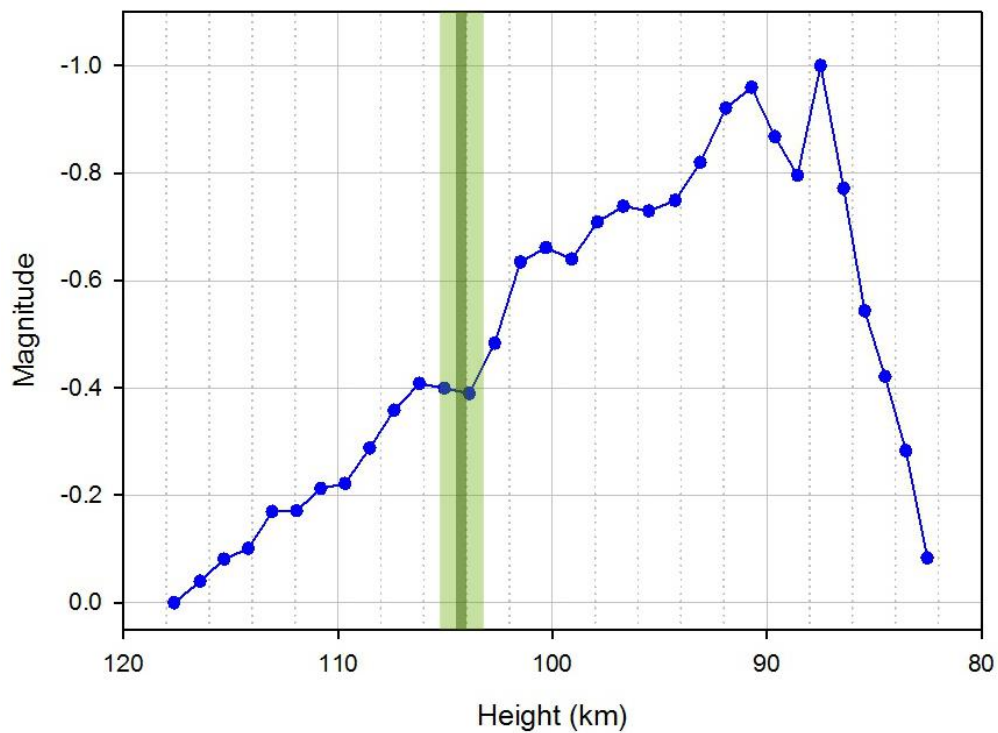


20080812 (cam 02)

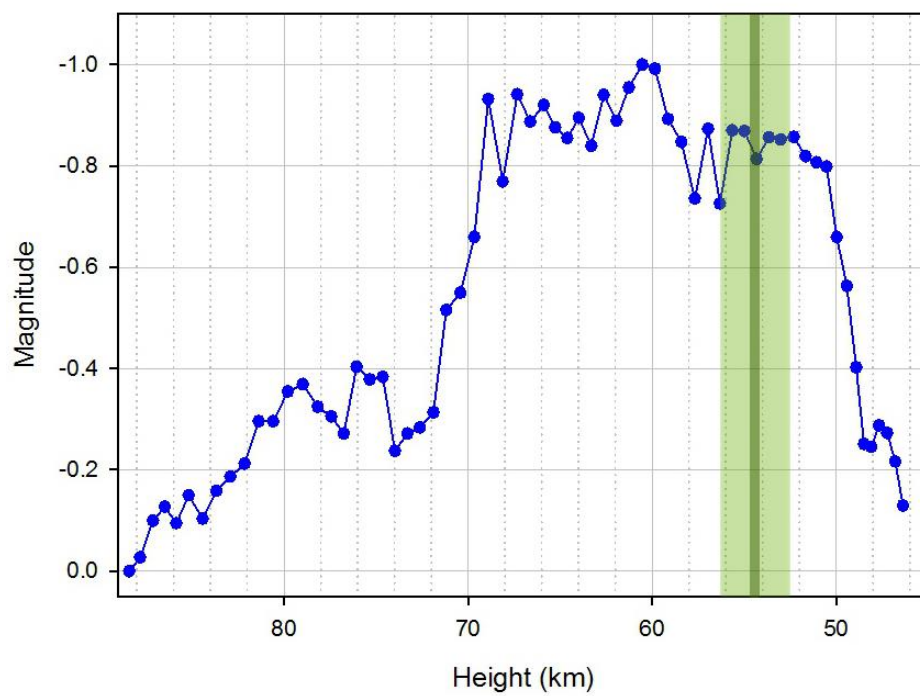
08:19:28



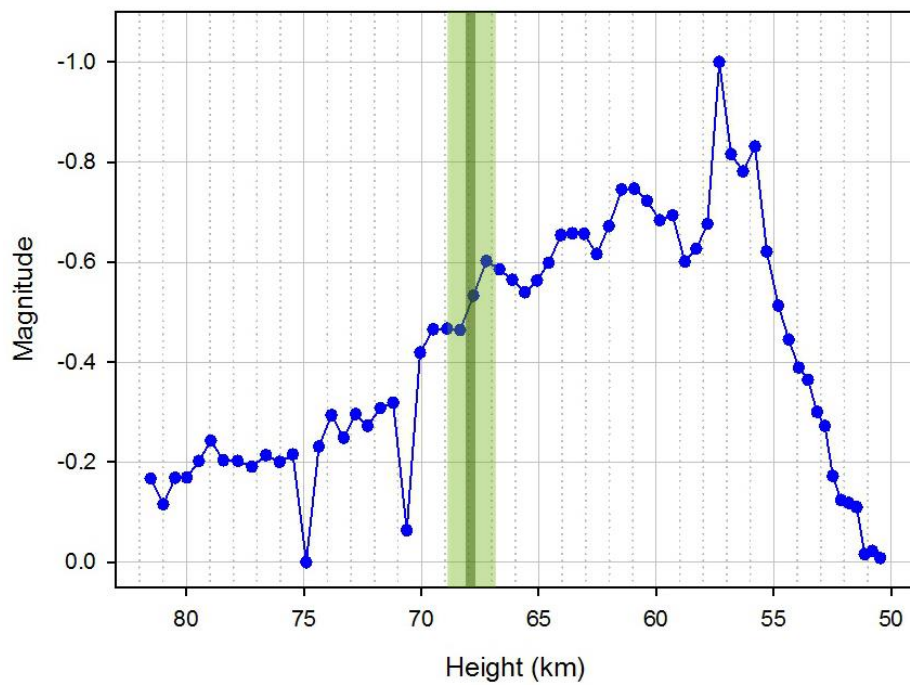
20080908 (cam 07)



20081005 (cam 07)

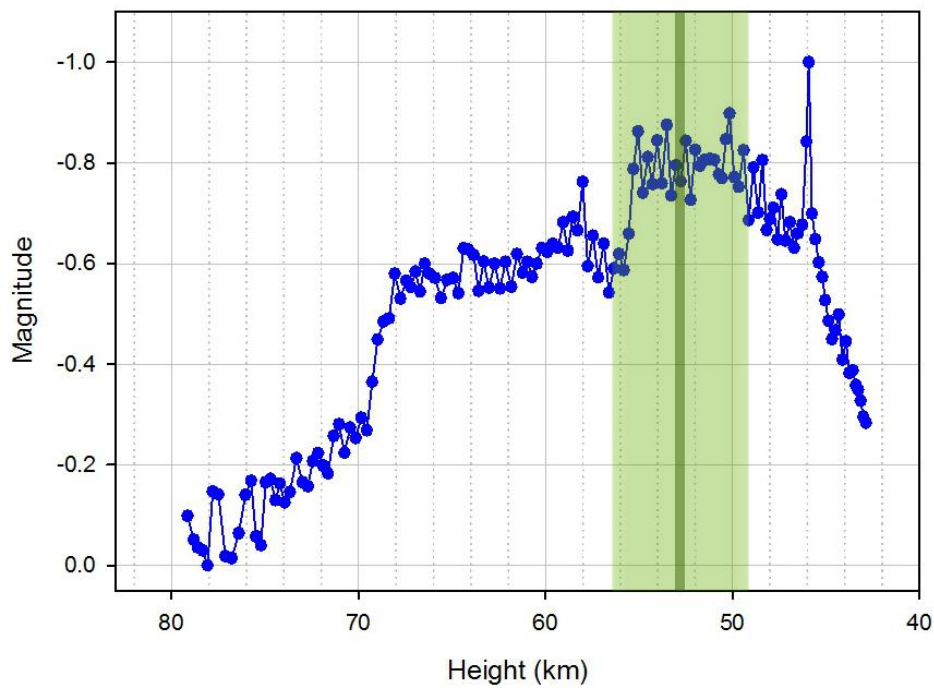


20081018 (cam 02)

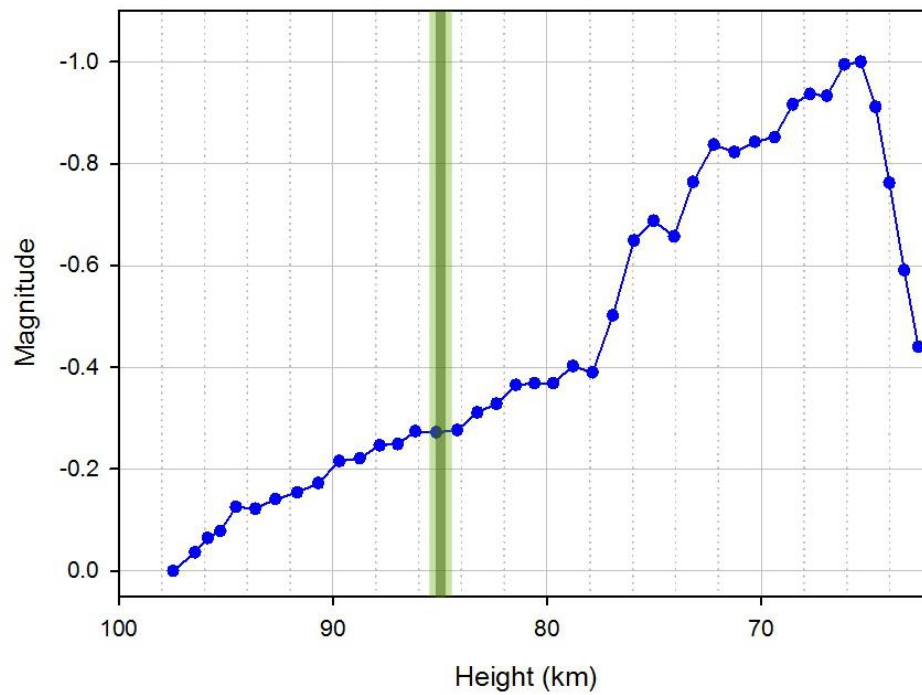




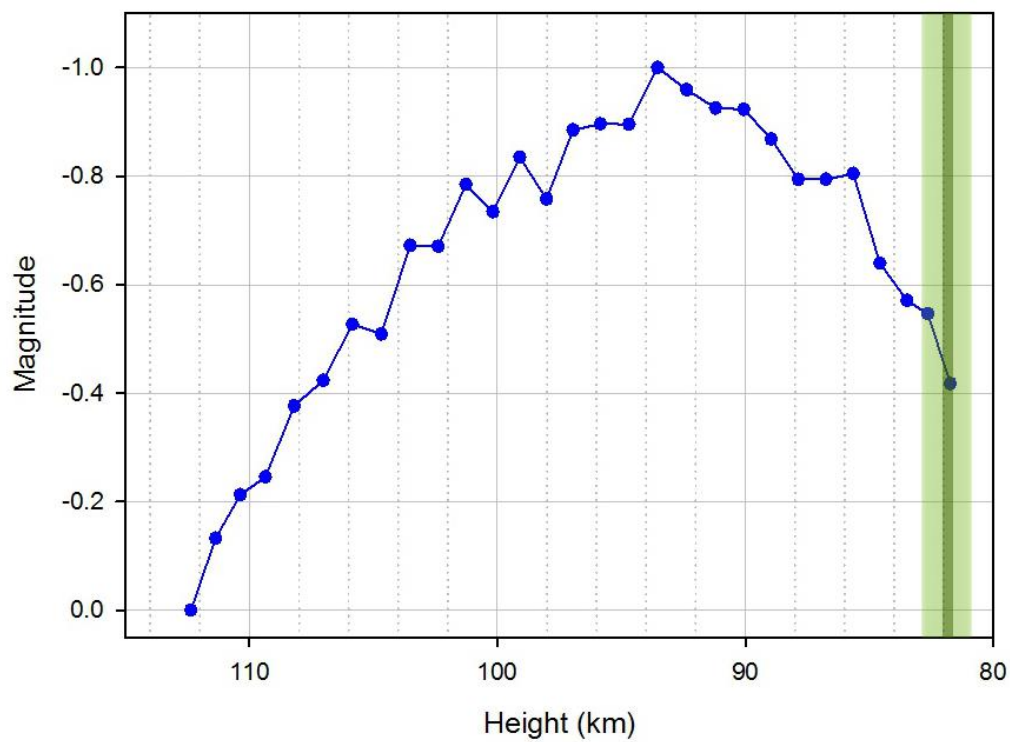
20081028 (cam 02)



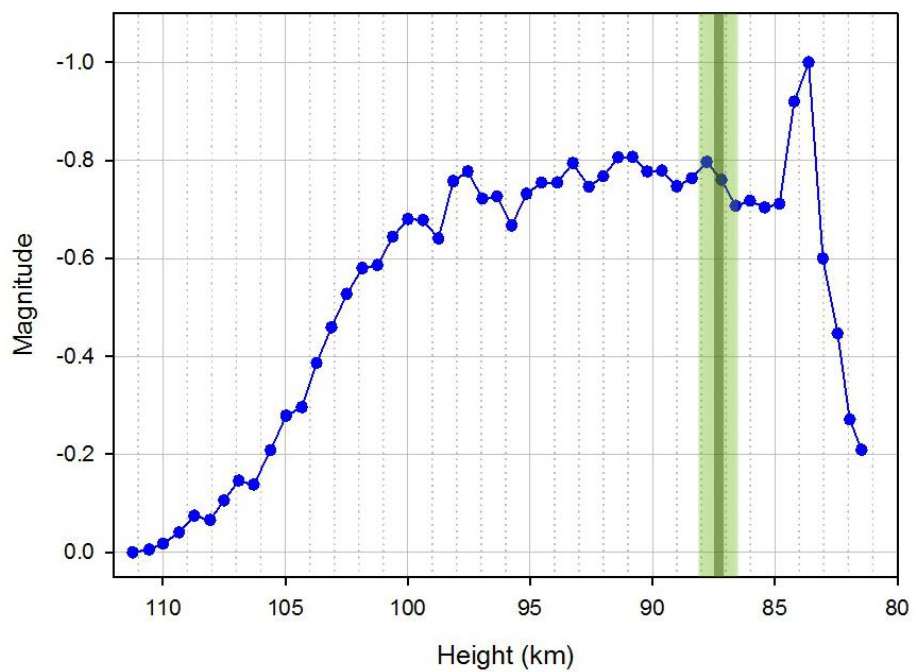
20081102 (cam 07)



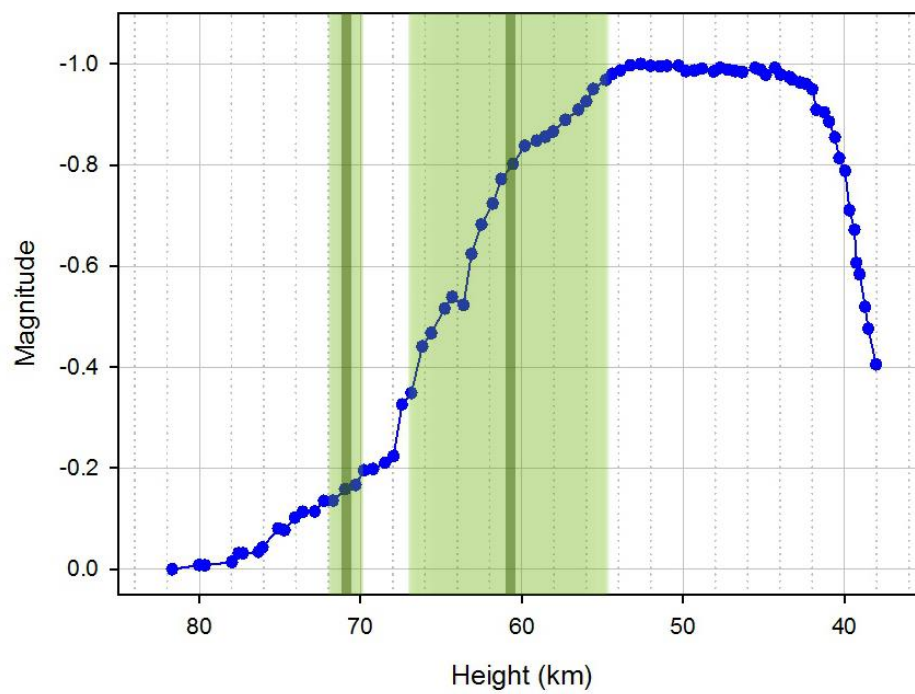
20081107 (cam 07)



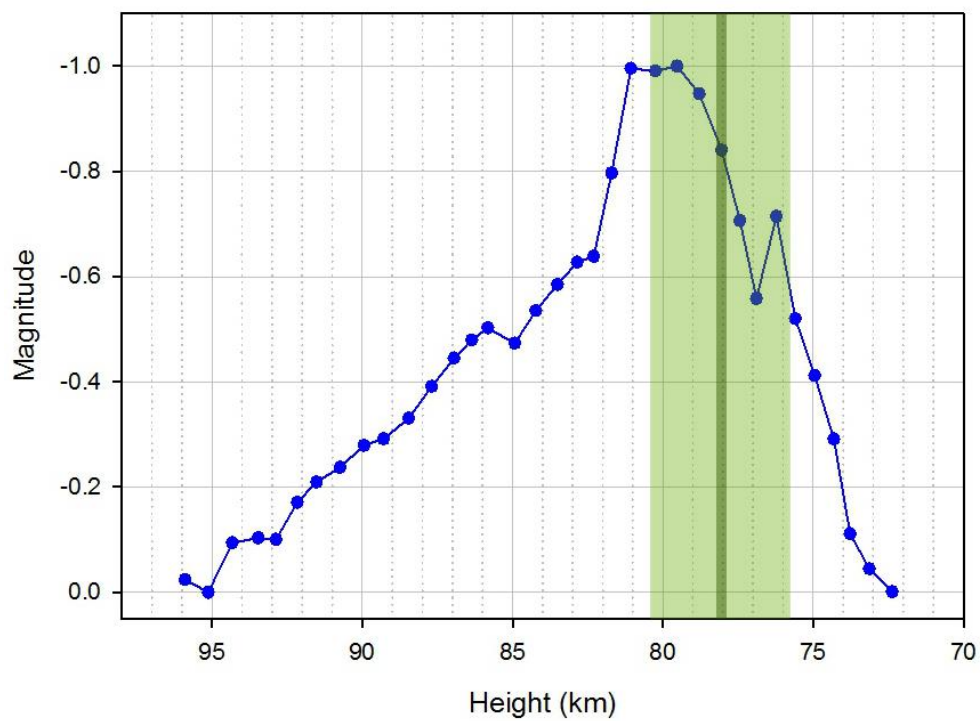
20090126 (cam 04)



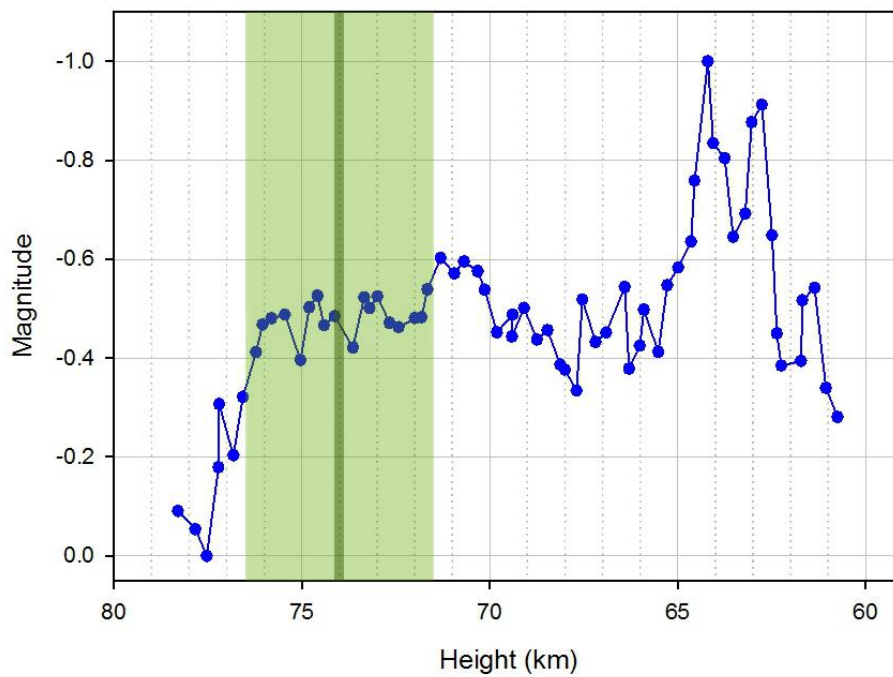
20090428 (cam 04)



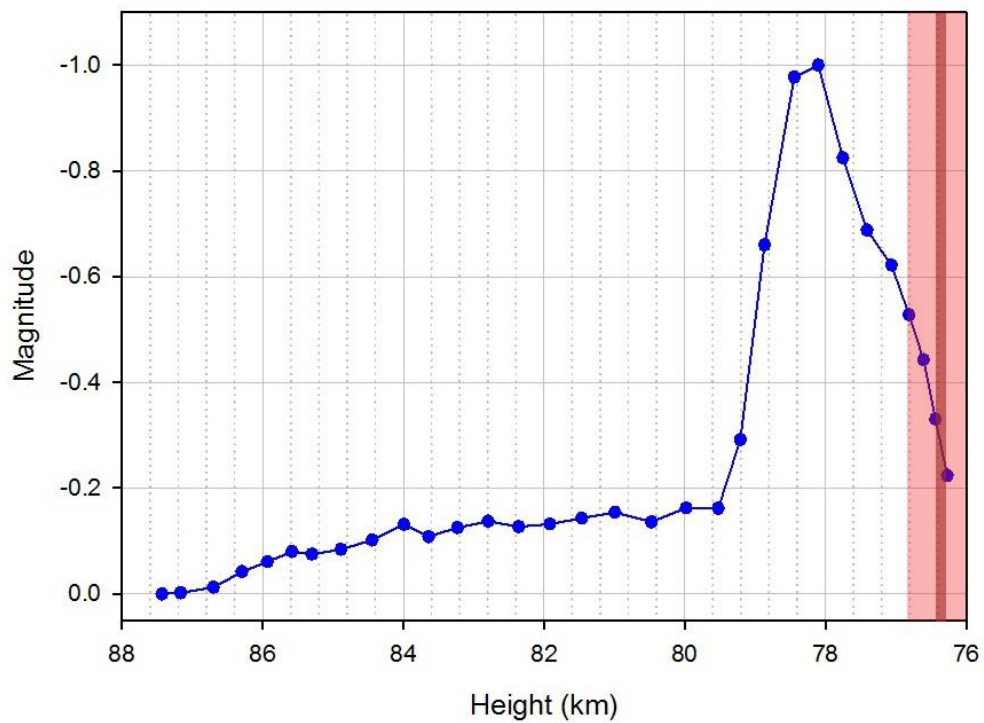
20090523 (cam 06)



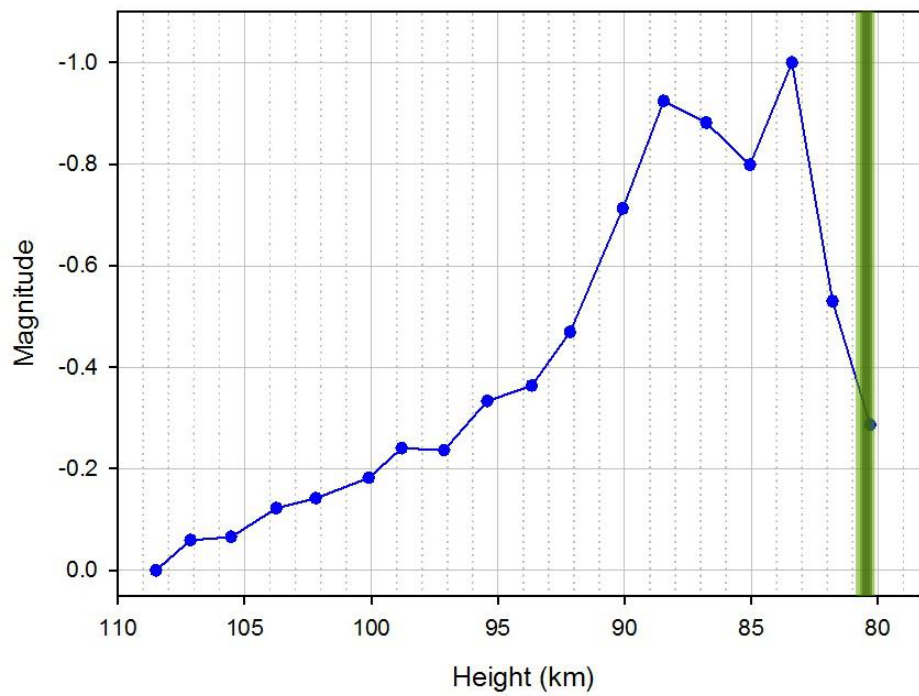
20090530 (cam 04)



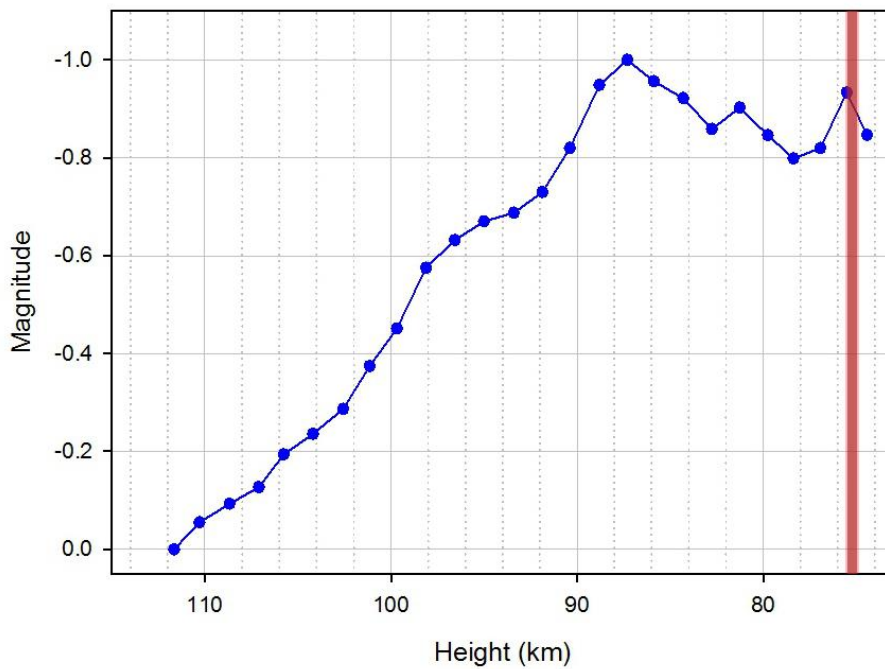
20090709 (cam 06)



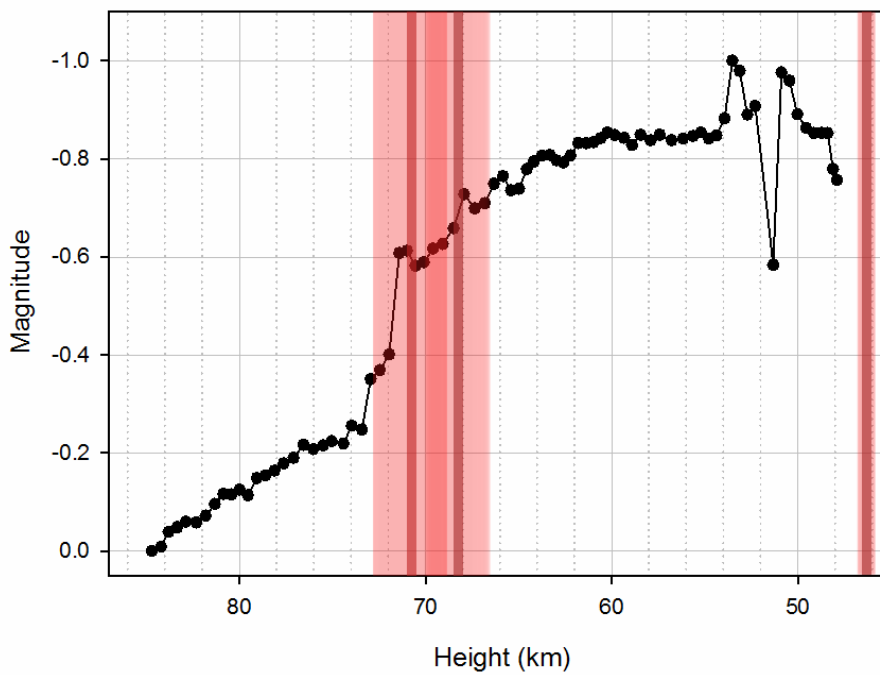
20090812 (cam 03)



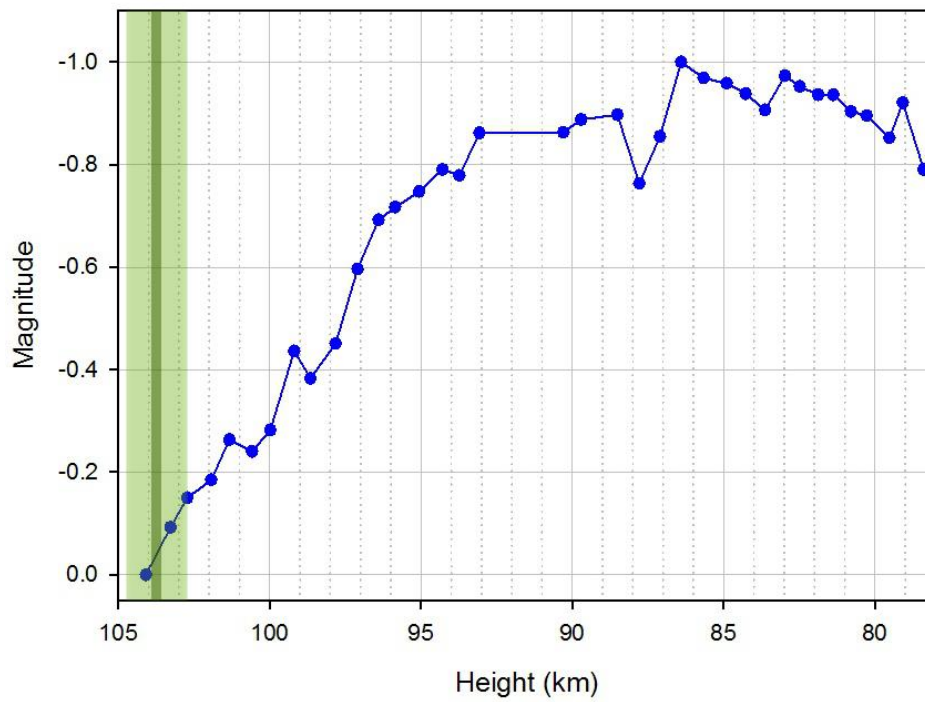
20090813 (cam 06)



20090825 (cam 06)

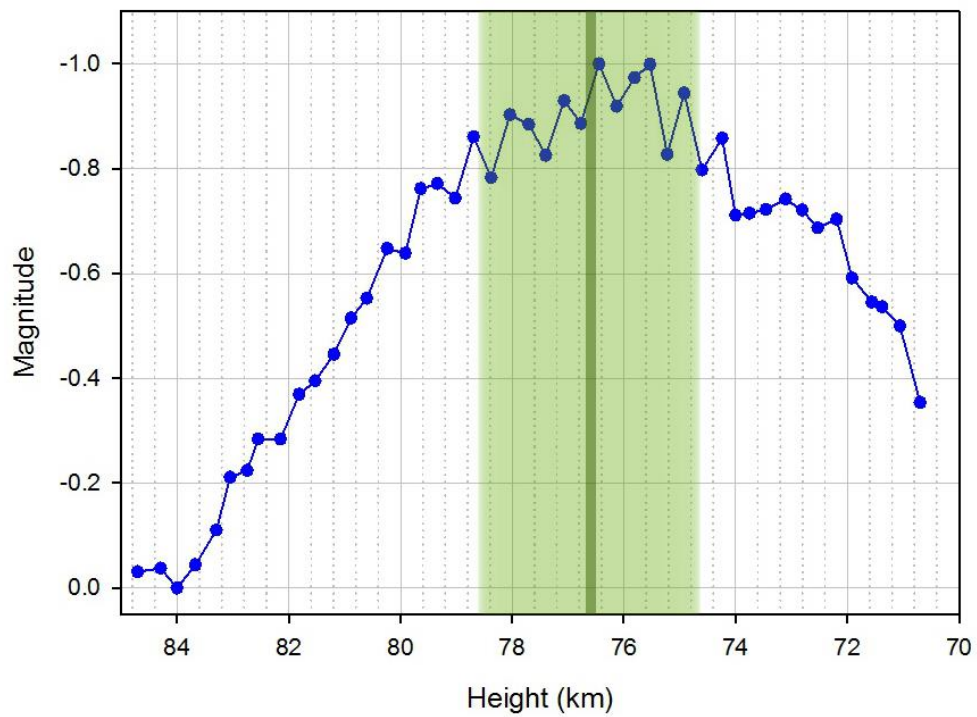


20090906 (cam 05)

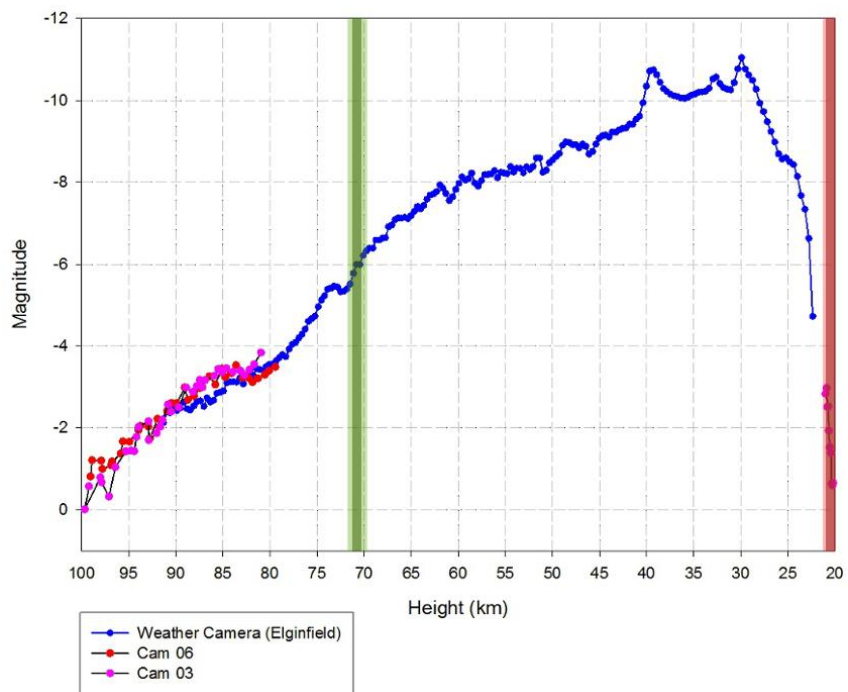




20090917 (cam 01)

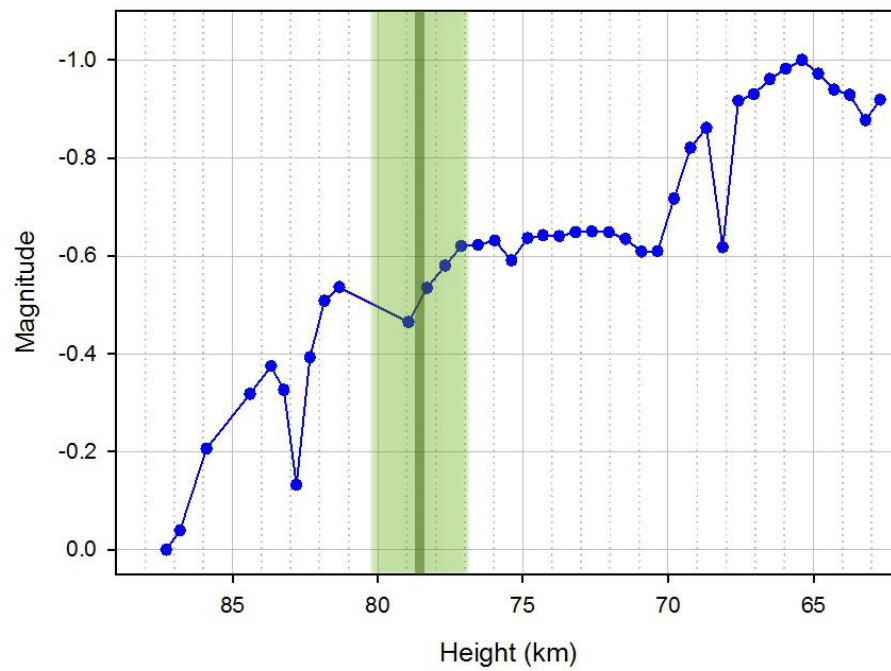


Grimsby Fireball 20090926

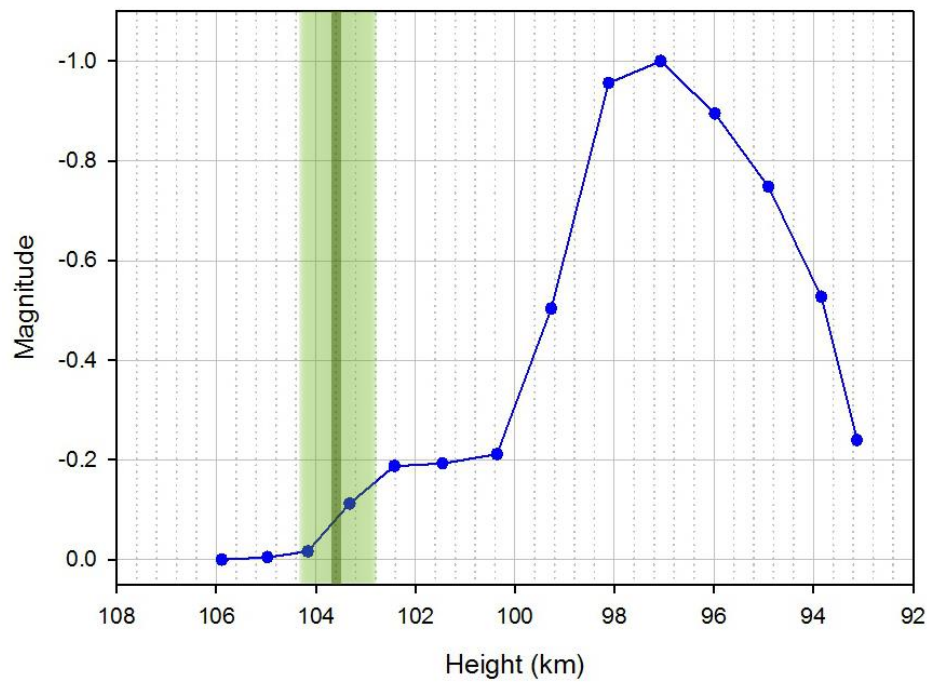




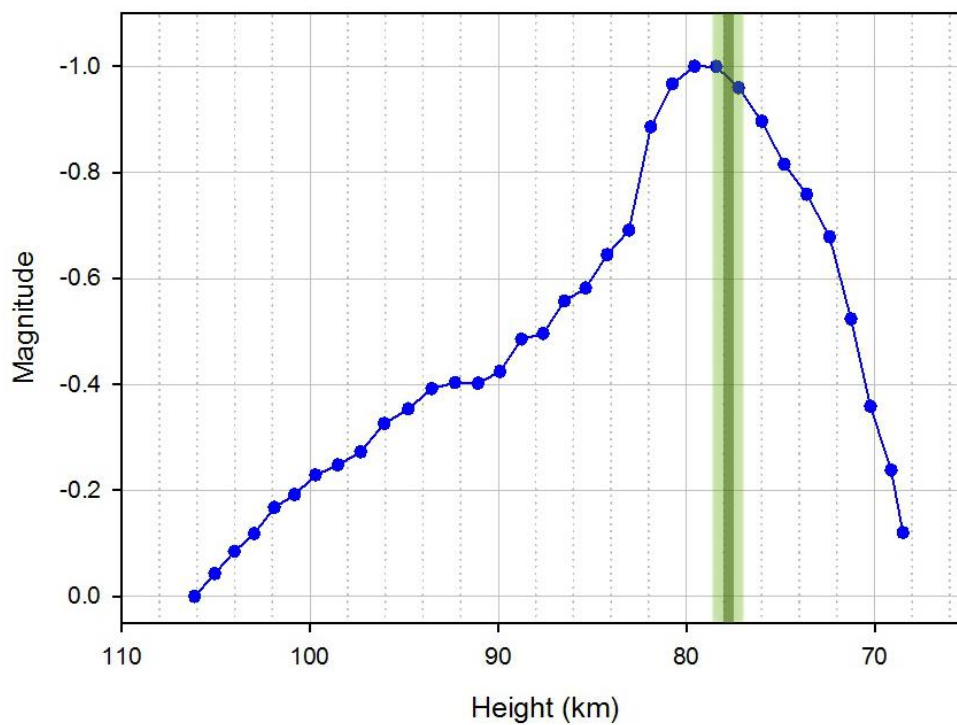
20100111 (cam 02)



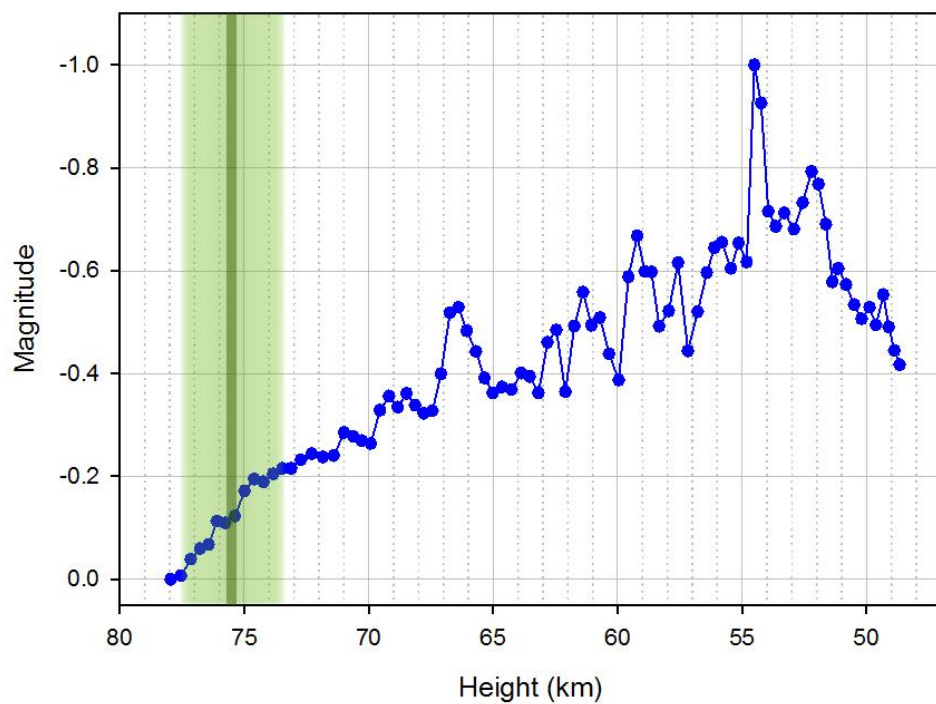
20100307 (cam 01)



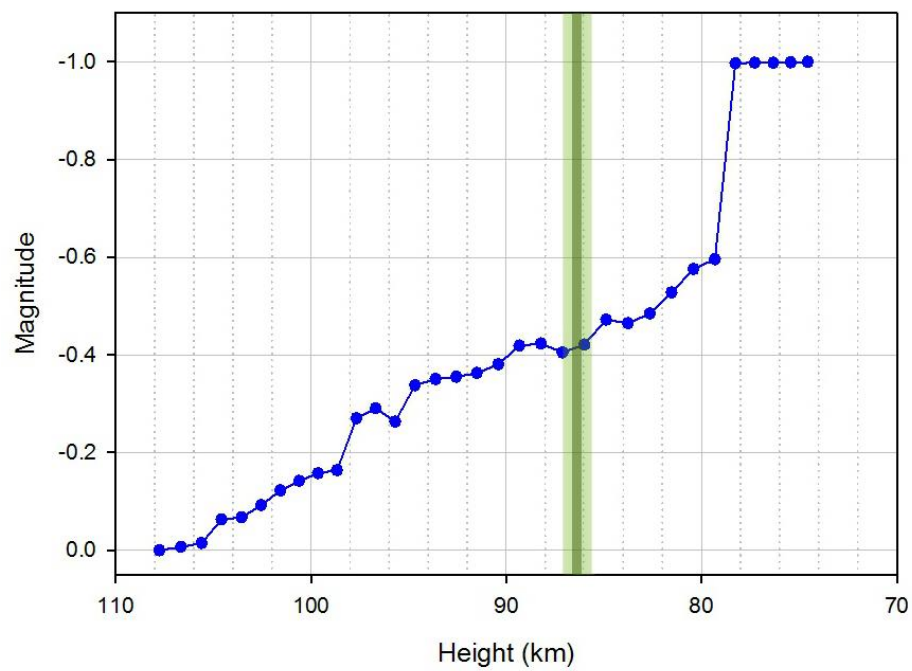
20100309 (cam 04)



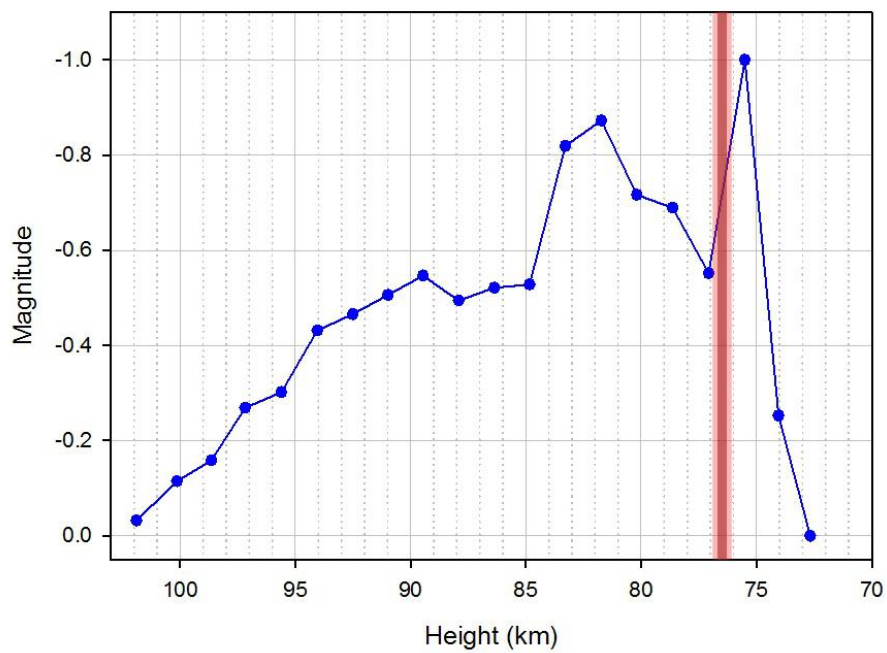
20100316 (cam 06)



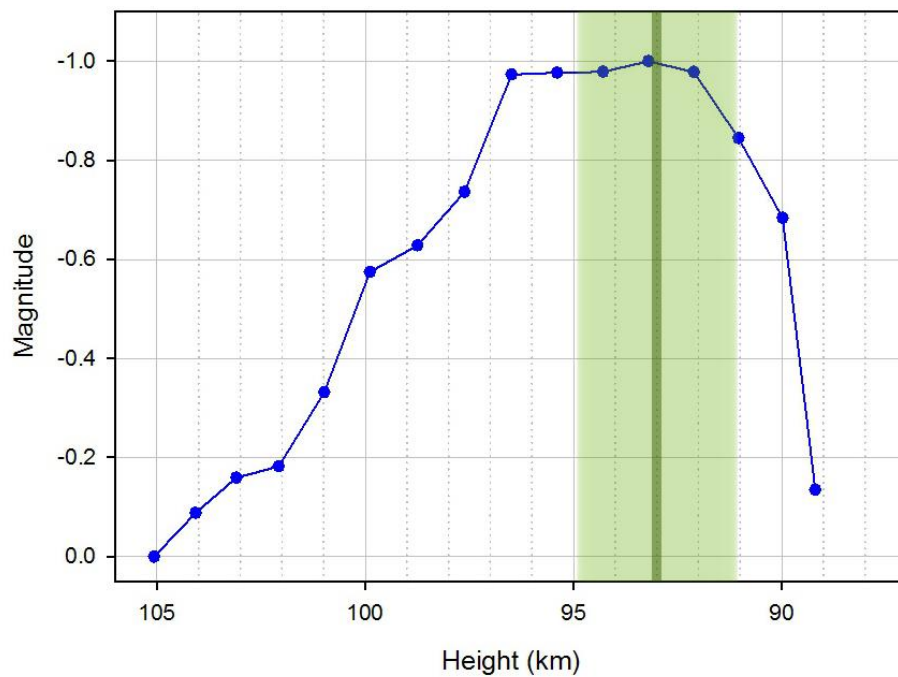
20100421 (cam 05)



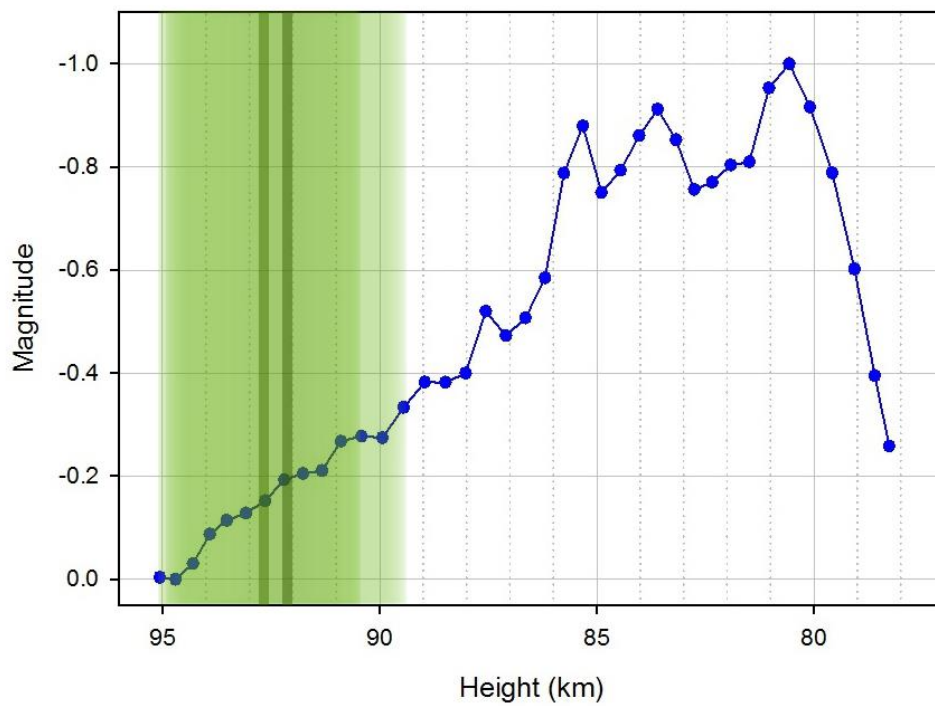
20100423 (cam 06)



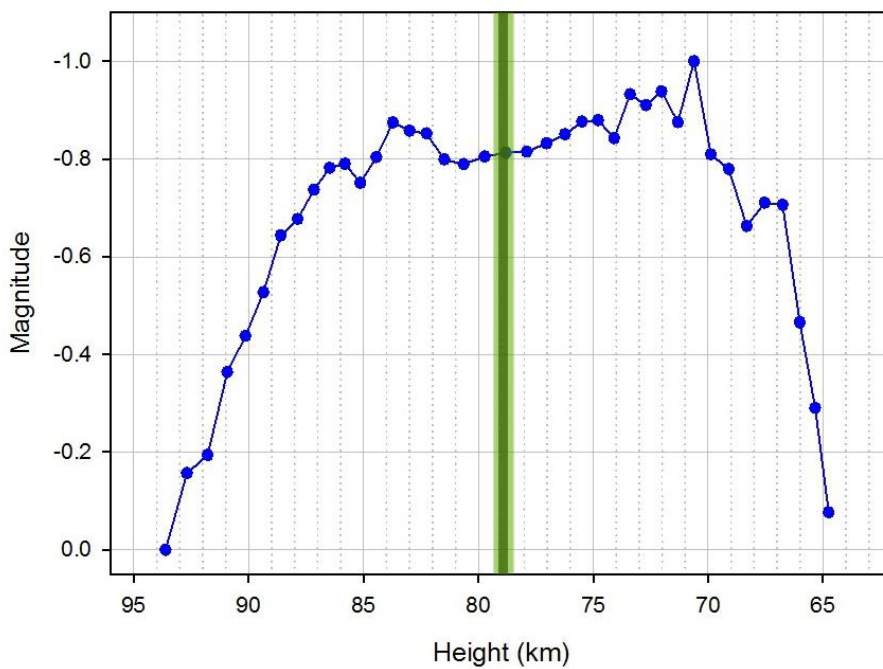
20100429 (cam 07)



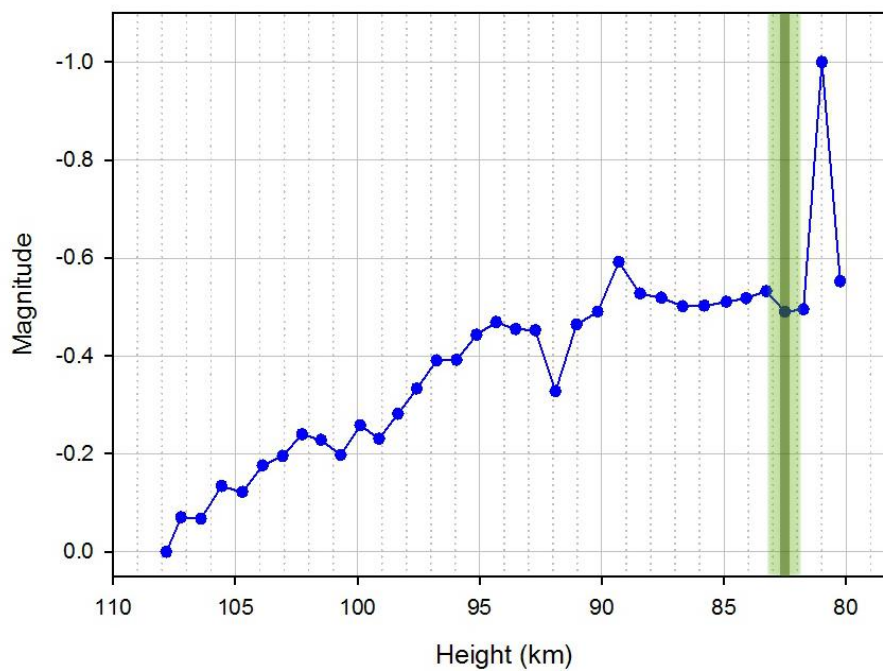
20100530 (cam 07)



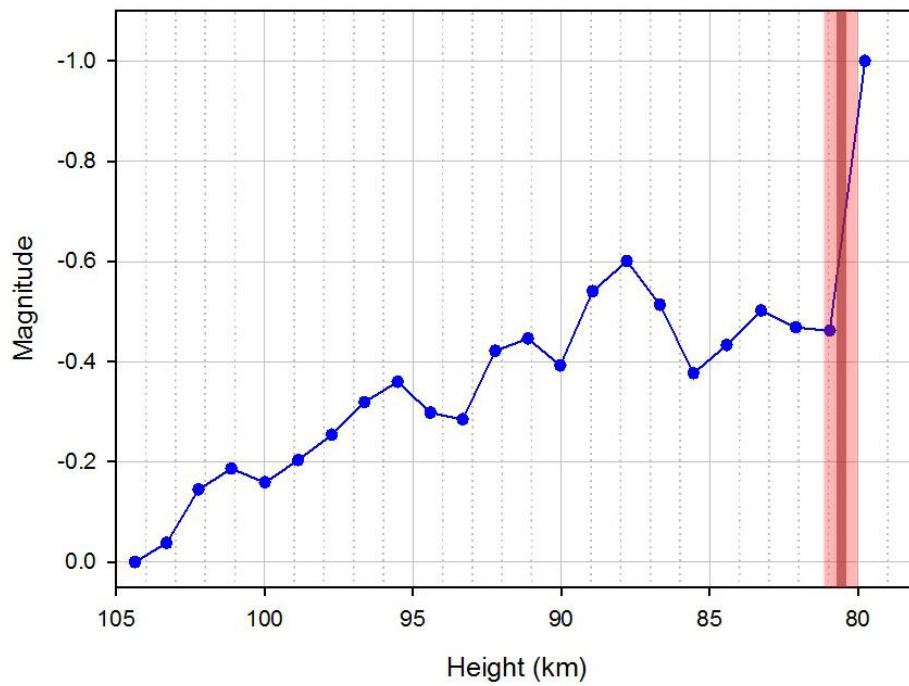
20100802 (cam 03)



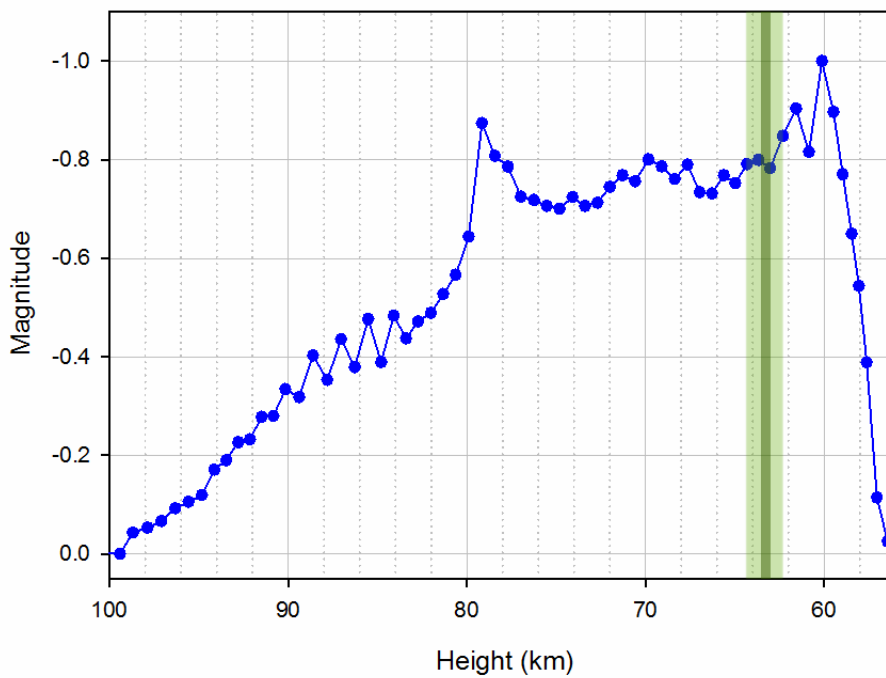
20100814 (cam 02)



20100914 (cam 03)

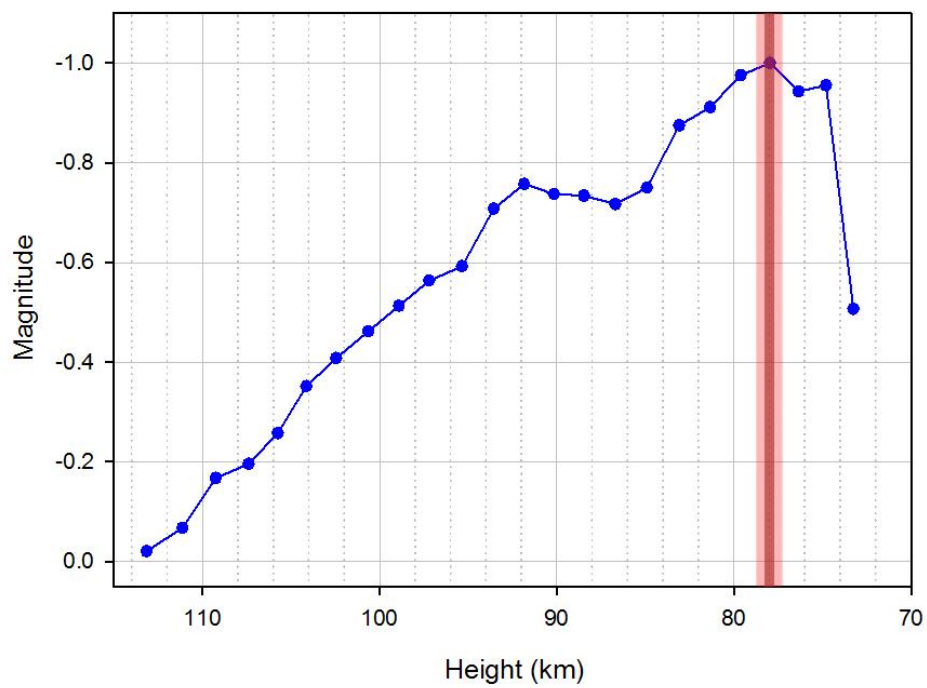


20101129 (cam 07)

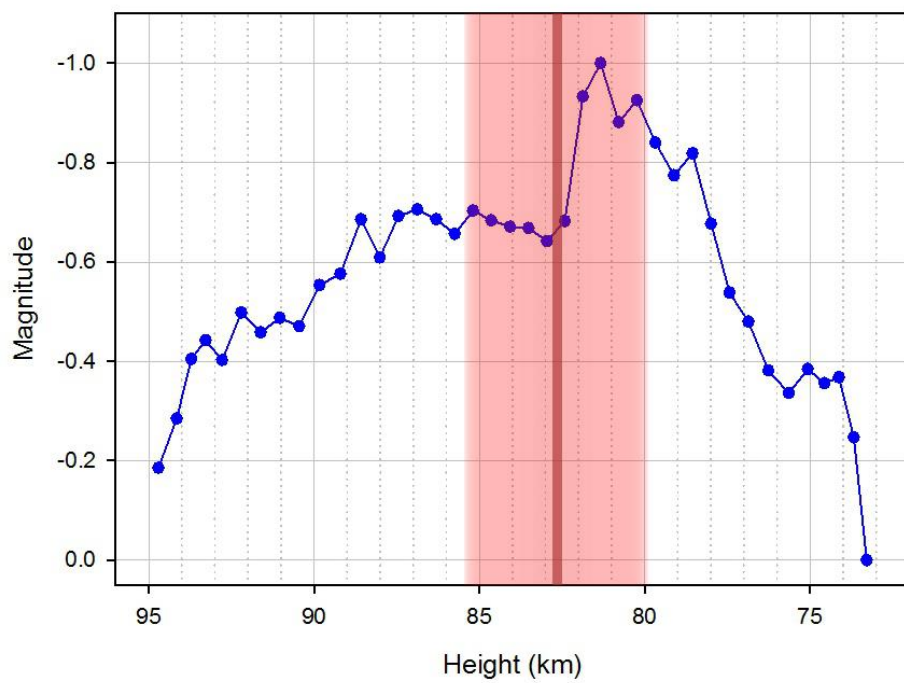




20110208 (cam 07)

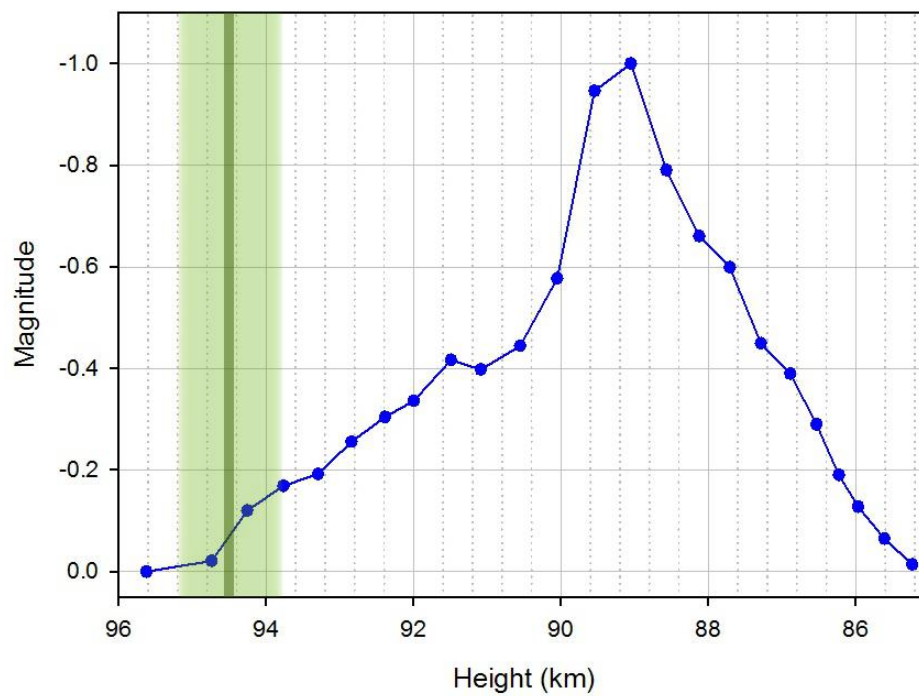


20110402 (cam 07)

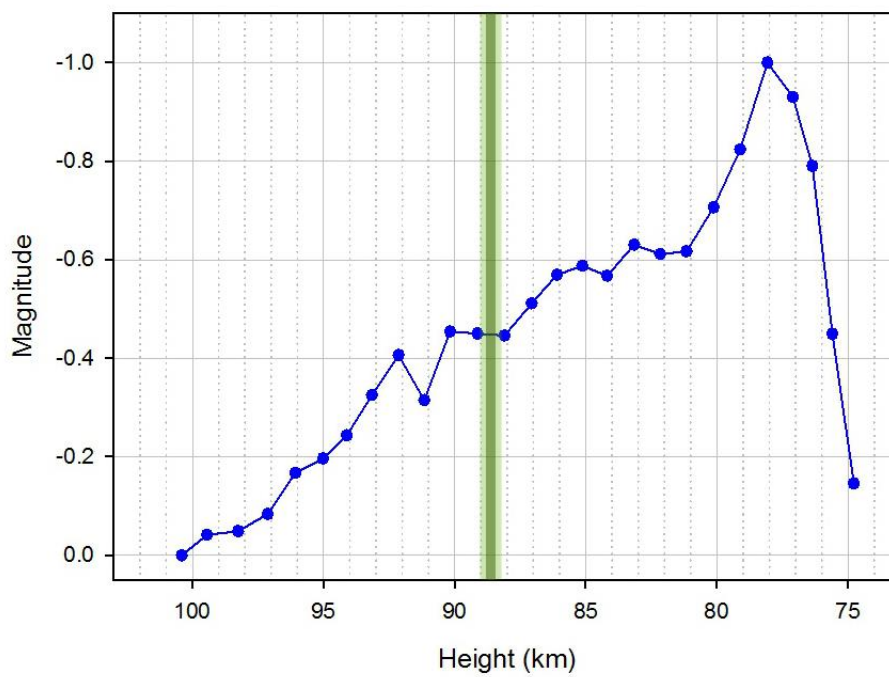




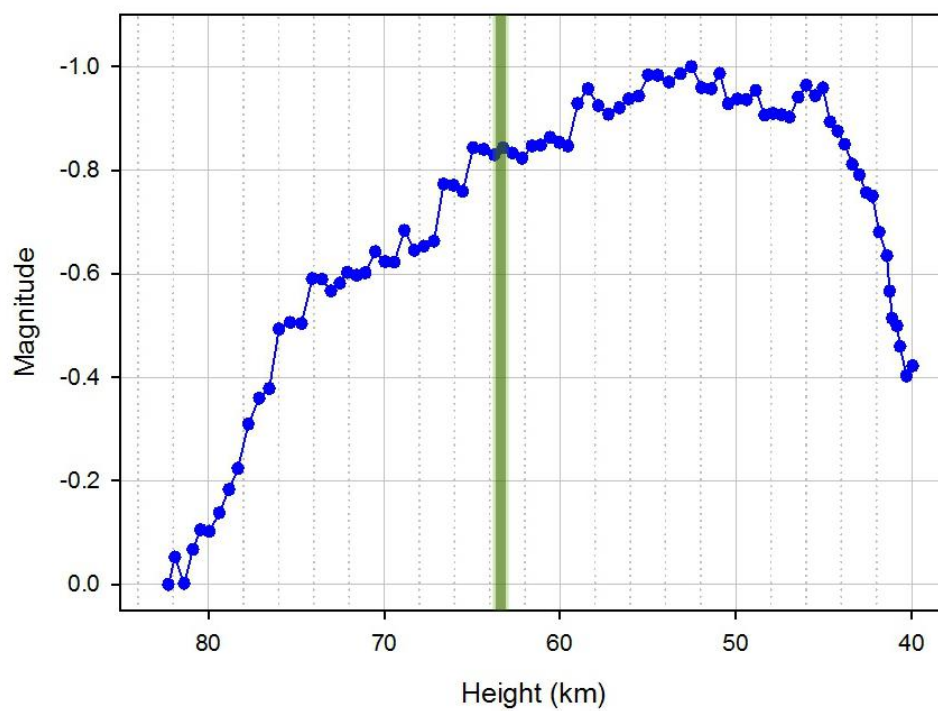
20110520 (cam 04)



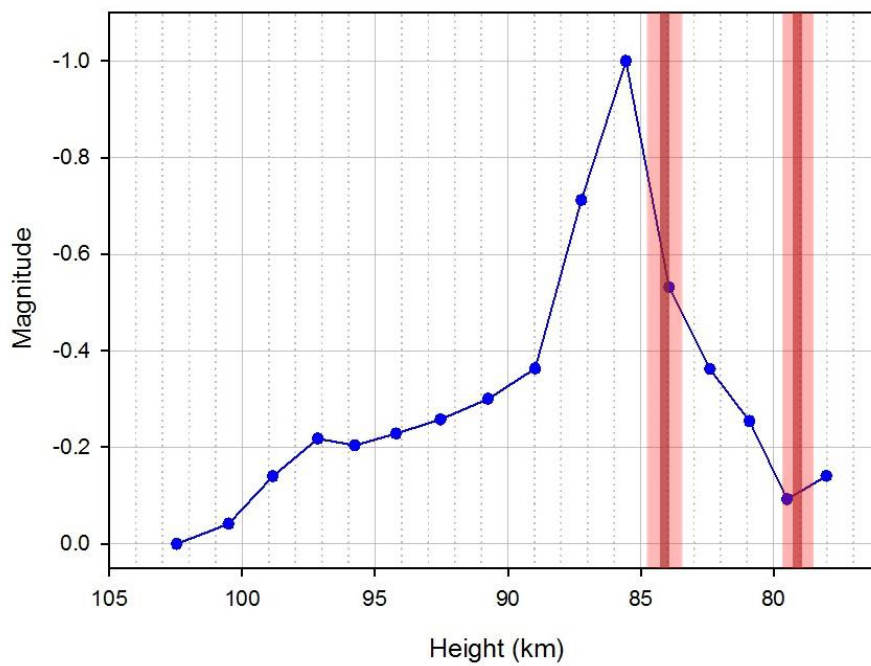
20110630 (cam 08)



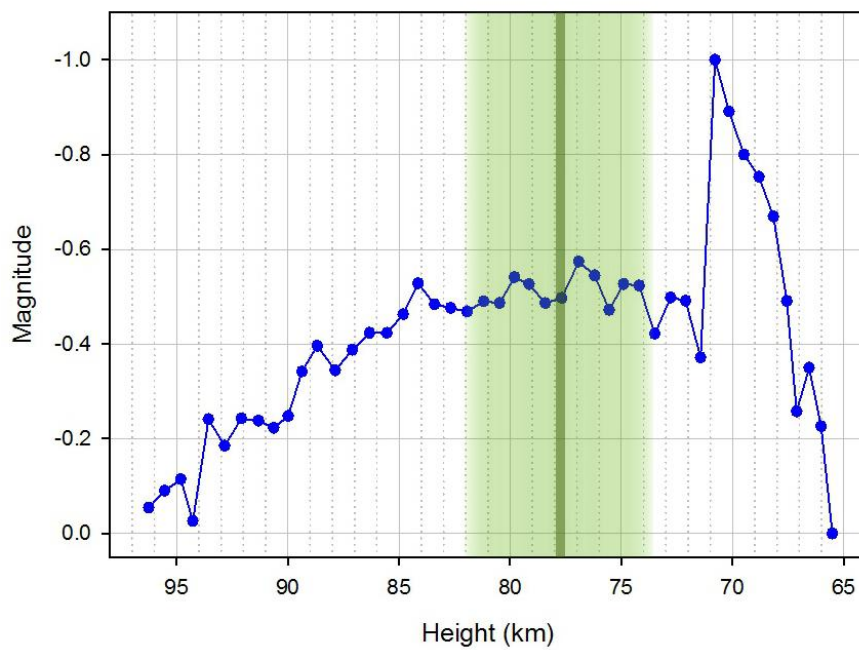
20110808 (cam 06)



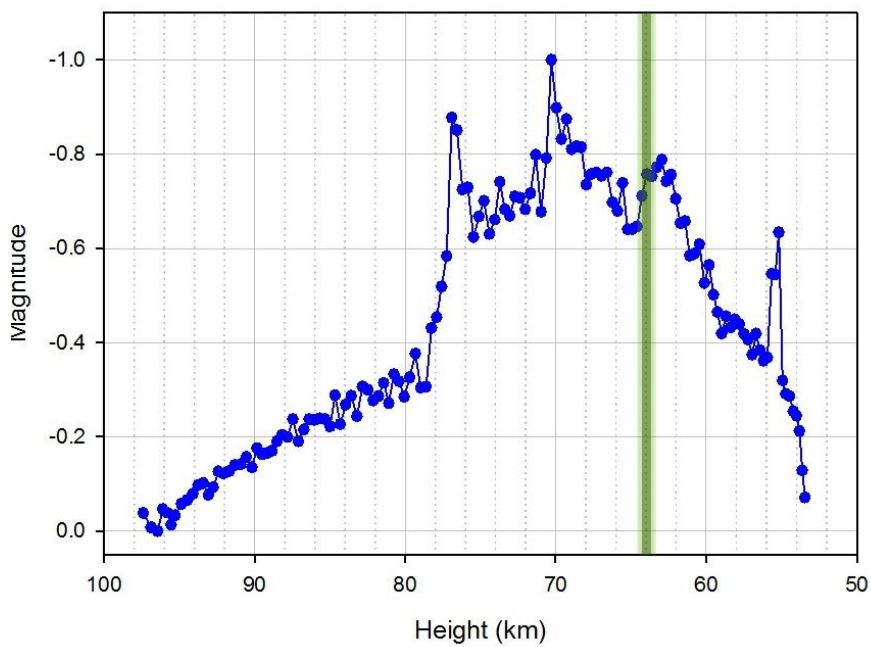
20110815 (cam 02)



20111005 (cam 06)



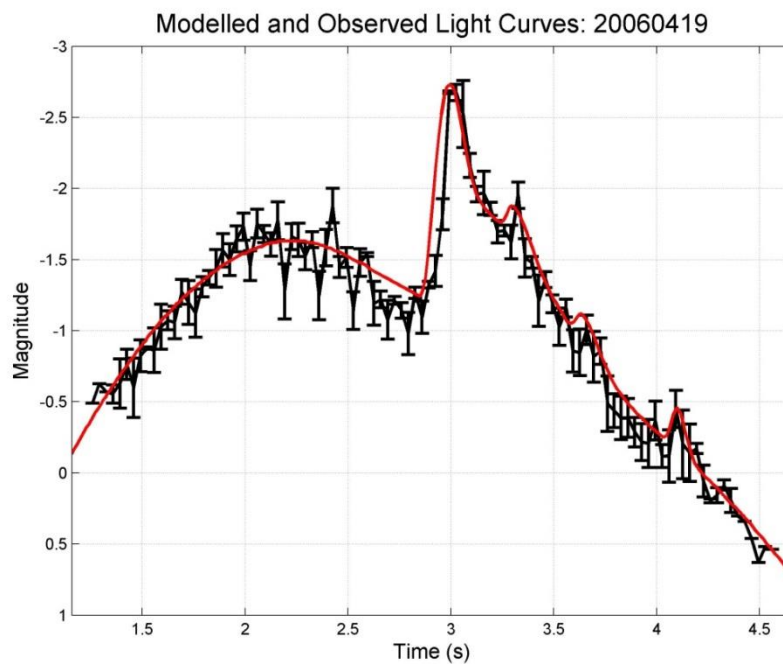
20111202 (cam 07)

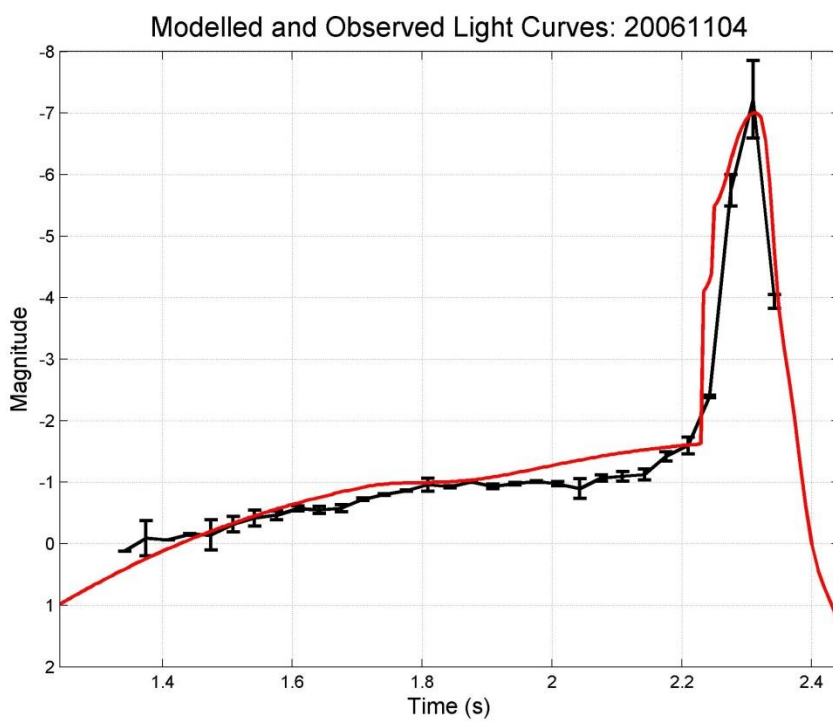
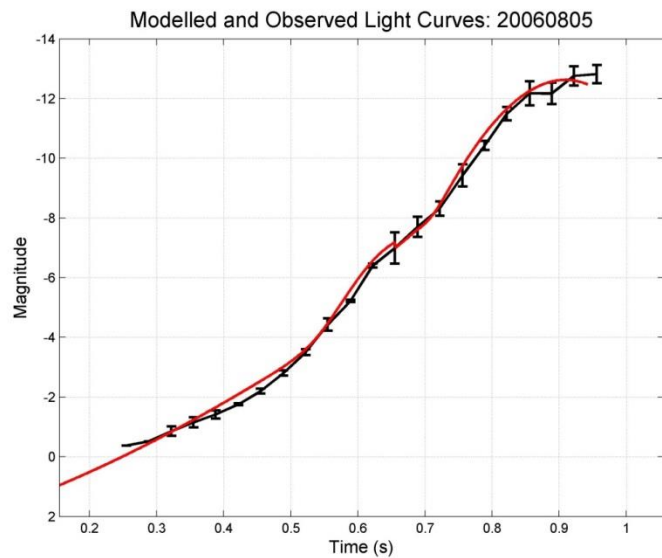


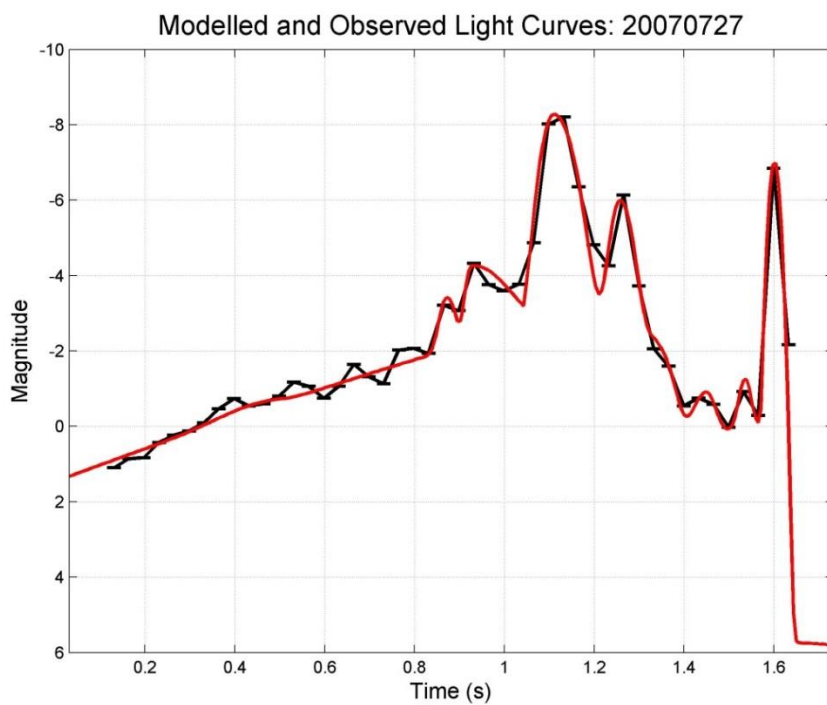
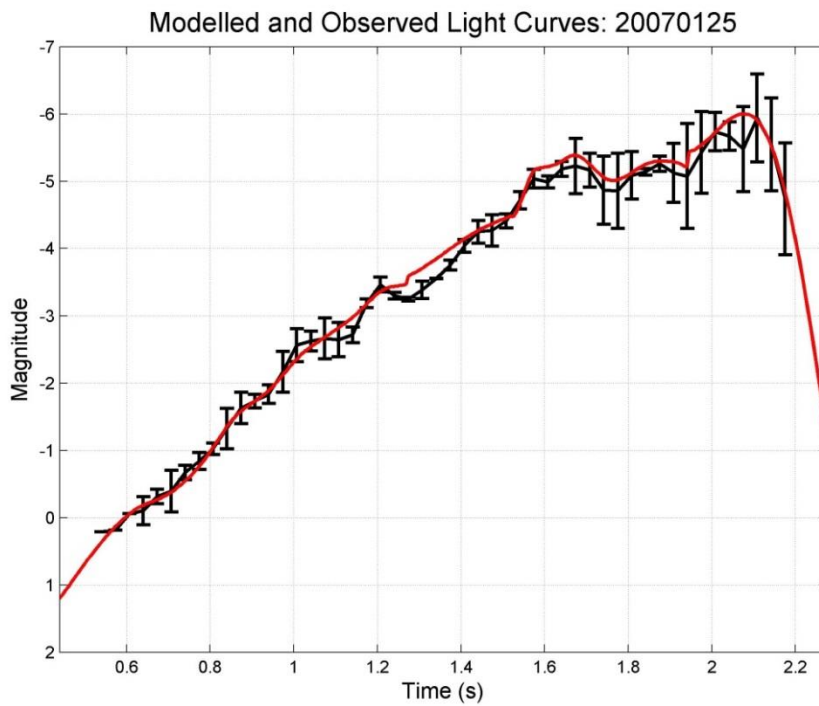
## Appendix 5

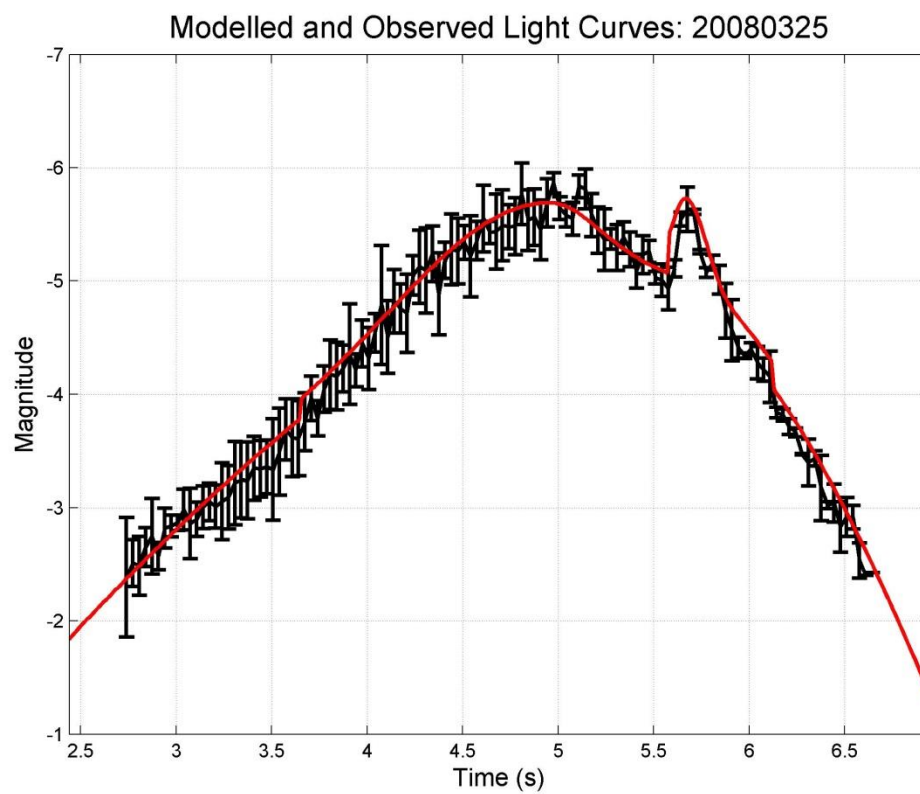
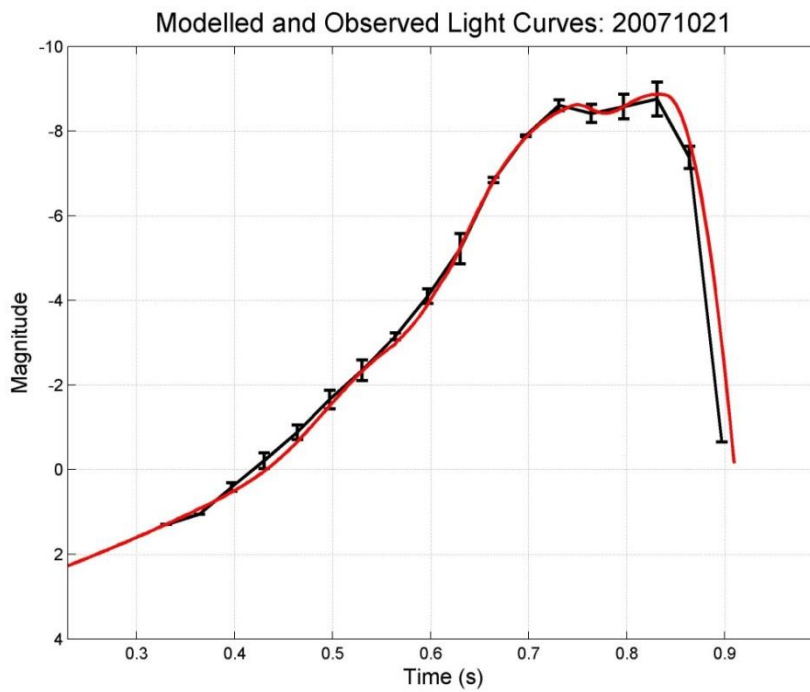
### Light Curve Fits from the FM Model

The figures in this section show each of the measured average absolute brightness light curves (black) and the fits (red) from the FM model for all events as described in Chapter 6. The brightness here is given in astronomical magnitudes in the HAD CCD bandpass (which is close to the R astronomical bandpass). The uncertainty bounds represent the standard deviation in absolute brightness as measured between cameras (at least two and up to six cameras for some events). Only two events have a single camera light curve due to adverse sky conditions at other sites. The events are named according to their date of appearance as YYYYMMDD.

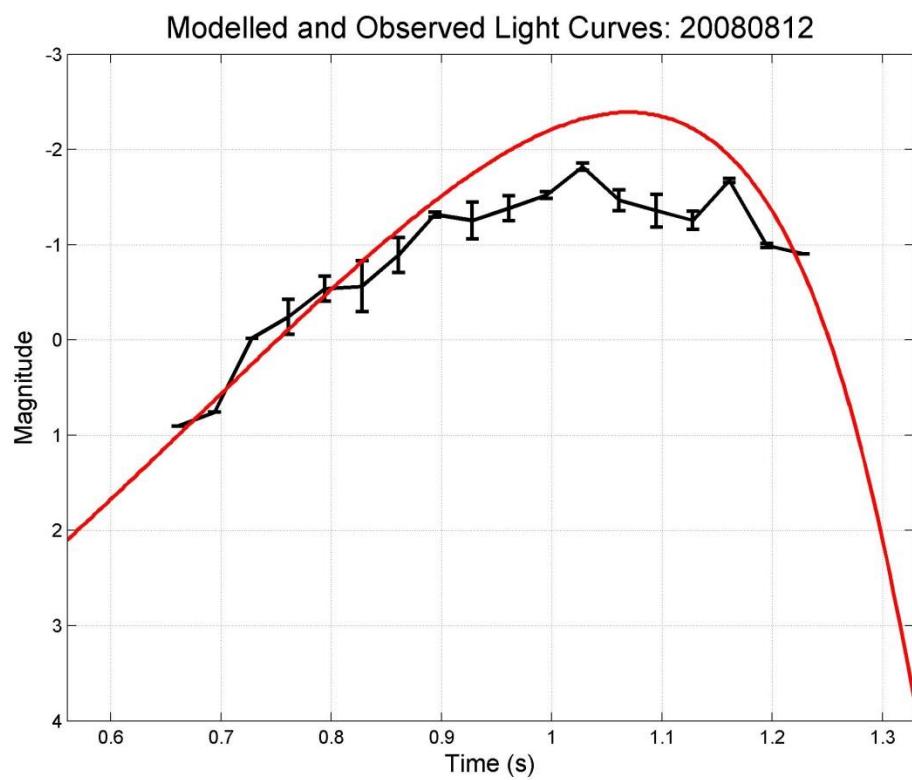
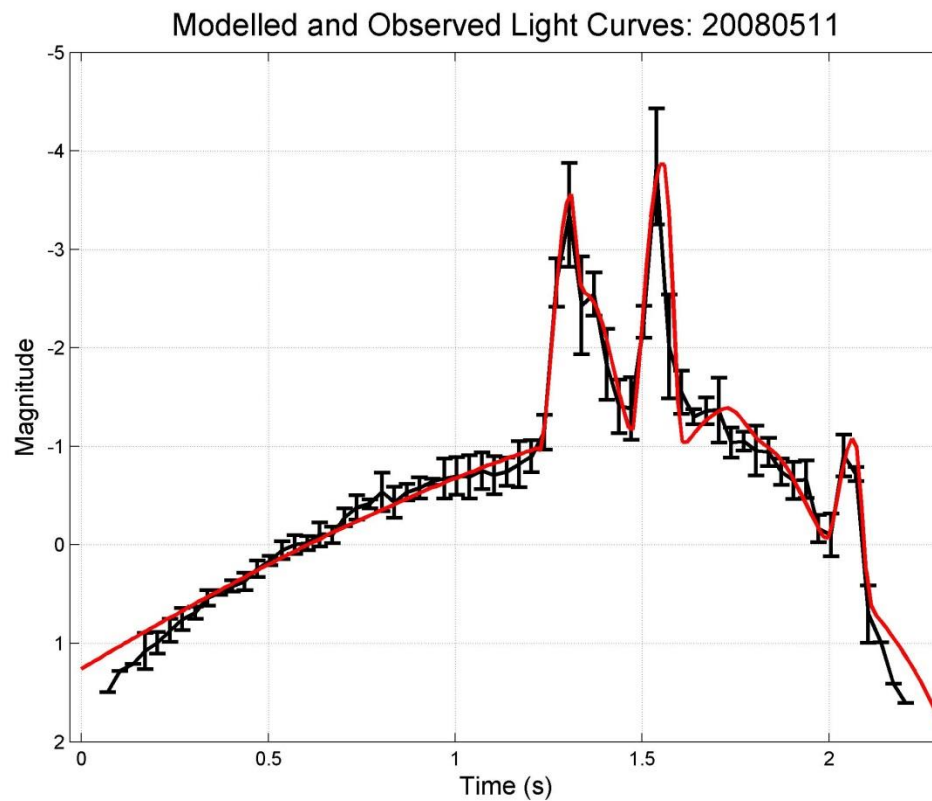


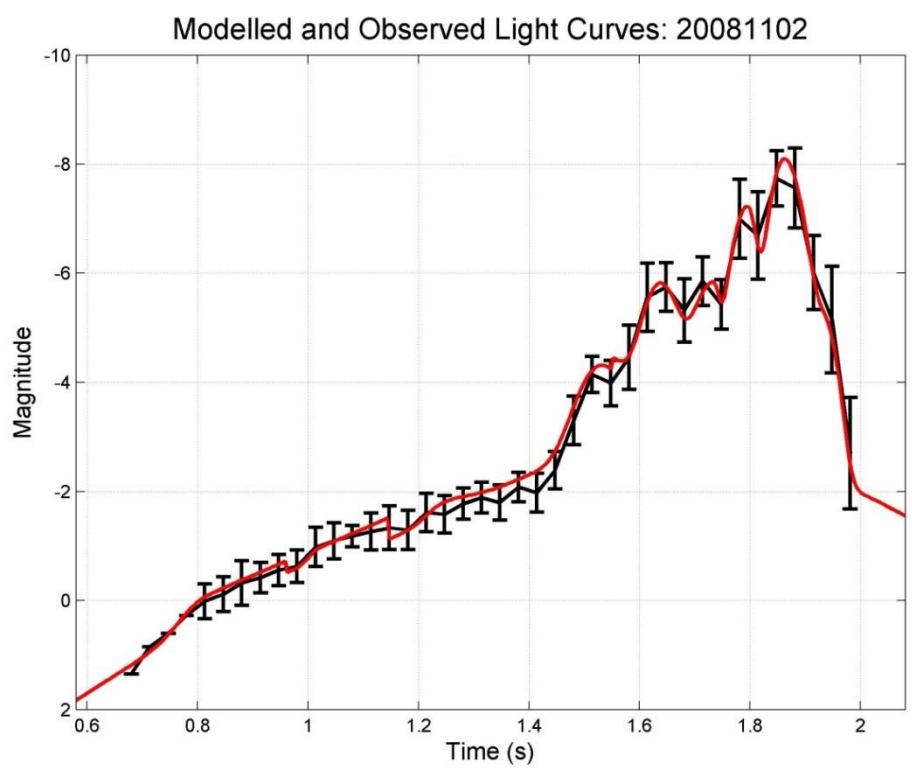
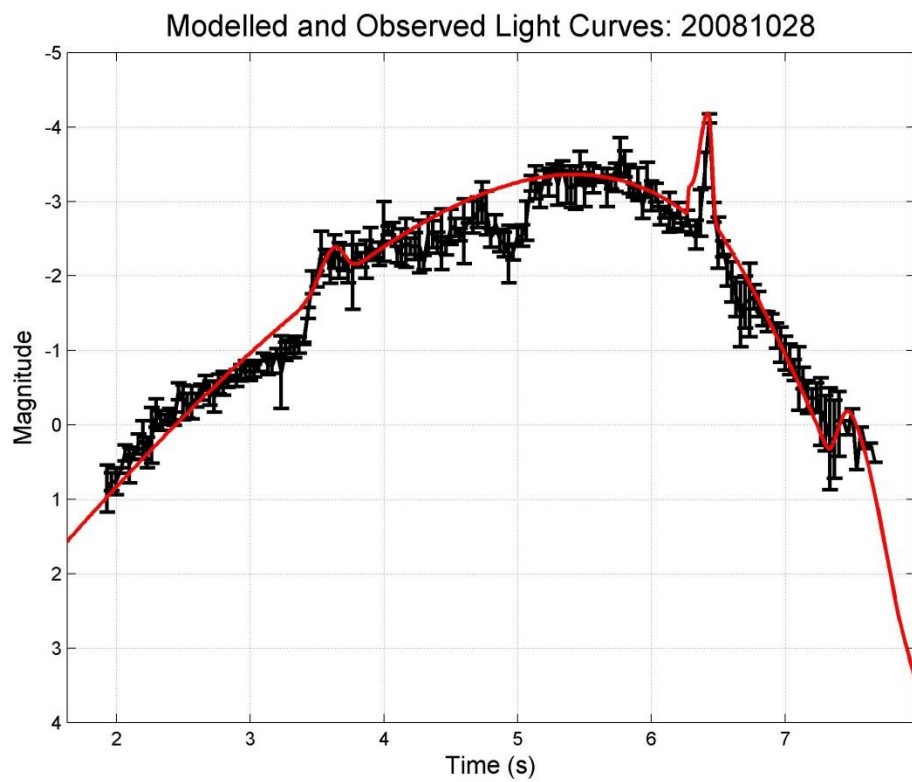


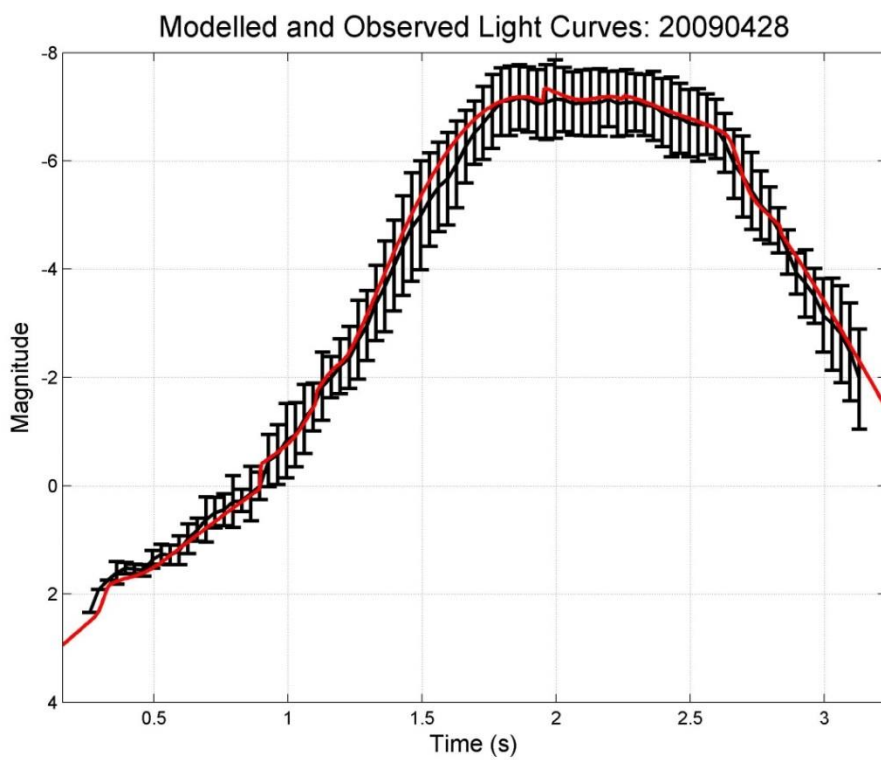
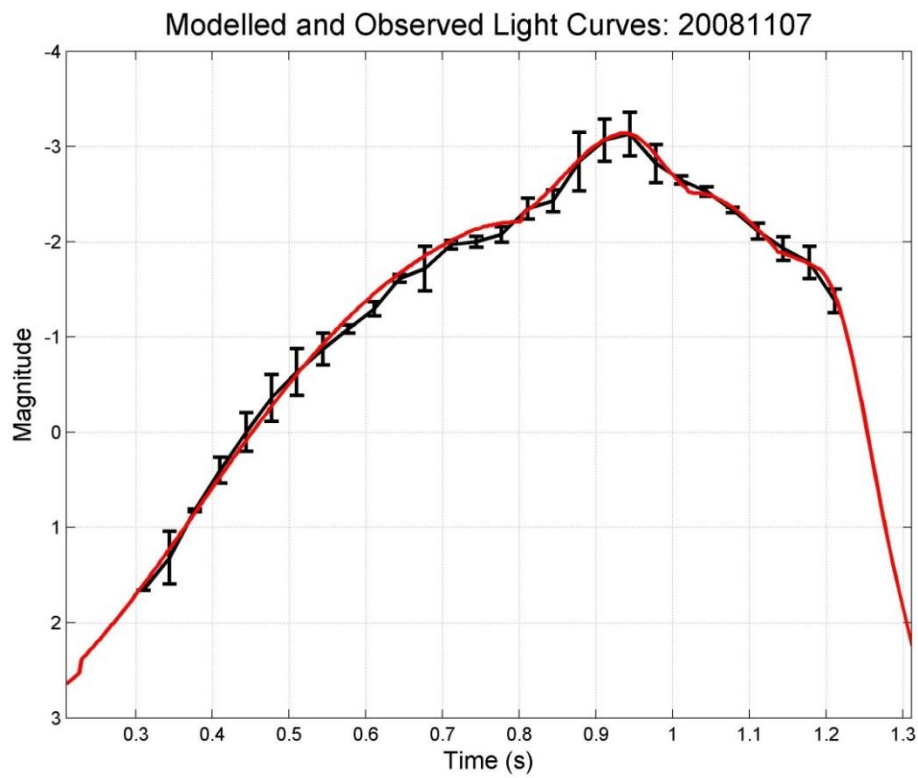


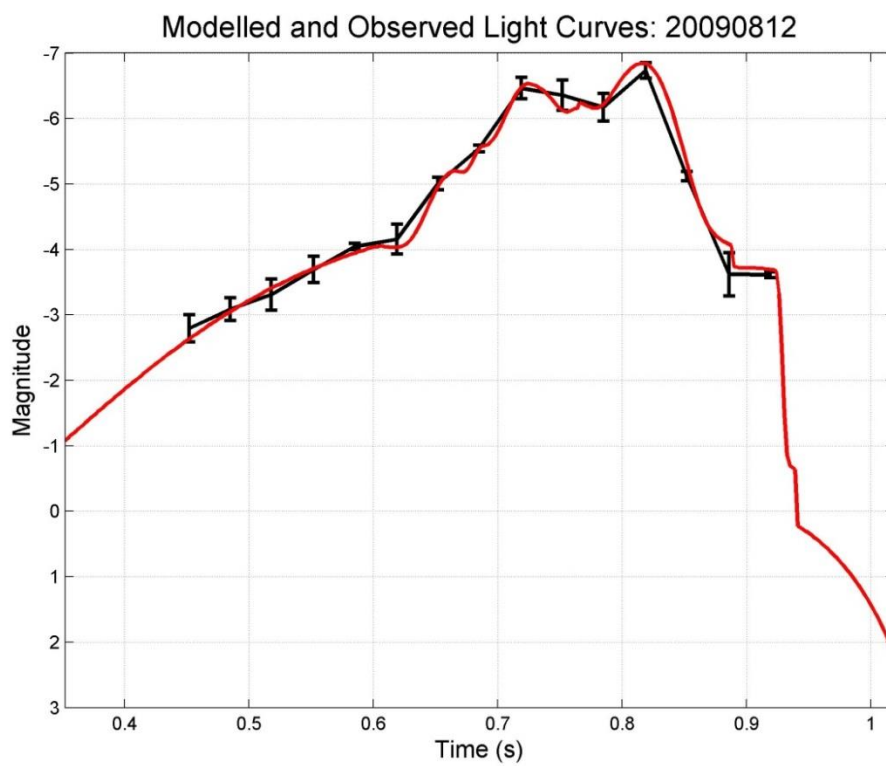
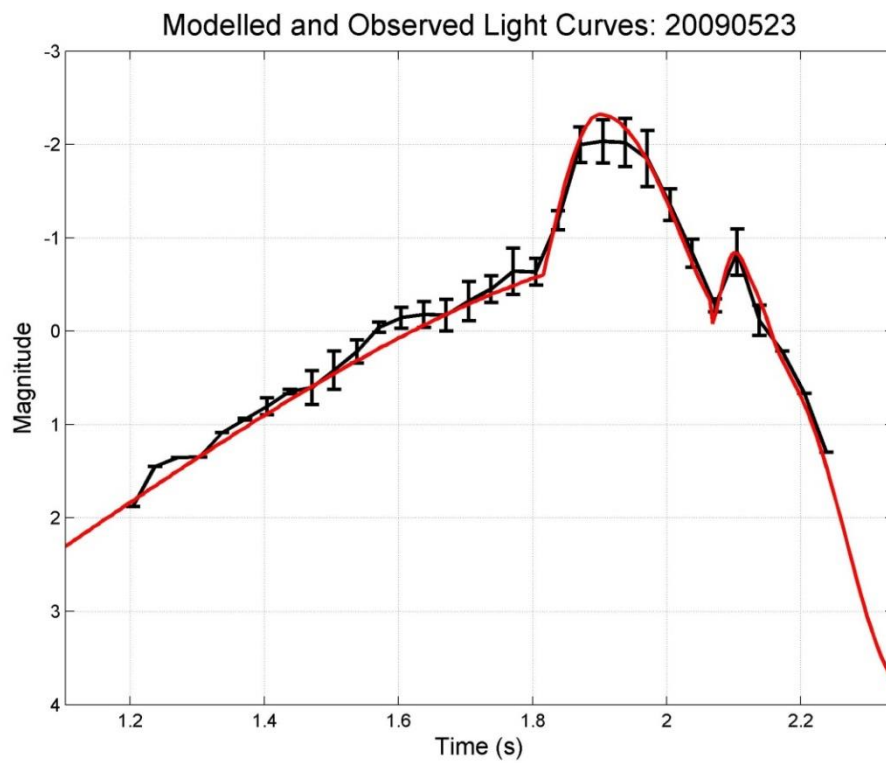


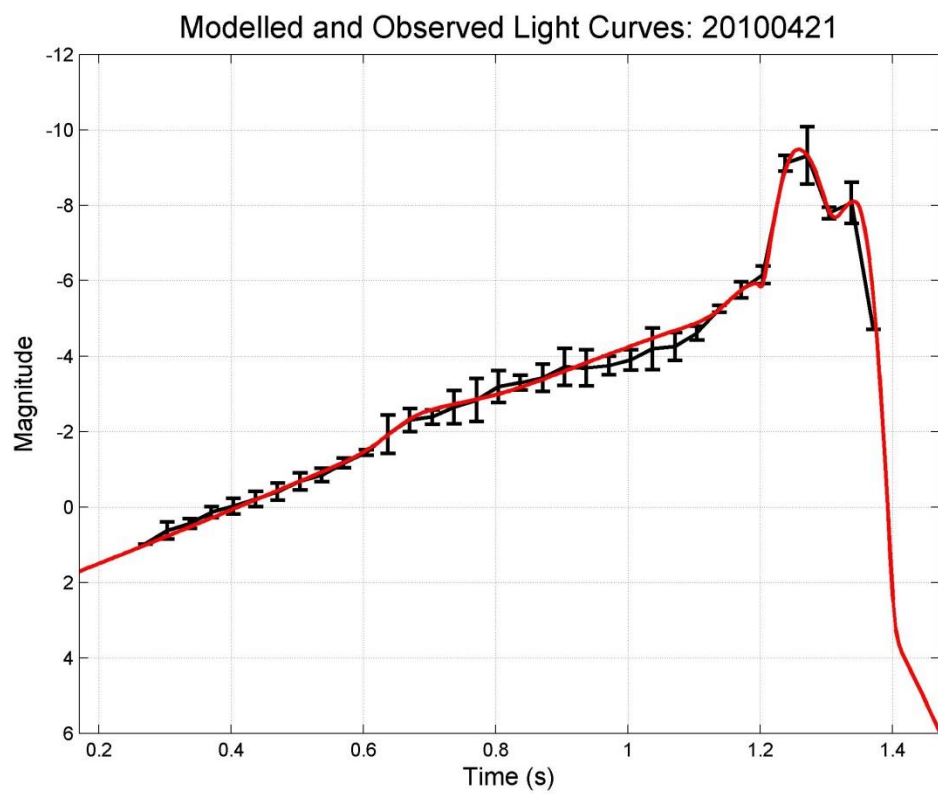
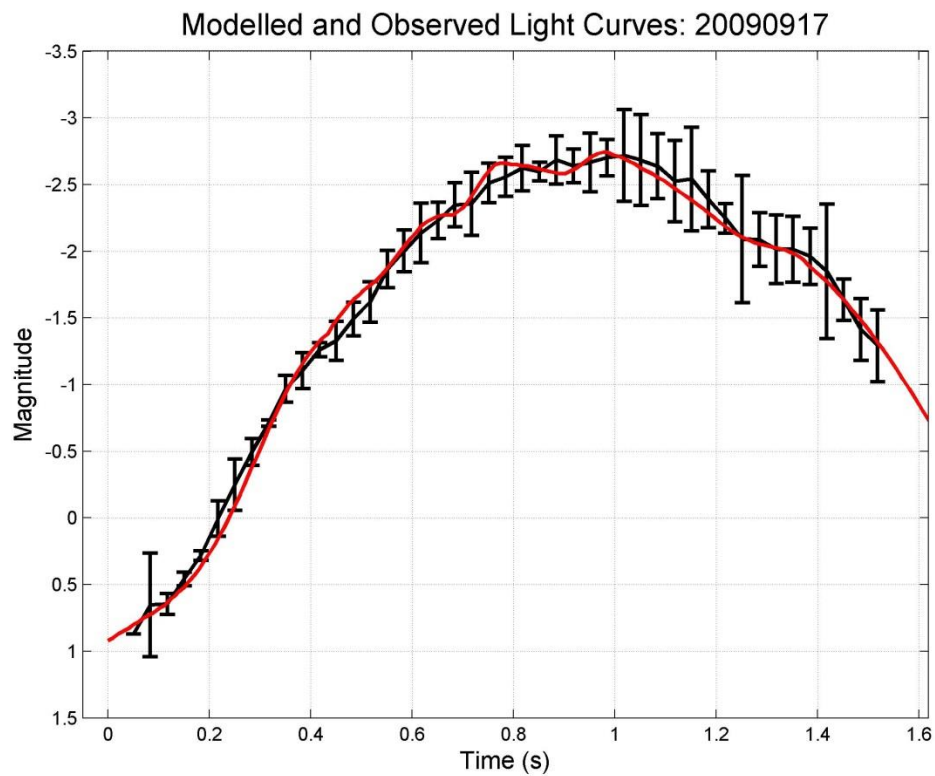


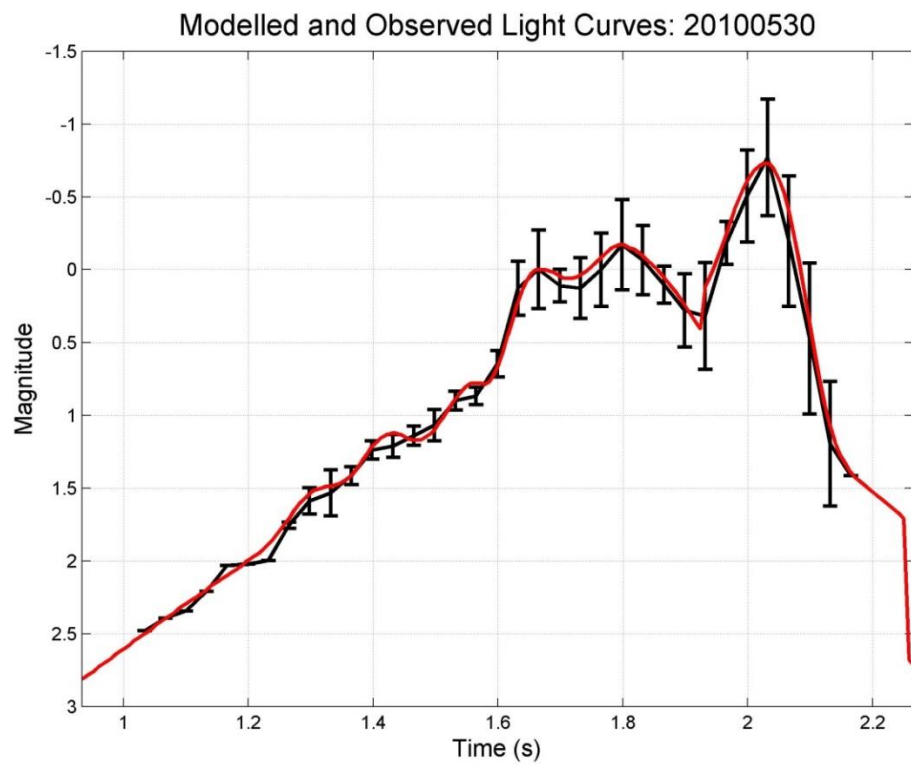
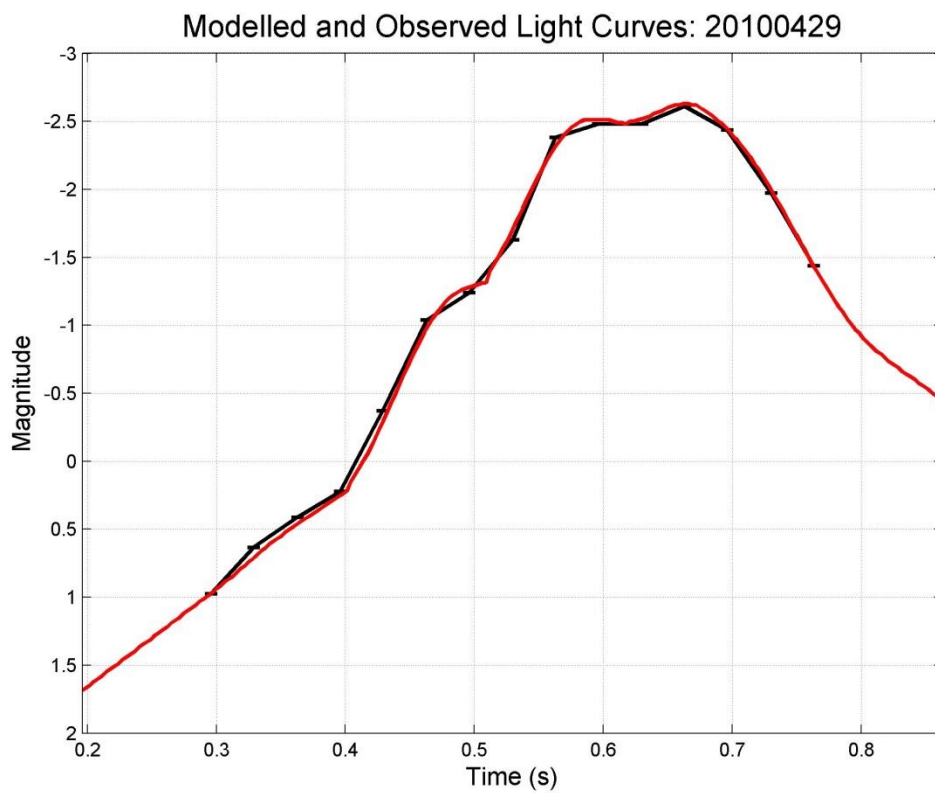


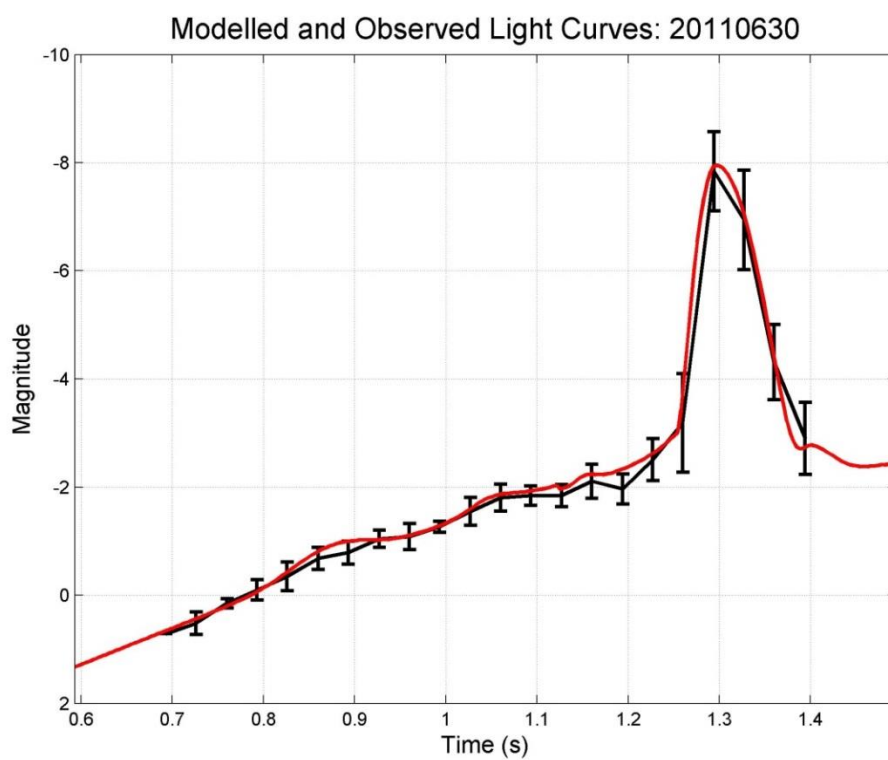
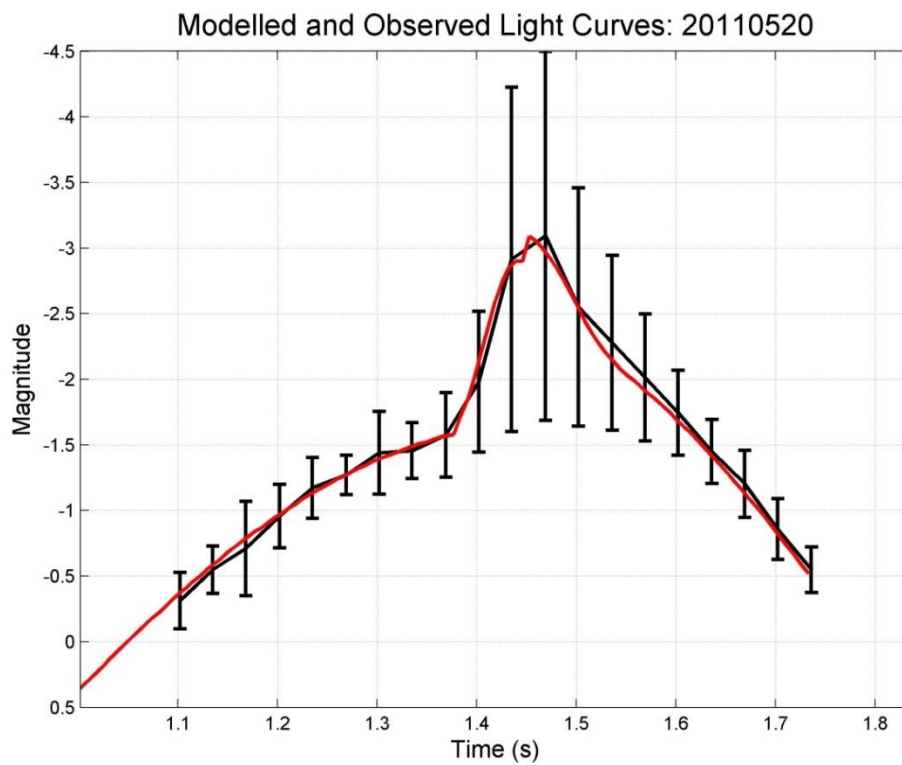




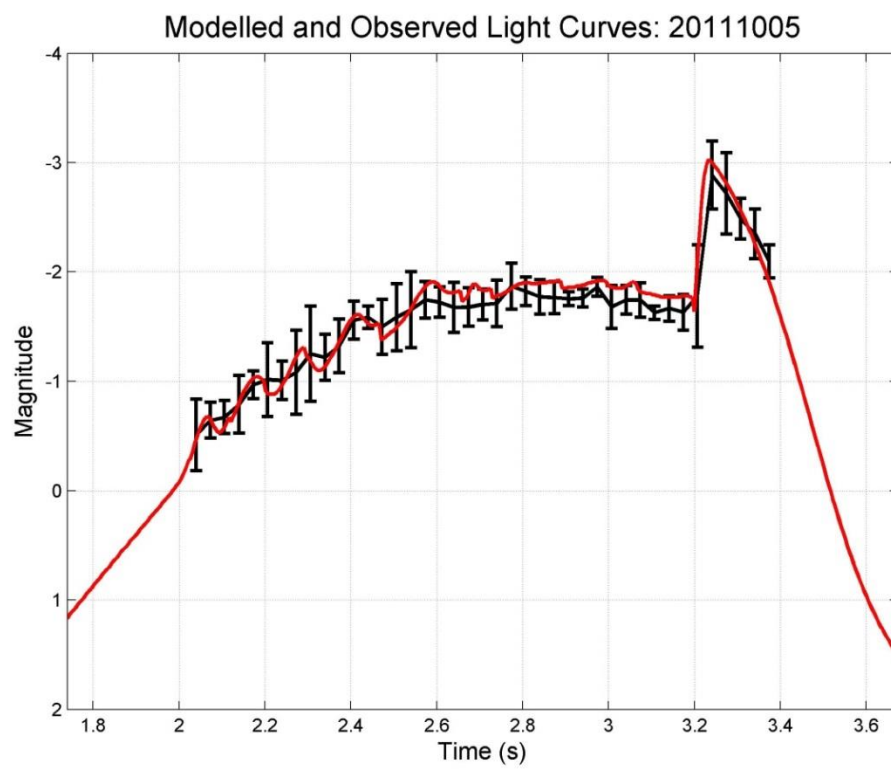
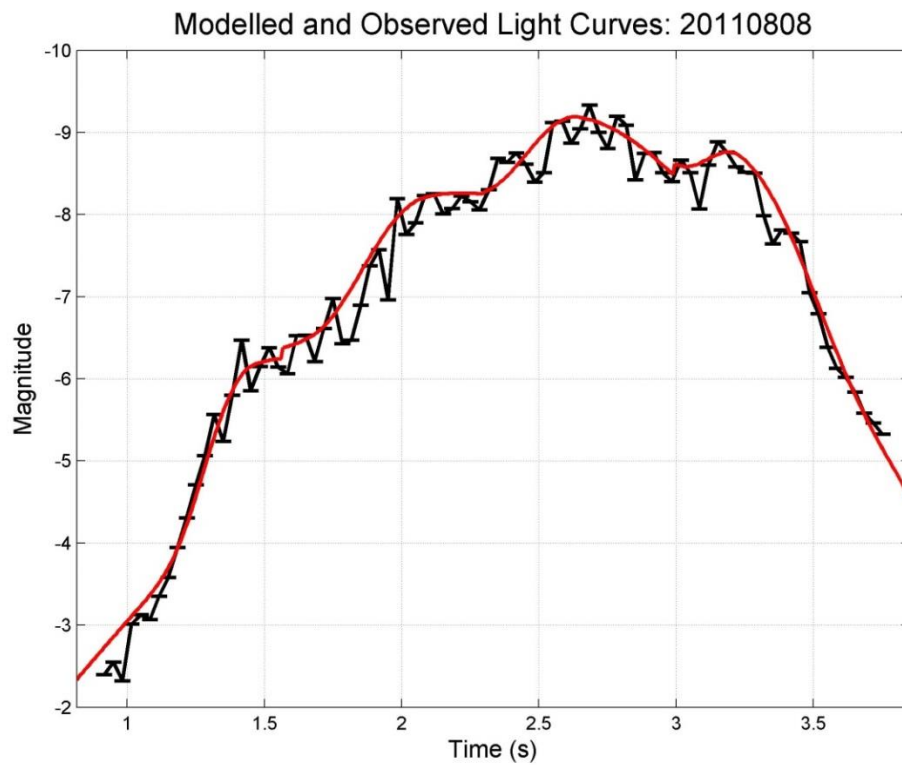


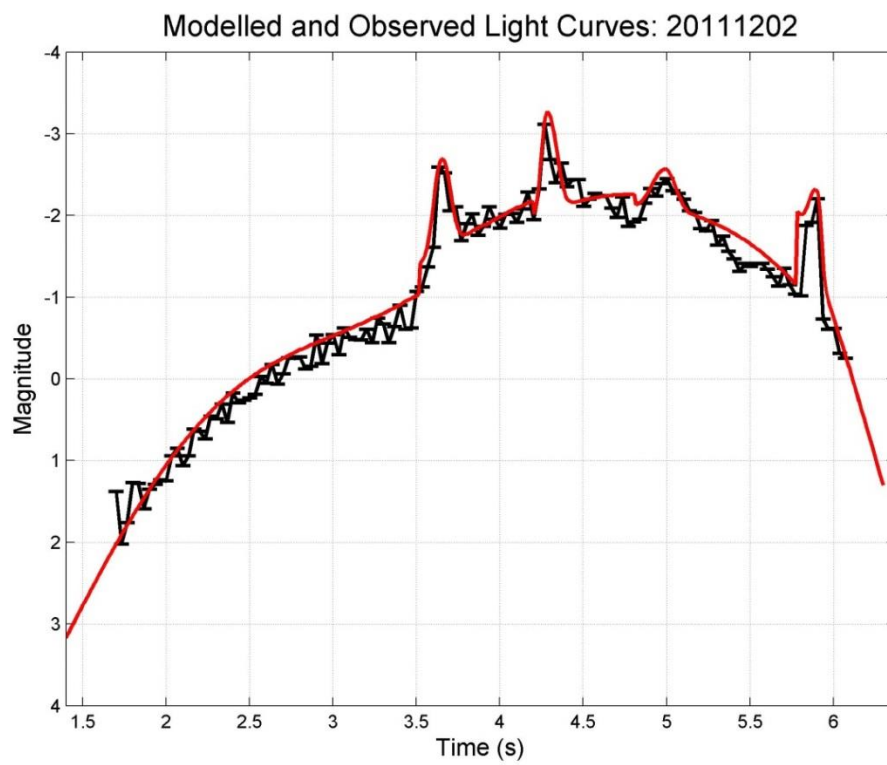












## Appendix 6

### Energy Deposition and Blast Radius Calculations from the FM Model

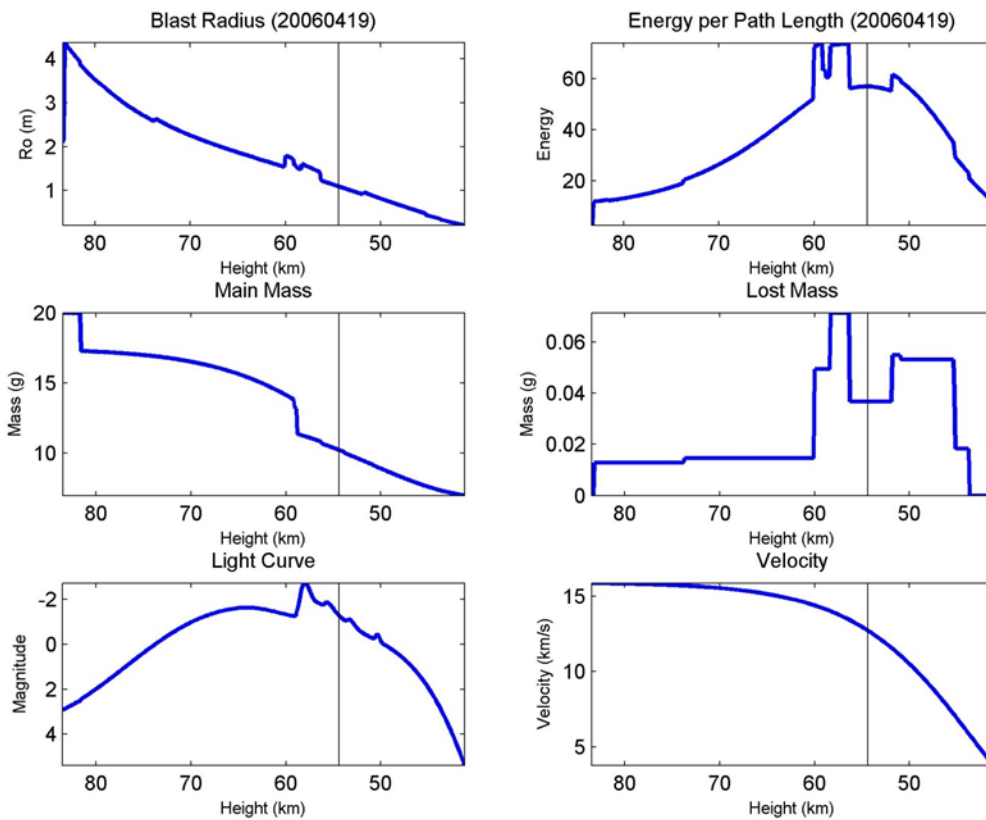
The figures in this section show the model fit to the observed light curve and dynamics. Based on these model fits, also shown are the inferred model blast radius calculations for all events as described in Chapter 6 in the top-down approach.

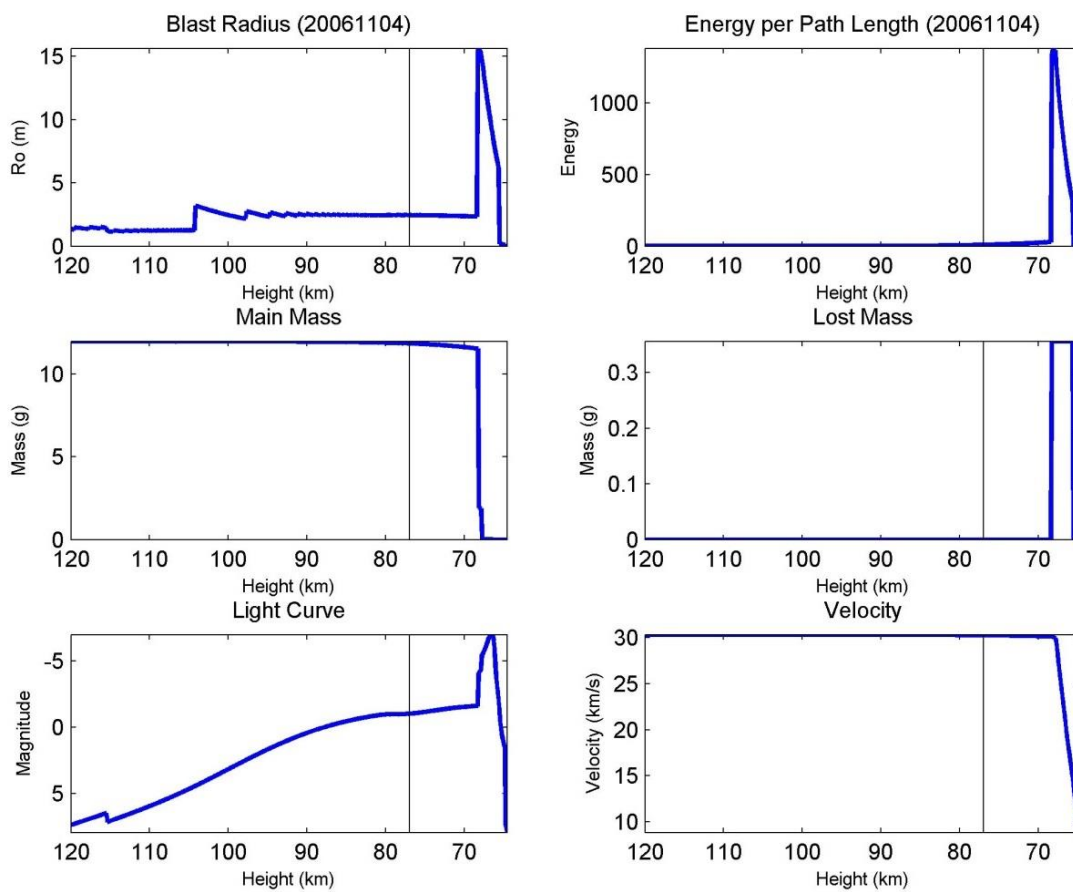
The figure panels show the following predictions for each simultaneous optical and infrasound meteor as modelled using the FM entry code: Upper left: FM predicted blast radius as a function of height

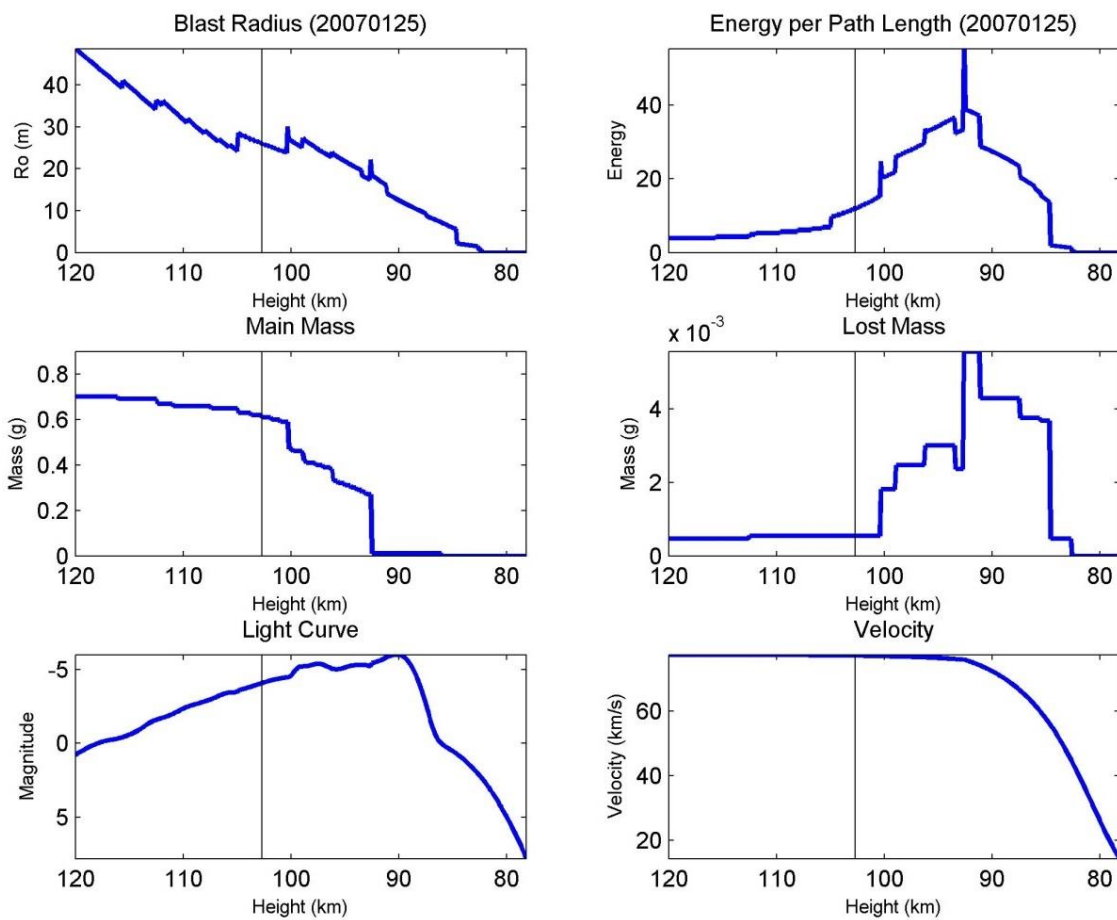
- Upper right: FM estimate of meteoroid energy per path length in units of J/m as a function of height
- Middle left: FM modelled meteoroid mass as a function of height
- Middle right: FM predicted meteoroid mass ablated as part of optical flares as a function of height.
- Lower left: FM modelled light curve as absolute meteor magnitude as a function of height
- Lower right: FM modelled meteoroid velocity as a function of height

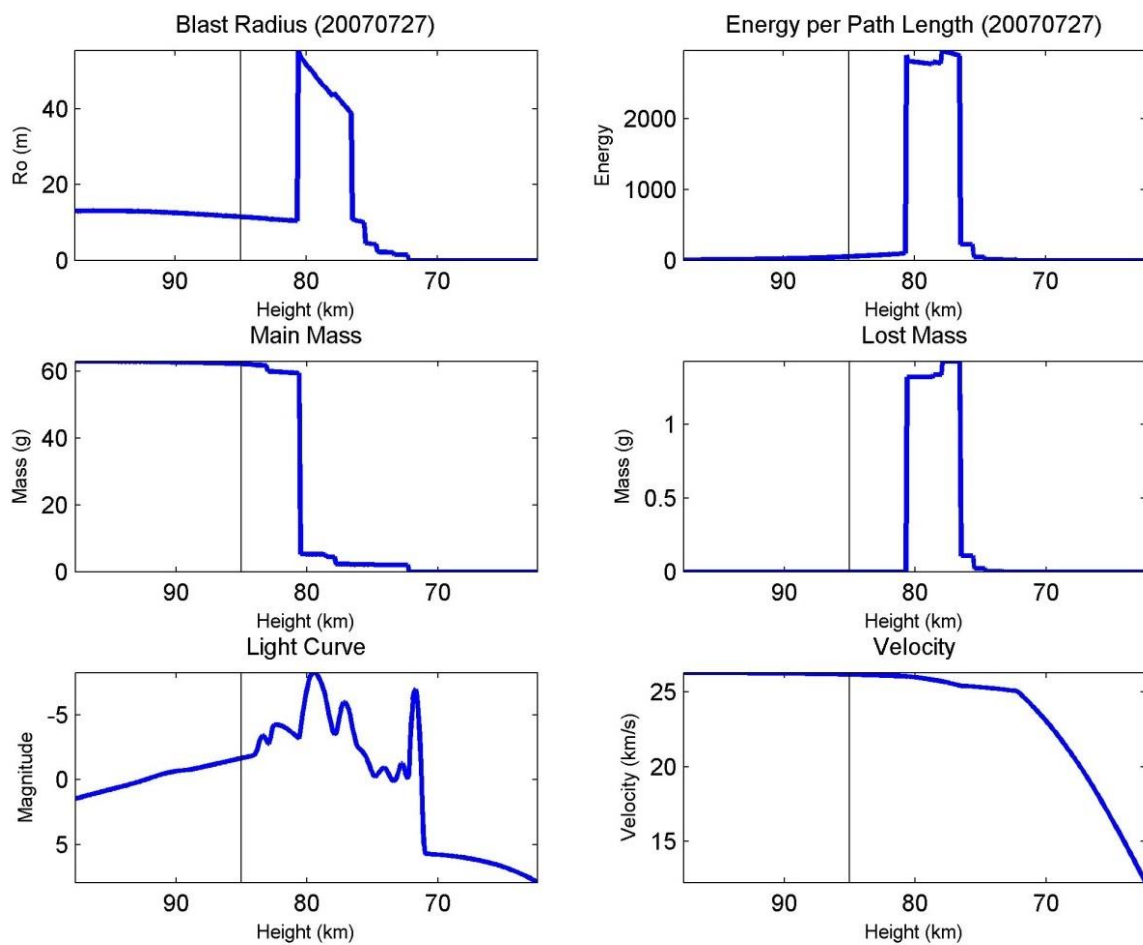
The black vertical lines in each plot represent the most likely shock source height of the observed meteor as derived from raytracing as shown in Appendix 4.

## Single Arrivals

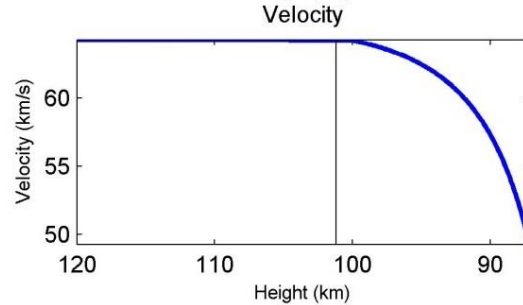
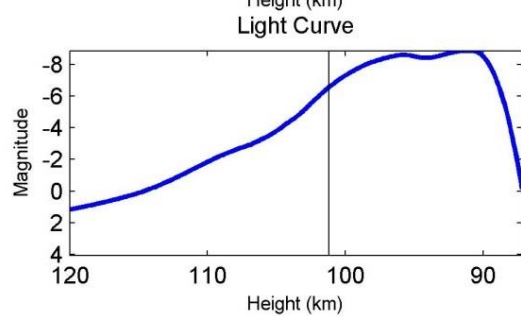
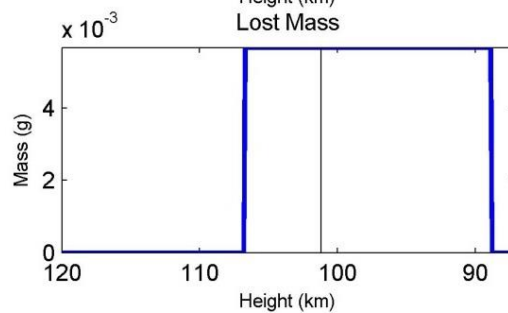
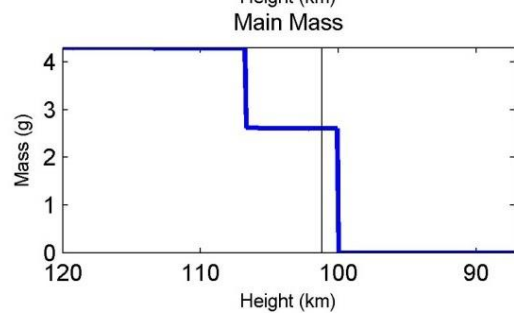
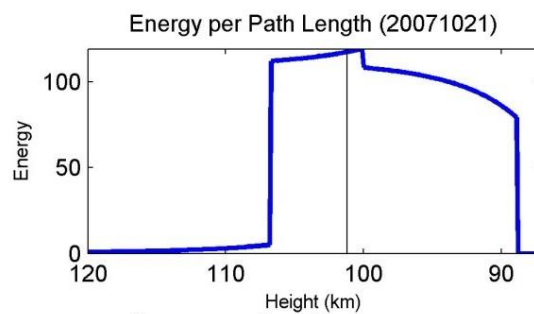
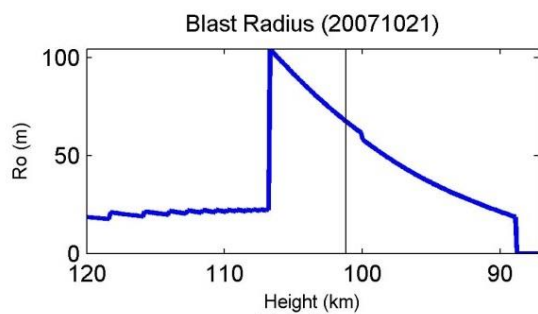


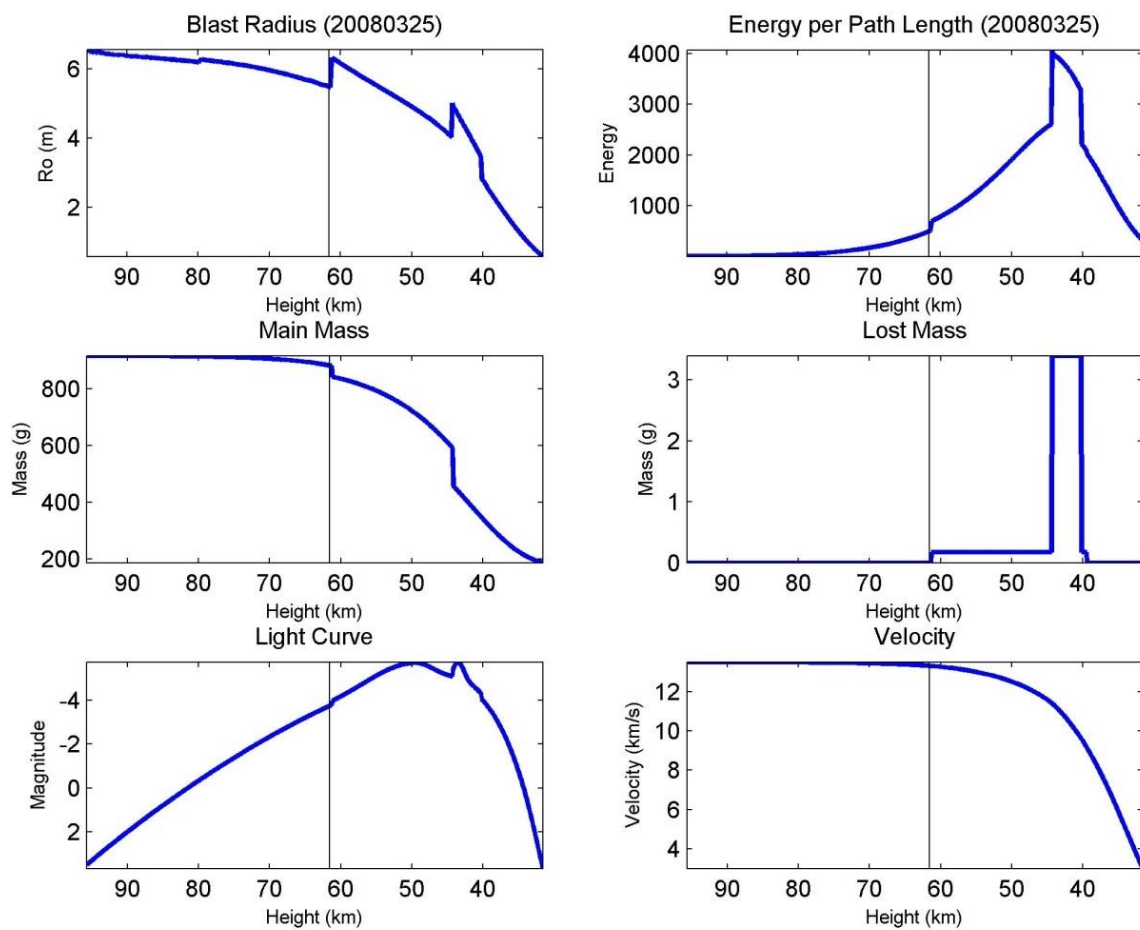


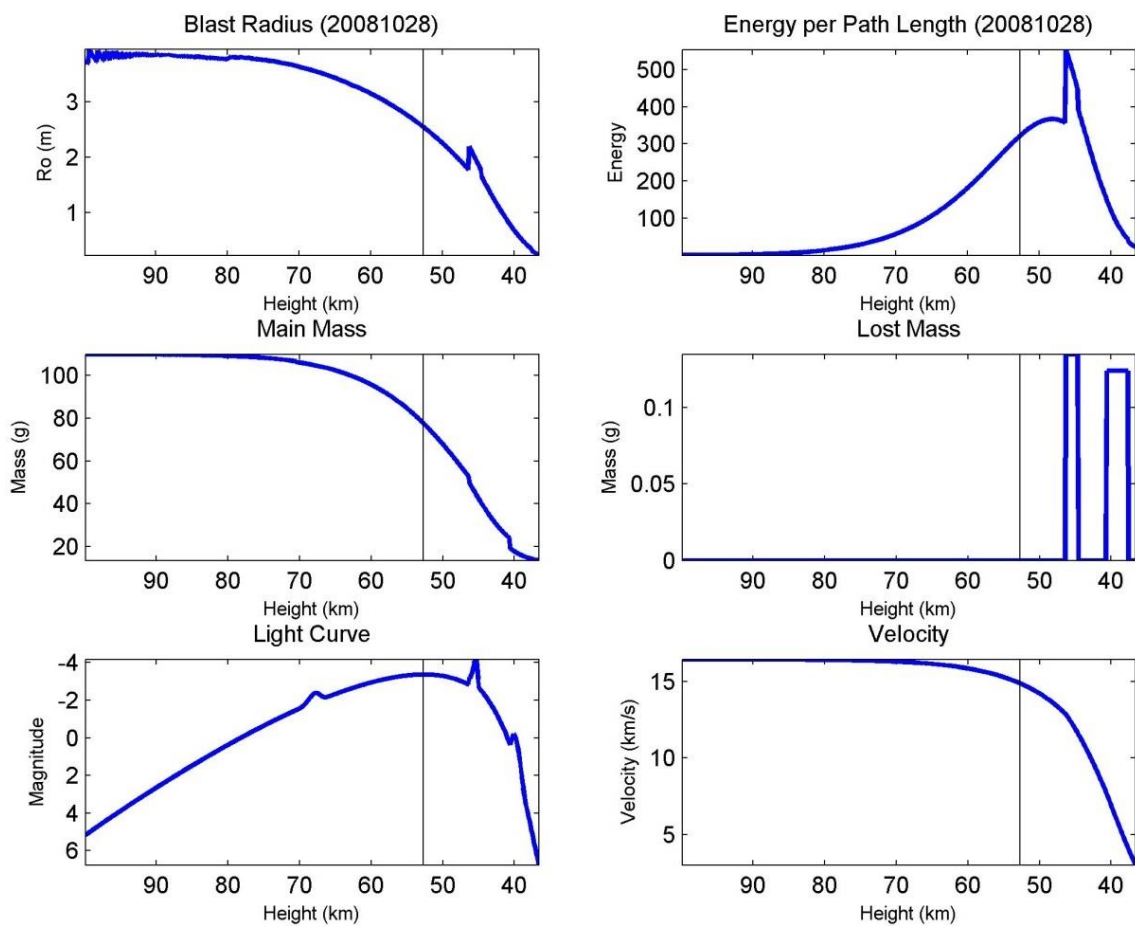


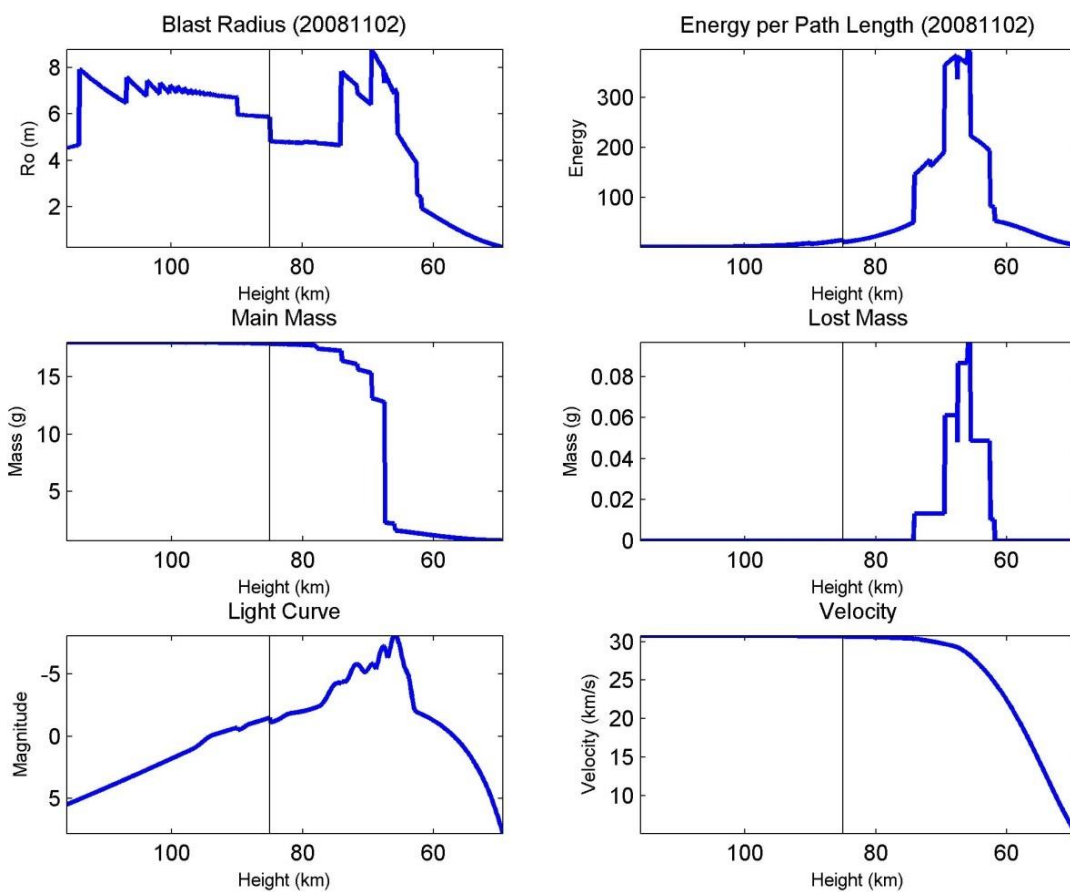


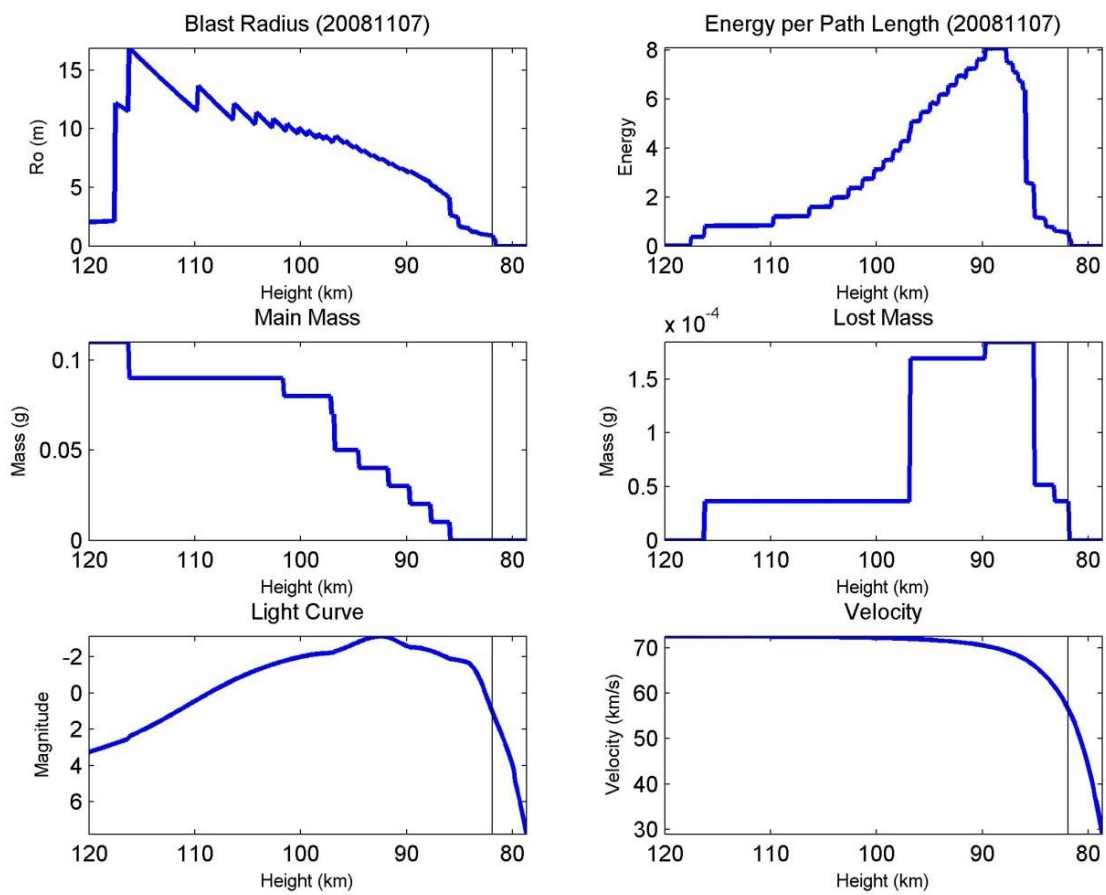


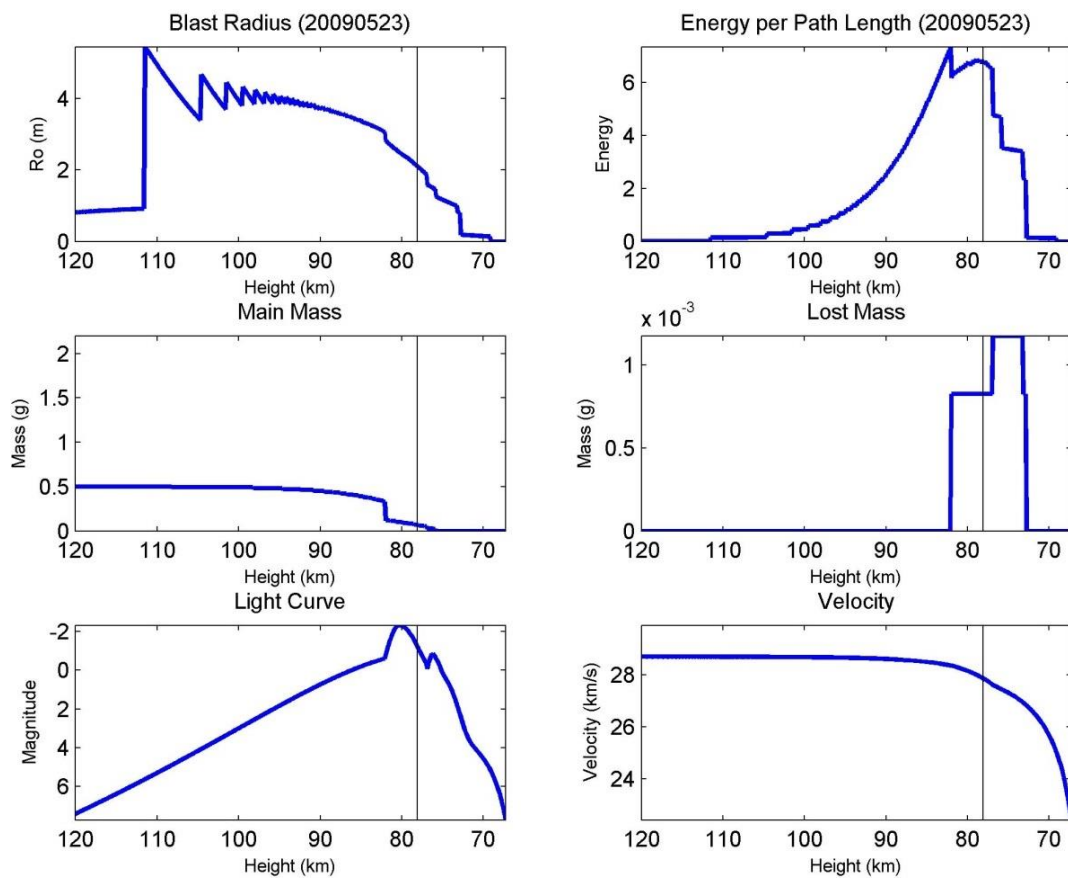


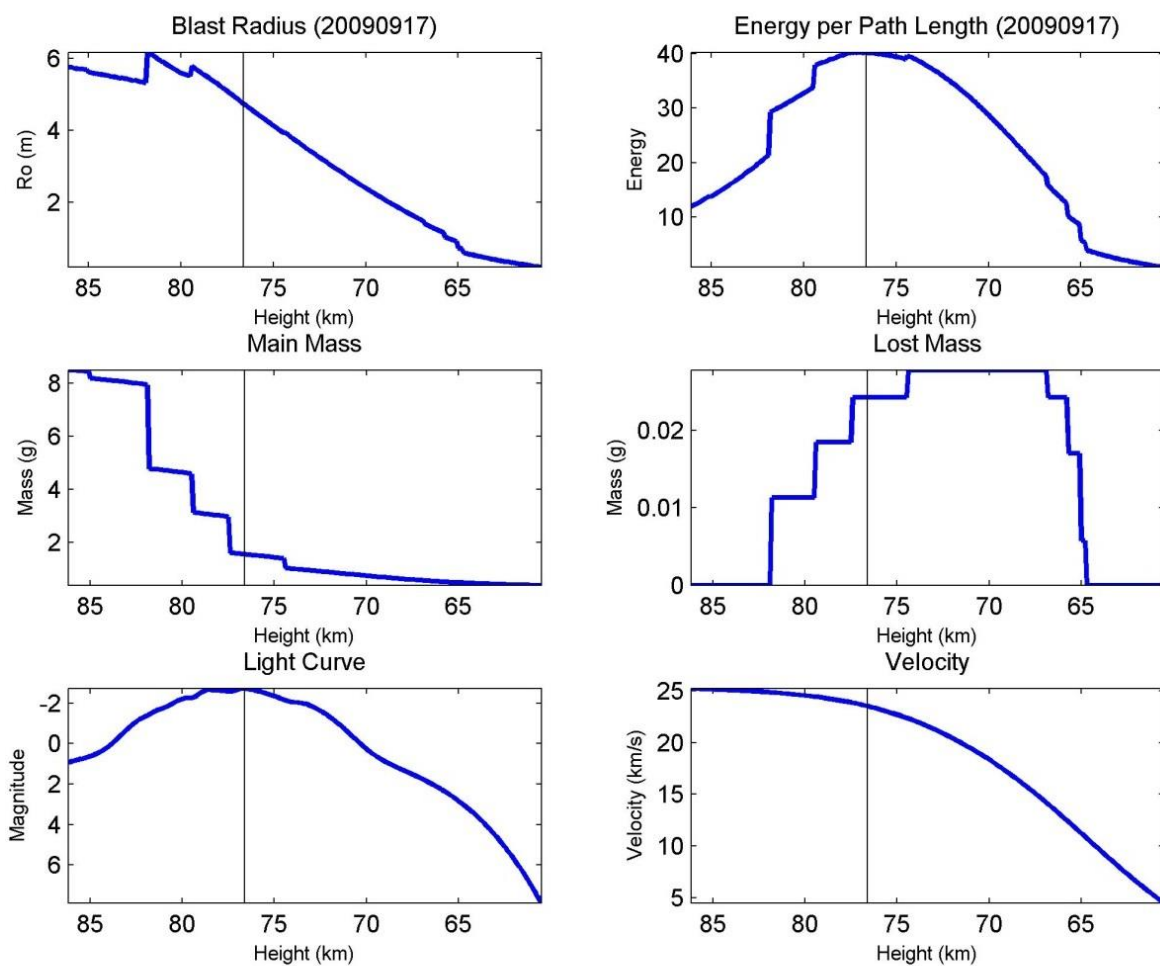




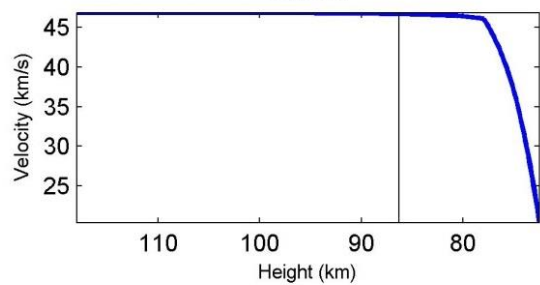
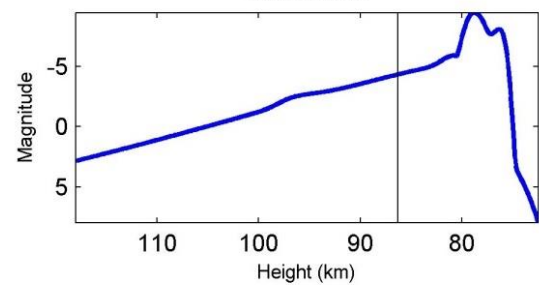
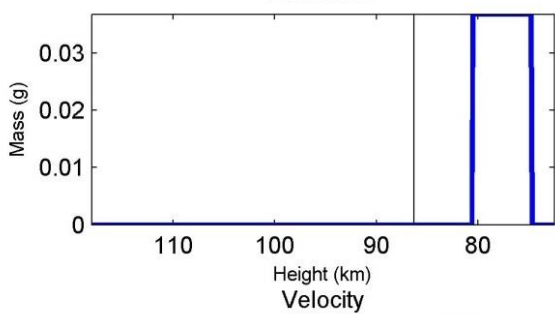
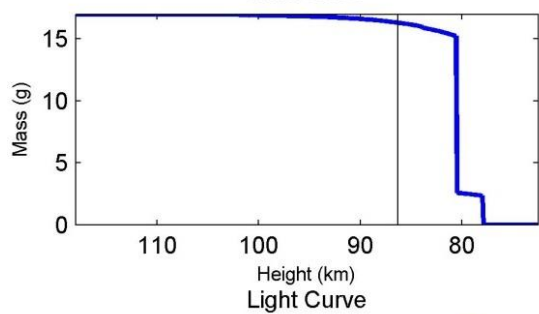
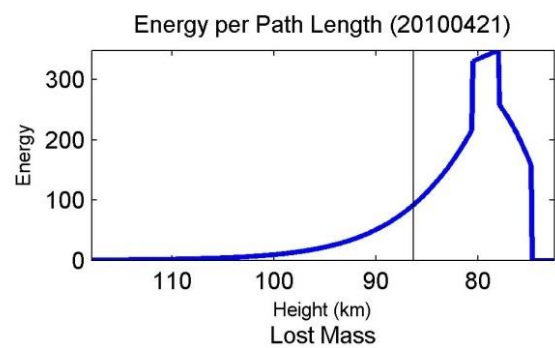
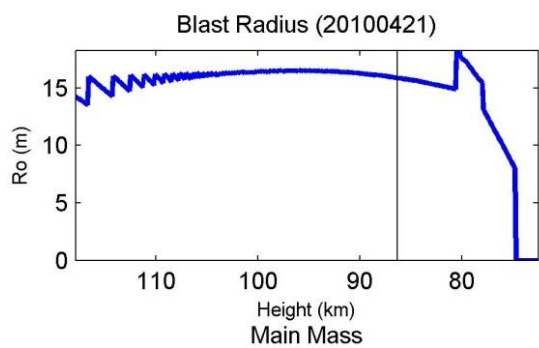


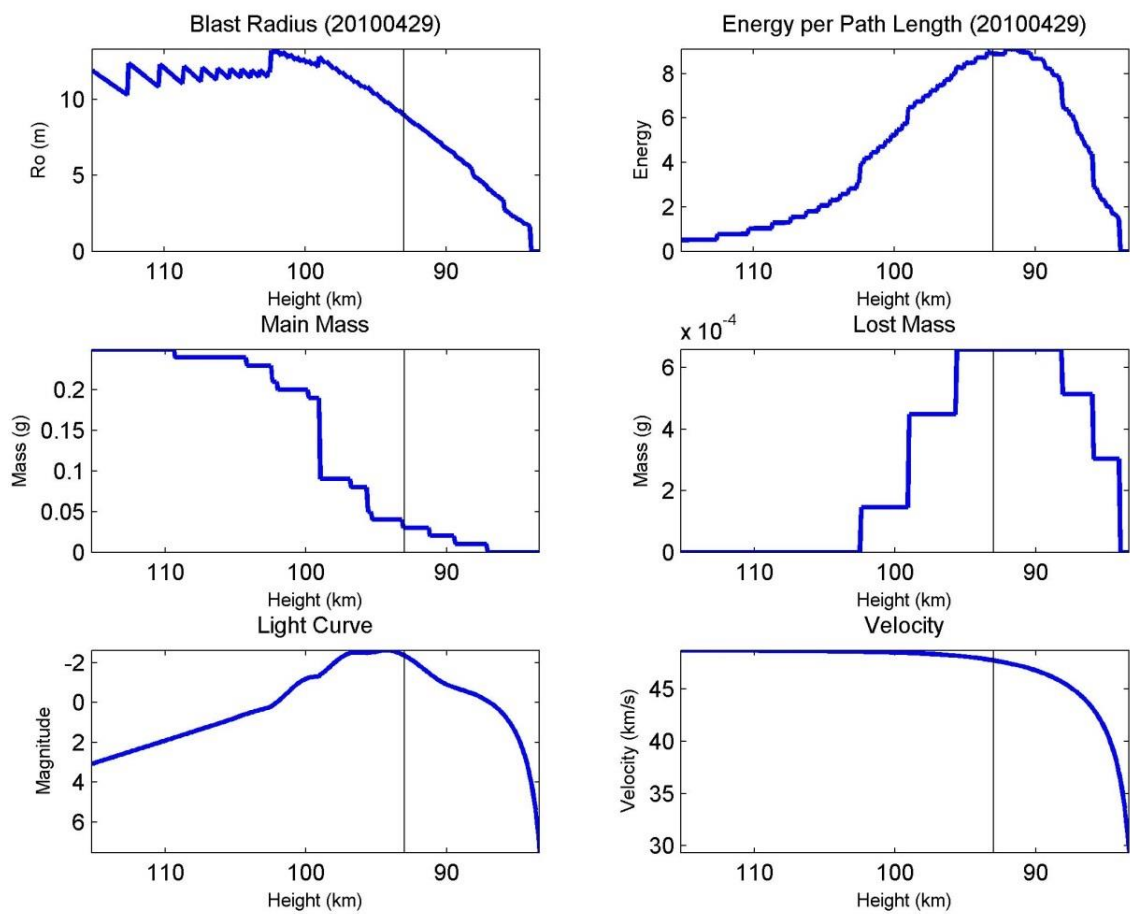


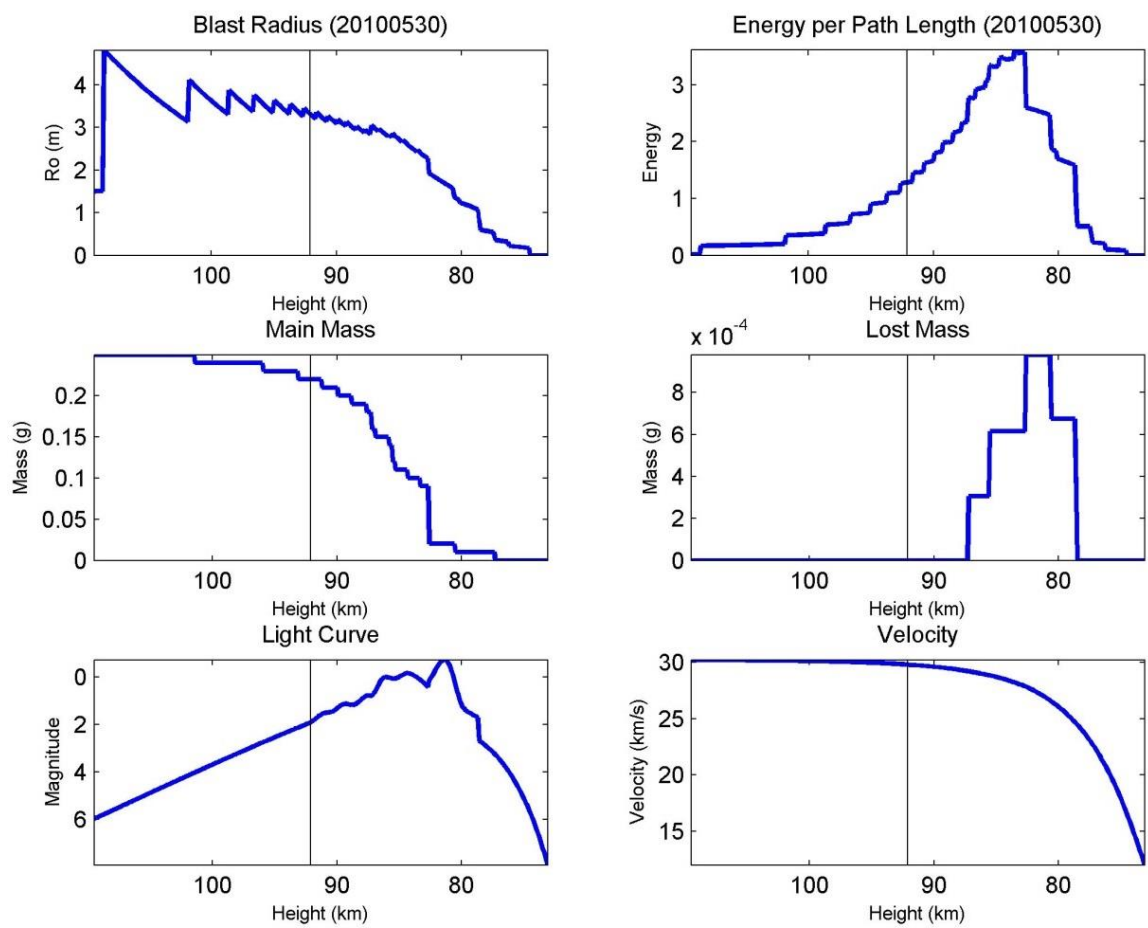


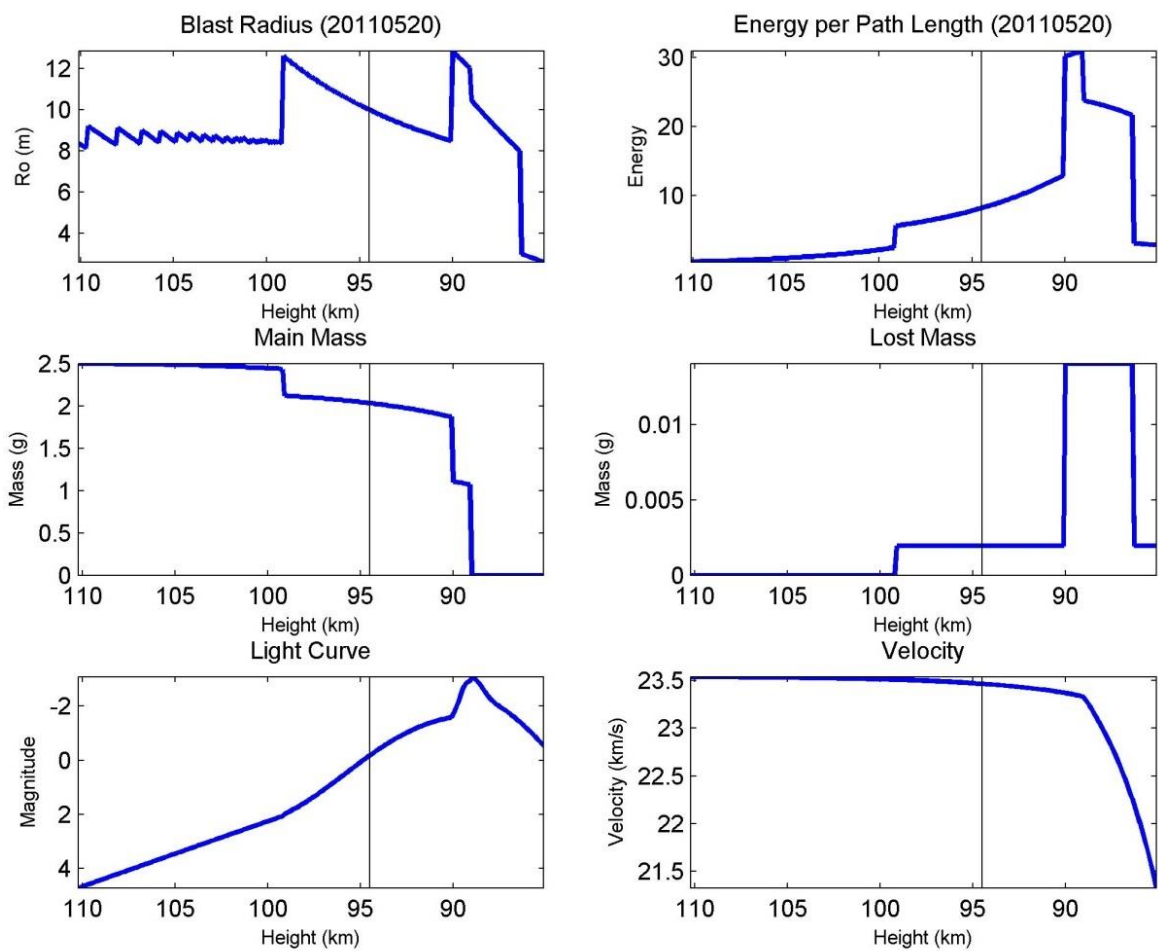


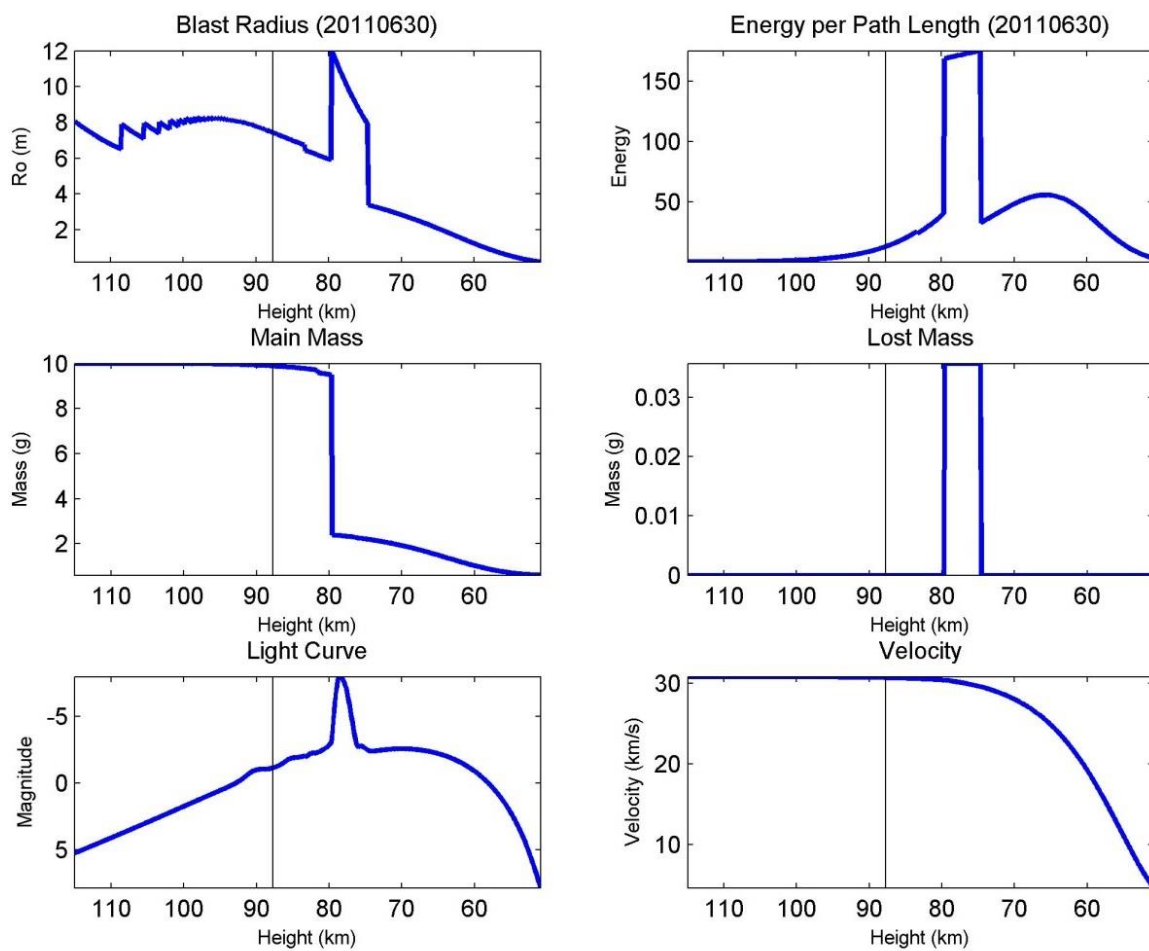


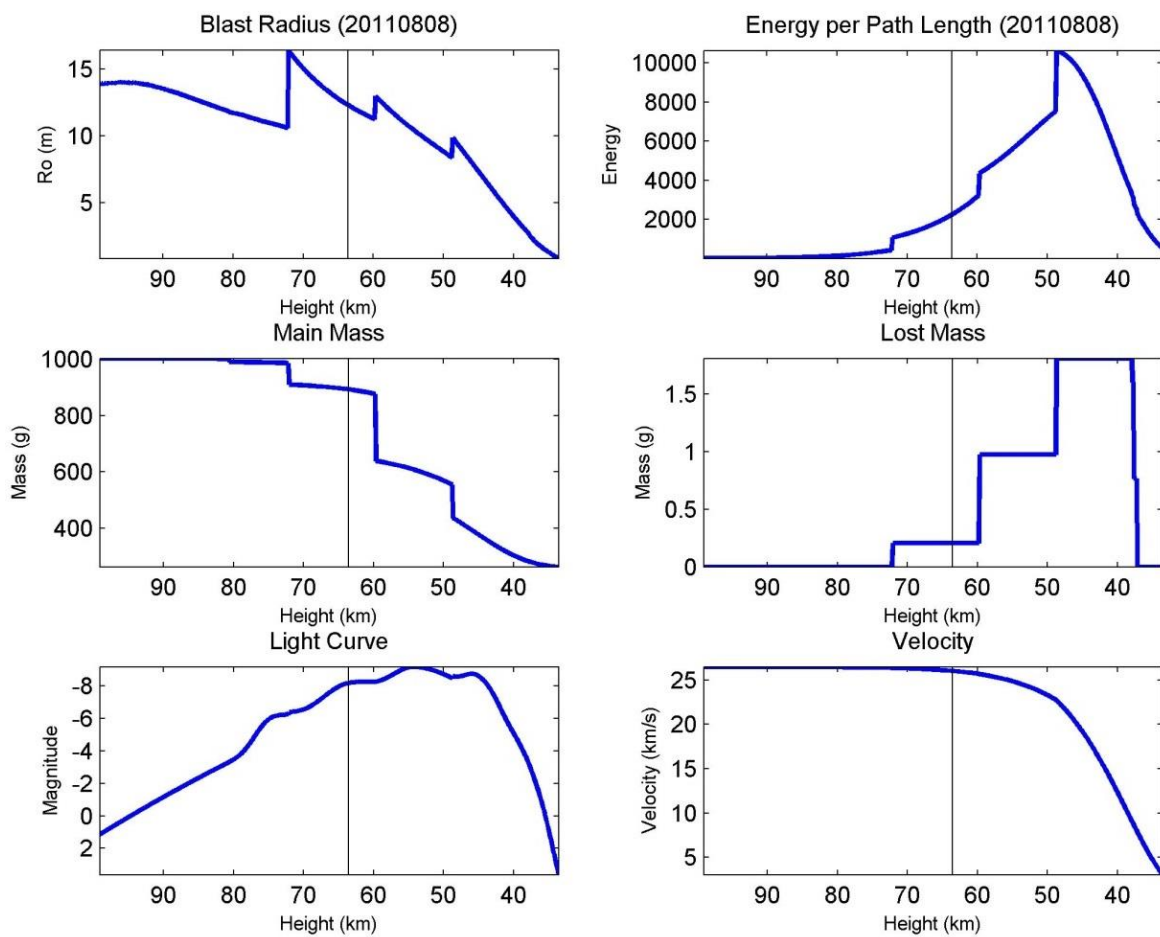


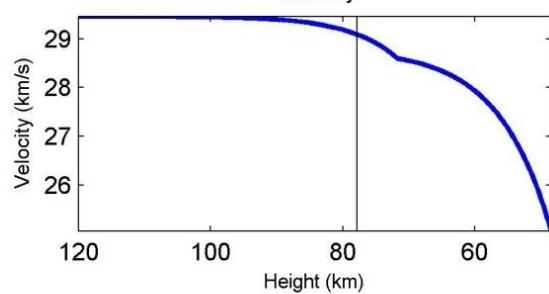
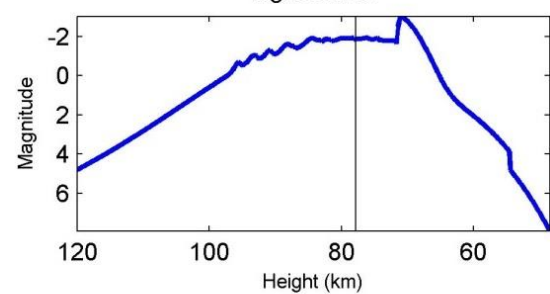
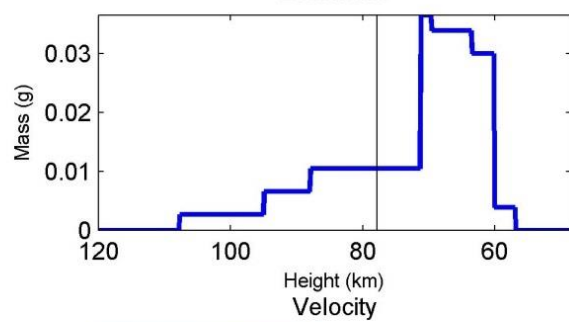
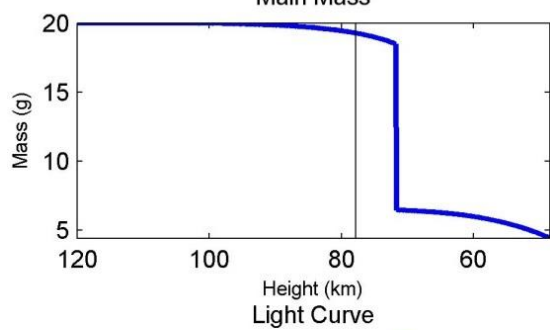
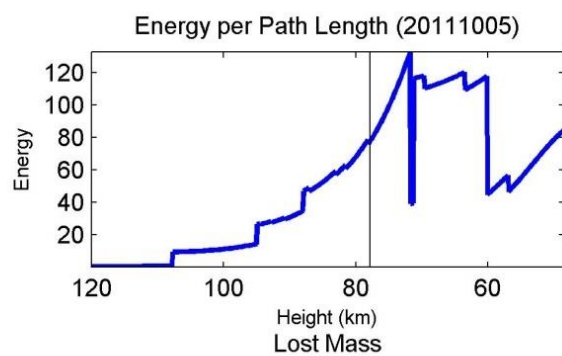
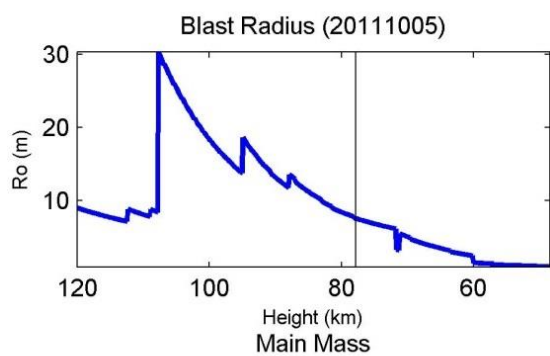




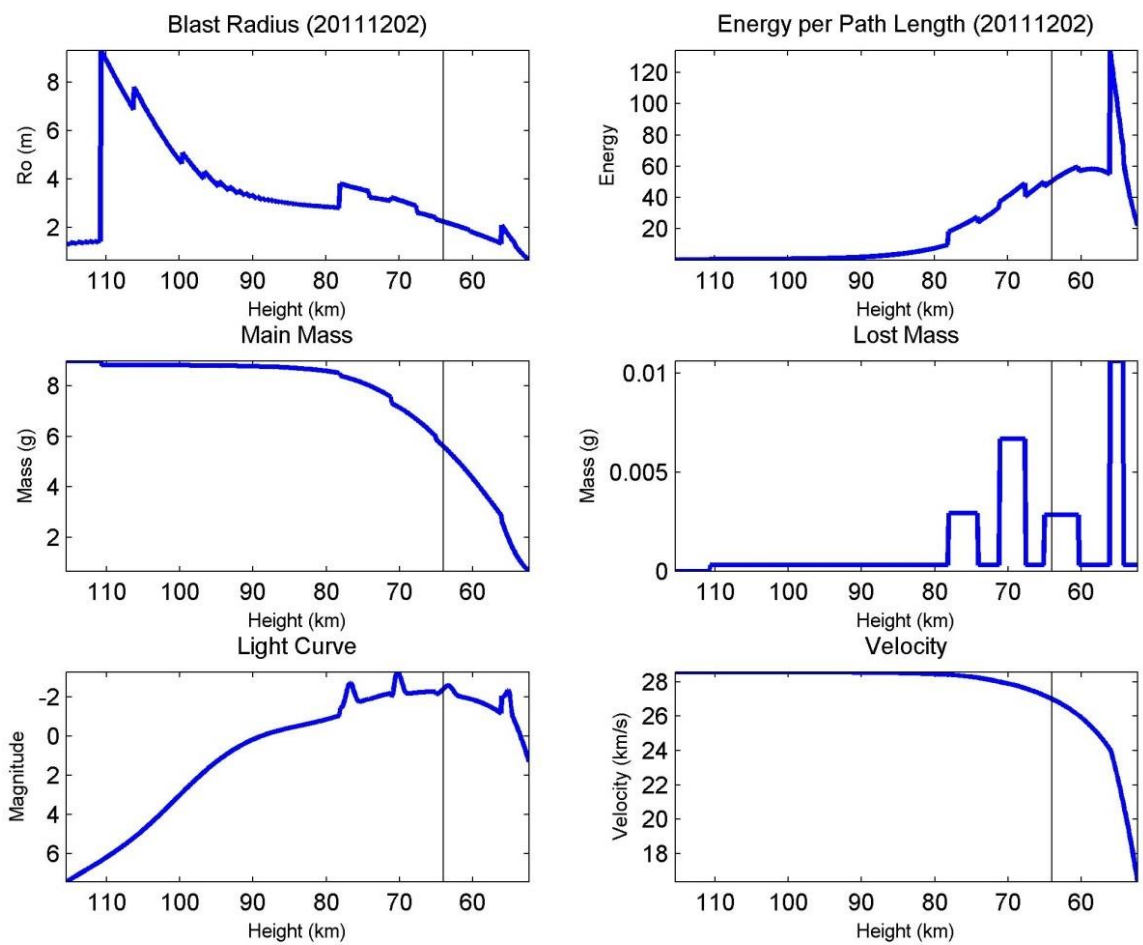




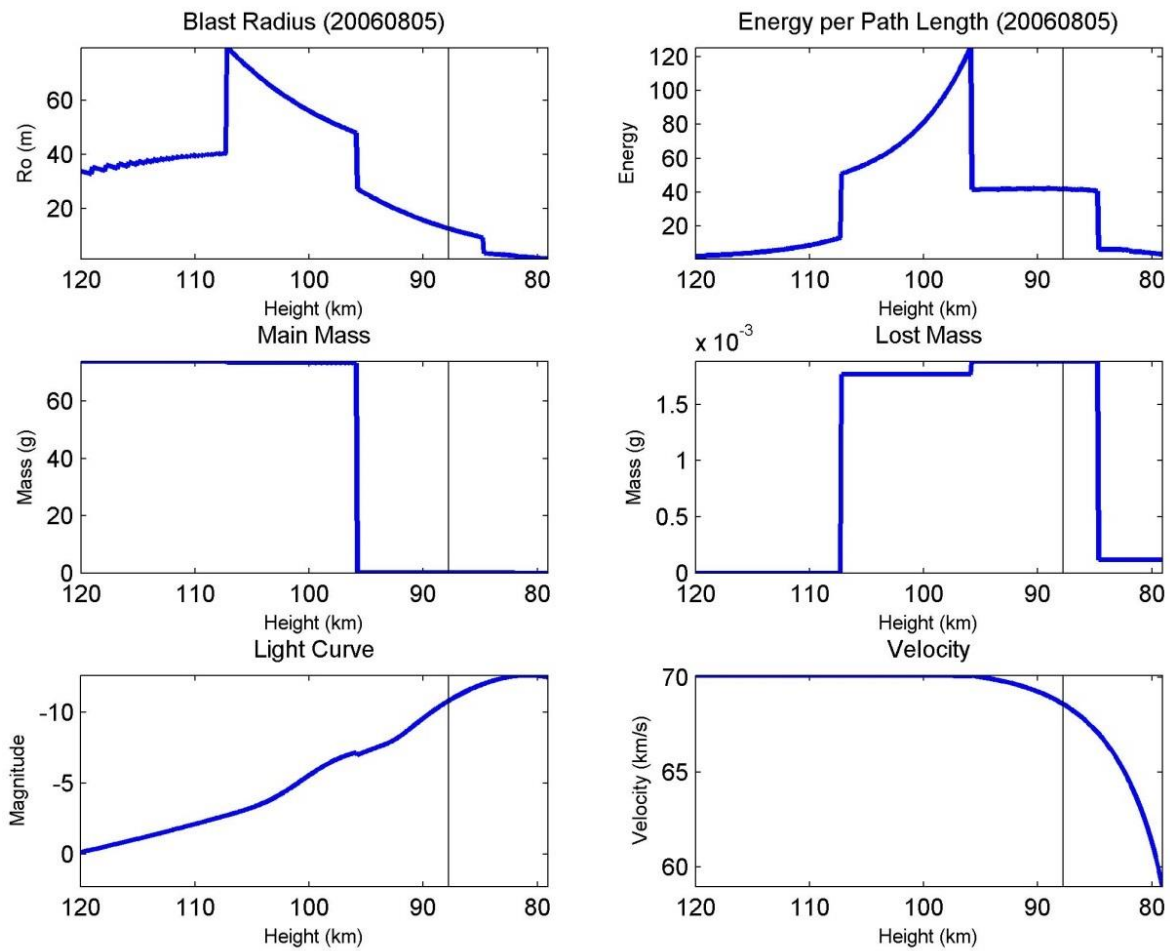


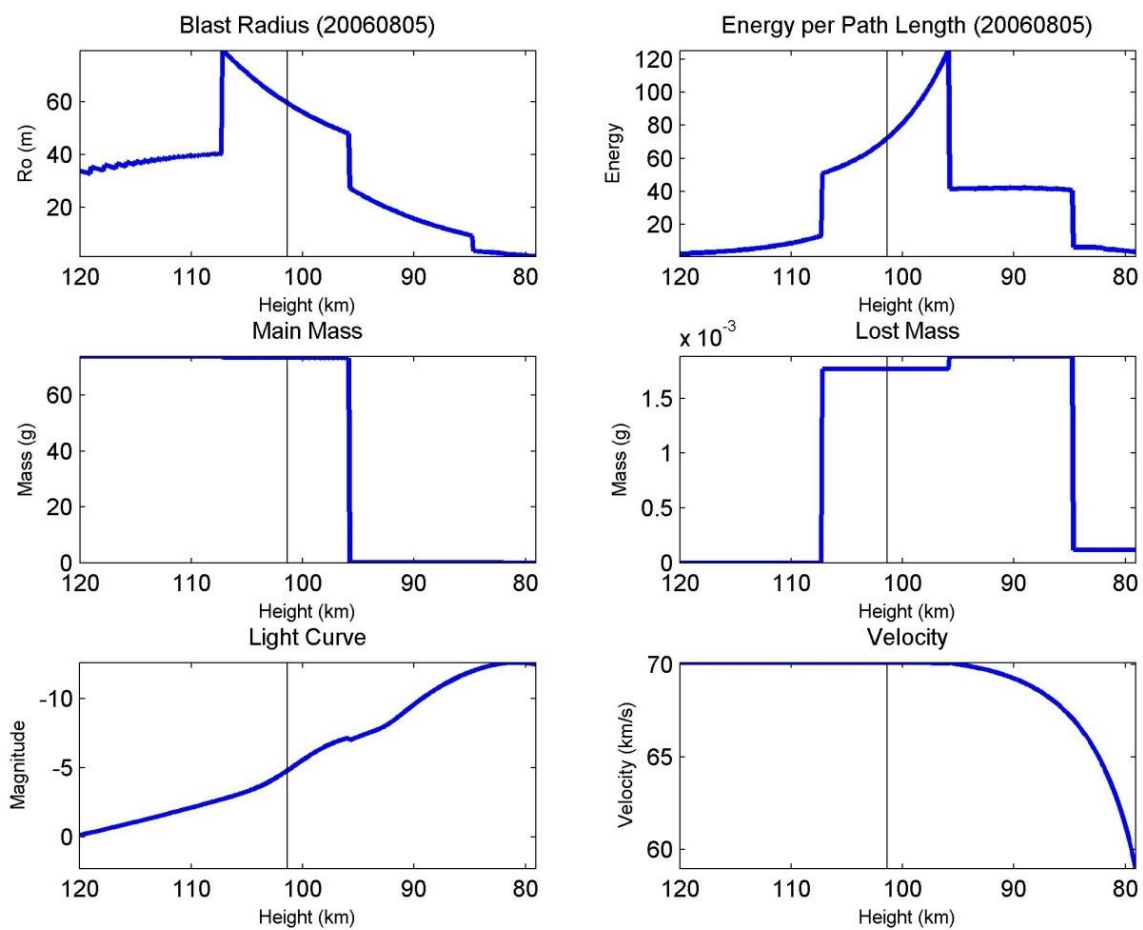


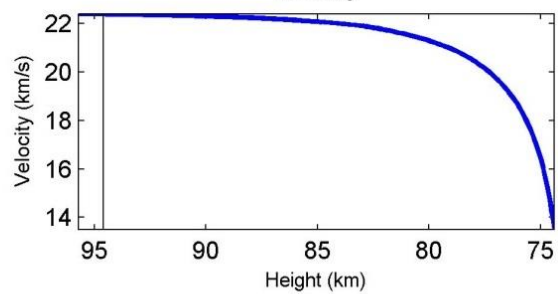
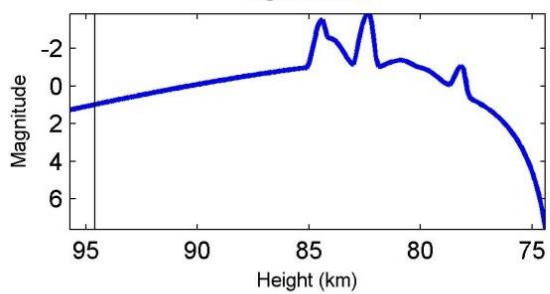
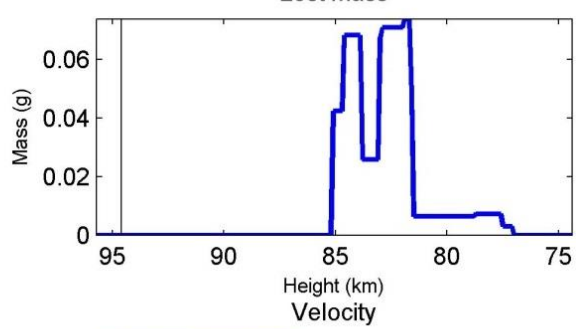
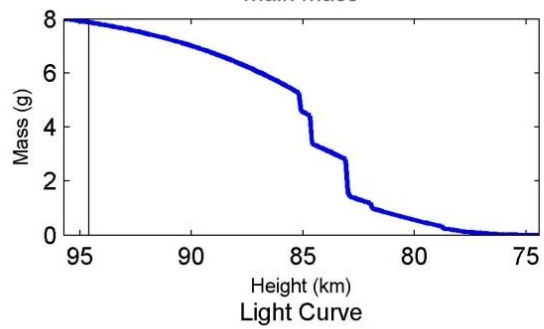
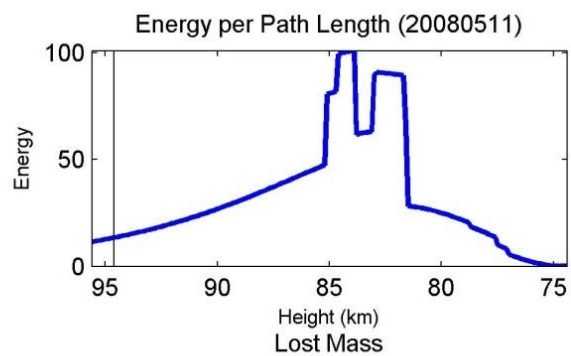
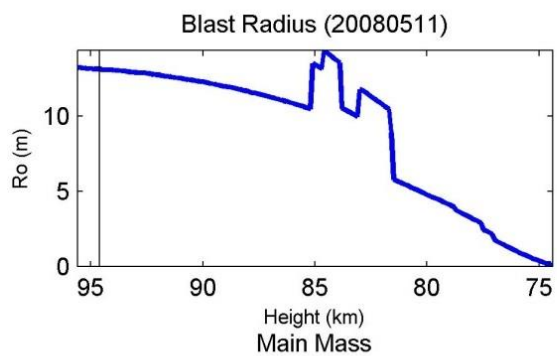


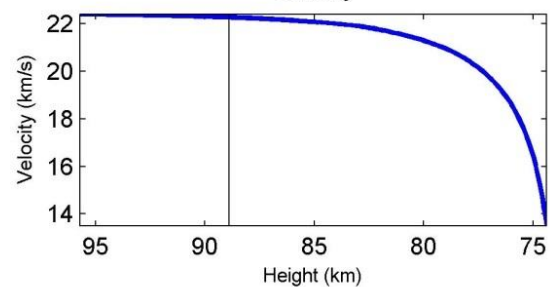
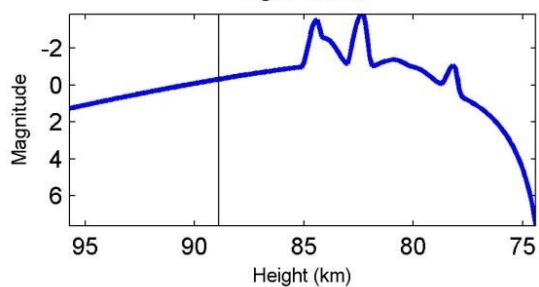
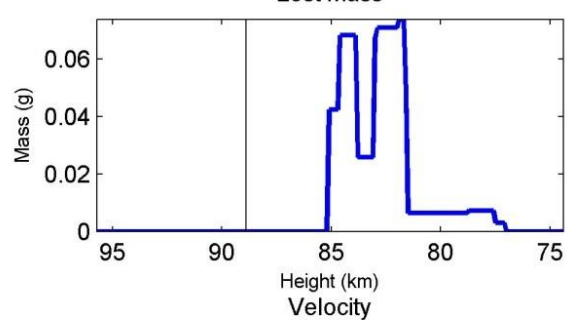
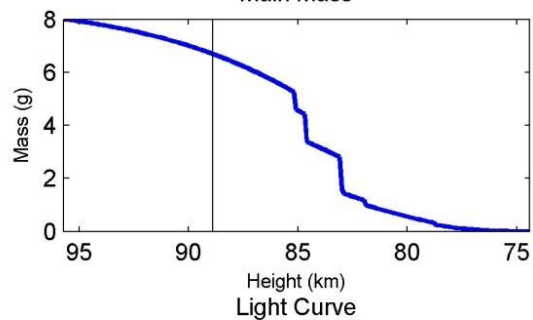
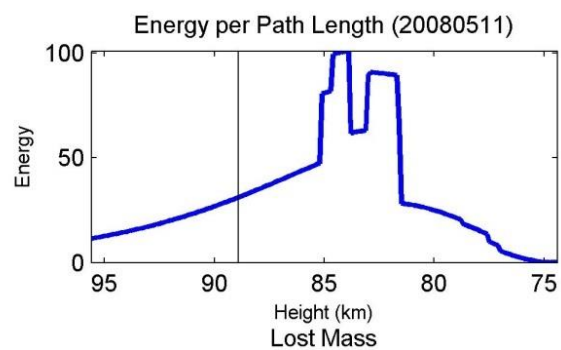
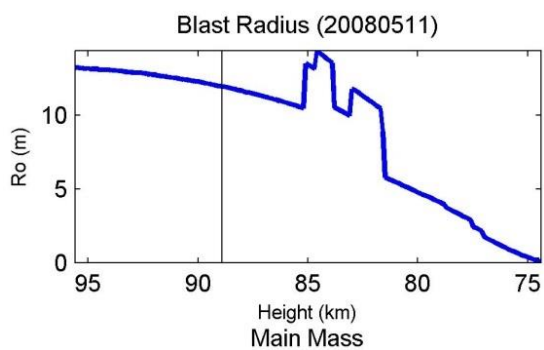


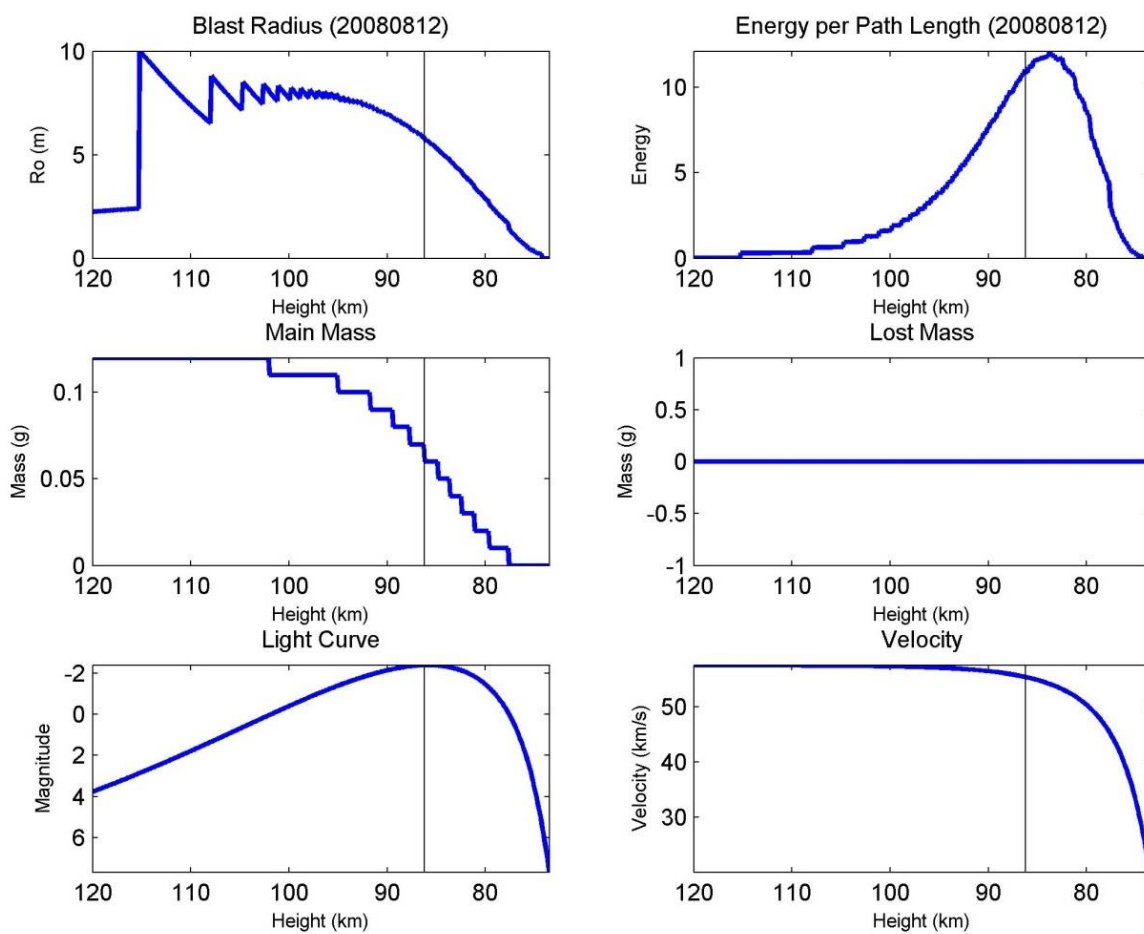
## Multi Arrivals

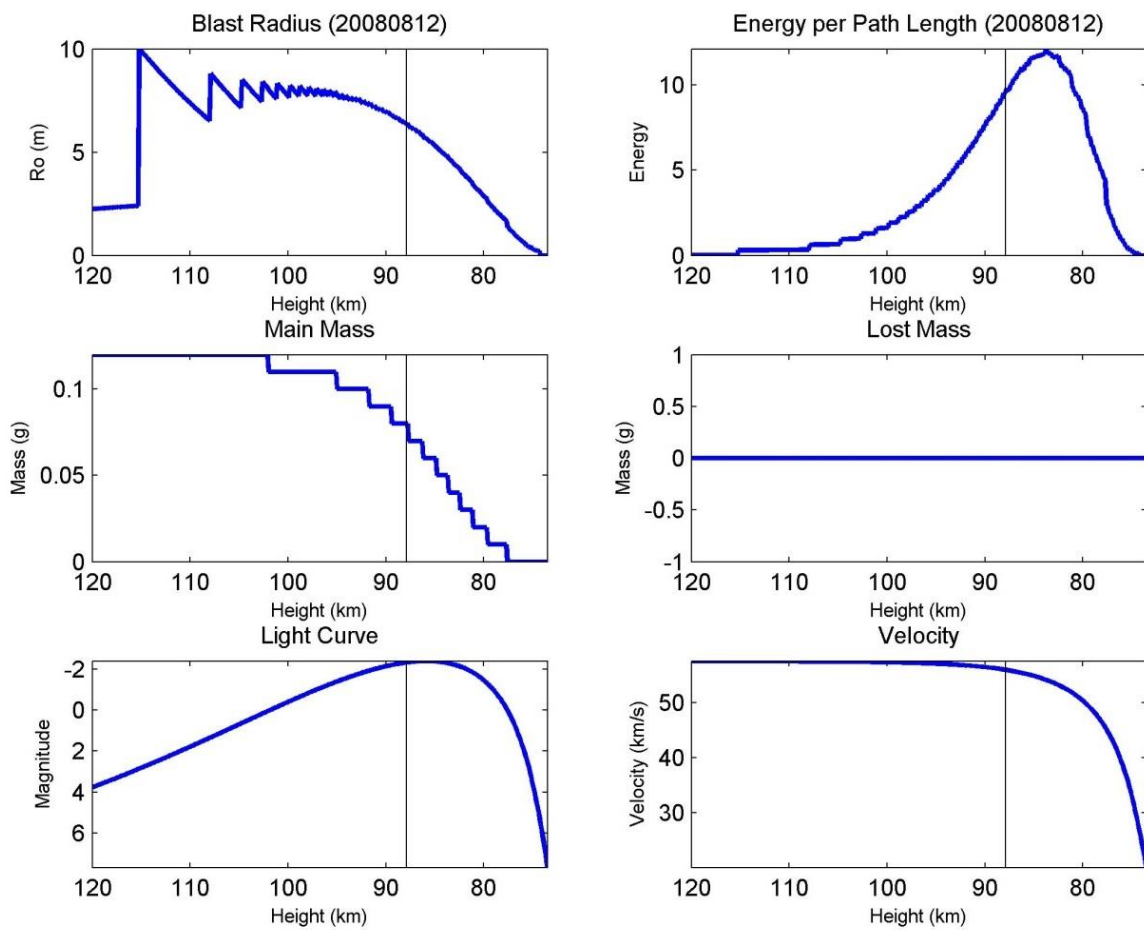




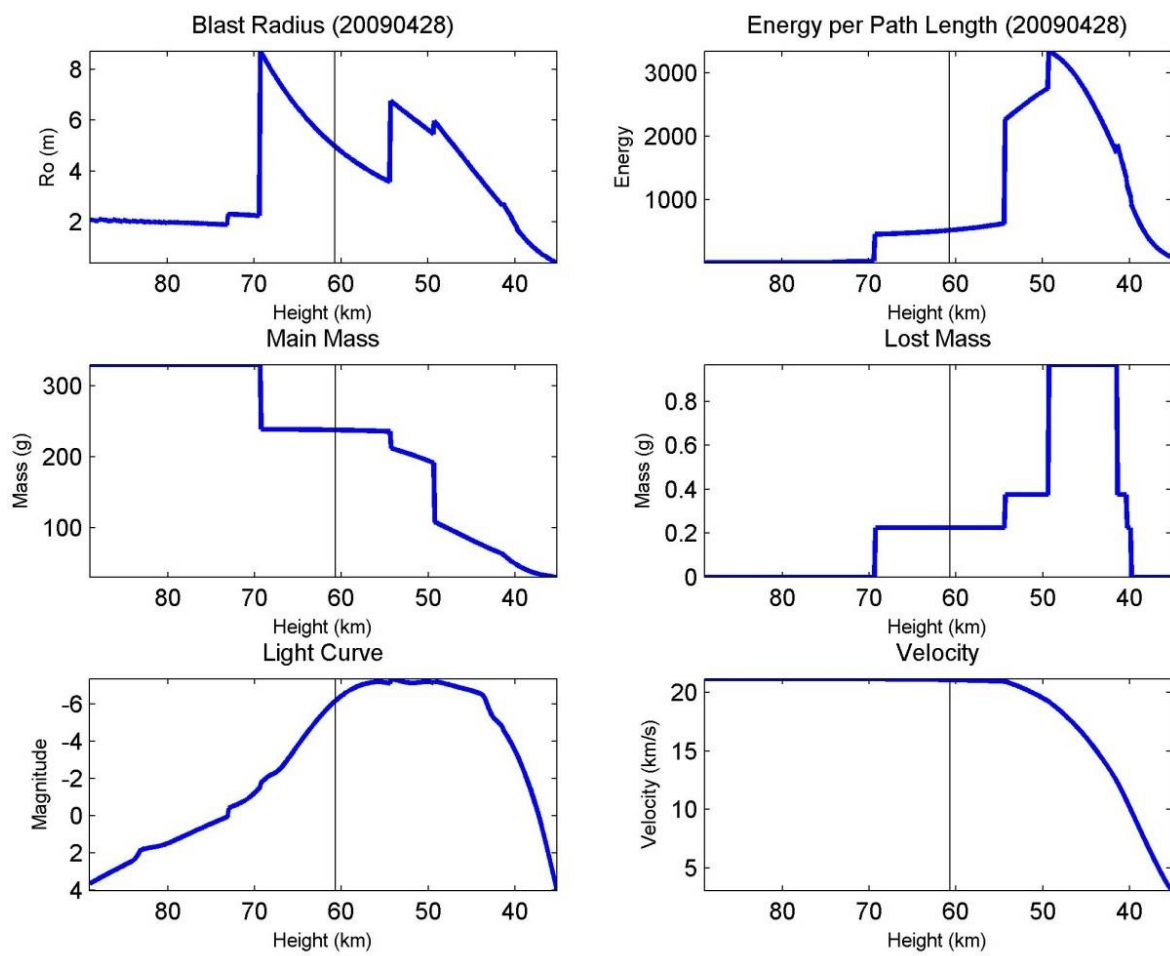


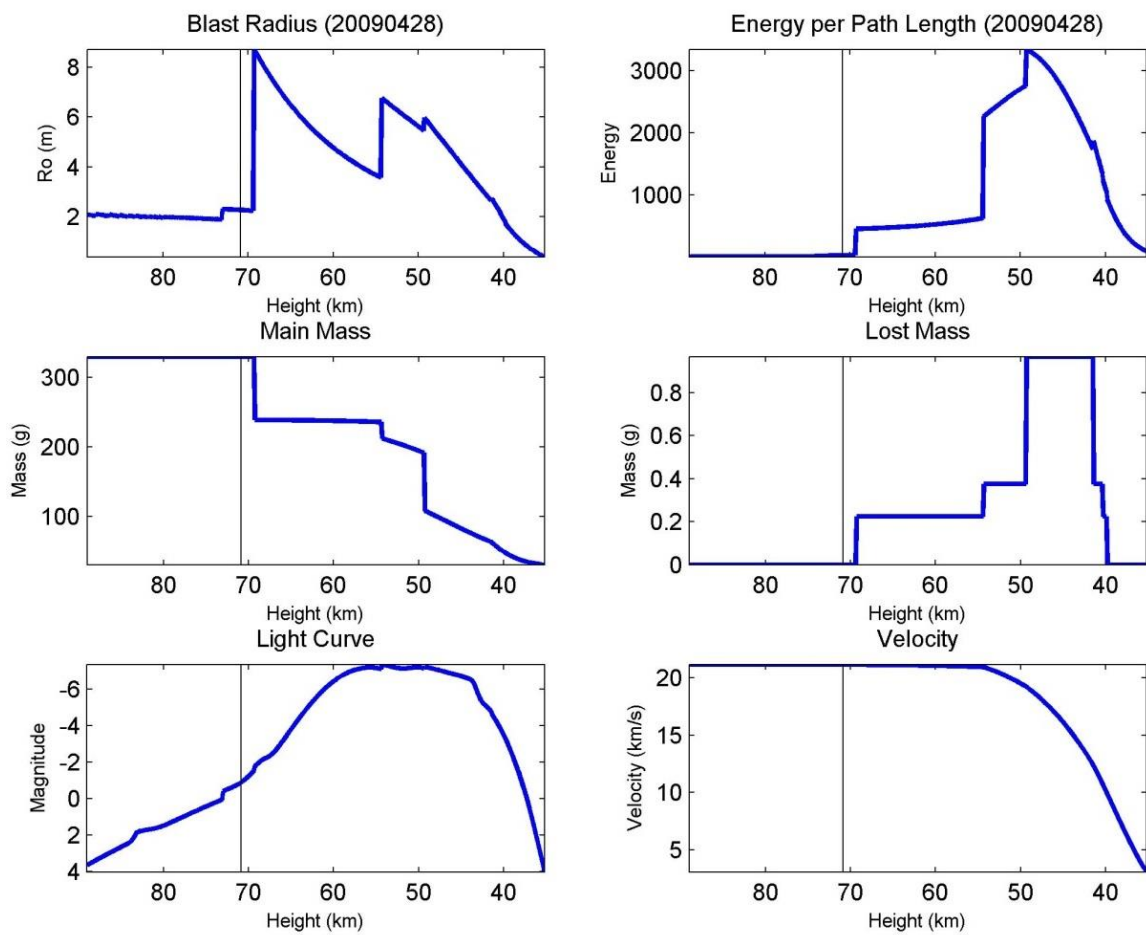


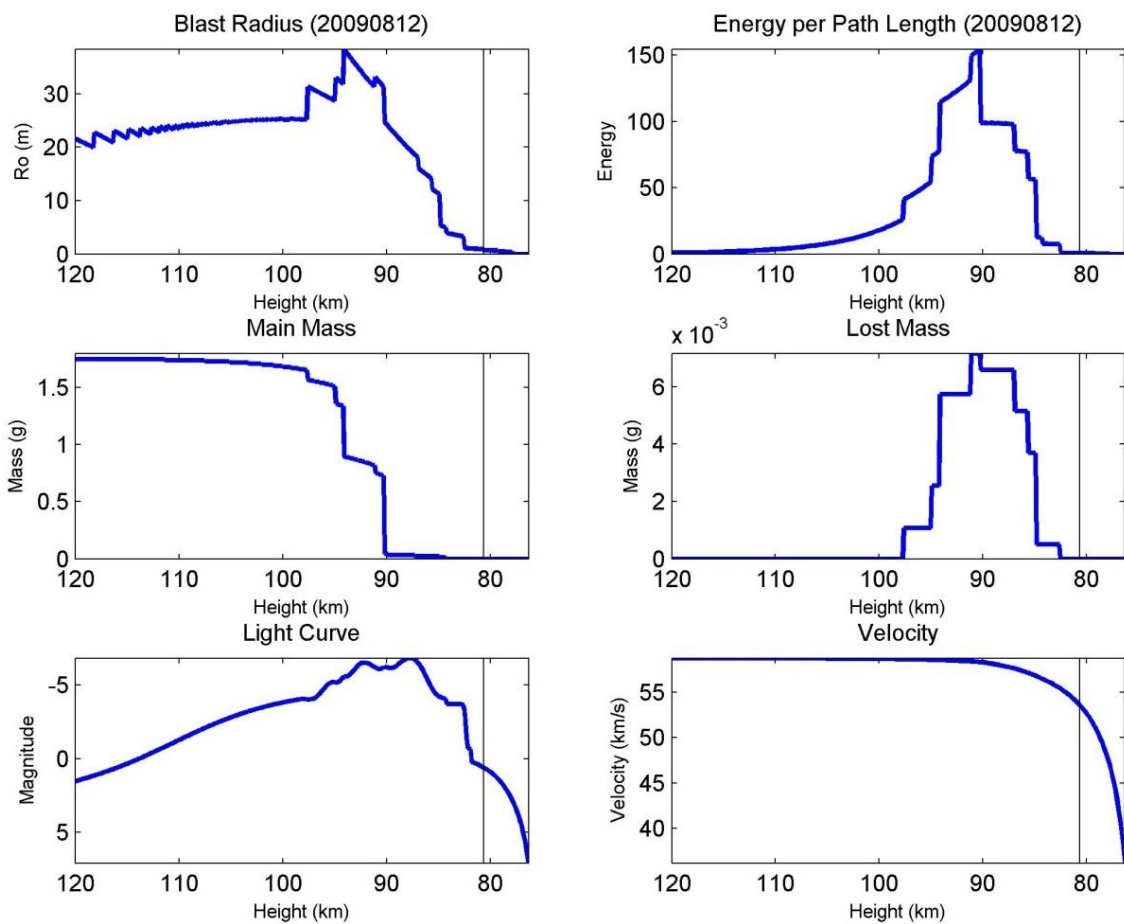


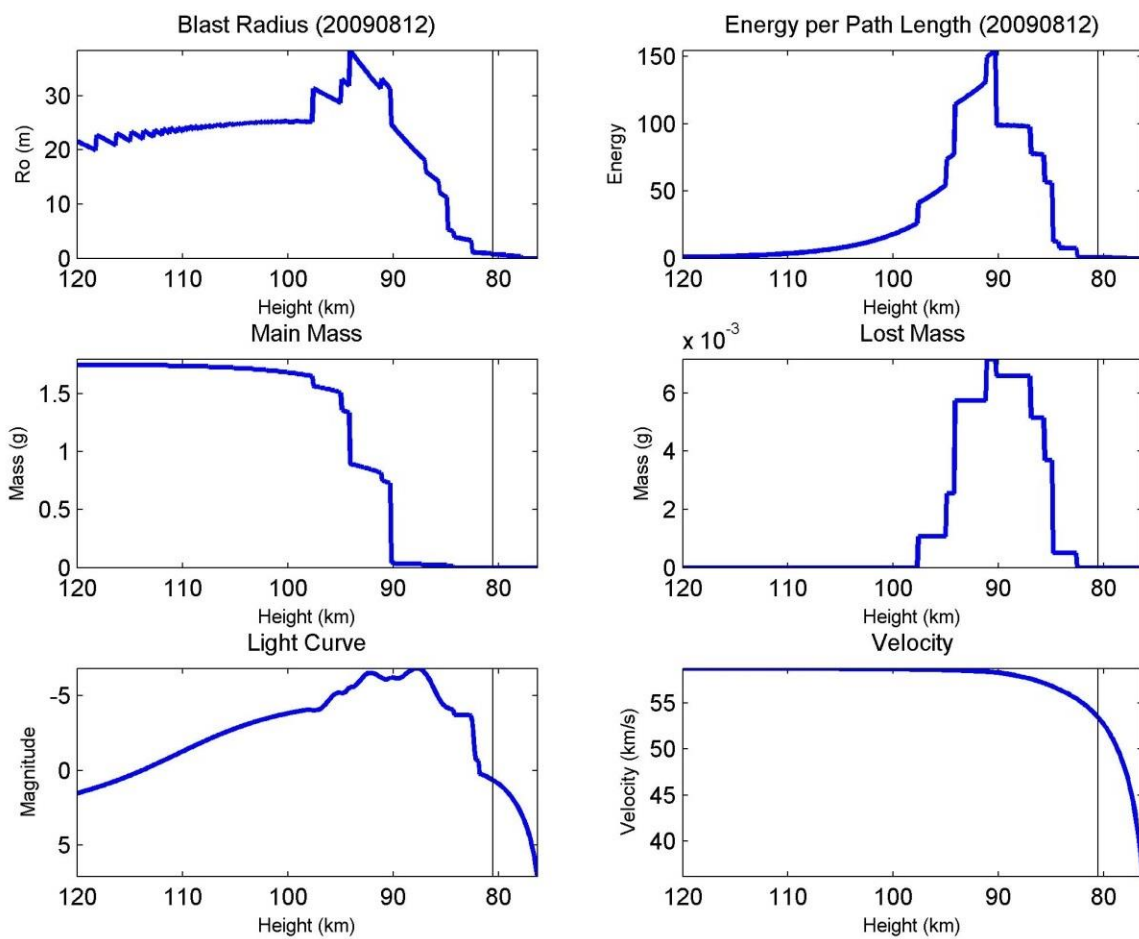


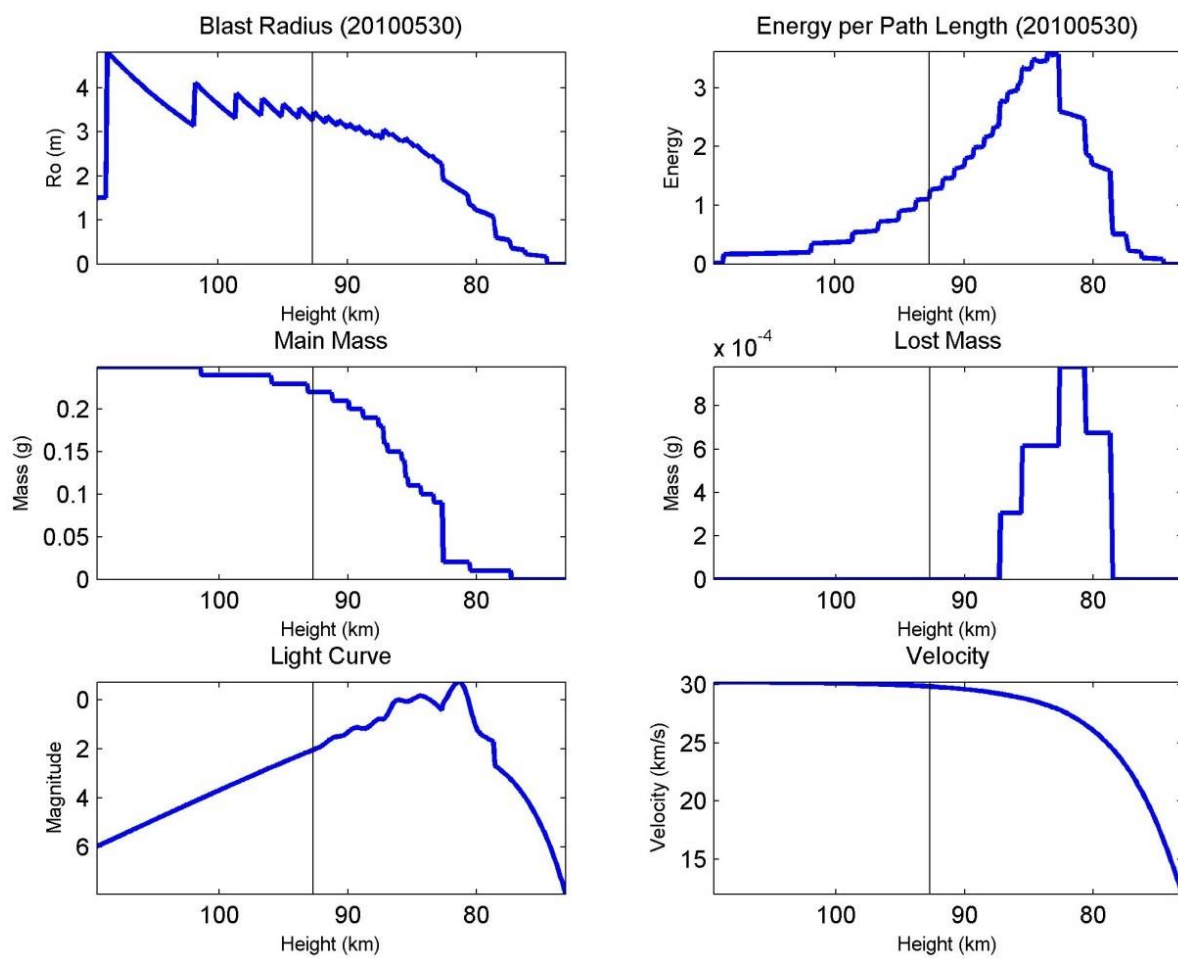


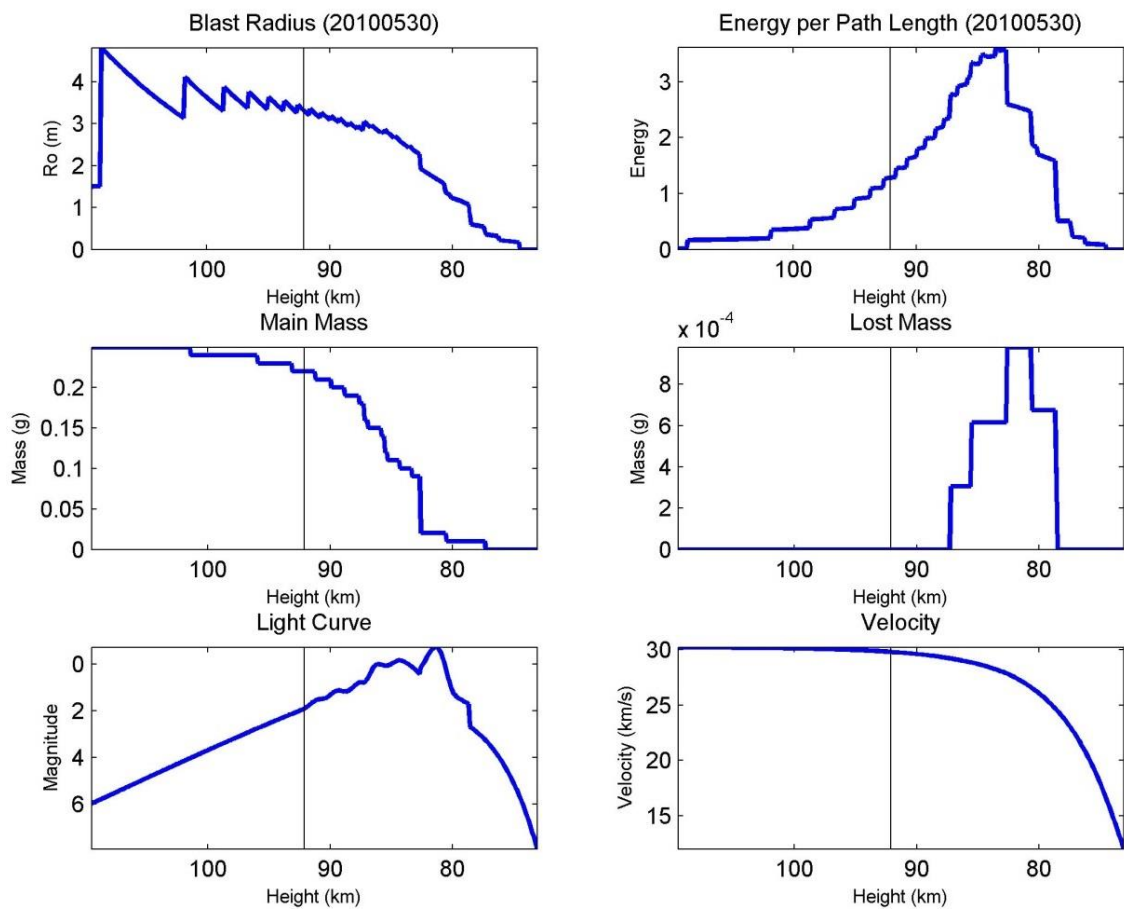












## Copyright Permissions

### JOHN WILEY AND SONS LICENSE TERMS AND CONDITIONS

Jun 22, 2014

---



---

This is a License Agreement between Elizabeth A Silber ("You") and John Wiley and Sons ("John Wiley and Sons") provided by Copyright Clearance Center ("CCC"). The license consists of your order details, the terms and conditions provided by John Wiley and Sons, and the payment terms and conditions.



**All payments must be made in full to CCC. For payment instructions, please see information listed at the bottom of this form.**

License Number	3384080261995
License date	May 08, 2014
Licensed content publisher	John Wiley and Sons
Licensed content publication	Journal of Geophysical Research: Planets
Licensed content title	An estimate of the terrestrial influx of large meteoroids from infrasonic measurements
Licensed copyright line	Copyright 2009 by the American Geophysical Union.
Licensed content author	Elizabeth A. Silber,Douglas O. ReVelle,Peter G. Brown,Wayne N. Edwards
Licensed content date	Aug 28, 2009
Start page	n/a
End page	n/a
Type of use	Dissertation/Thesis
Requestor type	Author of this Wiley article
Format	Electronic
Portion	Full article
Will you be translating?	No
Title of your thesis / dissertation	Observational and theoretical investigation of cylindrical line source blast theory using meteors
Expected completion date	Jun 2014
Expected size (number of pages)	500
Total	0.00 USD
Terms and Conditions	

### TERMS AND CONDITIONS

This copyrighted material is owned by or exclusively licensed to John Wiley & Sons, Inc.



or one of its group companies (each a "Wiley Company") or handled on behalf of a society with which a Wiley Company has exclusive publishing rights in relation to a particular work (collectively "WILEY"). By clicking  accept  in connection with completing this licensing transaction, you agree that the following terms and conditions apply to this transaction (along with the billing and payment terms and conditions established by the Copyright Clearance Center Inc., ("CCC's Billing and Payment terms and conditions"), at the time that you opened your Rightslink account (these are available at any time at <http://myaccount.copyright.com>).

### **Terms and Conditions**

- The materials you have requested permission to reproduce or reuse (the "Wiley Materials") are protected by copyright.
- You are hereby granted a personal, non-exclusive, non-sub licensable (on a stand-alone basis), non-transferable, worldwide, limited license to reproduce the Wiley Materials for the purpose specified in the licensing process. This license is for a one-time use only and limited to any maximum distribution number specified in the license. The first instance of republication or reuse granted by this licence must be completed within two years of the date of the grant of this licence (although copies prepared before the end date may be distributed thereafter). The Wiley Materials shall not be used in any other manner or for any other purpose, beyond what is granted in the license. Permission is granted subject to an appropriate acknowledgement given to the author, title of the material/book/journal and the publisher. You shall also duplicate the copyright notice that appears in the Wiley publication in your use of the Wiley Material. Permission is also granted on the understanding that nowhere in the text is a previously published source acknowledged for all or part of this Wiley Material. Any third party content is expressly excluded from this permission.
- With respect to the Wiley Materials, all rights are reserved. Except as expressly granted by the terms of the license, no part of the Wiley Materials may be copied, modified, adapted (except for minor reformatting required by the new Publication), translated, reproduced, transferred or distributed, in any form or by any means, and no derivative works may be made based on the Wiley Materials without the prior permission of the respective copyright owner. You may not alter, remove or suppress in any manner any copyright, trademark or other notices displayed by the Wiley Materials. You may not license, rent, sell, loan, lease, pledge, offer as security, transfer or assign the Wiley Materials on a stand-alone basis, or any of the rights granted to you hereunder to any other person.
- The Wiley Materials and all of the intellectual property rights therein shall at all times remain the exclusive property of John Wiley & Sons Inc, the Wiley Companies, or their respective licensors, and your interest therein is only that of having possession of and the right to reproduce the Wiley Materials pursuant to

Section 2 herein during the continuance of this Agreement. You agree that you own no right, title or interest in or to the Wiley Materials or any of the intellectual property rights therein. You shall have no rights hereunder other than the license as provided for above in Section 2. No right, license or interest to any trademark, trade name, service mark or other branding ("Marks") of WILEY or its licensors is granted hereunder, and you agree that you shall not assert any such right, license or interest with respect thereto.

- NEITHER WILEY NOR ITS LICENSORS MAKES ANY WARRANTY OR REPRESENTATION OF ANY KIND TO YOU OR ANY THIRD PARTY, EXPRESS, IMPLIED OR STATUTORY, WITH RESPECT TO THE MATERIALS OR THE ACCURACY OF ANY INFORMATION CONTAINED IN THE MATERIALS, INCLUDING, WITHOUT LIMITATION, ANY IMPLIED WARRANTY OF MERCHANTABILITY, ACCURACY, SATISFACTORY QUALITY, FITNESS FOR A PARTICULAR PURPOSE, USABILITY, INTEGRATION OR NON-INFRINGEMENT AND ALL SUCH WARRANTIES ARE HEREBY EXCLUDED BY WILEY AND ITS LICENSORS AND WAIVED BY YOU
- WILEY shall have the right to terminate this Agreement immediately upon breach of this Agreement by you.
- You shall indemnify, defend and hold harmless WILEY, its Licensors and their respective directors, officers, agents and employees, from and against any actual or threatened claims, demands, causes of action or proceedings arising from any breach of this Agreement by you.
- IN NO EVENT SHALL WILEY OR ITS LICENSORS BE LIABLE TO YOU OR ANY OTHER PARTY OR ANY OTHER PERSON OR ENTITY FOR ANY SPECIAL, CONSEQUENTIAL, INCIDENTAL, INDIRECT, EXEMPLARY OR PUNITIVE DAMAGES, HOWEVER CAUSED, ARISING OUT OF OR IN CONNECTION WITH THE DOWNLOADING, PROVISIONING, VIEWING OR USE OF THE MATERIALS REGARDLESS OF THE FORM OF ACTION, WHETHER FOR BREACH OF CONTRACT, BREACH OF WARRANTY, TORT, NEGLIGENCE, INFRINGEMENT OR OTHERWISE (INCLUDING, WITHOUT LIMITATION, DAMAGES BASED ON LOSS OF PROFITS, DATA, FILES, USE, BUSINESS OPPORTUNITY OR CLAIMS OF THIRD PARTIES), AND WHETHER OR NOT THE PARTY HAS BEEN ADVISED OF THE POSSIBILITY OF SUCH DAMAGES. THIS LIMITATION SHALL APPLY NOTWITHSTANDING ANY FAILURE OF ESSENTIAL PURPOSE OF ANY LIMITED REMEDY PROVIDED HEREIN.
- Should any provision of this Agreement be held by a court of competent jurisdiction to be illegal, invalid, or unenforceable, that provision shall be deemed amended to achieve as nearly as possible the same economic effect as the original provision, and the legality, validity and enforceability of the remaining provisions of this Agreement shall not be affected or impaired thereby.

- The failure of either party to enforce any term or condition of this Agreement shall not constitute a waiver of either party's right to enforce each and every term and condition of this Agreement. No breach under this agreement shall be deemed waived or excused by either party unless such waiver or consent is in writing signed by the party granting such waiver or consent. The waiver by or consent of a party to a breach of any provision of this Agreement shall not operate or be construed as a waiver of or consent to any other or subsequent breach by such other party.
- This Agreement may not be assigned (including by operation of law or otherwise) by you without WILEY's prior written consent.
- Any fee required for this permission shall be non-refundable after thirty (30) days from receipt by the CCC.
- These terms and conditions together with CCC's Billing and Payment terms and conditions (which are incorporated herein) form the entire agreement between you and WILEY concerning this licensing transaction and (in the absence of fraud) supersedes all prior agreements and representations of the parties, oral or written. This Agreement may not be amended except in writing signed by both parties. This Agreement shall be binding upon and inure to the benefit of the parties' successors, legal representatives, and authorized assigns.
- In the event of any conflict between your obligations established by these terms and conditions and those established by CCC's Billing and Payment terms and conditions, these terms and conditions shall prevail.
- WILEY expressly reserves all rights not specifically granted in the combination of (i) the license details provided by you and accepted in the course of this licensing transaction, (ii) these terms and conditions and (iii) CCC's Billing and Payment terms and conditions.
- This Agreement will be void if the Type of Use, Format, Circulation, or Requestor Type was misrepresented during the licensing process.
- This Agreement shall be governed by and construed in accordance with the laws of the State of New York, USA, without regards to such state's conflict of law rules. Any legal action, suit or proceeding arising out of or relating to these Terms and Conditions or the breach thereof shall be instituted in a court of competent jurisdiction in New York County in the State of New York in the United States of America and each party hereby consents and submits to the personal jurisdiction of such court, waives any objection to venue in such court and consents to service of process by registered or certified mail, return receipt requested, at the last known address of such party.

## **WILEY OPEN ACCESS TERMS AND CONDITIONS**

Wiley Publishes Open Access Articles in fully Open Access Journals and in Subscription

journals offering Online Open. Although most of the fully Open Access journals publish open access articles under the terms of the Creative Commons Attribution (CC BY) License only, the subscription journals and a few of the Open Access Journals offer a choice of Creative Commons Licenses:: Creative Commons Attribution (CC-BY) license [Creative Commons Attribution Non-Commercial \(CC-BY-NC\) license](#) and [Creative Commons Attribution Non-Commercial-NoDerivs \(CC-BY-NC-ND\) License](#). The license type is clearly identified on the article.

Copyright in any research article in a journal published as Open Access under a Creative Commons License is retained by the author(s). Authors grant Wiley a license to publish the article and identify itself as the original publisher. Authors also grant any third party the right to use the article freely as long as its integrity is maintained and its original authors, citation details and publisher are identified as follows: [Title of Article/Author/Journal Title and Volume/Issue. Copyright (c) [year] [copyright owner as specified in the Journal]. Links to the final article on Wiley's website are encouraged where applicable.

### **The Creative Commons Attribution License**

The [Creative Commons Attribution License \(CC-BY\)](#) allows users to copy, distribute and transmit an article, adapt the article and make commercial use of the article. The CC-BY license permits commercial and non-commercial re-use of an open access article, as long as the author is properly attributed.

The Creative Commons Attribution License does not affect the moral rights of authors, including without limitation the right not to have their work subjected to derogatory treatment. It also does not affect any other rights held by authors or third parties in the article, including without limitation the rights of privacy and publicity. Use of the article must not assert or imply, whether implicitly or explicitly, any connection with, endorsement or sponsorship of such use by the author, publisher or any other party associated with the article.

For any reuse or distribution, users must include the copyright notice and make clear to others that the article is made available under a Creative Commons Attribution license, linking to the relevant Creative Commons web page.

To the fullest extent permitted by applicable law, the article is made available as is and without representation or warranties of any kind whether express, implied, statutory or otherwise and including, without limitation, warranties of title, merchantability, fitness for a particular purpose, non-infringement, absence of defects, accuracy, or the presence or absence of errors.

### **Creative Commons Attribution Non-Commercial License**

The [Creative Commons Attribution Non-Commercial \(CC-BY-NC\) License](#) permits use, distribution and reproduction in any medium, provided the original work is properly cited

and is not used for commercial purposes.(see below)

### **Creative Commons Attribution-Non-Commercial-NoDerivs License**

The [Creative Commons Attribution Non-Commercial-NoDerivs License](#) (CC-BY-NC-ND) permits use, distribution and reproduction in any medium, provided the original work is properly cited, is not used for commercial purposes and no modifications or adaptations are made. (see below)

#### **Use by non-commercial users**

For non-commercial and non-promotional purposes, individual users may access, download, copy, display and redistribute to colleagues Wiley Open Access articles, as well as adapt, translate, text- and data-mine the content subject to the following conditions:

- The authors' moral rights are not compromised. These rights include the right of "paternity" (also known as "attribution" - the right for the author to be identified as such) and "integrity" (the right for the author not to have the work altered in such a way that the author's reputation or integrity may be impugned).
- Where content in the article is identified as belonging to a third party, it is the obligation of the user to ensure that any reuse complies with the copyright policies of the owner of that content.
- If article content is copied, downloaded or otherwise reused for non-commercial research and education purposes, a link to the appropriate bibliographic citation (authors, journal, article title, volume, issue, page numbers, DOI and the link to the definitive published version on **Wiley Online Library**) should be maintained. Copyright notices and disclaimers must not be deleted.
- Any translations, for which a prior translation agreement with Wiley has not been agreed, must prominently display the statement: "This is an unofficial translation of an article that appeared in a Wiley publication. The publisher has not endorsed this translation."

#### **Use by commercial "for-profit" organisations**

Use of Wiley Open Access articles for commercial, promotional, or marketing purposes requires further explicit permission from Wiley and will be subject to a fee. Commercial purposes include:

- Copying or downloading of articles, or linking to such articles for further redistribution, sale or licensing;
- Copying, downloading or posting by a site or service that incorporates advertising

with such content;

- The inclusion or incorporation of article content in other works or services (other than normal quotations with an appropriate citation) that is then available for sale or licensing, for a fee (for example, a compilation produced for marketing purposes, inclusion in a sales pack)
- Use of article content (other than normal quotations with appropriate citation) by for-profit organisations for promotional purposes
- Linking to article content in e-mails redistributed for promotional, marketing or educational purposes;
- Use for the purposes of monetary reward by means of sale, resale, licence, loan, transfer or other form of commercial exploitation such as marketing products
- Print reprints of Wiley Open Access articles can be purchased from:  
[corporatesales@wiley.com](mailto:corporatesales@wiley.com)

Further details can be found on Wiley Online Library  
<http://olabout.wiley.com/WileyCDA/Section/id-410895.html>

Other Terms and Conditions:

#### **v1.9**

**If you would like to pay for this license now, please remit this license along with your payment made payable to "COPYRIGHT CLEARANCE CENTER" otherwise you will be invoiced within 48 hours of the license date. Payment should be in the form of a check or money order referencing your account number and this invoice number 501297592.**

**Once you receive your invoice for this order, you may pay your invoice by credit card. Please follow instructions provided at that time.**

**Make Payment To:  
Copyright Clearance Center  
Dept 001  
P.O. Box 843006  
Boston, MA 02284-3006**

**For suggestions or comments regarding this order, contact RightsLink Customer Support: [customercare@copyright.com](mailto:customercare@copyright.com) or +1-877-622-5543 (toll free in the US) or +1-978-646-2777.**

**Gratis licenses (referencing \$0 in the Total field) are free. Please retain this printable license for your reference. No payment is required.**

JOHN WILEY AND SONS LICENSE  
TERMS AND CONDITIONS

Jun 22, 2014


---

This is a License Agreement between Elizabeth A Silber ("You") and John Wiley and Sons ("John Wiley and Sons") provided by Copyright Clearance Center ("CCC"). The license consists of your order details, the terms and conditions provided by John Wiley and Sons, and the payment terms and conditions.

**All payments must be made in full to CCC. For payment instructions, please see information listed at the bottom of this form.**

License Number	3384080410695
License date	May 08, 2014
Licensed content publisher	John Wiley and Sons
Licensed content publication	Geophysical Research Letters
Licensed content title	Infrasonic detection of a near-Earth object impact over Indonesia on 8 October 2009
Licensed copyright line	Copyright 2011 by the American Geophysical Union.
Licensed content author	Elizabeth A. Silber,Alexis Le Pichon,Peter G. Brown
Licensed content date	Jun 24, 2011
Start page	n/a
End page	n/a
Type of use	Dissertation/Thesis
Requestor type	Author of this Wiley article
Format	Electronic
Portion	Full article
Will you be translating?	No
Title of your thesis / dissertation	Observational and theoretical investigation of cylindrical line source blast theory using meteors
Expected completion date	Jun 2014
Expected size (number of pages)	500
Total	0.00 USD
Terms and Conditions	

**TERMS AND CONDITIONS**

This copyrighted material is owned by or exclusively licensed to John Wiley & Sons, Inc. or one of its group companies (each a "Wiley Company") or handled on behalf of a society with which a Wiley Company has exclusive publishing rights in relation to a particular work (collectively "WILEY"). By clicking  in connection with completing this



licensing transaction, you agree that the following terms and conditions apply to this transaction (along with the billing and payment terms and conditions established by the Copyright Clearance Center Inc., ("CCC's Billing and Payment terms and conditions"), at the time that you opened your Rightslink account (these are available at any time at <http://myaccount.copyright.com>).

### **Terms and Conditions**

- The materials you have requested permission to reproduce or reuse (the "Wiley Materials") are protected by copyright.
- You are hereby granted a personal, non-exclusive, non-sub licensable (on a stand-alone basis), non-transferable, worldwide, limited license to reproduce the Wiley Materials for the purpose specified in the licensing process. This license is for a one-time use only and limited to any maximum distribution number specified in the license. The first instance of republication or reuse granted by this licence must be completed within two years of the date of the grant of this licence (although copies prepared before the end date may be distributed thereafter). The Wiley Materials shall not be used in any other manner or for any other purpose, beyond what is granted in the license. Permission is granted subject to an appropriate acknowledgement given to the author, title of the material/book/journal and the publisher. You shall also duplicate the copyright notice that appears in the Wiley publication in your use of the Wiley Material. Permission is also granted on the understanding that nowhere in the text is a previously published source acknowledged for all or part of this Wiley Material. Any third party content is expressly excluded from this permission.
- With respect to the Wiley Materials, all rights are reserved. Except as expressly granted by the terms of the license, no part of the Wiley Materials may be copied, modified, adapted (except for minor reformatting required by the new Publication), translated, reproduced, transferred or distributed, in any form or by any means, and no derivative works may be made based on the Wiley Materials without the prior permission of the respective copyright owner. You may not alter, remove or suppress in any manner any copyright, trademark or other notices displayed by the Wiley Materials. You may not license, rent, sell, loan, lease, pledge, offer as security, transfer or assign the Wiley Materials on a stand-alone basis, or any of the rights granted to you hereunder to any other person.
- The Wiley Materials and all of the intellectual property rights therein shall at all times remain the exclusive property of John Wiley & Sons Inc, the Wiley Companies, or their respective licensors, and your interest therein is only that of having possession of and the right to reproduce the Wiley Materials pursuant to Section 2 herein during the continuance of this Agreement. You agree that you own no right, title or interest in or to the Wiley Materials or any of the intellectual property rights therein. You shall have no rights hereunder other than the license as

provided for above in Section 2. No right, license or interest to any trademark, trade name, service mark or other branding ("Marks") of WILEY or its licensors is granted hereunder, and you agree that you shall not assert any such right, license or interest with respect thereto.

- NEITHER WILEY NOR ITS LICENSORS MAKES ANY WARRANTY OR REPRESENTATION OF ANY KIND TO YOU OR ANY THIRD PARTY, EXPRESS, IMPLIED OR STATUTORY, WITH RESPECT TO THE MATERIALS OR THE ACCURACY OF ANY INFORMATION CONTAINED IN THE MATERIALS, INCLUDING, WITHOUT LIMITATION, ANY IMPLIED WARRANTY OF MERCHANTABILITY, ACCURACY, SATISFACTORY QUALITY, FITNESS FOR A PARTICULAR PURPOSE, USABILITY, INTEGRATION OR NON-INFRINGEMENT AND ALL SUCH WARRANTIES ARE HEREBY EXCLUDED BY WILEY AND ITS LICENSORS AND WAIVED BY YOU
- WILEY shall have the right to terminate this Agreement immediately upon breach of this Agreement by you.
- You shall indemnify, defend and hold harmless WILEY, its Licensors and their respective directors, officers, agents and employees, from and against any actual or threatened claims, demands, causes of action or proceedings arising from any breach of this Agreement by you.
- IN NO EVENT SHALL WILEY OR ITS LICENSORS BE LIABLE TO YOU OR ANY OTHER PARTY OR ANY OTHER PERSON OR ENTITY FOR ANY SPECIAL, CONSEQUENTIAL, INCIDENTAL, INDIRECT, EXEMPLARY OR PUNITIVE DAMAGES, HOWEVER CAUSED, ARISING OUT OF OR IN CONNECTION WITH THE DOWNLOADING, PROVISIONING, VIEWING OR USE OF THE MATERIALS REGARDLESS OF THE FORM OF ACTION, WHETHER FOR BREACH OF CONTRACT, BREACH OF WARRANTY, TORT, NEGLIGENCE, INFRINGEMENT OR OTHERWISE (INCLUDING, WITHOUT LIMITATION, DAMAGES BASED ON LOSS OF PROFITS, DATA, FILES, USE, BUSINESS OPPORTUNITY OR CLAIMS OF THIRD PARTIES), AND WHETHER OR NOT THE PARTY HAS BEEN ADVISED OF THE POSSIBILITY OF SUCH DAMAGES. THIS LIMITATION SHALL APPLY NOTWITHSTANDING ANY FAILURE OF ESSENTIAL PURPOSE OF ANY LIMITED REMEDY PROVIDED HEREIN.
- Should any provision of this Agreement be held by a court of competent jurisdiction to be illegal, invalid, or unenforceable, that provision shall be deemed amended to achieve as nearly as possible the same economic effect as the original provision, and the legality, validity and enforceability of the remaining provisions of this Agreement shall not be affected or impaired thereby.
- The failure of either party to enforce any term or condition of this Agreement shall not constitute a waiver of either party's right to enforce each and every term and condition of this Agreement. No breach under this agreement shall be deemed

waived or excused by either party unless such waiver or consent is in writing signed by the party granting such waiver or consent. The waiver by or consent of a party to a breach of any provision of this Agreement shall not operate or be construed as a waiver of or consent to any other or subsequent breach by such other party.

- This Agreement may not be assigned (including by operation of law or otherwise) by you without WILEY's prior written consent.
- Any fee required for this permission shall be non-refundable after thirty (30) days from receipt by the CCC.
- These terms and conditions together with CCC's Billing and Payment terms and conditions (which are incorporated herein) form the entire agreement between you and WILEY concerning this licensing transaction and (in the absence of fraud) supersedes all prior agreements and representations of the parties, oral or written. This Agreement may not be amended except in writing signed by both parties. This Agreement shall be binding upon and inure to the benefit of the parties' successors, legal representatives, and authorized assigns.
- In the event of any conflict between your obligations established by these terms and conditions and those established by CCC's Billing and Payment terms and conditions, these terms and conditions shall prevail.
- WILEY expressly reserves all rights not specifically granted in the combination of (i) the license details provided by you and accepted in the course of this licensing transaction, (ii) these terms and conditions and (iii) CCC's Billing and Payment terms and conditions.
- This Agreement will be void if the Type of Use, Format, Circulation, or Requestor Type was misrepresented during the licensing process.
- This Agreement shall be governed by and construed in accordance with the laws of the State of New York, USA, without regards to such state's conflict of law rules. Any legal action, suit or proceeding arising out of or relating to these Terms and Conditions or the breach thereof shall be instituted in a court of competent jurisdiction in New York County in the State of New York in the United States of America and each party hereby consents and submits to the personal jurisdiction of such court, waives any objection to venue in such court and consents to service of process by registered or certified mail, return receipt requested, at the last known address of such party.

## **WILEY OPEN ACCESS TERMS AND CONDITIONS**

Wiley Publishes Open Access Articles in fully Open Access Journals and in Subscription journals offering Online Open. Although most of the fully Open Access journals publish open access articles under the terms of the Creative Commons Attribution (CC BY) License only, the subscription journals and a few of the Open Access Journals offer a choice of

Creative Commons Licenses:: Creative Commons Attribution (CC-BY) license [Creative Commons Attribution Non-Commercial \(CC-BY-NC\) license](#) and [Creative Commons Attribution Non-Commercial-NoDerivs \(CC-BY-NC-ND\) License](#). The license type is clearly identified on the article.

Copyright in any research article in a journal published as Open Access under a Creative Commons License is retained by the author(s). Authors grant Wiley a license to publish the article and identify itself as the original publisher. Authors also grant any third party the right to use the article freely as long as its integrity is maintained and its original authors, citation details and publisher are identified as follows: [Title of Article/Author/Journal Title and Volume/Issue. Copyright (c) [year] [copyright owner as specified in the Journal]. Links to the final article on Wiley's website are encouraged where applicable.

### **The Creative Commons Attribution License**

The [Creative Commons Attribution License \(CC-BY\)](#) allows users to copy, distribute and transmit an article, adapt the article and make commercial use of the article. The CC-BY license permits commercial and non-commercial re-use of an open access article, as long as the author is properly attributed.

The Creative Commons Attribution License does not affect the moral rights of authors, including without limitation the right not to have their work subjected to derogatory treatment. It also does not affect any other rights held by authors or third parties in the article, including without limitation the rights of privacy and publicity. Use of the article must not assert or imply, whether implicitly or explicitly, any connection with, endorsement or sponsorship of such use by the author, publisher or any other party associated with the article.

For any reuse or distribution, users must include the copyright notice and make clear to others that the article is made available under a Creative Commons Attribution license, linking to the relevant Creative Commons web page.

To the fullest extent permitted by applicable law, the article is made available as is and without representation or warranties of any kind whether express, implied, statutory or otherwise and including, without limitation, warranties of title, merchantability, fitness for a particular purpose, non-infringement, absence of defects, accuracy, or the presence or absence of errors.

### **Creative Commons Attribution Non-Commercial License**

The [Creative Commons Attribution Non-Commercial \(CC-BY-NC\) License](#) permits use, distribution and reproduction in any medium, provided the original work is properly cited and is not used for commercial purposes.(see below)

### **Creative Commons Attribution-Non-Commercial-NoDerivs License**

The [Creative Commons Attribution Non-Commercial-NoDerivs License](#) (CC-BY-NC-ND) permits use, distribution and reproduction in any medium, provided the original work is properly cited, is not used for commercial purposes and no modifications or adaptations are made. (see below)

### **Use by non-commercial users**

For non-commercial and non-promotional purposes, individual users may access, download, copy, display and redistribute to colleagues Wiley Open Access articles, as well as adapt, translate, text- and data-mine the content subject to the following conditions:

- The authors' moral rights are not compromised. These rights include the right of "paternity" (also known as "attribution" - the right for the author to be identified as such) and "integrity" (the right for the author not to have the work altered in such a way that the author's reputation or integrity may be impugned).
- Where content in the article is identified as belonging to a third party, it is the obligation of the user to ensure that any reuse complies with the copyright policies of the owner of that content.
- If article content is copied, downloaded or otherwise reused for non-commercial research and education purposes, a link to the appropriate bibliographic citation (authors, journal, article title, volume, issue, page numbers, DOI and the link to the definitive published version on **Wiley Online Library**) should be maintained. Copyright notices and disclaimers must not be deleted.
- Any translations, for which a prior translation agreement with Wiley has not been agreed, must prominently display the statement: "This is an unofficial translation of an article that appeared in a Wiley publication. The publisher has not endorsed this translation."

### **Use by commercial "for-profit" organisations**

Use of Wiley Open Access articles for commercial, promotional, or marketing purposes requires further explicit permission from Wiley and will be subject to a fee. Commercial purposes include:

- Copying or downloading of articles, or linking to such articles for further redistribution, sale or licensing;
- Copying, downloading or posting by a site or service that incorporates advertising with such content;
- The inclusion or incorporation of article content in other works or services (other than normal quotations with an appropriate citation) that is then available for sale or licensing, for a fee (for example, a compilation produced for marketing purposes,

inclusion in a sales pack)

- Use of article content (other than normal quotations with appropriate citation) by for-profit organisations for promotional purposes
- Linking to article content in e-mails redistributed for promotional, marketing or educational purposes;
- Use for the purposes of monetary reward by means of sale, resale, licence, loan, transfer or other form of commercial exploitation such as marketing products
- Print reprints of Wiley Open Access articles can be purchased from: [corporatesales@wiley.com](mailto:corporatesales@wiley.com)

Further details can be found on Wiley Online Library  
<http://olabout.wiley.com/WileyCDA/Section/id-410895.html>

Other Terms and Conditions:

**v1.9**

**If you would like to pay for this license now, please remit this license along with your payment made payable to "COPYRIGHT CLEARANCE CENTER" otherwise you will be invoiced within 48 hours of the license date. Payment should be in the form of a check or money order referencing your account number and this invoice number 501297597.**

**Once you receive your invoice for this order, you may pay your invoice by credit card. Please follow instructions provided at that time.**

**Make Payment To:  
Copyright Clearance Center  
Dept 001  
P.O. Box 843006  
Boston, MA 02284-3006**

**For suggestions or comments regarding this order, contact RightsLink Customer Support: [customercare@copyright.com](mailto:customercare@copyright.com) or +1-877-622-5543 (toll free in the US) or +1-978-646-2777.**

**Gratis licenses (referencing \$0 in the Total field) are free. Please retain this printable license for your reference. No payment is required.**

## Curriculum Vitae

<b>Name</b>	Elizabeth A. Silber
<b>Education</b>	<p>PhD. Physics, 2008-2014 University of Western Ontario London, Ontario</p> <p>MSc. Physics, 2007-2008 Transferred to PhD. University of Western Ontario London, Ontario</p> <p>Hon. BSc. Astrophysics and Planetary Science, 2003-2007 Graduated with Distinction The University of Western Ontario London, Ontario</p>
<b>Honours and Awards</b>	<p>CTBTO Award for Young Scientists and Engineers, 2013</p> <p>The Graduate Research Award for Disarmament, Arms Control and Non-Proliferation, 2013</p> <p>Western Graduate Thesis Research Award, 2009, 2011, 2013</p> <p>GTA Outstanding Research Contributions Scholarship, 2012</p> <p>The Graduate Research Award for Disarmament, Arms Control and Non-Proliferation, 2011</p> <p>Alexander Graham Bell NSERC CGS D3, 2009-2012</p> <p>Province of Ontario Graduate Scholarship (declined), 2009-2010</p> <p>Province of Ontario Graduate Scholarship, 2008-2009</p> <p>Western Graduate Scholarship, 2007-2012</p> <p>Faculty of Science Teaching Assistant Award of Excellence, 2007-2008</p> <p>Physics Graduate Entrance Scholarship, 2007</p>



**Related Work Experience**      Instructor, 2012-Present  
The University of Western Ontario  
London, Ontario

Graduate Research Assistant, 2007-2014  
The University of Western Ontario  
London, Ontario

Teaching Assistant, 2007-2012  
The University of Western Ontario  
London, Ontario

### **Refereed Journal Articles**

**Silber, E. A.** and Brown, P. G. (2014) Optical Observations of Meteors Generating Infrasound – I: Acoustic Signal Identification and Phenomenology, JASTP, submitted (#ATP3766)

Jenniskens, P, and 48 authors (24th author) (2014) Fall, Recovery and Characterization of the Novato L6 Chondrite Breccia, MAPS, accepted for publication

Brown, P.G. and 32 authors (25th author) (2013) A 500-kiloton airburst over Chelyabinsk and an enhanced hazard from small impactors, Nature

Borovička, J., Toth, J., Igaz, A., Spurny, P., Kalenda, P., Haloda, J., Svoren, J., Kornos, L., **Silber, E.**, Brown, P., Husarik, M. (2013) The Košice meteorite fall: Atmospheric trajectory, fragmentation, and orbit, Meteoritics & Planetary Science, 1-23

Jenniskens, P. and 68 authors, (52nd author) (2012) Radar enabled recovery of Sutter's Mill, a unique carbonaceous chondrite regolith breccia, Science, 338, 1583-1587

Ens, T., Brown, P. Edwards, W., **Silber, E. A.** (2012) Infrasound production by bolides: A global statistical study, Journal of Atmospheric and Solar-Terrestrial Physics, Vol. 80, p. 208-229

**Silber, E.A.**, Le Pichon, A. Brown, P. (2011) Infrasonic Detection of a Near-Earth Object Impact over Indonesia on 8 October, 2009, Geophysical Research Letters, Vol. 38, L12201

The above paper was featured in Nature Research Highlights: Nuclear network detects fireball (2011), Nature, Vol. 475, pp. 9

Brown, P., McCausland, P.J.A., Fries, M., **Silber, E.**, Edwards, W.N., Wong, D.K., Weryk, R.J., Fries J., Krzeminski, Z. (2011) The Fall of the Grimsby Meteorite - I: Fireball dynamics and 6 orbit from radar, video and infrasound records, Meteoritics and Planetary Science, Vol. 46, Issue 3, pp. 1-25

**Silber, E.A.**, ReVelle, D.O., Brown, P.G., Edwards, W.N. (2009) An estimate of the terrestrial influx of large meteoroids from infrasonic measurements, *JGR-Planets*, 114, E08006

Brown, P.G., ReVelle, D.O., **Silber, E.A.**, Edwards, W.N., Arrowsmith, S., Jackson Jr., L.E., Tancredi, G., Eaton, D. (2008) Analysis of a Crater Forming Meteorite Impact in Peru, *Journal of Geophysical Research – Planets*, Vol. 113, E09007

ReVelle, D.O., **Silber, E.A.**, Edwards, W.N., Brown, P.G. (2008), Reanalysis of the Historic AFTAC Bolide Infrasonic database, *The Earth, Moon and Planets*, Vol. 102, issue 1-4, pp. 337-344

### **Non-Refereed Journal Articles**

**Silber, E.A.** and Brown, P.G. (2013) Scientific Research to Characterize and Localize the Windsor Hum: Final Report, Final Report for Department of Foreign Affairs and International Trade, Contract #7294374

**Silber, E.A.** and Brown, P.G. (2013) Scientific Research to Characterize and Localize the Windsor Hum: Preliminary Report, Preliminary Report for Department of Foreign Affairs and International Trade, Contract #7294374

**Silber, E. A.** (2013) Transparency and Freedom of Information for Dual-use Research, published in 2012-2013 Graduate Research Awards Debates on Disarmament, Arms Control and Non-Proliferation, The Simons Foundation, pp. 52-57

**Silber, E. A.**, LePichon, A., Brown, P. (2011) Infrasonic Detection of a Large Bolide Over South Sulawesi, Indonesia on October 8, 2009: Preliminary Results, *Meteoroids: The Smallest Solar System Bodies*, NASA Technical report, Proceedings of the Meteoroids 2010 Conference held in Breckenridge, Colorado, USA, May 24–28, 2010

**Silber, E. A.** (2011) Contemplating solutions to annihilation, Invited Article, *Western News*, Western University

**Silber, E. A.** (2011) Should the Biological Weapons Convention Review Conference in 2011 revive the verification debate or focus instead on compliance?, published in 2010-2011 Graduate Research Awards Debates on Disarmament, Arms Control and Non-Proliferation, The Simons Foundation, pp. 28-32

Brown, P.G., Edwards, W.N., **Silber, E.A.** (2006) The Potential of the International Monitoring System Infrasonic Network for the Detection of Rocket Launches, Department of Foreign Affairs and International Trade (DFAIT), Canada Report, 43 Pages + Appendix, Contract #IDC 0061

**Silber, E.A.** (2007) A theoretical and experimental investigation of hypersonically generated cylindrical line source blastwaves using meteors, Undergraduate Honors Thesis, Western University

### **Talks and Presentations**

**Silber, E.A.** and Brown, P.G. (2013) Simultaneous Infrasonic and Optical observations of bright meteors: analysis of acoustic source heights and signal classification, Meteoroids 2013 Conference, Poznan, Poland, Aug 26 – 30, 2013

**Silber, E.A.** (2013) Infrasonic as a scientific tool to study meteors, International Meteor Conference (IMC 2013), Poznan, Poland, Aug 22 – 25, 2013, Keynote Lecture

**Silber, E. A.** and Brown, P.G. (2013) Model validation of explosive atmospheric sources, S&T 2013, Vienna, Austria, Jun 17 – 24, 2013

**Silber, E. A.** (2013) Infrasonic as a scientific tool: from geopolitics to meteors, Dalhousie University, Halifax, Invited Lecture

Brown, P. and **Silber, E. A.** (2013) The Sutter's Mill Meteorite: Fall and Recovery, CPSX Research Forum, Western University, January, 2013

Brown, P., Ens, T., Edwards, W., **Silber, E. A.** (2012) Global Detection of Airbursts: A Combined Satellite-Infrasonic Study, 43rd Lunar and Planetary Science Conference, held March 19–23, 2012 at The Woodlands, Texas. LPI Contribution No. 1659, id.1581

**Silber, E. A.** (2012) Silent Sound: Infrasonic Demystified, Society of Graduate Students 25th Annual Western Research Forum, Western University, London, ON, March 26-27, 2012

Popova, O., **Silber, E. A.**, Rybnov, Y. (2011) The detection of a superbolide over Tajikistan (July 23, 2008), Physics of Surrounding Environments Conference, held in Tomsk, Russia, June 27 – July 1, 2011

**Silber, E. A.**, Le Pichon, A., Brown, P. (2011) Infrasonic detection and analysis of the Oct 8, 2009 Bolide over Indonesia, CASCA Conference, held in London, Ontario, May 30 – June 2, 2011

**Silber, E. A.**, Le Pichon, A., Brown, P. (2010) Infrasonic detection and analysis of the Oct 8, 2009 Bolide over Indonesia, Infrasonic Technology Workshop (ITW) 2010, Tunis, Tunisia

**Silber, E. A.**, Brown, P. G., McCausland, P. J., Fries, M., Edwards, W.N., Wong, D. K., Weryk, R. J., Fries J. and Krzeminski, Z. (2010) Infrasonic Observations of the Grimsby Meteorite Fall, Infrasonic Technology Workshop (ITW) 2010, Tunis, Tunisia

**Silber, E. A.**, Le Pichon, A., Brown, P. (2010) Infrasonic detection and analysis of the Oct 8, 2009 superbolide near Indonesia, Conference Proceedings, CAP Congress 2010, Toronto, ON, Canada, June 6-11, 2010

**Silber, E. A.**, Le Pichon, A., Brown, P. (2010) Infrasonic detection and analysis of the Oct 8, 2009 superbolide near Indonesia, Conference Proceedings, Meteoroids 2010, Breckenridge, CO, May 24-28, 2010

**Silber, E.A.**, ReVelle, D. O., Brown, P. (2010) Development and testing of a weak shock model of infrasonic propagation using regional observations of meteors, Meteoroids 2010, Breckenridge, CO, May 24-28, 2010

**Silber, E. A.** (2010) Cratering Processes in the Solar System, Invited Talk, AB Lucas Secondary School, London, Ontario

**Silber, E. A.** (2009) Infrasonic Observations of Meteors and Weak Shock Theory, Graduate Research Symposium, Western University

Revelle, D. O., **Silber, E.A.**, Brown, P.G., Edwards, W.N. (2008) An Estimate of the Terrestrial Influx of Large Meteoroids from Infrasonic Measurements, Infrasound Technical Workshop Proceedings, Bermuda, USA

**Silber, E. A.**, ReVelle, D.O., Brown, P.G., Edwards, W.N. (2008) An Estimate of the Terrestrial Influx of Large Meteoroids from Infrasonic Measurements, Meteor Group Seminar, Western University

**Silber, E.A.** (2007) The Hayabusa Mission, The Undergraduate Physics Conference, Western University

ReVelle, D.O., **Silber, E.A.**, Edwards, W.N., Brown, P.G. (2007), Reanalysis of the historic AFTAC bolide infrasound database, Meteoroids 2007 Conference Proceedings, Barcelona, Spain